A STUDY OF THE RESPONSE OF REINFORCED CONCRETE FRAMES WITH AND WITHOUT MASONRY INFILL WALLS TO SIMULATED EARTHQUAKES

by

Jonathan Monical

A Dissertation

Submitted to the Faculty of Purdue University

In Partial Fulfillment of the Requirements for the degree of

Doctor of Philosophy

Lyles School of Civil Engineering

West Lafayette, Indiana

December 2021

THE PURDUE UNIVERSITY GRADUATE SCHOOL
STATEMENT OF COMMITTEE APPROVAL

Dr. Santiago Pujol, Co-Chair
Department of Civil and Natural Resources Engineering
University of Canterbury

Dr. Ayhan Irfanoglu, Co-Chair
Lyles School of Civil Engineering
Purdue University

Dr. Thomas H. Heaton
Department of Mechanical and Civil Engineering
California Institute of Technology

Dr. James V. Krogmeier
Elmore Family School of Electrical and Computer Engineering
Purdue University

Dr. Julio Ramirez
Lyles School of Civil Engineering
Purdue University

Approved by:
Dr. Dulcy Abraham

To my family

ACKNOWLEDGMENTS

I am grateful to my family for raising me to be a gentleman and forgiving me at times when I am not. I am especially grateful to my mother and father as they have given me countless rides to and from campus and have been willing to cook for me, house me, love me. My mother, who never shied away from sharing a cup of coffee and a bite to eat with me, has spent more time in the "civil building" than any other parent I know of looking at portraits and memorizing names of professors that may or may not have taught me. I appreciated the company sitting on the couch together - her solving the daily Jumble and me writing.

I am thankful to my professor, Santiago Pujol, who first taught me the principles of reinforced concrete design and inspired me to think for myself. Because of him, I worked as a teaching assistant, investigated a bridge collapse in Colombia, and spent two months researching with students at Tohoku University. I am grateful for his careful, meticulous review of anything I attempted to put in writing.

I am thankful to my committee members, Professors Tom Heaton, Ayhan Irfanoglu, Jim Krogmeier, and Julio Ramirez, for giving me advice along the way and allowing me to defend my thesis. I am thankful to Ashlee Messersmith, Carla Coffey, and Chelsea Cummings for assisting me in formatting this document.

I am thankful to Ann Christine Catlin who offered me funding over several semesters to help compile research projects for an online database. I admire her strong work ethic and endless supply of enthusiasm which she brought to each conversation, meeting, project - even email - and I may never meet another person who displays both qualities as consistently as she does.

I am thankful to the staff at Bowen Laboratory including Kevin Brower, Molly Stetler, and Harry Tidrick. On the few occasions that I got to the lab before Harry, it was a pleasure to begin the morning drinking great coffee with a good friend.

I am thankful to the Maeda Lab at Tohoku University. Maeda Sensei, a kind and funny teacher, offered me a unique opportunity to experience the beauty of Japan. My friend and senpai, Hamood Alwashali, welcomed me into his family and gave me valuable insight. Discussing his research and reading his thesis sparked my interest in masonry infill walls.

I am thankful to Prateek Shah, a brilliant student and deeply talented researcher. He helped me conduct my experiments and spoke to me with the same constructive criticism as that of an advisor. Working together through the challenges we encountered while completing our own research projects was beyond helpful to me and any of the better ideas presented in this investigation I attribute to him.

I am thankful to Kinsey Skillen who knew the inner workings of Bowen Laboratory better than most and usually had a quick suggestion for simplifying the task at hand. I am thankful to William Pollalis who did not hesitate to help me instrument and test my specimens.

Finally, I am thankful to the late Mete Sozen who undoubtedly shaped the way I think about structures in earthquakes. A quote of his which stays with me is, “In the practice of engineering, simplicity is almost always better than complexity, but not all engineers think so and it takes rare genius to understand the full complexity of a problem and charity to make it simple for others.”

TABLE OF CONTENTS

LIST OF TABLES

LIST OF FIGURES

LIST OF SYMBOLS

Symbol or Abbreviation	Description
A_b	Area of longitudinal bars in column
A_g	Gross cross-sectional area of masonry unit
A_{net}	Net cross-sectional area of masonry unit
D	Cross-sectional dimension of column in direction of motion
D_{SDOF}	Peak drift ratio of SDOF
D_{max}	Maximum lateral displacement of SDOF
E_c	Elastic modulus of concrete
E_m	Elastic modulus of masonry
F	Peak lateral force
$F(t)$	Lateral force history
F_{Sa}	Spectral acceleration amplification factor
F_{Sd}	Spectral displacement amplification factor
F_{eff}	Force solution produced from CSM using effective period
F_{lin}	Force solution produced from CSM using linear response
F_v	Velocity amplification factor
F_y	Lateral force at yield displacement
H_{SDOF}	Height of SDOF
$H_i - H_{i-1}$	Story height between level i and level i-1
H_r	Height of MDOF measured from top of foundation to roof
I_c	Moment of inertia of column
I_{inf}	Total moment of inertia of infilled frame
K_{eff}	Effective lateral stiffness of specimen
K_{frame}	Initial lateral stiffness of bare frame
K_{inf}	Initial lateral stiffness of infilled frame (tested in-plane)
K_o	Initial lateral stiffness of specimen

K_{oop}	Initial lateral stiffness of infilled frame (tested out-of-plane)
K_s	Effective lateral stiffness of earthquake simulator
K_s	Inferred effective lateral stiffness of earthquake simulator
L	Distance between optical targets t_0 and t_3
L_i	Distance between column centerlines
L_{inf}	Length of infill wall
M	Peak overturning moment at top of foundation
M_n	Nominal moment capacity of column
P	Axial load
S_{a_A}	Spectral acceleration reduced using substitute damping
S_{a_B}	Spectral acceleration reduced using equivalent damping
$S_{a_{sm}}$	Smoothed spectral acceleration
S_{d_A}	Spectral displacement reduced using substitute damping
S_{d_B}	Spectral displacement reduced using equivalent damping
$S_{d_{sm}}$	Smoothed spectral displacement
S_a	Spectral acceleration
S_d	Spectral displacement
T_{CSM}	Period defined by intersection of demand and capacity curves (CSM)
T_{Four}	Period at peak amplitude of Fourier transform of absolute acceleration response at roof of specimen
T_{eff}	Effective period of specimen
T_g	Characteristic period of ground motion, base motion
T_i	Period of oscillator
T_o	Initial fundamental translational period of specimen
T_y	Period corresponding to yield displacement
V_{frame}	Lateral strength of bare frame
V_{inf}	Lateral strength of infill wall
V_{max}	Lateral strength of infilled frame
a	Shear span of column
b	Width of column

d	Effective depth of longitudinal reinforcement in column
f'_c	Compressive strength of concrete cylinder
f'_m	Gross compressive strength of masonry prism
f_{Four}	Frequency at peak amplitude of Fourier transform of absolute acceleration response at roof of specimen
f_{mortar}	Compressive strength of mortar coupon
f_u	Strength of longitudinal bars in column
f_y	Yield stress of longitudinal bars in column
f_{yt}	Yield stress of transverse reinforcement in column
g	Acceleration of gravity
h	Total height of specimen
h_c	Clear height of column
k	Lateral story stiffness proposed by Schultz (1986)
m	Effective mass of specimen
mg	Effective weight of specimen
n	Total number of infilled bays
n_{col}	Total number of columns
r	Transverse reinforcement ratio in column
s	Spacing of transverse reinforcement (ties) in column
t_0, t_1, t_2, t_3	Designation of optical targets installed on wide-flange steel beam attached to earthquake simulator
t_{inf}	Thickness of infill wall
v_{max}	Maximum shear demand for story mechanism
v_s	Transverse reinforcement index
Δ	Estimated drift demand
Δ_{frame}	Drift capacity of bare frame
Δ_{inf}	Drift capacity of infilled frame
Γ	Fundamental mode participation factor
α	Fraction of column dimension projected into foundation beam
β_{20}	20% damping ratio

β_A	Substitute damping ratio
β_B	Equivalent damping ratio
β_o	Light damping ratios (2%, 5%)
$\delta(t)$	Drift history
δ_h	Peak lateral displacement
δ_{eff}	Displacement solution produced from CSM using effective period
δ_{lin}	Displacement solution produced from CSM using linear response
δ_{sol}	Displacement solution produced from CSM
δ_v	Peak vertical displacement of optical target t_3 relative to optical target t_0
δ_y	Yield displacement
θ	Peak rotation of simulator
μ	Ductility ratio
ρ	Longitudinal reinforcement ratio in column
ω_o	Initial natural frequency of specimen
ϕ_i	Fundamental mode shape ordinate at level i
ϕ_{i-1}	Fundamental mode shape ordinate at level i-1
1-B	One-bay frame
1-S	One-story frame
2-B	Two-bay frame
2-S	Two-story frame
CSM	Capacity Spectrum Method
DR	Drift ratio
EW	East-west
FA_{proj}	Projected floor area
F_{tc}	Compression factor used to scale time step in acceleration record
GMP	Ground motion parameter
LVDT	Linear variable differential transformer
MDOF	Multiple-degree-of-freedom
MDR	Peak mean (roof) drift ratio

NS	North-south
PEER	Pacific Earthquake Engineering Research Center
PGA	Peak ground acceleration, peak base acceleration
PGD	Peak ground displacement, peak base displacement
PGV	Peak ground velocity, peak base velocity
R1	Reference run
R2, R3	Repeat runs
RC	Reinforced concrete
RSN	Record sequence number
SDOF	Single-degree-of-freedom
SDR	Peak story drift ratio
TC	Time compression
VOD	Velocity of Displacement method
WA	Cross-sectional area of infill wall
WR	Infill wall ratio

ABSTRACT

This study focuses on non-ductile reinforced concrete (RC) frames built outside current practices. These structures are quite vulnerable to collapse during earthquakes. One option to retrofit buildings with poorly detailed RC columns is to construct full-height masonry infill walls to provide additional means to resist loads caused by gravity and increase lateral stiffness resulting in a reduction in drift demand. On the other hand, infill can cause reductions in drift capacity that offset the benefits of reductions in drift demand. Given these two opposing effects, this investigation addresses the following question: are poorly detailed RC frames with masonry infill walls any safer than similar RC frames without infill walls?

To investigate the effects of infill on drift demand and drift capacity, two one-bay one-story reinforced concrete frames were built with minimal column shear reinforcement. The frames were tested on a unidirectional earthquake simulator. Ties in columns were spaced at a distance equal to the effective depth of columns ($s = d$) to represent details common in older construction. Each specimen was subjected to simulated earthquakes in four series of tests including configurations of frames with infill walls and configurations of frames without infill. External confinement consisting of post-tensioned clamping devices was installed on columns in some tests of bare frames and infilled frames. These devices present an additional option to retrofit buildings by increasing drift capacities of flexural elements. The advantages of both retrofit options - infill walls and clamping devices - are that each can be built, fabricated, and installed with minimal expertise using readily available and inexpensive materials and tools. In total, five different configurations of frames were tested in this investigation:

- Bare frame
- Frame with infill
- Frame with column external transverse reinforcement (clamps)
- Frame with infill and clamps
- Frame with infill and clamps tested at 90 degrees to direction of motion (out-of-plane)

The sequence in which tests were conducted is described in Table 1-1.

In this investigation and one other (Lee & Woo, 2002), it was observed that infilled frames drifted no more than one-third the amount that similar frames without infill drifted when both were subjected to nominally identical simulated ground motions. Drift capacities of bare frames and infilled frames were not reached in tests conducted in this investigation because of the limits of the earthquake simulator. Nevertheless, wide inclined cracks associated with the onset of shear failure were observed in tests of bare frames and infilled frames without external confinement. Inclined cracks formed in columns of the bare frame in less intense simulations compared with simulations causing inclined cracks in columns of the infilled frame.

In other investigations of non-ductile bare frames and infilled frames, drift capacities of infilled frames were no less than half the drift capacities of bare frames when the latter was not larger than 4% (that is when the latter referred to relatively vulnerable frames). For frames with columns with minimal transverse reinforcement and assuming the infilled frame drifts one-third the amount of the bare frame, an infilled frame with a 50% reduction in drift capacity is safer than the associated bare frame because the drift capacity of the system without infill is reached before the drift capacity of the system with infill.

In addition to experimental evidence obtained in the laboratory showing the benefits of infill, field data consisting of surveys of school buildings conducted in the aftermath of major earthquakes suggest that schools with more full-height infill walls tend to have less damage than schools with fewer infill walls. An infill wall ratio defined as the ratio of cross-sectional area of masonry infill wall in one direction on ground floor to total floor area is useful in organizing the extent of structural damage. Projections of the data obtained from the mentioned surveys suggest that if a school building has an infill wall ratio of at least 0.5% in both directions, the likelihood of severe damage decreases by a factor of 3. An infill wall ratio of 0.5% represents modest amounts of infill as ratios larger than 0.5% were observed to be common in surveyed buildings (Table 6-1 through Table 6-5).

Because the nature of future earthquakes is anything but known and the protection of children in school buildings is nothing short of essential, it is recommended to construct additional full-height infill walls in any direction quantified to have an infill wall ratio less than 1% in the absence of financing a more elaborate strengthening system. Using a lower-bound approximation, an infilled frame with an infill wall ratio of 1% is safer than the associated bare frame without infill and the peak story drift of said infilled frame subjected to a base motion with a peak base velocity of 15 in./sec. (40 cm/sec.) is estimated to be no larger than 1% while the peak story drift of the associated bare frame without infill is estimated to drift to approximately 3%.

CHAPTER 1. INTRODUCTION

1.1 Background

The use of masonry to construct infill walls in buildings in active seismic regions is common because of the low cost and availability of bricks and mortar. Infill walls serve as partitions and to enclose buildings. Often infill walls are ignored when considering structural response. But the effect of infill on lateral stiffness and strength of structures has been studied extensively beginning in the latter half of the twentieth century and it is widely believed that infill increases both the lateral stiffness and lateral strength of a frame. Studies focusing on differences in drift capacities - defined as the lateral displacement or drift ratio corresponding to a 20% reduction in lateral resistance - between infilled frames and similar frames without infill have suggested that the stiffer infilled frames tend to have smaller drift capacities. But structures with larger lateral stiffnesses have smaller drift demands - defined as the lateral displacement or drift ratio of a story relative to other stories or foundation - than structures with smaller lateral stiffnesses. Although studies have shown infill to decrease drift capacities of RC frames, only one quantified the decrease in drift demand attributed to infill (Lee & Woo, 2002).

To investigate the effect of infill on drift capacities of RC frames, results from static tests of bare frames and infilled frames are compiled in Table 1-2 through Table 1-18 and are presented in this chapter. For static tests, only infilled frames with full-height infill walls and without openings are considered. To investigate the effect of infill on drift demands of RC frames, results from uniaxial earthquake simulations of bare frames and infilled frames are compiled and are presented in Section 5.12. For dynamic tests, infilled frames with and without openings are considered. In studies where bare frames and infilled frames were both tested and when data were available, initial lateral stiffnesses, peak lateral strengths, drift demands, and drift capacities are compared.

Caution was taken in tabulating key parameters and measurements obtained in tests conducted by other researchers. Nevertheless, there may be discrepancies between values listed in Table 1-2 through Table 1-18 and those mentioned elsewhere because of differences in the definitions of terms. The definitions of terms used throughout this document are given below:

- Measured lateral strengths of bare frames and infilled frames reported here are the maximum lateral forces reached in either direction and not the mean of peak loads measured in both directions. In the case of the infilled frame, the total resistance of the system (bare frame plus infill wall) is used.

- Estimates of base-shear strengths of bare frames reported here are approximated using limit analysis assuming story mechanisms form in the first stories of said frames and from nominal moment capacities calculated using a moment-curvature program developed by Pujol (2001) assuming a limiting strain in concrete of 0.004.

- Drift ratios are computed as the ratio of lateral displacement to total height of frame measured from top of foundation to mid-depth of top beam or slab unless stated otherwise.

- In static cyclic tests, values of drift capacities reported here are the mean of peak drifts measured in both directions corresponding to a 20% reduction in lateral load from maximum resistance measured in each direction.

Reporting drift capacities of infilled frames without bias is difficult (and to a lesser extent bare frames) because there exists no universal method used to conduct cyclic tests specifying when to unload, how many times to cycle at a certain drift ratio or lateral load, and most critical of all, at what drift ratio testing should stop. To be consistent and fair in the selection of values representing the drift capacities of bare frames and infilled frames, figures showing measured force vs. displacement relationships detailing the graphical procedure used to obtain drift capacities are provided for each specimen (discussed in Appendix A). The graphical procedure is described next.

Envelopes were drawn on typical force-displacement graphs by connecting peak values as shown in Figure 1-1. The drift associated with the point on the envelope corresponding to a 20% decrease in lateral resistance is assumed to be the drift capacity of the tested specimen. For nine infilled frames and three bare frames, tests were concluded before a 20% drop in lateral resistance was reached and the maximum measured drift or mean of maximum drifts (in both directions for cyclic tests) is taken to be the drift capacity. Values of initial lateral stiffness included in the compiled database include, exclusively, values reported by researchers as numerical quantities. Estimates of initial lateral stiffness could not be obtained from reported load-deflection graphs with sufficient reliability.

Table 1-2 through Table 1-18 include key parameters and data obtained from experiments conducted on planar bare frame and infilled frame specimens. Here planar refers to frames with columns arranged along a single column line. In addition to 41 one-bay one-story (1-B, 1-S) infilled frames, 3 two-bay one-story (2-B, 1-S) infilled frames and 5 one-bay two-story (1-B, 2-S) infilled frames are included in this investigation. A short description of each experiment is summarized next.

1.2 Summary of Previous Research of Bare Frames and Infilled Frames

Mehrabi (1994) conducted monotonic tests on 1 one-bay one-story bare frame and 3 one-bay one-story infilled frames. He conducted cyclic tests on 7 one-bay one-story infilled frames and 2 two-bay one-story infilled frames. Mehrabi observed that lateral stiffnesses measured at 50% of lateral strengths of frames with infill walls made from hollow and solid masonry units were approximately 15 and 50 times as large as the initial lateral stiffness of the associated bare frame. Measured lateral strengths of infilled frames were between 1.5 and 3 times as strong as the lateral strength of the associated bare frame.

Kakaletsis (2008) conducted cyclic tests on 1 one-bay one-story bare frame and 2 one-bay one-story infilled frames, one with weaker solid clay bricks with compressive strengths of approximately 450 psi and the other with stronger vitrified solid ceramic bricks with compressive strengths of approximately 3800 psi. Kakaletsis observed that lateral stiffnesses of infilled frames measured prior to initial cracking (which occurred at a drift ratio of approximately 0.25%) were approximately 2.5 times as large as the lateral stiffness of the associated bare frame and lateral strengths of infilled frames were between 1.5 and 2 times as strong as the lateral strength of the associated bare frame.

Imran (2009) conducted cyclic tests on 2 one-bay one-story frames with infill walls made from normal-weight clay units and lightweight autoclaved aerated concrete units. The compressive strengths of masonry prisms constructed using the mentioned masonry units were between 400 and 600 psi. Imran observed that initial cracking of infilled frames occurred at a drift ratio of approximately 0.1% and drift capacities of both infilled frames exceeded 3%.

Blackard (2009) conducted a cyclic test on 1 one-bay one-story frame with a two-wythe full-height infill wall. Column ties were spaced at $s = 1.1d$ where d is effective depth defined as the distance from extreme fiber in compression to centroid of tensile reinforcement. Blackard observed an inclined 'shear' crack forming near the top of one column at a drift ratio of approximately 0.6% accompanied by a sudden drop in lateral resistance by 25%. The measured lateral load remained above 50% of the lateral strength up to drift ratios of 1.25% when testing stopped.

Baran (2010) conducted cyclic tests on 3 one-bay one-story infilled frames, 1 one-bay two-story bare frame, and 3 one-bay two-story infilled frames. Column ties were spaced at $s = 1.2d$. Baran observed that lateral strengths of two-story infilled frames were between three and five times as strong as the lateral strength of the associated two-story bare frame. Drift capacities of two-story infilled frames were between one-third and three-quarters of the drift capacity of the associated two-story bare frame.

Jin (2012) conducted cyclic tests on 2 one-bay one-story infilled frames, one with a stronger top beam with a depth that was nearly 3.5 times the size of the column dimension and one with a weaker top beam with a depth that was approximately 1.5 times the size of the column dimension. Column ties were spaced at $s = 0.8d$. The compressive strength of masonry prisms constructed using hollow concrete block units were approximately 950 psi. Jin observed that drift capacities of both infilled frames exceeded 2% and lateral strengths differed by less than 20%.

Cavaleri (2014) conducted cyclic tests on 8 one-bay one-story infilled frames. Cavaleri reported that lateral stiffnesses measured at a drift ratio of 0.1% of frames with 8 by 8 in. columns with weak and strong infill (with masonry prism compressive strengths of approximately 400 and 1300 psi) were approximately 10 times as large as the lateral stiffness of the associated bare frame. Lateral stiffnesses measured at a drift ratio of 0.1% of frames with 12 by 12 in. columns with weak infill (with a masonry prism strength of approximately 250 psi) were approximately twice as large as the initial lateral stiffness of the associated bare frame.

Al-Nimry (2014) conducted cyclic tests on 2 one-bay one-story frames with infill walls each built from a combination of stone masonry, concrete masonry, and plain concrete. One infilled frame had an axial load ratio (defined as the total axial load applied to frame divided by the sum of axial strengths of columns) of 14% and the other had an axial load ratio of 10%. Drift capacities of both infilled frames exceeded 1%.

Bose (2016) conducted a monotonic test on 1 one-bay one-story bare frame and a cyclic test on 1 one-bay one-story infilled frame. The lateral strength of the infilled frame was approximately 60% larger than the lateral strength of the associated bare frame and the drift capacity of the infilled frame was 40% of the drift capacity of the associated bare frame.

Diawati (2016) conducted cyclic tests on 1 one-bay one-story bare frame and 3 one-bay one-story infilled frames. Column ties were spaced at $s = 0.8d$. The lateral strengths of infilled frames were between 4 and 7 times as large as the lateral strength of the associated bare frame and drift capacities of infilled frames were no less than half of the drift capacity of the associated bare frame.

Suzuki (2017) conducted cyclic tests on 1 one-bay one-story bare frame and 1 one-bay one-story infilled frame. He also conducted cyclic tests on 1 two-bay one-story infilled frame and 1 one-bay two-story infilled frame. The lateral strength of the one-bay one-story infilled frame was approximately three times as large as the lateral strength of the associated bare frame and the lateral strength of the two-bay one-story infilled frame was approximately five times as large as the lateral strength of the one-bay one-story bare frame. Drift capacities of infilled frames varied between 1.5 and 2.5%.

Alwashali (2018) conducted cyclic tests on 5 one-bay one-story infilled frames. The frame with an infill wall constructed with weak mortar (Specimen WM) reached a drift capacity of nearly 4%. The other infilled frames had drift capacities between approximately 1.5 and 3%.

Han (2020) conducted cyclic tests on 1 one-bay one-story bare frame and 1 one-bay one-story infilled frame. Column ties were spaced at $s = d$. The initial lateral stiffness of the infilled frame was approximately 50% larger than the initial lateral stiffness of the associated bare frame. The drift capacity of the infilled frame was approximately 80% of the drift capacity of the associated bare frame.

Drift capacities obtained from tests of bare frame and infilled frame specimens described above are discussed next.

1.3 Poorly Detailed Bare Frames and Infilled Frames

Comparisons of measured drift capacities of infilled frames and measured drift capacities of the associated poorly detailed bare frames with transverse reinforcement ratios between 0.1 and 0.3% and measured drift capacities not exceeding 4% are shown in Figure 1-2. Of the ten vulnerable frames with infill, drift capacities of infilled frames were at least half the drift capacities of the associated bare frames except in test SP5 by Baran (2010). In a cyclic test of a two-story infilled frame conducted by Baran, Specimen SP5 was pushed to a story drift ratio of only 1% in one direction and less than 4% in the other direction and the resulting drift capacity obtained from the mentioned graphical procedure was approximately 0.9%. In all other tests by Baran, infilled frames were pushed to story drift ratios of at least 3% in both directions. It is plausible that the drift capacity of the mentioned specimen was reduced because of the differences in loading procedures.

1.4 Infilled Frames

Trends observed in the data obtained solely from tests of infilled frames are described next, beginning with comparisons of measurements and estimates of initial lateral stiffness and lateral strength.

1.4.1 Initial Lateral Stiffness

Measured initial lateral stiffnesses of frames with infill are compared with values calculated from Equation 1-1 which resembles the equation used to estimate the lateral stiffness of a cantilever but has two modifications. The first modification is the fraction $\frac{9}{25}$ which is a rough estimate used to account for the reduction in lateral stiffness attributable to shear distortions of infill. The second modification is the ratio of the net cross-sectional area to the gross cross-sectional area of masonry units which accounts for voids in units used to construct the infill wall. Measurements of the elastic modulus of masonry were not reported in all investigations described in Section 1.2. Nevertheless, Almesfer (2014) showed a nearly linear relationship between the measured elastic modulus and measured gross compressive strength of masonry prisms (described in Section 1.4.3.1) obtained from field work carried out in New Zealand in addition to other prisms built and tested in the laboratory. Based on work done by Almesfer (2014) and from measurements obtained in this investigation (described in Appendix B), the elastic modulus of masonry was estimated as the product of 450 and the gross compressive strength of the associated masonry prism. A comparison of measured and estimated values shows that Equation 1-1 is an adequate approximation of the initial lateral stiffness of frames with infill (Figure 1-3).

$$K_{inf} = \frac{9}{25} * \frac{A_{net}}{A_g} * \frac{3E_m I_{inf}}{h^3} \qquad 1\text{-}1$$

Definitions:

$$K_{inf} = initial\ lateral\ stiffness\ of\ infilled\ frame$$

$$A_{net} = net\ cross - sectional\ area\ of\ masonry\ unit$$

$$A_g = gross\ cross - sectional\ area\ of\ masonry\ unit$$

$$E_m = elastic\ modulus\ of\ masonry\ estimated\ as\ 450 * f'_m$$

$$f'_m = gross\ compressive\ strength\ of\ masonry\ prism$$

$$I_{inf} = \sum_{i=1}^{n} \frac{1}{12} * t_{inf} * L_i^3 = total\ moment\ of\ inertia\ of\ infilled\ frame$$

$$n = total\ number\ of\ infilled\ bays$$

$$t_{inf} = thickness\ of\ infill\ wall$$

$$L_i = distance\ between\ column\ centerlines$$

$$h = total\ height\ (from\ top\ of\ foundation\ to\ mid - depth\ of\ topmost\ beam)$$

Measurements of initial lateral stiffnesses of infilled frames as reported by investigators were obtained using one of seven different procedures summarized in Table 1-6 and each value was obtained at a drift ratio no larger than 0.25%. Some researchers reported values of lateral stiffnesses measured at half the lateral strengths of infilled frames. These measurements were overestimated using Equation 1-1 by as much as 100% compared with other reported values of lateral stiffnesses (measured at drift ratios not exceeding 0.2%) which had smaller margins of error. One estimate of the initial lateral stiffness of an infilled frame was four times as large as the measurement obtained at a drift ratio of approximately 0.25% (Figure 1-3).

1.4.2 Lateral Strength

Multiple sources including Liauw (1985), Paulay (1992), FEMA 306 (1998), and Flanagan (1999) have offered expressions for estimating lateral strengths of infilled frames. Alwashali (2018) showed that more complex expressions do not reduce scatter between observed and calculated values of lateral strength. An appropriate equation must compromise complexity with reliability. Fiorato (1970) suggested multiplying the lateral strength of the bare frame by a factor of two to estimate the strength of the infilled frame claiming that the effective height of columns in frames with infill was reduced to half of the clear height. This simple approximation seems to be a reasonable lower-bound estimate as the measured lateral strengths of infilled frames were smaller than twice the estimated lateral strengths of the associated bare frames in less than 15% of tests described in Section 1.2 and detailed in Table 1-16 through Table 1-18. Fiorato also suggested increasing the lateral strength of an infilled frame by adding the horizontal friction force generated by axial loads acting on the infill wall and estimated the coefficient of friction between bricks and mortar to be approximately 0.5 based on laboratory tests conducted on masonry panels.

Alwashali (2018) proposed a simple method to estimate the lateral strength of the infill wall (without contribution of bare frame) based on material properties of masonry and infill wall dimensions. His approximation was modified in this investigation by multiplying the lateral strength of the infill wall by the ratio of net cross-sectional area to gross cross-sectional area of masonry unit and adding the contribution of the bare frame (Equation 1-2). Figure 1-4 shows that measured lateral strengths of infilled frames described in Section 1.2 were 25% larger than estimates on average.

$$V_{max} = V_{inf} + V_{frame} = \frac{A_{net}}{A_g} * 0.07f'_m * t_{inf} * L_{inf} + n_{col} * 2\frac{M_n}{h_c} \qquad \text{1-2}$$

Definitions:

$$V_{max} = lateral\ strength\ of\ infilled\ frame$$

$$V_{inf} = lateral\ strength\ of\ infill\ wall$$

$$V_{frame} = lateral\ strength\ of\ bare\ frame$$

$$A_{net} = net\ cross - sectional\ area\ of\ masonry\ unit$$

$$A_g = gross\ cross - sectional\ area\ of\ masonry\ unit$$

$$f'_m = gross\ compressive\ strength\ of\ masonry\ prism$$

$$t_{inf} = thickness\ of\ infill\ wall$$

$$L_{inf} = length\ of\ infill\ wall$$

$$n_{col} = total\ number\ of\ columns$$

$$2\frac{M_n}{h_c} = lateral\ strength\ of\ fixed - fixed\ RC\ column$$

$$M_n = moment\ capacity\ of\ column$$

$$h_c = clear\ height\ of\ column$$

Infill wall length is defined as the clear length of the bay (or bays for two-bay specimens) with infill. The coefficient 0.07 is the mean ratio of the measured shear strength to the measured compressive strength of masonry coupons reported in tests compiled by Alwashali (2018).

1.4.3 Drift Capacity

Drift capacities as defined in Section 1.1 were measured for each infilled frame listed in Table 1-2 through Table 1-18 and described in Section 1.2 and ranged between approximately 0.75 and 4%. Parameters affecting drift capacities of infilled frames are discussed next.

1.4.3.1 Gross Compressive Strength of Masonry Prisms

Prisms built using three to five bricks, stones, or other masonry units stacked vertically on top of each other with mortar bed joints between units were tested in uniaxial compression to quantify the compressive strength of the masonry used to construct infill walls of specimens described in Section 1.2. The gross compressive strength of masonry prisms is computed as the ratio of the peak load applied perpendicular to mortar bed joints to the gross cross-sectional area of the masonry unit. Figure 1-5 shows a decreasing lower-bound trend between drift capacities of infilled frames and gross compressive strength of masonry prisms suggesting that frames with weaker infill are likely to have larger drift capacities than similar frames with stronger infill. More scatter in drift capacities was observed for prism strengths between 2000 and 3000 psi. It is plausible that other variables affect more the drift capacities of infilled frames with stronger masonry units with compressive strengths larger than 2000 psi.

1.4.3.2 Transverse Reinforcement

An increasing lower-bound trend between the amount of transverse reinforcement in RC columns and drift capacities of infilled frames is observed in Figure 1-6 and Figure 1-7. Two indices are used to quantify the amount of transverse reinforcement (ties) in columns: 1) the ratio of the effective depth of longitudinal reinforcement to spacing of transverse reinforcement (d/s) and 2) the transverse reinforcement ratio (r) defined as the cross-sectional area of column ties divided by the product of the width of the column and the spacing (s) of the ties. Both parameters suggest that increasing the amount of transverse reinforcement by a factor of four doubles the measured lower-bound drift capacity of infilled frames (Figure 1-6 and Figure 1-7). These trends are consistent with work done by Alwashali (2018) which shows a decreasing trend between drift capacity and 1) masonry prism strength and 2) the ratio of lateral strength of infilled frame to lateral strength of bare frame which is discussed next.

1.4.3.3 Relative Lateral Strength

The "relative lateral strength" of the infilled frame is computed as the ratio of the result obtained from Equation 1-2 to lateral strength of bare frame estimated as $n_{col} * 2\frac{M_n}{h_c}$ where n_{col} is the total number of columns, M_n is the nominal moment capacity of each column, and h_c is the clear height of columns. A decreasing lower-bound trend between drift capacities and relative lateral strengths of infilled frames is observed in Figure 1-8.

Measured drift capacities of infilled frames and the key parameters affecting said measurements are the focus of this chapter. The next four chapters (Chapters 2-5) discuss experiments conducted in this investigation used to compare drift demands of bare frames and infilled frames.

CHAPTER 2. EXPERIMENTAL DESIGN AND PROGRAM

2.1 Scope

The purpose of the experiments described in this section was to quantify differences in drift demands between reinforced concrete frames and RC frames with masonry infill walls. Sequences of tests and testing configurations are listed in Table 1-1. To test the hypothesis that infilled frames drift less than similar frames without infill, two nominally identical one-story RC frames (Specimens F1 and F2) with and without infill were subjected to simulated earthquakes. Four series of tests were conducted on each specimen: two series of tests were conducted on frames with infill and two series of tests were conducted on frames with no infill. External confinement (referred to as 'clamps' in this investigation) similar to devices tested by Skillen (2020) was installed on columns in three of four series of tests done on each specimen to control inclined cracks and increase drift capacities. The addition of clamps was assumed not to not affect drift demands.

2.2 Test Specimens

Specimens were tested one at a time. Each specimen was clamped to a unidirectional earthquake simulator. A 44,500-lb reinforced concrete block suspended from an overhead crane was connected to top beams of each specimen (Figure 2-1). The center of mass of suspended block and top beam were aligned. In all but one test series base motions occurred in the direction of the frame. No prototype was used to guide the design of the scaled frames as the main objective of this investigation was to test the idea that infilled frames drift less than similar frames without infill, not to represent a hypothetical or an existing structure. Frames had an out-of-plane dimension of 8 in. and columns had square cross sections of 8 in. by 8 in. Top and bottom beams were 20-in. deep and 8-in. wide. Clear height of columns was h_c = 40 in. resulting in a column aspect ratio of 5 (Figure 2-2). Additional details of the test specimens are discussed in Appendix B.

The effective weight of the system (discussed in more detail in Section 4.3) was approximately 49 kips which included half the weight of the specimen, the concrete block suspended from an overhead crane and attached to said specimen, and hardware used to connect specimen with concrete block. Base shear coefficients of the bare frame and infilled frame were estimated to be approximately 0.45 and 1.1 (discussed in Section 4.4). Initial fundamental periods of the bare frame and infilled frame were estimated to be approximately 0.15 and 0.07 second (discussed in Section 4.3). Additional details of the test specimens are described in Appendix B.

2.3 Materials

The mean compression strength of concrete measured from compression tests of standard 6x12-in. cylinders was f'_c = 3800 psi. The mean elastic modulus of the mentioned cylinders was approximately E_c = 3200 ksi. Additional details of the material properties of concrete are given in Appendix B.

Longitudinal reinforcement in columns consisted of four 5/8-in. diameter bars each with an area A_b = 0.31 in.^{2} resulting in a longitudinal reinforcement ratio ρ = 1.9% (Figure 2-3). The mean yield stress of longitudinal reinforcement in columns was approximately f_y = 63 ksi and strength was approximately f_u = 99 ksi (Figure 2-4). The effective depth of column longitudinal reinforcement was d = 6 in. Transverse reinforcement in columns was designed to represent details common in older construction vulnerable to the formation of inclined cracks caused by strong ground motions leading to severe damage. Column transverse reinforcement consisted of 3/8-in. ties spaced at $s = d$ = 6 in. with 90-degree hooks at each end (Figure 2-5). The resulting transverse reinforcement ratio r = 0.45% is not small compared with typical ratios in “non-conforming” columns (0.1-0.2%) and was a consequence of 1) the need to test reduced-scale specimens to meet the capacity of the earthquake simulator, and 2) unavailability of smaller deformed bars. Nevertheless, inclined cracks formed in bare frames and infilled frames in the spaces between the mentioned internal column ties. The mean yield stress and strength of reinforcing ties in columns were approximately 70 and 97 ksi (Figure 2-6).

External clamps were similar to devices designed by Skillen (2020) and consisted of 3x2x3/8 A36 steel angles and 1/2-in. high-strength (Grade 8) threaded rods [Figure 2-7 (a, b)]. Clamps were snugged along each corner of columns and threaded rods in both directions were prestressed to approximately 40 ksi using a calibrated torque wrench. The yield stress and strength of 1/2-in. high-strength threaded rods were approximately 150 ksi (using initial stiffness of rod and 0.2% offset) and 175 ksi (Figure 2-8). Spacing of clamps near column ends was $d/2$ = 3 in. and d near mid-height [Figure 2-7 (c)]. The initial confining stress attributed to clamps near column ends was approximately 470 psi. Assuming the shear demand per column of the bare frame is approximately 10.5 kips using simple approximations of yield moment ($A_s * f_y * 0.9d = 210\ kip - in.$) and base-shear strength ($4 * \frac{210\ kip-in.}{40\ in.} = 21\ kip$), the minimum prestress required in reinforcement near column ends (spaced at $d/2$) to resist said demand would be approximately 400 psi estimated as 10.5 $kip \div \left(b * \frac{d}{2}\right)$.

Masonry infill walls were constructed using clay bricks and bags of pre-blended mortar mix. Clay bricks were selected because of their availability and their size relative to column dimensions of test specimens. Lengths and heights of walls were L_{inf} = 64 in. and h_c = 40 in. (Figure 2-9). The bricks (Figure 2-10) were 7 5/8 in. by 3 5/8 in. by 2 1/4 in. (length by width by height) and typical mortar head joints and bed joints were 3/8-in. thick. Each brick contained three openings with a total void ratio of 25% calculated as the ratio of cross-sectional area of voids to gross cross-sectional area of brick ($1 - \frac{A_{net}}{A_g}$). Bricks were laid with their long dimension parallel to the longitudinal direction of the frame and openings oriented in the vertical direction, resulting in infill thickness (t_{inf}) equal to brick width (3 5/8 in.). In the lowest brick layer, to allow hardware clamping the specimen to the earthquake simulator to 'pass through' the infill and to minimize cutting, bricks were laid at 90-degrees relative to the plane of the wall (Figure 2-11). Additional details of masonry used to build infill walls are discussed in Appendix B.

Masonry prisms built from the same materials as infill walls had a mean compressive strength f'_m = 2800 psi and a mean modulus of elasticity E_m = 1400 ksi. Both values were based on the gross cross-sectional area of prisms (7 5/8 in. by 3 5/8 in.). The mean shear strength of masonry coupons (discussed in Appendix B) was approximately 100 psi and the mean compressive strength of 4-in. by 8-in. mortar cylinders was approximately 1700 psi. Additional details of the material properties of masonry are given in Appendix B.

2.4 Test Setup

An isometric view of the test setup is shown in Figure 2-12. Elevations of the test setup and specimen are shown in Figure 2-13 and Figure 2-14.

2.4.1 Connection of Specimen to Test Platform

A layer of gypsum was applied between the top surface of simulator platform and bottom face of foundation beam to ensure uniform contact of specimen with platform. Hardware was used to clamp foundation beam to simulator to prevent uplift of base for a total clamping force of approximately 220 kips. Two steel channels were bolted to both ends of simulator to strengthen the lateral connection between center and outer segments of the test platform. Adjustable bolts bore on the mentioned channels and steel plates bearing against both ends of foundation beam to prevent the specimen from sliding (Figure 2-15).

2.4.2 Connection of Specimen to Suspended Mass

2.4.2.1 Channels Flanking the Top Beam of Specimen

The suspended mass was connected to the top beam through two channels flanking each side of the top beam, a load cell, and a stiff link with small-play swivels at each of its two ends. Steel channels (each with a splice described in Appendix B) sandwiched the top beam of the test frame. A layer of gypsum was applied between west channel and concrete to ensure uniform contact. The channels provided a slip-critical connection between the mass and specimen for a total clamping force of approximately 300 kips. The connection between channels and specimen was made near the point of contra-flexure to reduce the effects of additional flexural stiffness provided by channels to top beam.

In addition to the mentioned slip-critical connection, adjustable bolts bore on hardware attached near ends of channels sandwiching the top beam and steel plates bearing against ends of top beam (Figure 2-16). The mentioned hardware consisted of pairs of angles bolted to interior and exterior faces of steel channels near north and south ends of specimen and steel plates bearing against south end of steel channels. The bolted connections between angles and channels were assumed to resist shear forces but not force couples, although it is plausible that they did provide some rotational restraint at either end of the top beam.

2.4.2.2 Two-Swivel Stiff Link and Load Cell between Specimen and Suspended Mass

A load cell was placed between the specimen and the stiff link attached to the suspended mass to measure directly inertial lateral forces (Figure 2-17). Two rods driven into holes in load cell and passing through steel plates butted against ends of load cell were tightened using mechanical nut tensioners to a clamping force of 100 kips each. Plate and load cell assembly was mounted to top of south end of specimen (aligned with the top beam) by lifting it with an overhead crane, butting one side against steel angles bolted to south end of top steel channels, and tightened to said angles using bolts to a total clamping force of approximately 160 kips (Figure 2-18).

The link consisted of two swivels connected to each other as shown in Figure 2-19. The link helped minimize application of vertical forces to the specimen. This was done to 1) minimize the eccentricity of forces applied to load cell, and 2) minimize tension in and uplift of columns. Details of swivels are discussed in Appendix B.

Steel socket head screws passing through holes in base tangs and threaded into high-strength steel coupling nuts connected both swivels to each other with a clamping force of 200 kips (Figure 2-19). The swivel at south end of link was attached to north face of suspended mass using high-strength threaded rods epoxy glued into suspended mass tightened to a total clamping force of approximately 200 kips (Figure 2-20). The north end of the link was fastened to a steel plate connected to the load cell using high-strength rods tightened to a total clamping force of approximately 180 kips (Figure 2-21). Three steel plates created a space between the mentioned steel plate and swivel at north end of link to accommodate a mechanical nut tensioner threaded on the rod driven into the load cell [Figure 2-21 (d)].

2.4.3 Suspended Mass

The suspended mass was a reinforced concrete prism with a length of 14 ft. and a 4 ft. by 5 ft. rectangular cross section. This concrete block served as the foundation of one of the RC walls tested by Pollalis (2021). It was suspended from an overhead crane using two lifting straps (Figure 2-22). The overhead crane was approximately 35 ft. above the centroid of the mass.

2.4.4 Out-of-plane Bracing

Four hollow steel tubes bolted to both sides of another reinforced concrete block (similar to the suspended mass) post-tensioned to the strong floor with a clamping force of 120 kips were used to reduce out-of-plane displacement of mass. Teflon pads were glued to surfaces of steel tubes and stainless-steel plates were attached to concrete surfaces of suspended mass to reduce friction (Figure 2-23). Initial gaps between surfaces of Teflon pads and stainless-steel plates were no larger than 1/4 in. Additional details of the test setup are described in Appendix B.

2.5 Instrumentation

An instrumentation layout is shown in Figure 2-24. Linear variable differential transformers (LVDTs), one load cell, strain gages, and accelerometers were sampled at a rate of 1,000 Hz to obtain measurements in runs of both specimens. Two optical particle-tracking systems were used (OptiTrack and Optotrak systems). OptiTrack was used in runs of both specimens, but Optotrak was used in runs of Specimen F2 only. They were sampled at a rate of 100 Hz and were used to 1) confirm measurements of displacements obtained with LVDTs, and 2) measure the flexibility of the earthquake simulator (described in Section 4.3). Additional details of the instrumentation used to obtain measurements in runs of bare frames and infilled frames tested in this investigation are described in Appendix B.

To highlight the discrepancies between base motion and structural response histories obtained or inferred from the different instruments described above, comparisons of the observed response from selected runs are described next.

2.5.1 Lateral Displacements

Measurements of displacements of simulator, specimens, and mass were obtained using one LVDT mounted inside the servoram (Figure 2-25), three LVDTs mounted to a steel column post-tensioned to the strong floor (Figure 2-26), OptiTrack (Figure 2-27 through Figure 2-30), and Optotrak (Figure 2-31 and Figure 2-32) systems. All positive values of base displacement indicate the platform moving to the south and all positive values of drift demand indicate the specimen drifting to the south as defined in Figure 2-24. Measurements of base displacement obtained during Run 48 of Specimen F2 were within 0.02 in. from one another in all systems (Figure 2-33) and measurements of peak drift obtained during the same run were within 0.03 in. from one another in all systems (Figure 2-34). Because measurements obtained using LVDTs were sampled at a rate ten times faster than OptiTrack and Optotrak systems, base displacements and drift demands reported in this investigation were based on measurements obtained from LVDTs (Figure 2-25 and Figure 2-26).

2.5.2 Lateral Forces

A load cell (Figure 2-35) was used to measure lateral forces as mentioned in Section 2.4.2. All positive values of lateral load indicate tension. Strain gages were attached to a “flexure link” that connects the test platform and the hydraulic actuator driving the simulator (Figure 2-36) to monitor residual strains of link. No yielding occurred in the link based on measurements of these strain gages. Discrepancies between measurements of peak lateral loads obtained from strain gages and load cell were no larger than 3 kips (base-shear coefficient of 0.06) in Run 12 of Specimen F1 (Figure 2-37). More noise was observed in measurements obtained from strain gages compared with those obtained from load cell near zero load during a motion. Plausible reasons for this noise are 1) differences related to the inertia of the mass of the simulator platform, foundations of specimens, and clamping hardware, 2) eccentricity of load resisted by servoram, and 3) misalignment of strain gages attached to flexure link. Because of this noise, lateral loads reported in this investigation are based on measurements obtained from load cell and not from strain gages.

2.5.3 Accelerometers

Accelerometers were mounted on specimens and the suspended mass (Figure 2-24) to measure base motions and compare the products of effective mass and measurements of absolute roof acceleration with measurements of lateral load obtained from load cell and strain gages. All positive values of acceleration, velocity, and displacement indicate southward motion as defined in Figure 2-24. The effective mass of frames tested in plane was 49,000 lb (discussed in Section 4.3). Two types of accelerometers were used in this investigation: triaxial ADXL accelerometers (which measured in-plane, out-of-plane, and vertical motion simultaneously) and uniaxial PCB accelerometers (Figure 2-38). ADXL and PCB accelerometers were mounted on top of top beams and foundation beams of each test frame at north and south ends (Figure 2-39). The suspended mass was instrumented with four PCB accelerometers: two accelerometers measured in-plane motion and two accelerometers measured vertical motion of mass (Figure 2-40). Acceleration histories obtained from ADXL accelerometers were reported in this investigation.

2.5.4 Processing Acceleration Data

Measurements of acceleration were processed in a series of four consecutive steps. The steps are filtering, trimming, integrating, and correcting and each is described next.

2.5.4.1 Filtering

First, raw acceleration histories were filtered using a fourth-order Butterworth bandpass filter with a high-pass cut-off frequency of 0.25 Hz and a low-pass cut-off frequency of 15 Hz. Although the minimum frequency of ADXL accelerometers specified by the manufacturer was 0.5 Hz, it was observed that the fit between target and measured displacement spectra calculated from base acceleration histories was better when the latter was filtered with a high-pass cut-off frequency of 0.25 Hz compared with 0.5 Hz (Figure 2-41). It was also observed that changing the low-pass cut-off frequency from 15 to 60 Hz had a negligible effect on spectral shape regardless of the high-pass cut-off frequency used. To select an appropriate low-pass cut-off frequency to reduce noise produced by the simulator-frame-mass system while preserving the frequency content of the scaled motion, target and measured base motions are compared using different filters as shown in Figure 2-42 through Figure 2-45 and tabulated in Table 2-1. Using a low-pass cut-off frequency of 15 Hz resulted in the closest fit between:

1) Target and measured values of peak base acceleration (PGA) which were 0.43 and 0.40 g,
2) Fourier decompositions of target and measured base acceleration histories (Figure 2-46)
3) Target and measured base acceleration histories (Figure 2-47).

Notice the bandpass filter does not eliminate completely all frequencies larger than the low-pass cut-off frequency but instead reduces the amplitudes of said frequencies gradually to zero at a frequency approximately 15 to 20 Hz larger than the specified low-pass cut-off frequency (Figure 2-42).

2.5.4.2 Trimming

Next, filtered measured base acceleration histories were trimmed by isolating the duration of the simulated earthquake from the entire recording.

2.5.4.3 Integrating

Once trimmed, filtered base acceleration histories were integrated with respect to time using trapezoidal rule.

2.5.4.4 Correcting

After integrating base acceleration histories, base velocity histories were corrected using a second-order polynomial to adjust baselines such that the base velocity at the beginning and end of a motion was approximately zero. Corrected base velocity histories were integrated using the procedure described in Section 2.5.4.3 and base displacement histories were corrected using again a second-order polynomial.

2.5.5 Comparisons of Target and Measured Base Motion Histories

Figure 2-42 through Figure 2-45 show comparisons of target and measured base motion histories using low-pass cut-off frequencies of 10, 15, 20, and 25 Hz for a selected run (Run 12 of Specimen F1). The base motion of the selected run filtered using a low-pass cut-off frequency of 25 Hz [Figure 2-43 (d)] had a PGA that was nearly twice as large as the result obtained from the same base motion filtered using a low-pass cut-off frequency of 10Hz [Figure 2-43 (a)]. Nevertheless, there was little difference between peak base velocities (Figure 2-44) and no difference between peak base displacements (Figure 2-45) when the base motion was filtered using low-pass cut-off frequencies between 10 and 25 Hz as suggested by Table 2-1. Measured peak base velocities (PGV) were approximately 1 in./sec. smaller than target PGV and measured peak base displacements (PGD) were approximately 0.2 in. smaller than target PGD. Figure 2-48 and Figure 2-49 show comparisons of target and measured base velocity and base displacement histories obtained with a low-pass cut-off frequency of 15 Hz.

2.5.6 Comparisons of Base Motion Histories Inferred from Accelerometers and LVDTs

Discrepancies between measurements of peak base accelerations and peak base velocities obtained from ADXL and PCB accelerometers were no larger than 0.04 g and 1 in./sec. in the selected run (Run 12 of Specimen F1) as shown in Figure 2-50 and Figure 2-51. Discrepancies between peak base displacements inferred from ADXL and PCB accelerometers and from the LVDT mounted inside the servoram driving the simulator platform were within 0.3 in. from one another in the selected run (Figure 2-52). Discrepancies between peak base displacements obtained from double integration of base acceleration histories and those obtained from the LVDT mounted inside the servoram may be the result of the baseline correction procedure used to correct base motion histories. It is plausible that peak measurements were less than target peak values because of the limits of the simulator and the inability of the servoram to replicate perfectly the selected scaled ground motions with high frequency contents used to shake specimens with an effective weight of nearly 50 kips.

2.5.7 Comparisons of Roof Acceleration and Lateral Load

Discrepancies between measurements of peak roof accelerations obtained from ADXL and PCB accelerometers were no larger than 0.05 g in the selected run (Figure 2-53). Spikes in the measured roof acceleration history obtained from the PCB accelerometer mounted near the middle of the east face of the suspended mass were observed in the second half of the motion (after 10 seconds). It is plausible that the mass and out-of-plane bracing system impacted each other and caused instantaneous acceleration spikes. Discrepancies between measurements of peak roof accelerations obtained from accelerometers and peak lateral loads obtained from load cell and strain gages were not larger than 5 kips (base-shear coefficient of 0.1) in the selected run (Figure 2-54). Additional details of the instrumentation used in this investigation are discussed in Appendix B.

2.6 Input Ground Motions

Table 2-2 shows the details of the strong ground motion records used in this investigation. A total of seven base motions modeled after “corrected” acceleration records obtained from the PEER NGA-West2 ground motion database (Ancheta, et al., 2014) were used to subject specimens to simulated earthquakes. For a given motion, the time step of the record was compressed and magnitudes of accelerations were amplified to generate the maximum possible motion that could be reproduced by the earthquake simulator (PGA = 2 g, PGV = 12 in./sec., PGD = 2 in.). Maximum motions so scaled are designated as motions with intensities of “100%” (described in Table 2-2) and only simulations of equal or smaller intensities were used in this investigation. Compressed acceleration records of each motion were integrated twice with respect to time to obtain displacement histories used to control the movement of the earthquake simulator. “Target” refers to the base motion input. Acceleration, velocity, and displacement histories of the 100% target motions used in this investigation are shown in Figure 2-55 through Figure 2-61. Spectra of the 100% target motions calculated for a damping ratio of 2% are shown in Figure 2-62 through Figure 2-64.

The selection of simulated ground motions was based on three criteria:

1) Ratios of PGV to PGA of scaled motions
2) Ratios of PGV to PGD of unscaled motions
3) Comparisons of target and measured displacement spectra

Each of these criteria is discussed next.

2.6.1 Ratios of PGV to PGA

The first criterion was based on work by Laughery (2016). Laughery claimed that for simulated motions with small, scaled ratios of PGV to PGA, measured drift demands tended to exceed estimates obtained with the method[1] proposed by Sozen (2003) by as much as 100%. To test this idea, simulations within the (scaled) range 0.03 sec. < PGV/PGA < 0.09 sec. were used in test Series F2-C.

2.6.2 Ratios of PGV to PGD

The second criterion was based on multiple studies summarized by Sozen (2003) which showed that drift demands of reinforced concrete frames tend to be linearly proportional to measurements of PGV. To increase the likelihood of nonlinear response and stay within the limits of the simulator,

[1] Method 5 as discussed in Chapter 5

motions with relatively large peak base velocities and relatively small peak displacements were selected. Only records with unscaled ratios of PGV to PGD larger than 1 Hz were considered. Target motions with intensities of 100% compressed in time and scaled (such that the peak displacement of the platform was smaller than the maximum stroke of the simulator ±2 in.) had target base velocities exceeding 8 in./sec.

2.6.3 Comparisons of Displacement Spectra

The third criterion was necessary to make fair comparisons of drift demand between bare frames and infilled frames. To ensure base motions would be replicated reliably by the earthquake simulator, accelerometers were mounted on top of platform to measure base motion histories and motions with intensities of 100% were simulated no fewer than three times before subjecting specimens to said simulations. Then, displacement spectra calculated from corrected measured base acceleration histories and for a damping ratio of 2% were compared with target spectral demands. An example of good fit between target and measured displacement spectra calculated from measurements obtained from corrected base acceleration histories is shown in Figure 2-65.

2.7 Simulation Protocol

Sozen (1969) and Gulkan (1971) provide detailed descriptions of the earthquake simulator. The simulator was operated using displacement control and the mentioned scaled displacement histories (discussed in Section 2.6). The order of simulated motions is summarized in Table 3-1 through Table 3-8. All series included base motions of increasing intensities. Here intensity is based on target values of PGV. The term ‘increasing intensities’ indicates that each series began with less intense motions (with small target values of PGV) followed by more intense motions (with large target values of PGV). Each series of Specimen F1 and the first series of Specimen F2 (Series F2-C) also included ground motions of ‘decreasing intensities’ meaning that PGV of subsequent motions following the most intense motion of a given series decreased gradually. Runs were repeated in each series to quantify drift demands of softened structures in subsequent motions. Repeats are discussed in detail in Section 4.6.

2.8 Testing Sequence

The testing sequences of Specimens F1 and F2 are summarized in Table 1-1. A total of 75 simulations were applied to Specimen F1. The first series of tests of Specimen F1 included fifteen runs of the bare frame (Series F1-B). Here a run is defined as a single simulated base motion. Next, clamps were installed on columns and a second series of tests was conducted on Specimen F1 that reached higher shaking intensity. After twenty-two runs of the frame with clamps (Series F1-C), and without removing clamps, the frame was infilled with a masonry wall. Mortar used in infill wall was also used to patch beam-column joints where concrete spalling had occurred. Then, nineteen runs were conducted on the infilled frame with clamps (Series F1-M-C). Next, the specimen was rotated 90-degrees such that the longitudinal axis of the frame was oriented perpendicular to the direction of motion of the simulator. The infilled frame was subjected to base motions in its weak direction to observe if out-of-plane failure would occur in the fourth and final series of tests of Specimen F1 which included twenty-two runs (Series F1-M-C-OOP).

A total of 97 simulations were applied to Specimen F2. Clamps were installed on columns prior to conducting the first series of tests on Specimen F2 which included sixty-nine runs (Series F2-C). Next, clamps were removed from columns and the frame was infilled with a masonry wall. Mortar used in infill wall was also used to patch beam-column joints where concrete spalling had occurred. After nine runs of the infilled frame (Series F2-M), testing stopped, and threaded rods were passed through holes drilled through bricks and mortar along vertical edges of infill wall to allow for installation of clamps on columns to reduce the likelihood of shear failure and a third series of tests was conducted on Specimen F2. After six runs of the infilled frame with clamps (Series F2-M-C-S), the infill wall was demolished but clamps remained on columns. The fourth and final series of tests of Specimen F2 included thirteen runs of the frame with clamps with no infill wall (Series F2-C-S). The number of motions applied to both frames is outside the realm of foreseeable possibilities for a structure in the field. Nevertheless, absence of failure 1) allowed the large number of motions achieved, and 2) demonstrated the tenacity of the studied retrofit systems (combining masonry infill to increase stiffness and reduce drift, and external transverse reinforcement to increase drift capacity and toughness).

CHAPTER 3. OBSERVED RESPONSE DURING EARTHQUAKE SIMLUATIONS

3.1 Simulation Identification

The simulation identification (ID) assigned to each run is described next. The 1940 El Centro record compressed in time by a factor of two - referred to as El Centro (TC2) - is the common motion used in runs of each series to allow for comparisons of drift demands of bare frames and infilled frames subjected to nominally identical simulations. In Series F2-C and F2-C-S, simulations modeled after other ground motions in addition to El Centro (TC2) were used.

Simulations IDs for each run are defined using three components:

1) Test Series
2) Intensity
3) Sequence

IDs of runs modeled after the common motion, El Centro (TC2), consist of one item from each column in the following table separated by hyphens.

Runs modeled after the common motion - El Centro (TC2)

Test Series		**Intensity**	**Sequence**
Specimen	Configuration	Percent	Order
F1	B	10	1
F2	C	20	2
	M-C	40	3
	M-C-OOP	60	4
	M	80	
	M-C-S	100	
	C-S		

IDs of runs of Series F2-C and F2-C-S consist of one item from each column in the following table separated by hyphens.

Runs of Series F2-C and F2-C-S

Test Series		Intensity		Sequence
Specimen	Configuration	RSN	PGV	Order
F2	C	RSN6-TC2	PGV-2	1
	C-S	RSN6-TC4	PGV-4	2
		RSN77	PGV-6	3
		RSN85	PGV-8	
		RSN1051	PGV-10	
		RSN2114	PGV-12	
		RSN6975		

Each component of the simulation ID is described next.

3.1.1 Test Series

The test series component consists of two items. The first item is a letter and number which represent the specimen tested, F1 or F2. The second item a single letter or letters representing the configuration of the frame: ‘B’ is for bare frame, ‘C’ is for clamps, ‘M’ is for frame with masonry infill wall, ‘OOP’ is for out-of-plane tests of infilled frame, and ‘S’ is designated for series tested after wide inclined ‘shear’ cracks formed at bases of columns during Series F2-M resulting in an abrupt pause in testing, installing clamps on columns, and continuing simulations beginning in Series F2-M-C-S. Multiple letters are used to represent combined configurations of specimens.

3.1.2 Intensity

Intensities of 1) runs modeled after El Centro (TC2) and 2) runs of Series F2-C and F2-C-S are defined separately.

3.1.2.1 Common Motion - El Centro (TC2)

The intensity component of a run modeled after El Centro (TC2) consists of one item which is a two or three-digit value referring to the target intensity of said run relative to the 100% target intensity motion expressed as a percent.

3.1.2.2 Runs of Series F2-C and F2-C-S

The intensity component of runs of Series F2-C and F2-C-S consists of two items. The first item consists of the acronym 'RSN' followed by a number or numbers assigned uniquely to records of strong ground motions by PEER (Ancheta, et al., 2014). RSN stands for Record Sequence Number and is jargon used in the NGA West-2 ground motion database compiled by Ancheta (2014) to catalogue and differentiate between records obtained from multiple stations during the same earthquake and between different earthquakes.

The second item consists of the acronym 'PGV' followed by a number representing the target PGV of a simulation in inches per second. Here PGV refers to the target peak base velocity expected to be measured in an ideal run with 'perfect' equipment. Two target motions (of seven) used in Series F2-C were modeled after the same motion, a record obtained from the 1940 El Centro earthquake. One motion was compressed in time by a factor of four and the other was compressed in time by a factor of two. To differentiate between the two El Centro motions used in Series F2-C, the acronym 'TC' followed by the number '2' or '4' representing the relevant 'time-compression' factor is used.

3.1.3 Sequence

The sequence component consists of one item which is a single-digit number which refers to the order in which nominally identical simulated motions occurred within the same test series. For example, the simulation identified as F1-M-C-40-4 was the fourth occurrence (third repetition) of the common motion, El Centro (TC2), with an intensity of 40% of the 100% target intensity and said simulation was used to test Specimen F1 with a configuration that included an infill wall and clamps in the direction of the longitudinal axis of the frame.

The results of each test series are described next.

3.2 Summaries of Peak Measurements

Peak measurements obtained in runs of each test series are summarized in Table 3-1 through Table 3-8. The term 'peak' used here and throughout this investigation refers to absolute maxima of measurements obtained in a run, and the term ‘drift’ often refers to a peak value. The following measurements are reported in each table:

- Peak base acceleration (PGA) and peak base velocity (PGV) obtained from ADXL accelerometers mounted on foundation beam (discussed in Section 2.5.3)

- Peak base displacement (PGD) obtained from LVDT mounted inside servoram (discussed in Section 2.5.1)

- Peak in-run and cumulative drift ratios (discussed in Section 4.1)

- Peak base shear coefficient computed as peak lateral load obtained from load cell (described in Section 2.5.2) divided by effective weight (discussed in Section 4.3)

Peak drift ratios are computed as ratios of relative peak lateral displacement of top beam to total height of frame (h = 50 in.) computed as the sum of column clear height (h_c) and half the depth of top beam of specimen (10 in.). The relative peak lateral displacement of top beam is computed as the difference in absolute displacements of mid-depth of top beam (mean of displacements obtained from LVDTs at top and soffit of top beam) and top of foundation.

3.3 Specimen F1

3.3.1 Series F1-B

Table 3-1 summarizes the measurements obtained in runs of Series F1-B. After the first four simulations (Runs 1-4) in Series F1-B, it was determined that there was excessive play between specimen and mass in the two-swivel link assembly as suggested from spikes in

1) measured force-displacement plots (Figure 3-1), and from

2) lateral load histories (Figure 3-2).

To reduce play in system and spikes in the observed response, the mentioned link was replaced with another link (Figure 3-3). Force-displacement relationships of the system with the link reducing play show no large spikes (Figure 3-4) which led to larger drift demands in the second half of the motion (after 10 seconds) as shown in Figure 3-5. Nevertheless, the system still had play which appears to be approximately 1/16 in. Details of both links are described in Appendix B.

Figure 3-6 shows the force-displacement relationship measured in runs of Series F1-B. The maximum in-run drift ratio reached in Series F1-B was approximately 2.6% and occurred during the first simulation with an intensity of 80% (F1-B-80-1). The base-shear strength of Specimen F1 without infill was approximately 24 kips which was nearly 50% of the effective weight (discussed in Section 4.4). Initial cracks at corners of joints followed by flexural cracks no further than $1.5d$ from column ends formed during runs of motions with intensities of 10% and 20% (Figure 3-7). Yielding occurred during the first simulation with an intensity of 40% (F1-B-40-1) producing a peak cumulative drift ratio of approximately 1.1% and hairline (< 0.005 in.) inclined cracks measured after testing initiated from flexural cracks (Figure 3-8). The next four simulations with intensities ranging from 60% to 80% and measured peak base velocities between 7 and 8 in./sec. resulted in more inclined cracks the largest of which was 0.075 in. wide measured after testing and severe concrete spalling at corners of joints (Figure 3-9). It was decided not to subject the bare frame to simulations with intensities of 100% because of the risk of columns being damaged beyond repair preventing further testing.

Series F1-B ended with two simulations with intensities of 40% producing a residual cumulative drift of approximately 0.45%. The permanent width of the inclined crack at top of north column was approximately 0.075 in. wide (Figure 3-10). Before testing the next series (Series F1-C), clamps were installed along clear heights of columns. Upon installation of the final clamp, the mentioned inclined crack was reduced to a width smaller than 0.010 in [Figure 3-10 (d)].

3.3.2 Series F1-C

Elevations of the frame before and after installation of clamps are shown in Figure 3-11. Values of ground motion parameters and the measured response of Specimen F1 in Series F1-C are quantified in Table 3-2. The force-displacement relationship obtained from peak values of lateral force and cumulative displacement measured in runs of Series F1-C is shown in Figure 3-12 (a). Peak in-run and cumulative drifts reached in runs with intensities of 80% in Series F1-C were approximately equal to drifts reached in Series F1-B for nominally identical simulations. Motions with intensities of 100% were included in Series F1-C and peak in-run drift ratios reached in those runs were approximately 3%. Several flexural and inclined cracks not wider than 0.005 in. formed during Series F1-C near ends of columns (Figure 3-13). Maximum permanent cracks widths measured before the beginning and after the end of the series increased from 0.020 in. to 0.030 in. After Series F1-C was completed, an infill wall was built in the frame and testing of Series F1-M-C began.

3.3.3 Series F1-M-C

An elevation of the infilled frame with clamps is shown in Figure 3-14. A second ADXL accelerometer was installed on the southwest corner of the foundation beam after Run 42 (F1-M-C-40-1) to compare measurements of base motions obtained from the other ADXL accelerometer mounted on the northeast corner of the foundation. Values of ground motion parameters and the measured response of Specimen F1 in Series F1-M-C are quantified in Table 3-3. The force-displacement relationship measured in runs of Series F1-M-C is shown in Figure 3-15 (a). Peak in-run drift ratios of the infilled frame reached in simulations with intensities of 80% were between 1% and 1.3% compared with peak in-run drift ratios of the bare frame between 2.3% and 2.6% reached in nominally identical simulations [Figure 3-15 (b)]. The maximum lateral load reached in runs of Series F1-M-C was approximately 44 kips (base-shear coefficient of 0.90) and occurred during the first simulation with an intensity of 80% (F1-M-C-80-1). This value of maximum lateral load does not represent the lateral strength of the infilled system as suggested by the force-displacement hysteretic curves measured in runs with intensities of 80% (Figure 3-16).

A horizontal crack formed along mortar joints spanning the full length of wall between the first and second layer of bricks during the first run with an intensity of 20% (F1-M-C-20-1) as shown in Figure 3-17. Mortar bed joints at top of wall began to separate from soffit of top beam. In the first run with an intensity of 40% (F1-M-C-40-1), an inclined crack formed running from center of top of wall to edge of wall near mid-height of north column (Figure 3-18). The inclined crack formed along mortar joints in upper portion of wall, but it formed through bricks near edge of wall and north column. A second inclined crack formed near top of wall and south column. In the same run, a flexural crack at top of north column formed in mortar used to patch beam-column joint prior to tests of Series F1-M-C.

Another inclined crack running from mid-height of wall near south column to inclined crack near top of wall and north column formed in the second run with an intensity of 60% (F1-M-C-60-2) as shown in Figure 3-19. A horizontal crack formed in mortar joints between second and third uppermost layers of bricks near top of wall. In the third layer of bricks (from bottom of wall), a portion of the brick next to south column fell out during the fourth run with an intensity of 60% (F1-M-C-60-4) as shown in Figure 3-20 and Figure 3-21. After subjecting the infilled frame to simulations of increasing and decreasing intensities in Series F1-M-C, the infilled frame with clamps was subjected to a third run with an intensity of 80% (F1-M-C-80-3). The state of the wall at the end of Series F1-M-C is shown in Figure 3-22. Portions of mortar head joints near base of wall fell out during the final run of Series F1-M-C.

Maximum permanent crack widths in wall increased from 0.005 in. measured after the first run with an intensity of 10% (F1-M-C-10-1) to 0.04 in. measured after the third run with an intensity of 80% (F1-M-C-80-3). In runs of decreasing intensities of the infilled frame with clamps (Runs 48-55) permanent crack widths in wall did not increase by more than 0.005 in. Permanent widths of inclined cracks that formed in columns in Series F1-B and F1-C remained between 0.01 and 0.03 in. and did not increase by more than 0.01 in. throughout Series F1-M-C. Flexural and inclined cracks not wider than 0.005 in. formed in columns in Series F1-M-C, mostly near mid-heights of columns.

After the final run of Series F1-M-C, the suspended mass was disconnected from the specimen and the infilled frame with clamps was rotated 90-degrees to subject the specimen to simulated base motions in its weak direction.

3.3.4 Series F1-M-C-OOP

The infilled frame with clamps as tested in its weaker out-of-plane orientation is shown in Figure 3-23. The effective weight of Series F1-M-C-OOP was approximately 4.5 kips (described in more detail in Section 4.3) which included half the weight of the specimen and the total weight of hardware attached to top beam of the specimen. Values of ground motion parameters and the measured response of Specimen F1 in Series F1-M-C-OOP are quantified in Table 3-4. The peak roof acceleration - peak cumulative drift ratio measured in runs of Series F1-M-C-OOP is shown in Figure 3-24. The maximum cumulative in-run drift ratio was approximately 2% and the peak roof acceleration was approximately 1.8 g (peak lateral load of 8 kips). Spalling of mortar along bed joints between the first and second layer of bricks (Figure 3-25) occurred during the first run with an intensity of 40% (F1-M-C-OOP-40-1) and a measured peak base velocity of approximately 5 in./sec. No bricks fell out and the state of the wall after the final run of Series F1-M-C-OOP was nearly identical to the state of the wall after the final run of Series F1-M-C suggesting that infill wall damage is more sensitive to in-plane motion than out-of-plane motion provided there is 1) no torsion and 2) the infill wall thickness is at least 40% of the column dimension.

3.4 Specimen F2

3.4.1 Series F2-C

Clamps were installed on columns prior to the first series of tests done on Specimen F2 (Figure 3-26). The force-displacement relationship measured in Series F2-C is shown in Figure 3-27 (a). The force-displacement response of the frame with clamps is similar to the force-displacement response observed in runs of Series F1-B and F1-C [Figure 3-27 (b)] suggesting drift demands are not sensitive to the addition of clamps. Also, lateral strengths of frames without infill are similar - the base-shear strength of Specimen F2 (without infill) was approximately 23 kips and the base-shear strength of Specimen F1 was approximately 24 kips. Nevertheless, differences between Specimens F1 and F2 without infill included peak drift demands and crack patterns.

Recall that the maximum in-run drift ratio reached in Series F1-C was approximately 3% in a simulation modeled after the 1940 El Centro motion with a measured peak base velocity of approximately 10 in./sec. (F1-C-100-2). But the maximum in-run drift ratio reached in Series F2-C was approximately 3.5% in a simulation modeled after the 1994 Northridge motion with a measured peak base velocity of approximately 8 in./sec. (F2-C-RSN1051-PGV8-1). Differences between drift demands and values of PGV in the two mentioned runs of nominally identical frames suggest that there is no trivial error associated with the assumption that drift demand is linearly proportional to peak base velocity (discussed in more detail in Section 4.5).

Flexural cracks formed along columns throughout Series F2-C (Figure 3-28). Inclined cracks not wider than 0.005 in. formed in runs at a target peak base velocity of 8 in./sec and these cracks did not increase to permanent widths larger than 0.010 in. throughout Series F2-C. Within regions between clamps, flexural cracks remained smaller than 0.015 in. At beam-column joints permanent widths of flexural cracks remained smaller than 0.05 in. Concrete spalling near joints at bases of columns was observed at the end of the most intense simulations (target PGV = 8 in./sec.) as shown in Figure 3-29. After Run 69, clamps were removed from columns and an infill wall was built within Specimen F2 before testing Series F2-M.

3.4.2 Series F2-M

An elevation of the infilled frame (without clamps) is shown in Figure 3-30. The force-displacement relationship of Series F2-M is shown in Figure 3-31 (a). The response of the infilled frame without clamps is similar to the response the infilled frame with clamps (Series F1-M-C) as shown in Figure 3-31 (b). The maximum in-run drift ratio reached in Series F2-M was approximately 1.1%. The maximum lateral load reached in Series F2-M was approximately 37 kips (base-shear coefficient of 0.75). But this value of maximum lateral load was observed not to be the lateral strength of the infilled frame based on the force-displacement hysteretic curve measured in the first and only run with an intensity of 80% of Series F2-M (Figure 3-32).

A horizontal crack formed through mortar bed joints between the first and second layer of bricks (Figure 3-33) during the first run with an intensity of 20% (F2-M-20-1). An inclined crack running from center of top of wall to mid-height of south column (Figure 3-34) formed in the second run with an intensity of 40% (F2-M-40-2). Another inclined crack formed from center of top of wall to near mid-height of north column (Figure 3-35) in the first run with an intensity of 60% (F2-M-60-1). During the first run with an intensity of 80% (F2-M-80-1), inclined cracks formed at column bases (Figure 3-36). It is plausible that those cracks formed because of mortar head joints falling out of wall resulting in stiffness discontinuities because of separation of wall with columns leading to the infamous captive column effect (Figure 3-37). The maximum permanent crack widths were approximately 0.1 and 0.035 in. at bottoms of south (Figure 3-38) and north (Figure 3-39) columns.

It was decided to pause testing after the first run with an intensity of 80% (F2-M-80-1) because of the mentioned wide inclined cracks, install clamps along clear heights of columns, and repair the infill wall prior to subjecting the infilled frame with clamps to additional simulations. To allow threaded rods to pass through edges of wall adjacent to columns to restrain inclined cracks from opening in subsequent motions, 1/2-in. diameter holes were drilled along the height of wall on both sides (Figure 3-40). Upon installation of clamps at the base of the north column, the permanent width of the inclined crack shown in Figure 3-41 reduced from 0.030 to 0.020 in. Openings in wall caused by damage from intense simulations and from drilling were filled with gypsum to repair infill and ensure uniform contact between wall and frame (Figure 3-42). The repaired infilled frame with clamps was tested in Series F2-M-C-S described next.

3.4.3 Series F2-M-C-S

Elevations of the repaired infilled frame with clamps are shown in Figure 3-43. The force-displacement relationship measured in Series F2-M-C-S is shown in Figure 3-44 (a). The force-displacement responses of infilled frames of Specimen F2 were similar to each other although the peak lateral load reached in the first run with an intensity of 80% of the repaired infilled frame with clamps (F2-M-C-S-80-1) was approximately 10% larger than the peak lateral load reached in the first run with an intensity of 80% of the infilled frame without clamps (F2-M-80-1) which was approximately 37 kips [Figure 3-44 (b)]. This suggests that the installation of clamps on columns and minor repairs made to infill wall were successful in controlling the inclined cracks that formed in Series F2-M. The peak in-run drift ratios reached in the final two runs with intensities of 80% of Series F2-M-C-S were approximately 1.1% and 1.2%.

Permanent widths of flexural and inclined cracks in columns did not increase by more than 0.01 in. throughout Series F2-M-C-S. Cracks in mortar head and bed joints at top of wall near columns (Figure 3-45) occurred during the first run with an intensity of 10% (F2-M-C-S-10-1). Inclined cracks formed in mortar joints near center of wall (Figure 3-46) during the first run with an intensity of 60% (F2-M-C-S-60-1). A horizontal crack through mortar bed joints formed during the first run with an intensity of 80% (F2-M-C-S-80-1) as shown in Figure 3-47 and a portion of a brick fell out of the wall near the bottom of the south column (Figure 3-48). The crack map at the end of Series F2-M-C-S is shown in Figure 3-49. After the final run of Series F2-M-C-S, the infill wall was demolished (Figure 3-50) and the frame with clamps was tested in Series F2-C-S.

3.4.4 Series F2-C-S

An elevation of the frame with clamps tested after the infill tests of Specimen F2 is shown in Figure 3-51. The force-displacement relationship measured in runs of Series F2-C-S is shown in

Figure 3-52 (a). Peak in-run drift ratios reached in the most intense simulations modeled after the 1940 El Centro (TC2) and the 1994 Northridge motions (with measured peak base velocities between 9 and 10.5 in./sec.) were approximately 3.2% and 4.6%. The maximum lateral load reached in Series F2-C-S was approximately 21 kips (base-shear coefficient of 0.43). The response measured in runs of Series F2-C-S in simulations modeled after the El Centro (TC2) motion was similar to the response measured in runs of decreasing intensities of the bare frame (F1-B) and frames with clamps (F1-C and F2-C) as shown in Figure 3-52 (b). No loss in lateral load carrying capacity associated with a 20% decrease from strength was observed even up to drift ratios exceeding 4%. Nevertheless, concrete spalling at base of columns was so severe that longitudinal bars became exposed by the end of Series F2-C-S (Figure 3-53).

CHAPTER 4. DISCUSSION OF OBSERVED RESPONSE

Drift is a simple yet useful indicator of damage potential. This chapter includes a discussion based primarily on measurements of drift. Drift demands - measured and estimated - are the focus of the remaining chapters. Differences between in-run and cumulative drift demands are described next.

4.1 In-run and Cumulative Drift

Measurements of in-run drift and cumulative drift are used in this investigation. In-run drift is measured relative to the initial position of the specimen at the beginning of a run. Even though specimens had permanent offsets after each test series, cumulative drift ratios are measured relative to the initial position of the specimen at the beginning of a given series. This "artificial zeroing" of cumulative drift at the beginning of each test series is reasonable because 1) the offset of a damaged frame is shifted after strengthening devices (clamps) are applied to said frame (discussed in Section 3.3.1), and 2) infill was set in the deformed shape of frames. Also, drift demands of repaired infilled frames are not sensitive to the accumulation of permanent drift occurring in previous simulations (discussed in Section 4.7).

Absolute differences between peak in-run and peak cumulative drift demands were not larger than 0.5% in each test series (Table 4-1). In runs of the bare frame and frames with clamps, maximum differences between peak in-run and peak cumulative drift demands varied between 0.2% and 0.45% [Table 4-1 (a)] up to drift ratios of nearly 5%. In runs of infilled frames, maximum differences remained smaller than 0.1% [Table 4-1 (b)]. Peak in-run and peak cumulative drift ratios did not differ from one another by more than 0.01% (in absolute terms) in Series F1-M-C-OOP.

Differences between in-run and cumulative drift increased with number of simulations. Total numbers of runs in each series do not represent the number of times most buildings are expected to be shaken in major earthquakes. It is likely that differences between in-run and cumulative drift in buildings in the field would not be larger than the differences observed in this investigation. Absolute differences between peak in-run drift ratios and peak cumulative drift ratios were smaller than 0.1% in 147 out of 175 total simulations (Table 4-1). There is no significant difference in the trends discussed in this investigation whether in-run or cumulative drift ratios are considered.

The variation of lateral load was plotted versus cumulative drift so that measured values of displacement would resemble those measured in typical monotonic and cyclic static-loading tests. In-run drifts were used in figures other than those showing force-displacement relationships because traditionally, peak in-run drifts have been used to quantify drift demands. In-run drifts were tabulated in multiple theses [(Takeda, 1970), (Gulkan & Sozen, 1971), (Aristizabal-Ochoa & Sozen, 1976), (Healey & Sozen, 1978), (Moehle & Sozen, 1978), (Cecen, 1979), (Moehle & Sozen, 1980), (Wolfgram, 1984), (Schultz, 1986), (Wood, 1985) (Bonacci, 1989), (Eberhard & Sozen, 1989)] covering a range of dynamic experiments conducted at the University of Illinois Urbana-Champaign (discussed in Section 5.11.3). Measured peak in-run drift demands of frames with and without infill are discussed next.

4.2 Effect of Infill on Drift Demands

The addition of masonry infill walls to frames reduced drift demands in simulations modeled after the El Centro (TC2) motion as shown in Figure 4-2. In reference runs (R1) only and excluding repeats (discussed in Section 4.6) the bare frame and frames with clamps drifted approximately 3.5 times more than infilled frames on average. Average values were computed as ratios of measured peak in-run drift ratios to measurements of peak base velocity. The trend in Figure 4-2 suggests that for the specimens and ground motions used in this investigation, drift demands of infilled frames were no larger than 30% of the drift demands of frames without infill for nominally identical simulations.

4.3 Initial Period

The fundamental translational periods of vibration of reinforced concrete frames and infilled frames tested in this investigation were computed using initial gross properties. The initial fundamental period T_o was calculated as the product of 2π and the inverse of the natural frequency ω_o of the specimen neglecting the effect of damping on ω_o (Equation 4-1).

$$T_o = \frac{2\pi}{\omega_o} = 2\pi\sqrt{\frac{m}{K_o}} \qquad 4\text{-}1$$

Definitions:

$$T_o = initial\ fundamental\ translational\ period\ of\ specimen$$

$$\omega_o = initial\ fundamental\ natural\ frequency\ of\ specimen$$

$$m = effective\ mass\ of\ specimen$$

$$K_o = initial\ lateral\ stiffness\ of\ specimen$$

The effective mass m of bare and infilled frames tested in-plane was approximately 49,000 lb neglecting half of the mass of infill (<500 lb). This mass included a 44,500-lb concrete block, hardware used to connect concrete block with frame, top beam, and half of columns (Table 4-1). In Series F1-M-C-OOP the effective mass m_{oop} was approximately 4,500 lb, which included hardware, top beam, half of columns, and half of masonry infill wall (Table 4-2). The height h of bare and infilled frames was selected to exceed clear heights of columns of one-story frames and was measured from the top of foundation to centroid of top beam and center of mass of frame-mass system (h = 50 in.) to be consistent with the selection of story heights of multiple-degree-of-freedom structures.

Bare frames were idealized as pairs of reinforced concrete columns with fixed ends (Series F1-B, F1-C, F2-C, F2-C-S). The initial lateral stiffness of bare frames K_{frame} was calculated using Equation 4-2.

$$K_{frame} = 2 * \frac{12E_cI_c}{h^3} = 210\ \frac{kip}{in.} \qquad \text{4-2}$$

Definitions:

$$E_c = elastic\ modulus\ of\ concrete = 3200\ ksi \text{ (Refer to Section 2.3)}$$

$$I_c = moment\ of\ inertia\ of\ column$$

$$h = height\ from\ top\ of\ foundation\ to\ center\ of\ mass\ of\ system = 50\ in.$$

The top beam was assumed to be rigid even though it had a finite flexural stiffness. The ratio of the moment of inertia of the top beam (approximately 5300 in.^{4}) to its length measured between column centerlines (72 in.) is approximately ten times as large as the ratio of the moment of inertia of a single column (approximately 340 in.^{4}) to its height measured from top of foundation to center of mass of system (50 in.). Based on work done by Chalah (2020), the effect of the flexible top beam reduces the initial lateral stiffness of the bare frame by no more than 5% from the result obtained from Equation 4-2 and the corresponding difference in initial periods is approximately 2%.

Infilled frames were idealized as cantilevers made of masonry units with lumped masses at free ends (Series F1-M-C, F2-M, F2-M-C-S). The initial lateral stiffness of infilled frames K_{inf} was calculated using Equation 4-3.

$$K_{inf} = \frac{9}{25} * \frac{3E_m\left(0.75 * I_{inf}\right)}{h^3} = 1000\ \frac{kip}{in.} \tag{4-3}$$

Definitions:

$$E_m = elastic\ modulus\ of\ masonry\ estimated\ to\ be\ 1400\ ksi \text{ (Refer to Section 2.3)}$$

$$I_{inf} = \frac{1}{12} * t_{inf} * (L_{inf} + 8\ in.)^3 = moment\ of\ inertia\ of\ infill\ wall\ (8\ in. \text{ is column dim.})$$

$$t_{inf} = thickness\ of\ infill\ wall = 3.6\ in.$$

$$L_{inf} = length\ of\ infill\ wall = 64\ in.$$

$$h = height\ from\ top\ of\ foundation\ to\ center\ of\ mass\ of\ system = 50\ in.$$

The fraction $\frac{9}{25}$ is a rough estimate used to account for the reduction in lateral stiffness attributable to shear distortions of infill. The coefficient 0.75 is the ratio of net cross-sectional area to gross cross-sectional area of the bricks used to build infill walls (described in Section 1.4.1).

The infilled frame with clamps tested in its out-of-plane direction (Series F1-M-C-OOP) was idealized as a pair of reinforced concrete cantilevers with a lumped mass at their ends (ignoring any stiffening attributable to the infill). The initial lateral stiffness of the infilled frame tested in its weak direction K_{oop} was calculated using Equation 4-4.

$$K_{oop} = 2 * \frac{3E_cI_c}{h^3} = 50\ \frac{kip}{in.} \tag{4-4}$$

Definitions:

$$E_c = elastic\ modulus\ of\ concrete = 3200\ ksi \text{ (Refer to Section 2.3)}$$

$$I_c = moment\ of\ inertia\ of\ column$$

$$h = height\ from\ top\ of\ foundation\ to\ centroid\ of\ top\ beam$$

The estimated initial lateral stiffness of infilled frames (K_{inf} = 1000 kip/in.) is approximately five times larger than the estimated initial lateral stiffness of bare frames (K_{frame} = 210 kip/in.). But the flexibility of the earthquake simulator decreased the effective lateral stiffness of the specimen-simulator system and elongated the periods of the response of specimens. To obtain measurements of deformations of the simulator, four optical targets (described in more detail in Appendix B) were installed along the centerline of the west face of a wide-flange steel beam attached to the simulator (Figure 4-3). The targets were used to measure vertical displacements during simulations of Specimen F2. The target layout and peak displacements of optical targets are illustrated in Figure 4-4 and Figure 4-5.

Peak vertical displacements of optical targets t_1, t_2, and t_3 relative to target t_0 appear to have varied linearly with distance from target t_0 (Figure 4-6) and rotations of lines drawn from t_0 to t_1, t_2, and t_3, computed as the ratio of relative displacement to distance from t_0 (Figure 4-7) are nearly constant independent of the target chosen in runs of Specimen F2. These consistent measurements of rotation suggest that the foundation of the frame and the testing platform rotated as a rigid body (Figure 4-5). Rotations of lines drawn from t_0 to t_3 are used to show the variation of overturning moment with rotation (Figure 4-8). The rotational stiffness (M/θ) of the simulator is defined by Equation 4-5.

$$\frac{M}{\theta} = \frac{F * h}{\frac{\delta_v}{L}} \qquad \text{4-5}$$

Definitions:

$$M = F * h = peak\ overturning\ moment\ at\ top\ of\ foundation$$

$$\theta = peak\ rotation\ of\ simulator$$

$$F = peak\ lateral\ force\ \text{(Obtained from load cell described in Section 2.4.2)}$$

$$h = height\ from\ top\ of\ foundation\ to\ center\ of\ mass\ of\ system$$

$$\delta_v = peak\ vertical\ displacement\ of\ optical\ target\ t_3\ relative\ to\ optical\ target\ t_0$$

$$L = distance\ between\ optical\ targets\ t_0\ and\ t_3$$

In Figure 4-8, the slope of the solid line shows the mean value of M/θ which is approximately $3.6 * 10^6\ \frac{kip-in.}{rad}$. Rearranging the terms in the moment-rotation relationship and projecting the rotation from top of foundation to center of mass of system gives Equation 4-6.

$$K_s = \frac{F}{\delta_h} = \frac{M}{\theta} * \frac{1}{h} * \frac{1}{h} = \frac{F}{\theta * h} \qquad 4\text{-}6$$

Definition:

$$K_s = inferred\ effective\ lateral\ stiffness\ of\ earthquake\ simulator$$
$$= lateral\ force\ (F) \div lateral\ displacement\ (\delta_h)\ caused\ by\ rotation\ (\theta)$$
$$F = peak\ lateral\ force\ at\ height\ h$$
$$\delta_h = peak\ lateral\ displacement\ at\ height\ h$$
$$M = F * h = peak\ overturning\ moment\ at\ top\ of\ foundation$$
$$\theta = peak\ rotation\ of\ simulator$$
$$h = height\ from\ top\ of\ foundation\ to\ center\ of\ mass\ of\ system$$

Estimates of the effective lateral stiffness of the simulator K_s are computed using Equation 4-6 in runs of Specimen F2 (Figure 4-9). The mean K_s represented by the horizontal line drawn in Figure 4-9 is approximately 1500 kip/in.

The initial lateral stiffness K_o estimated assuming fixity at base for each frame configuration is shown in Table 4-3, column 2. Estimates of the effective initial lateral stiffness of the specimen-simulator system were computed by idealizing the frame-simulator system as two springs in series (Equation 4-7) and are listed in column 4 of Table 4-3.

$$K_{eff} = \frac{1}{\frac{1}{K_o} + \frac{1}{K_s}} \qquad 4\text{-}7$$

Definitions:

$$K_{eff} = effective\ lateral\ stiffness$$
$$K_o = initial\ lateral\ stiffness$$
$$K_s = inferred\ effective\ lateral\ stiffness\ of\ the\ simulator$$

The estimated effective initial lateral stiffness of the infilled frame is approximately 3.5 times larger than the estimated effective initial lateral stiffness of the bare frame. Initial K_{eff} of the bare frame (180 kip/in.) is smaller than K_o of the bare frame (210 kip/in.) by 15%. K_s was 50% larger than K_o of infilled frames (1000 kip/in.) and the resulting estimated effective initial lateral stiffness of infilled frames was approximately 600 kip/in. The base was assumed fixed (with zero rotation attributed to simulator) for Series F1-M-C-OOP.

Measurements[1] and estimates of the effective initial lateral stiffnesses and the associated initial translational periods are compared for bare frames and infilled frames (Table 4-4). Measurements of effective lateral stiffnesses K_{eff} were obtained as the ratio of ‘a’ to ‘b’ (Equation 4-8) in initial runs of Series F1-B (Run 1 of Specimen F1), Series F1-M-C (Run 38 of Specimen F1), Series F2-C (Run 1 of Specimen F2), and Series F2-M (Run 70 of Specimen F2):

a) The sum of absolute values of measurements of maximum and minimum lateral forces obtained from load cell placed between specimen and added mass (Section 2.4.2)

b) The sum of absolute values of measurements of maximum and minimum drifts measured in the same run and along the centerline of top beam

$$K_{eff} = \frac{a}{b} = \frac{|\max(F(t))| + |\min(F(t))|}{|\max(\delta(t))| + |\min(\delta(t))|} \qquad 4\text{-}8$$

Definitions:

$$K_{eff} = effective\ lateral\ stiffness$$

$$F(t) = measured\ lateral\ force\ history$$

$$\delta(t) = measured\ drift\ history$$

Equation 4-9 defines the effective translational period T_{eff} for any given run.

$$T_{eff} = 2\pi * \sqrt{\frac{m}{K_{eff}}} \qquad 4\text{-}9$$

Definitions:

[1] Values reported as measurements of lateral stiffness and translational period are inferred from measurements of peak lateral forces and peak drifts.

$$T_{eff} = effective\ translational\ period$$
$$m = effective\ mass$$
$$K_{eff} = effective\ lateral\ stiffness$$

Figure 4-10 compares measured and estimated values of effective initial lateral stiffnesses and initial periods. Initial K_{eff} of the bare frame inferred from measurements obtained in Run 1 of Specimen F1 (F1-B-10-1) is approximately 70% of the estimated value (from Equation 4-7). Measured and estimated initial periods of the bare frame (Specimen F1) differ by 15%. Prior to testing Specimen F2, shrinkage cracks observed near joints at base of columns were expected to reduce the measured initial lateral stiffness of the frame with clamps tested in Series F2-C. Initial K_{eff} inferred from measurements obtained in Run 1 of Specimen F2 (F2-C-RSN6975-PGV2-1) is less than half (approximately 40%) of the estimated initial lateral stiffness of the bare frame and measured and estimated initial periods differ by approximately 40%. There is less error between measurements and estimates for infilled frames. Initial K_{eff} and T_o inferred from measurements obtained during initial runs of tests of infilled frames are within 30% and 10% of estimated K_{eff} and T_o of the infilled frames tested in Series F1-M-C and F2-M.

Free vibration tests were conducted prior to simulations but the structural response died out in less than two seconds and no reliable measurements of fundamental periods of specimens were obtained. It is plausible that large lateral stiffnesses of test specimens (>100 kips/in.) combined with excessive damping attributed to the servoram attached to the simulator platform resisting movement of said platform during intervals between simulations shortened the duration of the free vibration response.

4.4 Force-Displacement Relationship

Frames with masonry infill walls have larger lateral strengths and lateral stiffnesses than similar frames without walls. These two features of infilled frames have been widely reported and were also observed in this investigation. Force-displacement relationships measured in each series tested in this investigation are shown in Figure 4-11 through Figure 4-14. These figures show 1) hysteretic curves and 2) envelopes or ‘backbone’ curves of said hysteretic curves. Each type of curve is explained next.

Hysteretic curves are based on measurements of peak cumulative drift ratios (in both directions) and the associated peak lateral loads obtained in runs of the tested specimens. For each run in a given test series, three line segments were used to connect four data points. The four data points are:

1) Permanent cumulative offset at beginning of run (x-axis) and zero lateral load (y-axis)
2) Peak positive cumulative drift ratio (x-axis) and peak positive lateral load (y-axis)
3) Peak negative cumulative drift ratio (x-axis) and peak negative lateral load (y-axis)
4) Permanent cumulative offset at end of run (x-axis) and zero lateral load (y-axis)

Envelopes of hysteretic curves were constructed using only those data points associated with the largest values of resistance at a given drift.

On average, the bare frame with and without clamps reached 24 kips that corresponds - within 10% - to the estimate:

$$4\frac{M_n}{h_c} = 22\ kip$$

Here M_n = 220 kip-in. is the nominal moment capacity (discussed in Section 1.1) corresponding to a limiting compressive strain in concrete ε_{cu} = 0.004 and h_c = 40 in. is the clear height of columns.

Infilled frames reached 40 kips on average. Although the measured hysteretic curves did not suggest that ‘plateauing’ or yielding occurred (Figure 3-16 and Figure 3-32), this peak lateral load (not lateral strength) corresponds - within 15% - to the estimate of strength obtained using the approximation by Fiorato (1970):

$$2 * 4\frac{M_n}{h_c} + 0.5 * (4.4\ kip) = 46\ kip$$

The expression (defined in Section 1.4.2) by Alwashali (2018) provides a larger estimate:

$$0.07f'_m * \frac{A_{net}}{A_g} * t_{inf} * L_{inf} + 4\frac{M_n}{h_c} = 53\ kip$$

The variation of drift with ground motion parameters is analyzed next.

4.5 Ground Motion Parameters

Drift demands tend to increase with earthquake intensity and intensity can be quantified with ground motion parameters (GMPs). The GMPs studied in this investigation included peak base acceleration (PGA), peak base velocity (PGV), and peak base displacement (PGD). Figure 4-15 shows the variation of drift demands of frames with and without infill in simulations modeled after El Centro (TC2). Each plot in Figure 4-15 shows a linear trend between drift and GMPs with relatively little scatter. Despite the many runs applied to Specimen F2, the trends between drift demand and GMPs of the El Centro (TC2) motion remained nearly linearly suggesting that, whatever the effects of the many repeats (discussed in Section 4.6), the frame remained intact as it kept being tested. The linear trend between drift and each GMP supports the idea that for a given motion, PGA, PGV, and PGD are linearly proportional to each other regardless of the intensity of the motion.

The trend between drift and GMPs is weaker for simulations modeled after the seven motions used in Series F2-C (Figure 4-16). Still, drift increases with intensity but the amount of scatter is larger. To visualize scatter in the mentioned simulations between drift and each GMP, mean ratios of drift ratios to GMPs are indicated in all three plots in Figure 4-16 (using solid black lines). Figure 4-16 also shows lines representing one standard deviation above and below mean values (labeled with dashed gray lines) as well as upper bounding lines passing through the origin and points in each plot such that all points lie along or below said lines (labeled with dashed red lines). Although there is more scatter in the plot showing variation of drift with PGD [Figure 4-16 (c)] than in plots showing drift vs. PGA and PGV [Figure 4-16 (a, b)], between two-thirds and three-quarters of points are within one standard deviation of mean values for all three GMPs. Based on Figure 4-16, the GMP that organized best measured drift demands is PGV for the following reasons:

1) The variation of drift with PGV shows the clearest linear trend. Points in plots showing the variation of drift with PGA and PGD are located further away from mean values and slopes of upper bounding lines are more than 2.5 times as large as mean ratios. In the plot showing drift vs. PGV, the slope of the upper bounding line is less than twice the mean ratio.

2) Differences between target and measured values of peak base acceleration and peak base velocity are as large as 0.1 g and 1 in./sec (Figure 4-17) in runs of Series F2-C. Using mean ratios of drift demand to GMP, a 0.1 g deviation in PGA corresponds to an absolute difference in drift ratio of nearly 0.6% compared with a 1 in./sec. deviation in PGV which corresponds to an absolute difference in drift ratio of approximately 0.3%.

3) PGA is more sensitive to filtering methods than PGV as suggested by Laughery (2016) and discussed in Section 2.5.4. Laughery reported that values of PGA differed by approximately 100% while values of PGV were within 10% of each other for low-pass cut-off frequencies between 15 Hz to 60 Hz. Using the data reported in this investigation tabulated in Table 2-1, maximum differences between values of PGA exceed 100% for the same low-pass cut-off frequencies as mentioned by Laughery while values of PGV are within 5% of each other.

For motions with peak base velocities exceeding 4 in./sec., drifts measured in the most-demanding motions (discussed in Section 5.6) are approximately twice as large as drifts of the least-demanding motions (discussed in Section 5.6) for approximately the same value of PGV. It follows that errors in estimates of drift computed using methods requiring values of PGV would be no less than 50% for a range of ground motions.

The effect of repeats on drift demands is discussed next.

4.6 Effect of Repeats on Drift Demands

Runs were repeated in each series to quantify drift demands of softened structures in subsequent motions. A run is labeled a repeat of another if the displacement inputs used to operate the earthquake simulator in both simulations are nominally identical to each other and both runs occurred in the same series (for the same specimen and in the same configuration). In other words, if the earthquake simulator moved the base of a specimen using the same target motion multiple times within a single series of tests, runs following the reference instance of that motion are labeled repeats. To differentiate between repeats and the reference instance of a motion, runs are abbreviated with the letter ‘R’ followed by a number corresponding to the sequence in which the motions occurred. Reference runs are designated as R1 and repeated runs are designated as R2. In

Series F2-C, some runs were repeated twice and these runs are designated as R2 and R3 according to their sequential order.

To compare between different kinds of repetitions, repeats are divided into three categories:

1) Consecutive repeats (following one another)
2) Repeats separated by motions with similar intensities (with the same target PGV)
3) Repeats separated by at least one stronger motion (with larger target PGV)

Although repeated runs separated by at least one weaker motion are not studied here, it is difficult to imagine that such a scenario would produce drift demands exceeding those in repeats in the second and third categories.

Runs were repeated in series of both specimens. There are 47 repeats in the first category, 24 repeats in the second category, and 54 repeats in the third category (34 repeats in Series F2-C and a total of 20 repeats in other test series). Each series except Series F2-C had repeats in the first category and only series F2-C had repeats in the second category. Each series of tests on Specimen F1 and Series F2-C had repeats in the third category.

4.6.1 Consecutive repeats

For repeats occurring immediately after the reference run, differences between drift ratios in the repeat run (R2) and the reference run (R1) do not exceed 0.2% in absolute terms (Figure 4-18) except in the most intense simulations of Series F1-B (Runs 10-13 of Specimen F1). In the high-intensity motions of the bare frame, the drift reached in the first run with an intensity of 60% (F1-B-60-1) is smaller than the drift reached in the repeated run with an intensity of 60% (F1-B-60-2) by a drift ratio of 0.25% [Figure 4-18 (a-i)]. But the drift in the first run with an intensity of 80% (F1-B-80-1) is larger than the drift in the repeated run with an intensity of 80% (F1-B-80-2) by a drift ratio exceeding 0.3%. Notice that the smoothed displacement spectra (discussed in Section 5.3.3) calculated for the El Centro (TC2) motion with intensities of 60% and 80% using a damping ratio of 2% shows that spectral drift increases with increases in period (Figure 4-19), which does not help explain the observations described.

In runs of infilled frames [Figure 4-18 (b-i)], maximum differences between drift ratios in repeated runs and reference runs are approximately 50% smaller than maximum differences between drift ratios in repeated runs and reference runs of the bare frame [Figure 4-18 (a-i)]. But maximum ratios of drift in R2 to drift in R1 in runs of infilled frames are nearly 25% larger than those in runs of the bare frame [Figure 4-18 (b-ii)] which is the result of comparing drifts in runs causing initial cracking of infill with drifts in runs immediately following them. In runs of the infilled frame tested in it its out-of-plane direction (Series F1-M-C-OOP), maximum absolute differences between drifts in repeated runs and initial runs are no larger than 0.1% [Figure 4-18 (c-i)].

For the 47 repeats in the first category, the absolute difference between drift ratios in consecutive runs is no larger than 0.05% on average.

4.6.2 Repeats Separated by Motions with Similar Intensities

For repeats in the second category in runs of Series F2-C with target PGV of 2, 4, and 6 in./sec., repeat runs (R2) and reference runs (R1) were separated by six motions with the same target PGV. There were three repeats with a target PGV of 8 in./sec. and each repeat run (R2) was separated from the reference run (R1) by at least two motions with a target PGV of 8 in./sec. Maximum differences between drift ratios in R2 and R1 are approximately 0.5% in absolute terms [Figure 4-20 (a)].

The largest ratios of drift in R2 to drift in R1 occurred in low-intensity runs of Series F2-C. In the initial three runs of the series, Specimen F2 remained uncracked and ratios of drift in repeat runs (of the cracked specimen) to drift in reference runs (of the uncracked specimen) are approximately 2.8 on average [Figure 4-20 (b)]. The trend in Figure 4-20 (b) is similar to the shape of the bounding curve representing the function $y = \frac{0.5\% + x}{x}$ and for small values of x (drift ratio), values of y (ratio of drifts) are large.

For the 24 repeats in the second category, the absolute difference between drift ratios in R2 and R1 is 0.25% on average.

4.6.3 Repeats Separated by at least One Stronger Motion

4.6.3.1 Specimen F1

For the 20 repeats in the third category in series of tests on Specimen F1, maximum differences between drift ratios in repeat runs and reference runs do not exceed 0.4% in absolute terms (Figure 4-21). The largest absolute difference in runs of infilled frames (Series F1-M-C, F1-M-C-OOP) is approximately 0.4% [Figure 4-21 (b, c)] but the largest absolute difference in runs of the bare frame and frame with clamps (Series F1-B, F1-C) is not larger than 0.3% [Figure 4-21 (a)].

4.6.3.2 Series F2-C

For the 34 repeats in the third category of Series F2-C, drift in repeat runs (R3) are compared with drift in previous repeat runs (R2) and reference runs (R1). Differences between drifts in R3 and R1 are larger than differences between drifts in R3 and R2 (Figure 4-22). The maximum absolute difference between drift ratios in R3 and R2 is approximately 0.5% and the maximum absolute difference between drift ratios in R3 and R1 is approximately 1% [Figure 4-22 (a)].

For repeats in the third category and for peak in-run drift ratios (in reference runs) exceeding 1.0%, the absolute difference between drift ratios in repeat runs and reference runs is approximately 0.2% on average.

4.6.4 Effects of Cracking and Yielding on Drift Demands

To highlight the effects of cracking and yielding on drift in repeat runs of Series F2-C, runs are sorted into three regions reflecting the state of Specimen F2. Regions are labeled ‘uncracked,’ ‘cracked’ (but not yielded), and ‘yielded’ based on the force-displacement relationship measured in reference runs (R1) and repeat runs (R2) of Series F2-C (Figure 4-23). R3 repeat runs are plotted as black circles and each R3 run occurred after the specimen yielded and drifted to a peak in-run drift ratio of approximately 3.5%. Figure 4-23 is plotted with measurements of peak in-run drift ratios instead of peak cumulative drift ratios.

For simulations of the uncracked and cracked specimen (but not yielded), drift in repeat runs (R2, R3) is larger than drift in the previous runs (R1, R2) by a drift ratio of approximately 0.5% on average [Figure 4-24 (a)]. In the nonlinear range of response, drift in repeat runs exceeds drift in previous runs by a drift ratio of approximately 0.2% on average.

4.6.5 Conclusion

A consistent increase in drift was observed only for repeats 1) not intense enough to cause yielding, and 2) separated by a more-demanding[2] motion (Figure 4-25).

Drift demands of repaired bare and infilled frames are investigated next.

4.7 Effect of Repairs on Drift Demands

In two series of tests, one of a frame without infill (Series F1-B) and another of a frame with infill (Series F2-M), specimens were repaired after inclined cracks formed near column ends. After a 0.075-in. wide inclined crack formed near the top of the north column of the bare frame (Series F1-B), clamps were installed along heights of columns and mortar was used to patch joints where concrete spalling occurred before testing was resumed (as Series F1-C). The frame with clamps drifted more than the bare frame by a drift ratio of 0.2% on average but there was no consistent trend [Figure 4-26 (a)].

After a 0.1-in. wide inclined crack formed at the base of the south column of the infilled frame (Series F2-M), clamps were installed along heights of columns and gypsum was used to fill voids in wall before testing the repaired infilled frame with clamps (Series F2-M-C-S). The repaired infilled frame with clamps drifted more than the infilled frame without clamps by a drift ratio of 0.05% on average [Figure 4-26 (b)].

Although clamps were not designed or expected to control drift, the repairs applied to the infilled frame were effective in that differences in drift demands between the ‘pristine’ and repaired infilled frames consistently decreased with increases in intensity.

[2] Here more-demanding refers to simulations producing larger drift demands than those reached in repeat runs and reference runs.

CHAPTER 5. EVALUATION OF METHODS TO ESTIMATE DRIFT DEMANDS

5.1 Introduction

This chapter is divided into two parts. The first part discusses the reliability of simple methods used to obtain estimates of drift demand relative to observations of drift for the frames with and without infill tested in this investigation. The second part discusses the reliability of the method shown to reduce errors between estimated and measured drift demands (Method 5) extended to include results of other single-degree-of-freedom and multiple-degree-of-freedom reinforced concrete structures with and without infill.

5.2 Part I - Reliability of Simple Methods Used to Estimate Drift Demands

Peak drifts measured in 153 earthquake simulations (described in Sections 3.3 and 3.4) conducted on two one-bay one-story RC frames (Specimens F1 and F2) with three different configurations[1] are compared with estimates of drift computed using five methods. Each method is described next, and plots of measured versus calculated drifts are provided to judge the merits of the methods.

Ranges of measurements

Measured parameter	Unit	Minimum value	Maximum value
Peak base acceleration (PGA)	g	0.1	0.9
Peak base velocity (PGV)	in./sec.	1	11
Peak base displacement (PGD)	in.	0.1	1.8
Compression factor used to scale time step in acceleration record (Section 2.6)		1	5
Peak in-run drift ratio	%	0.03	4.7
Base-shear coefficient		0.02	0.88
Estimated initial period (Section 4.3)	sec.	0.10	0.17
Effective period (Section 5.4)	sec.	0.10	0.74
Fourier period (Section 5.5)	sec.	0.17	0.92

[1] The three configurations were Series F1-B (bare frame), Series F1-C, F2-C, and F2-C-S (frames with clamps), and Series F1-M-C, F2-M, and F2-M-C-S (frames with masonry infill walls tested in-plane).

5.3 Description of Methods

The five methods used to estimate peak displacement (using a given base motion) are:

5.3.1 Methods 1-4

Methods 1-4 are based on the format of the Capacity Spectrum Method (CSM) proposed by Freeman (1975). In this method ground motion demand is represented by a response spectrum produced for increased damping, and capacity is defined by the load-deflection curve of the structure. The intersection of capacity and demand defines the expected drift response. Methods 1-4 make use of a ‘smoothed’ representation of linear response to quantify demand, as well as increased damping to reduce said linear demand. Section 5.3.3 explains how spectra were smoothed and Section 5.3.4 describes increases in damping and reduction of spectra.

Methods 1-4 follow different alternatives to increase damping, reduce demand, and represent initial linear response. Methods also differ in how peak displacement is estimated once damping is selected and the intersection between demand and capacity is set. In Methods 1 and 2, estimated peak displacement corresponds to periods measured during testing. In Methods 3 and 4, estimated peak displacement corresponds to periods defined by intersections between demand and capacity.

5.3.2 Method 5

Method 5 does not require linear spectra nor estimates of increased damping. Instead, estimated peak displacement corresponds to initial period. A summary of the methods used is given below:

Method	Initial damping	Increased damping	Reduction in response	Period associated with solution
1	2%	Eq. 5-3	Eqs. 5-4 and 5-5	T_{eff}
2	2%	Eq. 5-3	Eqs. 5-4 and 5-5	T_{Four}
3	2%	Eq. 5-3	Eqs. 5-4 and 5-5	T_{CSM}
4	5%	Eq. 5-6	Eqs. 5-7 and 5-8	T_{CSM}
5	N/A	N/A	N/A	T_o

T_{eff} is effective period defined in Section 5.4, T_{Four} is 'Fourier period' defined in Section 5.5, T_{CSM} is period defined by intersection of demand and capacity curves, and T_o is initial period estimated using uncracked, gross sections as defined in Section 4.3.

5.3.3 Smoothed Linear Spectra

Methods 1-4 require response spectra. Spectra were calculated for base motions measured using accelerometers attached to foundations of specimens. Spectra were 'smoothed' by eliminating peaks and valleys typical of lightly damped systems by amplifying response spectra calculated for larger damping ratios (Figure 5-1). For each run, spectral amplification factors were computed as the means of ratios of linear response calculated for damping ratios of 2 and 5% to linear response calculated for a damping ratio of 20% for periods between 0.01 and 1.15 seconds. A cut-off period of 1.15 seconds was selected to try to bracket the plausible ranges of interest of periods associated with the tested specimens defined in Section 4.3. Lightly damped smoothed spectra were computed as the products of spectral amplification factors and linear response calculated for a damping ratio of 20% (Equations 5-1 and 5-2).

$$S_{a_{sm}}(\beta_o) = F_{Sa} * S_a(\beta_{20}) \tag{5-1}$$

$$S_{d_{sm}}(\beta_o) = F_{Sd} * S_d(\beta_{20}) \tag{5-2}$$

Definitions:

$$\beta_o = damping\ ratios\ (2\ and\ 5\%)$$

$$\beta_{20} = damping\ ratio\ (20\%)$$

$$S_{a_{sm}} = smoothed\ spectral\ acceleration$$

$$S_{d_{sm}} = smoothed\ spectral\ displacement$$

$$F_{Sa} = spectral\ acceleration\ amplification\ factor$$

$$F_{Sd} = spectral\ displacement\ amplification\ factor$$

$$S_a = spectral\ acceleration$$

$$S_d = spectral\ displacement$$

Amplification factors were computed separately for acceleration and displacement spectra in each run. Average spectral amplification factors in runs of each series are listed in Table 5-1.

5.3.4 Procedures used to Increase Damping to Estimate Drift in Methods 1-4

After generating smoothed spectra for a given damping ratio, spectral demands were overlaid on measured force-displacement or 'capacity' curves (assuming a modal-participation factor of unity) to determine a unique set of force and displacement solutions using the Capacity Spectrum Method (Figure 5-2) proposed by Freeman (1975). If multiple intersections occurred, the one associated with the maximum displacement was selected. Spectral acceleration values were divided by the acceleration of gravity g and measured force values of specimens tested in-plane were divided by effective weight (49 kips) to have consistent units. Force-displacement curves of frames with and without infill are shown in Figure 5-3. Force-displacement curves were obtained by selecting the points of maximum resistance of envelope curves shown in Figure 4-14 and connecting those points with line segments.

If the displacement at the intersection of demand and capacity was larger than the yield displacement, an iterative procedure was carried out to reduce demands by increasing the amount of damping computed as a function of the ductility ratio. Two sets of smoothed demand curves were used: one for a damping ratio of 2% (Methods 1-3), and one for 5% (Method 4). Demands calculated for 2% were reduced using Equations 5-3 through 5-5 [Shibata (1974), Gulkan (1974), Shibata (1976)] and demands calculated for 5% were reduced using Equations 5-6 through 5-8 (Shibata, Saito, & Masuno, 2020) as explained next. These combinations of assumptions of initial demands and increased damping ratios represent different approaches perceived to be common in structural engineering practice.

Following the format by Shibata (1974) and Gulkan (1974) to define increased damping, Equations 5-3 through 5-8 operate on the ratio of peak displacement to yield displacement called ductility. Yield displacement occurred at a drift ratio of approximately 1% for the bare frame and frames with clamps (Figure 5-3). Yield displacements of infilled frames were estimated to be approximately 1%. In iterative steps, damping was increased and demands were reduced until the ductility associated with the displacement at intersection of demand and capacity matched the ductility used to estimate the increased damping (in Equations 5-3 through 5-8).

Equations 5-3 through 5-5 are interpreted to reduce the entire spectral demand curve as a function of damping and ductility (Figure 5-4). But Equations 5-6 through 5-8 are interpreted to reduce the spectral demand curve only for periods larger than the period corresponding to yield displacement (Figure 5-5).

From Shibata (1974):

$$\beta_A = 0.2 * \left(1 - \frac{1}{\sqrt{\mu}}\right) + 0.02 \geq 0.02 \quad \text{5-3}$$

$$S_{a_A} = \frac{8}{6 + 100 * \beta_A} * S_{a_{sm}}(\beta_A) \quad \text{5-4}$$

$$S_{d_A} = \frac{8}{6 + 100 * \beta_A} * S_{d_{sm}}(\beta_A) \quad \text{5-5}$$

From Shibata (2020):

$$\beta_B = 0.25 * \left(1 - \frac{1}{\sqrt{\mu}}\right) + 0.05 \geq 0.05 \quad \text{5-6}$$

$$S_{a_B} = \frac{1.5}{1+10*\beta_B} * S_{a_{sm}}(T_i, \beta_B) \text{ for } T_i > T_y \quad \text{5-7}$$

$$S_{d_B} = \frac{1.5}{1+10*\beta_B} * S_{d_{sm}}(T_i, \beta_B) \text{ for } T_i > T_y \quad \text{5-8}$$

Note: $\mu = \frac{\delta_{sol}}{\delta_y}$, $T_y = 2\pi * \sqrt{\frac{m}{F_y \div \delta_y}}$

Definitions:

$$\beta_A = substitute\ damping\ ratio \text{ (Shibata \& Sozen, 1974)}$$

$$\beta_B = equivalent\ damping\ ratio \text{ (Shibata, Saito, \& Masuno, 2020)}$$

$$S_{a_A} = spectral\ acceleration\ reduced\ using\ substitute\ damping$$

$$S_{d_A} = spectral\ displacement\ reduced\ using\ substitute\ damping$$

$$S_{a_B} = spectral\ acceleration\ reduced\ using\ equivalent\ damping$$

$$S_{d_B} = spectral\ displacement\ reduced\ using\ equivalent\ damping$$

$$\mu = ductility\ ratio$$

$$\delta_{sol} = displacement\ solution$$

$$\delta_y = yield\ displacement$$

$$T_i = period\ of\ oscillator$$

$$T_y = period\ corresponding\ to\ yield\ displacement$$

$$m = effective\ mass = \ 49{,}000\ lb \text{ (Refer to Section 4.3)}$$

$$F_y = lateral\ force\ at\ yield\ displacement$$

Estimates of drift computed using each method are shown in Table 5-2 through Table 5-8.

5.4 Method 1 - Based on Effective Periods Estimated from Measurements of Lateral Stiffness

Method 1 requires an estimate of an effective translational period. This effective period was computed as $2\pi\sqrt{\frac{m}{K_{eff}}}$ with m referring to the measured effective mass (49,000 lb), and K_{eff} referring to effective lateral stiffness calculated from measurements as discussed in Section 4.3 instead of estimates that could be obtained a priori. In that sense, Method 1, as presented here, is not directly applicable to design or structural evaluation. The evaluation presented next was done to try to isolate the variables that affect drift the most.

For each run, drift was approximated as the spectral displacement corresponding to the effective period T_{eff} and a smoothed spectrum reduced (by increasing damping and using Equations 5-3 through 5-5) from the spectrum calculated for a damping ratio of 2% (Figure 5-6). The ductility ratio μ used in Equation 5-3 was selected to correspond to the x-coordinate of the intersection of the curves representing demand and capacity.

Figure 5-7 (a) shows the relationship between measured drifts and drifts computed using Method 1 for Specimens F1 and F2 and the three mentioned test configurations (bare frame, frames with clamps, and infilled frames). Method 1 showed excellent correlation between measurements and estimates. For infilled frames, all estimated drifts were within a drift ratio of 0.25% of measured drifts. For RC frames, estimated drifts were within a drift ratio of 0.5% of measured drifts in approximately 90% of runs of Specimen F1 (Series F1-B and F1-C) and approximately 85% of runs of Specimen F2 (Series F2-C and F2-C-S). Estimates of drift were smaller than measured drifts for drift ratios larger than 2%. Beyond 2%, ductility exceeded 2, and Equation 5-3 produced damping estimates exceeding 8%. The mentioned mismatch suggests that it is plausible that "effective" damping (understood as the increased damping required to match nonlinear response and the response of a linear representation of the softened structure) did not exceed 8%.

5.5 Method 2 - Based on Estimates of Periods Obtained through Fourier Transforms

Method 2 also requires a smoothed spectrum reduced (by increasing damping) from the spectrum calculated for a damping ratio of 2%. Instead of calculating an effective period (from measurements of effective stiffness), the absolute roof acceleration history (obtained from accelerometers mounted on the top beam) was decomposed by a Fourier transform into a range of frequencies and the frequency at the peak Fourier amplitude (f_{Four}) was recorded. For each run, drift was approximated as the spectral displacement corresponding to the associated Fourier period $T_{Four} = (f_{Four})^{-1}$ and the described smoothed spectrum reduced using Equations 5-3 through 5-5 (Figure 5-8). In Equation 5-3, μ was selected again to correspond to the x-coordinate of the intersection of the curves representing demand and capacity. On average, Fourier periods were 0.12 seconds longer than effective periods (Figure 5-9) used for Method 1 (Section 5.4) It follows that estimates of drift computed using T_{Four} (Method 2) would be expected to be larger than estimates of drift computed using T_{eff} (Method 1) as confirmed Figure 5-7.

Estimates computed using Method 2 were larger than measurements in all simulations of infilled frames and <u>absolute</u> errors were larger than 0.5% in nearly half of runs of Series F1-M-C, F2-M, and F2-M-C-S. Fourier periods were 0.08 seconds longer than effective periods on average in runs of frames with uncracked walls [Figure 5-10 (a)]. But in runs following those which caused initial cracking of masonry walls, Fourier periods abruptly increased from approximately 0.23 seconds to 0.34 seconds. It is plausible that this increase in Fourier period relative to effective period affected drift estimated using Method 2 for cracked infilled frames.

In runs of frames without infill, approximately 70% of estimates of drift computed using Method 2 were larger than measured drifts. Absolute errors between estimated and measured drifts were less than 0.5% in approximately 95% of runs of Series F1-B and F1-C and 85% of runs of Series F2-C and F2-C-S. Estimates of drift computed using Fourier periods tended to be smaller than measured drifts for drift ratios larger than 2.5% which suggests again that the increased damping ratios used were too large. But for drift ratios smaller than 2.5% estimates exceeded measurements by a larger margin in runs of infilled frames than in runs of frames without infill.

Methods 1 and 2 require information about the structure that a designer would not have including measurements of the effective lateral stiffness and the period of the softened structure. These methods are included to quantify the minimum error one should expect when estimating drift demand. Based on the results of Methods 1 and 2 and the general trends in Figure 5-7, the idea of a substitute structure suggested by Shibata and Sozen (1974) is reasonable.

5.6 Method 3 - Based on the Capacity Spectrum Method and Increased Damping Estimated using Equations 5-3 through 5-5

Method 3 was an application of the Capacity Spectrum Method as it was intended for use in design and evaluation. Demand was represented by reducing the linear response associated with a damping ratio of 2% using Equations 5-3 through 5-5 (Shibata & Sozen, 1974). Capacity was represented by the load-deflection curves shown in Figure 5-3. Both the ductility ratio μ used in Equation 5-3 and the value of displacement reported here as result of Method 3 correspond to the x-coordinate of the intersection of demand and capacity.

Figure 5-11 (a) shows the variation between measured drifts and drifts computed using Method 3 for Specimens F1 and F2. Approximately 65% of estimates in runs of Series F1-B and F1-C and in all but one run of Series F1-M-C were within a drift ratio of 0.5% of measurements. Estimates of drift of Specimen F2 were not as good. Absolute differences larger than 1.5% were observed and 55% of estimates in runs of Series F2-C had absolute errors larger than 0.5%. Plausible explanations for these large differences follow.

A plausible reason for large differences between measured and calculated drift may be related to spikes that were observed in base acceleration histories in runs causing initial cracking of masonry walls. These spikes resulted in larger spectral displacement demands that amplified drift estimates. In those cases, estimated drifts exceeded measurements by drift ratios larger than approximately 0.5% (0.72% in Series F1-M-C and 0.48% in Series F2-M). But the mentioned spikes did not affect Series F2-C where the worst match (or lack of) between calculations and observations occurred. The main difference between this series (Series F2-C) and other series was related to the sequence of base motions in it. The sequence included a) more repeats and b) a larger set of motions with widely different spectral shapes. It is plausible that the larger errors seen for Series F2-C are related to these differences in testing protocols.

Motion repeats are defined in Section 4.6. To investigate whether repeated motions affected the scatter in Figure 5-11 (a-ii), the data in it were plotted again for all runs [Figure 5-12 (a-i)] and for only reference runs (R1) excluding repeats [Figure 5-12 (a-ii)] of Series F2-C. Approximately half (46%) of estimates in reference runs (R1) had absolute errors larger than 0.5% which was similar to the percentage of estimates with absolute errors larger than 0.5% in all runs of Series F2-C (53%). Excluding repeats did not decrease maximum differences between estimates and observations.

Consider now the mentioned differences in spectral shapes among the seven motions used in Series F2-C that produced the scatter in Figure 5-11 (a-ii). Figure 5-13 shows smoothed displacement spectra calculated for a damping ratio of 2% of the mentioned motions at equivalent peak base velocities at an arbitrary intensity (PGV = 2 in./sec.). The curves in the figure can be classified in two distinct groups of simulated motions: 1) Darfield, San Fernando, Denali, and 2) El Centro (TC2), Northridge, Managua, with El Centro (TC4) being somewhere in between. Spectral displacements of the second group were nearly twice as large as those of the first group for periods between 0.25 and 0.45 seconds. Drift demands in simulations modeled after the El Centro (TC4) motion were closer to drift demands in other simulations in Group 1 and El Centro (TC4) was assumed to be in Group 1. Measurements of effective periods in the mentioned range of 0.25-0.45 seconds were recorded in more than half (53%) of the runs in Group 1 and approximately two-thirds of the absolute differences exceeding 0.5% occurred in runs in Group 1.

Figure 5-14 (a-i) shows measured and calculated drifts for the first group (of less-demanding motions). Figure 5-14 (a-ii) shows the same quantities but for the second group (of more-demanding motions). Comparing estimates of reference runs (R1) with those of repeat runs (R2, R3) showed no difference in maximum differences because large errors occurred in all three types of runs. And only a small reduction was observed in maximum absolute differences from approximately 1.8% to 1.3% in reference runs in Group 1 and Group 2. Nevertheless, there is a clear difference in the scatter in these figures [Figure 5-14 (a)] especially for estimated drift ratios smaller than 1%. Absolute differences larger than 0.5% occurred in approximately two-thirds of Group 1 runs but less than 40% of Group 2 runs which suggests that one problem with the use of CSM as described in Method 3 is that a structure softened by a previous earthquake is treated as if it were a new structure. An explanation of this problem follows.

For a small-intensity motion, the Capacity Spectrum Method produces a displacement estimate (δ_{lin}) at the intersection of spectral demand and the linear portion of the force-displacement curve (represented as 'Capacity' in Figure 5-15). But a structure that has survived a previous and more intense motion (represented as 'Demand (Group 2)' in Figure 5-15) may have an effective lateral stiffness that is much smaller than the initial stiffness ($K_{eff} < K_o$) and an effective period which has elongated from its initial period ($T_{eff} > T_o$). As a result, the intercept of the radial line corresponding to the longer effective period T_{eff} of the 'softer' structure and the demand curve of a less intense motion (represented as 'Demand (Group 1)' in Figure 5-15) can produce a larger drift ($\delta_{eff} > \delta_{lin}$). The demand curve may need to be drawn for increased damping for the case of a structure that has survived a previous earthquake but it is not clear how the additional damping should be quantified. It is plausible that increased damping ratios calculated using Method 3 are too large even for a pristine structure. This idea is investigated next.

It is possible that damping ratios increase too rapidly with ductility as described by Equation 5-3 because maximum absolute differences exceeding 1% were observed in each attempt to isolate the variables affecting the error in the estimation of drift. To avoid the mentioned instances of underestimating drift in runs of less-demanding motions following more-demanding motions [Figure 5-16 (a-i)] referred to here as 'Case A' runs, runs following less-demanding runs only ('Case B' runs) were plotted in Figure 5-16 (a-ii). In other words, a run is classified as a Case B run if measurements in each preceding run were smaller than the drift measured in said run. Similar to the trends observed in runs in Group 1 and Group 2 motions, absolute differences larger than 0.5% occurred in approximately 60% of Case A runs and 40% of Case B runs. And in both cases maximum absolute differences exceeded 1.5%.

All attempts to reduce maximum differences in the estimation of drift using Method 3 to values smaller than 1.5% were unsuccessful. It was decided next to investigate differences between linear and nonlinear response by separating runs of the linear specimen from runs of the nonlinear specimen in Series F2-C. This was done to test the following hypothesis: if the increased damping ratios set by Equation 5-3 are too large, then errors in estimates of drift computed using Method 3 in runs testing a linear specimen (which has not yielded) are smaller than errors of estimates of the nonlinear specimen (which has reached or exceeded its yield displacement). It is clear from Figure 5-17 (a) that the Capacity Spectrum Method as described in Method 3 estimated drift well in runs of the linear specimen but underestimated drift in runs of the nonlinear specimen tested in Series F2-C. All estimates of drift in runs of the linear specimen were within a drift ratio of 0.5% of measurements [Figure 5-17 (a-i)]. But estimates in all but one run of the nonlinear specimen were smaller than measurements and absolute errors larger than 0.5% occurred in more than half of the runs in Series F2-C [Figure 5-17 (a-ii)]. The trend of underestimating drift demands of a nonlinear specimen (in addition to the trends discussed earlier) support the idea that the increased damping ratios computed using Equation 5-3 increase too rapidly with ductility.

5.7 Method 4 - Based on the Capacity Spectrum Method and Increased Damping Estimated using Equations 5-6 through 5-8

Method 4 was also based on the Capacity Spectrum Method but differed from Method 3 in that initial spectral demands were calculated for a damping ratio of 5% and were reduced using Equations 5-6 through 5-8. The ductility ratio μ used in Equation 5-6 and the value of the displacement solution reported in Method 4 correspond to the x-coordinate of the intersection of demand and capacity curves. Each trend discussed in Method 3 holds true for Method 4 but the latter method resulted in more runs with absolute errors exceeding 0.5%.

Approximately 55% of estimates computed using Method 4 were within a drift ratio of 0.5% of measurements in runs of Series F1-B and F1-C [Figure 5-11 (b-i)]. Only two estimates of drift in runs of Series F1-M-C exceeded measurements by a drift ratio larger than 0.5%. There were no absolute errors larger than 0.5% in runs of Series F2-M and F2-M-C-S [Figure 5-11 (b-ii)]. Estimates computed using Method 4 in runs of Series F2-C were not as close to measurements. Approximately two-thirds of estimates in runs of Series F2-C had absolute errors larger than 0.5% [Figure 5-12 (b-i)]. Nearly 30% of estimates had absolute errors larger than 1%. More than half (54%) of measurements in reference runs (R1) of Series F2-C exceeded estimates by a drift ratio larger than 0.5% [Figure 5-12 (b-ii)].

No difference was observed in the number of runs with absolute errors exceeding 0.5% for estimates of drift computed using Methods 3 and 4 in runs in Group 1 (25 of 38 runs) as shown in [Figure 5-14 (b-i)]. But the number of runs in Group 2 with absolute errors exceeding 0.5% increased from 12 to 20 runs for estimates computed using Methods 3 and 4 [Figure 5-14 (b-ii)]. Approximately 75% and 45% of estimates in Case A and Case B runs had absolute errors larger than 0.5% as shown in Figure 5-16 (b). No estimate computed using Method 4 resulted in an absolute error larger than 0.5% in runs of the linear specimen tested in Series F2-C [Figure 5-17 (b-i)] but in approximately 90% of runs of the nonlinear specimen absolute differences were larger than 0.5% [Figure 5-17 (b-ii)].

5.8 Method 5 - Velocity of Displacement Method

Method 5 requires estimates of only two parameters, the initial fundamental translational period of the structure and the peak ground velocity of the earthquake motion. The method was introduced first by Sozen (2003), in a paper titled The Velocity of Displacement, in which he suggested it as a procedure for initial proportioning that does not require detailed information about the structure. The method as it appears in Sozen’s paper was based on the results of dynamic experiments conducted on a small-scale earthquake simulator at the University of Illinois Urbana-Champaign (Sozen, Otani, Gulkan, & Nielsen, 1969).

The Velocity of Displacement (VOD) method is based on the idea that linear oscillators have nearly constant velocity response for intermediate periods in the idealized displacement spectrum developed by Newmark (1973, 1982). Figure 5-18 shows a smoothed displacement spectrum calculated for a damping ratio of 2% using the NS component of the unscaled 1940 El Centro record. The spectrum was divided into three sections representing regions of nearly constant acceleration, velocity, and displacement. For oscillators with periods shorter than two seconds, drift was approximated as the product of initial period and the slope of a line projected from the origin equal to half of the peak ground velocity (PGV). The approximation of drift is observed to be satisfactory for oscillators in regions of nearly constant acceleration and velocity. For periods longer than 2-3 seconds the approximation is not expected to work for similar records.

A plausible derivation of Method 5 is described by Equations 5-9 through 5-16. Linear spectral displacement is related to spectral velocity by the initial fundamental natural frequency of an oscillator computed using uncracked sections (Equation 5-9). Spectral velocity may be expressed as the product of peak base velocity and a velocity amplification factor (Equations 5-10 and 5-11). Newmark (1973, 1982) analyzed vertical and horizontal earthquake spectra calculated using twenty-eight records of strong ground motions and reported amplification factors relating single-degree-of-freedom (SDOF) response to ground motion parameters. A velocity amplification factor $F_v = \pi$ is plausible based on the statistical analysis done by Newmark. Sozen never made this choice explicitly, but Equations 5-12 through 5-16 imply he did use $F_v = \pi$. With that assumption, spectral displacement becomes a function of two terms - peak base velocity and initial period (Equation 5-12). Lepage (1997) suggested multiplying the initial period by the square root of two, based on work by Shimazaki (1984). Equation 5-13 shows the Velocity of Displacement method as it is used today to estimate the maximum lateral displacement of the SDOF system. Equations 5-14 through 5-16 show the method as it is used to estimate peak drift ratio of single-degree-of-freedom structures and peak mean (roof) drift ratio (MDR) and peak story drift ratio (SDR) of multiple-degree-of-freedom (MDOF) structures.

$$S_d * \omega_o = S_v \tag{5-9}$$

$$S_d * \frac{2\pi}{T_o} = PGV * F_v \tag{5-10}$$

$$S_d = \frac{PGV}{2\pi} * F_v * T_o \tag{5-11}$$

$$S_d = \frac{PGV}{2} * T_o \tag{5-12}$$

$$D_{max} = S_d * \sqrt{2} = \frac{PGV}{\sqrt{2}} * T_o \tag{5-13}$$

$$D_{SDOF} = D_{max} \div H_{SDOF} \tag{5-14}$$

$$MDR = D_{max} * \Gamma \div H_r \tag{5-15}$$

$$SDR = D_{max} * \Gamma * (\phi_i - \phi_{i-1}) \div (H_i - H_{i-1}) \tag{5-16}$$

Definitions:

$$S_d = spectral\ displacement$$

$$\omega_o, T_o = initial\ fundamental\ natural\ frequency, period$$
$$S_v = spectral\ velocity$$
$$PGV = peak\ base\ velocity$$
$$F_v = velocity\ amplification\ factor$$
$$D_{max} = \ maximum\ lateral\ displacement\ of\ SDOF$$
$$D_{SDOF} = peak\ drift\ ratio\ of\ SDOF$$
$$H_{SDOF} = height\ of\ SDOF$$
$$MDR = peak\ mean\ (roof)\ drift\ ratio$$
$$\Gamma = fundamental\ mode\ participation\ factor$$
$$H_r = height\ of\ MDOF\ measured\ from\ top\ of\ foundation\ to\ roof$$
$$SDR = peak\ story\ drift\ ratio$$
$$\phi_i = fundamental\ mode\ shape\ ordinate\ at\ level\ i$$
$$\phi_{i-1} = fundamental\ mode\ shape\ ordinate\ at\ level\ i-1$$
$$H_i - H_{i-1} = story\ height\ between\ level\ i\ and\ level\ i-1$$

The advantage of the Velocity of Displacement method is the combination of simplicity and reliability [Laughery (2016), Shah (2021)]. Peak base velocities were calculated for each run by integrating ‘corrected’ measured base acceleration histories (described in detail in Section 2.5.4). Estimated initial periods of bare frames and infilled frames were 0.10 and 0.17 seconds (discussed in Section 4.3). Figure 5-11 (c) shows that drifts computed using VOD (Method 5) reduced error between estimates and observations compared with methods based on the Capacity Spectrum Method as it would be applied knowing only base motion and specimen properties (Methods 3-4). For infilled frames, all estimates of drift computed using VOD were within a drift ratio of 0.5% of measurements. For frames without infill, estimated drifts were within a drift ratio of 0.5% of measured drifts in approximately 70% of runs of Specimen F1 (Series F1-B and F1-C) and approximately 55% of runs of Specimen F2 (Series F2-C and F2-C-S).

Approximately 35% of estimates computed using VOD in runs of Series F2-C had absolute errors exceeding 0.5% and less than 10% of estimates had absolute errors larger than 1%. There was little difference between reference runs (R1) and repeat runs (R2, R3) as absolute differences in each type of run were larger than 0.5% in approximately one-third of both reference and repeat runs

[Figure 5-12 (c)]. For VOD (Method 5), maximum differences were smaller in runs of less-demanding motions (defined as Group 1 in Figure 5-15) than in runs of more-demanding motions (defined as Group 2 in Figure 5-15) as shown in Figure 5-14 (c) which was the opposite trend observed for estimates computed using Methods 3 and 4.

Measurements exceeded estimates computed using VOD by drift ratios exceeding 0.5% in approximately 35% of Case A runs (defined in Section 5.6) and 45% of Case B runs (defined in Section 5.6) as shown in Figure 5-16 (c). For Case A runs, the number of estimates of drift computed using VOD resulting in absolute errors exceeding 0.5% (17 runs) was less than half the number of estimates computed using CSM resulting in absolute errors exceeding 0.5% (37 runs). This difference suggests that estimates of drift obtained using the Velocity of Displacement method (Method 5) are not as sensitive to the plausible effects of previous motions as are estimates computed using the Capacity Spectrum Methods (Methods 3-4).

No estimates of drift in runs of the linear specimen (F2) tested in Series F2-C differed from measurements by a drift ratio larger than 0.5% [Figure 5-17 (c-i)] and approximately half (49%) of measurements exceeded estimates by a drift ratio of at least 0.5% in runs of the nonlinear specimen (F2) as shown in Figure 5-17 (c-ii).

5.9 Comparisons of Results of Methods 3-5

Methods 1 and 2 were shown to be more reliable than Methods 3-5 because the former methods used information about the specimen which would not be known to the designer. To compare methods which could be used in the initial proportioning of a structure, only Methods 3-5 are considered here. Table 5-9 and Table 5-10 summarize the number of runs with absolute errors exceeding 0.5 and 1% of Methods 3, 4, and 5 in runs of each test series. Figure 5-19 shows comparisons of measured and estimated drifts computed using Methods 3-5 in runs of Specimens F1 and F2 subjected to simulations of the El Centro (TC2) motion. The mentioned simulation was selected here as a convenient way to compare results of each method because each test series included multiple runs at different intensities of this motion (55 runs of frames without infill and 34 runs of frames with infill).

For frames without infill, approximately 65% of estimates of drift computed using Methods 3 and 5 were within a drift ratio of 0.5% of measured drifts and no absolute differences were larger than 1%. Both methods estimated drift well within the linear range of response but tended to underestimate measurements exceeding yield displacements (drift demands larger than 1%). On the other hand, Method 4 underestimated drifts in all but a single run simulating the El Centro (TC2) motion and maximum differences exceeded 0.5% and 1% in approximately 50% and 15% of runs of frames without infill.

For frames with infill, there was a single run resulting in an absolute error exceeding 0.5% for estimates of drift computed using Method 3 and there were no instances of absolute errors larger than 0.5% for estimates computed using Method 5 in runs simulating the El Centro (TC2) motion. Two estimates computed using Method 4 resulted in absolute differences exceeding 0.5% and occurred in runs of Series F1-M-C.

Method 3 and Method 5 were observed to be the most reliable methods discussed in this investigation when considering only methods which could be used to estimate drift without detailed knowledge of the structure. Because of 1) the reality of error in the estimation of drift even for meticulously built specimens shaken in simulated motions of known intensities, and 2) the impracticability of predicting drift of actual buildings in unknown future earthquakes, one perspective is to estimate drift using the simplest method if the results are likely to be wrong anyway. There is no denying the simplicity of the Velocity of Displacement method. And to illustrate its reliability, comparisons of measurements and estimates of drift computed using VOD for a wider range of tests are described next.

5.10 Part II - Reliability of the Velocity of Displacement Method

Estimates of drift computed using the Velocity of Displacement method (Method 5) described by Equations 5-14 through 5-16 are compared with measurements of peak drift reached in runs of single-degree-of-freedom and multiple-degree-of-freedom reinforced concrete structures with and without infill walls. Dynamic experiments of RC structures without infill are discussed in Section 5.11 and dynamic experiments of RC structures with infill are discussed in Section 5.12.

5.11 Reinforced Concrete Structures without Infill

5.11.1 Single-Degree-of-Freedom Tests

Test results of single-degree-of-freedom (SDOF) reinforced concrete structures without infill are summarized in Table 5-11. Estimates of peak drift ratios were computed using the Velocity of Displacement method (VOD) given by Equation 5-14. Initial periods were estimated using Equation 4-1. Initial lateral stiffnesses of one-story frames were estimated using Equation 4-2 and initial lateral stiffnesses of cantilevers with lumped masses at tops of cantilevers were estimated using $3E_cI_c/h^3$. The total height of each specimen was taken as the distance from top of foundation to center of mass of system. The effective mass of each specimen was estimated as the sum of mass of reinforced concrete above mid-height of column(s) and additional mass attached to tops of specimens. Additional information about SDOF test structures and base motions are given in Appendix C. Total heights, initial lateral stiffnesses, and effective masses of specimens tested by Bonacci (1989) were obtained using procedures described in Appendix C.

Specimens built by Takeda (1970), Gulkan (1971), Bonacci (1989), and Laughery (2016) were tested using the same earthquake simulator (Sozen, Otani, Gulkan, & Nielsen, 1969) used for the one-story frames tested in this investigation. Reductions in lateral stiffnesses of the mentioned specimens assuming the inferred flexibility of the earthquake simulator (described in Section 4.3) were no larger than 10% of the estimated initial lateral stiffnesses K_o. Because differences in estimates of initial periods T_o were no larger than 5% (considering a mean effective lateral stiffness of simulator K_s = 1500 kip/in.), it is assumed there was no contribution of simulator flexibility to periods of specimens.

Unfortunately, there are no recordings of accelerations measured during tests by Takeda (1970) and Gulkan (1971). But target records and time-compression factors F_{tc} used to scale simulated motions were known. A graphical procedure illustrated in Figure 5-20 was used to approximate graphs of base motions. Target motions as reported by PEER (Ancheta, et al., 2014) were scaled in time and amplitude to match peaks in acceleration graphs. Once a satisfactory match was achieved, the approximate record was integrated with respect to time to obtain an estimate of the peak base velocity (PGV). With a credible approximation of PGV and an estimate of the initial period of a specimen, drift was computed using VOD. A description of each experiment follows.

Takeda (1970) subjected a pair of RC cantilevers to simulated motions modeled after the 1940 El Centro (NS comp.) and 1952 Taft (N21E) earthquakes. Estimates of drift were computed (using Equation 5-14) in three simulations carried out by Takeda. In runs where simulated motions lasted longer than four seconds, estimates were within a drift ratio of 0.5% of measurements (Figure 5-21). Nevertheless, in the one run lasting only two and half seconds ($F_{tc} = 16$), the estimated drift was smaller than the measured drift by a drift ratio exceeding 1.5% indicating that the estimation of drift (computed using VOD) may be less reliable for simulations produced using highly compressed records ($F_{tc} > 10$).

Gulkan (1971) built one-story RC frames with two different sizes and tested them in static and dynamic experiments classified in two test series: H and F. Specimens in Series H had linear dimensions half as long as dimensions of specimens in Series F. Specimens in Series H were subjected to simulated motions modeled after the 1940 El Centro (NS comp.) earthquake and specimens in Series F were subjected to simulated motions modeled after the 1952 Taft (N21E) earthquake. Estimates of drift were computed (using Equation 5-14) for four runs of Series H and ten runs of Series F (Figure 5-22). It was observed that simulations in Series H were less intense than those in Series F: approximations of peak base velocity (PGV) in Series H were no larger than 10 in./sec. but approximations of PGV in each run in Series H exceeded 15 in./sec. Drift ratios measured in Series H were approximately 2% or smaller and drift ratios measured in Series F exceeded 2%. Absolute differences between measurements and estimates were larger than drift ratios of approximately 0.5% in 7 out of 14 runs but no difference was larger than 1.0%.

Bonacci (1989) tested single-degree-of-freedom oscillators. Simulated motions were modeled after the 1940 El Centro (NS comp.), 1952 Taft (Santa Barbara, S48E), and 1971 San Fernando (Castaic, N21E) earthquakes. Approximately 60% of estimates computed using VOD (Equation 5-14) were within a drift ratio of 0.5% of measurements and 10% of estimates had absolute errors larger than 1% (Figure 5-23).

Schoettler (2015) subjected a full-scale reinforced concrete bridge column to simulated motions modeled after records obtained during the 1989 Loma Prieta earthquake. Estimates of drift (computed using Equation 5-14) were smaller than observations and absolute differences between measured and estimated drifts did not exceed a drift ratio of approximately 1% (Figure 5-24).

Laughery (2016) built and tested four one-story RC frames similar to those built and tested by Gulkan (1971). Laughery subjected his frames to simulated motions modeled after the 1994 Northridge (EW comp.) earthquake. All but one estimate of drift computed using VOD (Equation 5-14) were smaller than measured drifts in runs of frames tested by Laughery (Figure 5-25). Approximately two-thirds of measurements exceeded estimates by a drift ratio larger than 0.5% and one-fifth of measurements exceeded estimates by a drift ratio larger than 1%.

Perhaps the most noticeable trend between measurements and estimates of drift computed using the Velocity of Displacement method (Method 5) of the mentioned SDOF tests [Takeda (1970), Gulkan (1971), Bonacci (1989), Laughery (2016)] was the underestimation of drift. Approximately 75% of estimates computed using VOD in runs of the mentioned SDOF tests were smaller than measurements (Figure 5-26). And measurements exceeded estimates by drift ratios exceeding 0.5% in approximately 40% of runs of those SDOF tests. Errors in Figure 5-26 tended to increase with increases in drift ratios exceeding 2% indicating the possibility that damage (cover crushing) may have affected lateral resistance and as a result the dynamic response.

Earlier it was demonstrated that the most effective grouping of runs of Series F2-C eliminating all absolute errors between measurements and estimates computed using VOD exceeding 0.5% was the separation of runs of the linear specimen from runs of the nonlinear specimen (Specimen F2) as shown in Figure 5-17. Comparisons of measured and estimated drifts computed using VOD in reference runs (R1) simulating the El Centro (TC2) motion of the bare frame (Series F1-B) and frames with clamps (Series F1-C, F2-C, F2-C-S) are shown in Figure 5-27. Estimates of drifts nearly matched measurements up to drift ratios of 1.75% in runs of the bare frame [Figure 5-27 (a)] and were within a drift ratio of 0.25% of measurements in low-intensity runs (PGV < 4 in./sec. and DR<1%) of frames with clamps [Figure 5-27 (b)]. But if a simulation was demanding enough to cause 1) yielding and 2) drift ratios larger than 2%, absolute errors between estimates and measurements of drift exceeded 0.5%. In summary, in the tests done in this study as well as the tests done by Takeda (1970), Gulkan (1971), Bonacci (1989), and Laughery (2016), measured drifts tended to exceed the results from the method called VOD here (Equation 5-14) for the assumptions given for SDOF structures.

It is plausible that differences between measured and estimated initial periods of the mentioned SDOF specimens led to absolute errors exceeding 0.5% in Figure 5-26 and Figure 5-27. This idea is explored next.

5.11.2 Comparisons of Estimated and Measured Initial Periods

The Velocity of Displacement method requires an estimate of the initial period of a structure. And the reliability of the method depends on how well estimates of initial period match with measurements. Lepage (1997) reported conservative estimates of drift for SDOF specimens using 1) a method similar to VOD and 2) measured initial periods (Figure 5-28). For the reduced-scale SDOF test specimens described in Section 5.11.1, measured initial periods were approximately 30% larger than estimated initial periods on average (Figure 5-29). The measured initial period of the full-scale bridge column tested by Schoettler (2015) as reported by Shah (2021) was approximately 10% larger than the estimated initial period ignoring any rotational effects of the lumped mass on period. But estimates of initial periods of multiple-degree-of-freedom structures (described in Section 5.11.3) were approximately equal to observations (on average). Scatter in Figure 5-29 is similar for both SDOF and MDOF specimens (with standard deviations of approximately 0.15).

It is plausible that reduced-scale SDOF specimens are more sensitive to the effects of the flexibility of foundation beams on initial periods than reduced-scale MDOF structures. To study the effect of foundation flexibility on period, consider idealized reduced-scale three-bay planar frames within the following ranges:

Parameter	Assumed value or range
Number of stories	1 to 10
Typical story height	50 in.
First story height	50 in. + α
α	0.5 to 2.0
Bay length	72 in.
Column dimensions	8 in by 8 in.
Beam dimensions	20 in. by 8 in.
Story weight	49 kips

Initial fundamental periods were calculated for frames in the defined ranges using the following assumptions:

- The effect of foundation flexibility can be idealized by increasing height of first-story columns
- Shear deformations are negligible
- Axial deformations are negligible
- Rigid offsets in joints are ignored
- Masses are concentrated at floor levels
- Lateral story stiffness k is approximated with an equation proposed by Schultz (1986):

$$k = \frac{24 * E}{h^2} * \frac{1}{\frac{1}{col * k_c} + \frac{1}{bay * k_{tb}} + \frac{1}{bay * k_{bb}}}$$

where E = elastic modulus of concrete, h = story height, l = bay length, col = number of columns, bay = number of bays, I_c = moment of inertia of column, I_{ba} = moment of inertia of top beam, I_{bb} = moment of inertia of bottom beam, $k_c = \frac{I_c}{h}$, $k_{ba} = \frac{I_{ba}}{l}, and\ k_{bb} = \frac{I_{bb}}{l}$.

- Mode shape can be idealized as the sin function within the range from 0 to $\frac{\pi}{2}$

Figure 5-30 shows values of initial fundamental periods T_o estimated using these assumptions (described by equations shown in Figure 5-31) for the idealized planar frames. First-story height was varied to observe the effect of foundation flexibility on initial period. Analogous to the treatment of joints by Lepage (1997) and Shah (2021), the heights of columns h framing into foundation beams were projected into said beams a distance $\alpha * D$, where D is cross-sectional dimension of column in direction of motion. Fraction α was varied from 0.5 to 2.0. The trend in Figure 5-30 suggests that shorter structures (SDOFs) are more sensitive to the flexibility of the foundation than taller structures (MDOFs). Ratios of estimated initial fundamental periods of one-story frames assuming rigid and flexible foundations were approximately 1.25 while those of ten-story frames were less than 1.05 for α = 1.0 (Figure 5-30).

Results of VOD computed for the SDOFs specimens (described in Section 5.11.1) using 1) estimated initial periods increased by 30% (to reflect the mean ratio of measured to estimated periods) and 2) measured initial periods (tabulated in Appendix C) show that means and standard deviations are similar to each other (Figure 5-32) which supports the idea that the effect of foundation flexibility on initial period of an SDOF specimen is not trivial. The mean ratio of measured to estimated drift (computed using the mentioned amplified estimates of initial period) is approximately 0.95 [Figure 5-32 (a)]. This mean is approximately 20% larger than the mean reported by Lepage for SDOFs (Figure 5-28). The use of peak base acceleration (instead of peak base velocity) and characteristic period (similar to the period separating regions of nearly constant acceleration and nearly constant velocity) to approximate spectral response may account for the remaining differences between the two methods - the method proposed by Lepage (1997) and VOD described here. Lepage's method is not explored further in this study because estimates of drift demand computed using the Velocity of Displacement method are larger than measurements (on average) for the SDOF specimens (described in Section 5.11.1) and the method suggested by Sozen (2003) is satisfactorily conservative with the mentioned caveat: increasing estimates of initial period by 30% to approximate measured initial periods of reduced-scale single-degree-of-freedom structures. Comparisons of measured and estimated drift demands of MDOF specimens are discussed next.

5.11.3 Multiple-Degree-of-Freedom Tests

Test results of multiple-degree-of-freedom (MDOF) reinforced concrete structures without infill are summarized in Table 5-12. Estimates of peak roof drift ratios and peak story drift ratios were computed using VOD given by Equations 5-15 and 5-16. Initial fundamental periods of each MDOF specimen were estimated using numerical models created by Shah (2021) assuming linear (elastic) beam-column elements, gross section properties, and no rigid offsets (in joints). For frame specimens with reinforced concrete walls, beam-wall joints were treated as rigid. Story heights and bay lengths were taken as centerline distances. The fundamental mode participation factor Γ and effective modal mass of each specimen were estimated using the linear mode shape obtained from eigenvalue analyses of the mentioned models. Additional information about MDOF test structures and base motions are given in Appendix C.

Estimates of peak roof drift ratio (computed using Equation 5-15) and peak story drift ratio (computed using Equation 5-16) are compared with observations of drift of MDOF structures

(Figure 5-33). VOD produces conservative estimates for peak roof drift in multistory test structures (on average) and approximately 90% of estimates exceed measurements [Figure 5-33 (a)]. Estimates of peak story drift are less conservative relative to observations [Figure 5-33 (b)] and there is more scatter compared with peak roof drift demand. Nevertheless, measured story drift is less than 10% larger (in relative terms) than story drift estimated using Equation 5-16 (on average). Referring to Figure 5-33 (b), it is plausible that linear mode shapes underestimate story drift of MDOFs in the nonlinear range of response for drift ratios exceeding 1.5%. This idea is explored next.

5.11.4 Linear Mode Shapes

For VOD, linear mode shapes of MDOF structures are used to estimate peak drift demand. And although fundamental mode participation factors used to estimate peak roof drift (computed using Equation 5-15) did so conservatively [Figure 5-33 (a)], it is plausible that fundamental mode shape ordinates of multistory structures deviate more from measured displaced shapes of said structures in the nonlinear range of response which leads to more scatter between measured and estimated story drift (computed using Equation 5-16) and less conservative results [Figure 5-33 (b)]. As story mechanisms form, ratios of peak story drift to peak roof drift tend to increase. Based on the measurements of peak drift demand of MDOF specimens listed in Table 5-12, peak story drift is at least 25% larger than peak roof drift in the linear range of response and as much as 300% larger than peak roof drift in the nonlinear range of response (Figure 5-34). Multiplying estimates of peak roof drift (computed using Equation 5-15) by the mean ratio of measured SDR to measured MDR (approximately 1.7) to approximate peak story drift leads to more conservative results (Figure 5-35) than those shown in Figure 5-33 (b).

Based on the trends described in Section 5.11.1 and Section 5.11.3, the Velocity of Displacement method estimated peak roof drift for MDOF structures conservatively but tended to underestimate peak story drift for the same MDOF structures and for SDOF structures. Another plausible explanation for this difference (other than explanations given in Section 5.11.2 and Section 5.11.4) may be related to the time-compression factors (F_{tc}) used to scale simulated motions. Recall that Takeda (1970) scaled a motion using F_{tc} = 16 which resulted in the specimen drifting approximately 3.5% but the estimate of drift computed using Equation 5-14 was approximately half of the measured value. Perhaps larger time-compression factors result in larger errors between observations and estimates of drift demand computed using VOD. This idea is explored next.

5.11.5 Ratio of PGV to PGA

The problem of underestimating drift computed using the Velocity of Displacement method was explored by Laughery (2016). Referring to Figure 5-36, Laughery stated that, in scaled motions with small (scaled) ratios of PGV to PGA, measurements of drift tended to be larger than estimated drifts computed using VOD for both MDOF and SDOF structures. In Figure 5-36, there does seem to be an exponentially decreasing trend in ratio of measured to estimated drift for ratios of PGV to PGA up to 0.03 seconds. Laughery used a low-pass cut-off frequency of 60 Hz when filtering raw acceleration histories (refer to Section 2.5.4 for filtering procedures used for tests done in this investigation). Other data in Figure 5-36 were obtained with low-pass cut-off frequencies between 15 and 25 Hz (Shah, 2021). That discrepancy may have influenced the trend shown in Figure 5-36 (a) as PGA is quite sensitive to filtering choices as discussed next.

Laughery tabulated estimates of PGA and PGV obtained using different low-pass cut-off frequencies ranging from 15 to 60 Hz. Estimates of PGV did not deviate from each other by more than 5% (on average) regardless of the cut-off frequency used. But estimates of PGA obtained using low-pass cut-off frequencies of 15 Hz, 30 Hz, and 45 Hz were on average 50%, 75%, and 90% of estimates of PGA obtained using a low-pass cut-off frequency of 60 Hz. These observations were consistent with trends discussed in Section 2.5.4 and values given in Table 2-1 of ground motion parameters obtained using different low-pass cut-off frequencies.

To address the described effects of the sensitivity of PGA to filtering, Figure 5-36 was recreated using simulations 1) with estimates of PGA and PGV filtered using low-pass cut-off frequencies between 15 and 25 Hz, and 2) modeled after the 1940 El Centro (NS comp.) record scaled in time by two and a half (F_{tc} = 2.5). The second criterion was selected to quantify the range of measured values of PGV/PGA for the same target motion. Tests of MDOF structures done by Aristizabal (1976), Healey (1978), Moehle (1978), Cecen (1979), Moehle (1980), Wood (1985), Schultz (1986), and Eberhard (1989) all used the mentioned target motion. The ratio of PGV to PGA of the unscaled 1940 El Centro (NS comp.) record obtained from PEER (Ancheta, et al., 2014) is approximately 0.1 seconds and the motion scaled in time by 2.5 produces a PGV/PGA of approximately 0.04 seconds.

Figure 5-37 shows the variation of ratios of measured to estimated drift (MDR and SDR) computed using VOD (Equations 5-15 and 5-16) with ratios of PGV to PGA for the same target base motion (1940 El Centro, F_{tc} = 2.5).The plot appears to suggest a weak trend showing a general decrease in the ratio of measured to estimated drift with PGV/PGA. But measurements obtained in tests with ratios of PGV to PGA smaller than 0.03 sec. overestimated PGA by as much as 100% assuming a target PGV/PGA of approximately 0.04 seconds. It is plausible that even with the given assumptions (low-pass cut-off frequencies between 15 and 25 Hz and simulations modeled after the same target motion) there is still too much error associated with measurements of PGA (caused by factors other than filtering methods) and too much variability between the mentioned test specimens to make a definite conclusion about the effect of PGV/PGA on drift.

To isolate the effect of PGV/PGA on drift demands for a single frame configuration, seven simulations with scaled target ratios of PGV to PGA between 0.03 and 0.09 seconds were used in Series F2-C (described in Section 2.6.1). Figure 5-38 (a) shows a weak decreasing trend between ratios of measured to estimated drift computed using VOD (Equation 5-14) and PGV/PGA. There is a stronger trend for average ratios (of drift and PGV to PGA) of each motion [Figure 5-38 (b)]. The trend becomes even stronger for ratios of PGV to PGA multiplied by time-compression factors (Ftc) used to scale each motion (tabulated in Table 2-2) as shown in Figure 5-38 (c), especially for average ratios [Figure 5-38 (d)].

The trend between ratios of measured to estimated drift and ratios of PGV to PGA multiplied by time-compression factors (to approximate unscaled target values of PGV/PGA) is much clearer than the trend between ratios of measured to estimated drift and ratios of PGV to PGA without multiplication by said time-compression factors. This suggests that the effect of time scaling on error associated with estimation of drift computed using VOD seems to be small (for motions with $F_{tc} < 5$) compared with the effect of motions with unscaled ratios of PGV to PGA smaller than approximately 0.075 seconds.

5.11.6 Story Drift Demand of RC Structures without Infill

In notes written for a course given in Jakarta, Indonesia, in 2013, M. Sozen wrote:

"The expectation is that the maximum story drift ratio in a frame with reasonably uniform distribution of mass and stiffness could approach twice the mean drift ratio. It should also be noted that the relatively low drift ratio calculated for the first story is due the arbitrary assumption of fixity at base."

The latter sentence relates to Figure 5-32 which shows that, after a crude consideration of the flexibility of the base, Method 5 (VOD) produced a mean drift ratio of measured to calculated drift of 0.86 for SDOF systems not exceeding a drift ratio of 2% (Figure 5-39). Base flexibility affects SDOFs more than it affects MDOFs. For MDOFs and ignoring base flexibility, Method 5 (VOD) produced a mean ratio of measured to calculated story drift of 1.06 for MDOF systems not exceeding a drift ratio of 2% and for ratios of story to mean drift ratio (SDR/MDR) estimated for linear 'wire-frame' idealizations as described in Section 5.11.3 (Figure 5-40). That mean changes to 0.62 if the ratio SDR/MDR is assumed to be 2.0 as suggested in the first sentence by Sozen (Figure 5-41).

Comparisons of measured and estimated drift computed using VOD (Equations 5-14 through 5-16) for frames with infill are discussed next.

5.12 Reinforced Concrete Structures with Infill

Results of 60 dynamic tests on 8 RC frames with masonry infill walls are studied here. Key parameters of SDOF and MDOF frames with infill are tabulated in Table 5-13. Values of PGV, measured peak drift demand, and estimated drift computed using VOD (Equations 5-14 through 5-16) for each simulation are tabulated in Table 5-14 and Table 5-15. Values of PGV were 1) reported by authors, 2) obtained from raw data, or 3) inferred from target motions in a procedure similar to the procedure described in Section 5.11.1. Additional information about PGV is given in Table 5-14, Table 5-15, and in Appendix C. Foundations of infilled frames were assumed to be rigid and no reduction in lateral stiffnesses of specimens described here because of the flexibility of earthquake simulators was considered. Openings in walls of infilled frames were ignored provided the vertical area of the opening was less than 25% of the total vertical area of the wall.

Initial lateral stiffnesses of infilled frames were estimated using Equation 1-1 and initial fundamental periods of infilled frames were computed using Equation 5-17. Lateral stiffnesses of adjacent bays containing infill were assumed not to increase with the cube of sum of lengths of walls but rather with the sum of cubes of lengths of walls because individual infill panels flanked by RC columns are expected to act independently from adjacent panels resisting lateral load. The total moment of inertia of the infilled frame I_{inf} is computed as the sum of the moments of inertia of individual infilled bays. Story heights and bay lengths were taken as centerline distances. Additional information about infilled frames and base motions are given in Appendix C.

$$T_o = \frac{5}{3} * \frac{2\pi}{3.5} * \sqrt{\frac{m * h^3}{E_m * I_{inf}}} \tag{5-17}$$

Definitions:

$$T_o = initial\ fundamental\ period\ of\ infilled\ frame$$

$$m = effective\ mass\ of\ infilled\ frame$$

$$h = total\ height$$

$$E_m = elastic\ modulus\ of\ masonry\ estimated\ as\ 450 * f'_m$$

$$I_{inf} = \sum_{i=1}^{n} \frac{1}{12} * t_{inf} * L_i^3 = total\ moment\ of\ inertia\ of\ infilled\ frame$$

$$n = total\ number\ of\ infilled\ bays$$

$$t_{inf} = thickness\ of\ infill\ wall$$

$$L_i = distance\ between\ column\ centerlines$$

5.12.1 One-story RC Frames with Infill

Among the 60 runs listed in Table 5-14, 3 runs refer to an SDOF structure comparable to specimens tested in Series F1-M-C, F2-M, and F2-M-C-S. Benavent-Climent (2018) subjected a one-story RC structure with two parallel one-bay frames with full-height infill walls to a series of four simulated motions modeled after the 1980 Campano-Lucano (NS comp.) earthquake (Figure 5-42). Three runs with PGV between 8 and 18 in./sec. resulted in minor to moderate damage in the infilled frame. The fourth and most intense simulation with a PGV of nearly 30 in./sec. severely damaged the specimen and was ignored here. Estimates of drift computed using VOD (Equation

5-14) exceeded measurements of peak drift in all three runs but not by more than a drift ratio of 0.5% (Figure 5-43).

5.12.2 Three-story RC Frames with Infill

Each MDOF structure studied here had three stories and equal story weights. The fundamental mode participation factor Γ calculated for a three-story structure with equal lumped masses assuming a linear mode shape with a unit value associated with the third level (roof) is approximately 1.3 (Figure 5-44). Each MDOF structure also had one or two (in parallel) two-bay frames with infill in the direction of motion. Two-bay three-story infilled frames were idealized as two adjacent and independent continuous masonry walls with equal lumped masses at each level and uniformly distributed lateral stiffnesses along heights of walls (Figure 5-45), assuming a fundamental mode participation factor of 1.3 and fundamental mode shape ordinates of approximately 0.18, 0.55 and 1.0 at first, second, and third levels (Figure 5-44). Additional information about three-story infilled frames and base motions are given in Appendix C.

Lee (2002) subjected a three-story RC frame with infill to simulated motions modeled after the 1952 Taft (N21E) earthquake in two series of tests. The specimen consisted of two parallel two-bay frames oriented in the direction of motion (Figure 5-46). The first series of tests (FIF) was conducted on the specimen with full-height infill walls in each bay of both frames - walls in one set of bays had no openings and walls in the other set had door openings not located next to boundary elements [Figure 5-46 (a)]. After four simulations, infill walls with openings were removed and a second series of tests (PIF) was conducted on the partially infilled frame [Figure 5-46 (d)]. Measurements of peak roof drift were smaller than estimates computed using VOD (Equations 5-15 and 5-16) in runs of both series tested by Lee (Figure 5-47). And estimates of peak roof drift did not exceed measured peak roof drifts by a drift ratio larger than 0.5% except in the most intense simulations. Estimates of peak story drift were larger than measured peak story drifts and absolute differences were less than 0.6% in the two low-intensity simulations (PGV < 4 in./sec.) and less than 1% in the larger intensity simulations (PGV > 6 in./sec.) in both series.

Stavridis (2009) subjected a planar two-bay three-story RC frame with infill to simulated motions modeled after the 1989 Loma Prieta (NS comp.) earthquake. One bay of the frame had full-height walls with no openings and the other bay had full-height walls with window openings not located next to columns (Figure 5-48). All estimates of peak roof drift computed using VOD (Equations 5-15 and 5-16) exceeded measurements and absolute errors were less than 0.5% (Figure 5-49). Measured peak story drift was larger than estimated story drift for the most intense motion but not by a drift ratio larger than 0.55%. For all other simulations, estimates exceeded measurements with absolute differences in peak story drift ratios smaller than 0.5%

Guljas (2020) subjected a three-story RC frame with infill to simulated motions modeled after the 1979 Montenegro (NS comp.) earthquake in two series of tests. The first series of tests (S1) was conducted on a specimen consisting of two parallel frames (oriented in the direction of motion) each of which contained full-height infill walls built with hollow masonry units (Figure 5-50). Walls in one set of bays had no openings and walls in the other set had door and window openings not located next to columns. A single transverse bay (oriented perpendicular to the direction of motion) was infilled with hollow masonry units. After ten simulations, repairs were made to the structure by 1) replacing hollow masonry units with solid clay bricks and 2) installing vertical reinforced concrete confining elements along perimeters of door and window openings located in first and second-story infill walls in frames oriented in the direction of motion (Figure 5-51). A second series of tests (S2) including eleven simulations were conducted on the repaired specimen.

In tests by Guljas, estimates of peak roof and story drift computed using VOD (Equations 5-15 and 5-16) were larger than measured peak roof and story drift in all runs of both series (Figure 5-52). Absolute errors in estimations of peak roof and peak story drift in runs of S2 were less than 0.5%. Absolute errors in estimations of peak roof drift in runs of S1 were less than 0.5% in the first six simulations (PGV < 8 in./sec.) and between 0.8 and 1.2% in the last four simulations (PGV > 14 in./sec.). Absolute differences between measured and estimated peak story drift were within a drift ratio of 0.5% in the first six simulations of S1 and in the next three simulations absolute differences ranged from 0.8% to 1.2%. In the final run of S1 (PGV = 25 in./sec.), estimated peak story drift exceeded measured peak story drift by a drift ratio smaller than 0.6%.

5.12.3 Reliability of VOD for RC Frames with Infill

Measurements and estimates of drift computed using VOD (Equations 5-14 through 5-16) of the infilled frames (described in Chapter 3 and Sections 5.12.1-5.12.2) are shown in Figure 5-53. A parabolic trend between measured drift and estimated drift suggests that the mentioned infilled frames tested in earthquake simulations responded in the region of nearly constant acceleration. Estimates of roof drift demand exceeded measurements of peak roof drift in every test [Figure 5-53 (a)]. And estimates of story drift demand were larger than observations in all runs (considering only reference runs, R1, of specimens tested in this investigation) except for the most intense simulation of the three-story infilled frame tested by Stavridis and in this case the measured story drift exceeded estimated story drift by a drift ratio not larger than 0.55% [Figure 5-53 (b)]. For all other runs, estimated story drift exceeded measurements and absolute differences were smaller than 0.5% in approximately 85% of runs.

For simulations producing roof drift ratios (of MDOF specimens) smaller than 1% and story drift ratios smaller than 1.5%, estimates of drift of infilled frames computed using VOD were satisfactorily conservative and the mentioned equations (Equations 5-14 through 5-16) are therefore deemed useful to make comparisons between estimated drift demands of RC frames with and without infill.

5.13 Summary

The reliability of the Velocity of Displacement method as described by Equation 5-14 through Equation 5-16 (without the modifications proposed in Sections 5.11.2 and 5.11.4) is evaluated relative to measurements from tests of RC frame and wall structures, and RC frames with infill as shown in Figure 5-54 for initial fundamental periods obtained using uncracked, gross cross sections. There is more scatter between measured and estimated story drift demands than between measured and estimated roof drift demands. Mean ratios of measured to estimated roof and story drift computed for frames without infill are approximately twice as large as mean ratios of measured to estimated roof and story drift for frames with infill. It is plausible that estimates of initial fundamental periods computed for frames with infill (Equation 5-17) overestimate measured initial periods while the discussion in Section 5.11.2 suggests that initial fundamental periods of frames without infill underestimate or are approximately equal to measured initial periods.

VOD seems to be less sensitive to the effects of previous loading history and repeats than the Capacity Spectrum Method as described in Methods 3 and 4. Also, VOD is simple and requires only an assumption of a design peak ground velocity and an estimate of the initial period of the structure. To obtain conservative results using VOD for drift ratios up to 6%, it is recommended to amplify 1) estimates of drift (computed using Equation 5-14) in runs of reduced-scale single-degree-of-freedom reinforced concrete structures without infill by a factor of 1.3 (discussed in Section 5.11.2), and 2) estimates of story drift (computed using Equation 5-15) in runs of multiple-degree-of-freedom RC structures without infill by a factor of 1.7 (discussed in Section 5.11.4).

CHAPTER 6. DAMAGE IN SCHOOL BUILDINGS WITH MASONRY INFILL WALLS

6.1 Background

Data from surveys of buildings conducted in the aftermath of earthquakes have been collected since the middle of the twentieth century and this type of data is the most valuable source of evidence about the seismic performance of structures. Unfortunately, because of 1) the subjective nature of the qualification of damage, 2) the difference in experience of the surveyors, 3) the short time periods spent at each building site, 4) the risk of surveying severely damaged buildings, and 5) uncertainties about shaking intensity of ground motions, it is not possible to obtain highly consistent information from surveys of buildings or at a minimum, the data can be more difficult to interpret than other data obtained from experiments in the laboratory. Nevertheless, the surveys are useful in the identification of structural features common in damaged buildings and other beneficial features common in buildings without damage [(Rosenblueth, 1960), (Sozen, 1964)].

Following the 1968 Tokachi-oki-ken earthquake in Japan, Shiga developed a method which organized reinforced concrete buildings by sizes of columns and walls into two regions - likely to be damaged and unlikely to be damaged (Shiga, 1977). Vertical elements resisting lateral loads were quantified using column and wall ratios computed as the ratio of the cross-sectional area of RC columns and RC walls on the ground floor in either direction to total floor area above the ground floor. Shiga also estimated the average axial stress in columns and walls as the ratio of total building weight to the sum of cross-sectional areas of columns and walls on the ground floor oriented in one direction. He assumed a building weight of approximately two hundred pounds per square foot.

Shiga created a figure ("Shiga Map") which shows the variation of average axial stresses in columns and walls (y-axis) with wall ratios (x-axis) and column ratios (decreasing curves) of surveyed Japanese buildings with their corresponding levels of damage (Figure 6-1). Buildings with small axial stresses and large wall ratios were observed to have little or no damage. The influence of columns on damage seems to be small compared with the advantages of structural walls, and no buildings with wall ratios exceeding 0.3% in both directions were severely damaged.

If the mentioned ratio of reinforced concrete shear walls was sufficient to prevent severe damage in Japanese buildings, then it is plausible that a minimum amount of full-height masonry infill walls may reduce the likelihood of severe damage in buildings surveyed elsewhere.

6.2 Surveys from 2007 through 2017

Investigations in the last decade and a half including surveys in the Department of Ica in Peru in 2007 (Sim, et al., 2016), the Meinong District in Taiwan in 2016 (NCREE, Purdue University, 2016), the Province of Manabí in Ecuador in 2016 (Sim, et al., 2016), Mexico City, Mexico in 2017 (Purdue University, 2018), and Pohang, South Korea in 2017 (Sim, Laughery, Chiou, & Weng, 2018) are considered here with a focus on school buildings of one to four stories that contained partial and full-height masonry infill walls (in at least one direction) used primarily as partitions between classrooms, and between classrooms and hallways. A total of 129 surveyed school buildings have been identified. Key properties of the surveyed school buildings are listed in Table 6-1 through Table 6-5. Ground motion parameters measured during earthquakes that affected schools are listed in Table 6-6.

Of the 129 surveyed school buildings selected, over 90% of them contained "captive columns" [Figure 6-2 (a)]. This structural feature has been known to cause damage in buildings [(Rosenblueth, 1960), (Sozen, 1964), (Guevara & Garcia, 2005)]. Levels of structural damage were divided into four classes:

1) None: No observable damage.
2) Light: Hairline inclined and flexural cracks with widths not exceeding 0.005 in. were observed in structural elements.
3) Moderate: Wider cracks (exceeding widths of 0.005 in.) or spalling of concrete was observed.
4) Severe: At least one element had a structural failure or one floor slab lost its elevation.

At least one school building from each survey was reported to not contain any captive columns and none of said buildings had moderate or severe damage [Figure 6-2 (b)]. Approximately one-quarter of schools with captive columns had severe structural damage and nearly 40% had moderate or severe structural damage [Figure 6-2 (c)]. One potential strategy to reduce the likelihood of severe damage in school buildings is removing window sills and infilling openings in partial-height walls to produce enough bays with full-height infill walls in both directions to reduce drift demands of school buildings. Evidence in support of the mentioned strategy based on a case study of a pair of school buildings with captive columns and slightly different amounts of infill is described next.

During the 2007 Pisco, Peru earthquake occurring on August 15, 2007, one station located on a school campus where building surveys were conducted in a city called Ica recorded a PGA of approximately 0.30 g and a PGV of approximately 17 in./sec. (Table 6-6). After the earthquake, it was observed that two two-story school buildings (“SP144” and “SP145”) located within 500 feet of each other having two separate wings per building in the mentioned city were observed to have different levels of damage (Figure 6-3). RC columns flanking partial-height infill walls in exterior bays in school building SP144 were observed to have light or no damage [Figure 6-3 (a)] but exterior columns in another school building with a similar structural layout (SP145) were severely damaged and photographs taken of the latter columns showed disintegration of concrete and exposed longitudinal and transverse reinforcement [Figure 6-3 (b)]. Rough sketches and photographs used to document structural layouts of the surveyed buildings suggest that the east wing of the school building with light damage (SP144) had three fully infilled bays and one infilled bay with a door opening along the middle EW column line [Figure 6-4 (a)]. But the drawing of the west wing of the severely damaged school building (SP145) shows only one infilled bay with a door opening along the middle EW column line [Figure 6-5 (a)]. Photographs showing the extent of damage in school buildings SP144 with fully infilled bays and SP145 with partially infilled bays are shown in Figure 6-4 (b) and Figure 6-5 (b).

Infill wall ratios in each floor-plan direction were computed for these buildings following the format by Shiga. That is, wall ratios were computed as the ratio of gross cross-sectional area of masonry infill walls on the ground floor in one direction to total floor area above the ground floor (example illustrated in Figure 6-6). Lengths and thicknesses of infill walls were documented in sketches of structural layouts. Lengths of walls were taken as distances between centerlines of columns and wall thickness was estimated to be 6 in. Infill was assumed to be solid even if noted otherwise. Openings in bays with infill were assumed to be one-quarter or one-half the lengths of bays which were estimated using photographs and rough sketches. Wall ratios representing the amount of infill wall in the NS direction varied between 0.6% and 1% in east and west wings of both school buildings (Table 6-1). But wall ratios in the EW direction were 0.05% and 0.2% in the west and east wings of building SP145 and approximately 0.35% in both wings of building SP144 which suggests that even modest amounts of infill may be enough to prevent severe damage in RC buildings.

In addition to school buildings SP144 and SP145, surveys of five two and three-story school buildings conducted in the Department of Ica (all located within 50 miles of the mentioned station) showed that approximately 90% of buildings with wall ratios smaller than 0.2% in at least one direction had moderate or severe damage [Figure 6-7 (a)]. One structure housed a staircase leading from the ground floor to classrooms on the second floor but was disconnected from adjacent buildings, and because of the small floor area, the minimum wall ratio was approximately 1.5% and no structural damage was observed in it. It is plausible that a wall ratio of no less than one-quarter of a percent in both directions is sufficient to prevent severe damage in buildings with captive columns in ground motions at similar intensities [Figure 6-7 (b)]. To test the mentioned hypothesis, plots showing infill wall ratios in school buildings surveyed after the other four earthquakes [Meinong (2016), Manabí (2016), Puebla (2018), and Pohang (2018)] are shown in Figure 6-8.

Intensities of earthquakes based on measurements of PGV obtained from stations located near the surveyed schools suggest that the motions in Taiwan and Ecuador were approximately twice as strong as the motions in Mexico and South Korea (Table 6-6). Nevertheless, school buildings in each location with infill wall ratios exceeding 0.25% in both directions had light or no damage (Figure 6-8) except for a few school buildings in Ecuador [Figure 6-8 (b)]. Schools surveyed in Ecuador were replotted in Figure 6-9 (a) with boundaries representing infill wall ratios of 0.5%. Two schools with infill wall ratios exceeding 0.5% in both directions were reported to have severe damage and one school with infill wall ratios exceeding 2% in both directions was reported to have moderate damage [Figure 6-9 (b)]. Photographs of elevations of these buildings and observed damage are shown in Figure 6-10 through Figure 6-12.

Exterior columns of both school buildings reported to have severe damage were exposed to the effects of weathering (Figure 6-10 and Figure 6-11). Photographs taken of the mentioned columns suggest that longitudinal and transverse reinforcement had corroded, and this type of damage could have been classified as moderate instead of severe damage. Photographs taken of the school reported to have moderate damage did not show wide cracks or concrete spalling [Figure 6-12 (a)], but paint wrinkling on column exteriors may have prompted surveyors to indicate there was structural damage [Figure 6-12 (b)].

6.3 Bare Frame and Infilled Frame Prototypes

To provide the reader with a practical example showing that the addition of enough full-height masonry infill walls (in both directions) to a typical low-rise bare frame school building increases the safety of the structure if shaken in earthquakes with intensities similar to those of the strong ground motions described in this chapter, a bare frame prototype and an infilled frame prototype (with an infill wall ratio of at least 0.5% in each direction) are analyzed. Properties of the bare frame prototype are detailed in Table 6-7, Figure 6-14, and Figure 6-15, and properties of the infilled frame prototype are detailed in Table 6-8, Figure 6-16, and Figure 6-17. Prototypes were modeled in a numerical analysis program called STERA 3D (Saito, 2021) using the assumptions listed in Table 6-9. Dimensions of prototypes are based on dimensions of the school buildings described in Section 6.2. To reduce the effects of torsion, floor plans of the RC frame and infill walls are symmetric in both directions.

Initial fundamental periods of the prototypes were estimated using the results from STERA 3D, the procedure described in Section 5.11.2, and Equation 5-17. Initial fundamental periods of the bare frame prototype are calculated to be between 0.55 and 0.65 seconds in both directions. Initial fundamental periods of the infilled frame prototype are calculated to be between 0.1 and 0.4 seconds in both directions. Differences between estimates of initial periods of the infilled frame are approximately three times larger than those of the bare frame which emphasizes the idea that an engineer must contend with unavoidable error in the analysis of frames, especially ones with infill walls. Nevertheless, based on a mean ratio of initial period of bare frame prototype to initial period of infilled frame prototype of 2.5, the infilled frame is expected to drift less than one-third the amount the bare frame drifts assuming 1) drift demand is linear proportional to initial period as suggested by Method 5 (described in Section 5.8) and 2) the mean ratio of measured to estimated drift of frames without infill is approximately twice as large as the mean ratio of measured to estimated drift of frames with infill (described in Section 5.13).

6.4 Summary

Of the schools reported to not contain any captive columns, none had moderate or severe damage. Nevertheless, over 90% of the surveyed schools did contain captive columns. Despite this critical structural weakness, school buildings with masonry infill wall ratios of at least 0.5% in both directions were three times less likely to have severe damage. In other words, the frequency of severe damage observed in buildings was reduced from one out of every four schools to one out of every twelve schools regardless of construction practices and earthquake intensities, based on surveys conducted in five different countries. Infilling enough bays in both directions such that the minimum infill wall ratio exceeds 0.5% is not impractical as more than 70% of the surveyed school buildings have more than 0.5% in at least one direction (Figure 6-13).

CHAPTER 7. EXPERIMENTAL EVIDENCE OF DRIFT CAPACITIES AND DRIFT DEMANDS OF RC FRAMES WITH AND WITHOUT INFILL

7.1 RC Frames with and without Infill

One set of experiments found in the literature provided an answer to the central question posed in this investigation which is “are poorly detailed RC frames with masonry infill walls any safer than similar RC frames without infill walls?”. Drift capacities and drift demands of vulnerable RC frames with and without infill walls were measured and a direct comparison between infilled and bare frames could be made. Lee (2002) tested three specimens on an earthquake simulator, a fully infilled frame (FIF), a partially infilled frame (PIF), and a bare frame (BF). Specimens FIF and PIF are briefly mentioned in Section 5.12.2. Each specimen was shaken in four earthquake simulations at incrementally increasing intensities. Simulated motions had target values of ground motion parameters ranging between 0.12 and 0.4 g and 2.5 and 8.3 in./sec. Measured roof and story drift ratios plotted against peak base velocities for each specimen are shown in Figure 7-1 and Figure 7-2. Best-fit lines drawn in each plot indicate that the fully and partially infilled frames drifted approximately 9 and 3 times less than the bare frame.

No drift capacities were obtained in dynamic tests but monotonic tests were conducted on the partially infilled frame and the bare frame. Roof drift capacities corresponding to a 15% decrease in lateral load carrying capacity were approximately 2% and 2.5% for Specimens PIF and BF (Figure 7-3). Story drift capacities measured in first and second stories of Specimens BF and PIF were approximately 4% and 4.6% (Figure 7-4 and Figure 7-5). It is interesting that the story drift capacity of the infilled frame was larger than that of the bare frame but the latter specimen had a larger roof drift capacity. The partially infilled frame had a story drift capacity no less than 80% of that of the associated bare frame and story drift demands of the partially infilled frame were approximately one-third of the drift demands of the bare frame. This suggests that even modest amounts of infill (WR = 0.7% for Specimen PIF) improve the safety of vulnerable bare frames by increasing the ratio of drift capacity to drift demand for frames with infill.

7.2 Drift Capacities

Chapter 1 and Table 1-2 through Table 1-18 describe the results of monotonic and cyclic lateral load tests of RC frames with masonry infill walls. Recall that Figure 1-8 shows a decreasing trend between measured drift capacities of infilled frames and the ratio of measured lateral strength of infilled frame to estimated lateral strength of the associated bare frame. Using the data obtained from the same experiments described in Chapter 1, Figure 7-6 shows the variation of measured drift capacities of infilled frames with the ratio of estimated initial lateral stiffness of infilled frame (computed using Equation 1-1) to estimated initial lateral stiffness of associated bare frame (estimated assuming fixity at bases of columns). As with ratios of lateral strength, lower-bound drift capacities of infilled frames decreased with increases in ratios of initial lateral stiffness. And the square root of the relative initial lateral stiffness - defined as the ratio of initial lateral stiffness of infilled frame to initial lateral stiffness of the associated bare frame - is a rough estimate of the ratio of drift demands of bare frames to drift demands of similar frames with infill walls assuming drift and initial period are linearly proportional to each other (as suggested by Method 5 discussed in Chapter 5). This crude approximation (square root of relative initial lateral stiffness) is used to compare lower-bound drift capacities with expected drift demands.

Figure 7-7 and Table 1-16 through Table 1-18 show measured drift capacities of the mentioned infilled frames divided by an estimate of the drift capacity of the associated bare frame computed using a lower-bound estimate proposed by Pujol (1999) described by Equation 7-1. Bare frames with estimated drift capacities exceeding 4% were not included in Figure 7-7. This was done to compare the effect of infill on drift capacities of relatively vulnerable frames that were likely to fail in shear. A rapidly decreasing trend between the relative drift capacity (measured drift capacity of infilled frame to estimated lower-bound drift capacity of the associated bare frame) and relative initial lateral stiffness of infilled frames is apparent in Figure 7-7. Nevertheless, in nearly all cases considered drift capacity of the infilled frame is no less than half of the result obtained from Equation 7-1. The mentioned decrease in drift capacity seems to be less pronounced for large values of relative initial lateral stiffness suggesting that reduction in drift capacity can be offset by increases in lateral stiffness resulting in smaller drift demand.

$$\frac{\Delta_{frame}}{h} = \frac{v_s}{v_{max}} * \frac{a}{d} \tag{7-1}$$

Definitions:

$$\Delta_{frame} = estimated\ lower - bound\ story\ drift\ capacity\ of\ bare\ frame$$

$$h = story\ height$$

$$v_s = transverse\ reinforcement\ index = r * f_{yt}$$

$$r = transverse\ reinforcement\ ratio\ in\ column$$

$$f_{yt} = yield\ stress\ of\ transverse\ reinforcement\ in\ column$$

$$v_{max} = maximum\ shear\ demand\ for\ story\ mechanism = n_{col} * 2\frac{M_n}{h_c} * \frac{1}{bd}$$

$$n_{col} = total\ number\ of\ columns$$

$$2\frac{M_n}{h_c} = lateral\ strength\ of\ fixed - fixed\ column$$

$$M_n = moment\ capacity\ of column$$

$$h_c = clear\ height\ of\ column$$

$$b = width\ of\ column$$

$$d = effective\ depth\ of\ longitudinal\ reinforcement\ in\ column$$

$$a = shear\ span\ of\ column = \frac{h_c}{2}\ for\ columns\ in\ double\ curvature$$

7.3 Drift Demands

Drift has been the focus of this investigation. Unfortunately, no measurements of drift were reported for any of the 129 surveyed school buildings (discussed in Chapter 6) which prevented correlating peak drift ratios of buildings with observations of structural damage. But it is possible to estimate wall ratios of the infilled frames tested on earthquake simulators (discussed in Section 5.12). Figure 7-8 shows the variation of measured drift demands with infill wall ratios of the mentioned specimens. Key parameters of infilled frames subjected to simulated earthquakes are listed in Table 7-1. Because not all test structures had slabs, effective weights of specimens (as reported by authors) were projected to floor areas which were used to estimate infill wall ratios as discussed next.

The infill wall ratio of each specimen was computed as the ratio of the cross-sectional area of infill walls in the first story oriented in the direction of motion to the projected floor area (Equation 7-

2). Projected floor areas FA_{proj} were computed as effective weights of specimens divided by 180 pounds per square foot representing the weight of a typical RC building. Here, wall lengths were assumed to be distances between centerlines of boundary elements flanking infill walls. Cross-sectional areas of infill walls were multiplied by the ratio of net cross-sectional area to gross cross-sectional area of masonry unit used to build infill walls.

$$WR = \frac{WA}{FA_{proj}} * \frac{A_{net}}{A_g} \qquad 7\text{-}2$$

Note: $FA_{proj} = \frac{mg}{180\ psf}$

Definitions:

$$WR = infill\ wall\ ratio$$

$$WA = cross - sectional\ area\ of\ infill\ wall$$

$$FA_{proj} = projected\ floor\ area$$

$$A_{net} = net\ cross - sectional\ area\ of\ masonry\ unit$$

$$A_g = gross\ cross - sectional\ area\ of\ masonry\ unit$$

$$m = effective\ mass\ \text{(as reported by authors)}$$

$$g = acceleration\ of\ gravity$$

The average ratio of thickness of infill wall (t_{inf}) to column dimension in the direction of motion was approximately 0.5 for all infilled frames except for the specimens tested by Guljas (2020) for which said ratio was 1.0. Infill wall ratios of specimens tested by Guljas computed using Equation 7-2 were reduced by 50% to adjust for the large ratio of infill thickness to column dimension.

To normalize drift demands of infilled frames, measured drift ratios were divided by peak base velocities measured in each run of each specimen. Although the measured response of infilled frames appeared to operate in the region of nearly constant acceleration as suggested by the parabolic trend between measured drift demand and intensity of motion shown in Figure 5-53, an average ratio of drift ratio to peak base velocity was necessary to compare measured drift demands of infilled frames with estimated drift demands of the associated bare frames.

Mean ratios of peak in-run story drift ratio to peak base velocity are computed for each test series and are tabulated in column 6 of Table 7-1. The resulting mean story drift ratios produced by a peak base velocity of 1 in./sec. are plotted against infill wall ratios to show the effect of infill on drift demands. An upper-bounding curve suggests that the addition of infill walls to frames dramatically reduces story drift demands (Figure 7-8). Another plot showing the variation of peak base velocity (plotted on y-axis) required to produce a story drift ratio of 1% in infilled frames (computed as the inverse of the mentioned mean ratio and tabulated in column 7 of Table 7-1) with the computed infill wall ratio (plotted on x-axis) was created (Figure 7-9). A lower-bounding curve suggests the peak base velocity required to produce similar story drift demands in frames with infill increases rapidly with infill wall ratio.

Series F1-B tested in this investigation and Specimen BF tested by Lee (2002) were assumed to represent typical bare frame structures without infill walls (WR = 0%). In Series F1-B, the mean peak in-run story drift ratio was approximately 0.25% for a peak base velocity of 1 in./sec. and the corresponding mean PGV required to produce a peak story drift ratio of 1% was approximately 4 in./sec. In runs of Specimen BF (tested by Lee), story drift ratios reached approximately 0.15% for a peak base velocity of 1 in./sec. on average and the corresponding PGV required to produce a peak story drift ratio of 1% was approximately 6 in./sec. The curves drawn in Figure 7-8 and Figure 7-9 suggest that a frame with infill and an infill wall ratio of 1% is expected to drift to approximately 1% for a ground motion with a PGV between 15 and 20 in./sec.

7.4 Comparisons of Drift Capacities and Drift Demands

No poorly detailed RC frames with masonry infill walls had measured drift capacities less than approximately half of those of the associated vulnerable bare frames. And the results shown in Figure 7-8 and Figure 7-9 suggest that no infilled frame with an infill wall ratio of 1% or larger drifted more than one-third the amount that bare frames drifted. The implied factor of safety estimated as the ratio of drift capacity to drift demand of the infilled frame with an infill wall ratio of 1% is 50% higher than that of the vulnerable bare frame and an infilled frame with properties similar to the test specimens discussed in this investigation is no less safe than the associated bare frame.

CHAPTER 8. CONCLUSIONS

8.1 Conclusions from This Investigation

- Measured drift demands of one-story RC frames with infill and an estimated wall ratio of approximately 0.5% were no larger than one-third of the measured drift demands of nominally identical one-story RC frames without infill.

- No inclined cracks resulting in a reduction in lateral load capacity formed in runs of specimens with and without infill walls with external clamps installed on columns. Clamps spaced at $d/2$ near column ends were prestressed to resist the total estimated shear demand assuming hinging occurs at column ends. Clamps were fabricated using structural steel angles, threaded rods, and nuts.

- Measured drift demands of structures increased in a nearly linear fashion with peak base velocity (PGV) with less scatter compared with variations of measured drift demands with peak base acceleration (PGA) and peak base displacement (PGD).

- Drift demands of RC frames with and without infill walls were estimated conservatively using a method suggesting that drift is proportional to the product of the initial fundamental period of the structure and the peak base velocity of the base motion (detailed in Sections 5.11 and 5.12).

8.2 Conclusions Drawn from Data Obtained from Other Investigations

8.2.1 Static Tests

- Measured drift capacities of one and two-story RC frames with 1) masonry infill walls, 2) column transverse reinforcement ratios between 0.1 and 0.3% and 3) wall ratios between 0.5 and 2.5% (estimated using axial loads and cross-sectional areas of infill walls) were no less than half of the measured drift capacities of nominally identical one and two-story RC frames without infill.

- Lower-bound ratios of measured drift capacities of infilled frames to estimated lower-bound drift capacities of bare frames were approximately 0.5 for relative initial lateral stiffnesses (defined as the ratio of initial lateral stiffness of infilled frame to estimated initial lateral stiffness of associated bare frame) smaller than 40 and relative lateral strengths (defined as ratio of total lateral strength of infilled frame to estimated lateral strength of associated bare frame) smaller than 7.

- Lower-bound measured drift capacities of infilled frames increased with column transverse reinforcement ratios at a rate of 1% to 1%. Lower-bound measured drift capacities of infilled frames decreased with masonry prism compressive strength at a rate of 1% to 2000 psi and decreased with relative lateral strength at a rate of 1% to 4 (kip/kip).

8.2.2 Dynamic Tests

- For an RC frame of one to three stories with infill and 1) a wall ratio of 1%, 2) a masonry prism compressive strength between 1500 and 3200 psi, and 3) an elastic modulus of masonry between 650 and 1400 ksi, peak story drift demand is expected to be no larger than 1% for a strong ground motion with a peak ground velocity of 15 in./sec. using a lower-bound approximation.

8.3 Conclusions from Data Collected After Earthquakes

- Approximately one out of every four school buildings of one to four stories with captive columns and infill walls with wall ratios between 0 and 3.5% surveyed after earthquakes had severe damage. For buildings with a masonry infill wall ratio of at least 0.5% or larger in each direction, the likelihood of severe damage was reduced to approximately one out of every twelve school buildings.

8.4 Final Note

This final note is about defining the appropriate domain in which the seismic performance of reinforced concrete buildings, including but not limited to school buildings, could be improved by increasing the amount of infill walls in each direction. The mentioned domain would include reinforced concrete frame structures within the following ranges:

Domain	**Range**	**Description**
Number of stories	1-4	Low-rise buildings
Story heights	Uniform	Equal story heights, no short-columns (Guevara, 2005)
	Rectangular	Frames in both directions
Floor plan	Regular	No stiffness discontinuities, initial periods are similar in both directions
	Symmetric	Layout should be symmetric in plan to minimize the effects of torsion
Type of walls	Masonry infill walls	Conclusions apply to masonry infill walls (not to confined masonry walls)
Wall construction	Full-height walls in each story	For bays with infill, walls should run from ground floor to roof such that each story has a full-height infill wall
Thickness of masonry wall	$t_{inf} > 0.4 *$ column dimension	Wall thickness should be no less than 40% of the cross-sectional dimension of the boundary column
Mortar joints	Solid and uniform	Mortar should be used to construct uniformly thick head joints and bed joints around each masonry unit to build 'solid' walls

To increase the safety of vulnerable RC structures in active seismic regions lacking the resources required to implement state-of-the-art retrofit methods, one practical solution is to rearrange enough partial-height infill walls into full-height infill walls in each direction of the structure to obtain infill wall ratios exceeding 1% to reduce the likelihood of severe damage observed often in buildings with captive columns shaken in strong ground motions.

TABLES

Table 1-1: Testing sequence of Specimen F1 and Specimen F2

Specimen	Series	Description of test series	Orientation of frame to direction of motion	Series run count	Run number	Effective mass, lb	Use of load cell to measure lateral forces
F1	F1-B	Bare frame	In-plane	15	1-15	49,000	✓
	F1-C	Frame with clamps	In-plane	22	16-37	49,000	✓
	F1-M-C	Frame with masonry infill wall and clamps	In-plane	19	38-56	49,000	✓
	F1-M-C-OOP	Frame with masonry infill wall and clamps	Out-of-plane	22	57-78	4,500	
F2	F2-C	Frame with clamps	In-plane	69	1-69	49,000	✓
	F2-M	Frame with masonry infill wall	In-plane	9	70-78	49,000	✓
	F2-M-C-S	Frame with masonry infill wall and clamps	In-plane	6	79-84	49,000	✓
	F2-C-S	Frame with clamps	In-plane	13	85-97	49,000	✓

Table 1-2: Summary of tests of bare frames and infilled frames

Source	Year	Specimen ID	Type of frame	Type of test	Number of bays	Number of stories
Mehrabi	1994	1	Bare frame	Monotonic	1	1
		3	Infilled frame	Monotonic	1	1
		4	Infilled frame	Cyclic	1	1
		5	Infilled frame	Cyclic	1	1
		6	Infilled frame	Cyclic	1	1
		7	Infilled frame	Cyclic	1	1
		8	Infilled frame	Monotonic	1	1
		9	Infilled frame	Monotonic	1	1
		10	Infilled frame	Cyclic	1	1
		11	Infilled frame	Cyclic	1	1
		12	Infilled frame	Cyclic	1	1
		13	Infilled frame	Cyclic	2	1
		14	Infilled frame	Cyclic	2	1
Kakaletsis	2007, 2008	B	Bare frame	Cyclic	1	1
		S	Infilled frame	Cyclic	1	1
		IS	Infilled frame	Cyclic	1	1
Imran	2009	1	Infilled frame	Cyclic	1	1
		2	Infilled frame	Cyclic	1	1
Blackard	2009	S	Infilled frame	Cyclic	1	1

Table 1-2 (continued): Summary of tests on bare frames and infilled frames

Source	Year	Specimen ID	Type of frame	Type of test	Number of bays	Number of stories
Baran	2010	SP1	Bare frame	Cyclic	1	2
		SP2	Infilled frame	Cyclic	1	2
		SP3	Infilled frame	Cyclic	1	2
		SP4	Infilled frame	Cyclic	1	2
		SP5	Infilled frame	Cyclic	1	2
		SP7	Infilled frame	Cyclic	1	1
		SP8	Infilled frame	Cyclic	1	1
		SP9	Infilled frame	Cyclic	1	1
Jin	2012, 2013	IFRB	Infilled frame	Cyclic	1	1
		IFFB	Infilled frame	Cyclic	1	1
Cavaleri	2014	S1A-1	Infilled frame	Cyclic	1	1
		S1A-2	Infilled frame	Cyclic	1	1
		S1B-1	Infilled frame	Cyclic	1	1
		S1B-2	Infilled frame	Cyclic	1	1
		S1C-1	Infilled frame	Cyclic	1	1
		S1C-2	Infilled frame	Cyclic	1	1
		S1C-3	Infilled frame	Cyclic	1	1
		S1C-4	Infilled frame	Cyclic	1	1
Al-Nimry	2014	IF4	Infilled frame	Cyclic	1	1
		IF5	Infilled frame	Cyclic	1	1

Table 1-2 (continued): Summary of tests on bare frames and infilled frames

Source	Year	Specimen ID	Type of frame	Type of test	Number of bays	Number of stories
Bose	2016	BF	Bare frame	Monotonic	1	1
		IF-AAC	Infilled frame	Cyclic	1	1
Diawati	2016	BF	Bare frame	Cyclic	1	1
		IFFB	Infilled frame	Cyclic	1	1
		IFSB-wo	Infilled frame	Cyclic	1	1
		IFSB	Infilled frame	Cyclic	1	1
Suzuki	2017	BF	Bare frame	Cyclic	1	1
		1S-1B	Infilled frame	Cyclic	1	1
		1S-2B	Infilled frame	Cyclic	2	1
		2S-1B	Infilled frame	Cyclic	1	2
Alwashali	2018	F-0.4	Infilled frame	Cyclic	1	1
		F-0.6	Infilled frame	Cyclic	1	1
		WM	Infilled frame	Cyclic	1	1
		F-1.5	Infilled frame	Cyclic	1	1
		WB	Infilled frame	Cyclic	1	1
Han	2020	S-NO	Bare frame	Cyclic	1	1
		S-Full	Infilled frame	Cyclic	1	1

Table 1-3: Infill properties of one-bay one-story infilled frames

Source	Specimen ID	$\frac{A_{net}}{A_g}$[1]	t_{inf}[2], in.	L_{inf}[3], in.	f'_m[4], psi	E_m[5], ksi	f_{mortar}[6], psi	Estimated V_{inf}[7], kip
Mehrabi	3	1.0	3.6	84	2200	1400	2300	47
	4	0.52	3.6	84	1500	670	1600	17
	5	1.0	3.6	84	2000	1300	1900	43
	6	0.52	3.6	84	1500	610	2400	16
	7	1.0	3.6	84	2000	1300	2300	42
	8	0.52	3.6	84	1400	740	2300	15
	9	1.0	3.6	84	2100	1200	1800	44
	10	0.52	3.6	116	1500	570	1700	24
	11	1.0	3.6	116	1700	1400	1900	49
	12	1.0	3.6	116	2000	1100	2600	58
Kakaletsis	S	0.64	2.4	47.2	380	100	220	2
	IS	0.77	2.0	47.2	2200	410	250	11
Imran	1	1.0	3.9	59.1	430	-	1600	7
	2	1.0	3.9	59.1	540	-	1500	9
Blackard	S	1.0	7.9	133	2800	-	1200	203

[1] Ratio of net cross-sectional area of masonry unit to gross cross-sectional area of masonry unit (assumed to be unity if not reported by source)
[2] Thickness of infill wall (width of masonry unit unless stated otherwise)
[3] Length of infill wall
[4] Measured gross compressive strength of masonry prism
[5] Measured elastic modulus of masonry prism
[6] Measured compressive strength of mortar coupon
[7] Estimated lateral strength of infill wall (without contribution of the associated bare frame) computed using Equation 1-2

Table 1-3 (continued): Infill properties of one-bay one-story infilled frames

Source	Specimen ID	$\frac{A_{net}}{A_g}$ [1]	t_{inf} [2], in.	L_{inf} [3], in.	f'_m [4], psi	E_m [5], ksi	f_{mortar} [6], psi	Estimated V_{inf} [7], kip
Baran	SP7	0.48	3.5	51.2	1200	-	890	7
	SP8	0.48	3.5	51.2	1100	-	750	7
	SP9	0.48	3.5	51.2	1100	-	710	7
Jin	IFRB	0.68	1.9	35.0	940	1600	-	3
	IFFB	0.68	1.9	35.0	940	1600	-	3
Cavaleri	S1A-1	1.0	8.3	63.0	390	570	440	14
	S1A-2	1.0	8.3	63.0	390	570	440	14
	S1B-1	1.0	5.9	63.0	1300	930	1300	33
	S1B-2	1.0	5.9	63.0	1300	930	1300	33
	S1C-1	1.0	11.8	63.0	250	660	1400	13
	S1C-2	1.0	11.8	63.0	250	660	1400	13
	S1C-3	1.0	11.8	63.0	250	660	1400	13
	S1C-4	1.0	11.8	63.0	250	660	1400	13
Al-Nimry	IF4	1.0	4.7	46.1	2400	-	1700	37
	IF5	1.0	4.7	46.1	2400	-	1700	37
Bose	IF-AAC	1.0	4.9	86.6	350	-	-	10
Diawati	IFFB	1.0	5.5	57.5	420	110	5900	9
	IFSB-wo	1.0	1.7	57.5	2400	630	6500	16
	IFSB	1.0	2.4	57.5	2700	1300	7000	25
Suzuki	1S-1B	0.42	1.9	45.7	1200	670	-	3

Table 1-3 (continued): Infill properties of one-bay one-story infilled frames

Source	Specimen ID	$\frac{A_{net}}{A_g}$ [1]	t_{inf} [2], in.	L_{inf} [3], in.	f'_m [4], psi	E_m [5], ksi	f_{mortar} [6], psi	Estimated V_{inf} [7], kip
Alwashali	F-0.4	1.0	3.9	82.7	2500	1100	2900	57
	F-0.6	1.0	3.9	82.7	2800	1500	4000	64
	WM	1.0	3.9	82.7	1900	790	700	44
	F-1.5	1.0	3.9	78.7	2700	1200	4200	59
	WB	1.0	3.9	82.7	2800	1500	4000	64
Han	S-Full	1.0	3.5	57.9	1200	-	-	17

Table 1-4: Infill properties of two-bay one-story infilled frames

Source	Specimen ID	$\frac{A_{net}}{A_g}$ [1]	t_{inf} [2], in.	L_{inf} [3], in.	f'_m [4], psi	E_m [5], ksi	f_{mortar} [6], psi	Estimated V_{inf} [7], kip
Mehrabi	13	0.52	3.6	168	2000	820	2100	44
	14	1.0	3.6	168	1700	930	2100	72
Suzuki	1S-2B	0.42	1.9	91.3	1200	670	-	6

[1] Ratio of net cross-sectional area of masonry unit to gross cross-sectional area of masonry unit (assumed to be unity if not reported by source)
[2] Thickness of infill wall (width of masonry unit unless stated otherwise)
[3] Length of infill wall
[4] Measured gross compressive strength of masonry prism
[5] Measured elastic modulus of masonry prism
[6] Measured compressive strength of mortar coupon
[7] Estimated lateral strength of infill wall (without contribution of the associated bare frame) computed using Equation 1-2

Table 1-5: Infill properties of one-bay two-story infilled frames

Source	Specimen ID	$\frac{A_{net}}{A_g}$ [1]	t_{inf}[2], in.	L_{inf}[3], in.	f'_m[4], psi	E_m[5], ksi	f_{mortar}[6], psi	Estimated V_{inf}[7], kip
Baran	SP2	0.48	2.7	51.2	1200	-	490	6
	SP3	0.48	3.5	51.2	1200	-	1200	7
	SP4	0.48	3.5	51.2	1200	-	940	7
	SP5	0.48	3.5	51.2	1100	-	510	6
Suzuki	2S-1B	0.42	1.9	45.7	1200	670	-	3

[1] Ratio of net cross-sectional area of masonry unit to gross cross-sectional area of masonry unit (assumed to be unity if not reported by source)
[2] Thickness of infill wall (width of masonry unit unless stated otherwise)
[3] Length of infill wall
[4] Measured gross compressive strength of masonry prism
[5] Measured elastic modulus of masonry prism
[6] Measured compressive strength of mortar coupon
[7] Estimated lateral strength of infill wall (without contribution of the associated bare frame) computed using Equation 1-2

Table 1-6: Procedures used to obtain measurements of initial lateral stiffnesses of infilled frames

Procedure used to measure K_{inf}	Description
DR = 0.05%	Inferred from measurements of lateral loads and drifts obtained at a measured drift ratio of 0.05%
DR = 0.10%	Inferred from measurements of lateral loads and drifts obtained at a measured drift ratio of 0.10%
DR = 0.15%	Inferred from measurements of lateral loads and drifts obtained at a measured drift ratio of 0.15%
50% of V_{max}	Inferred from measurements of lateral loads and drifts obtained at half the lateral strength of the infilled frame at measured drift ratio no larger than 0.2%
First load step	Inferred from measurements of lateral loads and drifts obtained at the end of the first load step at a measured drift ratio no larger than 0.1%
Initial cracking	Inferred from measurements of lateral loads and drifts obtained at initial cracking of masonry infill wall at a measured drift ratio of approximately 0.25%
Uncracked K_{inf}	Inferred from measurements of lateral loads and drifts obtained prior to initial cracking of masonry infill wall at a measured drift ratio no larger than 0.1%

Table 1-7: Initial lateral stiffnesses of one-bay one-story infilled frames

Source	Specimen ID	Procedure used to measure K_{inf}[1]	DR[2], %	L[3], in.	h[4], in.	Estimated E_m[5], ksi	I_{inf}[6], x 10^3 in.^{4}	Measured K_{inf}[7], kip/in.	Estimated K_{inf}[8], kip/in.
Mehrabi	3	50% of V_{max}	<0.15	91	60.5	990	228	740	1100
	4	50% of V_{max}	<0.15	91	60.5	690	228	430	400
	5	50% of V_{max}	<0.15	91	60.5	910	228	1300	1000
	6	50% of V_{max}	<0.20	92	60.5	660	235	480	400
	7	50% of V_{max}	<0.20	92	60.5	890	235	1500	1000
	8	50% of V_{max}	<0.15	91	60.5	620	228	330	360
	9	50% of V_{max}	<0.20	91	60.5	930	228	590	1000
	10	50% of V_{max}	<0.20	123	60.5	690	562	400	990
	11	50% of V_{max}	<0.20	123	60.5	750	562	1500	2000
	12	50% of V_{max}	<0.20	123	60.5	890	562	2000	2400
Kakaletsis	S	Initial cracking	0.25	53.1	35.4	170	29.6	120	80
	IS	Initial cracking	0.25	53.1	35.4	990	25.6	120	470
Imran	1	Uncracked K_{inf}	<0.10	65.9	64.0	190	94.1	130	80
	2	Uncracked K_{inf}	<0.10	65.9	64.0	240	94.1	220	90
Blackard	S	-	-	144	80.8	1200	1960	-	5000

[1] Procedure used to obtain measured initial lateral stiffness of infilled frame as specified in Table 1-6
[2] Drift ratio associated with measurement of initial lateral stiffness
[3] Distance between column centerlines
[4] Total height of infilled frame (clear height of column plus half of depth of top beam)
[5] Estimated elastic modulus of masonry computed as $E_m = 450 * f'_m$
[6] Moment of inertia of masonry infill wall computed as $I_{inf} = \frac{1}{12} * t_{inf} * L^3$
[7] Measured initial lateral stiffness as reported by source and measured as indicated in column 3
[8] Estimated initial lateral stiffness computed using Equation 1-1

Table 1-7 (continued): Initial lateral stiffnesses of one-bay one-story infilled frames

Source	Specimen ID	Procedure used to measure K_{inf}[1]	DR[2], %	L[3], in.	h[4], in.	Estimated E_m[5], ksi	I_{inf}[6], x 10^3 in.^{4}	Measured K_{inf}[7], kip/in.	Estimated K_{inf}[8], kip/in.
Baran	SP7	First load step	<0.05	55.1	32.5	520	48.8	550	380
	SP8	First load step	<0.10	55.1	32.5	510	48.8	340	370
	SP9	First load step	<0.10	55.1	32.5	500	48.8	340	370
Jin	IFRB	-	-	39.4	31.9	420	9.6	-	90
	IFFB	-	-	39.4	27.4	420	9.6	-	150
Cavaleri	S1A-1	-	-	70.9	70.9	170	245	-	130
	S1A-2	-	-	70.9	70.9	170	245	-	130
	S1B-1	-	-	70.9	70.9	570	175	-	300
	S1B-2	-	-	70.9	70.9	570	175	-	300
	S1C-1	-	-	74.8	70.9	110	412	-	140
	S1C-2	-	-	74.8	70.9	110	412	-	140
	S1C-3	-	-	74.8	70.9	110	412	-	140
	S1C-4	-	-	74.8	70.9	110	412	-	140
Al-Nimry	IF4	50% of V_{max}	<0.20	52.8	42.2	1100	57.8	590	900
	IF5	50% of V_{max}	<0.20	52.8	42.2	1100	57.8	840	900
Bose	IF-AAC	DR = 0.15%	0.15	94.5	56.3	160	346	360	330
Diawati	IFFB	-	-	63.0	50.2	190	115	-	190
	IFSB-wo	-	-	63.0	50.2	1100	36.1	-	330
	IFSB	-	-	63.0	50.2	1200	49.2	-	510
Suzuki	1S-1B	-	-	50.0	29.9	550	19.5	-	180

Table 1-7 (continued): Initial lateral stiffnesses of one-bay one-story infilled frames

Source	Specimen ID	Procedure used to measure K_{inf}[1]	DR[2], %	L[3], in.	h[4], in.	Estimated E_m[5], ksi	I_{inf}[6], x 10^3 in.^{4}	Measured K_{inf}[7], kip/in.	Estimated K_{inf}[8], kip/in.
Alwashali	F-0.4	DR = 0.05%	0.05	90.6	63.0	1100	244	1400	1200
	F-0.6	DR = 0.05%	0.05	90.6	63.0	1300	244	1400	1300
	WM	DR = 0.05%	0.05	90.6	63.0	870	244	1300	910
	F-1.5	DR = 0.05%	0.05	90.6	63.0	1200	244	1400	1300
	WB	DR = 0.05%	0.05	90.6	63.0	1300	244	1100	1300
Han	S-Full	DR = 0.10%	0.10	66.1	72.0	550	85.4	170	140

Table 1-8: Initial lateral stiffnesses of two-bay one-story infilled frames

Source	Specimen ID	Procedure used to measure K_{inf}[1]	DR[2], %	L[3], in.	h[4], in.	Estimated E_m[5], ksi	I_{inf}[6], x 10^3 in.^{4}	Measured K_{inf}[7], kip/in.	Estimated K_{inf}[8], kip/in.
Mehrabi	13	50% of V_{max}	<0.15	91	60.5	900	455	830	1000
	14	50% of V_{max}	<0.20	91	60.5	760	455	1500	1700
Suzuki	1S-2B	-	-	50.0	29.9	550	39.0	-	360

[1] Procedure used to obtain measured initial lateral stiffness of infilled frame as specified in Table 1-6
[2] Drift ratio associated with measurement of initial lateral stiffness
[3] Distance between column centerlines (of one bay of two-bay infilled frames)
[4] Total height of infilled frame (clear height of column plus half of depth of top beam)
[5] Estimated elastic modulus of masonry computed as $E_m = 450 * f'_m$
[6] Moment of inertia of masonry infill wall computed as $I_{inf} = 2 * \frac{1}{12} * t_{inf} * L^3$ (for two-bay infilled frames)
[7] Measured initial lateral stiffness as reported by source and measured as indicated in column 3
[8] Estimated initial lateral stiffness computed using Equation 1-1

Table 1-9: Initial lateral stiffnesses of one-bay two-story infilled frames

Source	Specimen ID	Procedure used to measure K_{inf}[1]	DR[2], %	L[3], in.	h[4], in.	Estimated E_m[5], ksi	I_{inf}[6], x 10^3 in.^{4}	Measured K_{inf}[7], kip/in.	Estimated K_{inf}[8], kip/in.
Baran	SP2	-	-	55.1	67.9	560	37.9	-	35
	SP3	-	-	55.1	67.9	550	48.8	-	44
	SP4	-	-	55.1	67.9	530	48.8	-	42
	SP5	-	-	55.1	67.9	480	48.8	-	39
Suzuki	2S-1B	-	-	50.0	62.0	550	19.5	-	20

[1] Procedure used to obtain measured initial lateral stiffness of infilled frame as specified in Table 1-6
[2] Drift ratio associated with measurement of initial lateral stiffness
[3] Distance between column centerlines
[4] Total height of infilled frame (from top of foundation to mid-depth of topmost beam)
[5] Estimated elastic modulus of masonry computed as $E_m = 450 * f'_m$
[6] Moment of inertia of masonry infill wall computed as $I_{inf} = \frac{1}{12} * t_{inf} * L^3$
[7] Measured initial lateral stiffness as reported by source and measured as indicated in column 3
[8] Estimated initial lateral stiffness computed using Equation 1-1

Table 1-10: Properties of reinforced concrete columns of one-bay one-story infilled frames

Source	Specimen ID	h_c[1], in.	a[2], in.	b[3], in.	d[4], in.	s[5], in.	r[6], %	v_s[7], psi	f'_c[8], psi	E_c[9], ksi	$\frac{P}{f'_c A_g}$[10]	Estimated M_n[11], kip-in.
Mehrabi	3	56	28	7.0	5.8	2.5	0.6	300	4500	3200	0.15	300
	4	56	28	7.0	5.8	2.5	0.6	300	3900	2500	0.17	290
	5	56	28	7.0	5.8	2.5	0.6	300	3000	2600	0.22	270
	6	56	28	8.0	6.7	1.5	0.8	440	3800	2900	0.14	470
	7	56	28	8.0	6.7	1.5	0.8	440	4900	2700	0.11	500
	8	56	28	7.0	5.8	2.5	0.6	300	3900	2500	0.17	290
	9	56	28	7.0	5.8	2.5	0.6	300	3900	2500	0.17	290
	10	56	28	7.0	5.8	2.5	0.6	300	3900	2900	0.17	290
	11	56	28	7.0	5.8	2.5	0.6	300	3700	2600	0.18	280
	12	56	28	7.0	5.8	2.5	0.6	300	3900	2900	0.26	300
Kakaletsis	S	31.5	15.8	5.9	5.3	1.3	0.3	90	4100	3700	0.08	70
	IS	31.5	15.8	5.9	5.3	1.3	0.3	90	4100	3700	0.08	70

---

[1] Clear height of column
[2] Shear span of column (half of clear height of column)
[3] Width of column (out-of-plane dimension)
[4] Effective depth of column
[5] Spacing of transverse reinforcement in column (spacing near column ends if multiple spacings)
[6] Transverse reinforcement ratio in column
[7] Transverse reinforcement index computed as $v_s = r * f_{yt}$ where f_{yt} is yield stress of transverse reinforcement in column
[8] Measured compressive strength of concrete cylinder
[9] Measured elastic modulus of concrete cylinder or computed as $E_c = 57{,}000 * \sqrt{f'_c}$ if not reported by source
[10] Axial load ratio where A_g refers to gross cross-sectional area of column
[11] Estimated moment capacity of column corresponding to a limiting compressive strain in concrete ε_{cu} = 0.004 (described in Section 1.1)

Table 1-10 (continued): Properties of reinforced concrete columns of one-bay one-story infilled frames

Source	Specimen ID	h_c[1], in.	a[2], in.	b[3], in.	d[4], in.	s[5], in.	r[6], %	v_s[7], in.	f'_c[8], psi	E_c[9], ksi	$\frac{P}{f'_c A_g}$[10]	Estimated M_n[11], kip-in.
Imran	1	59.1	29.5	6.9	5.6	5.3	0.5	200	3900	3600	0	150
	2	59.1	29.5	6.9	5.6	5.3	0.5	200	3800	3500	0	150
Blackard	S	73.5	36.8	11	9.9	10.5	0.1	90	4400	3800	0.07	540
Baran	SP7	29.5	14.8	5.9	3.3	3.9	0.2	50	2300	2700	0.25	40
	SP8	29.5	14.8	5.9	3.3	3.9	0.2	70	1600	2200	0.13	30
	SP9	29.5	14.8	5.9	3.3	3.9	0.2	50	1400	2100	0.13	30
Jin	IFRB	24.0	12.0	4.3	3.5	2.8	0.2	110	4200	3000	0.14	40
	IFFB	24.0	12.0	4.3	3.5	2.8	0.2	110	4200	3000	0.14	40
Cavaleri	S1A-1	63.0	31.5	7.9	6.6	3.9	0.3	190	3600	3700	0.20	220
	S1A-2	63.0	31.5	7.9	6.6	3.9	0.3	190	3600	3700	0.20	220
	S1B-1	63.0	31.5	7.9	6.6	3.9	0.3	190	3600	3700	0.20	220
	S1B-2	63.0	31.5	7.9	6.6	3.9	0.3	190	3600	3700	0.20	220
	S1C-1	63.0	31.5	11.8	10.5	3.9	0.2	120	3600	3700	0.09	450
	S1C-2	63.0	31.5	11.8	10.5	3.9	0.2	120	3600	3700	0.09	450
	S1C-3	63.0	31.5	11.8	10.5	3.9	0.2	120	3600	3700	0.09	450
	S1C-4	63.0	31.5	11.8	10.5	3.9	0.2	120	3600	3700	0.09	450
Al-Nimry	IF4	40.3	20.1	3.9	6.1	2.6	0.5	420	3000	3100	0.14	80
	IF5	40.3	20.1	3.9	6.1	2.6	0.5	420	3000	3100	0.10	80
Bose	IF-AAC	52.4	26.2	7.9	7.1	2.0	1.0	590	5500	4200	0.03	230

Table 1-10 (continued): Properties of reinforced concrete columns of one-bay one-story infilled frames

Source	Specimen ID	h_c[1], in.	a[2], in.	b[3], in.	d[4], in.	s[5], in.	r[6], %	v_s[7], in.	f'_c[8], psi	E_c[9], ksi	$\frac{P}{f'_c A_g}$[10]	Estimated M_n[11], kip-in.
Diawati	IFFB	39.4	19.7	5.5	4.7	3.9	0.2	130	3000	2800	0.23	80
	IFSB-wo	39.4	19.7	5.5	4.7	3.9	0.2	130	3900	3200	0.18	80
	IFSB	39.4	19.7	5.5	4.7	3.9	0.2	130	4000	3500	0.17	80
Suzuki	1S-1B	27.8	13.9	4.3	3.4	1.0	0.9	520	3500	3000	0.13	30
Alwashali	F-0.4	55.1	27.6	7.9	6.8	3.9	0.3	200	3500	3400	0.21	210
	F-0.6	55.1	27.6	7.9	6.7	2.0	1.6	880	3700	3500	0.20	320
	WM	55.1	27.6	7.9	6.7	2.0	1.6	880	3700	3500	0.19	320
	F-1.5	55.1	27.6	11.8	10.4	3.2	1.3	730	4100	3900	0.08	830
	WB	58.1	29.0	7.9	6.7	2.0	1.6	880	3400	3400	0.21	320
Han	S-Full	66.1	33.1	8.3	6.8	7.1	0.1	70	3700	3500	0.14	530

Table 1-11: Properties of reinforced concrete columns of two-bay one-story infilled frames

Source	Specimen ID	h_c[1], in.	a[2], in.	b[3], in.	d[4], in.	s[5], in.	r[6], %	v_s[7], psi	f'_c[8], psi	E_c[9], ksi	$\frac{P}{f'_c A_g}$[10]	Estimated M_n[11], kip-in.
Mehrabi	13	56	28	7.0	5.8	2.5	0.6	310	4000	2800	0.17	290
	14	56	28	7.0	5.8	2.5	0.6	310	4000	2800	0.17	290
Suzuki	2B-1S	27.8	13.9	4.3	3.4	1.0	0.9	520	3500	3000	0.13	30

Table 1-12: Properties of reinforced concrete columns of one-bay two-story infilled frames

Source	Specimen ID	h_c[1], in.	a[2], in.	b[3], in.	d[4], in.	s[5], in.	r[6], %	v_s[7], in.	f'_c[8], psi	E_c[9], ksi	$\frac{P}{f'_c A_g}$[10]	Estimated M_n[11], kip-in.
Baran	SP2	29.5	14.8	5.9	3.3	3.9	0.2	50	1900	2500	0.11	31
	SP3	29.5	14.8	5.9	3.3	3.9	0.2	50	1800	2400	0.11	31
	SP4	29.5	14.8	5.9	3.3	3.9	0.2	50	2400	2800	0.19	37
	SP5	29.5	14.8	5.9	3.3	3.9	0.2	50	1200	2000	0.30	31
Suzuki	1B-2S	27.8	13.9	4.3	3.4	1.0	0.9	520	3500	3000	0.13	30

[1] Clear height of column
[2] Shear span of column (half of clear height of column)
[3] Width of column (out-of-plane dimension)
[4] Effective depth of column
[5] Spacing of transverse reinforcement in column (spacing near column ends if multiple spacings)
[6] Transverse reinforcement ratio in column
[7] Transverse reinforcement index computed as $v_s = r * f_{yt}$ where f_{yt} is yield stress of transverse reinforcement in column
[8] Measured compressive strength of concrete cylinder
[9] Measured elastic modulus of concrete cylinder or computed as $E_c = 57{,}000 * \sqrt{f'_c}$ if not reported by source
[10] Axial load ratio where A_g refers to gross cross-sectional area of column
[11] Estimated moment capacity of column corresponding to a limiting compressive strain in concrete ε_{cu} = 0.004 (described in Section 1.1)

Table 1-13: Summary of drift capacities and lateral strengths of one-bay one-story bare and infilled frames

Source	Specimen ID	Measured Δ_{frame}/h[1], %	Estimated Δ_{frame}/h[2], %	Measured V_{frame}[3], kip	Estimated V_{frame}[4], kip	Measured Δ_{inf}/h[5], %	Measured V_{max}[6], kip	Estimated V_{max}[7], kip
Mehrabi	3	6.8[m]	2.8	24	21	2.9	62	68
	4	6.8[m]	2.9	24	20	2.0	37	37
	5	6.8[m]	3.1	24	19	1.5	60	62
	6	-	2.9	-	34	1.8	47	50
	7	-	2.8	-	36	1.3	110	78
	8	6.8[m]	2.9	24	20	2.6	43	36
	9	6.8[m]	2.9	24	20	2.3	66	64
	10	-	2.9	-	20	2.0	43	44
	11	-	3.0	-	20	1.6	66	69
	12	-	2.8	-	21	1.2	82	79
Kakaletsis	S	4.0[c]	0.9	10	9	2.9	19	11
	IS	4.0[c]	0.9	10	9	3.9	17	20
Imran	1	-	4.1	-	10	3.0	25	17
	2	-	4.1	-	10	3.3	24	19

[1] Measured drift capacity of the associated RC bare frame corresponding to a 20% reduction in lateral load from strength (c-cyclic test, m-monotonic test)
[2] Estimated lower-bound drift capacity of the associated bare frame computed using Equation 7-1
[3] Measured lateral strength of the associated bare frame
[4] Estimated lateral strength of the associated bare frame computed as $V_{frame} = 4\frac{M_n}{h_c}$
[5] Measured drift capacity of infilled frame corresponding to a 20% reduction in lateral resistance or maximum drift reached in test if no 20% reduction was observed
[6] Measured peak lateral strength of the infilled frame
[7] Estimated lateral strength of the infilled frame computed as $V_{max} = V_{inf} + V_{frame}$

Table 1-13 (continued): Summary of drift capacities and lateral strengths of one-bay one-story bare and infilled frames

Source	Specimen ID	Measured Δ_{frame}/h^{1}, %	Estimated Δ_{frame}/h^{2}, %	Measured $V_{frame}{}^{3}$, kip	Estimated $V_{frame}{}^{4}$, kip	Measured Δ_{inf}/h^{5}, %	Measured $V_{max}{}^{6}$, kip	Estimated $V_{max}{}^{7}$, kip
Blackard	S	-	1.2	-	29	0.7	153	232
Baran	SP7	-	0.9	-	5	1.4	20	12
	SP8	-	1.3	-	4	1.8	14	11
	SP9	-	1.2	-	4	2.4	15	11
Jin	IFRB	-	0.8	-	7	2.4*	14	10
	IFFB	-	0.8	-	7	2.2*	11	10
Cavaleri	S1A-1	-	3.3	-	14	1.7	40	28
	S1A-2	-	3.3	-	14	2.5	47	28
	S1B-1	-	3.3	-	14	1.5	47	47
	S1B-2	-	3.3	-	14	1.4	42	47
	S1C-1	-	1.6	-	29	1.7	49	42
	S1C-2	-	1.6	-	29	1.7	61	42
	S1C-3	-	1.6	-	29	2.1	66	42
	S1C-4	-	1.6	-	29	1.8	70	42
Al-Nimry	IF4	-	4.0	-	8	1.1	45	45
	IF5	-	4.4	-	7	1.0	35	44
Bose	IF-AAC	9.4[m]	7.0	20.0	17	3.8	33	28
Diawati	IFFB	3.6[c]	1.7	8	8	1.8	39	18
	IFSB-wo	3.6[c]	1.6	8	9	3.1	39	25
	IFSB	3.6[c]	1.6	8	9	2.9	58	34

* Measured story drift capacities represent lateral displacement measured at soffit of top beam (h_c above top of foundation)

Table 1-13 (continued): Summary of drift capacities and lateral strengths of one-bay one-story bare and infilled frames

Source	Specimen ID	Measured Δ_{frame}/h[1], %	Estimated Δ_{frame}/h[2], %	Measured V_{frame}[3], kip	Estimated V_{frame}[4], kip	Measured Δ_{inf}/h[5], %	Measured V_{max}[6], kip	Estimated V_{max}[7], kip
Suzuki	1S-1B	-	7.2	5	4	2.3	13	7
Alwashali	F-0.4	-	2.8	-	15	1.4	64	72
	F-0.6	-	8.1	-	23	2.7	66	88
	WM	-	8.1	-	23	3.8	67	67
	F-1.5	-	4.0	-	60	1.7	131	118
	WB	-	9.1	-	22	2.0	58	86
Han	S-Full	2.2[c]	0.6	38	32	1.7	48	50

Table 1-14: Summary of drift capacities and lateral strengths of two-bay one-story bare and infilled frames

Source	Specimen ID	Measured Δ_{frame}/h^{1}, %	Estimated Δ_{frame}/h^{2}, %	Measured $V_{frame}{}^{3}$, kip	Estimated $V_{frame}{}^{4}$, kip	Measured Δ_{inf}/h^{5}, %	Measured $V_{max}{}^{6}$, kip	Estimated $V_{max}{}^{7}$, kip
Mehrabi	13	-	2.0	-	31	1.1	68	75
	14	-	2.0	-	31	1.1	101	102
Suzuki	1S-2B	-	4.8	5	6	2.3	23	13

[1] Measured drift capacity of the associated RC bare frame corresponding to a 20% reduction in lateral load from strength (c-cyclic test, m-monotonic test)
[2] Estimated lower-bound drift capacity of the associated bare frame computed using Equation 7-1
[3] Measured lateral strength of the associated bare frame
[4] Estimated lateral strength of the associated bare frame computed as $V_{frame} = 6\frac{M_n}{h_c}$ for two-bay bare frames
[5] Measured drift capacity of infilled frame corresponding to a 20% reduction in lateral resistance or maximum drift reached in test if no 20% reduction was observed
[6] Measured peak lateral strength of the infilled frame
[7] Estimated lateral strength of the infilled frame computed as $V_{max} = V_{inf} + V_{frame}$

Table 1-15: Summary of drift capacities and lateral strengths of one-bay two-story bare and infilled frames

Source	Specimen ID	Measured Δ_{frame}/h [1], %	Estimated Δ_{frame}/h [2], %	Measured V_{frame} [3], kip	Estimated V_{frame} [4], kip	Measured Δ_{inf}/h [5], %	Measured V_{max} [6], kip	Estimated V_{max} [7], kip
Baran	SP2	2.9[c]	1.1	4	4	2.2	11	10
	SP3	2.9[c]	1.1	4	4	1.7	16	12
	SP4	2.9[c]	0.9	4	5	1.3	18	12
	SP5	2.9[c]	1.1	4	4	0.9	17	11
Suzuki	2S-1B	-	7.2	-	4	1.6*	12	7

* Measured roof drift capacity

[1] Measured story drift capacity of the associated RC bare frame corresponding to a 20% reduction in lateral load from strength (c-cyclic test, m-monotonic test)
[2] Estimated lower-bound story drift capacity of the associated bare frame computed using Equation 7-1
[3] Measured lateral strength of the associated bare frame
[4] Estimated lateral strength of the associated bare frame computed as $V_{frame} = 4\frac{M_n}{h_c}$ for one-bay bare frames
[5] Measured story drift capacity of infilled frame corresponding to a 20% reduction in lateral resistance or maximum drift reached in test if no 20% reduction was observed
[6] Measured peak lateral strength of the infilled frame
[7] Estimated lateral strength of the infilled frame computed as $V_{max} = V_{inf} + V_{frame}$

Table 1-16: Summary of nondimensional parameters of one-bay one-story bare frames and infilled frames

Source	Specimen ID	d/s[1]	Estimated K_{inf}/ Estimated K_{frame}[2]	Measured Δ_{inf}/ Estimated Δ_{frame}[3]	Measured V_{max}/ Estimated V_{frame}[4]
Mehrabi	3	2.3	16	0.5	3.0
	4	2.3	7	0.7	1.8
	5	2.3	18	0.5	3.2
	6	4.5	4	0.6	1.4
	7	3.8	10	0.5	3.1
	8	2.3	7	0.9	2.1
	9	2.3	19	0.8	3.2
	10	2.3	16	0.7	2.1
	11	2.3	36	0.5	3.3
	12	2.3	38	0.4	3.8
Kakaletsis	S	4.0	0.4	3.3	2.1
	IS	4.0	2	4.4	1.8
Imran	1	2.2	1	0.7	2.5
	2	2.2	2	0.8	2.4

[1] Ratio of effective depth to spacing of transverse reinforcement in column

[2] Ratio of estimated initial lateral stiffness of infilled frame computed using Equation 1-1 to estimated initial lateral stiffness of the associated bare frame computed as $K_{frame} = 2 * 12 * E_c * \frac{1}{12} * b * (L - L_{inf})^3 \div h^3$

[3] Ratio of measured drift capacity of infilled frame to estimated lower-bound drift capacity of the associated bare frame computed using Equation 7-1

[4] Ratio of measured peak lateral strength of infilled frame to estimated lateral strength of the associated bare frame computed as $V_{frame} = 4\frac{M_n}{h_c}$

Table 1-16 (continued): Summary of nondimensional parameters of one-bay one-story bare frames and infilled frames

Source	Specimen ID	d/s[1]	Estimated K_{inf}/ Estimated K_{frame}[2]	Measured Δ_{inf}/ Estimated Δ_{frame}[3]	Measured V_{max}/ Estimated V_{frame}[4]
Blackard	S	0.9	24	0.6	5.2
Baran	SP7	0.8	7	1.6	3.7
	SP8	0.8	8	1.4	3.1
	SP9	0.8	8	2.0	3.9
Jin	IFRB	1.3	1	2.8	2.0
	IFFB	1.3	1	2.6	1.6
Cavavleri	S1A-1	1.7	2	0.5	2.8
	S1A-2	1.7	2	0.8	3.4
	S1B-1	1.7	4	0.5	3.4
	S1B-2	1.7	4	0.4	3.0
	S1C-1	2.7	0.4	1.1	1.7
	S1C-2	2.7	0.4	1.1	2.1
	S1C-3	2.7	0.4	1.3	2.3
	S1C-4	2.7	0.4	1.1	2.4
Al-Nimry	IF4	2.3	9	0.3	5.5
	IF5	2.3	9	0.2	4.7
Bose	IF-AAC	3.6	2	0.5	1.9
Diawati	IFFB	1.2	5	1.1	4.7
	IFSB-wo	1.2	7	1.9	4.6
	IFSB	1.2	10	1.8	6.8
Suzuki	1S-1B	3.5	2	0.3	3.1

Table 1-16 (continued): Summary of nondimensional parameters of one-bay one-story bare frames and infilled frames

Source	Specimen ID	d/s[1]	Estimated K_{inf}/ Estimated K_{frame}[2]	Measured Δ_{inf}/ Estimated Δ_{frame}[3]	Measured V_{max}/ Estimated V_{frame}[4]
Alwashali	F-0.4	1.7	12	0.5	4.2
	F-0.6	3.4	12	0.3	2.8
	WM	3.4	8	0.5	2.8
	F-1.5	3.3	2	0.4	2.2
	WB	3.4	13	0.2	2.6
Han	S-Full	1.0	2	2.9	1.5

Table 1-17: Summary of nondimensional parameters of two-bay one-story bare frames and infilled frames

Source	Specimen ID	d/s[1]	Estimated K_{inf}/ Estimated K_{frame}[2]	Measured Δ_{inf}/ Estimated Δ_{frame}[3]	Measured V_{max}/ Estimated V_{frame}[4]
Mehrabi	13	2.3	11	0.6	2.2
	14	2.3	18	0.6	3.3
Suzuki	1S-2B	3.5	3	0.5	3.6

[1] Ratio of effective depth to spacing of transverse reinforcement in column
[2] Ratio of estimated initial lateral stiffness of infilled frame computed using Equation 1-1 to estimated initial lateral stiffness of the associated bare frame computed as $K_{frame} = 3 * 12 * E_c * \frac{1}{12} * b * (L - L_{inf})^3 \div h^3$ for two-bay bare frames
[3] Ratio of measured drift capacity of infilled frame to estimated lower-bound drift capacity of the associated bare frame computed using Equation 7-1
[4] Ratio of measured peak lateral strength of infilled frame to estimated lateral strength of the associated bare frame computed as $V_{frame} = 6\frac{M_n}{h_c}$ for two-bay bare frames

Table 1-18: Summary of nondimensional parameters of one-bay two-story bare frames and infilled frames

Source	Specimen ID	d/s[1]	Estimated K_{inf}/ Estimated K_{frame}[2]	Measured Δ_{inf}/ Estimated Δ_{frame}[3]	Measured V_{max}/ Estimated V_{frame}[4]
Baran	SP2	0.8	3	2.0	2.7
	SP3	0.8	4	1.5	3.7
	SP4	0.8	4	1.4	3.5
	SP5	0.8	5	0.8	4.0
Suzuki	2S-1B	3.5	2	0.2*	2.8

* Ratio of measured roof drift capacity of infilled frame to estimated lower-bound story drift capacity of associated bare frame

[1] Ratio of effective depth to spacing of transverse reinforcement in column

[2] Ratio of estimated initial lateral stiffness of infilled frame computed using Equation 1-1 to estimated initial lateral stiffness of the associated bare frame computed as the equivalent stiffness of first and second stories where story stiffness is computed as $Q_s = \frac{24E_c}{h^2} * [\frac{1}{\frac{1}{k_c}+\frac{1}{k_{ga}}+\frac{1}{k_{gb}}}]$ and k is member stiffness index computed as I_c/h or I_g/L for column and girders (c = columns, ga = girders above story, and gb = girders below story)

[3] Ratio of measured story drift capacity of infilled frame to estimated lower-bound story drift capacity of the associated bare frame computed using Equation 7-1

[4] Ratio of measured peak lateral strength of infilled frame to estimated lateral strength of the associated bare frame computed as $V_{frame} = 4\frac{M_n}{h_c}$ for one-bay bare frames

Table 2-1: Variation of measured peak ground motion parameters with low-pass cut-off frequency

Parameter	Low-pass cut-off frequency							
	10 Hz	15 Hz	20 Hz	25 Hz	30 Hz	40 Hz	50 Hz	60 Hz	Target
Peak base acceleration (PGA), g	0.34	0.40	0.52	0.60	0.66	0.78	0.88	0.94	0.43
Peak base velocity (PGV), in./sec.	8.0	8.2	8.4	8.4	8.4	8.4	8.5	8.5	9.3
Peak base displacement (PGD), in.	1.11	1.11	1.11	1.11	1.11	1.11	1.11	1.11	1.30

Note: The raw measured acceleration history obtained from the ADXL accelerometer mounted on northeast corner of foundation beam in Run 12 of Specimen F1 (F1-B-80-1) was filtered using a high-pass cut-off frequency of 0.25 Hz and specified low-pass cut-off frequencies followed by trimming, correcting, and integrating procedures (discussed in Section 2.5.4) to obtain the peak values of ground motion parameters shown in Table 2-1.

Table 2-2: Records used to simulate scaled earthquake motions

Record	RSN	Direction	Unscaled			Unscaled time step, sec.	F_{tc}[1]	Amplitude scaling factor	Scaled (100% intensity)		
			PGA, g	PGV, in./sec.	PGD, in.				PGA, g	PGV, in./sec.	PGD, in.
1940 El Centro	6 (TC2)	NS	0.28	12.2	3.41	0.010	2.0	1.90	0.53	11.6	1.62
1940 El Centro	6 (TC4)	NS	0.28	12.2	3.41	0.010	4.0	3.80	1.07	11.6	0.81
1971 San Fernando	77	S16E	1.22	45.1	15.4	0.010	2.0	0.50	0.61	11.3	1.92
1972 Managua	95	NS	0.33	12.1	2.42	0.005	1.25	1.20	0.40	11.6	1.86
1994 Northridge	1051	S76E	1.58	21.6	2.17	0.020	1.0	0.55	0.87	11.9	1.19
2002 Denali	2114	N43W	0.30	26.0	14.4	0.005	2.5	0.85	0.25	8.8	1.96
2010 Darfield	6975	N27W	0.30	30.0	31.3	0.005	5.0	1.55	0.46	9.3	1.94

[1] Compression factor used to scale time step in acceleration record

Table 3-1: Summary of peak measurements in runs of Series F1-B

Run	Simulation ID	PGA[1], g	PGV[1], in./sec.	PGD[2], in.	Peak in-run drift ratio[3], %	Peak cumulative drift ratio[4], %	Peak base-shear coefficient[5]
1*	F1-B-10-1	0.11	1.3	0.16	0.12	0.12	0.15
2*	F1-B-10-2	0.10	1.4	0.16	0.13	0.13	0.14
3*	F1-B-10-3	0.11	1.3	0.16	0.14	0.15	0.17
4*	F1-B-20-1	0.23	3.0	0.32	0.34	0.34	0.27
5	F1-B-10-4	0.11	1.3	0.16	0.25	0.26	0.15
6	F1-B-10-5	0.10	1.5	0.16	0.24	0.25	0.15
7	F1-B-20-2	0.17	2.2	0.32	0.56	0.56	0.33
8	F1-B-40-1	0.27	4.5	0.65	1.10	1.08	0.49
9	F1-B-40-2	0.22	4.7	0.65	1.18	1.16	0.47
10	F1-B-60-1	0.28	7.1	0.97	1.68	1.73	0.49
11	F1-B-60-2	0.36	6.9	0.97	1.93	1.98	0.46
12	F1-B-80-1	0.40	8.2	1.29	2.58	2.62	0.47
13	F1-B-80-2	0.41	8.1	1.29	2.26	2.60	0.44
14	F1-B-40-3	0.25	4.9	0.64	1.37	1.82	0.24
15	F1-B-40-4	0.25	5.1	0.64	1.36	1.81	0.24

* Runs with two-swivel link allowing play

[1] Obtained from measurements of the one ADXL accelerometer mounted on base of specimen corrected using procedures described in Section 2.5.3
[2] Obtained from measurements of LVDT mounted inside servoram driving simulator platform
[3] Obtained from measurements of LVDTs attached to specimen and measured relative to initial position of specimen at beginning of run
[4] Obtained from measurements of LVDTs attached to specimen and measured relative to initial position of specimen at beginning of series
[5] Ratio of peak lateral load obtained from measurements of load cell to effective mass of series (49,000 lb)

Table 3-2: Summary of peak measurements in runs of Series F1-C

Run	Simulation ID	PGA[1], g	PGV[1], in./sec.	PGD[2], in.	Peak in-run drift ratio[3], %	Peak cumulative drift ratio[4], %	Peak base-shear coefficient[5]
16	F1-C-10-1	0.12	1.4	0.16	0.45	0.45	0.07
17	F1-C-10-2	0.11	1.0	0.16	0.45	0.48	0.08
18	F1-C-20-1	0.15	2.1	0.32	0.74	0.77	0.14
19	F1-C-20-2	0.15	2.4	0.32	0.72	0.76	0.14
20	F1-C-40-1	0.26	4.1	0.64	1.54	1.58	0.35
21	F1-C-40-2	0.28	4.2	0.65	1.58	1.60	0.36
22	F1-C-60-1	0.33	6.6	0.97	2.09	2.12	0.46
23	F1-C-60-2	0.33	6.0	0.97	2.15	2.16	0.45
24	F1-C-80-1	0.38	7.8	1.29	2.40	2.46	0.47
25	F1-C-80-2	0.40	7.8	1.29	2.34	2.41	0.45
26	F1-C-100-1	0.45	9.5	1.61	2.91	2.84	0.45
27	F1-C-100-2	0.47	9.8	1.61	2.95	2.88	0.44
28	F1-C-80-3	0.39	8.1	1.29	2.59	2.71	0.42
29	F1-C-80-4	0.39	8.2	1.29	2.58	2.76	0.42
30	F1-C-60-3	0.33	6.5	0.97	2.14	2.36	0.35
31	F1-C-60-4	0.34	6.7	0.97	2.17	2.36	0.35
32	F1-C-40-3	0.29	4.6	0.64	1.45	1.64	0.21
33	F1-C-40-4	0.29	4.8	0.64	1.45	1.64	0.21
34	F1-C-20-3	0.20	2.5	0.32	0.78	0.97	0.09
35	F1-C-20-4	0.20	2.4	0.32	0.79	0.97	0.09
36	F1-C-10-3	0.11	1.3	0.16	0.43	0.62	0.04
37	F1-C-10-4	0.11	1.3	0.16	0.43	0.62	0.04

[1] Obtained from measurements of the one ADXL accelerometer mounted on base of specimen corrected using procedures described in Section 2.5.4
[2] Obtained from measurements of LVDT mounted inside servoram driving simulator platform
[3] Obtained from measurements of LVDTs attached to specimen and measured relative to initial position of specimen at beginning of run
[4] Obtained from measurements of LVDTs attached to specimen and measured relative to initial position of specimen at beginning of series
[5] Ratio of peak lateral load obtained from measurements of load cell to effective mass of series (49,000 lb)

Table 3-3: Summary of peak measurements in runs of Series F1-M-C

Run	Simulation ID	PGA[1], g	PGV[1], in./sec.	PGD[2], in.	Peak in-run drift ratio[3], %	Peak cumulative drift ratio[4], %	Peak base-shear coefficient[5]
38	F1-M-C-10-1	0.19	2.0	0.17	0.07	0.07	0.27
39	F1-M-C-10-2	0.15	1.8	0.16	0.07	0.07	0.27
40	F1-M-C-20-1	0.16	2.9	0.32	0.12	0.12	0.39
41	F1-M-C-20-2	0.16	3.0	0.32	0.13	0.13	0.33
42	F1-M-C-40-1	0.26	5.9	0.65	0.34	0.34	0.52
43	F1-M-C-40-2	0.29	5.4	0.65	0.51	0.52	0.63
44	F1-M-C-60-1	0.43	7.7	0.97	0.73	0.75	0.71
45	F1-M-C-60-2	0.37	6.9	0.97	0.75	0.77	0.74
46	F1-M-C-80-1	0.52	9.6	1.30	1.03	1.04	0.88
47	F1-M-C-80-2	0.51	8.2	1.30	1.12	1.17	0.86
48	F1-M-C-60-3	0.38	6.5	0.97	0.94	1.03	0.58
49	F1-M-C-60-4	0.37	6.5	0.97	0.98	1.05	0.61
50	F1-M-C-40-3	0.28	4.5	0.65	0.76	0.83	0.35
51	F1-M-C-40-4	0.28	4.6	0.65	0.78	0.85	0.36
52	F1-M-C-20-3	0.19	2.5	0.32	0.52	0.61	0.17
53	F1-M-C-20-4	0.20	2.6	0.32	0.52	0.62	0.18
54	F1-M-C-10-3	0.13	1.4	0.16	0.28	0.34	0.06
55	F1-M-C-10-4	0.13	1.4	0.16	0.29	0.34	0.06
56	F1-M-C-80-3	0.47	8.4	1.30	1.29	1.35	0.77

[1] Obtained from measurements of ADXL accelerometer(s) mounted on base of specimen corrected using procedures described in Section 2.5.4
[2] Obtained from measurements of LVDT mounted inside servoram driving simulator platform
[3] Obtained from measurements of LVDTs attached to specimen and measured relative to initial position of specimen at beginning of run
[4] Obtained from measurements of LVDTs attached to specimen and measured relative to initial position of specimen at beginning of series
[5] Ratio of peak lateral load obtained from measurements of load cell to effective mass of series (49,000 lb)

Table 3-4: Summary of peak measurements in runs of Series F1-M-C-OOP

Run	Simulation ID	PGA[1], g	PGV[1], in./sec.	PGD[2], in.	Peak in-run drift ratio[3], %	Peak cumulative drift ratio[4], %	Peak roof acceleration, g[5]
57	F1-M-C-OOP-10-1	0.13	1.4	0.16	0.23	0.23	0.18
58	F1-M-C-OOP-10-2	0.13	1.4	0.16	0.24	0.24	0.19
59	F1-M-C-OOP-20-1	0.18	2.5	0.33	0.45	0.46	0.35
60	F1-M-C-OOP-20-2	0.19	2.4	0.32	0.46	0.46	0.35
61	F1-M-C-OOP-40-1	0.28	4.8	0.65	0.90	0.90	0.71
62	F1-M-C-OOP-40-2	0.28	4.6	0.65	0.96	0.95	0.72
63	F1-M-C-OOP-60-1	0.36	7.2	0.97	1.40	1.40	1.08
64	F1-M-C-OOP-60-2	0.36	7.0	0.97	1.48	1.48	1.16
65	F1-M-C-OOP-80-1	0.42	9.0	1.29	1.69	1.69	1.43
66	F1-M-C-OOP-80-2	0.42	9.4	1.29	1.77	1.77	1.41
67	F1-M-C-OOP-100-1	0.50	10.8	1.61	2.00	2.00	1.74
68	F1-M-C-OOP-100-2	0.49	11.0	1.61	2.02	2.02	1.74
69	F1-M-C-OOP-80-3	0.42	9.4	1.29	1.93	1.93	1.52
70	F1-M-C-OOP-80-4	0.43	9.2	1.29	1.99	1.99	1.58
71	F1-M-C-OOP-60-3	0.34	6.9	0.97	1.67	1.67	1.24
72	F1-M-C-OOP-60-4	0.34	6.7	0.97	1.68	1.68	1.25
73	F1-M-C-OOP-40-3	0.26	4.6	0.65	1.26	1.26	0.87
74	F1-M-C-OOP-40-4	0.26	4.6	0.65	1.27	1.27	0.87
75	F1-M-C-OOP-20-3	0.18	2.4	0.32	0.54	0.54	0.29
76	F1-M-C-OOP-20-4	0.18	2.4	0.32	0.54	0.54	0.29
77	F1-M-C-OOP-10-3	0.11	1.3	0.16	0.25	0.25	0.15
78	F1-M-C-OOP-10-4	0.12	1.3	0.16	0.25	0.25	0.15

[1] Obtained from measurements of ADXL accelerometers mounted on base of specimen corrected using procedures described in Section 2.5.4
[2] Obtained from measurements of LVDT mounted inside servoram driving simulator platform
[3] Obtained from measurements of LVDTs attached to specimen and measured relative to initial position of specimen at beginning of run
[4] Obtained from measurements of LVDTs attached to specimen and measured relative to initial position of specimen at beginning of series
[5] Obtained from measurements of ADXL accelerometers mounted on top of top beam of specimen

Table 3-5: Summary of peak measurements in runs of Series F2-C

Run	Simulation ID	PGA[1], g	PGV[1], in./sec.	PGD[2], in.	Peak in-run drift ratio[3], %	Peak cumulative drift ratio[4], %	Peak base-shear coefficient[5]
1	F2-C-RSN6975-PGV2-1	0.08	2.1	0.41	0.10	0.10	0.08
2	F2-C-RSN77-PGV2-1	0.09	2.2	0.34	0.13	0.12	0.08
3	F2-C-RSN2114-PGV2-1	0.08	2.0	0.44	0.17	0.16	0.10
4	F2-C-RSN6-TC4-PGV2-1	0.16	1.7	0.14	0.33	0.33	0.19
5	F2-C-RSN6-TC2-PGV2-1	0.13	1.9	0.28	0.37	0.36	0.19
6	F2-C-RSN1051-PGV2-1	0.14	2.1	0.20	0.53	0.52	0.27
7	F2-C-RSN95-PGV2-1	0.12	1.7	0.32	0.66	0.67	0.33
8	F2-C-RSN6975-PGV2-2	0.11	2.2	0.42	0.31	0.30	0.11
9	F2-C-RSN77-PGV2-2	0.10	1.9	0.34	0.37	0.38	0.15
10	F2-C-RSN2114-PGV2-2	0.10	1.9	0.44	0.45	0.44	0.17
11	F2-C-RSN6-TC4-PGV2-2	0.24	2.1	0.14	0.47	0.46	0.20
12	F2-C-RSN6-TC2-PGV2-2	0.14	2.1	0.28	0.55	0.55	0.26
13	F2-C-RSN1051-PGV2-2	0.13	1.9	0.20	0.76	0.75	0.35
14	F2-C-RSN95-PGV2-2	0.11	1.9	0.32	0.60	0.59	0.24
15	F2-C-RSN6975-PGV4-1	0.15	3.8	0.83	0.57	0.57	0.23
16	F2-C-RSN77-PGV4-1	0.22	3.7	0.68	0.57	0.57	0.26
17	F2-C-RSN2114-PGV4-1	0.12	3.8	0.89	0.71	0.70	0.30
18	F2-C-RSN6-TC4-PGV4-1	0.42	3.8	0.28	0.75	0.75	0.35
19	F2-C-RSN6-TC2-PGV4-1	0.20	3.8	0.56	1.00	1.00	0.44
20	F2-C-RSN1051-PGV4-1	0.22	3.7	0.40	1.25	1.26	0.48
21	F2-C-RSN95-PGV4-1	0.17	3.4	0.64	1.53	1.39	0.46
22	F2-C-RSN6975-PGV4-2	0.19	3.5	0.83	0.81	0.82	0.19

[1] Obtained from measurements of ADXL accelerometers mounted on base of specimen corrected using procedures described in Section 2.5.4
[2] Obtained from measurements of LVDT mounted inside servoram driving simulator platform
[3] Obtained from measurements of LVDTs attached to specimen and measured relative to initial position of specimen at beginning of run
[4] Obtained from measurements of LVDTs attached to specimen and measured relative to initial position of specimen at beginning of series
[5] Ratio of peak lateral load obtained from measurements of load cell to effective mass of series (49,000 lb)

Table 3-5 (continued): Summary of peak measurements in runs of Series F2-C

Run	Simulation ID	PGA[1], g	PGV[1], in./sec.	PGD[2], in.	Peak in-run drift ratio[3], %	Peak cumulative drift ratio[4], %	Peak base-shear coefficient[5]
23	F2-C-RSN77-PGV4-2	0.15	3.6	0.68	1.06	1.07	0.31
24	F2-C-RSN2114-PGV4-2	0.12	3.9	0.89	1.16	1.17	0.35
25	F2-C-RSN6-TC4-PGV4-2	0.33	3.7	0.28	1.32	1.31	0.43
26	F2-C-RSN6-TC2-PGV4-2	0.26	4.1	0.56	1.47	1.45	0.43
27	F2-C-RSN1051-PGV4-2	0.22	4.2	0.40	1.76	1.74	0.46
28	F2-C-RSN95-PGV4-2	0.21	3.6	0.64	0.98	1.04	0.22
29	F2-C-RSN6975-PGV6-1	0.25	5.3	1.24	1.24	1.18	0.29
30	F2-C-RSN77-PGV6-1	0.22	5.4	1.02	1.59	1.63	0.41
31	F2-C-RSN2114-PGV6-1	0.15	5.8	1.33	1.69	1.62	0.41
32	F2-C-RSN6-TC4-PGV6-1	0.52	5.0	0.42	2.00	1.96	0.45
33	F2-C-RSN6-TC2-PGV6-1	0.31	5.3	0.83	2.02	1.91	0.44
34	F2-C-RSN1051-PGV6-1	0.43	5.8	0.60	2.35	2.38	0.46
35	F2-C-RSN95-PGV6-1	0.30	5.6	0.96	1.79	1.75	0.34
36	F2-C-RSN6975-PGV6-2	0.19	5.3	1.24	1.18	1.25	0.18
37	F2-C-RSN77-PGV6-2	0.26	5.3	1.02	1.90	1.97	0.38
38	F2-C-RSN2114-PGV6-2	0.16	5.7	1.33	2.00	2.02	0.36
39	F2-C-RSN6-TC4-PGV6-2	0.44	5.1	0.42	2.23	2.26	0.42
40	F2-C-RSN6-TC2-PGV6-2	0.31	5.5	0.83	1.79	1.70	0.36
41	F2-C-RSN1051-PGV6-2	0.43	5.7	0.60	2.78	2.85	0.47
42	F2-C-RSN95-PGV6-2	0.26	5.6	0.96	2.04	1.88	0.38
43	F2-C-RSN6975-PGV8-1	0.27	6.9	1.66	1.54	1.72	0.24
44	F2-C-RSN77-PGV8-1	0.31	6.9	1.36	2.46	2.40	0.44
45	F2-C-RSN2114-PGV8-1	0.18	7.4	1.77	2.71	2.76	0.43
46	F2-C-RSN6-TC4-PGV8-1	0.58	6.7	0.56	2.96	2.99	0.45
47	F2-C-RSN6-TC2-PGV8-1	0.38	7.1	1.11	2.47	2.39	0.40
48	F2-C-RSN1051-PGV8-1	0.63	7.8	0.80	3.53	3.72	0.47

Table 3-5 (continued): Summary of peak measurements in runs of Series F2-C

Run	Simulation ID	PGA[1], g	PGV[1], in./sec.	PGD[2], in.	Peak in-run drift ratio[3], %	Peak cumulative drift ratio[4], %	Peak base-shear coefficient[5]
49	F2-C-RSN95-PGV8-1	0.32	7.2	1.27	2.86	2.53	0.40
50	F2-C-RSN6975-PGV8-2	0.31	7.4	1.66	1.70	1.80	0.21
51	F2-C-RSN6-TC2-PGV8-2	0.37	7.7	1.11	2.43	2.58	0.36
52	F2-C-RSN95-PGV8-2	0.35	7.1	1.27	2.80	2.59	0.42
53	F2-C-RSN6975-PGV6-3	0.22	5.9	1.24	1.37	1.40	0.18
54	F2-C-RSN6-TC2-PGV6-3	0.35	5.8	0.84	1.73	1.80	0.26
55	F2-C-RSN95-PGV6-3	0.30	5.4	0.96	2.30	2.29	0.36
56	F2-C-RSN6975-PGV4-3	0.16	4.1	0.83	1.04	1.09	0.13
57	F2-C-RSN77-PGV4-3	0.26	3.6	0.68	1.66	1.60	0.20
58	F2-C-RSN2114-PGV4-3	0.13	3.8	0.89	1.78	1.76	0.22
59	F2-C-RSN6-TC4-PGV4-3	0.37	4.1	0.28	1.69	1.71	0.21
60	F2-C-RSN6-TC2-PGV4-3	0.24	4.0	0.56	1.33	1.36	0.17
61	F2-C-RSN1051-PGV4-3	0.25	3.6	0.40	2.17	2.21	0.29
62	F2-C-RSN95-PGV4-3	0.19	3.6	0.64	1.54	1.41	0.21
63	F2-C-RSN6975-PGV2-3	0.09	1.9	0.42	0.68	0.76	0.06
64	F2-C-RSN77-PGV2-3	0.14	1.8	0.34	0.93	1.03	0.08
65	F2-C-RSN2114-PGV2-3	0.11	2.0	0.44	0.96	1.06	0.09
66	F2-C-RSN6-TC4-PGV2-3	0.25	2.6	0.14	0.55	0.64	0.05
67	F2-C-RSN6-TC2-PGV2-3	0.14	2.0	0.28	0.86	0.95	0.09
68	F2-C-RSN1051-PGV2-3	0.12	1.8	0.20	0.97	1.06	0.11
69	F2-C-RSN95-PGV2-3	0.11	1.8	0.32	0.85	0.94	0.08

Table 3-6: Summary of peak measurements in runs of Series F2-M

Run	Simulation ID	PGA[1], g	PGV[1], in./sec.	PGD[2], in.	Peak in-run drift ratio[3], %	Peak cumulative drift ratio[4], %	Peak base-shear coefficient[5]
70	F2-M-10-1	0.09	1.4	0.16	0.03	0.03	0.16
71	F2-M-10-2	0.10	1.5	0.16	0.04	0.04	0.18
72	F2-M-20-1	0.18	2.7	0.32	0.11	0.11	0.28
73	F2-M-20-2	0.16	2.6	0.32	0.16	0.17	0.29
74	F2-M-40-1	0.24	4.8	0.65	0.38	0.39	0.48
75	F2-M-40-2	0.27	4.8	0.65	0.43	0.49	0.53
76	F2-M-60-1	0.43	7.2	0.97	0.72	0.79	0.71
77	F2-M-60-2	0.38	6.4	0.97	0.82	0.92	0.69
78	F2-M-80-1	0.50	8.4	1.29	1.14	1.24	0.75

[1] Obtained from measurements of ADXL accelerometers mounted on base of specimen corrected using procedures described in Section 2.5.4
[2] Obtained from measurements of LVDT mounted inside servoram driving simulator platform
[3] Obtained from measurements of LVDTs attached to specimen and measured relative to initial position of specimen at beginning of run
[4] Obtained from measurements of LVDTs attached to specimen and measured relative to initial position of specimen at beginning of series
[5] Ratio of peak lateral load obtained from measurements of load cell to effective mass of series (49,000 lb)

Table 3-7: Summary of peak measurements in runs of Series F2-M-C-S

Run	Simulation ID	PGA[1], g	PGV[1], in./sec.	PGD[2], in.	Peak in-run drift ratio[3], %	Peak cumulative drift ratio[4], %	Peak base-shear coefficient[5]
79	F2-M-C-S-10-1	0.11	1.3	0.16	0.13	0.13	0.13
80	F2-M-C-S-20-1	0.15	2.3	0.32	0.24	0.25	0.25
81	F2-M-C-S-40-1	0.24	4.3	0.65	0.48	0.49	0.45
82	F2-M-C-S-60-1	0.33	6.2	0.97	0.74	0.77	0.68
83	F2-M-C-S-80-1	0.46	8.1	1.29	1.12	1.16	0.82
84	F2-M-C-S-80-2	0.45	8.3	1.29	1.22	1.29	0.72

[1] Obtained from measurements of ADXL accelerometers mounted on base of specimen corrected using procedures described in Section 2.5.4
[2] Obtained from measurements of LVDT mounted inside servoram driving simulator platform
[3] Obtained from measurements of LVDTs attached to specimen and measured relative to initial position of specimen at beginning of run
[4] Obtained from measurements of LVDTs attached to specimen and measured relative to initial position of specimen at beginning of series
[5] Ratio of peak lateral load obtained from measurements of load cell to effective mass of series (49,000 lb)

Table 3-8: Summary of peak measurements in runs of Series F2-C-S

Run	Simulation ID	PGA[1], g	PGV[1], in./sec.	PGD[2], in.	Peak in-run drift ratio[3], %	Peak cumulative drift ratio[4], %	Peak base-shear coefficient[5]
85	F2-C-S-10-1	0.13	1.3	0.16	0.35	0.35	0.04
86	F2-C-S-20-1	0.22	2.7	0.33	0.72	0.71	0.09
87	F2-C-S-40-1	0.29	4.6	0.65	1.61	1.61	0.25
88	F2-C-S-60-1	0.38	6.7	0.97	2.41	2.41	0.38
89	F2-C-S-80-1	0.43	8.8	1.29	2.84	2.87	0.42
90	F2-C-S-100-1	0.48	10.3	1.62	3.17	3.26	0.43
91	F2-C-S-100-2	0.49	10.3	1.62	3.21	3.30	0.41
92	F2-C-S-RSN1051-PGV8-1	0.58	7.0	0.80	3.31	3.53	0.42
93	F2-C-S-RSN1051-PGV8-2	0.56	6.9	0.80	3.44	3.57	0.41
94	F2-C-S-RSN1051-PGV10-1	0.75	8.3	1.00	4.02	4.24	0.43
95	F2-C-S-RSN1051-PGV10-2	0.71	8.4	1.00	3.91	4.36	0.42
96	F2-C-S-RSN1051-PGV12-1	0.89	9.2	1.19	4.51	4.81	0.42
97	F2-C-S-RSN1051-PGV12-2	0.87	9.3	1.19	4.68	4.83	0.40

[1] Obtained from measurements of ADXL accelerometers mounted on base of specimen corrected using procedures described in Section 2.5.4
[2] Obtained from measurements of LVDT mounted inside servoram driving simulator platform
[3] Obtained from measurements of LVDTs attached to specimen and measured relative to initial position of specimen at beginning of run
[4] Obtained from measurements of LVDTs attached to specimen and measured relative to initial position of specimen at beginning of series
[5] Ratio of peak lateral load obtained from measurements of load cell to effective mass of series (49,000 lb)

Table 4-1: Summary of components of effective mass of frame-mass system (tested in-plane)

Component	Mass, lb
RC block (suspended mass)	44,500
Hardware	2,500
RC frame (top beam plus half of RC columns)	1,900
Total	48,900

Table 4-2: Summary of components of effective mass of infilled frame with clamps tested out-of-plane (Series F1-M-C-OOP)

Component	Mass, lb
Hardware	2,000
RC frame (top beam plus half of RC columns)	1,900
Half of masonry infill wall	450
Total	4,350

Table 4-3: Summary of values of initial lateral stiffnesses

Type of frame	Series	Estimated K_o[1], kip/in.	Inferred K_s[2], kip/in.	Estimated K_{eff}[3], kip/in.
RC frame	F1-B, F1-C, F2-C, F2-C-S	210	1500	180
Infilled frame tested in-plane	F1-M-C, F2-M, F2-M-C-S	1000	1500	600
Infilled frame tested out-of-plane	F1-M-C-OOP	50	Inf.	50

Table 4-4: Summary of measured and estimated initial lateral stiffnesses and initial periods

Series	Simulation ID[4]	m[5], lb	Measured K_{eff}[6], kip/in.	Estimated K_{eff}[3], kip/in.	Measured T_o[7], sec.	Estimated T_o, sec.
F1-B	F1-B-10-1	49,000	120	180	0.20	0.17
F1-M-C	F1-M-C-10-1		420	600	0.11	0.10
F2-C	F2-C-RSN6975-PGV2-1		70	180	0.26	0.17
F2-M	F2-M-10-1		450	600	0.10	0.10

[1] Initial lateral stiffness of frame estimated assuming fixity at base
[2] Mean effective lateral stiffness of simulator
[3] Effective initial lateral stiffness
[4] Simulation ID of initial runs of mentioned series associated with measured values of K_{eff} and T_o
[5] Effective mass of frames with and without infill tested in-plane
[6] Inferred from measurements of lateral loads and drifts obtained in initial runs of the mentioned series
[7] Inferred from measurements of effective mass and K_{eff} computed using measurements obtained in initial runs of the mentioned series

Table 5-1: Mean spectral amplification factors

Series	$S_{2\%}$ / $S_{20\%}$		$S_{5\%}$ / $S_{20\%}$	
	F_{Sa}	F_{Sd}	F_{Sa}	F_{Sd}
F1-B	2.0	2.2	1.5	1.7
F1-C	2.0	2.2	1.6	1.7
F1-M-C	1.9	2.1	1.5	1.7
F1-M-C-OOP	2.0	2.2	1.6	1.7
F2-C	1.8	2.0	1.5	1.6
F2-M	2.0	2.2	1.5	1.7
F2-M-C-S	1.9	2.1	1.5	1.7
F2-C-S	1.9	2.1	1.5	1.7
Mean	**2.0**		**1.6**	

Note: Spectral amplification factors are computed for periods between 0.01 and 1.15 seconds.

Table 5-2: Summary of estimated drift demands in runs of Series F1-B

Run	T_{eff}[1], sec.	T_{Four}[2], sec.	M1 Δ/h[3], %	M2 Δ/h[4], %	M3 Δ/h[5], %	M4 Δ/h[6], %	M5 Δ/h[7], %
1	0.20	0.34	0.13	0.29	0.14	0.11	0.31
2	0.20	0.34	0.14	0.29	0.15	0.11	0.33
3	0.21	0.35	0.13	0.28	0.13	0.10	0.31
4	0.24	0.35	0.37	0.76	0.66	0.43	0.72
5	0.28	0.34	0.22	0.26	0.13	0.10	0.32
6	0.28	0.34	0.20	0.26	0.14	0.10	0.35
7	0.28	0.34	0.42	0.60	0.40	0.25	0.54
8	0.32	0.35	1.02	1.08	1.09	0.83	1.07
9	0.34	0.44	1.04	1.38	1.06	0.82	1.14
10	0.40	0.46	1.37	1.79	1.35	1.19	1.70
11	0.44	0.50	1.57	1.86	1.37	1.23	1.65
12	0.49	0.60	1.97	2.39	1.77	1.53	1.97
13	0.50	0.62	1.98	2.41	1.71	1.52	1.96
14	0.55	0.63	1.54	1.70	1.16	0.95	1.17
15	0.54	0.63	1.50	1.66	1.14	0.90	1.22

[1] Effective period (described in Section 5.4)
[2] Fourier period (described in Section 5.5)
[3] Estimated drift ratio computed using Method 1
[4] Estimated drift ratio computed using Method 2
[5] Estimated drift ratio computed using Method 3
[6] Estimated drift ratio computed using Method 4
[7] Estimated drift ratio computed using Method 5

Table 5-3: Summary of estimated drift demands in runs of Series F1-C

Run	T_{eff}[8], sec.	T_{Four}[9], sec.	M1 Δ/h[10], %	M2 Δ/h[11], %	M3 Δ/h[12], %	M4 Δ/h[13], %	M5 Δ/h[14], %
16	0.53	0.63	0.40	0.51	0.16	0.12	0.33
17	0.52	0.62	0.37	0.48	0.15	0.12	0.25
18	0.50	0.63	0.77	0.98	0.44	0.28	0.52
19	0.50	0.63	0.71	0.97	0.42	0.29	0.58
20	0.47	0.63	1.34	1.80	1.12	0.87	0.99
21	0.46	0.63	1.36	1.79	1.11	0.88	1.01
22	0.47	0.59	1.63	2.04	1.36	1.23	1.58
23	0.47	0.59	1.69	2.09	1.37	1.23	1.45
24	0.49	0.59	1.97	2.32	1.70	1.50	1.89
25	0.50	0.59	1.99	2.30	1.70	1.50	1.88
26	0.54	0.63	2.32	2.69	2.13	1.92	2.28
27	0.55	0.64	2.39	2.66	2.15	1.95	2.36
28	0.55	0.70	2.14	2.66	1.71	1.51	1.95
29	0.55	0.70	2.16	2.63	1.71	1.50	1.96
30	0.55	0.70	1.94	2.35	1.38	1.24	1.57
31	0.55	0.70	1.93	2.26	1.39	1.24	1.61
32	0.59	0.70	1.66	1.84	1.12	0.90	1.10
33	0.58	0.70	1.63	1.86	1.12	0.90	1.14
34	0.66	0.89	0.91	1.61	0.53	0.32	0.60
35	0.66	0.91	0.89	1.56	0.53	0.31	0.57
36	0.72	0.89	0.51	0.75	0.14	0.11	0.32
37	0.73	0.90	0.51	0.80	0.14	0.11	0.32

[8] Effective period (described in Section 5.4)
[9] Fourier period (described in Section 5.5)
[10] Estimated drift ratio computed using Method 1
[11] Estimated drift ratio computed using Method 2
[12] Estimated drift ratio computed using Method 3
[13] Estimated drift ratio computed using Method 4
[14] Estimated drift ratio computed using Method 5

Table 5-4: Summary of estimated drift demands in runs of Series F1-M-C

Run	T_{eff}[1], sec.	T_{Four}[2], sec.	M1 Δ/h[3], %	M2 Δ/h[4], %	M3 Δ/h[5], %	M4 Δ/h[6], %	M5 Δ/h[7], %
38	0.11	0.17	0.09	0.29	0.31	0.18	0.28
39	0.11	0.19	0.07	0.25	0.10	0.06	0.25
40	0.12	0.19	0.13	0.40	0.43	0.26	0.40
41	0.14	0.23	0.16	0.52	0.26	0.11	0.42
42	0.17	0.23	0.37	0.89	1.06	0.67	0.84
43	0.19	0.34	0.45	1.40	0.67	0.39	0.76
44	0.21	0.34	0.59	1.72	0.86	0.65	1.09
45	0.22	0.34	0.73	1.74	0.93	0.60	0.98
46	0.23	0.34	0.83	1.89	1.08	0.99	1.36
47	0.24	0.35	0.99	1.69	1.21	0.99	1.16
48	0.27	0.35	1.16	1.53	1.02	0.64	0.92
49	0.28	0.35	1.19	1.52	1.01	0.64	0.92
50	0.32	0.44	1.03	1.39	0.49	0.25	0.63
51	0.31	0.44	1.04	1.40	0.49	0.25	0.65
52	0.38	0.46	0.57	0.68	0.17	0.12	0.35
53	0.38	0.43	0.58	0.64	0.19	0.13	0.37
54	0.44	0.56	0.30	0.42	0.10	0.08	0.20
55	0.44	0.59	0.30	0.45	0.10	0.07	0.19
56	0.28	0.44	1.26	2.40	1.30	1.02	1.19

[1] Effective period (described in Section 5.4)
[2] Fourier period (described in Section 5.5)
[3] Estimated drift ratio computed using Method 1
[4] Estimated drift ratio computed using Method 2
[5] Estimated drift ratio computed using Method 3
[6] Estimated drift ratio computed using Method 4
[7] Estimated drift ratio computed using Method 5

Table 5-5: Summary of estimated drift demands in runs of Series F2-C

Run	T_{eff}[1], sec.	T_{Four}[2], sec.	M1 Δ/h[3], %	M2 Δ/h[4], %	M3 Δ/h[5], %	M4 Δ/h[6], %	M5 Δ/h[7], %
1	0.26	0.39	0.15	0.30	0.21	0.16	0.50
2	0.26	0.44	0.14	0.53	0.18	0.13	0.52
3	0.26	0.42	0.15	0.45	0.20	0.16	0.47
4	0.28	0.39	0.30	0.40	0.31	0.25	0.41
5	0.30	0.34	0.38	0.43	0.41	0.31	0.46
6	0.30	0.39	0.37	0.65	0.39	0.29	0.50
7	0.31	0.37	0.43	0.61	0.44	0.31	0.41
8	0.38	0.48	0.26	0.38	0.18	0.11	0.53
9	0.35	0.47	0.29	0.58	0.20	0.16	0.46
10	0.35	0.43	0.23	0.42	0.16	0.12	0.47
11	0.34	0.43	0.37	0.60	0.32	0.26	0.51
12	0.32	0.40	0.42	0.62	0.42	0.32	0.50
13	0.31	0.38	0.49	0.71	0.50	0.37	0.45
14	0.34	0.47	0.52	0.66	0.48	0.34	0.46
15	0.34	0.44	0.39	0.62	0.31	0.24	0.90
16	0.33	0.46	0.48	1.06	0.42	0.33	0.89
17	0.32	0.40	0.41	0.72	0.35	0.28	0.90
18	0.32	0.39	0.66	0.88	0.67	0.54	0.90
19	0.32	0.39	0.87	1.06	0.92	0.70	0.92
20	0.35	0.42	1.11	1.59	1.23	0.88	0.88
21	0.37	0.48	1.08	1.28	1.07	0.83	0.82
22	0.45	0.51	0.55	0.69	0.30	0.24	0.84
23	0.40	0.47	0.68	1.07	0.36	0.29	0.87
24	0.39	0.51	0.60	1.16	0.34	0.28	0.94
25	0.38	0.48	0.86	1.33	0.71	0.58	0.90
26	0.39	0.44	0.99	1.09	0.97	0.74	1.00
27	0.42	0.51	1.55	2.09	1.20	0.91	1.02
28	0.48	0.62	1.25	1.91	1.04	0.80	0.88
29	0.45	0.52	0.83	1.07	0.49	0.36	1.28
30	0.43	0.53	1.24	1.97	0.64	0.51	1.30
31	0.43	0.58	1.18	2.14	0.60	0.49	1.39
32	0.45	0.54	1.67	2.36	1.06	0.84	1.21

[1] Effective period (described in Section 5.4)
[2] Fourier period (described in Section 5.5)
[3] Estimated drift ratio computed using Method 1
[4] Estimated drift ratio computed using Method 2
[5] Estimated drift ratio computed using Method 3
[6] Estimated drift ratio computed using Method 4
[7] Estimated drift ratio computed using Method 5

Table 5-5 (continued): Summary of estimated drift demands in runs of Series F2-C

Run	T_{eff}[1], sec.	T_{Four}[2], sec.	M1 Δ/h[3], %	M2 Δ/h[4], %	M3 Δ/h[5], %	M4 Δ/h[7], %	M5 Δ/h[9], %
33	0.46	0.63	1.59	2.17	1.37	1.17	1.27
34	0.48	0.66	1.96	2.55	1.59	1.42	1.40
35	0.50	0.62	1.51	2.41	1.51	1.28	1.36
36	0.55	0.62	1.19	1.43	0.50	0.37	1.28
37	0.49	0.60	1.64	2.29	0.62	0.49	1.28
38	0.49	0.58	1.53	2.04	0.58	0.46	1.36
39	0.49	0.69	2.03	2.37	1.10	0.86	1.24
40	0.50	0.62	1.73	2.09	1.35	1.16	1.32
41	0.51	0.66	2.16	2.53	1.53	1.36	1.38
42	0.52	0.63	1.72	2.45	1.50	1.30	1.34
43	0.54	0.62	1.51	1.85	0.69	0.53	1.66
44	0.52	0.60	2.41	3.00	0.95	0.75	1.66
45	0.53	0.64	2.31	3.19	0.91	0.70	1.77
46	0.53	0.69	2.51	2.58	1.29	1.26	1.61
47	0.54	0.62	2.06	2.31	1.65	1.45	1.72
48	0.57	0.66	2.73	2.72	2.20	2.06	1.86
49	0.58	0.65	2.48	2.84	1.79	1.62	1.74
50	0.59	0.66	1.73	2.03	0.74	0.57	1.78
51	0.57	0.70	2.20	2.49	1.69	1.47	1.84
52	0.58	0.65	2.43	2.84	1.79	1.62	1.72
53	0.62	0.69	1.39	1.69	0.52	0.39	1.43
54	0.59	0.70	2.01	2.20	1.39	1.21	1.40
55	0.57	0.76	2.06	2.51	1.53	1.31	1.31
56	0.66	0.72	1.07	1.29	0.32	0.26	0.99
57	0.61	0.73	1.54	1.82	0.32	0.26	0.86
58	0.61	0.75	1.46	1.90	0.35	0.29	0.92
59	0.60	0.72	1.70	1.50	0.70	0.56	1.00
60	0.62	0.78	1.59	1.92	1.05	0.80	0.97
61	0.58	0.67	2.19	2.15	1.20	0.92	0.87
62	0.62	0.89	1.87	1.82	1.11	0.84	0.86
63	0.74	0.86	0.72	1.14	0.13	0.09	0.46
64	0.70	0.82	0.84	0.95	0.15	0.12	0.44
65	0.71	0.90	0.91	1.04	0.17	0.14	0.47
66	0.74	0.83	0.69	0.76	0.37	0.30	0.61
67	0.70	0.92	0.86	1.42	0.50	0.38	0.47
68	0.67	0.83	1.09	1.22	0.51	0.40	0.44
69	0.71	0.88	1.03	0.89	0.51	0.36	0.44

Table 5-6: Summary of estimated drift demands in runs of Series F2-M

Run	T_{eff}[1], sec.	T_{Four}[2], sec.	M1 Δ/h[3], %	M2 Δ/h[4], %	M3 Δ/h[5], %	M4 Δ/h[6], %	M5 Δ/h[7], %
70	0.10	0.22	0.04	0.23	0.11	0.05	0.21
71	0.11	0.19	0.05	0.18	0.09	0.04	0.21
72	0.13	0.21	0.13	0.37	0.34	0.23	0.38
73	0.15	0.23	0.17	0.49	0.37	0.16	0.36
74	0.17	0.23	0.34	0.73	0.85	0.68	0.68
75	0.19	0.34	0.39	1.29	0.57	0.35	0.68
76	0.21	0.35	0.57	1.54	0.77	0.68	1.02
77	0.23	0.35	0.70	1.34	0.87	0.67	0.91
78	0.28	0.44	1.05	2.18	1.09	0.95	1.19

Table 5-7: Summary of estimated drift demands in runs of Series F2-M-C-S

Run	T_{eff}[1], sec.	T_{Four}[2], sec.	M1 Δ/h[3], %	M2 Δ/h[4], %	M3 Δ/h[5], %	M4 Δ/h[6], %	M5 Δ/h[7], %
79	0.20	0.35	0.16	0.33	0.07	0.05	0.18
80	0.21	0.35	0.28	0.61	0.17	0.10	0.33
81	0.22	0.34	0.56	1.24	0.65	0.35	0.61
82	0.23	0.34	0.67	1.52	0.83	0.64	0.88
83	0.25	0.35	0.86	1.51	1.05	0.89	1.14
84	0.28	0.44	1.09	2.15	1.12	0.98	1.17

[1] Effective period (described in Section 5.4)
[2] Fourier period (described in Section 5.5)
[3] Estimated drift ratio computed using Method 1
[4] Estimated drift ratio computed using Method 2
[5] Estimated drift ratio computed using Method 3
[6] Estimated drift ratio computed using Method 4
[7] Estimated drift ratio computed using Method 5

Table 5-8: Summary of estimated drift demands in runs of Series F2-C-S

Run	T_{eff}[1], sec.	T_{Four}[2], sec.	M1 Δ/h[3], %	M2 Δ/h[4], %	M3 Δ/h[5], %	M4 Δ/h[6], %	M5 Δ/h[7], %
85	0.64	0.77	0.43	0.57	0.25	0.20	0.31
86	0.62	0.77	0.88	1.09	0.59	0.46	0.64
87	0.56	0.72	1.66	1.95	1.22	0.93	1.11
88	0.55	0.62	2.00	2.19	1.54	1.35	1.61
89	0.57	0.71	2.26	2.57	1.95	1.70	2.12
90	0.59	0.70	2.61	2.87	2.34	2.13	2.47
91	0.61	0.70	2.66	2.86	2.35	2.14	2.48
92	0.62	0.67	2.76	2.63	2.19	2.05	1.69
93	0.63	0.81	2.76	3.06	2.19	2.06	1.67
94	0.65	0.82	2.90	3.31	2.92	2.81	2.00
95	0.67	0.82	2.85	3.29	2.93	2.82	2.01
96	0.70	0.81	3.30	3.66	3.36	3.30	2.22
97	0.71	0.82	3.38	3.63	3.36	3.29	2.23

[1] Effective period (described in Section 5.4)
[2] Fourier period (described in Section 5.5)
[3] Estimated drift ratio computed using Method 1
[4] Estimated drift ratio computed using Method 2
[5] Estimated drift ratio computed using Method 3
[6] Estimated drift ratio computed using Method 4
[7] Estimated drift ratio computed using Method 5

Table 5-9: Accuracy of methods used to estimate drift in runs of Specimens F1 and F2

Series	Total run count	Number of runs with absolute[1] errors (in drift ratios)					
		exceeding 0.5%			exceeding 1.0%		
		Method 3	Method 4	Method 5	Method 3	Method 4	Method 5
F1-B	15	3	3	1	0	1	0
F1-C	22	10	14	11	0	2	0
F1-M-C	19	1	2	0	0	0	0
F2-C	69	37	45	25	12	20	6
F2-M	9	0	0	0	0	0	0
F2-M-C-S	6	0	0	0	0	0	0
F2-C-S	13	10	11	10	5	10	6

Table 5-10: Accuracy of methods used to estimate drift in runs of Series F2-C

Run category	Total run count	Number of runs with absolute[1] errors (in drift ratios)					
		exceeding 0.5%			exceeding 1.0%		
		Method 3	Method 4	Method 5	Method 3	Method 4	Method 5
F2-C	69	37	45	25	12	20	6
$R1$	28	13	15	10	6	10	3
$R2$	24	14	16	8	4	6	2
$R3$	17	10	14	7	2	4	1
Group 1	38	25	25	10	9	14	1
Group 2	31	12	20	15	3	6	5
Case A	51	30	37	17	9	16	3
Case B	18	7	8	8	3	4	3
Linear specimen (F2)	19	0	0	0	0	0	0
Nonlinear specimen (F2)	50	37	45	25	12	20	6

[1] Absolute refers to absolute values of differences between measured and estimated drift ratios

Table 5-11: Summary of tests of SDOF reinforced concrete structures subjected to simulated earthquakes

Source, year	Specimen, run	PGA, g	PGV, in./sec.	Peak in-run drift ratio, %	m[1], lb	h[2], in.	K_o[3], kip/in.	T_o[4], sec.	M5 Δ/h[5], %
Takeda, 1970*	T2-11	1.3	8.6	2.2	4200	24	80	0.07	1.8
	T2-12	2.4	8.2	3.5					1.7
	T5-21	2.7	11.3	2.3					2.4
Gulkan, 1971*	HE1-1	1.2	7.8	0.7	690	15.5	80	0.03	1.1
	HE2-1	1.5	10.0	1.9					1.4
	HE2-2	1.5	9.4	2.1					1.3
	HE2-3	1.5	9.8	1.8					1.3
	FE1-1	2.2	16.4	2.1	4300	31	160	0.05	1.9
	FE1-2	2.5	18.6	2.3					2.2
	FE1-3	2.5	18.5	2.1					2.2
	FE1-4	2.4	17.7	2.1					2.1
	FE2-1	2.3	17.0	2.7					2.0
	FE2-2	2.6	19.1	2.6					2.3
	FE2-3	2.4	17.5	2.8					2.1
	FE2-4	2.9	21.3	3.1					2.5
	FE2-5	3.1	22.4	3.4					2.7
	FE2-6	2.9	21.3	3.4					2.5
Bonacci, 1989**	B-01-1	1.3	12.8	1.2	3900	49.3	60	0.08	1.5
	B-01-2	2.3	15.6	2.2					1.8
	B-01-3	2.7	15.6	2.4					1.8
	B-02-1	0.93	11.9	1.9	5000	60.3	30	0.13	1.8
	B-02-2	3.1	15.0	3.7					2.2

[1] Effective mass of specimen
[2] Total height of specimen
[3] Estimated initial lateral stiffness of specimen
[4] Estimated initial fundamental period of specimen
[5] Estimated drift ratio computed using Method 5

Table 5-11 (continued): Summary of tests of SDOF reinforced concrete structures subjected to simulated earthquakes

Source, year	Specimen, run	PGA, g	PGV, in./sec.	Peak in-run drift ratio, %	m[1], lb	h[2], in.	K_o[3], kip/in.	T_o[4], sec.	M5 Δ/h[5], %
Bonacci, 1989**	B-03-1	0.85	11.4	1.3	3900	49.3	60	0.08	1.3
	B-03-2	3.1	15.1	3.4					1.7
	B-04-1	0.87	10.8	2.4	5600	60.9	20	0.15	1.9
	B-04-2	3.1	15.0	3.5					2.7
	B-05-2	3.3	15.2	3.0	5000	60.3	30	0.13	2.3
	B-05-3	2.8	15.6	3.9					2.3
	B-06-1	0.43	4.8	0.7	5000	60.3	30	0.13	0.7
	B-06-2	0.89	8.8	1.6					1.3
	B-06-3	1.6	12.1	2.5					1.8
	B-07-1	0.67	11.5	2.1	5600	60.9	20	0.15	2.0
	B-07-2	1.3	14.6	2.4					2.6
	B-08-1	0.33	6.7	1.0	5600	60.9	20	0.15	1.2
	B-08-2	0.59	10.2	2.9					1.8
	B-09-1	0.42	8.5	0.9	5000	60.3	30	0.13	1.3
	B-09-2	1.2	14.1	3.7					2.1
	B-10-1	0.55	8.7	1.9	5600	60.9	20	0.15	1.6
	B-10-2	1.4	13.6	2.6					2.4
	B-10-4	1.4	13.6	2.6					2.4
	B-11-2	0.85	9.3	1.5	3900	49.3	60	0.08	1.1
	B-11-3	1.6	13.5	2.4					1.5
	B-11-4	2.6	14.4	3.6					1.6
	B-12-1	0.59	6.9	1.0	3900	49.3	60	0.08	0.8
	B-12-2	1.0	10.0	1.4					1.1
	B-12-3	1.4	13.3	1.8					1.5
	B-13-1	0.72	11.5	0.9	3900	49.3	60	0.08	1.3
	B-13-2	2.0	15.4	1.4					1.8

Table 5-11 (continued): Summary of tests of SDOF reinforced concrete structures subjected to simulated earthquakes

Source, year	Specimen, run	PGA, g	PGV, in./sec.	Peak in-run drift ratio, %	m[1], lb	h[2], in.	K_o[3], kip/in.	T_o[4], sec.	M5 Δ/h[5], %
Bonacci, 1989**	B-14-1	0.94	8.7	0.5	3900	49.3	60	0.08	1.0
	B-14-2	1.2	14.5	1.8					1.7
	B-14-3	1.5	15.6	1.9					1.8
	B-15-1	0.46	7.8	0.9	5000	60.3	30	0.13	1.2
	B-15-2	1.3	14.5	2.0					2.2
	B-15-3	1.5	15.7	2.2					2.3
Laughery, 2016**	C1-25	0.51	3.8	0.5	5000	47	30	0.13	0.7
	C1-50	0.93	7.6	1.7					1.4
	C1-75	1.3	8.9	2.5					1.7
	C1-100-1	1.8	10.9	3.5					2.1
	C1-100-2	1.5	11.7	3.0					2.2
	C2-100-1	1.9	12.0	3.5					2.3
	C2-75	1.4	9.7	2.2					1.8
	C2-50	0.82	6.6	1.8					1.2
	C2-25	0.64	3.6	0.8					0.7
	C2-100-2	1.7	11.5	3.5					2.2
	H1-25	0.58	3.3	0.9					0.6
	H1-50	0.90	6.5	1.7					1.2
	H1-75	1.2	8.9	2.2					1.7
	H1-100-1	1.4	12.0	3.0					2.3
	H1-100-2	1.4	12.1	3.4					2.3
	H2-100-1	1.6	11.7	3.0					2.2
	H2-75	1.2	9.3	2.7					1.7
	H2-50	0.95	6.3	2.1					1.2
	H2-25	0.62	3.4	1.1					0.6
	H2-100-2	1.6	11.5	3.1					2.2

Table 5-11 (continued): Summary of tests of SDOF reinforced concrete structures subjected to simulated earthquakes

Source, year	Specimen, run	PGA, g	PGV, in./sec.	Peak in-run drift ratio, %	m[1], lb	h[2], in.	K_o[3], kip/in.	T_o[4], sec.	M5 Δ/h[5], %
Schoettler (UCSD), 2015**	EQ1	0.20	5.4	0.8	540000	288	110	0.72	1.0
	EQ2	0.40	14.2	1.8					2.5
	EQ3	0.51	31.6	5.0					5.6
	EQ4	0.44	15.0	1.6					2.6
	EQ6	0.49	30.9	5.1					5.5

* Measured values of PGA and peak in-run drift ratios are taken from the specified source, measured values of PGV were obtained using the graphical procedure (described in Section 5.11.1)

** Measured values of PGA, PGV, and peak-in run drift ratios as reported by Shah (2021)

Table 5-12: Summary of tests of MDOF reinforced concrete frame and wall structures subjected to simulated earthquakes

Source, year	Specimen, run	No. stories	PGA[1], g	PGV[2], in./sec.	Peak in-run MDR[3], %	Peak in-run SDR[4], %	T_o[5], sec.	M5 MDR[6], %	M5 SDR[7], %
Aristizabal, 1976	D1-1	10	0.50	4.2	1.2	1.8	0.19	0.9	1.1
	D1-2		1.7	9.9	2.0	5.1		2.1	2.7
	M1-1	10	0.83	7.0	2.3	4.2	0.18	1.4	1.8
Healey, 1978	MF1-1	10	0.41	5.3	1.0	1.7	0.25	1.3	1.8
	MF1-2		0.91	8.9	2.1	3.4		2.1	3.0
	MF1-3		1.4	9.4	2.8	4.3		2.3	3.2
Moehle, 1978	MF2-1	10	0.37	6.2	1.1	1.7	0.27	1.6	2.4
	MF2-2		0.82	10.4	2.0	2.9		2.8	4.0
	MF2-3		1.3	11.4	2.6	3.5		3.0	4.4
Cecen, 1979	H1-1	10	0.34	5.3	1.3	2.0	0.25	1.4	1.9
	H1-2		0.79	11.1	2.3	3.4		2.8	3.9
	H1-3		1.6	14.0	4.4	6.9		3.6	4.9
	H2-1	10	0.16	2.2	0.4	0.8	0.25	0.6	0.8
	H2-2		0.30	3.9	0.8	1.8		1.0	1.4
	H2-3		0.45	6.3	1.1	2.7		1.6	2.2
	H2-4		0.44	6.3	1.1	3.2		1.6	2.2
	H2-5		0.68	9.4	1.7	4.4		2.4	3.3
	H2-6		0.98	12.2	2.6	5.4		3.1	4.3
	H2-7		2.5	13.6	4.4	5.6*		3.5	4.8

* Modified from value reported by Shah (2021) to reflect value tabulated by Cecen (1979)

[1] Measured peak base acceleration corrected as reported by Shah (2021)
[2] Measured peak base velocity corrected as reported by Shah (2021)
[3] Measured peak in-run mean (roof) drift ratio as reported by Shah (2021)
[4] Measured peak in-run story drift ratio as reported by Shah (2021)
[5] Estimated initial fundamental period computed using elastic elements, gross properties, and no rigid beam-column offsets as reported by Shah (2021)
[6] Estimated peak mean (roof) drift ratio computed using Method 5 as reported by Shah (2021)
[7] Estimated peak story drift ratio computed using Method 5 as reported by Shah (2021)

Table 5-12 (continued): Summary of tests of MDOF reinforced concrete frame and wall structures subjected to simulated earthquakes

Source, year	Specimen, run	No. stories	PGA[1], g	PGV[2], in./sec.	Peak in-run MDR[3], %	Peak in-run SDR[4], %	T_o[5], sec.	M5 MDR[6], %	M5 SDR[7], %
Moehle, 1980	FFW-1	9	0.31	5.2	1.1	N/A	0.21	1.2	1.5
	FHW-1	9	0.30	5.2	1.0	N/A	0.22	1.2	1.6
	FNW-1	9	0.36	5.4	1.1	2.0	0.26	1.4	2.1
	FNW-2		0.73	9.7	1.8	3.4		2.5	3.8
	FNW-3		1.2	14.2	3.6	8.5		3.7	5.6
	FSW-1	9	0.33	5.3	1.0	2.0	0.23	1.2	1.9
	FSW-2		0.55	9.6	1.7	4.0		2.3	3.4
	FSW-3		1.1	15.6	3.0	5.1		3.7	5.5
Wolfgram, 1984	NS2-1	7	0.56	7.4	0.7	0.9	0.10	0.9	1.2
	NS3-1	7	0.49	6.9	0.6	1.5	0.10	0.8	1.1
	NS3-2		0.79	10.2	1.1	N/A		1.2	1.6
	NS3-3		1.5	14.1	1.2	N/A		1.7	2.2
Wood, 1985	TW-1	9	0.38	5.9	1.1	1.6	0.17	1.3	1.8
	TW-2		0.57	8.6	1.7	2.7		1.8	2.6
	TW-3		0.77	10.7	2.1	3.2		2.3	3.3
	TW-4		1.1	14.6	2.7	5.1		3.1	4.5
	STP-1	9	0.29	2.2	0.2	0.3	0.17	0.5	0.7
	STP-2		1.5	8.3	0.9	1.6		1.8	2.6
	STP-3		0.09	1.3	0.3	0.5		0.3	0.4
	STP-4		0.39	6.3	1.0	1.6		1.3	2.0
	STP-5		0.55	8.6	1.4	2.7		1.8	2.7
	STP-6		0.79	11.6	1.6	4.5		2.5	3.6
Schultz, 1986	SS1-1	9	0.34	6.2	1.2	3.1	0.25	1.7	2.7
	SS1-2		0.33	5.7	1.0	2.4		1.5	2.5
	SS1-3		0.50	8.2	1.5	4.3		2.2	3.6

Table 5-12 (continued): Summary of tests of MDOF reinforced concrete frame and wall structures subjected to simulated earthquakes

Source, year	Specimen, run	No. stories	PGA[1], g	PGV[2], in./sec.	Peak in-run MDR[3], %	Peak in-run SDR[4], %	T_o[5], sec.	M5 MDR[6], %	M5 SDR[7], %
Schultz, 1986	SS2-1	9	0.33	5.2	1.1	1.4	0.26	1.4	2.3
	SS2-2		0.36	5.2	1.3	2.2		1.4	2.3
	SS2-3		0.33	4.9	1.0	1.4		1.3	2.2
	SS2-4		0.63	8.8	1.8	2.9		2.4	3.9
	SS2-5		0.96	12.6	2.4	4.7		3.5	5.6
	SS2-6		1.2	15.6	3.1	9.0		4.3	6.9
Shahrooz, 1987	Long-1	6	0.08	1.4	0.1	0.2	0.28	0.2	0.2
	Long-2		0.16	3.2	0.3	0.5		0.4	0.5
	Long-3		0.49	8.9	1.1	1.6		1.2	1.4
	Long-4		0.48	9.6	0.9	1.1		1.3	1.5
	Long-5		0.62	11.8	1.5	2.0		1.6	1.9
	Long-6		0.33	11.9	2.0	3.3		1.6	1.9
	Short-4	6	0.48	9.6	1.0	1.5	0.22	1.0	1.2
	Short-5		0.62	11.8	2.2	3.0		1.3	1.5
	Short-6		0.33	11.9	1.9	2.8		1.3	1.5
Eberhard, 1989	ES1-1	9	0.35	5.2	0.9	1.2	0.19	1.0	1.5
	ES1-2		0.50	7.6	1.4	2.3		1.5	2.1
	ES1-3		0.62	10.0	2.0	4.0		2.0	2.8
	ES2-1	9	0.35	5.1	0.8	1.3	0.19	1.0	1.5
	ES2-2		0.50	7.5	1.5	3.1		1.5	2.1
	ES2-3		0.60	9.8	1.9	4.6		2.0	2.8

Table 5-12 (continued): Summary of tests of MDOF reinforced concrete frame and wall structures subjected to simulated earthquakes

Source, year	Specimen, run	No. stories	PGA[1], g	PGV[2], in./sec.	Peak in-run MDR[3], %	Peak in-run SDR[4], %	T_o[5], sec.	M5 MDR[6], %	M5 SDR[7], %
Kajiwara (E-Defense), 2015	Frame-1	10	0.07	3.4	0.2	0.3	0.67	0.2	0.3
	Frame-2		0.21	8.5	0.5	0.7		0.5	0.7
	Frame-3		0.42	17.1	1.0	1.7		1.0	1.4
	Frame-4		1.0	33.0	1.8	3.0		2.0	2.6
	Frame-5		0.46	18.3	0.7	1.3		1.1	1.5
	Wall-1	10	0.06	2.5	0.1	0.1	0.50	0.1	0.1
	Wall-2		0.16	6.6	0.2	0.2		0.3	0.4
	Wall-3		0.32	12.2	0.4	0.6		0.6	0.7
	Wall-4		0.75	21.9	0.8	1.3		1.0	1.3
	Wall-5		0.45	18.3	0.7	1.1		0.9	1.1
Kajiwara (E-Defense), 2018	Frame-1	10	0.09	3.7	0.2	0.3	0.67	0.2	0.3
	Frame-2		0.25	9.5	0.6	0.8		0.6	0.8
	Frame-3		0.50	19.3	1.0	1.5		1.2	1.5
	Frame-4		0.83	36.4	1.8	2.7		2.2	2.9
	Frame-5		1.2	37.8	1.9	2.7		2.3	3.0
	Frame-6		0.87	32.0	1.2	1.8		1.9	2.6
	Wall-1	10	0.07	2.9	0.1	0.1	0.50	0.1	0.2
	Wall-2		0.17	7.2	0.3	0.4		0.3	0.4
	Wall-3		0.37	15.5	0.6	0.8		0.7	0.9
	Wall-4		0.62	28.9	1.0	1.3		1.4	1.7
	Wall-5		0.88	30.7	1.0	1.3		1.5	1.8
	Wall-6		1.3	36.7	1.3	2.1		1.7	2.1

Table 5-13: Summary of properties of SDOF and MDOF infilled frame structures subjected to simulated earthquakes

Source, year	Test series	No. stories	No. bays[1]	$\frac{A_{net}}{A_g}$[2]	t_{inf}[3], in.	I_{inf}[4], x 10^3 in.^{4}	f'_m[5], psi	E_m[6], ksi	m[7], lb	h[8], in.	K_{inf}[9], kip/in.	T_o[10], sec.
Lee, 2002	FIF	3	2x1	1.0	1.5*	61.0	3200	1400	27700	87.4	140	0.07
	PIF	3	2x1	1.0	1.5*	30.5	3200	1400	26300	87.4	70	0.10
Stavridis, 2009		3	2x0	1.0	7.9*	3930	3200	1400	145000	257	240	0.10
Benavent, 2018		1	2x1	1.0	1.6	128	1500	650	27400	68.9	280	0.05
Guljas, 2020	S1	3	2x1	0.32	4.7	833	1500	650	53800	142	70	0.14
	S2	3	2x1	1.0	4.7	833	2900	1300	53800	142	410	0.06
This investigation, 2021	F1-M-C, F2-M, F2-M-C-S	1	1x0	0.75	3.6	112	2800	1400	48900	50	500	0.10

* Two-wythe infill wall

[1] Number of bays - first number is number of bays in direction of motion, second number is number of bays perpendicular to direction of motion. "0" indicates planar frames where columns are arranged along a single column line.
[2] Ratio of net cross-sectional area of masonry unit to gross cross-sectional area of masonry unit (assumed to be unity if not mentioned)
[3] Thickness of infill wall (width of masonry unit unless stated otherwise)
[4] Total moment of inertia of infilled frame computed as $I_{inf} = \sum_{i=1}^{n} \frac{1}{12} * t_{inf} * L_i^3$ where n is number of infilled bays of length L_i
[5] Measured gross compressive strength of masonry prism
[6] Estimated elastic modulus of masonry computed as $E_m = 450 * f'_m$
[7] Effective mass of infilled frame as reported by source
[8] Total height of infilled frame
[9] Estimated initial lateral stiffness of infilled frame computed using Equation 1-1
[10] Estimated initial fundamental period of infilled frame computed using Equation 5-17

Table 5-14: Summary of tests of SDOF infilled frame structures subjected to simulated earthquakes

Source	Specimen, run	PGV, in./sec.	Peak in-run drift ratio, %	M5 Δ/h^1, %
Benavent	C100	7.9	0.15	0.50
	C100B	7.9	0.18	0.50
	C200	17.3	1.07	1.11
This investigation	F1-M-C-10-1	2.0	0.07	0.28
	F1-M-C-20-1	2.9	0.12	0.40
	F1-M-C-40-1	5.9	0.34	0.84
	F1-M-C-60-1	7.7	0.73	1.09
	F1-M-C-80-1	9.6	1.03	1.36
	F2-M-10-1	1.4	0.03	0.21
	F2-M-20-1	2.7	0.11	0.38
	F2-M-40-1	4.8	0.38	0.68
	F2-M-60-1	7.2	0.72	1.02
	F2-M-80-1	8.4	1.14	1.19
	F2-M-C-S-10-1	1.3	0.13	0.18
	F2-M-C-S-20-1	2.3	0.24	0.33
	F2-M-C-S-40-1	4.3	0.48	0.61
	F2-M-C-S-60-1	6.2	0.74	0.88
	F2-M-C-S-80-1	8.1	1.12	1.14

[1] Estimated drift ratio of infilled frame computed using Method 5

Table 5-15: Summary of tests of MDOF infilled frame structures subjected to simulated earthquakes

Source	Specimen, run	PGV, in./sec.	Peak in-run MDR[1], %	Peak in-run SDR[2], %	M5 MDR[3], %	M5 SDR[4], %
Lee*	FIF-012	3.8	0.03	0.04	0.28	0.38
	FIF-02	6.5	0.07	0.11	0.48	0.66
	FIF-03	7.7	0.08	0.11	0.56	0.78
	FIF-04	10.9	0.11	0.19	0.80	1.11
	PIF-012	4.3	0.14	0.24	0.44	0.61
	PIF-02	5.2	0.19	0.28	0.52	0.72
	PIF-03	7.1	0.26	0.30	0.72	1.00
	PIF-04	8.8	0.33	0.51	0.89	1.23
	*BF-012***	*2.9*	*0.20*	*0.26*	N/A	N/A
	*BF-02***	*4.3*	*0.63*	*0.78*		
	*BF-03***	*6.4*	*0.80*	*1.08*		
	*BF-04***	*8.3*	*1.35*	*1.68*		
Stavridis***	gil10	1.7	0.01	0.02	0.06	0.08
	gil20a	3.5	0.02	0.04	0.12	0.16
	gil40a	6.9	0.01	0.08	0.25	0.32
	gil20b	3.4	0.01	0.03	0.12	0.16
	gil20c	3.5	0.01	0.03	0.12	0.16
	gil40b	7.1	0.03	0.03	0.26	0.34
	gil67a	10.9	0.06	0.10	0.39	0.51
	gil20d	3.0	0.01	0.02	0.11	0.14
	gil67b	10.2	0.11	0.22	0.36	0.48
	gil83	13.2	0.18	0.40	0.47	0.62
	gil91	14.2	0.23	0.55	0.51	0.67
	gil100	15.0	0.27	0.67	0.54	0.71
	gil120	17.3	0.49	1.33	0.62	0.81

* Measured values of PGV were obtained using the procedure described in Appendix C

** Specimen is a bare frame tested by Lee (2002)

*** Measured values of PGV, peak in-run MDR, and peak in-run SDR were obtained using raw data provided by Stavridis (2009)

---

[1] Measured peak in-run mean (roof) drift ratio of infilled frame
[2] Measured peak in-run story drift ratio of infilled frame
[3] Estimated peak in-run mean (roof) drift ratio of infilled frame computed using Method 5
[4] Estimated peak in-run story drift ratio of infilled frame computed using Method 5

Table 5-15 (continued): Summary of tests of MDOF infilled frame structures subjected to simulated earthquakes

Source	Specimen, run	PGV, in./sec.	Peak in-run MDR[1], %	Peak in-run SDR[2], %	M5 MDR[3], %	M5 SDR[4], %
Guljas	S1-5%	0.9	0.03	0.05	0.09	0.12
	S1-10%	2.1	0.05	0.07	0.19	0.26
	S1-20%	3.2	0.08	0.10	0.30	0.40
	S1-30%	3.9	0.17	0.23	0.36	0.49
	S1-40%	5.5	0.17	0.28	0.51	0.69
	S1-60%	7.5	0.30	0.43	0.69	0.94
	S1-70%	14.2	0.47	0.73	1.31	1.77
	S1-80%	14.2	0.54	0.93	1.31	1.77
	S1-100%	22.4	0.93	1.66	2.08	2.81
	S1-120%	24.8	1.29	2.55	2.30	3.10
	S2-5%	1.0	0.03	0.04	0.04	0.05
	S2-10%	2.1	0.06	0.07	0.08	0.11
	S2-20%	3.0	0.08	0.11	0.11	0.15
	S2-30%	4.3	0.12	0.14	0.16	0.22
	S2-40%	5.1	0.11	0.13	0.19	0.26
	S2-60%	7.9	0.13	0.14	0.29	0.39
	S2-70%	10.2	0.18	0.20	0.38	0.51
	S2-80%	14.2	0.27	0.30	0.53	0.71
	S2-100%	22.0	0.64	0.93	0.82	1.10
	S2-120%	34.3	0.87	1.25	1.27	1.71
	S2-140%	33.1	0.99	1.63	1.23	1.66

Table 6-1: Properties of school buildings surveyed after 2007 Pisco, Peru earthquake

No.	School ID	No. floors	Tot. floor area[1], ft^2	NS infill WA[2], ft^2	EW infill WA[2], ft^2	NS infill WR[3], %	EW infill WR[3], %	Structural damage	Infill damage	Captive columns
1	142E	2	380	13	6	3.3	1.5	None	None	No
2	142W	3	7250	49	0	0.7	0.0	Moderate	Moderate	Yes
3	143	2	1770	0	61	0.0	3.4	Severe	Moderate	Yes
4	144W	2	7710	75	26	1.0	0.3	Light	Severe	Yes
5	144E	2	7710	68	26	0.9	0.3	Light	Severe	Yes
6	145W	2	7710	68	7	0.9	0.1	Severe	Severe	Yes
7	145E	2	7710	49	12	0.6	0.2	Severe	Severe	Yes
8	146	3	8320	50	0	0.6	0.0	Severe	Severe	Yes
9	147W	2	7710	55	14	0.7	0.2	Light	Severe	Yes
10	147E	2	7710	62	12	0.8	0.2	Moderate	Severe	Yes

Table 6-2: Properties of school buildings surveyed after 2016 Meinong, Taiwan earthquake

No.	School ID	No. floors	Tot. floor area[1], ft^2	NS infill WA[2], ft^2	EW infill WA[2], ft^2	NS infill WR[3], %	EW infill WR[3], %	Structural damage	Infill damage	Captive columns
11	A03	2	13620	157	70	1.2	0.5	Light	Light	Yes
12	A04	2	8970	93	0	1.0	0.0	Severe	Light	Yes
13	A05	3	33140	0	19	0.0	0.1	Moderate	Moderate	Yes
14	A08	2	16960	198	69	1.2	0.4	None	None	Yes
15	A10	2	6850	47	0	0.7	0.0	None	Light	Yes
16	B01	3	13850	39	0	0.3	0.0	Severe	Moderate	Yes
17	B04	3	26480	0	226	0.0	0.9	Severe	Severe	Yes
18	B05	2	13240	159	38	1.2	0.3	Light	Light	Yes
19	B06	3	26060	0	199	0.0	0.8	Light	Light	Yes
20	B07	3	27130	0	180	0.0	0.7	Light	None	Yes
21	B08	3	10740	42	0	0.4	0.0	Light	Light	Yes

[1] Total floor area is product of typical floor area and number of floors in building
[2] WA is “wall area” defined as cross-sectional area of infill wall on ground floor
[3] WR is “wall ratio” defined as ratio of cross-sectional area of infill wall to total floor area

Table 6-2 (continued): Properties of school buildings surveyed after 2016 Meinong, Taiwan earthquake

No.	School ID	No. floors	Tot. floor area[1], ft^2	NS infill WA[2], ft^2	EW infill WA[2], ft^2	NS infill WR[3], %	EW infill WR[3], %	Structural damage	Infill damage	Captive columns
22	B11	3	29740	227	0	0.8	0.0	Moderate	Moderate	Yes
23	B14	4	8310	54	0	0.6	0.0	Light	Light	No
24	B15	4	58130	37	118	0.1	0.2	None	None	Yes
25	B16-A	3	41980	181	46	0.4	0.1	None	Light	Yes
26	B16-B	3	53060	199	117	0.4	0.2	None	Light	Yes
27	B25	2	4570	8	23	0.2	0.5	None	None	Yes
28	C06	3	11820	73	15	0.6	0.1	Light	Light	Yes
29	C07	3	8280	67	22	0.8	0.3	None	Light	Yes
30	C08	3	17040	197	17	1.2	0.1	Moderate	Light	Yes
31	C10	2	10120	122	58	1.2	0.6	None	Light	Yes
32	C18	2	12140	151	40	1.2	0.3	Light	Moderate	Yes
33	C23	3	9750	91	4	0.9	0.0	None	None	Yes
34	D18	1	1930	50	16	2.6	0.8	None	Light	Yes
35	D19	2	12510	168	80	1.3	0.6	None	None	Yes
36	D20	2	2350	0	42	0.0	1.8	None	None	Yes
37	D21	2	19700	187	78	1.0	0.4	None	Light	Yes
38	D22	3	19780	0	227	0.0	1.1	None	None	Yes
39	D23	3	26230	164	40	0.6	0.2	None	Light	Yes
40	D24	4	17390	0	124	0.0	0.7	None	None	Yes
41	D25	2	18460	146	13	0.8	0.1	None	None	Yes
42	E10	3	9150	37	0	0.4	0.0	Severe	Light	Yes
43	F06	2	12060	103	0	0.9	0.0	None	None	Yes
44	F07	4	89040	194	164	0.2	0.2	None	Light	Yes
45	F10	1	10010	98	56	1.0	0.6	None	Severe	Yes
46	F11	1	2490	15	23	0.6	0.9	None	None	Yes

Table 6-3: Properties of school buildings surveyed after 2016 Manabí, Ecuador earthquake

No.	School ID	No. floors	Tot. floor area[1], ft^2	NS infill WA[2], ft^2	EW infill WA[2], ft^2	NS infill WR[3], %	EW infill WR[3], %	Structural damage	Infill damage	Captive columns
47	A05	2	6910	40	31	0.6	0.5	Light	Light	Yes
48	A30	3	16860	78	66	0.5	0.4	Severe	Severe	Yes
49	A32	1	11050	74	78	0.7	0.7	Light	Moderate	Yes
50	A33	2	7070	30	57	0.4	0.8	Moderate	Moderate	Yes
51	A34-I	2	6710	64	56	0.9	0.8	Light	Severe	Yes
52	A34-II	2	7560	54	70	0.7	0.9	Severe	Severe	Yes
53	A36	2	2430	0	29	0.0	1.2	Light	Light	Yes
54	A37	2	3380	22	42	0.6	1.2	Light	Severe	Yes
55	A38-I	3	7410	0	29	0.0	0.4	Severe	Severe	Yes
56	A38-II	3	7280	0	30	0.0	0.4	Moderate	Moderate	Yes
57	A39	3	9170	37	0	0.4	0.0	Severe	Severe	Yes
58	A40	4	9410	20	23	0.2	0.2	Severe	Severe	Yes
59	A41	3	7410	37	0	0.5	0.0	Light	Light	Yes
60	A42	3	7660	42	0	0.5	0.0	Light	Severe	Yes
61	A45	2	3480	29	4	0.8	0.1	Light	Light	Yes
62	A47	2	3830	5	37	0.1	1.0	Moderate	Severe	Yes
63	A48	1	1770	30	23	1.7	1.3	Light	Severe	Yes
64	A57	2	3390	33	0	1.0	0.0	Severe	Severe	Yes
65	A58	2	2930	0	18	0.0	0.6	Moderate	Moderate	Yes
66	A59	2	2500	0	14	0.0	0.6	Moderate	Severe	Yes
67	A60	2	4700	43	0	0.9	0.0	Severe	Severe	Yes
68	A61	2	3720	23	15	0.6	0.4	Moderate	Severe	Yes
69	A62	2	3360	26	0	0.8	0.0	Moderate	Severe	Yes
70	A63	2	3120	22	16	0.7	0.5	Moderate	Severe	Yes
71	B21	2	4940	0	15	0.0	0.3	Light	Light	Yes

[1] Total floor area is product of typical floor area and number of floors in building
[2] WA is “wall area” defined as cross-sectional area of infill wall on ground floor
[3] WR is “wall ratio” defined as ratio of cross-sectional area of infill wall to total floor area

Table 6-3 (continued): Properties of school buildings surveyed after 2016 Manabí, Ecuador earthquake

No.	School ID	No. floors	Tot. floor area[1], ft^2	NS infill WA[2], ft^2	EW infill WA[2], ft^2	NS infill WR[3], %	EW infill WR[3], %	Structural damage	Infill damage	Captive columns
72	B22	1	2400	15	0	0.6	0.0	Light	Light	Yes
73	B23	3	11100	17	26	0.2	0.2	Severe	Severe	Yes
74	B24	3	8200	12	0	0.1	0.0	Light	Light	Yes
75	B25	2	9300	25	54	0.3	0.6	Light	Light	Yes
76	B26	2	10190	25	55	0.2	0.5	Light	Moderate	No
77	B27	1	1980	32	3	1.6	0.2	Light	Light	Yes
78	B28	2	4940	6	9	0.1	0.2	Light	Severe	Yes
79	B29	1	2490	43	0	1.7	0.0	Light	Light	Yes
80	B30	2	3140	26	26	0.8	0.8	Light	Moderate	Yes
81	B31	3	7420	14	0	0.2	0.0	Light	Moderate	Yes
82	B32a	3	7140	17	20	0.2	0.3	Severe	Moderate	Yes
83	B32b	3	11890	19	25	0.2	0.2	Severe	Moderate	Yes
84	B32c	3	10390	28	20	0.3	0.2	Severe	Moderate	Yes
85	B33	3	7580	54	0	0.7	0.0	Moderate	Light	Yes
86	B34	3	7530	62	0	0.8	0.0	Light	Severe	Yes
87	B35	3	7410	9	28	0.1	0.4	Light	Moderate	Yes
88	B36	2	7230	26	0	0.4	0.0	Severe	Severe	Yes
89	B37	2	3900	24	0	0.6	0.0	Light	Light	Yes
90	B38	2	4770	39	4	0.8	0.1	Light	Light	Yes
91	B39	1	2380	4	32	0.2	1.4	Severe	Light	Yes
92	B40	2	7520	33	18	0.4	0.2	Severe	Moderate	Yes
93	B41	3	7230	41	0	0.6	0.0	Light	Light	Yes
94	B42	2	3410	19	0	0.6	0.0	Light	Light	Yes
95	B43	2	4850	45	37	0.9	0.8	Light	Light	Yes
96	B44	2	3140	29	0	0.9	0.0	Light	Light	Yes
97	B45	1	1710	25	13	1.4	0.8	Light	Light	Yes
98	B53	1	1880	33	0	1.8	0.0	Moderate	Light	Yes
99	B54	1	1970	40	45	2.0	2.3	Light	Light	No
100	C16	2	3770	33	29	0.9	0.8	Light	Light	Yes

Table 6-3 (continued): Properties of school buildings surveyed after 2016 Manabí, Ecuador earthquake

No.	School ID	No. floors	Tot. floor area[1], ft^2	NS infill WA[2], ft^2	EW infill WA[2], ft^2	NS infill WR[3], %	EW infill WR[3], %	Structural damage	Infill damage	Captive columns
101	C17	1	2790	20	19	0.7	0.7	Severe	Light	Yes
102	C20	3	9150	76	40	0.8	0.4	Severe	Severe	Yes
103	C23	3	7580	29	0	0.4	0.0	Light	Light	No
104	C24	3	7320	4	29	0.1	0.4	Severe	Severe	Yes
105	C25	3	6660	0	30	0.0	0.5	Severe	Severe	Yes
106	C26	3	6390	29	3	0.5	0.1	Moderate	Severe	Yes
107	C27	3	5630	0	29	0.0	0.5	Light	Light	Yes
108	C29	2	4340	29	29	0.7	0.7	Light	Light	Yes
109	C30	3	7590	44	25	0.6	0.3	Severe	Severe	Yes
110	C31	1	4450	88	132	2.0	3.0	Moderate	Moderate	Yes
111	C32	2	3840	31	24	0.8	0.6	Moderate	Moderate	Yes
112	C33	2	4620	31	4	0.7	0.1	Light	Light	Yes
113	C34	2	4620	39	36	0.8	0.8	Light	Light	Yes

Table 6-4: Properties of school buildings surveyed after 2017 Puebla, Mexico earthquake

No.	School ID	No. floors	Tot. floor area[1], ft^2	NS infill WA[1], ft^2	EW infill WA[1], ft^2	NS infill WR[2], %	EW infill WR[2], %	Structural damage	Infill damage	Captive columns
114	A5	2				0.7	0.0	None	None	No
115	A20-A	4				0.5	0.0	None	None	No
116	A20-B	4				0.5	0.4	None		Yes
117	A20-C	4				0.0	0.2	None	None	Yes
118	A49	2				1.5	0.0	None	None	Yes
119	A52	2				0.7	0.6	None	None	Yes
120	A63	4				0.0	0.3	Severe	Severe	Yes
121	A64	2				0.8	0.1	Light	None	Yes
122	A65	2				0.5	0.5	None	None	Yes
123	A66	2				1.1	0.6	None	None	Yes
124	A68	3				0.0	0.1	None	None	No
125	A69	3				0.0	0.8	None	Light	Yes

Table 6-5: Properties of school buildings surveyed after 2017 Pohang, South Korea earthquake

No.	School ID	No. floors	Tot. floor area[3], ft^2	NS infill WA[4], ft^2	EW infill WA[4], ft^2	NS infill WR[2], %	EW infill WR[2], %	Structural damage	Infill damage	Captive columns
126	A01	3	27040	177	60	0.7	0.2	Severe	Severe	Yes
127	A02	3	25960	257	60*	1.0	0.2*	Severe	Severe	Yes
128	A14	3	12230	127	43	1.0	0.4	Light	Moderate	No
129	C10	3.5	33700	192	44	0.6	0.1	Light	Moderate	No

* Modified from values listed on datacenterhub.org to match EW infill WA and WR calculated for School ID A01 (No. 126)

[1] No values were reported for total floor area or cross-sectional areas of NS and EW infill walls on ground floor for surveys in Mexico City
[2] WR is "wall ratio" defined as ratio of cross-sectional area of infill wall to total floor area
[3] Total floor area is product of typical floor area and number of floors in building
[4] WA is "wall area" defined as cross-sectional area of infill wall on ground floor

Table 6-6: Average ground motion parameters measured during earthquakes

Earthquake	Date	Location where records were obtained	Source	Average PGA, g	Average PGV, in./sec.	Average PGD, in.
Pisco, Peru	15 August 2007	Ica, Peru	DataHub[1]	0.30	17.1	5.5
Meinong, Taiwan	6 February 2016	Tainan City, Taiwan	DataHub[2]	0.31	19.7	5.4
Manabí, Ecuador	16 April 2016	Manta, Ecuador Portoviejo, Ecuador	DataHub[3]	0.41	15.4	3.5
Puebla, Mexico	19 September 2017	Mexico City, Mexico	DataHub[4]	0.13	11.6	3.3
Pohang, South Korea	15 November 2017	Pohang, South Korea	DataHub[5]	0.33	5.7	0.9

[1] Sim (2016)
[2] NCREE (2016)
[3] Sim (2016)
[4] Purdue University (2018)
[5] Sim (2018)

Table 6-7: Properties of bare frame prototype

Parameter	Value	Unit
Number of stories	3	
Story height	3.2	m
Story weight	2800	kN
Typical floor area	320	m^2
Depth of beam	0.5	m
Width of beam	0.3	m
Thickness of slab	0.15	m
Short direction		
Number of bays	2	
Bay length	8	m
Column dimension	0.5	m
Initial fundamental period		
STERA 3D	0.55	sec.
Procedure described in Sec. 5.11.2*	0.65	sec.
Long direction		
Number of bays	5	
Bay length	4	m
Column dimension	0.3	m
Initial fundamental period		
STERA 3D	0.55	sec.
Procedure described in Sec. 5.11.2*	0.65	sec.
Compressive strength of concrete	24	MPa
Elastic modulus of concrete	23000	MPa
Yield stress of steel reinforcement	295	MPa
Elastic modulus of steel reinforcement	205000	MPa

* Initial fundamental periods were estimated assuming the bare frame prototype has flexible beams using the procedure described in Section 5.11.2.

Table 6-8: Properties of infilled frame prototype

Parameter	Value	Unit
Infill wall		
Wall thickness	0.15	m
Height of masonry unit	0.1	m
Thickness of mortar joint	0.02	m
Void ratio of masonry unit	0	
Short direction		
Number of bays with full-height infill walls	4	
Infill wall ratio	0.50	%
Initial fundamental period		
STERA 3D	0.15	sec.
Equation 5-17	0.20	sec.
Long direction		
Number of bays with full-height infill walls	9	
Infill wall ratio	0.56	%
Initial fundamental period		
STERA 3D	0.10	sec.
Equation 5-17	0.40	sec.
Compressive strength		
Masonry unit	20	MPa
Mortar	10	MPa
Elastic modulus of masonry prism	6000	MPa

Table 6-9: Analysis assumptions for prototypes modeled in STERA 3D

Parameter	Assumption
Connection panel (beam-column joint)	Rigid zone, reduction ratio set to ‘0’
Slab effect (on beam)	Amplification factor set to ‘1’
Floor assumption (slab)	Rigid
Restrained freedom number	Value set to ‘0’
P-Delta effect	Ignored
Nonlinear shear spring	Ignored
Mass distribution	Same for all nodes
Passive damper element	Ignored
Isolator	Ignored
Masonry wall	Stiffness reduction factor set to ‘5’

Table 7-1: Summary of parameters of infilled frames subjected to simulated earthquakes

Source	Specimen	WA[1], in.^{2}	FA$_{proj}$[2], ft.^{2}	WR[3], %	Mean SDR$_{inf}$[4], %	PGV prod. SDR$_{inf}$ =1%[5], in./sec.
Lee	FIF	300	150	1.3	0.01	68
	PIF	150	150	0.7	0.05	19
Stavridis		2270	810	2.0	0.02	46
Benavent		250	150	1.1	0.03	29
Guljas	S1	1400	300	0.5*	0.06	17
	S2	1400	300	1.6*	0.03	31
This investigation	F1-M-C	260	270	0.5	0.07	15
	F2-M	260	270	0.5	0.08	13
	F2-M-C-S	260	270	0.5	0.11	9

* Reduced from result obtained using Equation 2 by 50%

[1] WA is “wall area” computed as cross-sectional area of infill walls (product of wall thicknesses and distances between centerlines of boundary elements flanking infill walls) in first story of specimen oriented in the direction of motion
[2] Projected floor area computed as the effective weight of specimen divided by 180 pounds per square foot
[3] WR is “wall ratio” computed using Equation 7-2
[4] Mean ratio of measured peak in-run story drift ratio produced by a peak base velocity of 1 in./sec. in runs of specified series
[5] Mean peak base velocity required to produce a story drift of 1% in runs of specified series computed as the inverse of the value listed in column 6 of Table 7-1

FIGURES

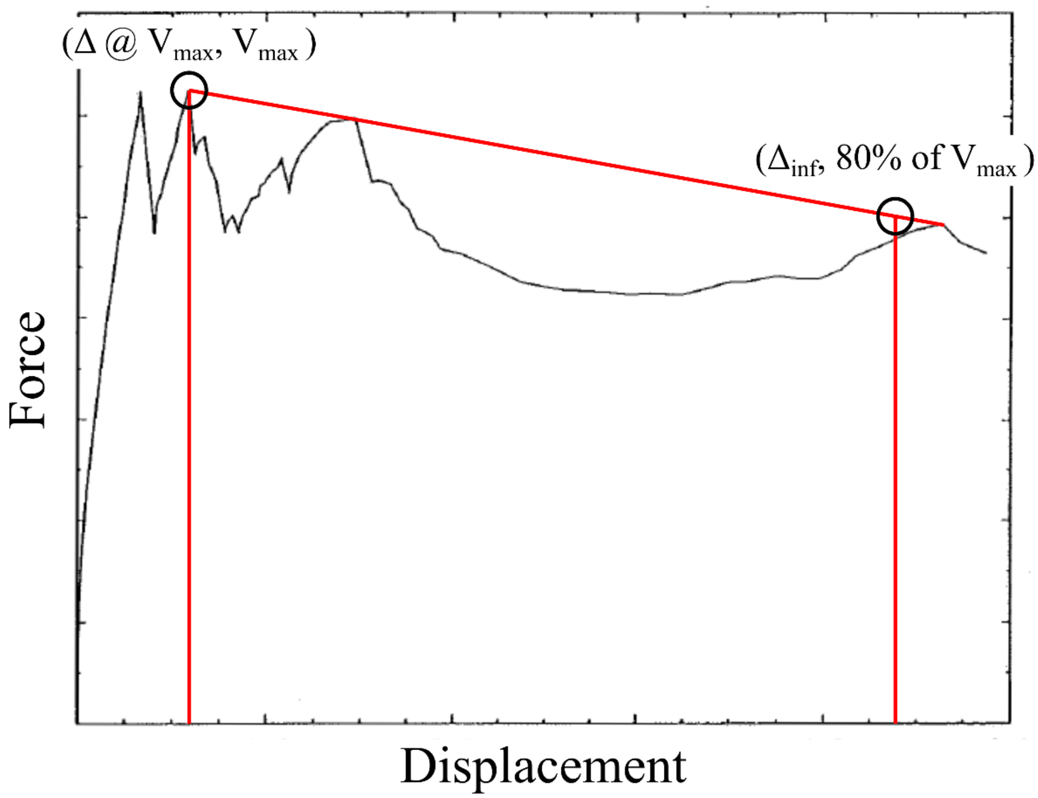

Figure 1-1: Graphical procedure used to obtain drift capacities from force-displacement plots

Note: Figure 1-1 is taken from Mehrabi (1994).

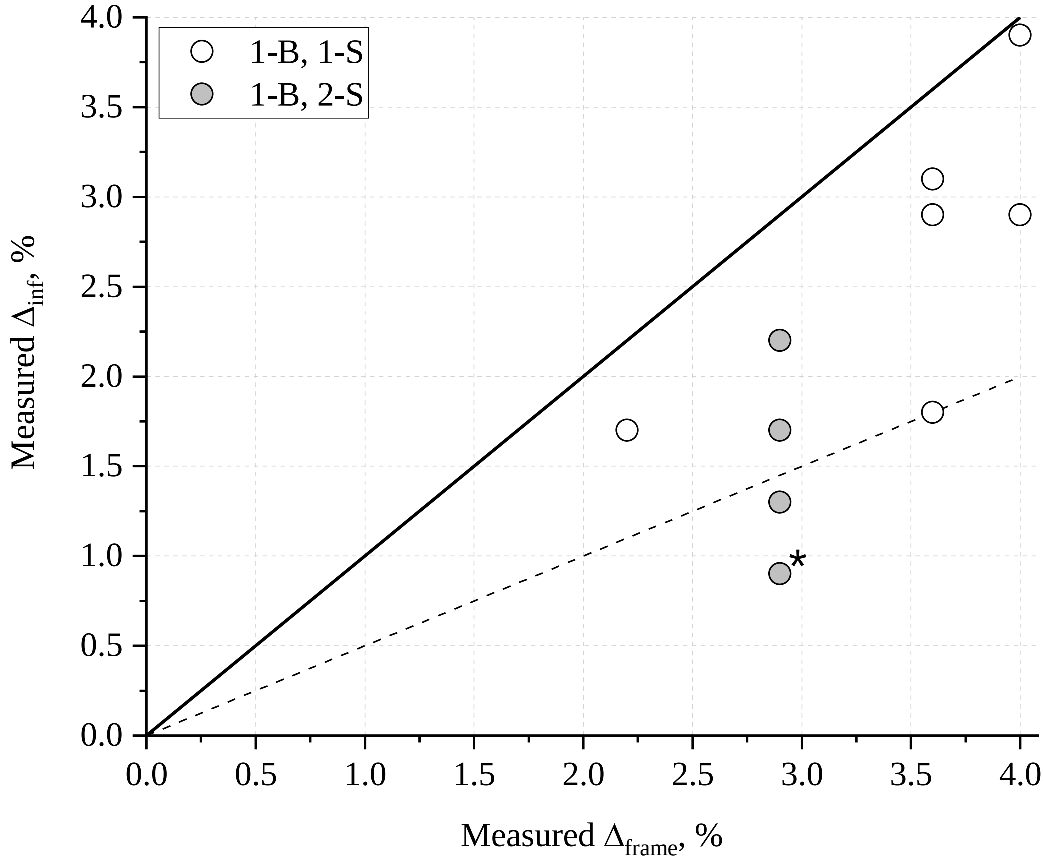

Figure 1-2: Variation of measured drift capacity of infilled frame with measured drift capacity of bare frame

Note: The infilled frame (indicated with asterisk) was pushed to a story drift ratio of only 1% in one direction of a cyclic test which may have reduced its drift capacity.

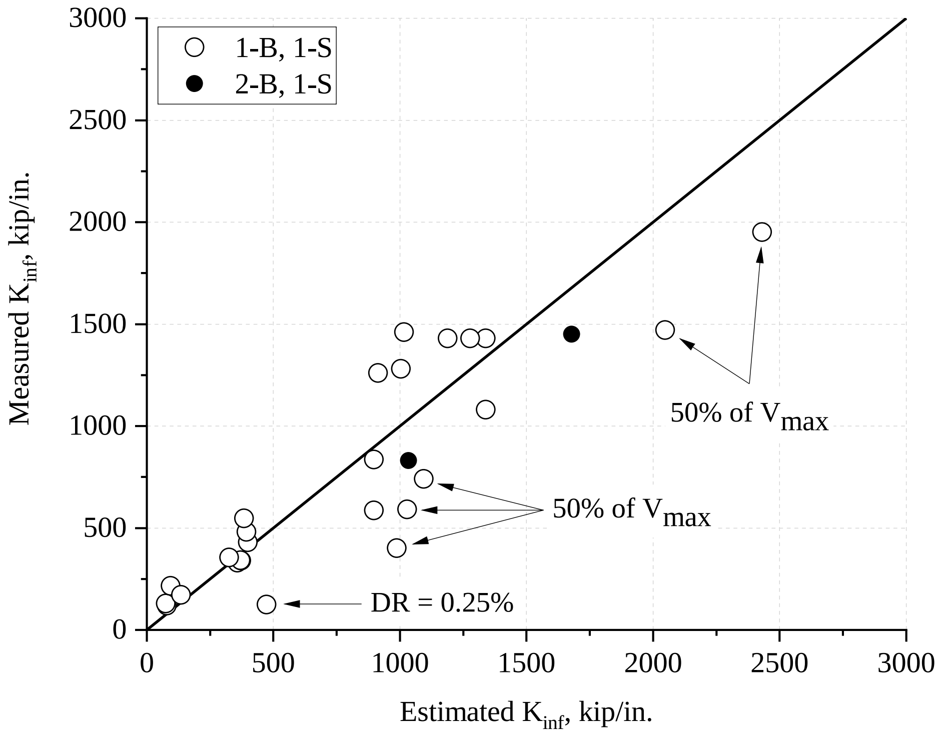

Figure 1-3: Measured vs. estimated initial lateral stiffness of infilled frames

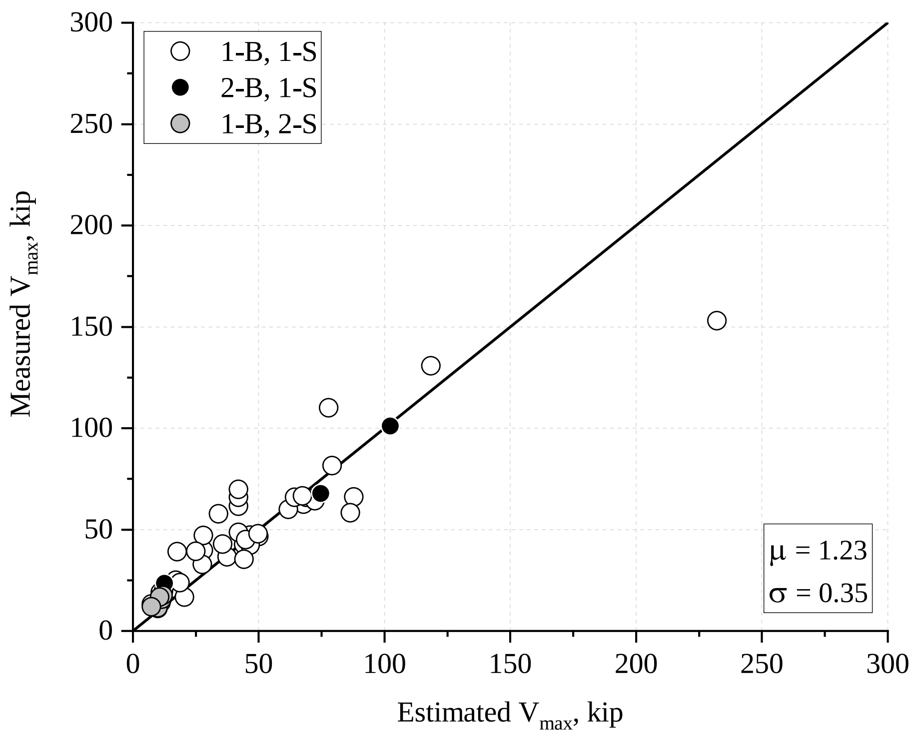

Figure 1-4: Measured vs. estimated peak lateral strength of infilled frames

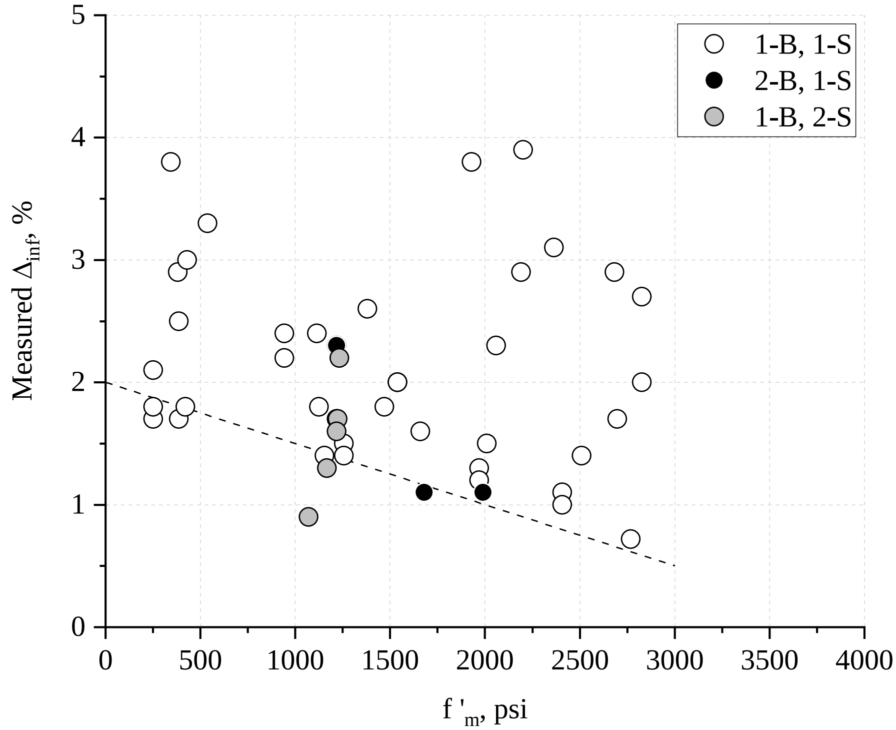

Figure 1-5: Variation of measured drift capacity of infilled frame with measured gross compressive strength of masonry prism

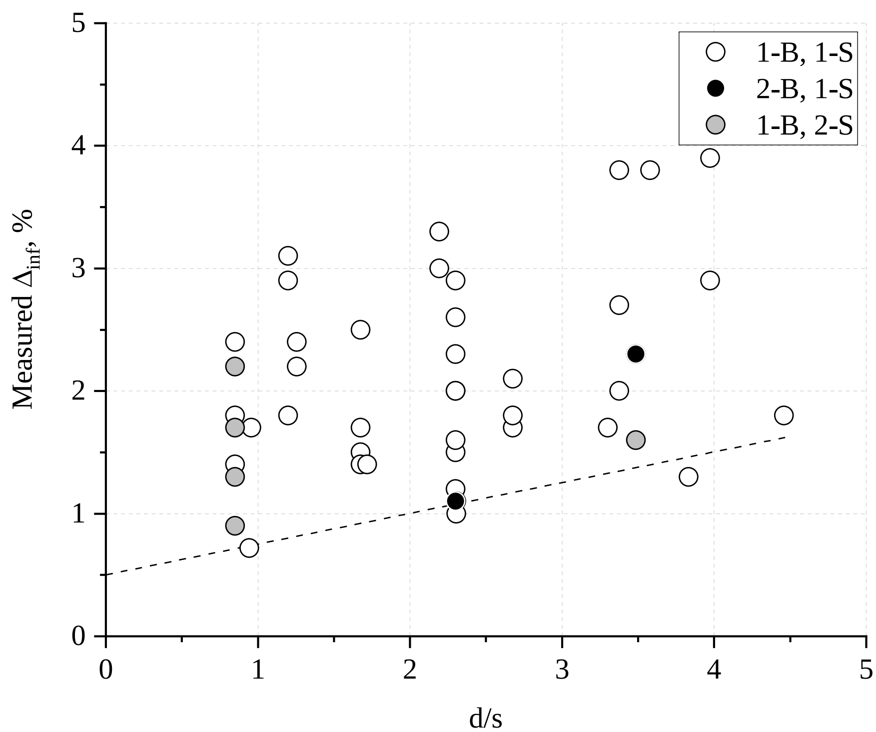

Figure 1-6: Variation of measured drift capacity of infilled frame with ratio of effective depth to spacing of transverse reinforcement in column

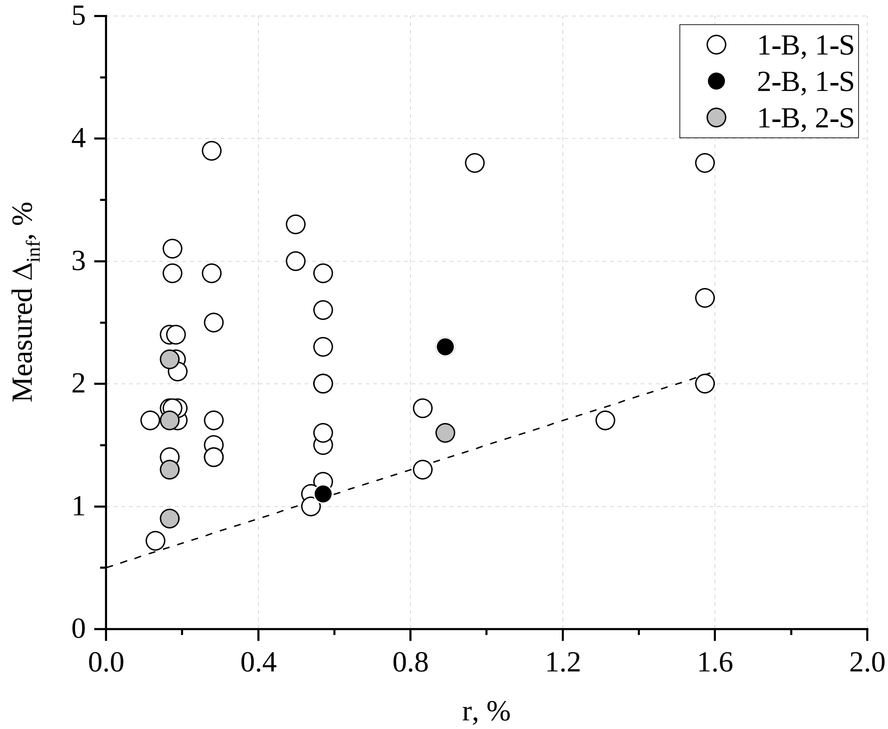

Figure 1-7: Variation of measured drift capacity of infilled frame with transverse reinforcement ratio in column

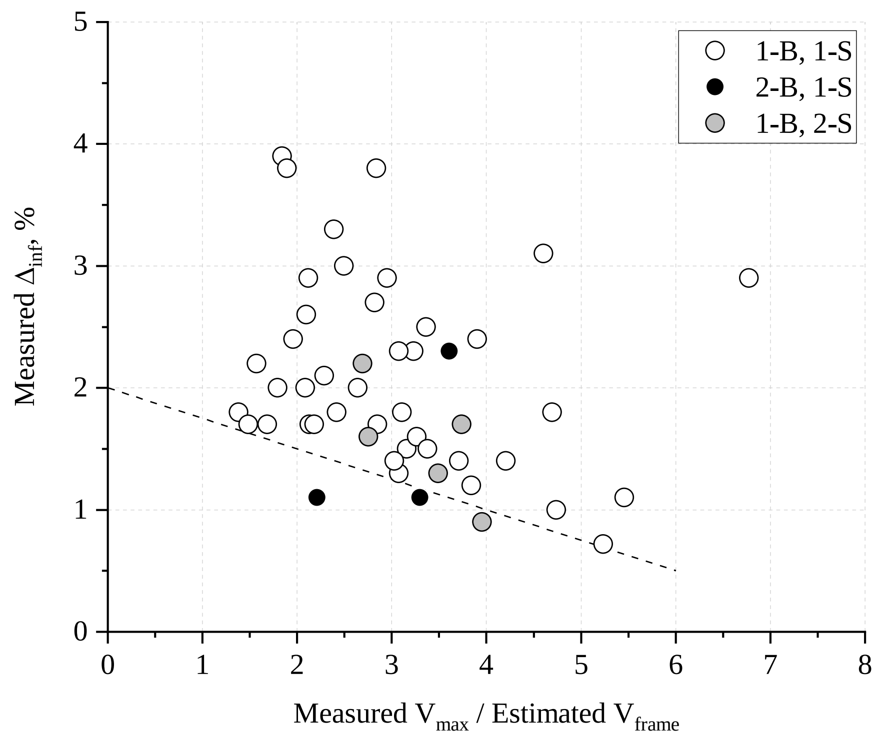

Figure 1-8: Variation of measured drift capacity of infilled frame with ratio of measured peak lateral strength of infilled frame to estimated strength of the associated bare frame

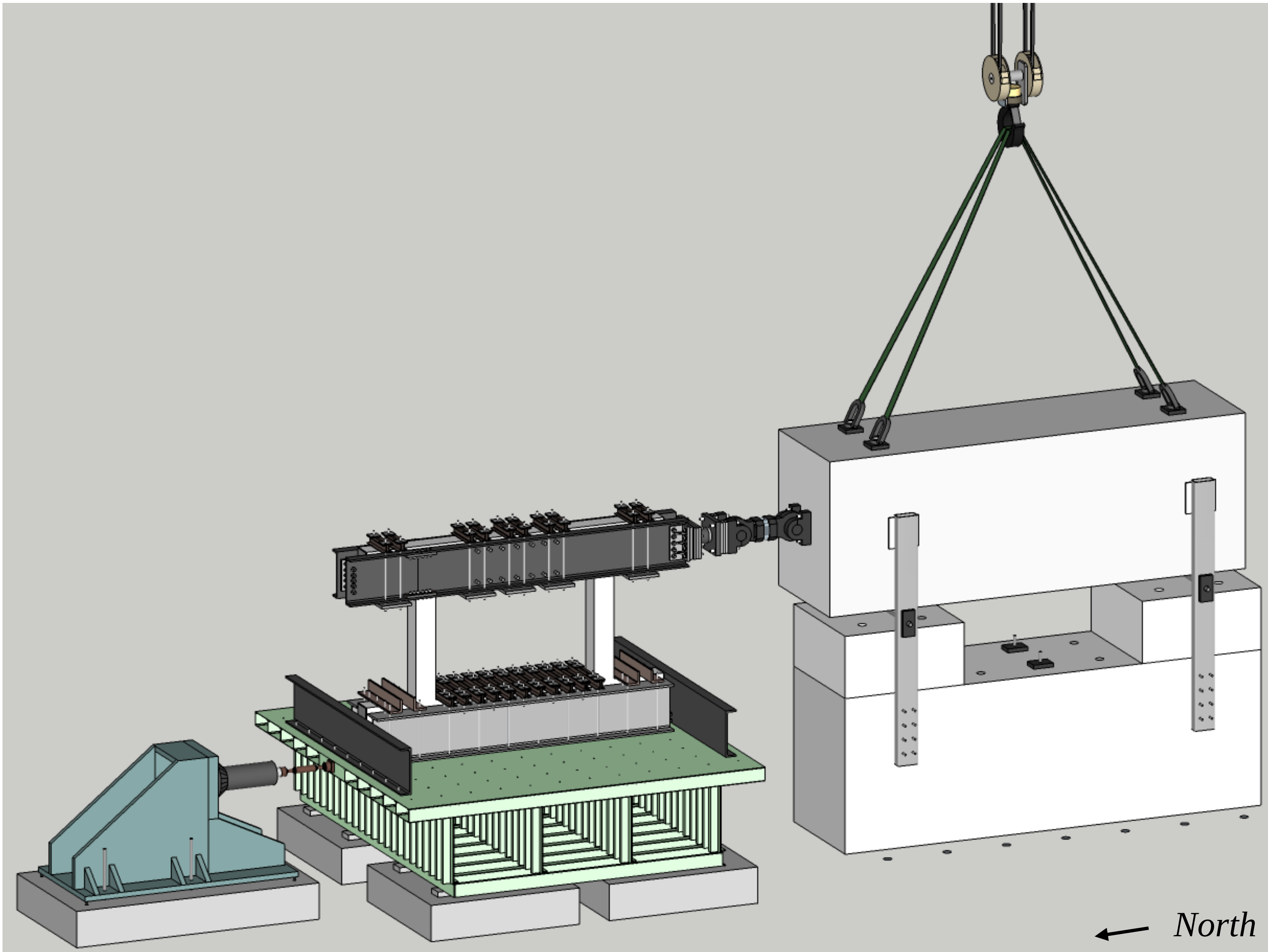

Figure 2-1: Isometric of test setup

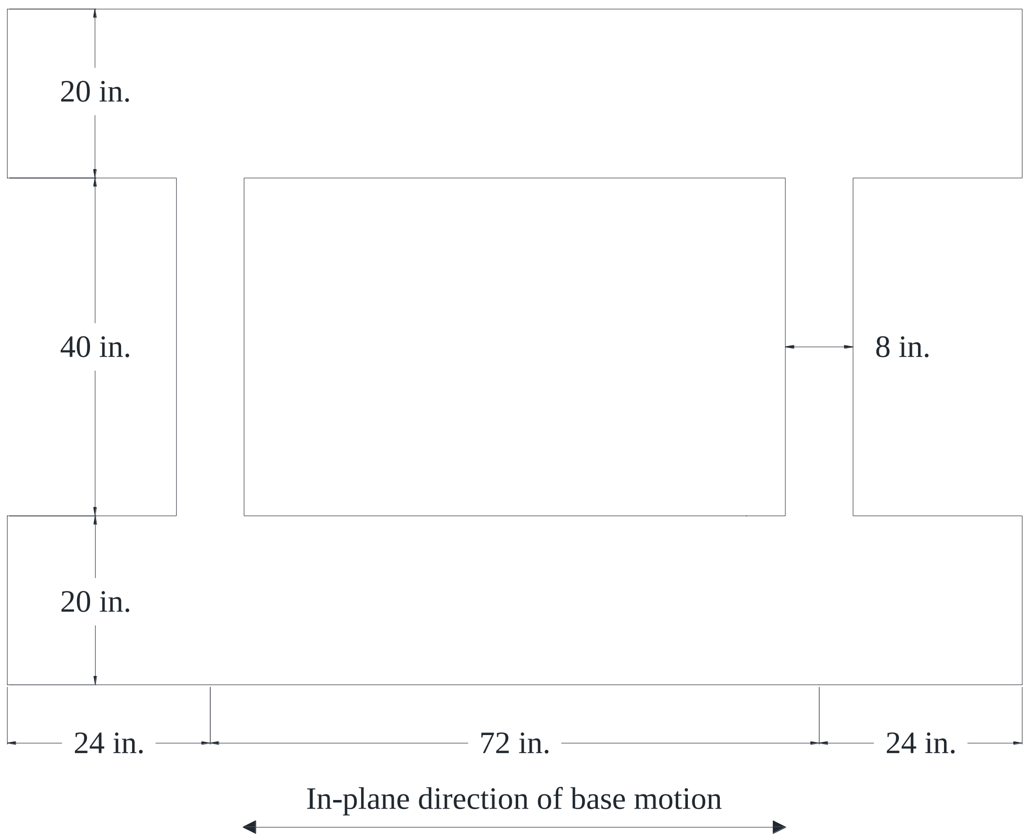

Figure 2-2: Elevation of test frame

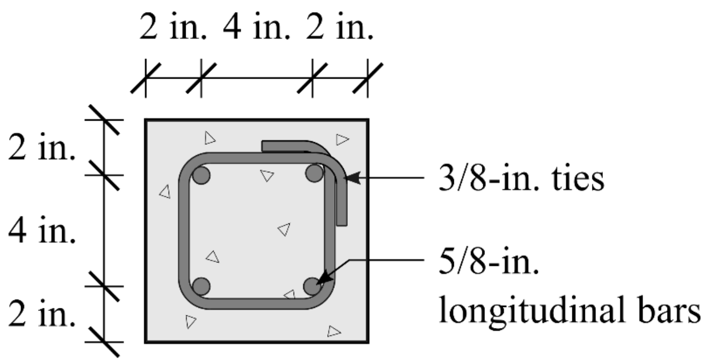

Figure 2-3: Column cross section

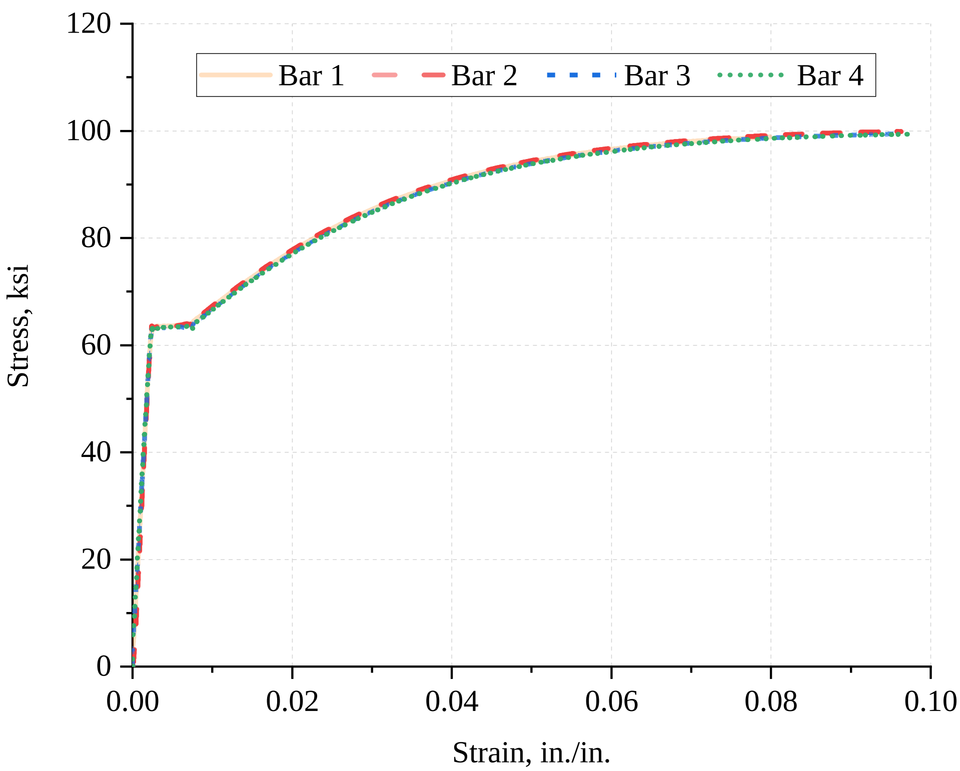

Figure 2-4: Measured stress-strain curves for 5/8-in. column longitudinal reinforcing bars

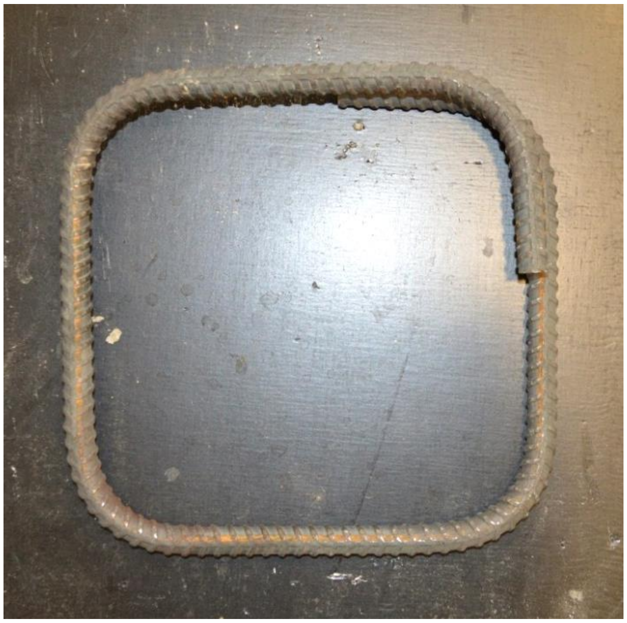

Figure 2-5: Reinforcing tie in column

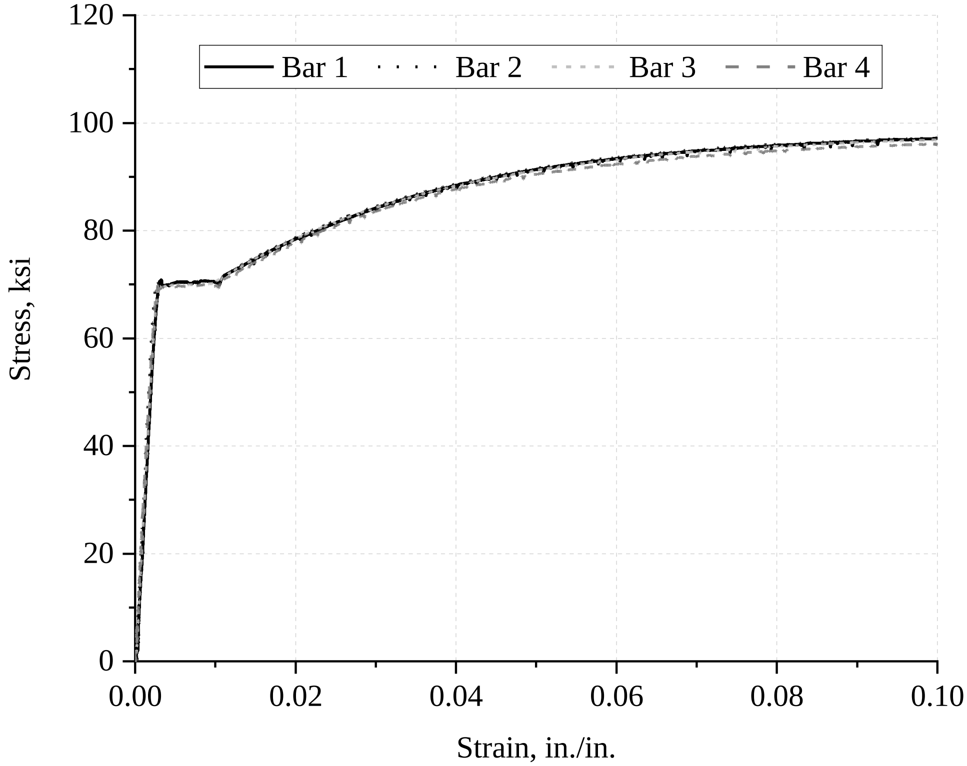

Figure 2-6: Measured stress-strain curves for 3/8-in. column reinforcing ties

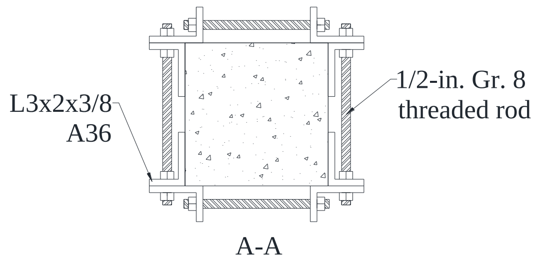

(a) Cross section

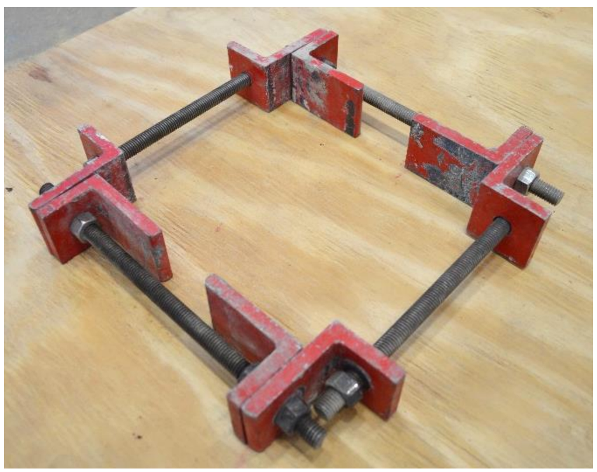

(b) Isometric

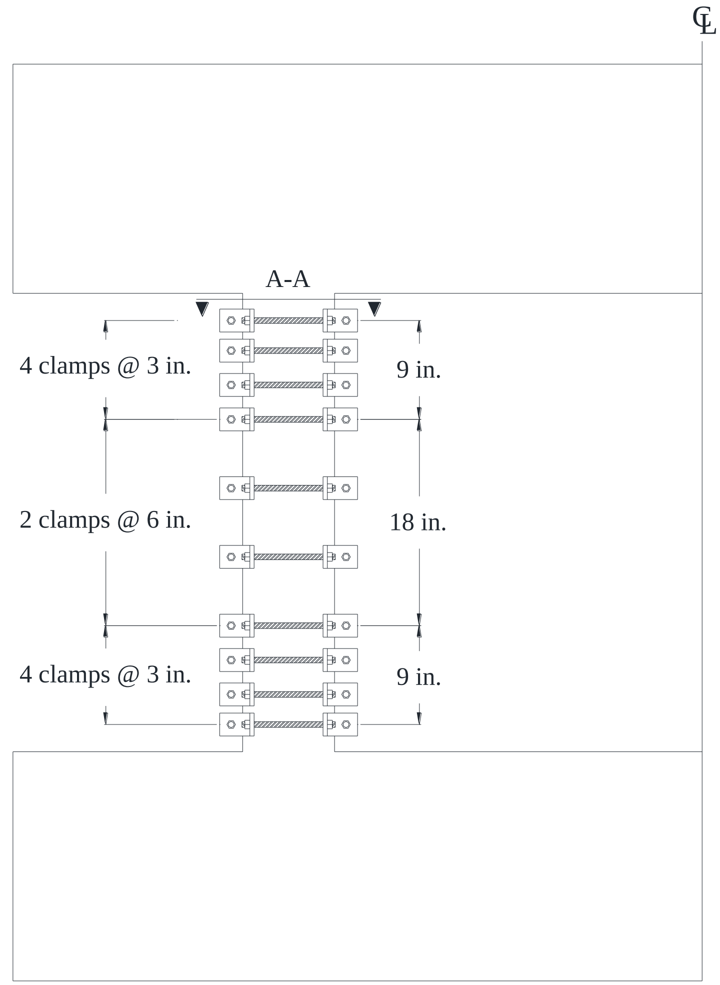

(c) Elevation

Figure 2-7: External transverse reinforcement (clamps)

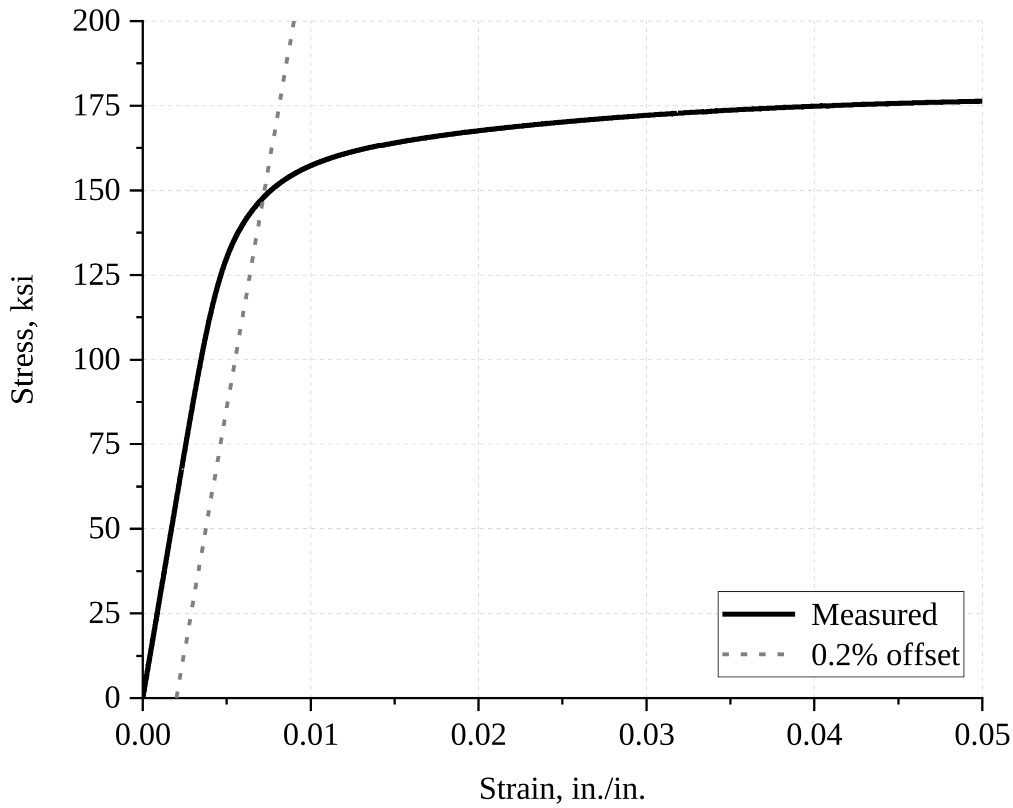

Figure 2-8: Measured stress-strain curve for 1/2-in. high-strength threaded rod

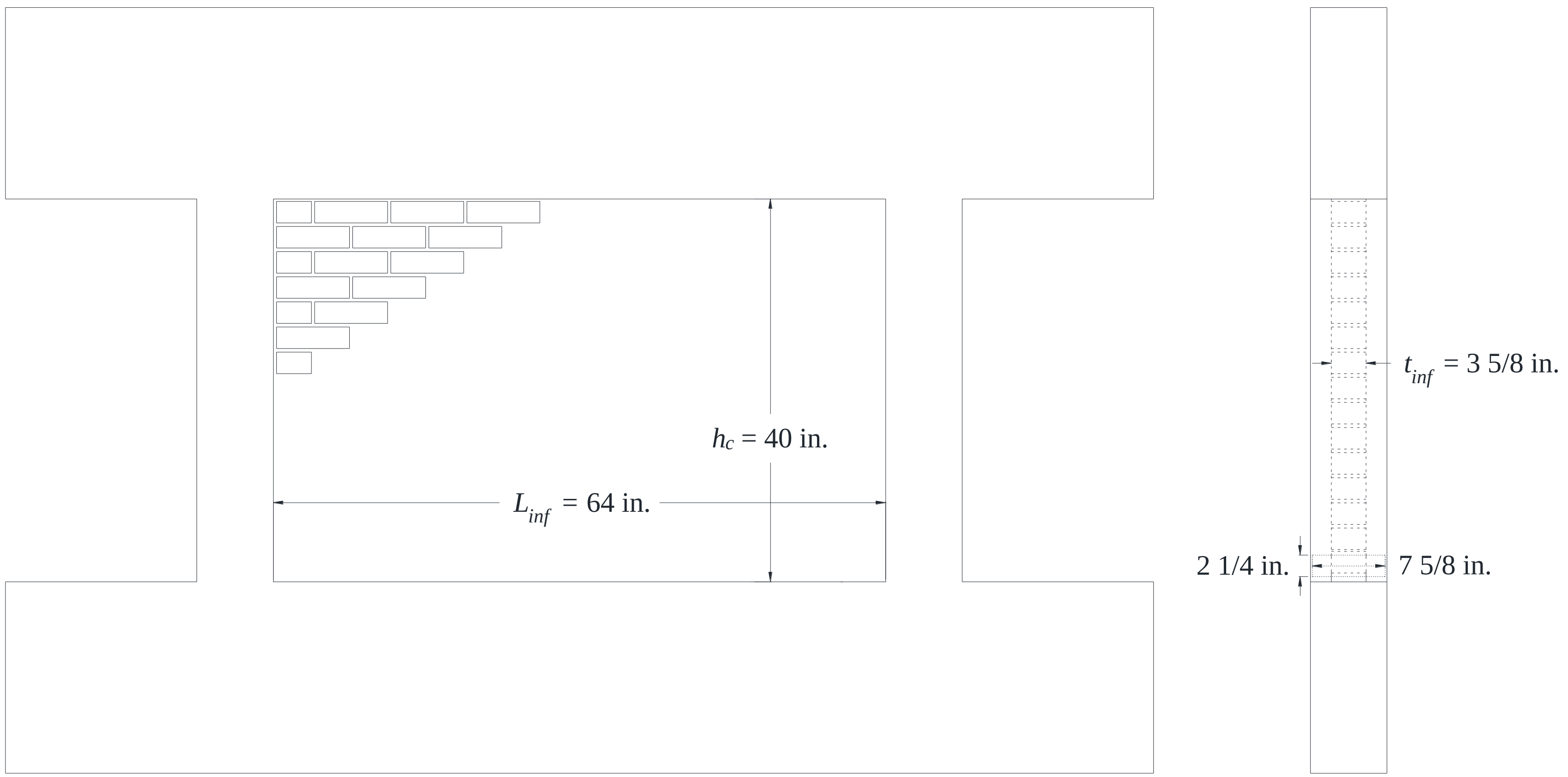

(a) Front view

(b) Side view

Figure 2-9: Dimensions of masonry infill wall

(a) Cross section

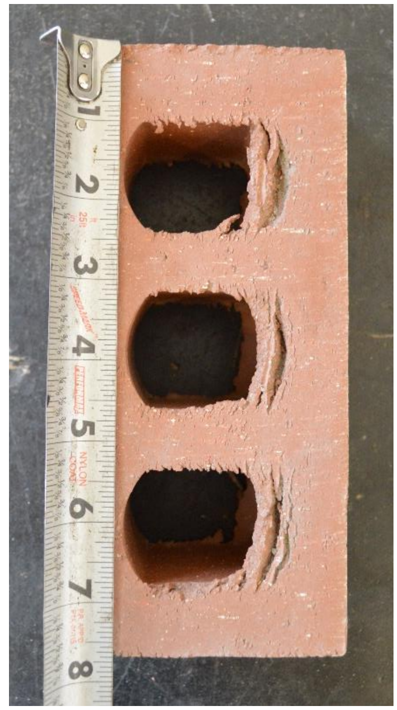

(b) Length = 7 5/8 in.

(c) Width = 3 5/8 in.

(d) Height = 2 1/4 in.

Figure 2-10: Dimensions of typical brick used to build masonry infill walls

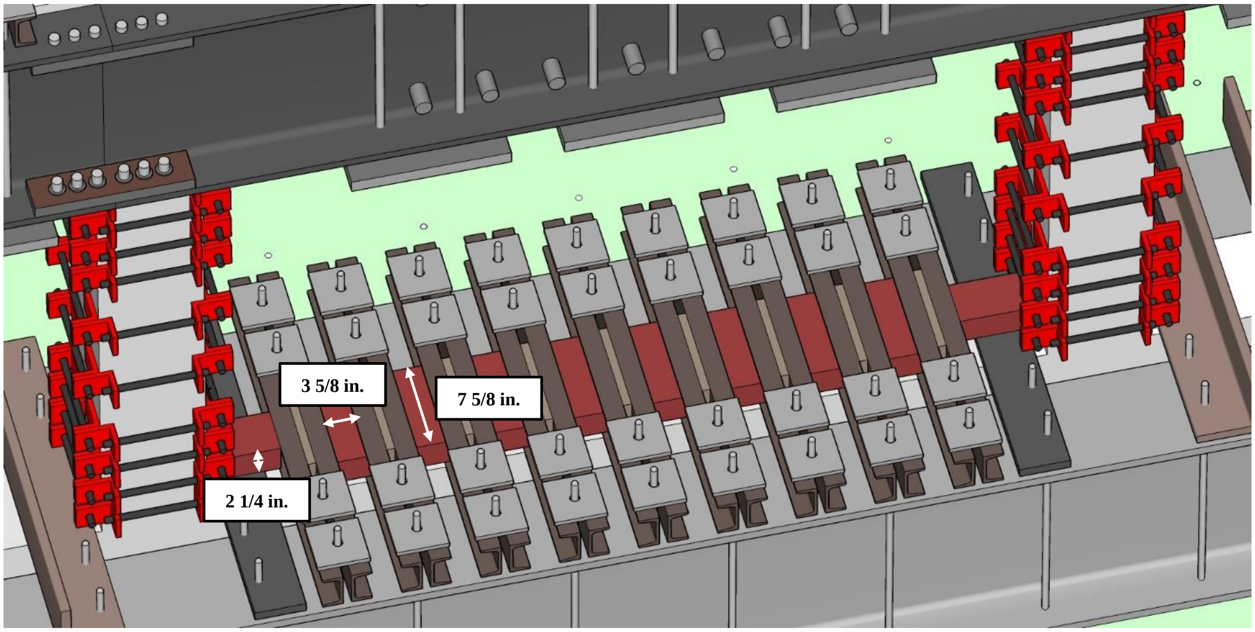

(a) Rendering

(b) Photograph
Figure 2-11: Isometric of base layer of wall

Figure 2-12: Test setup

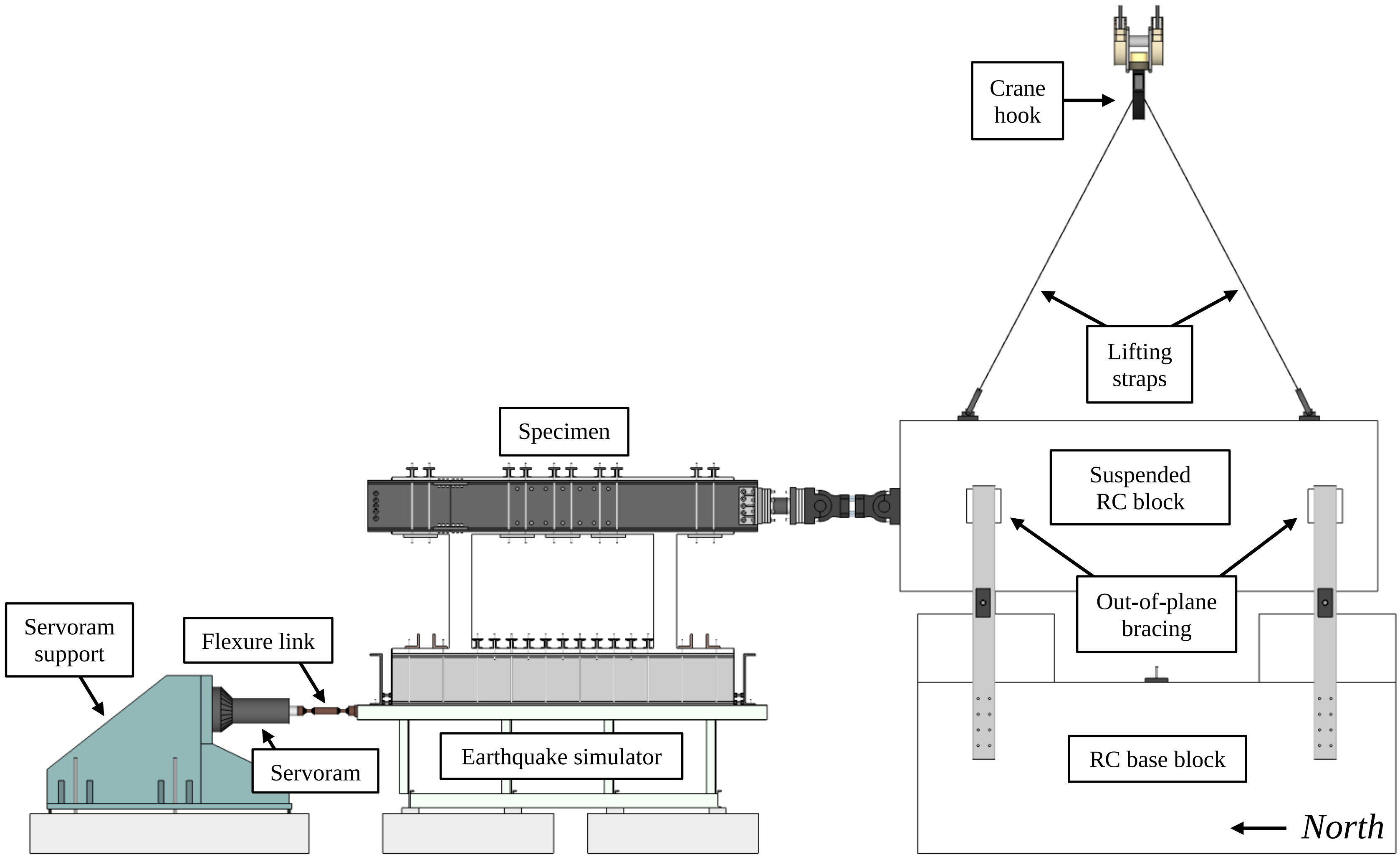

Figure 2-13: Elevation of test setup

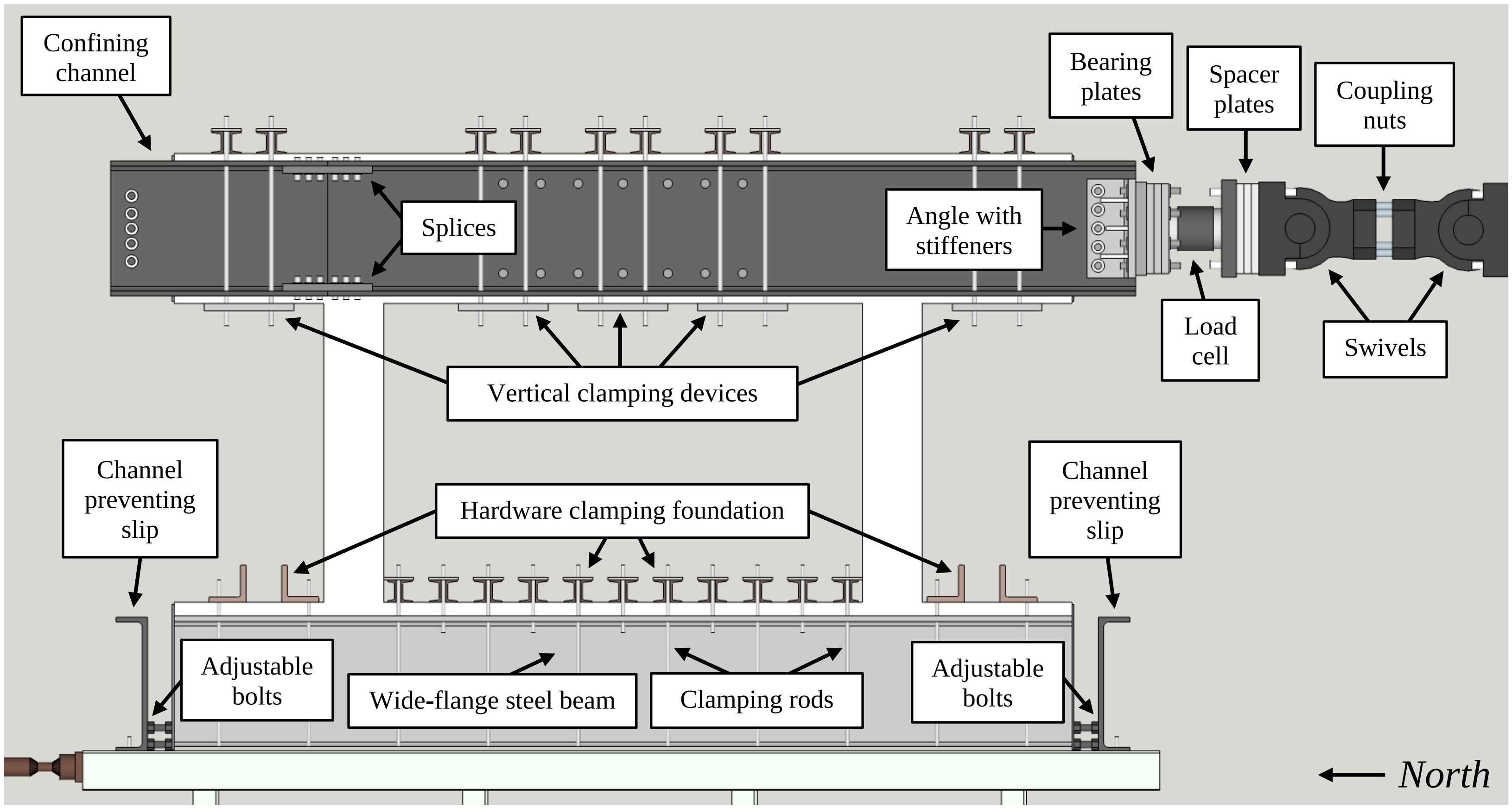

Figure 2-14: Elevation of specimen and connection to suspended mass

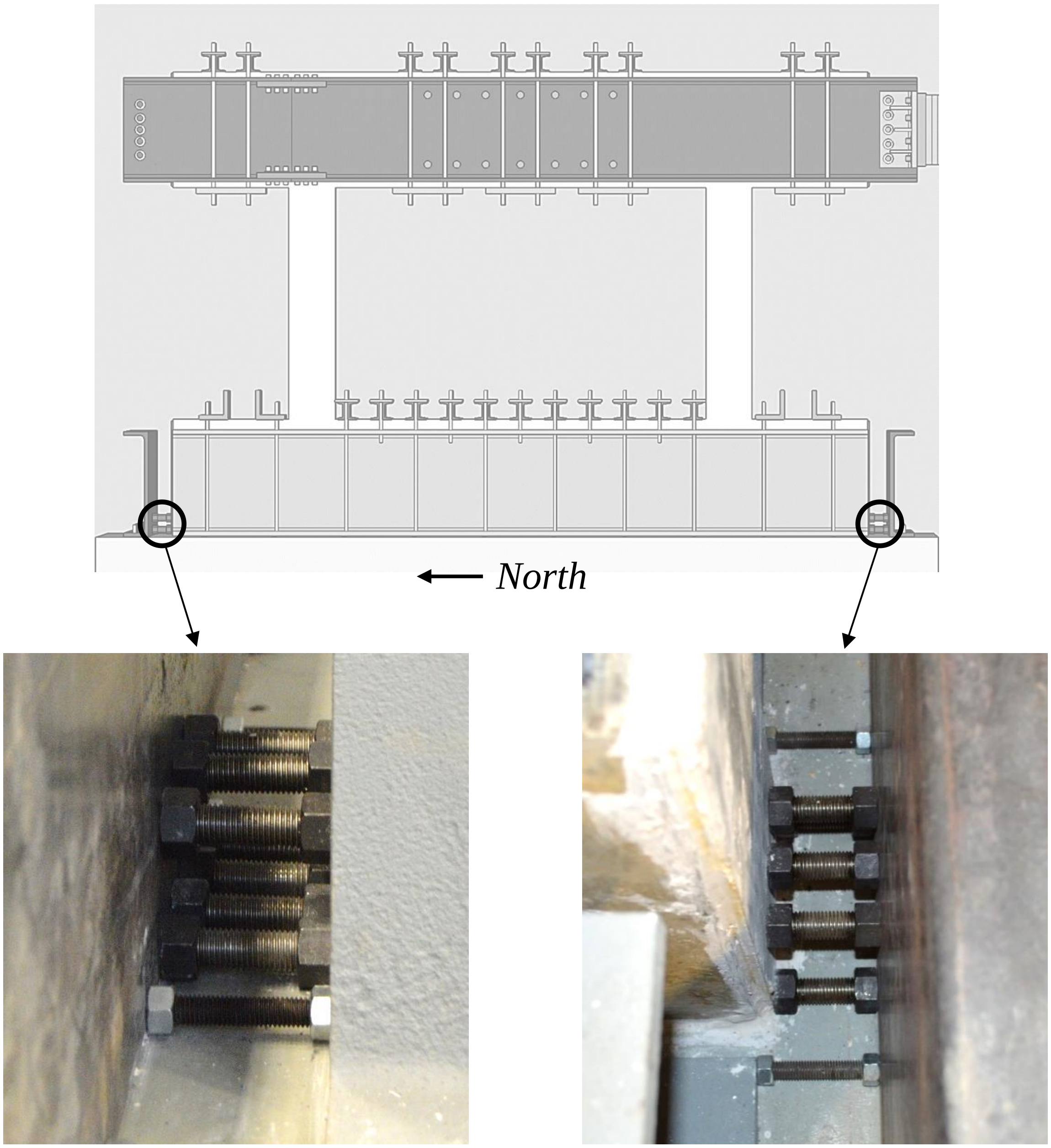

(a) (b)

Figure 2-15: Adjustable bolts preventing sliding of base of specimen

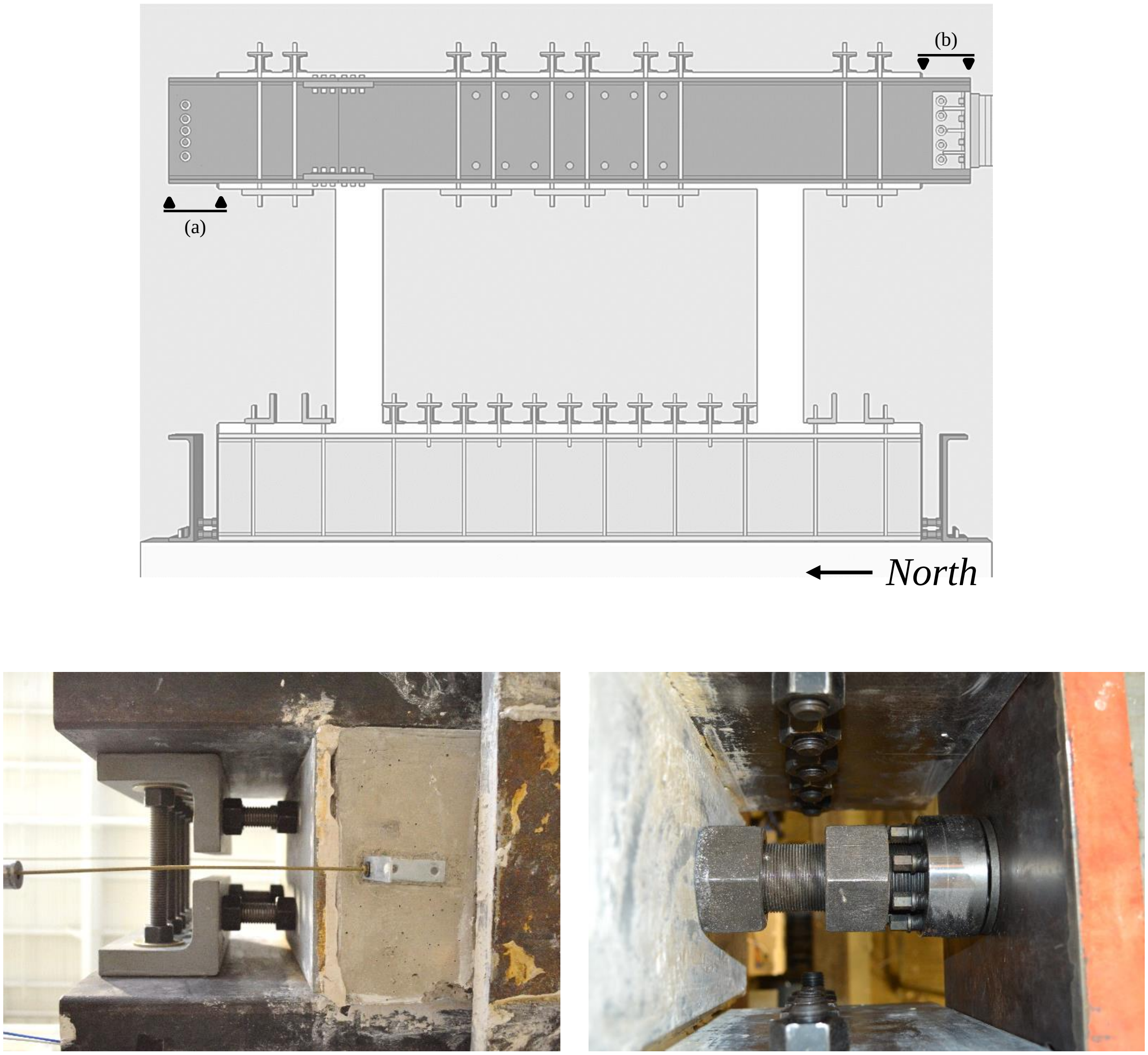

(a) (b)

Figure 2-16: Adjustable bolts preventing slip between confining channels and top beam

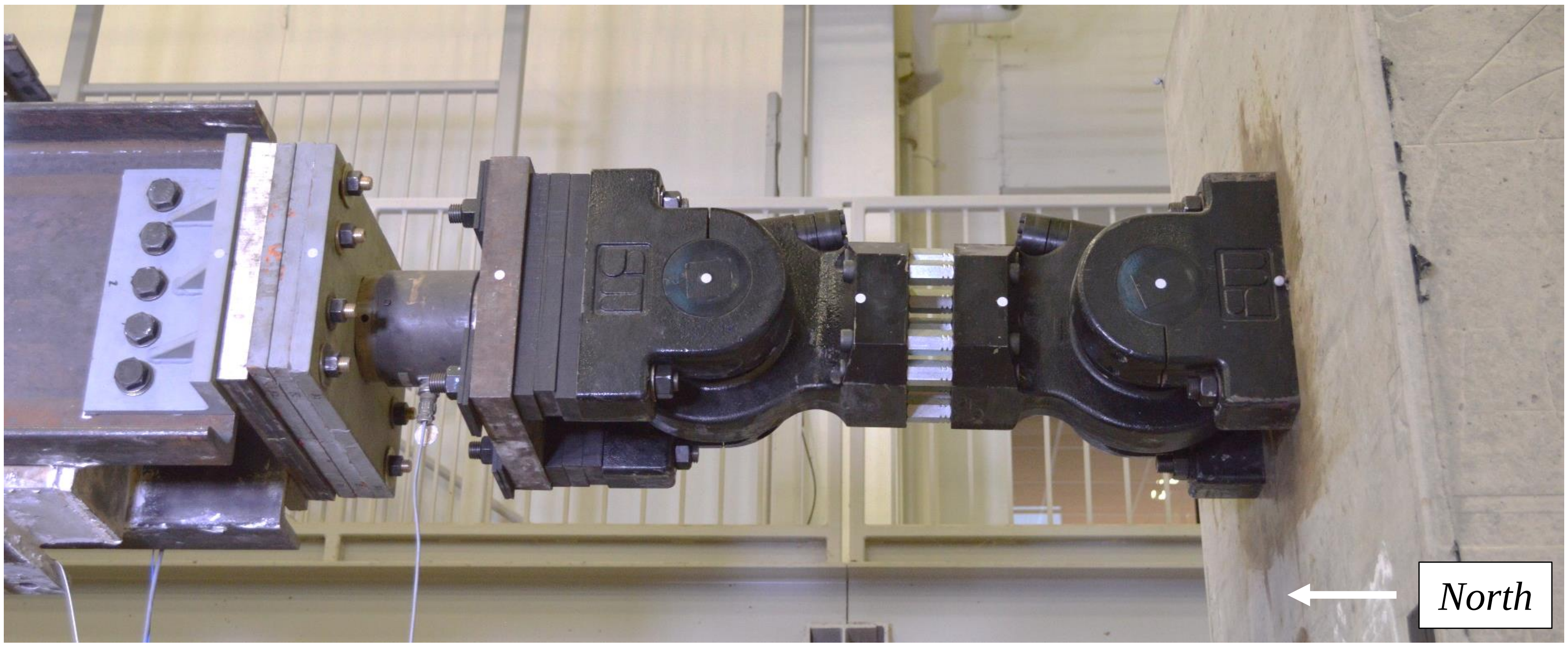

Figure 2-17: Two-swivel stiff link and load cell between specimen and suspended mass

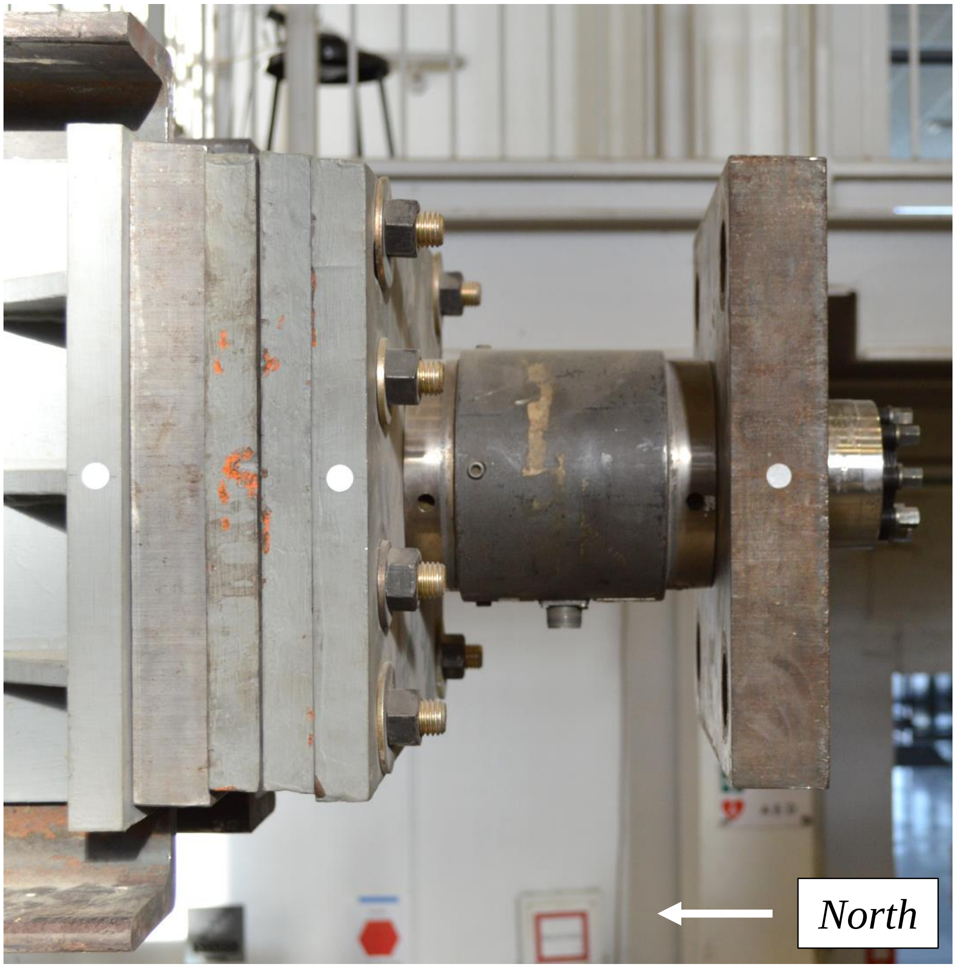

Figure 2-18: Load cell attached to south end of top beam of specimen

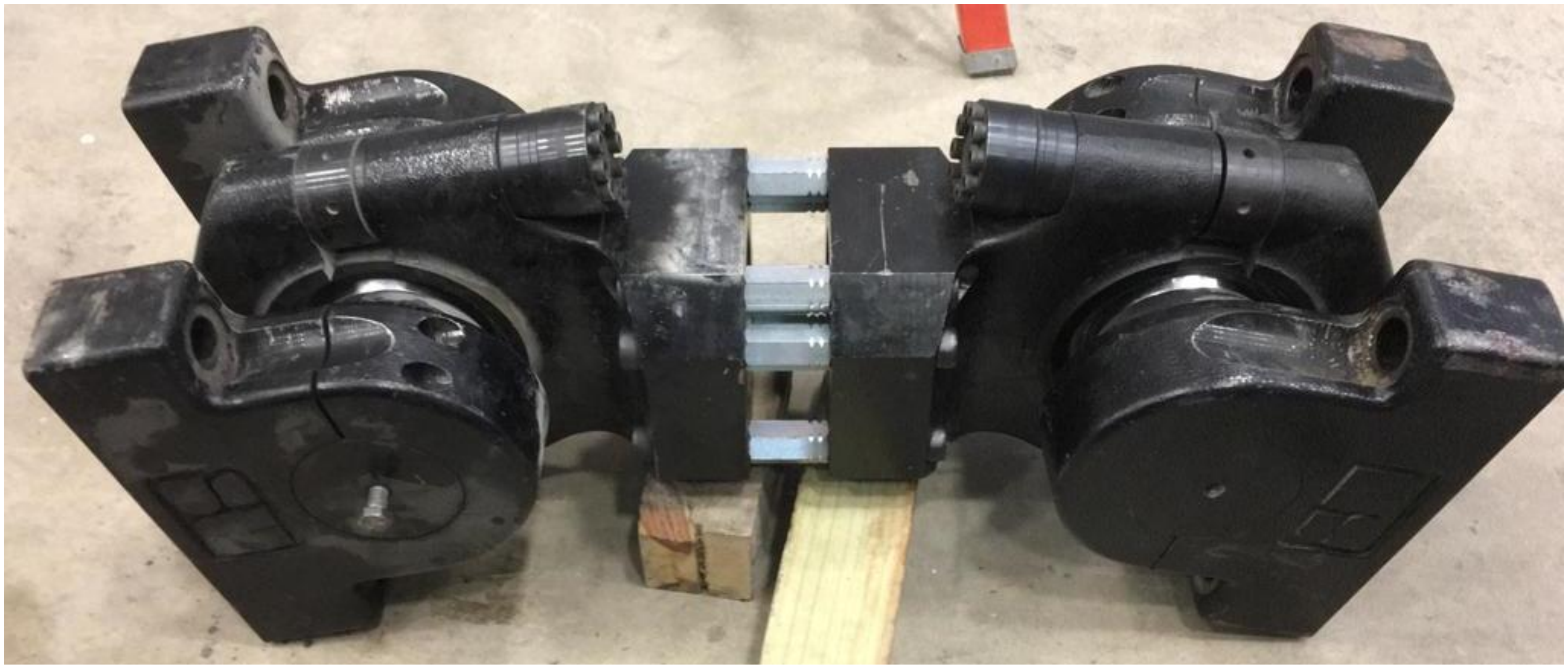

Figure 2-19: Two-swivel stiff link

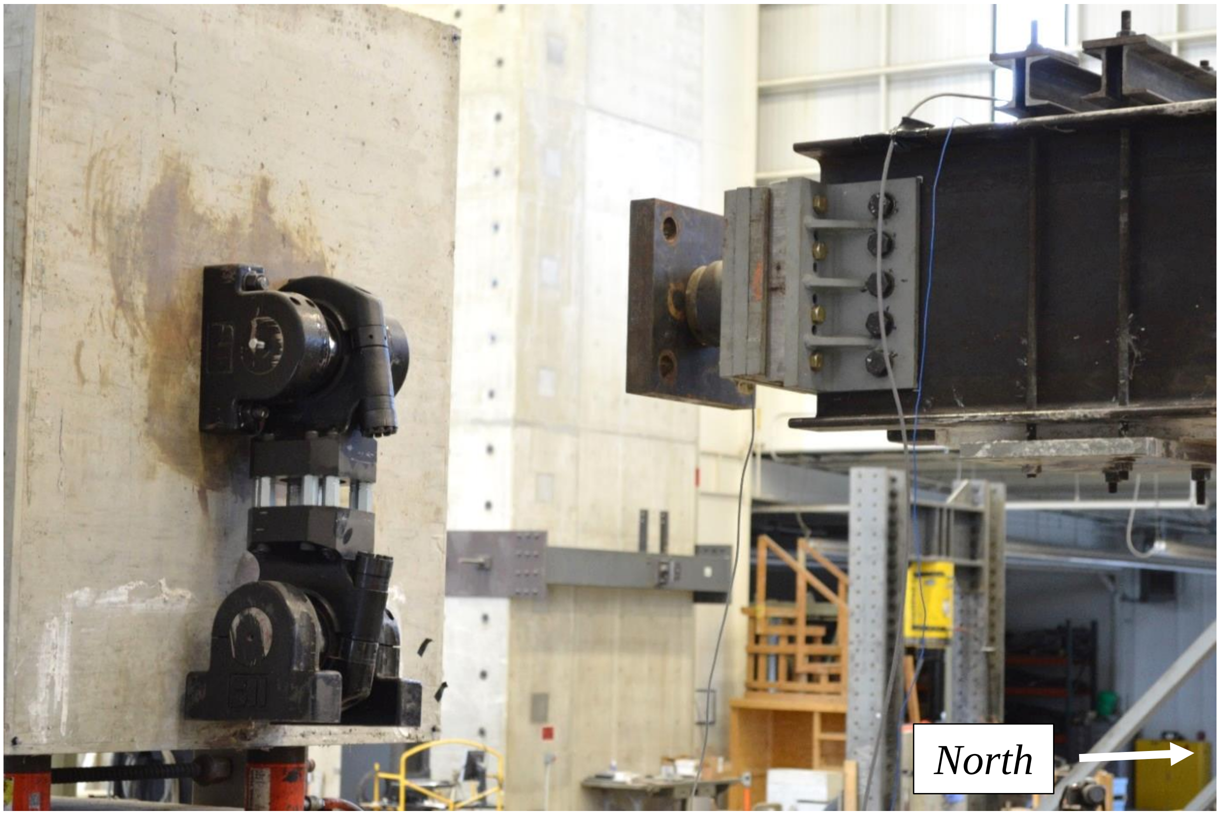

Figure 2-20: Swivel at south end of link attached to north face of suspended mass

(a) Isometric

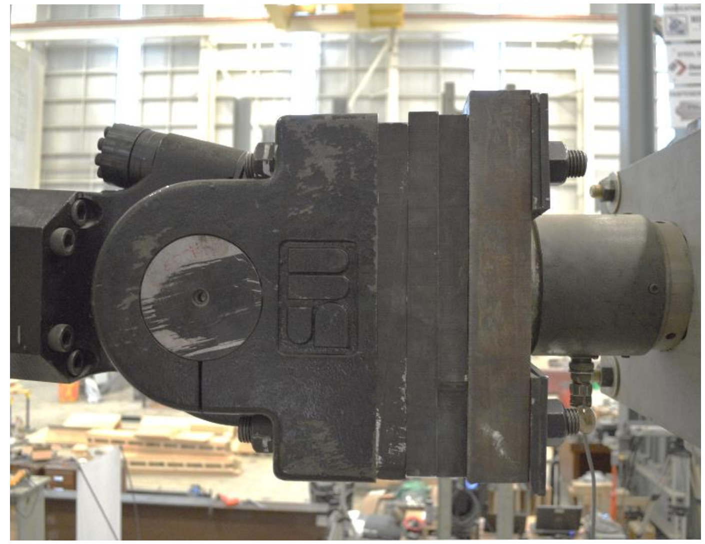

(b) Side view

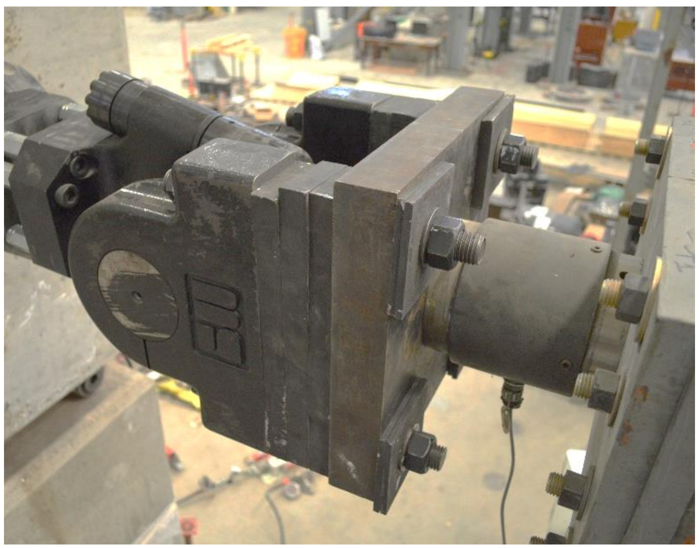

(c) Close-up

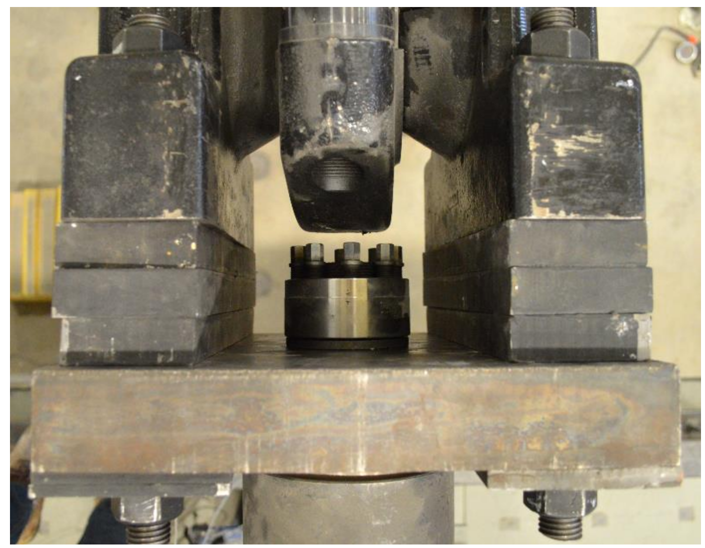

(d) Top view

Figure 2-21: Connection of link to specimen

Figure 2-22: Suspended mass

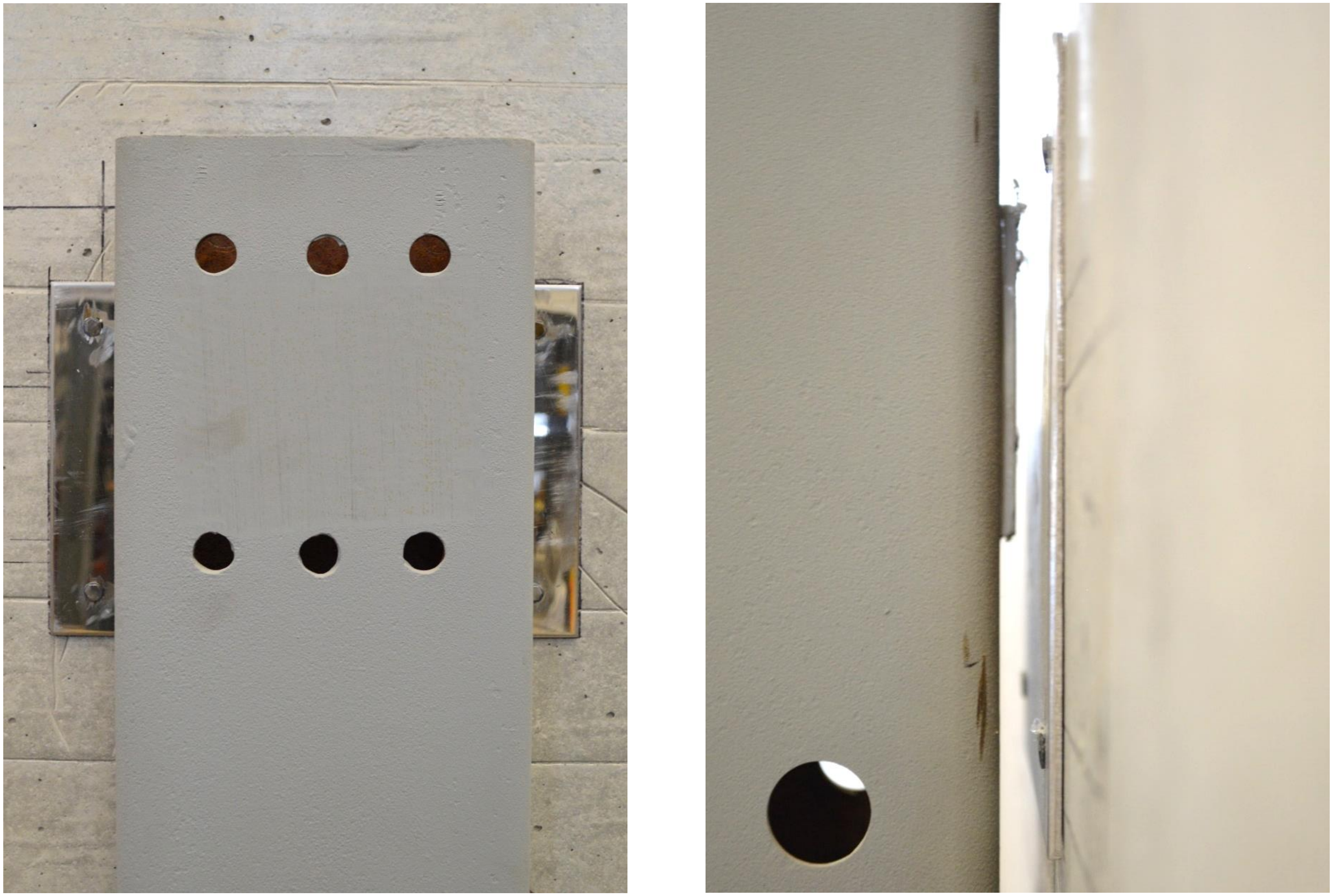

(a) Front view (b) Side view

Figure 2-23: Out-of-plane bracing

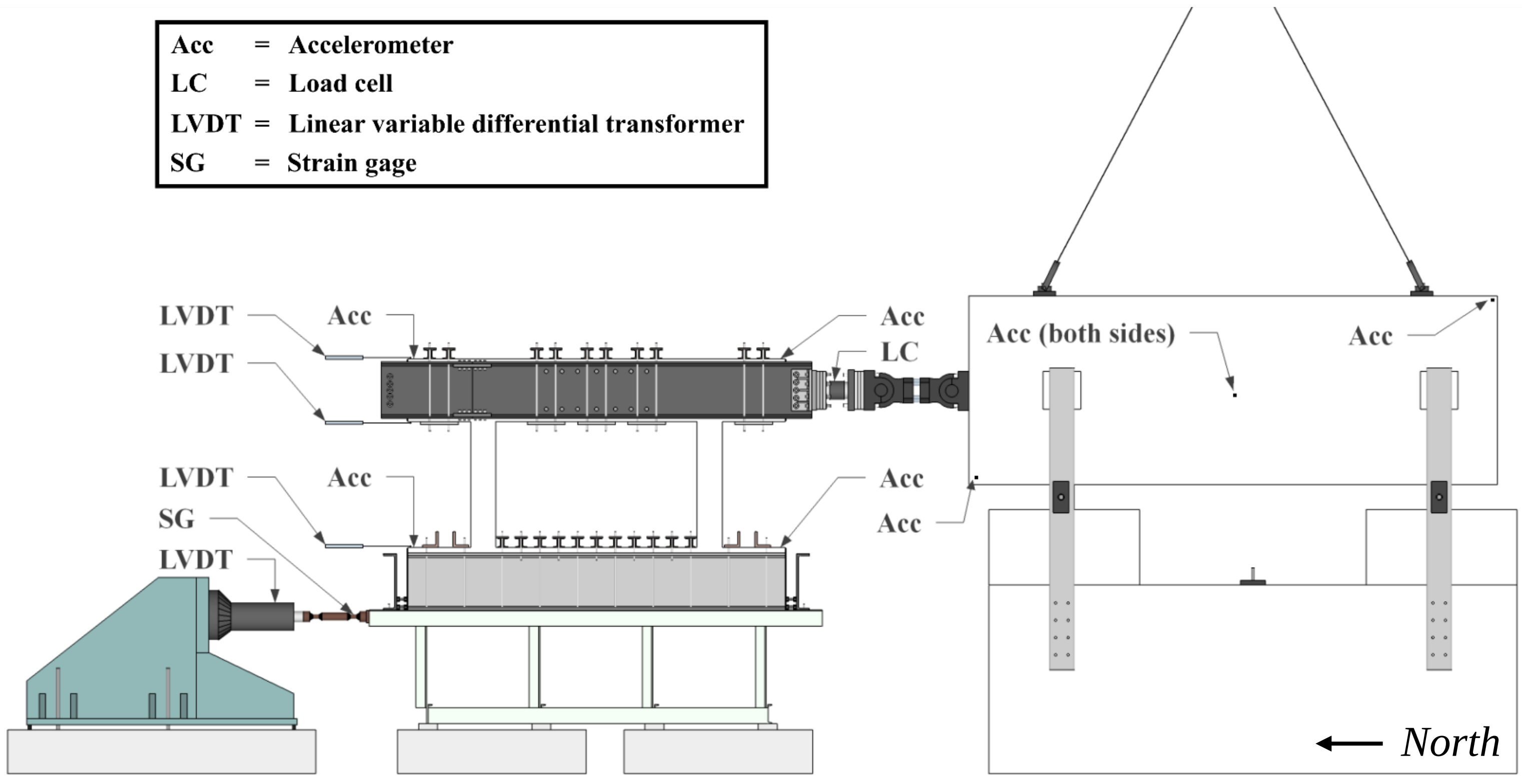

Figure 2-24: Elevation of instrumentation layout

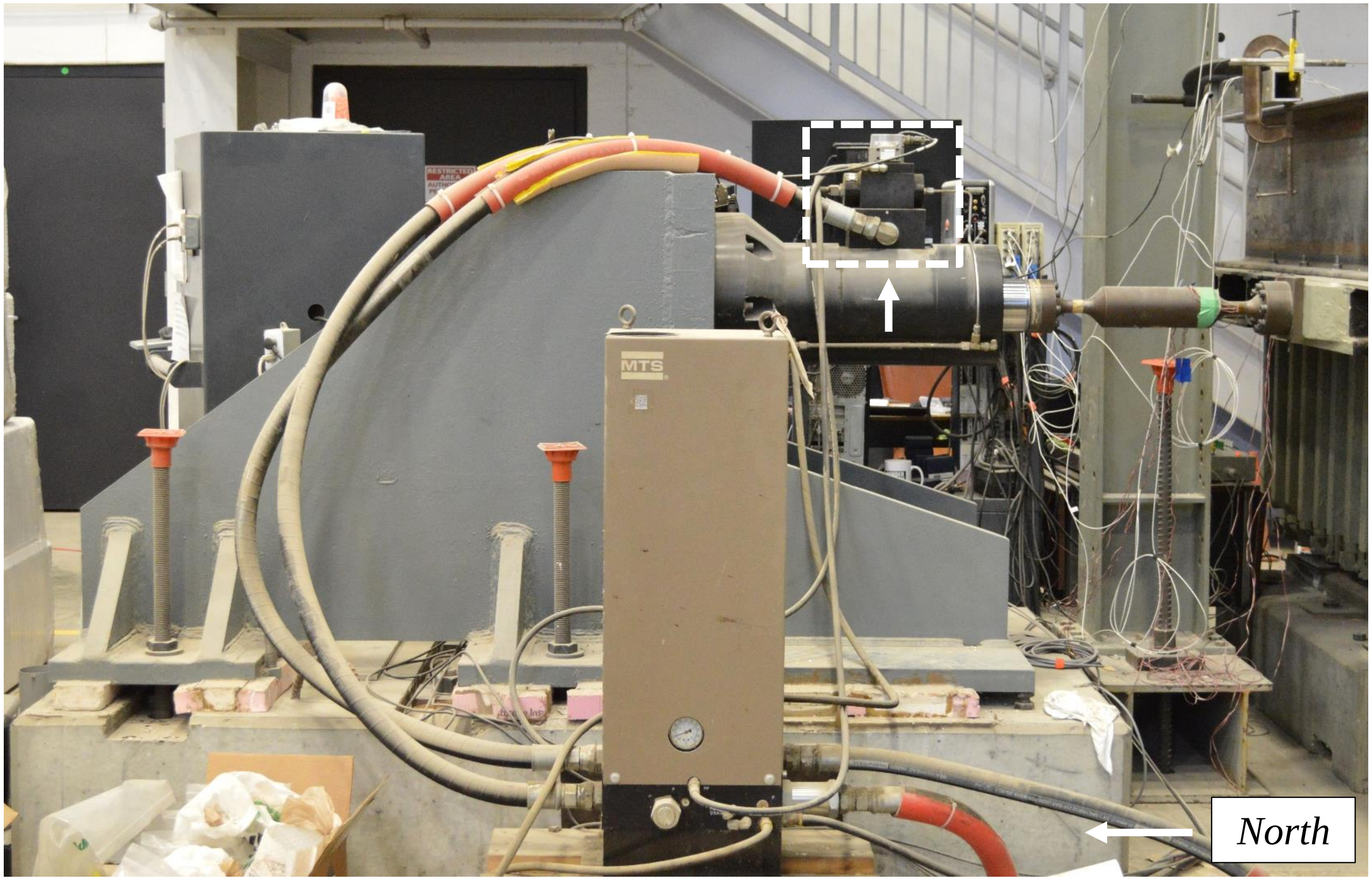

Figure 2-25: LVDT mounted inside servoram

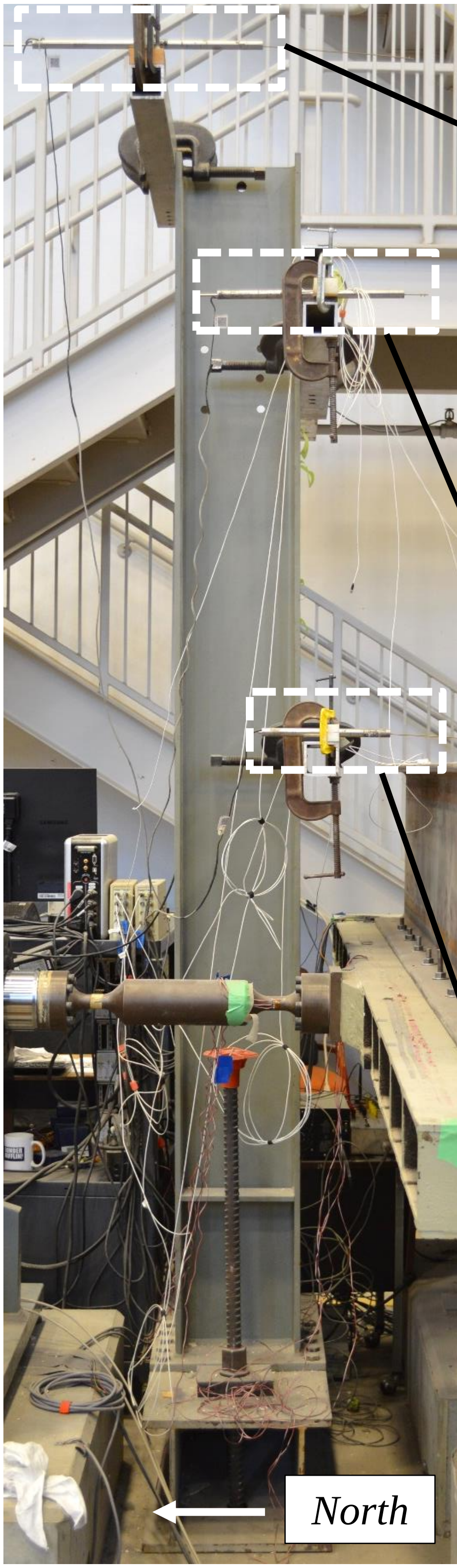

(a) LVDT layout

(b) LVDT at top of top beam

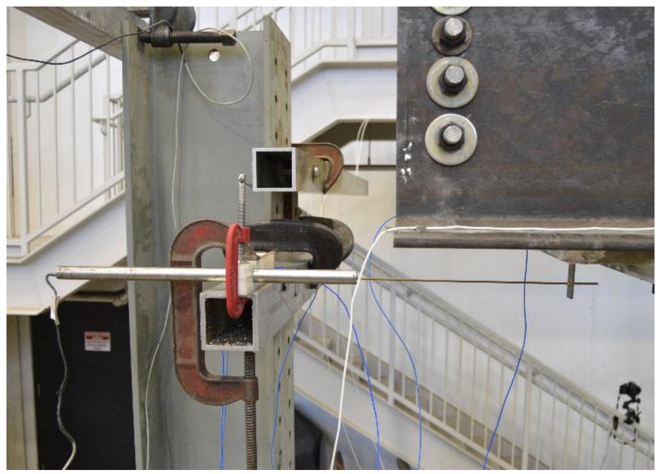

(c) LVDT at soffit of top beam

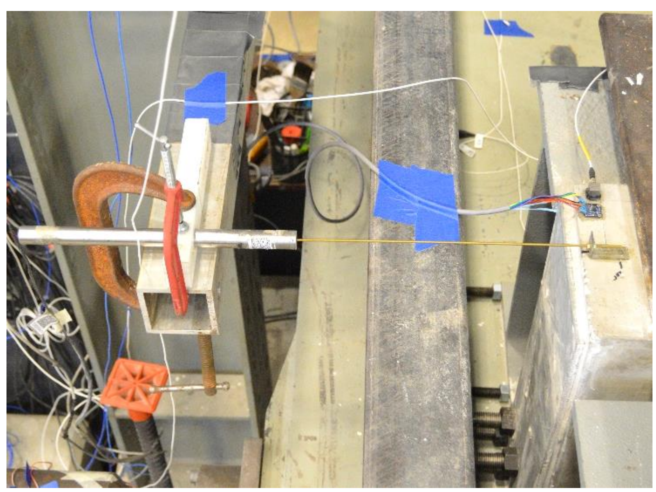

(d) LVDT at top of foundation beam

Figure 2-26: LVDTs mounted on steel column post-tensioned to strong floor

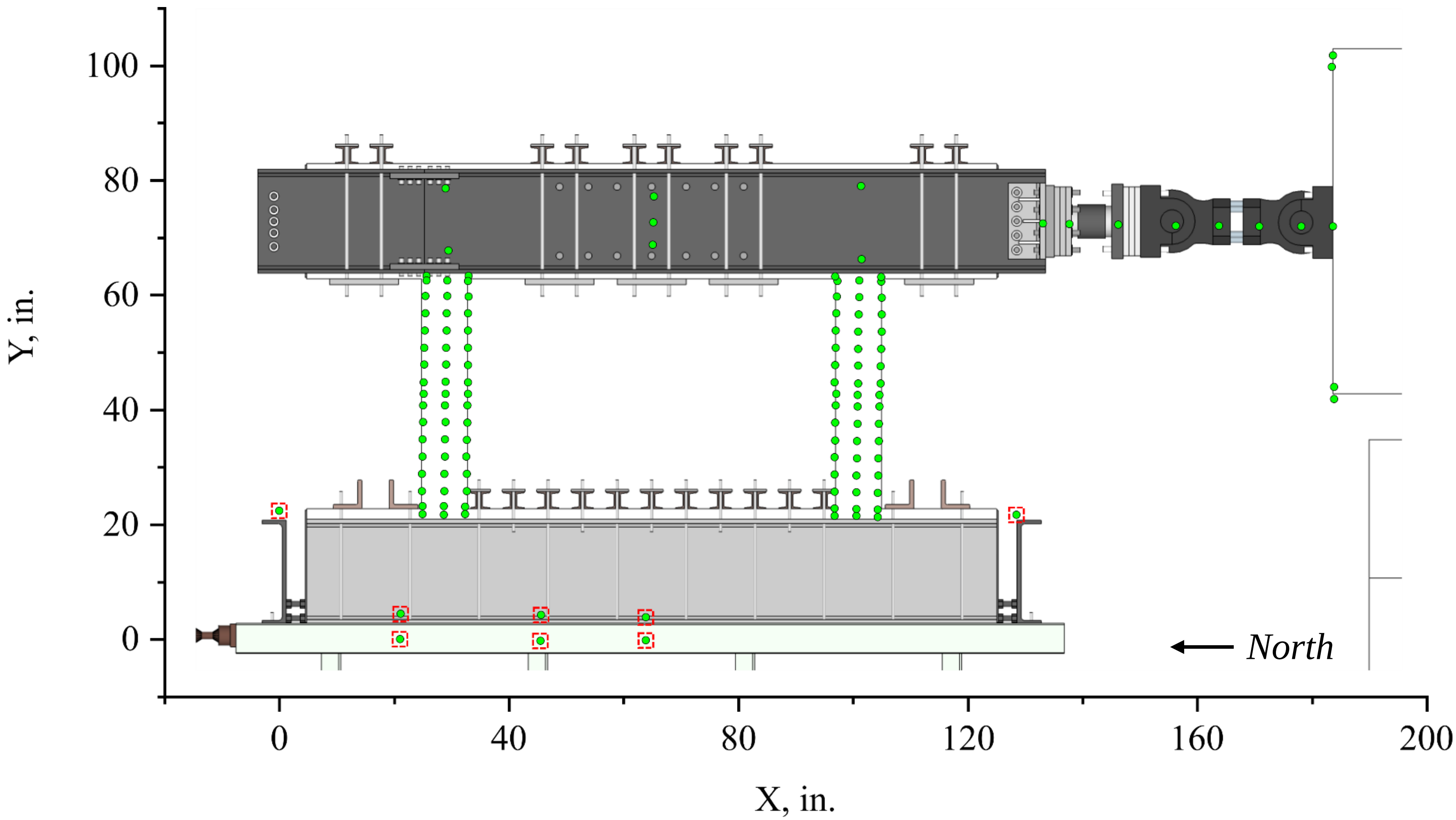

Figure 2-27: OptiTrack layout of Specimen F1

Note: Points labeled with green circles represent measured positions of OptiTrack targets. Points outlined in red indicate discrepancies between measurements and estimates of dimensions in rendering of test setup.

Figure 2-28: Photograph of OptiTrack layout of Specimen F1

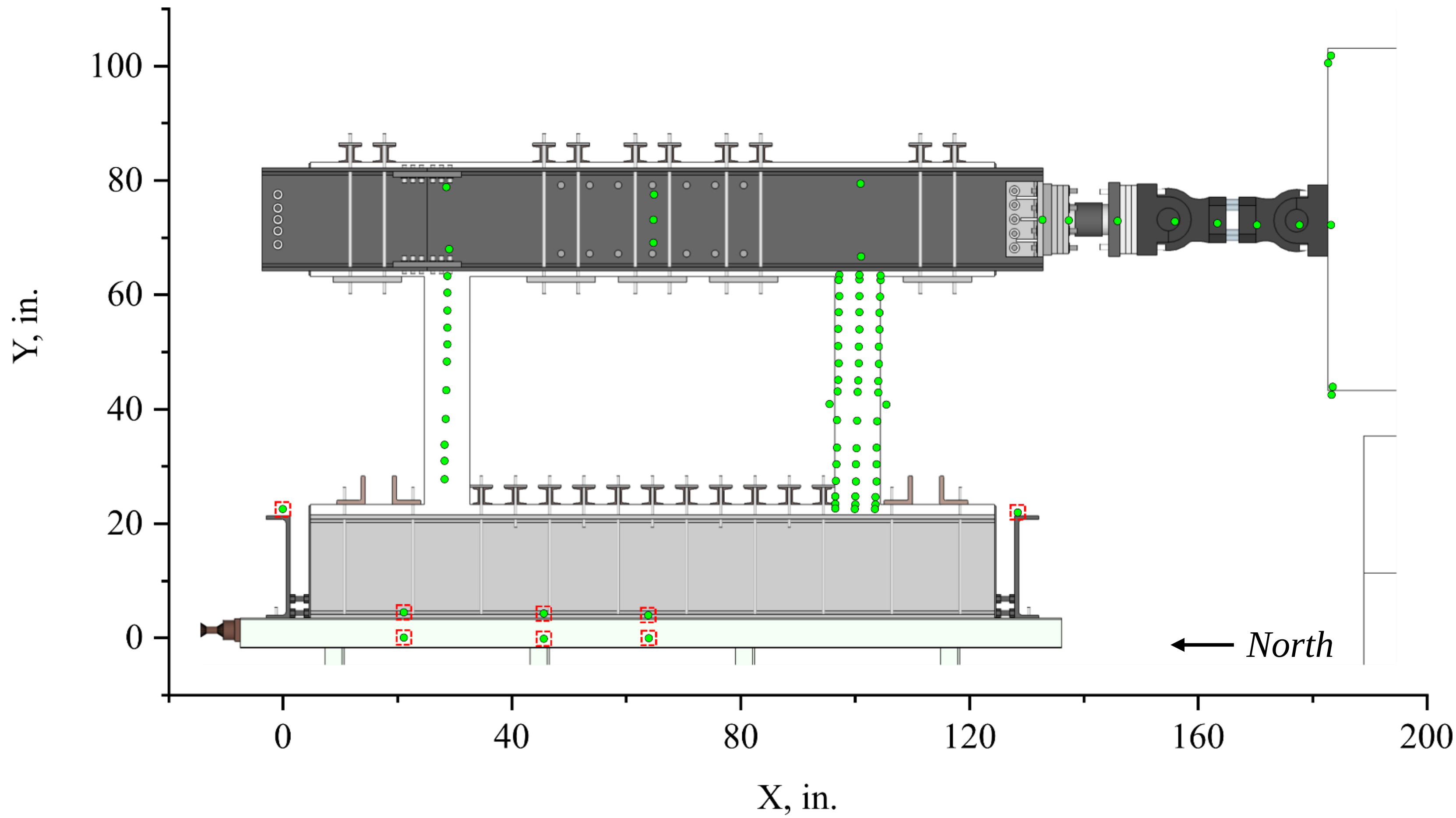

Figure 2-29: OptiTrack layout of Specimen F2

Note: Points labeled with green circles represent measured positions of OptiTrack targets. Points outlined in red indicate discrepancies between measurements and estimates of dimensions in rendering of test setup.

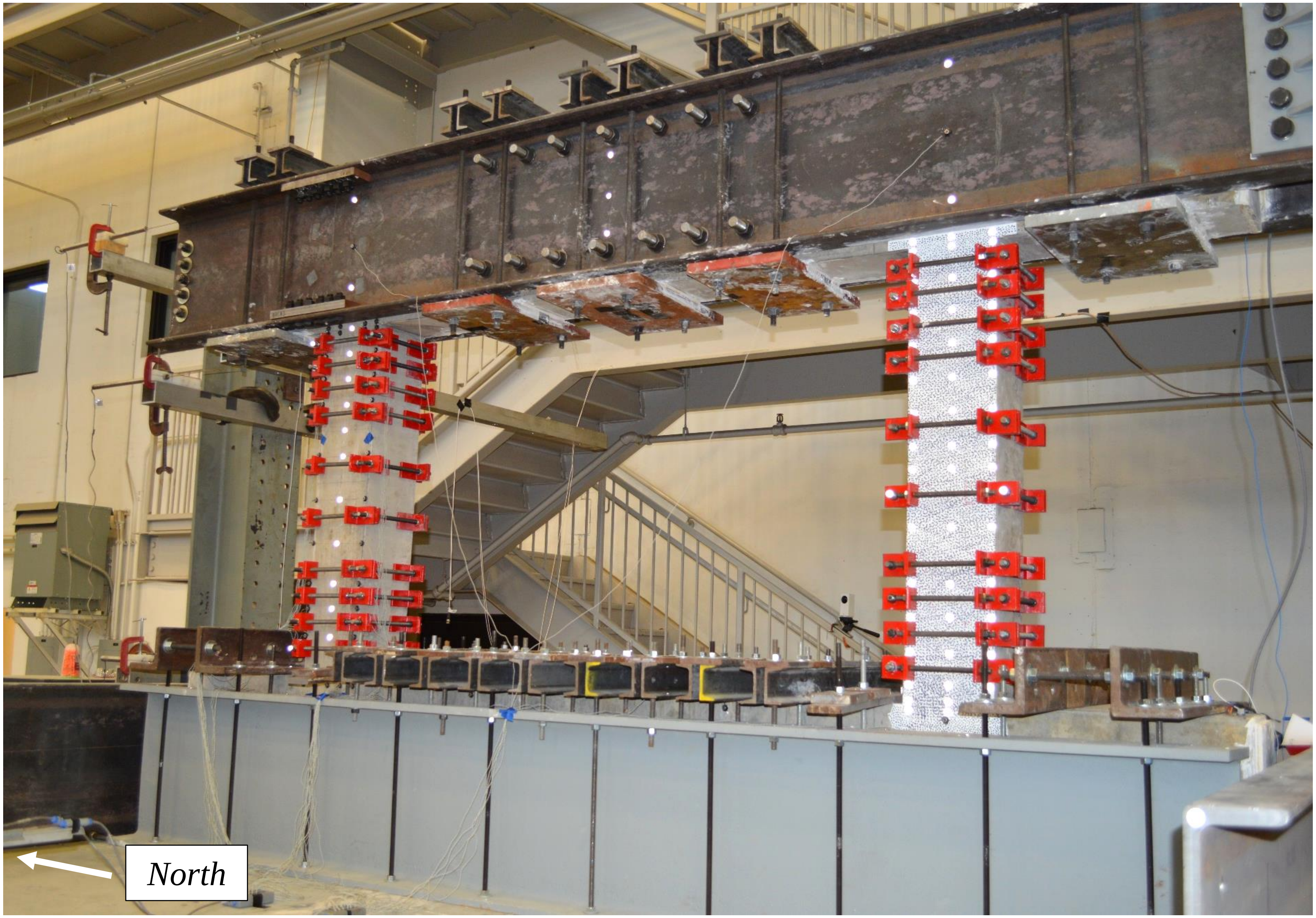

Figure 2-30: Photograph of OptiTrack layout of Specimen F2

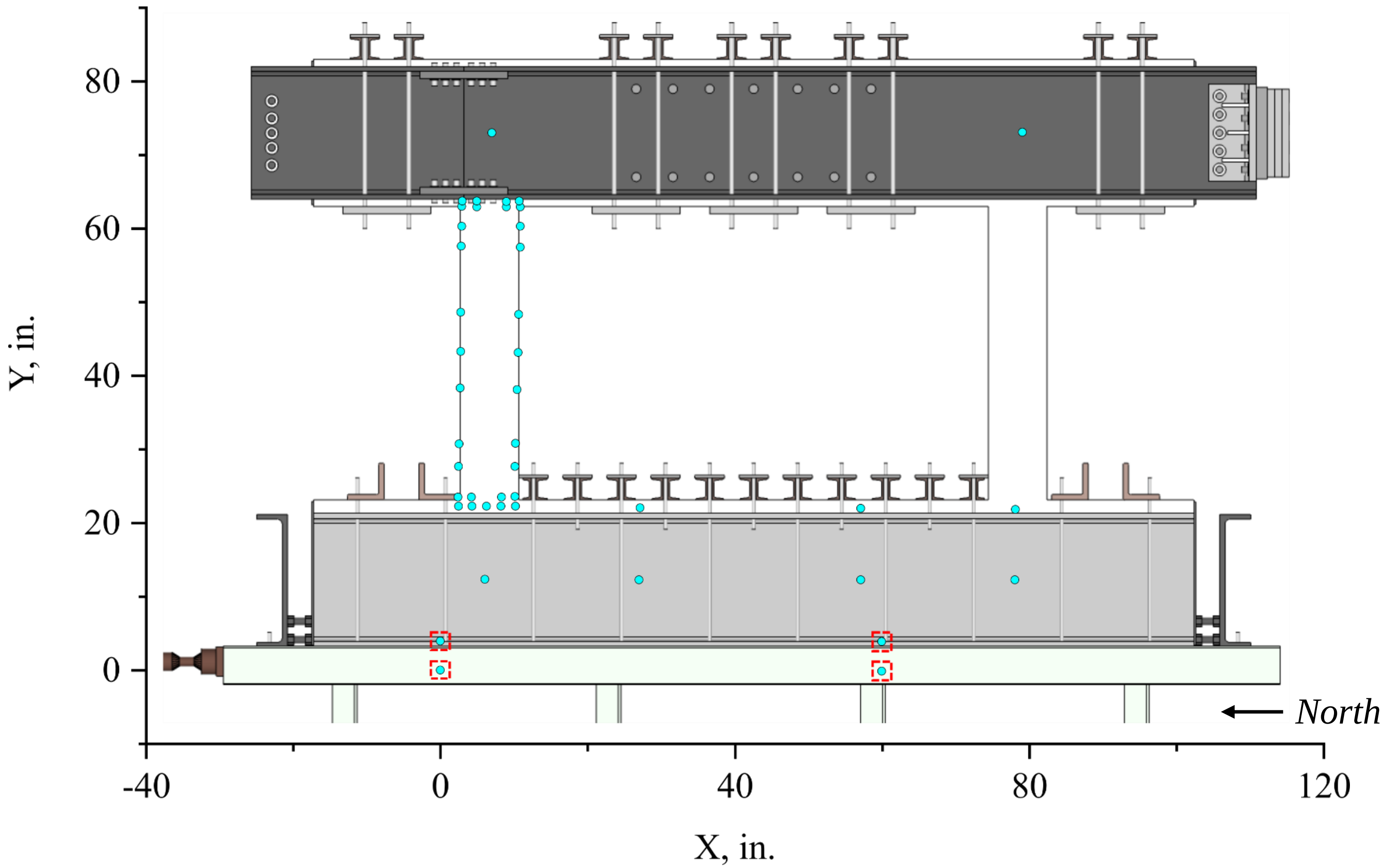

Figure 2-31: Optotrak layout of Specimen F2

Note: Points labeled with cyan circles represent measured positions of Optotrak targets. Points outlined in red indicate discrepancies between measurements and estimates of dimensions in rendering of test setup

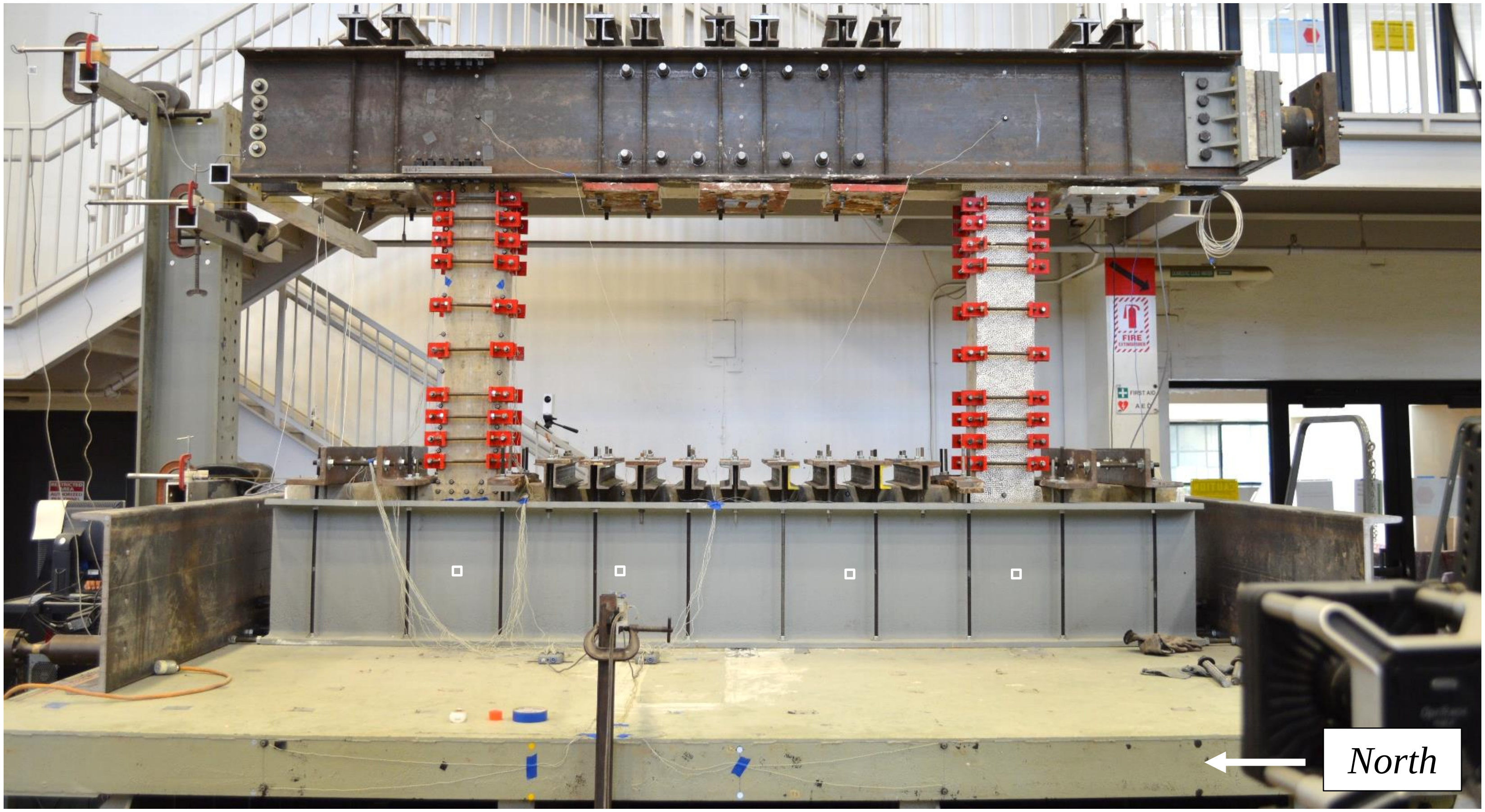

Figure 2-32: Photograph of Optotrak layout of Specimen F2

Note: Regions outlined in white indicate Optotrak targets used to measure flexibility of simulator installed after photograph was taken but before tests were conducted on Specimen F2

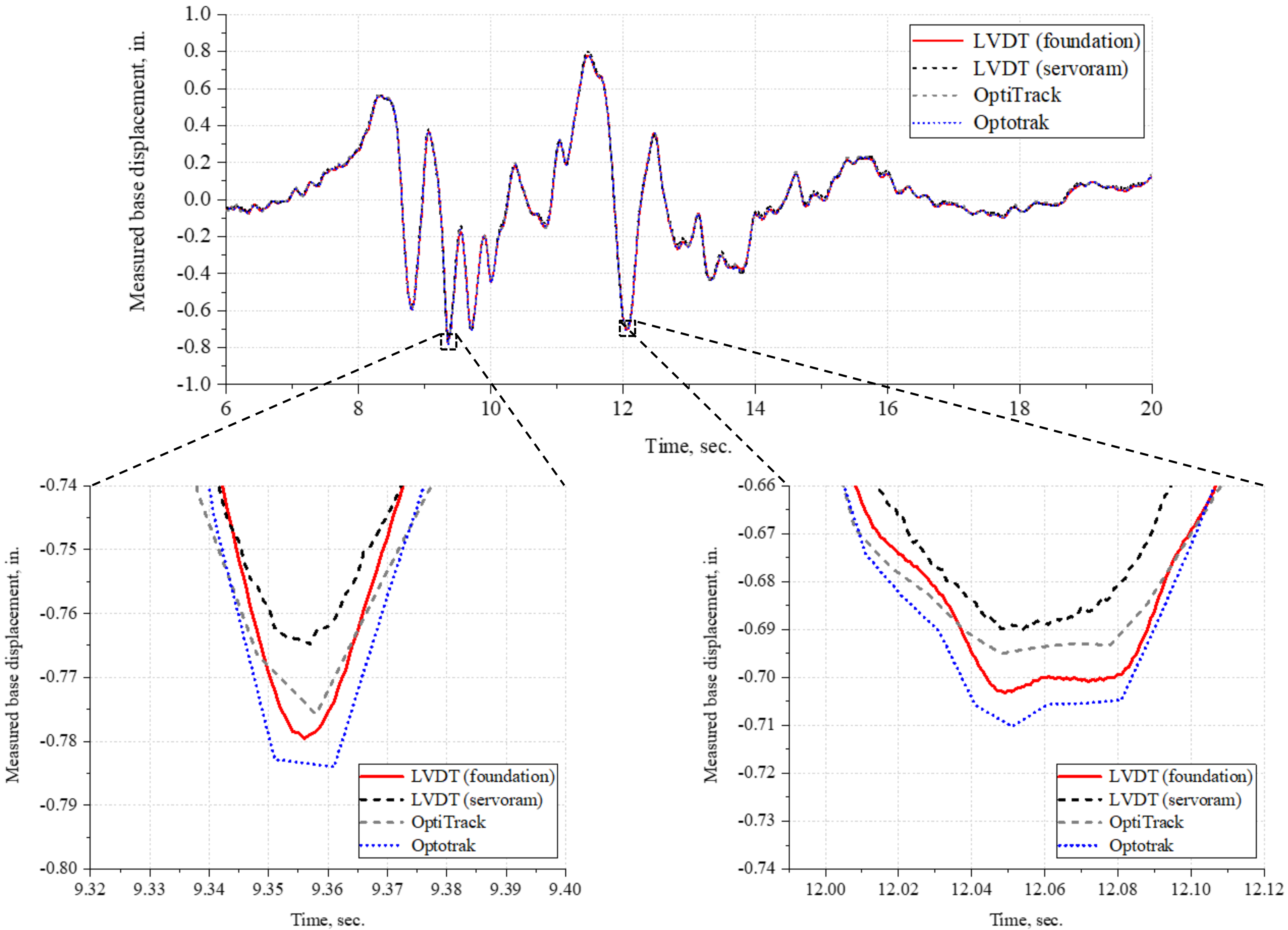

Figure 2-33: Comparisons of measurements of base displacement histories in F2-C-RSN1051-PGV8-1 (Run 48 of Specimen F2)

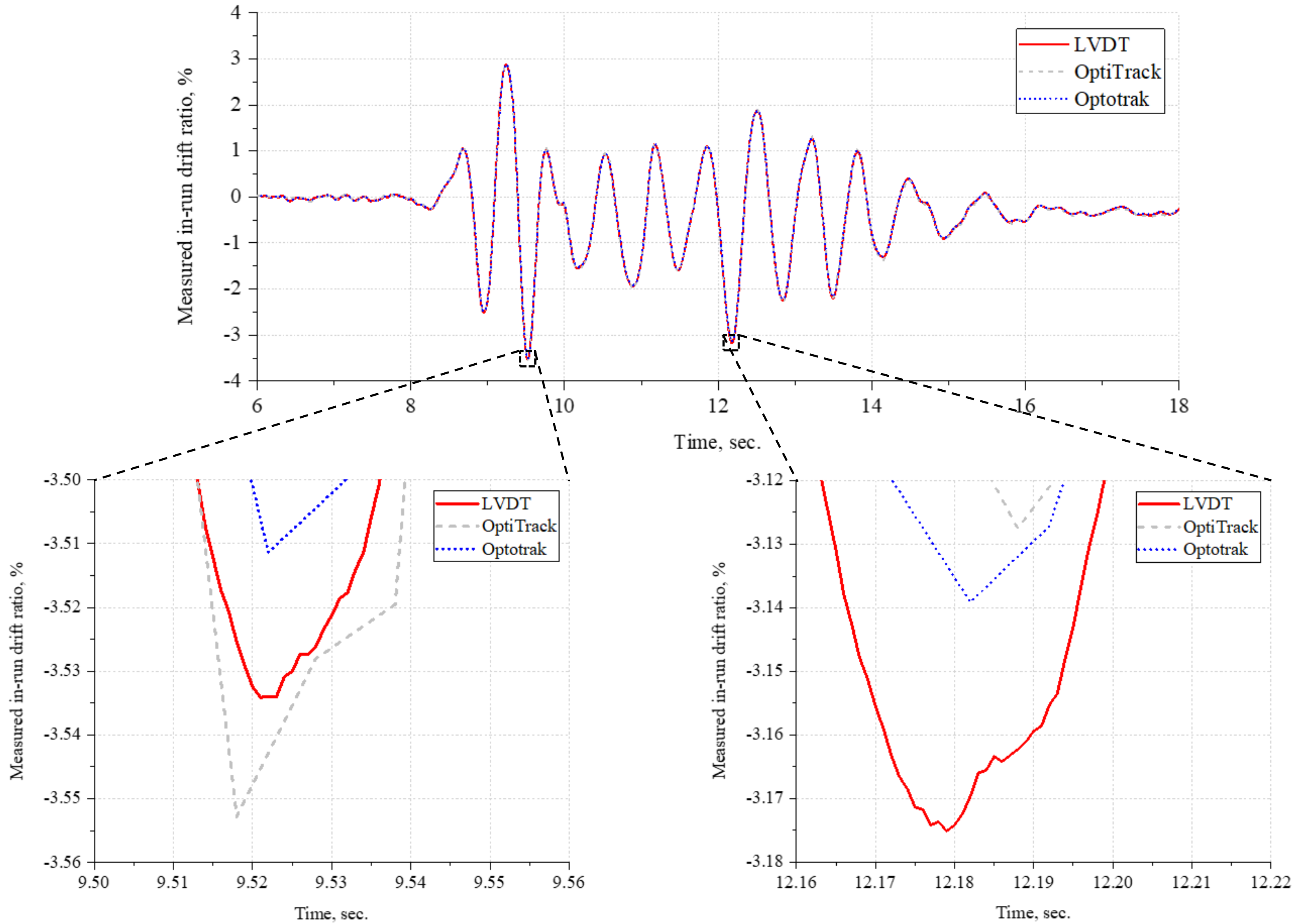

Figure 2-34: Comparisons of measurements of in-run drift histories in F2-C-RSN1051-PGV8-1 (Run 48 of Specimen F2)

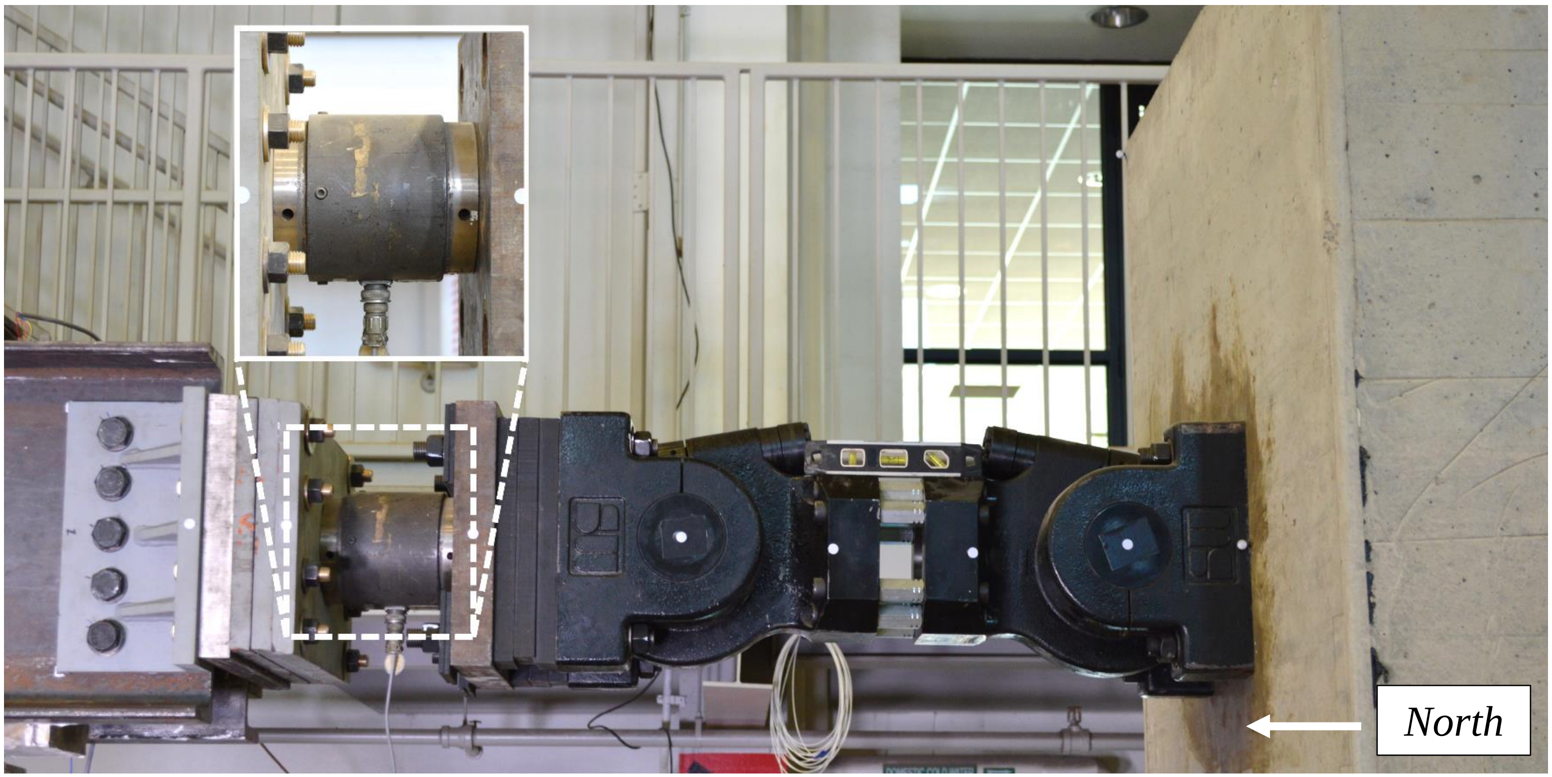

Figure 2-35: Load cell attached to south end of top beam of specimen and swivel at north end of link

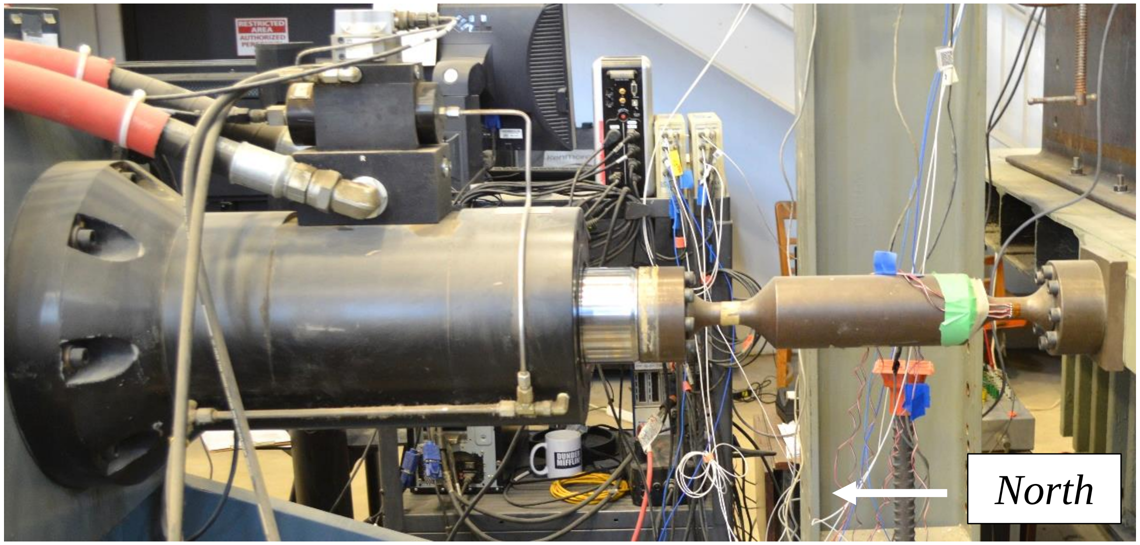

(a) Servoram and flexure link

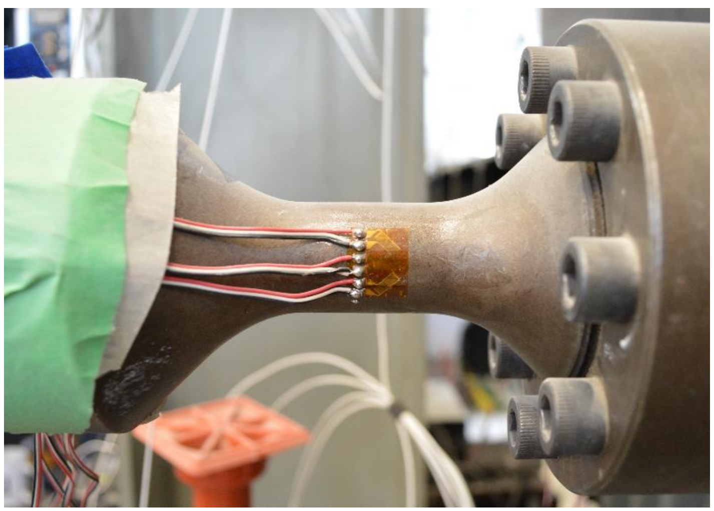

(b) West face

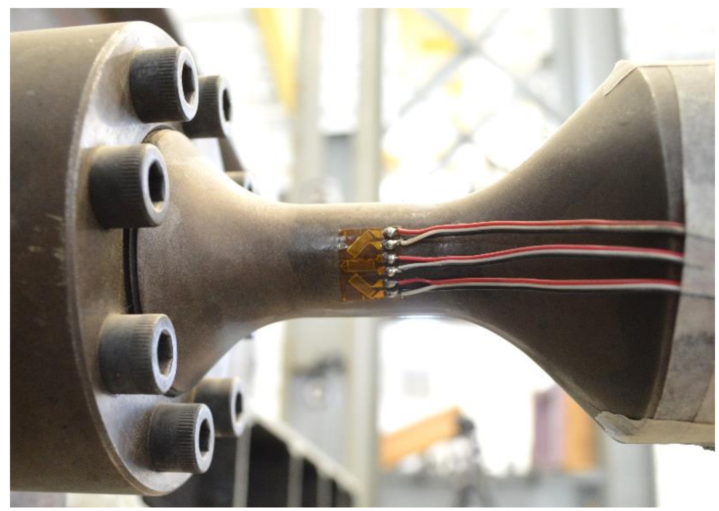

(c) East face

Figure 2-36: Strain gages on flexure link

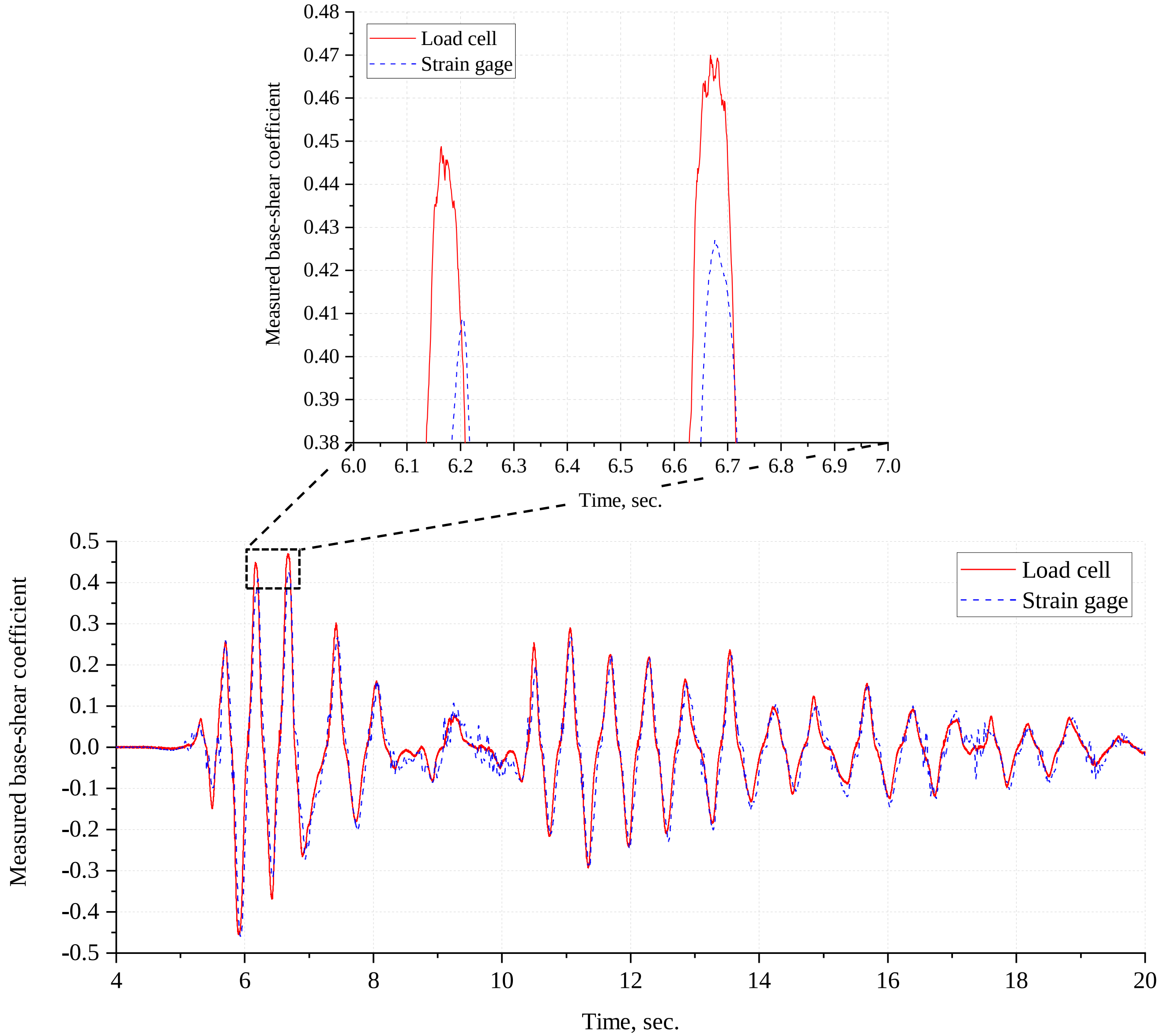

Figure 2-37: Comparisons of measurements of lateral load histories in F1-B-80-1 (Run 12 of Specimen F1)

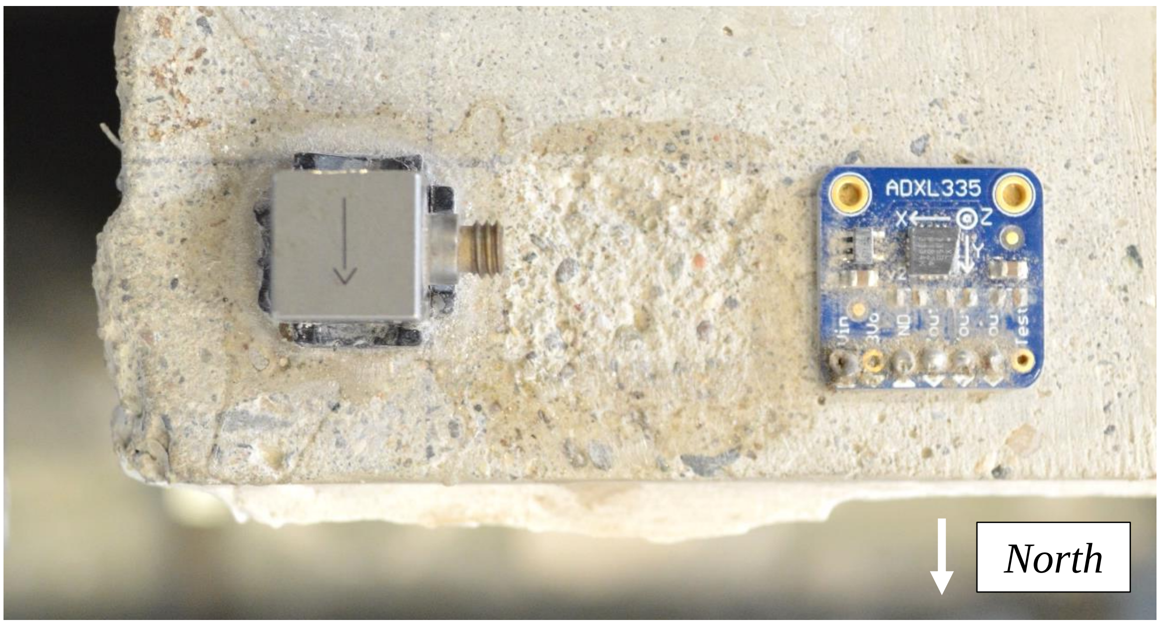

Figure 2-38: PCB (left) and ADXL (right) accelerometers mounted on top of foundation beam (Base NE)

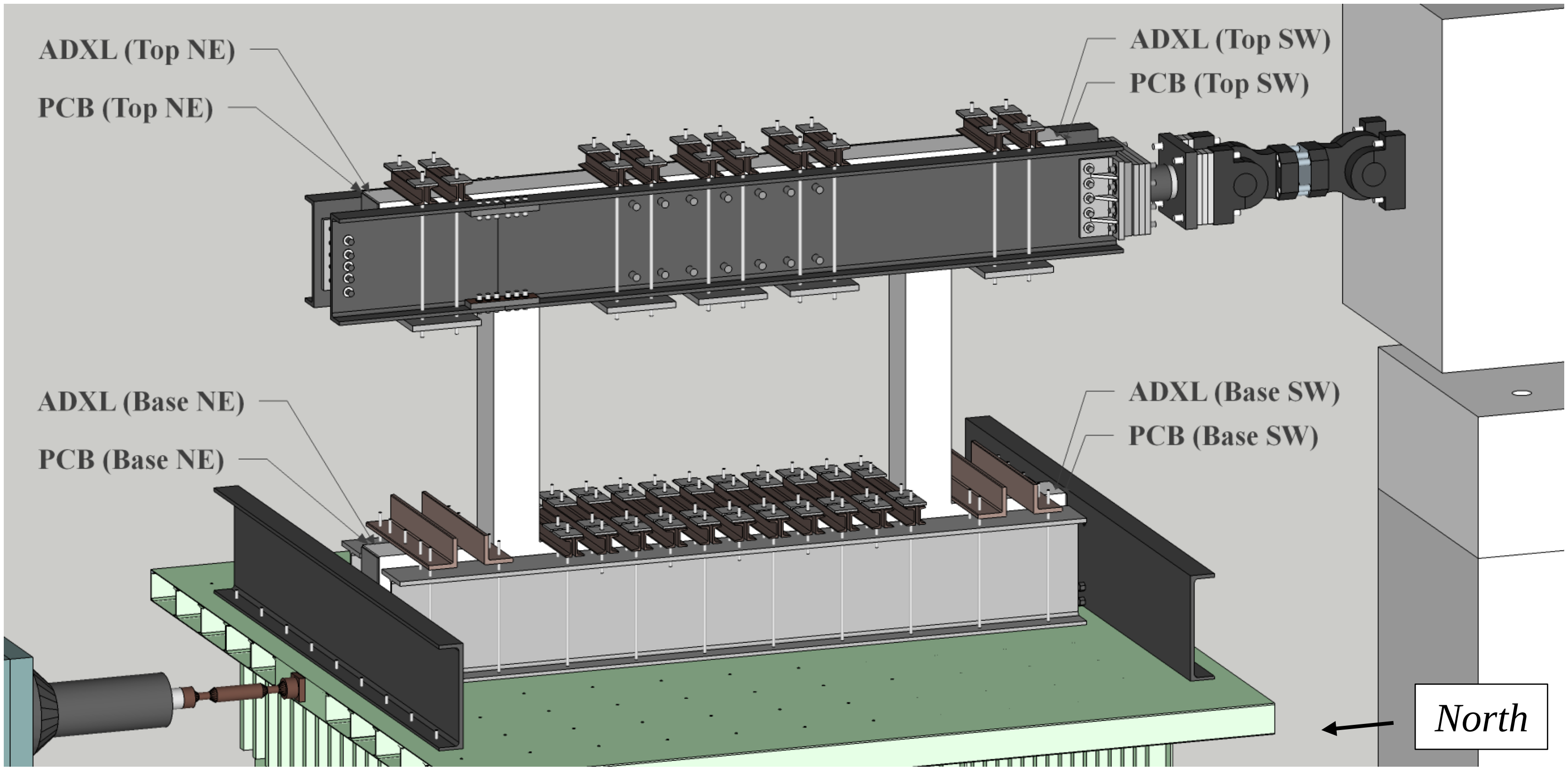

Figure 2-39: Accelerometer layout on specimen

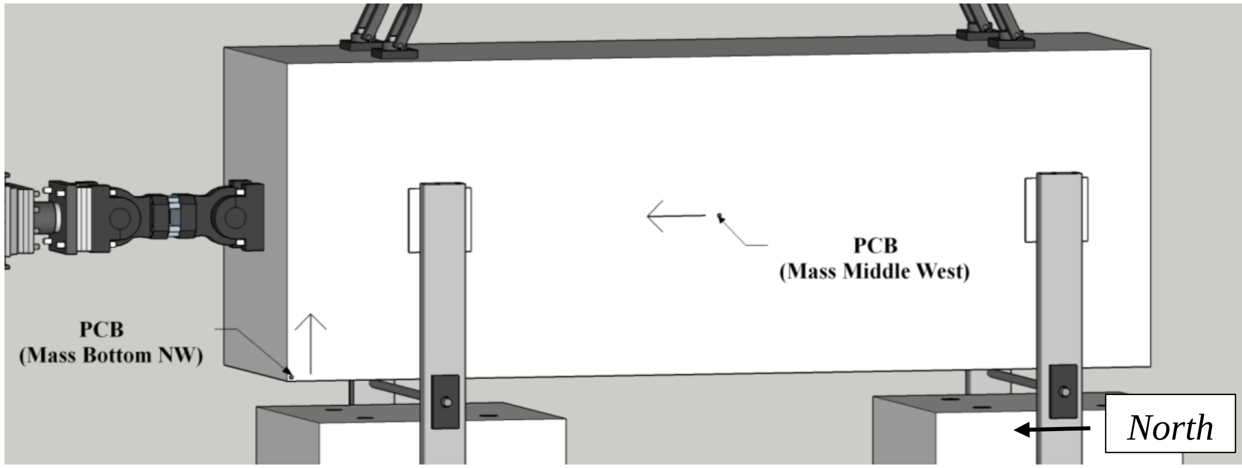

(a) West face

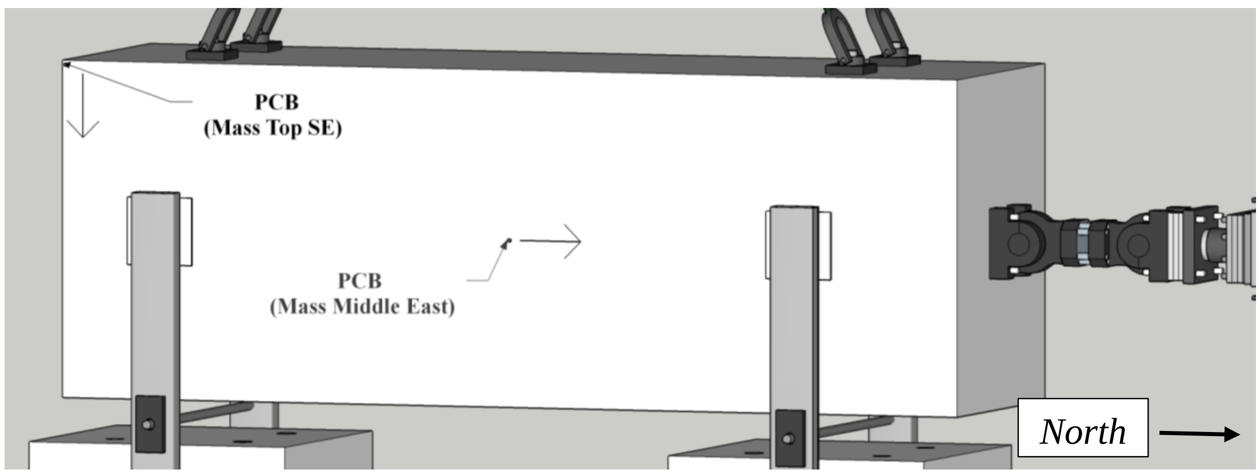

(b) East face

Figure 2-40: Accelerometer layout on suspended mass

Note: Arrows denote orientation of accelerometers.

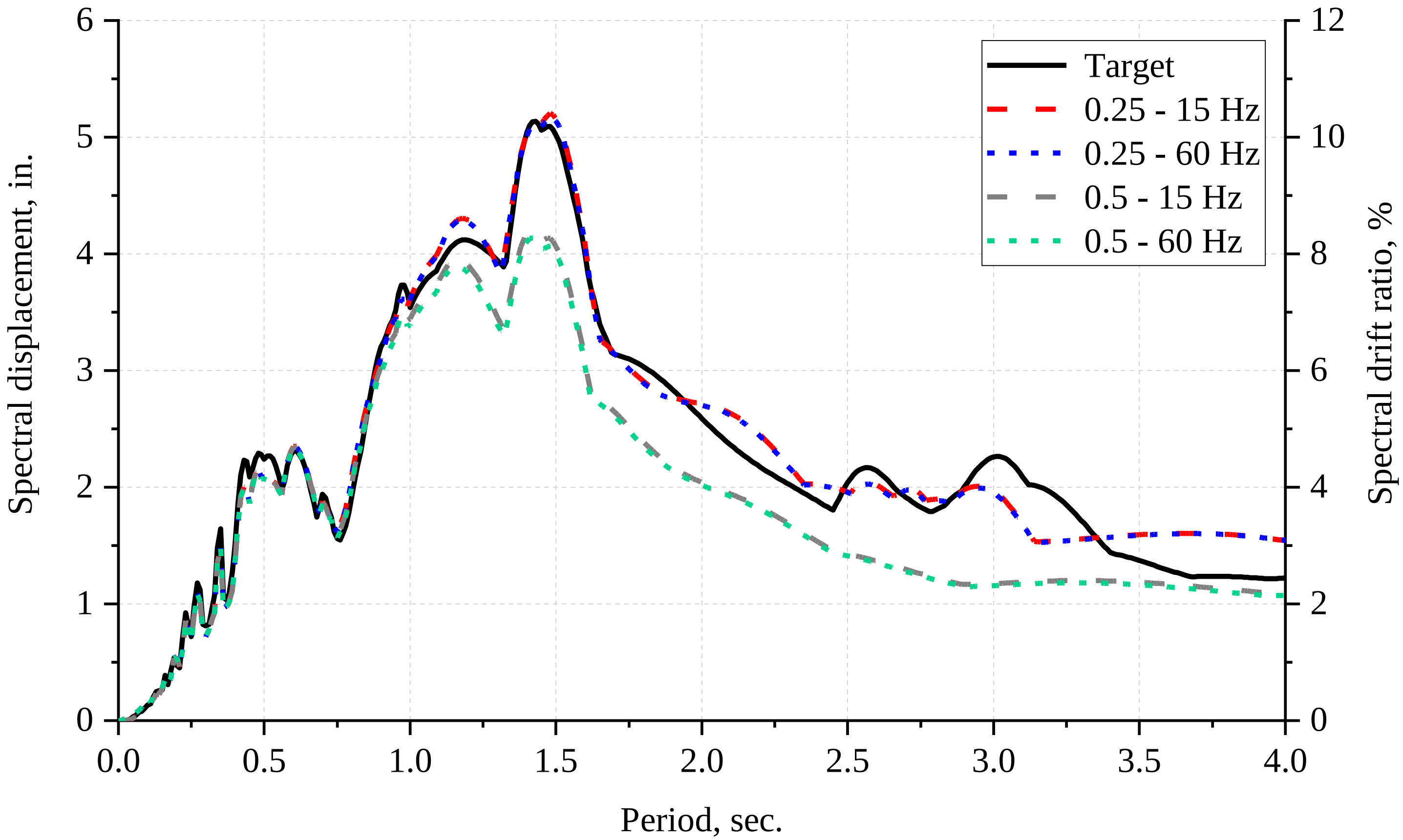

Figure 2-41: Comparisons of displacement spectra (2% damping) calculated using target and measured base acceleration histories of F1-B-80-1 (Run 12 of Specimen F1) filtered with different cut-off frequencies

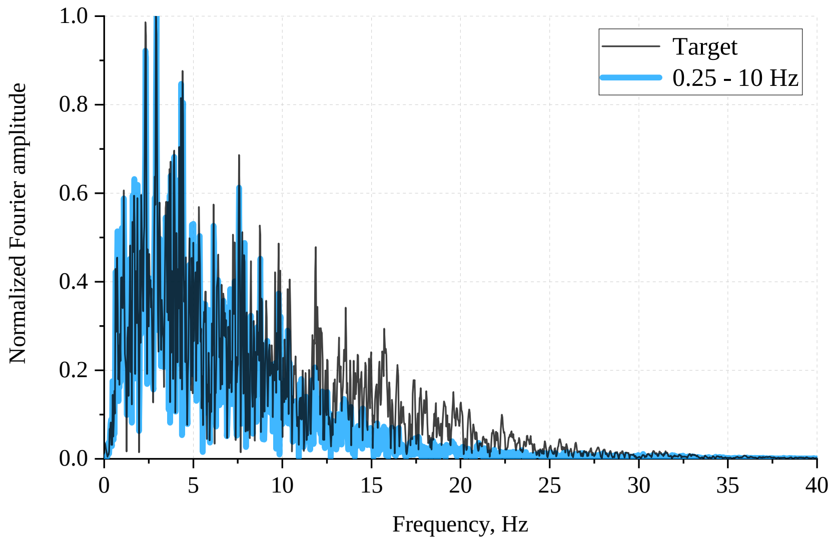

(a) Low-pass cut-off frequency of 10 Hz

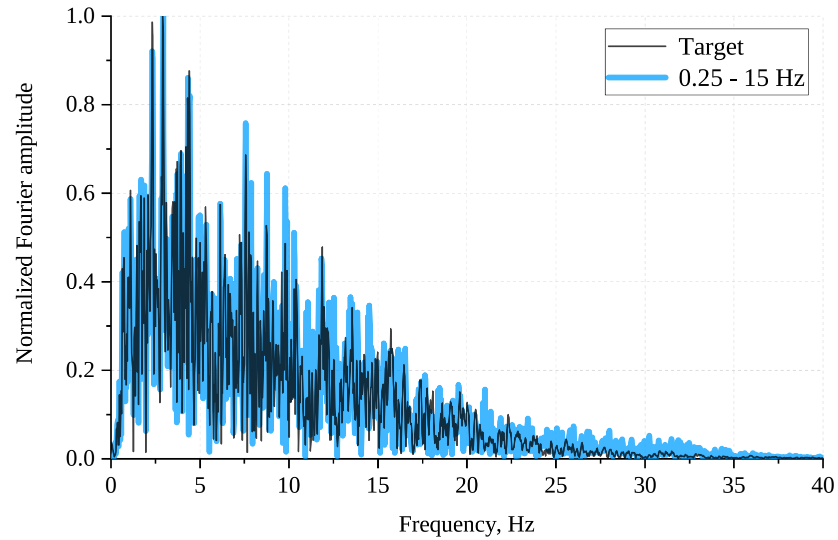

(b) Low-pass cut-off frequency of 15 Hz

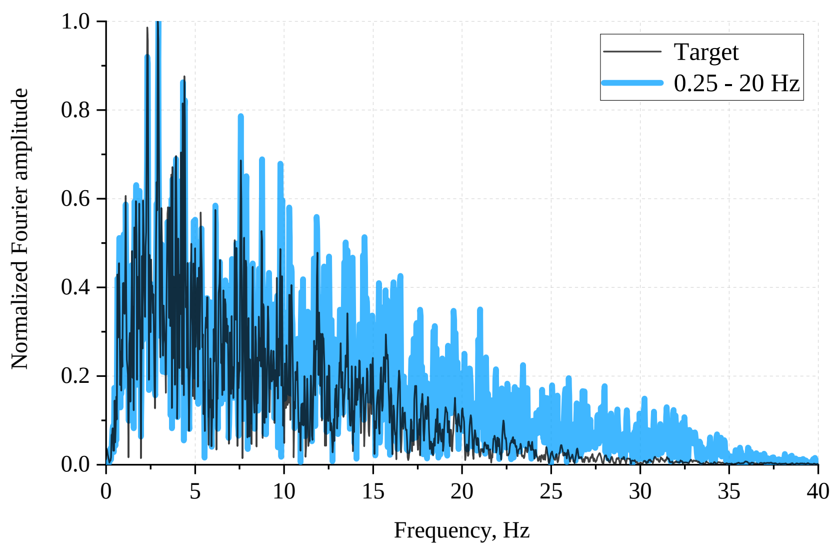

(c) Low-pass cut-off frequency of 20 Hz

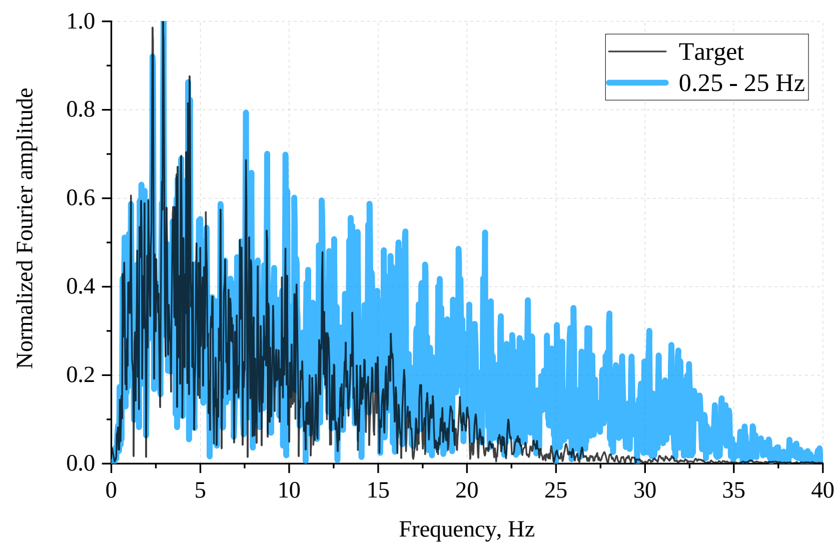

(d) Low-pass cut-off frequency of 25 Hz

Figure 2-42: Comparisons of Fourier decompositions of measured base acceleration histories of F1-B-80-1 (Run 12 of Specimen F1)

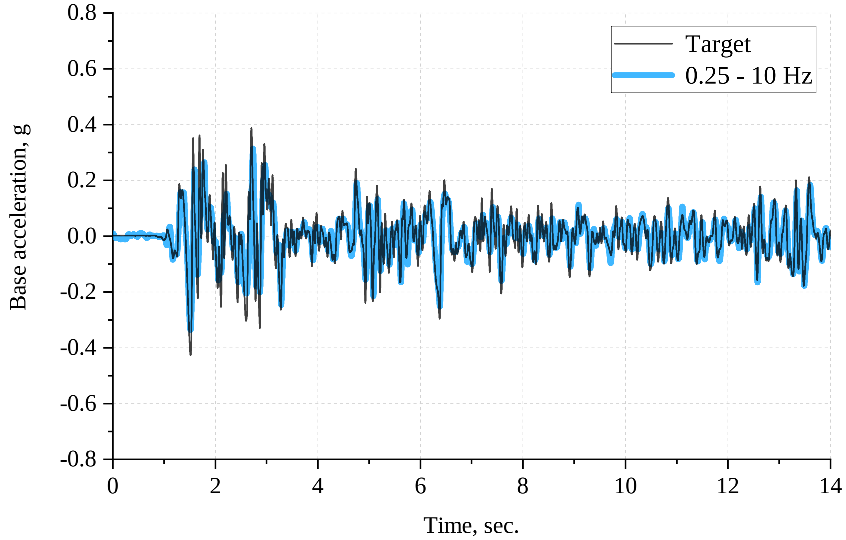

(a) Low-pass cut-off frequency of 10 Hz

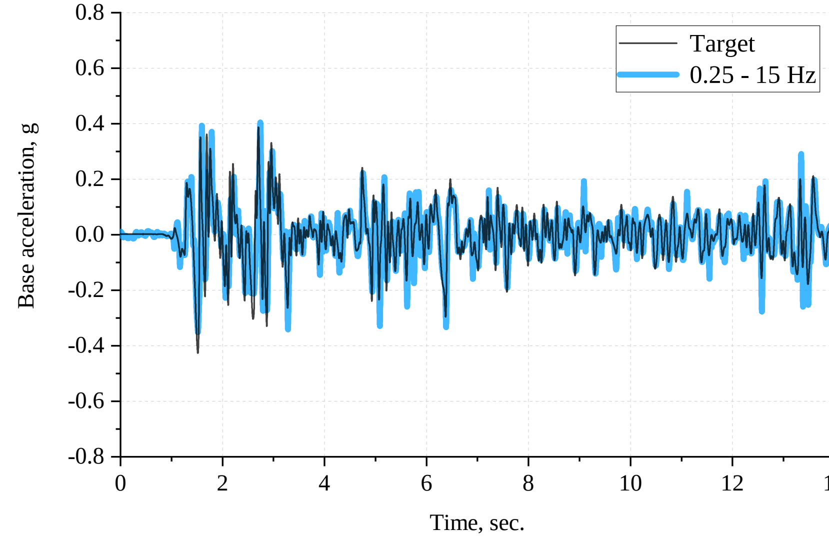

(b) Low-pass cut-off frequency of 15 Hz

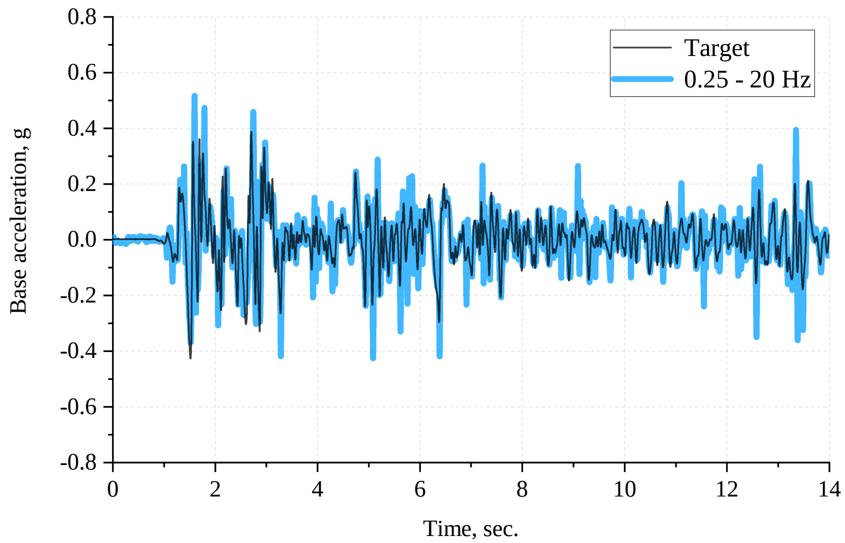

(c) Low-pass cut-off frequency of 20 Hz

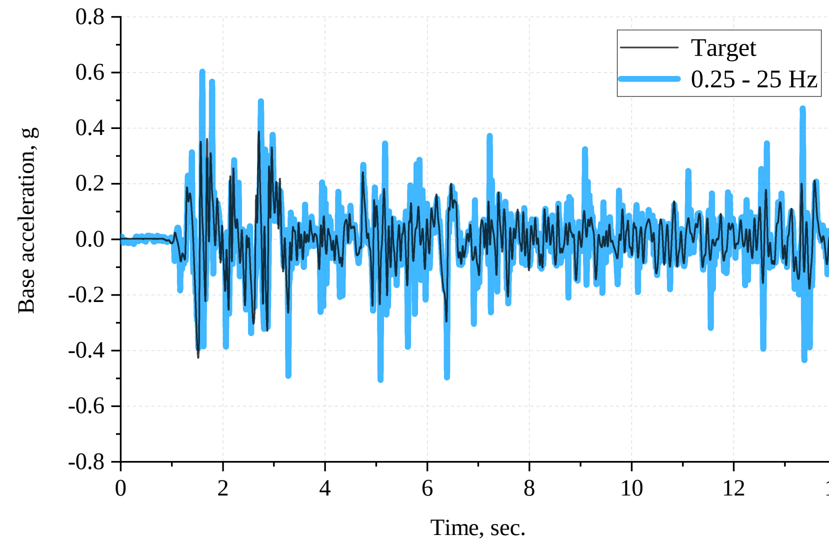

(d) Low-pass cut-off frequency of 25 Hz

Figure 2-43: Comparisons of measured base acceleration histories of F1-B-80-1 (Run 12 of Specimen F1)

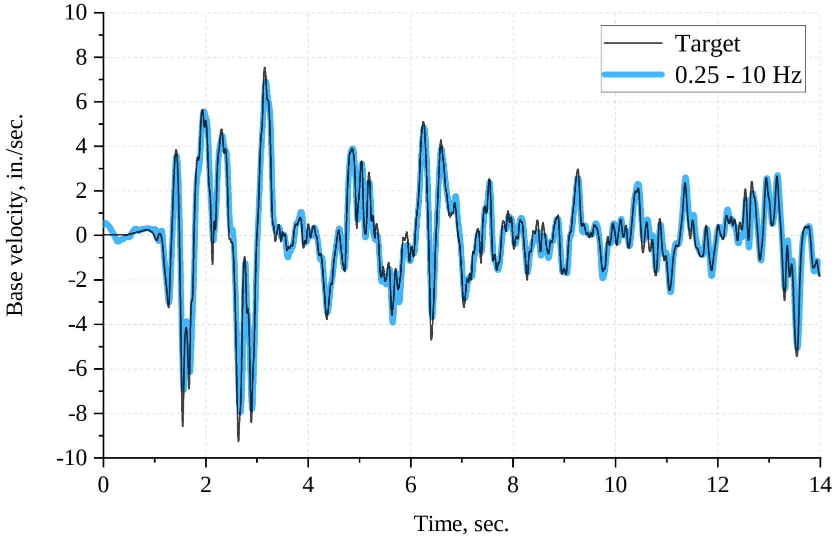

(a) Low-pass cut-off frequency of 10 Hz

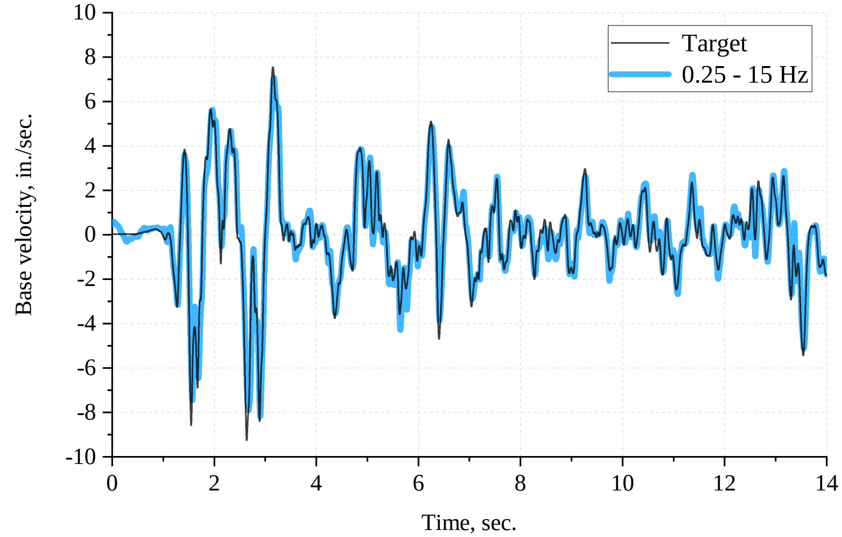

(b) Low-pass cut-off frequency of 15 Hz

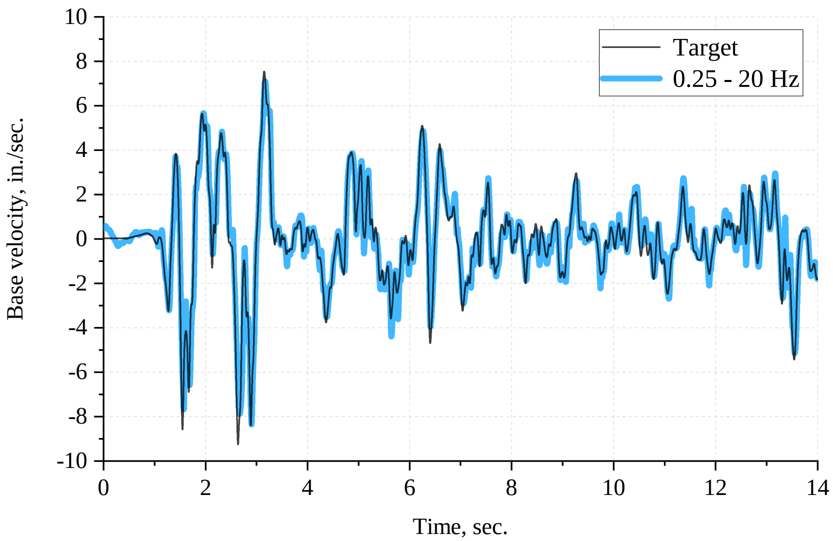

(c) Low-pass cut-off frequency of 20 Hz

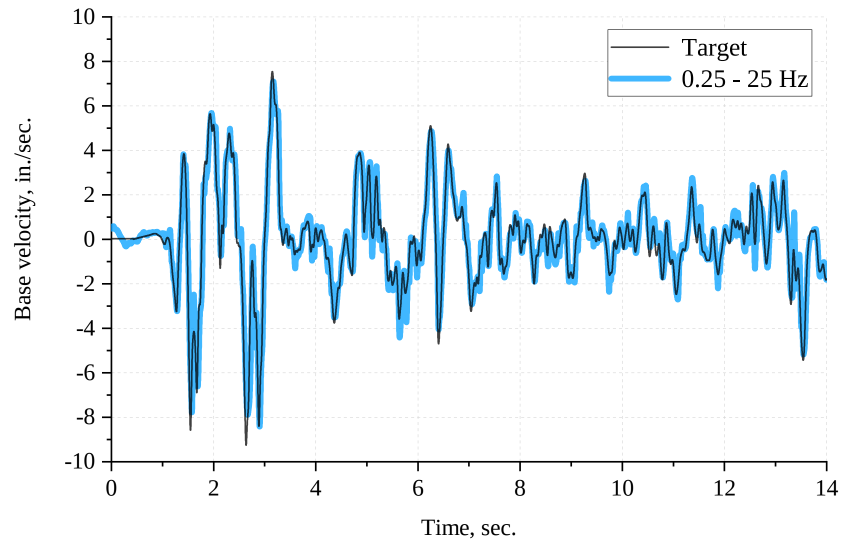

(d) Low-pass cut-off frequency of 25 Hz

Figure 2-44: Comparisons of measured base velocity histories of F1-B-80-1 (Run 12 of Specimen F1)

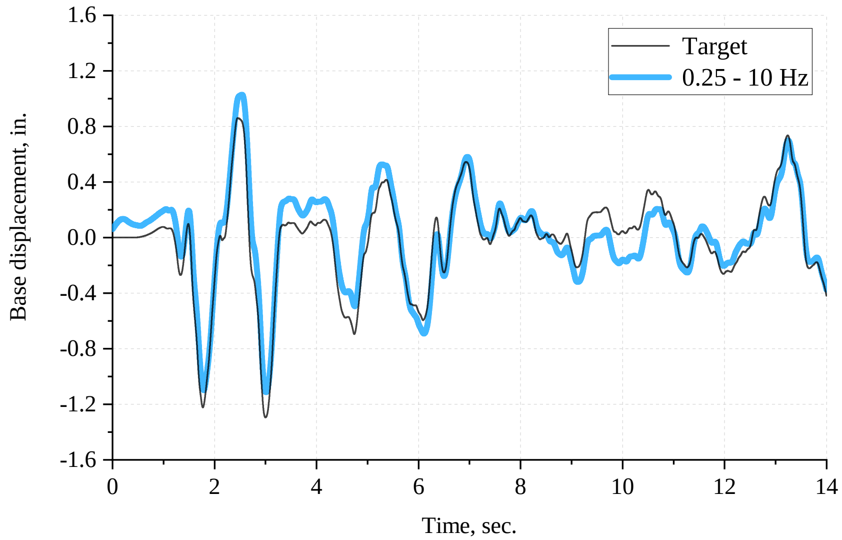

(a) Low-pass cut-off frequency of 10 Hz

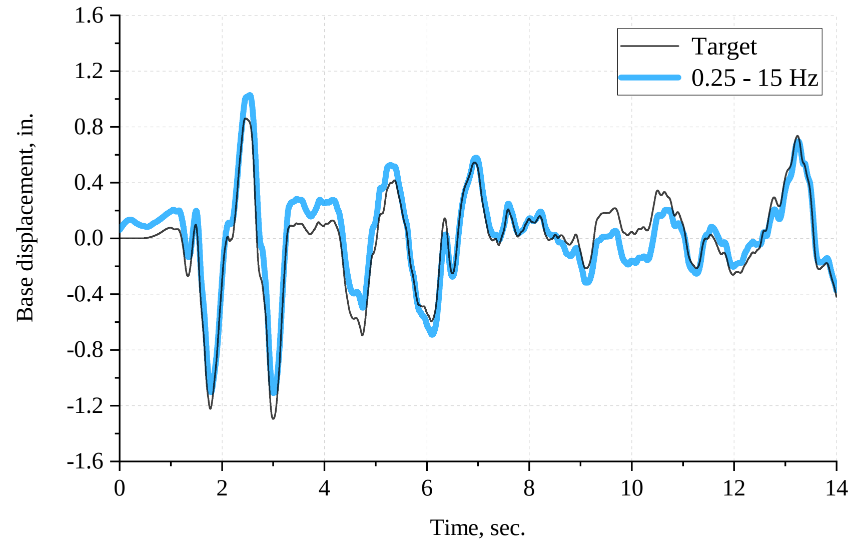

(b) Low-pass cut-off frequency of 15 Hz

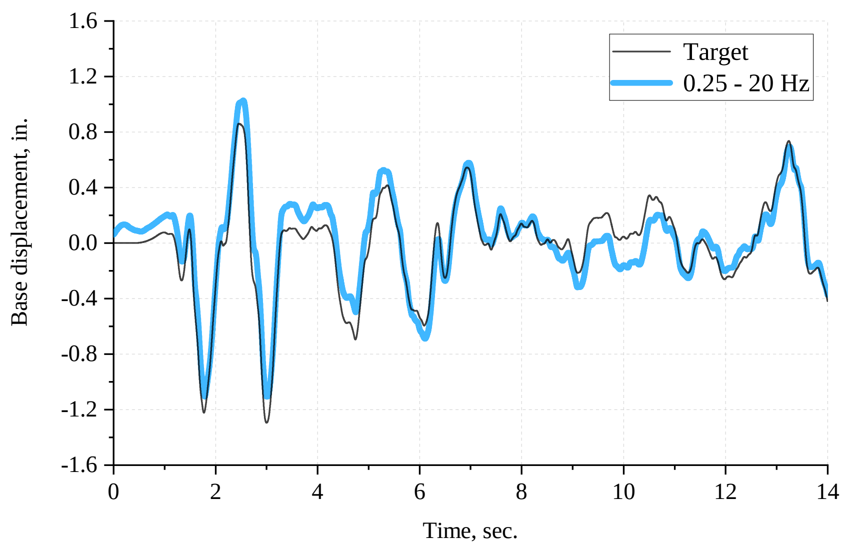

(c) Low-pass cut-off frequency of 20 Hz

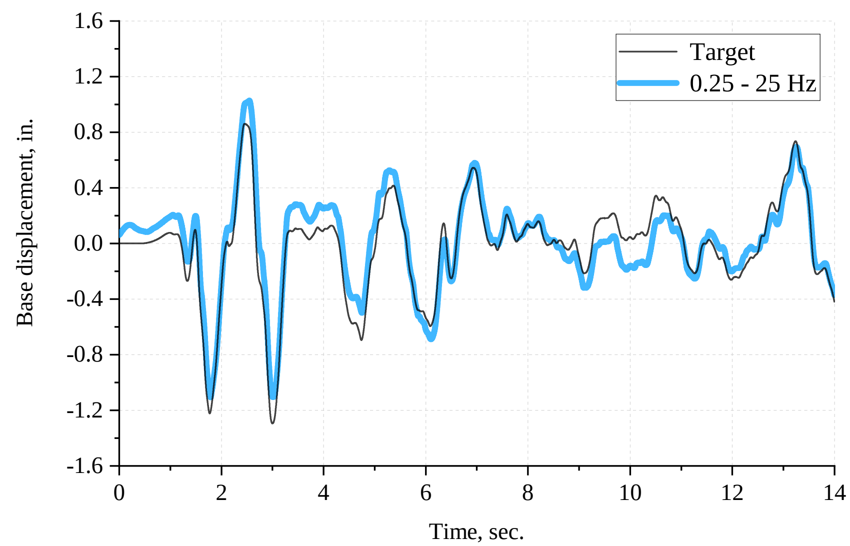

(d) Low-pass cut-off frequency of 25 Hz

Figure 2-45: Comparisons of measured base displacement histories of F1-B-80-1 (Run 12 of Specimen F1)

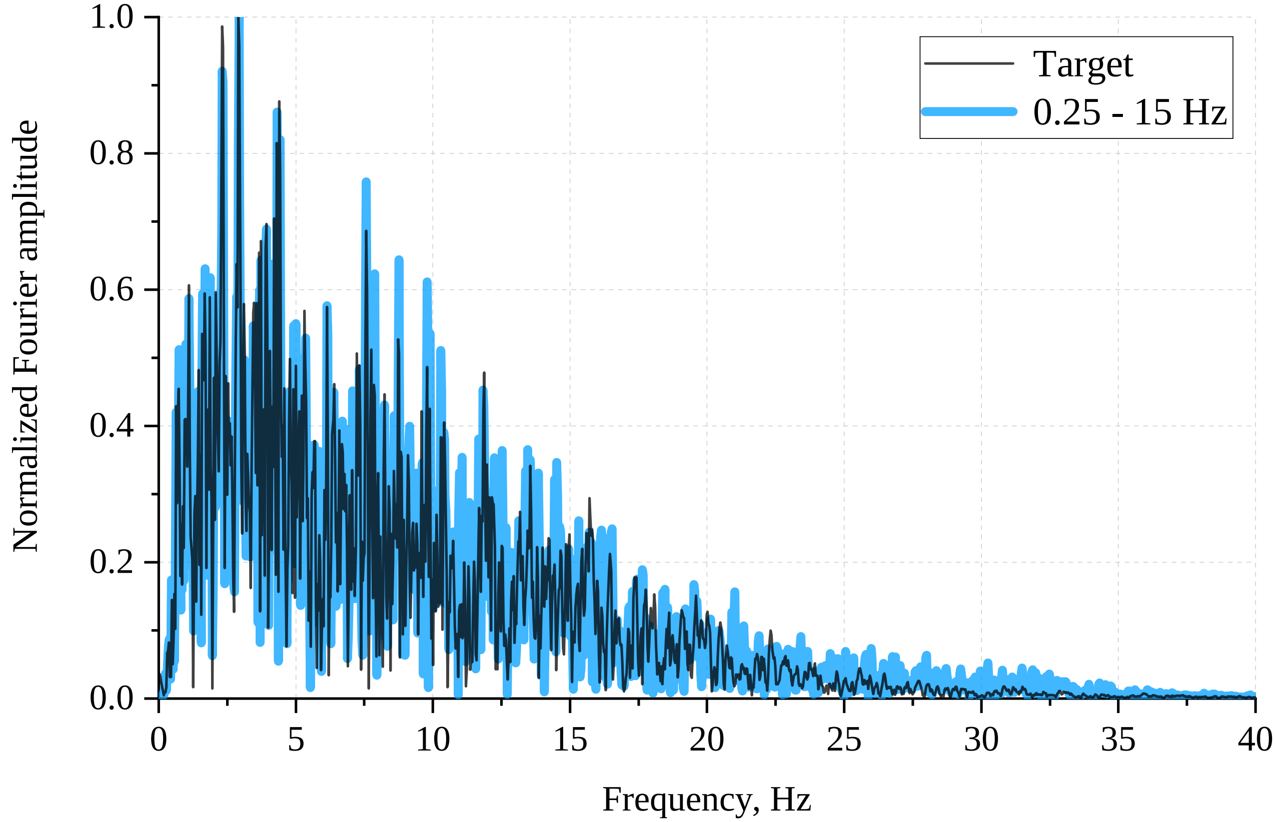

Figure 2-46: Comparisons of Fourier decompositions of target and measured base acceleration histories of F1-B-80-1 (Run 12 of Specimen F1) filtered with fourth-order Butterworth bandpass filter with high-pass and low-pass cut-off frequencies of 0.25 and 15 Hz

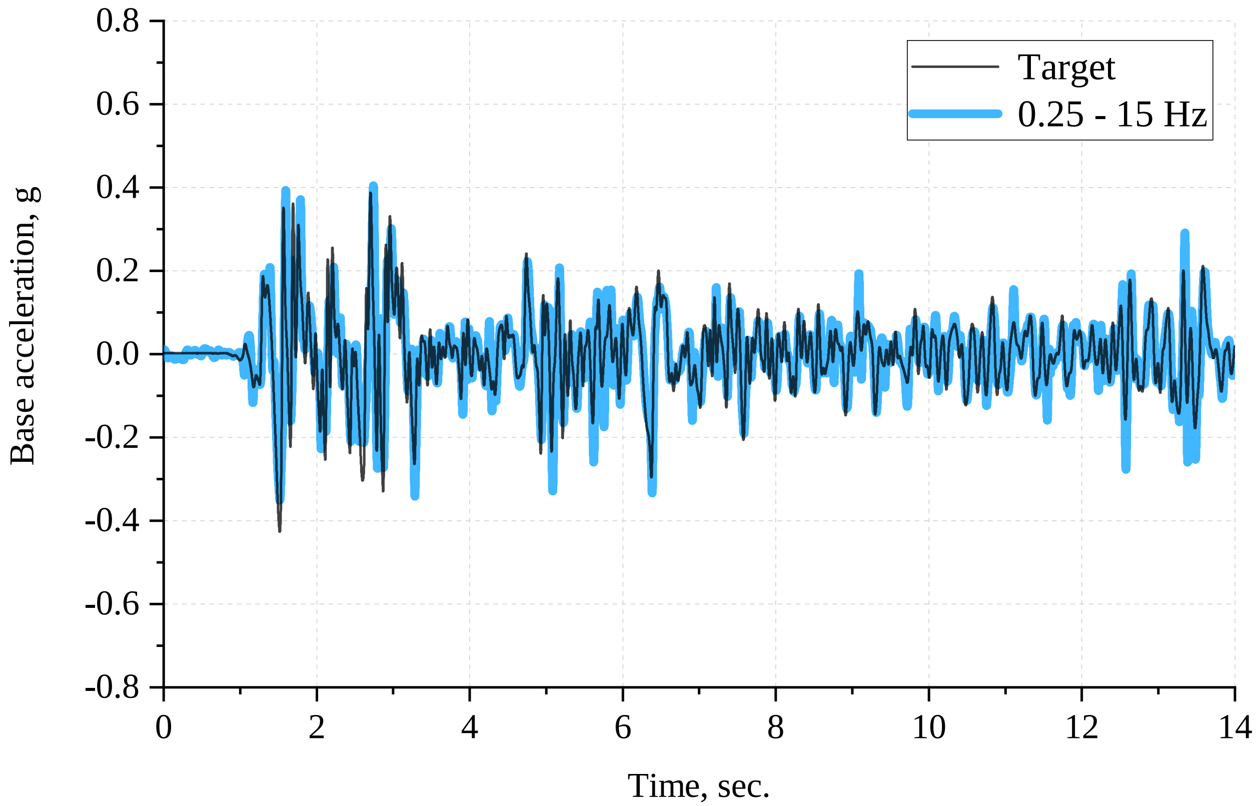

Figure 2-47: Comparisons of target and measured base acceleration histories of F1-B-80-1 (Run 12 of Specimen F1) filtered with fourth-order Butterworth bandpass filter with high-pass and low-pass cut-off frequencies of 0.25 and 15 Hz

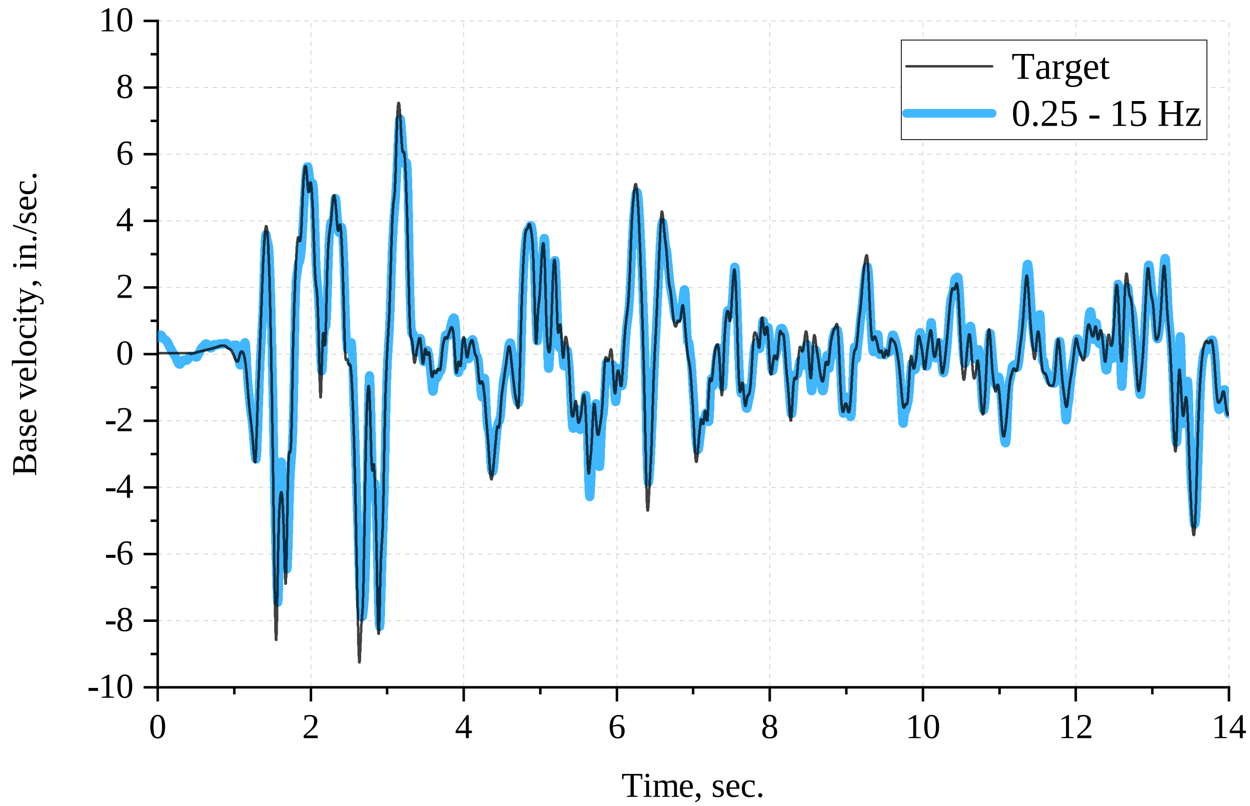

Figure 2-48: Comparisons of target and measured base velocity histories of F1-B-80-1 (Run 12 of Specimen F1) filtered with fourth-order Butterworth bandpass filter with high-pass and low-pass cut-off frequencies of 0.25 and 15 Hz

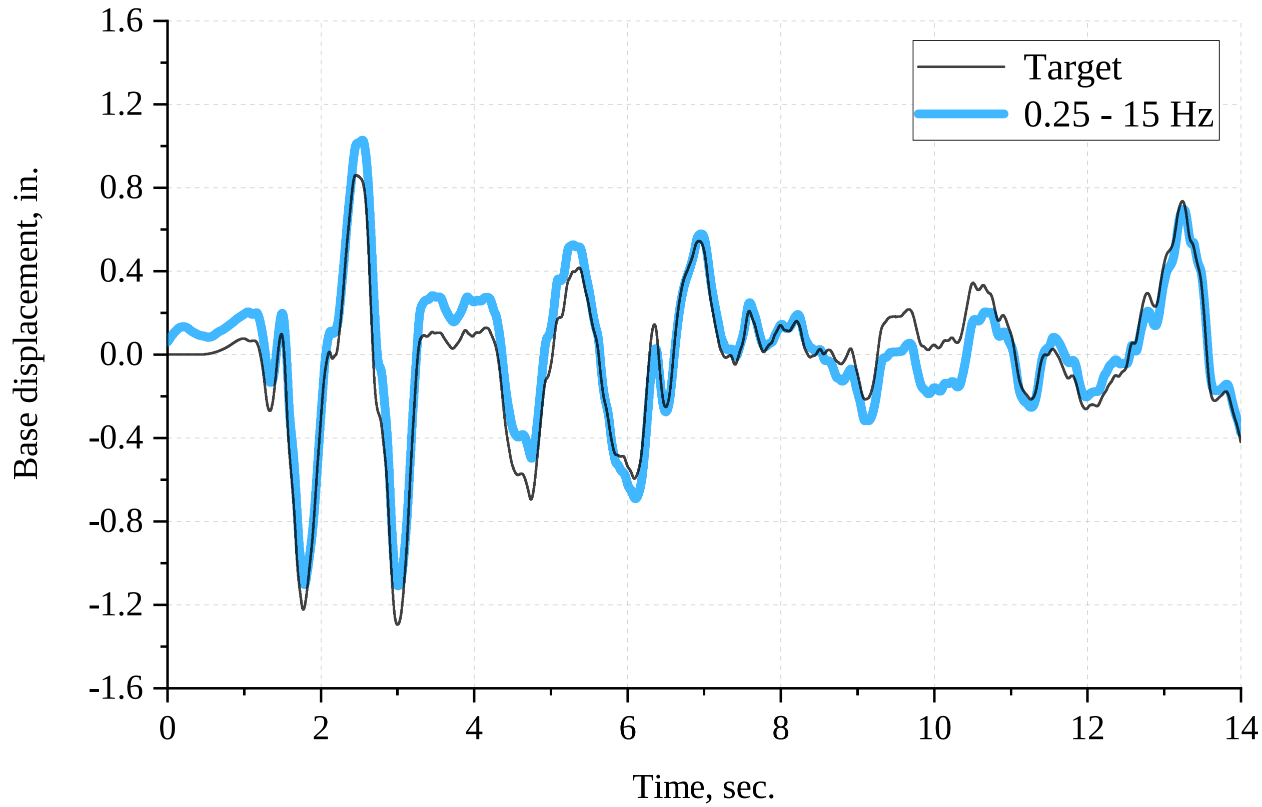

Figure 2-49: Comparisons of target and measured base displacement histories of F1-B-80-1 (Run 12 of Specimen F1) filtered with fourth-order Butterworth bandpass filter with high-pass and low-pass cut-off frequencies of 0.25 and 15 Hz

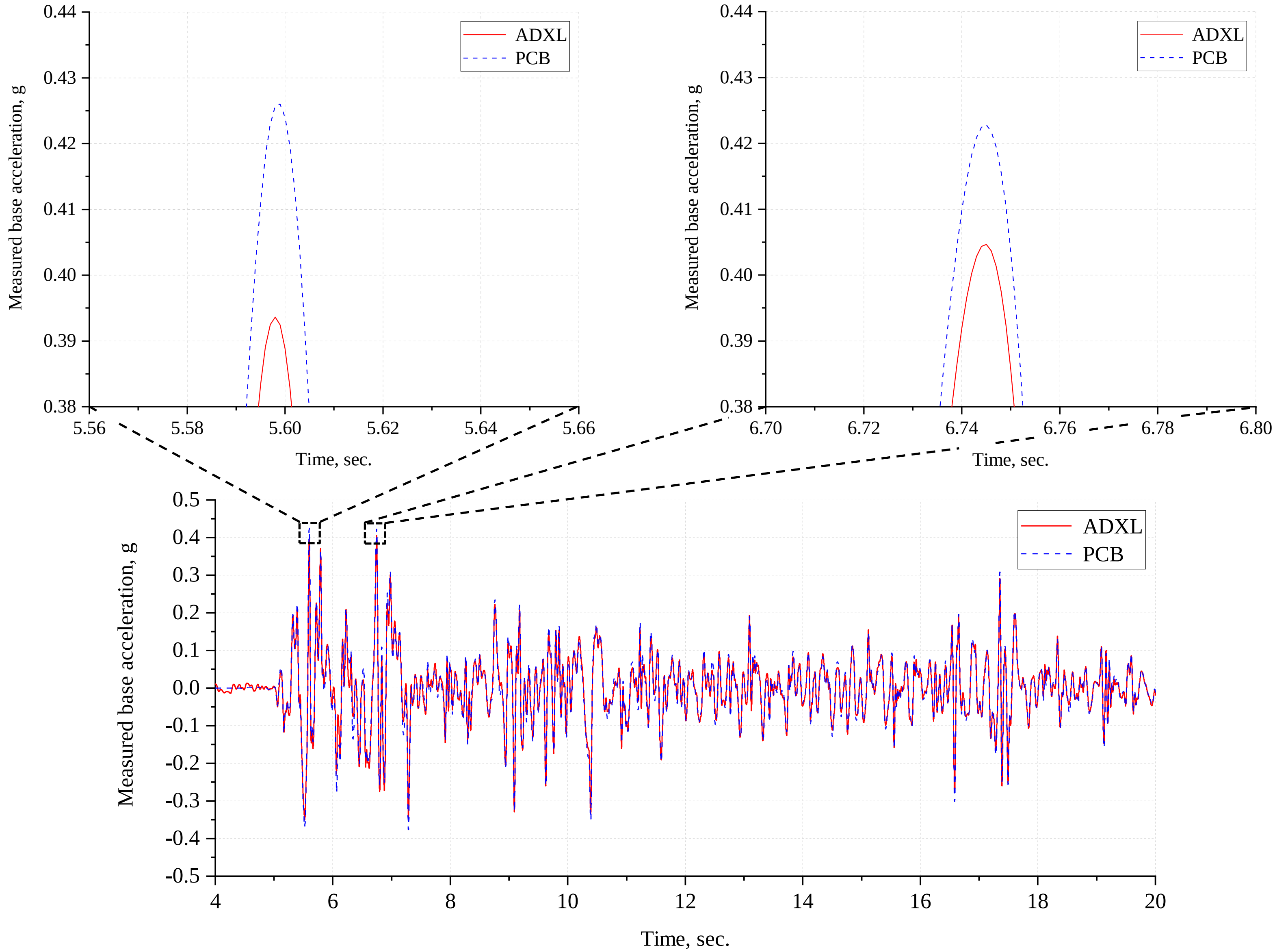

Figure 2-50: Comparisons of measurements of base acceleration histories in F1-B-80-1 (Run 12 of Specimen F1)

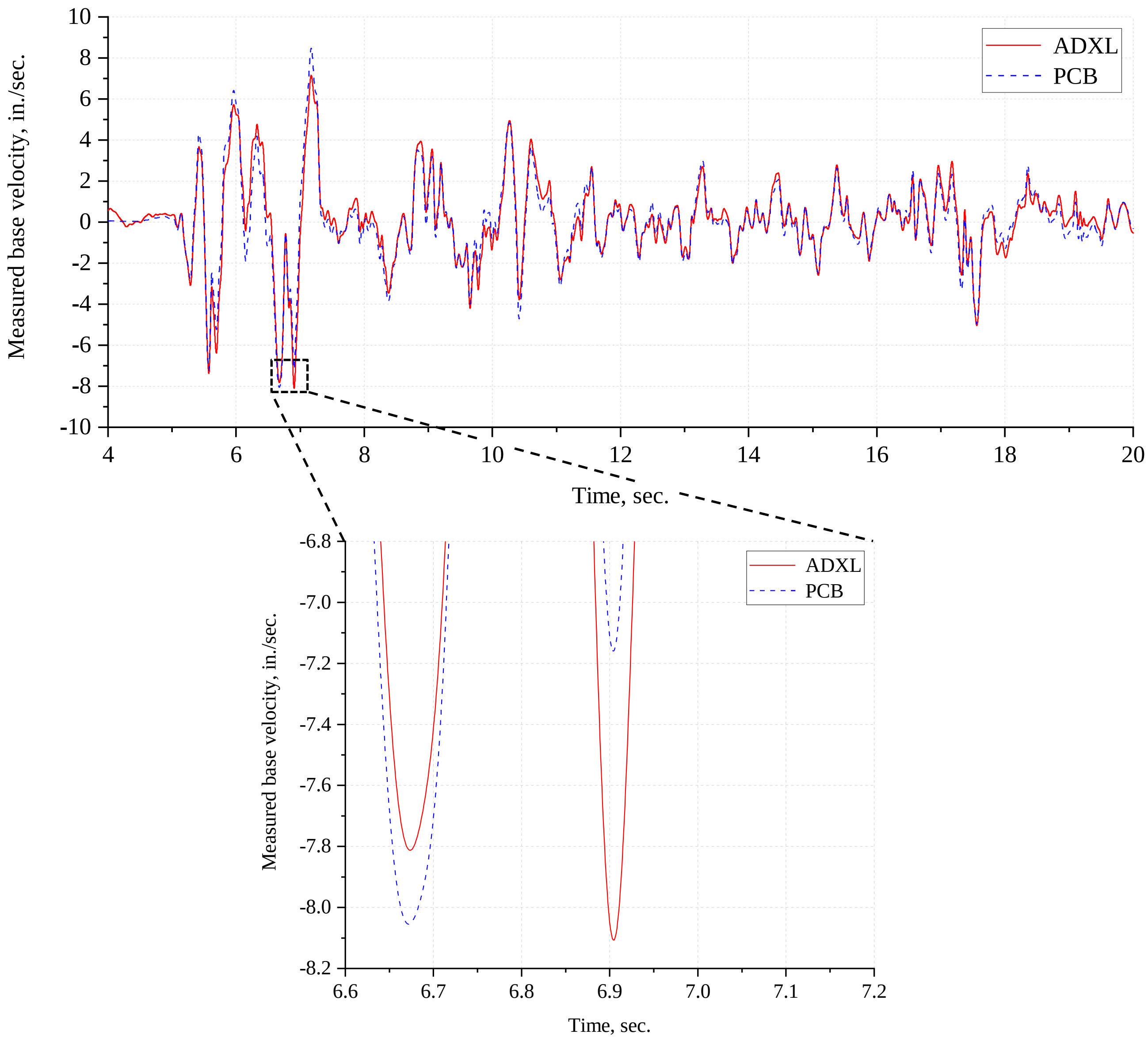

Figure 2-51: Comparisons of measurements of base velocity histories in F1-B-80-1 (Run 12 of Specimen F1)

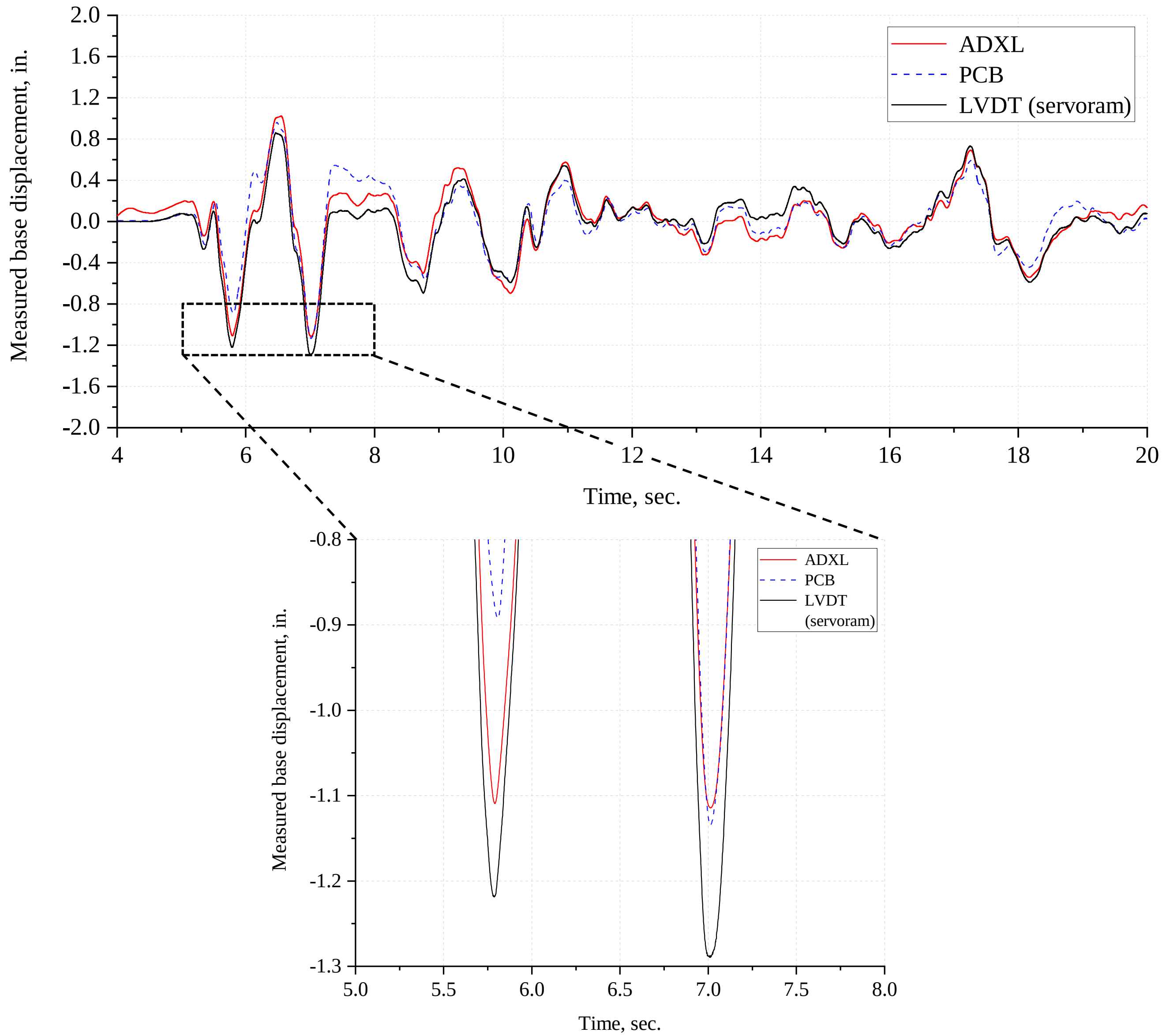

Figure 2-52: Comparisons of measurements of base displacement histories in F1-B-80-1 (Run 12 of Specimen F1)

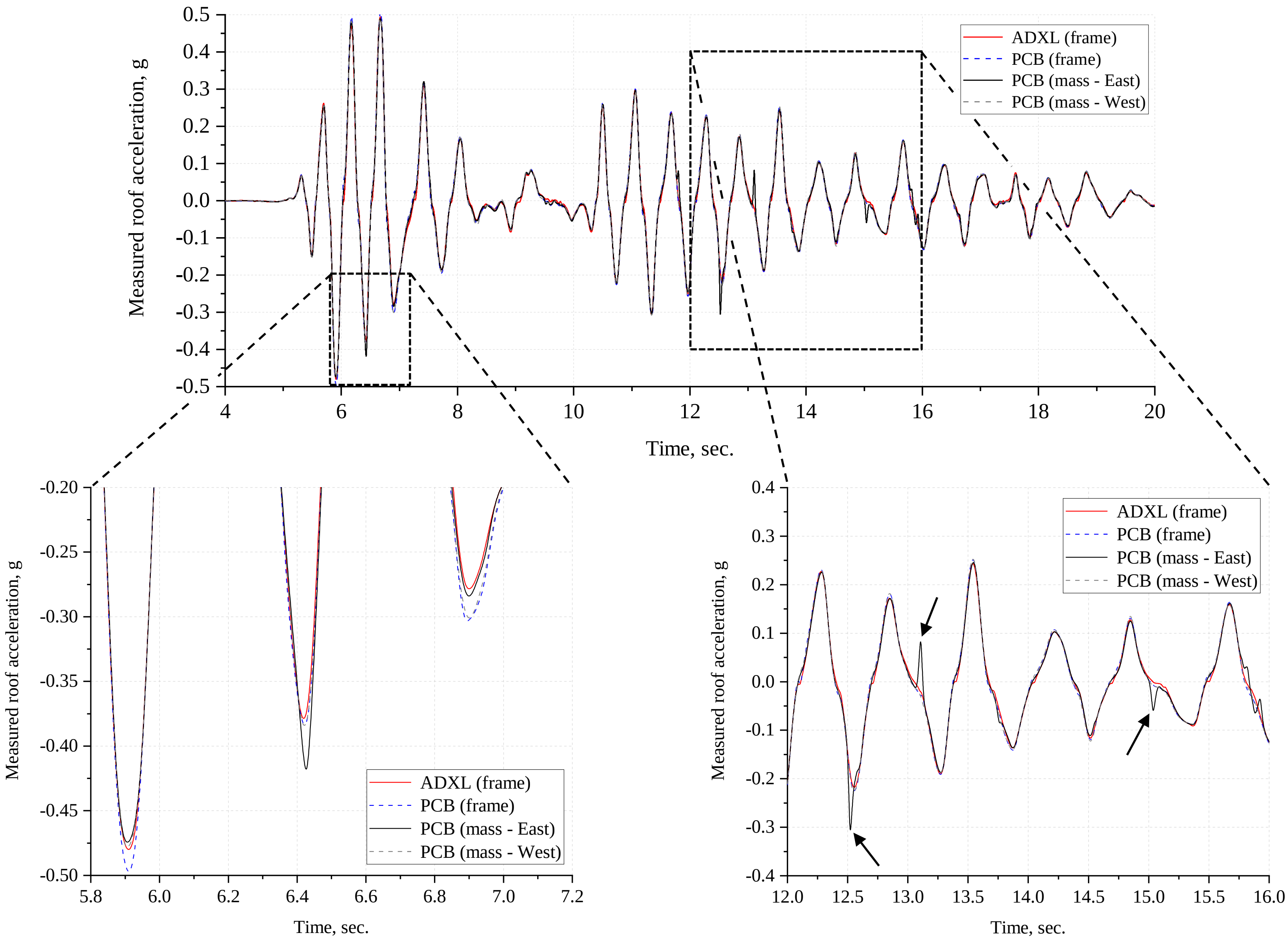

Figure 2-53: Comparisons of measurements of roof acceleration histories in F1-B-80-1 (Run 12 of Specimen F1)

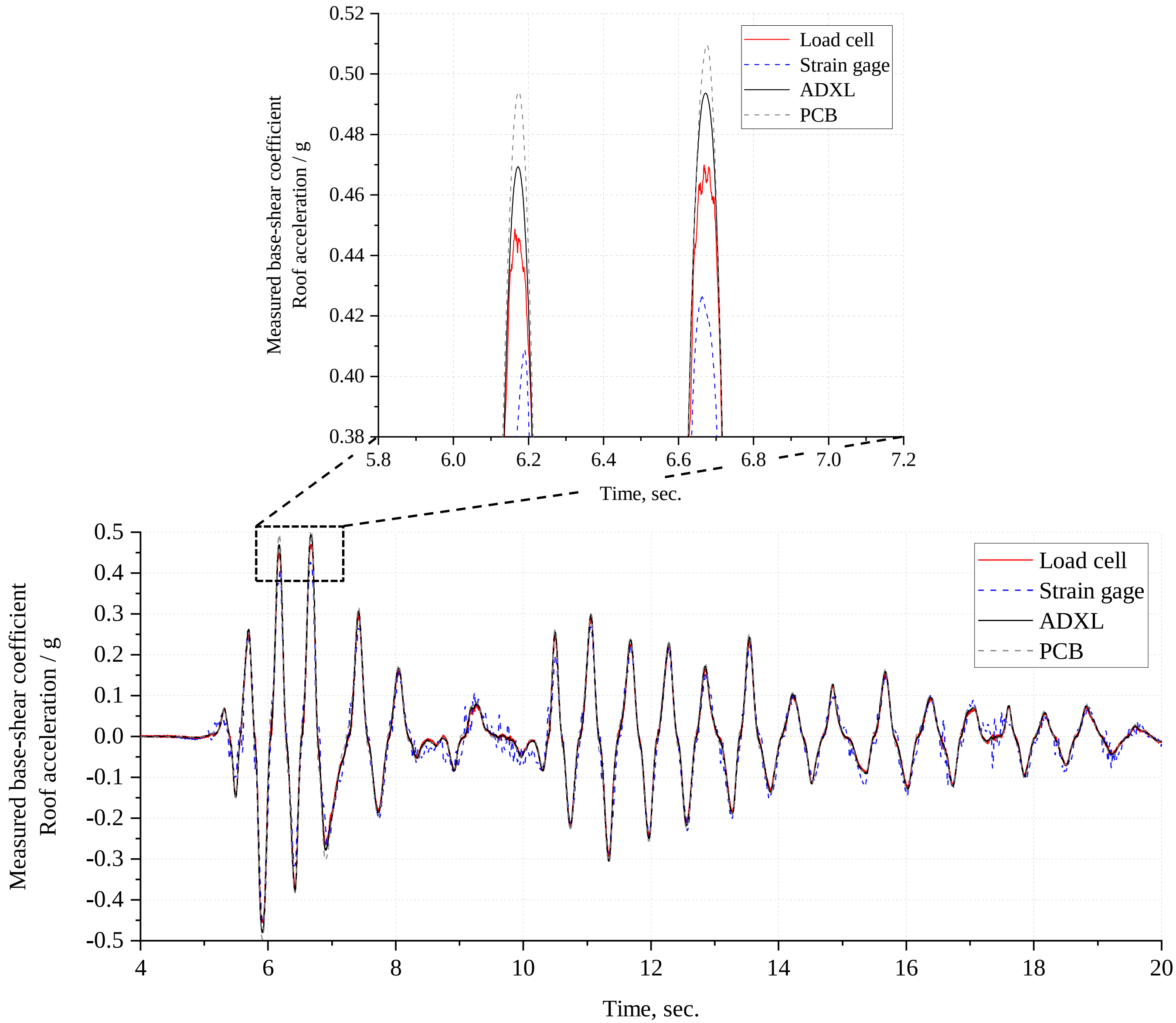

Figure 2-54: Comparisons of measurements of roof acceleration and lateral load histories in F1-B-80-1 (Run 12 of Specimen F1)

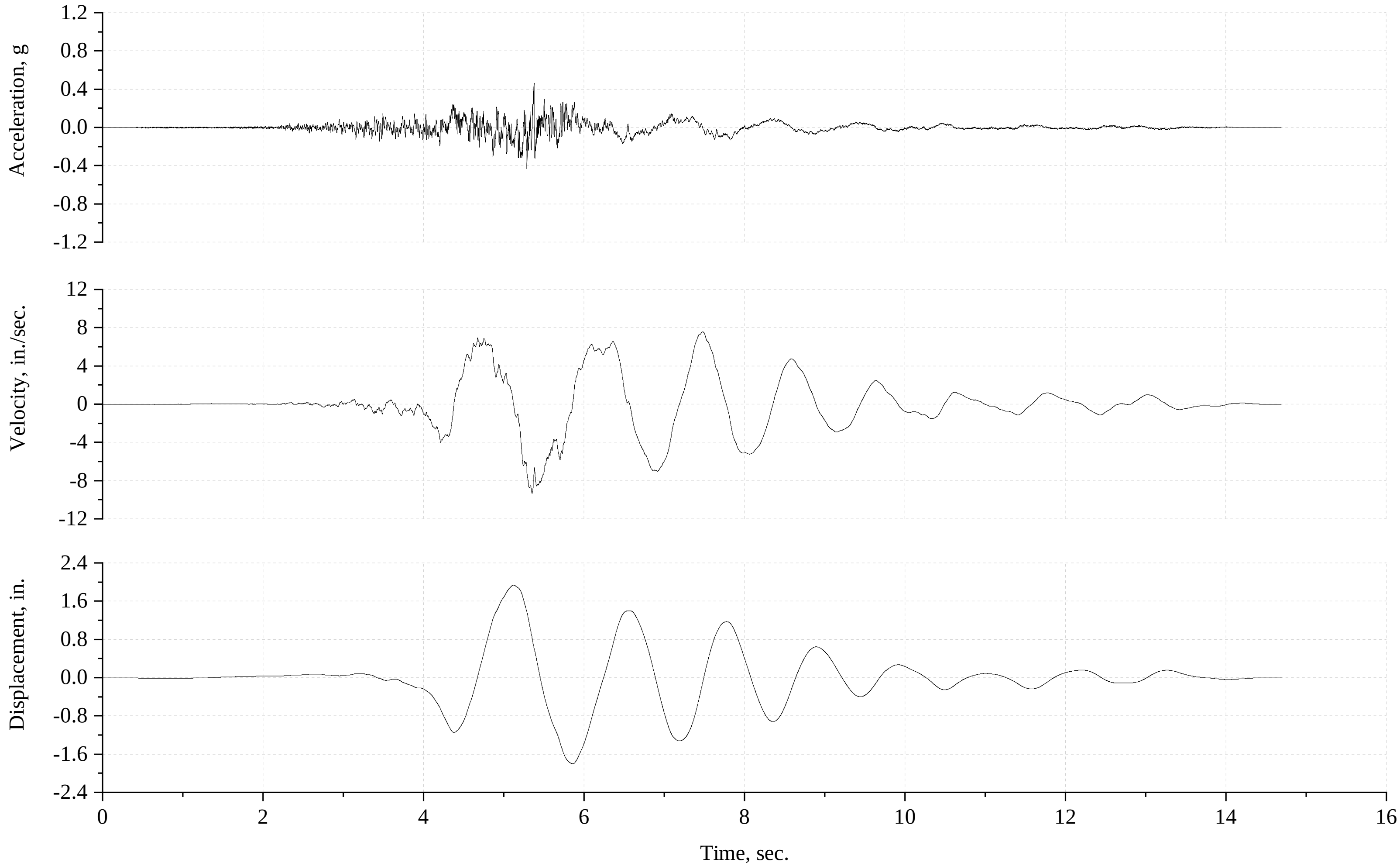

Figure 2-55: Target ground motion history of N27W component of scaled 2010 Darfield earthquake (RSN 6975) at 100% intensity

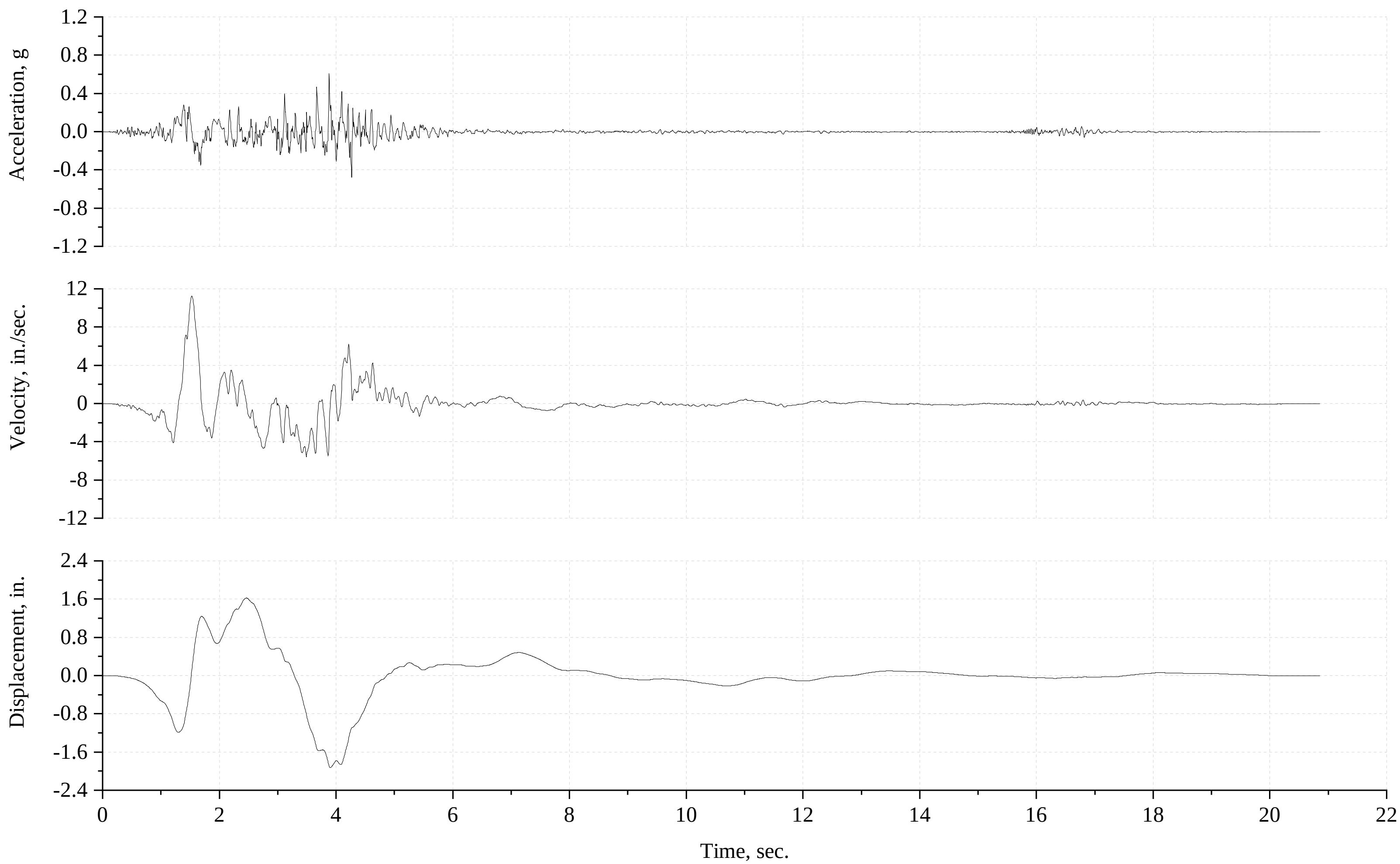

Figure 2-56: Target ground motion history of S16E component of scaled 1971 San Fernando earthquake (RSN 77) at 100% intensity

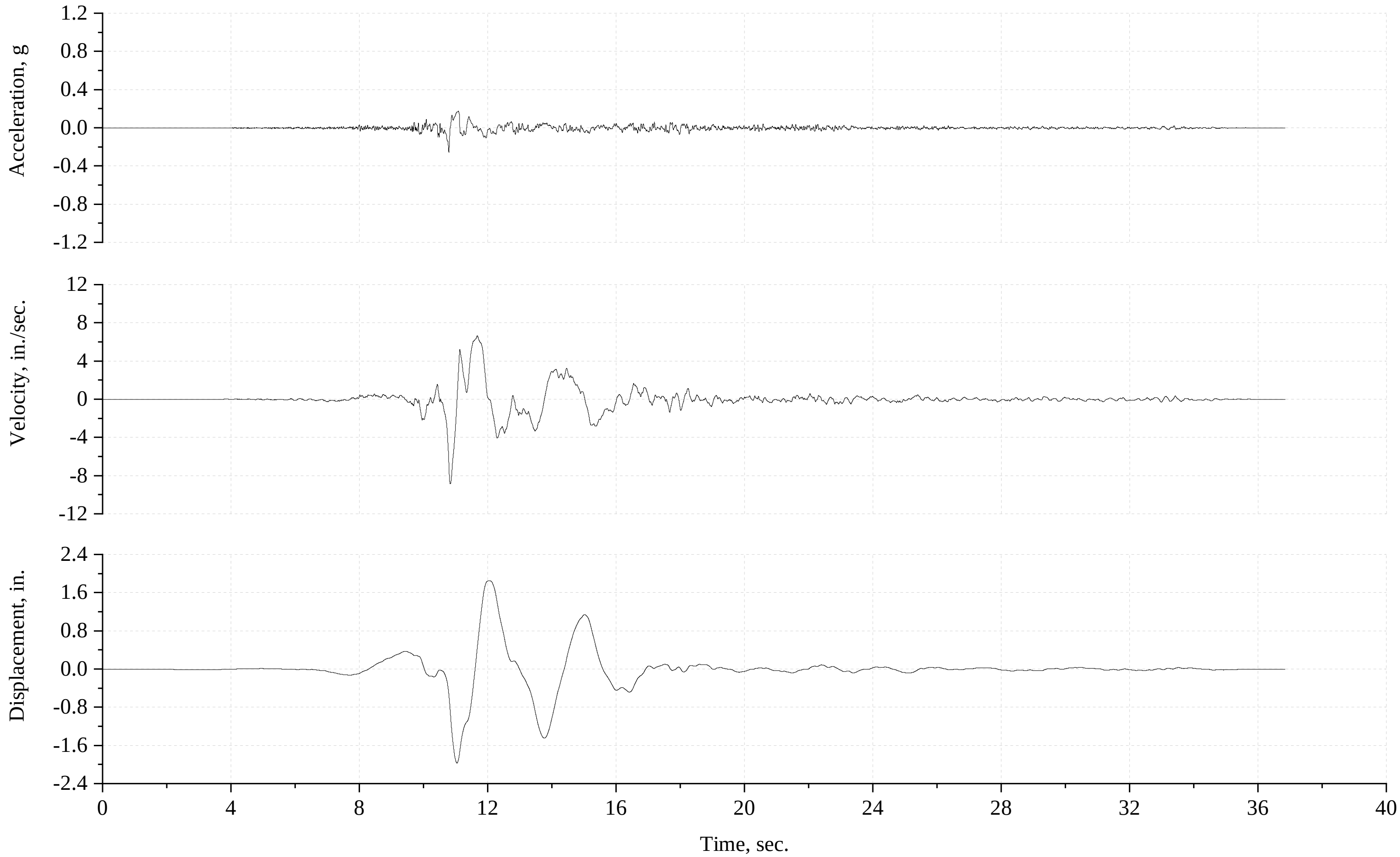

Figure 2-57: Target ground motion history of N43W component of scaled 2002 Denali earthquake (RSN 2114) at 100% intensity

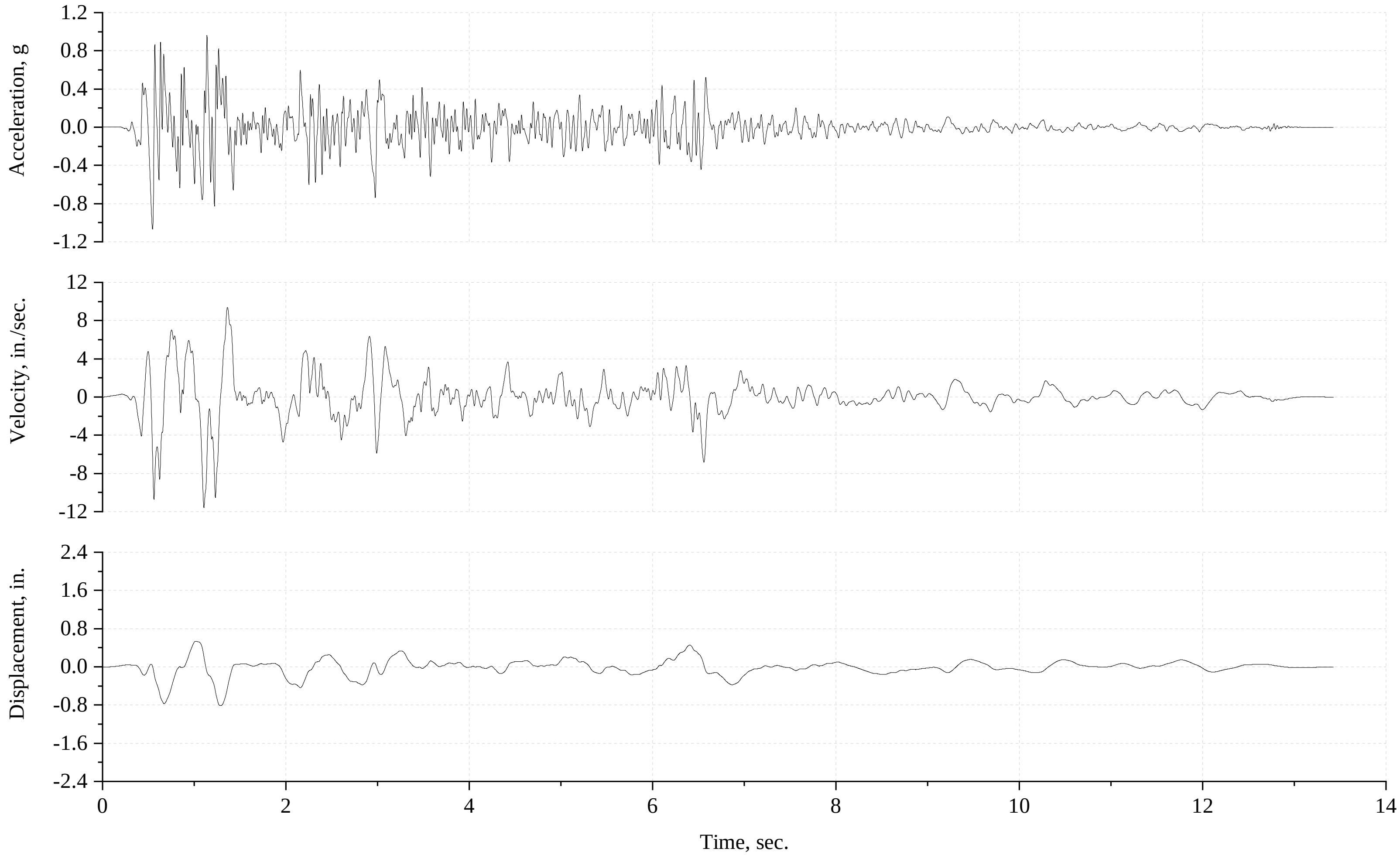

Figure 2-58: Target ground motion history of NS component of scaled 1940 El Centro earthquake (RSN 6 - TC4) at 100% intensity

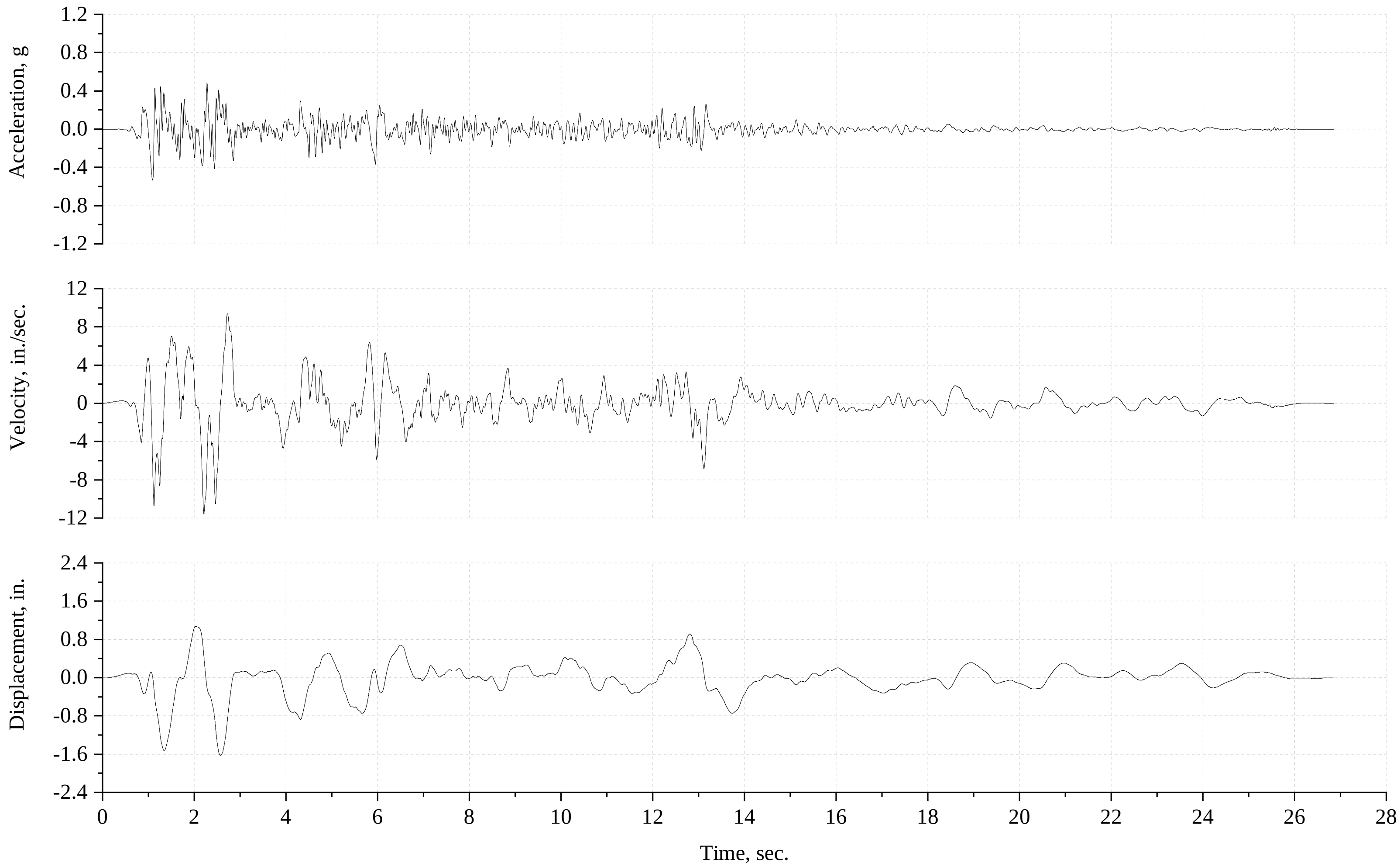

Figure 2-59: Target ground motion history of NS component of scaled 1940 El Centro earthquake (RSN 6 - TC2) at 100% intensity

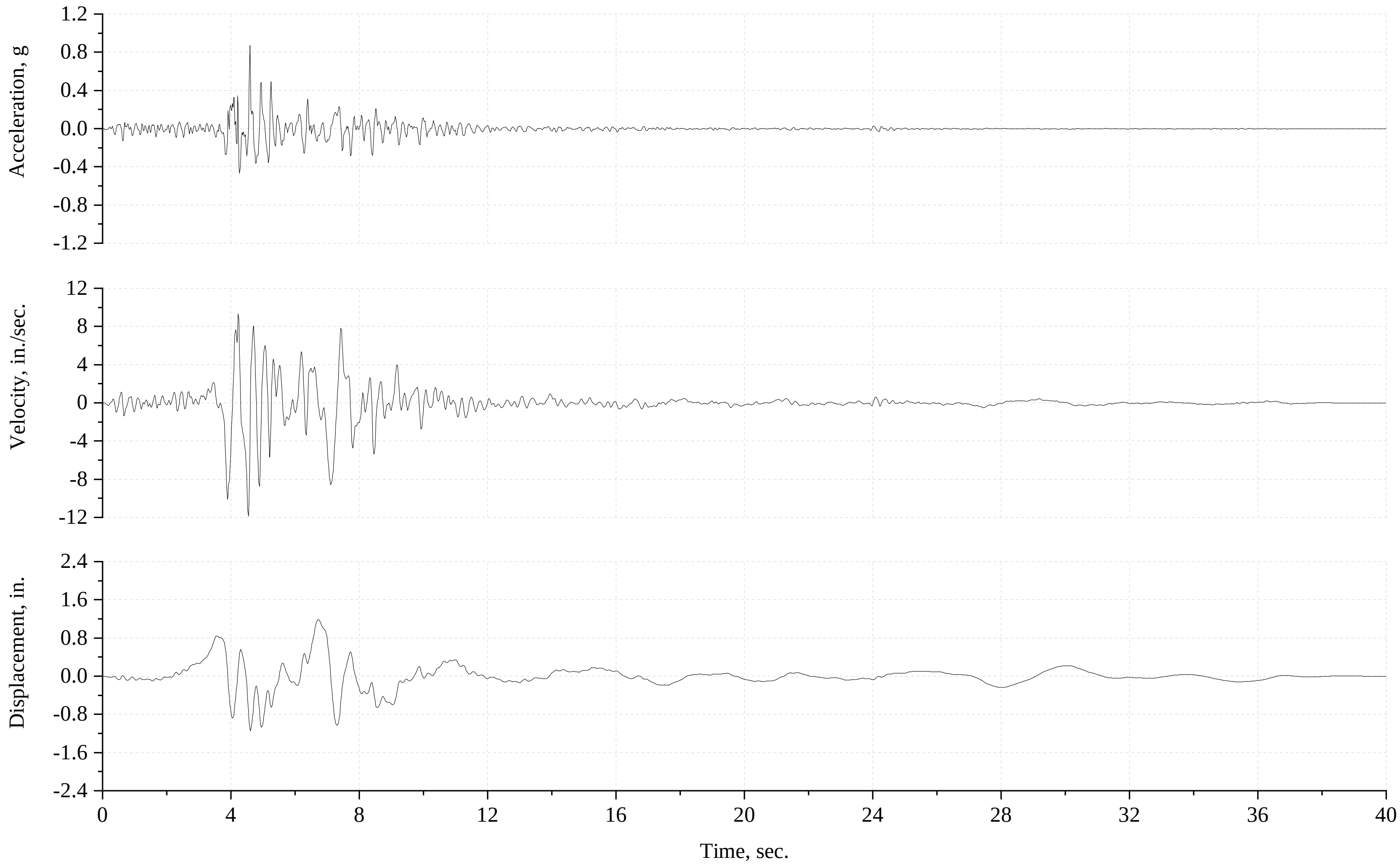

Figure 2-60: Target ground motion history of S76E component of scaled 1994 Northridge earthquake (RSN 1051) at 100% intensity

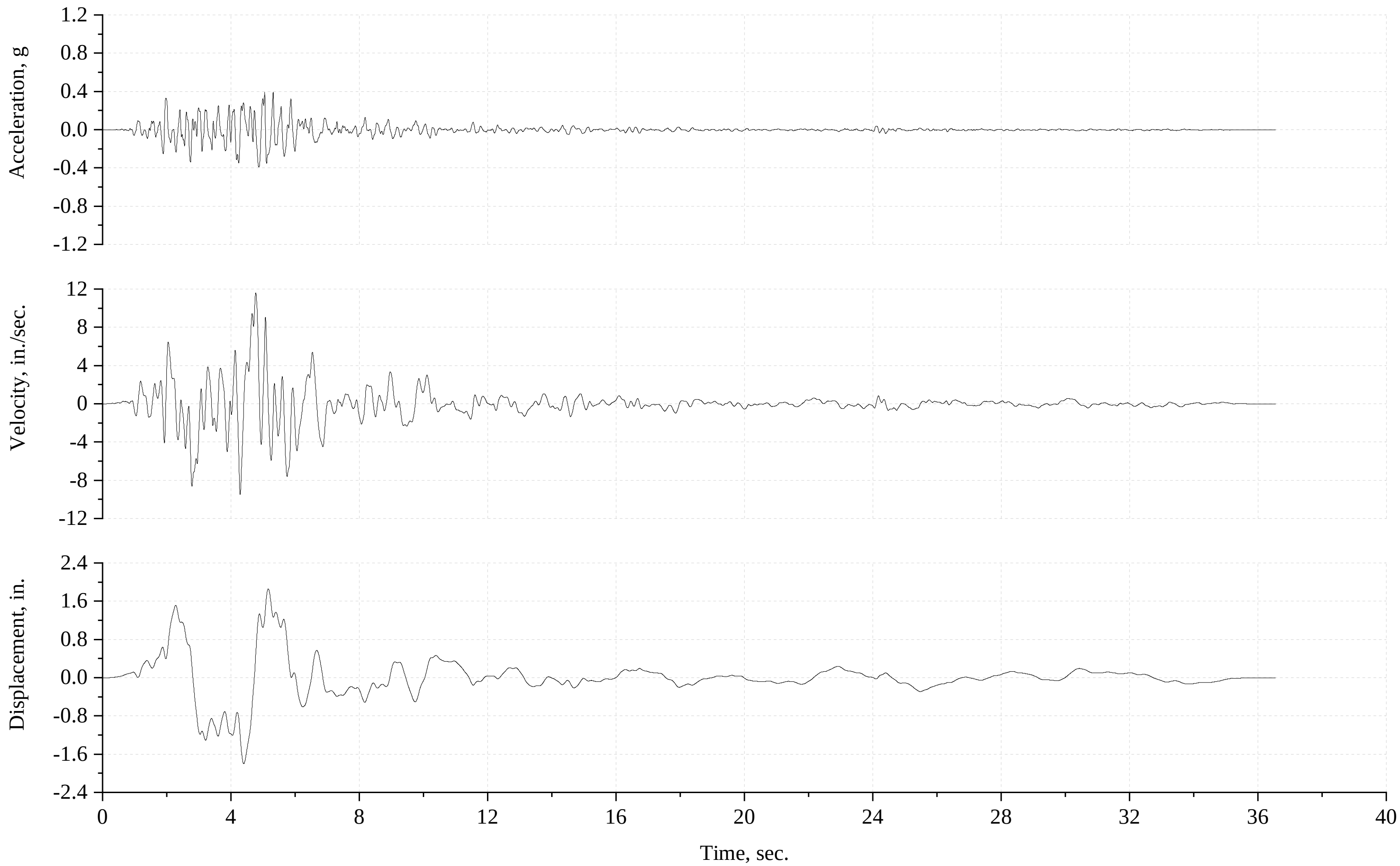

Figure 2-61: Target ground motion history of NS component of scaled 1972 Managua earthquake (RSN 95) at 100% intensity

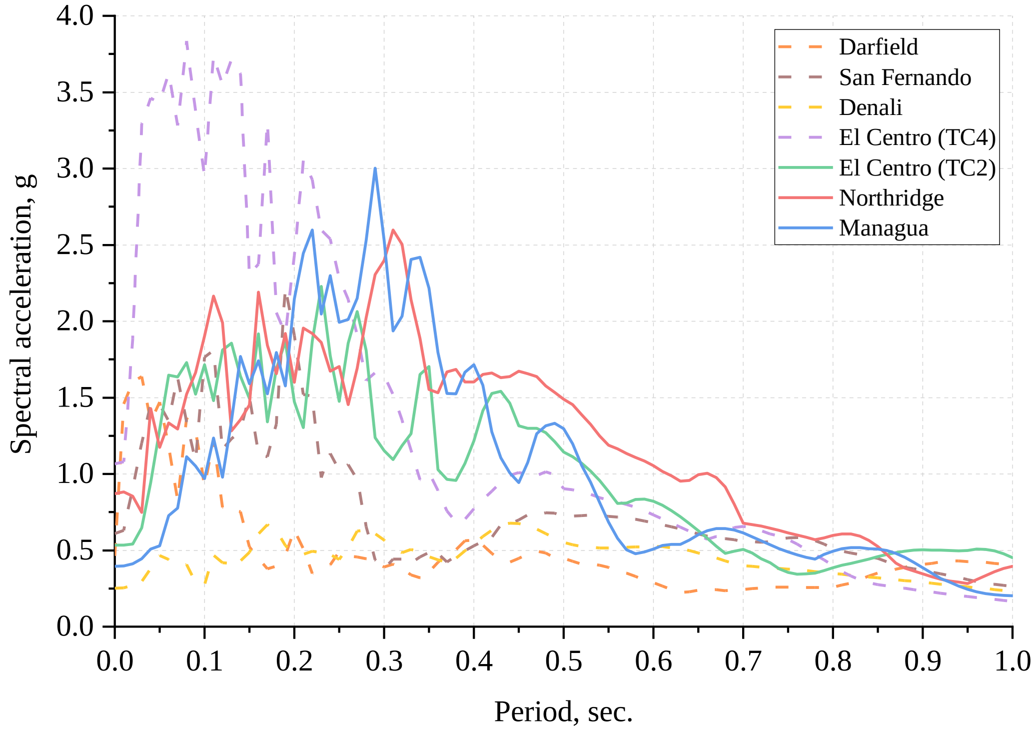

Figure 2-62: Target acceleration spectra (2% damping) at 100% intensities

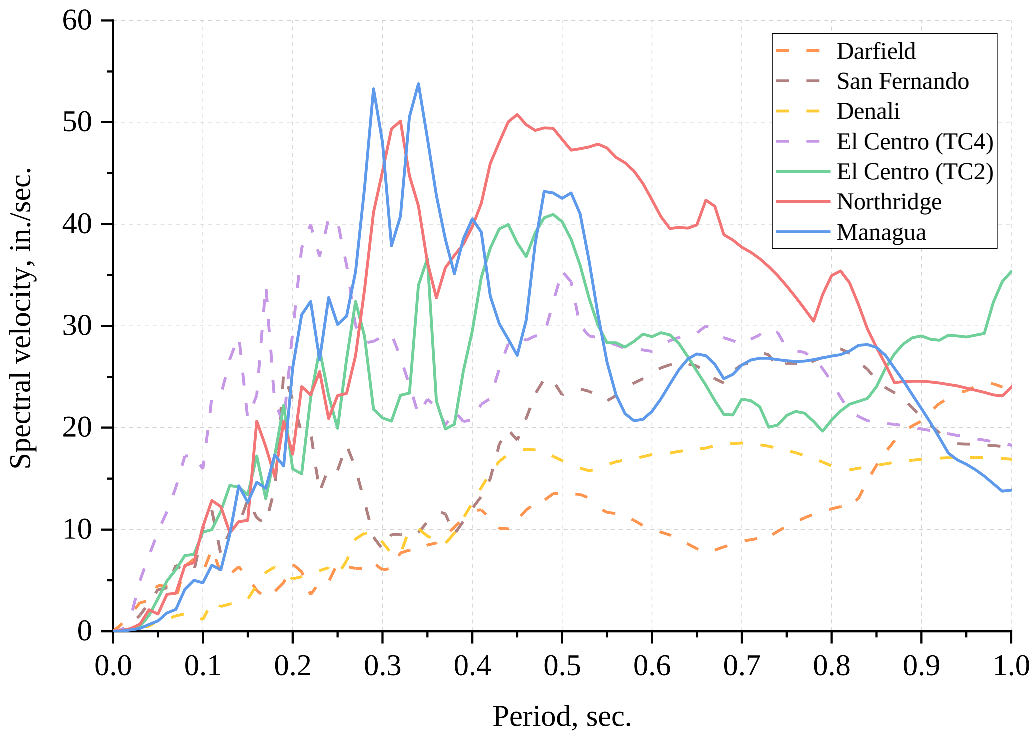

Figure 2-63: Target velocity spectra (2% damping) at 100% intensities

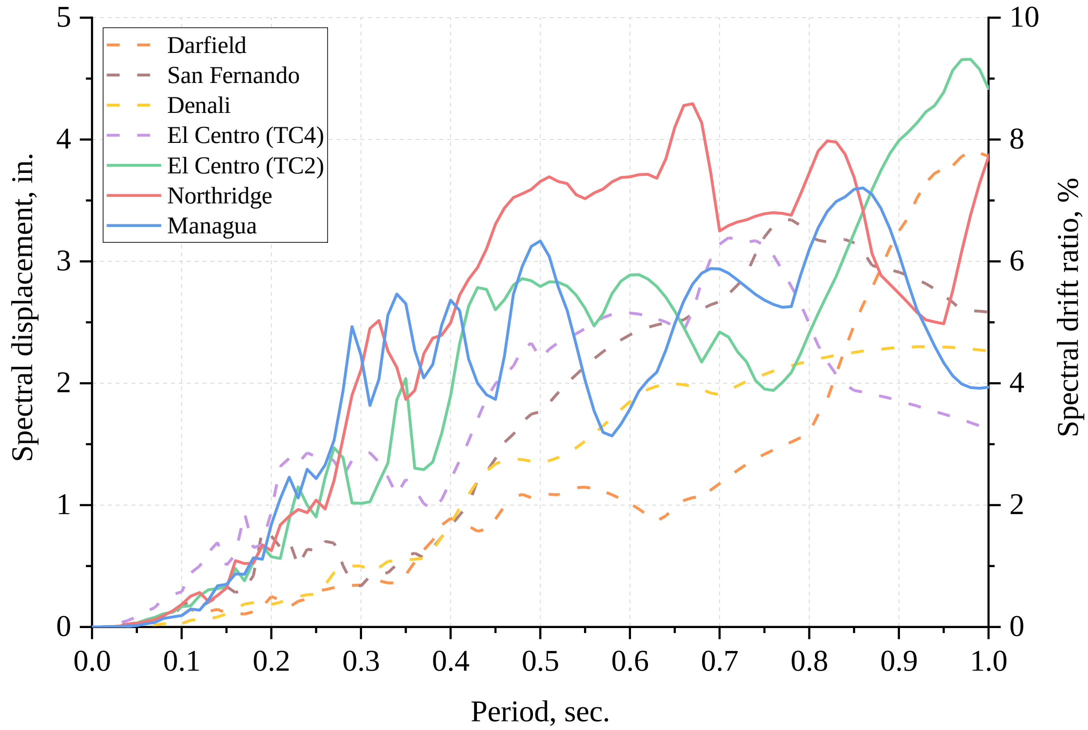

Figure 2-64: Target displacement spectra (2% damping) at 100% intensities

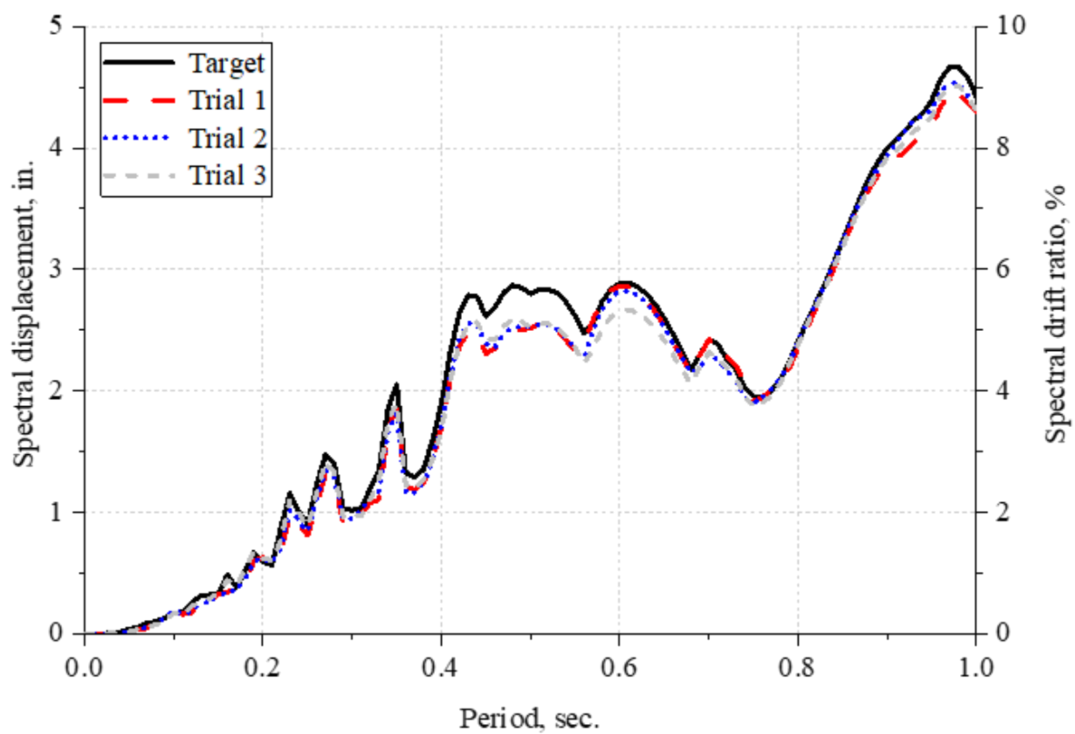

Figure 2-65: Target vs. measured displacement spectra (2% damping) calculated from measured base acceleration histories of 100% intensities of El Centro (TC2) motion

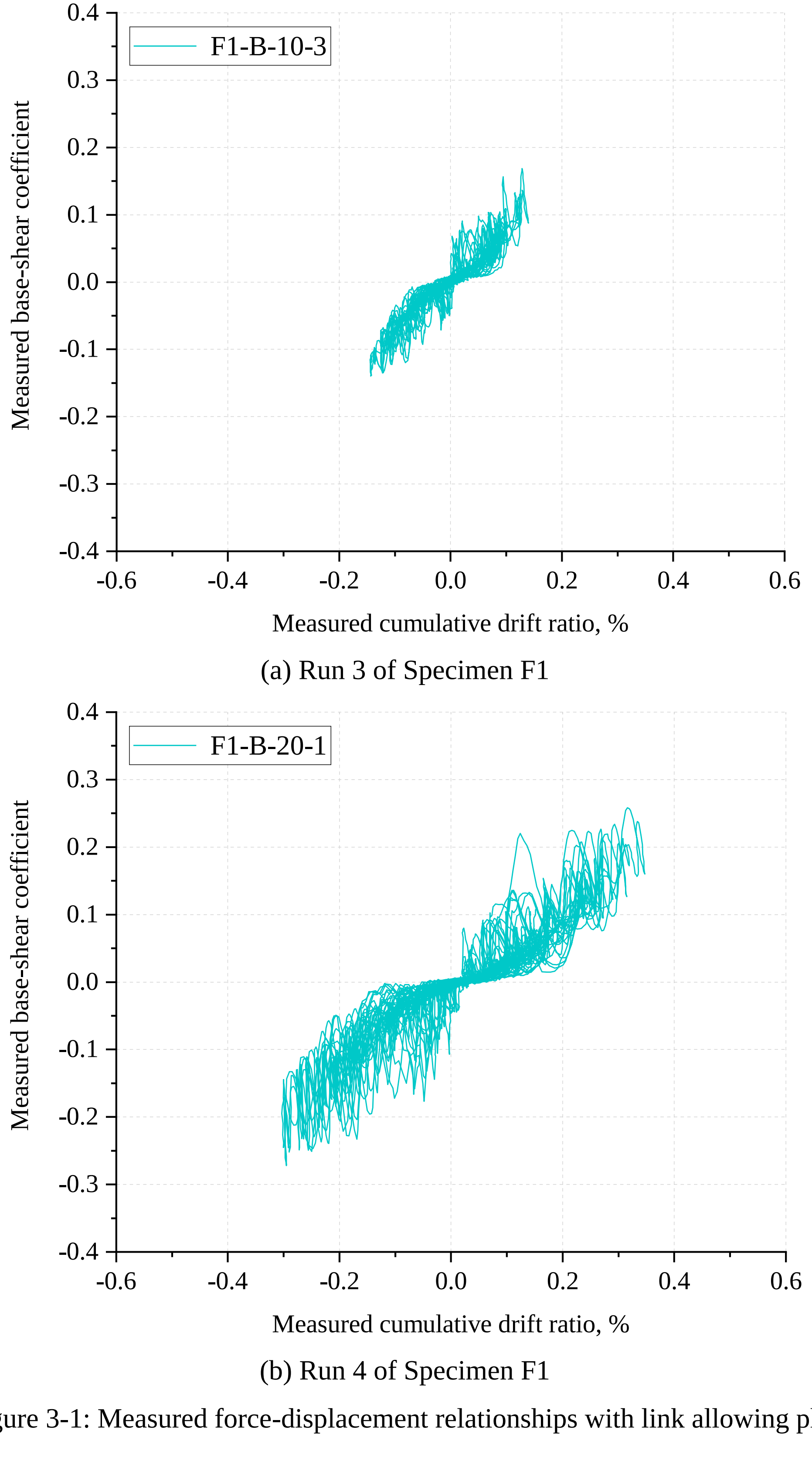

(a) Run 3 of Specimen F1

(b) Run 4 of Specimen F1

Figure 3-1: Measured force-displacement relationships with link allowing play

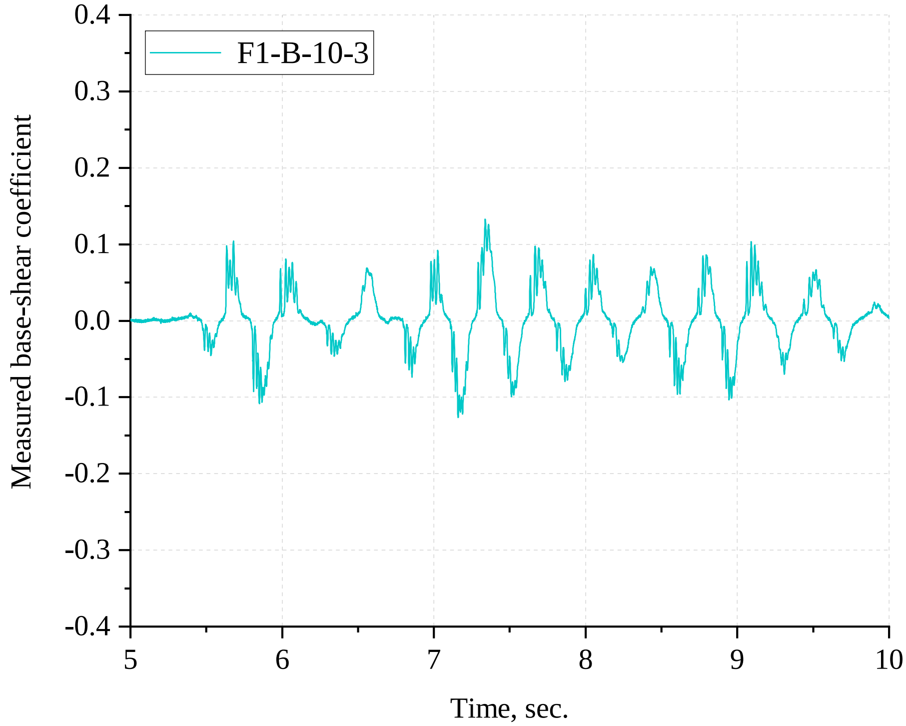

(a) Run 3 of Specimen F1

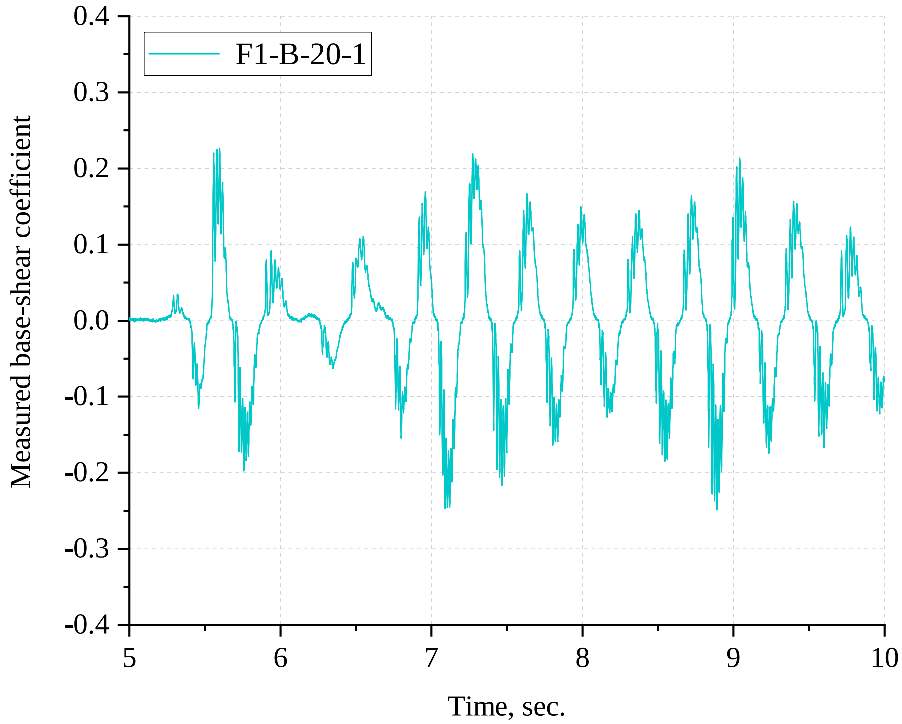

(b) Run 4 of Specimen F1

Figure 3-2: Measured lateral load histories with link allowing play

(a) Two-swivel link allowing play

(b) Two-swivel link reducing play

Figure 3-3: Test setup of bare frame (Series F1-B)

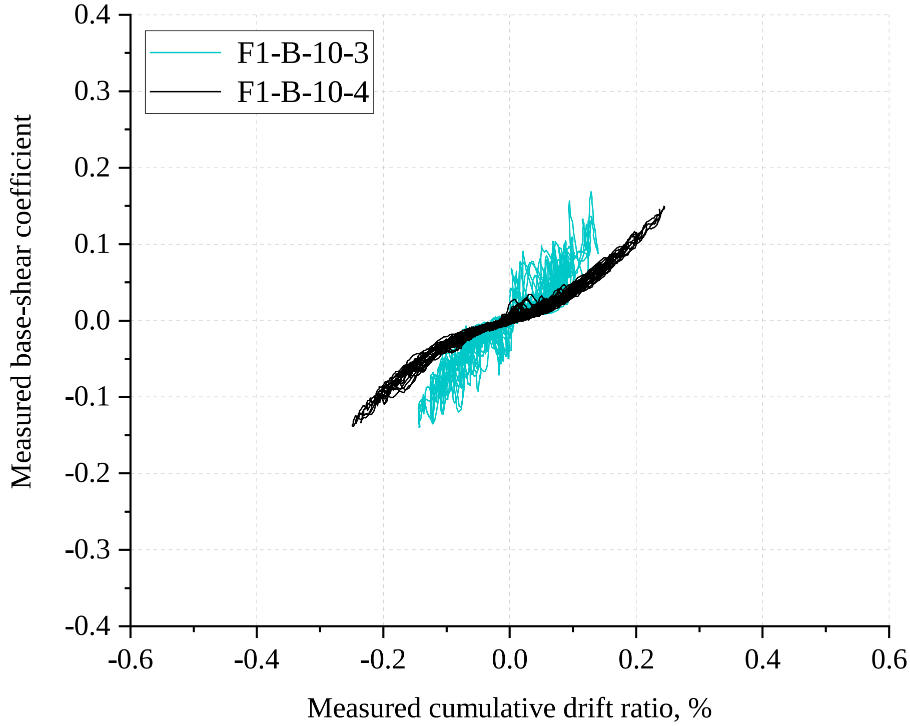

(a) Runs with intensities of 10%

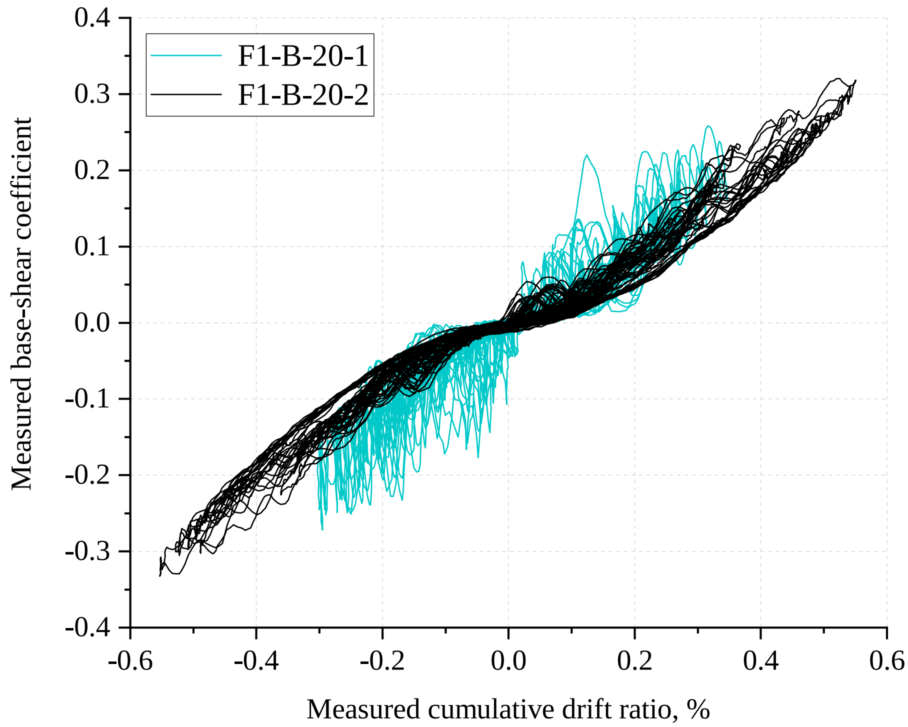

(b) Runs with intensities of 20%

Figure 3-4: Comparisons of force-displacement relationships in Series F1-B

Note: Curves labeled with teal lines indicate response of specimen with link allowing play.

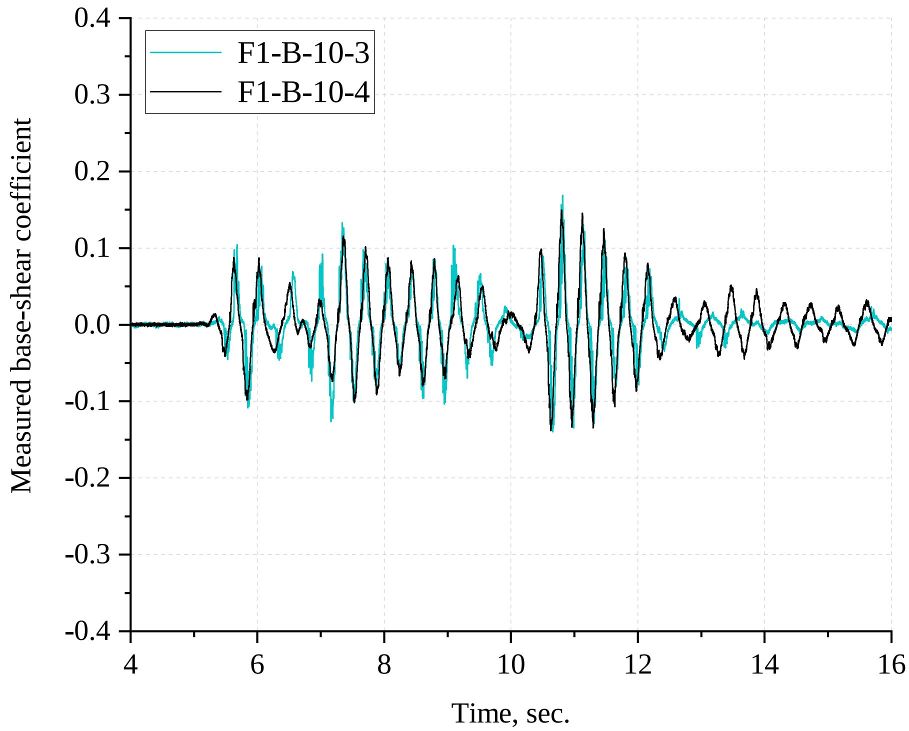

(a) Runs with intensities of 10%

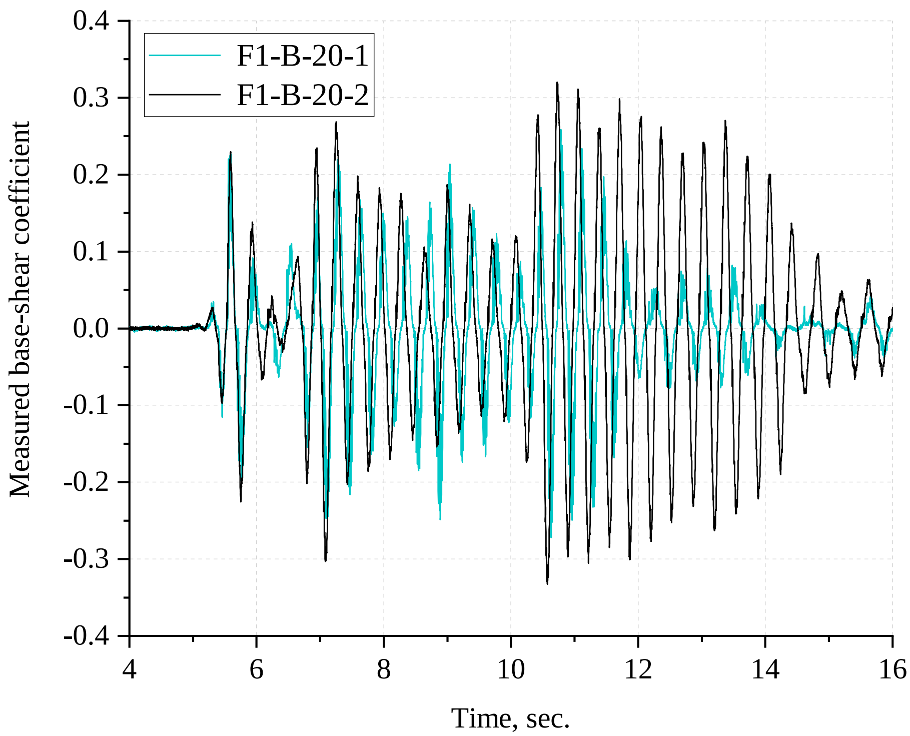

(b) Runs with intensities of 20%

Figure 3-5: Comparisons of target and measured displacement spectra in Series F1-B

Note: Curves labeled with teal lines indicate response of specimen with link allowing play.

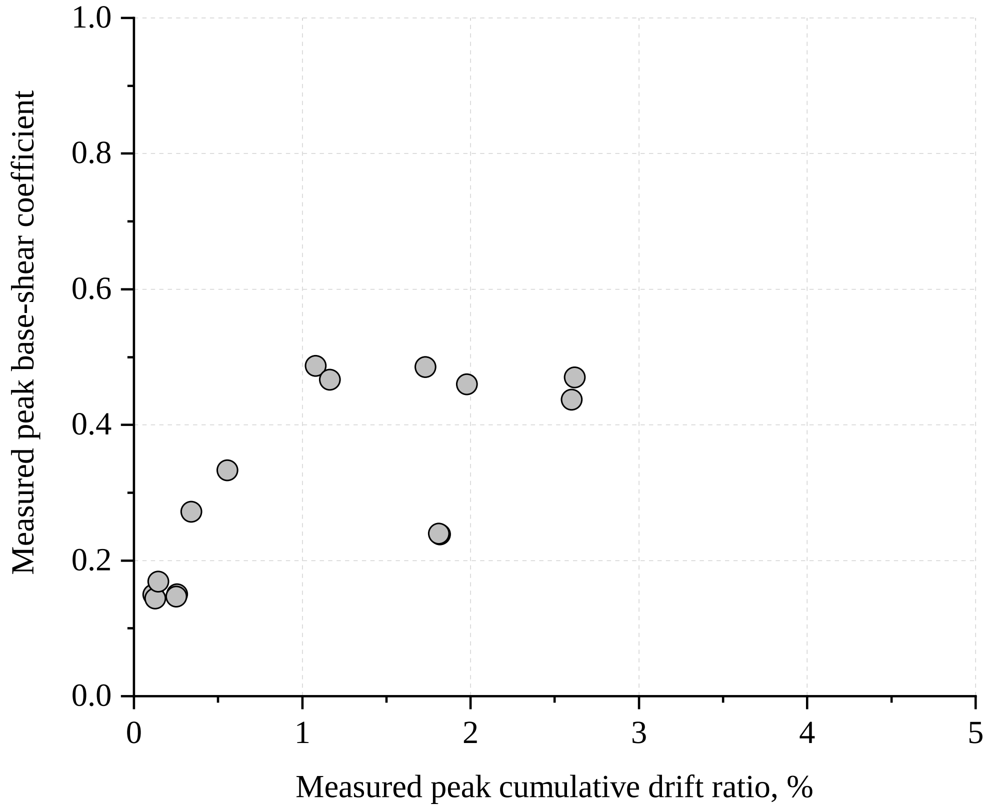

Figure 3-6: Force-displacement relationship of bare frame (Series F1-B)

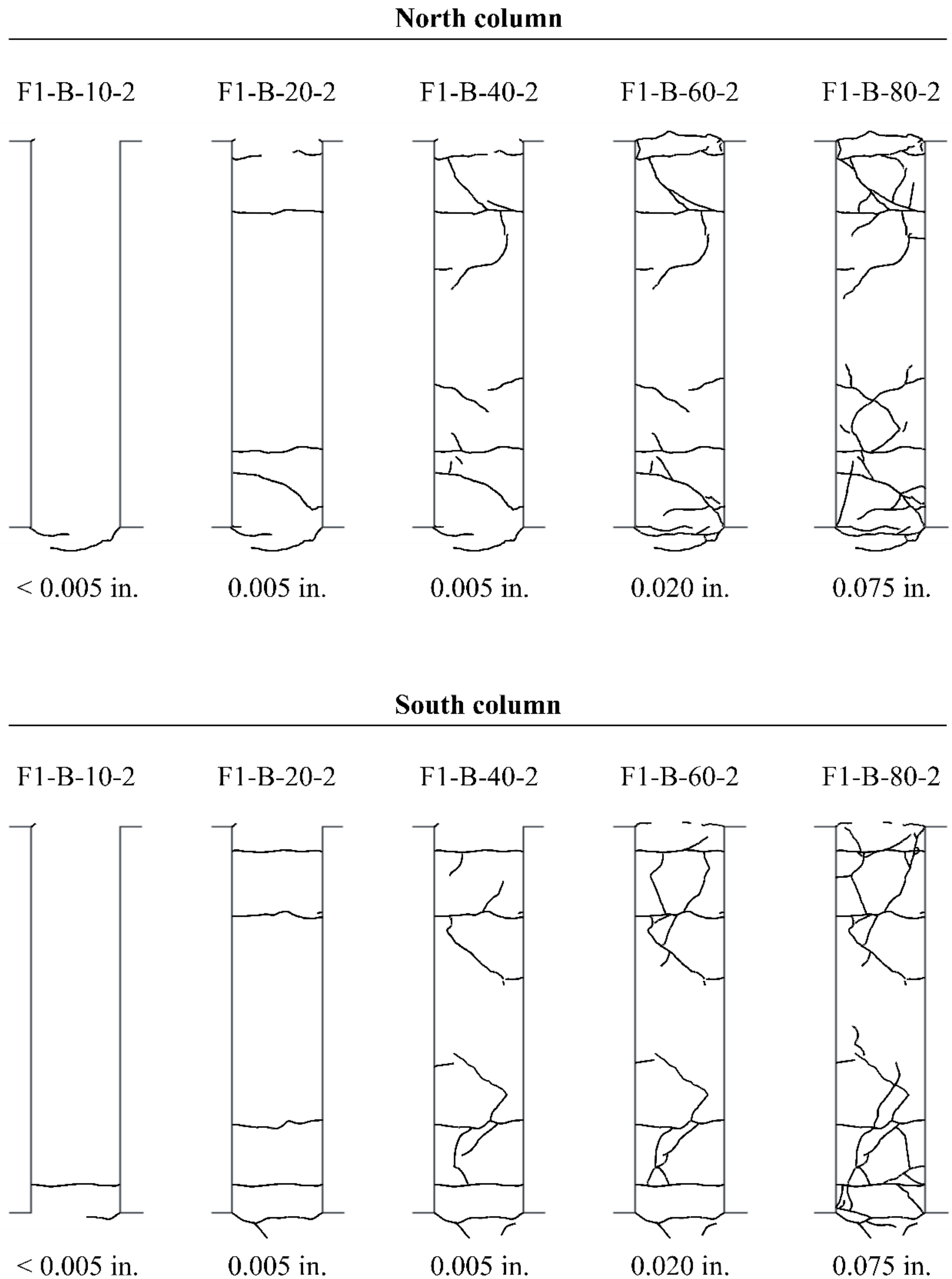

Figure 3-7: Crack maps of east face of columns in bare frame (Series F1-B)

Note: Values below crack maps are maximum permanent crack widths measured after the indicated runs.

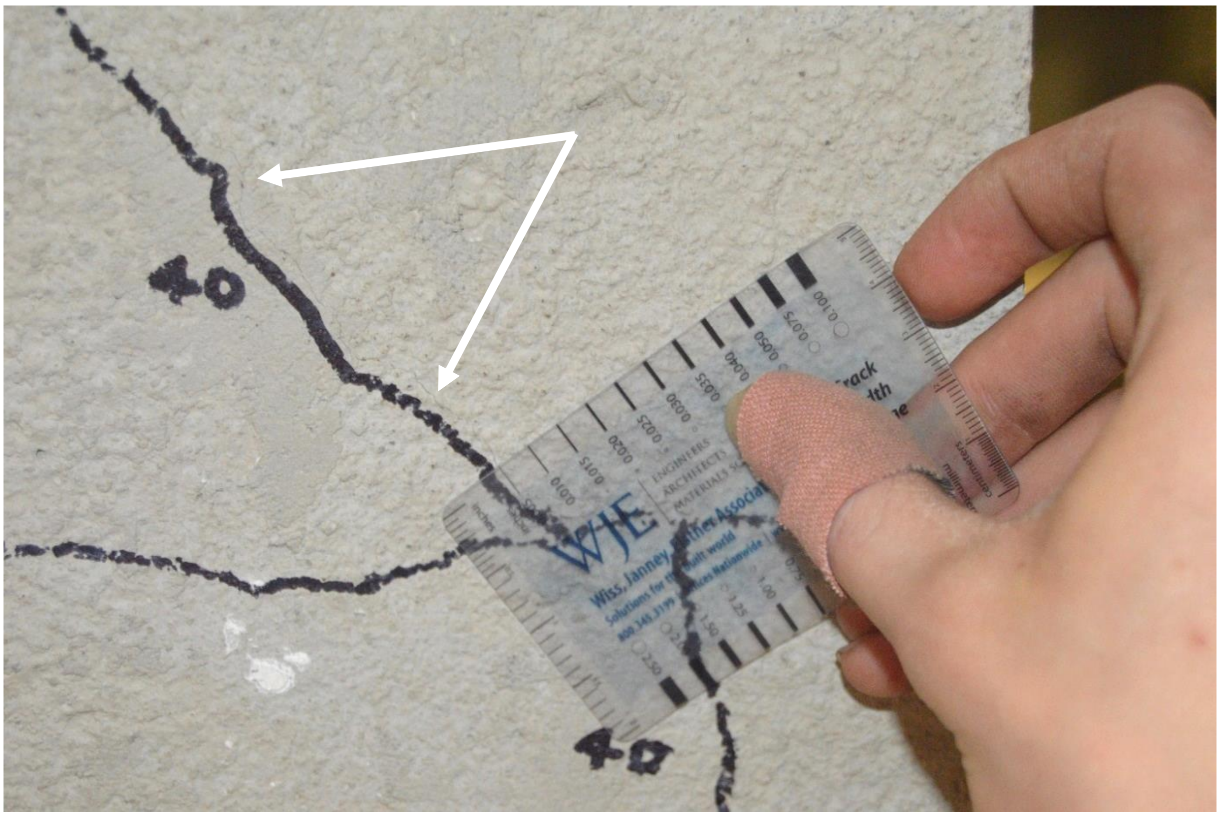

Figure 3-8: Inclined cracks observed after F1-B-40-1 (Run 8 of Specimen F1)

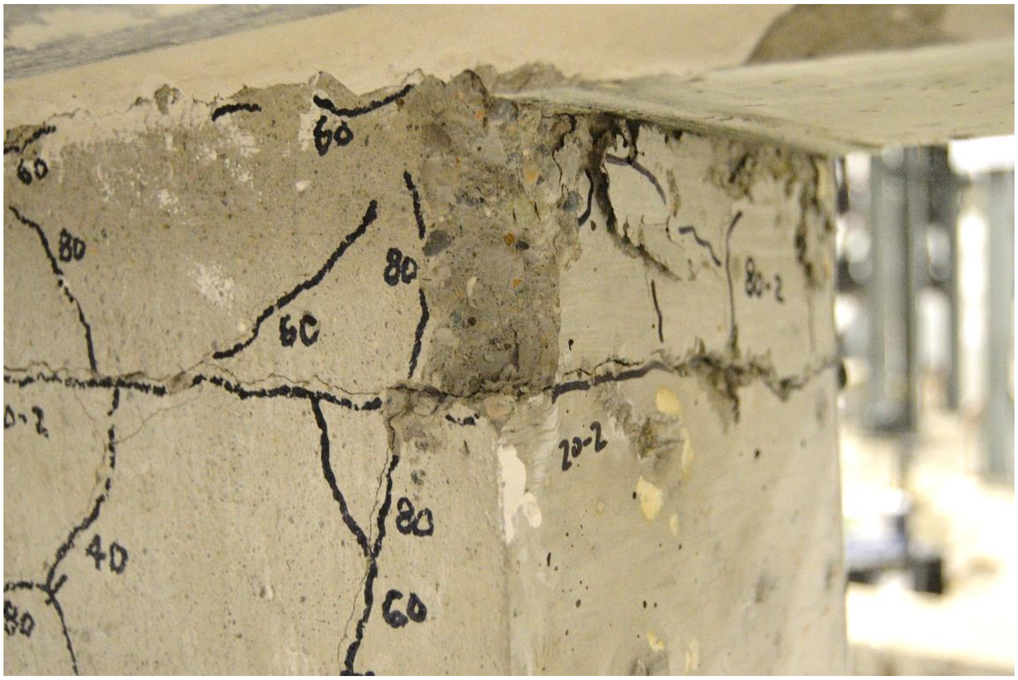

(a) South column

(b) North column

Figure 3-9: Concrete spalling at end of Series F1-B at tops of columns

(a) End of Series F1-B

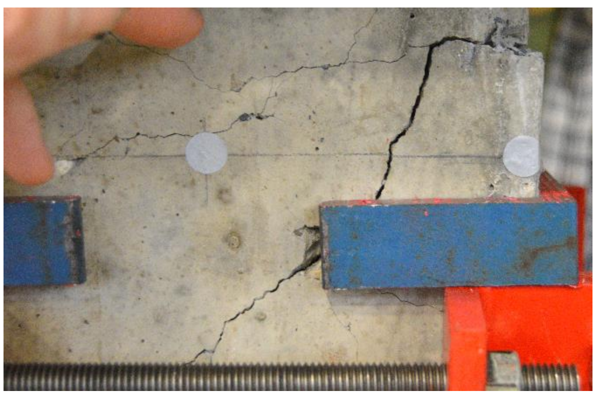

(b) Before installation of final clamp

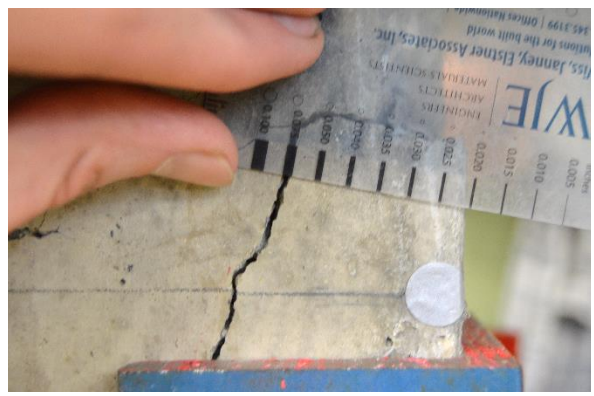

(c) Crack width = 0.075 in.

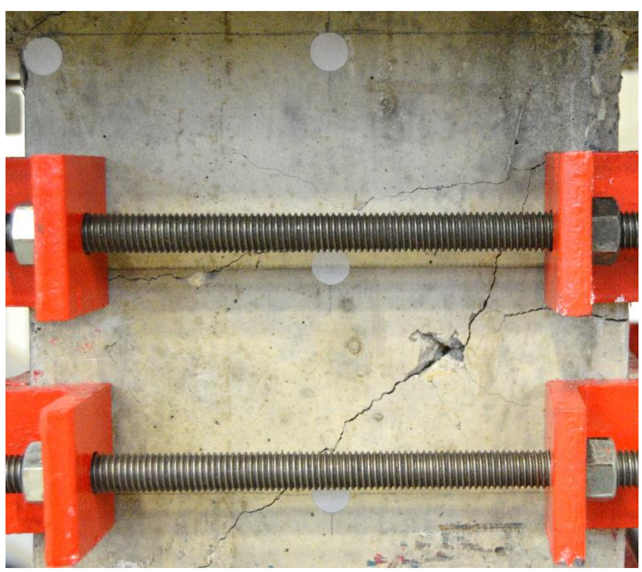

(d) After installation of final clamp (crack width = 0.010 in.)

Figure 3-10: Installation of clamps at top of north column

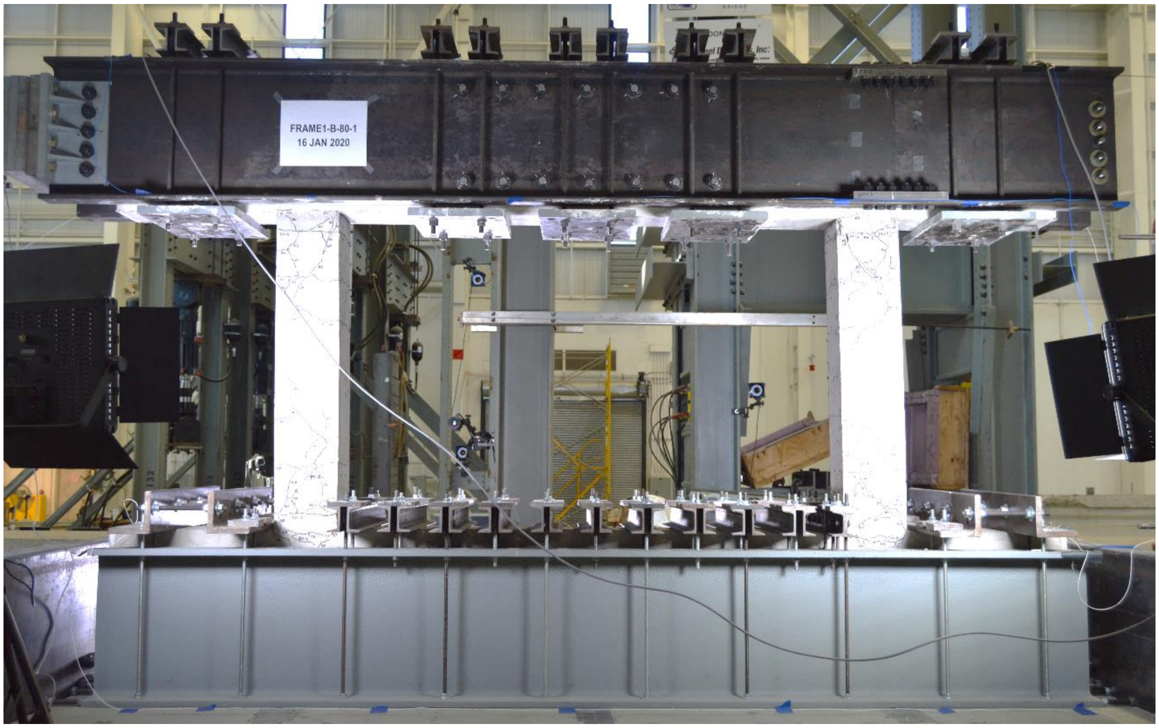

(a) Bare frame before installation of clamps (Series F1-B)

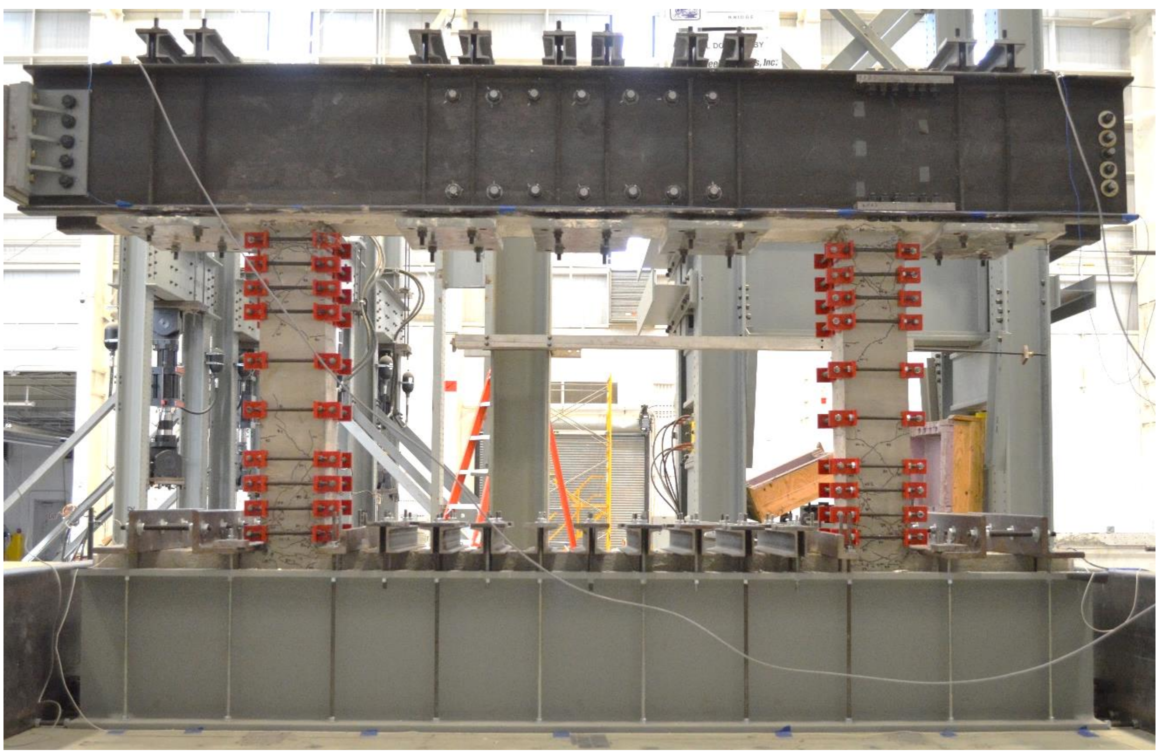

(b) Frame with clamps after installation of clamps (Series F1-C)

Figure 3-11: Elevations of bare frame and frame with clamps

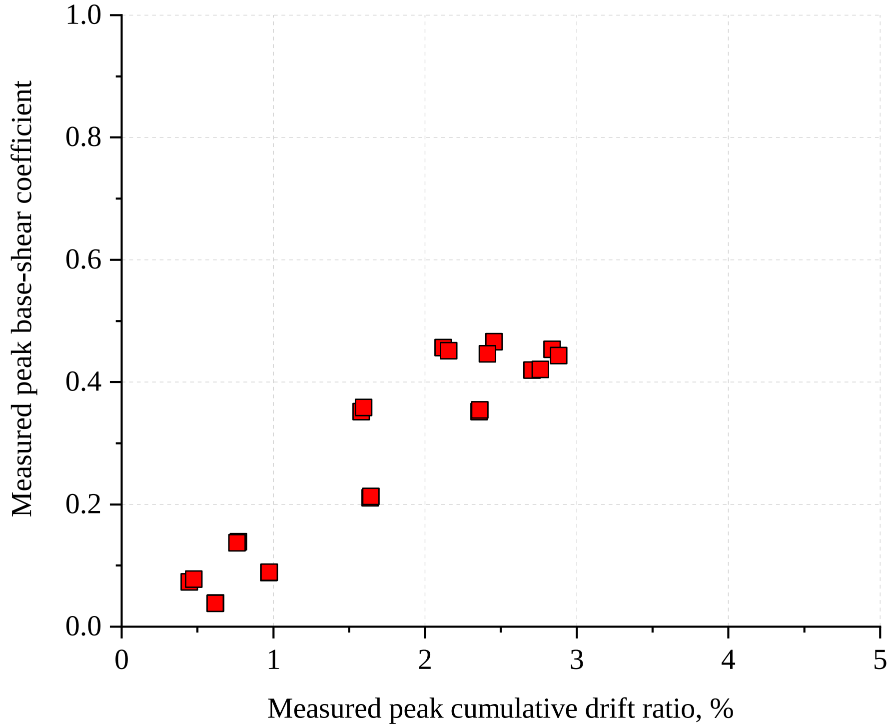

(a) Frame with clamps (Series F1-C)

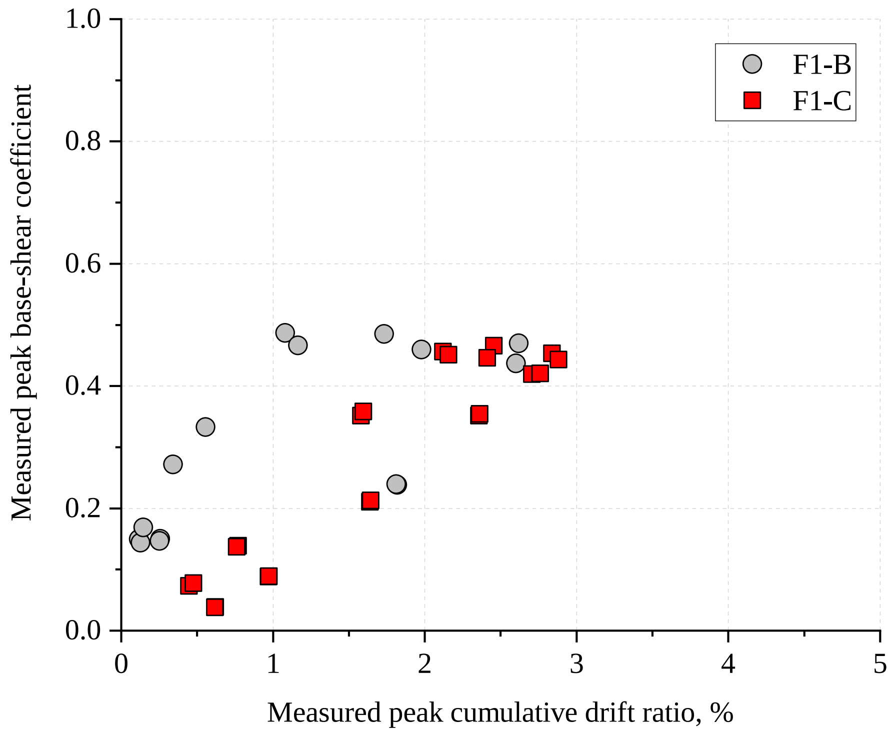

(b) Bare frame and frame with clamps

Figure 3-12: Force-displacement relationship of Series F1-C

North column

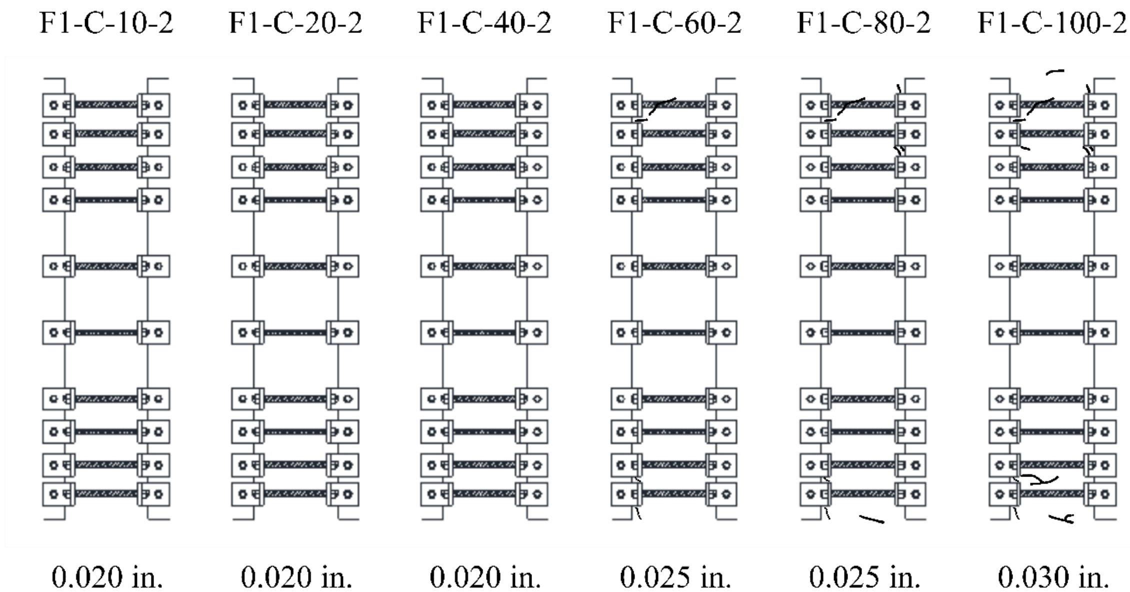

South column

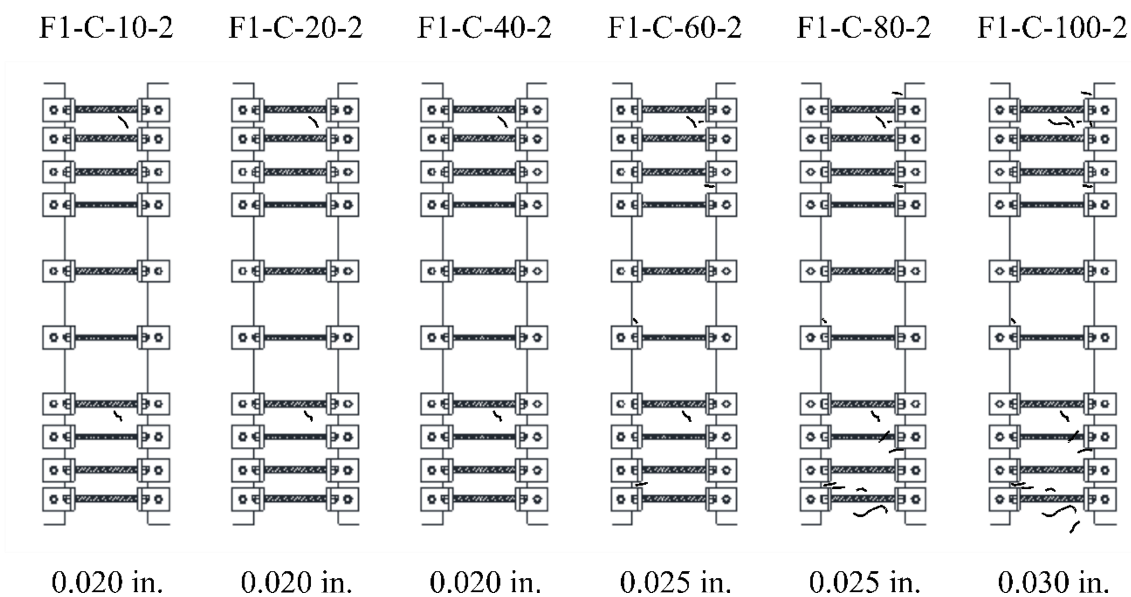

Figure 3-13: Crack maps of east face of columns in frame with clamps (Series F1-C)

Note: Values below crack maps are maximum permanent crack widths measured after the indicated runs

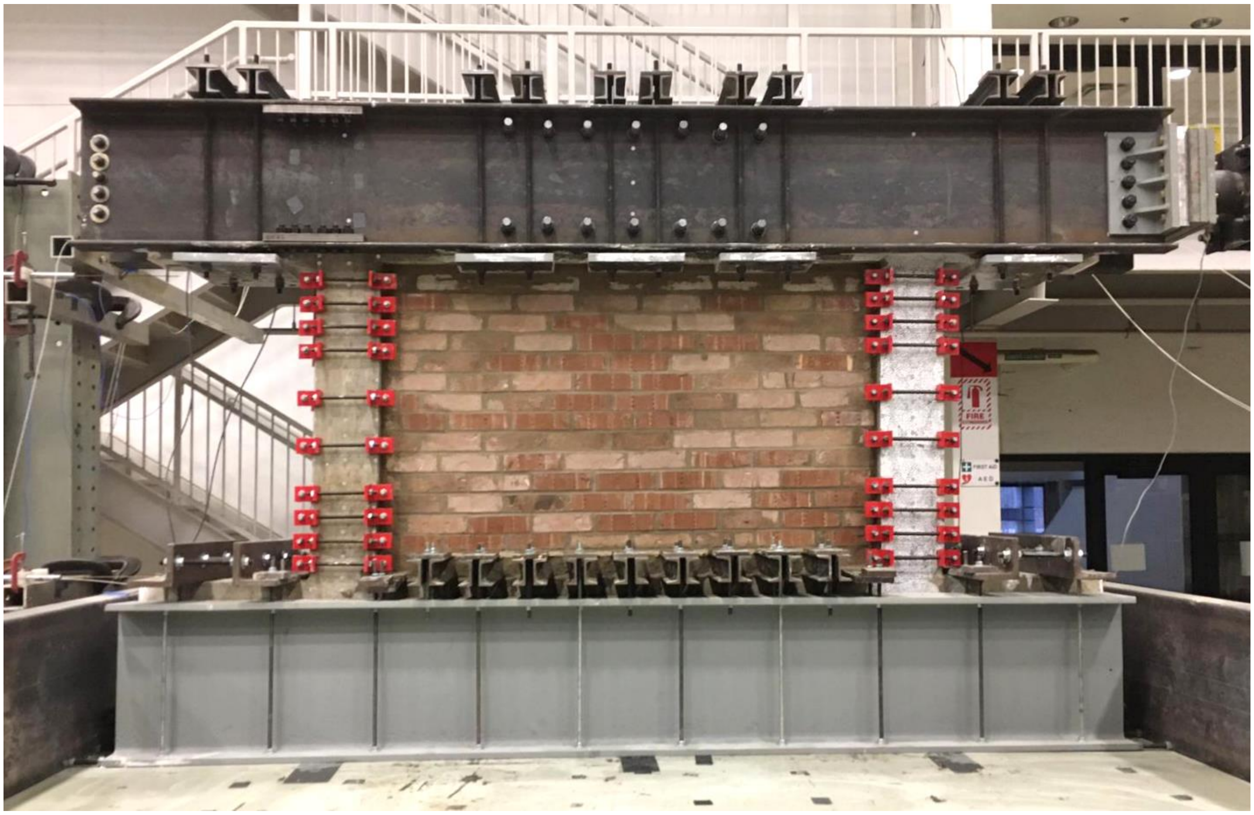

Figure 3-14: Elevation of infilled frame with clamps (Series F1-M-C)

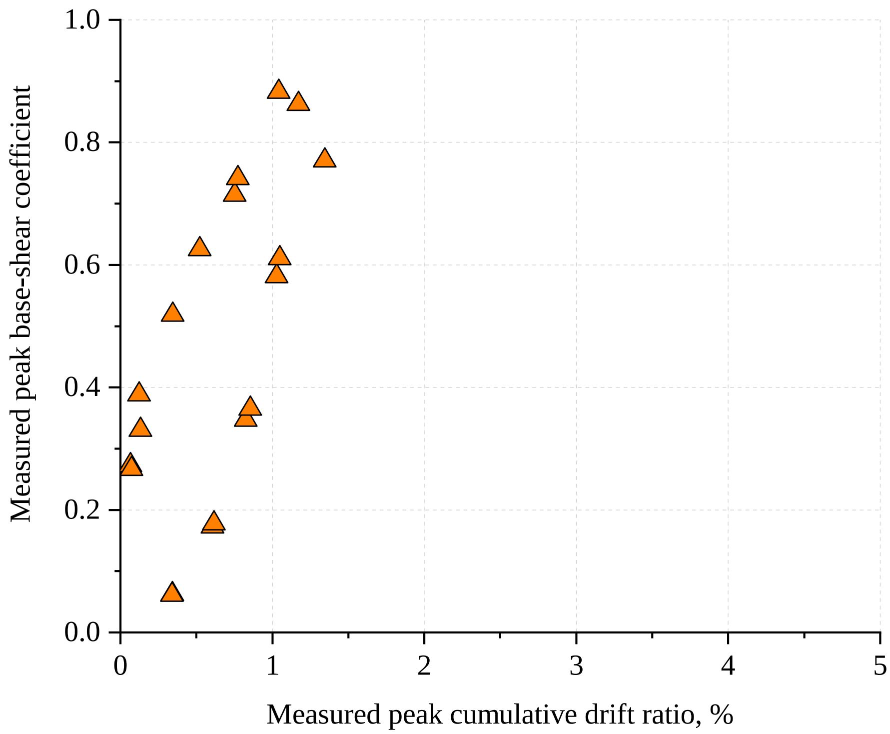

(a) Infilled frame with clamps (Series F1-M-C)

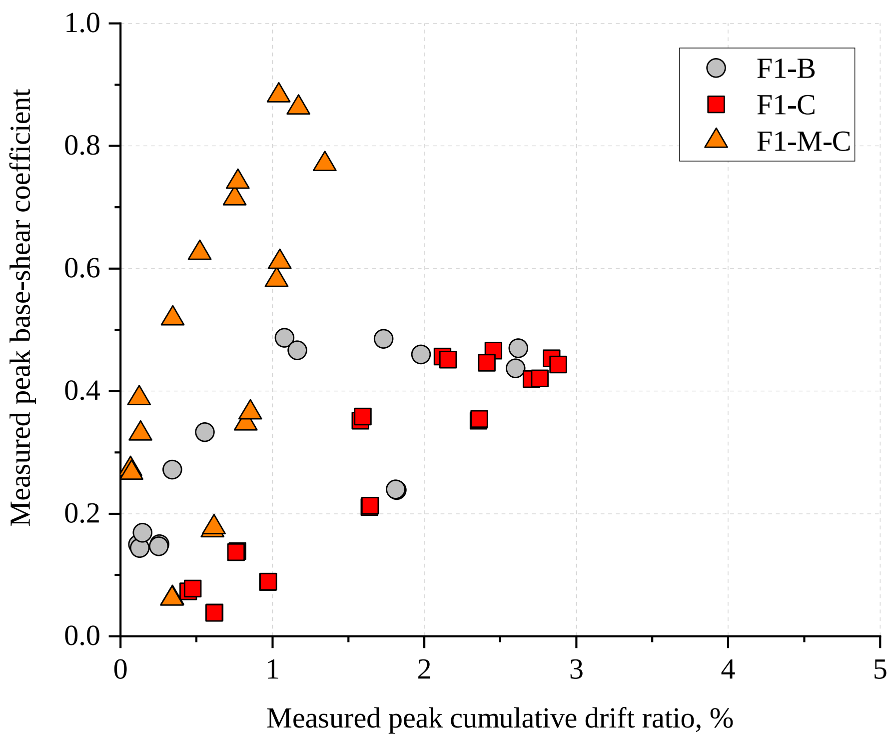

(b) Bare frame, frame with clamps, and infilled frame with clamps

Figure 3-15: Force-displacement relationship of Series F1-M-C

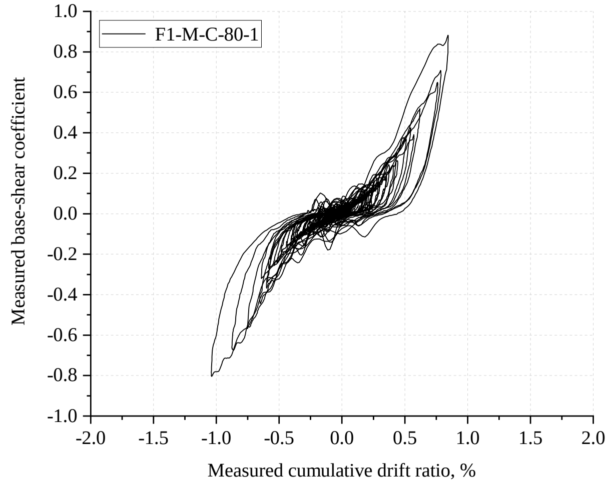

(a) Run 46 of Specimen F1 (F1-M-C-80-1)

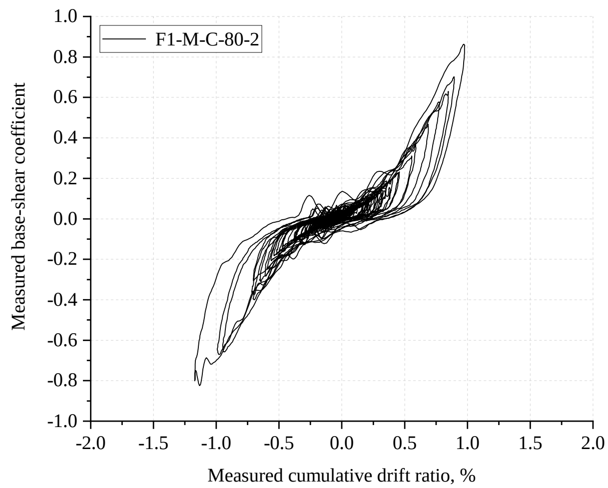

(b) Run 47 of Specimen F1 (F1-M-C-80-2)

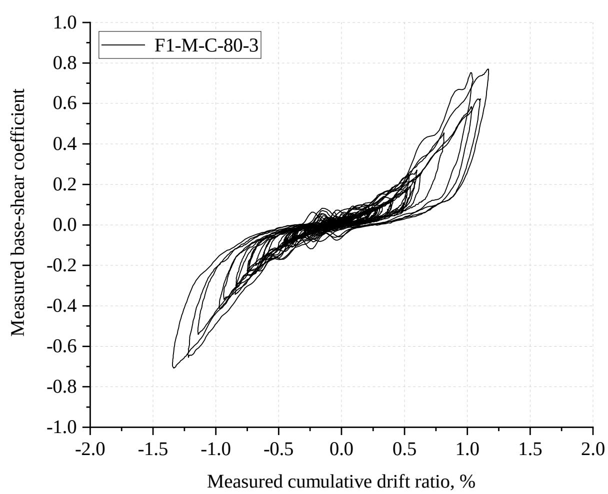

(c) Run 56 of Specimen F1 (F1-M-C-80-3)

Figure 3-16: Force-displacement histories measured in runs at 80% intensity of Series F1-M-C

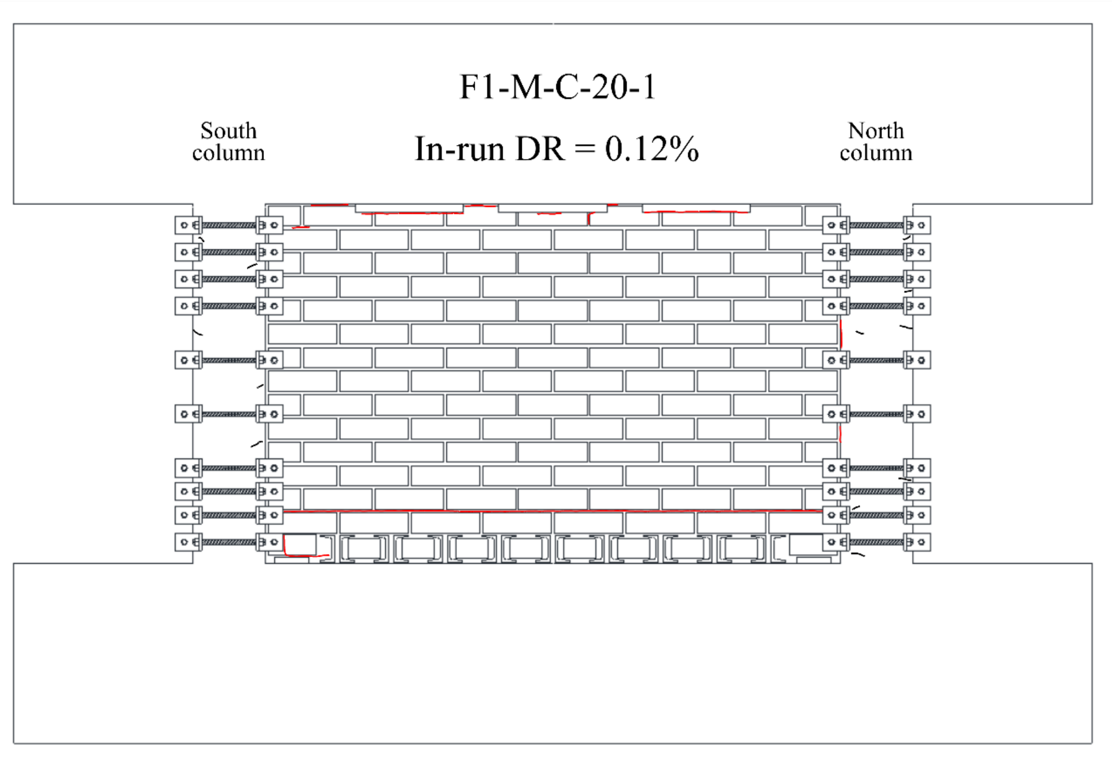

Figure 3-17: Crack map after Run 40 of Specimen F1

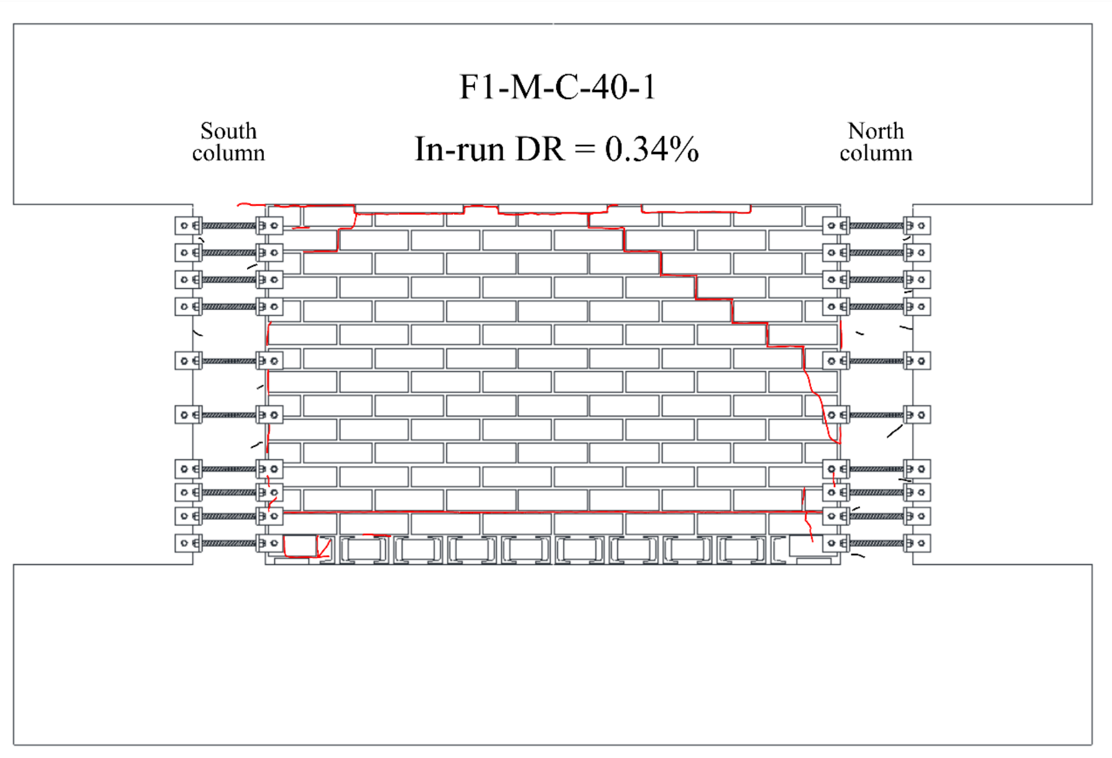

Figure 3-18: Crack map after Run 42 of Specimen F1

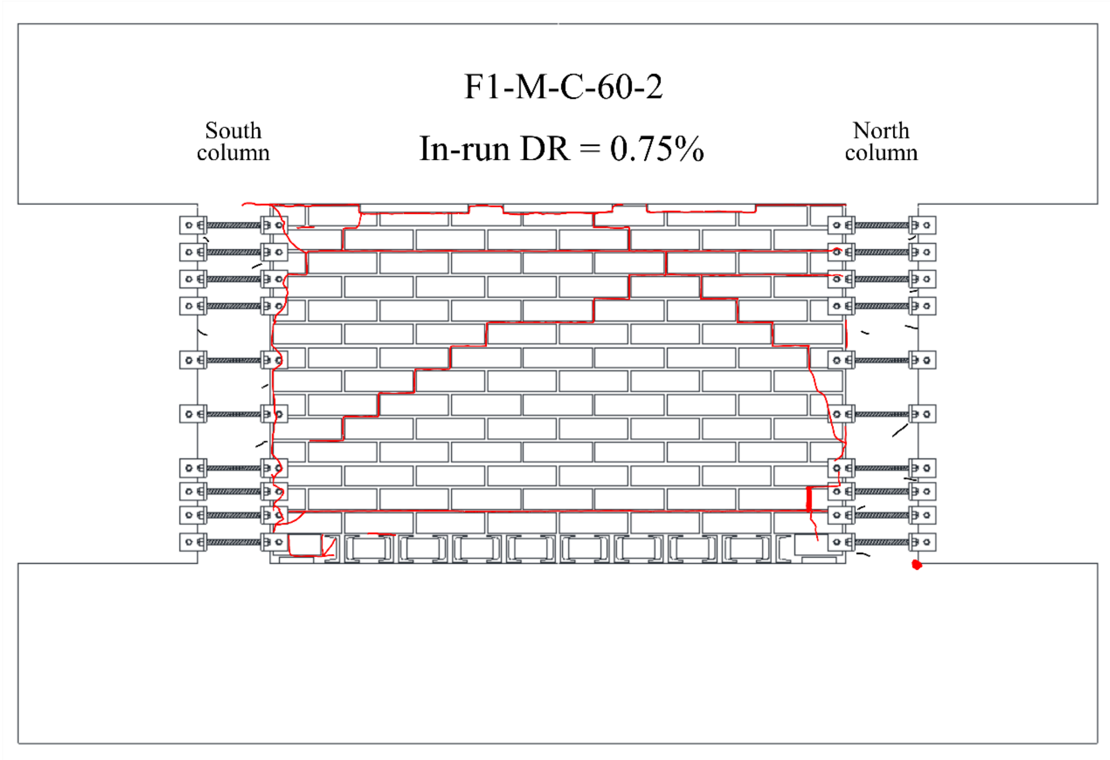

Figure 3-19: Crack map after Run 45 of Specimen F1

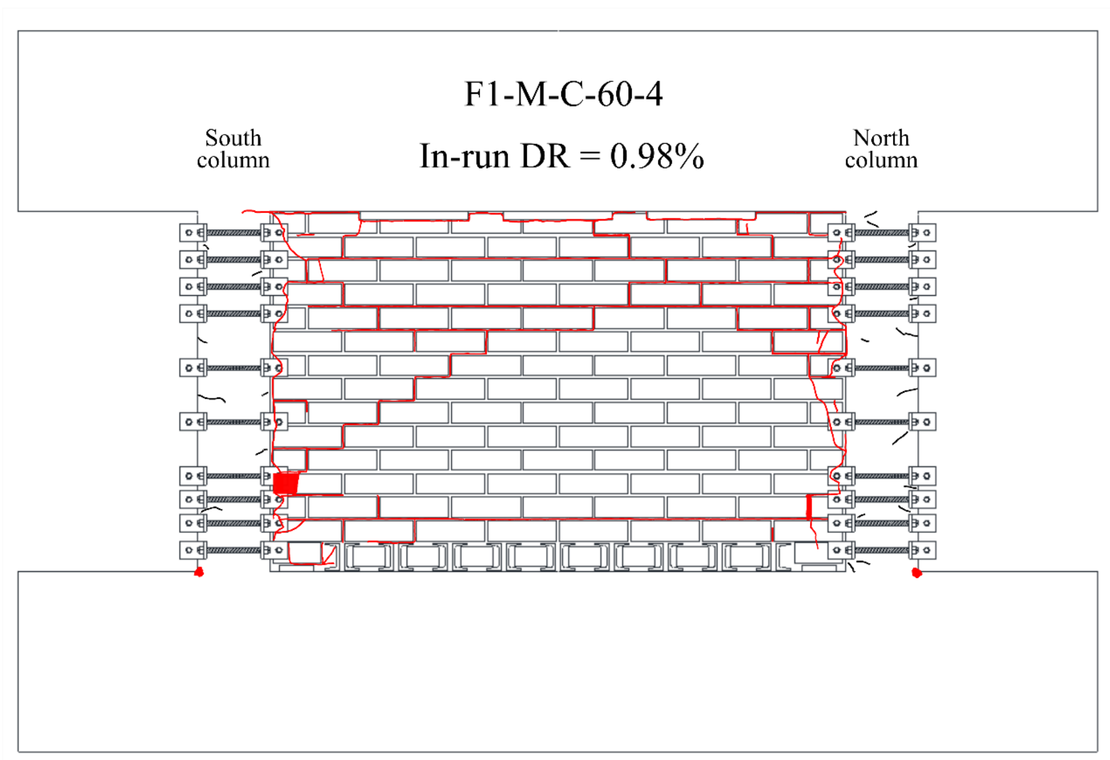

Figure 3-20: Crack map after Run 49 of Specimen F1

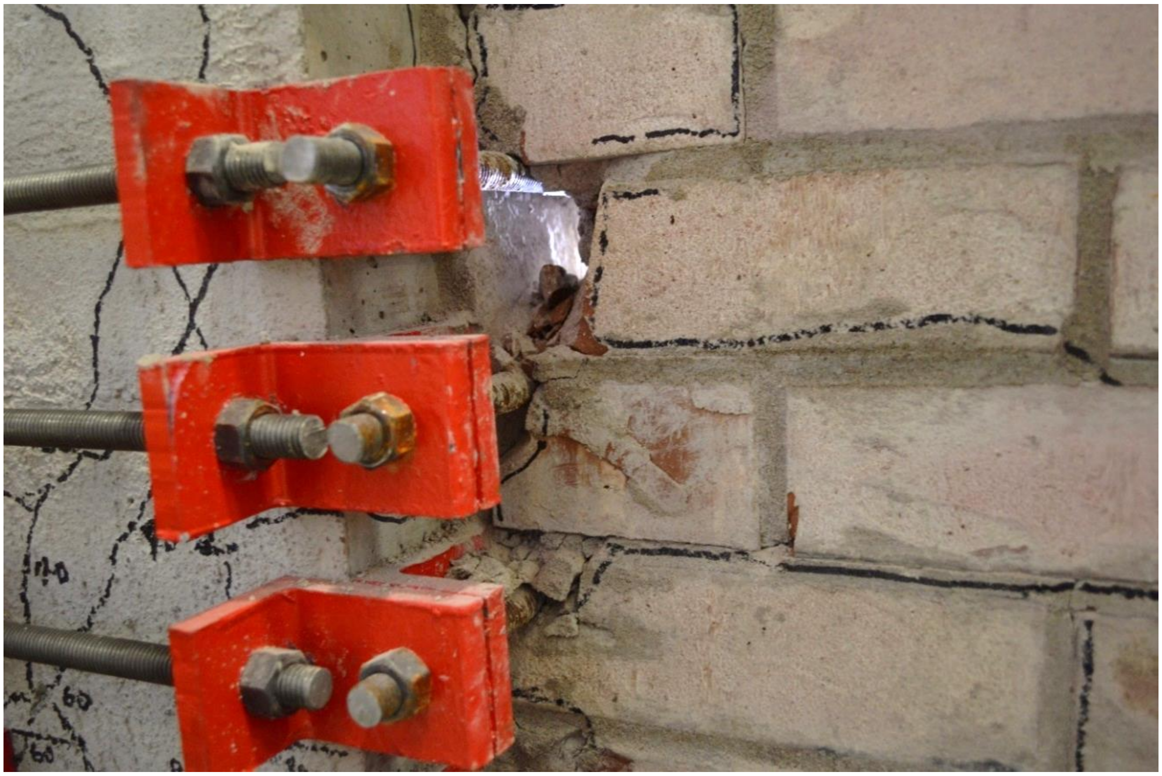

Figure 3-21: Gap where brick fell out of wall in Run 49 of Specimen F1 (F1-M-C-60-4)

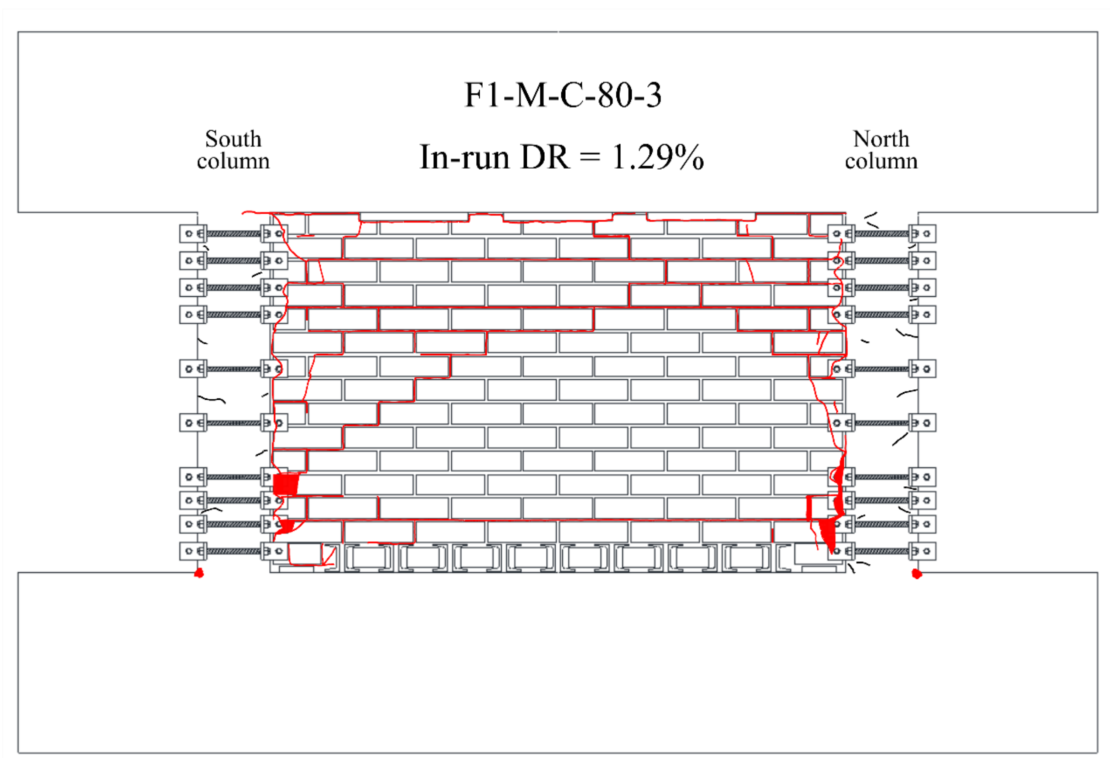

Figure 3-22: Crack map after Run 56 of Specimen F1

(a) Isometric of out-of-plane orientation of infilled frame with clamps

(b) Elevation of infilled frame with clamps tested in its weak direction

Figure 3-23: Test setup of Series F1-M-C-OOP

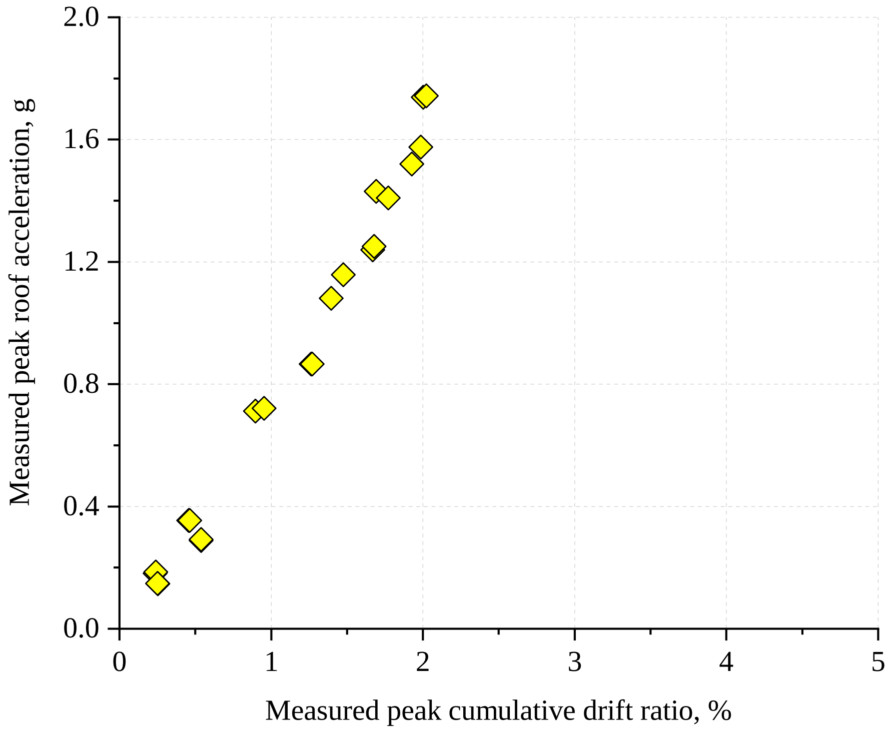

Figure 3-24: Force-displacement relationship measured in Series F1-M-C-OOP

Note: Effective mass of Specimen F1 tested in its out-of-plane direction was m_{oop} = 4,500 lb.

Figure 3-25: Spalling of mortar in Run 61 of Specimen F1 (F1-M-C-OOP-40-1)

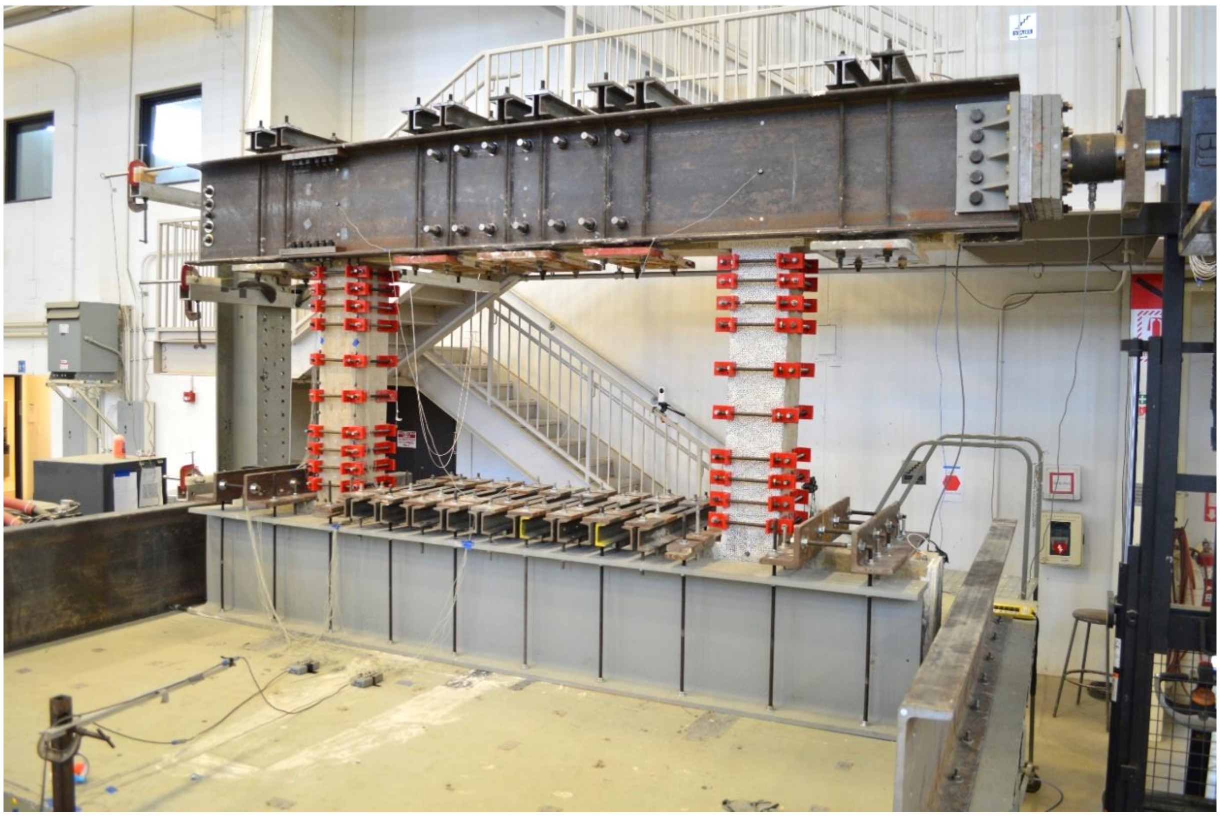

Figure 3-26: Frame with clamps tested in Series F2-C

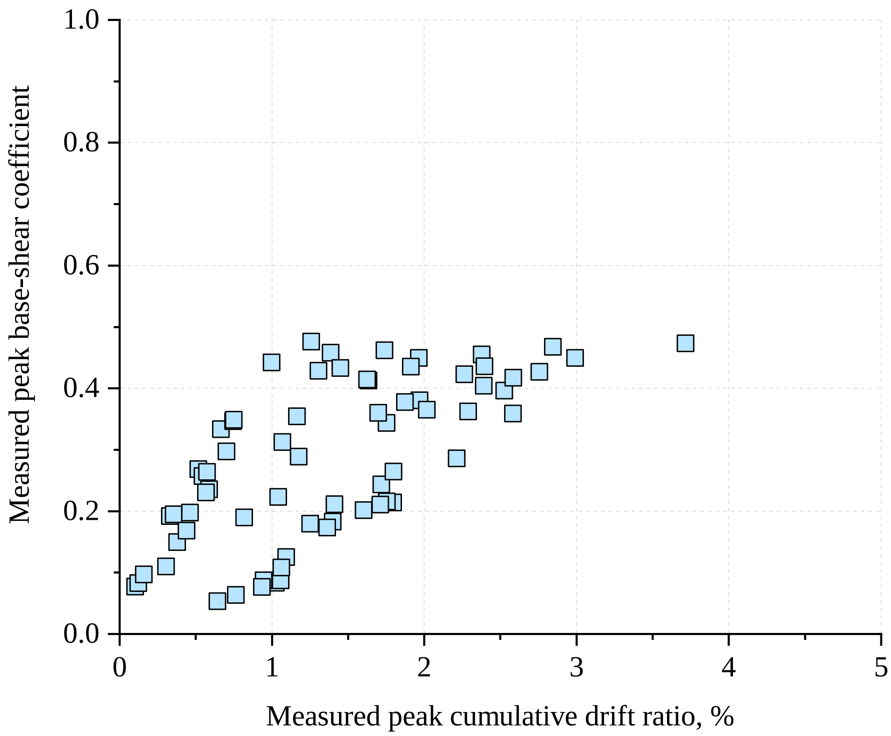

(a) Frame with clamps (Series F2-C)

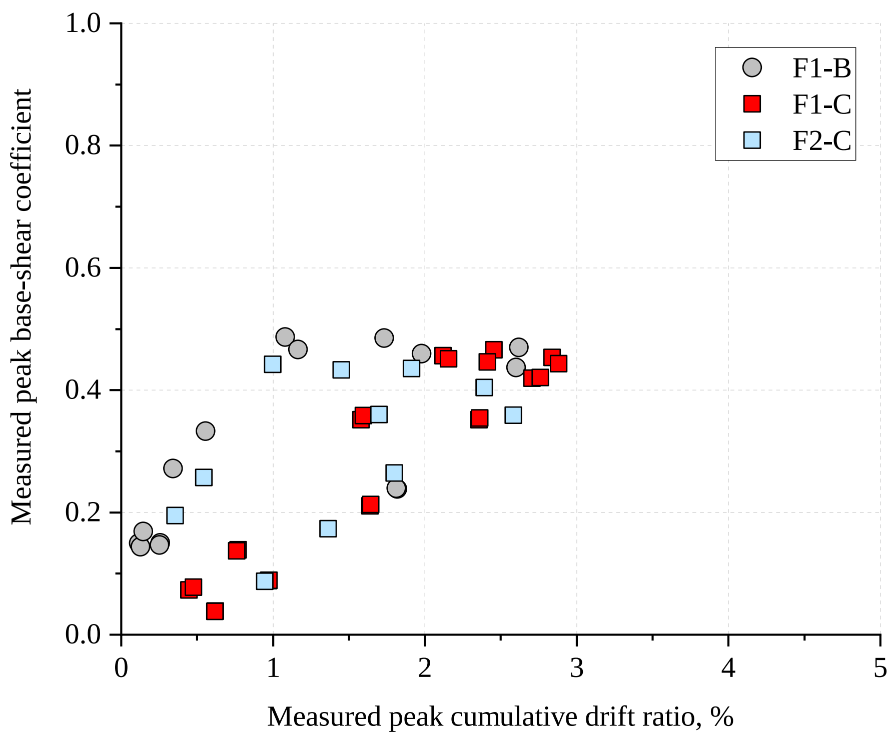

(b) Bare frame and frames with clamps subjected to El Centro (TC2) motions

Figure 3-27: Force-displacement relationship of Series F2-C

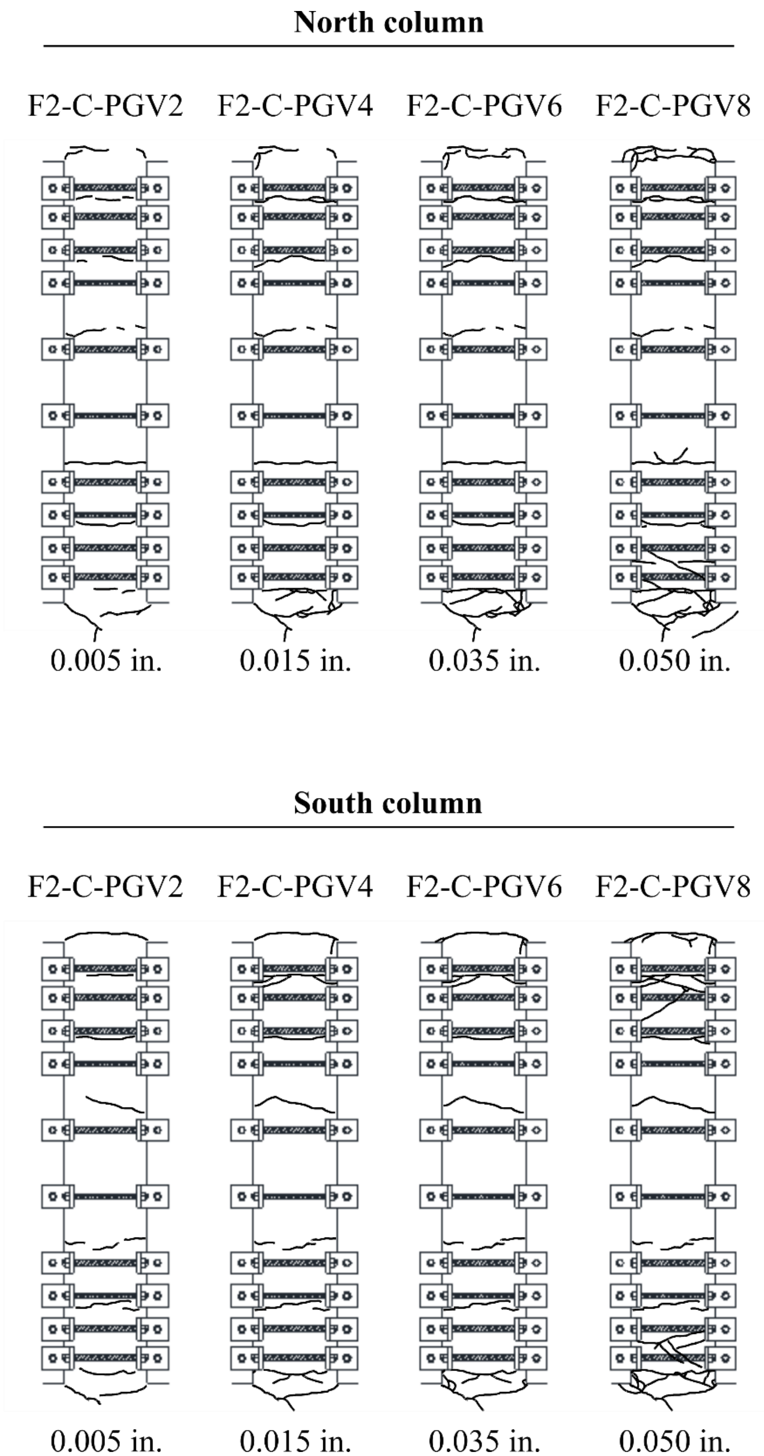

Figure 3-28: Crack maps of east face of columns in frame with clamps (Series F2-C)

Note: Values below crack maps are maximum permanent crack widths measured after the indicated sequence of runs at the same target peak base velocities.

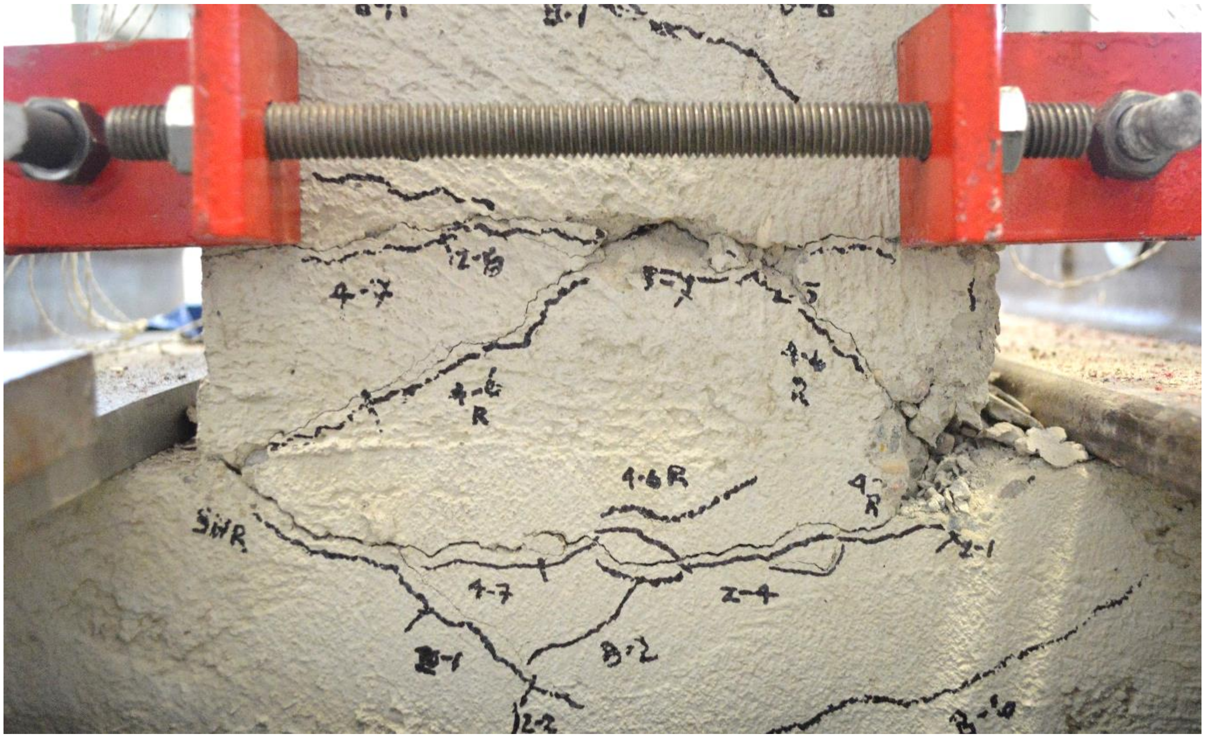

(a) Concrete spalling at base of north column

(b) Concrete spalling at base of south column

Figure 3-29: Concrete spalling at base of columns at end of Series F2-C

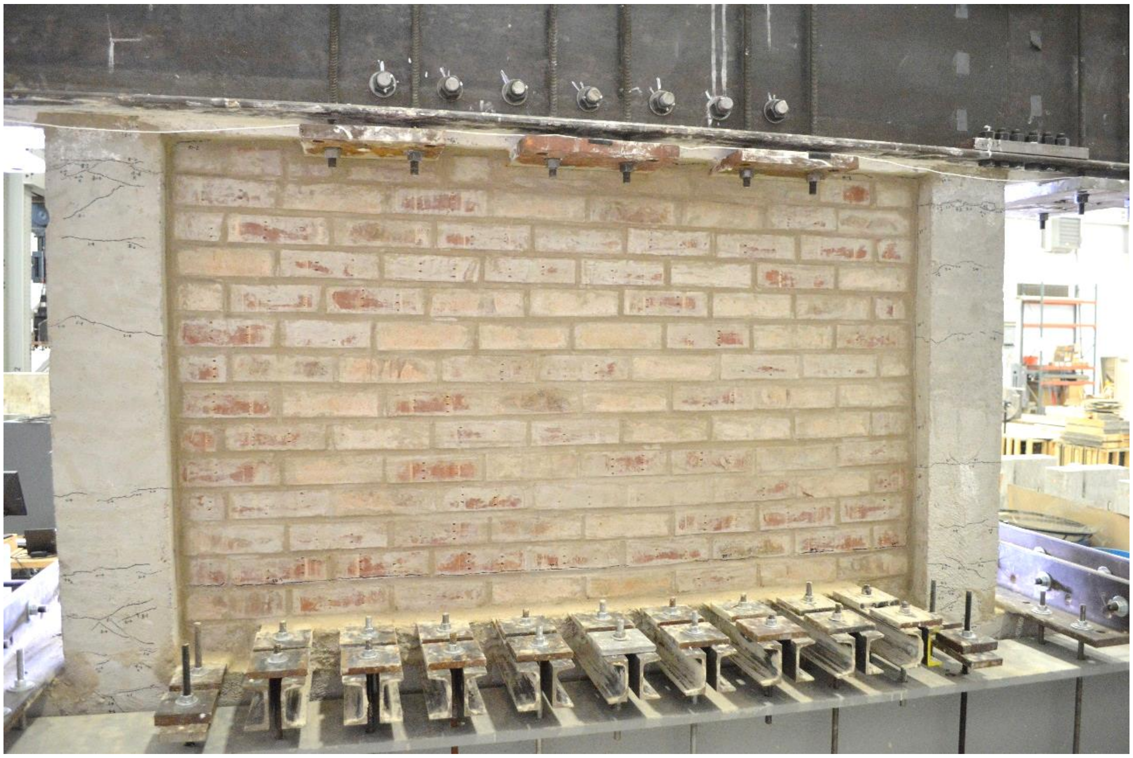

(a) Close-up of masonry infill wall

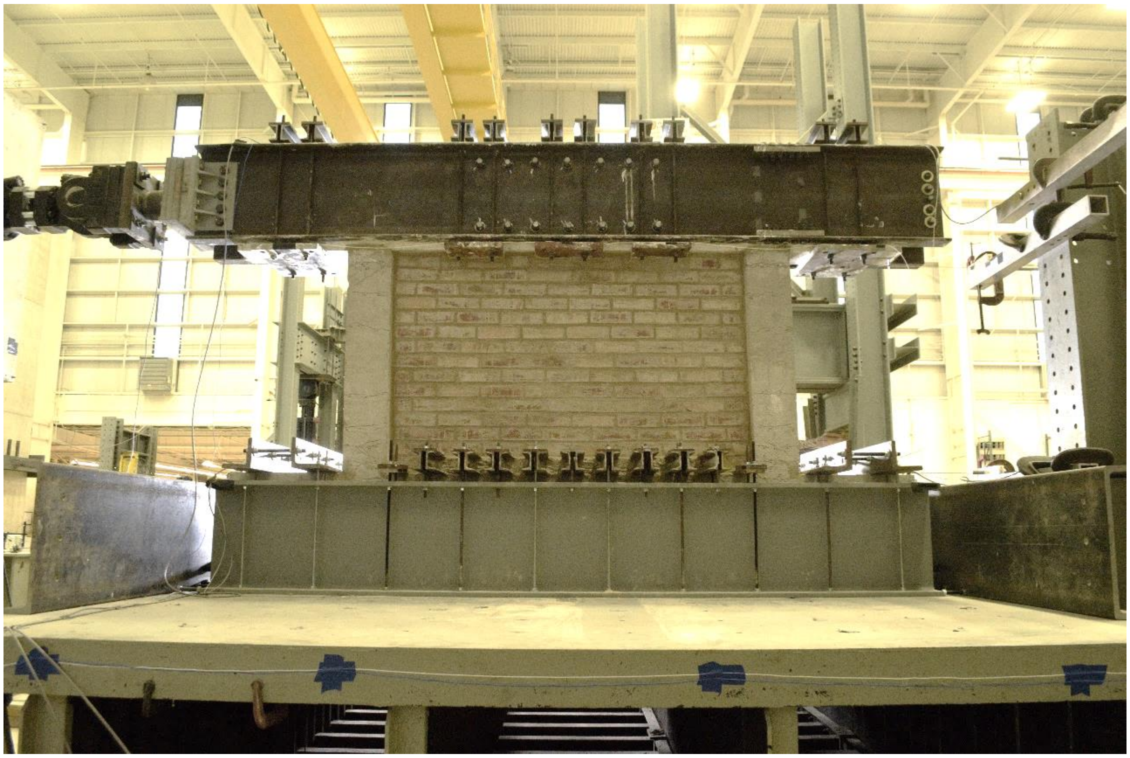

(b) Elevation of infilled frame without clamps

Figure 3-30: Infilled frame tested in Series F2-M

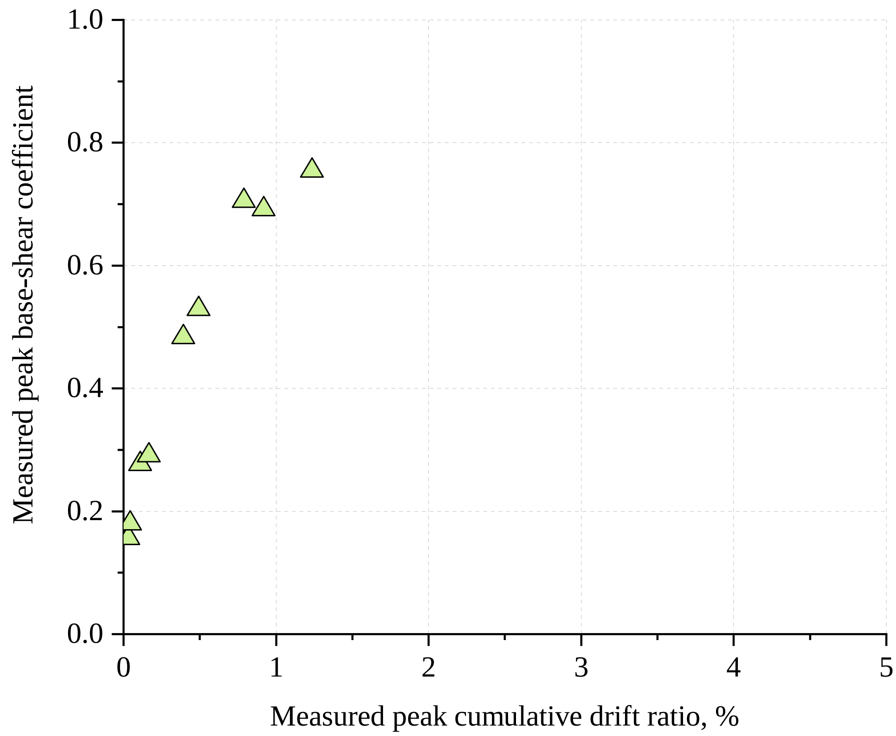

(a) Infilled frame without clamps (Series F2-M)

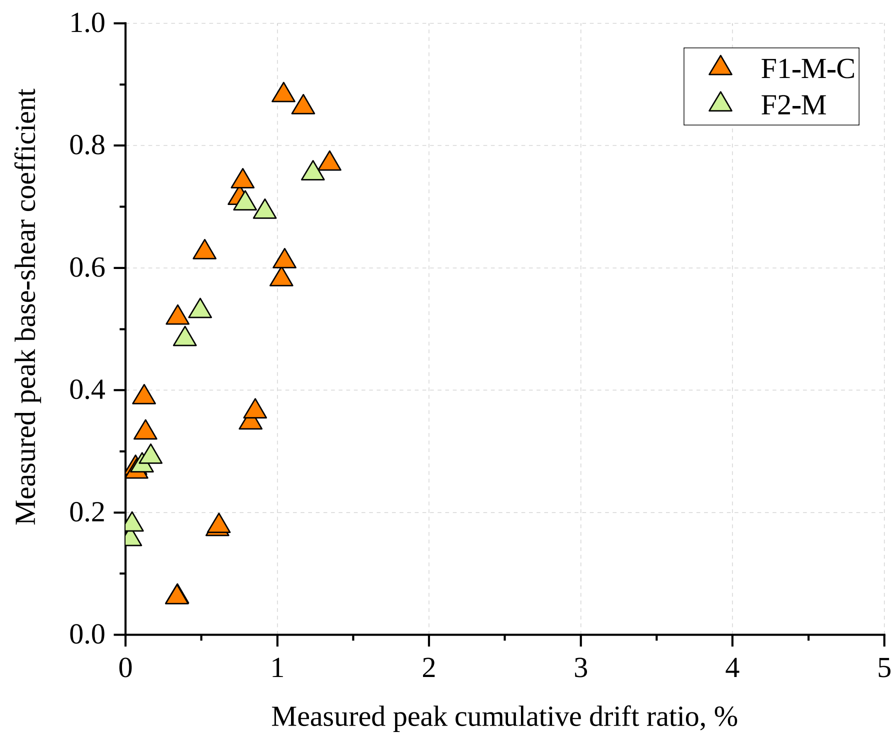

(b) Infilled frames (with and without clamps)

Figure 3-31: Force-displacement relationship of Series F2-M

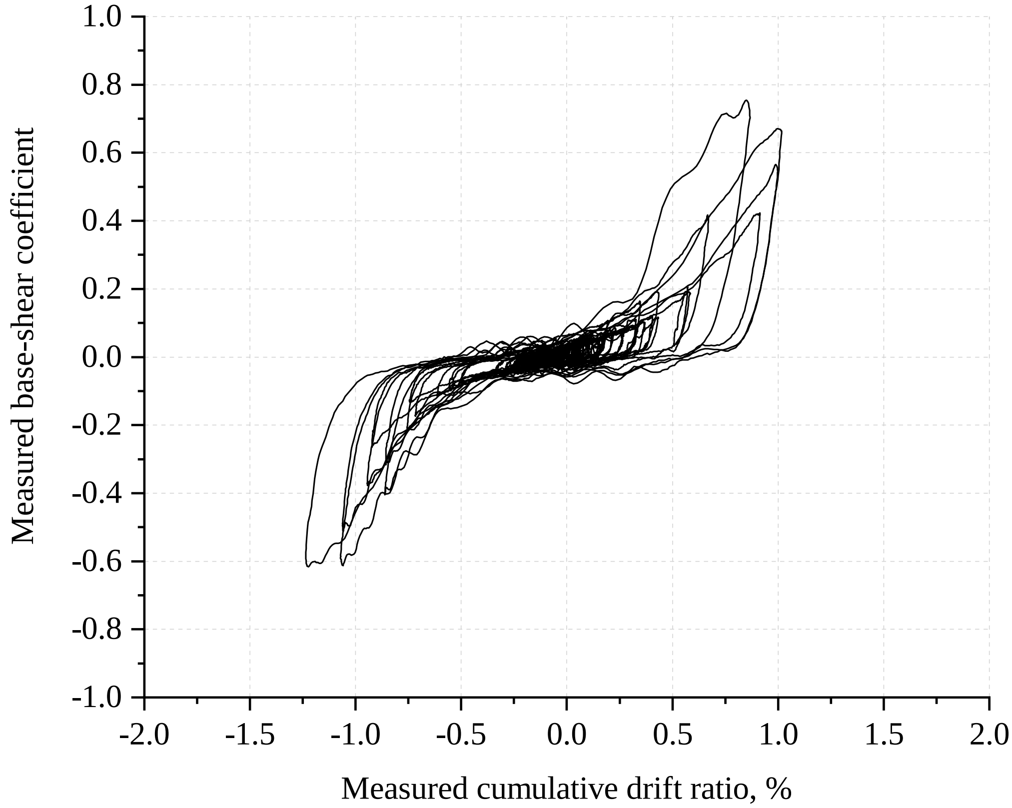

Figure 3-32: Force-displacement history measured in run at 80% intensity of Series F2-M

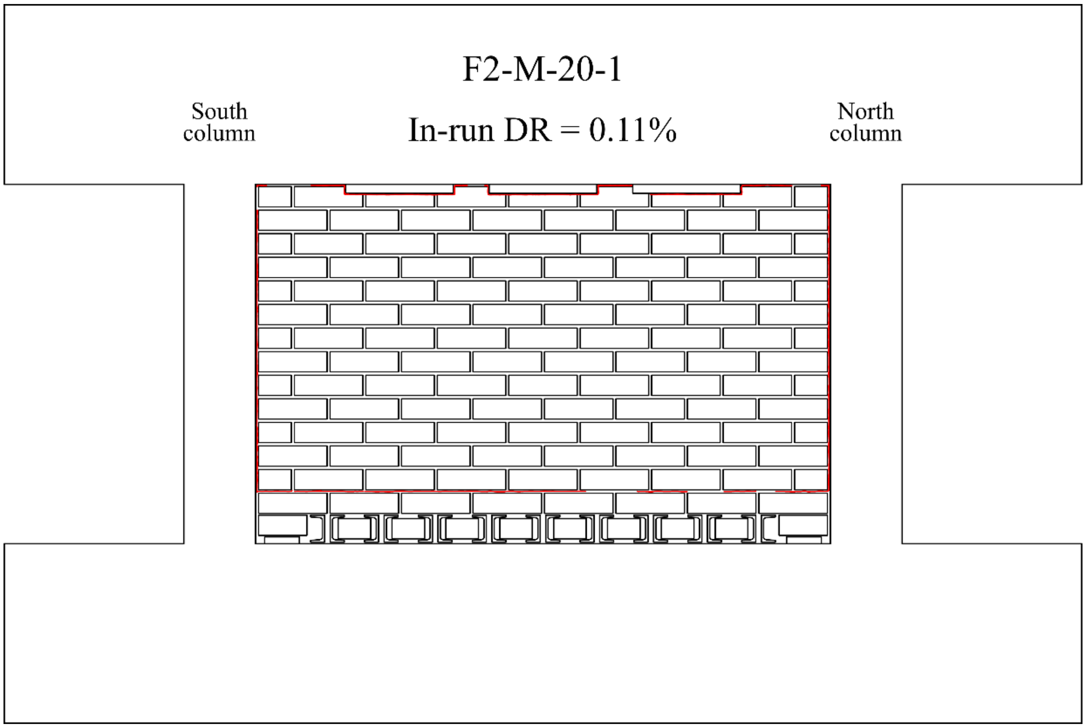

Figure 3-33: Crack map after Run 72 of Specimen F2

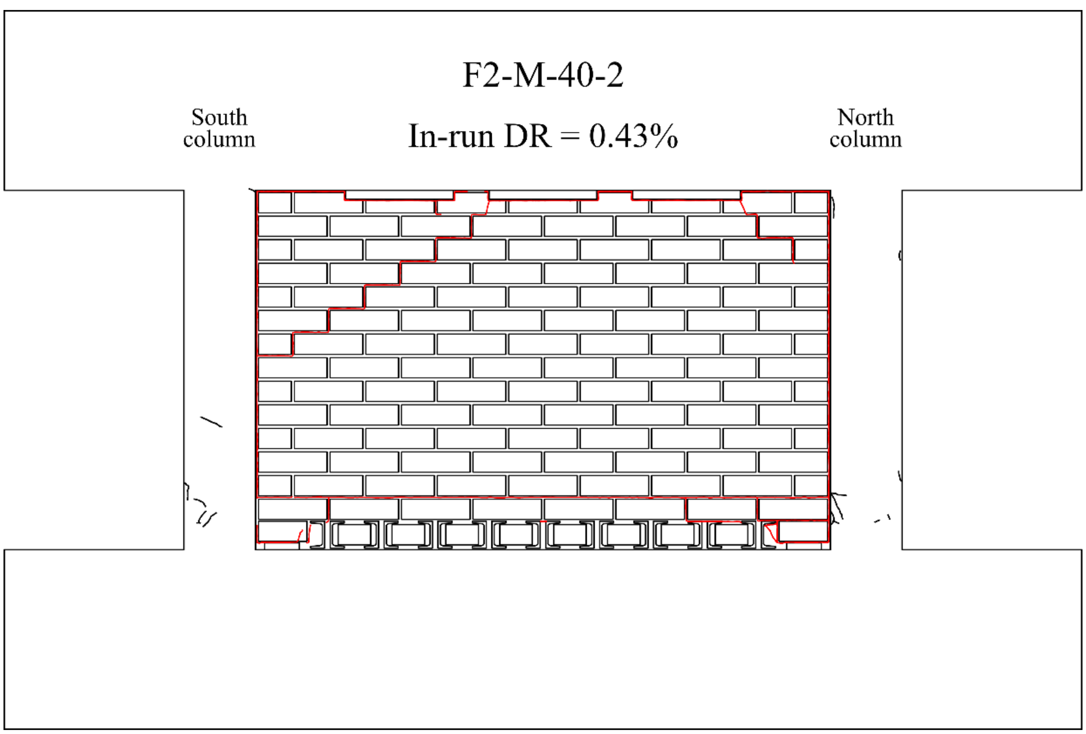

Figure 3-34: Crack map after Run 75 of Specimen F2

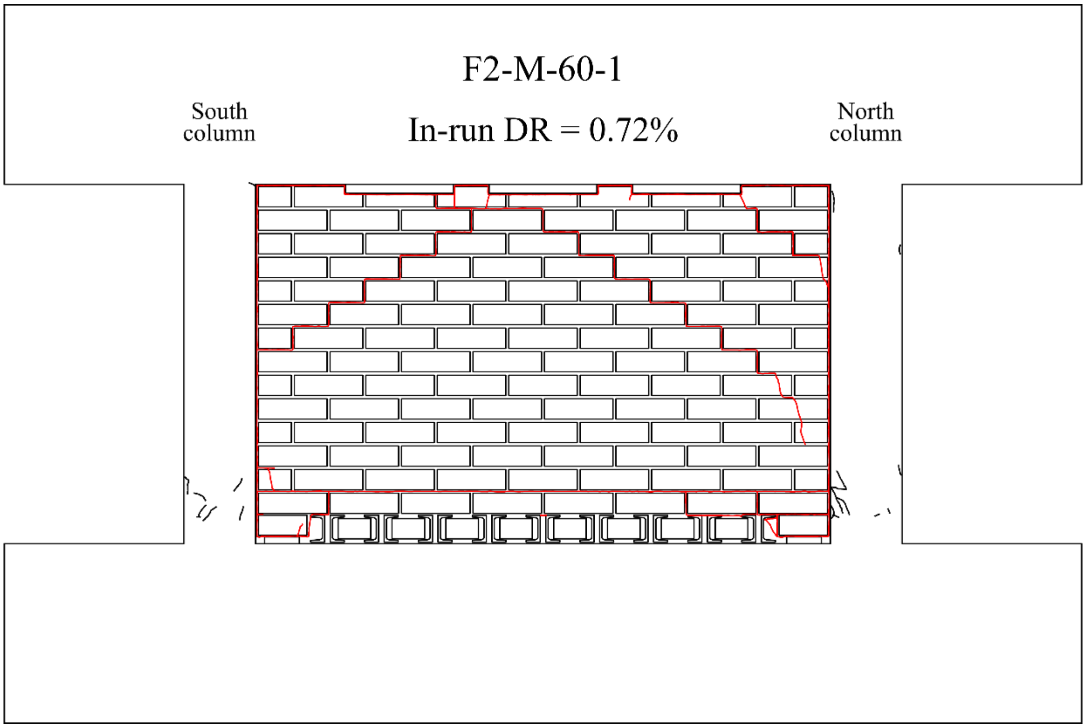

Figure 3-35: Crack map after Run 76 of Specimen F2

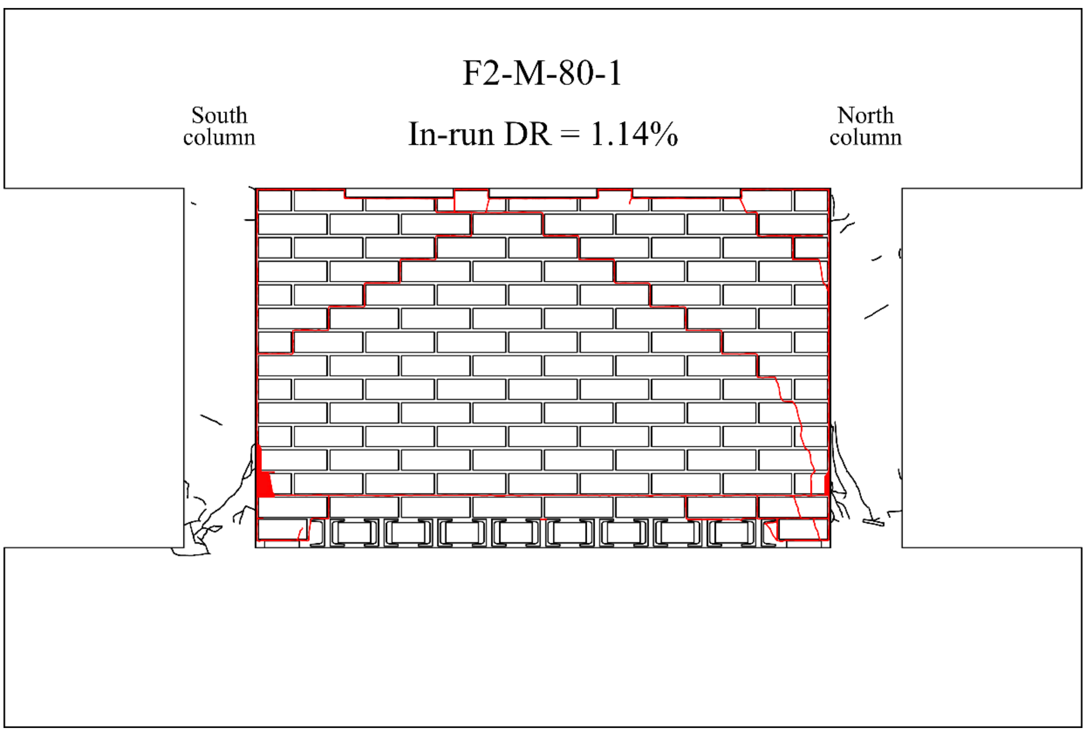

Figure 3-36: Crack map after Run 78 of Specimen F2

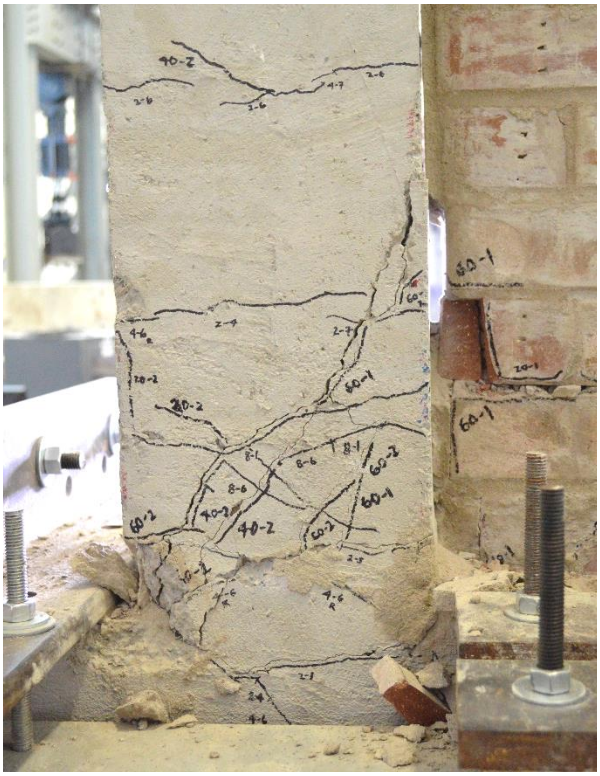

(a) East face of south column

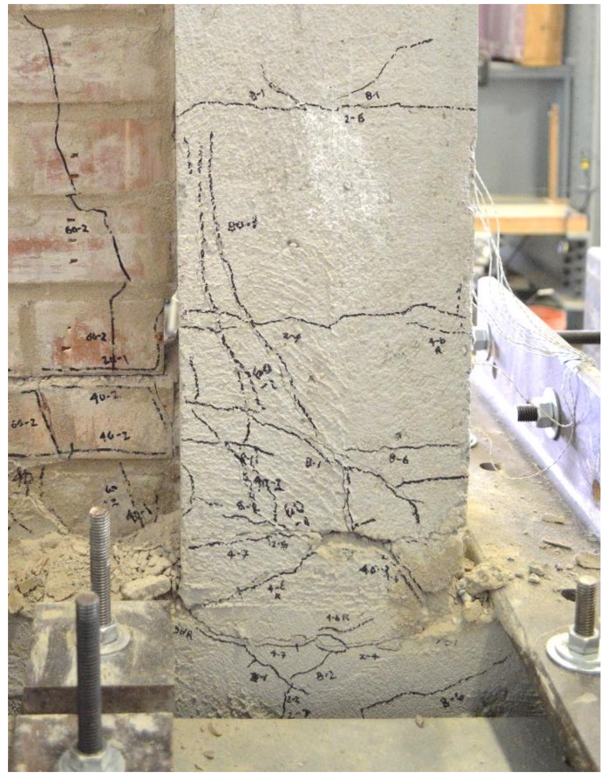

(b) East face of north column

(a) West face of south column

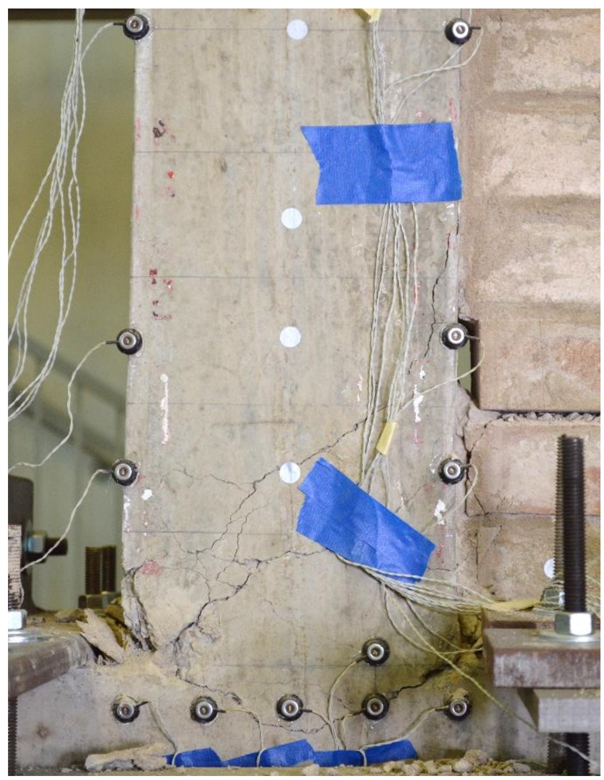

(b) West face of north column

Figure 3-37: Inclined cracks at bases of columns at end of Series F2-M

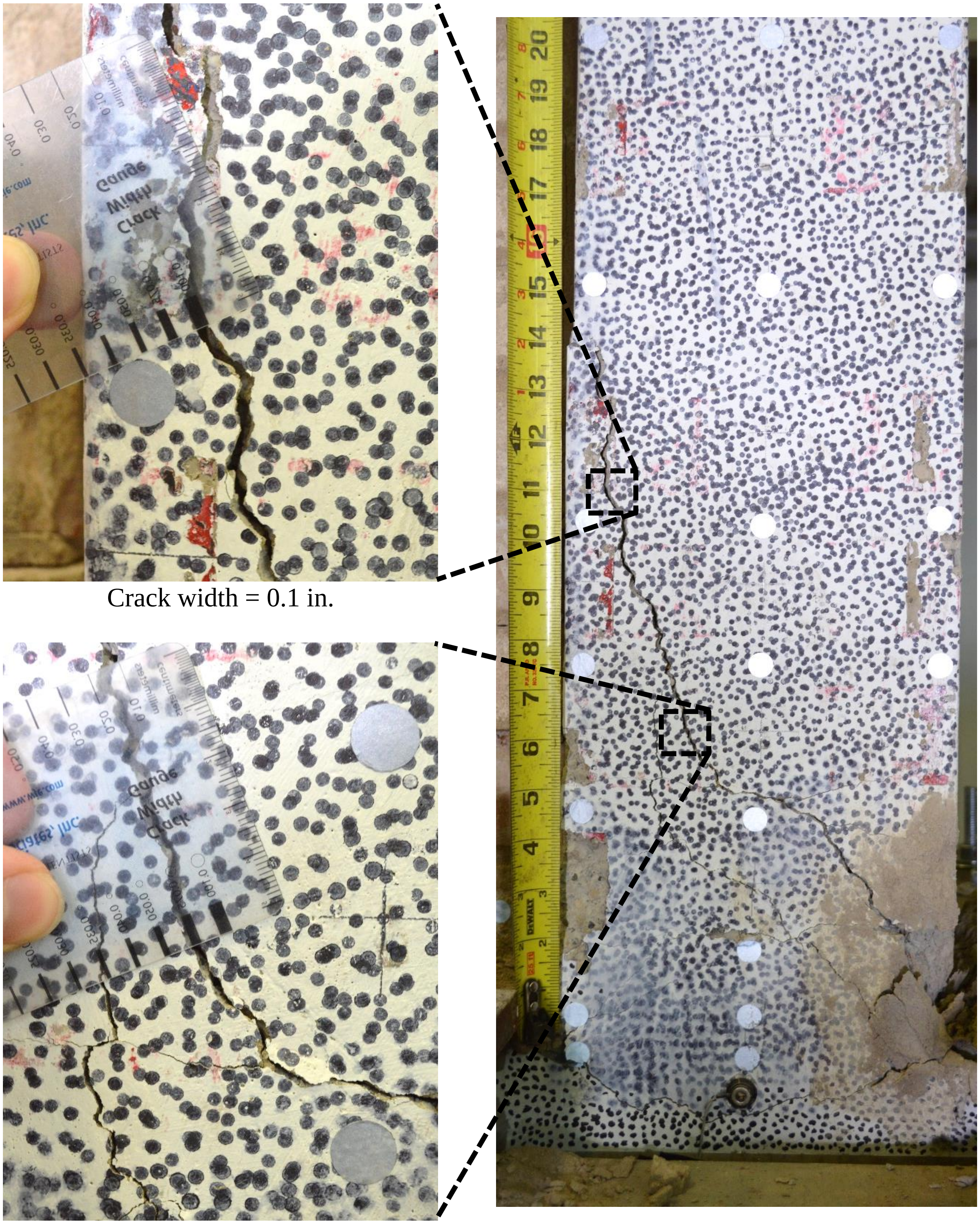

Crack width = 0.1 in.

Crack width = 0.075 in.

Figure 3-38: Inclined crack at base of south column at end of Series F2-M

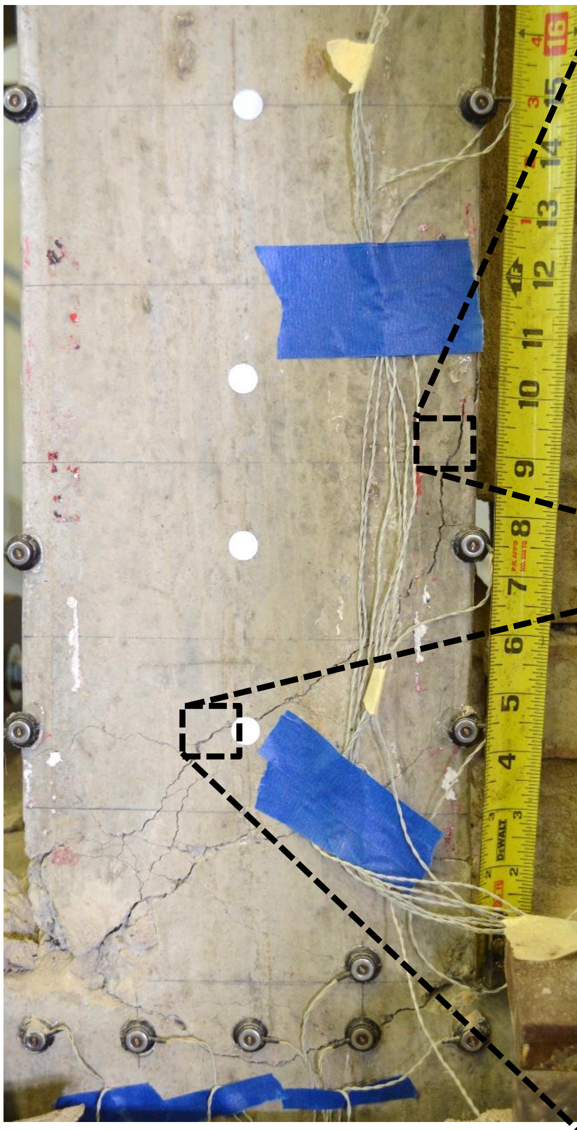

Crack width = 0.035 in.

Crack width = 0.030 in.

Figure 3-39: Inclined crack at base of north column at end of Series F2-M

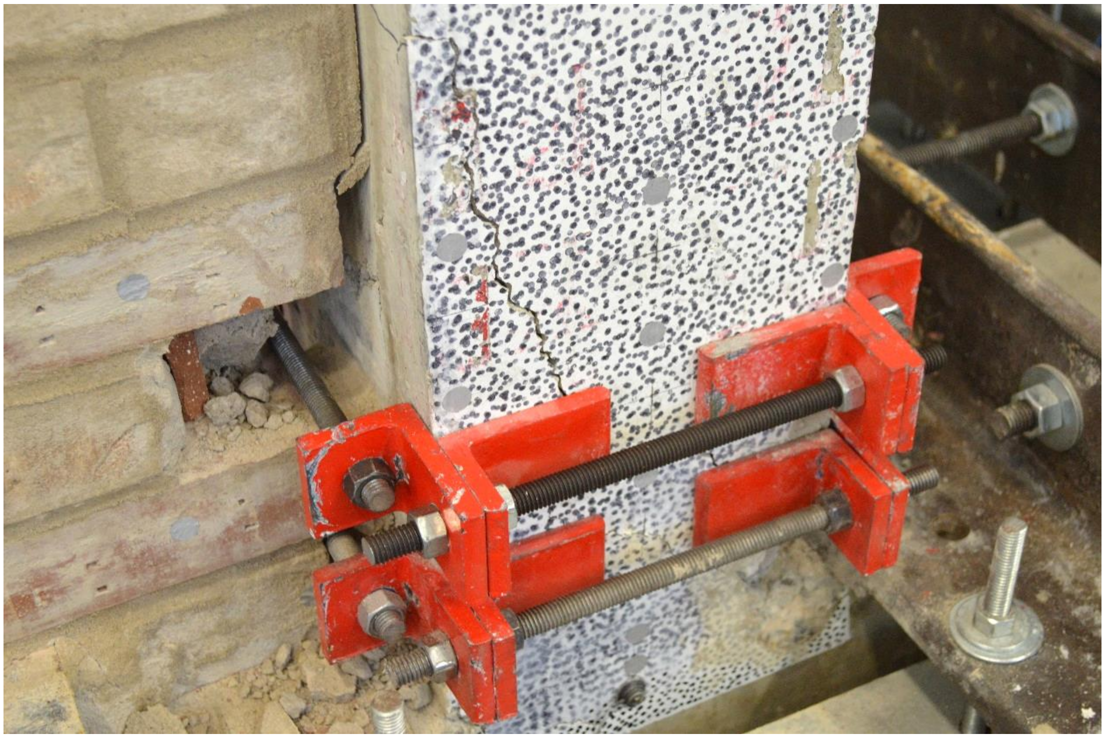

(a) Installing clamps at base of south column

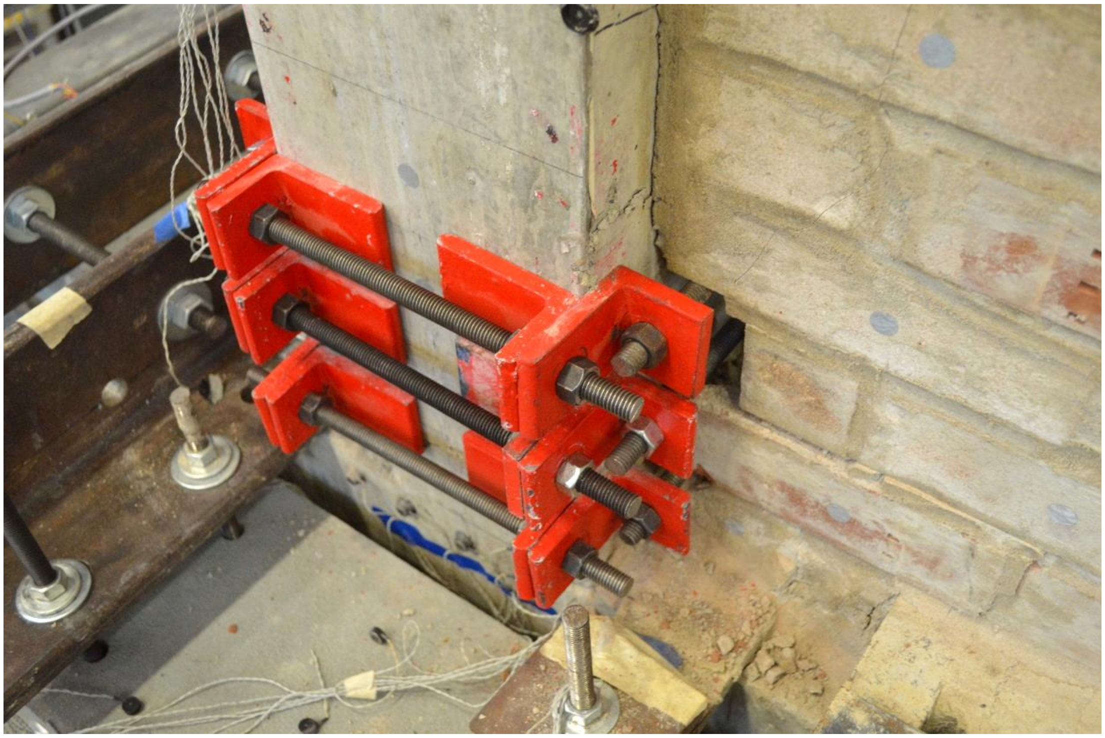

(b) Installing clamps at base of north column

Figure 3-40: Installation of clamps on columns of infilled frame

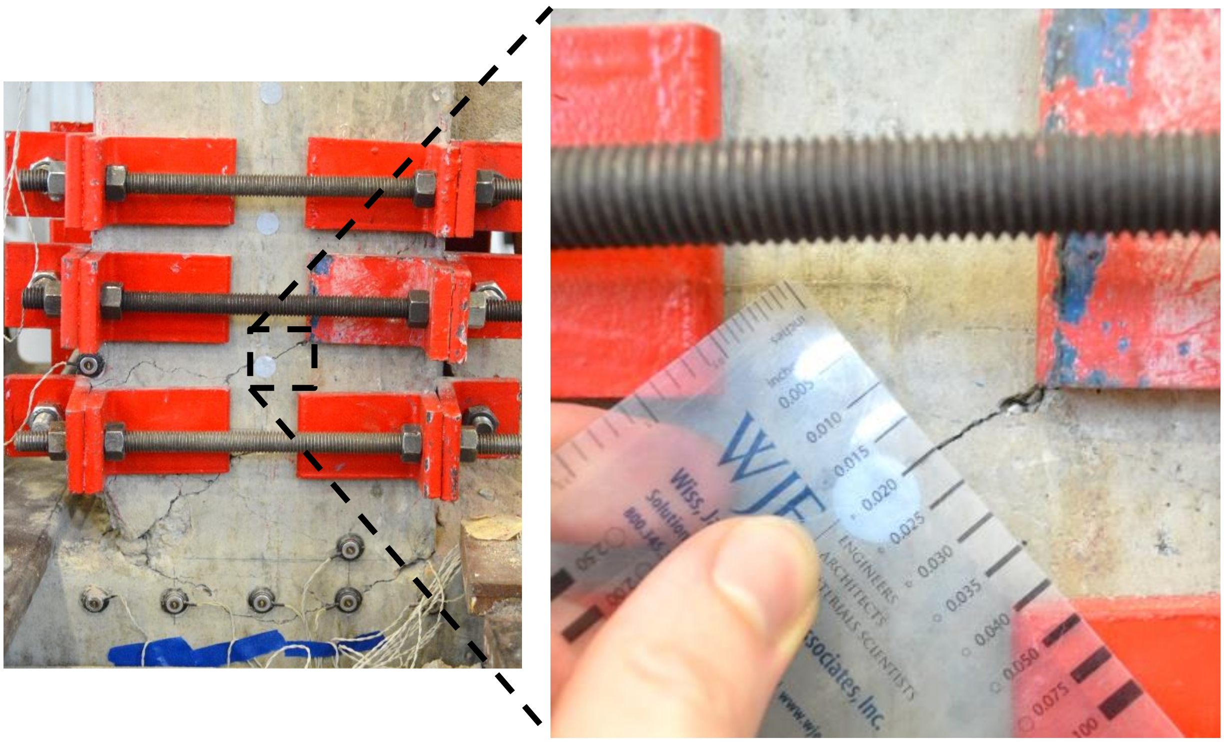

Crack width = 0.020 in.

Figure 3-41: Inclined crack after installing clamps at base of north column

(a) Infill wall before repairs

(b) Infill wall after repairs

(c) Close-up before repairs

(d) Close-up after repairs

Figure 3-42: Repair of infill wall near north column before Series F2-M-C-S

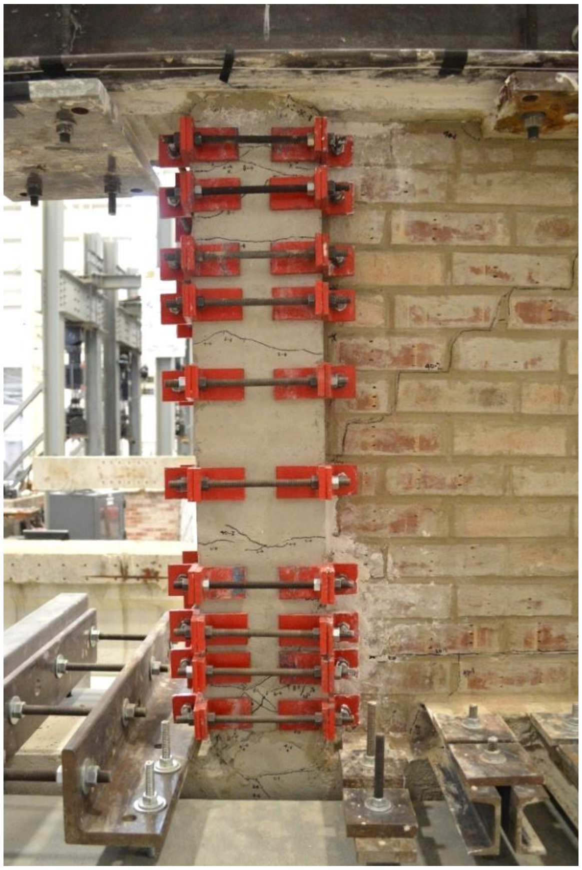

(a) Repaired south column - east face

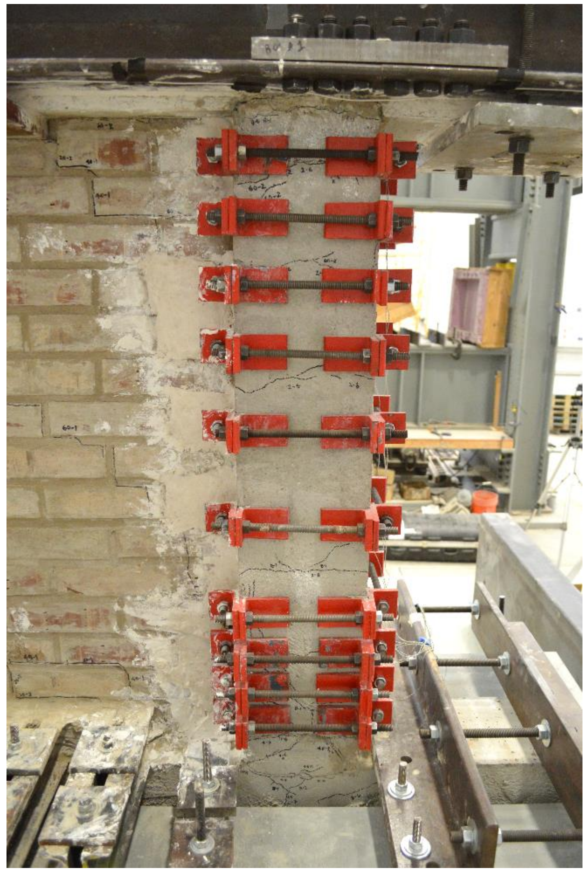

(b) Repaired north column - east face

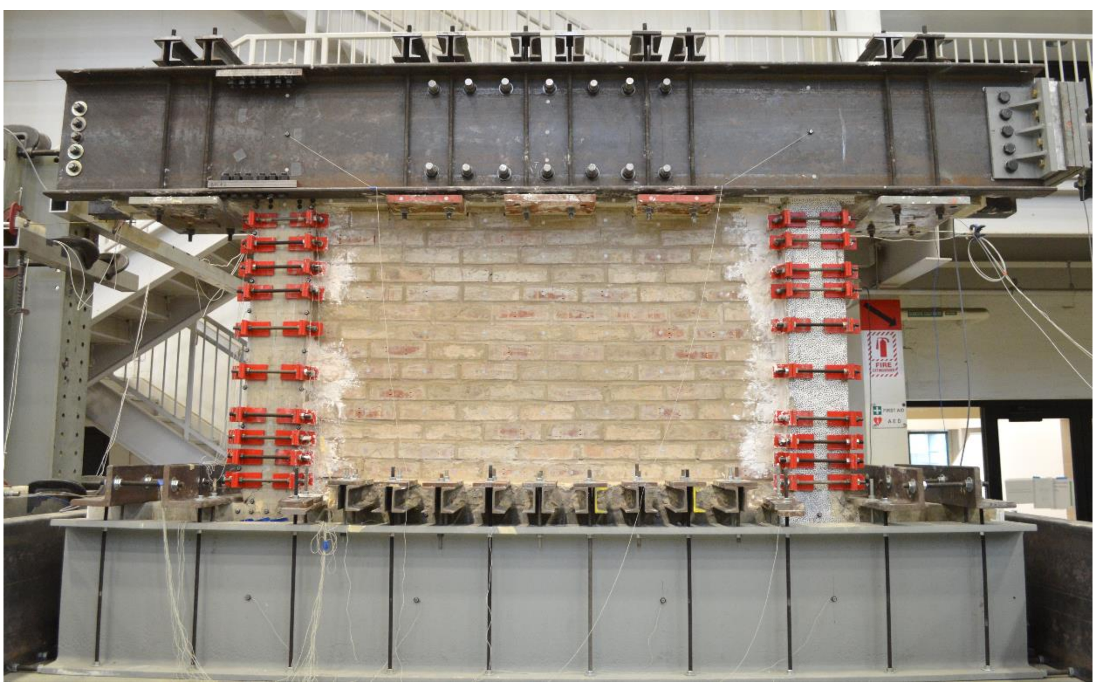

(c) Repaired infilled frame with clamps - west face

Figure 3-43: Elevations of (repaired) infilled frame with clamps tested in Series F2-M-C-S

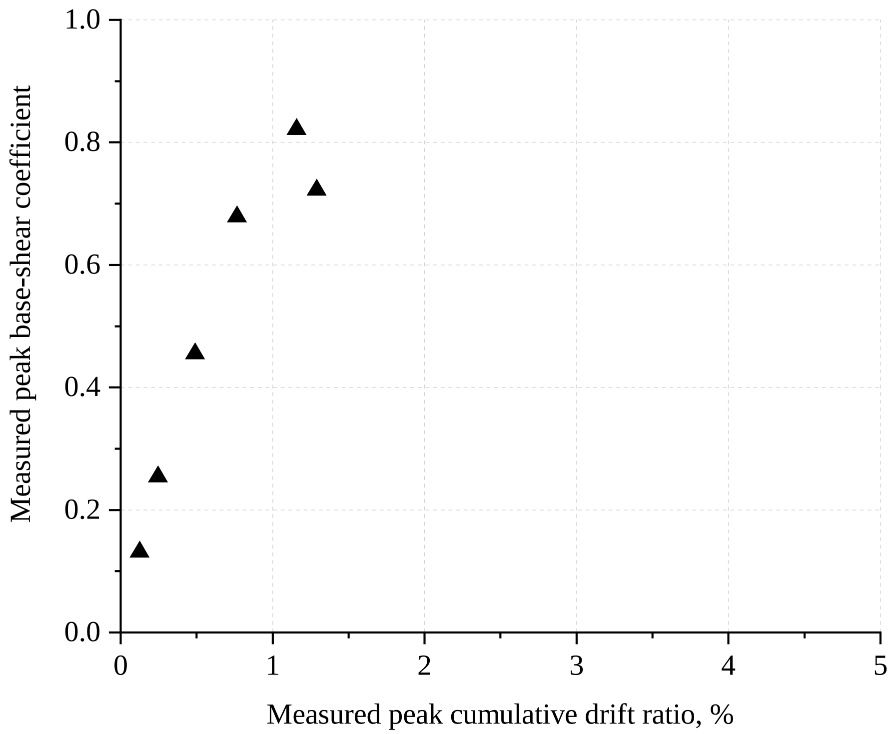

(a) Repaired infilled frame without clamps (Series F2-M-C-S)

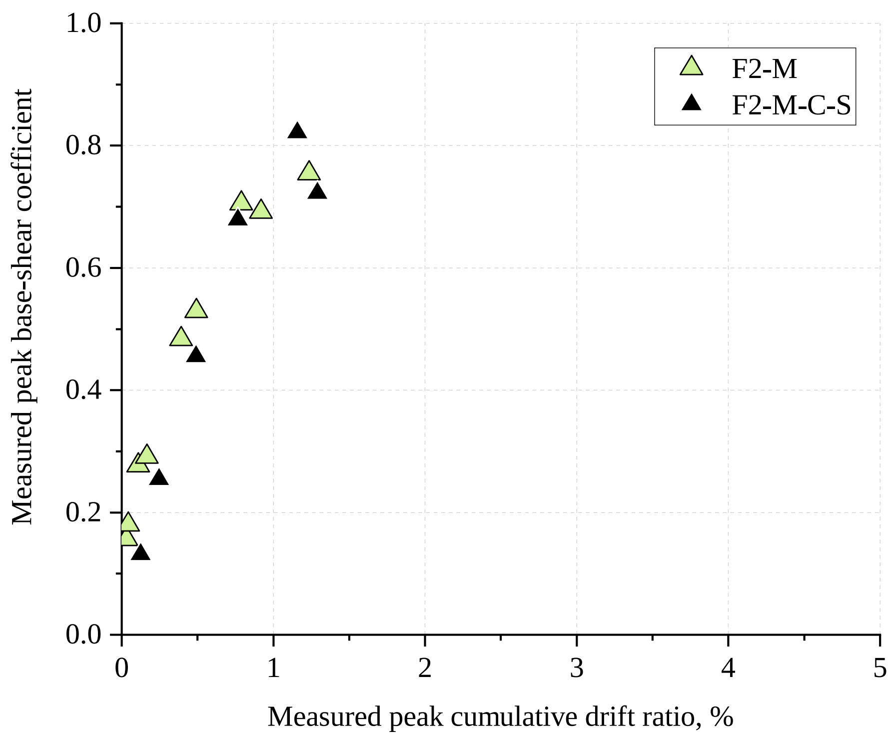

(b) Infilled frames of Specimen F2

Figure 3-44: Force-displacement relationship of Series F2-M-C-S

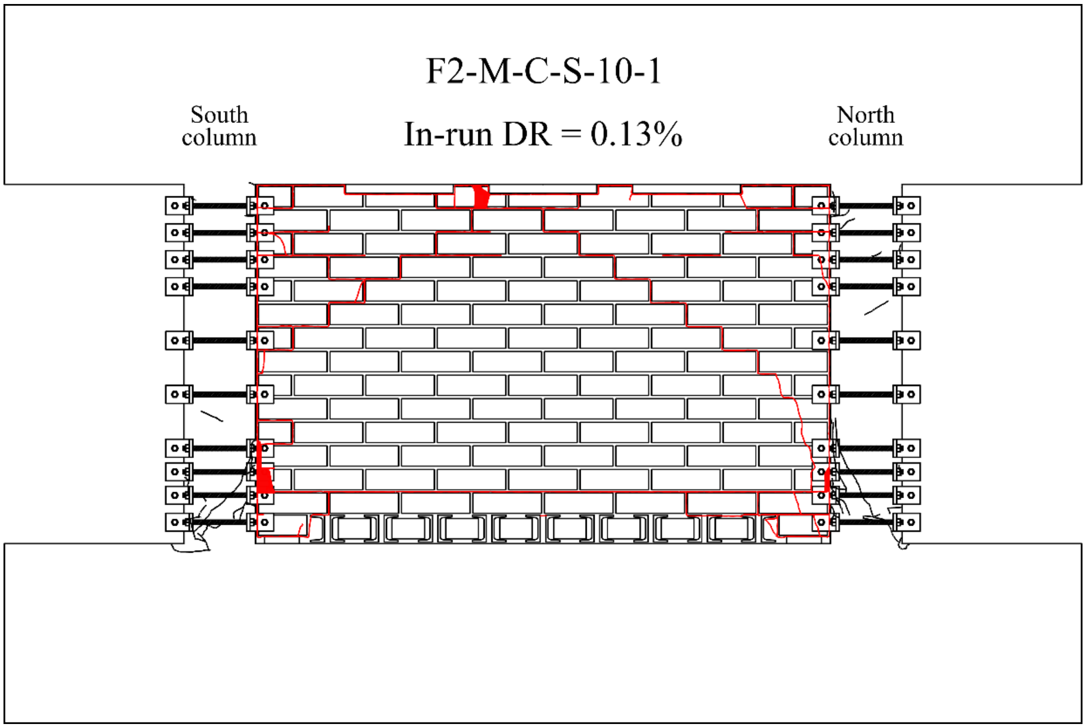

Figure 3-45: Crack map after Run 79 of Series F2-M-C-S

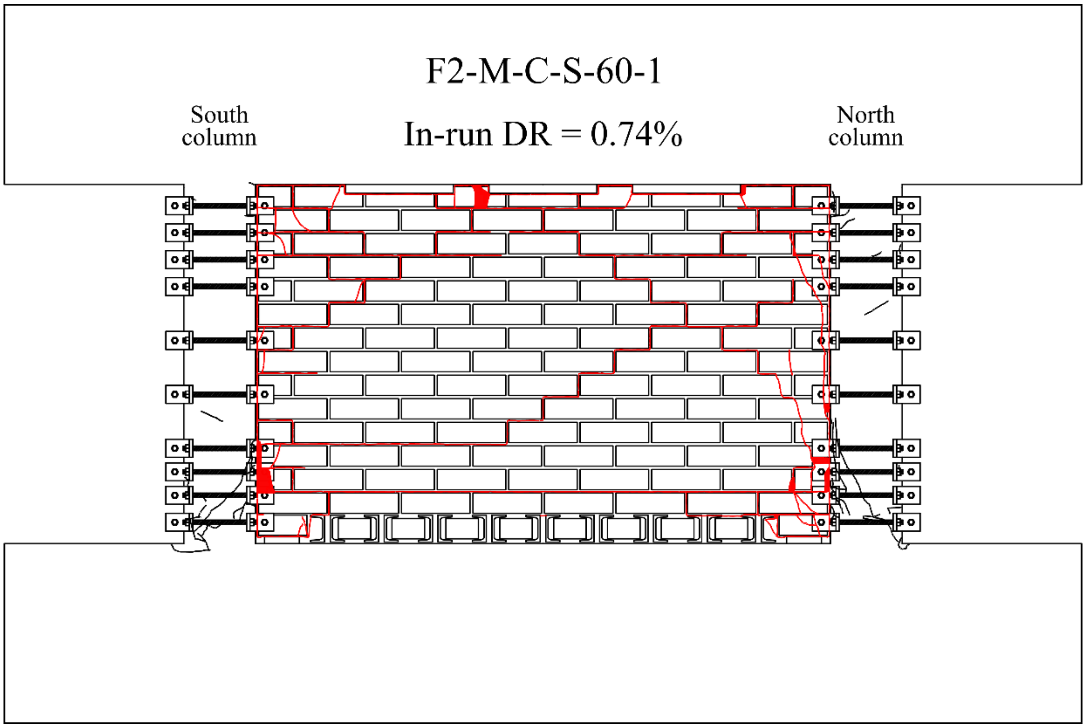

Figure 3-46: Crack map after Run 82 of Series F2-M-C-S

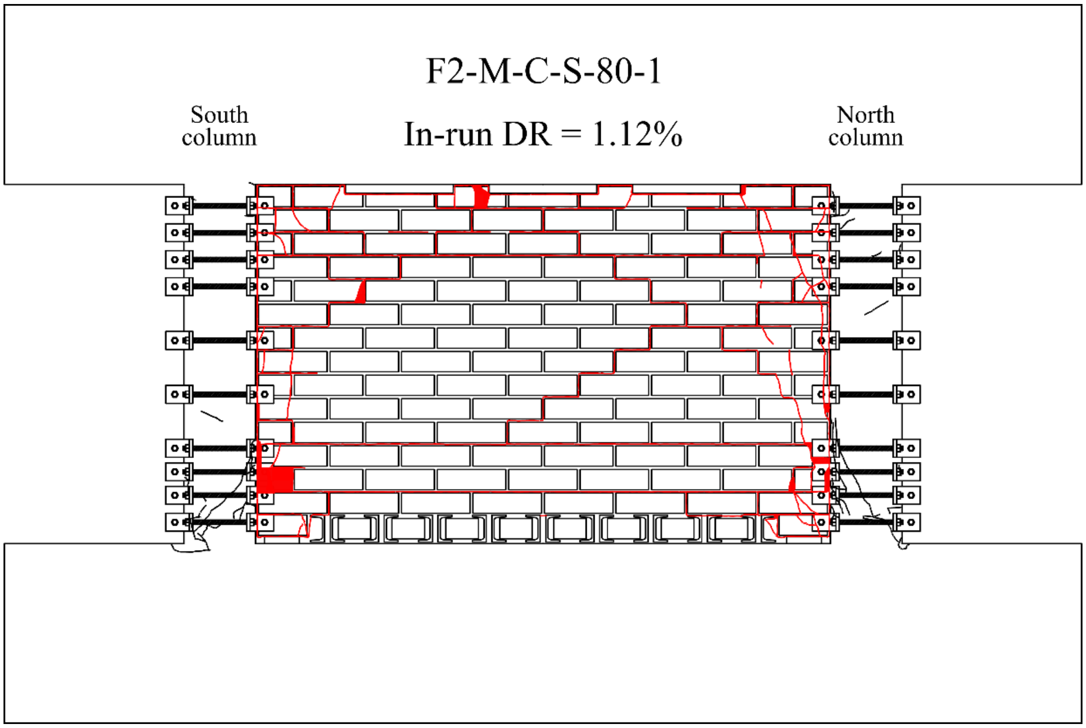

Figure 3-47: Crack map after Run 83 of Series F2-M-C-S

Figure 3-48: Gap where brick fell out of wall in Run 83 of Specimen F2 (F2-M-C-S-80-1)

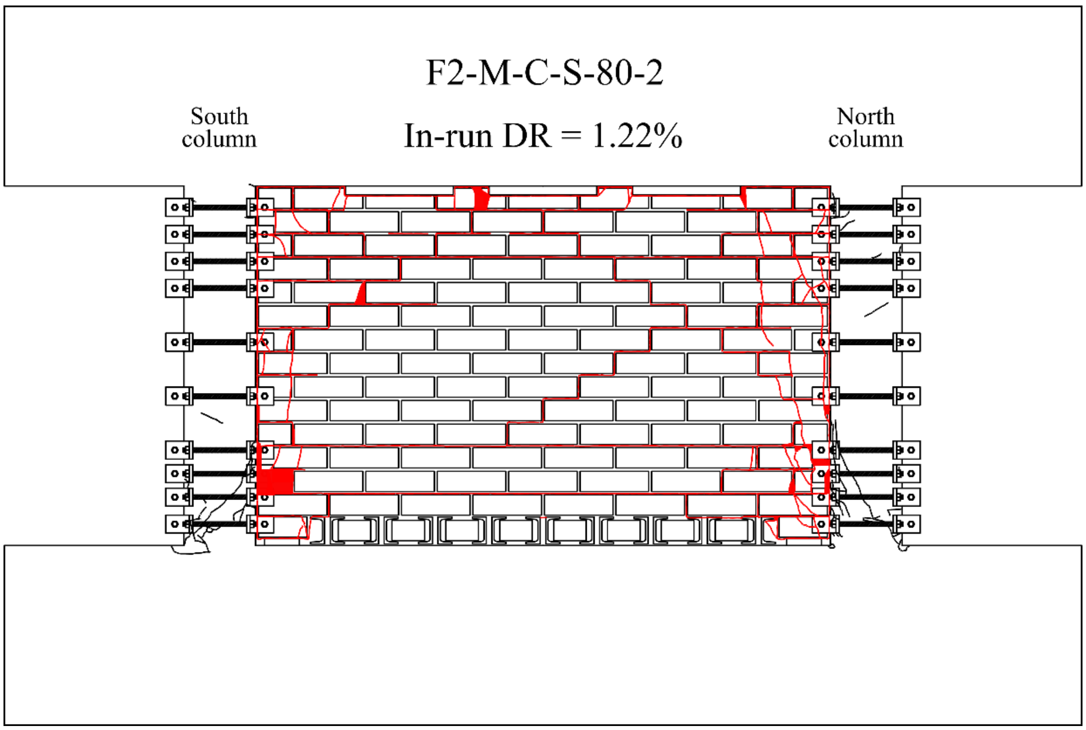

Figure 3-49: Crack map after Run 84 of Series F2-M-C-S

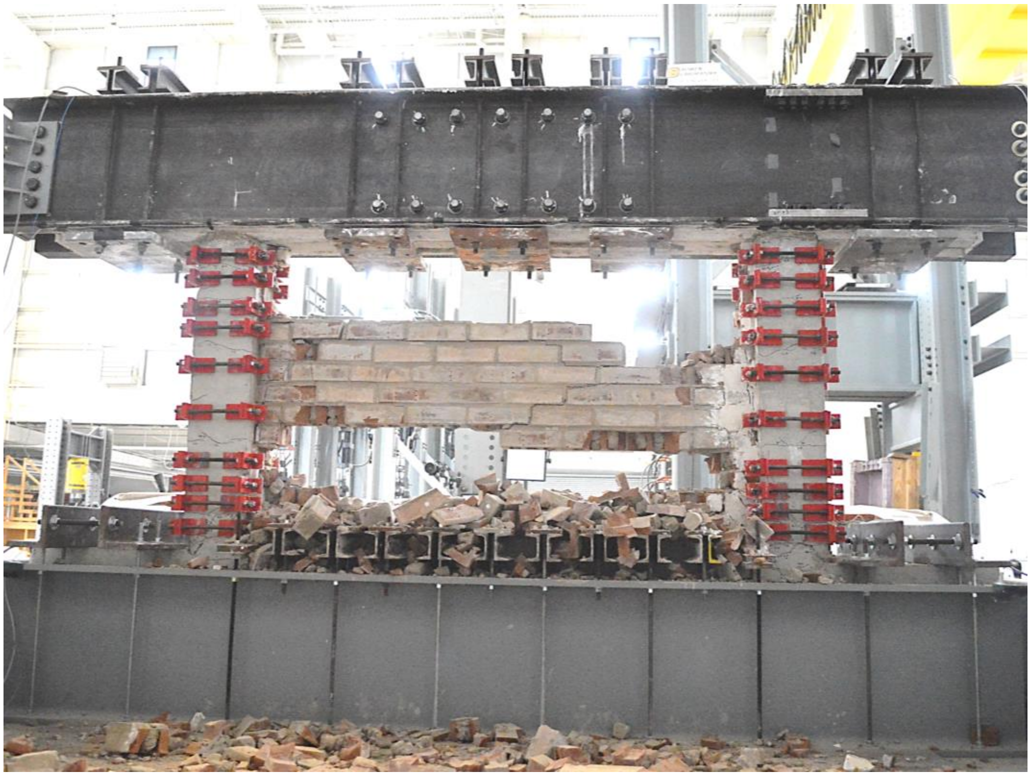

Figure 3-50: Demolishing infill wall

Figure 3-51: Elevation of frame with clamps (Series F2-C-S)

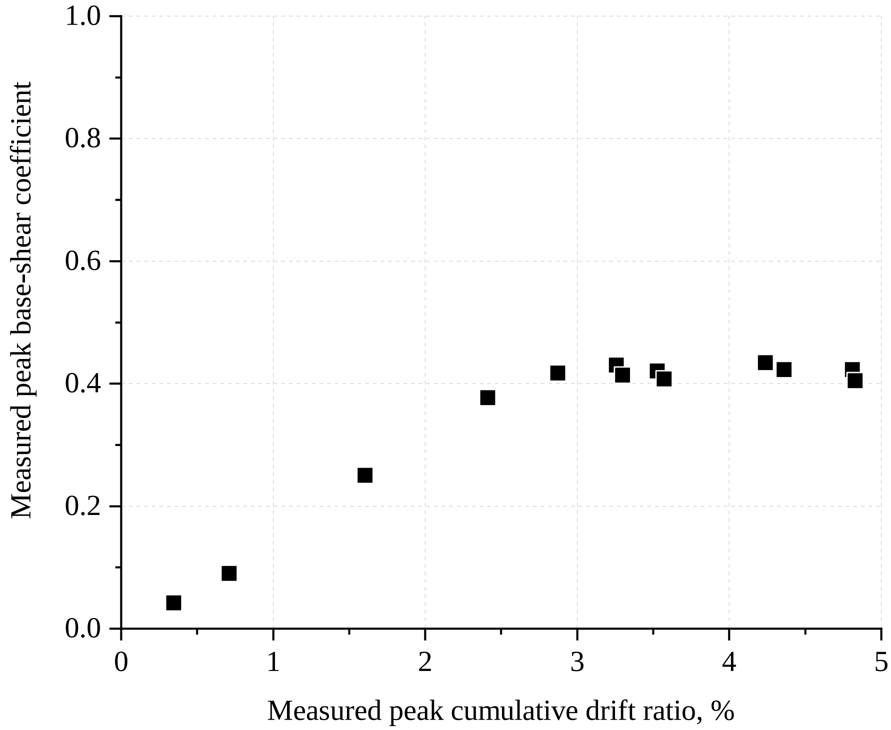

(a) Frame with clamps (Series F2-C-S)

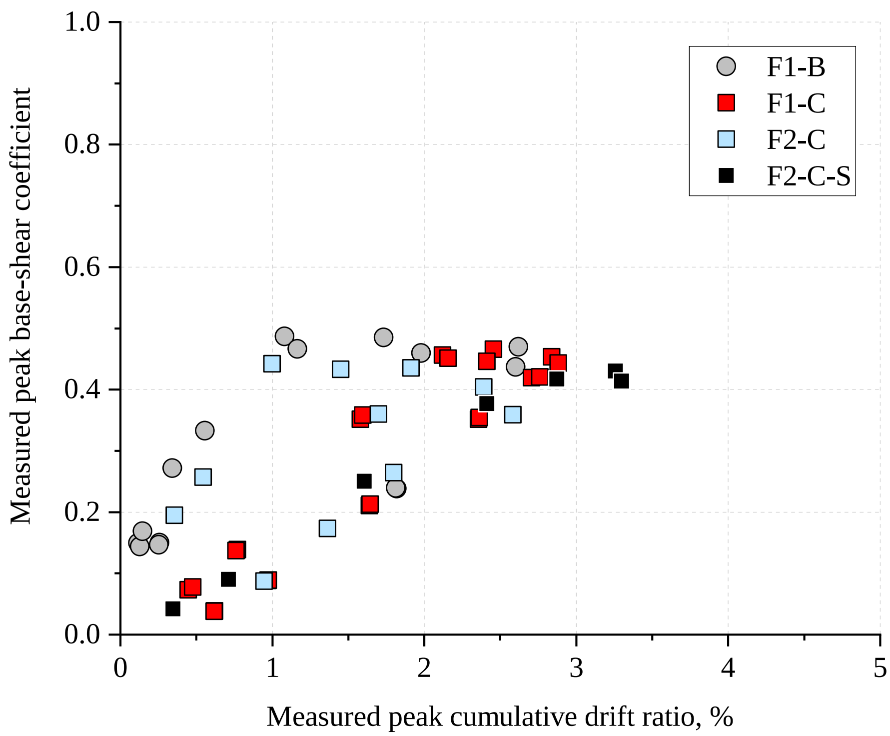

(b) Bare frame and frames with clamps subjected to El Centro (TC2) motions

Figure 3-52: Force-displacement relationship of Series F2-C-S

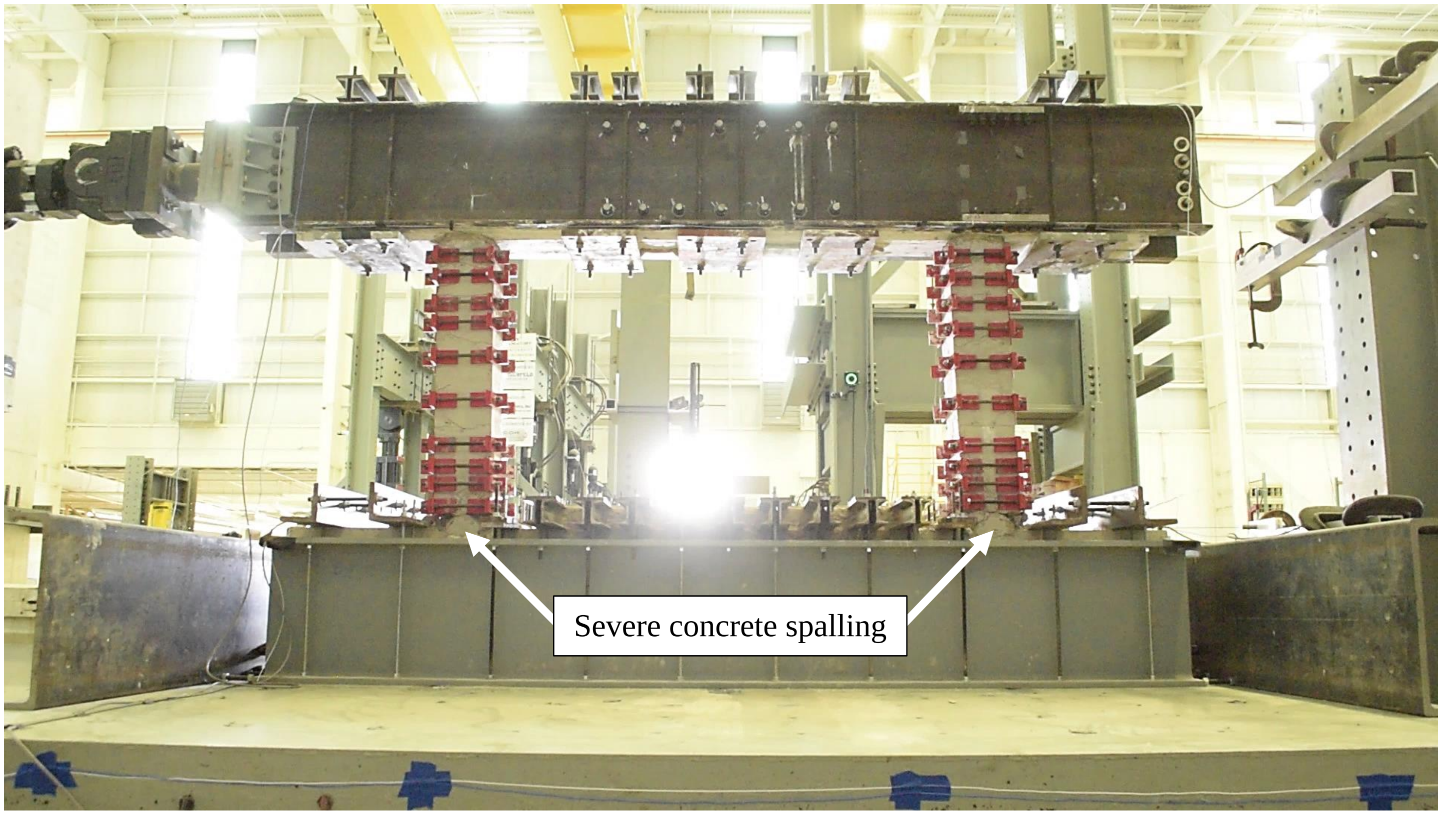

Figure 3-53: Elevation of frame with clamps at end of Series F2-C-S

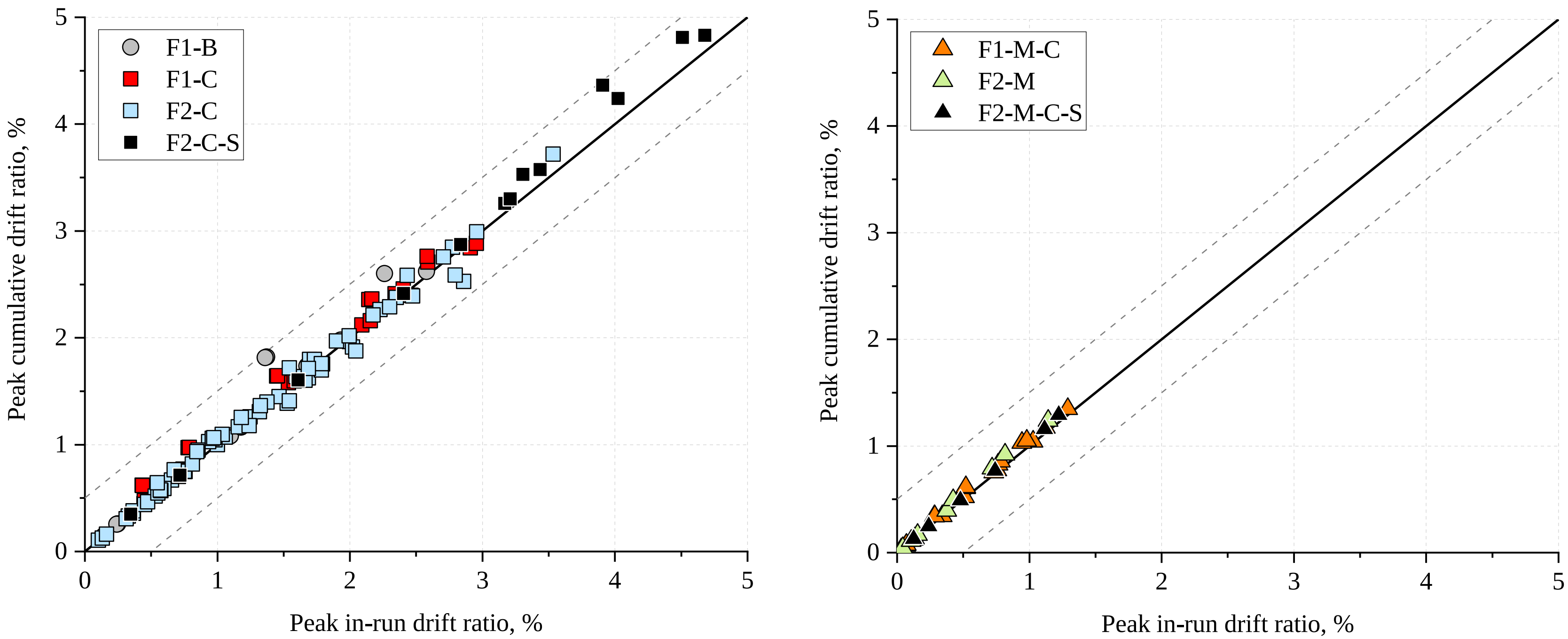

(a) Bare frame and frames with clamps

(b) Infilled frames

Figure 4-1: Comparisons of in-run and cumulative drift demands of frames with and without infill

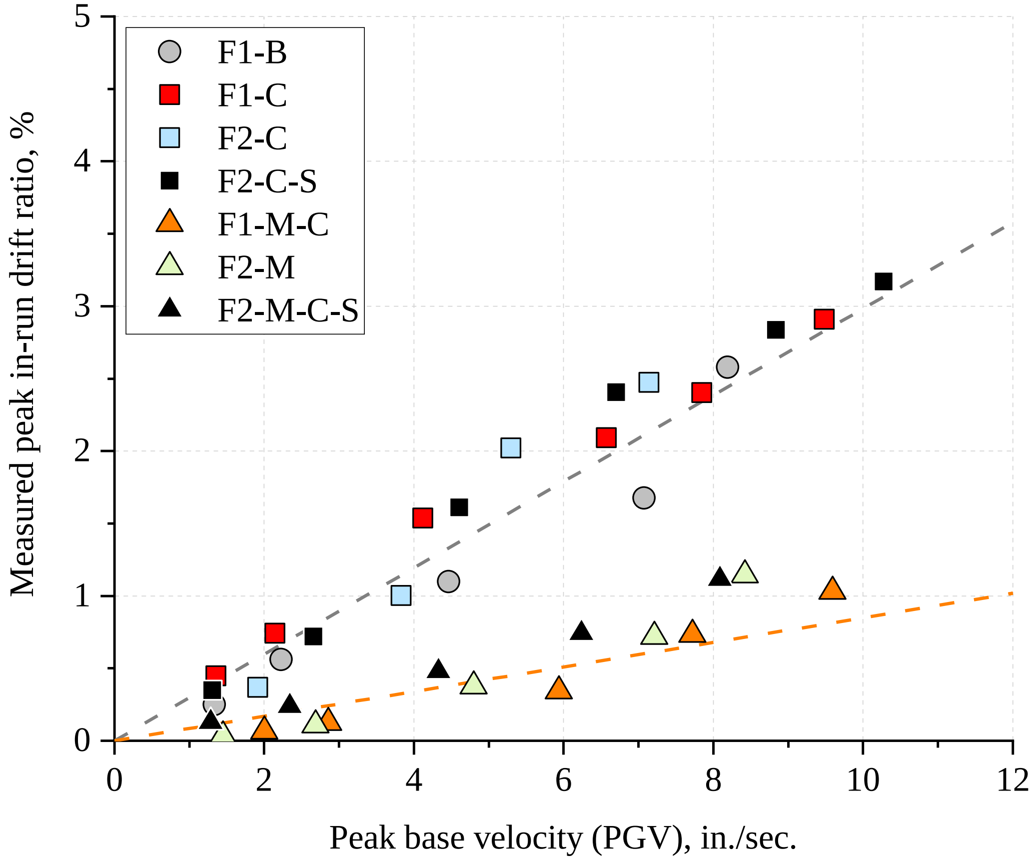

Figure 4-2: Comparisons of drift demands of frames with and without infill

Note: Reference runs (R1) excluding repeat runs (R2, R3) are used in Figure 4-2. Repeats are discussed in Section 4.6.

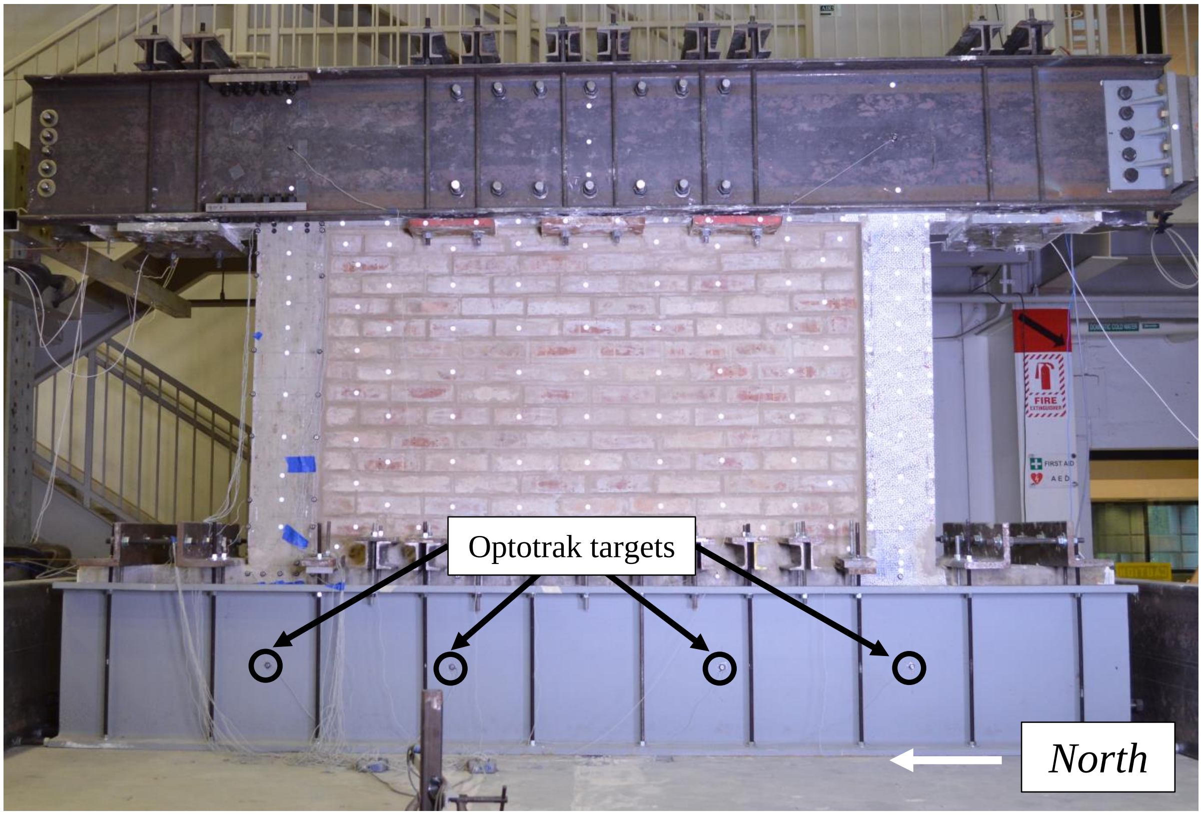

Figure 4-3: Optical targets attached to wide-flange steel beam attached to earthquake simulator

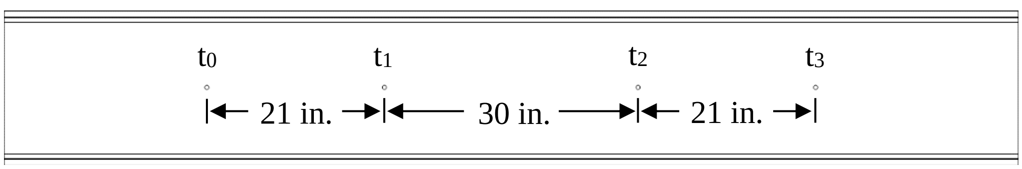

Figure 4-4: Optical target layout

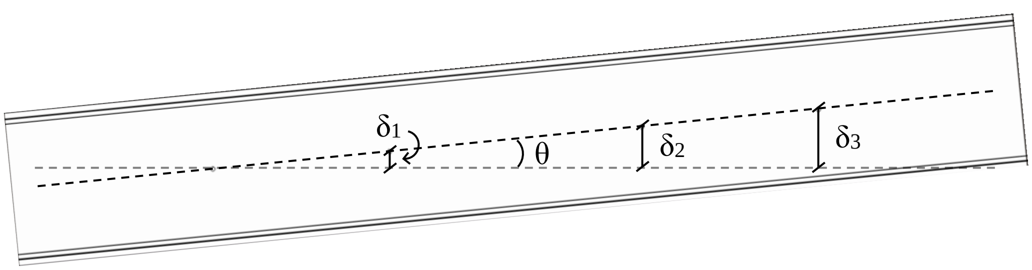

Figure 4-5: Peak displacements of optical targets t_1, t_2, and t_3 relative to optical target t_0

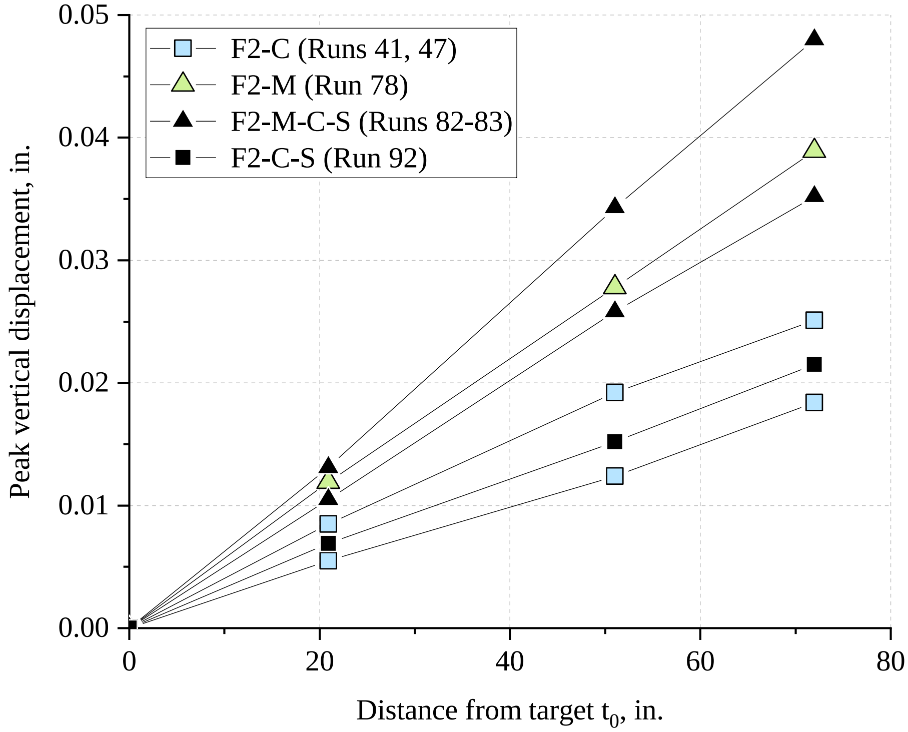

Figure 4-6: Peak vertical displacements of optical targets t_1, t_2, and t_3 relative to optical target t_0 in selected runs of Specimen F2

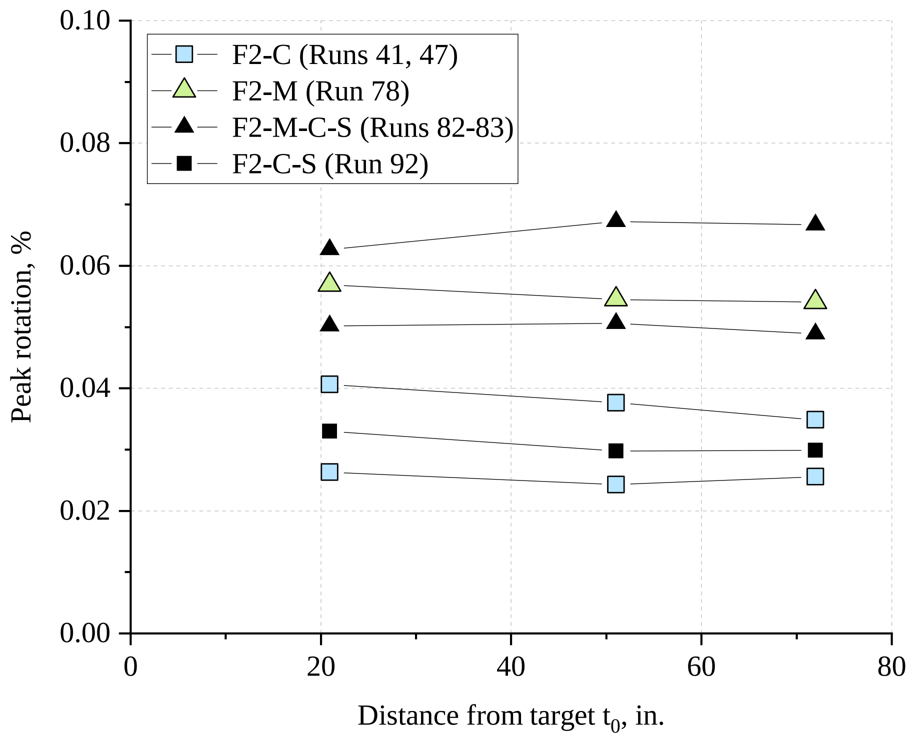

Figure 4-7: Peak rotations of lines drawn from optical target t_0 to optical targets t_1, t_2, and t_3 in selected runs of Specimen F2

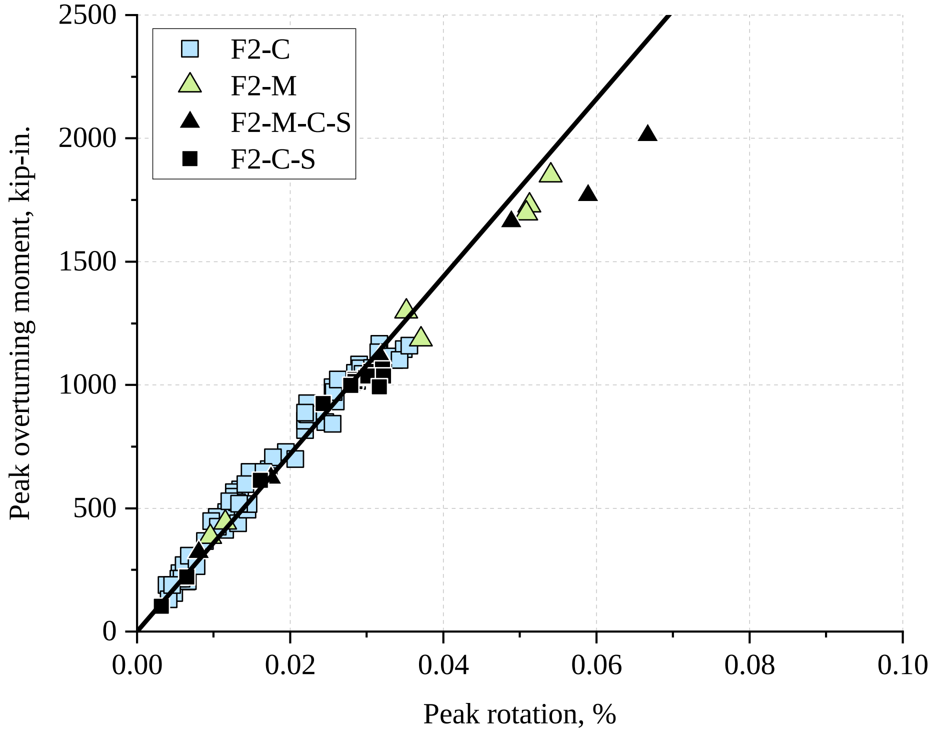

Figure 4-8: Moment-rotation relationship of simulator in runs of Specimen F2

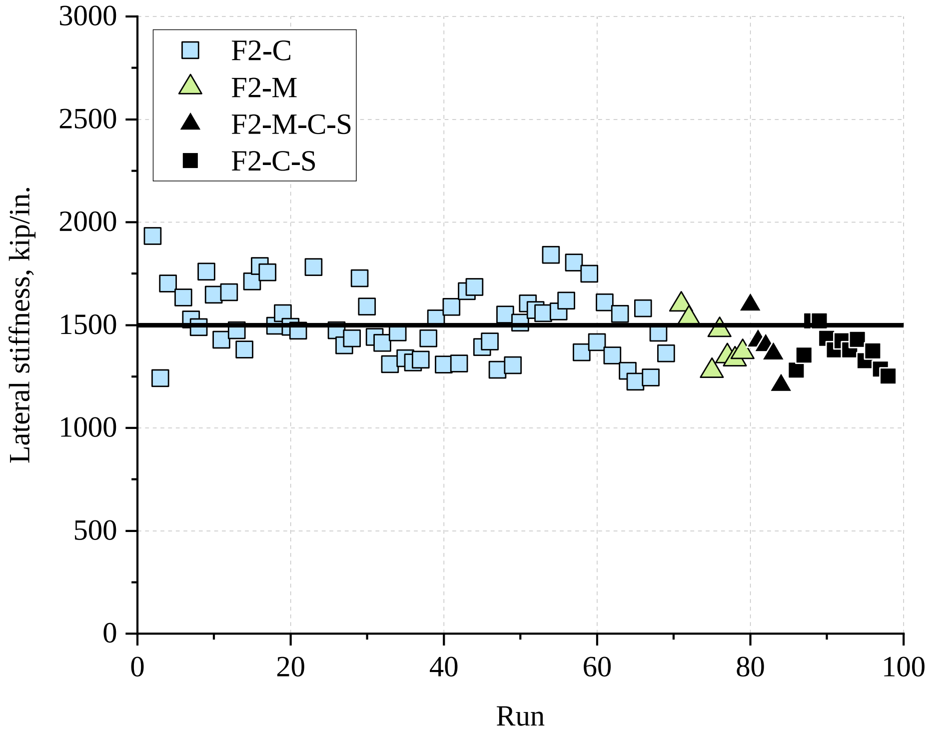

Figure 4-9: Measurements of effective lateral stiffness of simulator in runs of Specimen F2

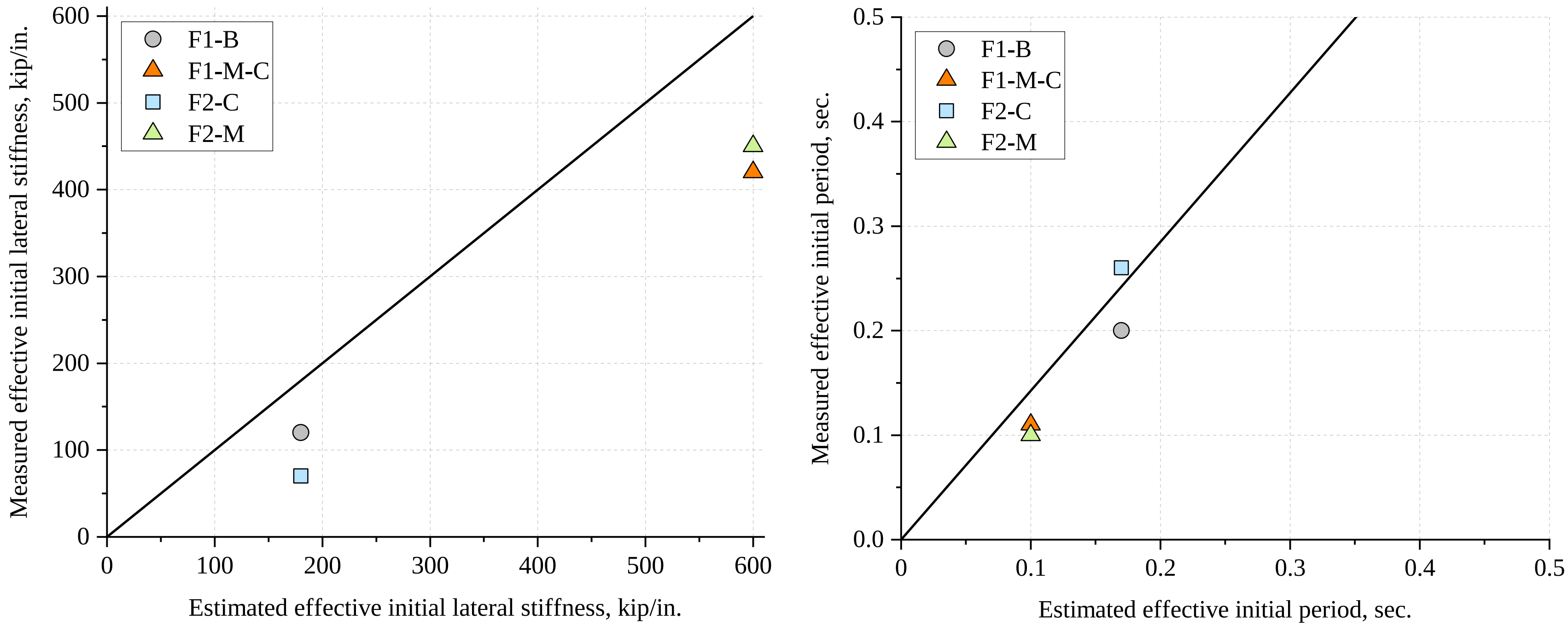

(a) Initial K_{eff} (b) Effective T_o

Figure 4-10: Comparisons of effective initial lateral stiffness and effective initial period

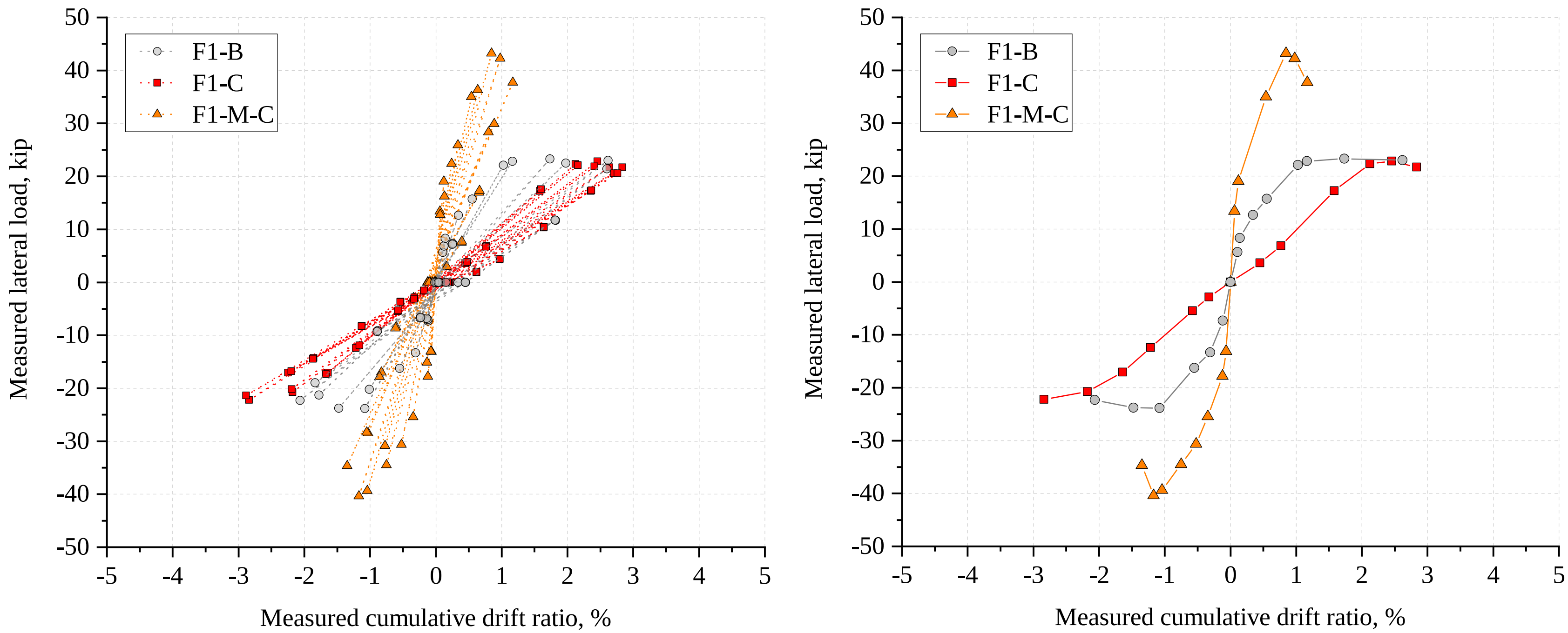

(a) Hysteresis curves (b) Envelopes

Figure 4-11: Force-displacement relationship measured in runs of Specimen F1

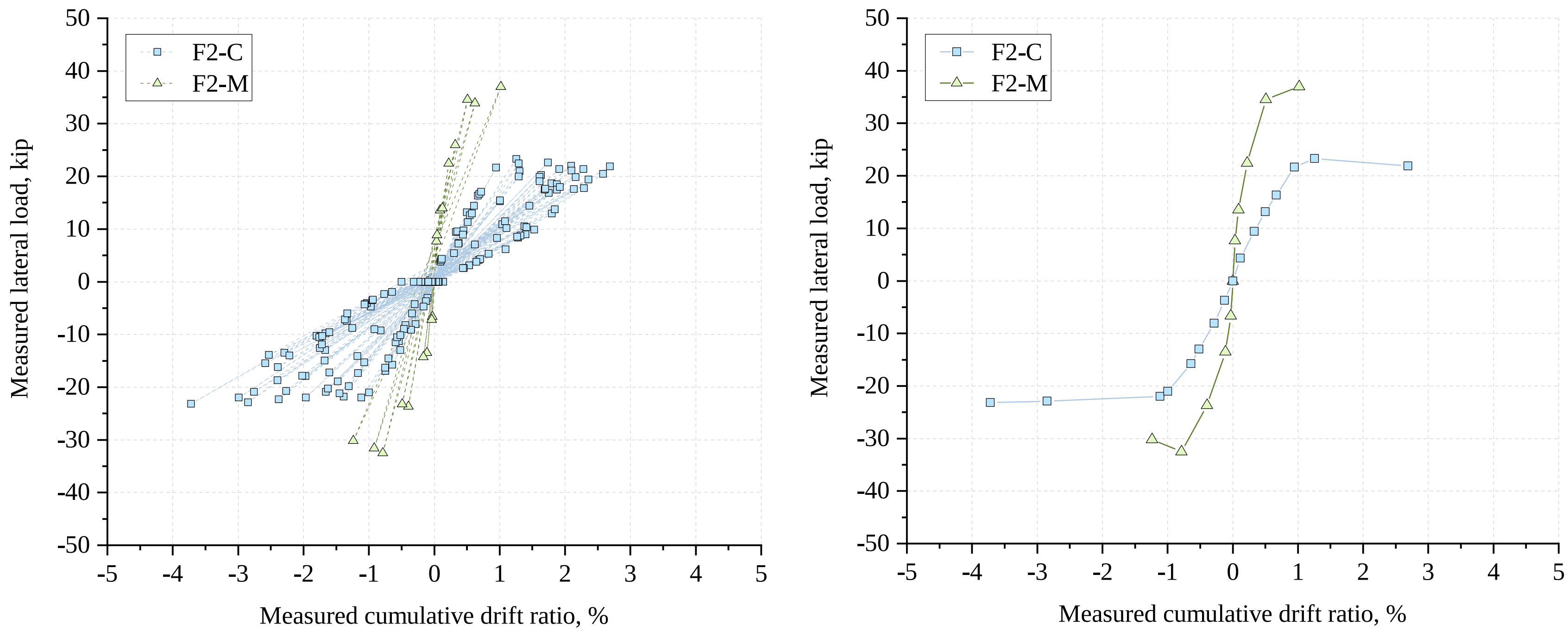

(a) Hysteresis curves (b) Envelopes

Figure 4-12: Force-displacement relationship measured in runs of Series F2-C and F2-M

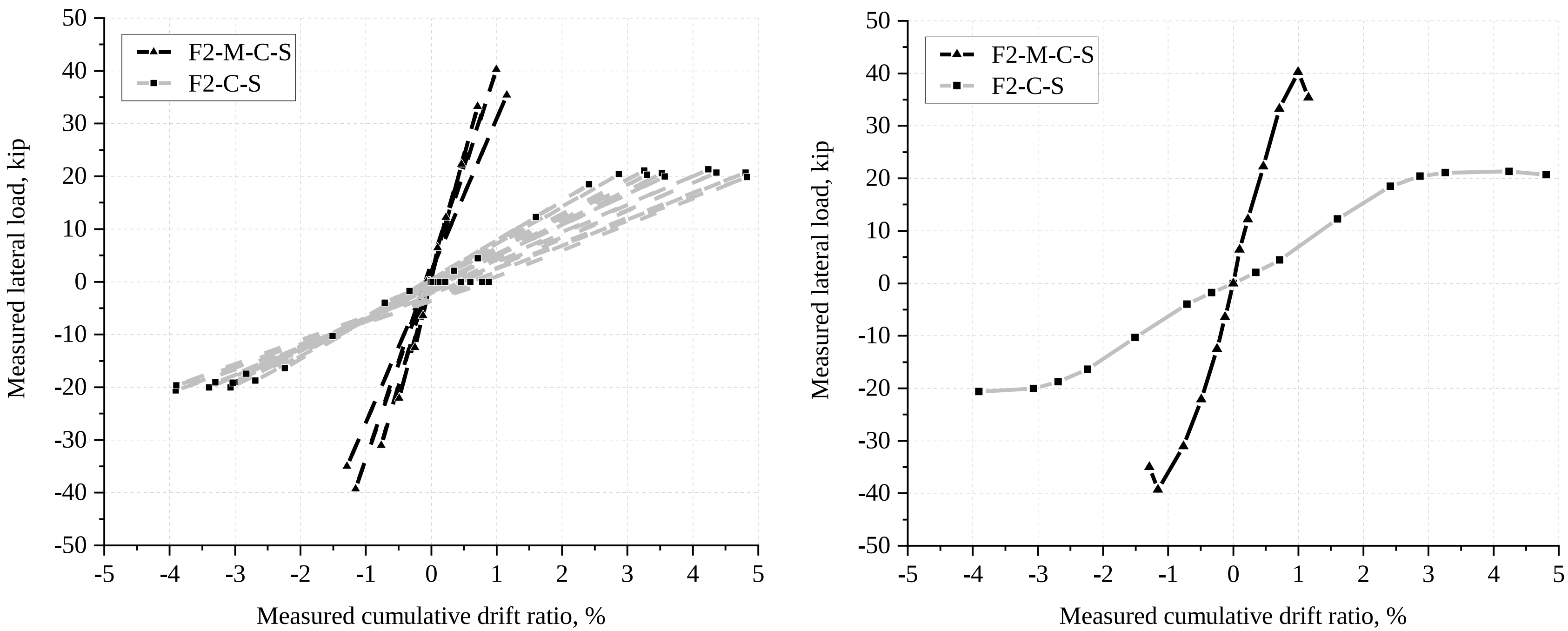

(a) Hysteresis curves

(b) Envelopes

Figure 4-13: Force-displacement relationship measured in runs of Series F2-M-C-S and F2-C-S

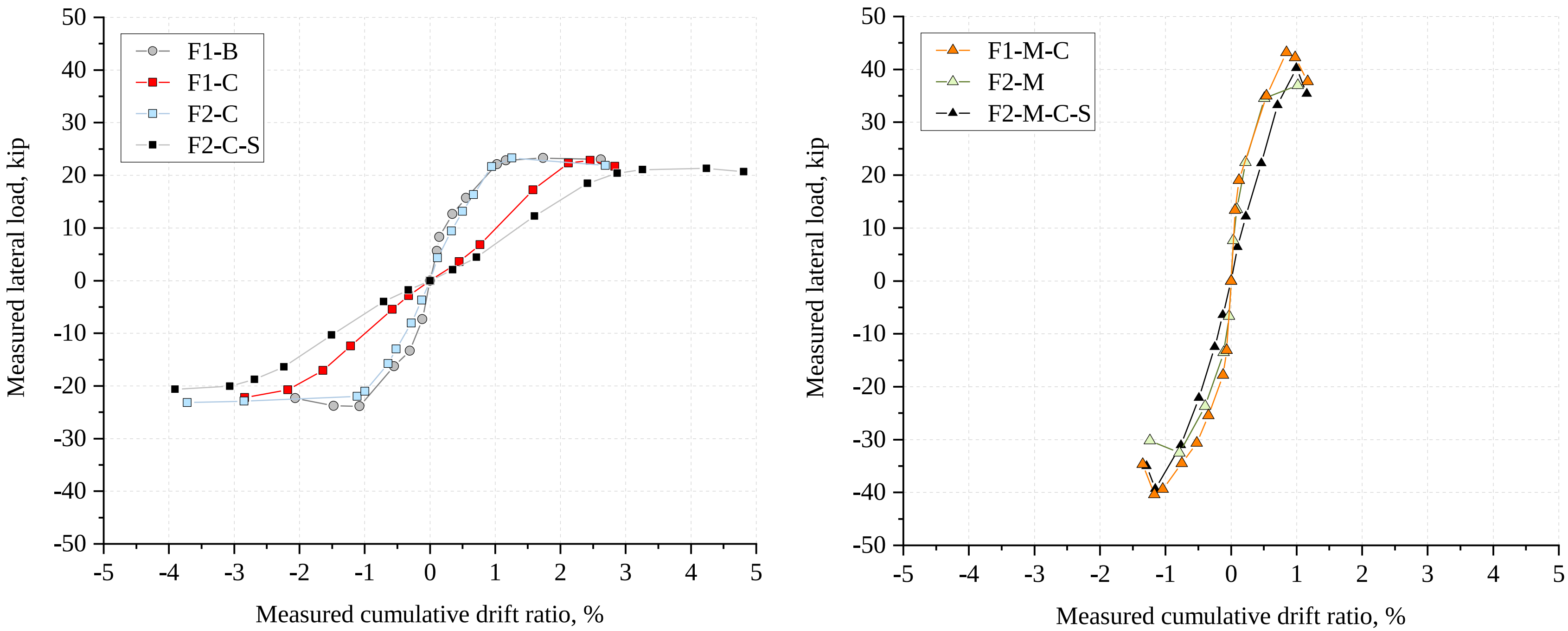

(a) Frames without infill
(b) Frames with infill

Figure 4-14: Measured force-displacement envelopes

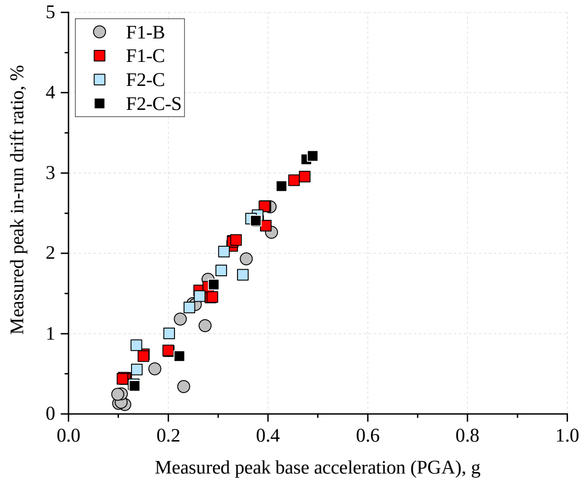

(a-i) PGA, Frames without infill

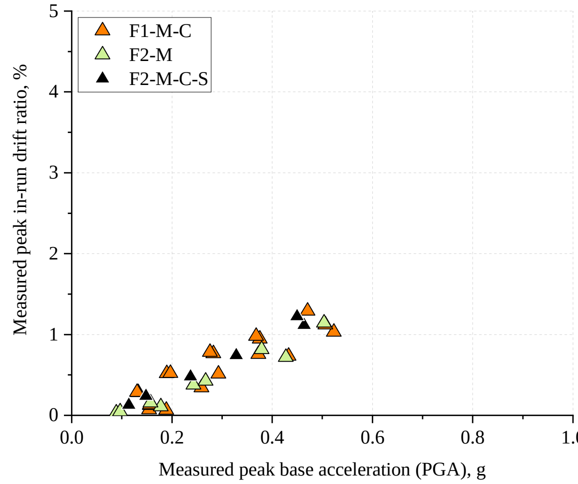

(a-ii) PGA, Frames with infill

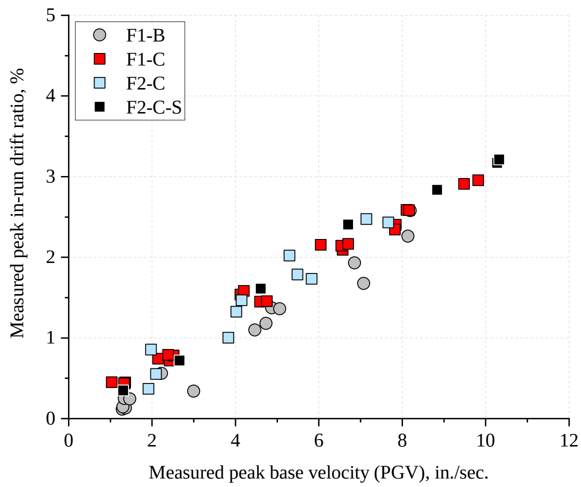

(b-i) PGV, Frames without infill

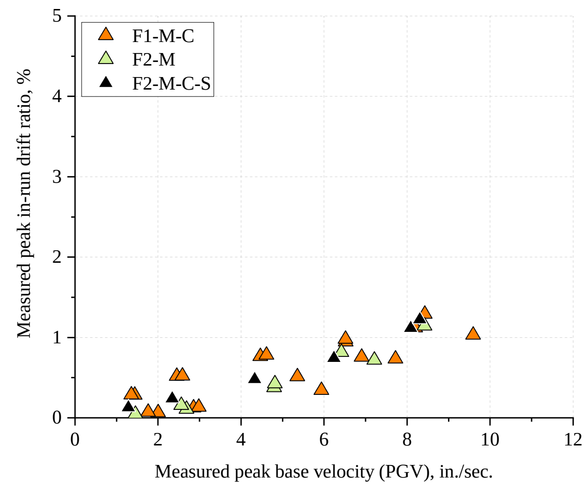

(b-ii) PGV, Frames with infill

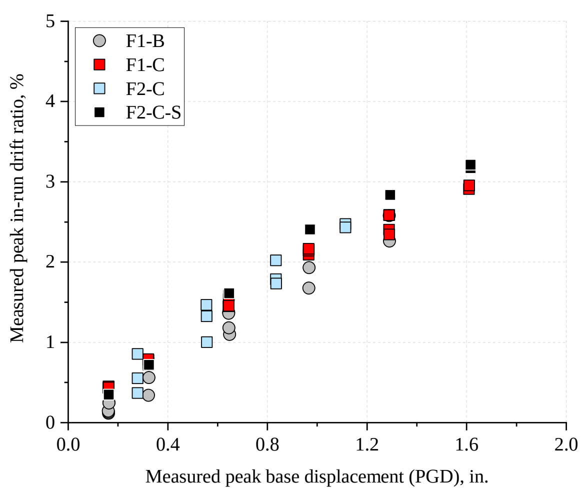

(c-i) PGD, Frames without infill

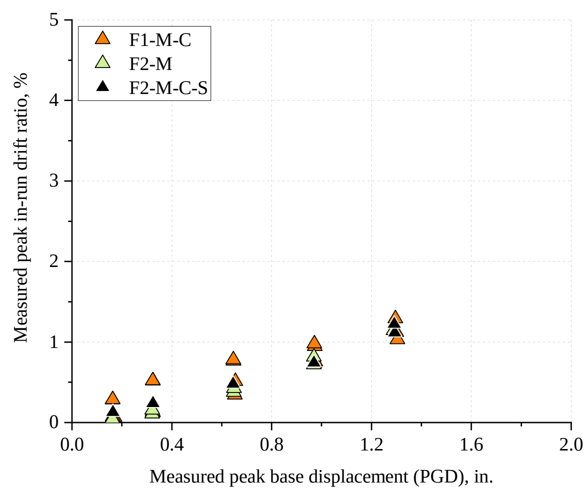

(c-ii) PGD, Frames with infill

Figure 4-15: Variation of drift demands with ground motion parameters in simulations modeled after the El Centro (TC2) motion

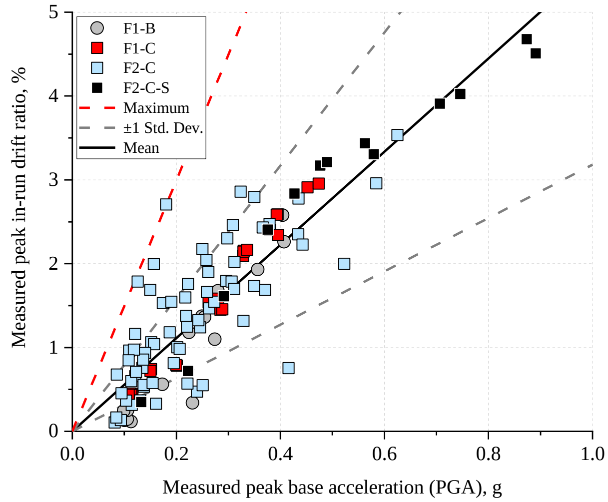

(a) PGA, Frames without infill

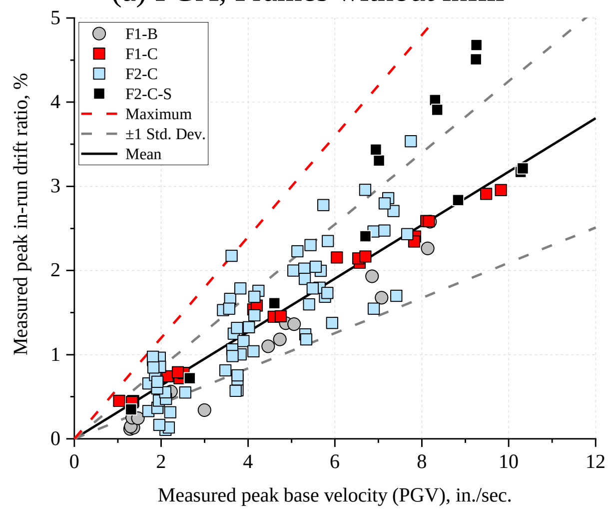

(b) PGV, Frames without infill

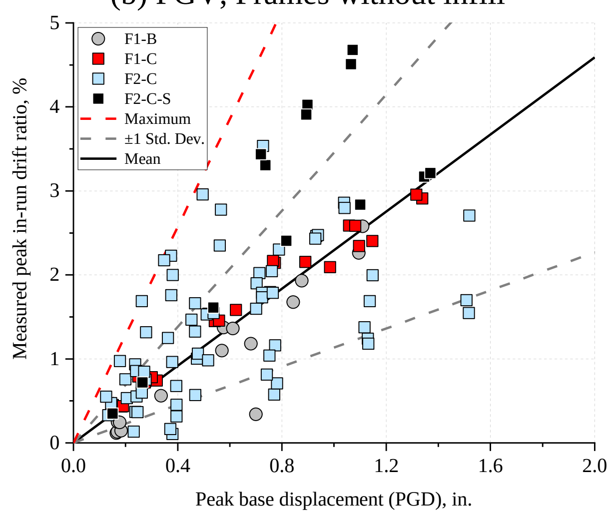

(c) PGD, Frames without infill

Figure 4-16: Variation of drift demands with ground motion parameters in runs of the bare frame and frames with clamps

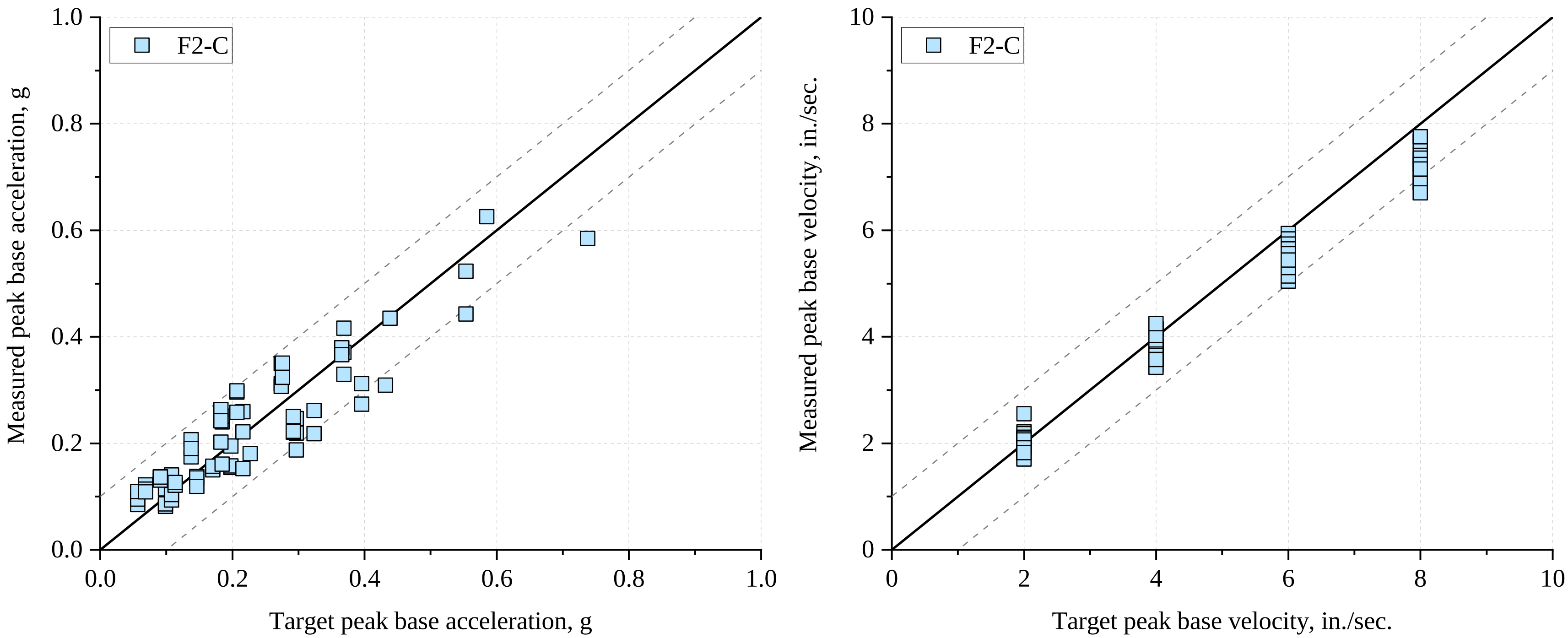

(a) PGA (a) PGV

Figure 4-17: Comparison of measured and target peak base acceleration and peak base velocity in runs of Series F2-C

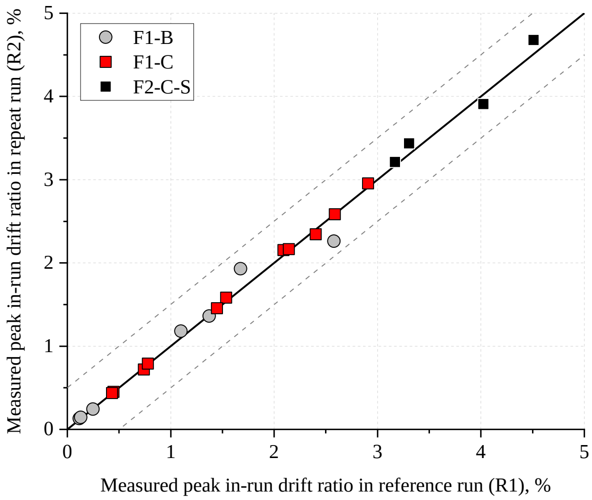

(a-i) R2 vs. R1, Frames without infill

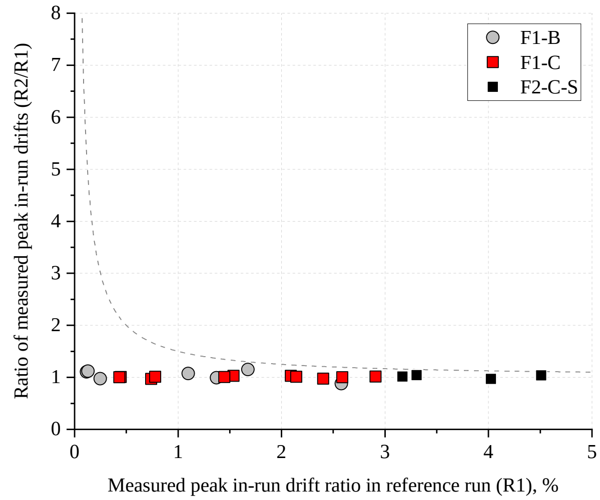

(a-ii) R2/R1, Frames without infill

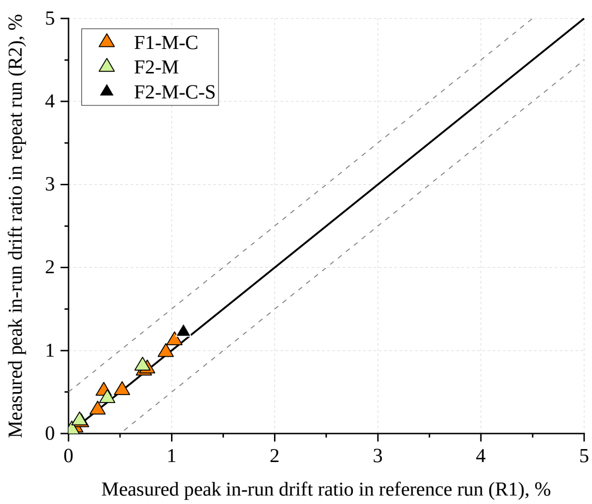

(b-i) R2 vs. R1, Frames with infill

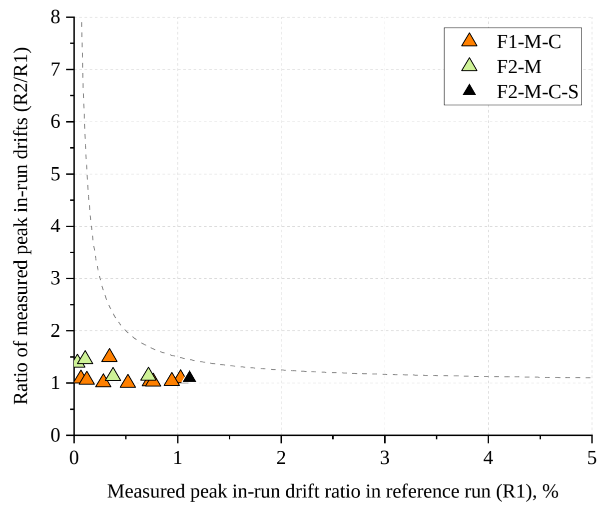

(b-ii) R2/R1, Frames with infill

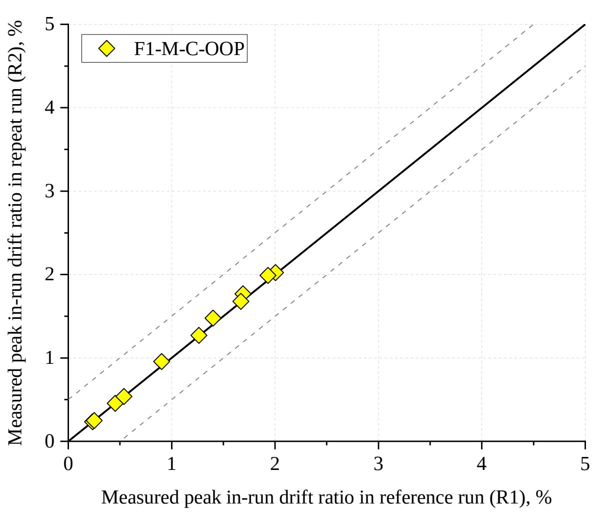

(c-i) R2 vs. R1, Series F1-M-C-OOP

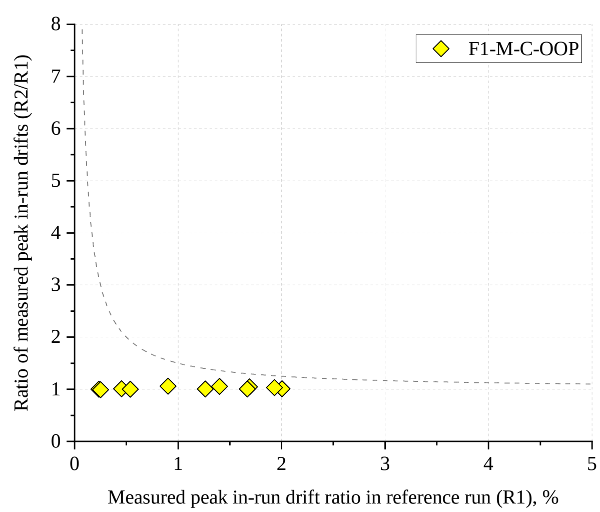

(c-ii) R2/R1, Series F1-M-C-OOP

Figure 4-18: Repeats in consecutive runs

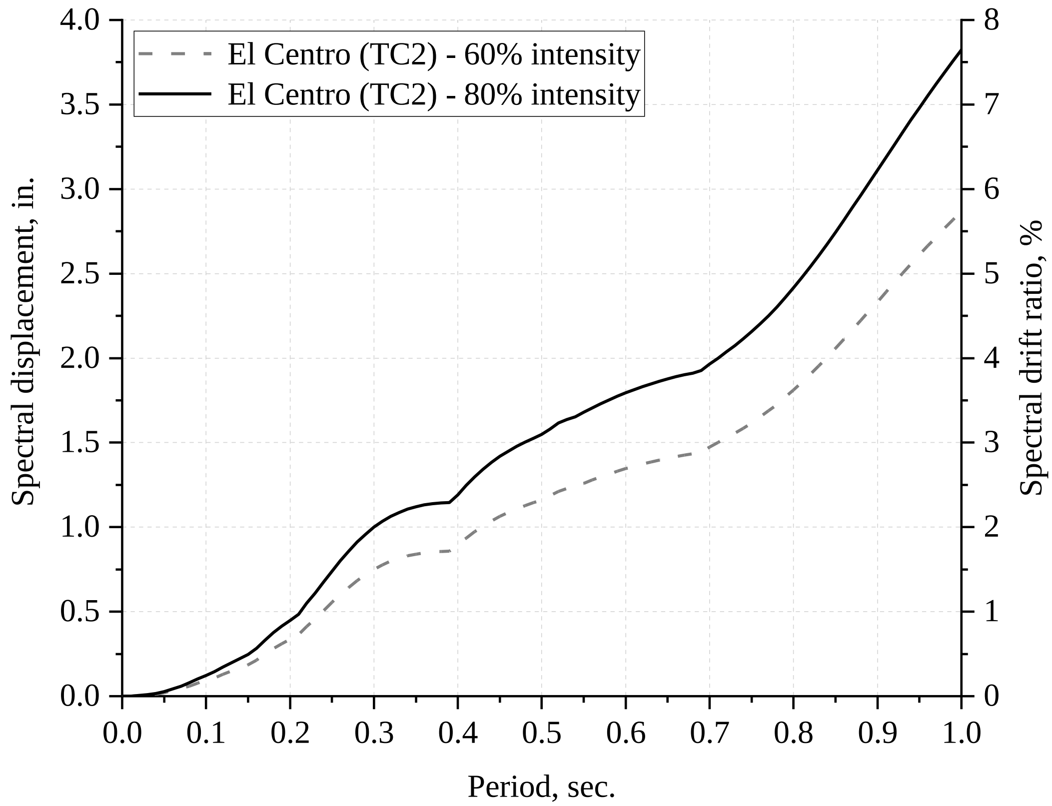

Figure 4-19: Smoothed displacement spectra for El Centro (TC2) motion

Note: Smoothed displacement spectra are discussed in Section 5.3.3.

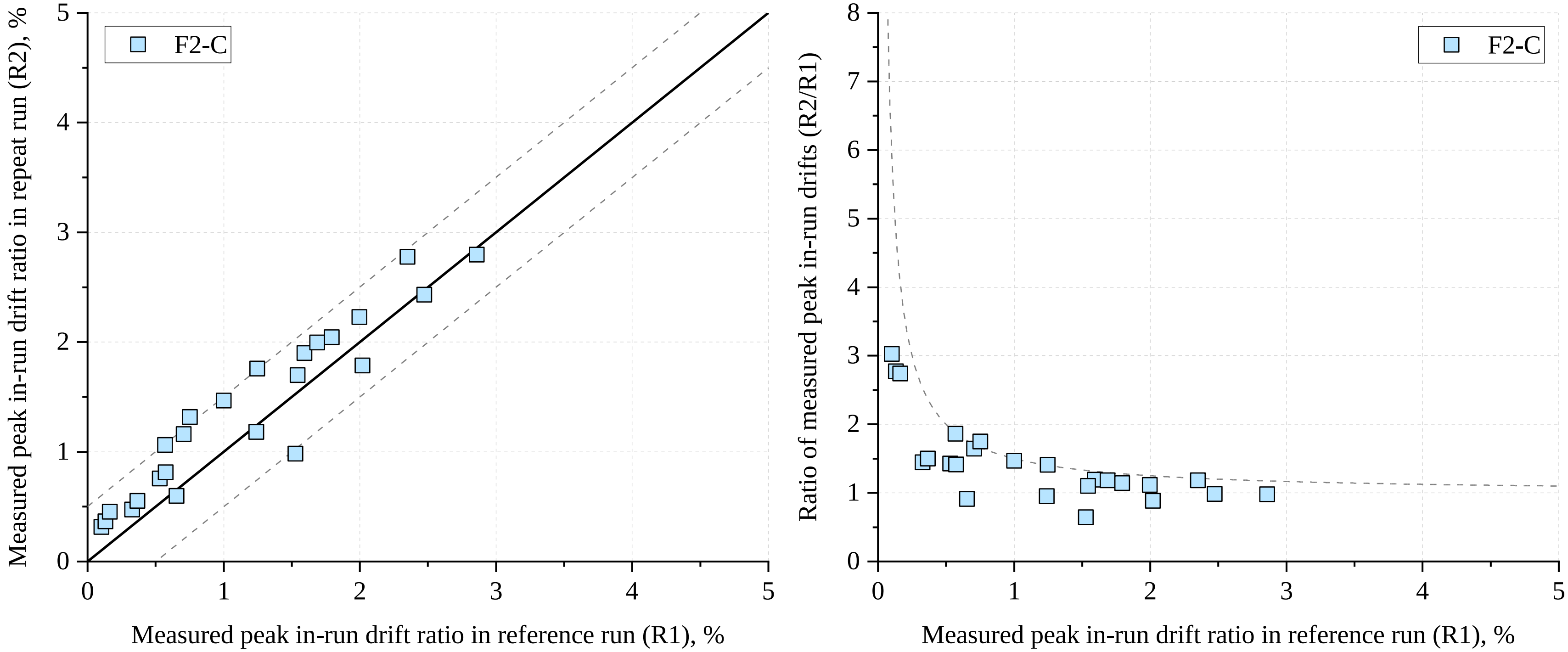

(a) R2 vs. R1 (b) R2/R1

Figure 4-20: Repeats separated by motions at similar intensities of Series F2-C

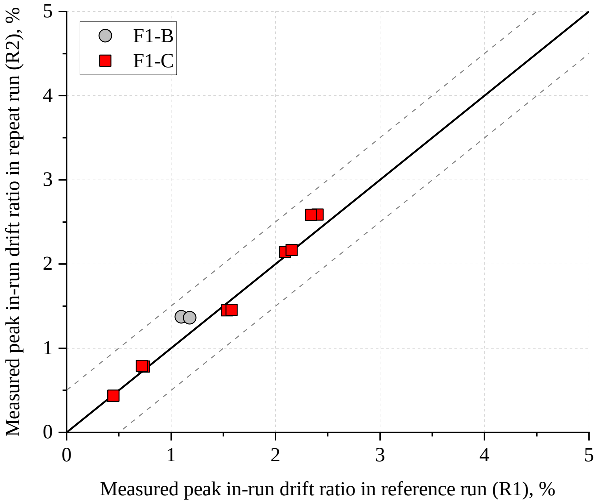

(a-i) R2 vs. R1, Frames without infill

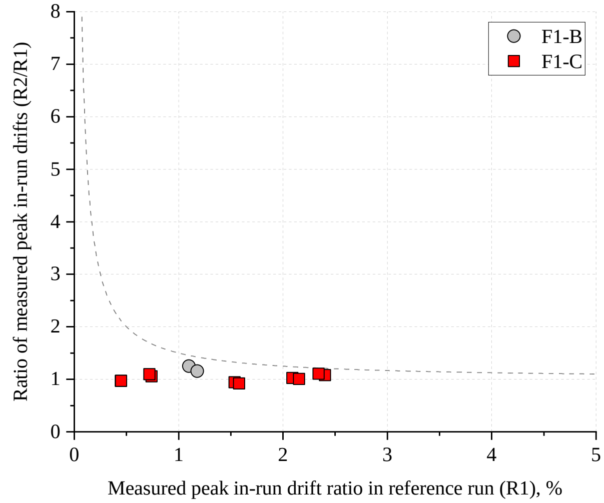

(a-ii) R2/R1 vs. R1, Frames without infill

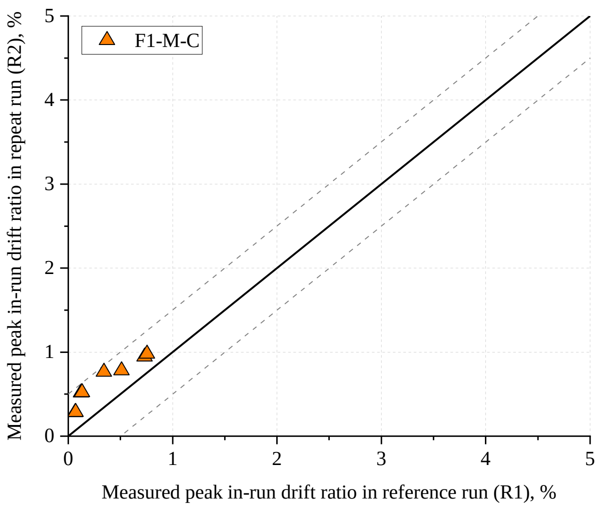

(b-i) R2 vs. R1, Frames with infill

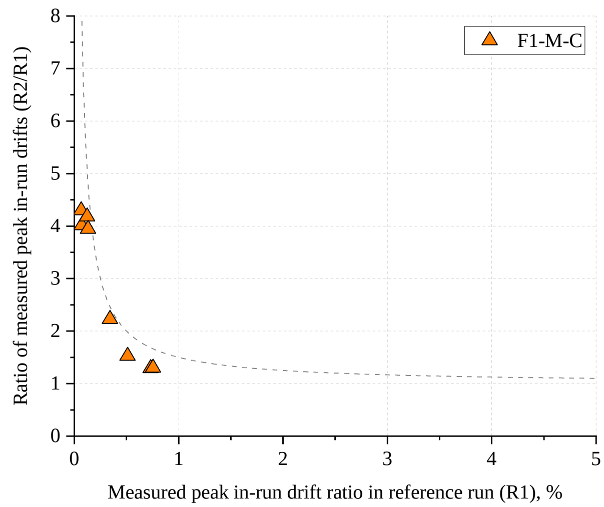

(b-ii) R2/R1 vs. R1, Frames with infill

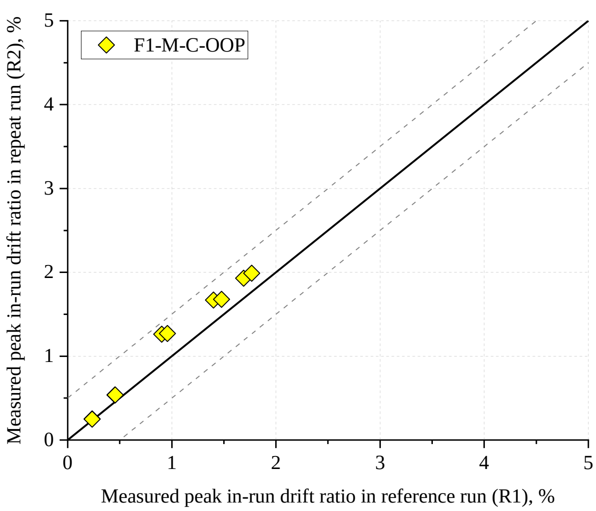

(c-i) R2 vs. R1, Series F1-M-C-OOP

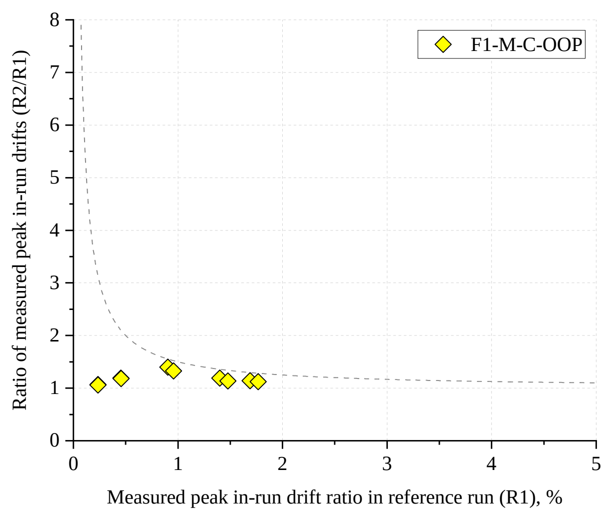

(c-ii) R2/R1 vs. R1, Series F1-M-C-OOP

Figure 4-21: Repeats separated by at least one stronger motion

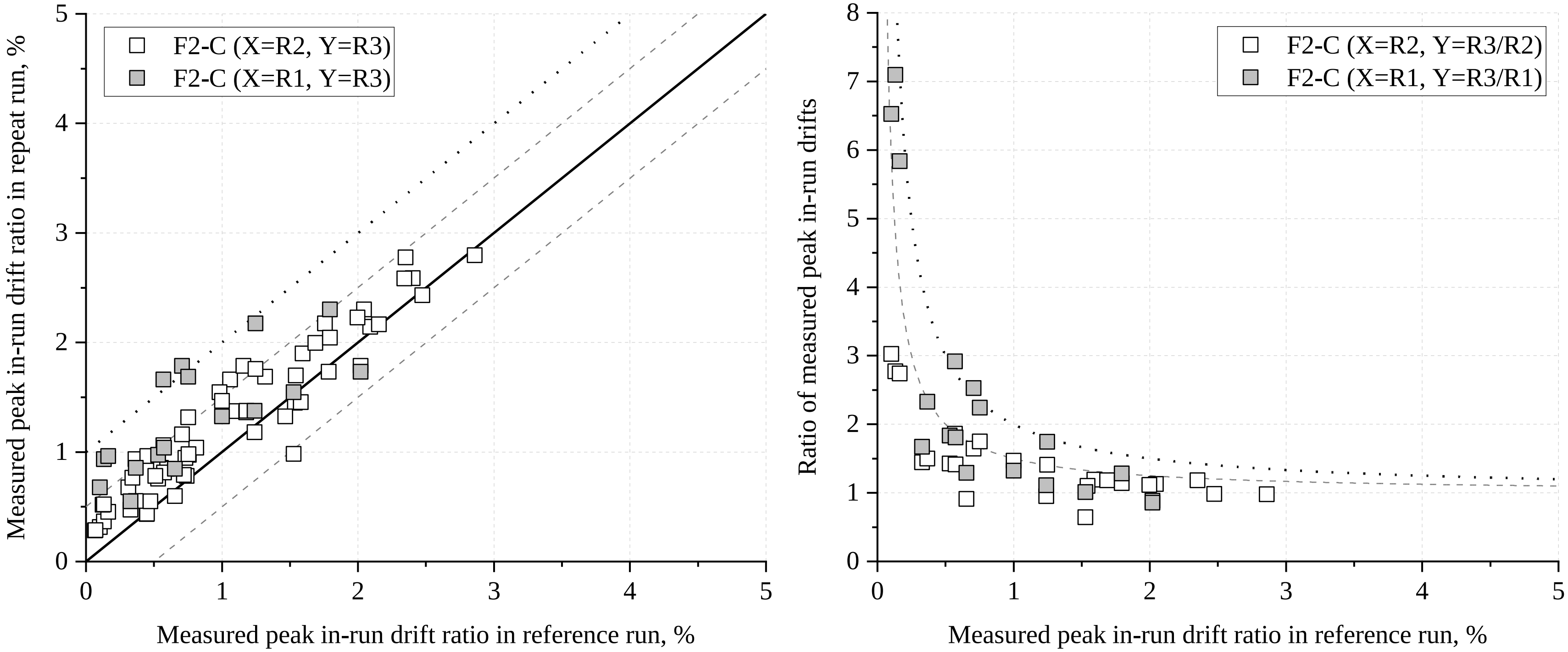

(a) R3 vs. R2, R3 vs. R1

(b) R3/R2 vs. R2, R3/R1 vs. R1

Figure 4-22: Repeats separated by at least one stronger motion of Series F2-C

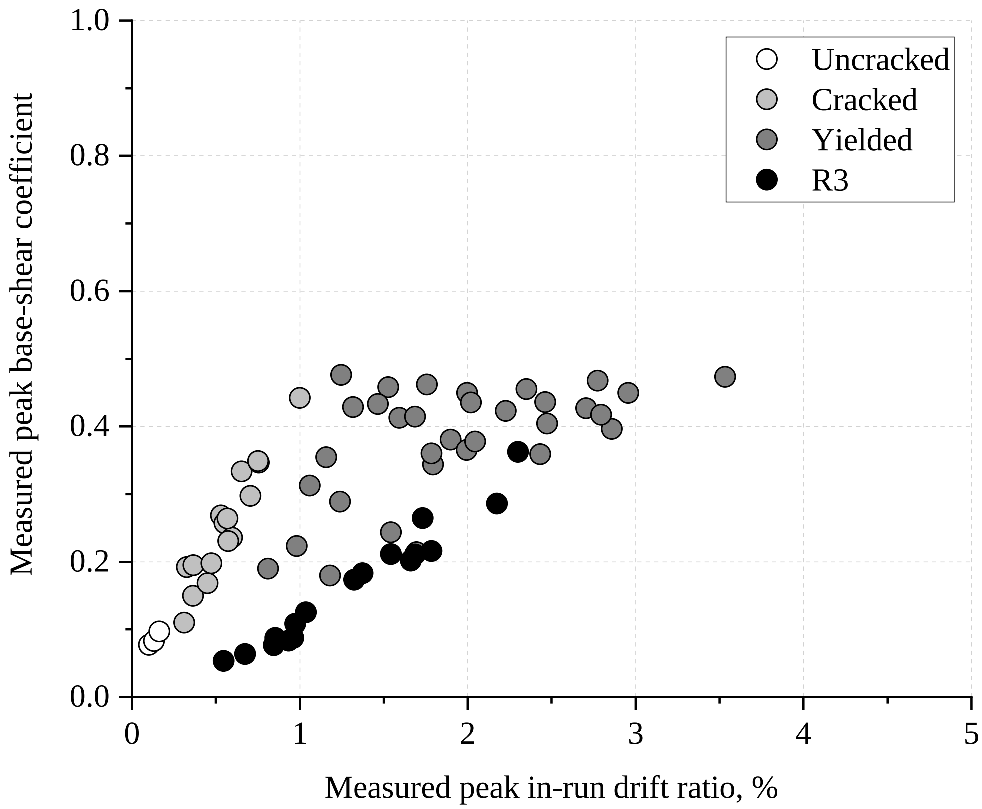

Figure 4-23: Force-displacement relationship in runs of Series F2-C

Note: Measurements of peak in-run drift ratios were used in Figure 4-23. ‘Cracked’ data points labeled with light gray circles indicate runs of the cracked specimen in the linear range of response.

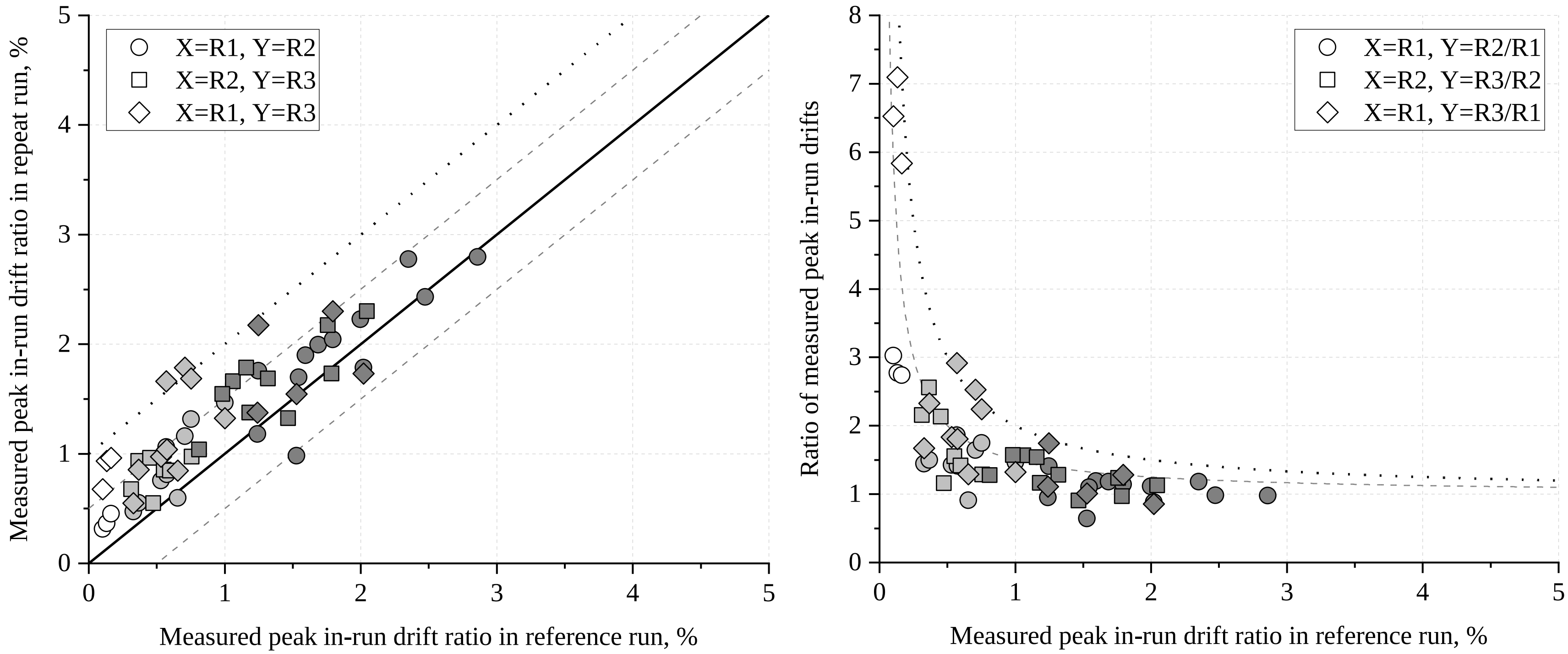

(a) R2 vs. R1, R3 vs. R2, R3 vs. R1

(b) R2/R1 vs. R1, R3/R2 vs. R2, R3/R1 vs. R1

Figure 4-24: Repeats in runs of Series F2-C

Note: Data points labeled in ‘white’ indicate reference runs of the uncracked specimen, ‘light gray’ indicate reference runs of the cracked specimen, and ‘dark gray’ indicate reference runs of the yielded specimen as depicted in Figure 4-23.

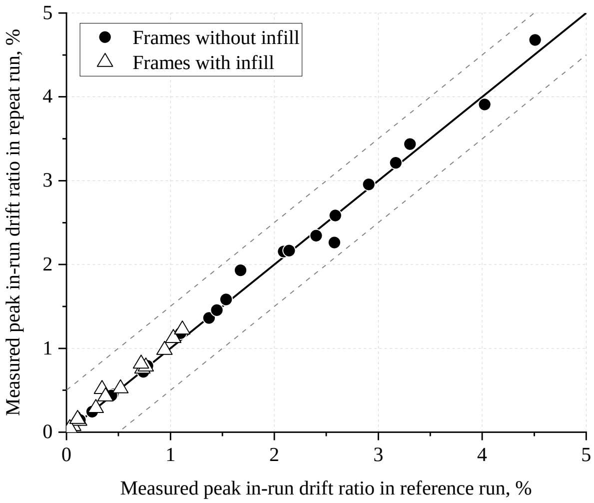

(a-i) R2 vs. R1

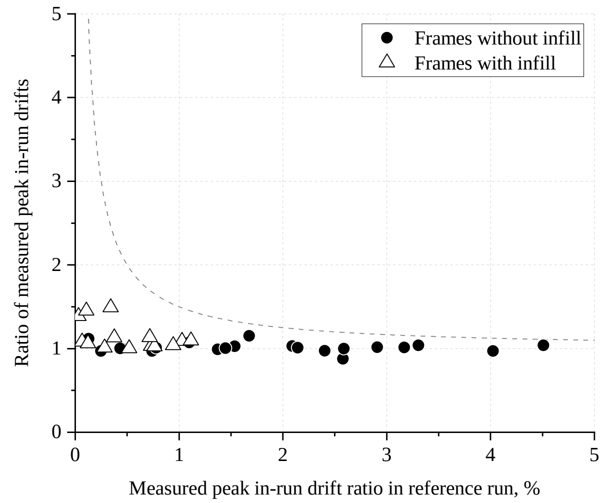

(a-ii) R2/R1 vs. R1

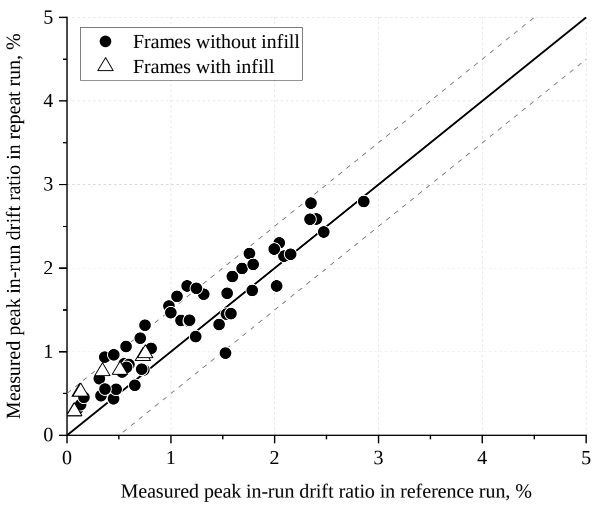

(b-i) R2 vs. R1, R3 vs. R2

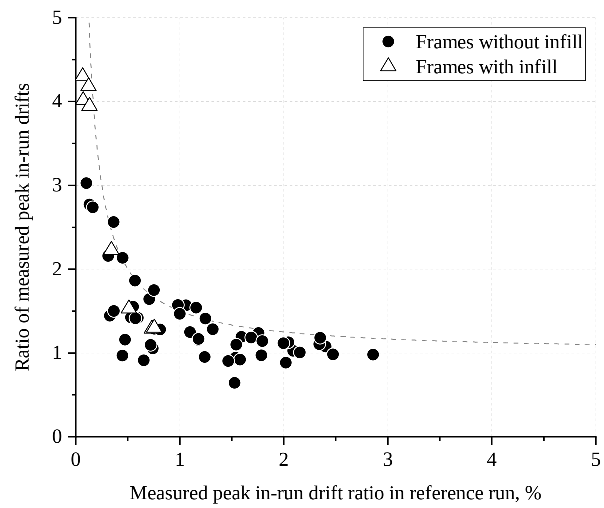

(b-ii) R2/R1 vs. R1, R3/R2 vs. R2

Figure 4-25: Effect of repeats on drift demands

Note: Plots at top show repeats in consecutive simulations [Figure 4-25 (a)] and plots at bottom show repeats in simulations separated by more-demanding motions [Figure 4-25 (b)].

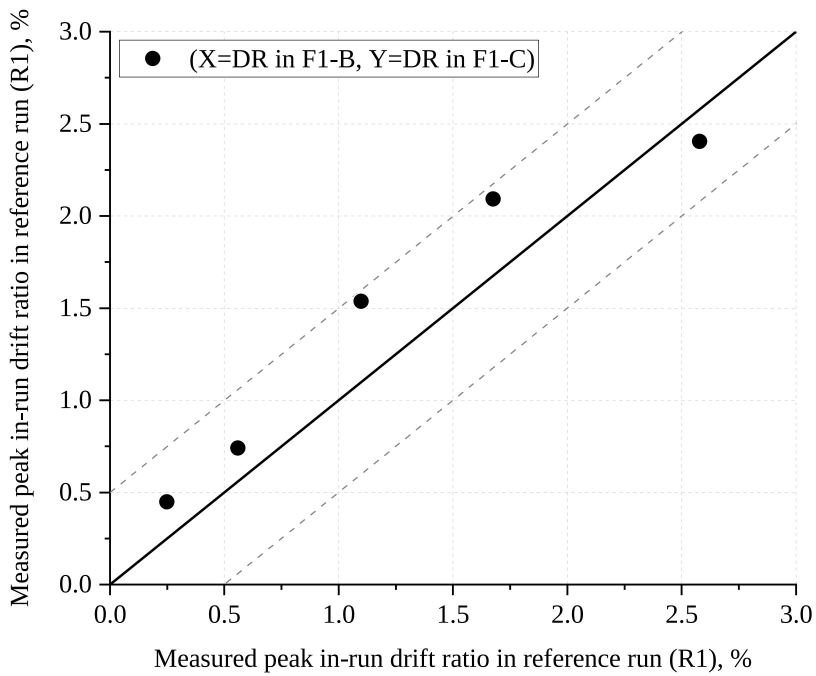

(a) Frames without infill

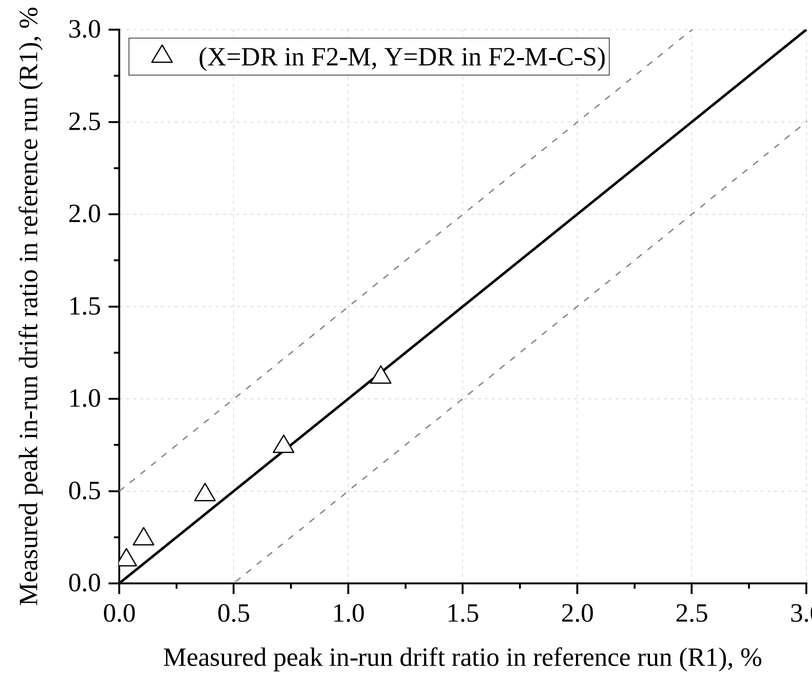

(b) Frames with infill

Figure 4-26: Effect of repairs on drift demands

Note: Drift ratios of repaired specimens are plotted on y-axes and drift ratios of the compared 'pristine' specimens are plotted on x-axes. Axes are plotted up to drift ratios of 3%.

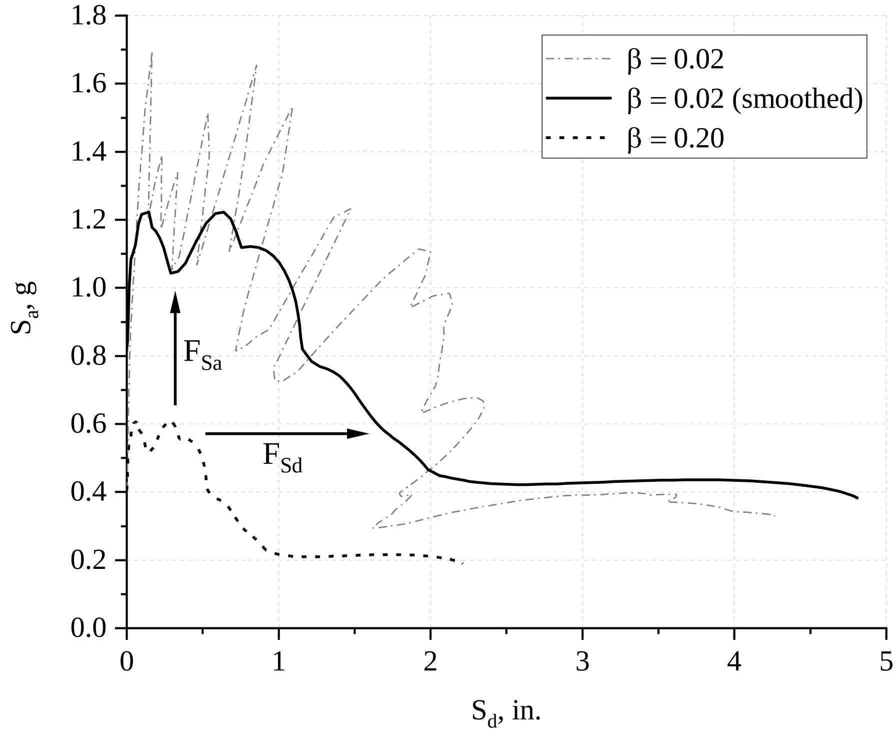

Figure 5-1: Amplification of linear spectra calculated for a damping ratio of 20%

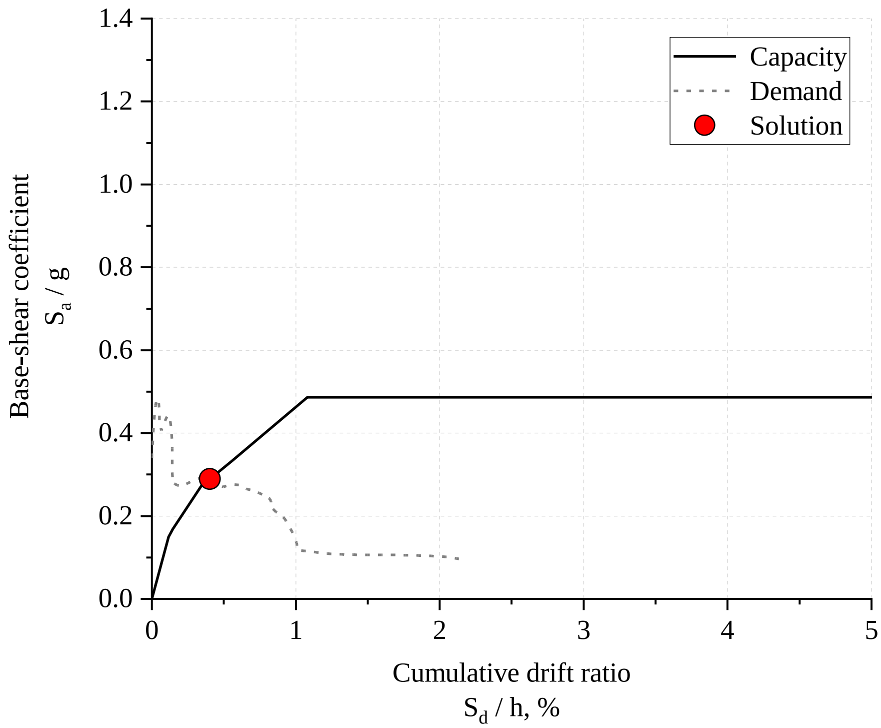

Figure 5-2: Capacity Spectrum Method

Note: The measured force-displacement curve is labeled as 'Capacity' and the smoothed response spectrum is labeled as 'Demand'.

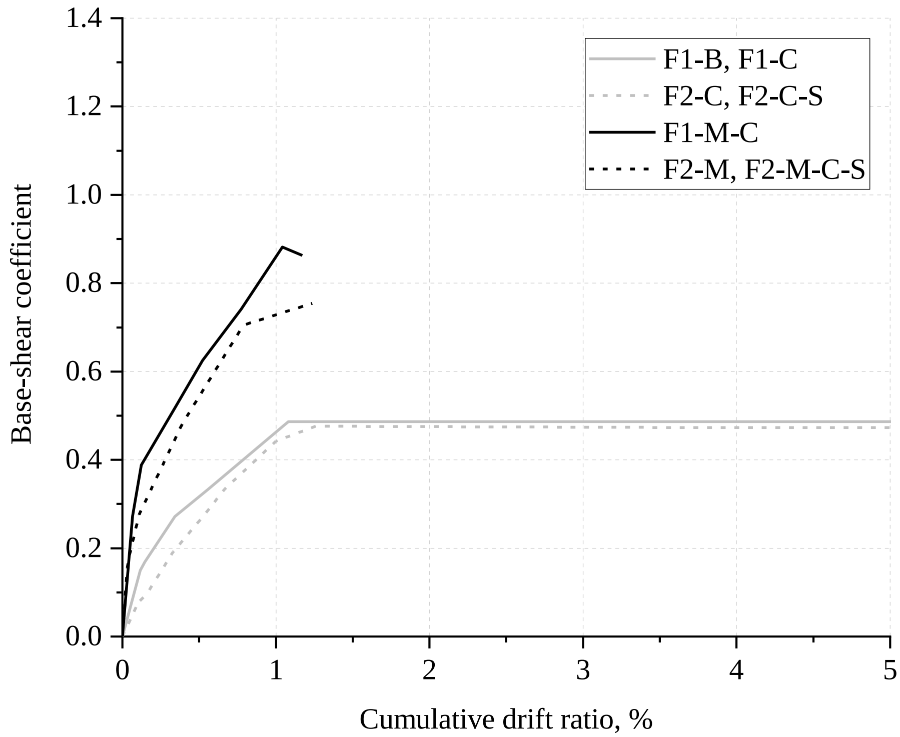

Figure 5-3: Measured force-displacement curves of frames with and without infill

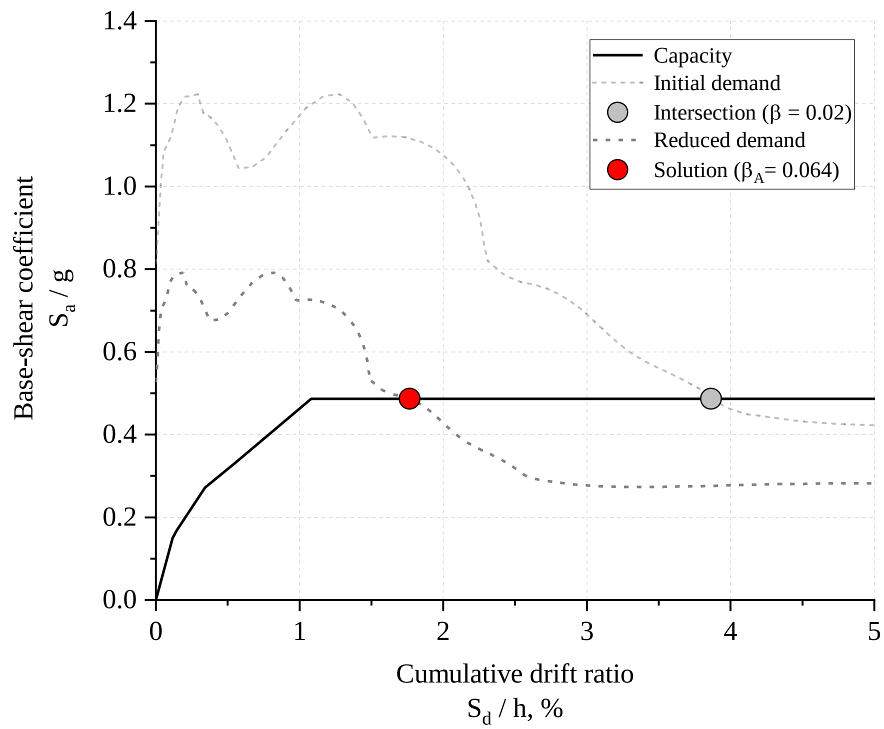

Figure 5-4: Capacity Spectrum Method using iterative procedure (Eqs. 3-5) to reduce demand

Note: Initial demand is calculated using a damping ratio β = 0.02.

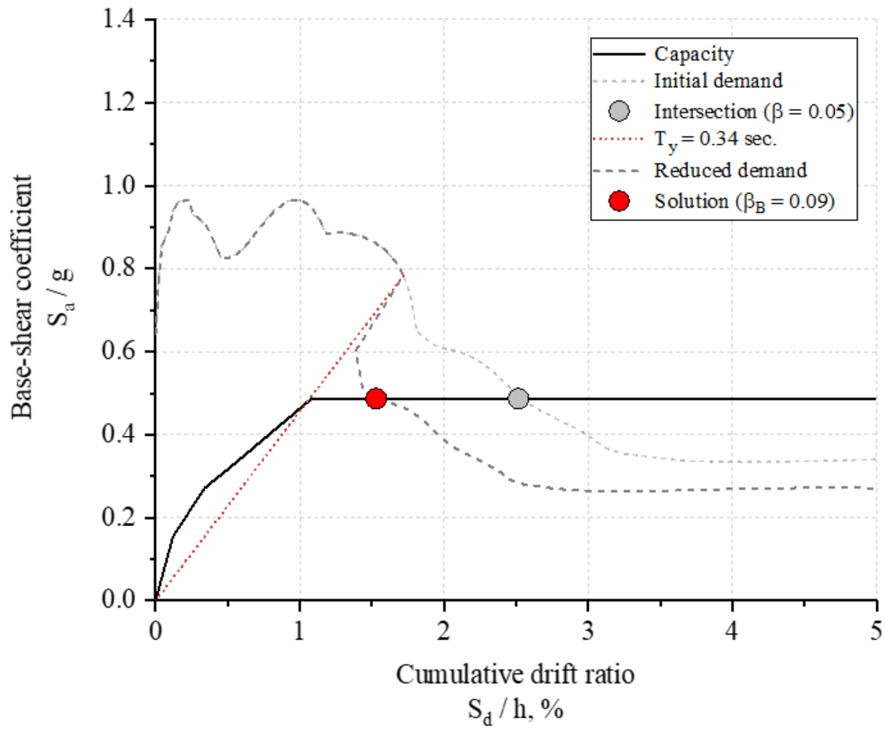

Figure 5-5: Capacity Spectrum Method using iterative procedure (Eqs. 6-8) to reduce demand

Note: Initial demand is calculated using a damping ratio β = 0.05.

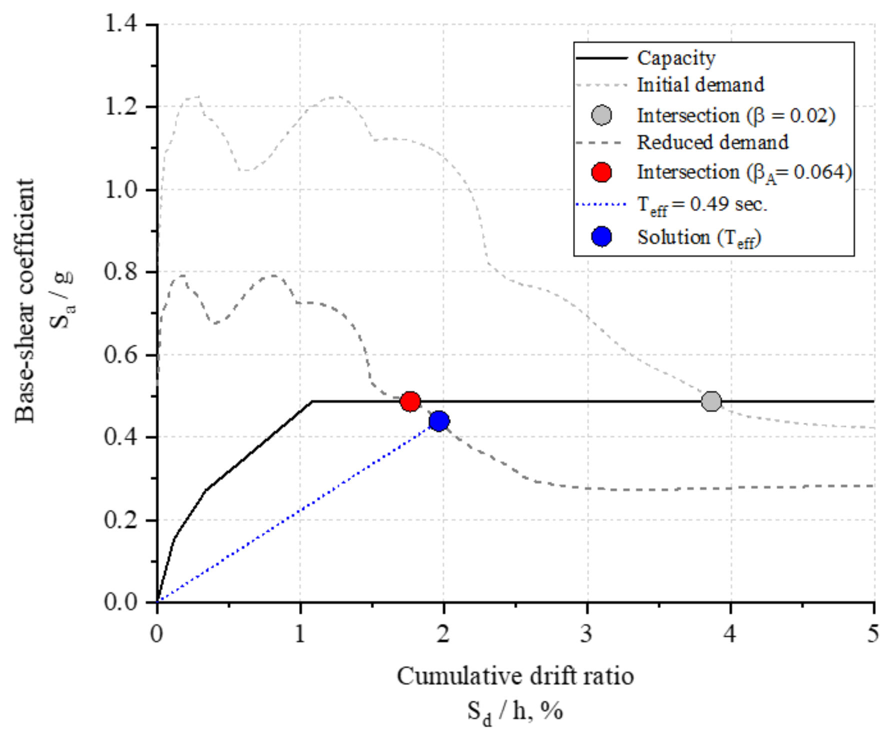

Figure 5-6: Method 1 - Capacity Spectrum Method using iterative procedure (Eqs. 3-5) and effective period T_{eff}

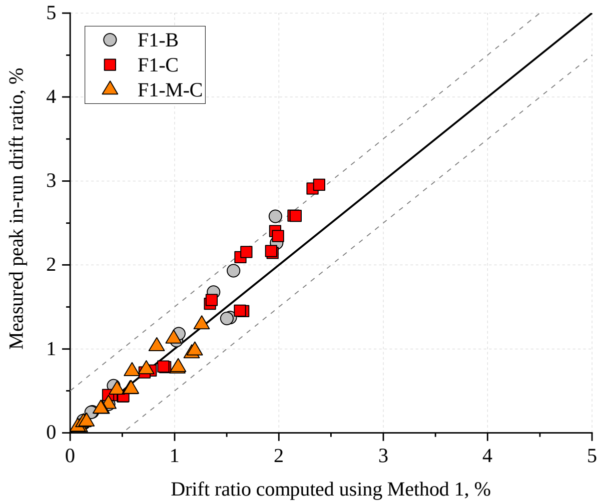

(a-i) Method 1, Specimen F1

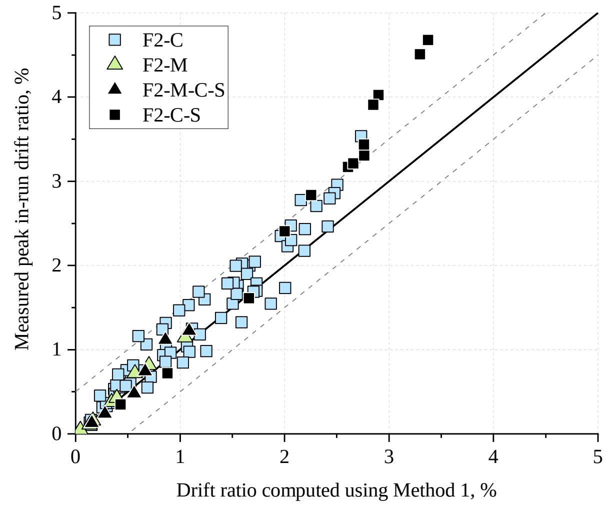

(a-ii) Method 1, Specimen F2

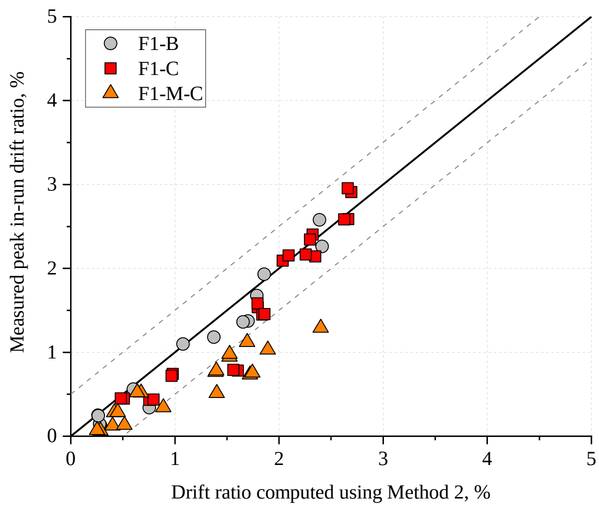

(b-i) Method 2, Specimen F1

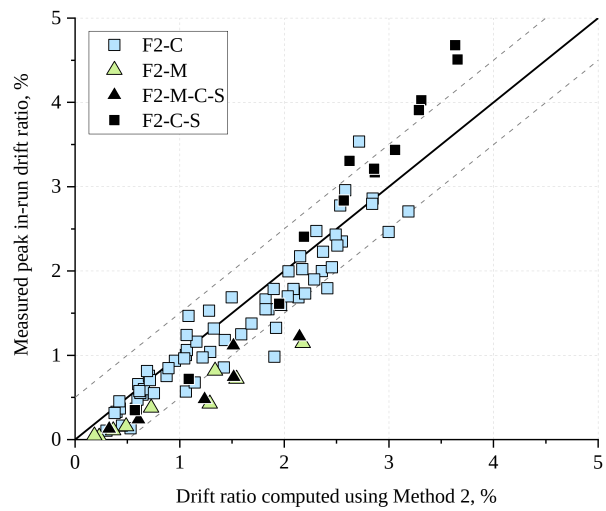

(b-ii) Method 2, Specimen F2

Figure 5-7: Comparisons of measured and estimated drift computed using Methods 1 and 2

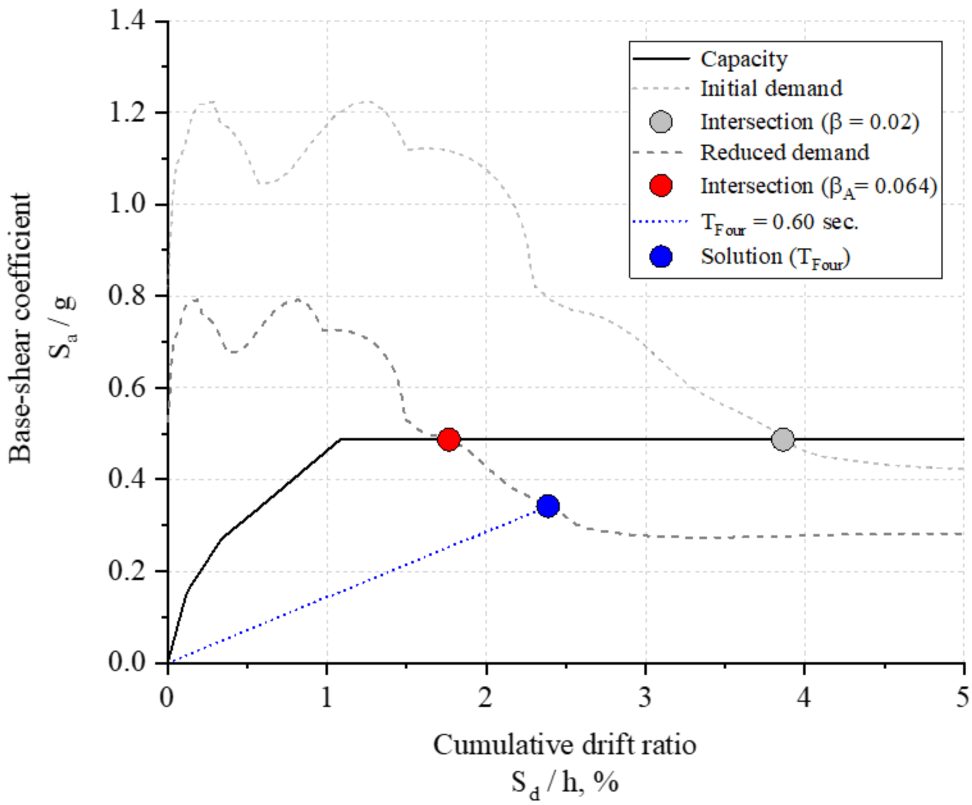

Figure 5-8: Method 2 - Capacity Spectrum Method using iterative procedure (Eqs. 5-3 through 5-5) and Fourier period T_{Four}

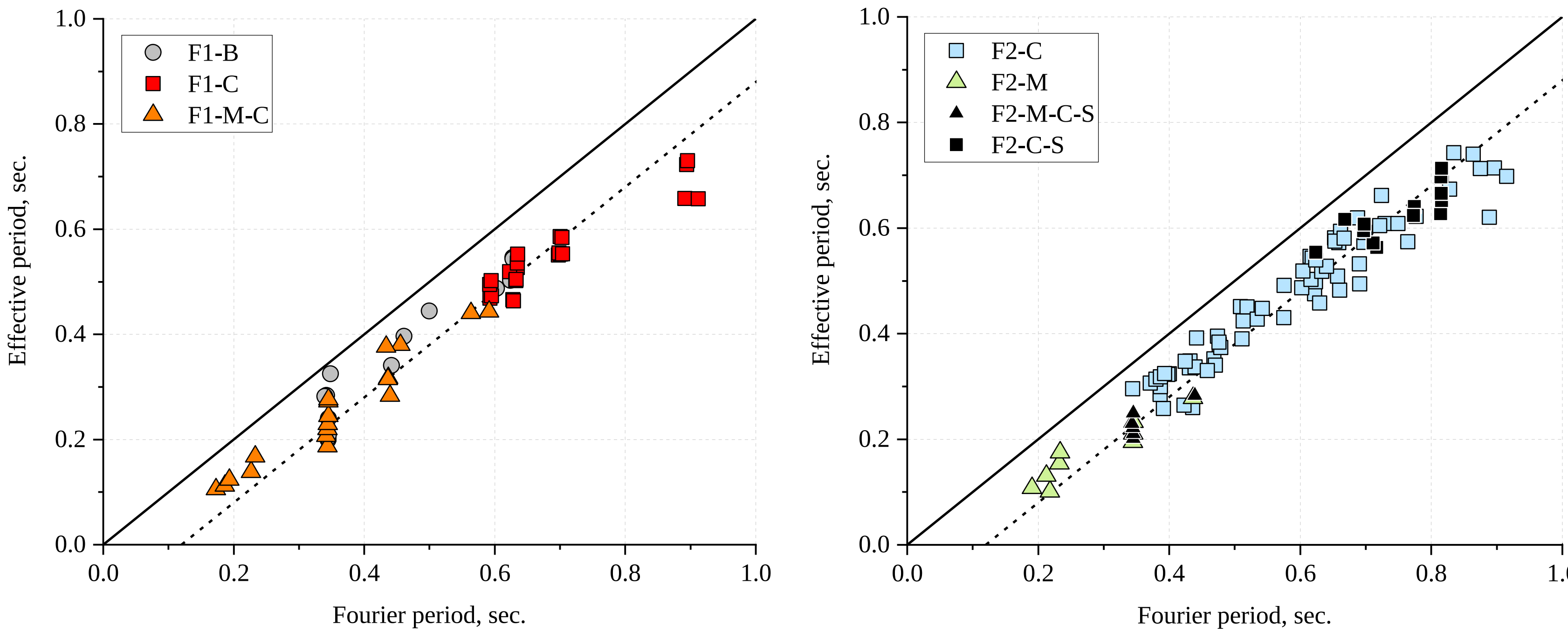

(a) Specimen F1

(b) Specimen F2

Figure 5-9: Comparisons of measurements of effective period with Fourier period

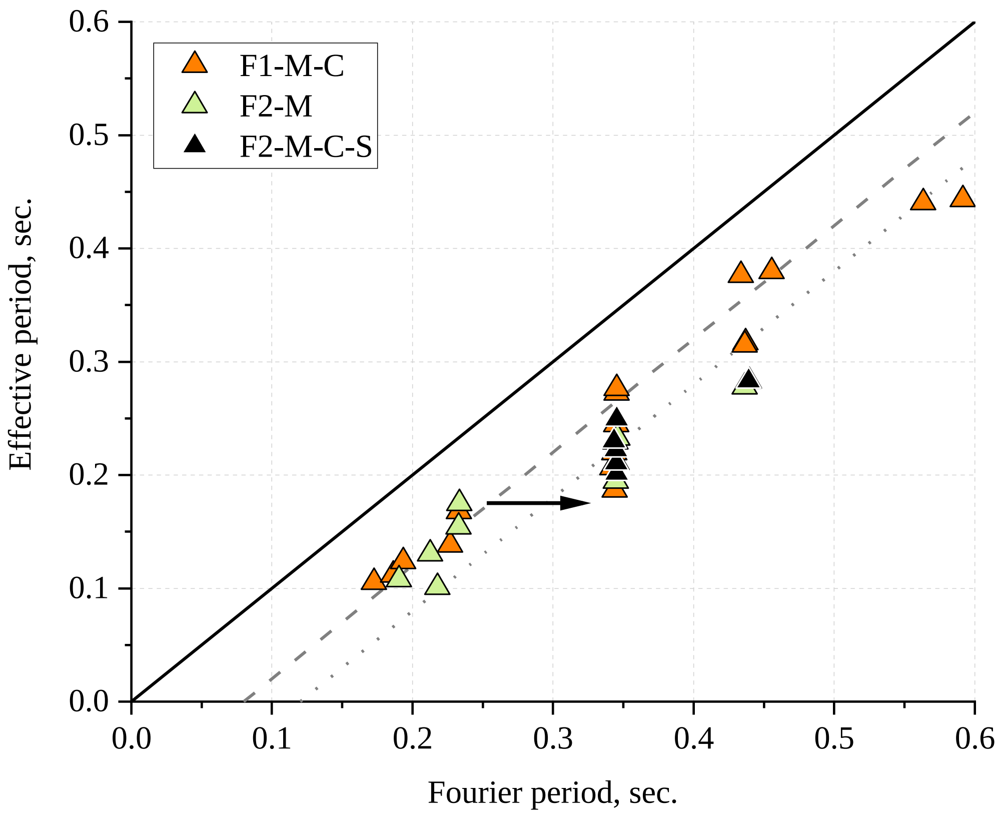

Figure 5-10: Comparisons of effective period and Fourier period in runs of infilled frames

Note: Arrow in Figure 5-10 (a) represents abrupt increase in Fourier periods after cracking of infill walls.

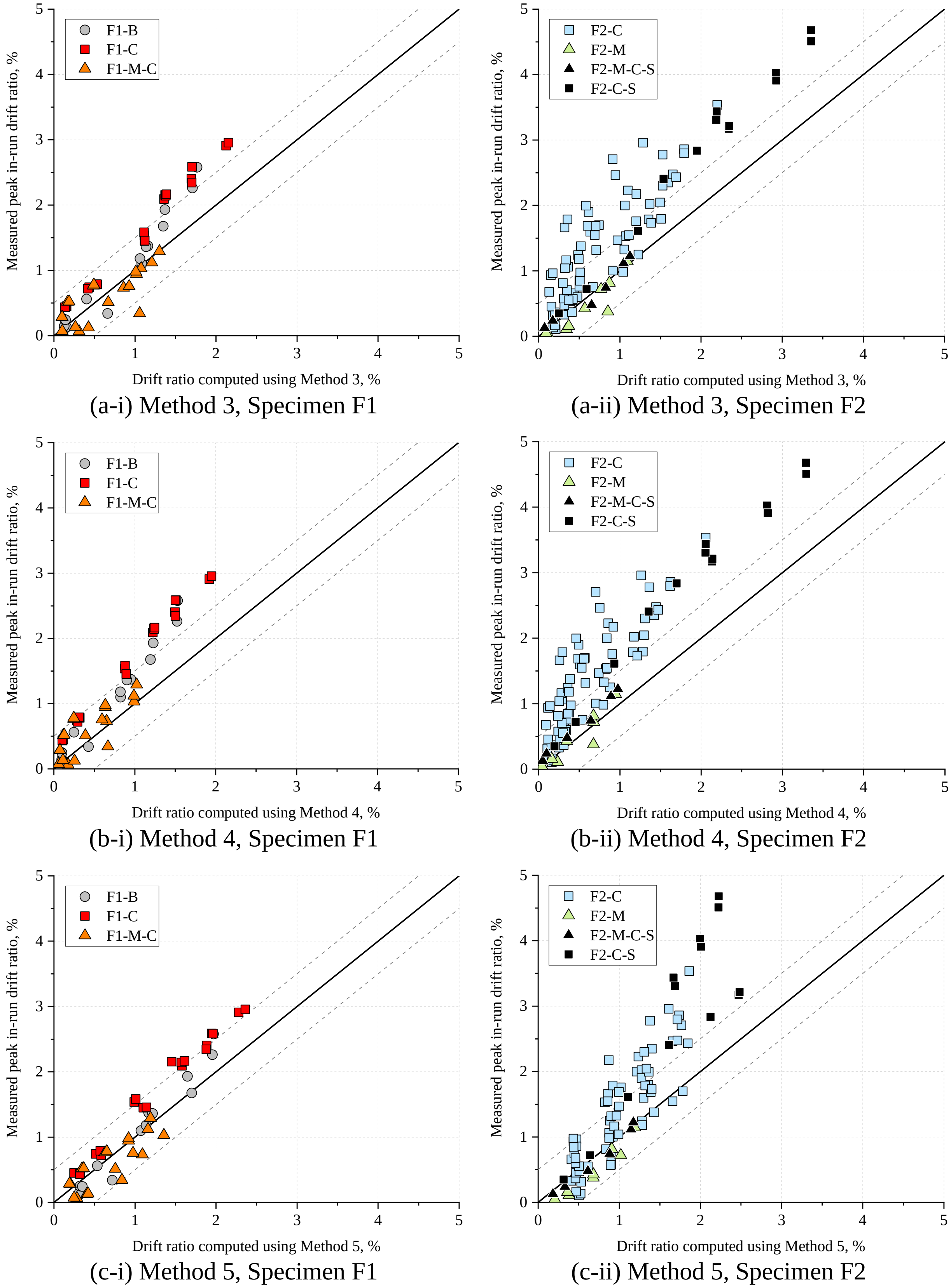

Figure 5-11: Comparisons of measured and estimated drift computed using Methods 3-5

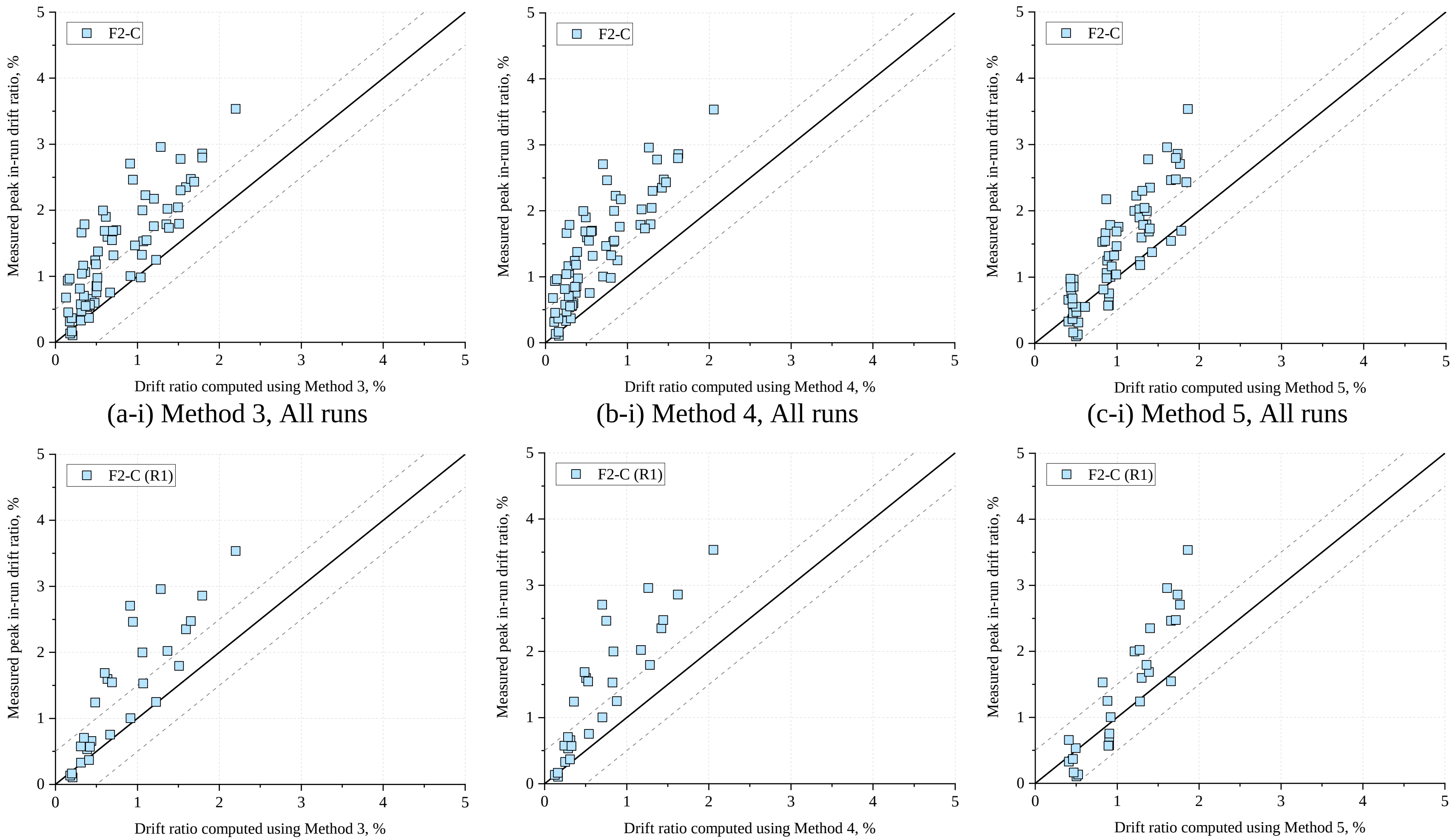

(a-i) Method 3, All runs

(b-i) Method 4, All runs

(c-i) Method 5, All runs

(a-ii) Method 3, Reference runs (R1)

(b-ii) Method 4, Reference runs (R1)

(c-ii) Method 5, Reference runs (R1)

Figure 5-12: Comparisons of measured and estimated drift in runs of Series F2-C in reference and all runs

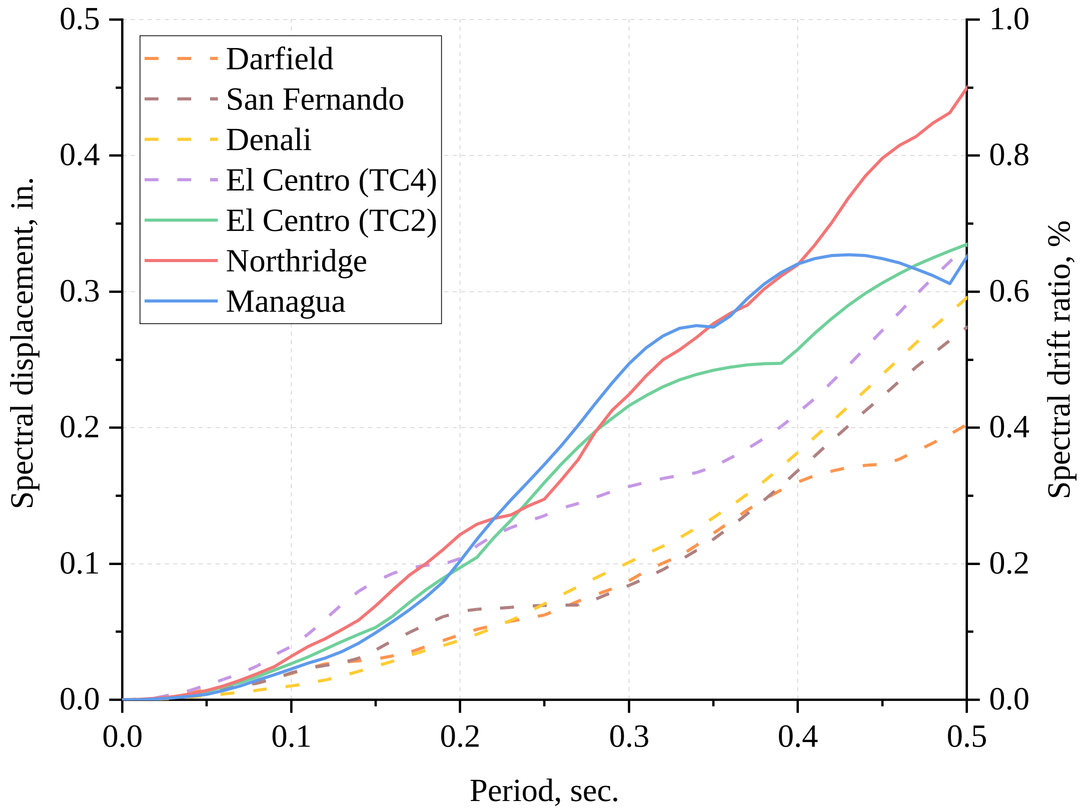

Figure 5-13: Smoothed displacement spectra (2% damped) of simulations modeled after the seven records used in Series F2-C at target PGV = 2 in./sec.

Note: Less-demanding motions (Group 1) are labeled with dashed lines and more-demanding motions (Group 2) are labeled with solid lines.

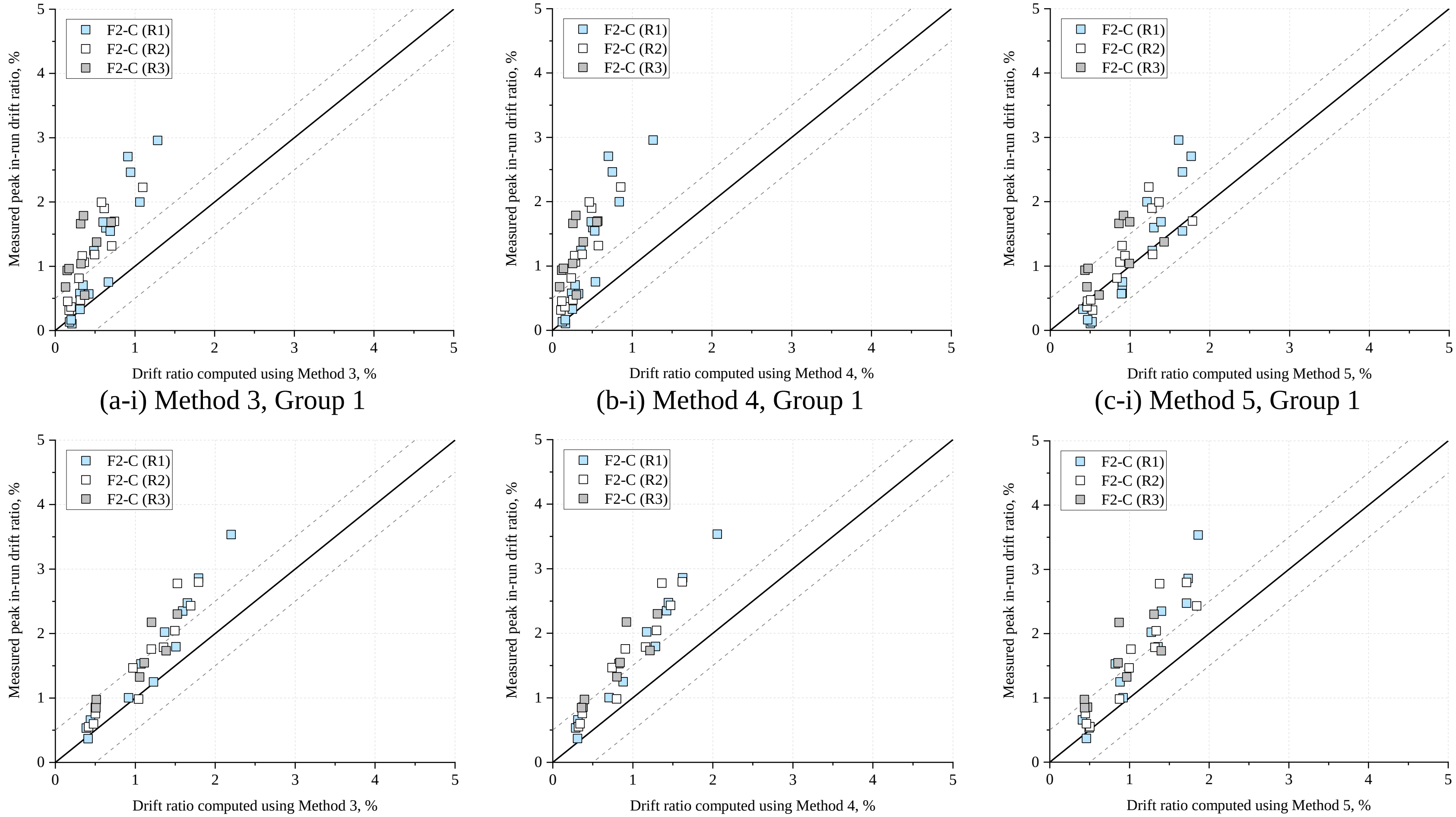

(a-i) Method 3, Group 1 (b-i) Method 4, Group 1 (c-i) Method 5, Group 1

(a-ii) Method 3, Group 2 (b-ii) Method 4, Group 2 (c-ii) Method 5, Group 2

Figure 5-14: Comparisons of measured and estimated drift in runs of Series F2-C in less-demanding and more-demanding motions

Note: Less-demanding motions are in Group 1 and more-demanding motions are in Group 2.

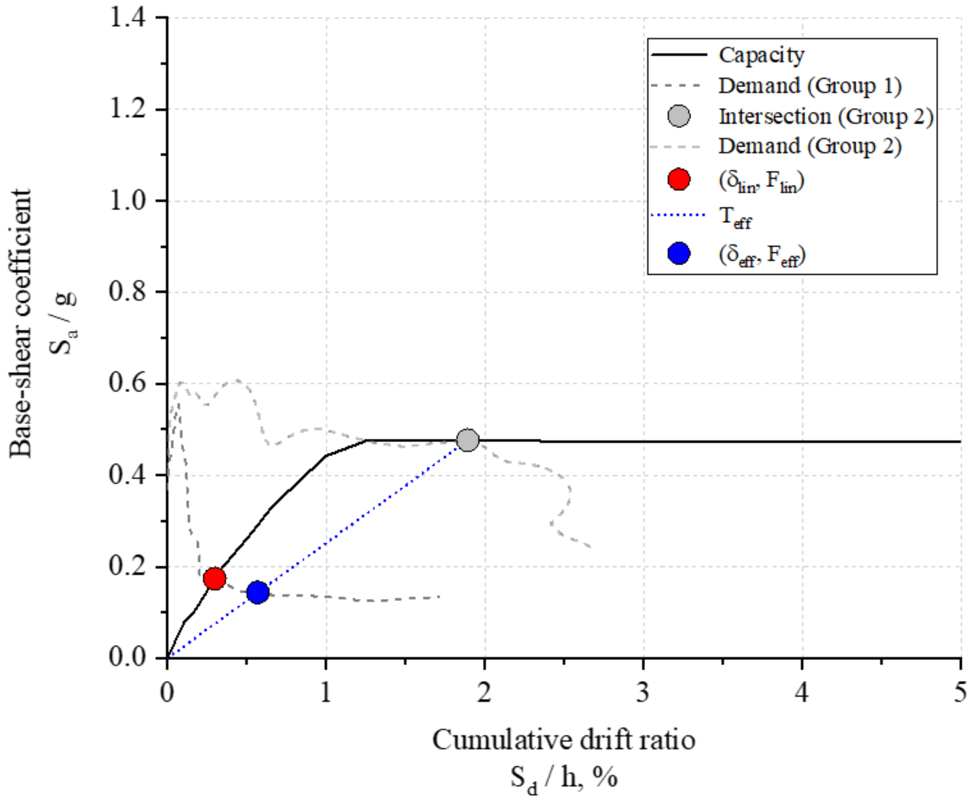

Figure 5-15: Estimates of drift computed using the Capacity Spectrum Method in a less-demanding motion (Group 1) following a more-demanding motion (Group 2)

Note: (δ_{lin}, F_{lin}) and (δ_{eff}, F_{eff}) are estimates of displacements and forces computed using linear response and effective period.

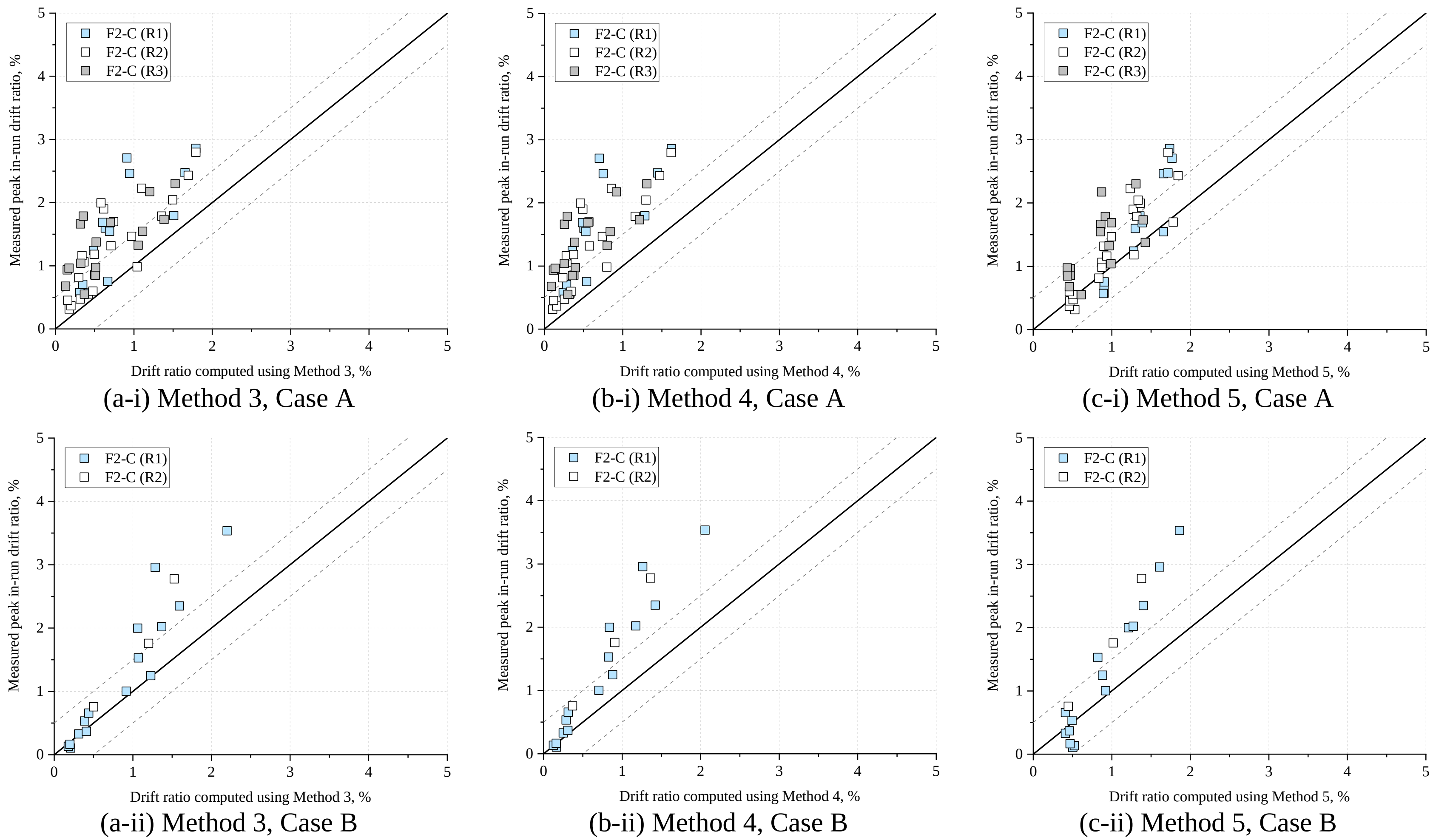

Figure 5-16: Comparisons of measured and estimated drift in Case A and Case B runs of Series F2-C

Note: ‘Case A’ refers to runs preceded by more-demanding motions and ‘Case B’ refers to runs preceded by less-demanding motions only.

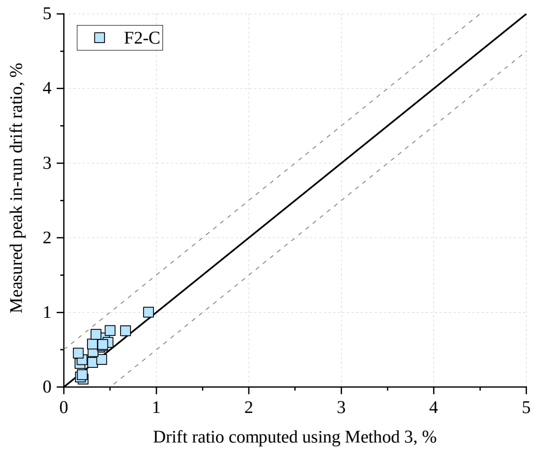

(a-i) Method 3, Linear specimen

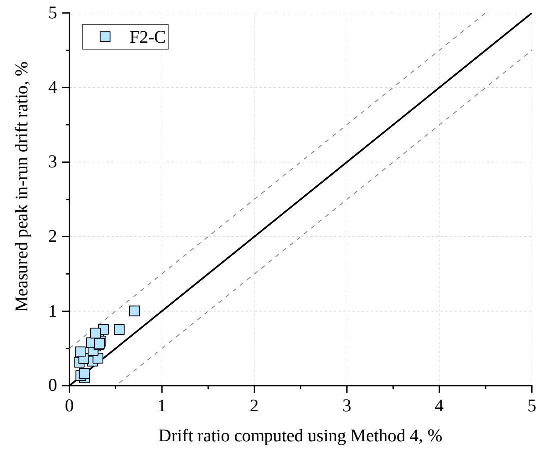

(b-i) Method 4, Linear specimen

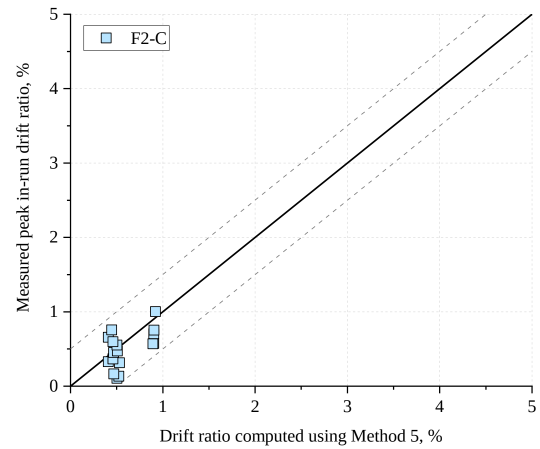

(c-i) Method 5, Linear specimen

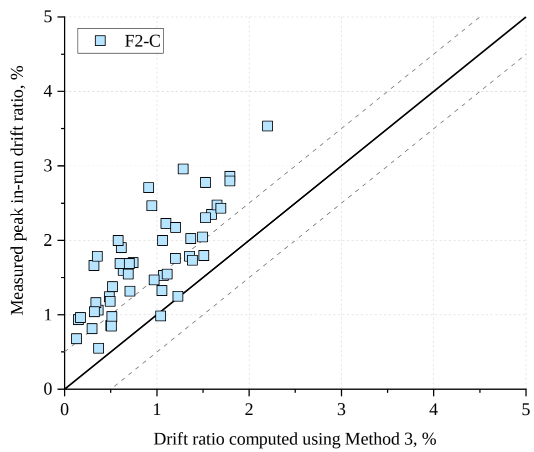

(a-ii) Method 3, Nonlinear specimen

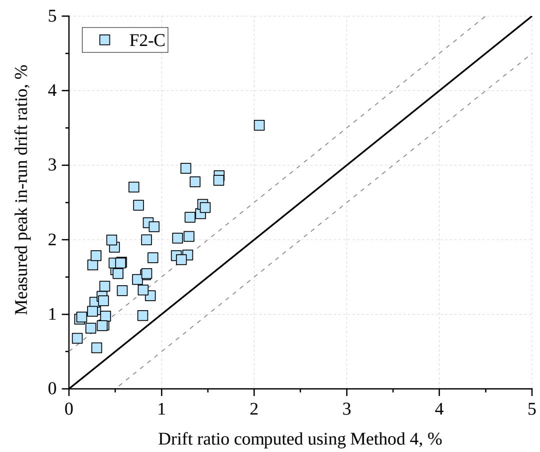

(b-ii) Method 4, Nonlinear specimen

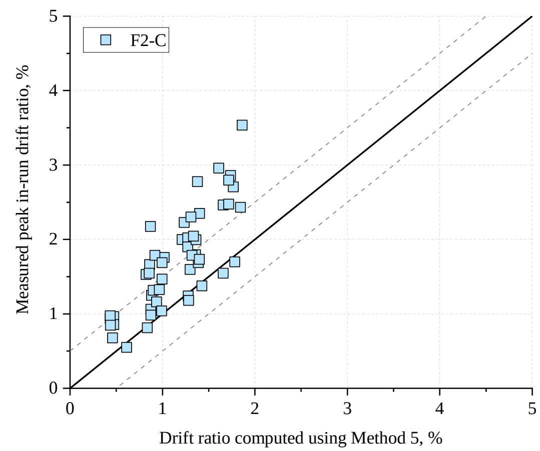

(c-ii) Method 5, Nonlinear specimen

Figure 5-17: Comparisons of measured and estimated drift in runs of the linear and nonlinear specimen (F2) tested in Series F2-C

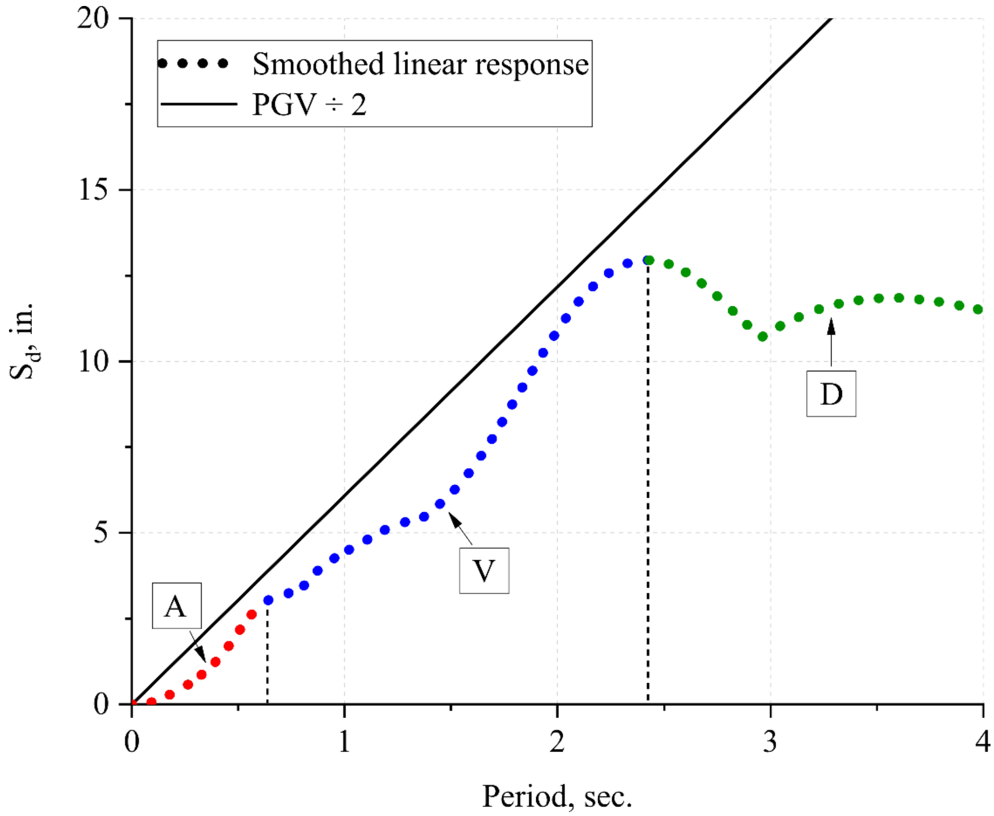

Figure 5-18: Displacement spectrum of the unscaled El Centro record

Note: Vertical lines divide spectrum into regions of nearly constant acceleration (A), velocity (V), and displacement (D).

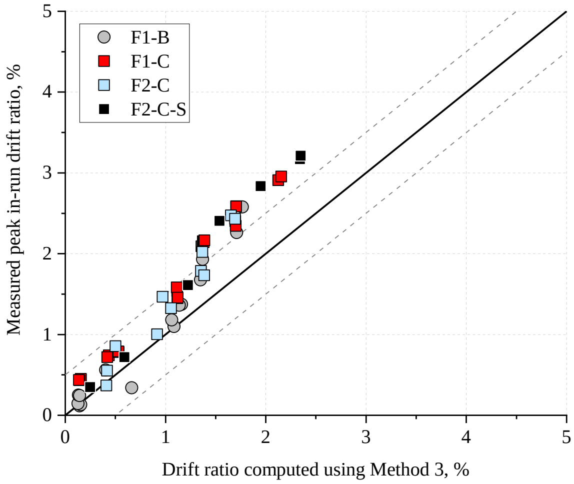

(a-i) Method 3, Frames without infill

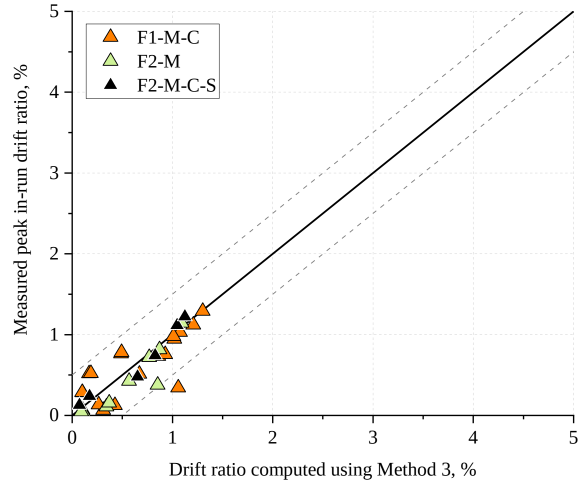

(a-ii) Method 3, Frames with infill

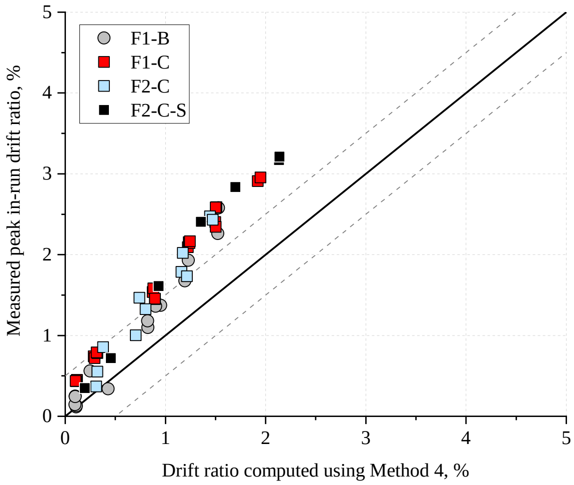

(b-i) Method 4, Frames without infill

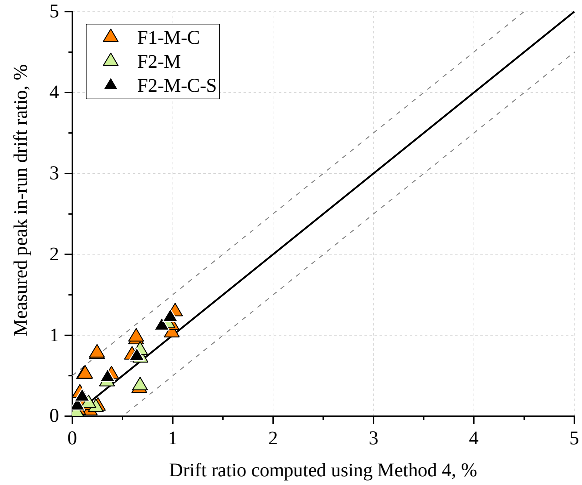

(b-ii) Method 4, Frames with infill

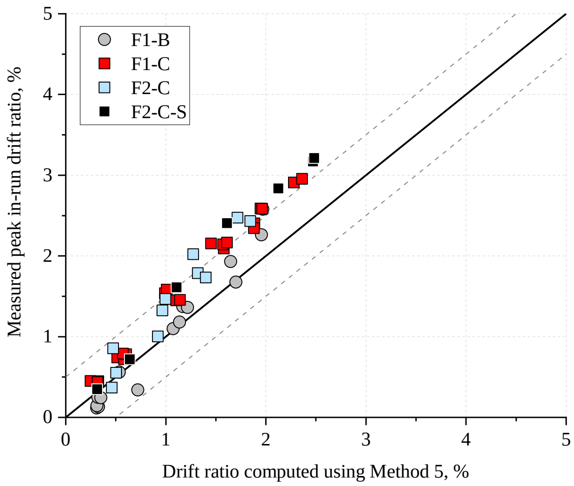

(c-i) Method 5, Frames without infill

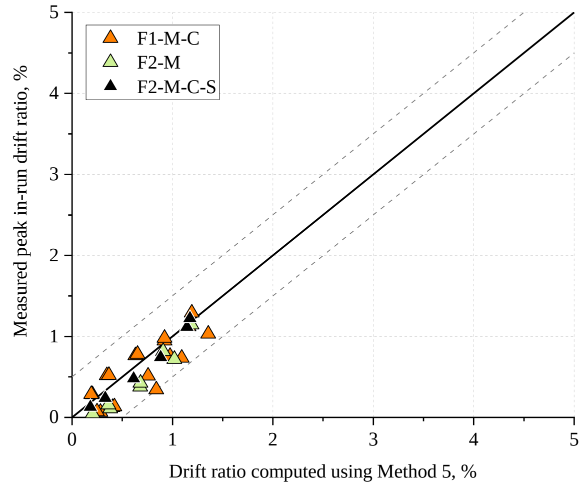

(c-ii) Method 5, Frames with infill

Figure 5-19: Comparisons of measured and estimated drift in simulations modeled after the El Centro (TC2) motion

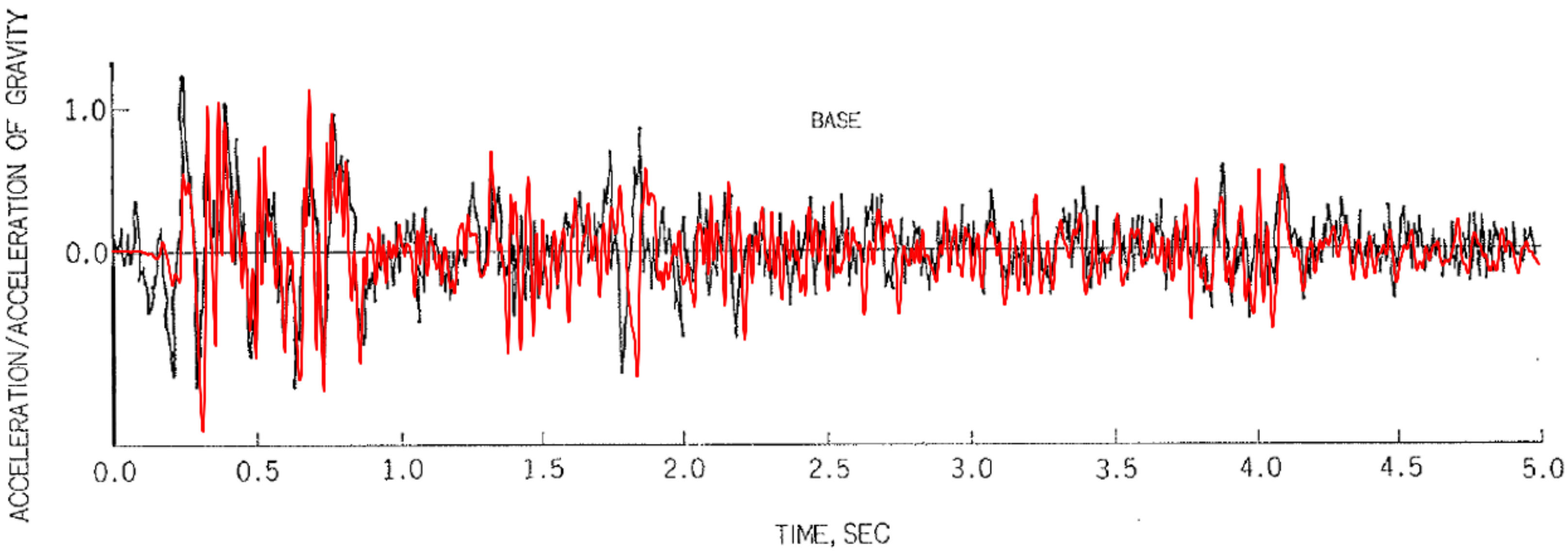

Figure 5-20: Graphical procedure used to match base acceleration histories

Note: Base acceleration history indicated with black line is taken from Takeda (1970) and approximation is labeled with red line.

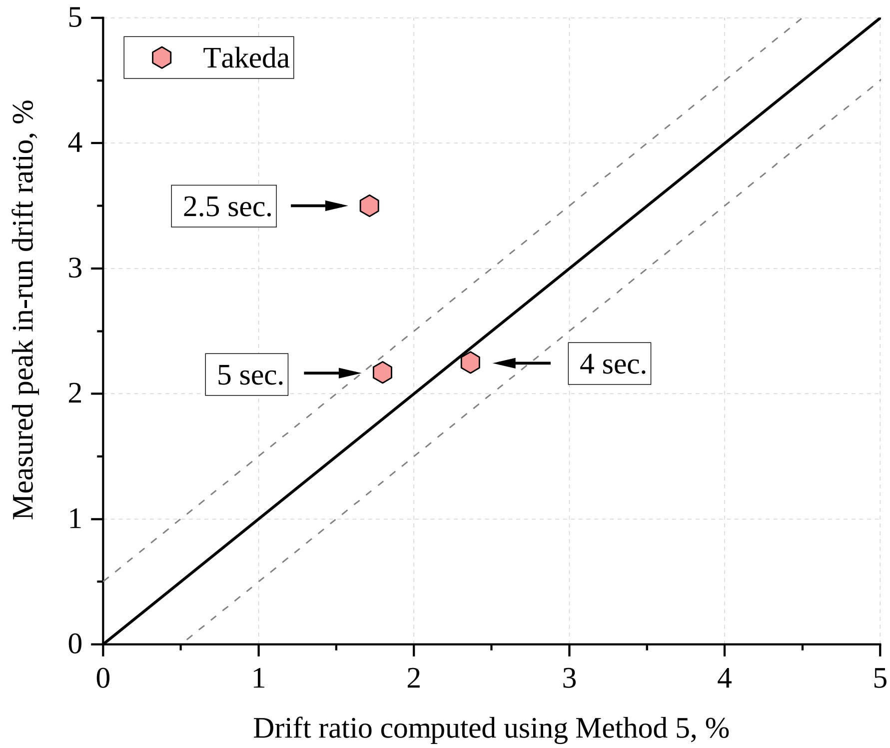

Figure 5-21: Measured vs. estimated drift computed using VOD in tests by Takeda (1970)

Note: Approximate durations of motions are indicated in boxes next to data points.

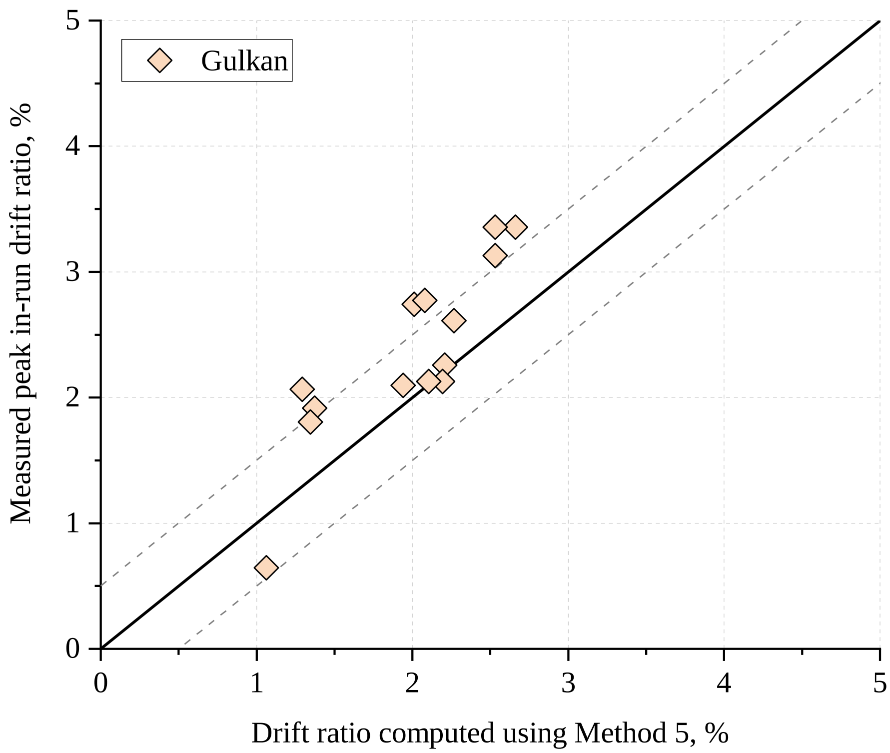

Figure 5-22: Measured vs. estimated drift computed using VOD in tests by Gulkan (1971)

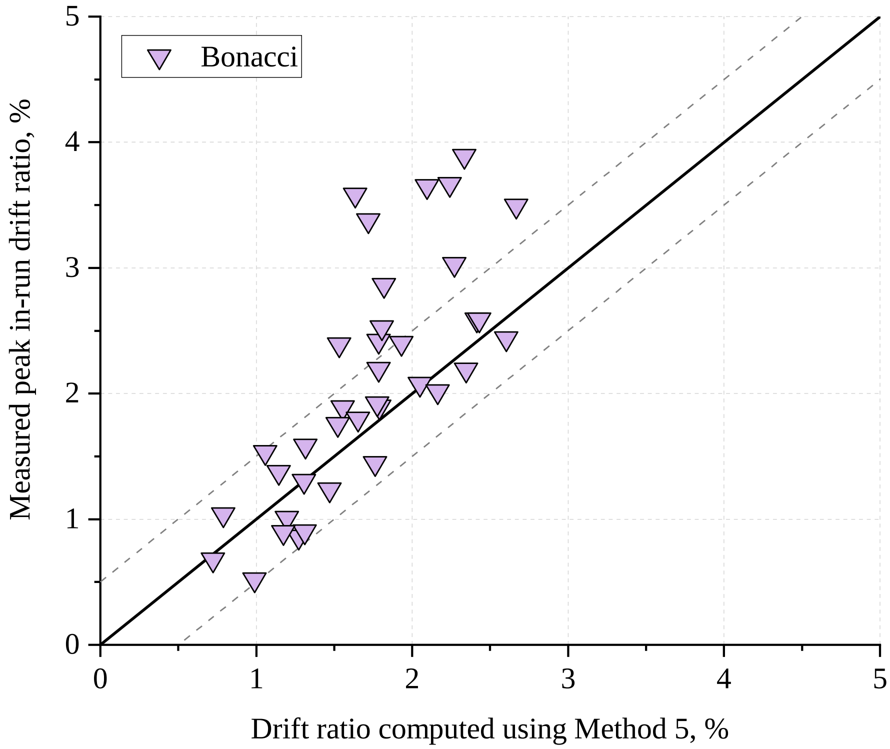

Figure 5-23: Measured vs. estimated drift computed using VOD in tests by Bonacci (1989)

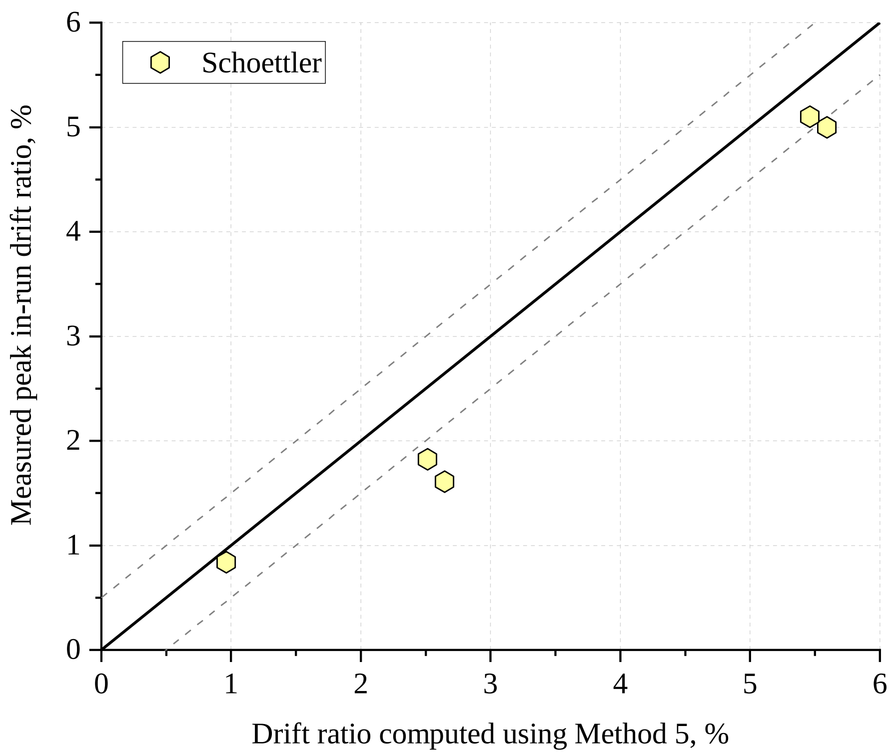

Figure 5-24: Measured vs. estimated drift computed using VOD in tests by Schoettler (2015)

Note: Axes in Figure 5-24 are plotted up to a drift ratio of 6% instead of 5%.

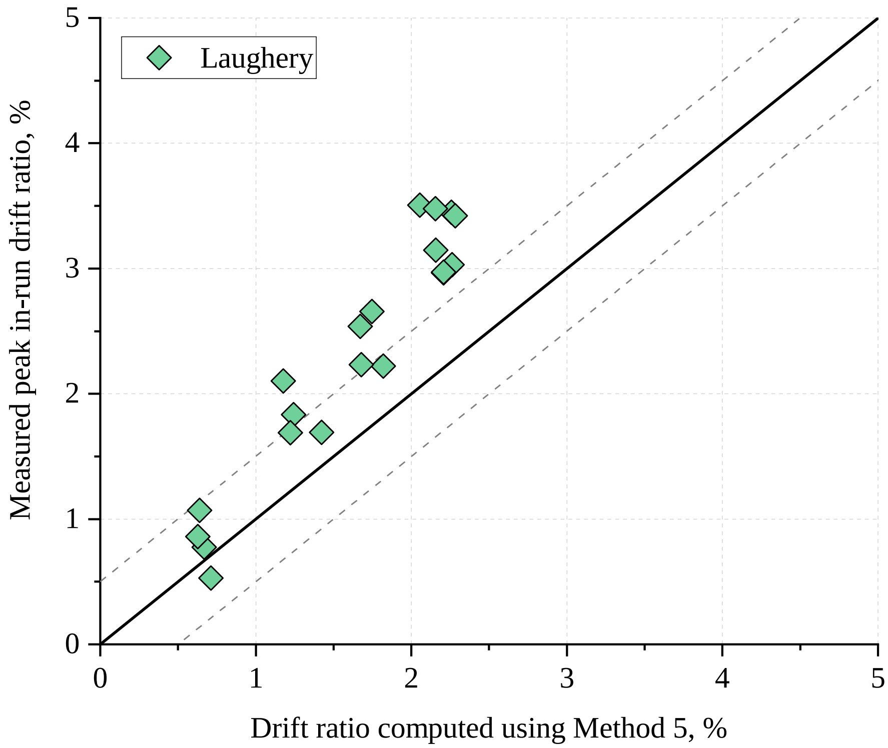

Figure 5-25: Measured vs. estimated drift computed using VOD in tests by Laughery (2016)

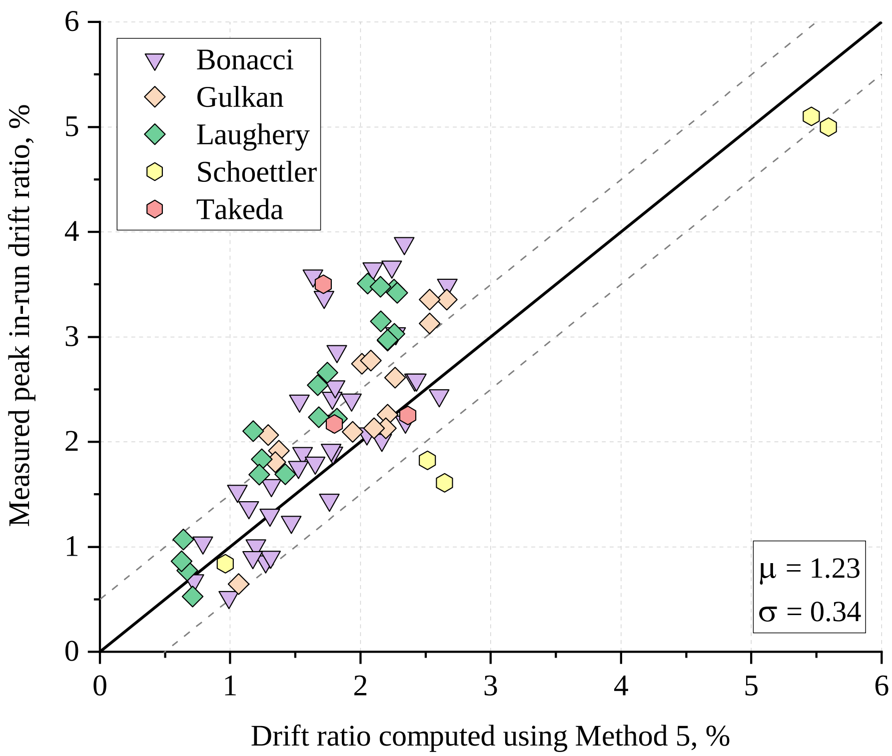

Figure 5-26: Measured vs. estimated drift computed using VOD in SDOF tests

Note: Axes in Figure 5-26 are plotted up to a drift ratio of 6% instead of 5%.

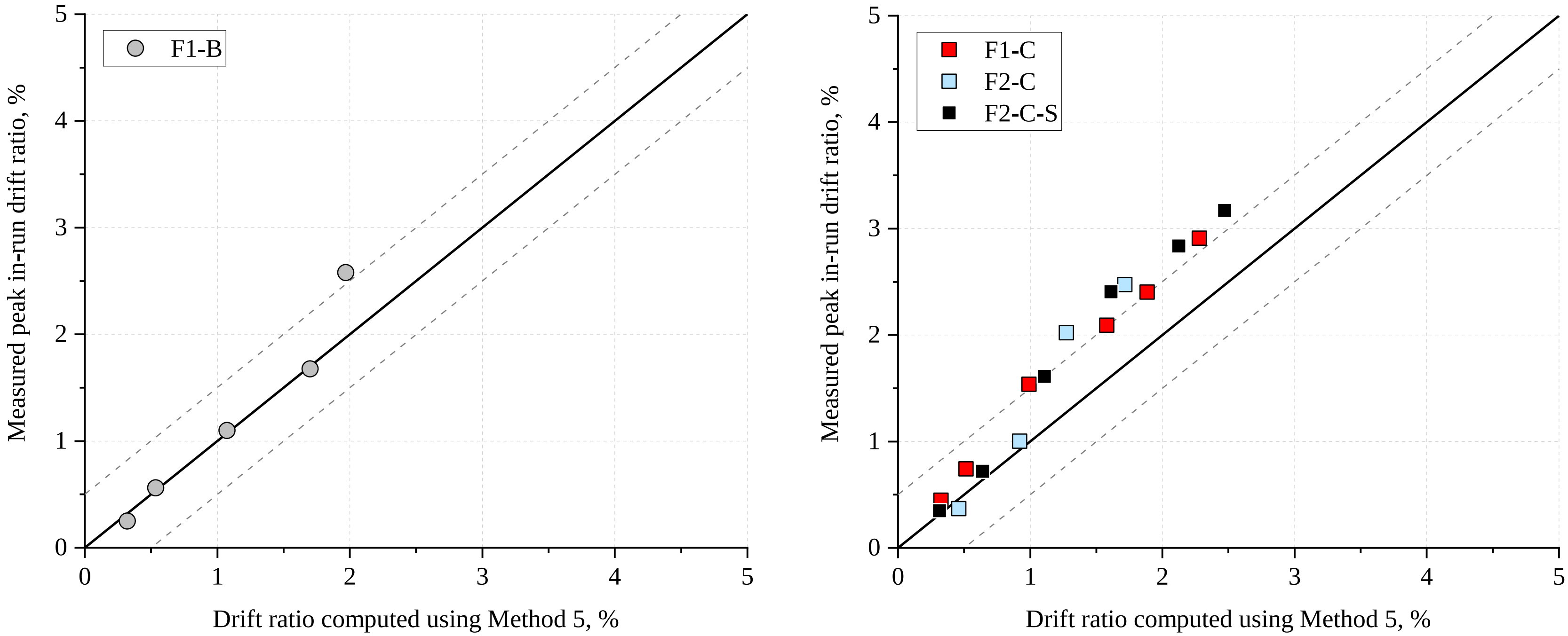

(a) Method 5, Bare frame

(b) Method 5, Frames with clamps

Figure 5-27: Comparisons of measured and estimated drift computed using VOD in simulations modeled after the El Centro (TC2) motion

Note: Reference runs (R1) excluding repeats (R2, R3) are used in Figure 5-27.

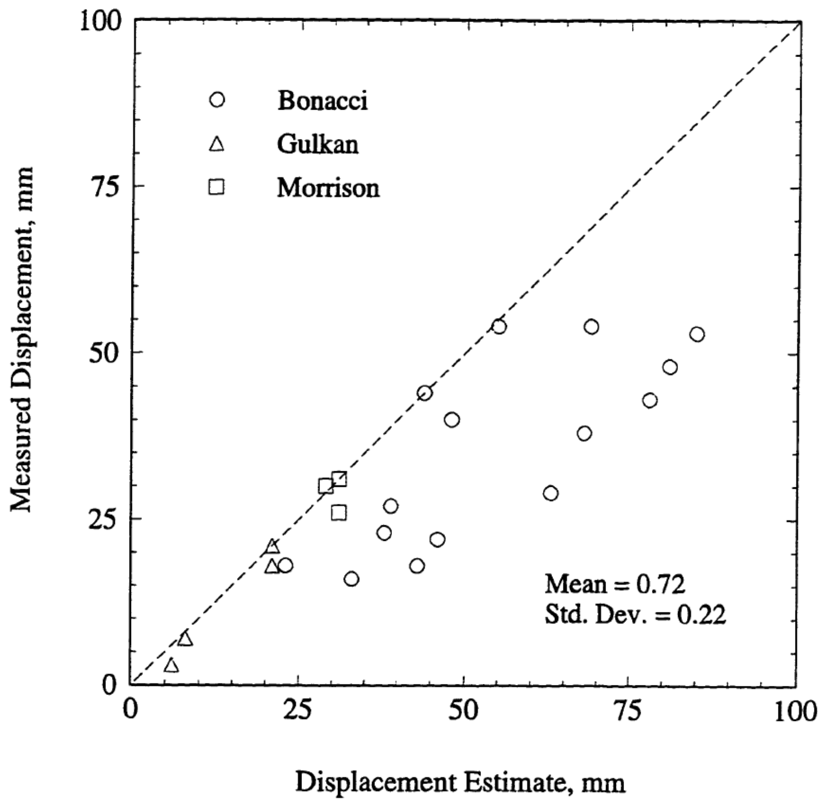

Figure 5-28: Measured vs. estimated drift in tests of SDOF specimens reported by Lepage (1997) Note: Plot is taken from Lepage (1997) and estimates of peak drift of SDOF specimens were computed using measured initial periods.

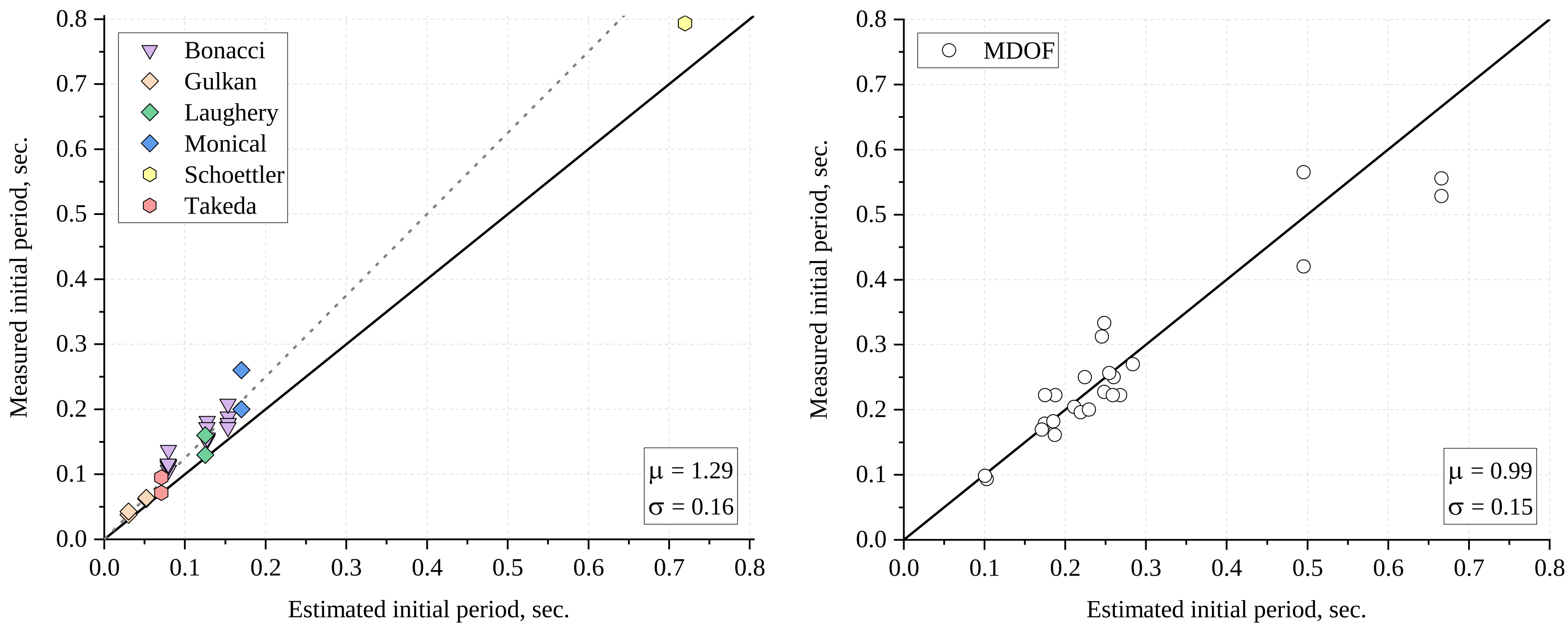

(a) SDOF specimens (b) MDOF specimens

Figure 5-29: Comparisons of measured and estimated periods of SDOF and MDOF specimens

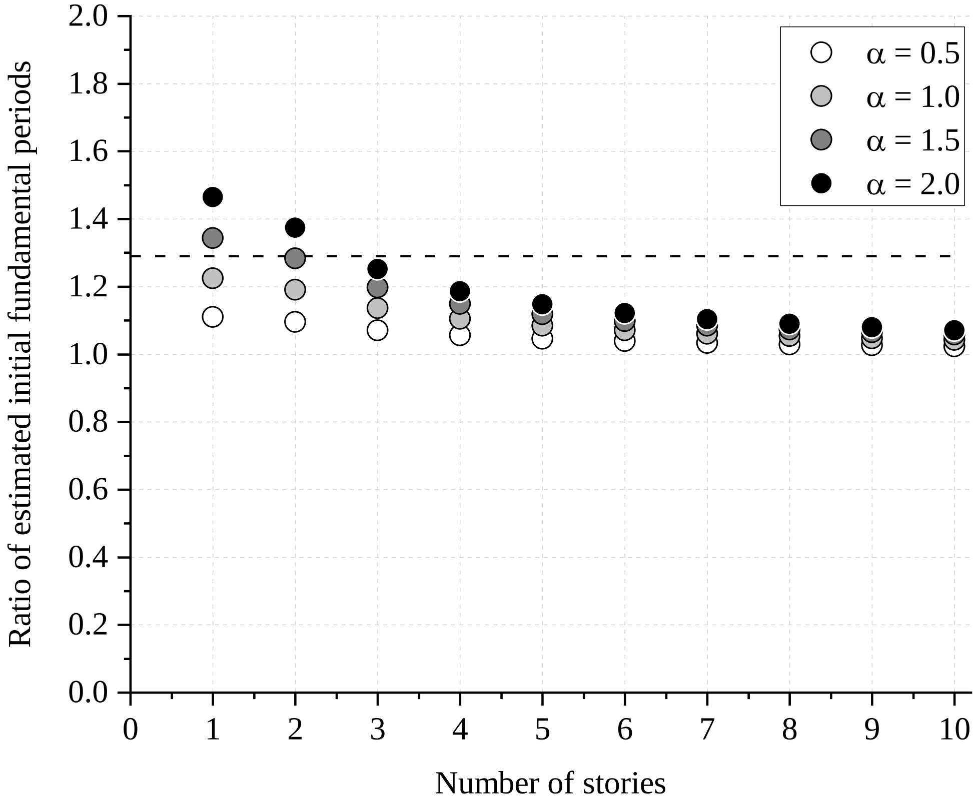

Figure 5-30: Ratio of estimated initial fundamental period of structure with flexible foundation to estimated initial fundamental period of structure with rigid foundations

Note: 'α' is a factor representing the percentage of column dimension projected into foundation of frames with flexible foundations. Horizontal line represents the average ratio of measured to estimated initial periods of the SDOF specimens shown in Figure 5-29 (a).

Assumed Properties of Three-bay Frames without Infill

$m := 49\ kip \div g$	story mass
$E := 3200\ ksi$	elastic modulus of concrete
$h := 50\ in$	story height
$l := 72\ in$	bay length
$bay := 3$	number of bays
$col := bay + 1$	number of columns
$D := 8\ in$	cross-sectional column dimension (square columns)
$b_b := 20\ in$	width of beam
$h_b := 8\ in$	height of beam
$I_c := \frac{1}{12} \cdot D^4$	moment of inertia of column
$I_b := \frac{1}{12} \cdot b_b \cdot {h_b}^3$	moment of inertia of beam
$k_c := \frac{I_c}{h}$	initial lateral stiffness of column
$k_{tb} := \frac{I_b}{l}$	initial lateral stiffness of top beam
$k_{bb} := \frac{I_b}{l}$	initial lateral stiffness of bottom beam

Assumed Linear Mode Shape for Frames without Infill

$\delta(N, i) := \sin\left(\frac{i}{N} \cdot \frac{\pi}{2}\right)$	mode shape

Figure 5-31: Estimation of initial fundamental periods of frame structures with rigid and flexible foundations

Initial Fundamental Period

$$k_1 := \frac{24 \cdot E}{h^2} \cdot \frac{1}{\frac{2}{col \cdot k_c} + \frac{1}{bay \cdot k_{tb}}}$$

initial lateral story stiffness of first story with rigid foundation

$$k := \frac{24 \cdot E}{h^2} \cdot \frac{1}{\frac{2}{col \cdot k_c} + \frac{1}{bay \cdot k_{tb}} + \frac{1}{bay \cdot k_{bb}}}$$

initial lateral story stiffness of stories above first story

$$K(i) := k_1 \cdot (i = 1) + k \cdot (i > 1)$$

initial lateral story stiffness of frame with rigid foundation

$$PE(N) := \frac{1}{2} \cdot \sum_{i=1}^{N} \left(K(i) \cdot (\delta(N,i) - \delta(N,i-1))^2 \right)$$

total potential energy of frame with rigid foundation

$$KE(N) := \frac{1}{2} \sum_{i=1}^{N} \left(m \cdot (\delta(N,i))^2 \right)$$

total kinetic energy of frame

$$T(N) := 2 \cdot \pi \cdot \sqrt{\frac{KE(N)}{PE(N)}}$$

initial fundamental period of frame with rigid foundation

$$k'_1(\alpha) := \frac{24 \cdot E}{(h + \alpha \cdot D)^2} \cdot \frac{1}{\frac{2}{col \cdot \frac{I_c}{(h + \alpha \cdot D)}} + \frac{1}{bay \cdot k_{tb}}}$$

initial lateral story stiffness of first story with flexible foundation

$$K'(i, \alpha) := k'_1(\alpha) \cdot (i = 1) + k \cdot (i > 1)$$

initial lateral story stiffness of frame with flexible foundation

$$PE'(N, \alpha) := \frac{1}{2} \cdot \sum_{i=1}^{N} \left(K'(i, \alpha) \cdot (\delta(N,i) - \delta(N,i-1))^2 \right)$$

total potential energy of frame with flexible foundation

$$T'(N, \alpha) := 2 \cdot \pi \cdot \sqrt{\frac{KE(N)}{PE'(N, \alpha)}}$$

initial fundamental period of frame with flexible foundation

$$Ratio(N, \alpha) := \frac{T'(N, \alpha)}{T(N)}$$

ratios of initial fundamental periods of frames with flexible and rigid foundations

Figure 5-31 (continued): Estimation of initial fundamental periods of frame structures with rigid and flexible foundations

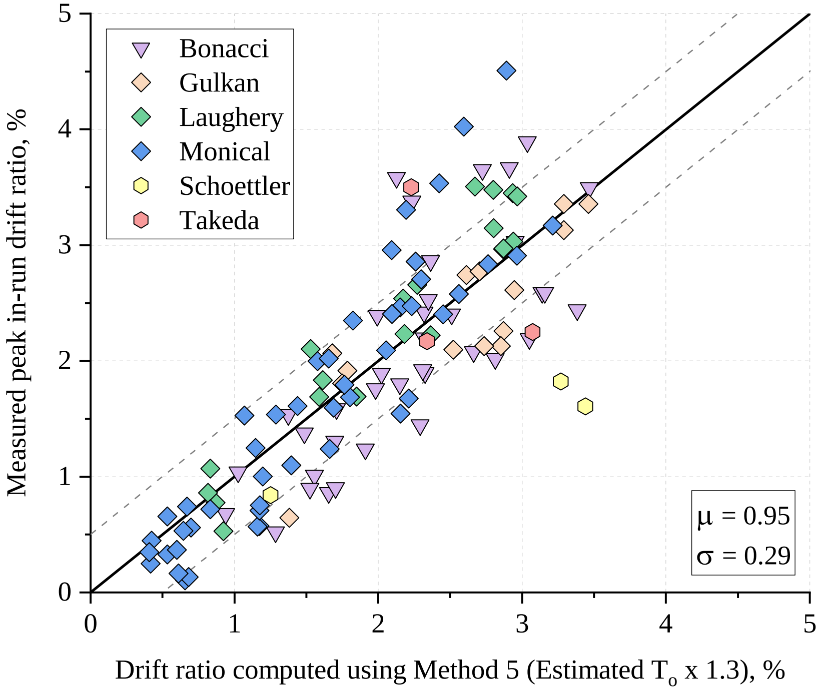

(a) VOD using estimated initial periods increased by 30%

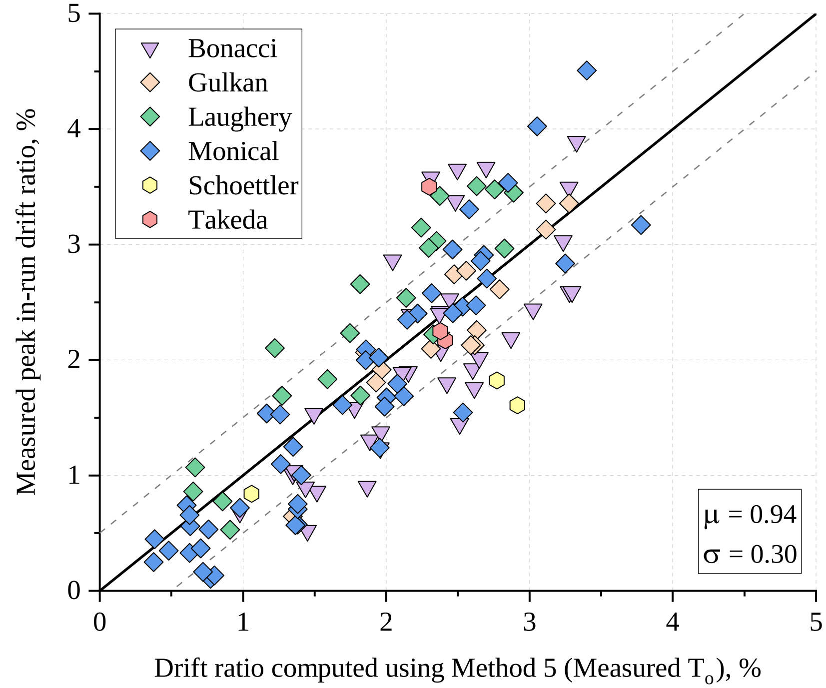

(a) VOD using measured initial periods

Figure 5-32: Results of VOD using estimated and measured initial periods of SDOF specimens

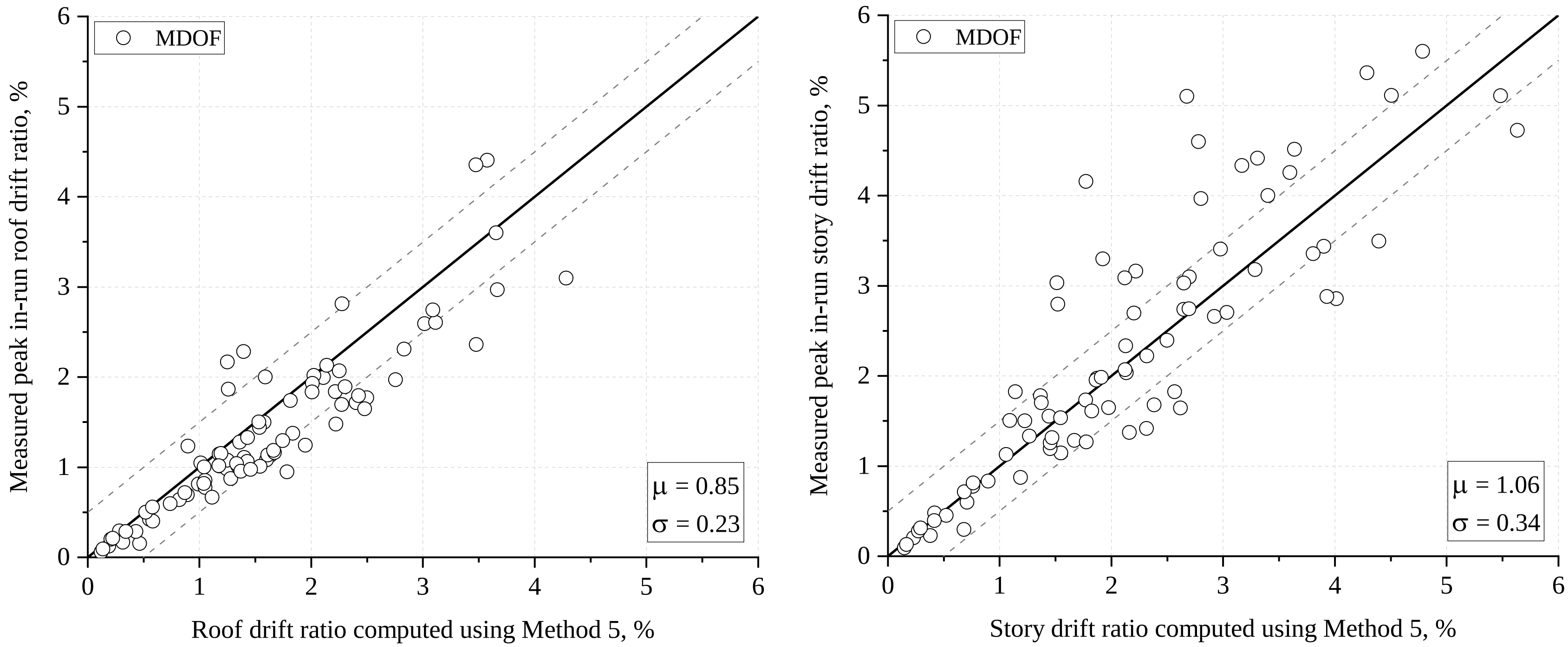

(a) Peak in-run roof drift of MDOF specimens

(b) Peak in-run story drift of MDOF specimens

Figure 5-33: Comparisons of measured and estimated peak drift computed using VOD of MDOF specimens

Note: Values of measured and estimated peak in-run drift in Figure 5-33 are taken from work by Shah (2021).

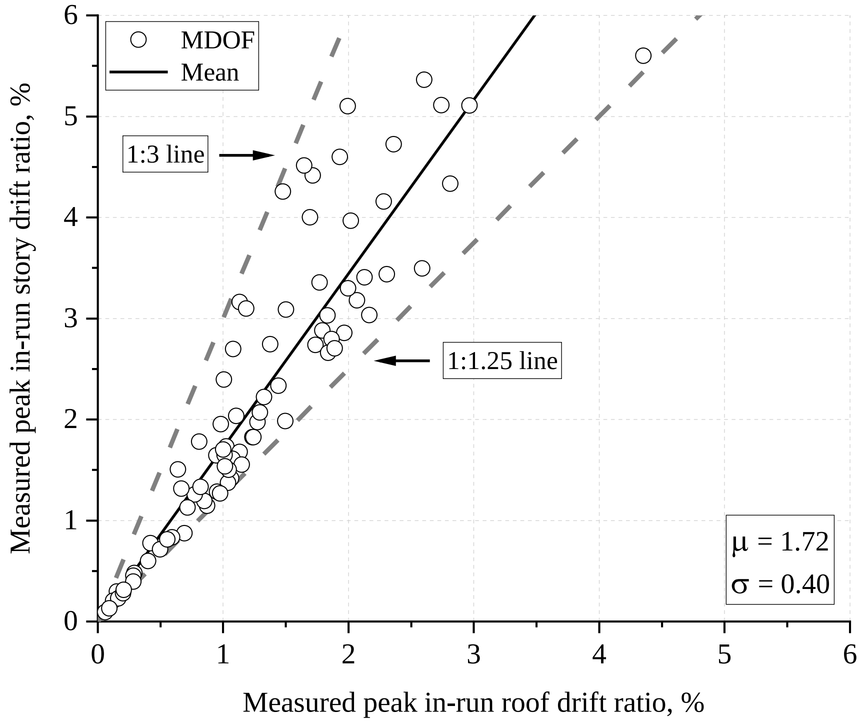

Figure 5-34: Measured peak story drift vs. measured peak roof drift of MDOF specimens

Note: Values of measured peak in-run drifts in Figure 5-34 are taken from Shah (2021).

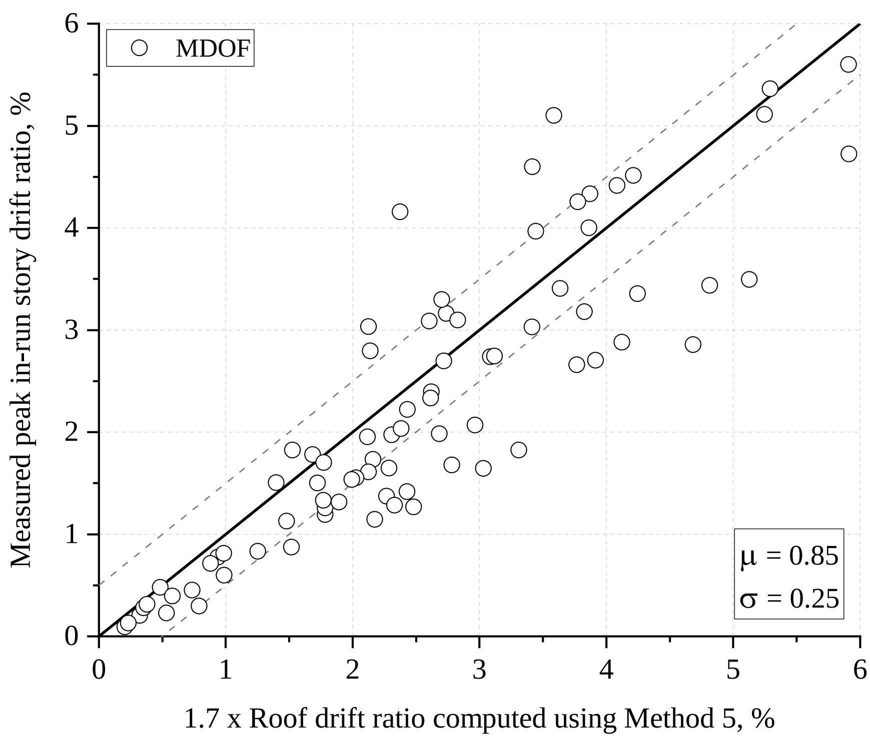

Figure 5-35: Measured peak story drift vs. estimated peak story drift of MDOF specimens computed using Eq. 5-15 increased by 70%

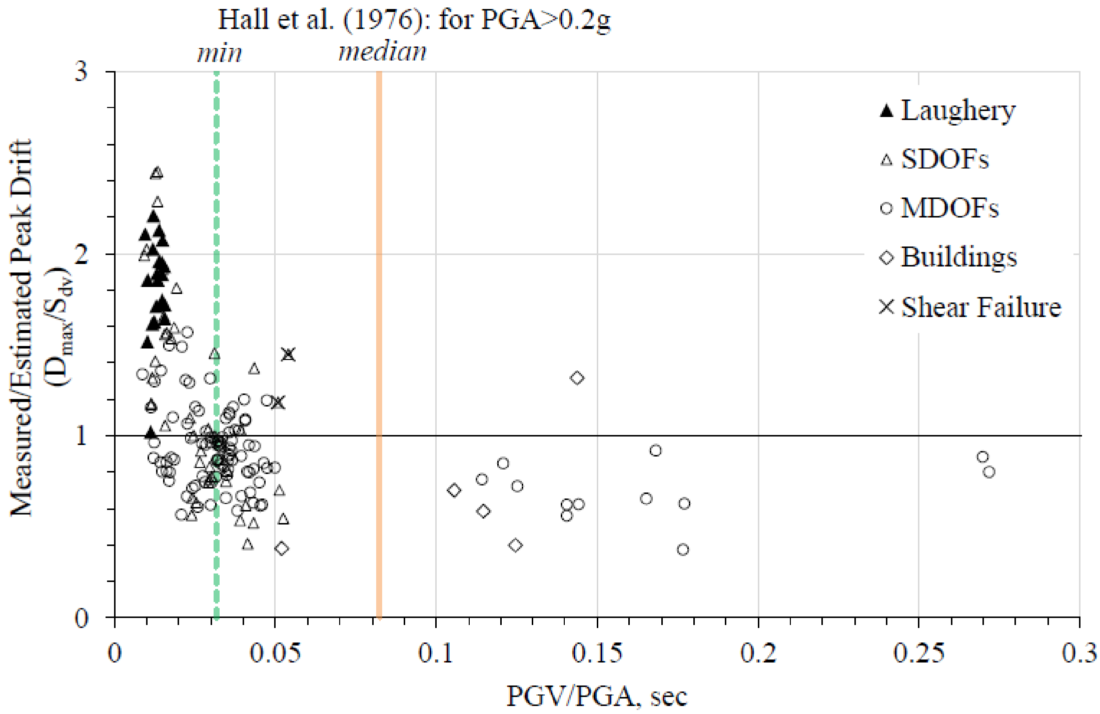

(a) Wide view of ratio of PGV to PGA

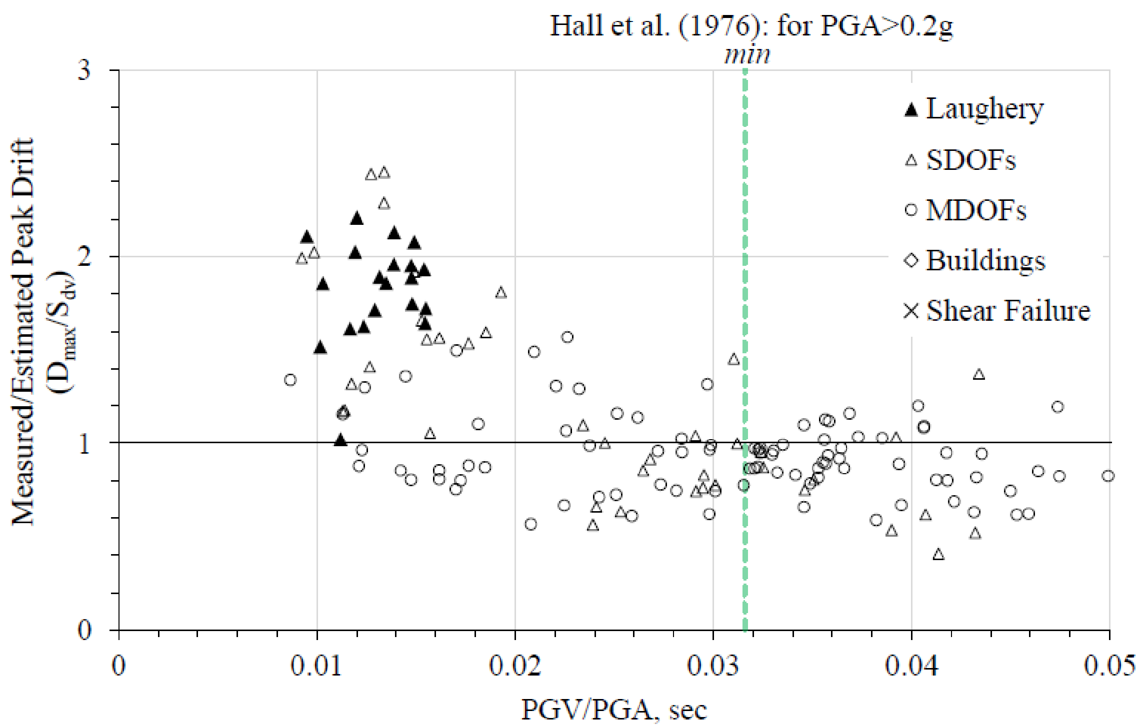

(b) Close-up view of ratio of PGV to PGA

Figure 5-36: Measured/Estimated drift computed using VOD vs. PGV/PGA

Note: Plots are taken from Laughery (2016). Estimates of peak drift of SDOFs were computed using Eq. 5-14 and estimates of peak roof drift of MDOFs were computed using Eq. 5-15.

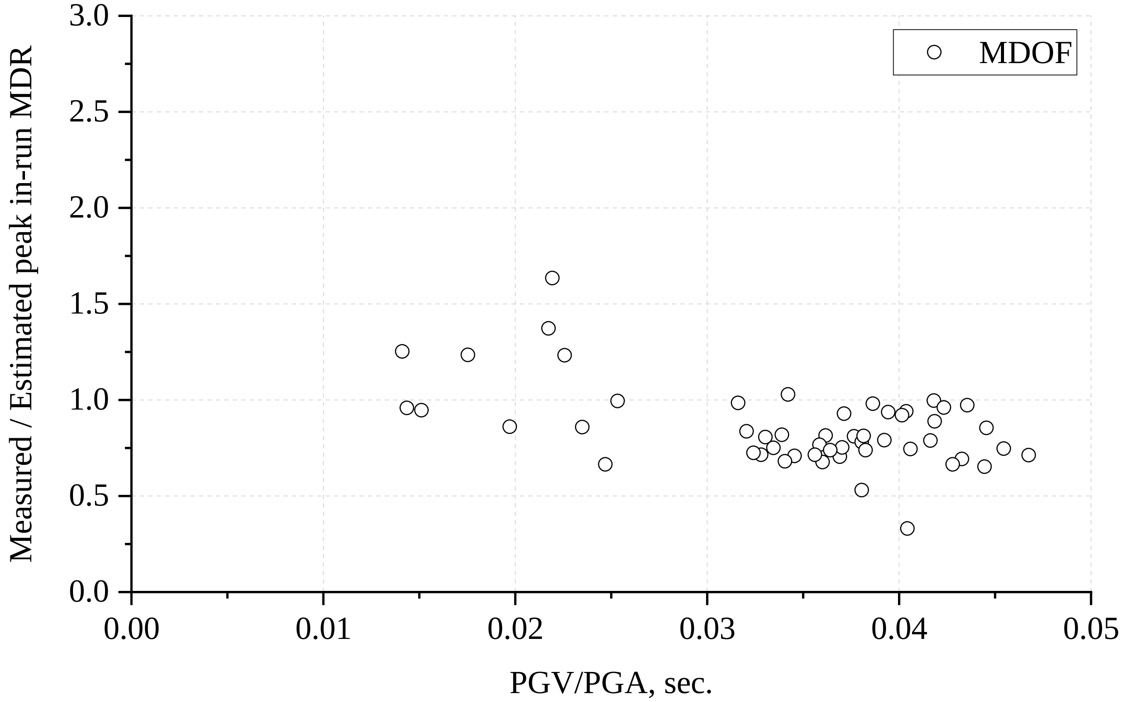

(a) Ratio of measured to estimated peak roof drift

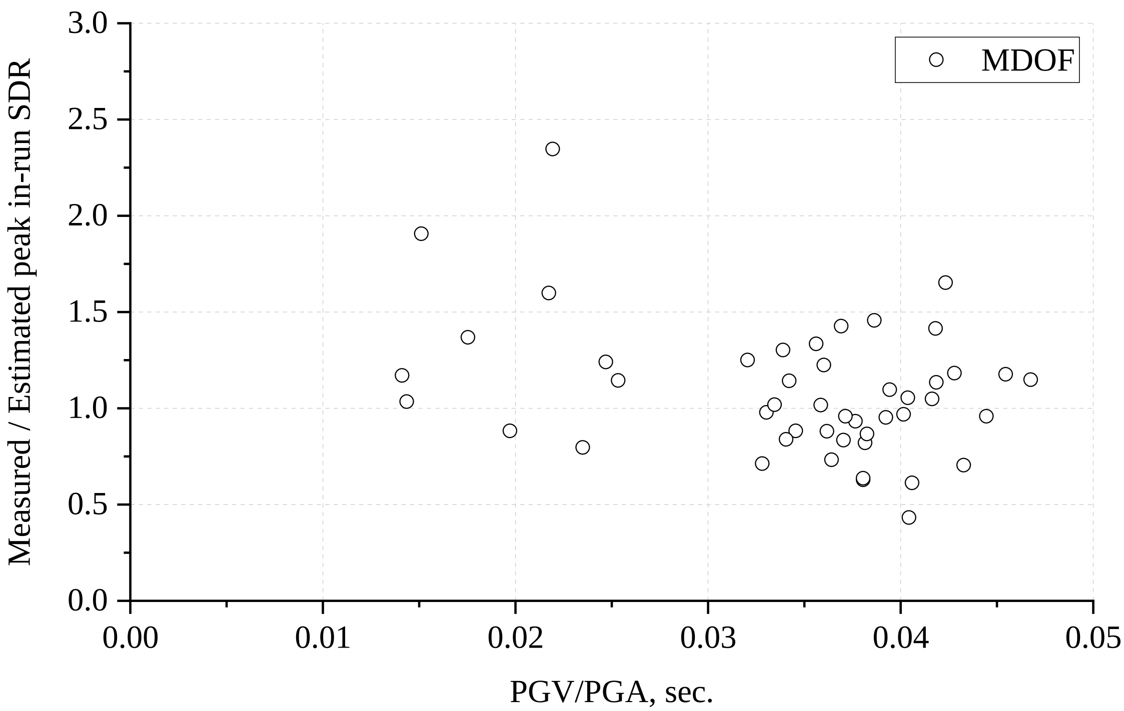

(b) Ratio of measured to estimated peak story drift

Figure 5-37: Measured / Estimated MDR and SDR computed using VOD vs. PGV/PGA

Note: Estimates of peak roof and story drift were computed using VOD (Eqs. 5-15 through 5-16).

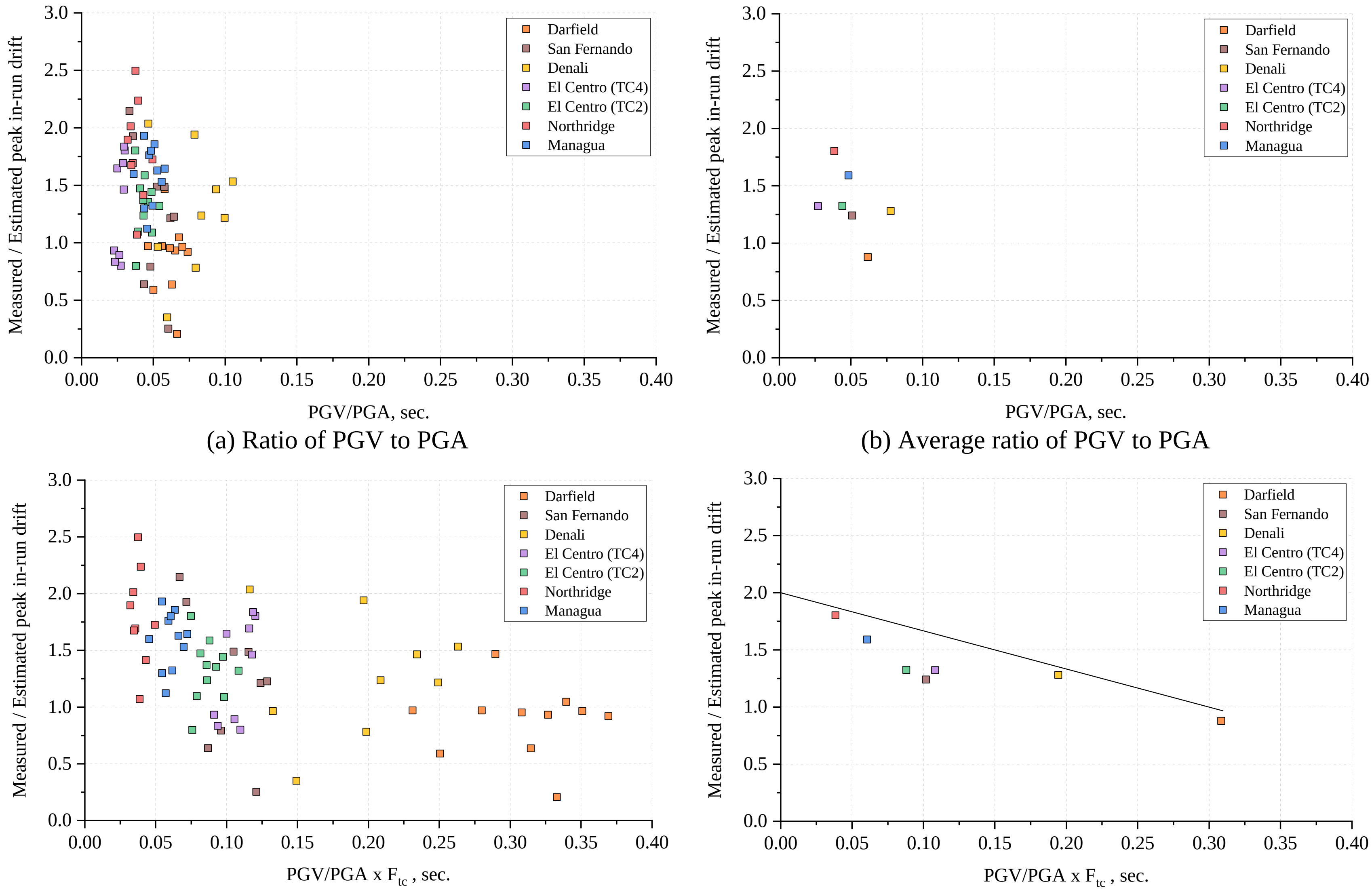

(a) Ratio of PGV to PGA

(b) Average ratio of PGV to PGA

(c) Ratio of PGV to PGA multiplied by F_{tc}

(d) Average ratio of PGV to PGA multiplied by F_{tc}

Figure 5-38: Variation of ratio of measured to estimated drift computed using VOD with PGV/PGA in Series F2-C

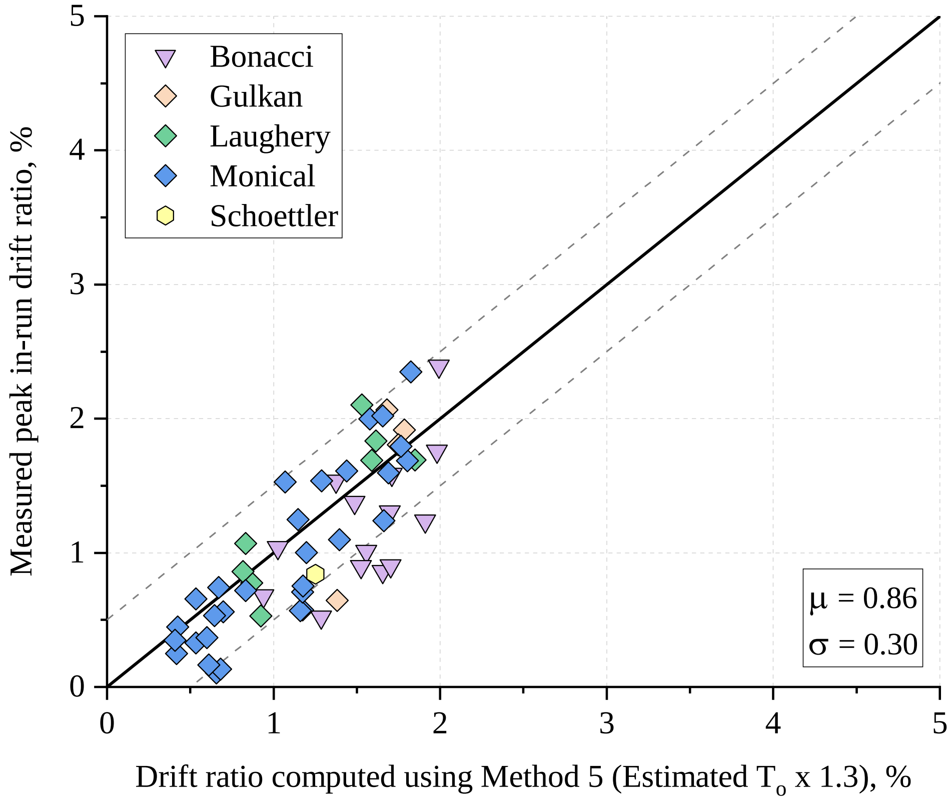

Figure 5-39: Measured peak drift vs. estimated peak story drift of SDOF specimens computed using VOD (Eq. 5-14) increased by 30% for drift demands smaller than 2%

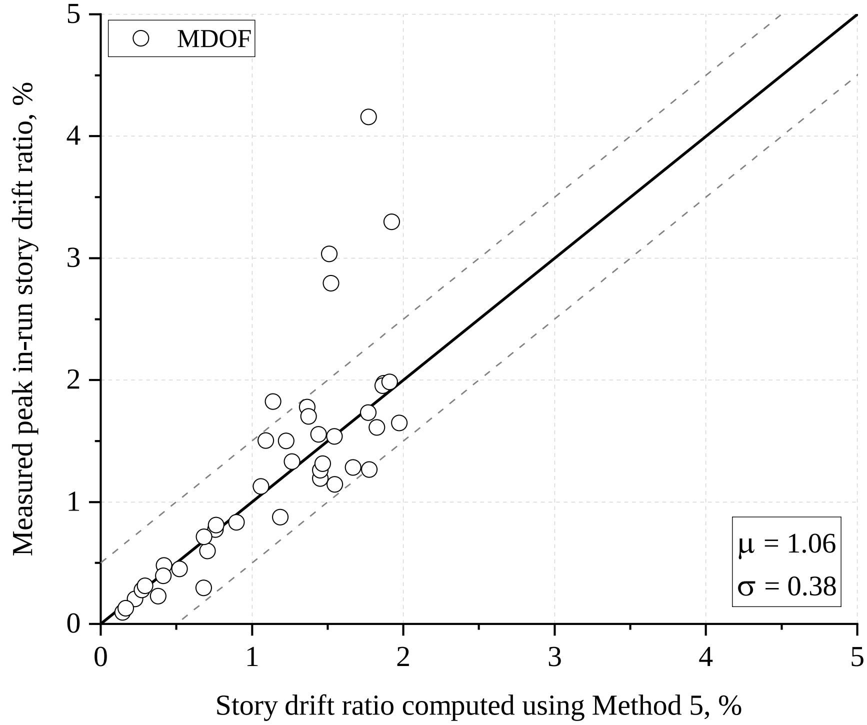

Figure 5-40: Measured peak story drift vs. estimated peak story drift of MDOF specimens computed using VOD (Eq. 5-16) for drift demands smaller than 2%

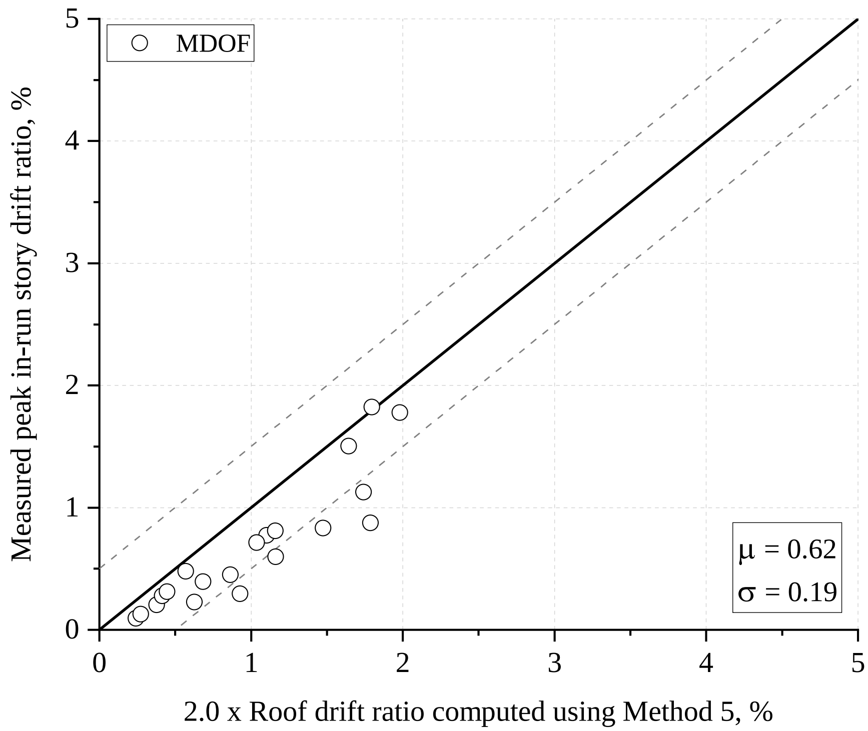

Figure 5-41: Measured peak story drift vs. estimated peak roof drift of MDOF specimens computed using VOD (Eq. 5-15) increased by 100% for drift demands smaller than 2%

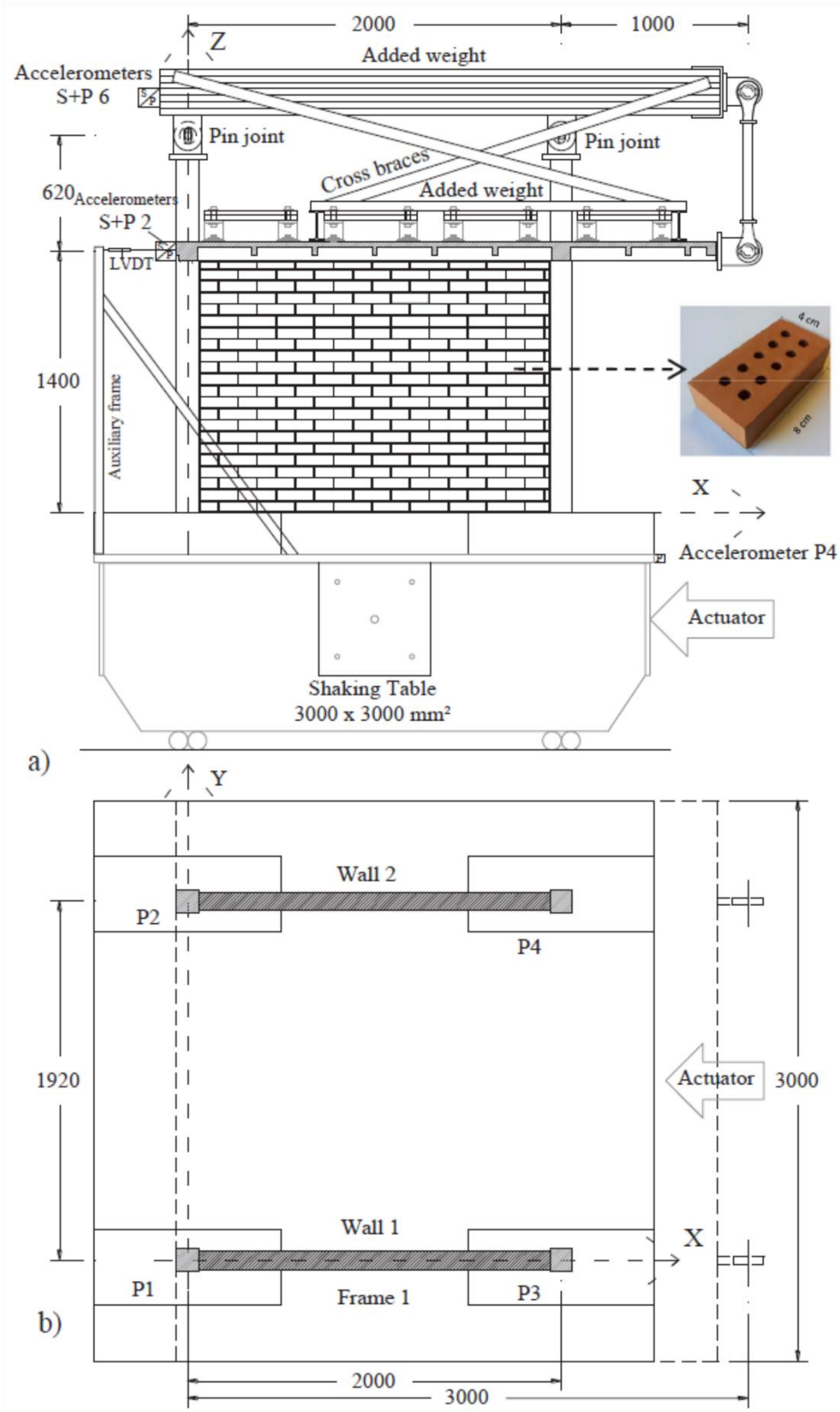

Figure 5-42: Test setup of one-story frame with infill tested by Benavent-Climent (2018)

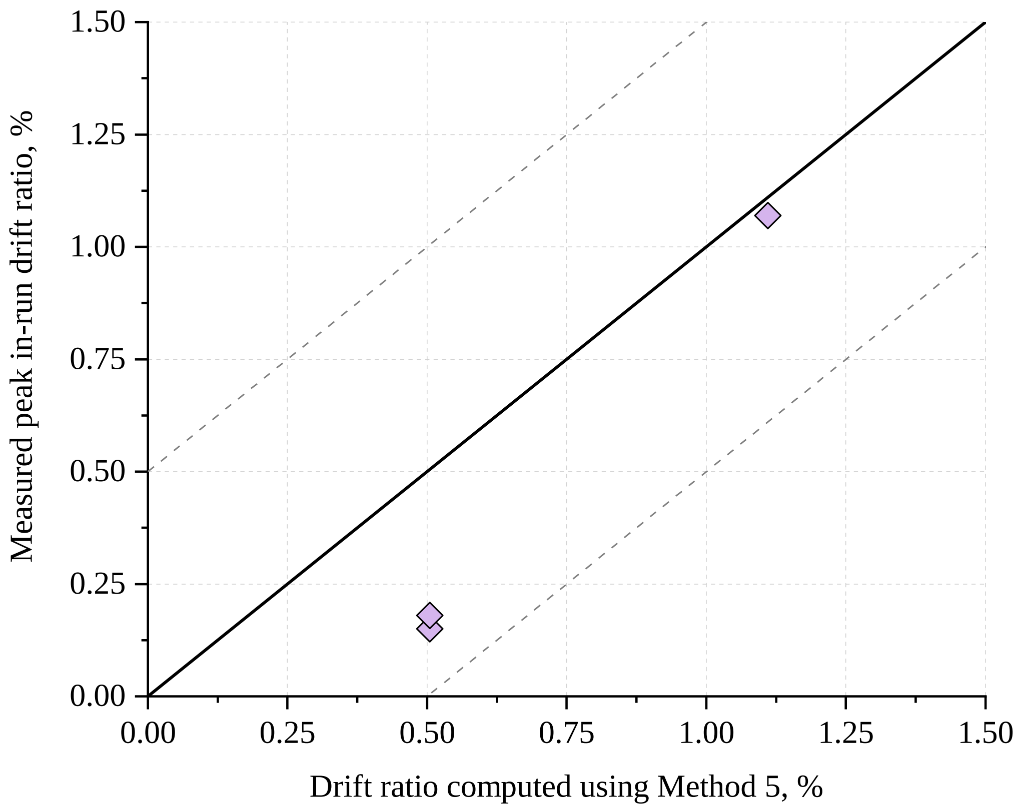

Figure 5-43: Measured vs. estimated drift computed using VOD of one-story infilled frame tested by Benavent-Climent (2018)

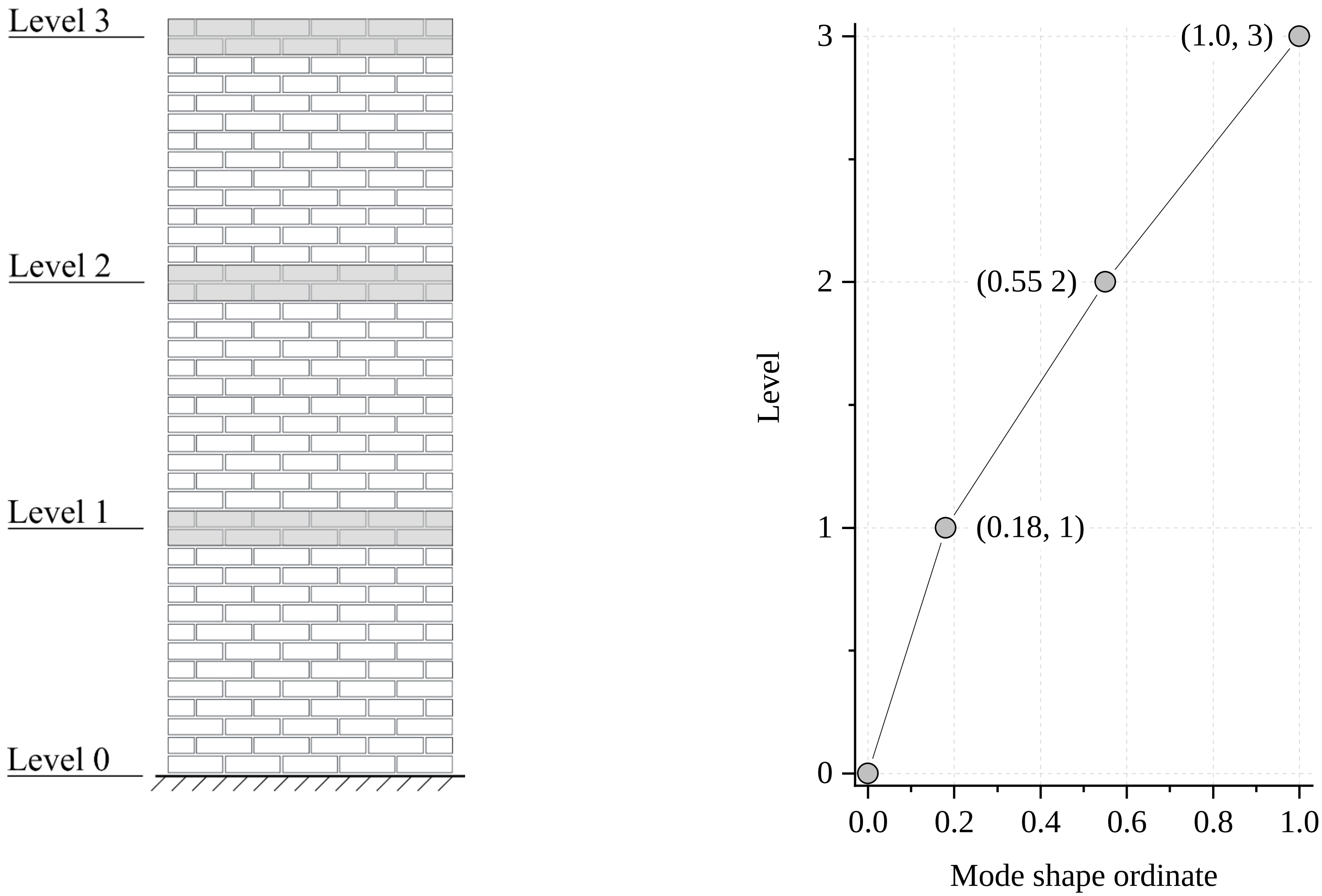

(a) Cantilever with three equal lumped masses and uniform lateral stiffness

(b) Mode shape

Figure 5-44: Linear mode shape of a three-degree-of-freedom cantilever structure

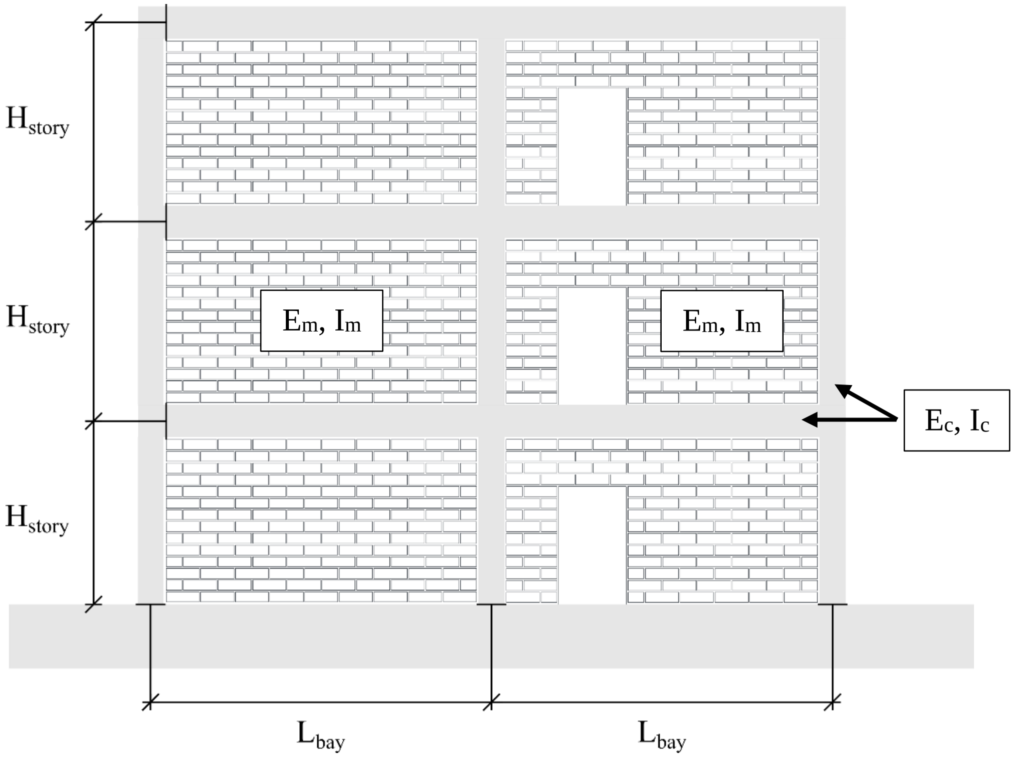

(a) Structural model - reinforced concrete frame with full-height masonry infill walls

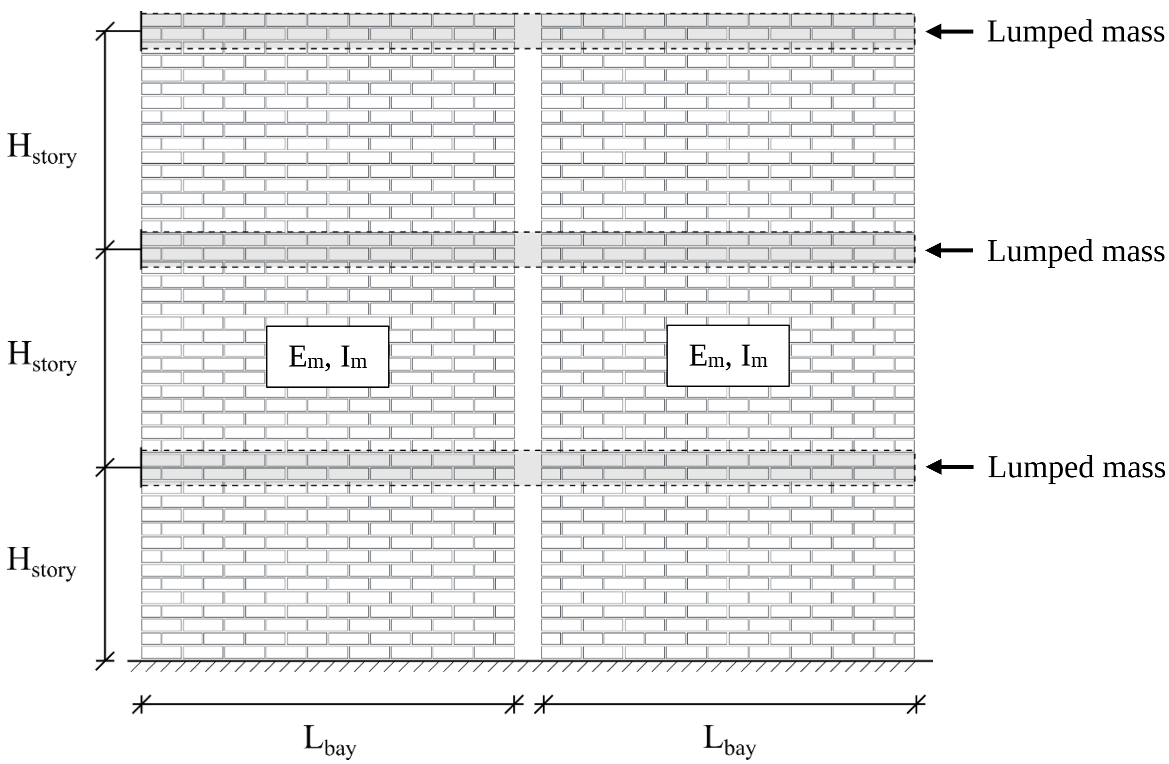

(b) Idealized model - continous masonry walls with equal lumped masses linked together with weak beams

Figure 5-45: Structural model and idealized model of a three-story infilled frame

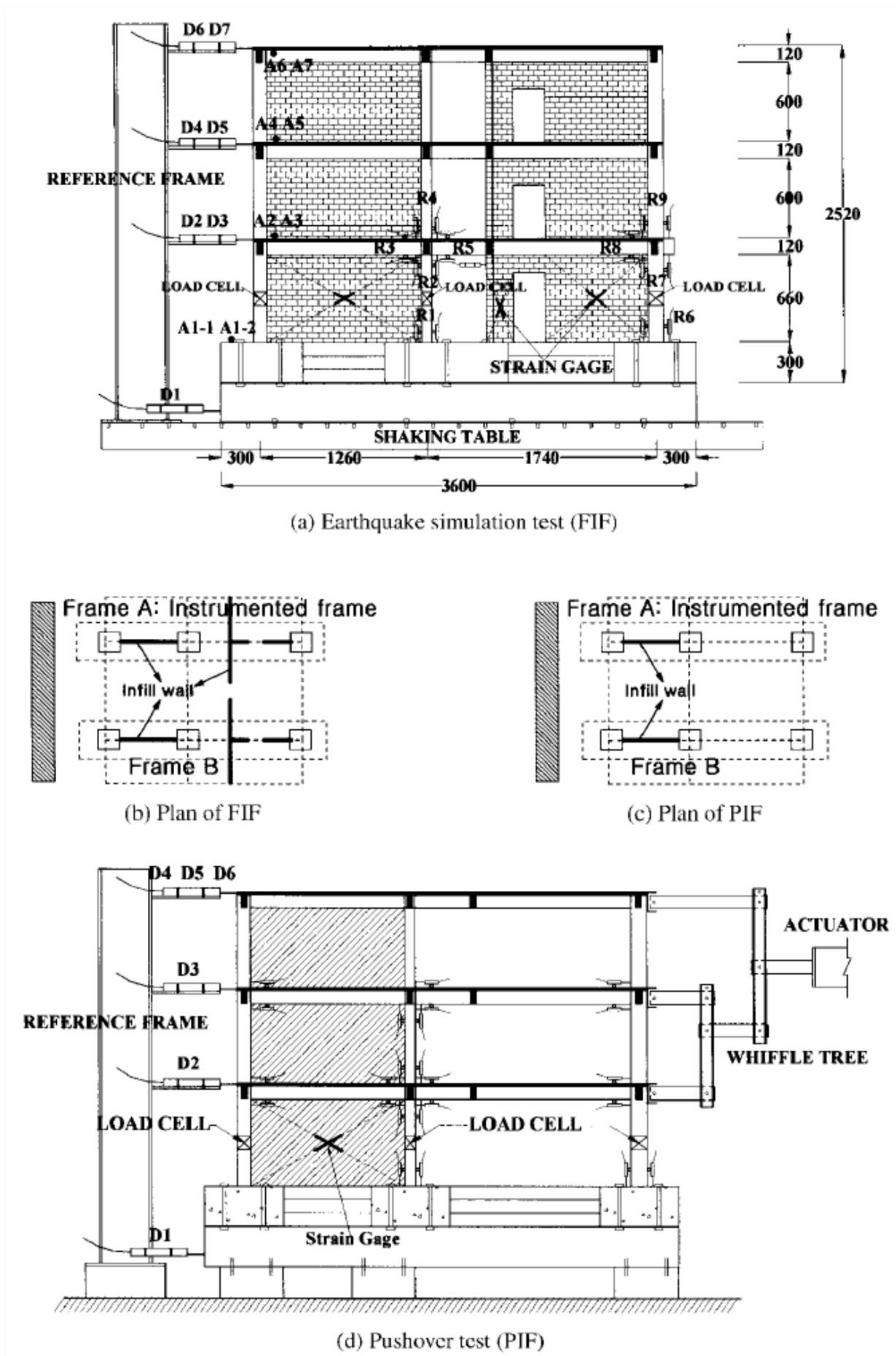

(a) Earthquake simulation test (FIF)

(b) Plan of FIF

(c) Plan of PIF

(d) Pushover test (PIF)

Figure 5-46: Test setup of three-story frame with infill tested by Lee (2002)

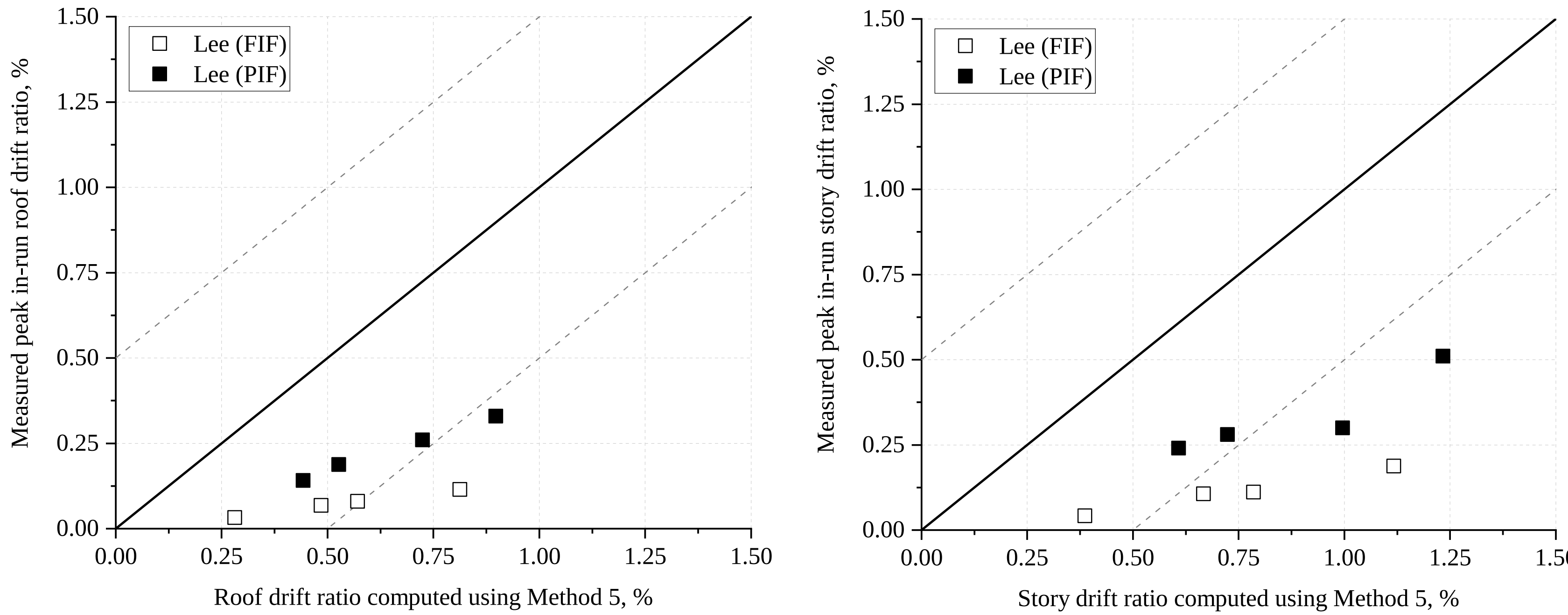

(a) Roof drift

(b) Story drift

Figure 5-47: Comparisons of measured and estimated peak drift computed using VOD of three-story infilled frames tested by Lee (2002)

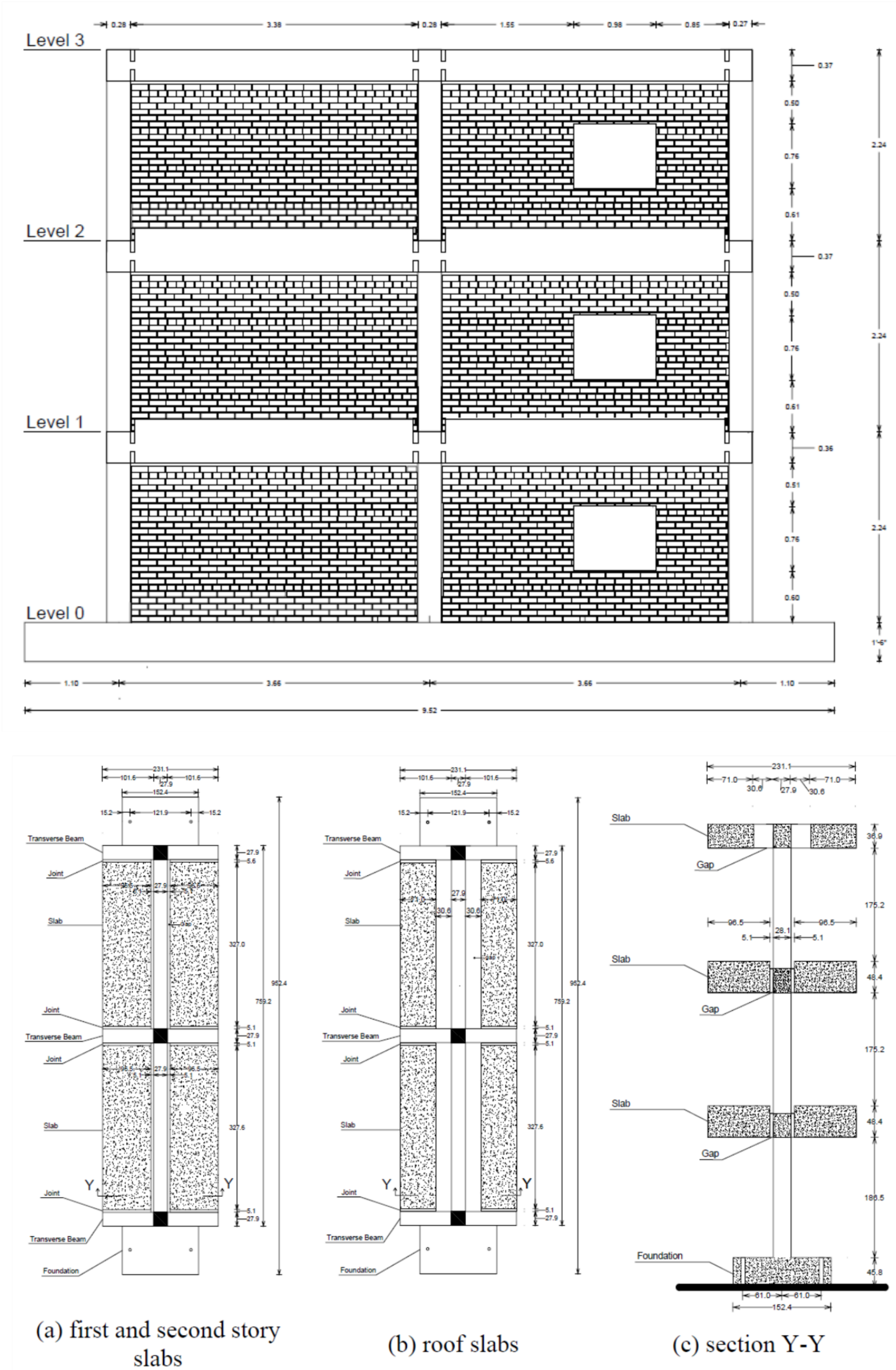

Figure 5-48: Test setup of three-story frame with infill tested by Stavridis (2009)

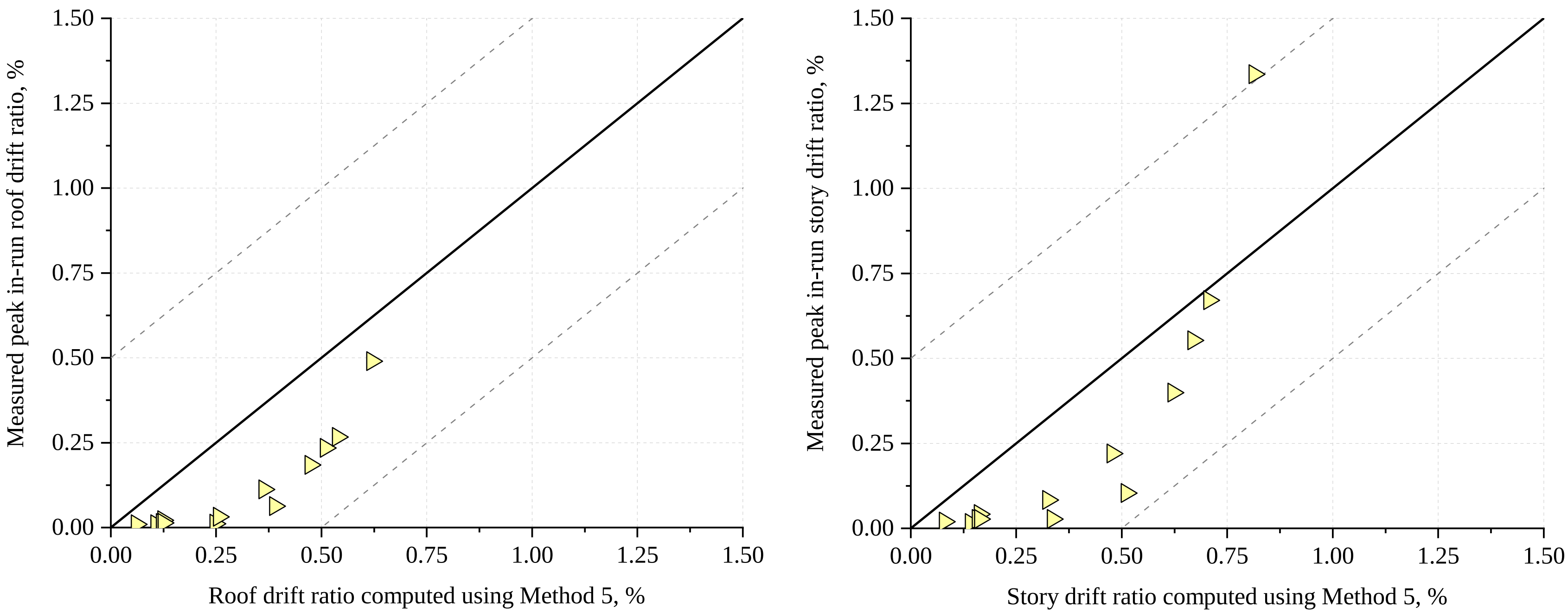

(a) Roof drift (b) Story drift

Figure 5-49: Comparisons of measured and estimated peak drift computed using VOD of three-story infilled frame tested by Stavridis (2009)

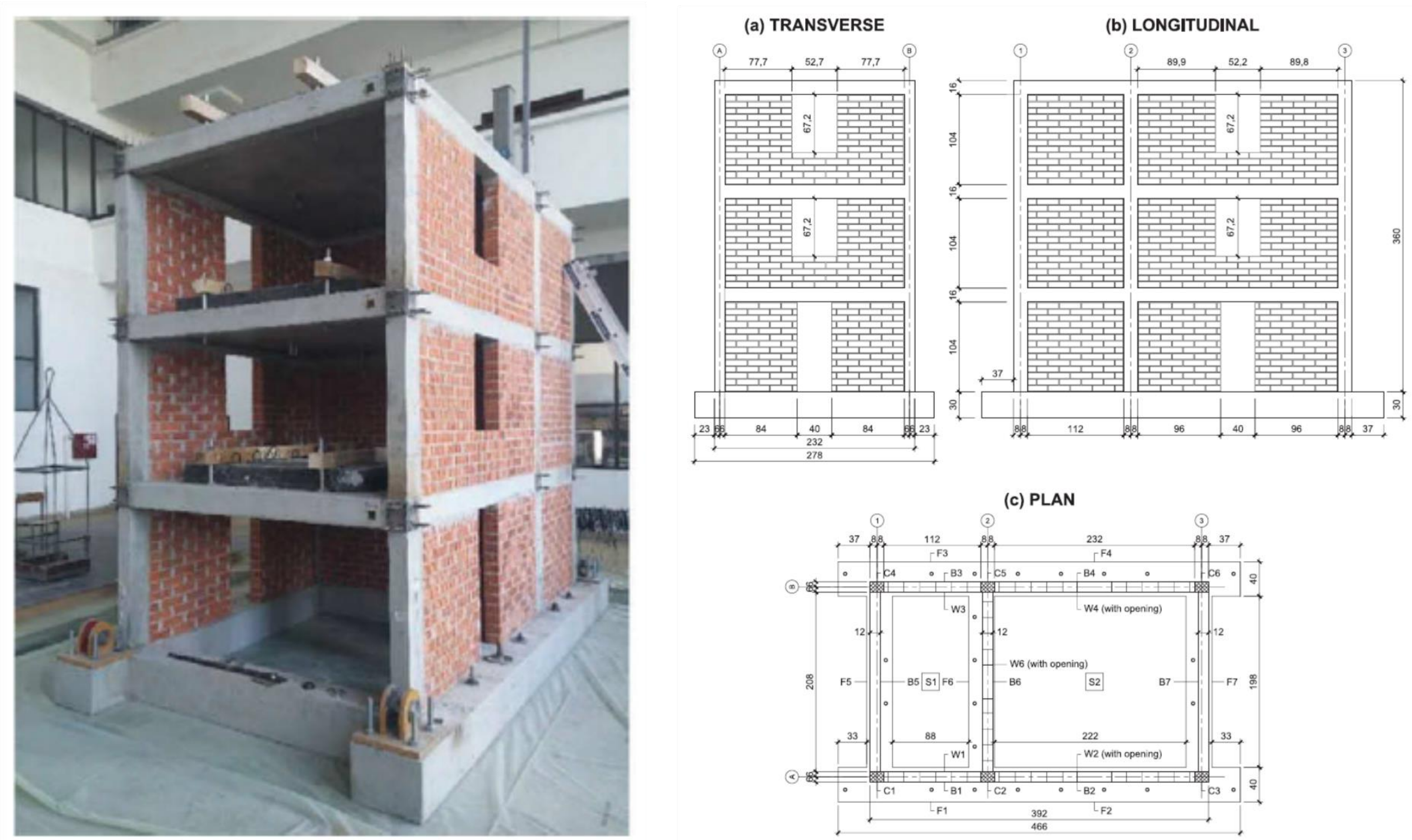

Figure 5-50: Test setup of three-story frame with infill tested in S1 by Guljas (2020)

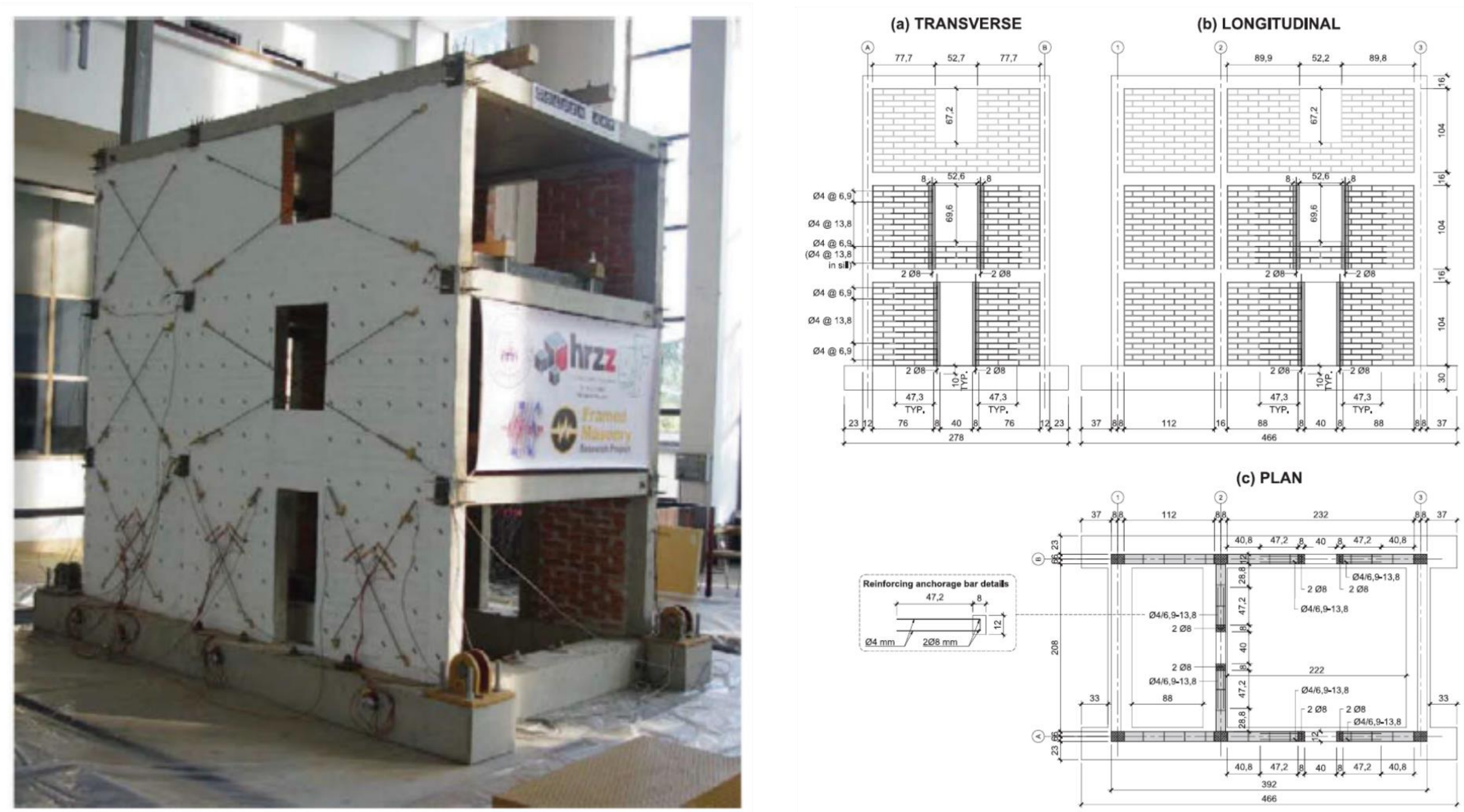

Figure 5-51: Test setup of three-story frame with infill tested in S2 by Guljas (2020)

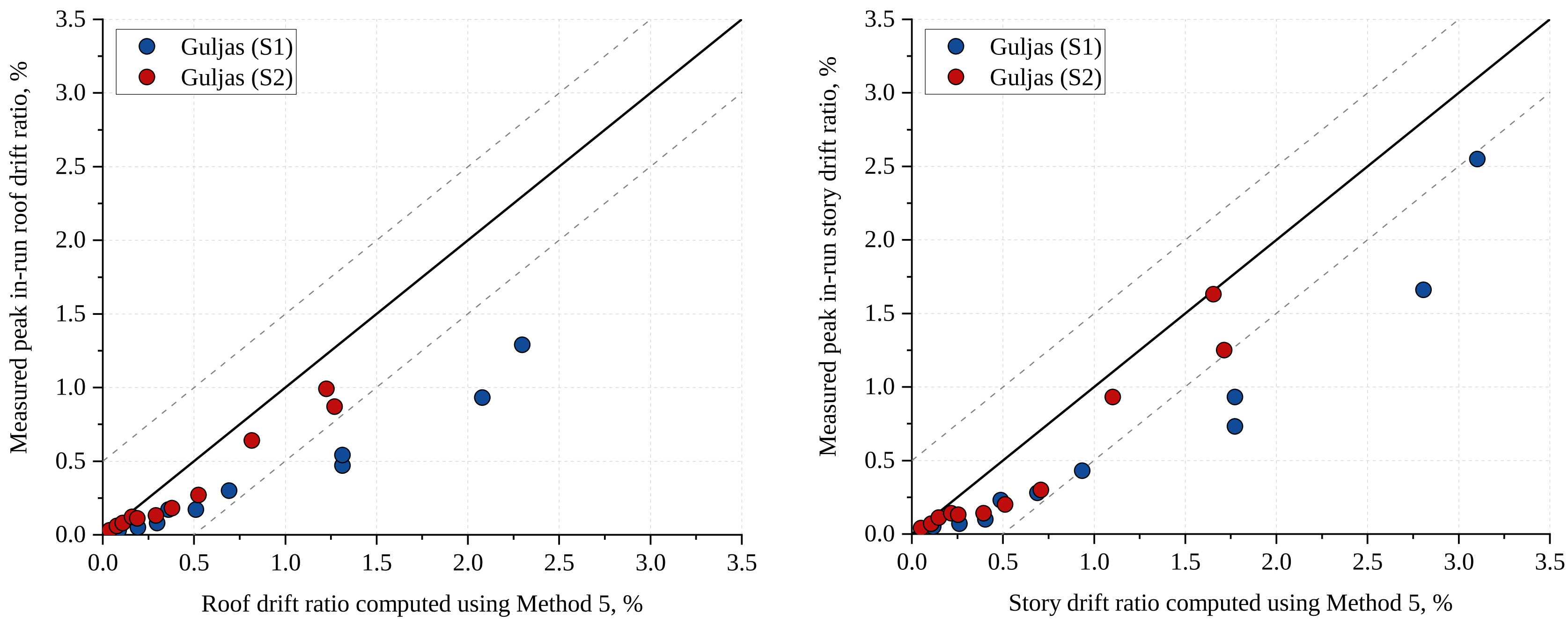

(a) Roof drift (b) Story drift

Figure 5-52: Comparisons of measured and estimated peak drift computed using VOD of three-story infilled frames tested by Guljas (2020)

Note: Axes in Figure 5-52 are plotted up to a drift ratio of 3.5% instead of 1.5%.

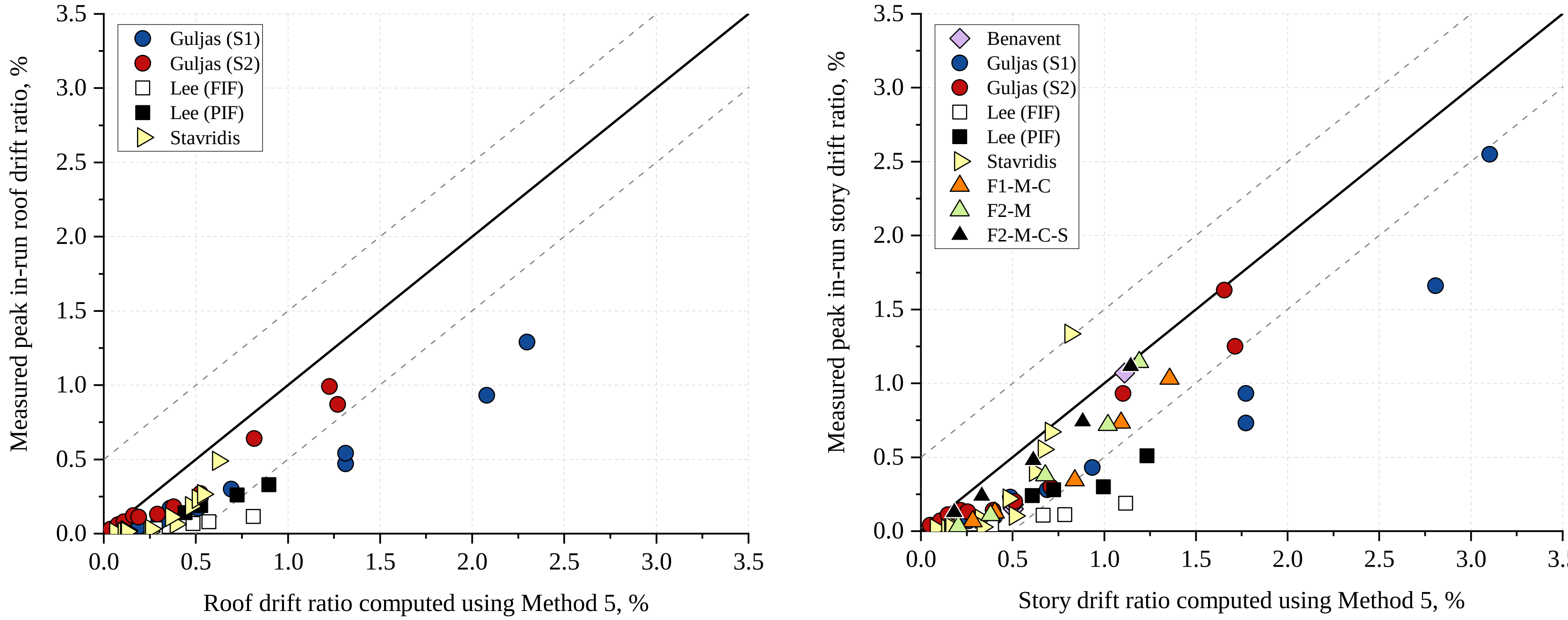

(a) Roof drift (b) Story drift

Figure 5-53: Comparisons of measured and estimated peak drift computed using VOD in tests of frames with infill

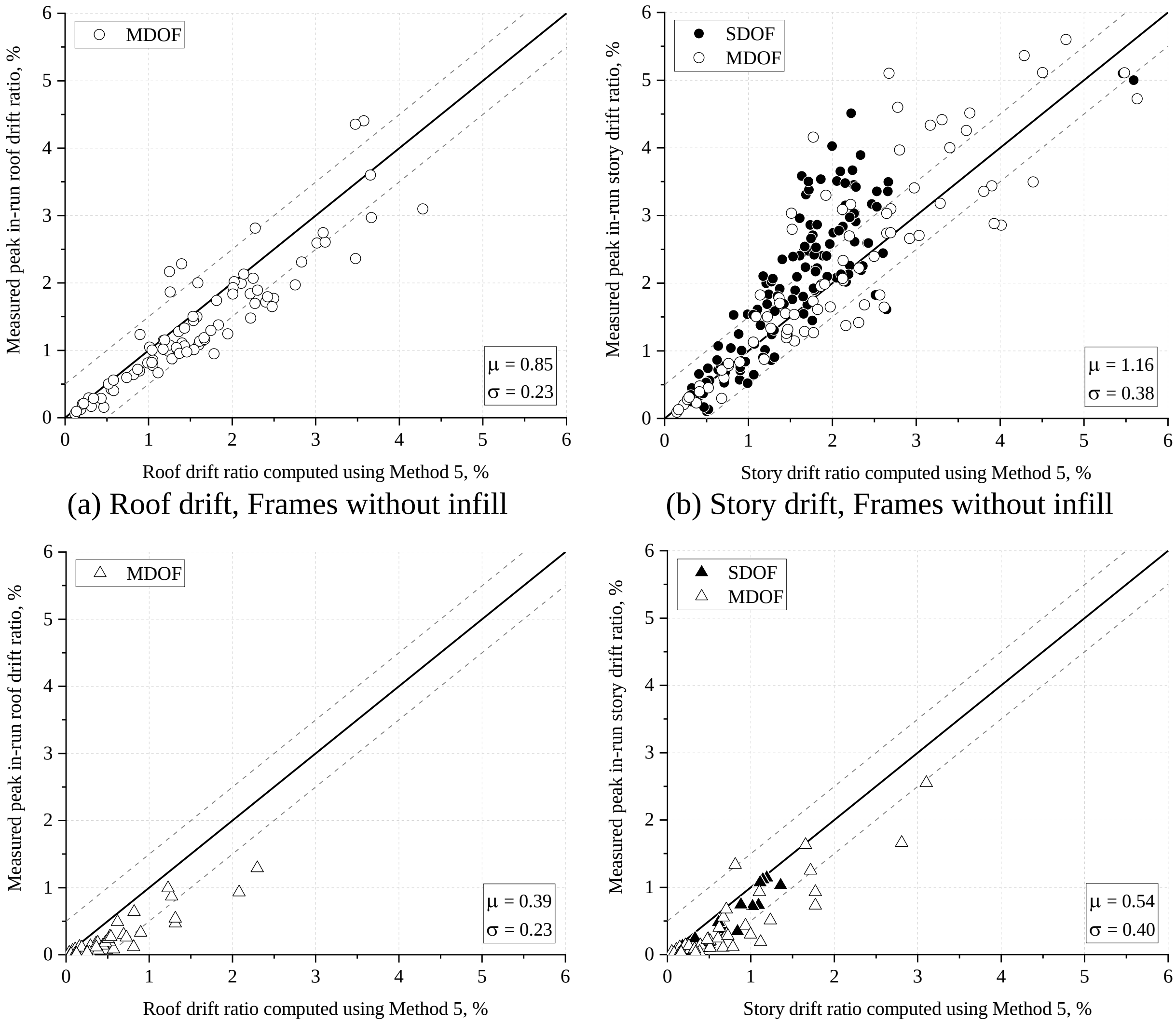

(a) Roof drift, Frames without infill

(b) Story drift, Frames without infill

(c) Roof drift, Frames with infill

(d) Story drift, Frames with infill

Figure 5-54: Comparisons of measured and estimated peak drift computed using VOD in tests of frames with and without masonry infill walls

Note: Estimates of drift were computed using Eqs. 5-14 through 5-16.

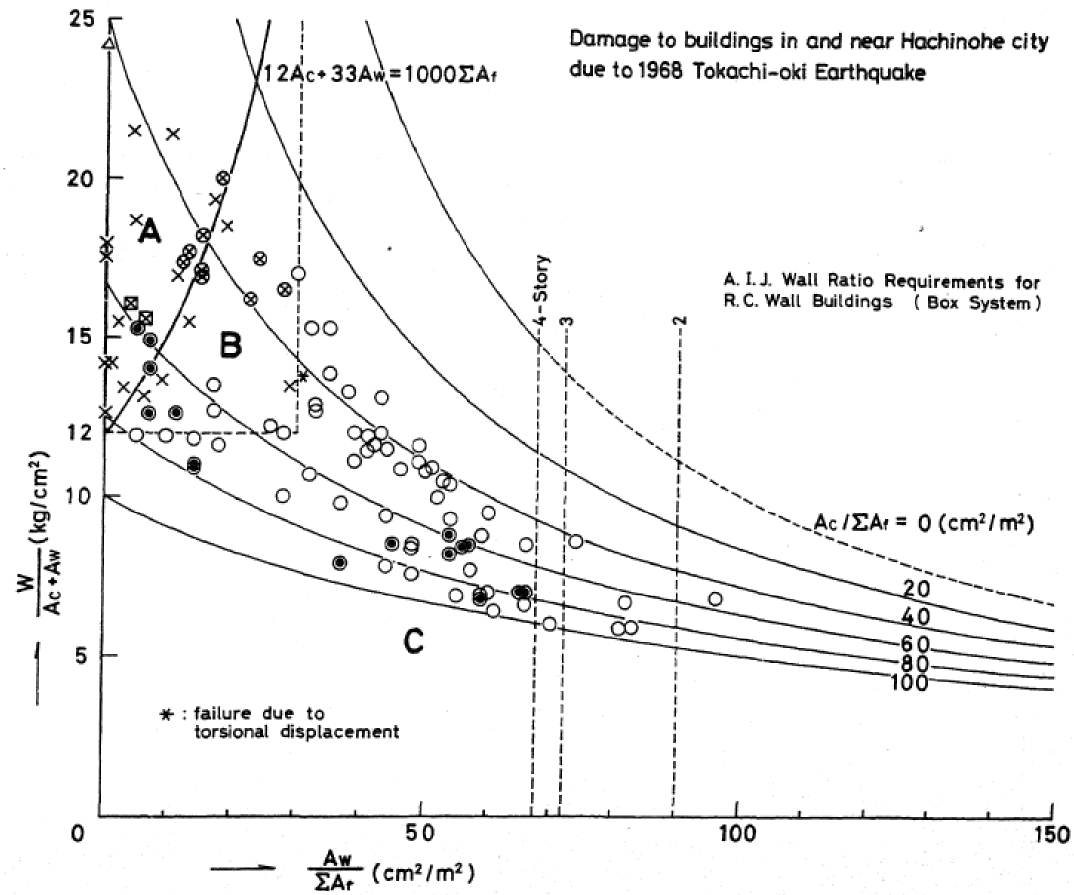

○ : Small or no damage in columns and shear walls
(◉ = C type school building)

△ : Collapse

× : Shear failure in most 1st-story columns

⊠ : Bending failure in about a half of 1st-story columns, shear failure in some 1st-story columns and slight shear cracks in shear walls

⊗ : Shear cracks in most 1st-story shear walls and slight damage in columns

Figure 6-1: Shiga Map

Note: Figure 6-1 is taken from Shiga (1977).

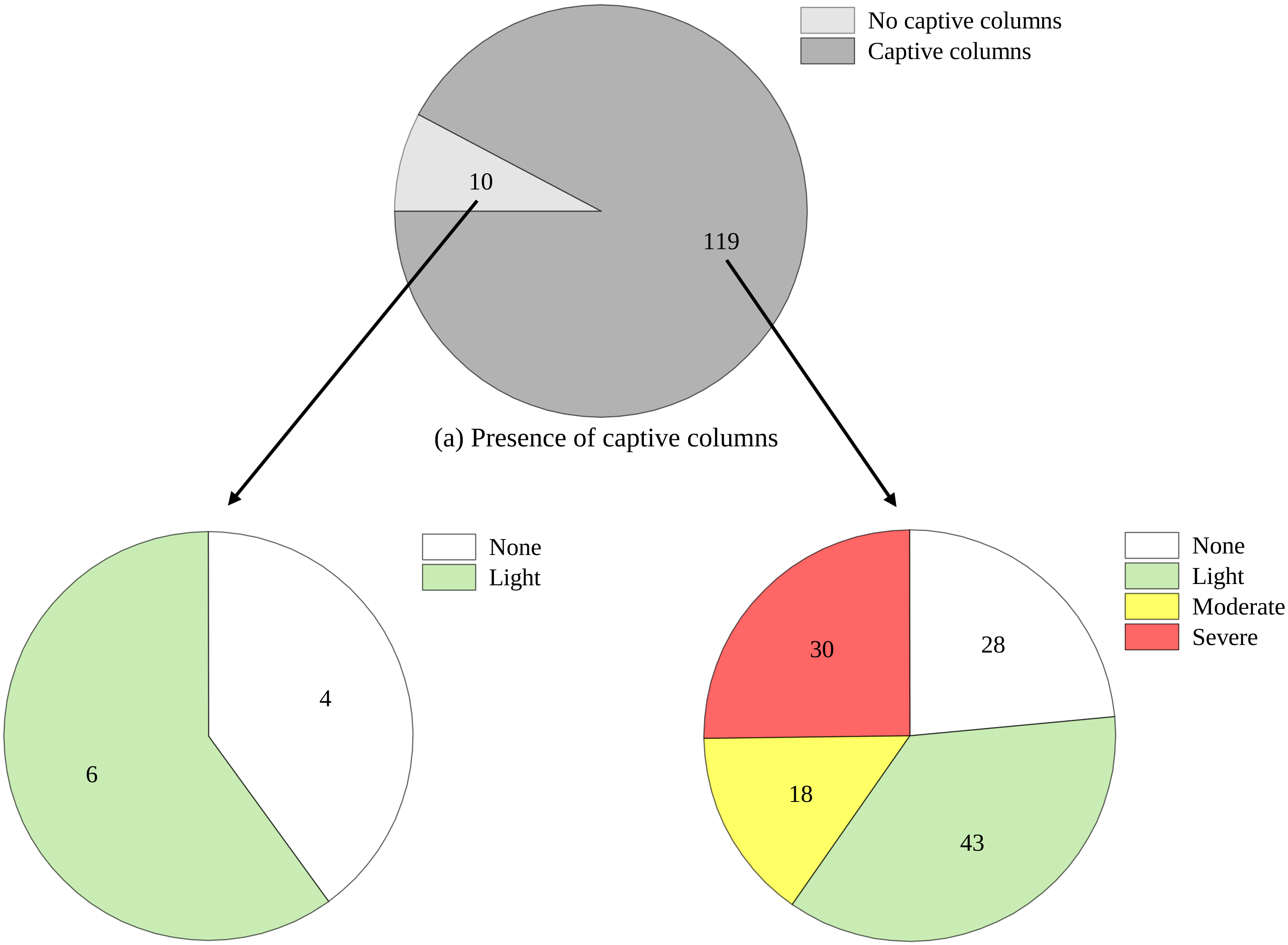

Figure 6-2: Type of structural damage in school buildings

(a-i) Exterior bay, SP144, east wing

(b-i) Exterior bay, SP145, west wing

(a-ii) Partial-height infill wall, SP144, east wing

(b-ii) Partial-height infill wall, SP145, west wing

Figure 6-3: Two school buildings surveyed after the 2007 Pisco earthquake

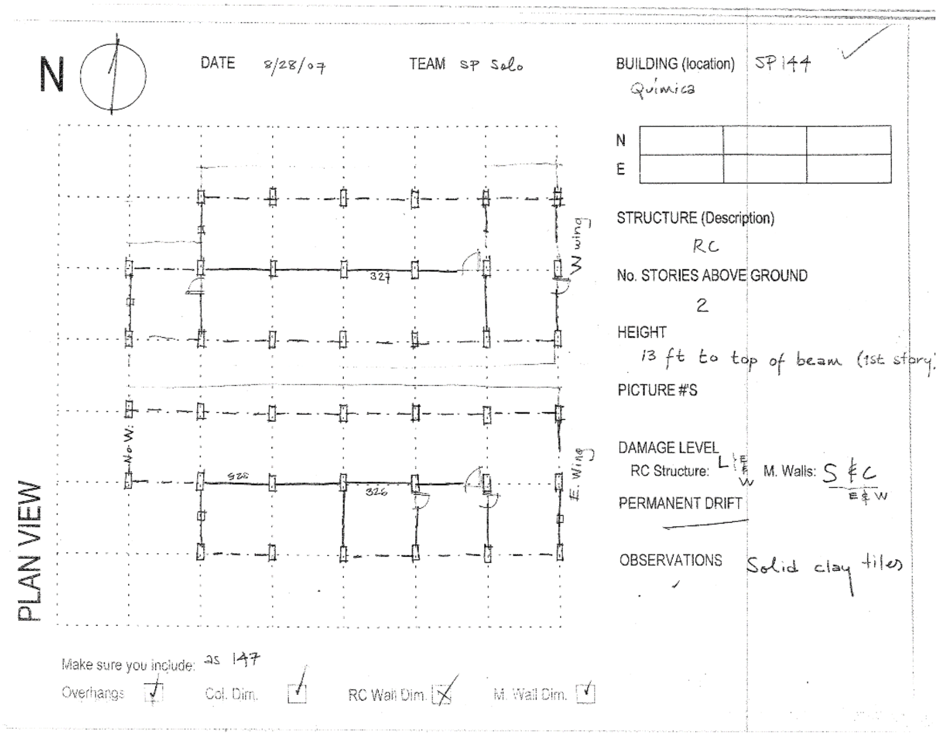

(a) Rough sketch of plan of building

(b) Fully infilled bays, east wing

Figure 6-4: School building SP144

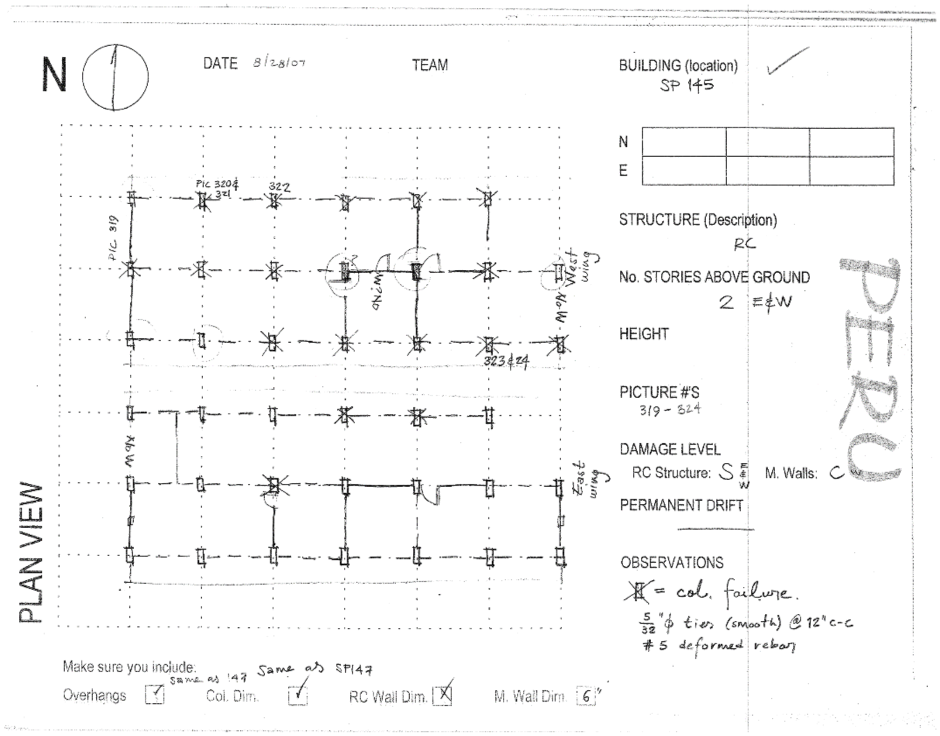

(a) Rough sketch of plan of building

(b) Partially infilled bays, west wing

Figure 6-5: School building SP145

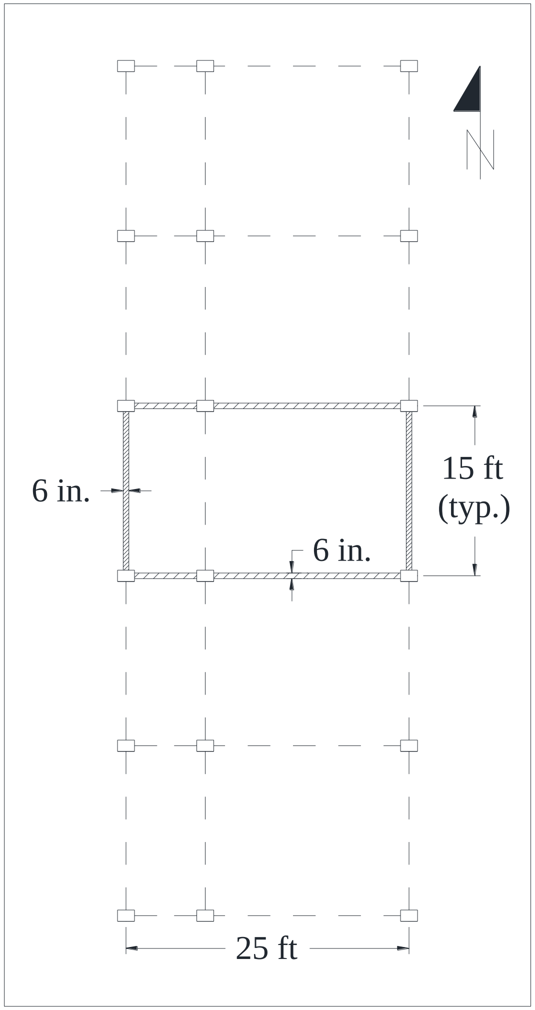

WA = "wall area" defined as cross-sectional area of infill wall on ground floor

WR = "wall ratio" defined as ratio of cross-sectional area of infill wall to total floor area

For a two-story school building with two fully infilled bays in NS and EW directions:

Tot. floor area = (2)·25 ft·(5·15 ft) = 3750 ft^2

NS infill WA = 2·(6 in.·15 ft) = 15 ft^2

NS infill WR = 15 ft^2 / 3750 ft^2 = 0.4%

EW infill WA = 2·(6 in.·25 ft) = 25 ft^2

EW infill WR = 25 ft^2 / 3750 ft^2 = 0.7%

Figure 6-6: Example of computing infill wall areas and infill wall ratios

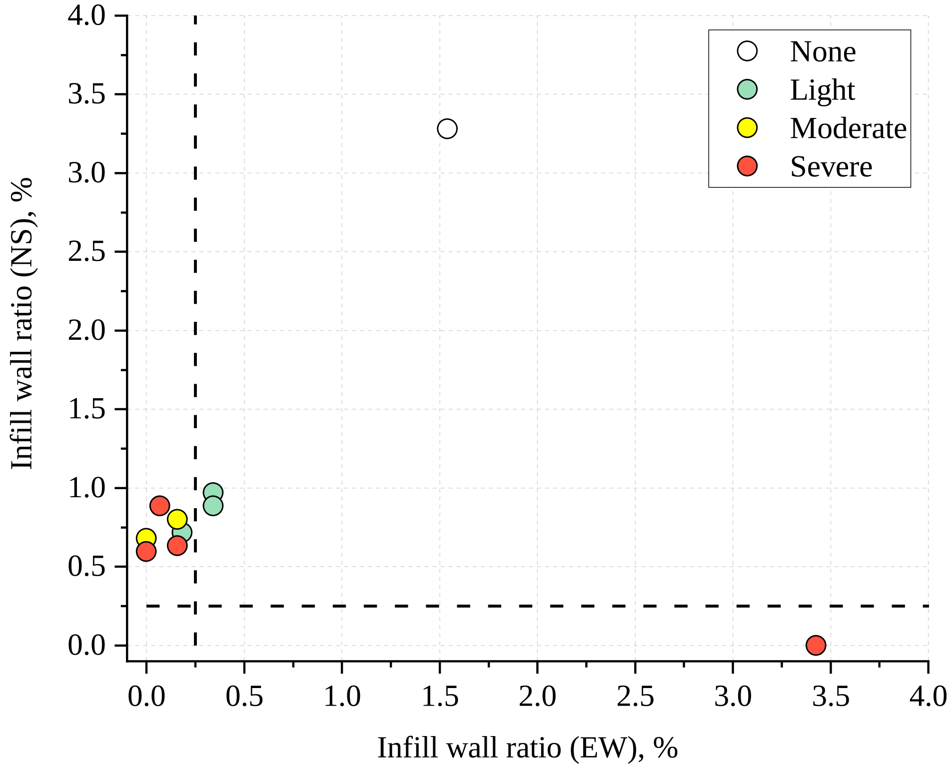

(a) Department of Ica, Ecuador, PGV = 17 in./sec.

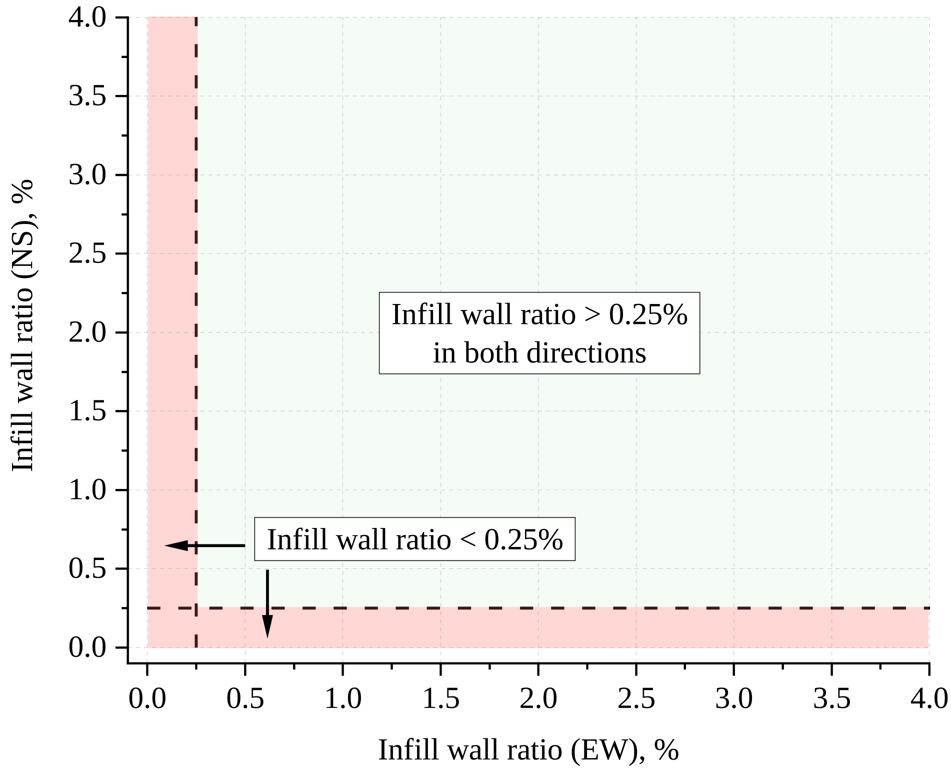

(b) Minimum infill wall ratio

Figure 6-7: Damaged school buildings surveyed after 2007 Pisco earthquake

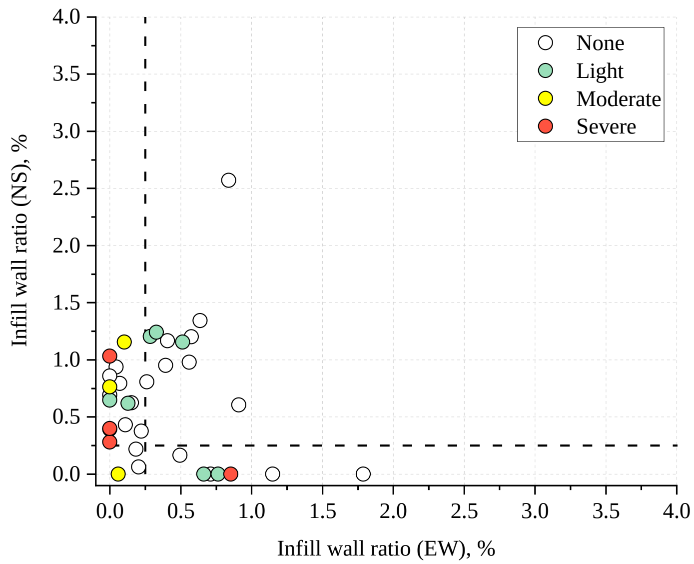

(a) Meinong District, Taiwan, PGV = 20 in./sec.

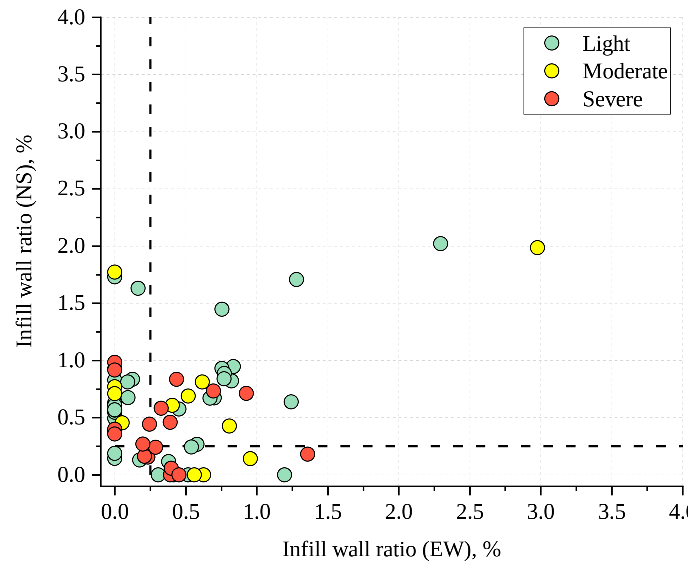

(b) Province of Manabí, Ecuador, PGV = 15 in./sec.

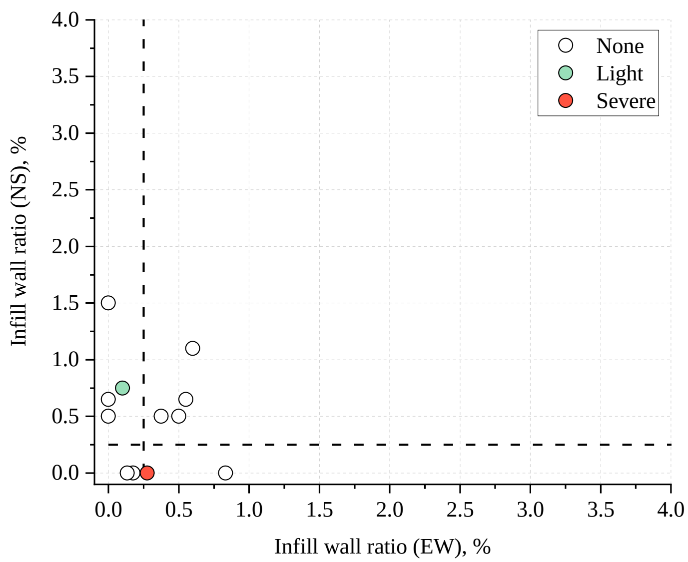

(c) Mexico City, Mexico, PGV = 12 in./sec.

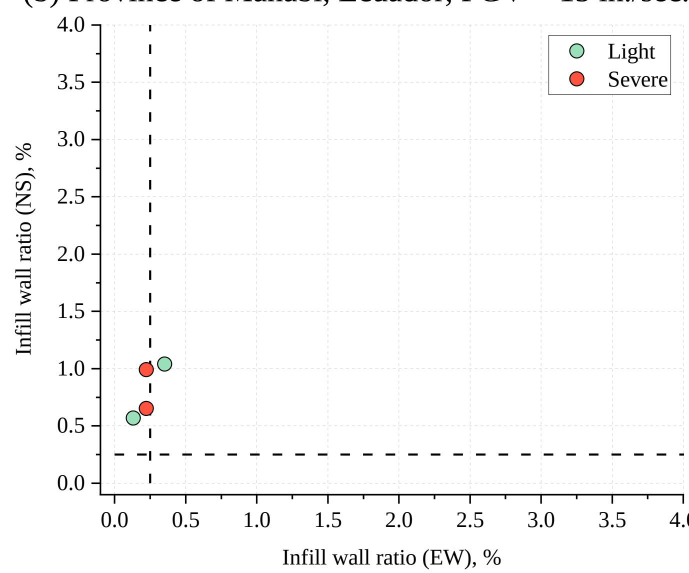

(d) Pohang, South Korea, PGV = 6 in./sec.

Figure 6-8: Infill wall ratios of damaged school buildings

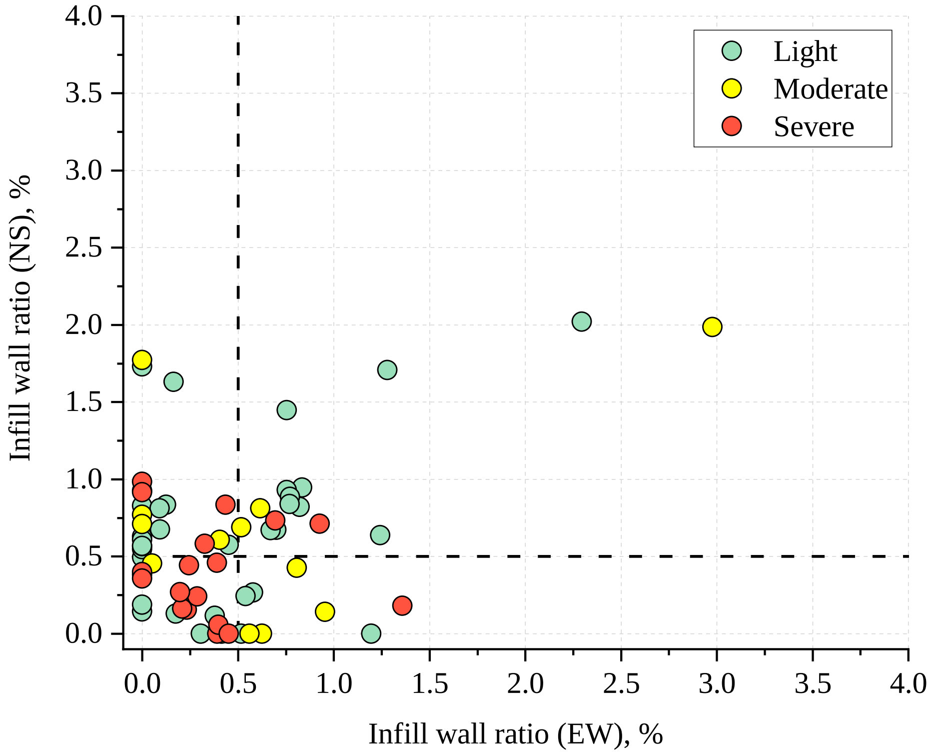

(a) Province of Manabí, Ecuador, PGV = 15 in./sec.

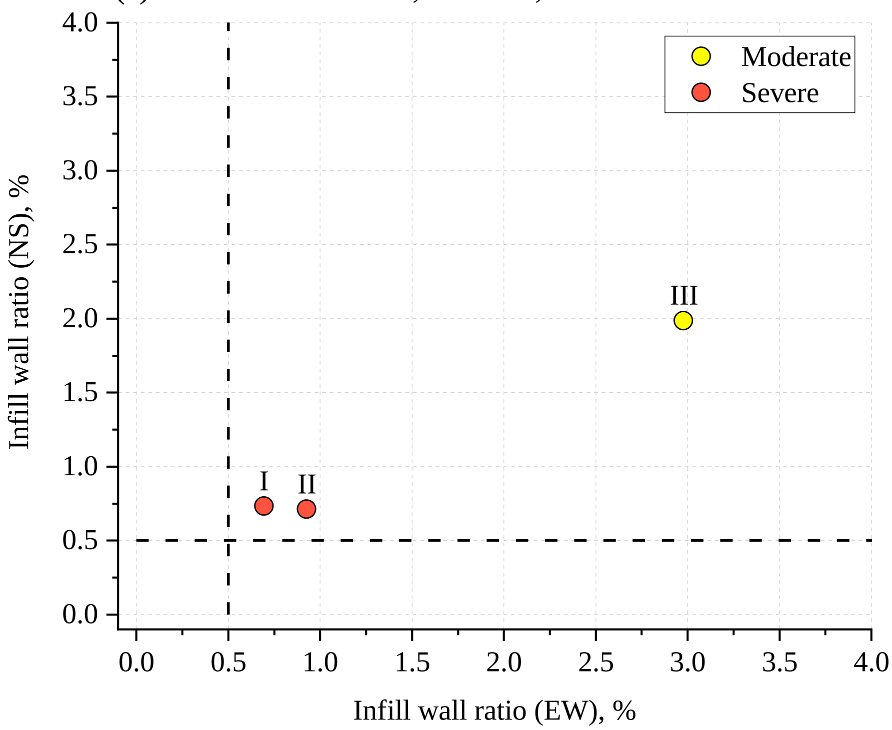

(b) School buildings with moderate and severe damage

Figure 6-9: Damaged school buildings surveyed after 2016 Manabí, Ecuador earthquake

Figure 6-10: School building I with severe damage

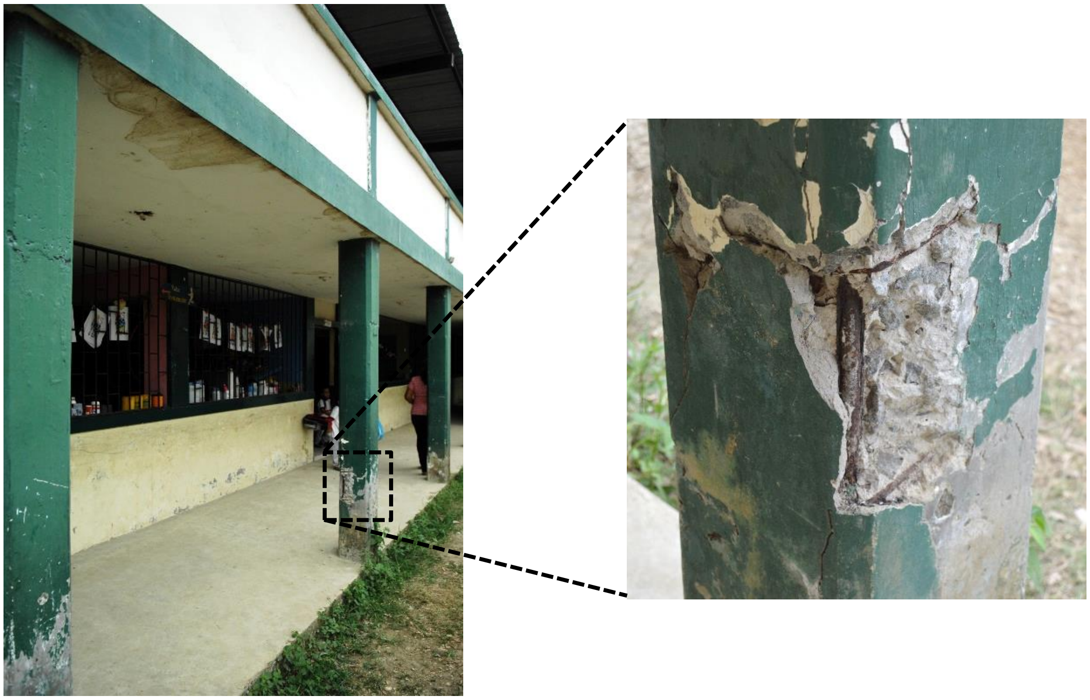

(a) Column line without partition walls

(b) Column line with partion walls

Figure 6-11: School building II with severe damage

Figure 6-12: School building III with moderate damage

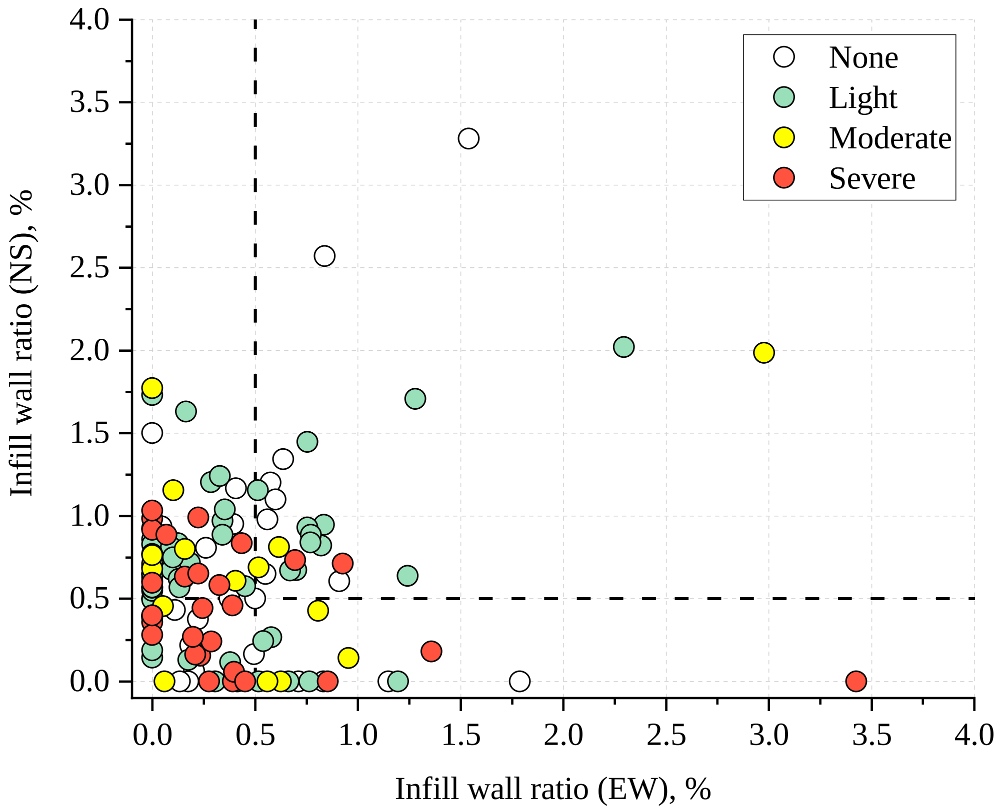

Figure 6-13: Damage in school buildings with masonry infill walls

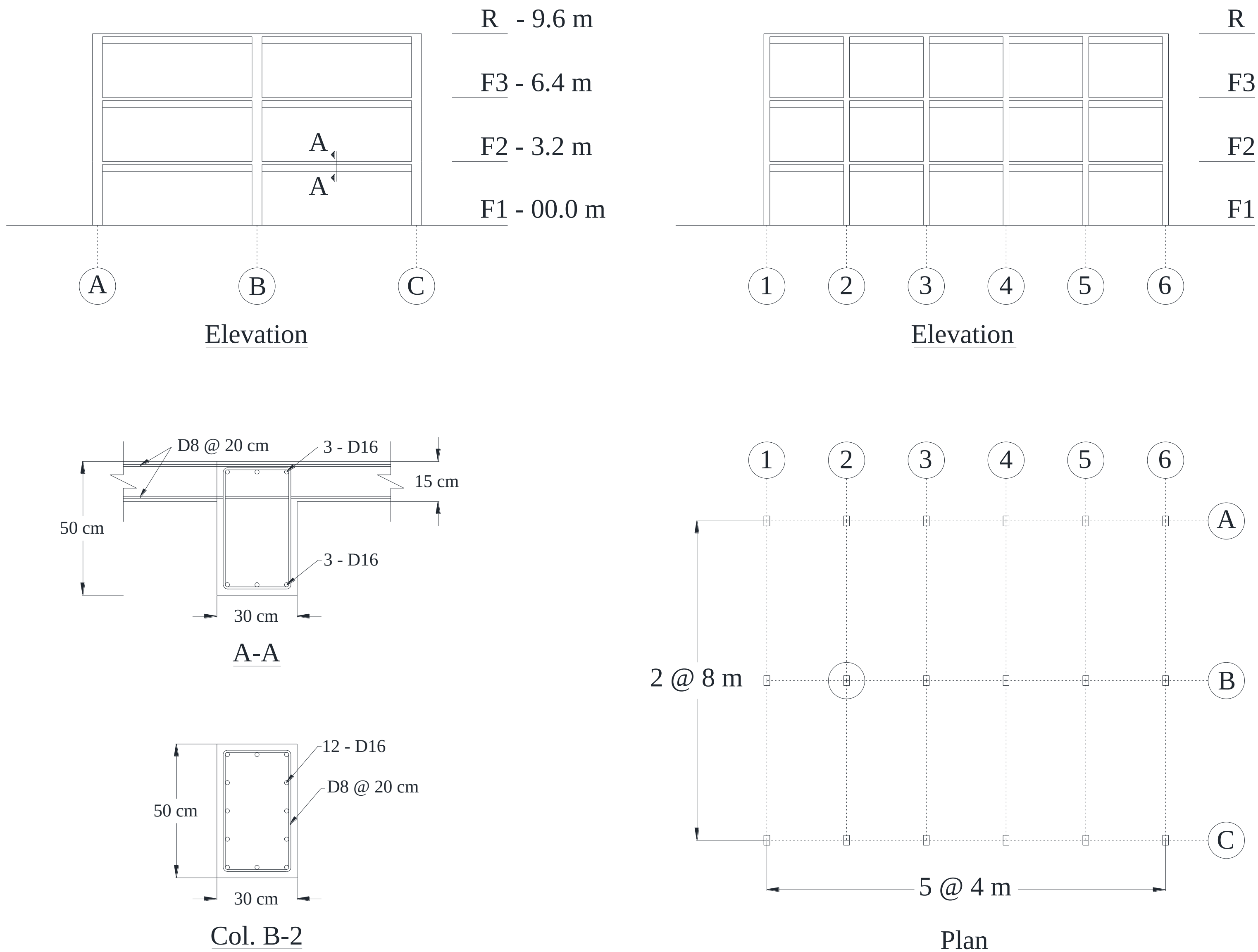

Figure 6-14: Bare frame prototype

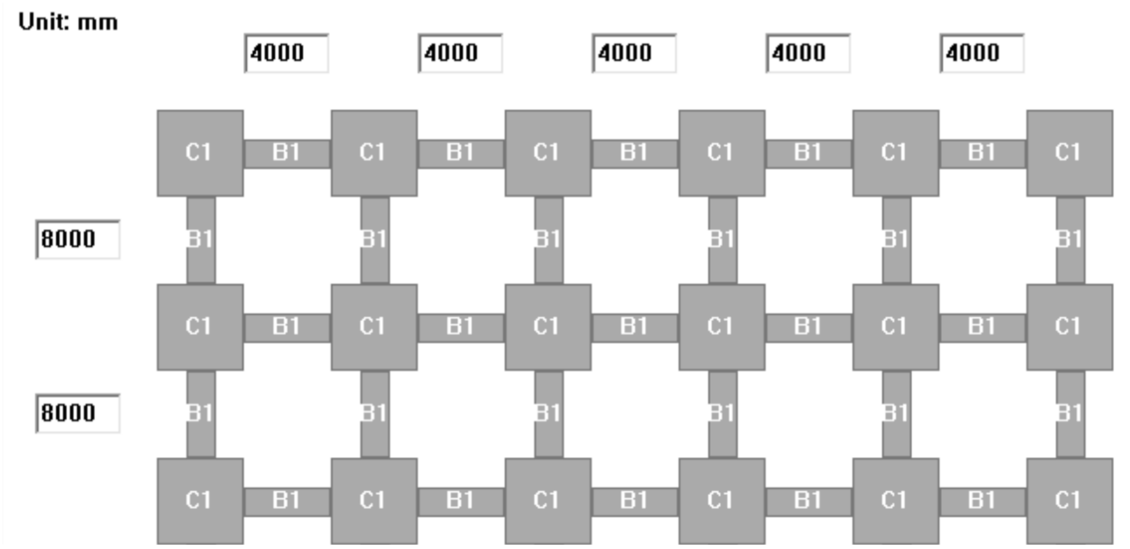

(a) Plan view

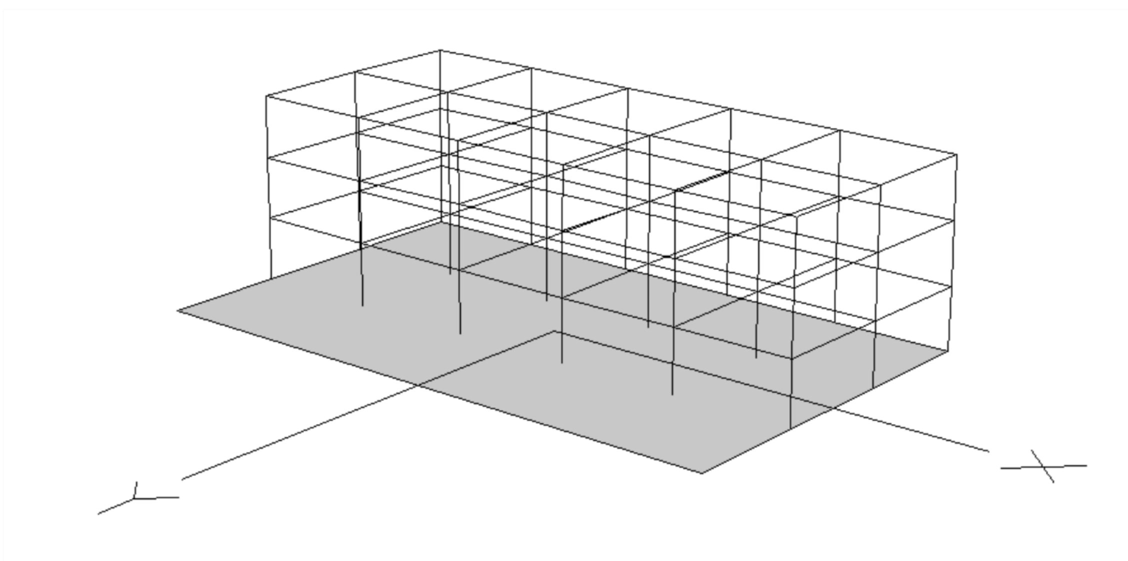

(b) Isometric view

Figure 6-15: Bare frame prototype modeled in STERA 3D

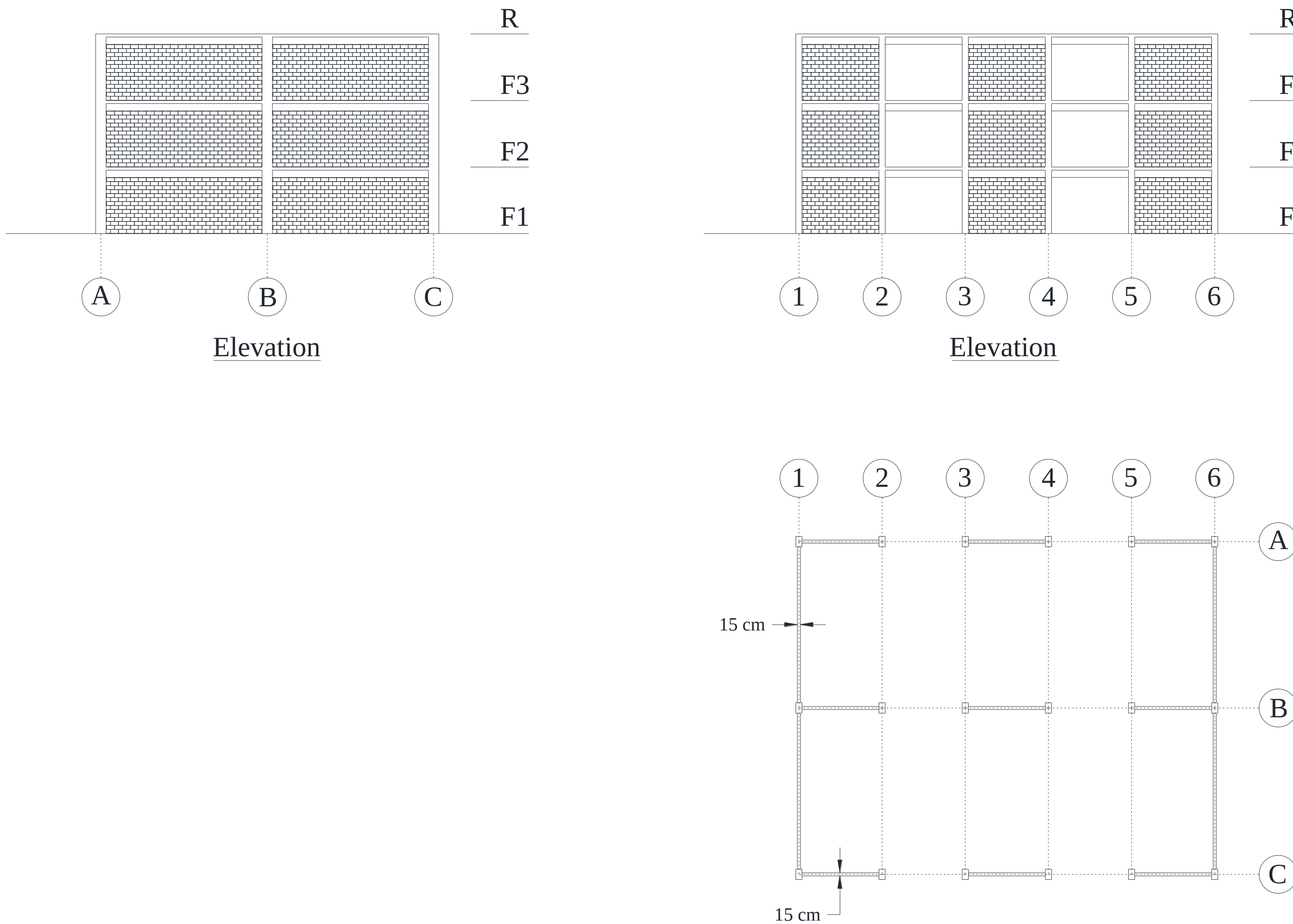

Figure 6-16: Infilled frame prototype

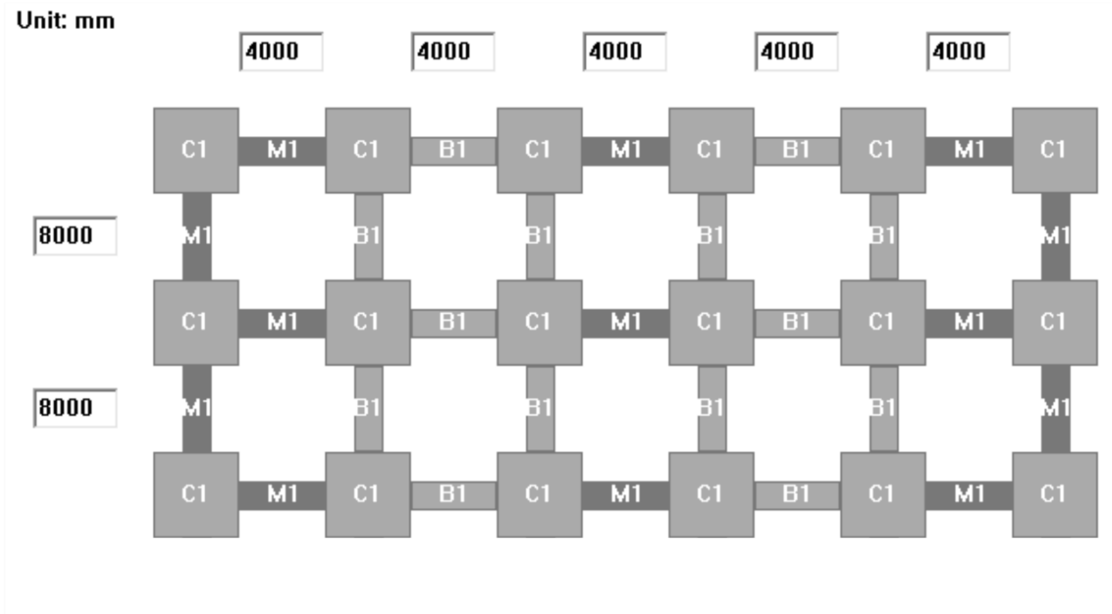

(a) Plan view

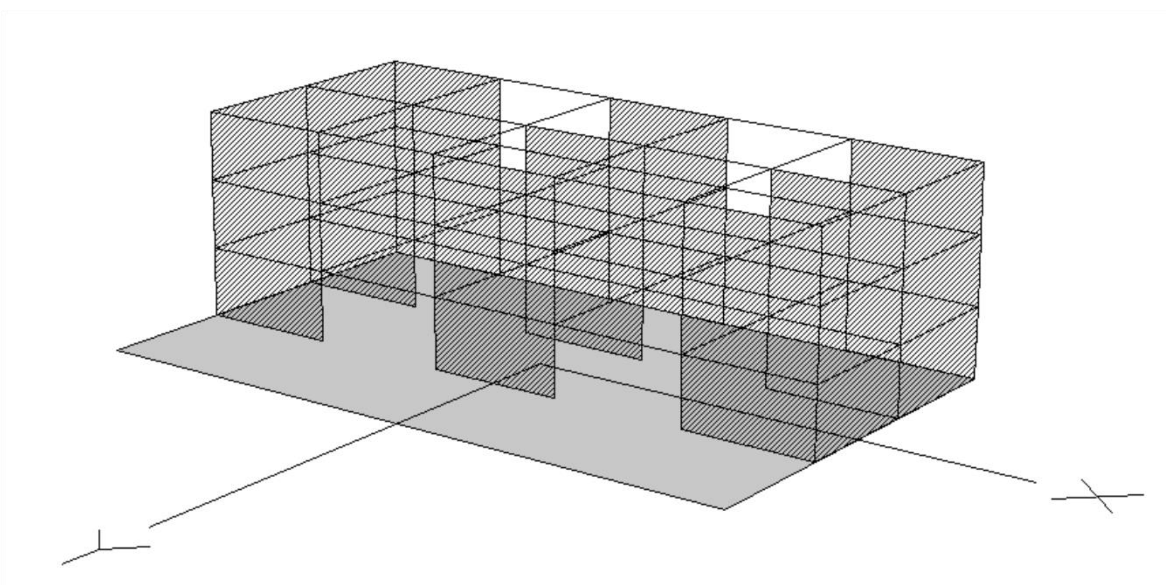

(b) Isometric view

Figure 6-17: Infilled frame prototype modeled in STERA 3D

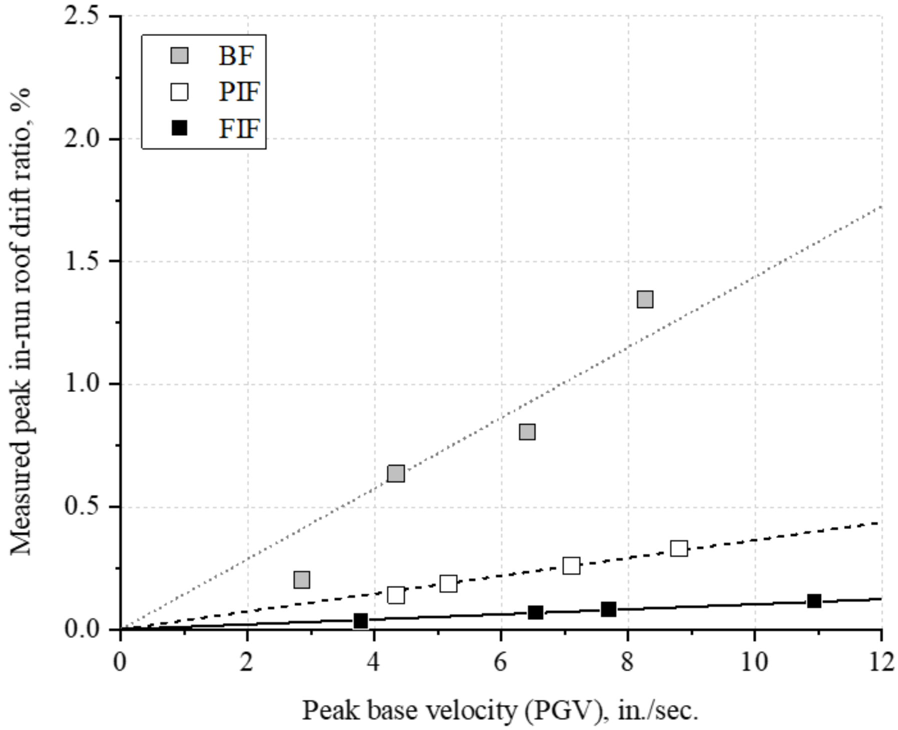

Figure 7-1: Variation of measured peak in-run roof drift ratio with PGV in tests by Lee (2002)

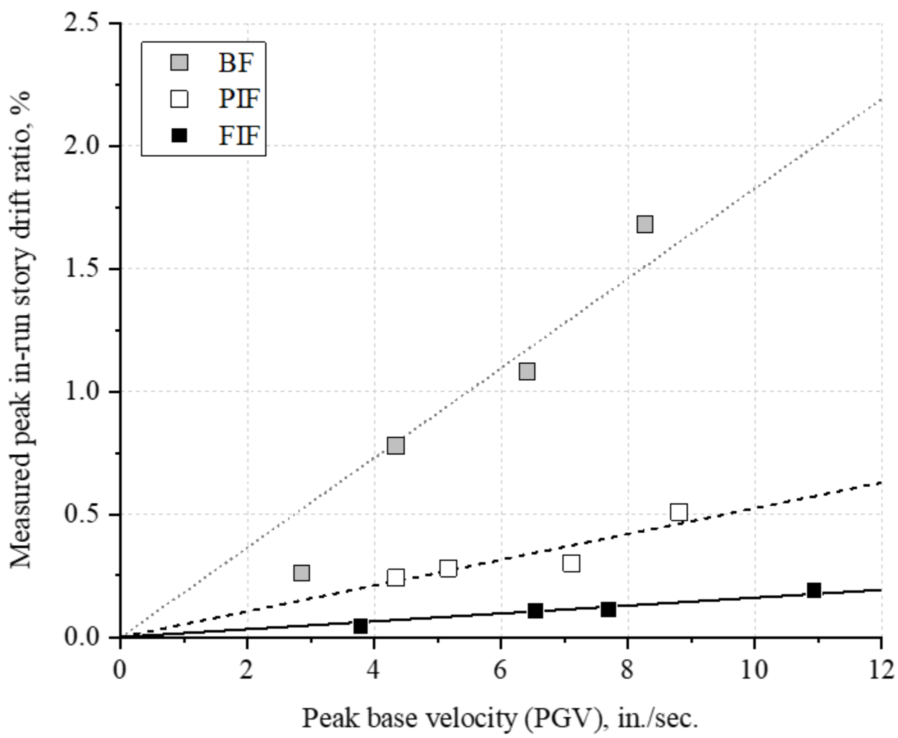

Figure 7-2: Variation of measured peak in-run story drift ratio with PGV in tests by Lee (2002)

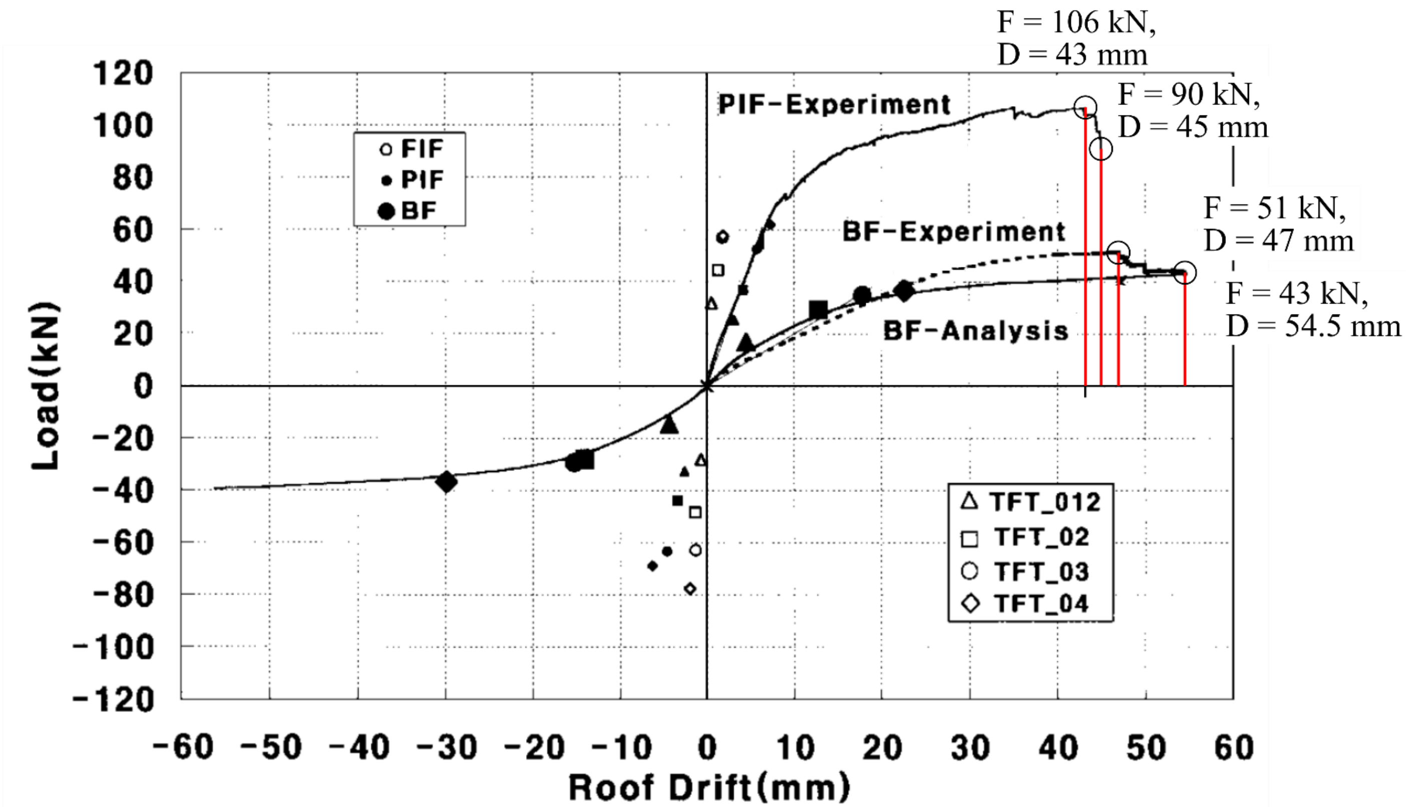

Figure 7-3: Force-displacement relationship of specimens tested by Lee (2002)

Note: Figure is taken from Lee (2002) and roof drift capacities of Specimens PIF and BF are 2 and 2.5%.

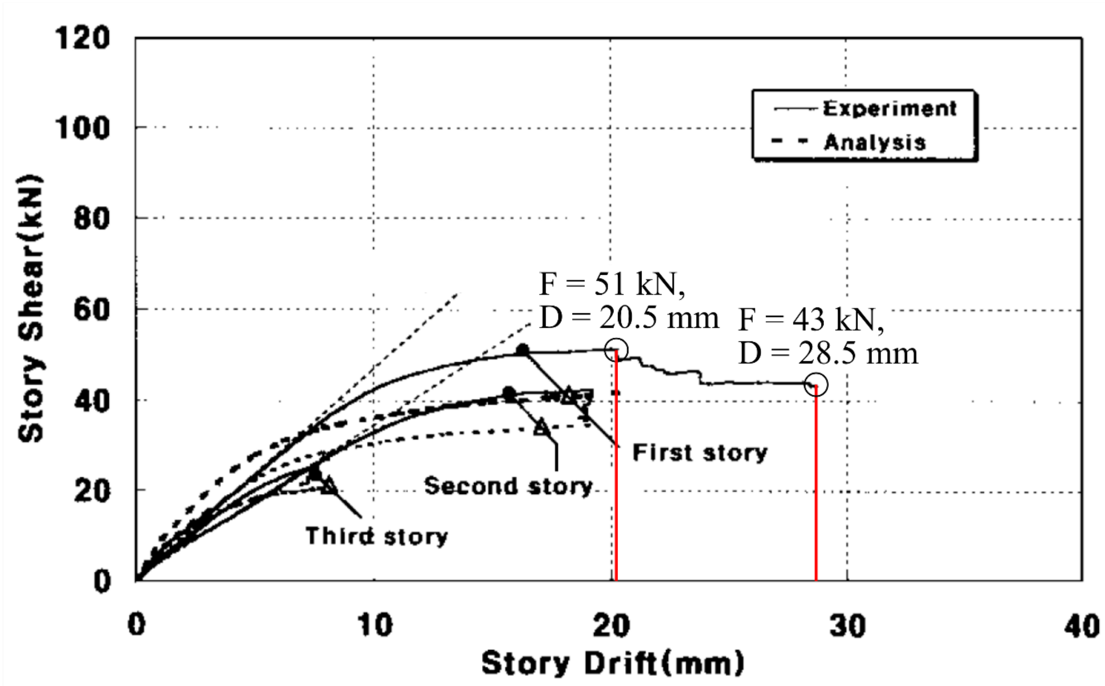

Figure 7-4: Force-displacement relationship of Specimen BF tested by Lee (2002)

Note: Figure is taken from Lee (2002) and story drift capacity of Specimen BF is 4%.

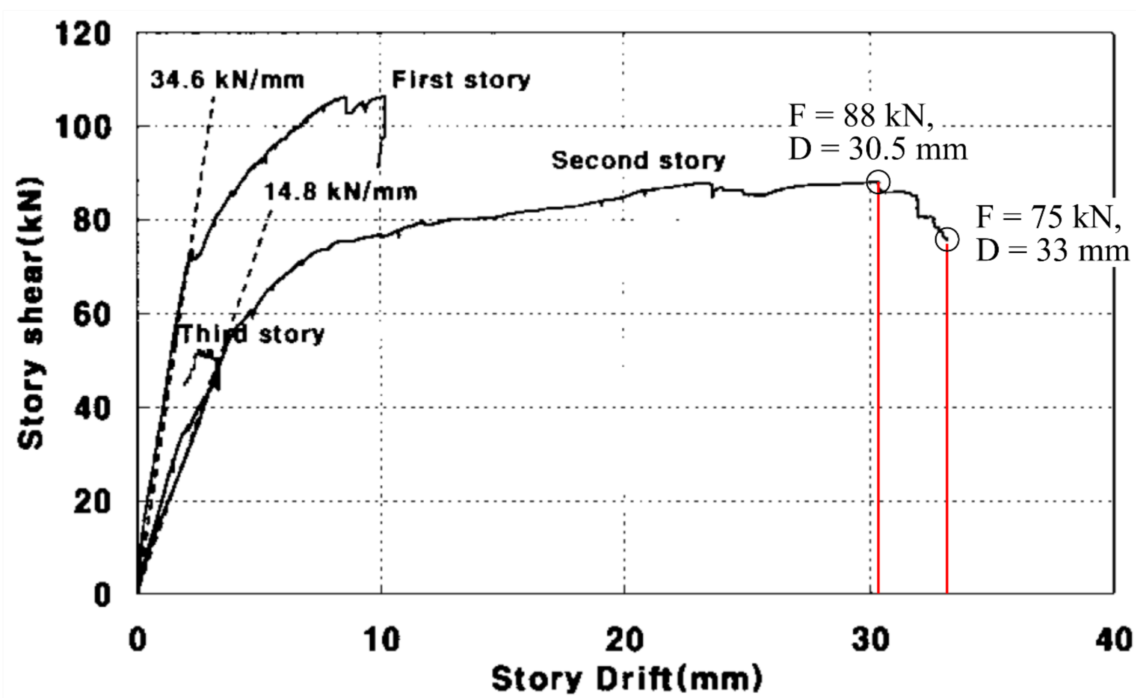

Figure 7-5: Force-displacement relationship of Specimen PIF tested by Lee (2002)

Note: Figure is taken from Lee (2002) and story drift capacity of Specimen PIF is 4.6%.

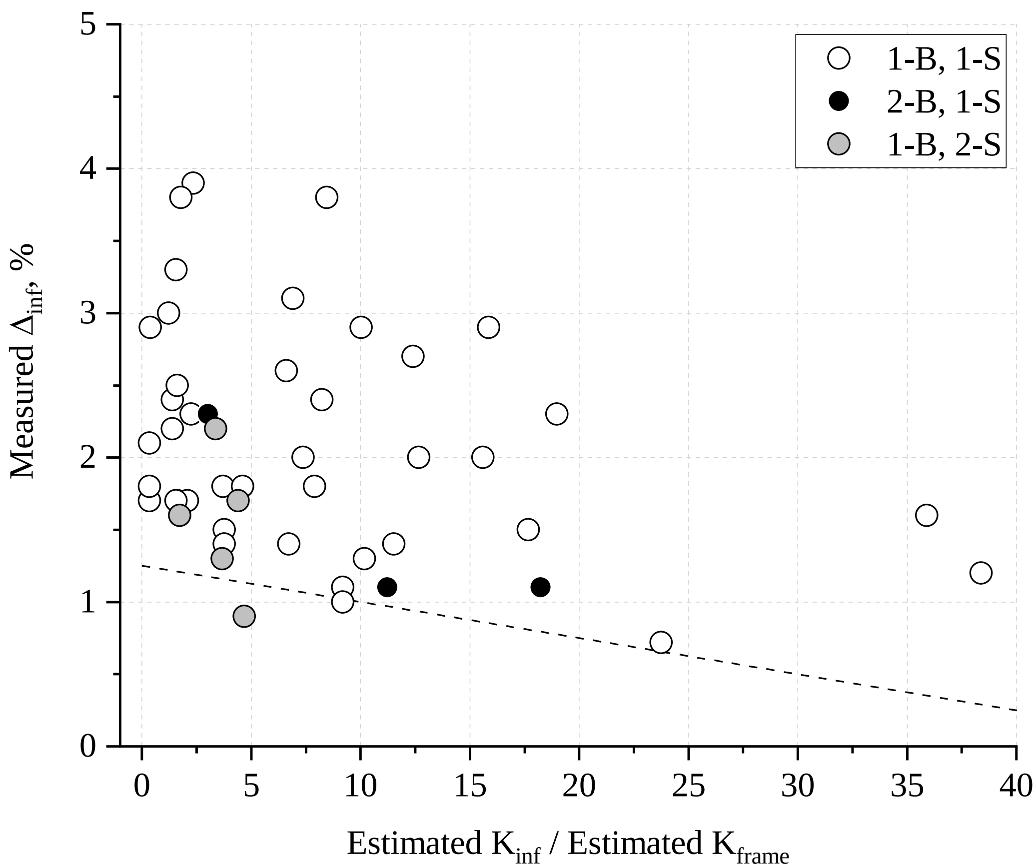

Figure 7-6: Variation of measured drift capacity of infilled frame to ratio of estimated initial lateral stiffness of infilled frame to estimated initial lateral stiffness of bare frame

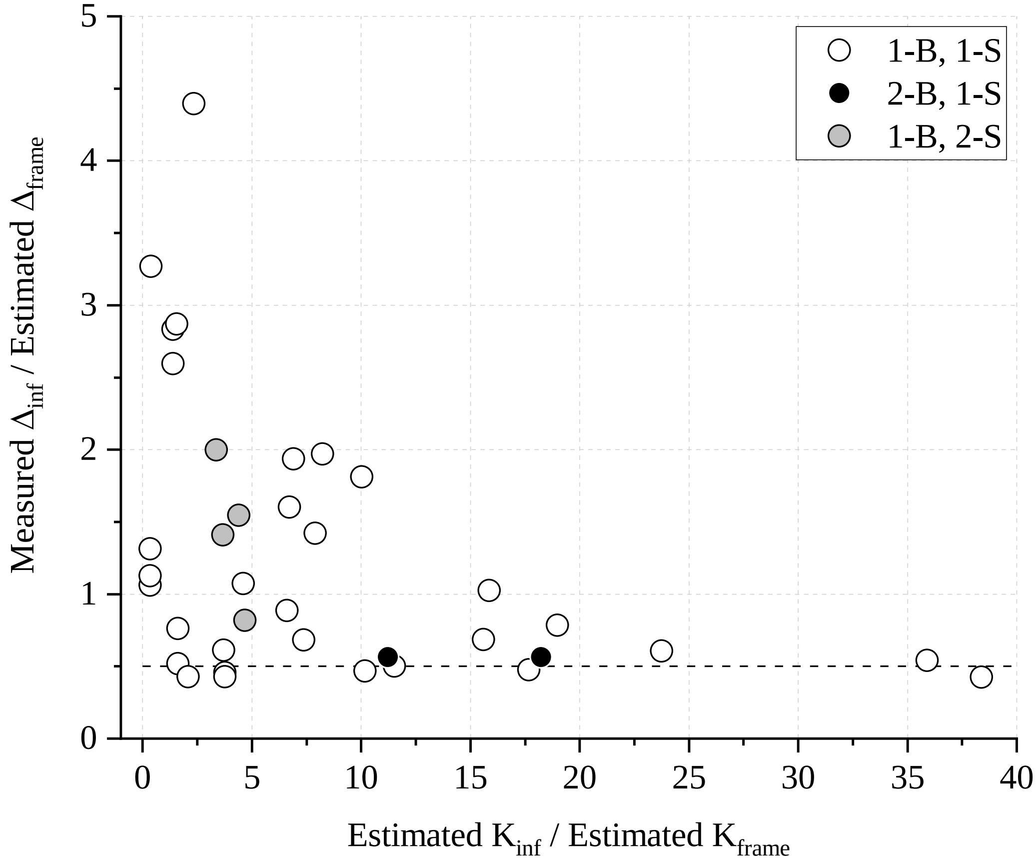

Figure 7-7: Variation of ratio of measured drift capacity of infilled frame to estimated lower-bound drift capacity of vulnerable bare frame with ratio of estimated initial lateral stiffness of infilled frame to estimated initial lateral stiffness of bare frame

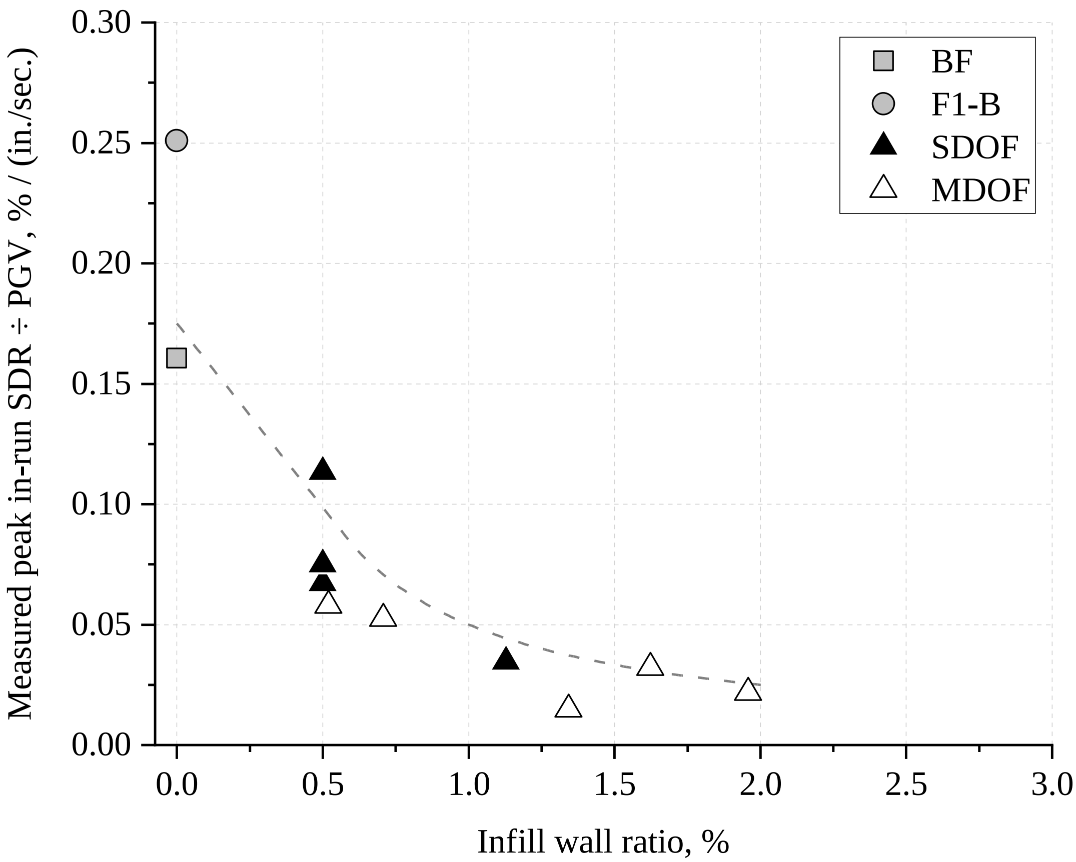

Figure 7-8: Measured peak in-run story drift ratio produced by a peak base velocity of 1 in./sec.

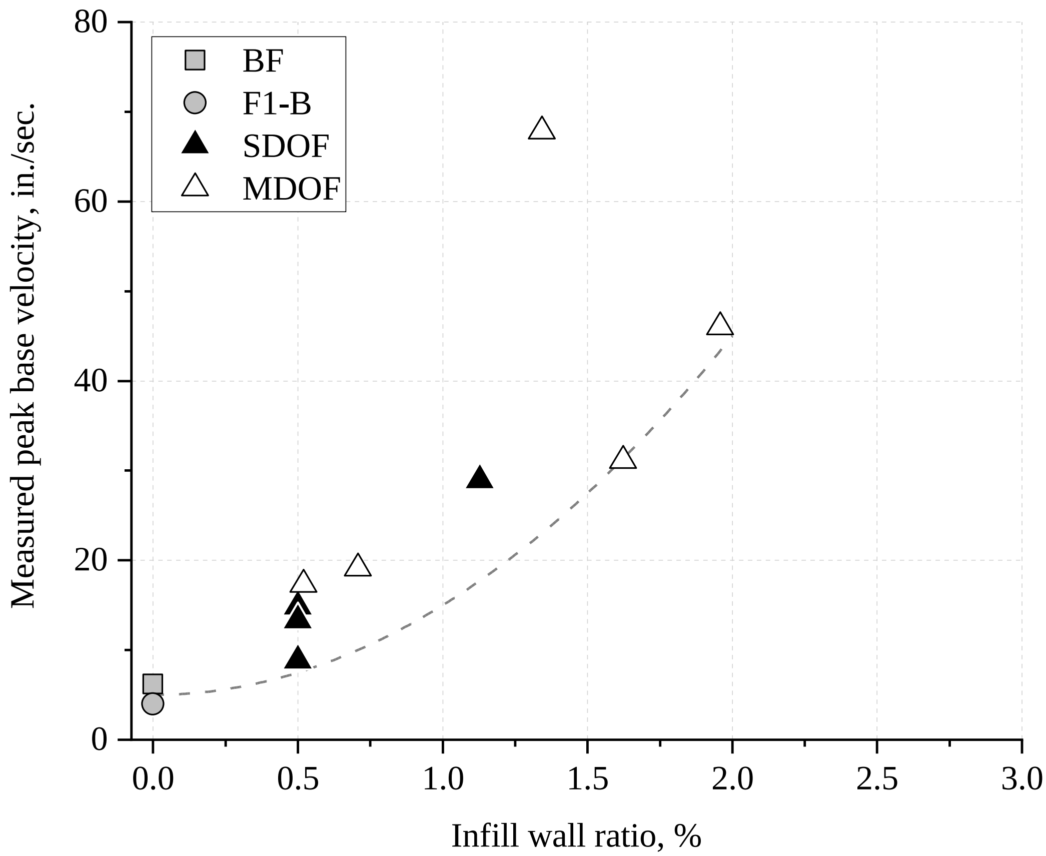

Figure 7-9: Peak base velocity required to produce a peak in-run story drift ratio of 1%

REFERENCES

Almesfer, N., Dizhur, D. Y., Lumantarna, R., & Ingham, J. M. (2014). Material Properties of Existing Unreinforced Clay Brick Masonry Buildings in New Zealand. *Bulletin of the New Zealand Society for Earthquake Engineering, 47(2)*, 75-96, https://doi.org/10.5459/bnzsee.47.2.75-96.

Al-Nimry, H. S. (2014). Quasi-Static Testing of RC Infilled Frames and Confined Stone-Concrete Bearing Walls. *Journal of Earthquake Engineering, 18(1)*, 1-23, https://dx.doi.org/10.1080/13632469.2013.835292.

Alwashali, H., Torihata, Y., Jin, K., & Maeda, M. (2018). Experimental Observations on the In-plane Behaviour of Masonry Wall Infilled RC Frames; Focusing on Deformation Limits and Backbone Curve. *Bulletin of Earthquake Engineering, 16(3)*, 1373-1397, https://doi.org/10.1007/s10518-017-0248-x.

Ancheta, T. D., Darragh, R. B., Stewart, J. P., Seyhan, E., Silva, W. J., Chiou, B. S.-J., . . . Donahue, J. L. (2014). NGA-West2 Database. *Earthquake Spectra, 30(3)*, 989-1005.

Aristizabal-Ochoa, J. D., & Sozen, M. A. (1976). *Behavior of Ten-Story Reinforced Concrete Walls Subjected to Earthquake Motions.* Civil Engineering Studies, Structural Research Series, University of Illinois at Urbana-Champaign, Vol. 431. Urbana, IL.

Baran, M., & Sevil, T. (2010). Analytical and Experimental Studies on Infilled RC Frames. *International Journal of the Physical Sciences, 5(13)*, 1981-1998.

Benavent-Climent, A., Ramirez-Marquez, A., & Pujol, S. (2018). Seismic Strengthening of Low-rise Reinforced Concrete Frame Structures with Masonry Infill Walls: Shaking-Table Test. *Engineering Structures, 165*, 142-151, https://doi.org/10.1016/j.engstruct.2018.03.026.

Blackard, B., Willam, K., & Mettupalayam, S. (2009). Experimental Observations of Masonry Infilled Reinforced Concrete Frames with Openings. *ACI Special Publication, SP-265-9*.

Bonacci, J. F. (1989). *Experiments to Study Seismic Drift of Reinforced Concrete Structures (PhD Thesis).* University of Illinois at Urbana-Champaign. Urbana, IL.

Bose, S., & Rai, D. C. (2016). Lateral Load Behavior of Open Ground Story RC Building with AAC Infills in Upper Stories. *Earthquake Spectra, 32(3)*, 1653-1674, https://doi.org/10.1193/121413EQS295M.

Cavaleri, L., & Di Trapani, F. (2014). Cyclic Response of Masonry Infilled RC Frames: Experimental Results and Simplified Modeling. *Soil Dynamics and Earthquake Engineering, 65*, 224-242, https://dx.doi.org/10.1016/j.soildyn.2014.06.016.

Cecen, H. (1979). *Response of Ten-Story, Reinforced Concrete Model Frames to Simulated Earthquakes (PhD Thesis).* University of Illinois at Urbana-Champaign. Urbana, IL.

Chalah, M., Chalah, F., Djellab, S. E., & Benouar, D. (2020). Effect of Beam Rigidity on the Lateral Stiffness of a One-Storey Frame. In A. Öchsner, & H. Altenbach, *Engineering Design Applications III, Advanced Structured Materials, Vol. 124.* (pp. 115-126). Springer, Cham. https://doi.org/10.1007/978-3-030-39062-4_11.

Diawati, M., & Sanada, Y. (2016). R/C Frame-infill Interaction Model and its Application to Indonesian Buildings. *Earthquake Engineering & Structural Dynamics, 46(2)*, 221-241, https://doi.org/10.1002/eqe.2787.

Eberhard, M. O., & Sozen, M. A. (1989). *Experiments and Analyses to Study the Seismic Response of Reinforced Concrete Frame-Wall Structures with Yielding Columns.* Civil Engineering Studies, Structural Research Series, University of Illinois at Urbana-Champaign, Vol. 548. Urbana, IL.

FEMA 306. (1998). *Evaluation of Earthquake Damaged Concrete and Masonry Wall Buildings.* Federal Emergency Management Agency. Washington, D.C.

Fiorato, A. E., Sozen, M. A., & Gamble, W. L. (1970). *An Investigation of the Interaction of Reinforced Concrete Frames with Masonry Filler Walls.* Civil Engineering Studies, Structural Research Series, University of Illinois at Urbana-Champaign, Vol. 370. Urbana, IL.

Flanagan, R. D., & Bennett, R. M. (1999). In-Plane Behavior of Structural Clay Tile Infilled Frames. *Journal of Structural Engineering, 125(6)*, 590-599, https://doi.org/10.1061/(ASCE)0733-9445(1999)125:6(590).

Freeman, S. A., Nicoletti, J. P., & Tyrell, J. V. (1975). Evaluations of Existing Bulidings for Seismic Risk - A Case Study of Puget Sound Naval Shipyard, Bremerton, Washington. *Proceedings of U.S. National Conference on Earthquake Engineering*, (pp. 113-122). Berkeley, USA.

Guevara, L. T., & Garcia, L. E. (2005). The Captive- and Short-Column Effects. *Earthquake Spectra, 21(1)*, 141-160, https://doi.org/10.1193/1.1856533.

Guljas, I., Penava, D., Laughery, L. A., & Pujol, S. (2020). Dynamic Tests of a Large-Scale Three-Story RC Structure with Masonry Infill Walls. *Journal of Earthquake Engineering, 24(11)*, 1675-1703, https://doi.org/10.1080/13632469.2018.1475313.

Gulkan, P., & Sozen, M. A. (1971). *Response and Energy-Dissipation of Reinforced Concrete Frames Subjected to Strong Base Motions.* Civil Engineering Studies, Structural Research Series, University of Illinois at Urbana-Champaign, Vol. 377. Urbana, IL.

Gulkan, P., & Sozen, M. A. (1974). Inelastic Responses of Reinforced Concrete Structures to Earthquake Motions. *ACI Journal, 71(12)*, 604-610.

Han, S. W., & Lee, C. S. (2020). Cyclic Behavior of Lightly Reinforced Concrete Moment Frames with Partial- and Full-height Masonry Walls. *Earthquake Spectra, 36(2)*, 599-628, https://doi.org/10.1177/8755293019899960.

Healey, T. J., & Sozen, M. A. (1978). *Experimental Study of the Dynamic Response of a Ten-Story Reinforced Concrete Frame with a Tall First Story.* Civil Engineering Studies, Structural Research Series, University of Illinois at Urbana-Champaign, Vol. 450. Urbana, IL.

Imran, L., & Aryanto, A. (2009). Behavior of Reinforced Concrete Frames In-Filled with Lightweight Materials under Seismic Loads. *Civil Engineering Dimension, 11(2)*, 69-77.

Jin, K., Choi, H., Matsukawa, K., & Nakano, Y. (2013). Symplified Backbone Curve Estimation Method of Unreinforced Masonry Infill in RC Frame. *International Symposium on Earthquake Engineering* (pp. 141-150). JAEE, Vol. 2.

Jin, K., Choi, H., Takahashi, N., & Nakano, Y. (2012). Seismic Capacity Evaluation of RC Frame with URM Wall Focused on Diagonal Strut Mechanism. *International Symposium on Earthquake Engineering* (pp. 481-490). JAEE, Vol. 1.

Kajiwara, K., Tosauchi, Y., Sato, E., Fukuyama, K., Inoue, T., Shiohara, H., . . . Mukai, T. (2017). 2015 Three-dimensional Shaking Table Test of a 10-story Reinforced Concrete Building on the E-Defense, Part 1: Overview and Specimen Design of the Base Slip and Base Fixed Tests. *16th World Conference on Earthquake Engineering.* Earthquake Engineering Research Institute.

Kakaletsis, D. J., & Karayannis, C. G. (2008). Influence of Masonry Strength and Openings on Infilled R/C Frames Under Cycle Loading. *Journal of Earthquake Engineering, 12(2)*, 197-221, https://doi.org/10.1080/13632460701299138.

Kakaletsis, D., & Karayannis, C. (2007). Experimental Investigation of Infilled R/C Frames with Eccentric Openings. *Structural Engineering and Mechanics, 26(3)*, 1-16, https://doi.org/10.12989/sem.2007.26.3.231.

Laughery, L. A. (2016). *Response of High-Strength Steel Reinforced Concrete Structures to Simulated Earthquakes (PhD Thesis).* Purdue University, West Lafayette, IN.

Lee, H. S., & Woo, S. W. (2002). Effect of Masonry Infills on Seismic Performance of a 3-Storey R/C Frame with Non-Seismic Detailing. *Earthquake Engineering and Structural Dynamics, 31(2)*, 353-378, https://doi.org/10.1002/eqe.112.

Lepage, A. (1997). *A Method for Drift-Control in Earthquake-Resistant Design of Reinforced Concrete Building Structures (PhD Thesis).* University of Illinois at Urbana-Champaign. Urbana, IL.

Liauw, T. C., & Kwan, K. H. (1985). Unified Plastic Analysis for Infilled Frames. *Journal of Structural Engineering, 111(7)*, 1427-1448, https://doi.org/10.1061/(ASCE)0733-9445(1985)111:7(1427).

MATLAB. (2020). *Version 9.8.0 (R2020a).* The MathWorks Inc. Natick, Massachusetts.

Mehrabi, A. B., Shing, P. B., Schuller, M. P., & Noland, J. L. (1994). *Performance of Masonry-Infilled R/C Frames Under In-Plane Lateral Loads.* Structural Engineering and Structural

Mechanics Research Series, University of Colorado at Boulder, Research Series No. CU/SR-94/6. Boulder, CO.

Moehle, J. P., & Sozen, M. A. (1978). *Earthquake-Simulation Tests of a Ten-Story Reinforced Concrete Frame with a Discontinued First-Level Beam.* Civil Engineering Studies, Structural Research Series, University of Illinois at Urbana-Champaign, Vol. 451. Urbana, IL.

Moehle, J. P., & Sozen, M. A. (1980). *Experiments to Study Earthquake Response of R/C Structures with Stiffness Interruptions.* Civil Engineering Studies, Structural Research Series, University of Illinois at Urbana-Champaign, Vol. 482. Urbana, IL.

Morrison, D. G., & Sozen, M. A. (1981). *Response of Reinforced Concrete Plate-Column Connections to Dynamic and Static Horizontal Loads.* Civil Engineering Studies, Structural Research Series, University of Illinois at Urbana-Champaign, Vol. 490. Urbana, IL.

NCREE, Purdue University. (2016). *2016 Taiwan (Meinong) Earthquake.* https://datacenterhub.org/deedsdv/publications/view/534.

Newmark, N. M. (1965). Current Trends in Seismic Analysis and Design of High Rise Structures. *Proceedings of the Symposium on Earthquake Engineering.* The University of British Columbia. Vancouver, B. C.

Newmark, N. M., & Hall, W. J. (1982). *Earthquake Spectra and Design.* Earthquake Engineering Research Institute.

Newmark, N. M., Hall, W. J., & Mohraz, B. (1973). *A Study of Vertical and Horizontal Earthquake Spectra.* United States Atomic Energy Commission. Washington D.C.

Paulay, T., & Priestly, M. J. (1992). *Seismic Design of Reinforced Concrete and Masonry Buildings.* John Wiley & Sons, Inc.

Pollalis, W. G. (2021). *Drift Capacity of Reinforced Concrete Walls with Lap Splices (PhD Thesis).* Purdue University. West Lafayette, IN.

Pujol, S. (2001). *Moment-Curvature Relationship Program - FLECHA.* https://datacenterhub.org/deedsdv/publications/view/659.

Pujol, S., Ramirez, J. A., & Sozen, M. A. (1999). Drift Capacity of Reinforced Concrete Columns Subjected to Cyclic Shear Reversals. *ACI Symposium Publication, 187*, 255-274.

Purdue University. (2018). *Buildings Surveyed after the 2017 Mexico City Earthquakes.* https://datacenterhub.org/deedsdv/publications/view/536.

Rosenblueth, E. (1960). The Earthquake of 28 July 1957 in Mexico City. *Proceedings of the Second World Conference on Earthquake Engineering*, (pp. 359-379). Tokyo and Kyoto, Japan.

Saito, T. (2021). *STERA 3D - Structural Earthquake Response Analysis 3D.* Technical Manual. Toyohashi University of Technology. Toyohashi, Japan.

Sato, E., Tosauchi, Y., Fukuyama, K., Inoue, T., Kajiwara, K., Shiohara, H., . . . Mukai, T. (2017). 2015 Three-dimensional Shaking Table Test of a 10-story Reinforced Concrete Building on the E-Defense, Part 2: Specimen Fabrication and Construction, Test Procedure, and Instrumentation Program. *16th World Conference on Earthquake Engineering.* Earthquake Engineering Research Institute.

Schoettler, M. J., Restrepo, J. I., Guerrini, G., Duck, D. E., & Carrea, F. (2015). *A Full-Scale, Single-Column Bridge Bent Tested by Shake-Table Excitation.* Pacific Earthquake Engineering Research Center. Berkeley, CA.

Schultz, A. E. (1986). *An Experimental and Analytical Study of the Earthquake Response of R/C Frames with Yielding Columns (PhD Thesis).* University of Illinois at Urbana-Champaign. Urbana, IL.

Shah, P. P. (2021). *Seismic Drift Demands (PhD Thesis).* Purdue University. West Lafayette, IN.

Shahrooz, B. M., & Moehle, J. P. (1987). *Experimental Study of Seismic Response of R.C. Setback Buildings.* Earthquake Engineering Research Center, College of Engineering, University of California, Berkeley. Berkeley, CA.

Shibata, A., & Sozen, M. A. (1974). *The Substitute-Structure Method for Earthquake-Resistant Design of Reinforced Concrete Frames.* Civil Engineering Studies, Structural Research Series, University of Illinois at Urbana-Champaign, Vol. 412. Urbana, IL.

Shibata, A., & Sozen, M. A. (1976). Substitute-Structure Method for Seismic Design in R/C. *Journal of the Structural Division, 102*, 1-18.

Shibata, A., Saito, T., & Masuno, H. (2020). Seismic Design Procedure for Building Structures Based on the Equivalent Linearization Method. *17th World Conference on Earthquake Engineering*, (pp. 1-12). Sendai, Japan.

Shiga, T. (1977). Earthquake Damage and the Amount of Walls in Reinforced Concrete Buildings. *Proceedings of the Sixth World Conference on Earthquake Engineering*, (pp. 2467-2472). New Delhi, India.

Shimazaki, K., & Sozen, M. A. (1984). *Seismic Drift of Reinforced Concrete Structures (Technical Report).* Hazama-Gumi. Tokyo, Japan.

Sim, C., Laughery, L. A., Chiou, T. C., & Weng, P. W. (2018). *2017 Pohang Earthquake.* https://datacenterhub.org/deedsdv/publications/view/296.

Sim, C., Skok, N., Irfanoglu, A., Pujol, S., Sozen, M., & Song, C. (2016). *Database of Low-rise Reinforced Concrete Buildings with Earthquake Damage.* https://datacenterhub.org/deedsdv/publications/view/454.

Sim, C., Villalobos, E., Smith, J. P., Rojas, P., Puranam, A. Y., Laughery, L. A., & Pujol, S. (2016). *2016 Ecuador Earthquake.* https://datacenterhub.org/deedsdv/publications/view/535.

Skillen, K. C. (2020). *The Effects of Transverse Reinforcement on the Strength and Deformability of Reinforced Concrete Elements (PhD Thesis).* Purdue University. West Lafayette, IN.

Sozen, M. A. (1964). *Structural Damage Caused by the Skopje Earthquake of 1963.* Civil Engineering Studies, Structural Research Series, University of Illinois at Urbana-Champaign, Vol. 279. Urbana, IL.

Sozen, M. A. (2003). The Velocity of Displacement. *Seismic Assessment and Rehabilitation and Existing Buildings,* (pp. 11-28). Dordrecht, Springer Netherlands. https://doi.org/10.1007/978-94-010-0021-5_2.

Sozen, M. A., Otani, S., Gulkan, P., & Nielsen, N. N. (1969). The University of Illinois Earthquake Simulator. *Proceedings of the Fourth World Conference on Earthquake Engineering*, (pp. 139–150). Santiago, Chile.

Stavridis, A. (2009). *Analytical and Experimental Study of Seismic Performance of Reinforced Concrete Frames Infilled with Masonry Walls (PhD Thesis).* University of California, San Diego. San Diego, CA.

Suzuki, T., Choi, H., Sanada, Y., Nakano, Y., Matsukawa, K., Paul, D., . . . Binici, B. (2017). Experimental Evaluation of the In-plane Behaviour of Masonry Wall Infilled RC Frames. *Bulletin of Earthquake Engineering, 15(10),* 4245-4267, https://doi.org/10.1007/s10518-017-0139-1.

Takeda, T., Sozen, M. A., & Nielsen, N. N. (1970). Reinforced Concrete Response to Simulated Earthquakes. *Journal of the Structural Division, 96(12)*, 2557-2573.

Tosauchi, Y., Sato, E., Fukuyama, K., Inoue, T., Kajiwara, K., Shiohara, H., . . . Mukai, T. (2017). 2015 Three-dimensional Shaking Table Test of a 10-story Reinforced Concrete Building on the E-Defense, Part 3: Base Slip and Base Fixed Test Results. *16th World Conference on Earthquake Engineering.* Earthquake Engineering Research Institute.

USGS. (2020). *ShakeMap Atlas*. Retrieved from USGS Earthquake Hazards Program: https://earthquake.usgs.gov/earthquakes/eventpage/usp000fjta/shakemap/stations

Wolfgram, C. E. (1984). *Experimental Modelling and Analysis of Three One-Tenth-Scale Reinforced Concrete Frame-Wall Structures.* Civil Engineering Studies, Structural Research Series, University of Illinois at Urbana-Champaign, Vol. 513. Urbana, IL.

Wood, S. L. (1985). *Experiments to Study the Earthquake Response of Reinforced Concrete Frames with Setbacks.* Civil Engineering Studies, Structural Research Series, University of Illinois at Urbana-Champaign, Vol. 544. Urbana, IL.

APPENDIX A. FORCE-DISPLACEMENT RELATIONSHIPS OF INFILLED FRAMES

This appendix (Figure A-1 through Figure A-88) shows test summaries, diagrams of experimental setups, elevations of test specimens, and graphs of force-displacement relationships measured in lateral load tests conducted on the bare frame and infilled frame specimens described in Section 1.2. Each force-displacement plot is overlaid with red or black lines connecting response extrema used to determine the drift capacity - defined as the displacement associated with a 20% reduction in lateral load from lateral strength - of each specimen. If the displacement associated with a 20% reduction in lateral load from lateral strength was not reached, the maximum displacement reached in one direction for monotonic tests or the mean of maximum displacements reached in both directions for cyclic tests is taken to be the drift capacity.

Spec. No.	Type of Frame	Type of Masonry Units	Panel Aspect Ratio(h/l)	Lateral Load	Vertical Load Distribution (Kips)		No. of Bays
					Columns	Beam	
1	weak	no infill	0.67	monotonic	66	---	1
2	weak - repaired (1)*	hollow	0.67	monotonic	66	---	1
3	weak - repaired (2)*	solid	0.67	monotonic	66	---	1
4	weak	hollow	0.67	cyclic	44	22	1
5	weak	solid	0.67	cyclic	44	22	1
6	strong	hollow	0.67	cyclic	44	22	1
7	strong	solid	0.67	cyclic	44	22	1
8	weak - repaired (4)*	hollow	0.67	monotonic	44	22	1
9	weak - repaired (8)*	solid	0.67	monotonic	44	22	1
10	weak	hollow	0.48	cyclic	44	22	1
11	weak	solid	0.48	cyclic	44	22	1
12	weak - repaired (10)*	solid	0.48	cyclic	66	33	1
13	weak	hollow	0.67	cyclic	99	---	2
14	weak - repaired (13)*	solid	0.67	cyclic	99	---	2

* Specimen repaired

Figure A-1: Summary of bare and infilled frames tested by Mehrabi (1994)

Note: Figure is taken from Mehrabi (1994).

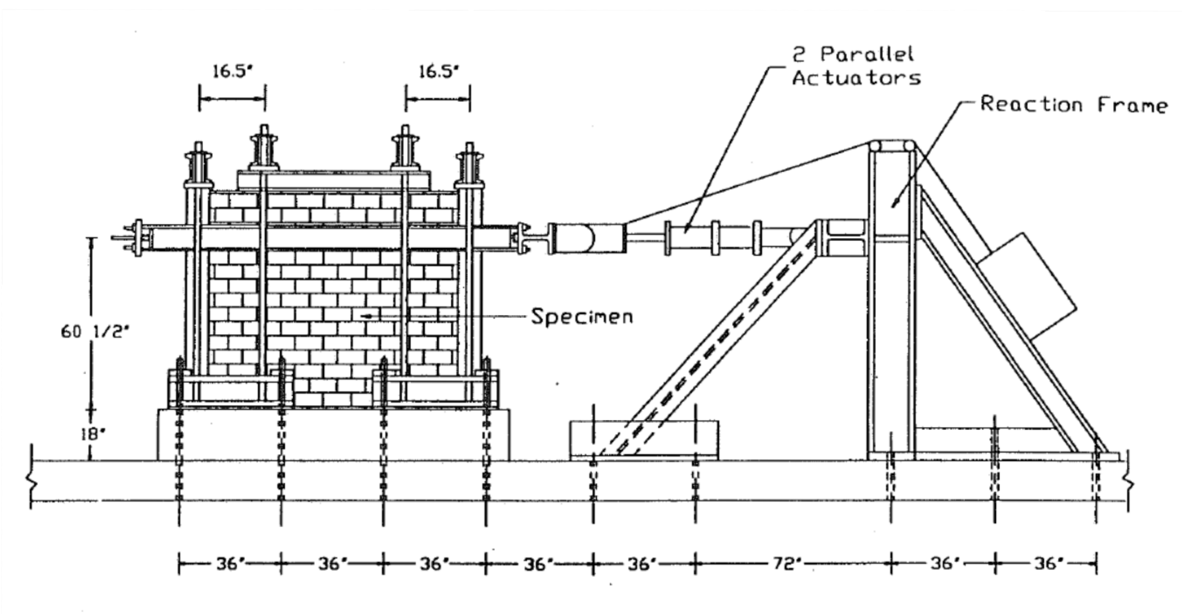

Figure A-2: Test setup of bare and infilled frames tested by Mehrabi (1994)

Note: Figure is taken from Mehrabi (1994).

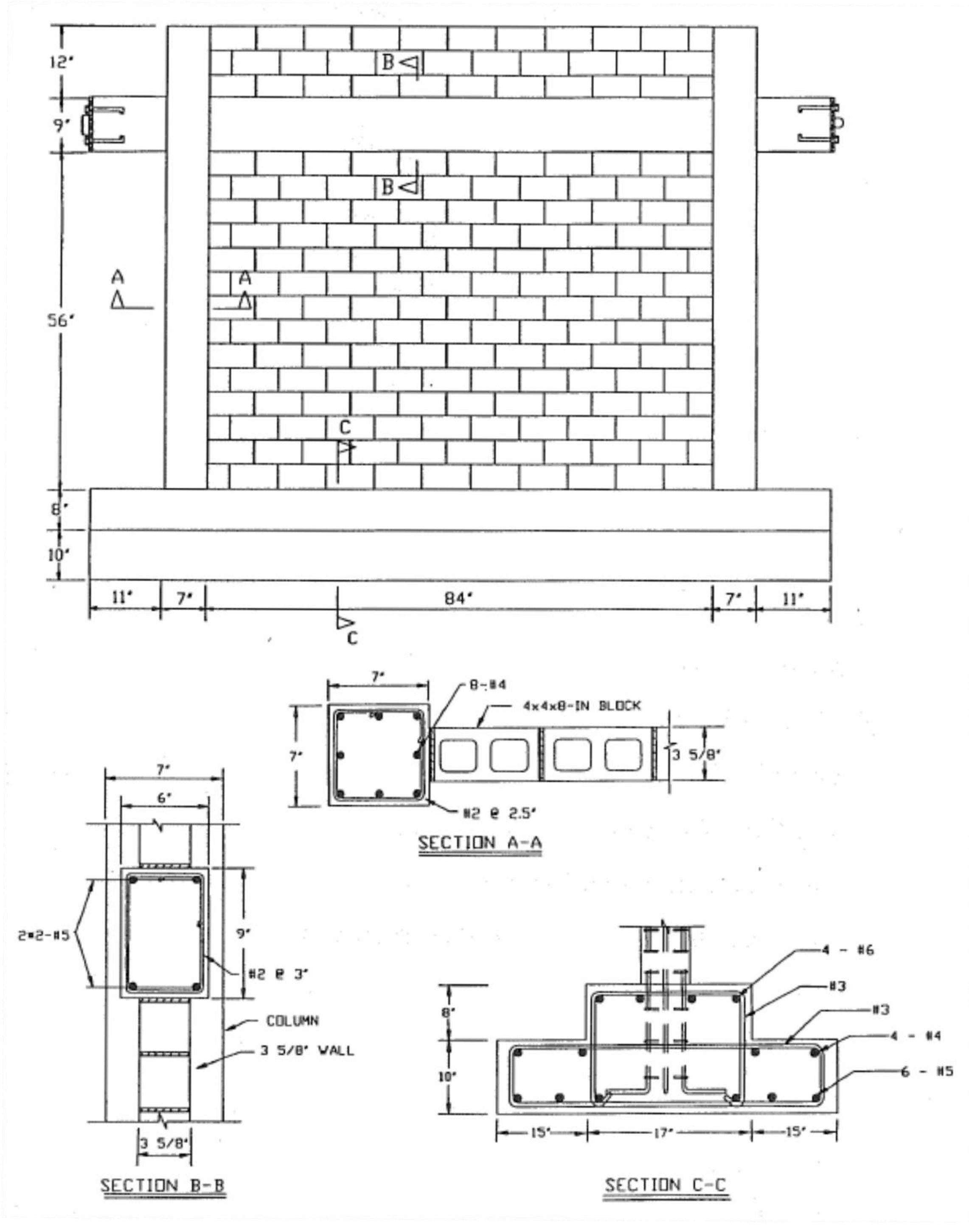

Figure A-3: Dimensions of weak frame (panel aspect ratio = 0.67) tested by Mehrabi (1994)

Note: Figure is taken from Mehrabi (1994).

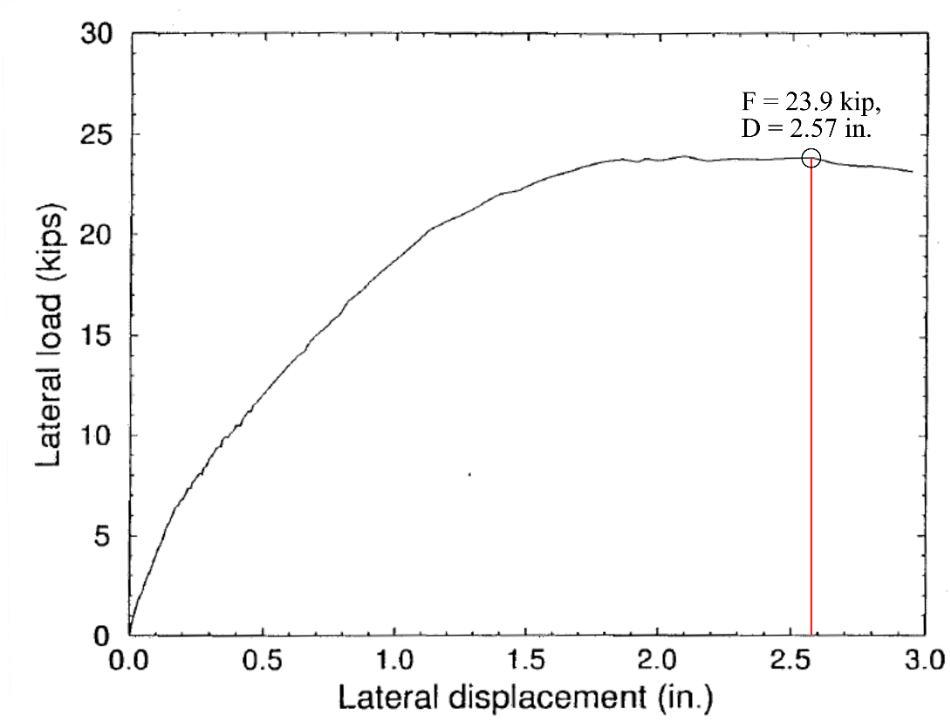

Figure A-4: Force-displacement relationship of Specimen 1 tested by Mehrabi (1994)

Note: Figure is taken from Mehrabi (1994) and drift capacity of Specimen 1 is 6.8%.

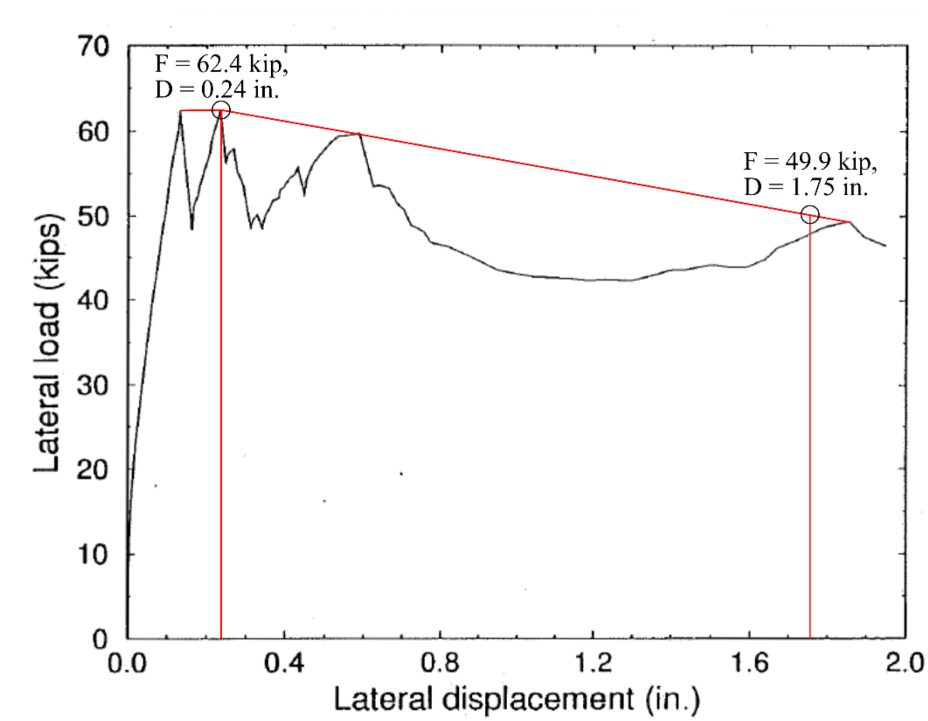

Figure A-5: Force-displacement relationship of Specimen 3 tested by Mehrabi (1994)

Note: Figure is taken from Mehrabi (1994) and drift capacity of Specimen 3 is 2.9%.

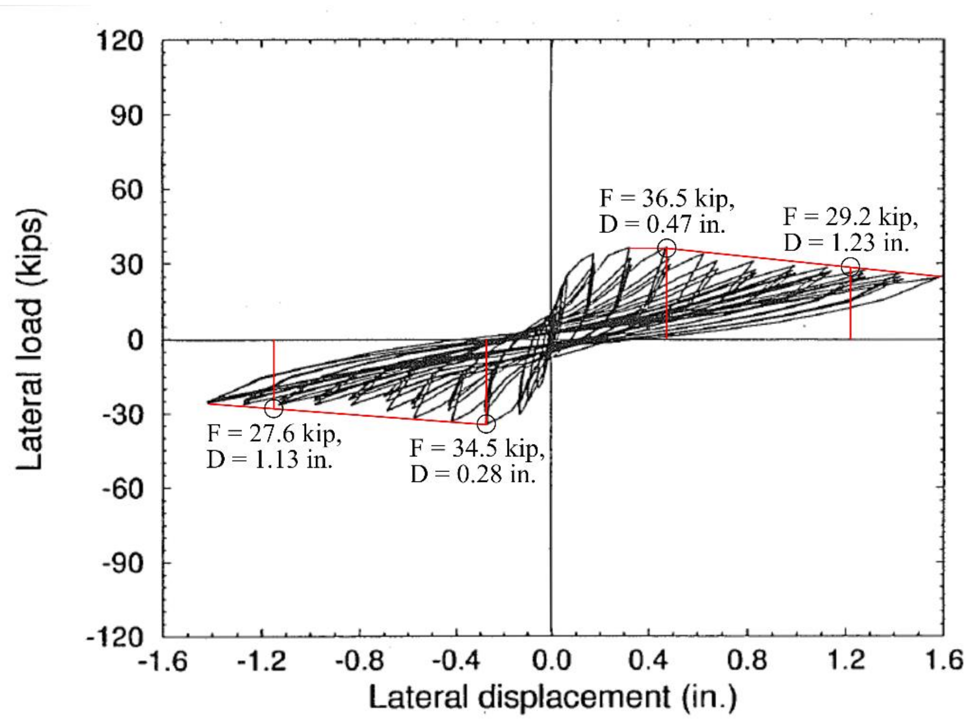

Figure A-6: Force-displacement relationship of Specimen 4 tested by Mehrabi (1994)

Note: Figure is taken from Mehrabi (1994) and drift capacity of Specimen 4 is 2.0%.

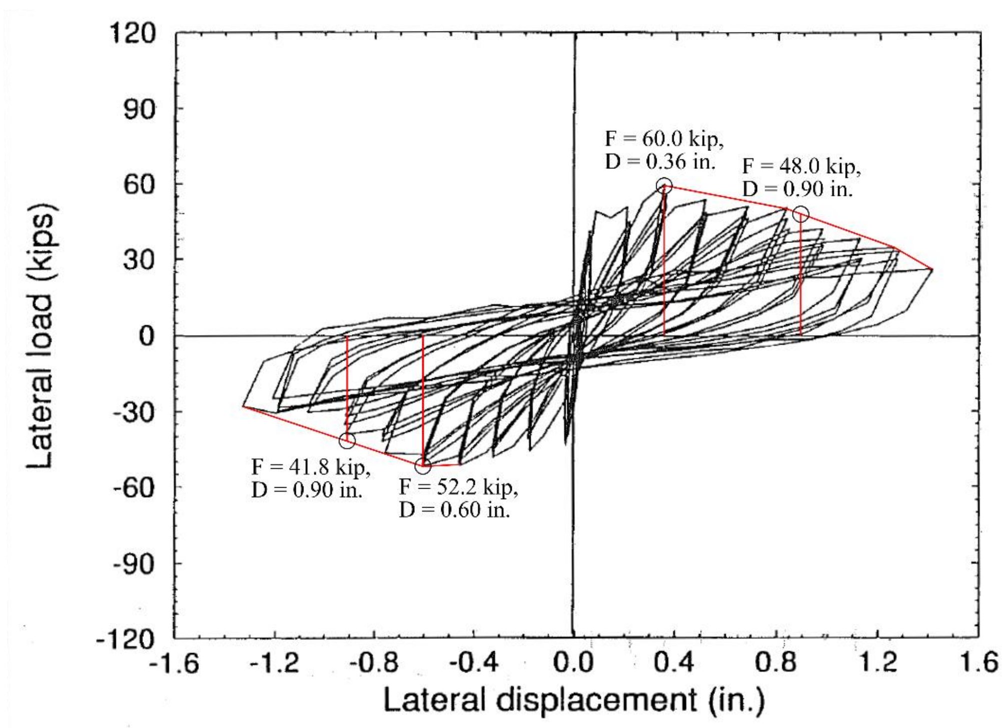

Figure A-7: Force-displacement relationship of Specimen 5 tested by Mehrabi (1994)

Note: Figure is taken from Mehrabi (1994) and drift capacity of Specimen 5 is 1.5%.

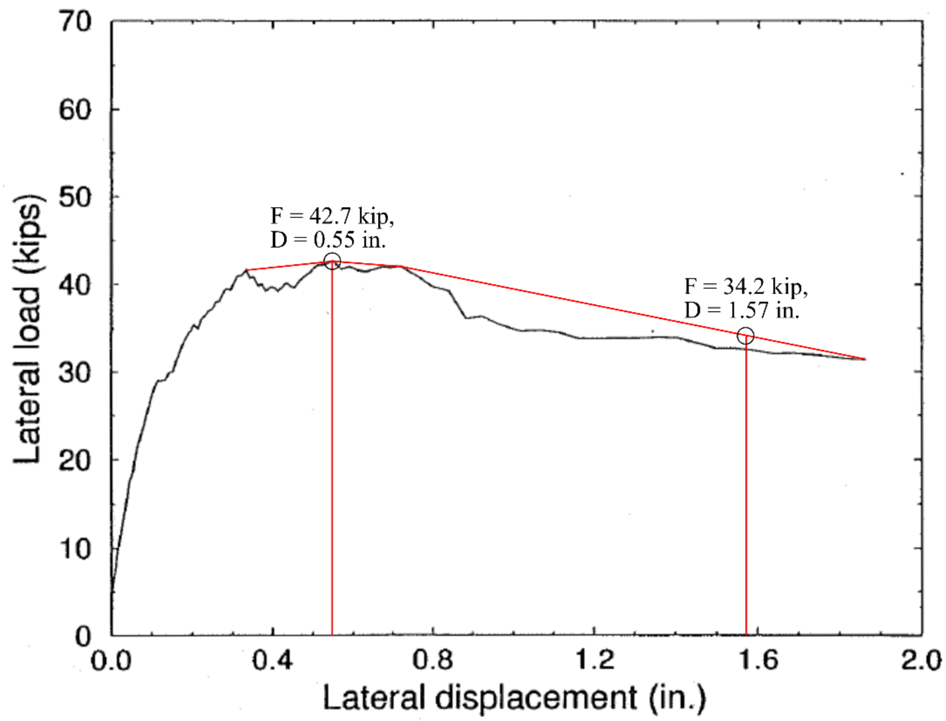

Figure A-8: Force-displacement relationship of Specimen 8 tested by Mehrabi (1994)

Note: Figure is taken from Mehrabi (1994) and drift capacity of Specimen 8 is 2.6%.

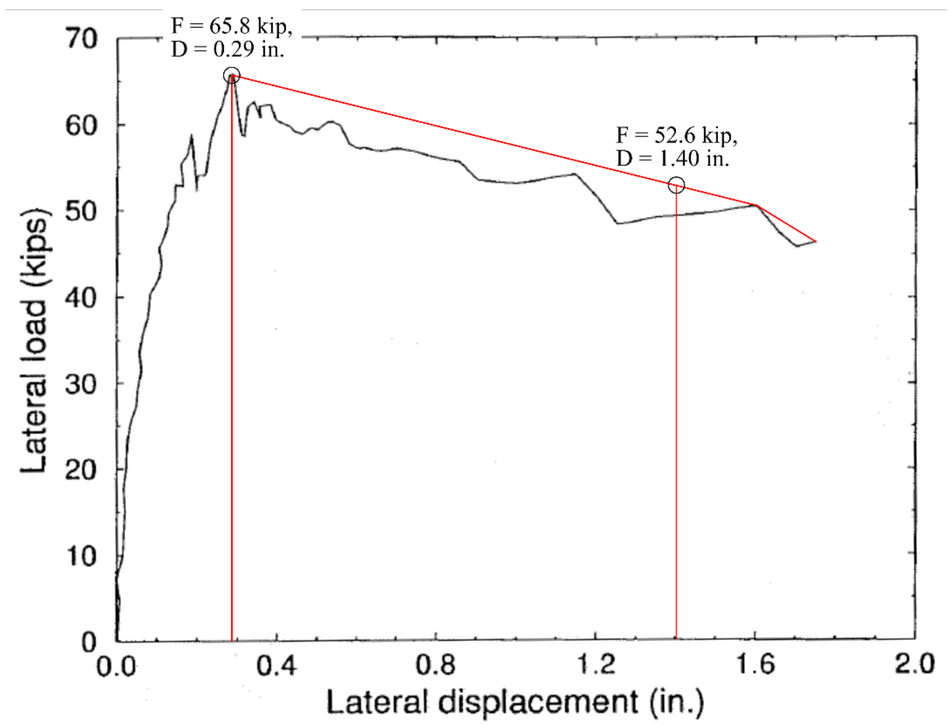

Figure A-9: Force-displacement relationship of Specimen 9 tested by Mehrabi (1994)

Note: Figure is taken from Mehrabi (1994) and drift capacity of Specimen 9 is 2.3%.

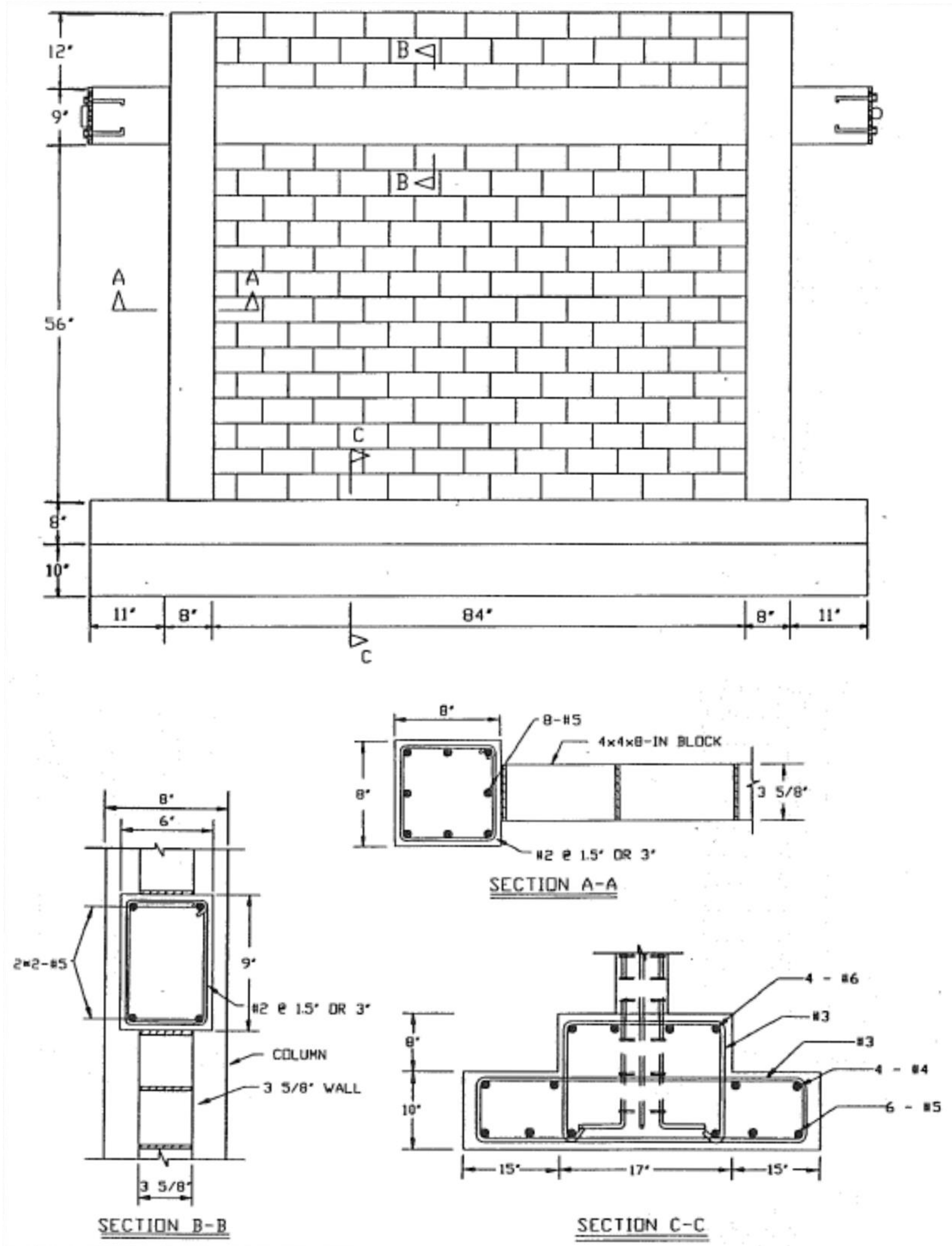

Figure A-10: Dimensions of strong frame (panel aspect ratio = 0.67) tested by Mehrabi (1994)

Note: Figure is taken from Mehrabi (1994).

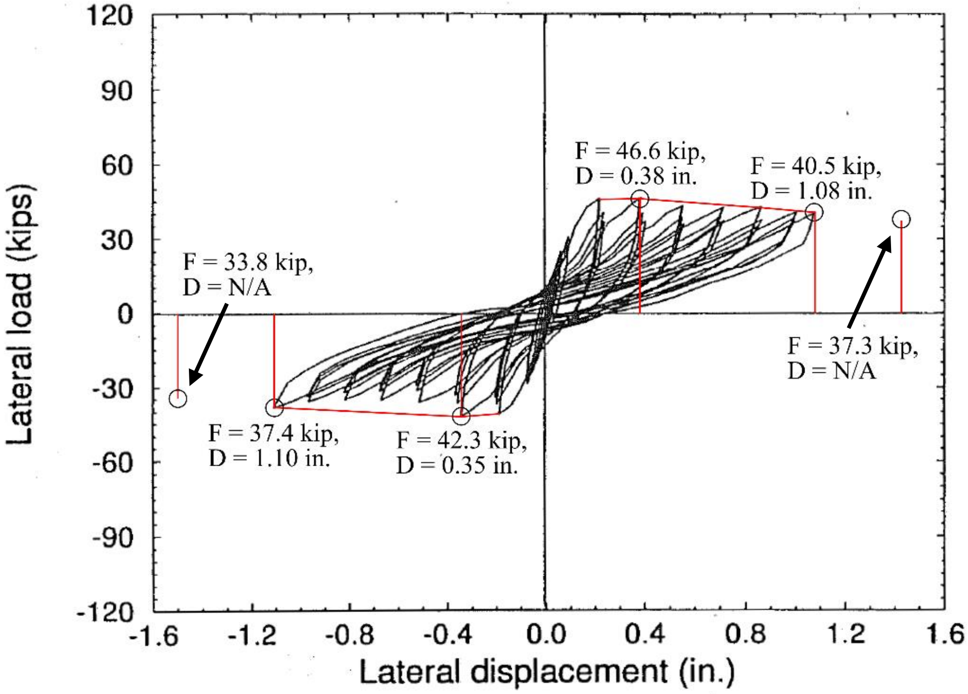

Figure A-11: Force-displacement relationship of Specimen 6 tested by Mehrabi (1994)

Note: Figure is taken from Mehrabi (1994) and drift capacity of Specimen 6 is 1.8%.

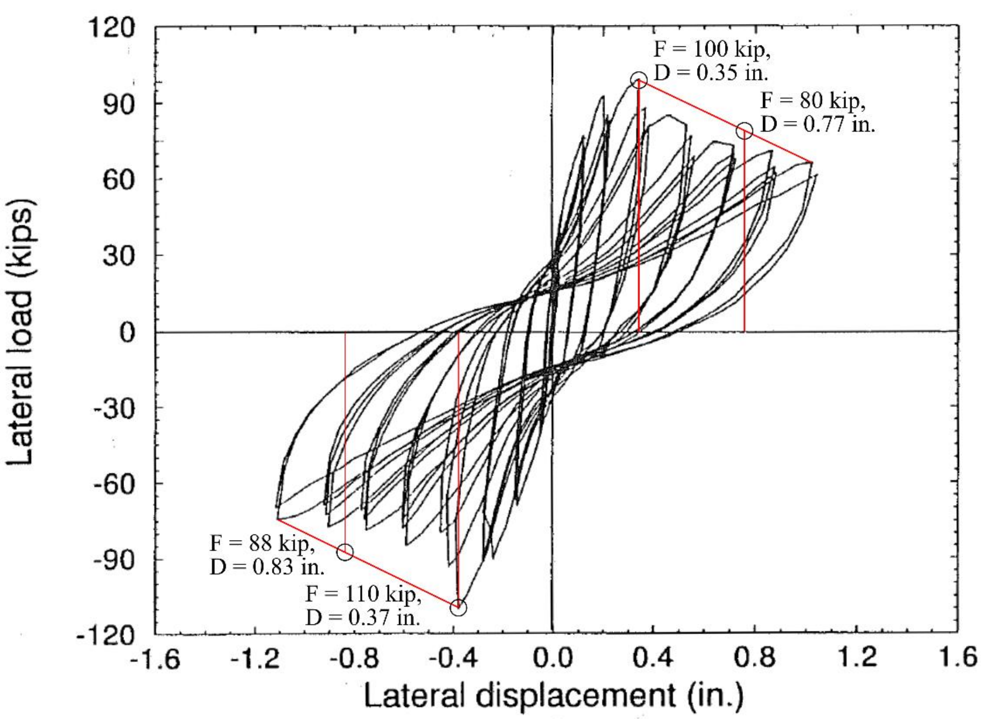

Figure A-12: Force-displacement relationship of Specimen 7 tested by Mehrabi (1994)

Note: Figure is taken from Mehrabi (1994) and drift capacity of Specimen 7 is 1.3%.

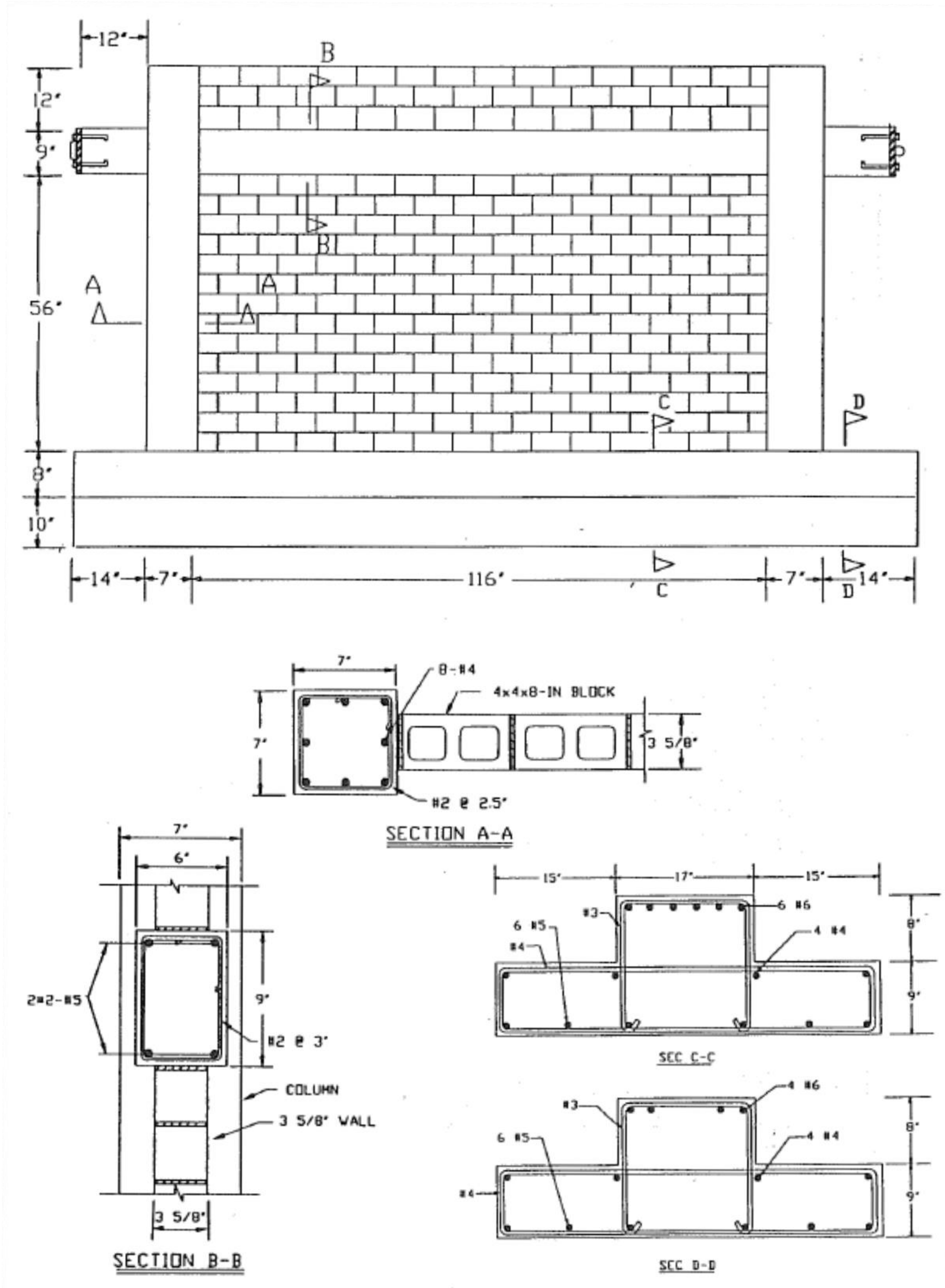

Figure A-13: Dimensions of weak frame (panel aspect ratio = 0.48) tested by Mehrabi (1994)
Note: Figure is taken from Mehrabi (1994).

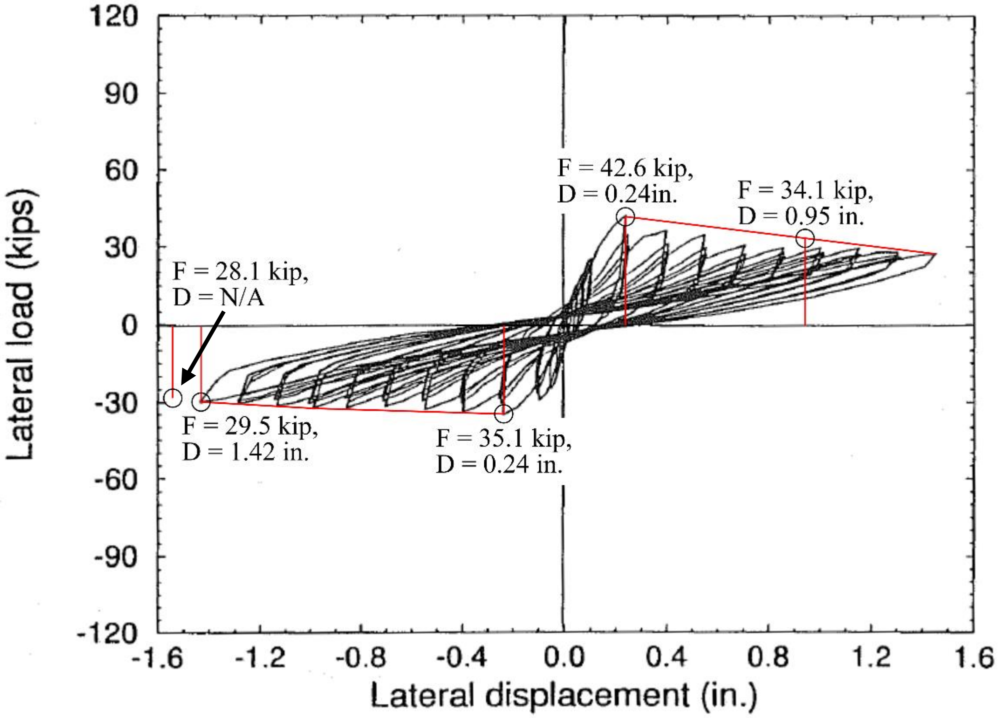

Figure A-14: Force-displacement relationship of Specimen 10 tested by Mehrabi (1994)

Note: Figure is taken from Mehrabi (1994) and drift capacity of Specimen 10 is 2.0%.

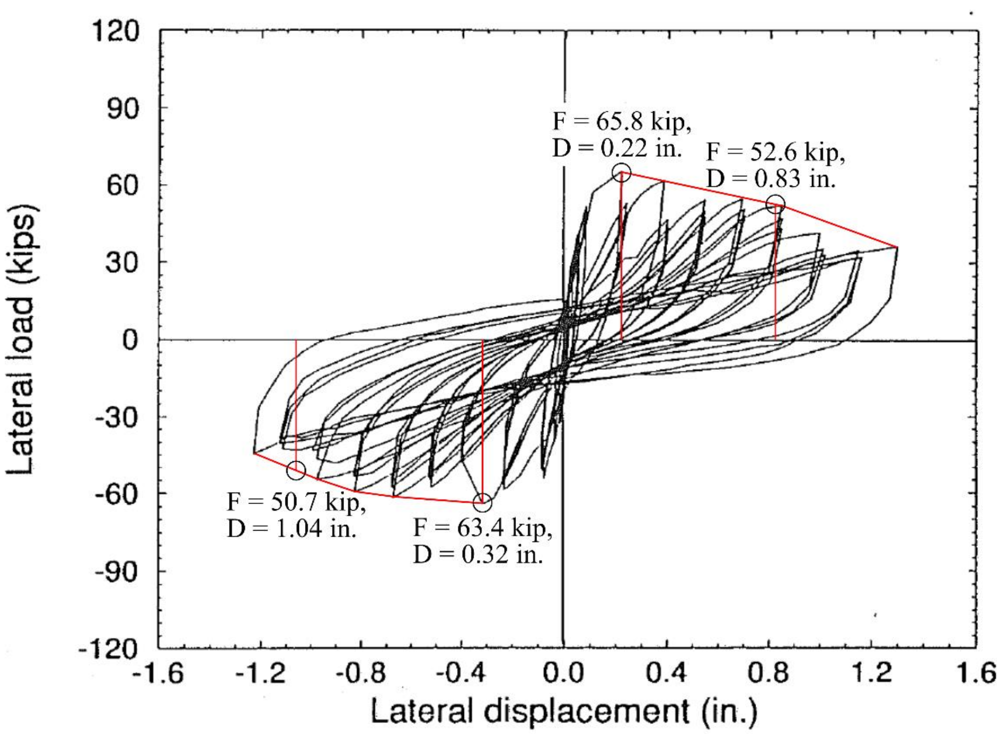

Figure A-15: Force-displacement relationship of Specimen 11 tested by Mehrabi (1994)

Note: Figure is taken from Mehrabi (1994) and drift capacity of Specimen 11 is 1.6%.

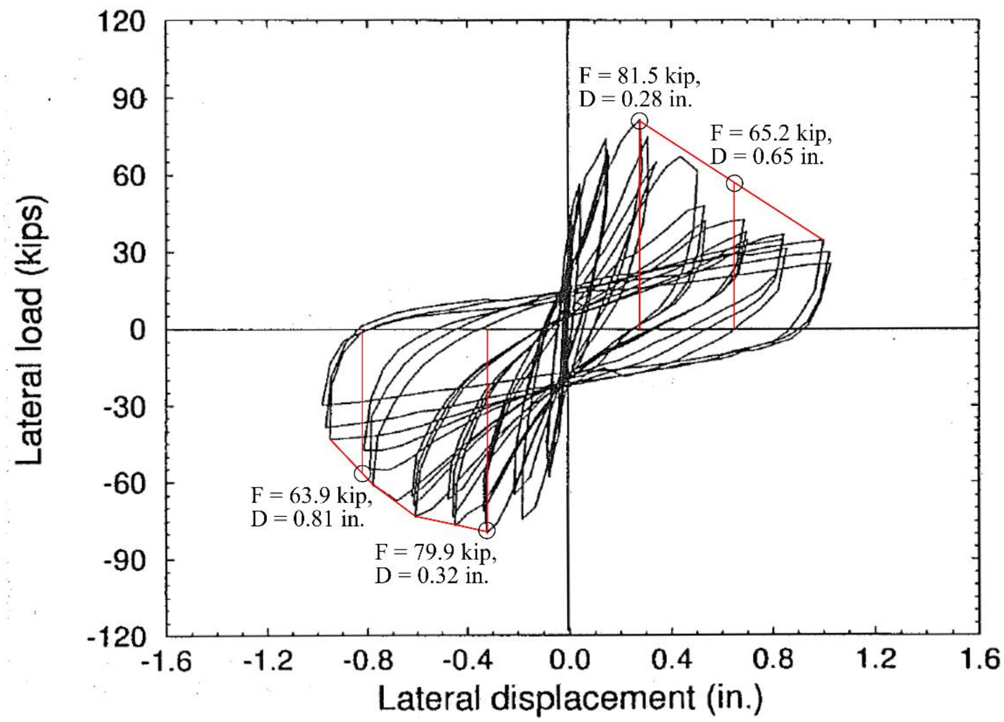

Figure A-16: Force-displacement relationship of Specimen 12 tested by Mehrabi (1994)

Note: Figure is taken from Mehrabi (1994) and drift capacity of Specimen 12 is 1.2%.

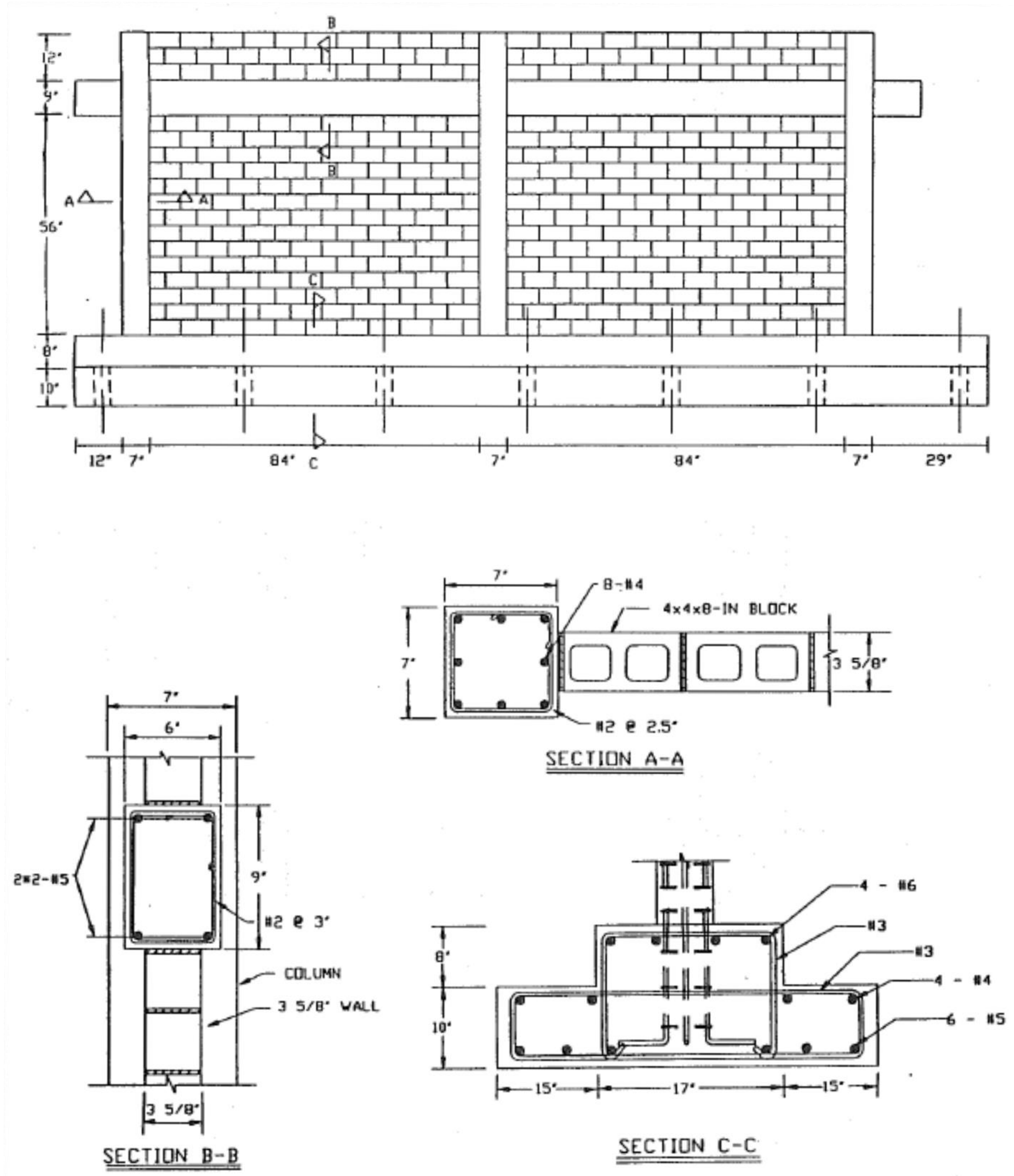

Figure A-17: Dimensions of two-bay weak frame (panel aspect ratio = 0.67) tested by Mehrabi (1994)

Note: Figure is taken from Mehrabi (1994).

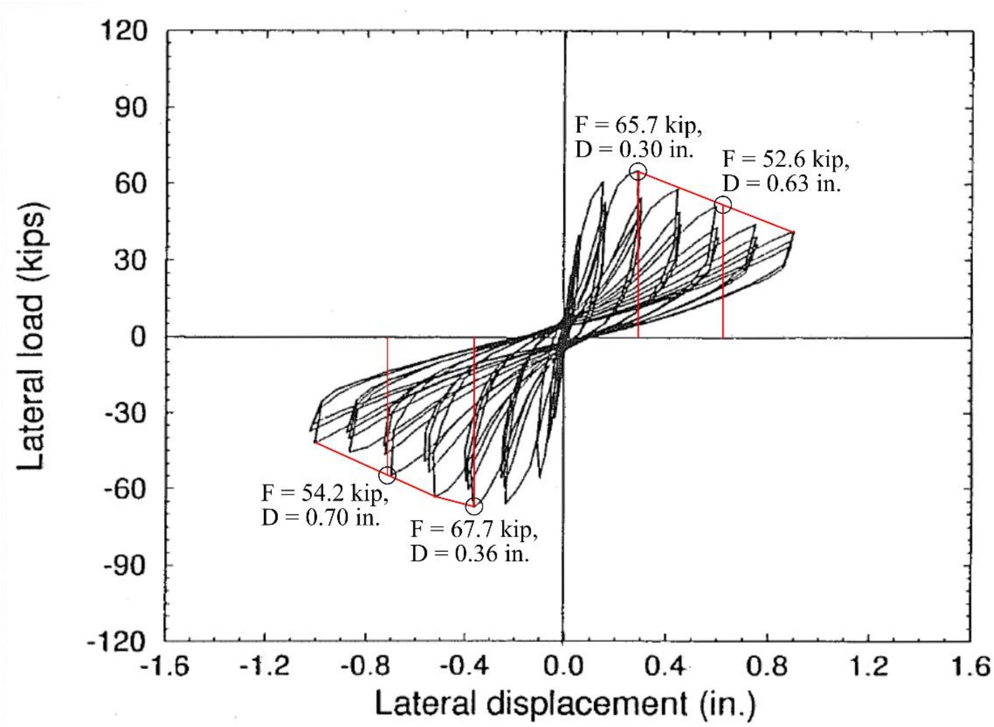

Figure A-18: Force-displacement relationship of Specimen 13 tested by Mehrabi (1994)

Note: Figure is taken from Mehrabi (1994) and drift capacity of Specimen 13 is 1.1%.

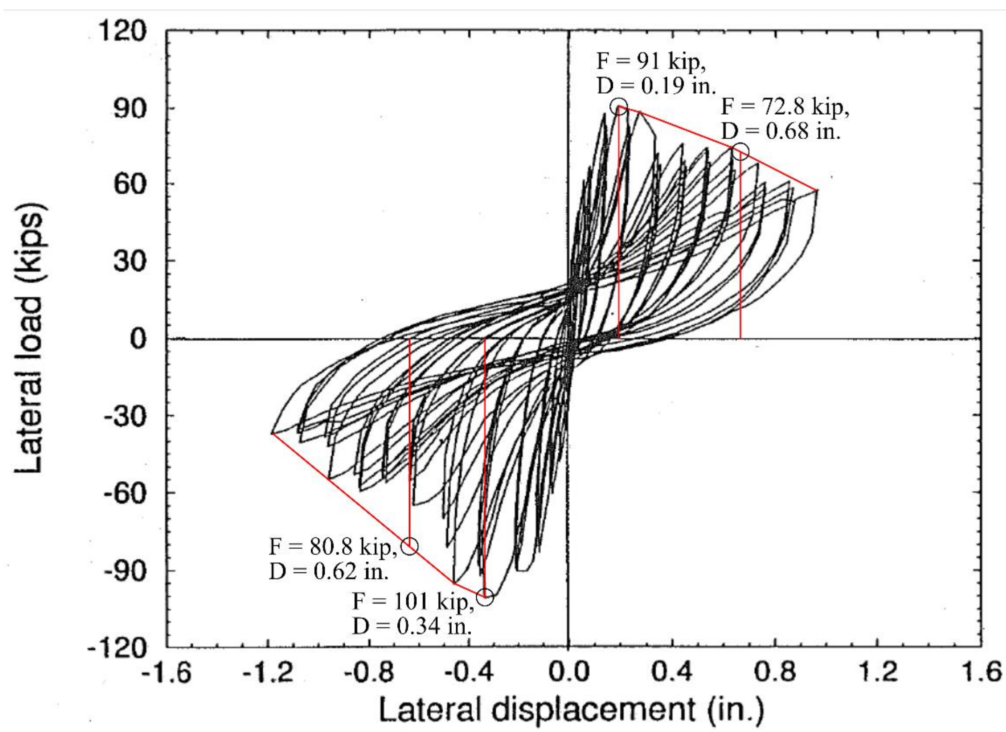

Figure A-19: Force-displacement relationship of Specimen 14 tested by Mehrabi (1994)

Note: Figure is taken from Mehrabi (1994) and drift capacity of Specimen 14 is 1.1%.

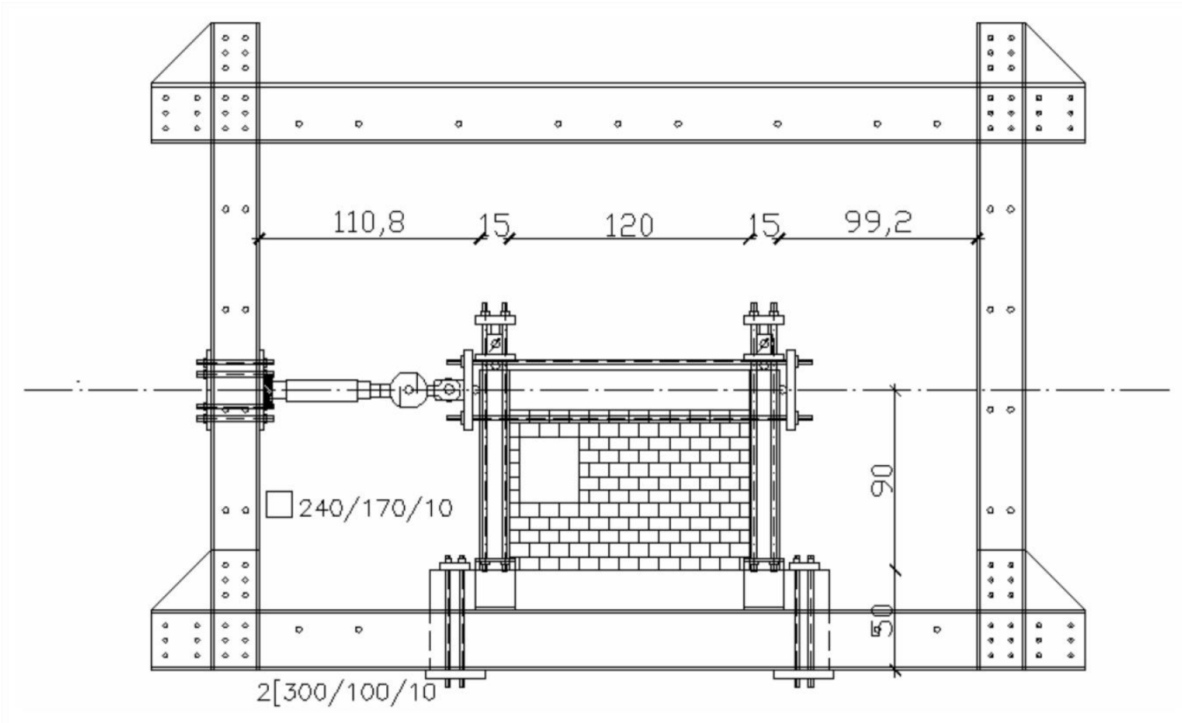

Figure A-20: Test setup of bare and infilled frames tested by Kakaletsis (2007)

Note: Figure is taken from Kakaletsis (2007) and dimensions are in cm.

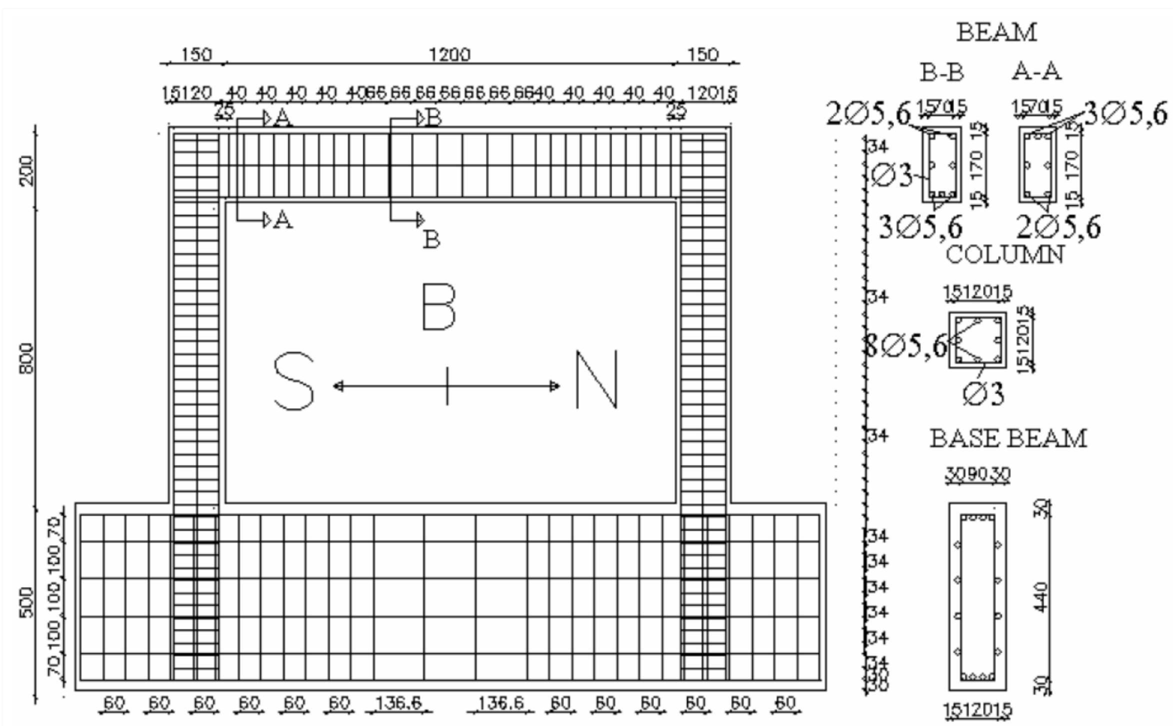

Figure A-21: Test setup of bare and infilled frames tested by Kakaletsis (2007)

Note: Figure is taken from Kakaletsis (2007) and dimensions are in mm.

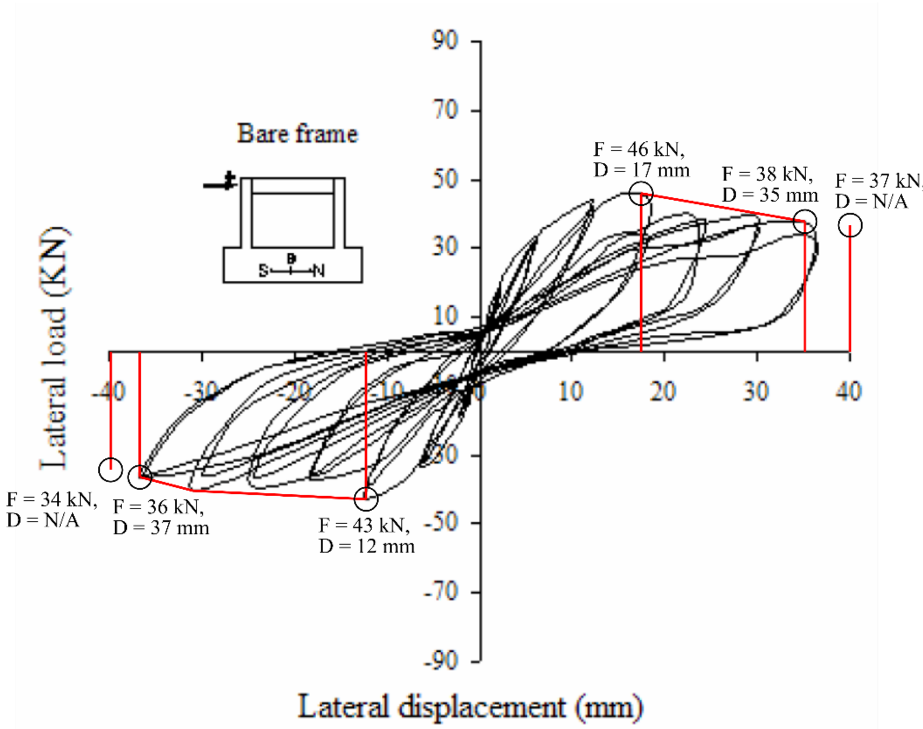

Figure A-22: Force-displacement relationship of Specimen B tested by Kakaletsis (2007)
Note: Figure is taken from Kakaletsis (2007) and drift capacity of Specimen B is 4.0%.

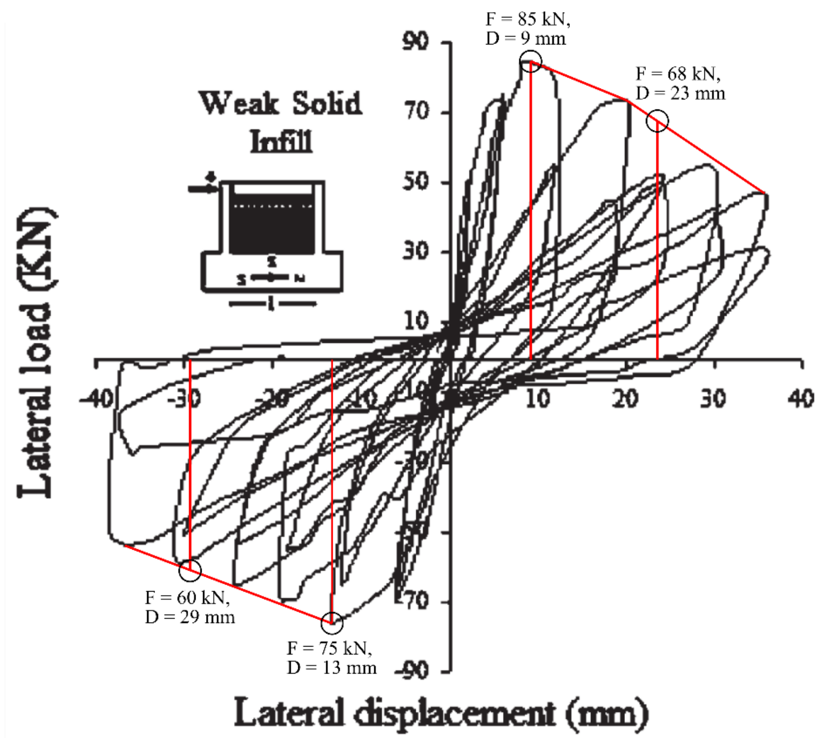

Figure A-23: Force-displacement relationship of Specimen S tested by Kakaletsis (2008)
Note: Figure is taken from Kakaletsis (2008) and drift capacity of Specimen S is 2.9%.

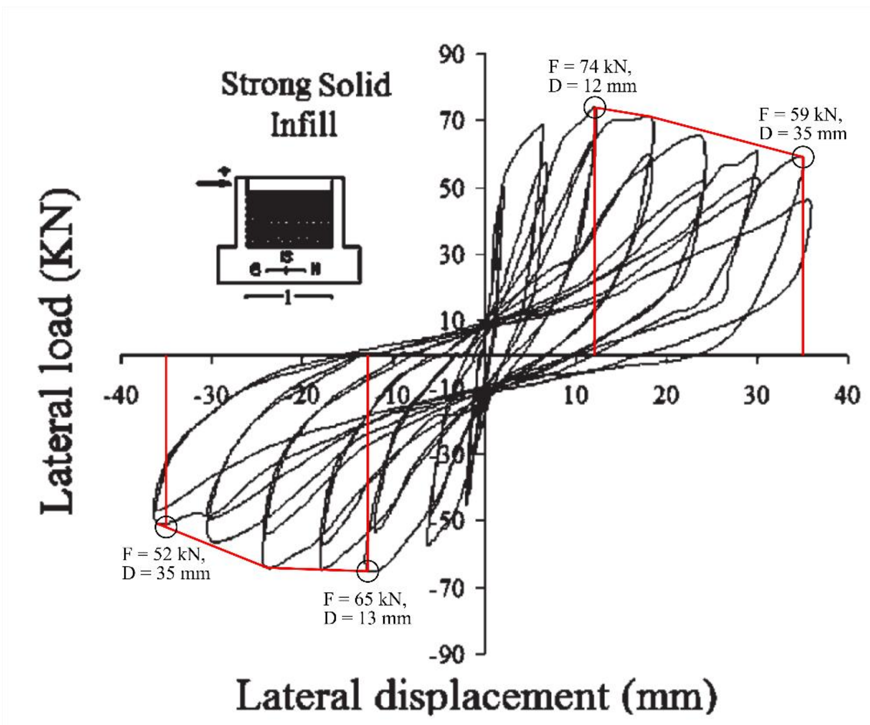

Figure A-24: Force-displacement relationship of Specimen IS tested by Kakaletsis (2008)

Note: Figure is taken from Kakaletsis (2008) and drift capacity of Specimen IS is 3.9%.

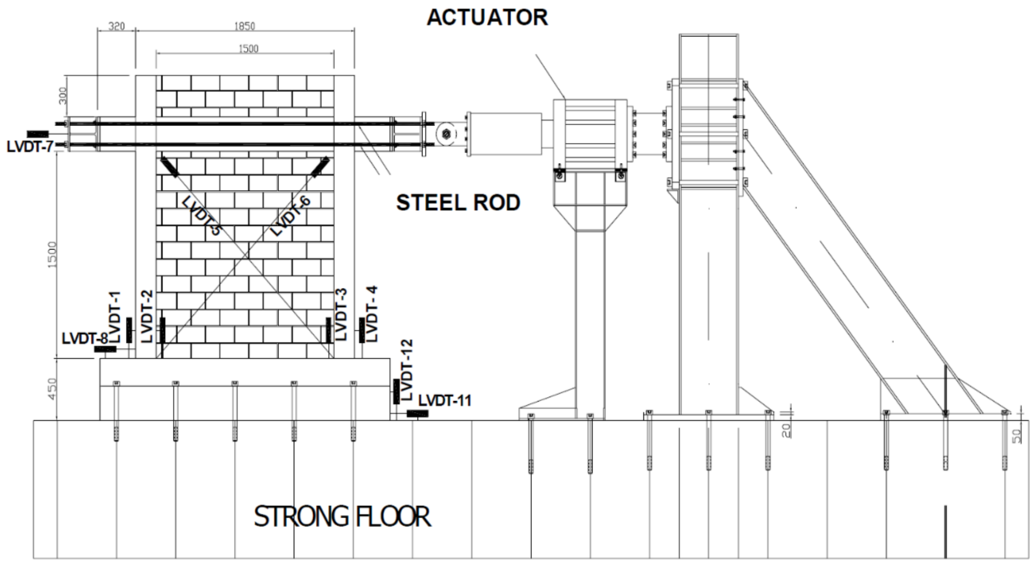

Figure A-25: Test setup of infilled frames tested by Imran (2009)

Note: Figure is taken from Imran (2009) and dimensions are in mm.

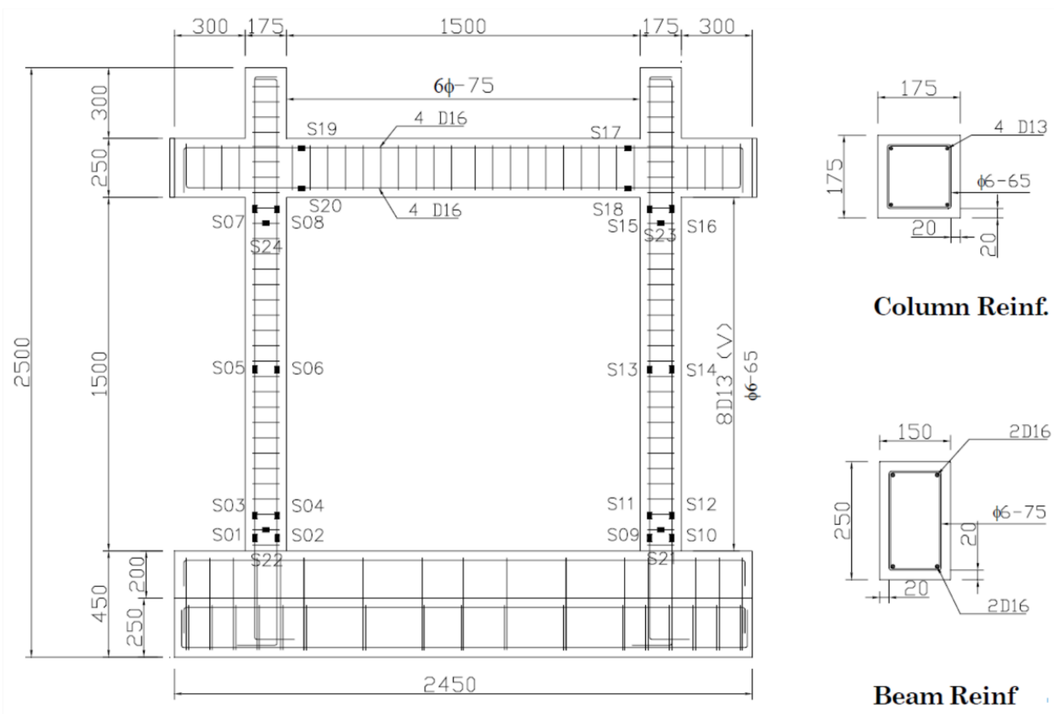

Figure A-26: Dimensions of infilled frames tested by Imran (2009)

Note: Figure is taken from Imran (2009) and dimensions are in mm.

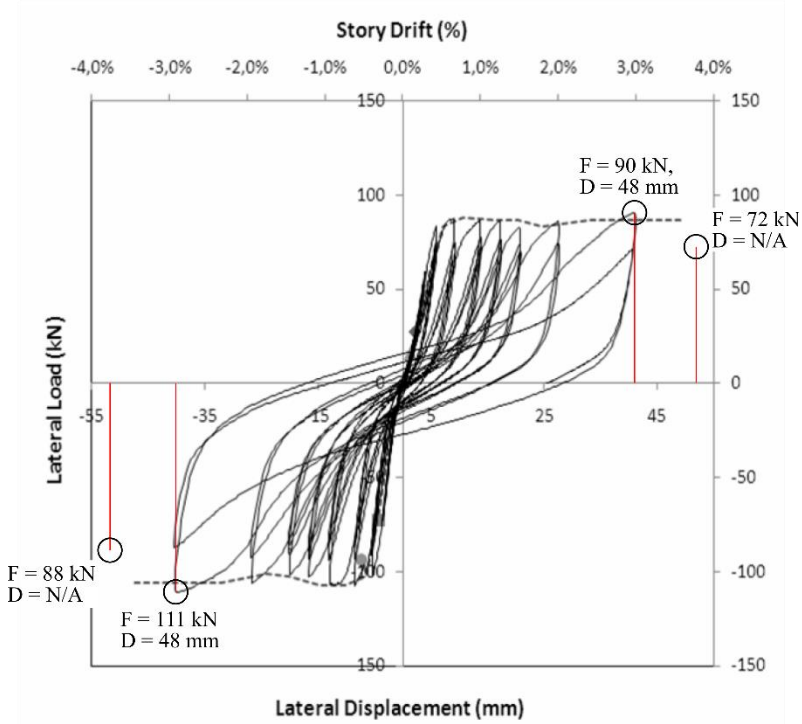

Figure A-27: Force-displacement relationship of Specimen 1 tested by Imran (2009)

Note: Figure is taken from Imran (2009) and drift capacity of Specimen 1 is 3.0%.

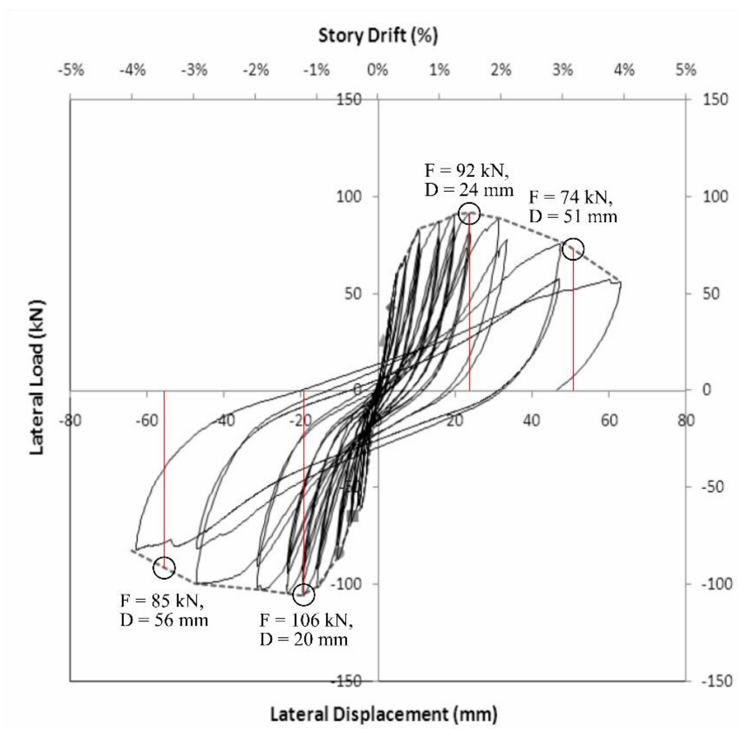

Figure A-28: Force-displacement relationship of Specimen 2 tested by Imran (2009)

Note: Figure is taken from Imran (2009) and drift capacity of Specimen 2 is 3.3%.

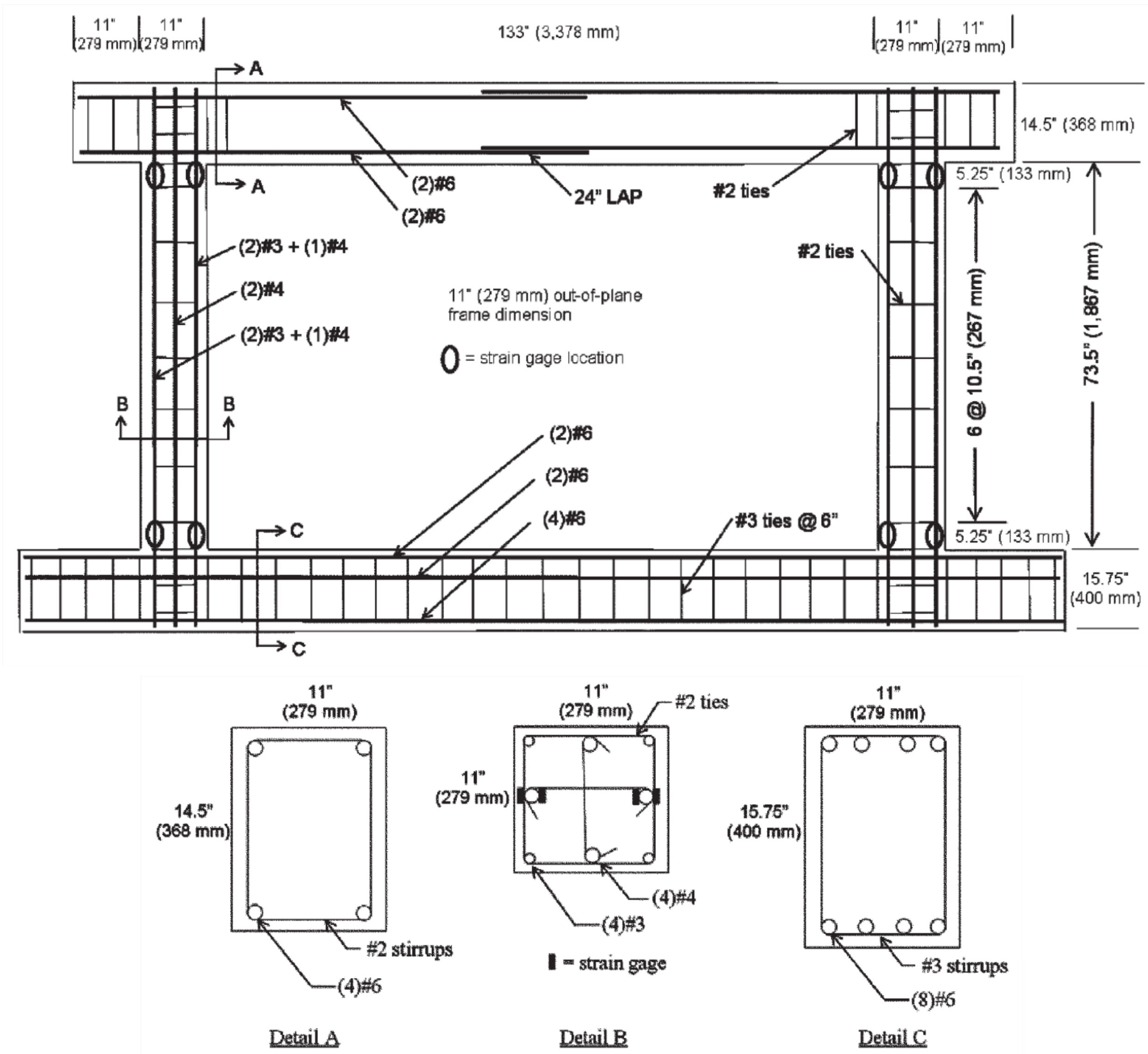

Figure A-29: Dimensions of infilled frame tested by Blackard (2009)

Note: Figure is taken from Blackard (2009).

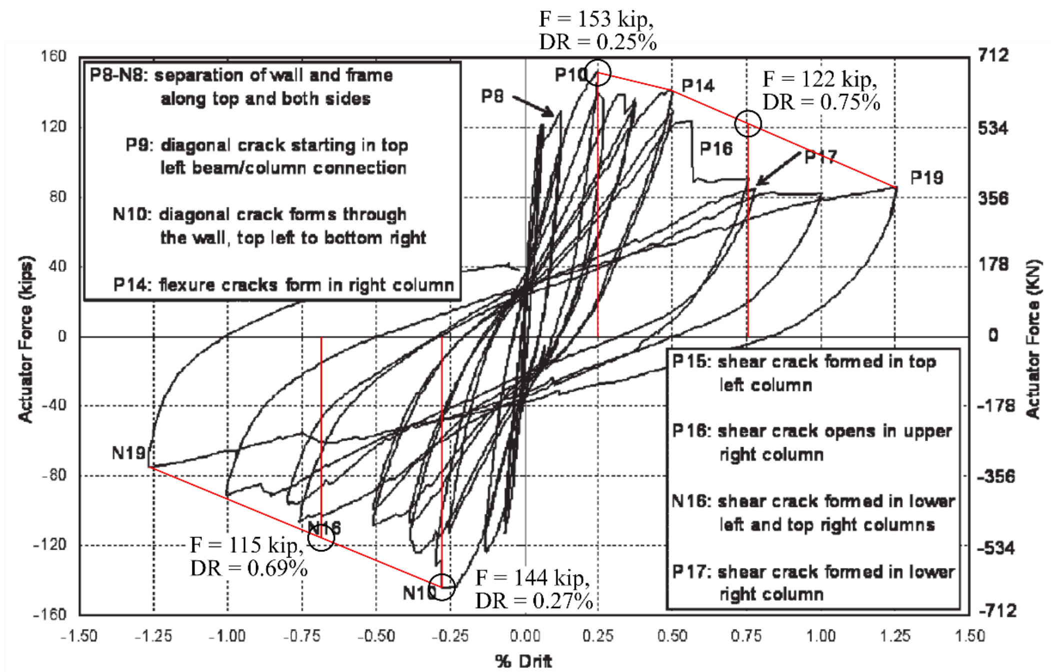

Figure A-30: Force-displacement relationship of Specimen S tested by Blackard (2009)

Note: Figure is taken from Blackard (2009) and drift capacity of Specimen S is 0.7%.

Test frame	Axial load N/N_o	No. of floors	Column steel	Lap-splice length	Long. Reinf. (MPa)	Trans. Reinf. (MPa)	Frame concrete (MPa)	Brick laying mortar (MPa)	Plaster (MPa)
SP1	0.11	2	Cont.	-	365	271	12.7	-	-
SP2	0.11	2	Cont.	-	365	271	13.3	3.4	-
SP3	0.11	2	Cont.	-	365	271	12.7	8.4	8.2
SP4	0.19	2	Cont.	-	330	220	16.6	6.5	6.5
SP5	0.30	2	Lapped	20 ϕ	330	220	8.6	3.5	3.5
SP6	0.10	2	Cont.	-	405	268	15.0	23.1[1]	-
SP7	0.25	1	Cont.	-	330	220	15.6	6.1	6.1
SP8	0.13	1	Cont.	-	405	268	10.7	5.2	5.2
SP9	0.13	1	Lapped	20 ϕ	330	220	9.7	4.9	4.9

[1] Compressive Strength of RC Infil.

Figure A-31: Summary of bare and infilled frames tested by Baran (2010)

Note: Figure is taken from Baran (2010).

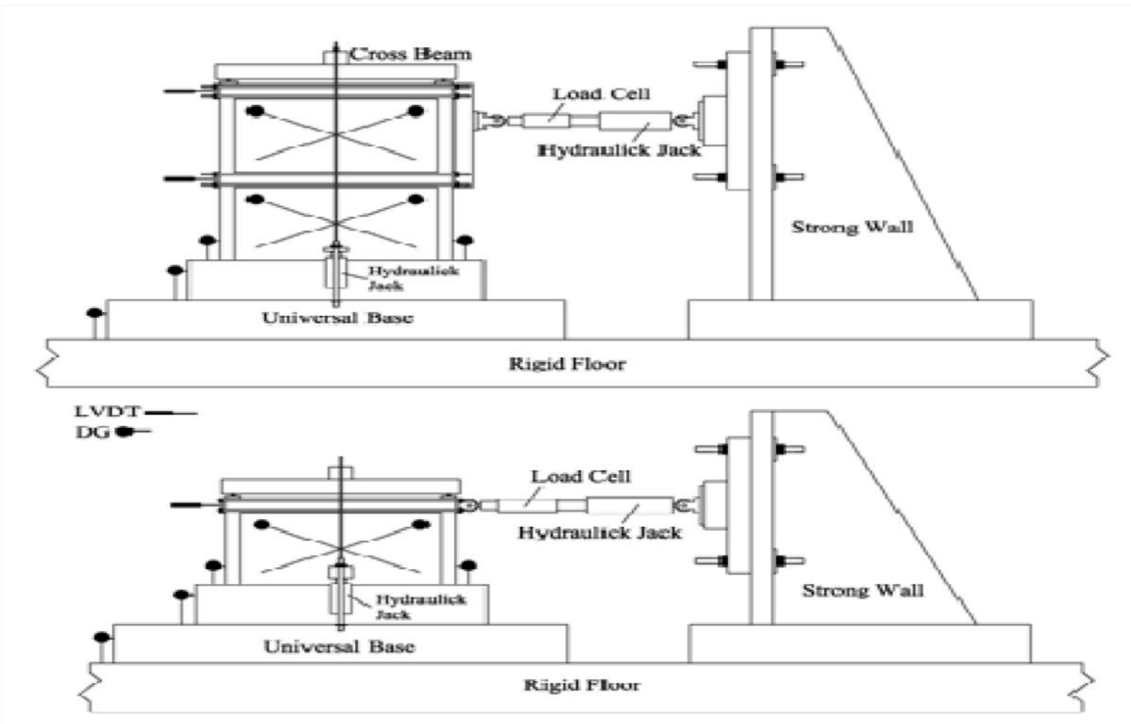

Figure A-32: Test setup of bare and infilled frames tested by Baran (2010)

Note: Figure is taken from Baran (2010).

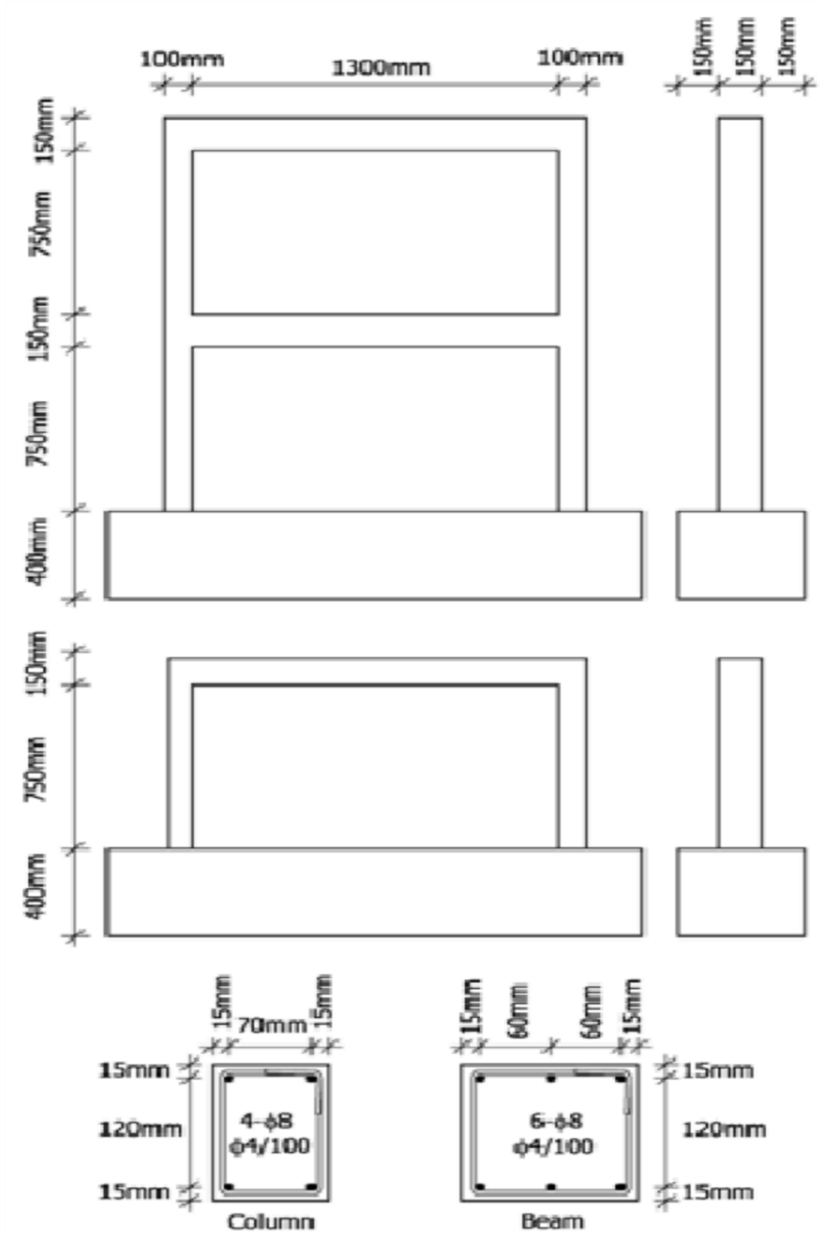

Figure A-33: Dimensions of bare and infilled frames tested by Baran (2010)

Note: Figure is taken from Baran (2010).

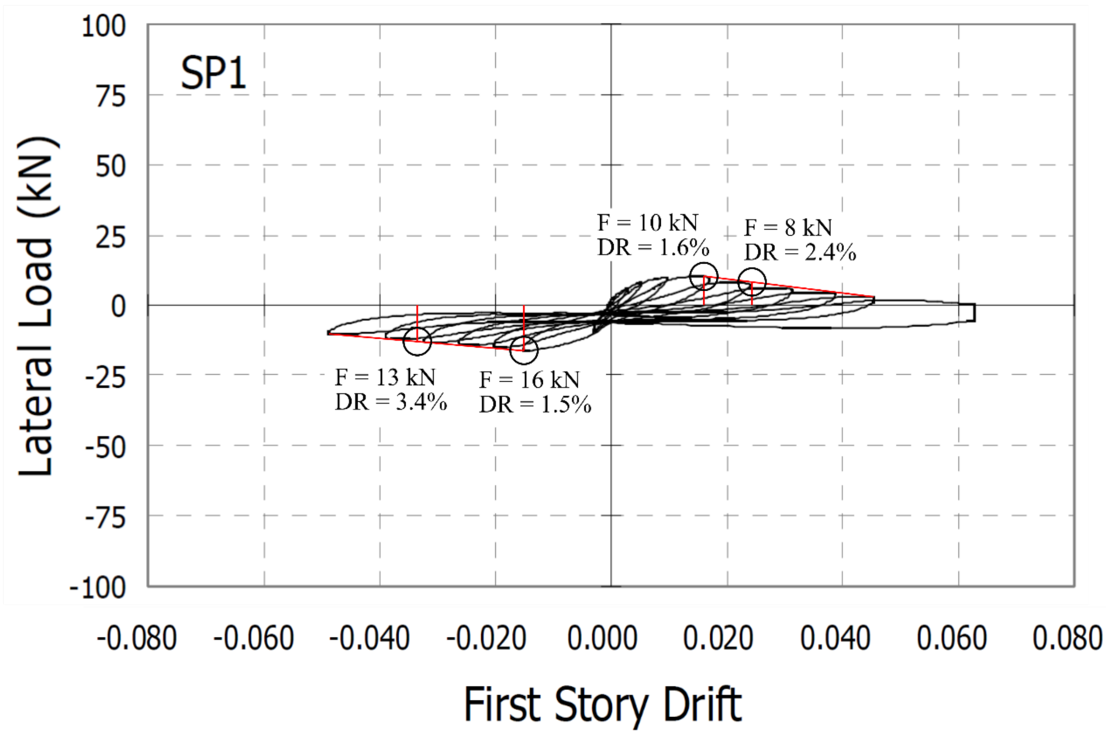

Figure A-34: Force-displacement relationship of Specimen SP1 tested by Baran (2010)

Note: Figure is taken from Baran (2010) and drift capacity of Specimen SP1 is 2.9%.

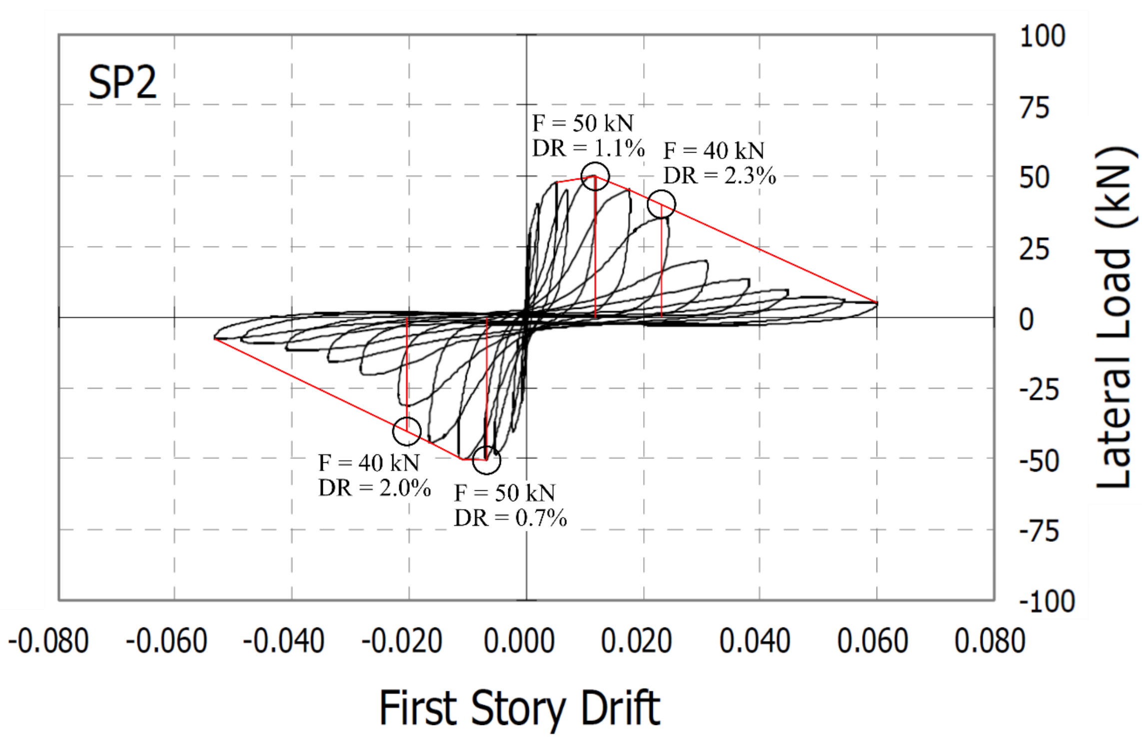

Figure A-35: Force-displacement relationship of Specimen SP2 tested by Baran (2010)

Note: Figure is taken from Baran (2010) and drift capacity of Specimen SP2 is 2.2%.

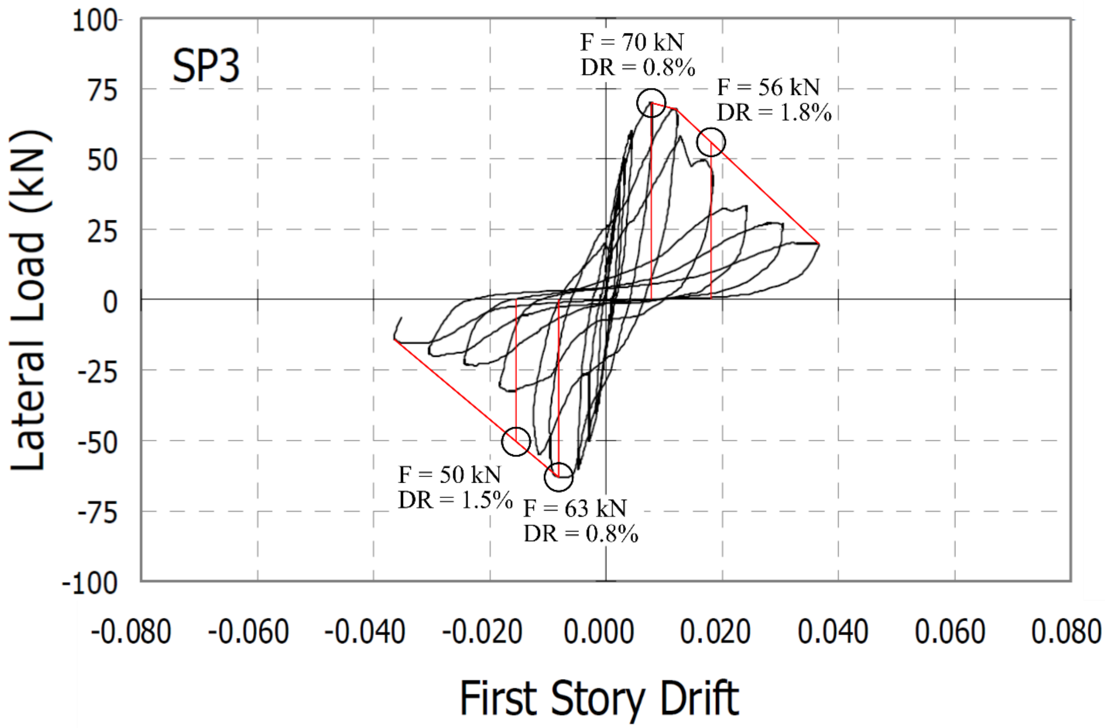

Figure A-36: Force-displacement relationship of Specimen SP3 tested by Baran (2010)

Note: Figure is taken from Baran (2010) and drift capacity of Specimen SP3 is 1.7%.

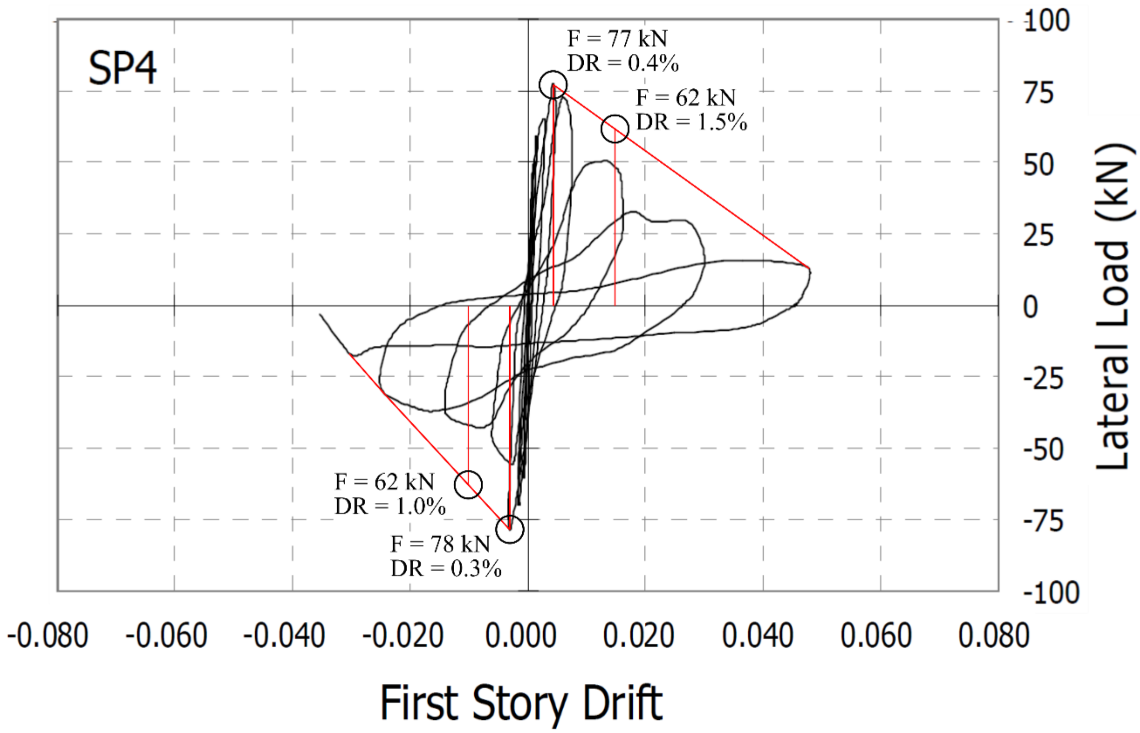

Figure A-37: Force-displacement relationship of Specimen SP4 tested by Baran (2010)

Note: Figure is taken from Baran (2010) and drift capacity of Specimen SP4 is 1.3%.

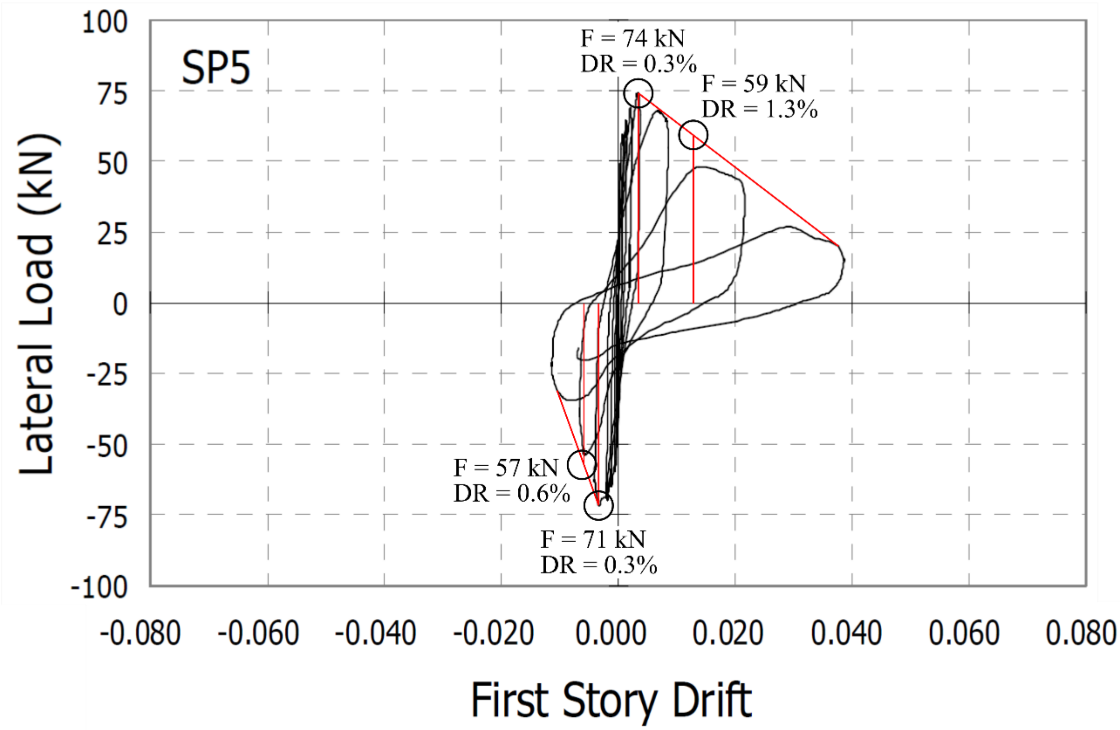

Figure A-38: Force-displacement relationship of Specimen SP5 tested by Baran (2010)

Note: Figure is taken from Baran (2010) and drift capacity of Specimen SP5 is 0.9%.

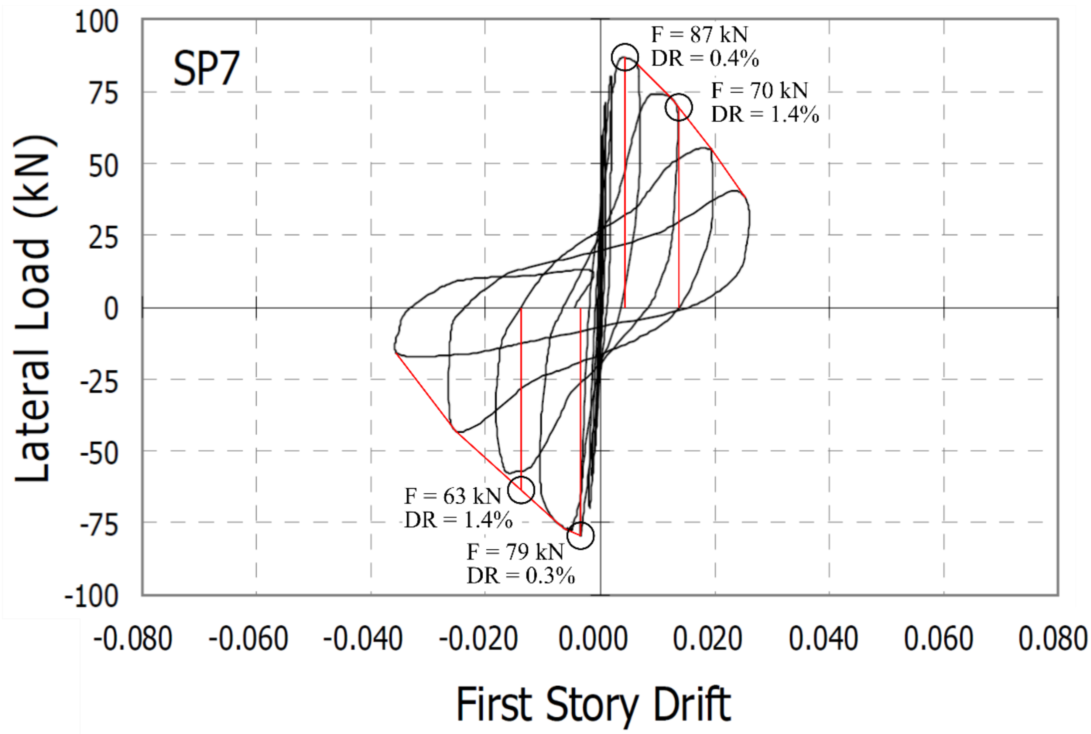

Figure A-39: Force-displacement relationship of Specimen SP7 tested by Baran (2010)

Note: Figure is taken from Baran (2010) and drift capacity of Specimen SP7 is 1.4%.

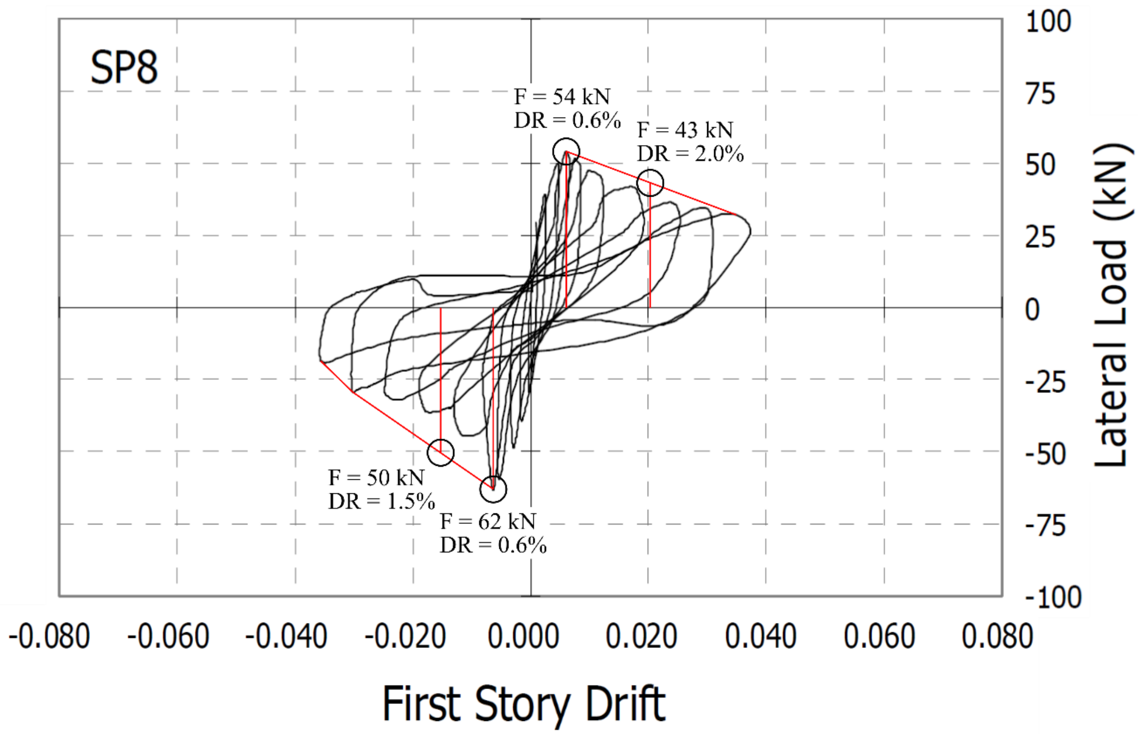

Figure A-40: Force-displacement relationship of Specimen SP8 tested by Baran (2010)

Note: Figure is taken from Baran (2010) and drift capacity of Specimen SP8 is 1.8%.

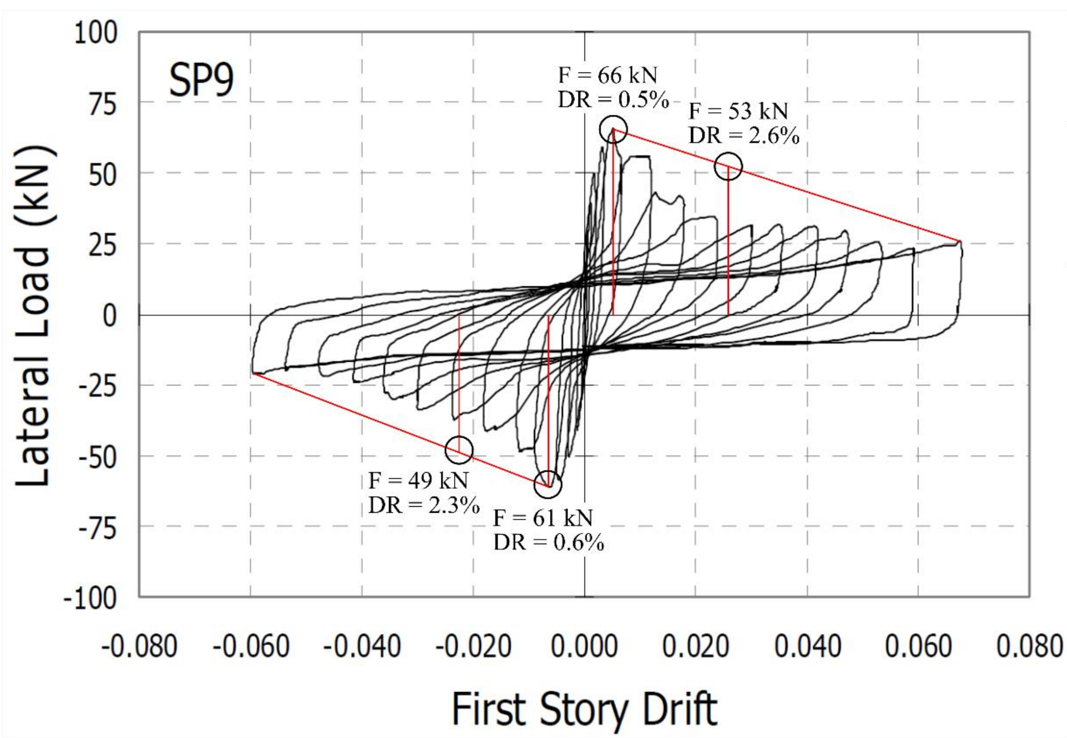

Figure A-41: Force-displacement relationship of Specimen SP9 tested by Baran (2010)

Note: Figure is taken from Baran (2010) and drift capacity of Specimen SP9 is 2.4%.

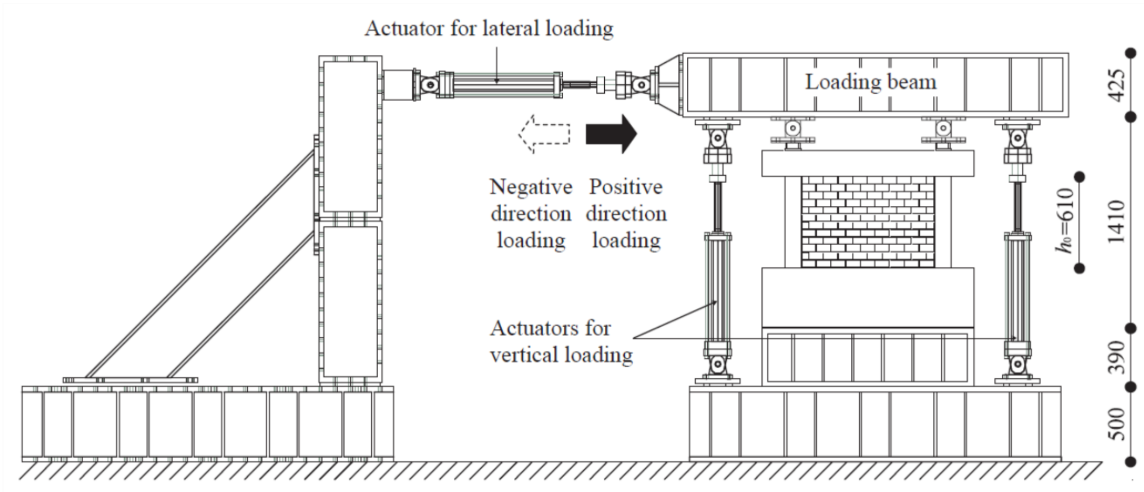

Figure A-42: Test setup of infilled frames tested by Jin (2012)

Note: Figure is taken from Jin (2012) and dimensions are in mm.

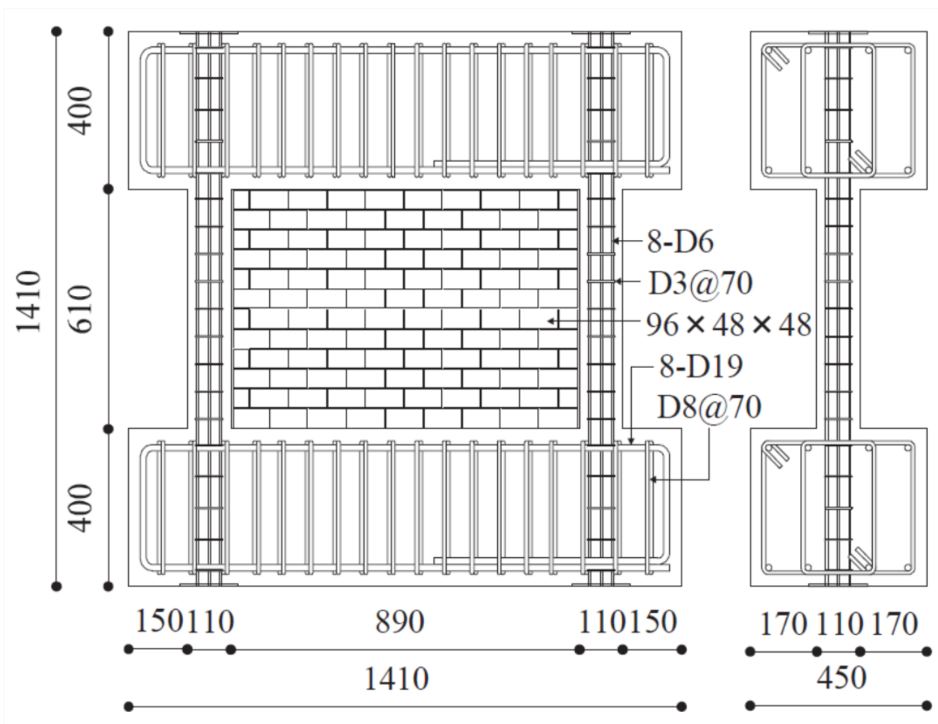

Figure A-43: Dimensions of Specimen IFRB tested by Jin (2012)

Note: Figure is taken from Jin (2012) and dimensions are in mm.

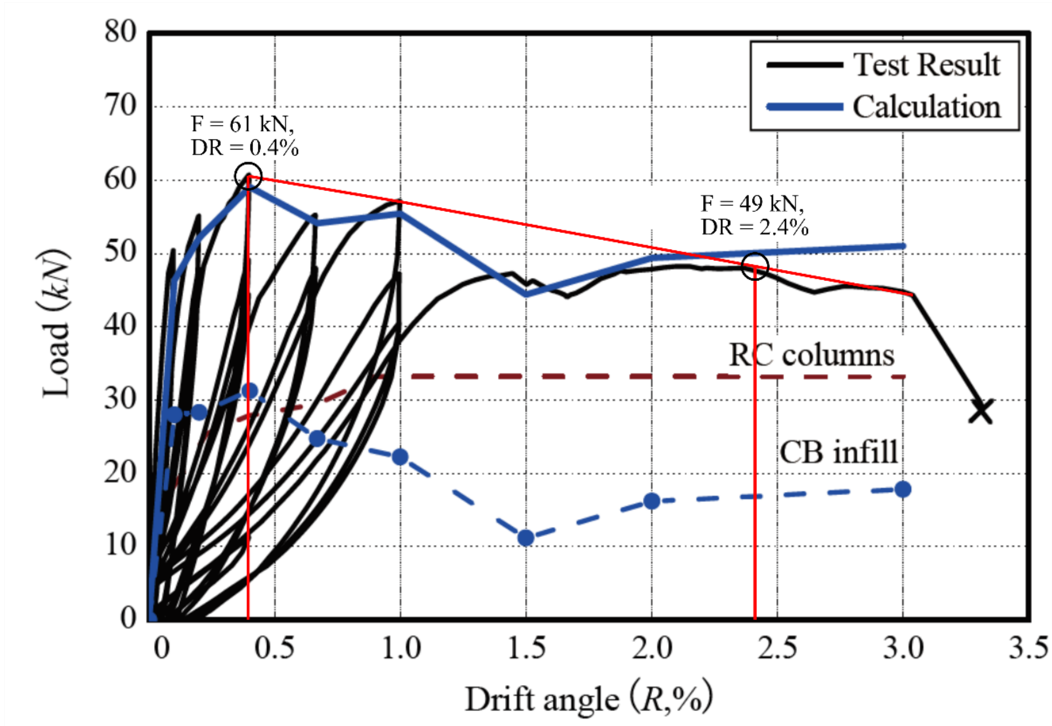

Figure A-44: Force-displacement relationship of Specimen IFRB tested by Jin (2013)

Note: Figure is taken from Jin (2013) and drift capacity of Specimen IFRB is 2.4%.

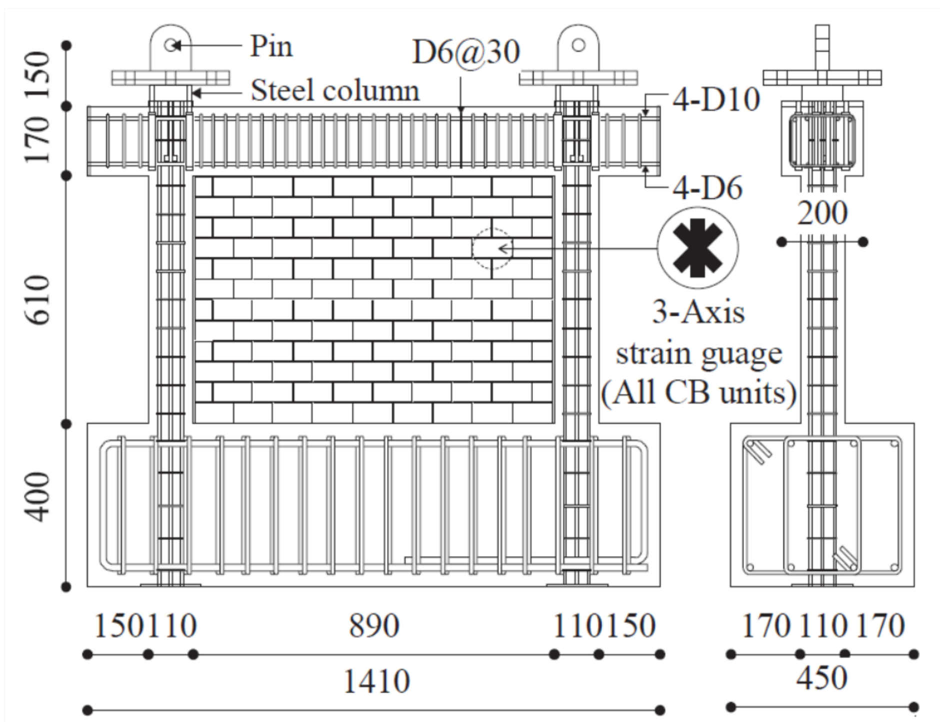

Figure A-45: Dimensions of Specimen IFFB tested by Jin (2012)

Note: Figure is taken from Jin (2012) and dimensions are in mm.

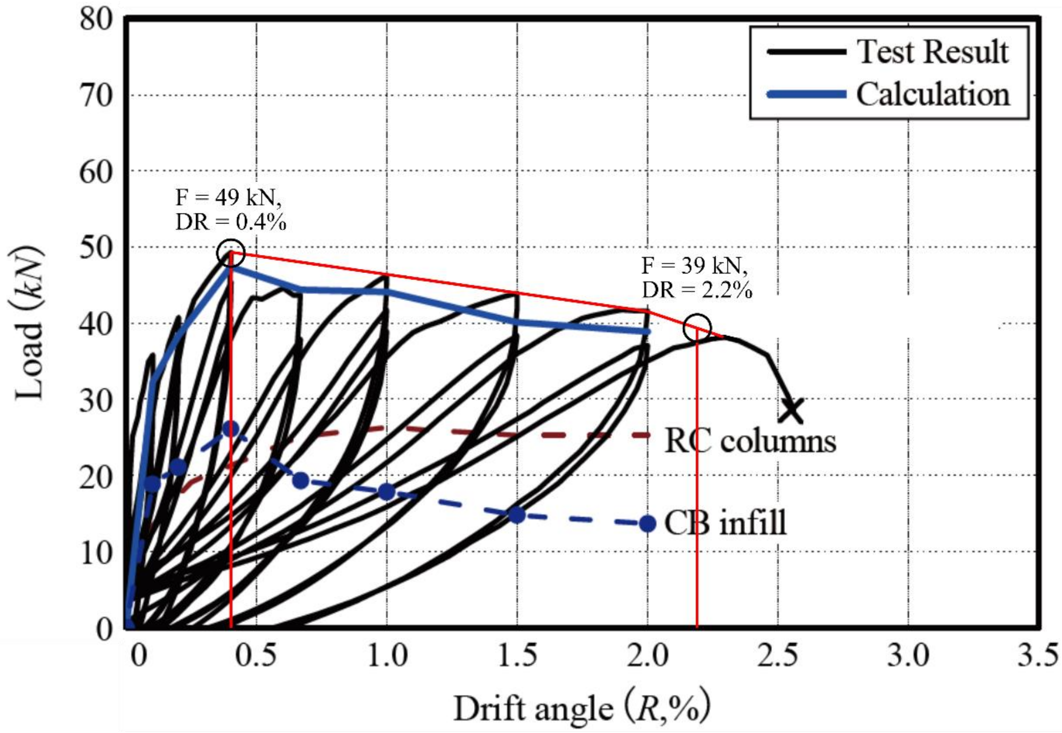

Figure A-46: Force-displacement relationship of Specimen IFFB tested by Jin (2013)

Note: Figure is taken from Jin (2013) and drift capacity of Specimen IFFB is 2.2%.

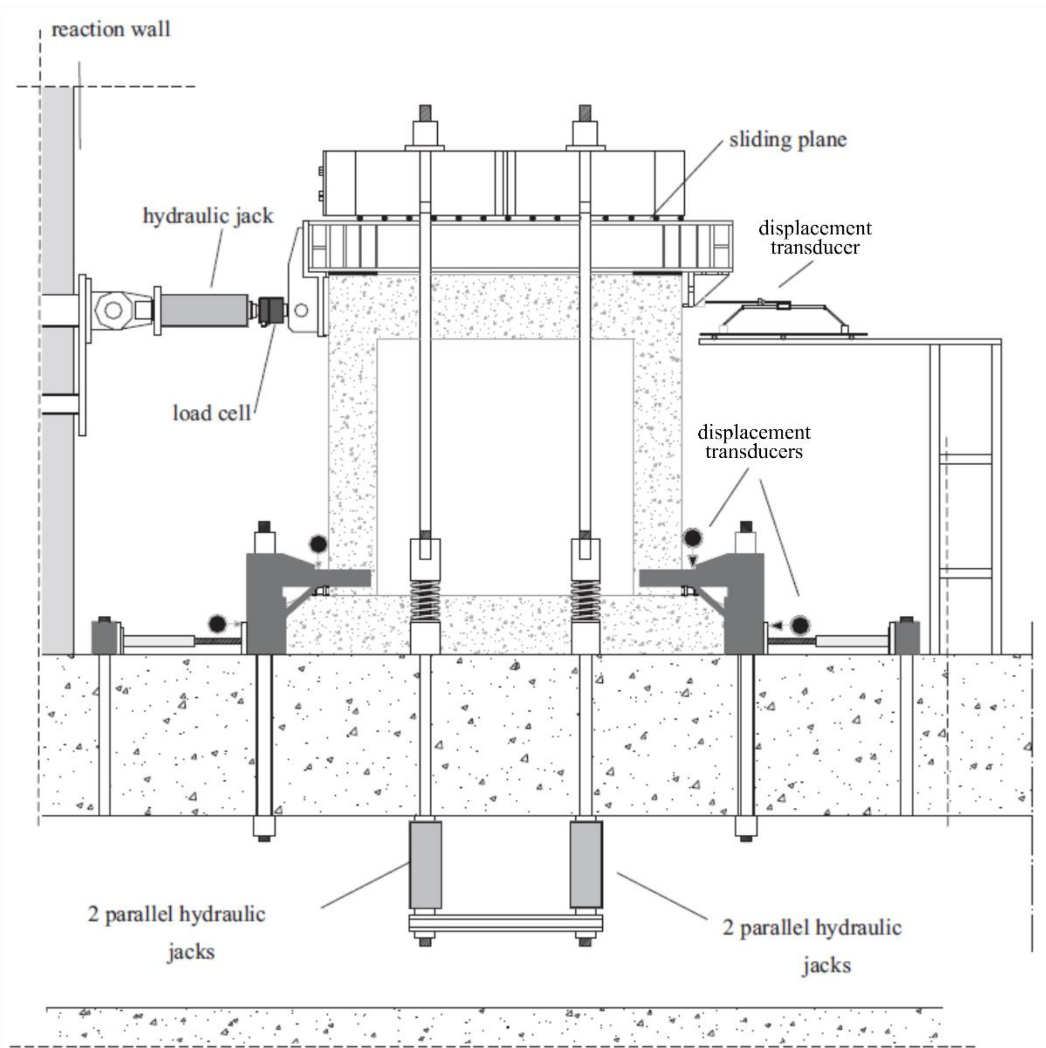

Figure A-47: Test setup of infilled frames tested by Cavaleri (2014)

Note: Figure is taken from Cavaleri (2014).

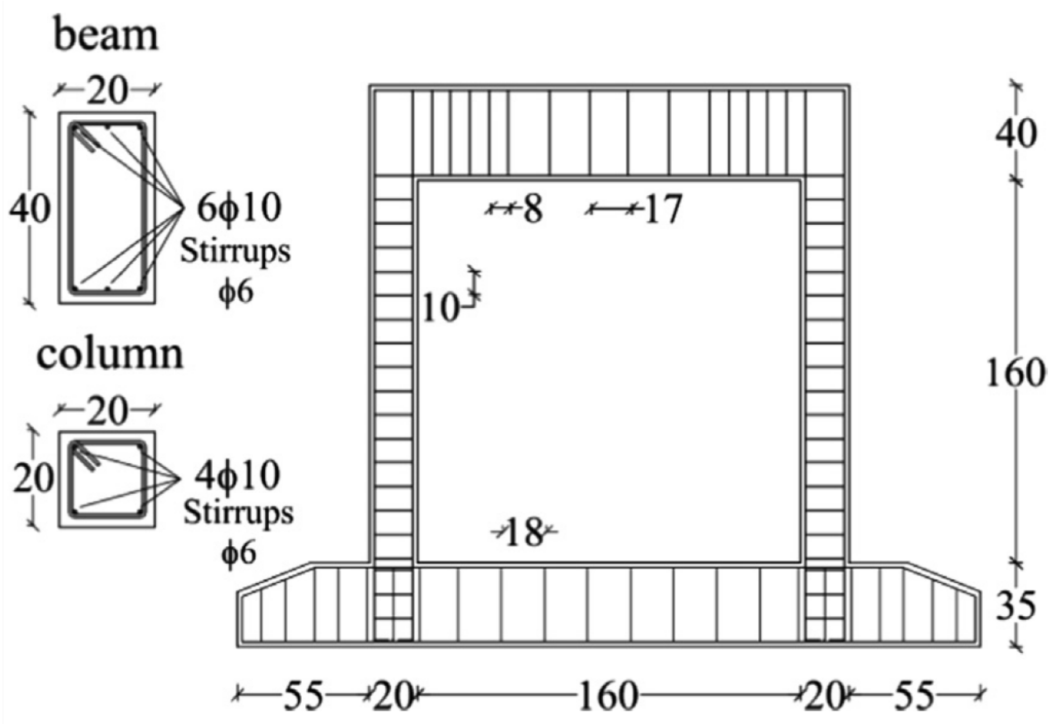

Figure A-48: Dimensions of S1A and S1B Specimens by Cavaleri (2014)

Note: Figure is taken from Cavaleri (2014) and dimensions are in cm.

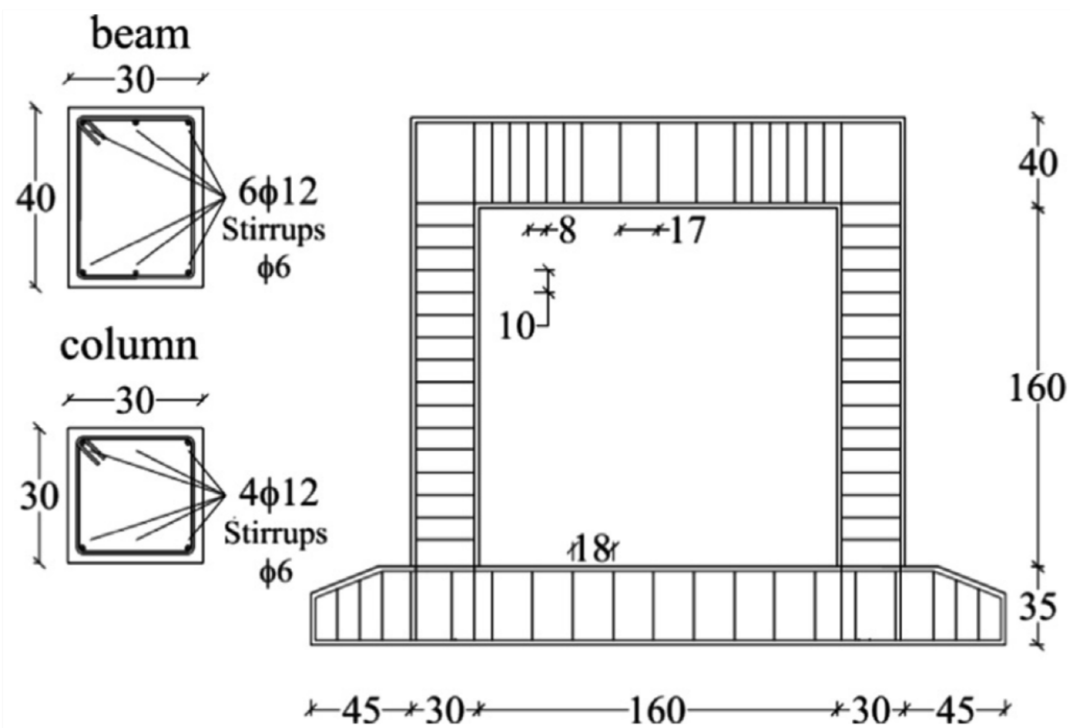

Figure A-49: Dimensions of S1C Specimens by Cavaleri (2014)

Note: Figure is taken from Cavaleri (2014) and dimensions are in cm.

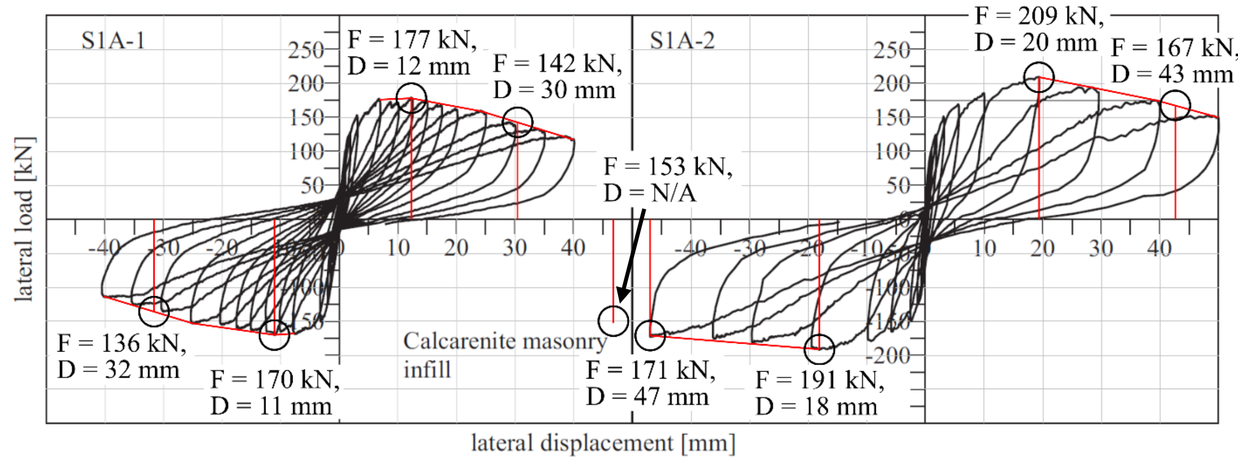

Figure A-50: Force-displacement relationship of S1A Specimens tested by Cavaleri (2014)

Note: Figure is taken from Cavaleri (2014) and drift capacities of Specimens S1A-1 and S1A-2 are 1.7 and 2.5%.

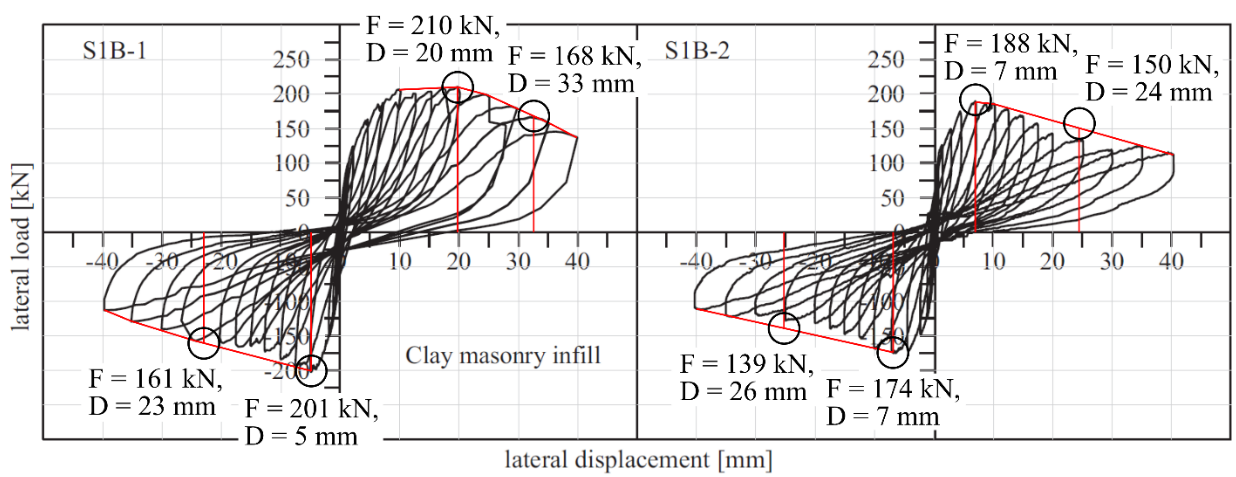

Figure A-51: Force-displacement relationship of S1B Specimens tested by Cavaleri (2014)

Note: Figure is taken from Cavaleri (2014) and drift capacities of Specimens S1B-1 and S1B-2 are 1.5 and 1.4%.

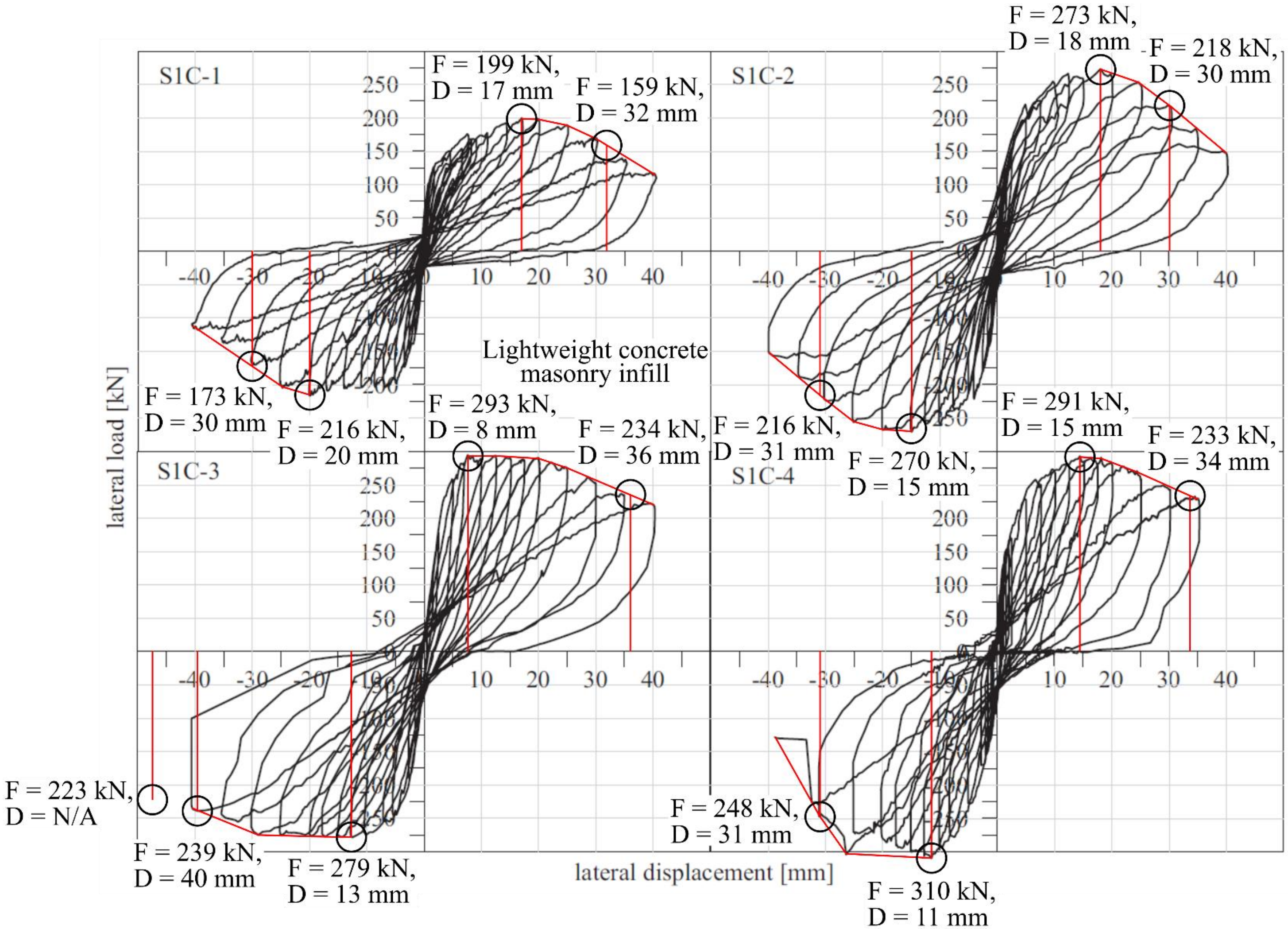

Figure A-52: Force-displacement relationship of S1C Specimens tested by Cavaleri (2014)

Note: Figure is taken from Cavaleri (2014) and drift capacities of Specimens S1C-1, S1C-2, S1C-3 and S1C-4 are 1.7, 1.7, 2.1 and 1.8%.

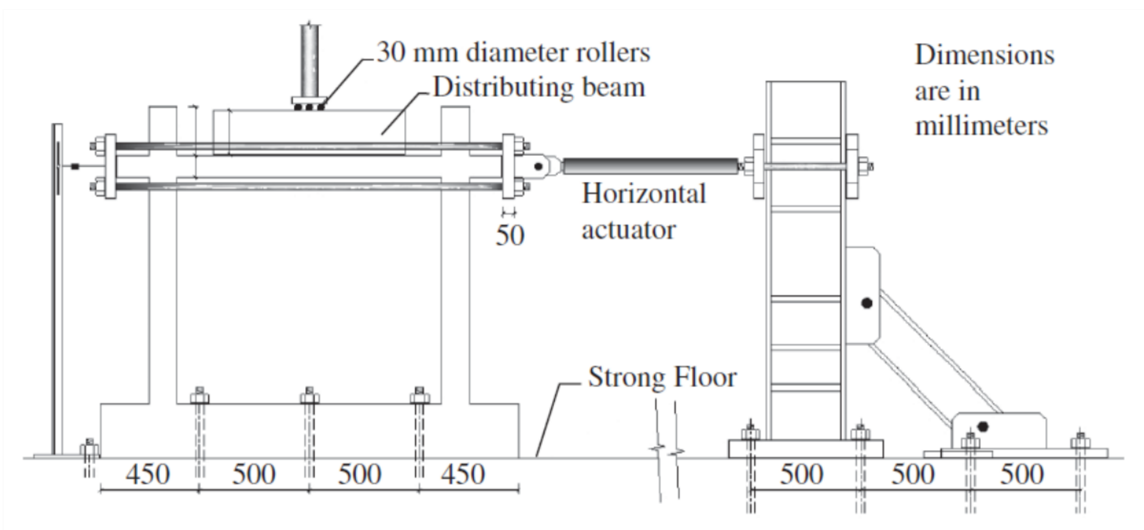

Figure A-53: Test setup of infilled frames tested by Al-Nimry (2014)

Note: Figure is taken from Al-Nimry (2014).

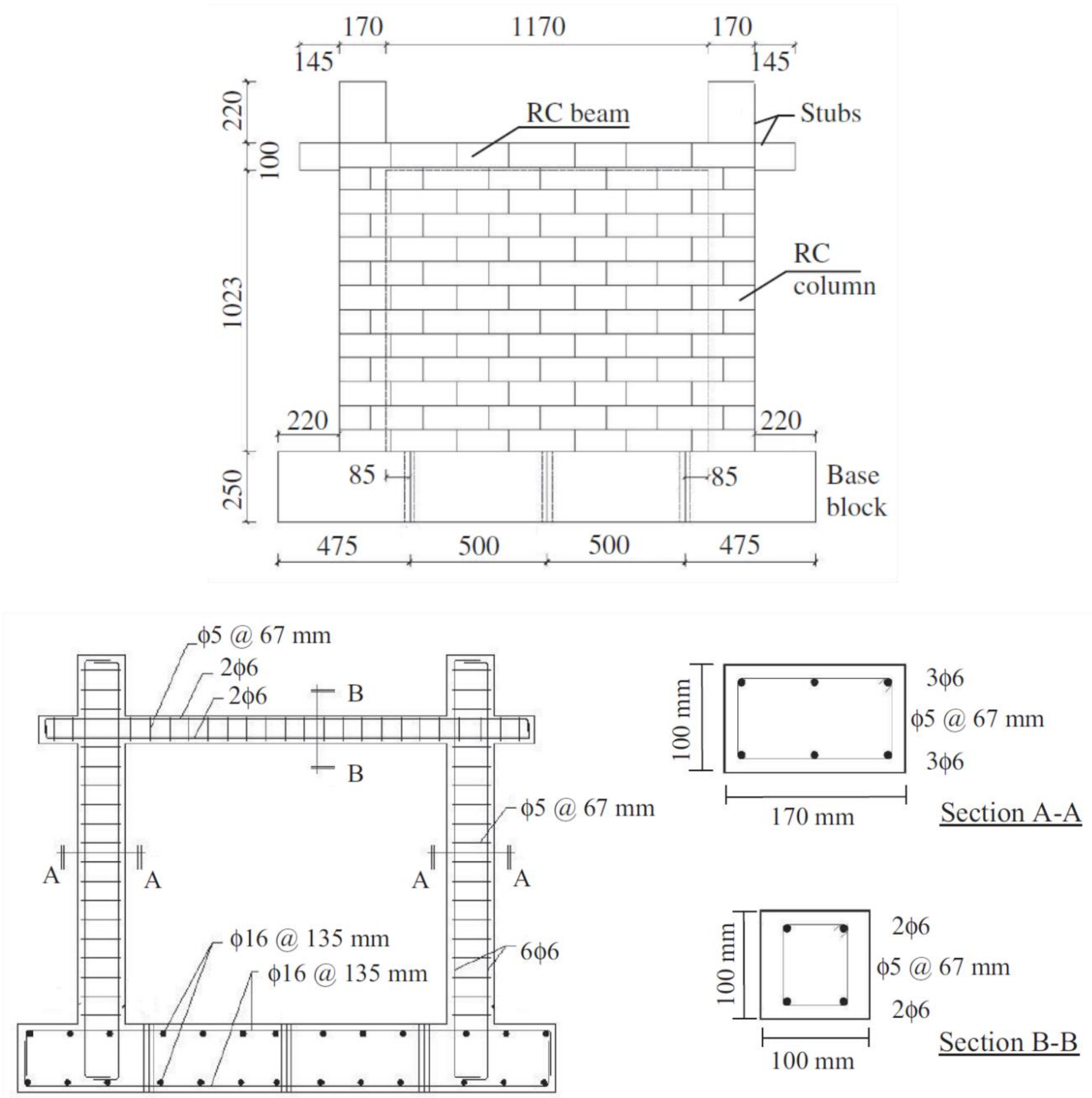

Figure A-54: Dimensions of infilled frames tested by Al-Nimry (2014)

Note: Figure is taken from Al-Nimry (2014) and dimensions are in mm.

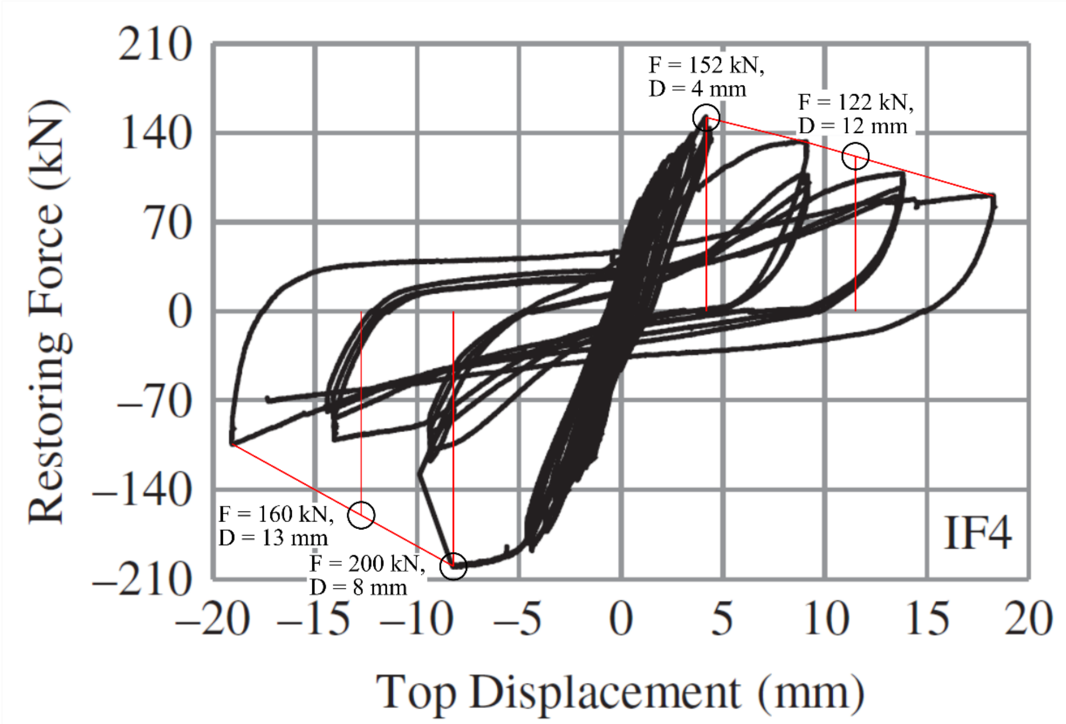

Figure A-55: Force-displacement relationship of Specimen IF4 tested by Al-Nimry (2014)

Note: Figure is taken from Al-Nimry (2014) and drift capacity of Specimen IF4 is 1.1%.

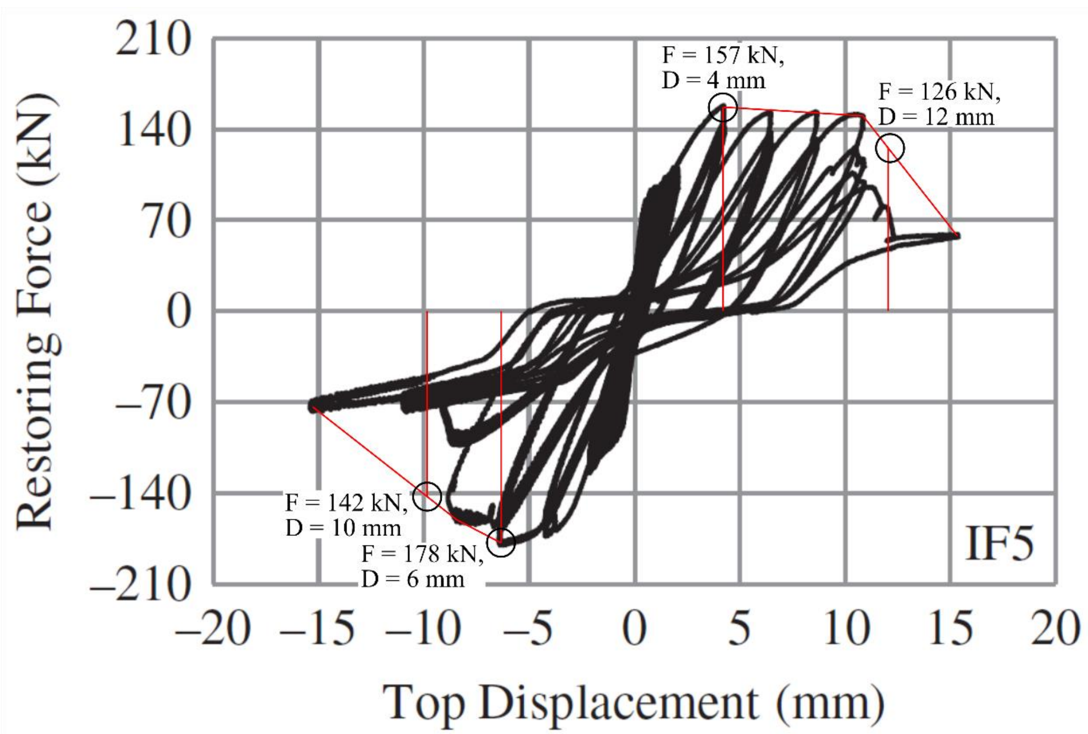

Figure A-56: Force-displacement relationship of Specimen IF5 tested by Al-Nimry (2014)

Note: Figure is taken from Al-Nimry (2014) and drift capacity of Specimen IF5 is 1.0%.

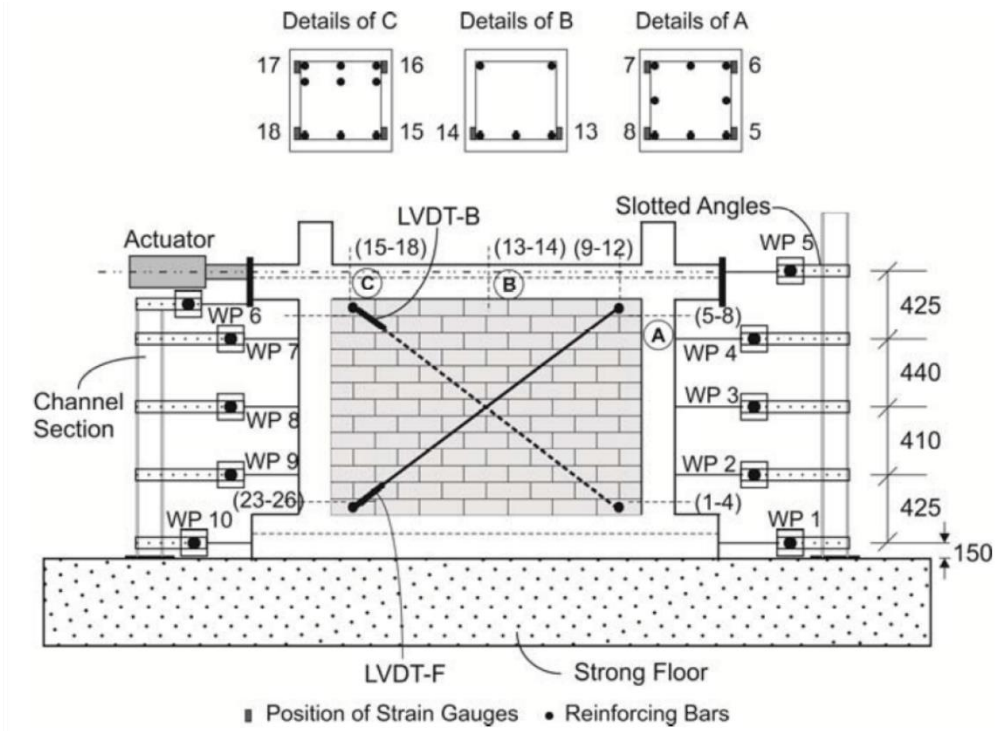

Figure A-57: Test setup of bare and infilled frames tested by Bose (2016)

Note: Figure is taken from Bose (2016).

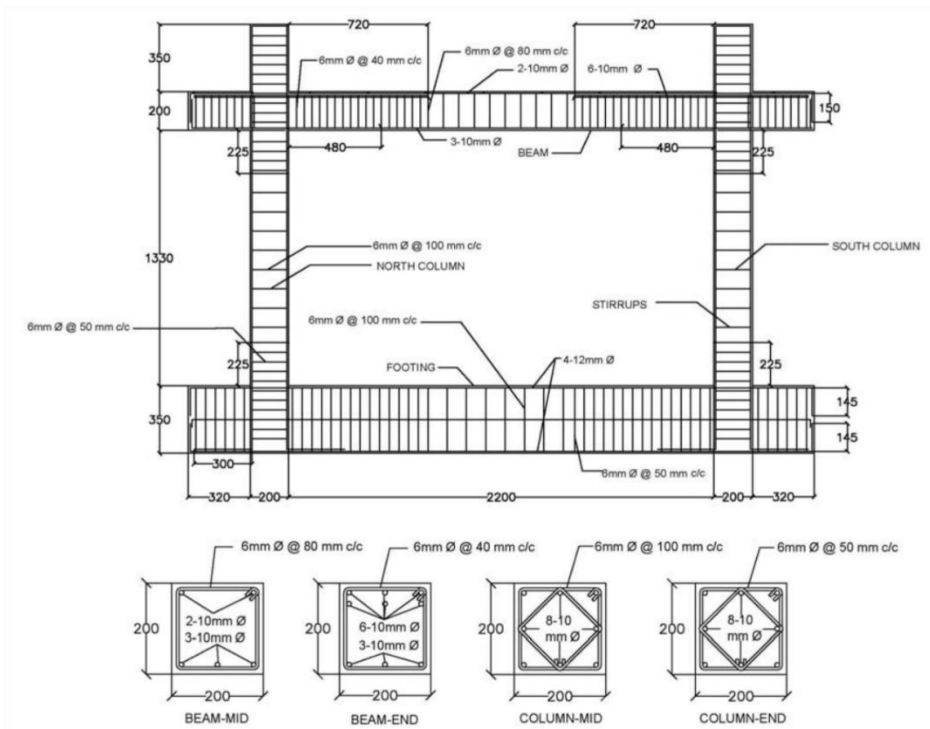

Figure A-58: Dimensions of bare and infilled frames tested by Bose (2016)

Note: Figure is taken from Bose (2016) and dimensions are in mm.

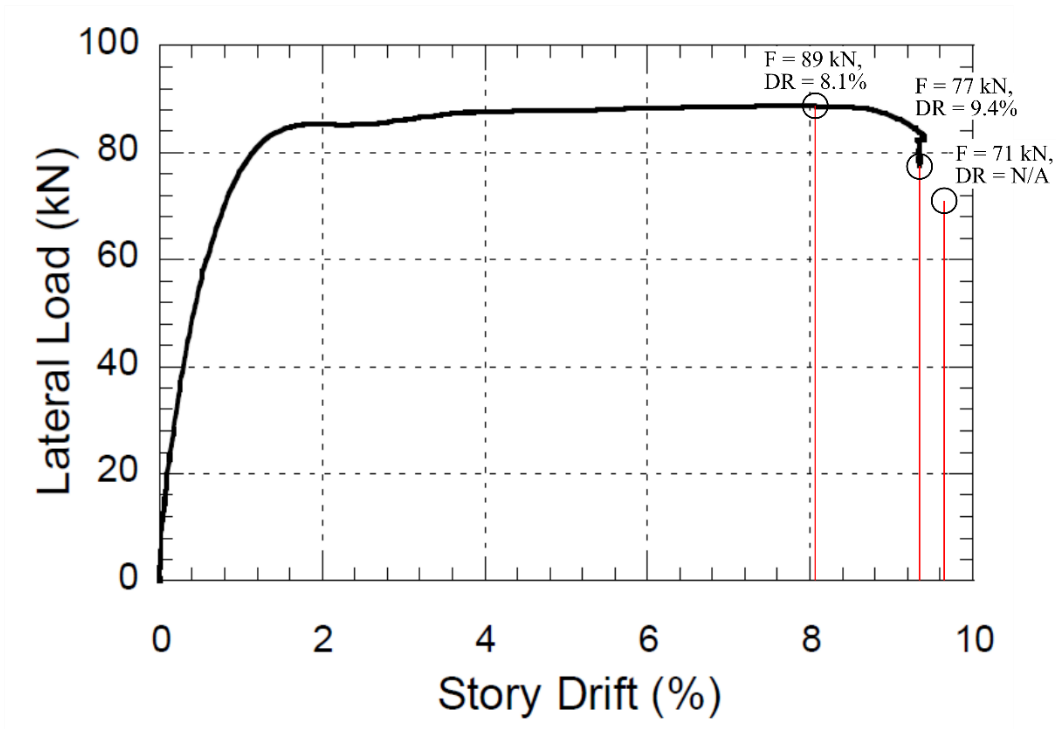

Figure A-59: Force-displacement relationship of Specimen BF tested by Bose (2016)

Note: Figure is taken from Bose (2016) and drift capacity of Specimen BF is 9.4%.

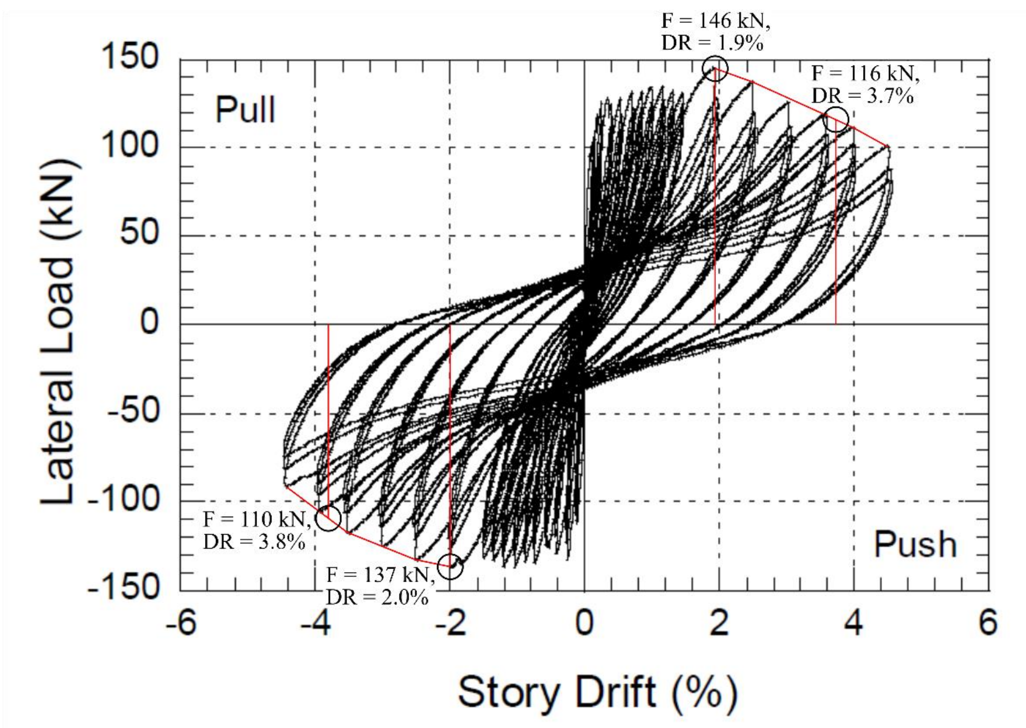

Figure A-60: Force-displacement relationship of Specimen IF-AAC tested by Bose (2016)

Note: Figure is taken from Bose (2016) and drift capacity of Specimen IF-AAC is 3.8%.

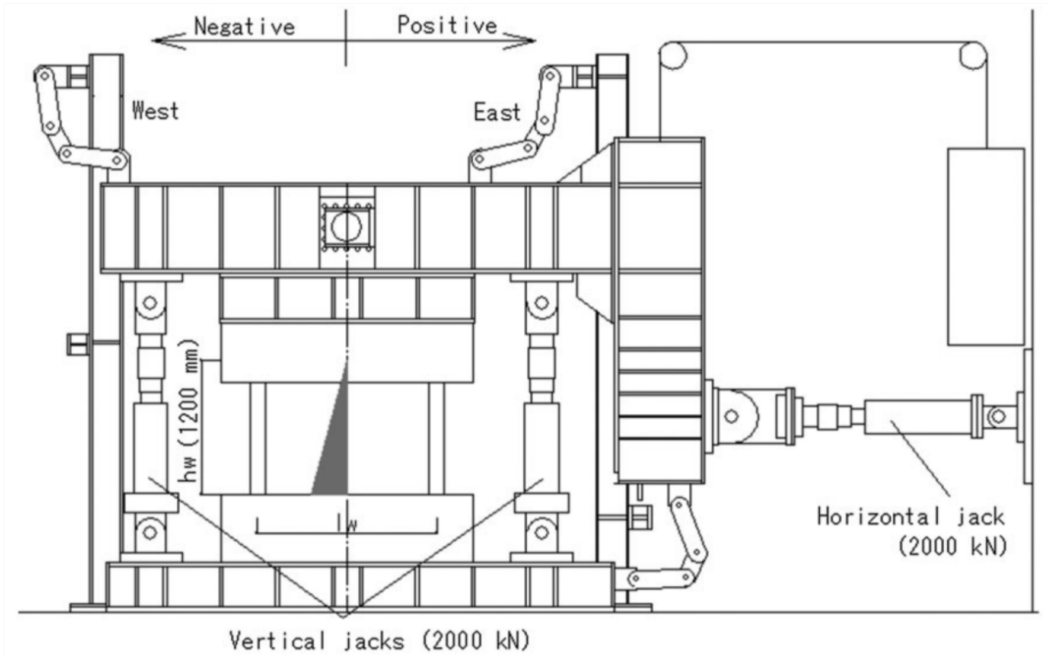

Figure A-61: Test setup of bare and infilled frames tested by Diawati (2016)

Note: Figure is taken from Diawati (2016).

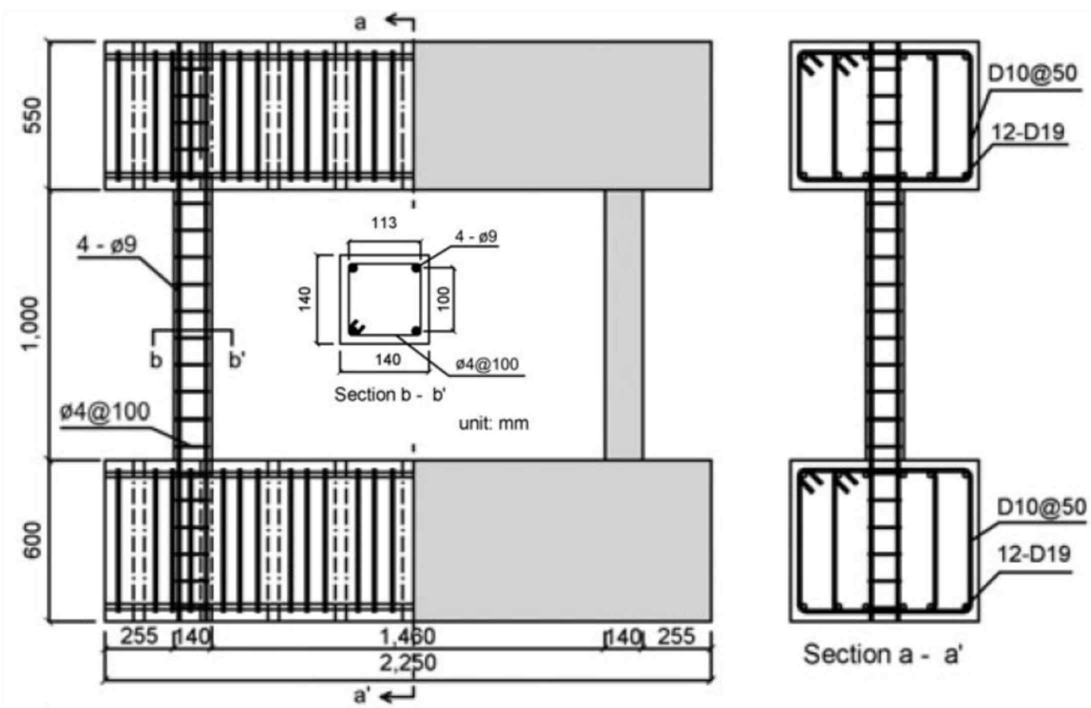

Figure A-62: Dimensions of Specimen BF tested by Diawati (2016)

Note: Figure is taken from Diawati (2016).

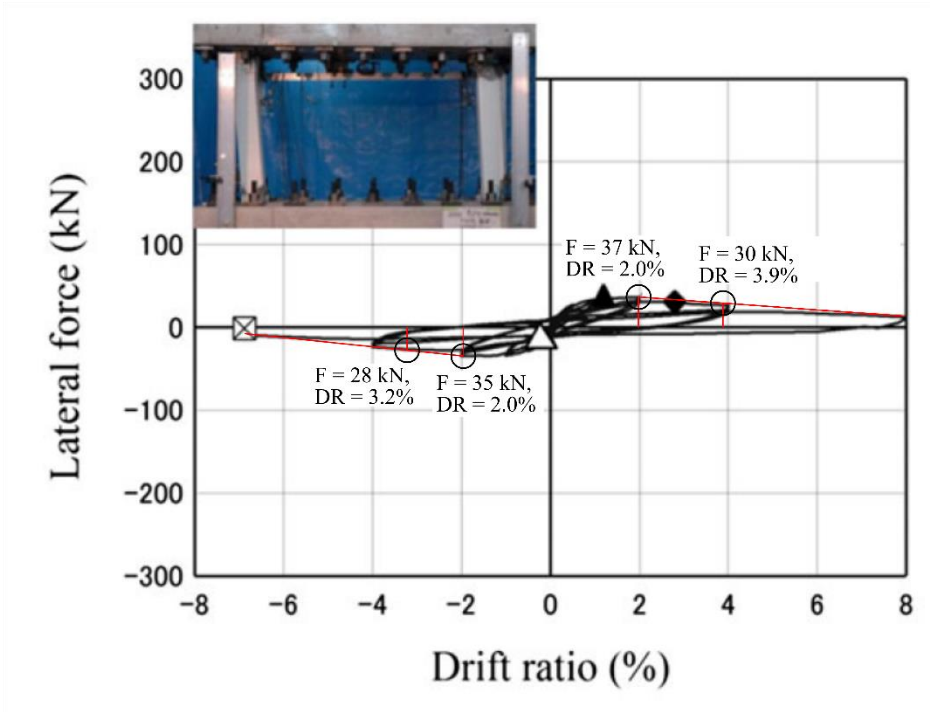

Figure A-63: Force-displacement relationship of Specimen BF tested by Diawati (2016)

Note: Figure is taken from Diawati (2016) and drift capacity of Specimen BF is 3.6%.

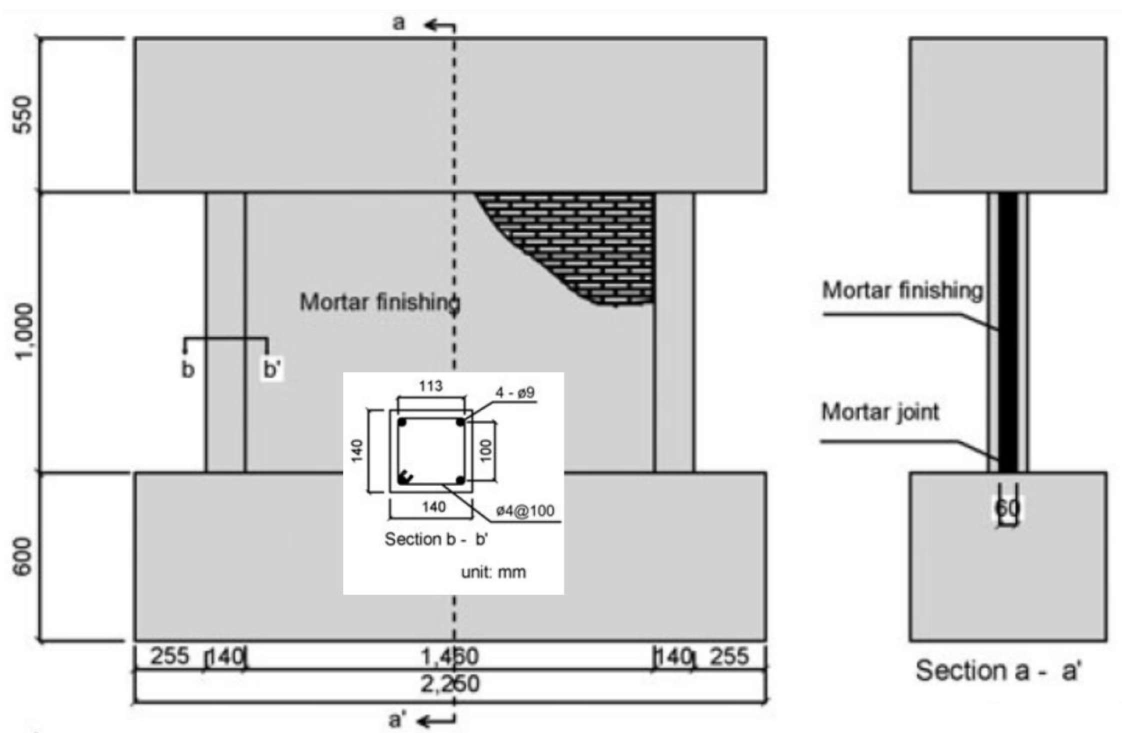

Figure A-64: Dimensions of infilled frames tested by Diawati (2016)

Note: Figure is taken from Diawati (2016).

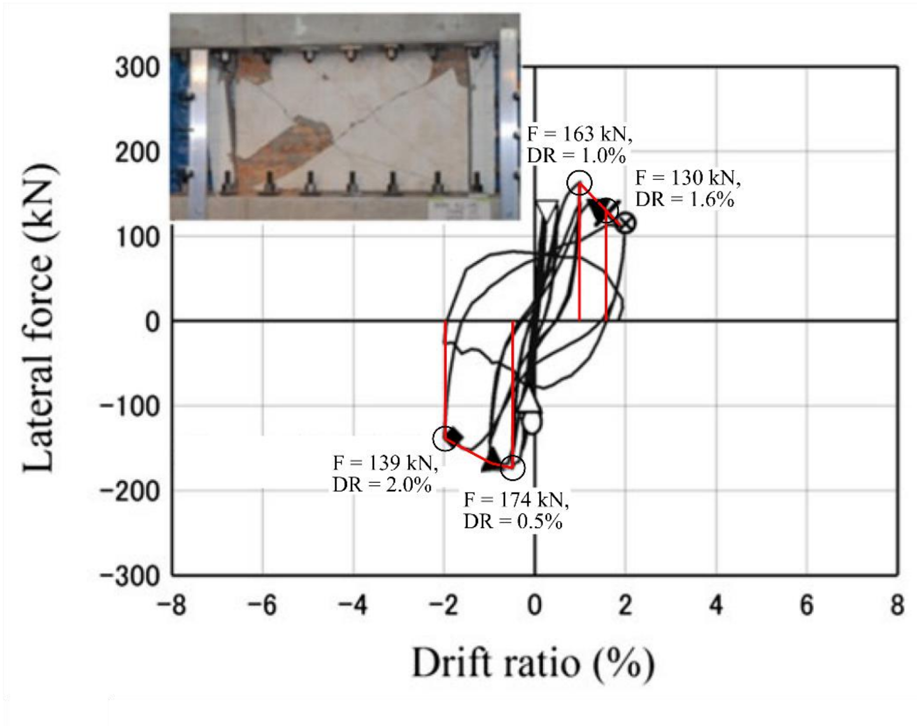

Figure A-65: Force-displacement relationship of Specimen IFFB tested by Diawati (2016)

Note: Figure is taken from Diawati (2016) and drift capacity of Specimen IFFB is 1.8%.

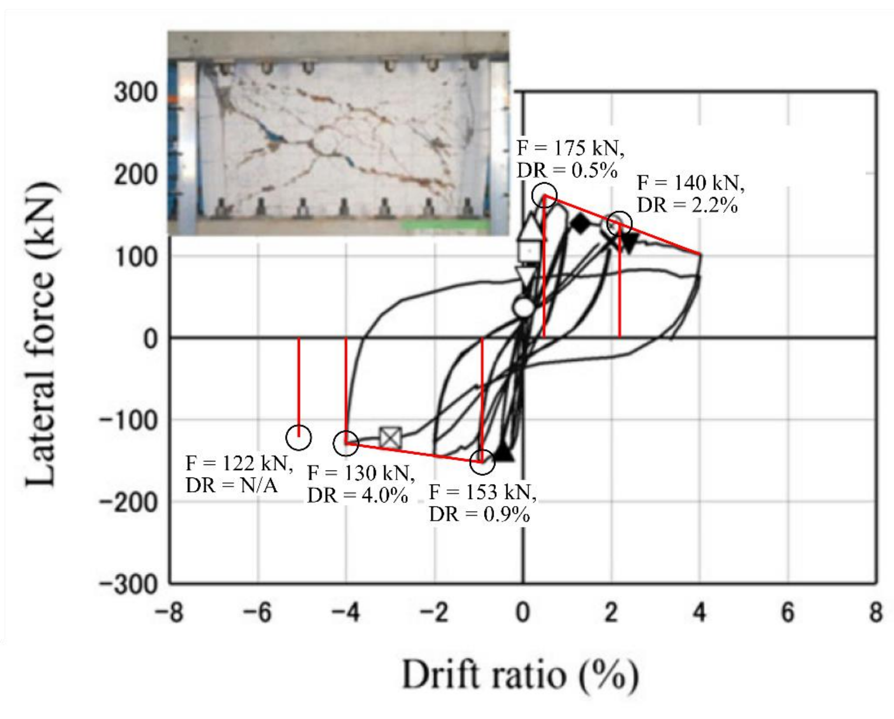

Figure A-66: Force-displacement relationship of Specimen IFSB-wo tested by Diawati (2016)

Note: Figure is taken from Diawati (2016) and drift capacity of Specimen IFSB-wo is 3.1%.

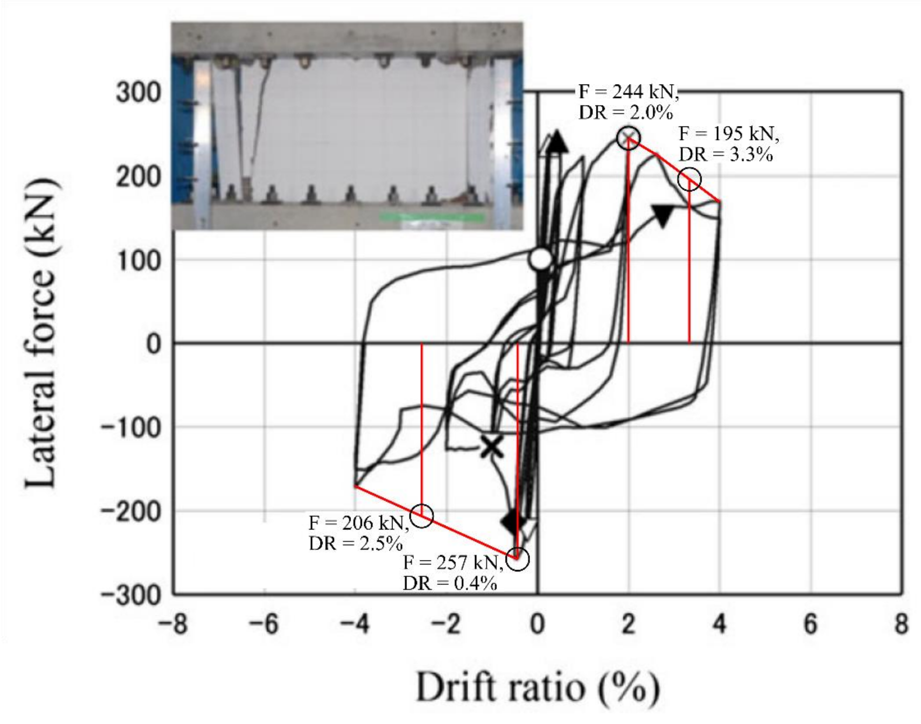

Figure A-67: Force-displacement relationship of Specimen IFSB tested by Diawati (2016)

Note: Figure is taken from Diawati (2016) and drift capacity of Specimen IFSB is 2.9%.

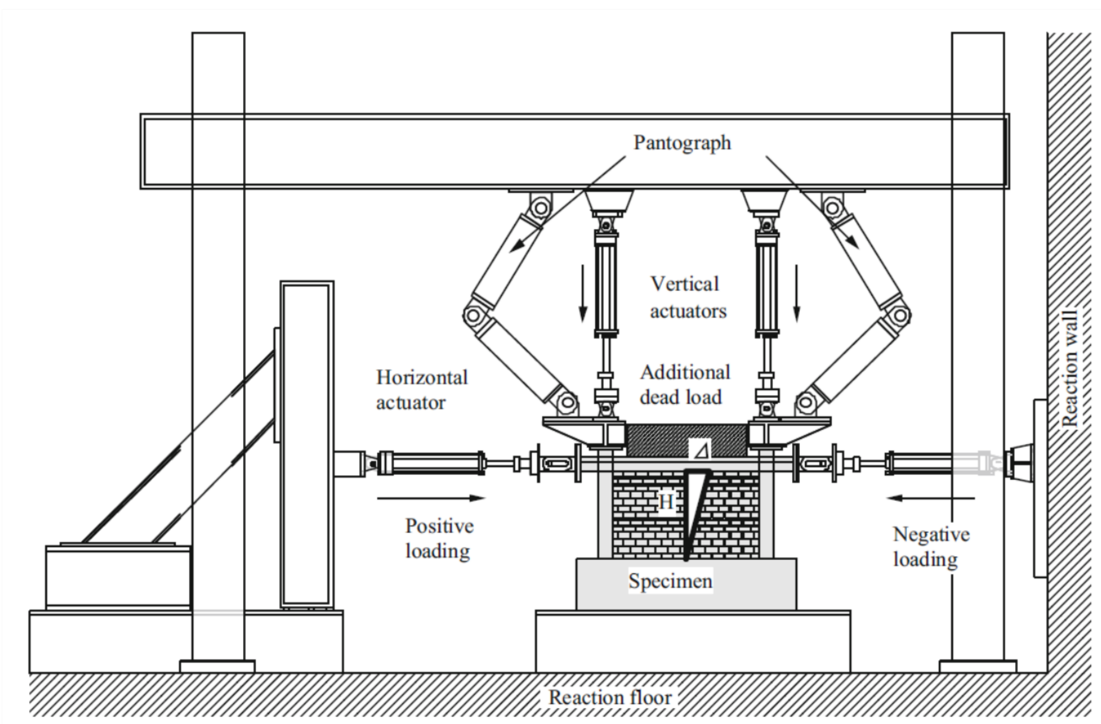

Figure A-68: Test setup of bare and infilled frames tested by Suzuki (2017)

Note: Figure is taken from Suzuki (2017).

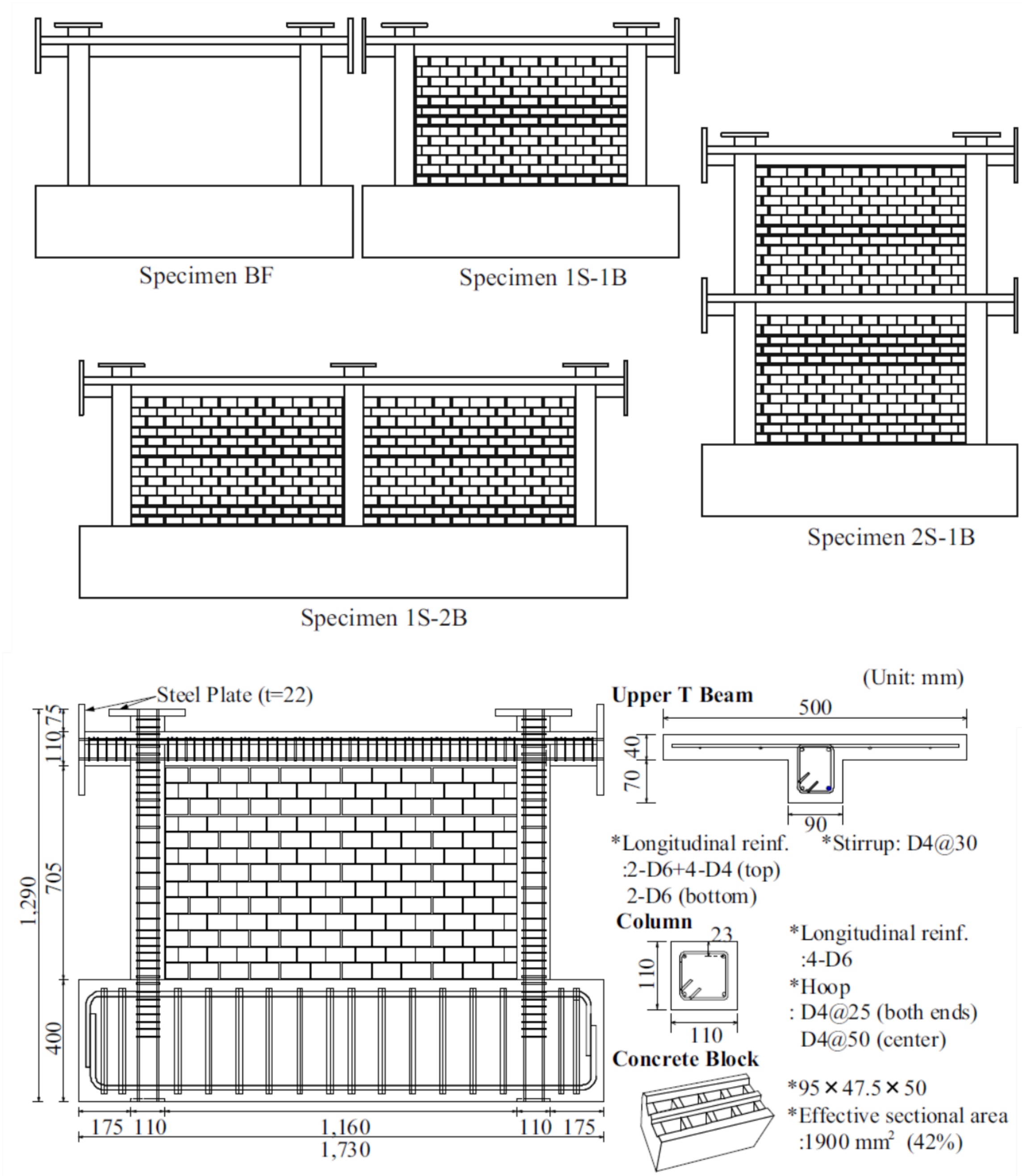

Figure A-69: Dimensions of bare and infilled frames tested by Suzuki (2017)

Note: Figure is taken from Suzuki (2017).

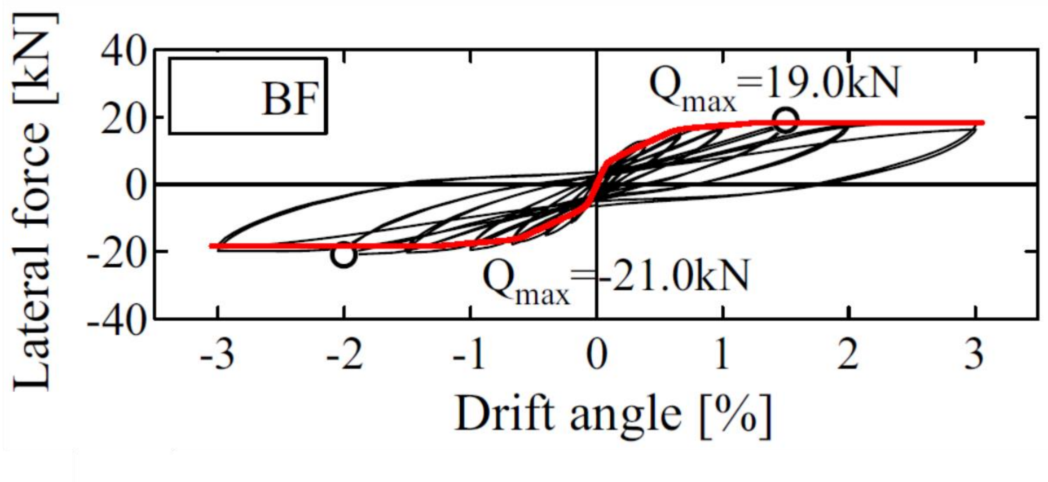

Figure A-70: Force-displacement relationship of Specimen BF tested by Suzuki (2017)

Note: Figure is taken from Suzuki (2017) and drift capacity of Specimen BF was not reached.

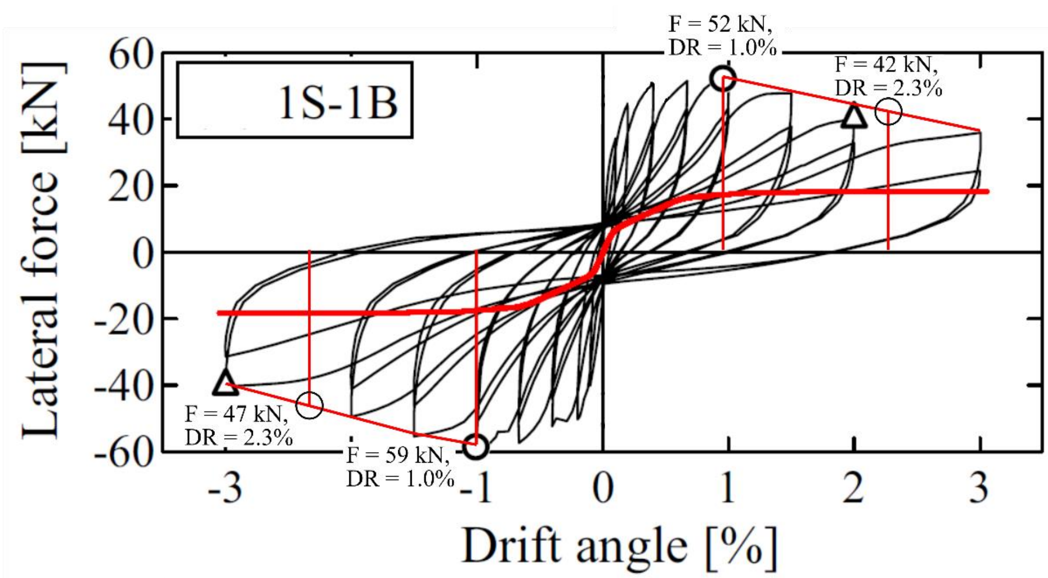

Figure A-71: Force-displacement relationship of Specimen 1S-1B tested by Suzuki (2017)

Note: Figure is taken from Suzuki (2017) and drift capacity of Specimen 1S-1B is 2.3%.

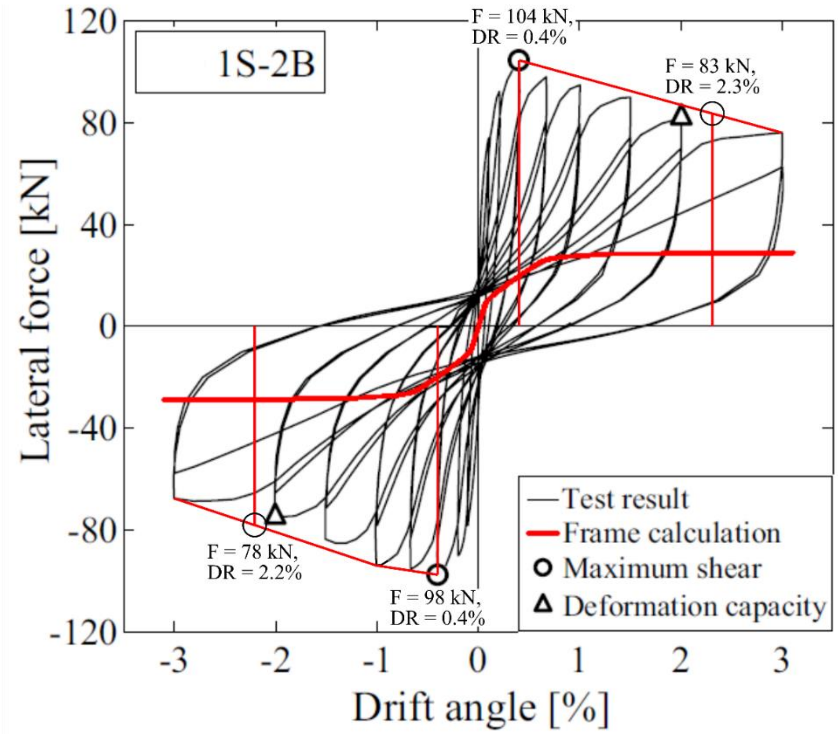

Figure A-72: Force-displacement relationship of Specimen 1S-2B tested by Suzuki (2017)

Note: Figure is taken from Suzuki (2017) and drift capacity of Specimen 1S-2B is 2.3%.

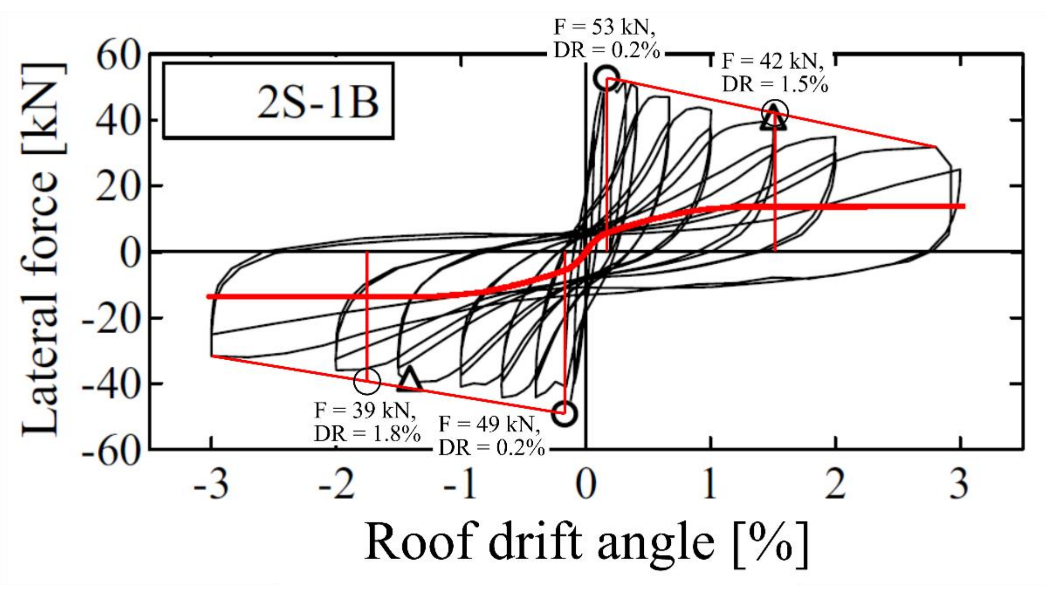

Figure A-73: Force-displacement relationship of Specimen 2S-1B tested by Suzuki (2017)

Note: Figure is taken from Suzuki (2017) and drift capacity of Specimen 2S-1B is 1.6%.

Series no.	Main varying parameter	Specimen name	β index	Column dimension (mm)	Beam dimension (bxd) (mm)	Ratio M_{ub}/M_{uc} *	Mortar strength
i	Strength of RC columns	F-1.5	1.51	300 x 300	600 x 400	3.3	Strong
		F-0.6	0.56	200 x 200		9.7	Strong
		F-0.4	0.39			5.9	Strong
ii	Weak beam	WB	0.43		200 x 250	0.7	Strong
iii	Weak mortar	WM	0.82		600 x 400	5.9	Weak
*ratio of beam to column`s plastic moment capacity							

Figure A-74: Summary of infilled frames tested by Alwashali (2018)

Note: Figure is taken from Alwashali (2018).

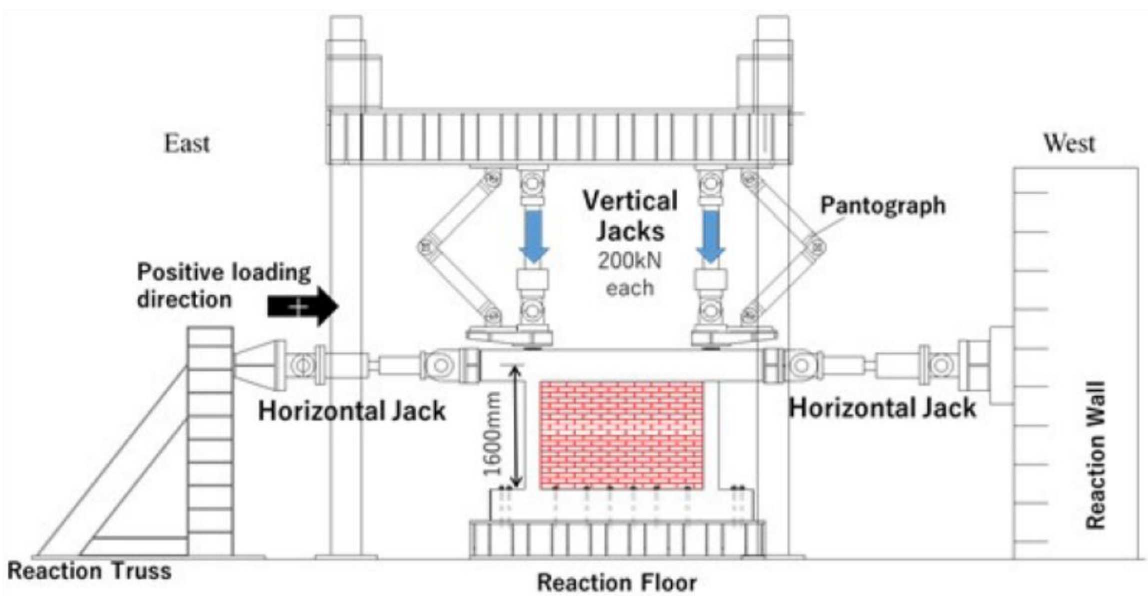

Figure A-75: Test setup of infilled frames tested by Alwashali (2018)

Note: Figure is taken from Alwashali (2018).

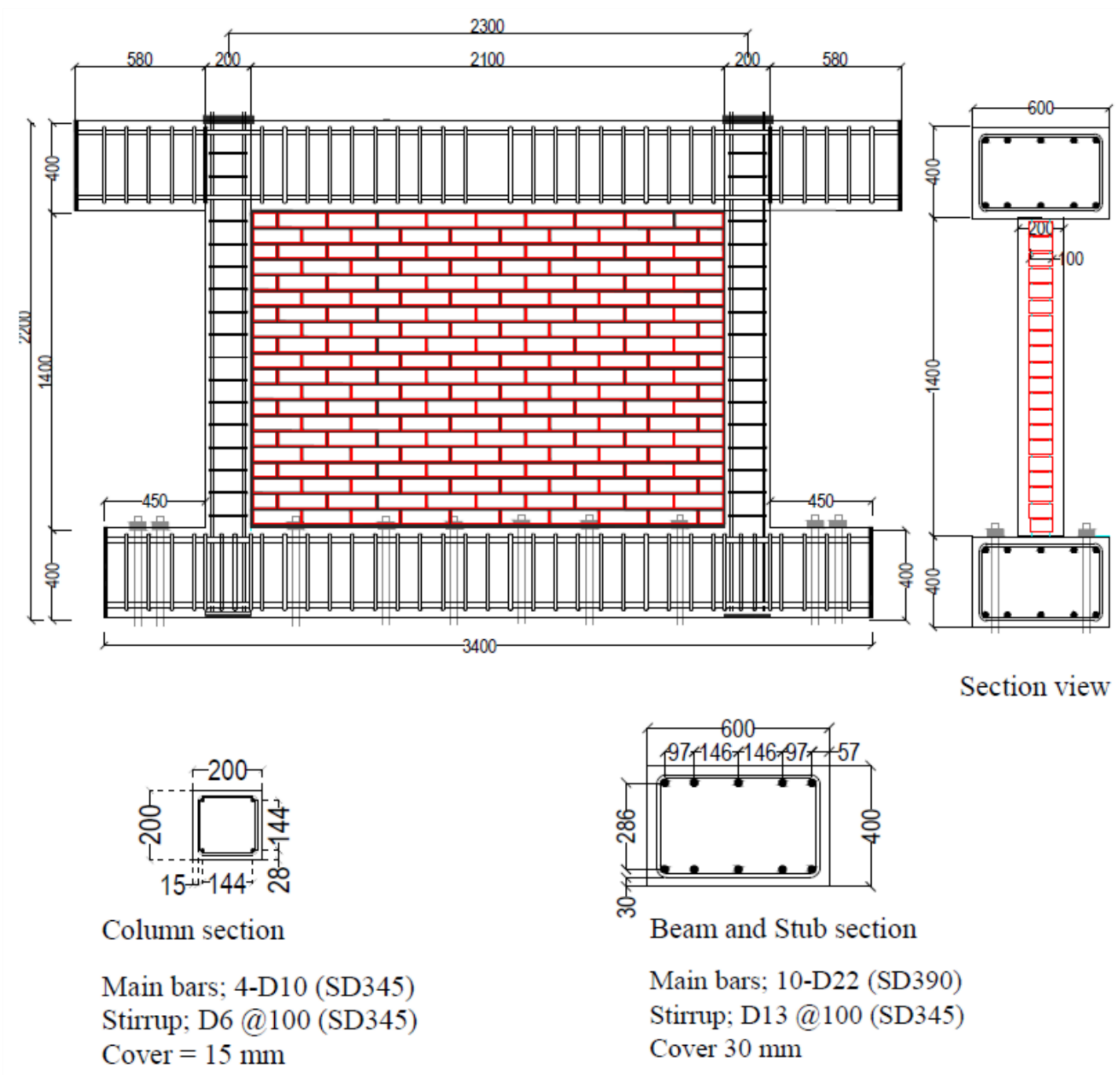

Figure A-76: Dimensions of Specimen F-0.4 tested by Alwashali (2018)

Note: Figure is taken from Alwashali (2018) and dimensions are in mm.

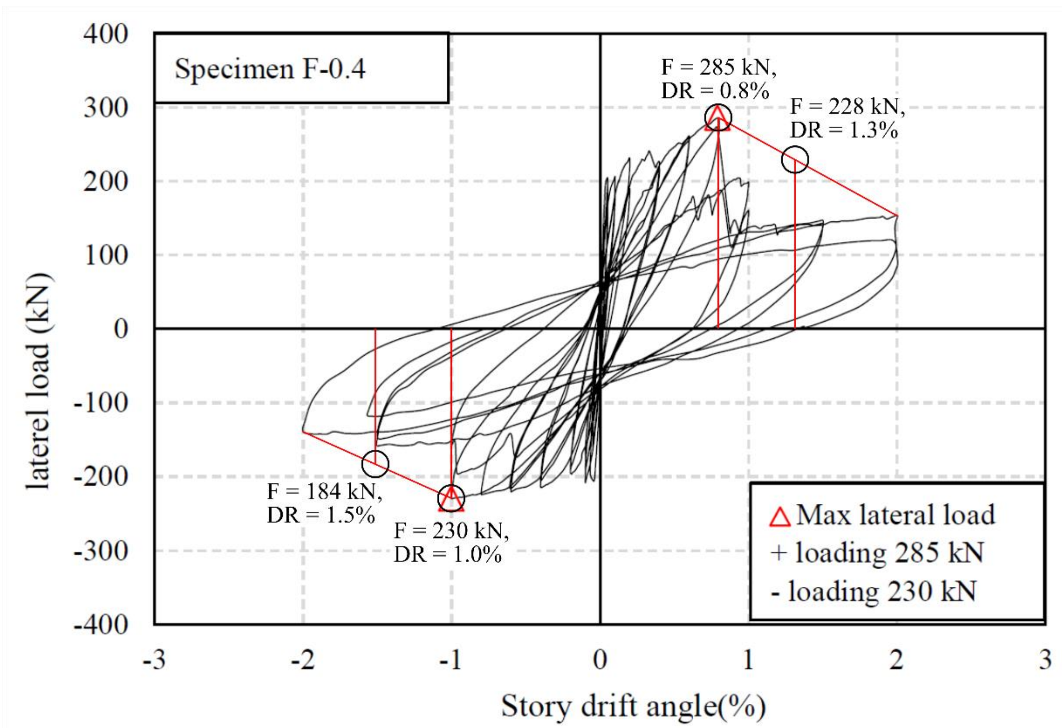

Figure A-77: Force-displacement relationship of Specimen F-0.4 tested by Alwashali (2018)

Note: Figure is taken from Alwashali (2018) and drift capacity of Specimen F-0.4 is 1.4%.

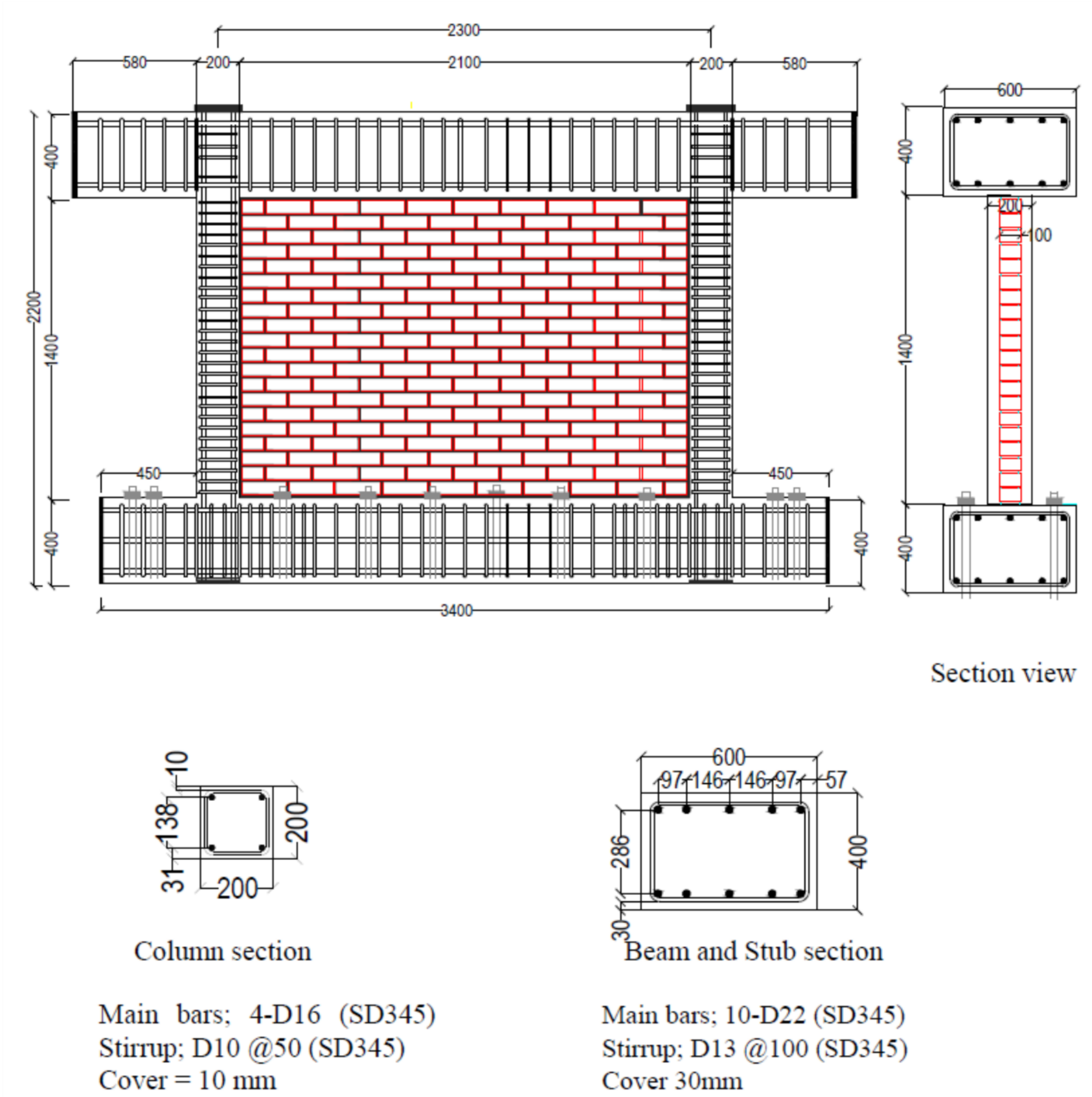

Figure A-78: Dimensions of Specimens F-0.6 and WM tested by Alwashali (2018)

Note: Figure is taken from Alwashali (2018) and dimensions are in mm.

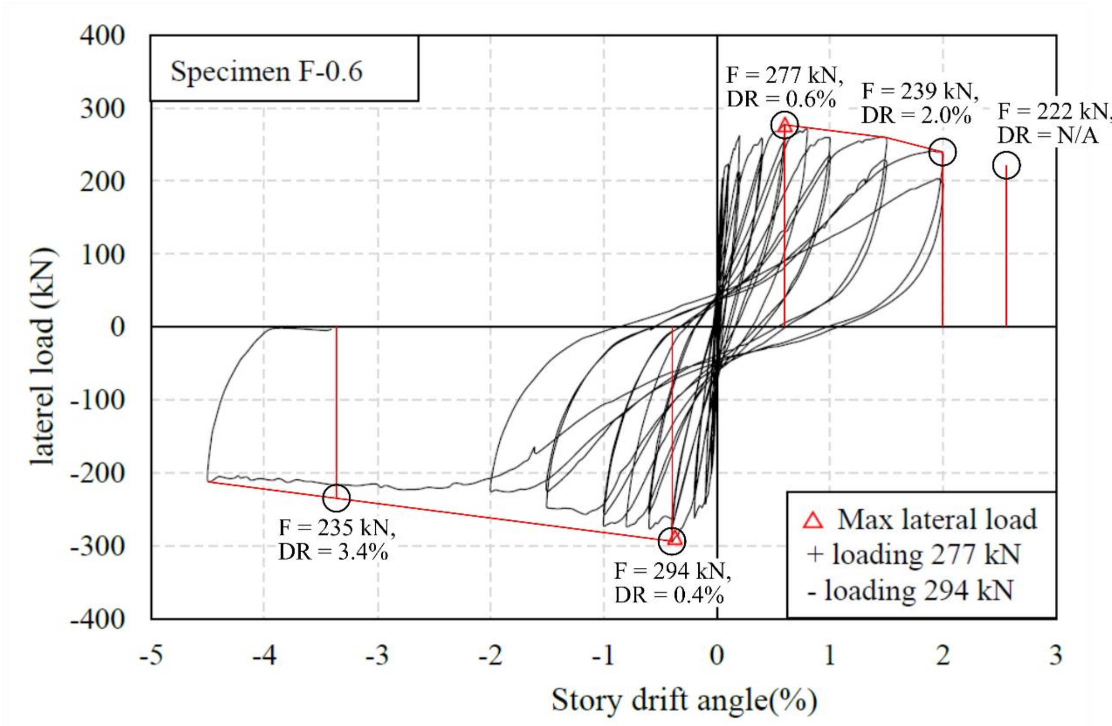

Figure A-79: Force-displacement relationship of Specimen F-0.6 tested by Alwashali (2018)

Note: Figure is taken from Alwashali (2018) and drift capacity of Specimen F-0.6 is 2.7%.

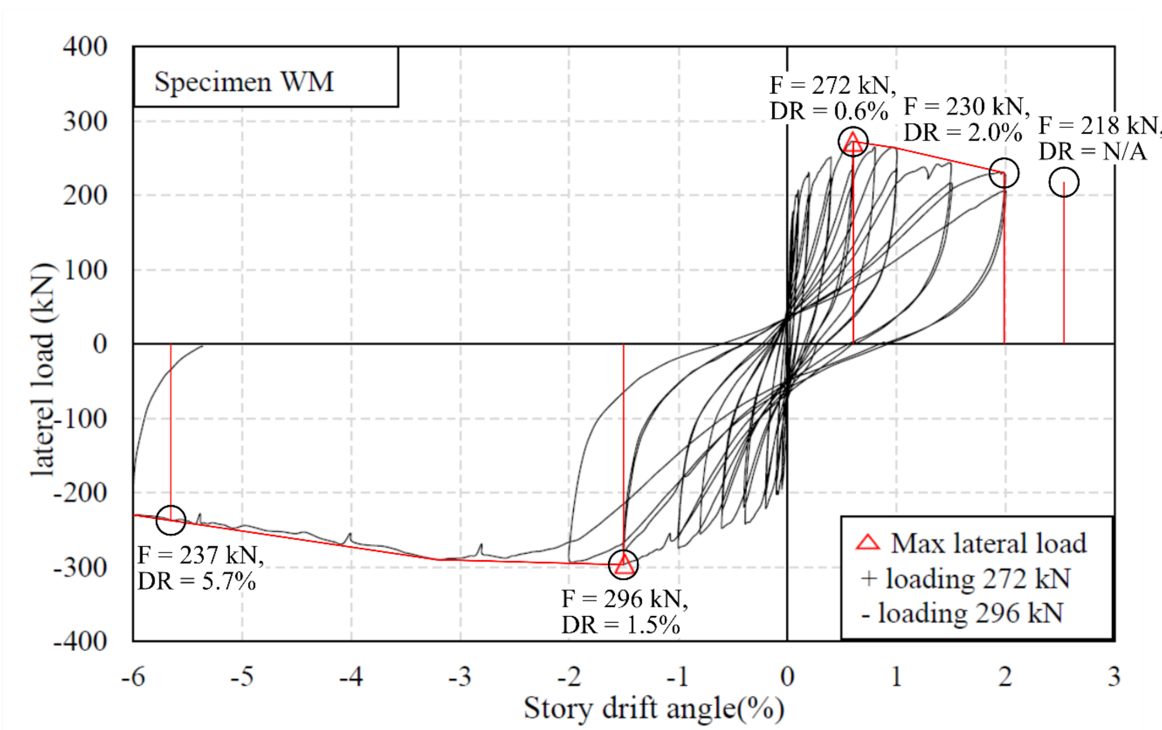

Figure A-80: Force-displacement relationship of Specimen WM tested by Alwashali (2018)

Note: Figure is taken from Alwashali (2018) and drift capacity of Specimen WM is 3.8%.

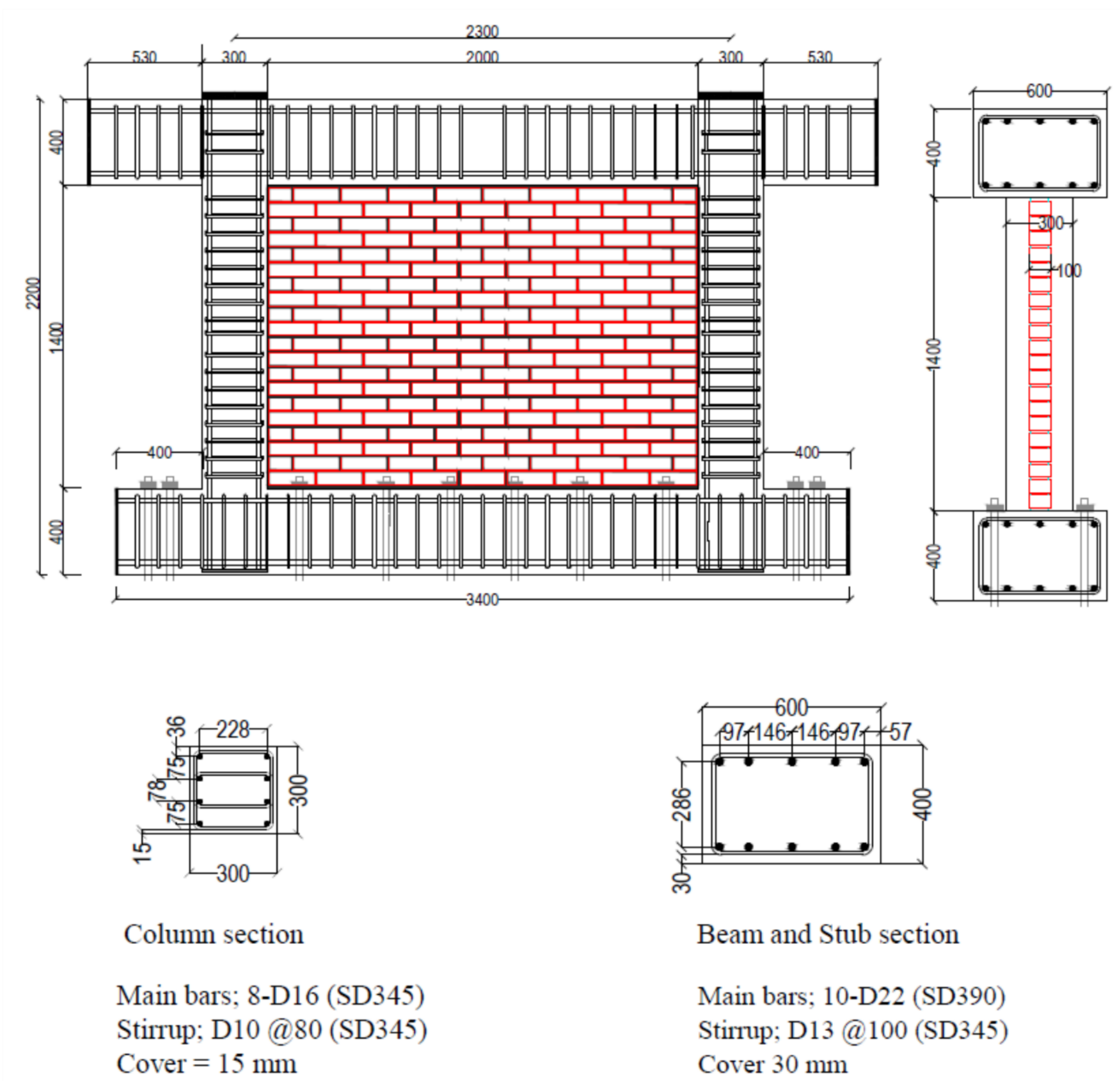

Figure A-81: Dimensions of Specimen F-1.5 tested by Alwashali (2018)

Note: Figure is taken from Alwashali (2018) and dimensions are in mm.

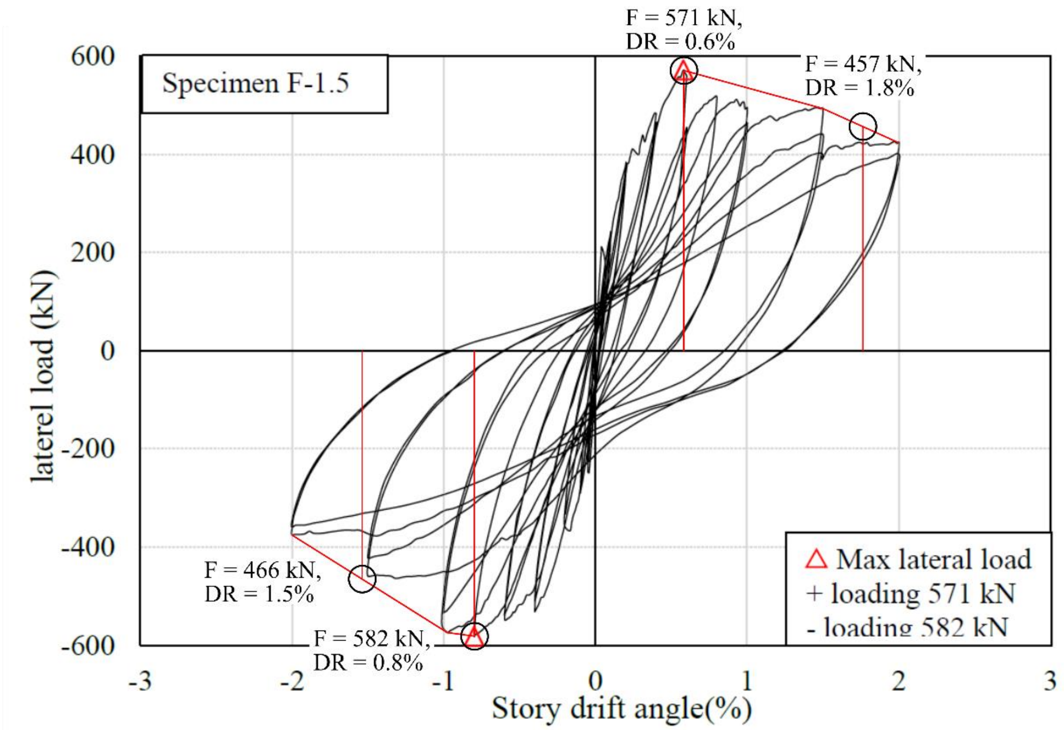

Figure A-82: Force-displacement relationship of Specimen F-1.5 tested by Alwashali (2018)

Note: Figure is taken from Alwashali (2018) and drift capacity of Specimen F-1.5 is 1.7%.

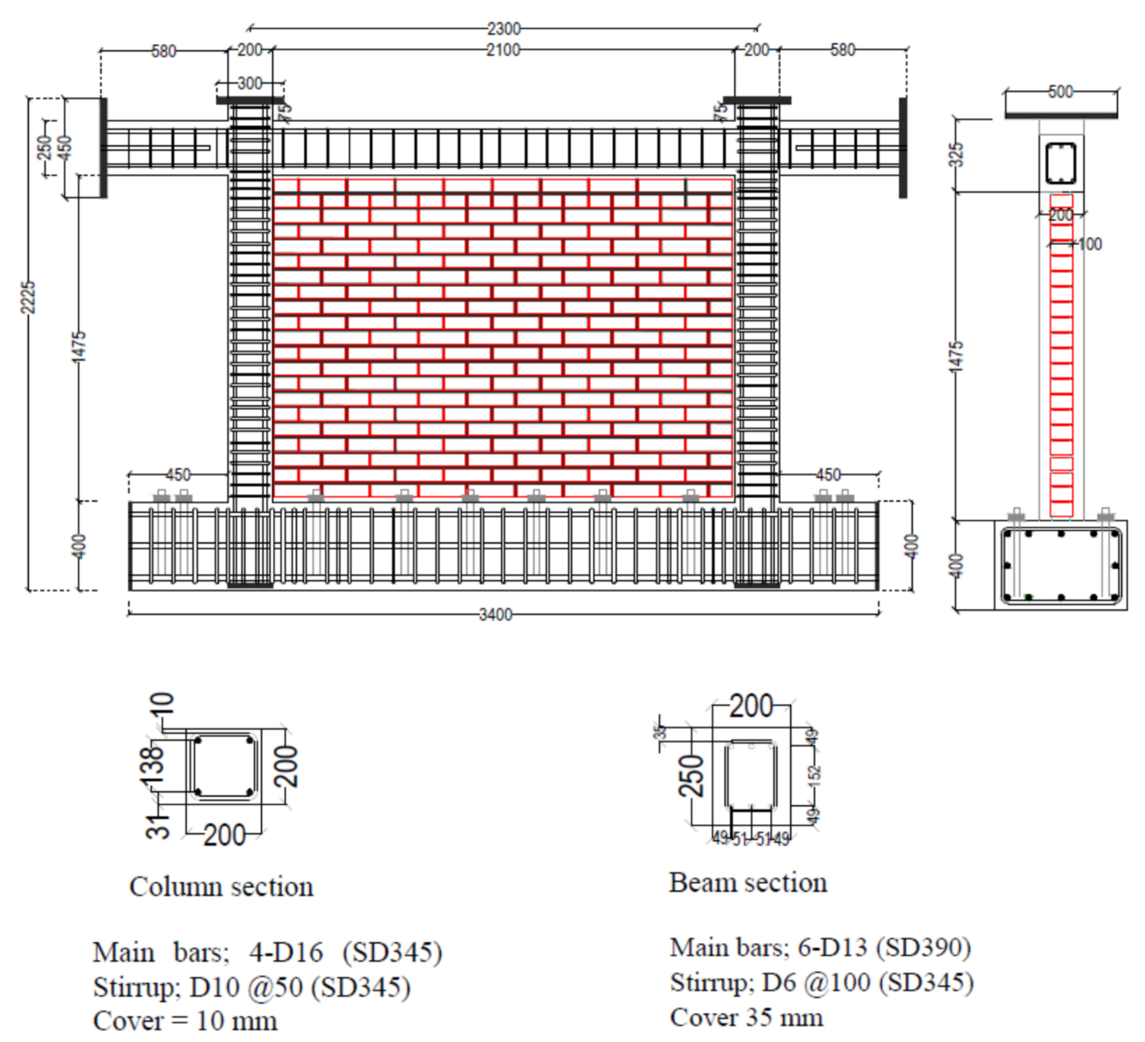

Figure A-83: Dimensions of Specimen WB tested by Alwashali (2018)

Note: Figure is taken from Alwashali (2018) and dimensions are in mm.

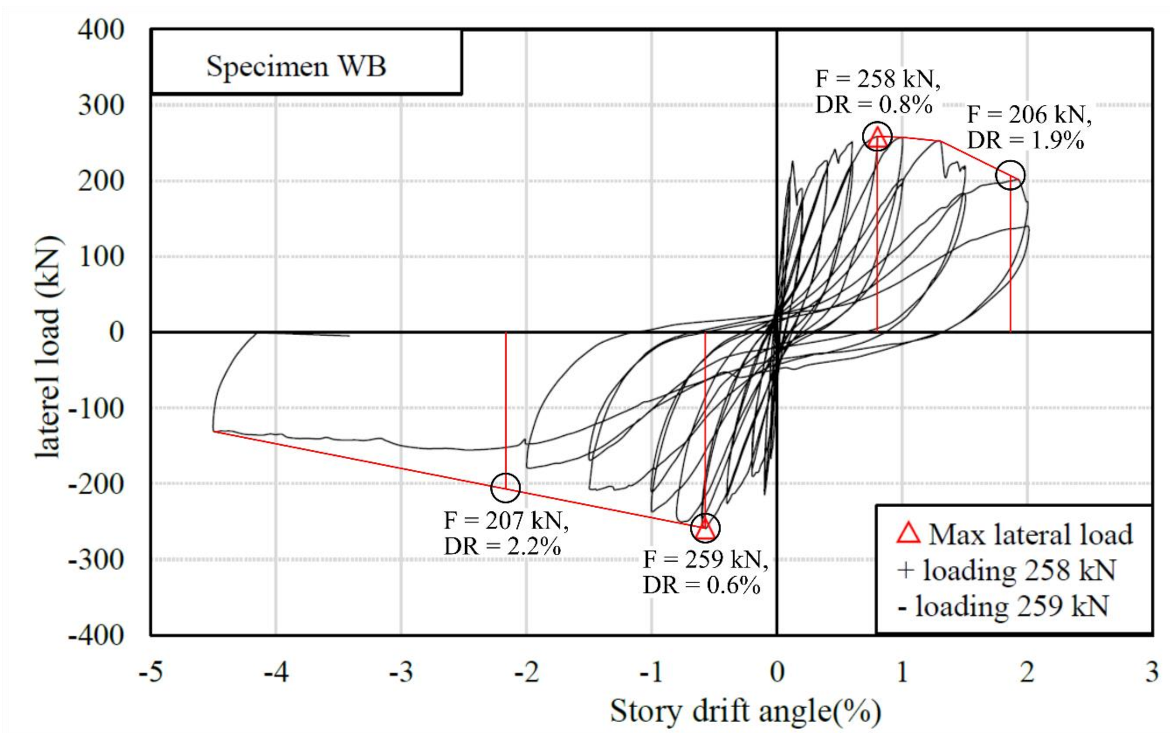

Figure A-84: Force-displacement relationship of Specimen WB tested by Alwashali (2018)

Note: Figure is taken from Alwashali (2018) and drift capacity of Specimen WB is 2.0%.

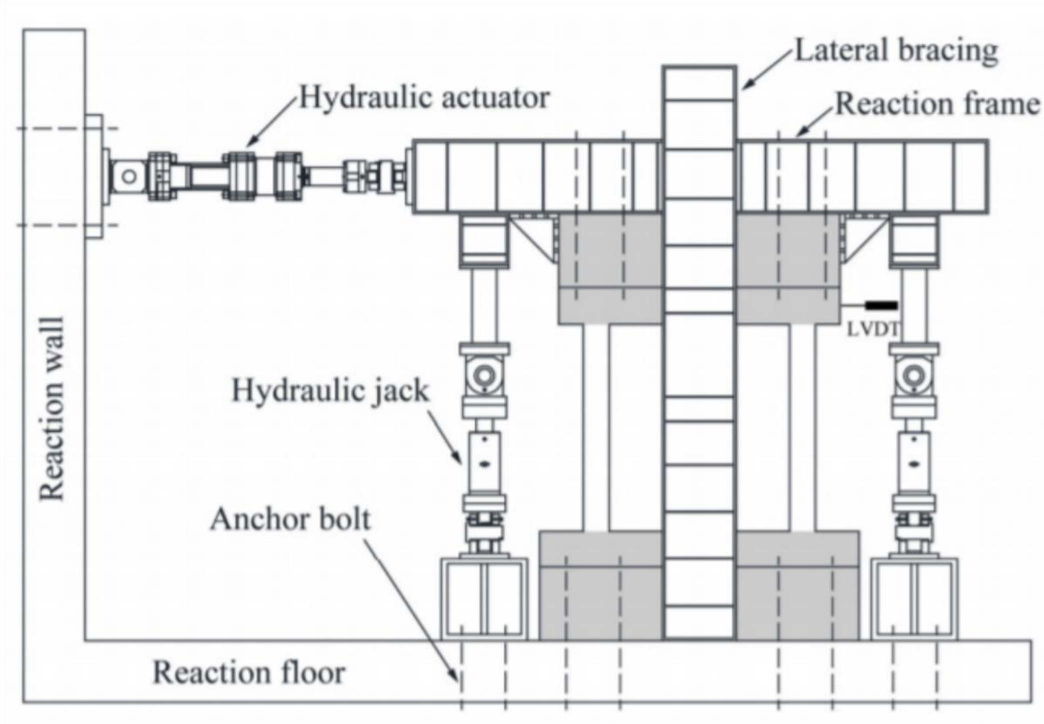

Figure A-85: Test setup of bare and infilled frames tested by Han (2020)

Note: Figure is taken from Han (2020).

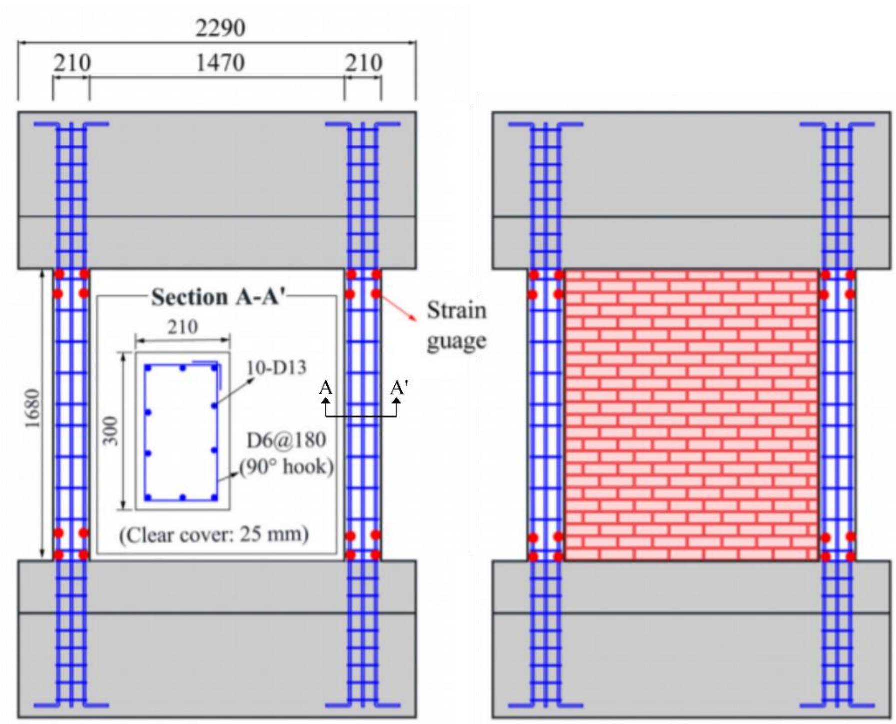

Figure A-86: Dimensions of bare and infilled frames tested by Han (2020)

Note: Figure is taken from Han (2020) and dimensions are in mm.

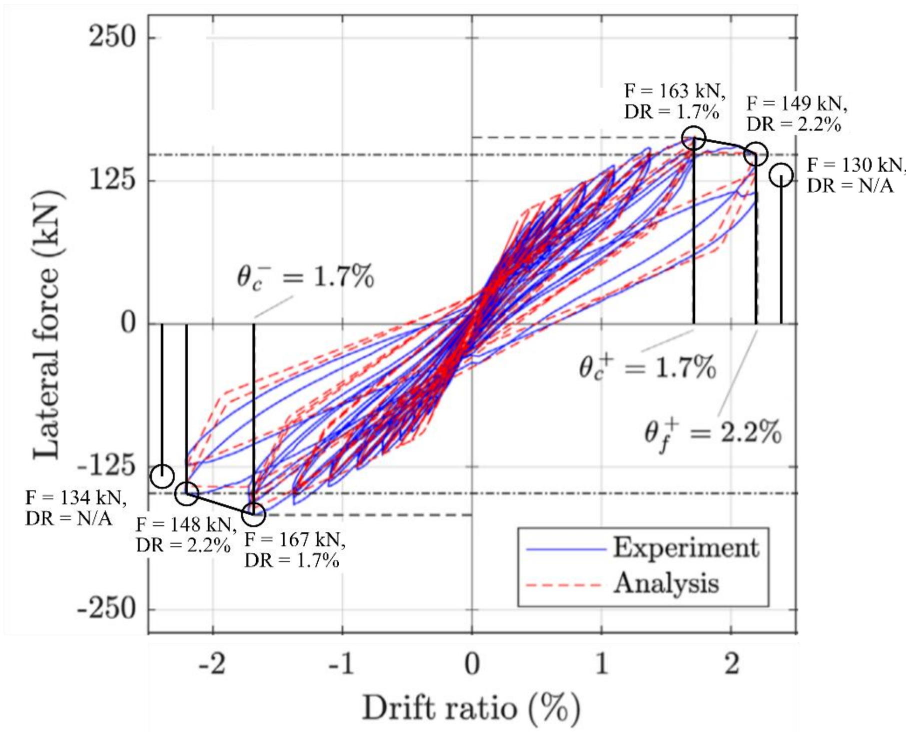

Figure A-87: Force-displacement relationship of Specimen S-NO tested by Han (2020)

Note: Figure is taken from Han (2020) and drift capacity of Specimen S-NO is 2.2%.

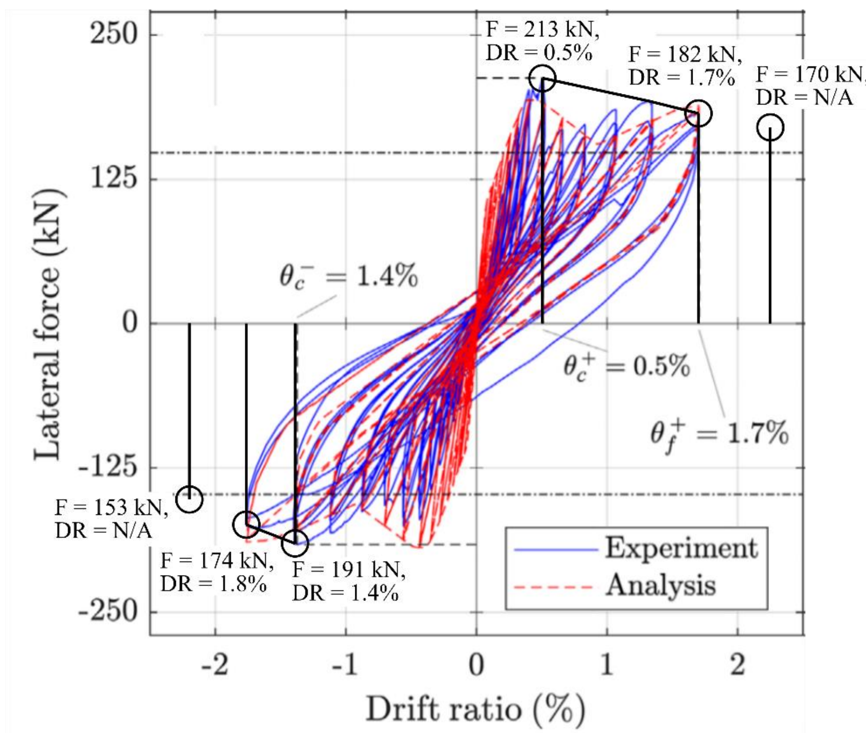

Figure A-88: Force-displacement relationship of Specimen S-Full tested by Han (2020)

Note: Figure is taken from Han (2020) and drift capacity of Specimen S-Full is 1.7%.

APPENDIX B. DESCRIPTION OF EXPERIMENTAL WORK

Photographs, diagrams, and figures of experimental work are available at https://datacenterhub.org /deedsdv/publications/view/208 (DOI: 10.7277/W61K-FB26).

B.1 Test Specimens

Reinforcement cages of specimens were constructed using steel spacers, reinforcing bars, and tie wire (Figure B-1). All transverse and longitudinal reinforcement consisted of deformed bars except for the smooth helical reinforcement used to provide extra confinement in joints. PVC pipes were positioned in top and foundation beams to create voids to allow threaded rods to pass through to clamp hardware to sides of specimens (Figure B-1). After clamping the first specimen to the simulator platform, it was decided to not clamp any hardware in the transverse (out-of-plane) direction of the foundation beam, but threaded rods were passed through holes in the vertical direction of the foundation beam to clamp specimen to simulator platform.

Both test frames were cast on their sides on the same day (Figure B-2). Frames were covered with wet burlap cloth and plastic sheeting for two weeks. Plastic sheeting was removed temporarily to dampen burlap daily (Figure B-3). After two weeks of curing, compression tests of the accompanying test cylinders suggested the concrete strength was approximately 2400 psi. It was decided to remove all burlap cloth, plastic sheeting, and wooden formwork. After two additional weeks without wet burlap and plastic sheeting, specimens were lifted from their sides by tilting them upward with an overhead crane and were stored near the earthquake simulator until they were tested (Figure B-4). PVC pipes were removed from holes prior to testing. Measured dimensions of column cross sections of test specimens are listed in Table B-1 and a diagram showing the locations where measurements were obtained is illustrated in Figure B-5.

B.2 Materials

B.2.1 Concrete

The mix design of the concrete used for both specimens was selected to have a 28-day concrete compressive strength of 3000 psi. The progression of concrete strength as measured from standard

6x12-in. test cylinders is listed in Table B-2. Measured properties of concrete on the first days of simulation tests of Specimens F1 and F2 are listed in Table B-3. The coarse aggregate used was pea gravel with a maximum aggregate size of 3/8 in. The water-cement ratio accounting for additional water in the aggregate was approximately 0.56. Additional details of the concrete mix design are listed in Table B-4.

B.2.2 Reinforcing Steel

Longitudinal reinforcement in columns consisted of four 5/8-in. deformed bars which where anchored 17.5 in. into joints and an additional 14.5 in. into top and foundation beams (Figure B-6). Column ties consisting of 3/8-in. deformed hoops with 90-degree hooks were spaced at 6 in. along clear heights of columns.

Tensile reinforcement in beams consisted of four 1-in. deformed bars resulting in a longitudinal reinforcement ratio in beams of 2.2% (Figure B-7). Helical steel reinforcement consisting of 1/4-in. smooth steel wire was used to confine concrete and column longitudinal reinforcement in joints (Figure B-8). Additional reinforcement details are shown in Figure B-6.

B.2.3 Masonry

Masonry infill walls were built using clay bricks and bags of pre-blended mortar mix. Clay bricks were modular bricks with a void ratio of 25% (Figure B-9). The mortar mix used was All-Star Mortar Mix (No. 1122-60) manufactured by Quikrete International, Inc in accordance with ASTM Standard C270 for Type N mortar (Figure B-10). Manufacturer mix proportions of the mortar mix are shown in Table B-5. Multiple batches of mortar were made in the construction of the infill walls of Specimens F1 and F2 as shown in the order illustrated in Figure B-11 and Figure B-12. The typical water-to-cement ratio of mortar was approximately 0.60. Details of mortar mix proportions of infill walls are shown in Table B-6 and Table B-7. Once infill walls were built, water was sprayed daily on brick and mortar surfaces on both sides of walls and then covered with plastic tarps for one week. Mean compressive strengths of mortar used to build walls of Specimens F1 and F2 measured from compression tests of 4-in. by 8-in. mortar cylinders conducted on the first test day of Series F1-M-C and F2-M were 1600 psi and 1800 psi. The progression of mortar strength as measured from 4-in. by 8-in. mortar cylinders is listed in Table B-8 and Table B-9.

A series of tests were devised using brick and mortar composite coupons to estimate material properties of masonry. Four and five-brick prisms with aspect ratios of 2.8 and 3.5 (computed as ratios of prism height to prism width) were constructed with steel loading plates on top and bottom of prism and subjected to compression loading perpendicular to mortar bed joints (Figure B-13). The mean compressive strength of prisms based on gross cross-sectional area of prisms (7 5/8 in. by 3 5/8 in.) was f'_m = 2800 psi and deviations in strengths between four and five-brick prisms were less than 15%. A summary of tests conducted on four and five-brick masonry prisms and the associated 4-in. by 8-in. mortar cylinders is given in Table B-10.

To obtain an estimate of the modulus of elasticity of masonry, Optotrak targets were attached near the four corners of masonry prisms on larger faces of coupons [Figure B-13 (a)]. In 10-kip loading intervals, the vertical and horizontal distances between all four targets were measured along 7.5 and 10.5-in. long gage lengths for four and five-brick prisms. Figure B-14 (a) shows relationships between unit stress estimated for the gross cross-sectional area of bricks and unit strain obtained from computing the means of shortenings measured along vertical edges of the coupon. The mean modulus of elasticity of masonry prisms was E_m = 1400 ksi estimated as the slope of the secant to the described stress-strain curve at a stress of approximately 1200 psi (approximately 40% of f'_m). Measurements of the elastic modulus of masonry obtained from four and five-brick masonry prisms are summarized in column 10 of Table B-10.

Diagonal compression coupons were loaded in compression at an angle of 45 degrees to mortar bed and head joints (Figure B-15 and Figure B-16). For these coupons, shear strength was estimated as the peak applied load divided by the product of length of diagonal and thickness of coupons (17 3/4 in. by 3 5/8 in.). The mean shear strength of diagonal coupons was approximately 110 psi. Shear triplet coupons were loaded in compression in the direction of mortar bed joints (Figure B-17). For these coupons, shear strength was estimated as the peak applied load divided by the resisting area of mortar (2 surfaces of 5 in. by 3 5/8 in.). The mean shear strength of triplet coupons was approximately 70 psi. The ratio of shear strength to compression strength of masonry coupons was approximately half the value suggested by the shear strength of masonry infill walls estimated using Equation 2. Differences between measurements obtained for shear strengths of the masonry coupons tested in this investigation and those reported by Alwashali (2018) may be a result of difficulty in loading coupons concentrically without eccentricities. Summaries of the results of diagonal compression and shear triplet coupon tests are given in Table B-11.

B.3 Earthquake Simulator

The earthquake motions used in this investigation were simulated using the unidirectional earthquake simulator currently housed at Bowen Laboratory for Large-Scale Civil Engineering Research at Purdue University (Figure B-18). A dynamic hydraulic actuator with a rated capacity of 75 kips mounted to a steel reaction block drove the earthquake simulator in displacement control procedures operated by an MTS FlexTest 60 digital controller. The earthquake simulator moved the base of the test specimen in the direction parallel to the longitudinal axis of the frame for in-plane tests. For out-of-plane tests the simulator moved the base of the test specimen in the direction perpendicular to the longitudinal axis of the frame. Details of the simulator are provided in Sozen (1969) and Gulkan (1971).

B.4 Test Setup

An isometric view of the test setup is shown in Figure B-19. The test setup sequence is described next. The procedure detailing the connection of the specimen to the suspended mass via the two-swivel stiff link is described next (Figure B-20).

B.4.1 Connection of Specimen to Suspended Mass

B.4.1.1 Connection of Load Cell to Specimen

Steel plates were clamped to north and south ends of load cell using two standard nut style mechanical tensioners (manufactured by Superbolt, Inc, S/N 2000190559, Model No. MT-200-12/W) threaded onto 2-in. steel studs threaded into voids in load cell (Figure B-21). The mentioned tensioning devices were tightened to a clamping force of approximately 100 kips each (Figure B-22). Bearing plates on the north end of the load cell butted against channels confining the top beam and angles bolted to said channels. Eight 7-in. long 3/4-in. ASTM A325 bolts clamped the bearing plates to angles and were pre-tensioned to approximately 160 kips. Five 7/8-in. ASTM A490 bolts connecting angles to channels were pre-tensioned to approximately 100 kips per angle designed as a slip-critical connection.

B.4.1.2 Connection of Two-Swivel Stiff Link to Suspended Mass

At the south end of the double-swivel assembly, the brackets of the south swivel were clamped to the north face of the RC block using four 1 in. high strength threaded rods tightened to approximately 50 kips per rod (Figure B-23). Rods were embedded 28 in. into the block measured from the concrete surface using high-strength epoxy adhesive (Figure B-24). The mentioned adhesive product consisted of Hilti HIT-RE 500 V3 epoxy cartridges and one 11 fl. oz. cartridge was used per rod (Figure B-25). Holes were drilled using a 36-in. long 1 1/8-in. Hilti TE-YX Imperial hammer drill bit (Figure B-26) and cleaned using a 28-in. long 1 1/8-in. Hilti wire brush (Figure B-27) in addition to blowing concrete dust and debris out of holes with pressurized air.

B.4.1.3 Connection of Load Cell to Two-Swivel Stiff Link

The final step in the setup of the frame-mass system was the connection of the load cell to the north end of the two-swivel link. A walkie-stacker forklift was used to raise the two-swivel link until it was horizontal and level with the top beam of the frame (Figure B-28). Then 1-in. thick steel plates were sandwiched between the 2-in. steel plate clamped to the south end of the load cell and the brackets of the north swivel. Three plates were required per bracket to provide sufficient space to accommodate the mechanical tensioner. Four 1-in. high-strength threaded rods passed through holes in the “spacer” plates and were tightened to a total clamping force of approximately 180 kips effectively creating a ‘rigid’ link connecting frame to RC block. The RC block was suspended in mid-air using lifting straps looped through the crane hook of the overhead crane while connecting load cell to two-swivel link to reduce the effects of accidental loading of test specimens.

B.4.2 Suspended Mass

A 14 ft. by 4 ft. by 5 ft. reinforced concrete block serving as the foundation of an RC wall specimen tested by Pollalis (2021) was used to provide additional mass to system (Figure B-29). It was suspended from an overhead crane (designed and installed by Dearborn Crane & Engineering Co., S/N 35001-2) using two 20-ft. long straps with flat tubing widths of 4 in. made with K-Spec core yarn consisting of a blend of high-performance fibers.

B.4.3 Out-of-plane Bracing

Four HSS8x4x1/4 steel tubes were used to reduce out-of-plane displacement of the mentioned block (Figure B-30). Each hollow steel tube was clamped to an RC base block using eight 5/8-in. threaded rods that were embedded 1 ft. into the concrete (Figure B-31). The base block was post-tensioned to the floor with a total clamping force of 130 kips (Figure B-32). Adjustable bolts bearing on the bottom of the base block and steel plates clamped to the floor prevented the block from rotating out-of-plane (Figure B-33). Hydraulic jacks were placed on top of support blocks and below the suspended mass to minimize movement of the mass as the crane hook was lowered daily at the end of laboratory operational hours and to reduce the likelihood of any accidental loading to the test frames (Figure B-34). The entire weight of the RC block was resisted by the hydraulic jacks when no simulations were being conducted.

Descriptions of individual test setup components are provided next.

B.4.4 Fabrication of Hardware

B.4.4.1 Splice of Top Channels

Four 1-ft long steel plates with a 2 7/8 in. by 1 in. cross section were designed to splice two 30-in. long steel channels with two 9-ft long steel channels used to transfer inertial forces from the suspended mass to the test specimen. Each steel plate was designed to resist 100 kips in shear (Figure B-35). Six 3-in. long 3/4-in. ASTM A325 steel bolts were tensioned to approximately 30 kip each, three bolts clamping one side of the splice to the shorter steel channel and three bolts clamping the other side of the splice to the longer steel section.

B.4.4.2 Top Steel Channels

Two MC18x58 ASTM A36 steel channels sandwiched the top beams of specimens (Figure B-36). Holes were drilled through webs of channels to allow threaded rods to pass through.

B.4.4.3 Clamping W-sections

Two wide-flange W18x65 steel beams flanking foundation beams of test specimens oriented in the direction of motion were used to provide additional restraint of simulator platform and additional stiffness to connections between foundation and clamping hardware (Figure B-37). Holes were drilled through top and bottom flanges to allow threaded rods to pass through to clamp frames to the platform of the earthquake simulator.

B.4.4.4 Slip Channels (Perpendicular to Direction of Motion)

Two MC18x58 ASTM A36 steel channels oriented perpendicular to the direction of motion were attached to north and south ends of simulator platform to strengthen test platform and prevent foundation beams of specimens from slipping (Figure B-38).

B.4.4.5 Swivels

The two-swivel link allowing excessive play is shown in Figure B-39. The stiff two-swivel link reducing play is shown in Figure B-40. The stiffer double-swivel assembly consisted of two 995 HT Shore Western hydraulic actuator base end swivels that were tightened to each other (Figure B-41).

B.5 Weights

The weights of each component used in earthquake simulations of test specimens were measured using two types of scales. Weights of components weighing less than 200 pounds were measured using an Ohaus Champ SQ bench scale (Model No. CQ100-L31) with a rated capacity of 250 lb. and a resolution of 0.02 lb. Weights of heavier steel hardware, RC frames, and the RC block used to provide additional mass to system were measured using an MSI Porta-Weigh Plus crane scale (Model No. 4300) with a rated capacity of 70 kips and a resolution of 20 lb. Objects weighing more than 200 pounds were lifted using straps looped through the digital crane scale attached to the crane hook of the overhead crane and the weight of the objects were recorded.

B.6 Instrumentation

An instrumentation layout is shown in Figure 2-24.

B.6.1 Lateral Displacements

Measurements of displacements of simulator, specimens, and mass were obtained using one LVDT mounted inside the servoram, three LVDTs mounted to a steel column post-tensioned to the strong floor, OptiTrack, and Optotrak systems. The 4-in. full-stroke LVDT mounted inside the servoram measured the position of the hydraulic actuator driving the simulator platform. Ends of rods threaded into cores housed in LVDTs mounted to steel column were bolted to angle brackets glued with epoxy to concrete surfaces of specimens. Two LVDTs measured absolute displacements at top and soffit of top beam and one LVDT measured the absolute displacement at top of foundation (bottom beam). Maximum errors of displacements measured during calibration of LVDTs were not larger than 0.01 in. (drift ratio of 0.02%) for LVDT at foundation (stroke was ± 2 in.) and not larger than 0.02 in. (drift ratio of 0.04%) for LVDTs at top beam (strokes were ± 3 in. and ± 5 in. at bottom and top of top beam).

Layouts of 127 OptiTrack targets used in runs of Specimen F1 are shown in Figure 2-27 and layouts of 88 OptiTrack targets used in runs of Specimen F2 are shown in Figure 2-29. Maximum errors of displacements measured during calibration of OptiTrack system was approximately 0.02 in. Layouts of 44 Optotrak targets used in runs of Specimen F2 are shown in Figure 2-31. Maximum errors of displacements measured during calibration of Optotrak system were approximately 0.002 in.

B.6.2 Lateral Forces

A load cell with a rated capacity of 100 kips was used to measure lateral forces. A calibration of the load cell was conducted by loading the instrument in 10-kip increments to its rated capacity followed by unloading in 10-kip increments back to zero load. The maximum error was not larger than 1 kip and the load cell measured no load at the end of the calibration procedure.

B.6.3 Accelerometers

Accelerometers were mounted on specimens and suspended mass to measure base motions. Two types of accelerometers were used in this investigation (triaxial ADXL and uniaxial PCB accelerometers). ADXL accelerometers manufactured by Analog Devices (model number 335) with frequency ranges of 0.5-1600 Hz for horizontal axes (north-south, east-west) and 0.5-550 Hz for vertical axis (up-down). PCB accelerometers manufactured by PCB Piezotronics (model number 333B52) with a frequency range of 0.5-3000 Hz (Figure 2-38). Two PCB accelerometers were attached to top of top beam and two PCB accelerometers were attached to top of foundation beam. Before tests were conducted on Specimen F1, two ADXL accelerometers were attached to top surfaces of top beam and one ADXL accelerometer was attached to top of northeast corner of foundation beam. A second ADXL accelerometer was added to top of southwest corner of foundation beam during Series F1-M-C and remained there during the remaining tests of Specimen F1 (Figure 2-39). Two ADXL accelerometers were attached to top of foundation and two ADXL accelerometers were attached to top surfaces of top beam prior to testing of Specimen F2. The suspended mass was instrumented with four PCB accelerometers: two accelerometers measured in-plane motion and two accelerometers measured vertical motion of mass (Figure 2-40).

B.6.4 Data Acquisition System

Details of the data acquisition systems used in this investigation are included in Table B-12 through Table B-23. Acceleration, displacement, force, and strain data measured during simulated earthquakes was recorded using a data acquisition system consisting of National Instruments SCXI-1000 chassis and a National Instruments SCB-68 connector block. The mentioned data acquisition system was formatted and operated using National Instruments LabVIEW software. Data was sampled continuously at 1000 Hz and stored into TDMS files.

In addition to the National Instruments data acquisition system, two optical data acquisition systems were used to measure and record the displacement of the simulator platform, test specimens, two-swivel link, and suspended block. A NaturalPoint Inc. OptiTrack optical tracking system measured three-dimensional displacement coordinates of circular targets cut from reflective tape attached to test setup components. The mentioned system consisted of four Prime 41 cameras which interfaced with OptiTrack's Motive software via ethernet switch. Data was sampled continuously at 100 Hz and stored into CSV files. A Northern Digital Inc. Optotrak Pro 600 optical tracking system measured three-dimensional displacement coordinates of infrared targets attached to test setup components. The mentioned system consisted of three laser tracker devices connected to Optotrak's system controller using a USB interface. Data was sampled continuously at 100 Hz and stored in TAK files.

B.6.5 Data Processing

Raw voltage data recorded using the National Instrument data acquisition system was transformed into the appropriate engineering units using the sensitivities listed in Table B-13, Table B-16, Table B-19, and Table B-22. Records were zeroed by subtracting mean values of the first 1000 data points (first one-second duration of record). The processing of data recorded using the optical data acquisition systems is described in detail in Shah (2021). Data obtained from each simulation was processed consistently using custom MATLAB (2020) scripts available at https://datacenterhub.org/deedsdv/publications/view/208 (DOI: 10.7277/W61K-FB26).

B.7 Test Schedule

The test schedule of both specimens is described in Table B-24.

Table B-1: Measured column cross section dimensions

Specimen	Section	In-plane dimension, in.		Out-of-plane dimension, in.	
		North column (N)	South column (S)	North column (N)	South column (S)
F1	1	7 15/16	7 7/8	8 1/16	8
	2	8	8	8 1/16	8 1/16
	3	8 1/16	8 1/16	8 1/16	8 1/8
	4	8 1/16	8 1/16	8 1/16	8 1/8
	5	8 1/16	8	8 1/16	8 1/8
	6	8	7 7/8	8	8 1/16
F2	1	7 7/8	8 1/16	8 1/8	8
	2	7 15/16	8 1/8	8 1/8	8 1/16
	3	8	8 3/16	8 1/8	8 3/16
	4	8	8 5/32	8 1/8	8 1/8
	5	8 1/16	8 1/8	8 1/8	8 1/8
	6	8 1/8	8	8 1/16	8 1/8

Table B-2: Compressive strength of standard 6x12-in. concrete test cylinders through 28 days after cast

Age, days	Compressive strength of test cylinders, psi		
	Each	Mean	Std. dev.
3	1600	1700	100
	1800		
	1650		
7	2000	2000	30
	2000		
	1950		
14	2400	2400	30
	2450		
	2450		
21	2800	2700	80
	2750		
	2650		
28	3200	3100	80
	3150		
	3050		

Table B-3: Measured properties of concrete on first day of simulation tests of Specimens F1 and F2

Specimen	Age, days	f'_c, psi		E_c, ksi		f_r, psi		f_t, psi	
		Each	Mean	Each	Mean	Each	Mean	Each	Mean
F1	129	3800	3800	3200	3200	500	500	450	400
		3750		3250		-		400	
		3850		3250		-		400	
F2	339	3550	3500	2950	3100	600	600	350	300
		3500		3100		600		300	
		3500		3150		-		300	

Table B-4: Concrete mix proportions

Material	Batched quantity, lb	Actual water, gal	Description	Source
Buzzi cement	1180	-	ASTM C150, Type I cement	Buzzi
Fly ash	440	-	ASTM C618, Class F fly ash	Headwaters
Pea gravel	6600	2	INDOT, 3/8-in. pea gravel	US Aggregates
#23 sand	6640	31	INDOT, natural sand	US Aggregates
Water	636	76.2	N/A	Irving Materials, Inc.
MasterGlenium 7511	29	-	Water-reducing admixture	Irving Materials, Inc.

Table B-5: Manufacturer mix proportions of mortar used to build masonry walls

Mix design	Specific gravity	Percent composition by weight
1 Part QUIKRETE® Masonry Cement T-N (#1125-70)	2.9	27%
3 Parts QUIKRETE® Mason Sand (#1952)	2.65	73%

Table B-6: Mortar mix proportions of mortar used to build masonry wall of Specimen F1

Date	Mix number	Brick layer	Mortar mix		Water, lb	Water-cement ratio
			Sand, lb	Cement, lb		
2020.01.25	1	0 (base)	91	34	18	0.53
2020.01.27	2	1-2	46	17	10	0.59
	3	3-6	89	33	20	0.61
2020.01.28	4	7-10	90	33	20	0.61
	5	11-12	45	16	10	0.63
2020.01.29	6	13	45	17	9	0.53
	7	14	43	16	10	0.63

Table B-7: Mortar mix proportions of mortar used to build masonry wall of Specimen F2

Date	Mix number	Brick layer	Mortar mix		Water, lb	Water-cement ratio
			Sand, lb	Cement, lb		
2020.08.19	1	0 (base)	44	16	11	0.69
2020.08.20	2	1-5	87	32	19	0.59
	3	6-10	88	33	19	0.58
	4	11-14	86	32	20	0.63

Table B-8: Compressive strength of mortar used to build masonry wall of Specimen F1

Mix number	Compressive strength of 4 in. by 8 in. mortar cylinders, psi		
	Age, days		
	7	28	39*
1	700	-	-
2	300	-	-
3	500	1400	1700
4	-	1500	1600
5	-	-	1500
6	-	1500	1700
7	-	-	1600

*First day of simulation tests of Series F1-M-C

Table B-9: Compressive strength of mortar used to build masonry wall of Specimen F2

Mix number	Compressive strength of 4 in. by 8 in. mortar cylinders, psi		
	Age, days		
	7	14	19*
1	-	-	-
2	1500	1800	1800
3	1500	1700	1800
4	1400	1600	1800

*First day of simulation tests of Series F2-M

Table B-10: Summary of 4-in. by 8-in. mortar cylinder and four and five-brick masonry prism tests

Specimen	Coupon No.	Mortar cylinder		Masonry prism					
		f_{mortar}, psi	E_{mortar}, ksi	No. bricks	Height, in.	Width, in.	Aspect ratio	f'_m, psi	E_m, ksi
F1	1	2000	-	4	10.1	3.6	2.8	1800	1000
	2	2450	-	4	10.1	3.6	2.8	3100	1400
	3	1750	-	4	10.1	3.6	2.8	2900	1000
	4	1700	-	4	10.1	3.6	2.8	3250	900
F2	1	1800	1950	4	10.1	3.6	2.8	2700	1400
	2	2600	2150	4	10.1	3.6	2.8	3250	2300
	3	1650	1850	5	12.8	3.6	3.5	2450	1100
	4	2350	2000	5	12.8	3.6	3.5	2650	1700

Table B-11: Summary of shear strengths of masonry coupon tests

Coupon	No.	Peak load, kip	Resisting area, in.^{2}	Shear strength, psi
Diagonal compression	1	7.8	64.3	120
Diagonal compression	2	6.4	64.3	100
Shear triplet	1	1.7	36.3	50
Shear triplet	2	3.0	36.3	80

Table B-12: Location of sensors used in Series F1-B and F1-C

Sensor number	Type	Location and description
0	LVDT	Below northeast side of simulator platform measuring displacement of platform
1	LVDT	Below northwest side of simulator platform measuring displacement of platform
2	LVDT	Below southwest side of simulator platform measuring displacement of platform
3	LVDT	Below southeast side of simulator platform measuring displacement of platform
4	LVDT	Soffit of top beam measuring in-plane roof displacement
5	LVDT	Top of top beam measuring in-plane roof displacement
6	LVDT	Top of foundation beam measuring in-plane base displacement
7	Strain gage*	Middle of east face of flexure link oriented 45° counterclockwise from horizontal
8	Strain gage**	Middle of east face of flexure link oriented along horizontal
9	Strain gage*	Middle of east face of flexure link oriented 45° clockwise from horizontal
10	Strain gage*	Middle of west face of flexure link oriented 45° counterclockwise from horizontal
11	Strain gage**	Middle of west face of flexure link oriented along horizontal
12	Strain gage*	Middle of west face of flexure link oriented 45° clockwise from horizontal
13	Load cell	Sandwiched between top beam and two-swivel link measuring lateral load
14	LVDT	Inside servoram measuring in-plane displacement of simulator platform (feedback signal)
15	LVDT	Inside servoram measuring in-plane displacement of simulator platform (command signal)

*Strain gage factor S_g = 2.090 and transverse sensitivity K_t = 0.8%

**Strain gage factor S_g = 2.135 and transverse sensitivity K_t = 0.4%

Table B-12 (continued): Location of sensors used in Series F1-B and F1-C

Sensor number	Type	Location and description
16	Accelerometer	Top northeast corner of top beam measuring vertical roof acceleration
17	Accelerometer	Top northeast corner of top beam measuring out-of-plane roof acceleration
18	Accelerometer	Top northeast corner of top beam measuring in-plane roof acceleration
19	Accelerometer	Top southwest corner of top beam measuring vertical roof acceleration
20	Accelerometer	Top southwest corner of top beam measuring out-of-plane roof acceleration
21	Accelerometer	Top southwest corner of top beam measuring in-plane roof acceleration
22	Accelerometer	Top northeast corner of foundation beam measuring vertical base acceleration
23	Accelerometer	Top northeast corner of foundation beam measuring in-plane base acceleration
24	Accelerometer	Top northeast corner of foundation beam measuring out-of-plane base acceleration
25	Accelerometer	Top northeast corner of foundation beam measuring in-plane base acceleration
26	Accelerometer	Top southwest corner of foundation beam measuring in-plane base acceleration
27	Accelerometer	Top northeast corner of top beam measuring in-plane roof acceleration
28	Accelerometer	Top southwest corner of top beam measuring in-plane roof acceleration
29	Accelerometer	Middle of east face of RC block measuring in-plane mass acceleration
30	Accelerometer	Bottom northwest corner of RC block on west face measuring vertical acceleration
31	Accelerometer	Top southeast corner of RC block on east face measuring vertical acceleration
32	Accelerometer	Middle of west face of RC block measuring in-plane mass acceleration

Table B-13: Summary of sensors used in Series F1-B and F1-C

Sensor number	Type	Model	Serial number	Direction	Sensitivity		Excitation, volts
					Calibration constant	Units	
0	LVDT	Schaevitz DC-E250	13292	-	39.554	V/in	±15
1	LVDT	Schaevitz DC-E250	13301	-	40.929	V/in	±15
2	LVDT	Schaevitz DC-E250	13609	-	41.910	V/in	±15
3	LVDT	Schaevitz DC-E250	12971	-	40.167	V/in	±15
4	LVDT	Schaevitz DC-E3000	1684	South	3.320	V/in	±15
5	LVDT	Schaevitz DC-E5000	1275	South	1.937	V/in	±15
6	LVDT	Schaevitz DC-E2000	2479	South	5.026	V/in	±15
7	Strain gage	CEA-06-250UR-350	1	-45°*	1.0	in./in.	2.5
8	Strain gage	CEA-06-250UR-350	2	0°*	1.0	in./in.	2.5
9	Strain gage	CEA-06-250UR-350	3	45°*	1.0	in./in.	2.5
10	Strain gage	CEA-06-250UR-350	4	-45°*	1.0	in./in.	2.5
11	Strain gage	CEA-06-250UR-350	5	0°*	1.0	in./in.	2.5
12	Strain gage	CEA-06-250UR-350	6	45°*	1.0	in./in.	2.5
13	Load cell	Lebow 3156-100K	2468	-	-0.00023941	V/kip	10
14	LVDT	-	-	South	1.812	V/in	-
15	LVDT	-	-	South	1.810	V/in	-

*Orientation relative to horizontal (positive values are in clockwise direction and negative values are counterclockwise direction)

Table B-13 (continued): Summary of sensors used in Series F1-B and F1-C

Sensor number	Type	Model	Serial number	Direction	Sensitivity		Excitation, volts
					Calibration constant	Units	
16	Accelerometer	ADXL335	1	Up	0.18	V/g	3.3
17	Accelerometer	ADXL335	1	East	0.33	V/g	3.3
18	Accelerometer	ADXL335	1	South	0.33	V/g	3.3
19	Accelerometer	ADXL335	2	Up	0.18	V/g	3.3
20	Accelerometer	ADXL335	2	East	0.33	V/g	3.3
21	Accelerometer	ADXL335	2	South	0.33	V/g	3.3
22	Accelerometer	ADXL335	3	Up	0.18	V/g	3.3
23	Accelerometer	ADXL335	3	North	0.33	V/g	3.3
24	Accelerometer	ADXL335	3	East	0.33	V/g	3.3
25	Accelerometer	PCB 333B52	34411	South	1.045	V/g	-
26	Accelerometer	PCB 333B52	34413	South	1.048	V/g	-
27	Accelerometer	PCB 333B52	34454	South	1.077	V/g	-
28	Accelerometer	PCB 333B52	34452	South	1.060	V/g	-
29	Accelerometer	PCB 333B52	34412	South	1.061	V/g	-
30	Accelerometer	PCB 333B52	34415	Up	1.051	V/g	-
31	Accelerometer	PCB 333B52	34453	Down	1.040	V/g	-
32	Accelerometer	PCB 333B52	34414	North	0.960	V/g	-

Table B-14: Summary of data acquisition system used in Series F1-B and F1-C

Sensor number	Chassis		Module		Card	
	Type	Number	Type	Number	Type	Channel number
0	SCXI-1000	1	SCXI-1520	1	SCXI-1314	0
1	SCXI-1000	1	SCXI-1520	1	SCXI-1314	1
2	SCXI-1000	1	SCXI-1520	1	SCXI-1314	2
3	SCXI-1000	1	SCXI-1520	1	SCXI-1314	3
4	SCXI-1000	1	SCXI-1520	1	SCXI-1314	4
5	SCXI-1000	1	SCXI-1520	1	SCXI-1314	5
6	SCXI-1000	1	SCXI-1520	1	SCXI-1314	6
7	SCXI-1000	1	SCXI-1521	2	SCXI-1317	0
8	SCXI-1000	1	SCXI-1521	2	SCXI-1317	1
9	SCXI-1000	1	SCXI-1521	2	SCXI-1317	2
10	SCXI-1000	1	SCXI-1521	2	SCXI-1317	3
11	SCXI-1000	1	SCXI-1521	2	SCXI-1317	4
12	SCXI-1000	1	SCXI-1521	2	SCXI-1317	5
13	SCXI-1000	1	SCXI-1121	3	SCXI-1321	3
14	SCXI-1000	1	SCXI-1121	4	SCXI-1321	0
15	SCXI-1000	1	SCXI-1121	4	SCXI-1321	1

Table B-14 (continued): Summary of data acquisition system used in Series F1-B and F1-C

Sensor number	Chassis		Module		Card	
	Type	Number	Type	Number	Type	Channel number
16	SCXI-1000	1	SCXI-1121	3	SCXI-1321	0
17	SCXI-1000	1	SCXI-1121	3	SCXI-1321	1
18	SCXI-1000	1	SCXI-1121	3	SCXI-1321	2
19	SCXI-1000	2	SCXI-1121	3	SCXI-1321	0
20	SCXI-1000	2	SCXI-1121	3	SCXI-1321	1
21	SCXI-1000	2	SCXI-1121	3	SCXI-1321	2
22	SCXI-1000	2	SCXI-1121	4	SCXI-1321	0
23	SCXI-1000	2	SCXI-1121	4	SCXI-1321	1
24	SCXI-1000	2	SCXI-1121	4	SCXI-1321	2
25	SCB68	-	-	-	-	0
26	SCB68	-	-	-	-	1
27	SCB68	-	-	-	-	2
28	SCB68	-	-	-	-	3
29	SCB68	-	-	-	-	4
30	SCB68	-	-	-	-	5
31	SCB68	-	-	-	-	6
32	SCB68	-	-	-	-	7

Table B-15: Location of sensors used in Series F1-M-C

Sensor number	Type	Location and description
0	LVDT	Below northeast side of simulator platform measuring displacement of platform
1	LVDT	Below northwest side of simulator platform measuring displacement of platform
2	LVDT	Below southwest side of simulator platform measuring displacement of platform
3	LVDT	Below southeast side of simulator platform measuring displacement of platform
4	LVDT	Soffit of top beam measuring in-plane roof displacement
5	LVDT	Top of top beam measuring in-plane roof displacement
6	LVDT	Top of foundation beam measuring in-plane base displacement
7	Strain gage*	Middle of east face of flexure link oriented 45° counterclockwise from horizontal
8	Strain gage**	Middle of east face of flexure link oriented along horizontal
9	Strain gage*	Middle of east face of flexure link oriented 45° clockwise from horizontal
10	Strain gage*	Middle of west face of flexure link oriented 45° counterclockwise from horizontal
11	Strain gage**	Middle of west face of flexure link oriented along horizontal
12	Strain gage*	Middle of west face of flexure link oriented 45° clockwise from horizontal
13	Accelerometer	Top northeast corner of top beam measuring vertical roof acceleration
14	Accelerometer	Top northeast corner of top beam measuring out-of-plane roof acceleration
15	Accelerometer	Top northeast corner of top beam measuring in-plane roof acceleration

*Strain gage factor S_g = 2.090 and transverse sensitivity K_t = 0.8%

**Strain gage factor S_g = 2.135 and transverse sensitivity K_t = 0.4%

Table B-15 (continued): Location of sensors used in Series F1-M-C

Sensor number	Type	Location and description
16	Load cell	Sandwiched between top beam and two-swivel link measuring lateral load
17	LVDT	Inside servoram measuring in-plane displacement of simulator platform (feedback signal)
18	LVDT	Inside servoram measuring in-plane displacement of simulator platform (command signal)
19	Accelerometer	Top southwest corner of top beam measuring vertical roof acceleration
20	Accelerometer	Top southwest corner of top beam measuring out-of-plane roof acceleration
21	Accelerometer	Top southwest corner of top beam measuring in-plane roof acceleration
22	Accelerometer	Top northeast corner of foundation beam measuring vertical base acceleration
23	Accelerometer	Top northeast corner of foundation beam measuring in-plane base acceleration
24	Accelerometer	Top northeast corner of foundation beam measuring out-of-plane base acceleration
25***	Accelerometer	Top southwest corner of foundation beam measuring vertical base acceleration
26***	Accelerometer	Top southwest corner of foundation beam measuring out-of-plane base acceleration
27***	Accelerometer	Top southwest corner of foundation beam measuring in-plane base acceleration
28	Accelerometer	Top northeast corner of foundation beam measuring in-plane base acceleration
29	Accelerometer	Top southwest corner of foundation beam measuring in-plane base acceleration
30	Accelerometer	Top northeast corner of top beam measuring in-plane roof acceleration
31	Accelerometer	Top southwest corner of top beam measuring in-plane roof acceleration
32	Accelerometer	Middle of east face of RC block measuring in-plane mass acceleration
33	Accelerometer	Bottom northwest corner of RC block on west face measuring vertical acceleration
34	Accelerometer	Top southeast corner of RC block on east face measuring vertical acceleration
35	Accelerometer	Middle of west face of RC block measuring in-plane mass acceleration

***Added after Run 42 of Specimen F1 (F1-M-C-40-1)

Table B-16: Summary of sensors used in Series F1-M-C

Sensor number	Type	Model	Serial number	Direction	Sensitivity		Excitation, volts
					Calibration constant	Units	
0	LVDT	Schaevitz DC-E250	13292	-	39.554	V/in	±15
1	LVDT	Schaevitz DC-E250	13301	-	40.929	V/in	±15
2	LVDT	Schaevitz DC-E250	13609	-	41.910	V/in	±15
3	LVDT	Schaevitz DC-E250	12971	-	40.167	V/in	±15
4	LVDT	Schaevitz DC-E3000	1684	South	3.320	V/in	±15
5	LVDT	Schaevitz DC-E5000	1275	South	1.937	V/in	±15
6	LVDT	Schaevitz DC-E2000	2479	South	5.026	V/in	±15
7	Strain gage	CEA-06-250UR-350	1	-45°*	1.0	in./in.	2.5
8	Strain gage	CEA-06-250UR-350	2	0°*	1.0	in./in.	2.5
9	Strain gage	CEA-06-250UR-350	3	45°*	1.0	in./in.	2.5
10	Strain gage	CEA-06-250UR-350	4	-45°*	1.0	in./in.	2.5
11	Strain gage	CEA-06-250UR-350	5	0°*	1.0	in./in.	2.5
12	Strain gage	CEA-06-250UR-350	6	45°*	1.0	in./in.	2.5
13	Accelerometer	ADXL335	1	Up	0.18	V/g	3.3
14	Accelerometer	ADXL335	1	East	0.33	V/g	3.3
15	Accelerometer	ADXL335	1	South	0.33	V/g	3.3

*Orientation relative to horizontal (positive values are in clockwise direction and negative values are counterclockwise direction)

Table B-16 (continued): Summary of sensors used in Series F1-M-C

Sensor number	Type	Model	Serial number	Direction	Sensitivity		Excitation, volts
					Calibration constant	Units	
16	Load cell	Lebow 3156-100K	2468	-	-0.00023941	V/kip	10
17	LVDT	-	-	South	1.812	V/in	-
18	LVDT	-	-	South	1.810	V/in	-
19	Accelerometer	ADXL335	2	Up	0.18	V/g	3.3
20	Accelerometer	ADXL335	2	East	0.33	V/g	3.3
21	Accelerometer	ADXL335	2	South	0.33	V/g	3.3
22	Accelerometer	ADXL335	3	Up	0.18	V/g	3.3
23	Accelerometer	ADXL335	3	North	0.33	V/g	3.3
24	Accelerometer	ADXL335	3	East	0.33	V/g	3.3
25**	Accelerometer	ADXL335	4	Up	0.18	V/g	3.3
26**	Accelerometer	ADXL335	4	East	0.33	V/g	3.3
27**	Accelerometer	ADXL335	4	South	0.33	V/g	3.3
28	Accelerometer	PCB 333B52	34411	South	1.045	V/g	-
29	Accelerometer	PCB 333B52	34413	South	1.048	V/g	-
30	Accelerometer	PCB 333B52	34454	South	1.077	V/g	-
31	Accelerometer	PCB 333B52	34452	South	1.060	V/g	-
32	Accelerometer	PCB 333B52	34412	South	1.061	V/g	-
33	Accelerometer	PCB 333B52	34415	Up	1.051	V/g	-
34	Accelerometer	PCB 333B52	34453	Down	1.040	V/g	-
35	Accelerometer	PCB 333B52	34414	North	0.960	V/g	-

**Added after Run 42 of Specimen F1 (F1-M-C-40-1)

Table B-17: Summary of data acquisition system used in Series F1-M-C

Sensor number	Chassis		Module		Card	
	Type	Number	Type	Number	Type	Channel number
0	SCXI-1000	1	SCXI-1520	1	SCXI-1314	0
1	SCXI-1000	1	SCXI-1520	1	SCXI-1314	1
2	SCXI-1000	1	SCXI-1520	1	SCXI-1314	2
3	SCXI-1000	1	SCXI-1520	1	SCXI-1314	3
4	SCXI-1000	1	SCXI-1520	1	SCXI-1314	4
5	SCXI-1000	1	SCXI-1520	1	SCXI-1314	5
6	SCXI-1000	1	SCXI-1520	1	SCXI-1314	6
7	SCXI-1000	1	SCXI-1521	2	SCXI-1317	0
8	SCXI-1000	1	SCXI-1521	2	SCXI-1317	1
9	SCXI-1000	1	SCXI-1521	2	SCXI-1317	2
10	SCXI-1000	1	SCXI-1521	2	SCXI-1317	3
11	SCXI-1000	1	SCXI-1521	2	SCXI-1317	4
12	SCXI-1000	1	SCXI-1521	2	SCXI-1317	5
13	SCXI-1000	1	SCXI-1121	3	SCXI-1321	0
14	SCXI-1000	1	SCXI-1121	3	SCXI-1321	1
15	SCXI-1000	1	SCXI-1121	3	SCXI-1321	2

Table B-17 (continued): Summary of data acquisition system used in Series F1-M-C

Sensor number	Chassis		Module		Card	
	Type	Number	Type	Number	Type	Channel number
16	SCXI-1000	1	SCXI-1121	3	SCXI-1321	3
17	SCXI-1000	1	SCXI-1121	4	SCXI-1321	0
18	SCXI-1000	1	SCXI-1121	4	SCXI-1321	1
19	SCXI-1000	2	SCXI-1121	3	SCXI-1321	0
20	SCXI-1000	2	SCXI-1121	3	SCXI-1321	1
21	SCXI-1000	2	SCXI-1121	3	SCXI-1321	2
22	SCXI-1000	2	SCXI-1121	4	SCXI-1321	0
23	SCXI-1000	2	SCXI-1121	4	SCXI-1321	1
24	SCXI-1000	2	SCXI-1121	4	SCXI-1321	2
25*	SCXI-1000	2	SCXI-1121	4	SCXI-1321	3
26*	SCXI-1000	2	SCXI-1121	4	SCXI-1321	4
27*	SCXI-1000	2	SCXI-1121	4	SCXI-1321	5
28	SCB68	-	-	-	-	0
29	SCB68	-	-	-	-	1
30	SCB68	-	-	-	-	2
31	SCB68	-	-	-	-	3
32	SCB68	-	-	-	-	4
33	SCB68	-	-	-	-	5
34	SCB68	-	-	-	-	6
35	SCB68	-	-	-	-	7

*Added after Run 42 of Specimen F1 (F1-M-C-40-1)

Table B-18: Location of sensors used in Series F1-M-C-OOP

Sensor number	Type	Location and description
0	LVDT	Below northeast side of simulator platform measuring displacement of platform
1	LVDT	Below northwest side of simulator platform measuring displacement of platform
2	LVDT	Below southwest side of simulator platform measuring displacement of platform
3	LVDT	Below southeast side of simulator platform measuring displacement of platform
4	LVDT	Soffit of top beam measuring in-plane roof displacement
5	LVDT	Top of top beam measuring in-plane roof displacement
6	LVDT	Top of foundation beam measuring in-plane base displacement
7	Strain gage*	Middle of east face of flexure link oriented 45° counterclockwise from horizontal
8	Strain gage**	Middle of east face of flexure link oriented along horizontal
9	Strain gage*	Middle of east face of flexure link oriented 45° clockwise from horizontal
10	Strain gage*	Middle of west face of flexure link oriented 45° counterclockwise from horizontal
11	Strain gage**	Middle of west face of flexure link oriented along horizontal
12	Strain gage*	Middle of west face of flexure link oriented 45° clockwise from horizontal
13	Accelerometer	Top southeast corner of top beam measuring vertical roof acceleration
14	Accelerometer	Top southeast corner of top beam measuring out-of-plane roof acceleration
15	Accelerometer	Top southeast corner of top beam measuring in-plane roof acceleration

*Strain gage factor S_g = 2.090 and transverse sensitivity K_t = 0.8%

**Strain gage factor S_g = 2.135 and transverse sensitivity K_t = 0.4%

Table B-18 (continued): Location of sensors used in Series F1-M-C-OOP

Sensor number	Type	Location and description
16	Load cell	Sandwiched between top beam and two-swivel link measuring lateral load
17	LVDT	Inside servoram measuring in-plane displacement of simulator platform (feedback signal)
18	LVDT	Inside servoram measuring in-plane displacement of simulator platform (command signal)
19	Accelerometer	Top northwest corner of top beam measuring vertical roof acceleration
20	Accelerometer	Top northwest corner of top beam measuring out-of-plane roof acceleration
21	Accelerometer	Top northwest corner of top beam measuring in-plane roof acceleration
22	Accelerometer	Top southeast corner of foundation beam measuring vertical base acceleration
23	Accelerometer	Top southeast corner of foundation beam measuring in-plane base acceleration
24	Accelerometer	Top southeast corner of foundation beam measuring out-of-plane base acceleration
25	Accelerometer	Top northwest corner of foundation beam measuring vertical base acceleration
26	Accelerometer	Top northwest corner of foundation beam measuring out-of-plane base acceleration
27	Accelerometer	Top northwest corner of foundation beam measuring in-plane base acceleration
28	Accelerometer	Top northeast corner of simulator platform measuring in-plane platform acceleration
29	Accelerometer	Top southeast corner of foundation beam measuring in-plane base acceleration
30	Accelerometer	Top northwest corner of top beam measuring in-plane roof acceleration
31	Accelerometer	Top southwest corner of simulator platform measuring in-plane platform acceleration
32	Accelerometer	Top southeast corner of top beam measuring in-plane roof acceleration
33	Accelerometer	Top northwest corner of foundation beam measuring in-plane base acceleration
34	Accelerometer	Not in use
35	Accelerometer	Not in use

Table B-19: Summary of sensors used in Series F1-M-C-OOP

Sensor number	Type	Model	Serial number	Direction	Sensitivity		Excitation, volts
					Calibration constant	Units	
0	LVDT	Schaevitz DC-E250	13292	-	39.554	V/in	±15
1	LVDT	Schaevitz DC-E250	13301	-	40.929	V/in	±15
2	LVDT	Schaevitz DC-E250	13609	-	41.910	V/in	±15
3	LVDT	Schaevitz DC-E250	12971	-	40.167	V/in	±15
4	LVDT	Schaevitz DC-E3000	1684	South	3.320	V/in	±15
5	LVDT	Schaevitz DC-E5000	1275	South	1.937	V/in	±15
6	LVDT	Schaevitz DC-E2000	2479	South	5.026	V/in	±15
7	Strain gage	CEA-06-250UR-350	1	-45°*	1.0	in./in.	2.5
8	Strain gage	CEA-06-250UR-350	2	0°*	1.0	in./in.	2.5
9	Strain gage	CEA-06-250UR-350	3	45°*	1.0	in./in.	2.5
10	Strain gage	CEA-06-250UR-350	4	-45°*	1.0	in./in.	2.5
11	Strain gage	CEA-06-250UR-350	5	0°*	1.0	in./in.	2.5
12	Strain gage	CEA-06-250UR-350	6	45°*	1.0	in./in.	2.5
13	Accelerometer	ADXL335	1	Up	0.18	V/g	3.3
14	Accelerometer	ADXL335	1	South	0.33	V/g	3.3
15	Accelerometer	ADXL335	1	West	0.33	V/g	3.3

*Orientation relative to horizontal (positive values are in clockwise direction and negative values are counterclockwise direction)

Table B-19 (continued): Summary of sensors used in Series F1-M-C-OOP

Sensor number	Type	Model	Serial number	Direction	Sensitivity		Excitation, volts
					Calibration constant	Units	
16	Load cell	Lebow 3156-100K	2468	-	-0.00023941	V/kip	10
17	LVDT	-	-	South	1.812	V/in	-
18	LVDT	-	-	South	1.810	V/in	-
19	Accelerometer	ADXL335	2	Up	0.18	V/g	3.3
20	Accelerometer	ADXL335	2	South	0.33	V/g	3.3
21	Accelerometer	ADXL335	2	West	0.33	V/g	3.3
22	Accelerometer	ADXL335	3	Up	0.18	V/g	3.3
23	Accelerometer	ADXL335	3	East	0.33	V/g	3.3
24	Accelerometer	ADXL335	3	South	0.33	V/g	3.3
25	Accelerometer	ADXL335	4	Up	0.18	V/g	3.3
26	Accelerometer	ADXL335	4	South	0.33	V/g	3.3
27	Accelerometer	ADXL335	4	West	0.33	V/g	3.3
28	Accelerometer	PCB 333B52	34414	North	0.960	V/g	-
29	Accelerometer	PCB 333B52	34454	South	1.077	V/g	-
30	Accelerometer	PCB 333B52	34413	North	1.048	V/g	-
31	Accelerometer	PCB 333B52	34412	North	1.061	V/g	-
32	Accelerometer	PCB 333B52	34452	South	1.060	V/g	-
33	Accelerometer	PCB 333B52	34411	North	1.045	V/g	-
34	Accelerometer	-	-	-	-	-	-
35	Accelerometer	-	-	-	-	-	-

Table B-20: Summary of data acquisition system used in Series F1-M-C-OOP

Sensor number	Chassis		Module		Card	
	Type	Number	Type	Number	Type	Channel number
0	SCXI-1000	1	SCXI-1520	0	SCXI-1314	0
1	SCXI-1000	1	SCXI-1520	0	SCXI-1314	1
2	SCXI-1000	1	SCXI-1520	0	SCXI-1314	2
3	SCXI-1000	1	SCXI-1520	0	SCXI-1314	3
4	SCXI-1000	1	SCXI-1520	0	SCXI-1314	4
5	SCXI-1000	1	SCXI-1520	0	SCXI-1314	5
6	SCXI-1000	1	SCXI-1520	0	SCXI-1314	6
7	SCXI-1000	1	SCXI-1521	1	SCXI-1317	0
8	SCXI-1000	1	SCXI-1521	1	SCXI-1317	1
9	SCXI-1000	1	SCXI-1521	1	SCXI-1317	2
10	SCXI-1000	1	SCXI-1521	1	SCXI-1317	3
11	SCXI-1000	1	SCXI-1521	1	SCXI-1317	4
12	SCXI-1000	1	SCXI-1521	1	SCXI-1317	5
13	SCXI-1000	1	SCXI-1121	2	SCXI-1321	0
14	SCXI-1000	1	SCXI-1121	2	SCXI-1321	1
15	SCXI-1000	1	SCXI-1121	2	SCXI-1321	2

Table B-20 (continued): Summary of data acquisition system used in Series F1-M-C-OOP

Sensor number	Chassis		Module		Card	
	Type	Number	Type	Number	Type	Channel number
16	SCXI-1000	1	SCXI-1121	2	SCXI-1321	3
17	SCXI-1000	1	SCXI-1121	3	SCXI-1321	0
18	SCXI-1000	1	SCXI-1121	3	SCXI-1321	1
19	SCXI-1000	2	SCXI-1121	0	SCXI-1321	0
20	SCXI-1000	2	SCXI-1121	0	SCXI-1321	1
21	SCXI-1000	2	SCXI-1121	0	SCXI-1321	2
22	SCXI-1000	2	SCXI-1121	2	SCXI-1321	0
23	SCXI-1000	2	SCXI-1121	2	SCXI-1321	1
24	SCXI-1000	2	SCXI-1121	2	SCXI-1321	2
25	SCXI-1000	2	SCXI-1121	3	SCXI-1321	0
26	SCXI-1000	2	SCXI-1121	3	SCXI-1321	1
27	SCXI-1000	2	SCXI-1121	3	SCXI-1321	2
28	SCB68	-	-	-	-	0
29	SCB68	-	-	-	-	1
30	SCB68	-	-	-	-	2
31	SCB68	-	-	-	-	3
32	SCB68	-	-	-	-	4
33	SCB68	-	-	-	-	5
34	SCB68	-	-	-	-	6
35	SCB68	-	-	-	-	7

Table B-21: Location of sensors used in tests on Specimen F2

Sensor number	Type	Location and description
0	LVDT	Below northeast side of simulator platform measuring displacement of platform
1	LVDT	Below northwest side of simulator platform measuring displacement of platform
2	LVDT	Below southwest side of simulator platform measuring displacement of platform
3	LVDT	Below southeast side of simulator platform measuring displacement of platform
4	LVDT	Soffit of top beam measuring in-plane roof displacement
5	LVDT	Top of top beam measuring in-plane roof displacement
6	LVDT	Top of foundation beam measuring in-plane base displacement
7	Strain gage*	Middle of east face of flexure link oriented 45° counterclockwise from horizontal
8	Strain gage**	Middle of east face of flexure link oriented along horizontal
9	Strain gage*	Middle of east face of flexure link oriented 45° clockwise from horizontal
10	Strain gage*	Middle of west face of flexure link oriented 45° counterclockwise from horizontal
11	Strain gage**	Middle of west face of flexure link oriented along horizontal
12	Strain gage*	Middle of west face of flexure link oriented 45° clockwise from horizontal
13	Accelerometer	Top northeast corner of top beam measuring vertical roof acceleration
14	Accelerometer	Top northeast corner of top beam measuring out-of-plane roof acceleration
15	Accelerometer	Top northeast corner of top beam measuring in-plane roof acceleration

*Strain gage factor S_g = 2.090 and transverse sensitivity K_t = 0.8%

**Strain gage factor S_g = 2.135 and transverse sensitivity K_t = 0.4%

Table B-21 (continued): Location of sensors used in tests on Specimen F2

Sensor number	Type	Location and description
16	Load cell	Sandwiched between top beam and two-swivel link measuring lateral load
17	LVDT	Inside servoram measuring in-plane displacement of simulator platform (feedback signal)
18	LVDT	Inside servoram measuring in-plane displacement of simulator platform (command signal)
19	Accelerometer	Top southwest corner of simulator platform measuring vertical simulator acceleration
20	Accelerometer	Top southwest corner of simulator platform measuring out-of-plane simulator acceleration
21	Accelerometer	Top southwest corner of simulator platform measuring in-plane simulator acceleration
22	Accelerometer	Top northeast corner of foundation beam measuring vertical base acceleration
23	Accelerometer	Top northeast corner of foundation beam measuring in-plane base acceleration
24	Accelerometer	Top northeast corner of foundation beam measuring out-of-plane base acceleration
25	Accelerometer	Top southwest corner of foundation beam measuring vertical base acceleration
26	Accelerometer	Top southwest corner of foundation beam measuring out-of-plane base acceleration
27	Accelerometer	Top southwest corner of foundation beam measuring in-plane base acceleration
28	Accelerometer	Top southwest corner of top beam measuring vertical roof acceleration
29	Accelerometer	Top southwest corner of top beam measuring out-of-plane roof acceleration
30	Accelerometer	Top southwest corner of top beam measuring in-plane roof acceleration
31	Accelerometer	Top northeast corner of simulator platform measuring vertical simulator acceleration
32	Accelerometer	Top northeast corner of simulator platform measuring out-of-plane simulator acceleration
33	Accelerometer	Top northeast corner of simulator platform measuring in-plane simulator acceleration
34	Accelerometer	Top of concrete pedestal supporting servoram measuring vertical acceleration
35	Accelerometer	Top of concrete pedestal supporting servoram measuring out-of-plane acceleration
36	Accelerometer	Top of concrete pedestal supporting servoram measuring in-plane acceleration

Table B-21 (continued): Location of sensors used in tests on Specimen F2

Sensor number	Type	Location and description
37	Accelerometer	Top northeast corner of foundation beam measuring in-plane base acceleration
38	Accelerometer	Top southwest corner of foundation beam measuring in-plane base acceleration
39	Accelerometer	Top northeast corner of top beam measuring in-plane roof acceleration
40	Accelerometer	Top southwest corner of top beam measuring in-plane roof acceleration
41	Accelerometer	Middle of east face of RC block measuring in-plane mass acceleration
42	Accelerometer	Bottom northwest corner of RC block on west face measuring vertical acceleration
43	Accelerometer	Top southeast corner of RC block on east face measuring vertical acceleration
44	Accelerometer	Middle of west face of RC block measuring in-plane mass acceleration

Table B-22: Summary of sensors used in tests on Specimen F2

Sensor number	Type	Model	Serial number	Direction	Sensitivity		Excitation, volts
					Calibration constant	Units	
0	LVDT	Schaevitz DC-E250	13292	-	39.554	V/in	±15
1	LVDT	Schaevitz DC-E250	13301	-	40.929	V/in	±15
2	LVDT	Schaevitz DC-E250	13609	-	41.910	V/in	±15
3	LVDT	Schaevitz DC-E250	12971	-	40.167	V/in	±15
4	LVDT	Schaevitz DC-E3000	1684	South	3.320	V/in	±15
5	LVDT	Schaevitz DC-E5000	1275	South	1.937	V/in	±15
6	LVDT	Schaevitz DC-E2000	2479	South	5.026	V/in	±15
7	Strain gage	CEA-06-250UR-350	1	-45°*	1.0	in./in.	2.5
8	Strain gage	CEA-06-250UR-350	2	0°*	1.0	in./in.	2.5
9	Strain gage	CEA-06-250UR-350	3	45°*	1.0	in./in.	2.5
10	Strain gage	CEA-06-250UR-350	4	-45°*	1.0	in./in.	2.5
11	Strain gage	CEA-06-250UR-350	5	0°*	1.0	in./in.	2.5
12	Strain gage	CEA-06-250UR-350	6	45°*	1.0	in./in.	2.5
13	Accelerometer	ADXL335	1	Up	0.18	V/g	3.3
14	Accelerometer	ADXL335	1	North	0.33	V/g	3.3
15	Accelerometer	ADXL335	1	East	0.33	V/g	3.3

*Orientation relative to horizontal (positive values are in clockwise direction and negative values are counterclockwise direction)

Table B-22 (continued): Summary of sensors used in tests on Specimen F2

Sensor number	Type	Model	Serial number	Direction	Sensitivity		Excitation, volts
					Calibration constant	Units	
16	Load cell	Lebow 3156-100K	2468	-	-0.00023941	V/kip	10
17	LVDT	-	-	South	1.812	V/in	-
18	LVDT	-	-	South	1.810	V/in	-
19	Accelerometer	ADXL335	2	Up	0.18	V/g	3.3
20	Accelerometer	ADXL335	2	South	0.33	V/g	3.3
21	Accelerometer	ADXL335	2	West	0.33	V/g	3.3
22	Accelerometer	ADXL335	3	Up	0.18	V/g	3.3
23	Accelerometer	ADXL335	3	North	0.33	V/g	3.3
24	Accelerometer	ADXL335	3	East	0.33	V/g	3.3
25	Accelerometer	ADXL335	4	Up	0.18	V/g	3.3
26	Accelerometer	ADXL335	4	East	0.33	V/g	3.3
27	Accelerometer	ADXL335	4	South	0.33	V/g	3.3
28	Accelerometer	ADXL335	5	Up	0.18	V/g	3.3
29	Accelerometer	ADXL335	5	East	0.33	V/g	3.3
30	Accelerometer	ADXL335	5	South	0.33	V/g	3.3
31	Accelerometer	ADXL335	6	Up	0.18	V/g	3.3
32	Accelerometer	ADXL335	6	North	0.33	V/g	3.3
33	Accelerometer	ADXL335	6	East	0.33	V/g	3.3
34	Accelerometer	ADXL335	7	Up	0.18	V/g	3.3
35	Accelerometer	ADXL335	7	South	0.33	V/g	3.3
36	Accelerometer	ADXL335	7	West	0.33	V/g	3.3

Table B-22 (continued): Summary of sensors used in tests on Specimen F2

Sensor number	Type	Model	Serial number	Direction	Sensitivity		Excitation, volts
					Calibration constant	Units	
37	Accelerometer	PCB 333B52	34413	South	1.048	V/g	-
38	Accelerometer	PCB 333B52	34454	South	1.077	V/g	-
39	Accelerometer	PCB 333B52	34411	South	1.045	V/g	-
40	Accelerometer	PCB 333B52	34452	South	1.060	V/g	-
41	Accelerometer	PCB 333B52	34412	South	1.061	V/g	-
42	Accelerometer	PCB 333B52	34415	Up	1.051	V/g	-
43	Accelerometer	PCB 333B52	34453	Down	1.040	V/g	-
44	Accelerometer	PCB 333B52	34414	North	0.960	V/g	-

Table B-23: Summary of data acquisition system used in tests on Specimen F2

Sensor number	Chassis		Module		Card	
	Type	Number	Type	Number	Type	Channel number
0	SCXI-1000	1	SCXI-1520	1	SCXI-1314	0
1	SCXI-1000	1	SCXI-1520	1	SCXI-1314	1
2	SCXI-1000	1	SCXI-1520	1	SCXI-1314	2
3	SCXI-1000	1	SCXI-1520	1	SCXI-1314	3
4	SCXI-1000	1	SCXI-1520	1	SCXI-1314	4
5	SCXI-1000	1	SCXI-1520	1	SCXI-1314	5
6	SCXI-1000	1	SCXI-1520	1	SCXI-1314	6
7	SCXI-1000	1	SCXI-1521	2	SCXI-1317	0
8	SCXI-1000	1	SCXI-1521	2	SCXI-1317	1
9	SCXI-1000	1	SCXI-1521	2	SCXI-1317	2
10	SCXI-1000	1	SCXI-1521	2	SCXI-1317	3
11	SCXI-1000	1	SCXI-1521	2	SCXI-1317	4
12	SCXI-1000	1	SCXI-1521	2	SCXI-1317	5
13	SCXI-1000	1	SCXI-1121	3	SCXI-1321	0
14	SCXI-1000	1	SCXI-1121	3	SCXI-1321	1
15	SCXI-1000	1	SCXI-1121	3	SCXI-1321	2

Table B-23 (continued): Summary of data acquisition system used in runs of Specimen F2

Sensor number	Chassis		Module		Card	
	Type	Number	Type	Number	Type	Channel number
16	SCXI-1000	1	SCXI-1121	3	SCXI-1321	3
17	SCXI-1000	1	SCXI-1121	4	SCXI-1321	0
18	SCXI-1000	1	SCXI-1121	4	SCXI-1321	1
19	SCXI-1000	2	SCXI-1121	1	SCXI-1321	0
20	SCXI-1000	2	SCXI-1121	1	SCXI-1321	1
21	SCXI-1000	2	SCXI-1121	1	SCXI-1321	2
22	SCXI-1000	2	SCXI-1121	2	SCXI-1321	0
23	SCXI-1000	2	SCXI-1121	2	SCXI-1321	1
24	SCXI-1000	2	SCXI-1121	2	SCXI-1321	2
25	SCXI-1000	2	SCXI-1121	3	SCXI-1321	0
26	SCXI-1000	2	SCXI-1121	3	SCXI-1321	1
27	SCXI-1000	2	SCXI-1121	3	SCXI-1321	2
28	SCXI-1000	2	SCXI-1121	4	SCXI-1321	0
29	SCXI-1000	2	SCXI-1121	4	SCXI-1321	1
30	SCXI-1000	2	SCXI-1121	4	SCXI-1321	2
31	SCXI-1000	3	SCXI-1121	1	SCXI-1321	0
32	SCXI-1000	3	SCXI-1121	1	SCXI-1321	1
33	SCXI-1000	3	SCXI-1121	1	SCXI-1321	2
34	SCXI-1000	3	SCXI-1121	2	SCXI-1321	0
35	SCXI-1000	3	SCXI-1121	2	SCXI-1321	1
36	SCXI-1000	3	SCXI-1121	2	SCXI-1321	2

Table B-23 (continued): Summary of data acquisition system used in runs of Specimen F2

Sensor number	Chassis		Module		Card	
	Type	Number	Type	Number	Type	Channel number
37	SCB68	-	-	-	-	0
38	SCB68	-	-	-	-	1
39	SCB68	-	-	-	-	2
40	SCB68	-	-	-	-	3
41	SCB68	-	-	-	-	4
42	SCB68	-	-	-	-	5
43	SCB68	-	-	-	-	6
44	SCB68	-	-	-	-	7

Table B-24: Test schedule

Specimen	Date cast	Series	Date(s) tested	Age on first day of test, days
F1	2019.08.30	F1-B	2020.01.06 - 2020.01.16	129
		F1-C	2020.01.19 - 2020.01.20	142
		F1-M-C	2020.03.05 - 2020.03.11	188
		F1-M-C-OOP	2020.06.18 - 2020.06.25	293
F2	2019.08.30	F2-C	2020.08.03 - 2020.08.12	339
		F2-M	2020.09.07 - 2020.09.08	374
		F2-M-C-S	2020.09.11	378
		F2-C-S	2020.09.14	381

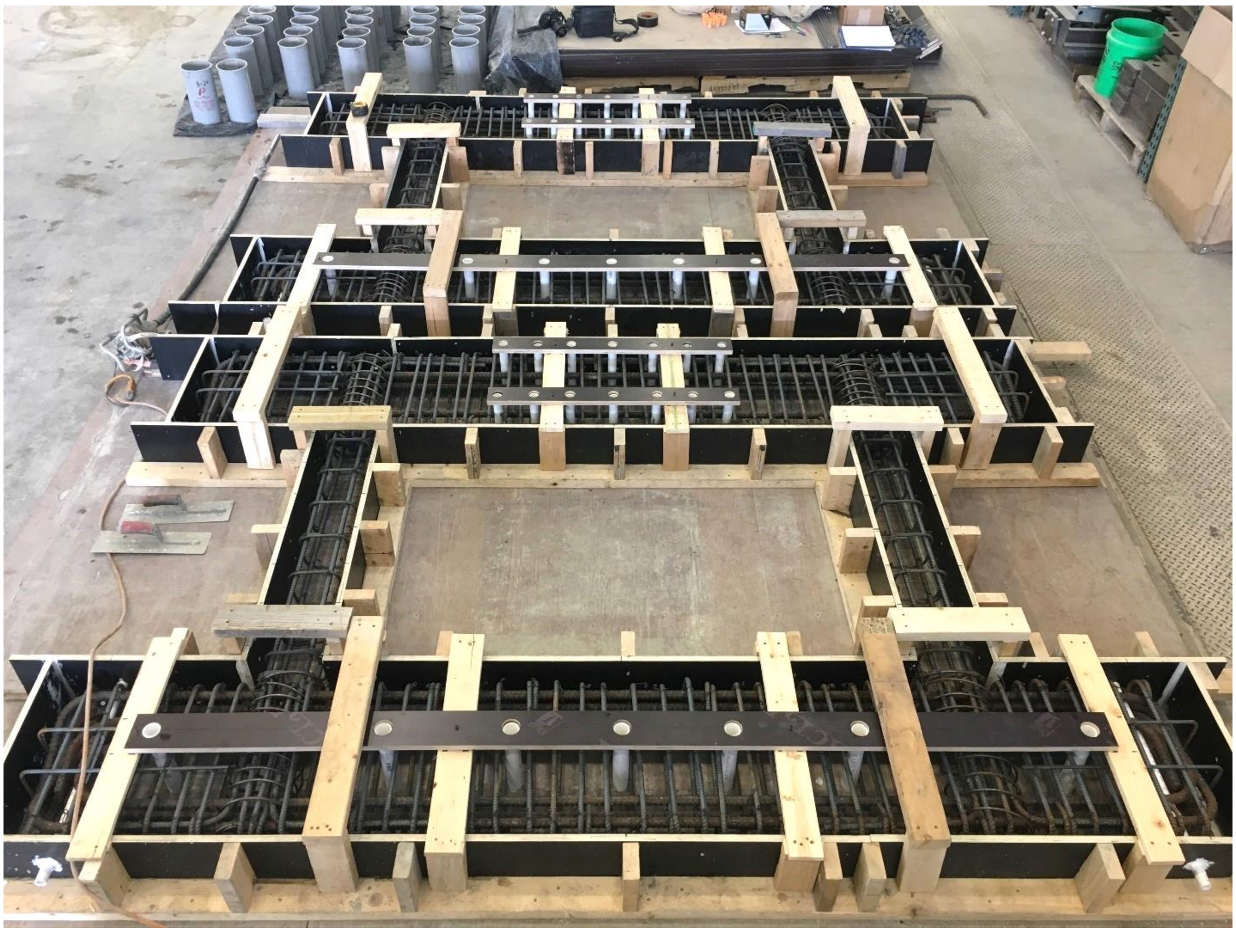

Figure B-1: Wooden formwork, reinforcement cage, and PVC pipes on day of cast

Figure B-2: Test frames immediately following cast

Figure B-3: Wet burlap over test frames

Figure B-4: Storing frames next to earthquake simulator

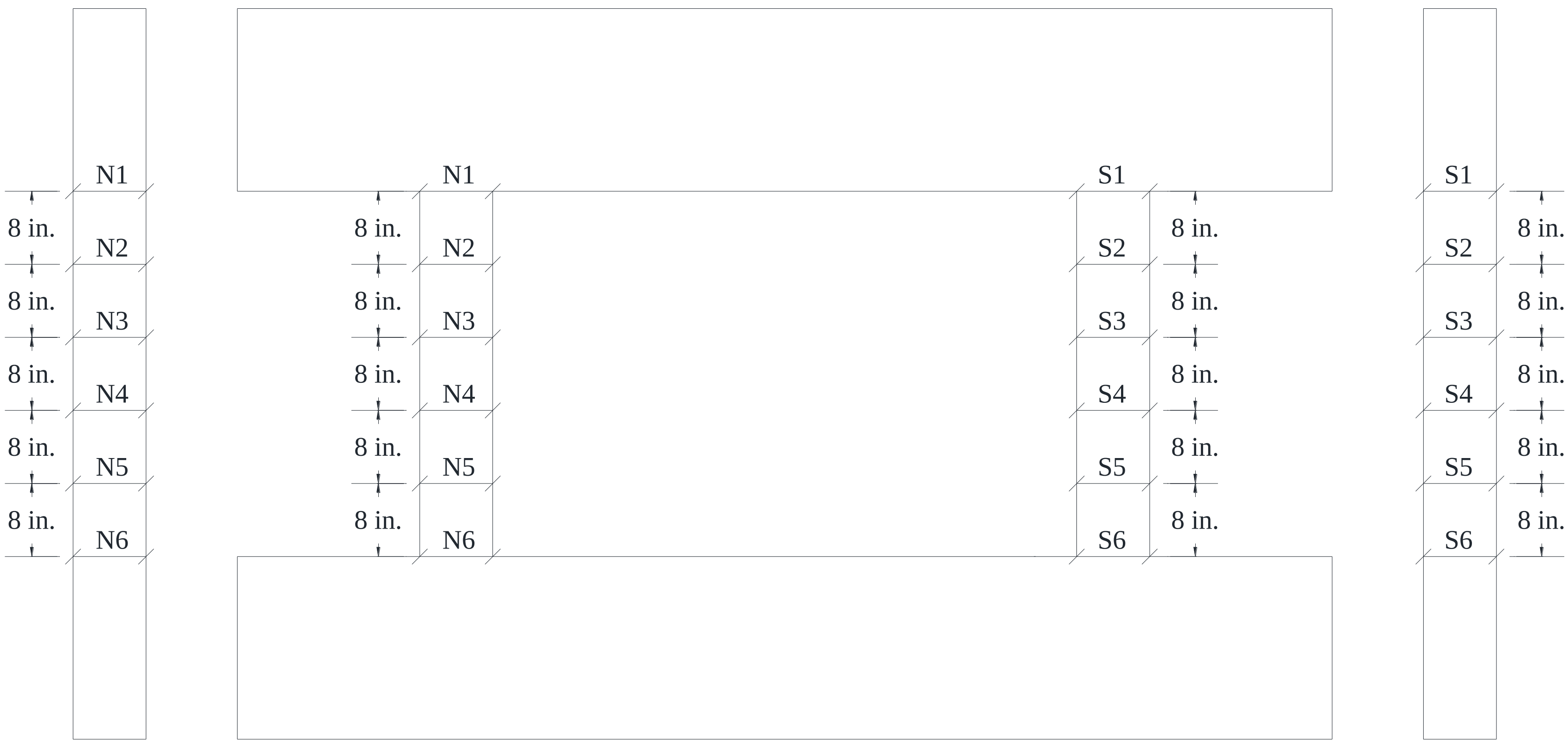

North column
Out-of-plane dimensions

North and south columns
In-plane dimensions

South column
Out-of-plane dimensions

Figure B-5: Column cross section dimension survey

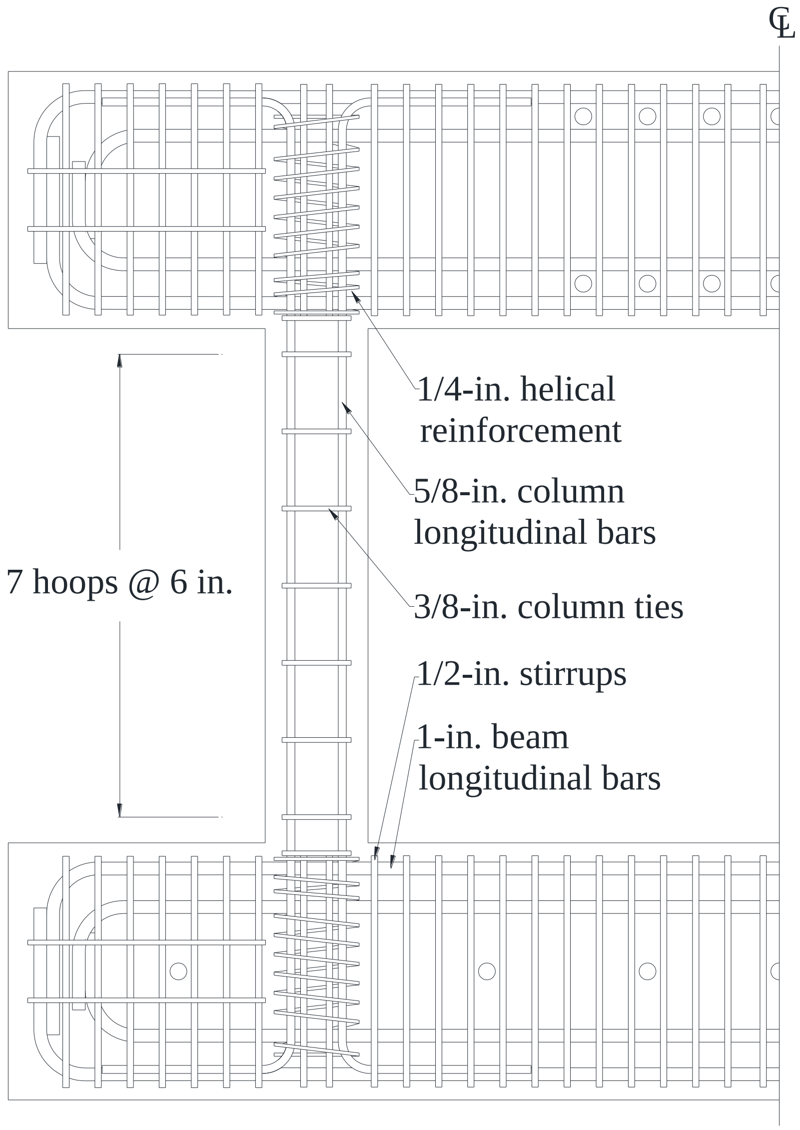

Figure B-6: Reinforcement layout

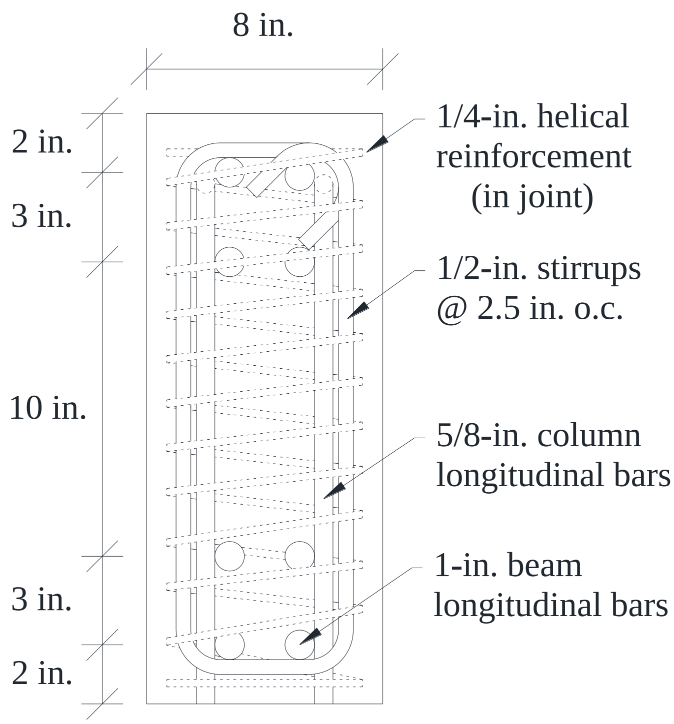

Figure B-7: Beam cross section

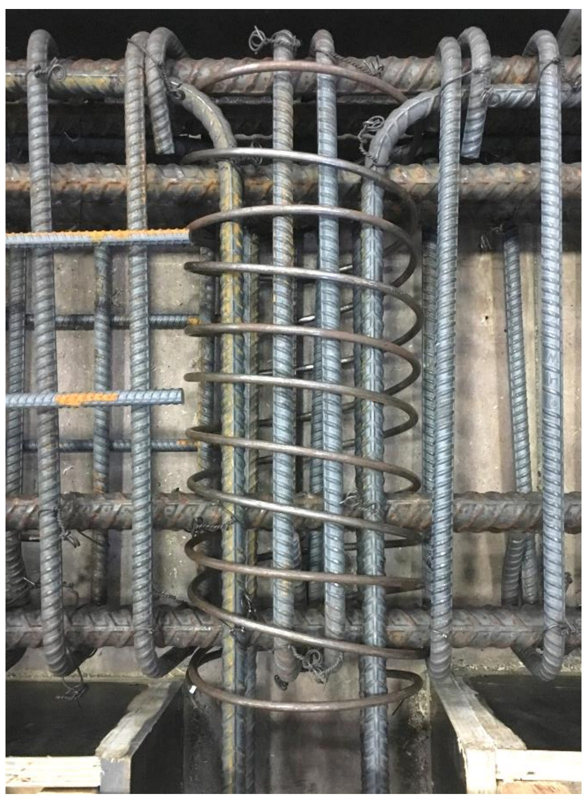

Figure B-8: Helical reinforcement in joint

Figure B-9: Bricks used to build masonry infill walls

Figure B-10: Bags of pre-blended mortar mix used to build masonry infill walls

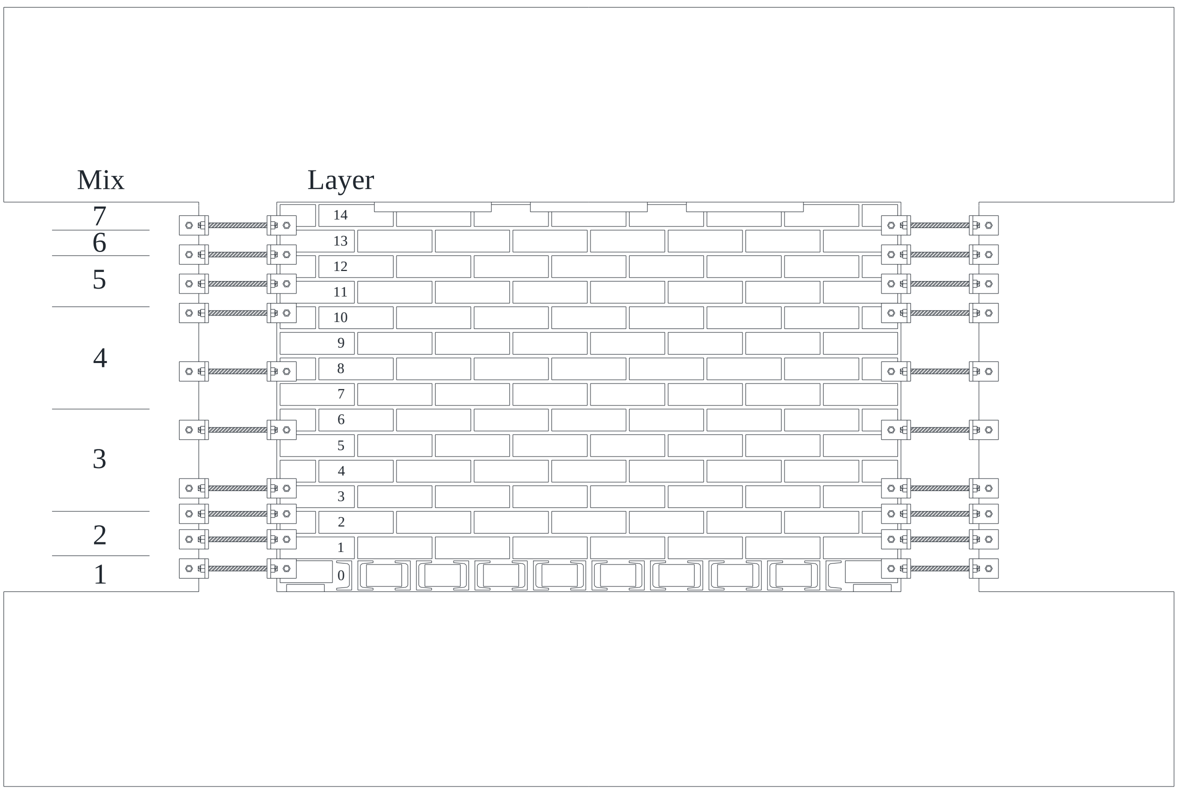

Figure B-11: Distribution of mortar mix along height of masonry wall of Specimen F1

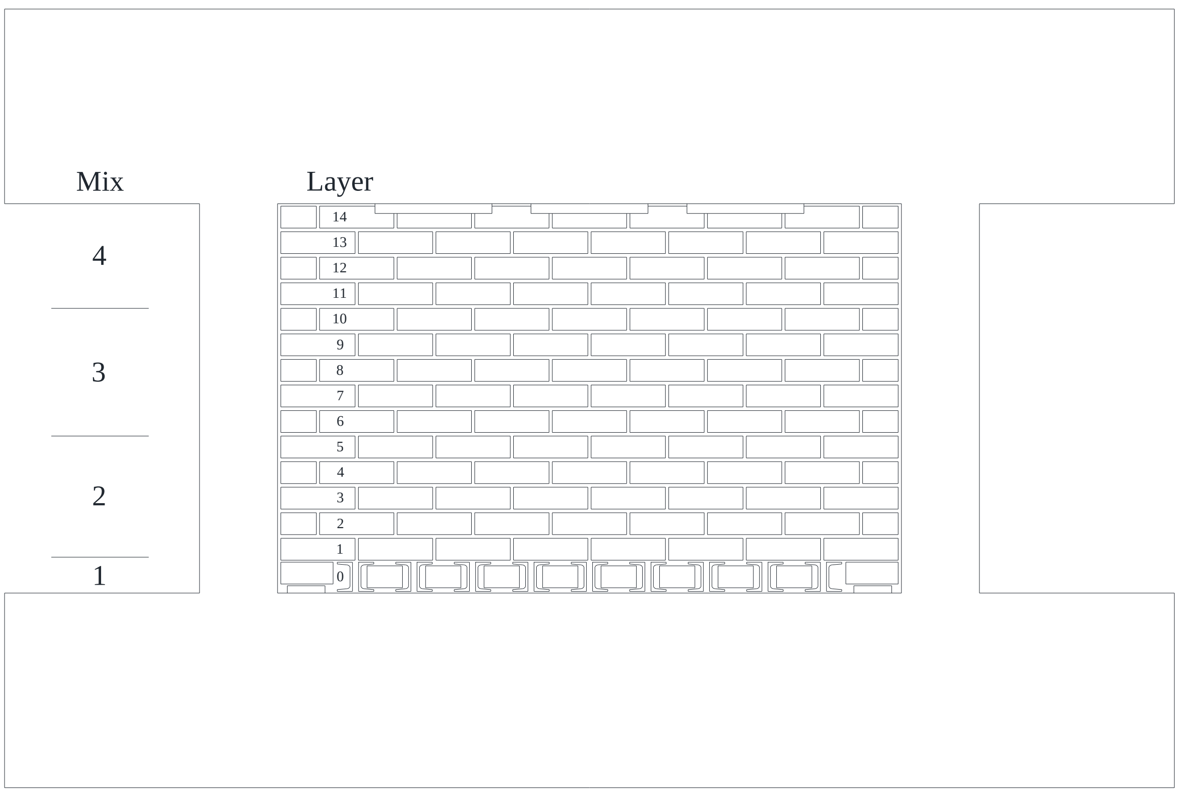

Figure B-12: Distribution of mortar mix along height of masonry wall of Specimen F2

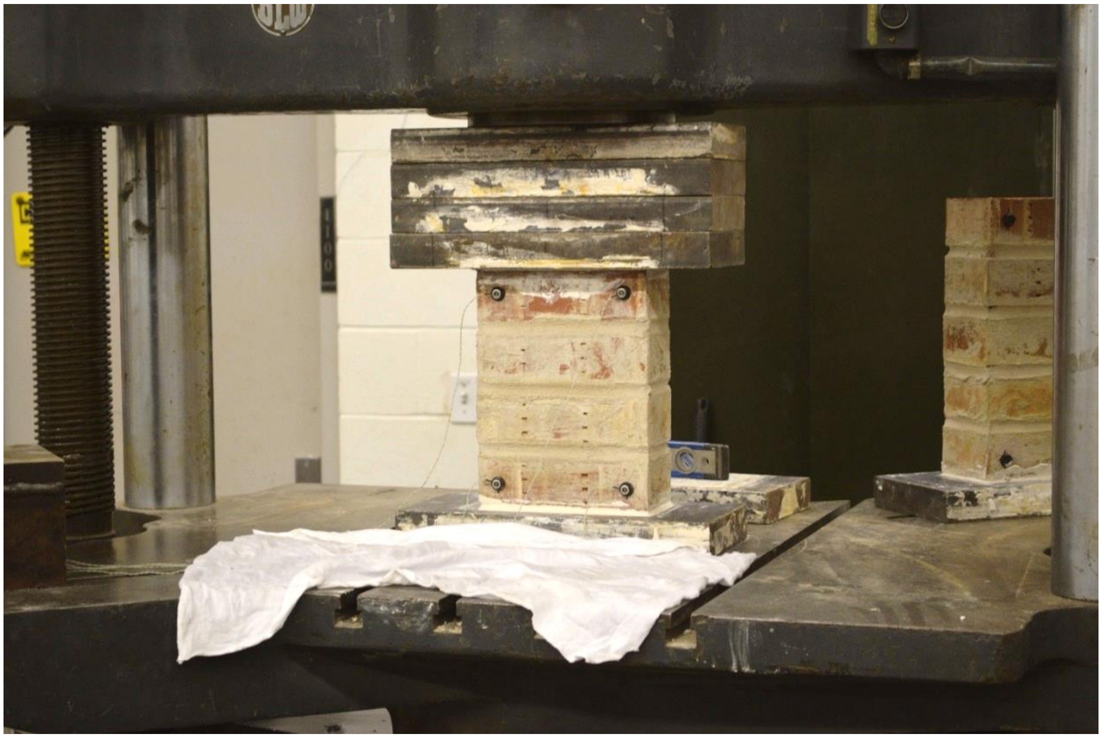

(a) Four-brick masonry prism with attached Optotrak targets

(b) Four-brick masonry prism

Figure B-13: Tests of masonry prisms

Note: Five-brick prism is shown in background of Figure B-13 (a).

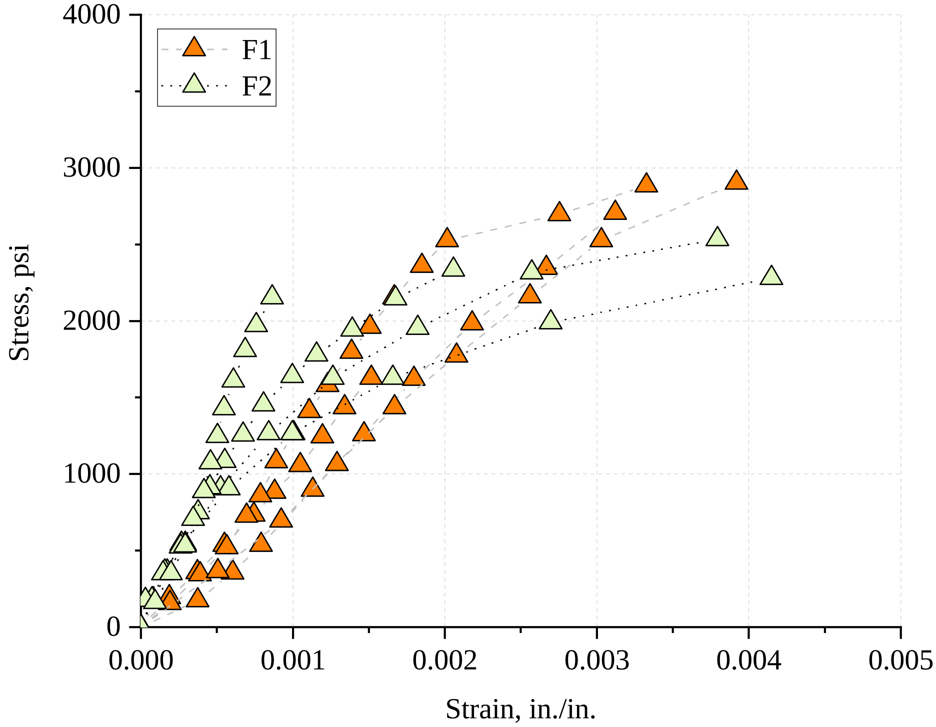

(a) Stress vs. strain

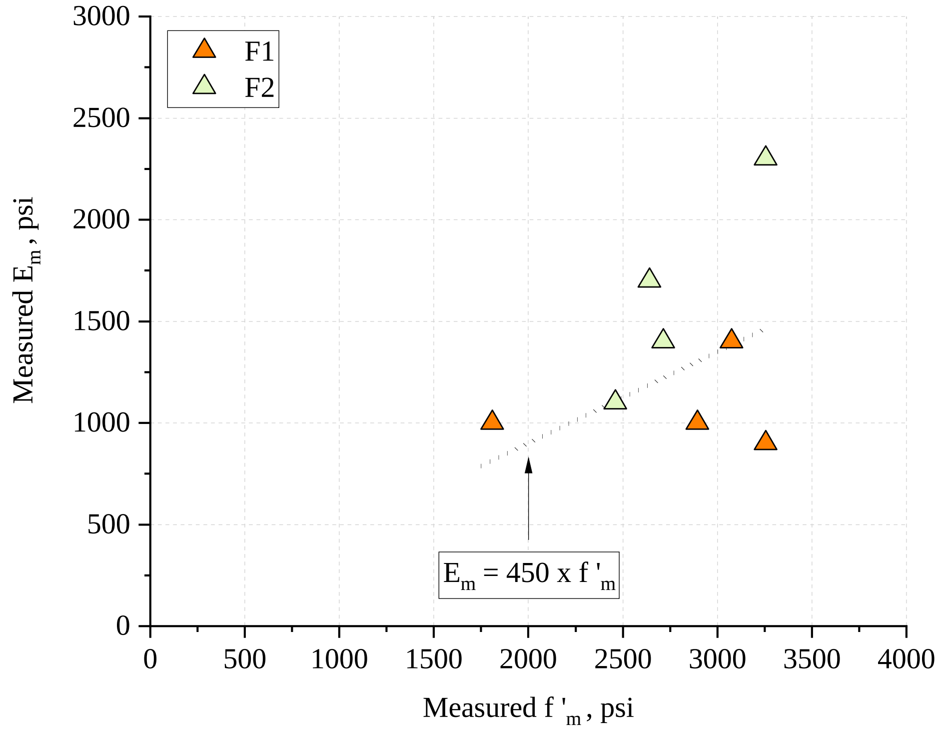

(b) Measured elastic modulus vs. measured gross compressive strength

Figure B-14: Measurements of gross compressive strength and elastic modulus of masonry prisms

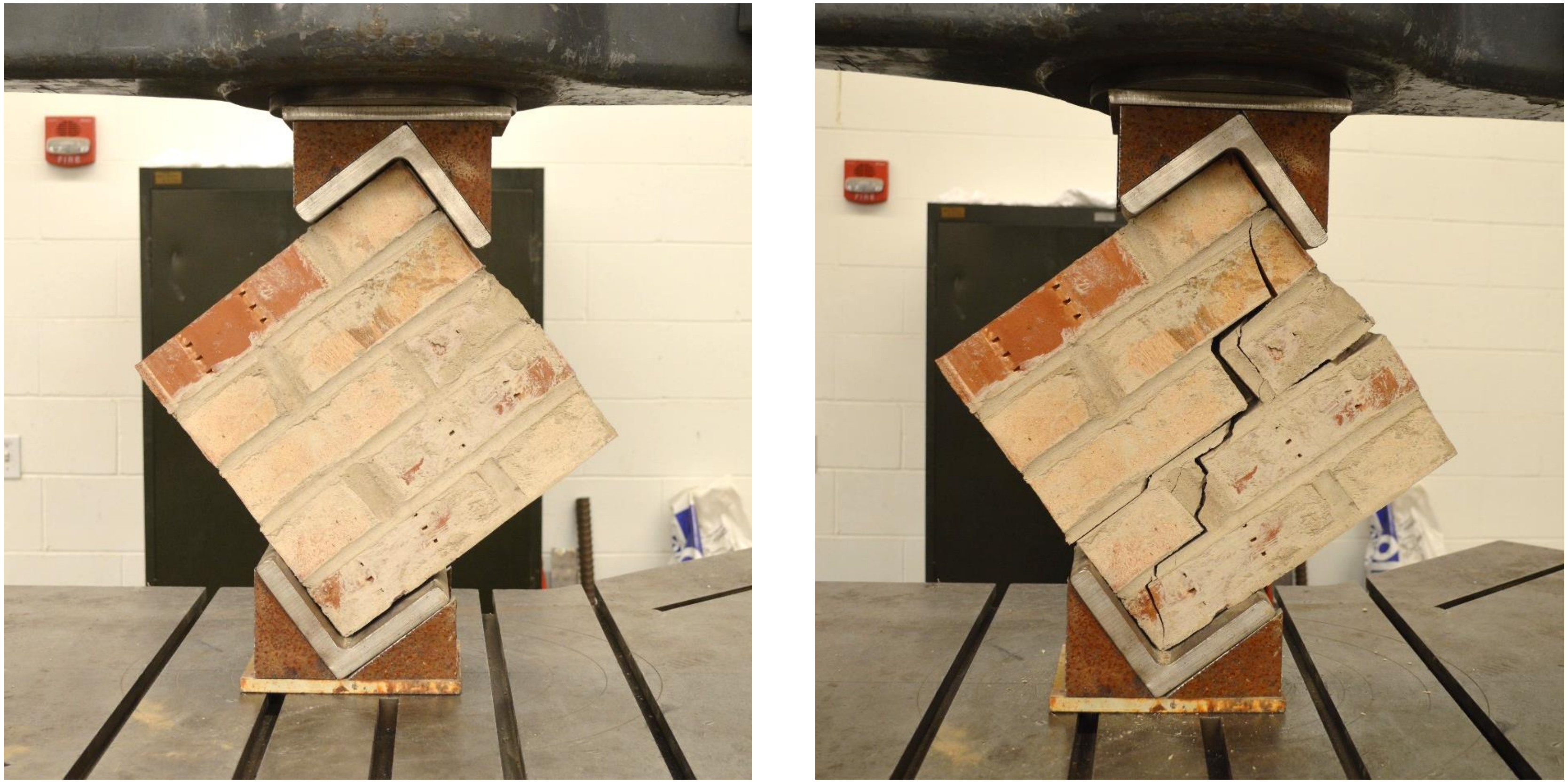

(a) Loading of coupon (b) Failure of coupon

Figure B-15: Diagonal compression Coupon No. 1

Figure B-16: Diagonal compression Coupon No. 2

Figure B-17: Shear triplet coupon

Figure B-18: Earthquake simulator housed at Bowen Laboratory at Purdue University

Figure B-19: Isometric of test setup

Figure B-20: Connection of frame to suspended mass via two-swivel link

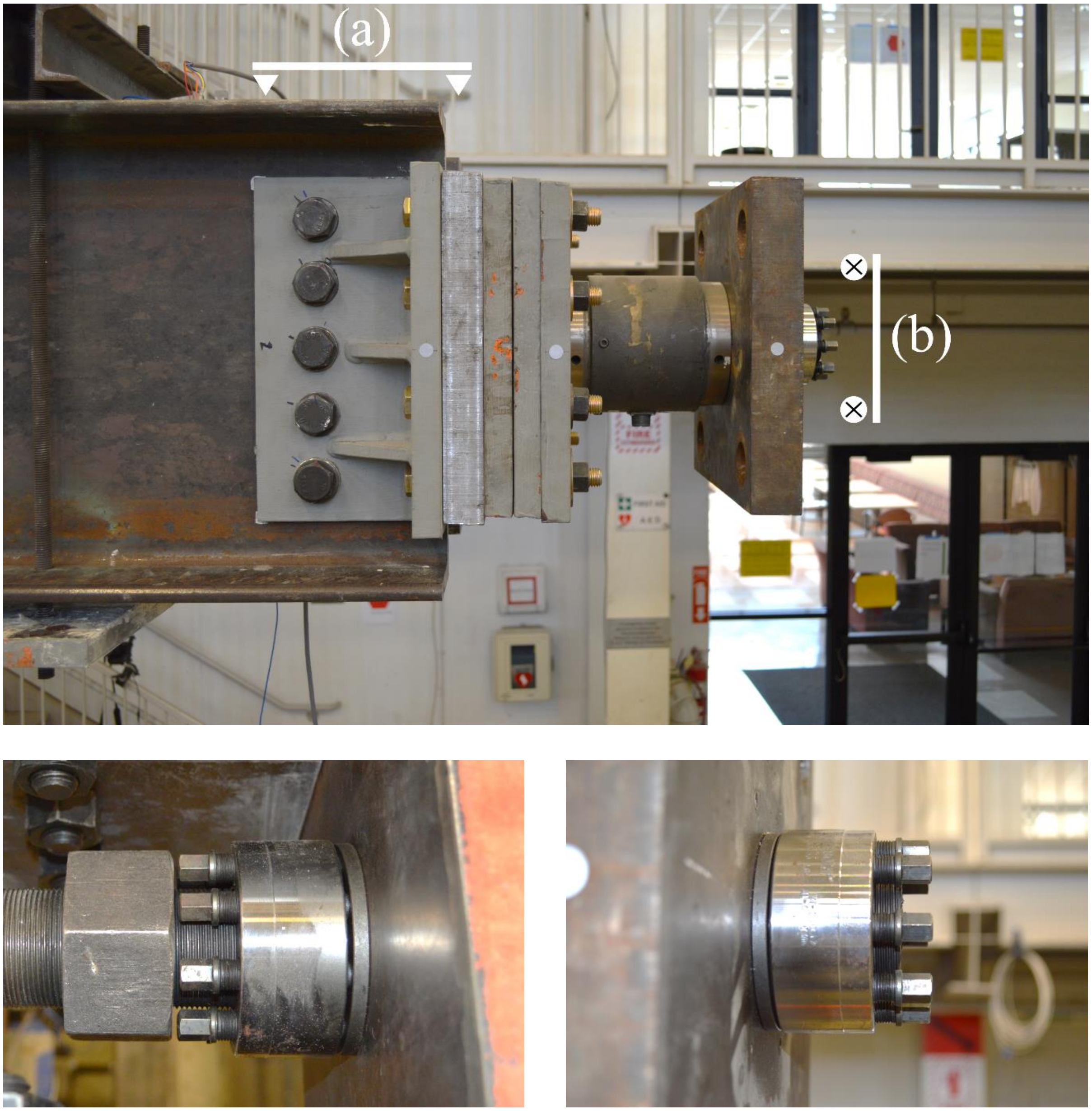

(a) (b)

Figure B-21: Steel plates clamped to ends of load cell using mechanical tensioners

Figure B-22: Standard nut style mechanical tensioner manufactured by Superbolt, Inc.

Figure B-23: Connection of swivel to north face of RC block

Figure B-24: Four 1-in. high-strength threaded rods embedded into north face of RC block

(a) Instruction pamphlet

(b) 11 fl. oz. Hilti HIT-RE 500 V3 epoxy cartridge

Figure B-25: High-strength epoxy adhesive used to anchor high-strength rods into RC block

Figure B-26: 1 1/8-in. Hilti TE-YX Imperial hammer drill bit used to drill holes in RC block

Figure B-27: 1 1/8-in. Hilti wire brush with extension used to remove concrete dust from holes drilled into RC block

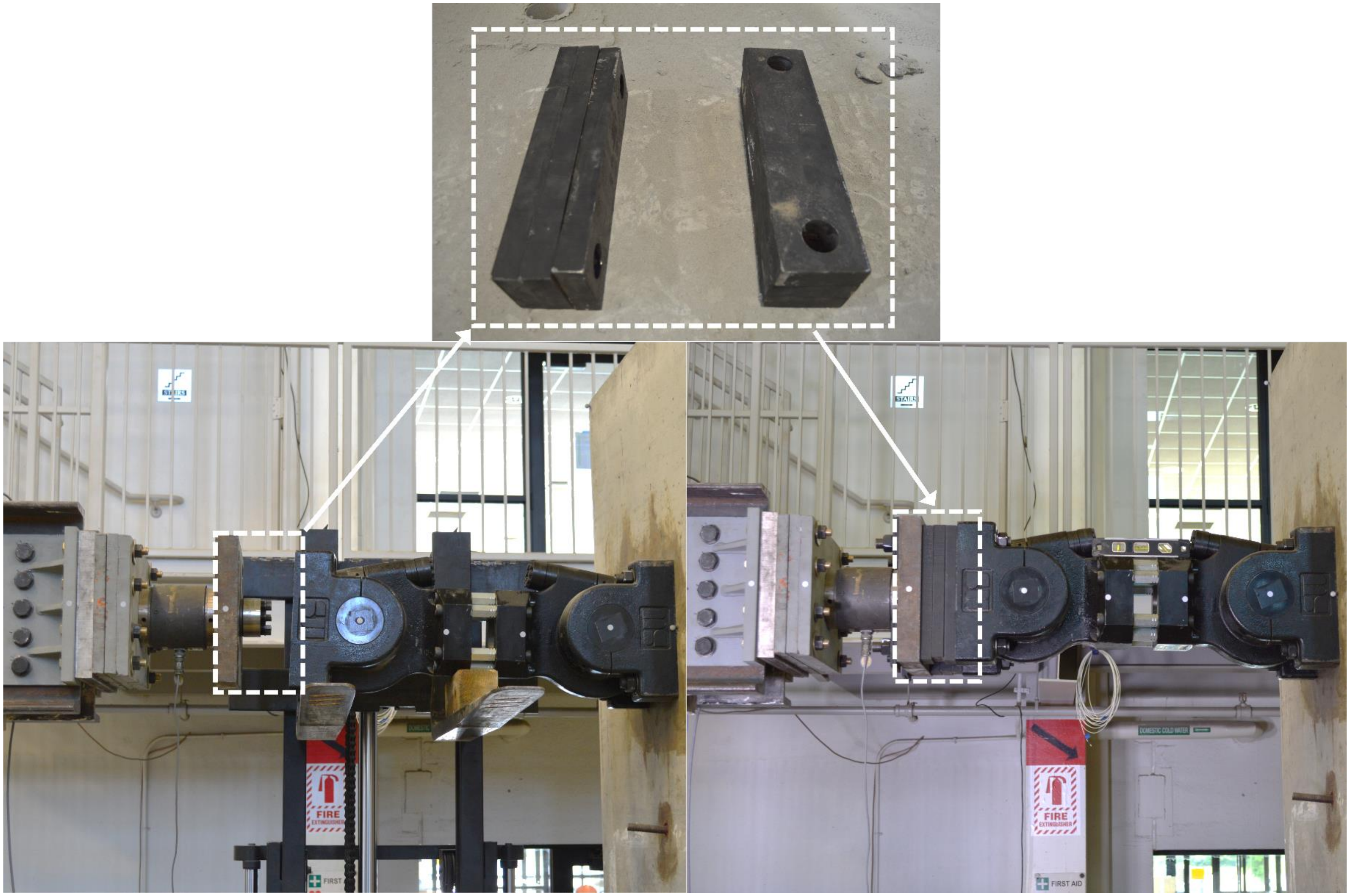

Figure B-28: Connection of load cell to north end of two-swivel link

Figure B-29: Reinforced concrete block serving as foundation of RC wall specimen tested by Pollalis (2021) used to provide additional mass to system

Figure B-30: Hollow steel tubes used to reduce out-of-plane displacement

Figure B-31: RC base block with 5/8-in. threaded rods embedded one foot into concrete

Figure B-32: RC base block clamped to strong floor

Figure B-33: Assembly used to prevent rotation of base block

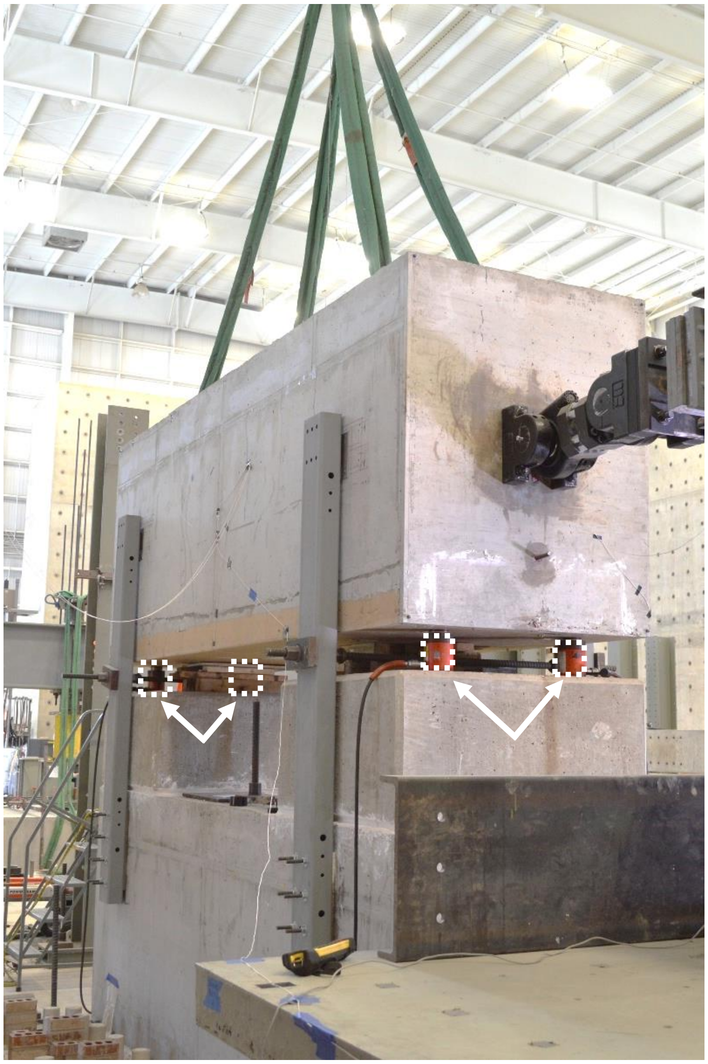

Figure B-34: Hydraulic jacks supporting weight of RC block in intervals between simulation tests

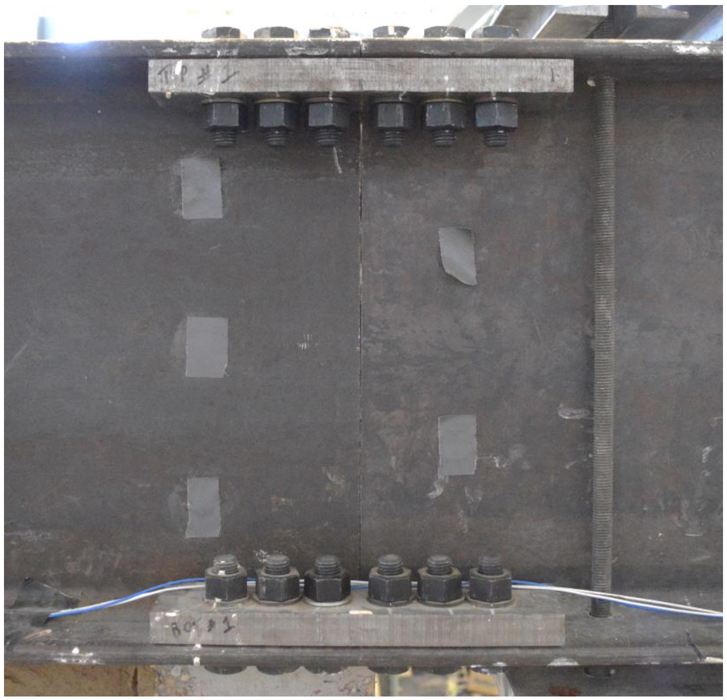

(a) Splice on east set of channels

(b) Top of top splice

(c) Top of bottom splice

Figure B-35: Splice detail

Figure B-36: Steel channels used to sandwich top beams of specimens

Figure B-37: Wide-flange steel beams used to flank foundation beams of specimens

Figure B-38: Steel channels used to strengthen simulator platform

Figure B-39: Initial two-swivel link allowing excessive play

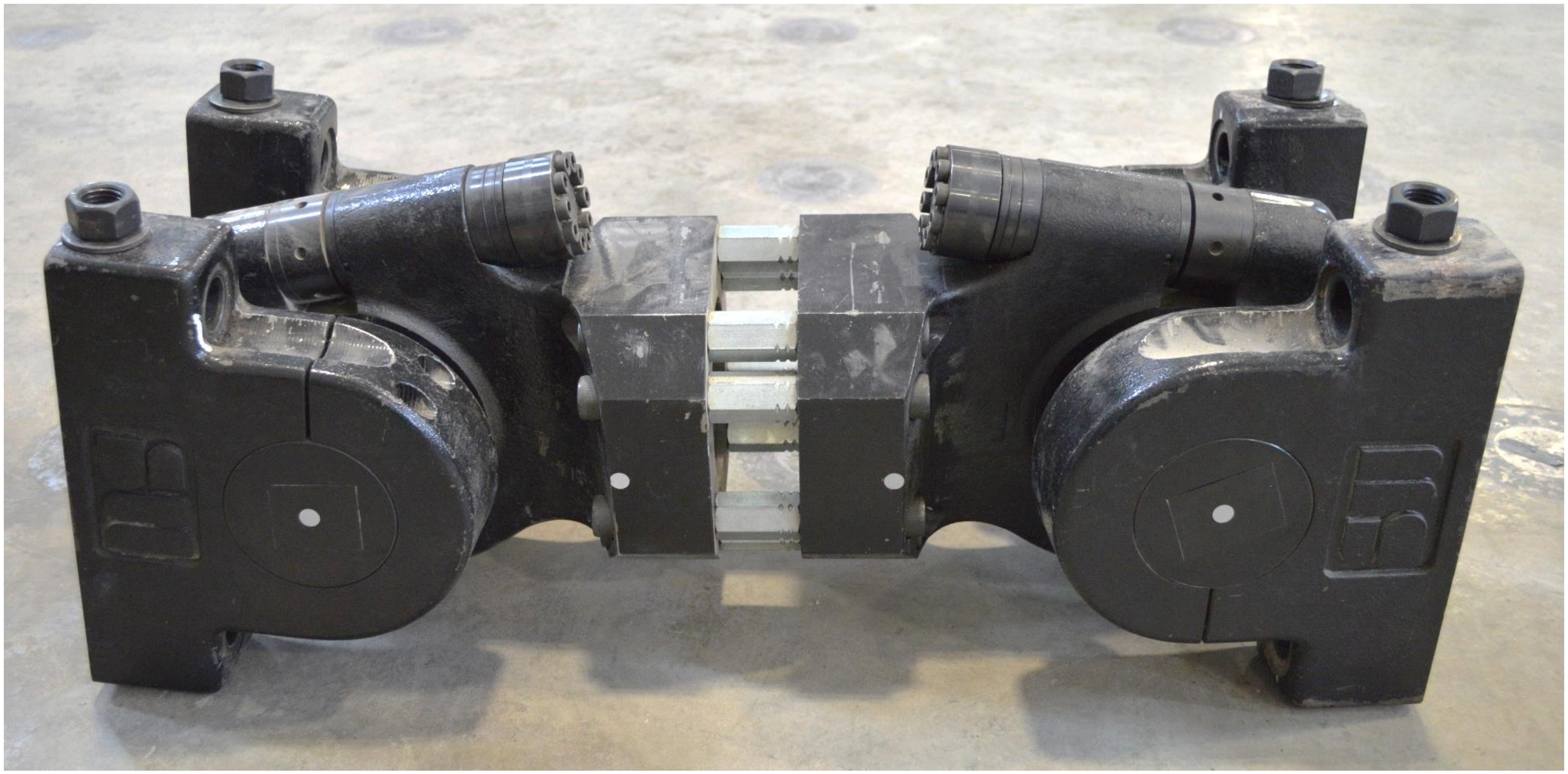

Figure B-40: Stiff two-swivel link reducing play

Shore Western

User Manual
Swivels

Models 980 thru 999

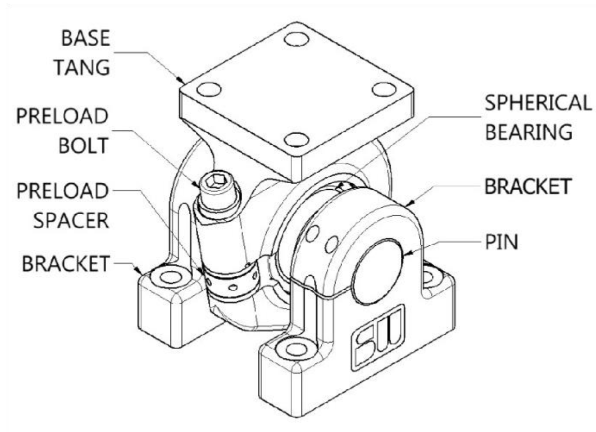

Specifications

Base End Swivels

Model Number	Force Rating Kip (KN)	Tilt Angle Degrees	Swivel Angle Degrees	Weight lbs (kg)
995 HT	110 (500)	±14	-35, +90	330 (150)

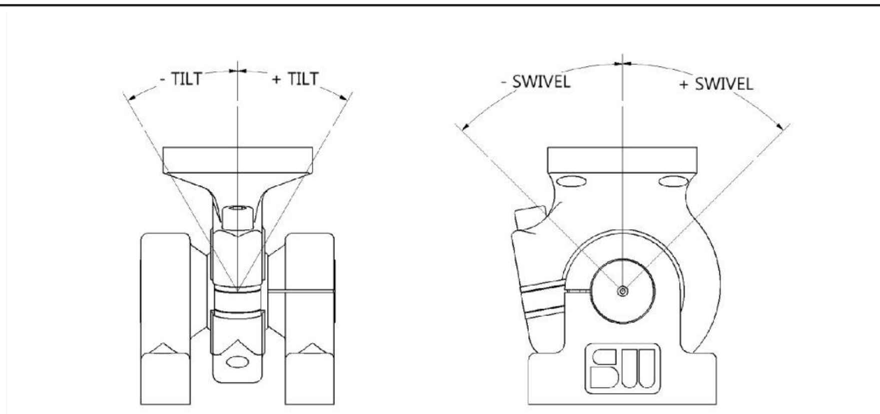

Figure B-41: Component description and dimensions of swivels used in link

APPENDIX C. DESCRIPTIONS OF ONE-STORY AND MULTISTORY RC STRUCTURES WITH AND WITHOUT INFILL

This appendix contains descriptions of the single and multiple-degree-of-freedom reinforced concrete structures with and without infill described in Section 5.10. Measurements of key parameters of the simulations and specimens listed in Table 5-11 and Table 5-12, and included in this appendix are taken from Shah (2021) unless noted otherwise. Details of the simulated motions are listed in Table C-1 through Table C-4. Measured initial fundamental periods of specimens with and without infill are given in Table C-5 and Table C-7. Photographs and drawings showing the test specimens and test setups are shown in Figure C-1 through Figure C-25. Each experiment is described next.

C.1 RC Structures without Infill

C.1.1 SDOF Tests

University of Illinois Urbana-Champaign

Takeda (1970) subjected a pair of reinforced concrete cantilevers to simulated motions modeled after the NS component of the 1940 El Centro earthquake and the N21E component of the 1952 Taft earthquake. The estimated effective mass and initial lateral stiffness of cantilevers were approximately 4200 lb and 85 kip/in. The height of the cantilever is taken as 24 in. measured from the top of foundation to center of mass of weights attached near the free end.

Gulkan (1971) built two types of one-story reinforced concrete bare frames and tested them in static and dynamic experiments. Series H specimens had one-half the linear dimensions of Series F specimens. Series H specimens and Series F specimens were subjected to simulated motions modeled after the NS component of the 1940 El Centro earthquake and the N21E component of the 1952 Taft earthquake. Estimates of effective mass and initial lateral stiffness of frames were approximately 690 lb and 80 kip/in. for Series H specimens and 4300 lb and 160 kip/in. for Series F specimens. The height of Series H frames is taken as 15.5 in. and the height of Series F frames is taken as 31 in. measured from top of foundation to center of mass of weights attached to top beam which were aligned along the centroidal axis of said beam for both series.

Bonacci (1989) tested single-degree-of-freedom oscillators. The response of specimens tested by Bonacci was idealized as that of an inverted pendulum comprised of a lumped weight (steel plates) connected to a flexural spring (reinforced concrete beam) by a weightless rod (stocky reinforced concrete panel). The derivation of the initial lateral stiffness of specimens tested by Bonacci is illustrated in Figure C-7.

Simulated motions were modeled after the NS component of the 1940 El Centro earthquake, the S48E component of the 1952 Taft (Santa Barbara) earthquake, and the N21E component of the 1971 San Fernando (Castaic) earthquake. Estimates of initial lateral stiffnesses of the fifteen specimens tested by Bonacci ranged from approximately 25 to 65 kip/in. Heights of specimens were taken to be between 49 and 61 in. measured from center of rotation (at pinned connection of base of panel) to effective center of mass of steel weights attached near top of RC panel. Clear lengths and total lengths (clear length plus half of width of RC panel) of reinforced concrete beams were taken to be between 30-42 in. and 45-57 in. Estimated initial periods ranged between 0.08 and 0.15 seconds.

University of California, San Diego

A full-scale 24-ft. tall reinforced concrete bridge column was subjected to ten simulated base motions on the George E. Brown, Jr. Network for Earthquake Engineering Simulation's earthquake simulator housed at the University of California, San Diego (UCSD). Five of the mentioned simulations were modeled after one of three records obtained during the 1989 Loma Prieta earthquake and resulted in measured drift demands ranging between approximately 1% and 6% (Schoettler, Restrepo, Guerrini, Duck, & Carrea, 2015). Each simulation had a time-compression factor (F_{tc}) equal to unity.

The single-degree-of-freedom system consisted of a circular column with a diameter of 4 ft. and a concrete block weighing over 500 kips cast on and clamped to the top portion of the column to ensure nonlinear response. The initial lateral stiffness of the column estimated as the lateral stiffness of a cantilever with a transverse load applied 24 ft. above the top of the foundation was approximately 100 kip/in.

Purdue University

Laughery (2016) built and tested four one-story reinforced concrete bare frames. Simulations were modeled after the EW component of the 1994 Northridge (Roscoe) earthquake. Estimates of effective mass and initial lateral stiffness of frames were approximately 5,000 lb and 33 kip/in. The height of frames is taken as 47 in. measured from top of foundation to mid-depth of top beam.

C.1.2 MDOF Tests

University of Illinois Urbana-Champaign

Aristizabal (1976) tested reduced-scale ten-story reinforced concrete specimens comprising two frames oriented in the direction of motion with each frame made up of two walls connected at each level by beams. Two types of frames were built, type-D and type-M, with different amounts of beam reinforcement. Specimens were subjected to simulated base motions on the earthquake simulator housed formerly at the University of Illinois Urbana-Champaign (UIUC). Simulations were modeled after the NS component of the 1940 El Centro earthquake. Each simulation was scaled in time by a factor of 2.5.

Healey (1978) subjected a reduced-scale ten-story reinforced concrete specimen comprising two frames oriented in the direction of motion to simulated base motions. Story heights of the first and tenth stories were 20% taller than those of the remaining stories. Simulations were modeled after the NS component of the 1940 El Centro earthquake. Each simulation was scaled in time by a factor of 2.5.

Moehle (1978) subjected a reduced-scale ten-story reinforced concrete specimen comprising two frames oriented in the direction of motion to simulated base motions. A first-level beam was discontinued in one bay of each frame creating two first-story columns to be nearly twice as tall as the other columns. Simulations were modeled after the NS component of the 1940 El Centro earthquake. Each simulation was scaled in time by a factor of 2.5.

Cecen (1979) subjected reduced-scale ten-story reinforced concrete specimens comprising two frames oriented in the direction of motion to simulated base motions. The frames were designed to be regular meaning there were no discontinuities in lateral stiffness and heights of each story were the same. Simulations were modeled after the NS component of the 1940 El Centro earthquake. Each simulation was scaled in time by a factor of 2.5.

Moehle (1980) subjected reduced-scale nine-story reinforced concrete specimens comprising two frames and a single wall oriented in the direction of motion to simulated base motions. Four types of frames were built with different wall configurations. Specimen FNW had no wall, Specimen FSW had a one-story “stub” wall, Specimen FHW had a four-story “half” wall, and Specimen FFW had a nine-story full-height wall. Simulations were modeled after the NS component of the 1940 El Centro earthquake. Each simulation was scaled in time by a factor of 2.5.

Wolfgram (1984) subjected one-tenth-scale seven-story reinforced concrete specimens comprising two exterior frames and one interior frame with a wall oriented in the direction of motion to simulated base motions. Three types of frames were built with different amounts of beam reinforcement and concrete strength. Simulations were modeled after the NS component of the 1978 Miyagi-ken-oki earthquake and the N21E component of the 1952 Taft earthquake. Each simulation was scaled in time by a factor of 5.

Wood (1985) subjected reduced-scale nine-story reinforced concrete specimens comprising two frames with setbacks oriented in the direction of motion to simulated base motions (Wood, 1985). Two types of frames were built, a symmetrical “tower” structure and an asymmetrical “stepped” structure defined relative to the centerline of the foundation. Simulations were modeled after the NS component of the 1940 El Centro earthquake. Each simulation was scaled in time by a factor of 2.5.

Schultz (1986) subjected reduced-scale nine-story reinforced concrete specimens comprising two frames oriented in the direction of motion to simulated base motions. Two types of frames were built with different amounts of column longitudinal reinforcement. Simulations were modeled after the NS component of the 1940 El Centro earthquake. Each simulation was scaled in time by a factor of 2.5.

Eberhard (1989) subjected reduced-scale nine-story reinforced concrete specimens comprising two frames with slender walls oriented in the direction of motion to simulated base motions. Two types of frames were built with different amounts of column reinforcement. Simulations were modeled after the NS component of the 1940 El Centro earthquake. Each simulation was scaled in time by a factor of 2.5.

University of California, Berkeley

Shahrooz (1987) subjected a one-fourth-scale six-story reinforced concrete frame specimen with a setback to simulated base motions on the earthquake simulator housed at the Earthquake Engineering Research Center of the University of California, Berkeley. The specimen was subjected to unidirectional and bidirectional simulations. Simulations were modeled after the NS component of the 1940 El Centro earthquake, the NS component of the 1978 Miyagi-ken-oki earthquake, and the S60E component of the 1985 Mexico City earthquake. Each simulation was scaled in time by a factor of 2 except for the 1985 Mexico City record which was scaled in time by a factor of 3.

E-Defense

The National Research Institute for Earth Science and Disaster Resilience (NIED) subjected full-scale ten-story reinforced concrete frame and wall specimens to simulated base motions on the E-Defense, a full-scale earthquake simulator housed in Miki, Japan (Kajiwara, et al., 2017). Specimens were subjected to simulations in three directions modeled after the NS, EW, and vertical components of the 1995 Kobe earthquake. Each simulation had a time-compression factor equal to unity.

C.2 RC Structures with Infill

C.2.1 SDOF Tests

University of Granada

Benavent-Climent (2018) subjected a one-bay by two-bay, one-story infilled reinforced concrete frame structure to a series of four simulated motions based on a record of the NS component of the 1980 Campano-Lucano (Italy) earthquake. Estimates of effective mass and initial lateral stiffness of the infilled frame were approximately 27,000 lb and 280 kip/in. Because of the configuration used for the additional weight applied to the specimen, the height of infilled frames is taken as approximately 69 in. to coincide with the center of mass of infilled frame and added mass system instead of the height of columns measured from top of foundation to mid-depth of top beam (which was approximately 55 in.). The estimated initial period was approximately 0.05 seconds.

C.2.2 MDOF Tests

Korea University

Lee (2002) subjected a three-story infilled reinforced concrete frame to two series (FIF and PIF) of simulated motions based on a record of the N21E component of the 1952 Taft earthquake. Estimates of effective masses of the specimen tested in FIF and PIF series were 27,500 and 26,500 lb and estimates of initial lateral stiffnesses were 145 and 70 kip/in. The height of the specimen is taken as approximately 87.5 in. measured from top of foundation to roof. Initial periods were estimated to be 0.07 and 0.10 seconds for the specimen tested in FIF and PIF series.

University of California, San Diego

Stavridis (2009) subjected a three-story reinforced concrete frame with masonry infill walls to simulations based on a record of the NS component of the 1989 Loma Prieta earthquake. The effective mass was estimated to be 145,000 lb and the estimated initial lateral stiffness was approximately 235 kip/in. The height of the specimen is taken as approximately 257 in. measured from top of foundation to roof. The initial period was estimated to be 0.10 seconds.

Josip Juraj Strossmayer University of Osijek

Guljas (2020) tested a three-story reinforced concrete frame with masonry infill walls. Motions based on a record of the NS component of the 1979 Montenegro earthquake were used in simulations in two series of tests (S1 and S2). The estimated effective mass of the specimen was approximately 54,000 lb. Estimates of initial lateral stiffness of infilled frames tested in S1 and S2 were approximately 65 and 410 kip/in. The height of specimens is taken as approximately 142 in. measured from top of foundation to roof. Estimates of initial periods of infilled frames tested in S1 and S2 were 0.14 and 0.06 seconds.

Table C-1: Simulated base motions used for SDOF specimens

Source, Year	Location	Specimen, Run	Ground motion	Component	Time-compression factor (F_{tc})
Takeda, 1970	UIUC	T2-11	1940 El Centro	NS	8.0
		T2-12	1940 El Centro	NS	16
		T5-21	1952 Taft	N21E	10
Gulkan, 1971	UIUC	Series-H	1940 El Centro	NS	8.0
		Series-F	1952 Taft	N21E	5.0
Bonacci, 1989	UIUC	B-01-B-05, B-10	1940 El Centro	NS	2.0
		B-06, B-11-B-12	1971 San Fernando (Castaic)	N21E	2.0
		B-07-B-09, B-13-B-15	1952 Taft (Santa Barbara)	S48E	2.0
Schoettler, 2015	UCSD	EQ1	1989 Loma Prieta (Agnew State Hospital)	EW	1.0
		EQ2	1989 Loma Prieta (Corralitos)	EW	1.0
		EQ3	1989 Loma Prieta (LGPC)	NS	1.0
		EQ4	1989 Loma Prieta (Corralitos)	EW	1.0
		EQ6	1989 Loma Prieta (LGPC)	NS	1.0
Laughery, 2016	Purdue University	All runs	1994 Northridge (Roscoe)	EW	3.0

Table C-2: Simulated base motions used for MDOF specimens tested at University of Illinois Urbana-Champaign

Source, Year	Specimen, Run	Ground motion	Component	Time-compression factor (F_{tc})
Aristizabal, 1976	All runs	1940 El Centro	NS	2.5
Healey, 1978	All runs	1940 El Centro	NS	2.5
Moehle, 1978	All runs	1940 El Centro	NS	2.5
Cecen, 1979	All runs	1940 El Centro	NS	2.5
Moehle, 1980	All runs	1940 El Centro	NS	2.5
Wolfgram, 1984	NS2-1	1978 Miyagi-ken-oki	NS	5.0
	NS3-1			
	NS3-2			
	NS3-3	1952 Taft	N21E	5.0
Wood, 1985	All runs	1940 El Centro	NS	2.5
Schultz, 1986	All runs	1940 El Centro	NS	2.5
Eberhard, 1989	All runs	1940 El Centro	NS	2.5

Table C-3: Simulated base motions used for MDOF specimen tested at the University of California, Berkeley

Source, Year	Specimen, Run	Ground motion	Component	Time-compression factor (F_{tc})
Shahrooz, 1987	Long-1	1940 El Centro	NS	2.0
	Long-2			
	Long-3			
	Long-4			
	Long-5	1978 Miyagi-ken-oki	NS	2.0
	Long-6	1985 Mexico City	S60E	3.0
	Short-4	1940 El Centro	NS	2.0
	Short-5	1978 Miyagi-ken-oki	NS	2.0
	Short-6	1985 Mexico City	S60E	3.0

Table C-4: Simulated base motions used for MDOF specimens tested on the E-Defense

Source, Year	Specimen, Run	Ground motion	Component	Time-compression factor (F_{tc})
	Frame-1			
	Frame-2			
	Frame-3	1995 Kobe (JMA)	NS	1.0
	Frame-4			
	Frame-5			
Kajiwara, 2015	Wall-1			
	Wall-2			
	Wall-3	1995 Kobe (JMA)	EW	1.0
	Wall-4			
	Wall-5			
	Frame-1			
	Frame-2			
	Frame-3	1995 Kobe (JMA)	NS	1.0
	Frame-4			
	Frame-5			
Kajiwara, 2018	Frame-6	1995 Kobe (JMA)	EW	1.0
	Wall-1			
	Wall-2			
	Wall-3	1995 Kobe (JMA)	EW	1.0
	Wall-4			
	Wall-5			
	Wall-6	1995 Kobe (JMA)	NS	1.0

Table C-5: Measured periods of SDOF specimens without infill

Source, Year	Specimen	Measured T_o[1], sec.
Takeda, 1970	T2	0.10
	T5	0.07
Gulkan, 1971	HE1	0.04
	HE2	0.04
	FE1	0.06
	FE2	0.06
Bonacci, 1989	B-01	0.11
	B-02	0.15
	B-03	0.11
	B-04	0.19
	B-05	0.18
	B-06	0.17
	B-07	0.18
	B-08	0.17
	B-09	0.15
	B-10	0.21
	B-11	0.11
	B-12	0.14
	B-13	0.11
	B-14	0.12
	B-15	0.16
Schoettler*, 2015		0.79
Laughery, 2016	C1	0.16
	C2	0.16
	H1	0.13
	H2	0.13

* Measured initial period of specimen tested by Schoettler (2015) is taken from Shah (2021).

[1] Measured initial fundamental period of specimen as reported by source

Table C-6: Measured periods of MDOF specimens without infill

Source, Year	Specimen	Measured T_o[1], sec.
Aristizabal, 1976	D1	0.22
	M1	0.22
Healey, 1978	MF1	0.31
Moehle, 1978	MF2	0.22
Cecen, 1979	H1	0.33
	H2	0.23
Moehle, 1980	FFW	0.20
	FHW	0.20
	FNW	0.25
	FSW	0.20
Wolfgram, 1984	NS2	0.09
	NS3	0.10
Wood, 1985	TW	0.18
	STP	0.17
Schultz, 1986	SS1	0.26
	SS2	0.22
Shahrooz, 1987	Long	0.27
	Short	0.25
Eberhard, 1989	ES1	0.18
	ES2	0.16
Kajiwara, 2015	Frame	0.56
	Wall	0.56
Kajiwara, 2018	Frame	0.53
	Wall	0.42

[1] Measured initial fundamental period of specimen as reported by Shah (2021)

Table C-7: Measured periods of SDOF and MDOF specimens with infill

Source, Year	Specimen	Measured T_o[1], sec.
Lee, 2002	FIF	0.06
	PIF	0.17
	BF	0.23
Stavridis, 2009		0.06
Benavent, 2018		0.09
Guljas, 2020	S1	0.11
	S2	0.13

[1] Measured initial fundamental period of specimen as reported by source

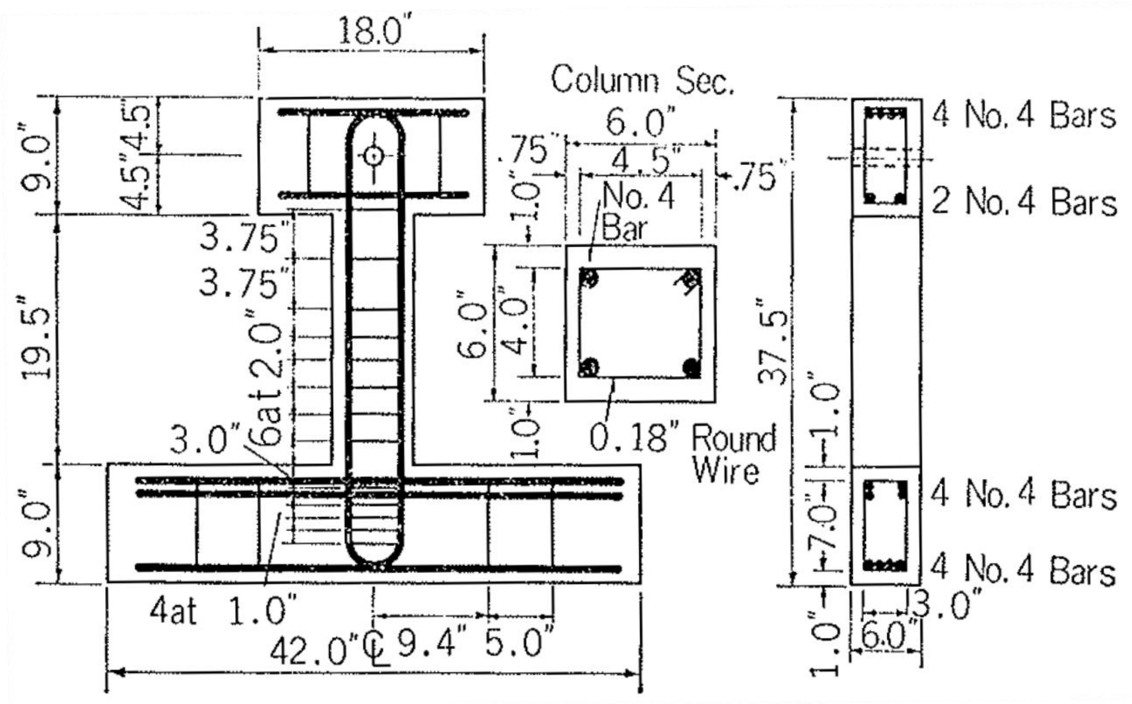

(a) Elevation of test specimens

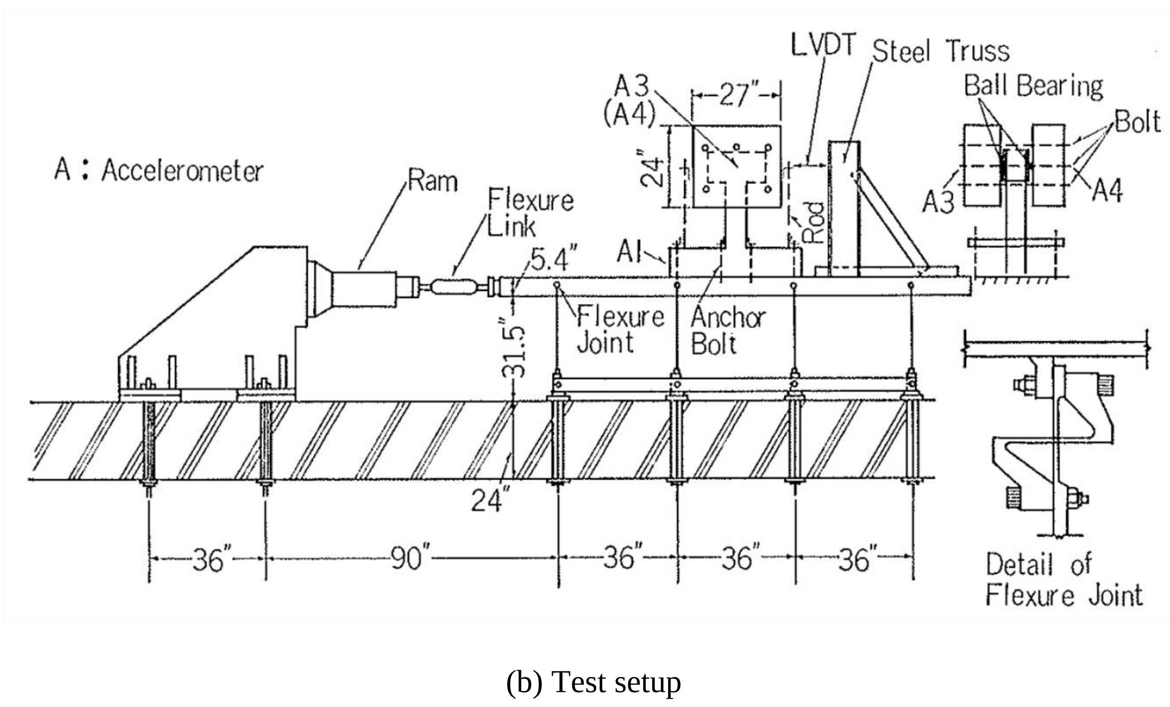

(b) Test setup

Figure C-1: Reinforced concrete cantilever specimens tested by Takeda (1970)

Note: Figures are taken from Takeda (1970).

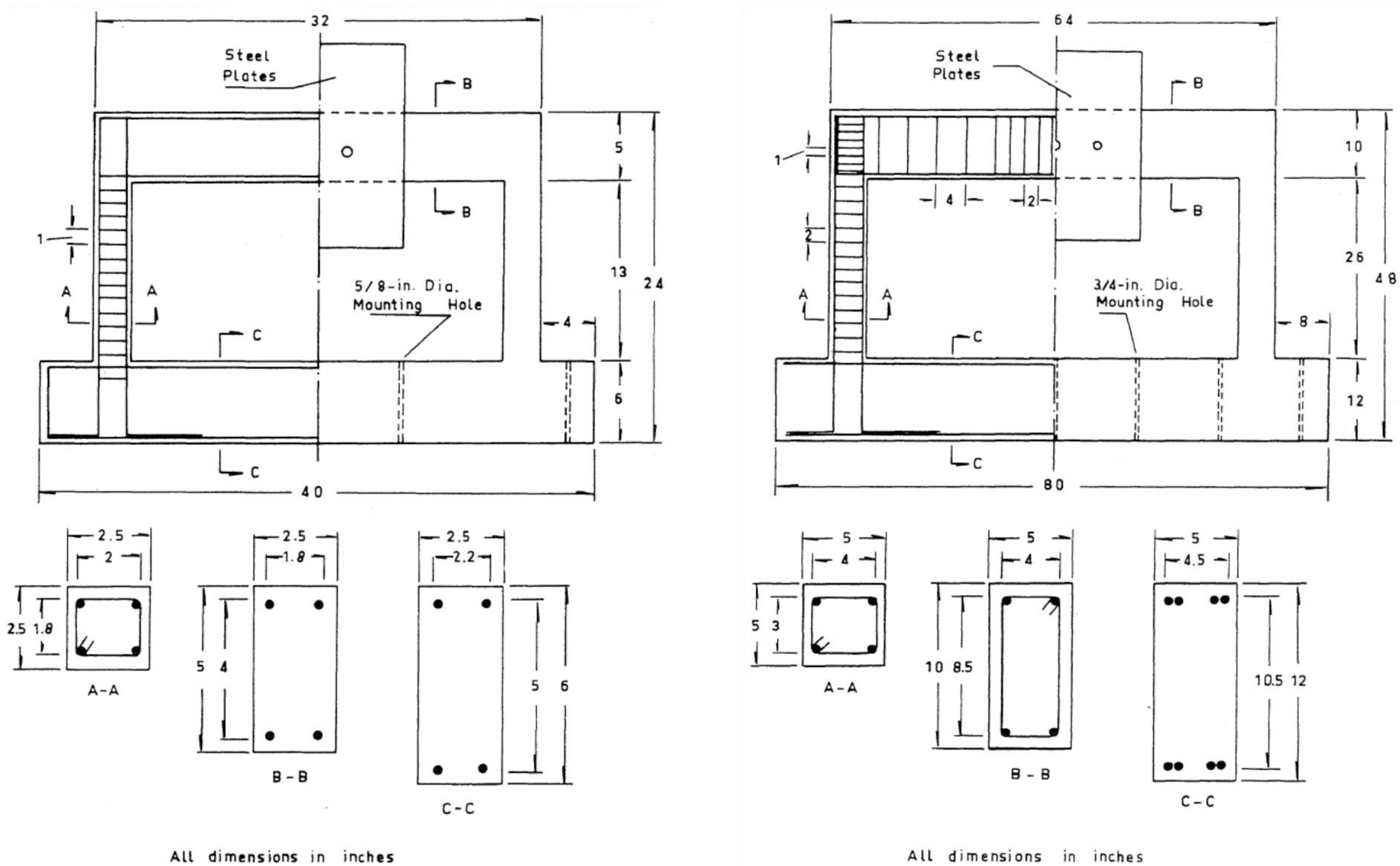

(a) Series H specimens (b) Series F specimens

Figure C-2: Elevations of reinforced concrete frame specimens tested by Gulkan (1971)

Note: Figures are taken from Gulkan (1971).

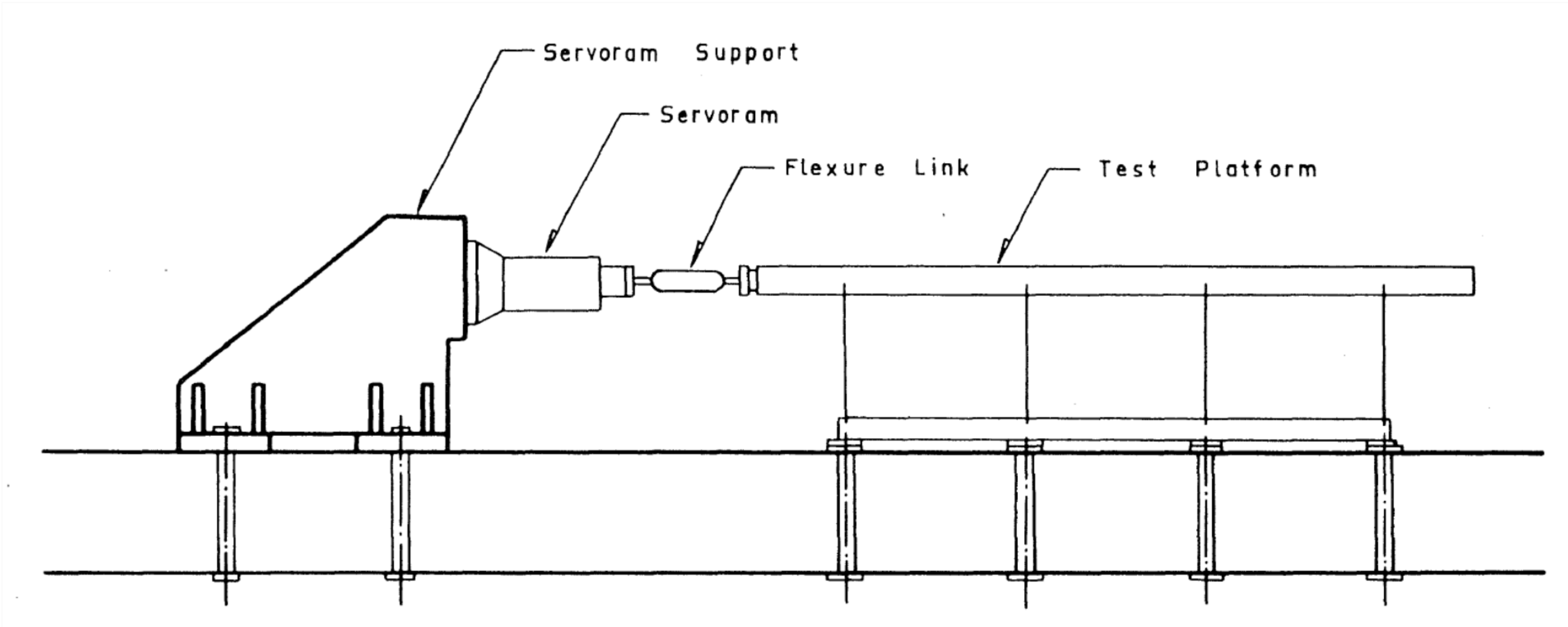

Figure C-3: Elevation of earthquake simulator used in tests done by Gulkan (1971)

Note: Figure is taken from Gulkan (1971).

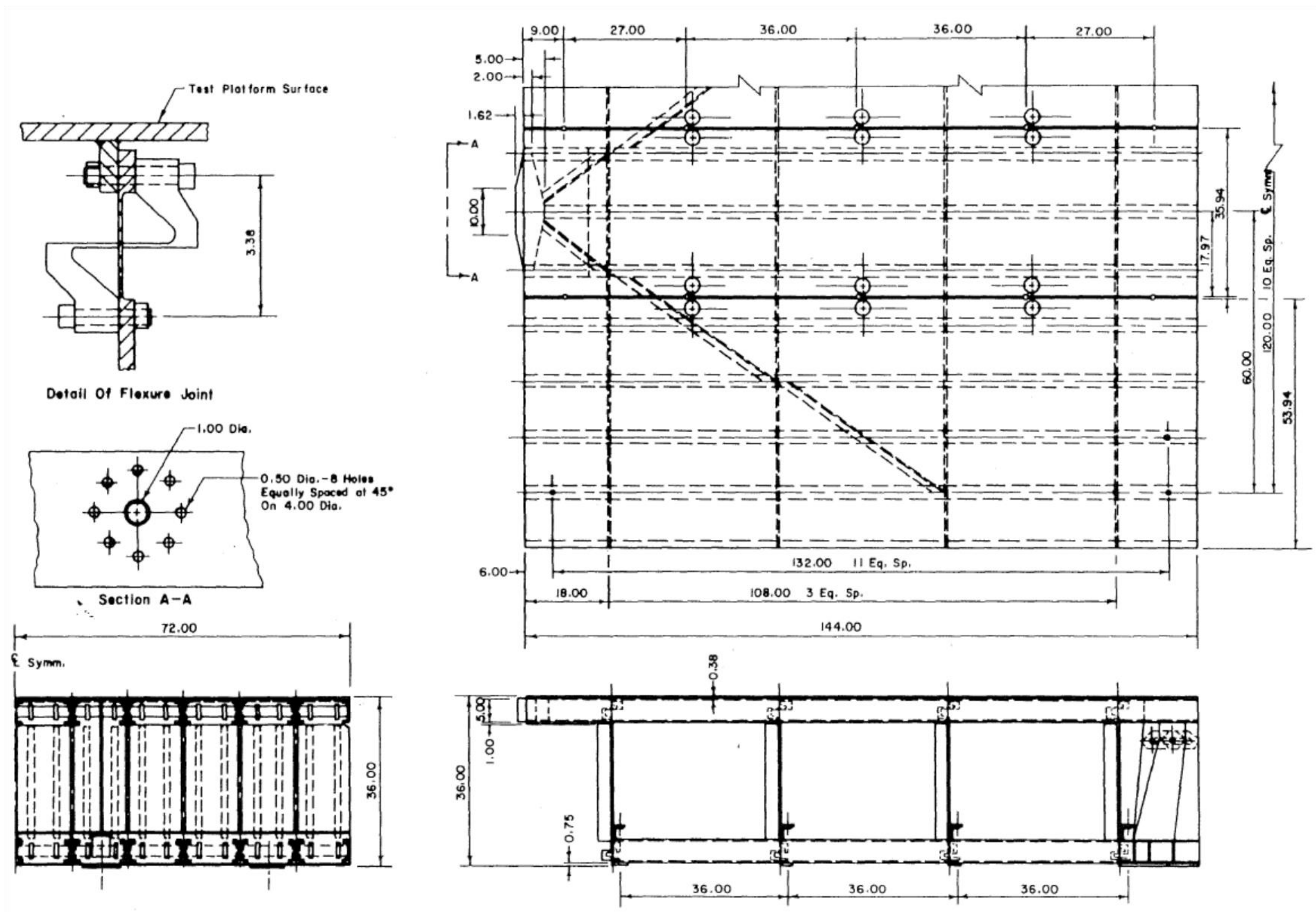

Figure C-4: Structural components of earthquake simulator used in tests done by Gulkan (1971)

Note: Figure is taken from Gulkan (1971).

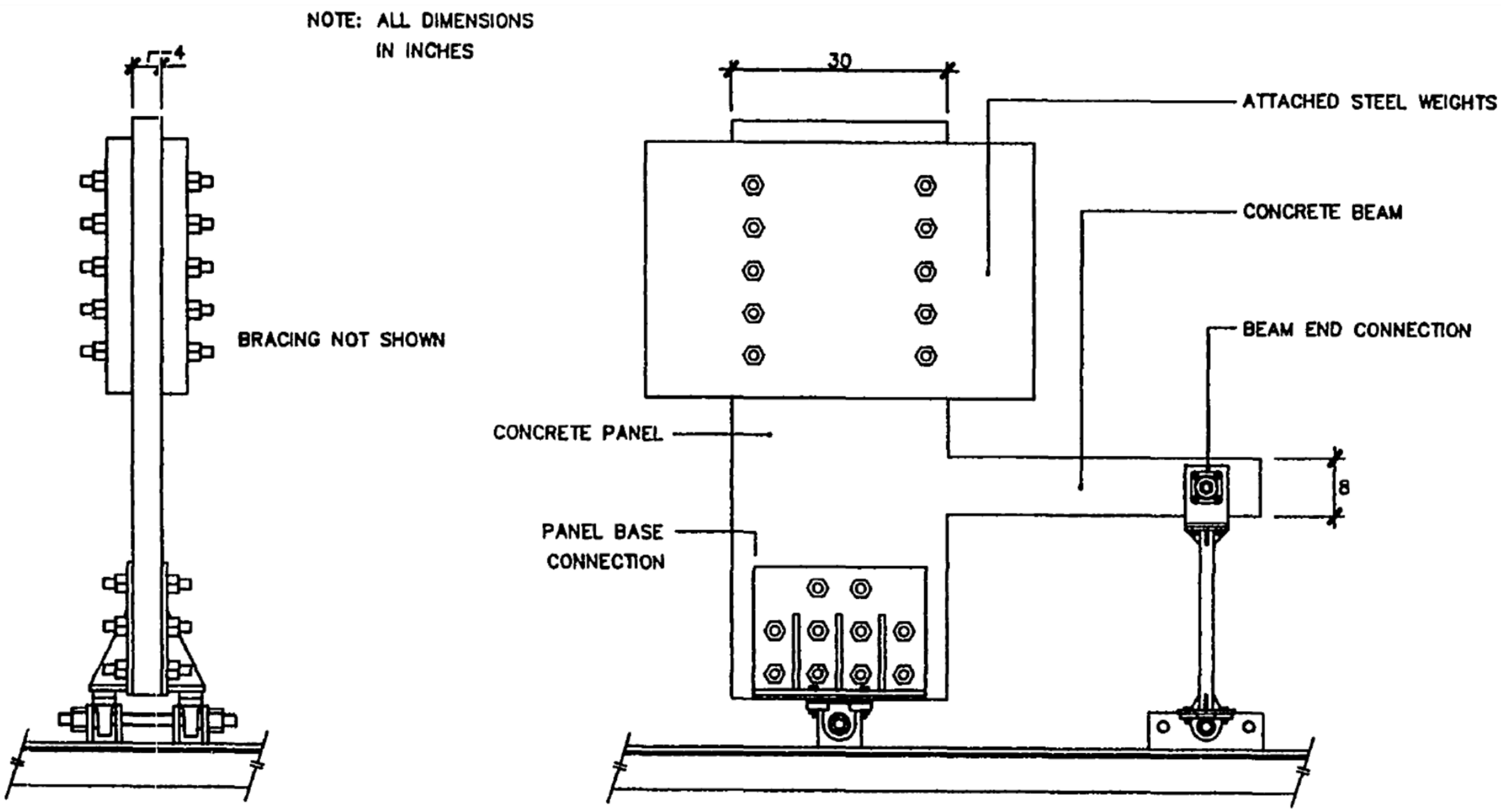

Figure C-5: Elevation of typical specimen tested by Bonacci (1989)

Note: Figure is taken from Bonacci (1989).

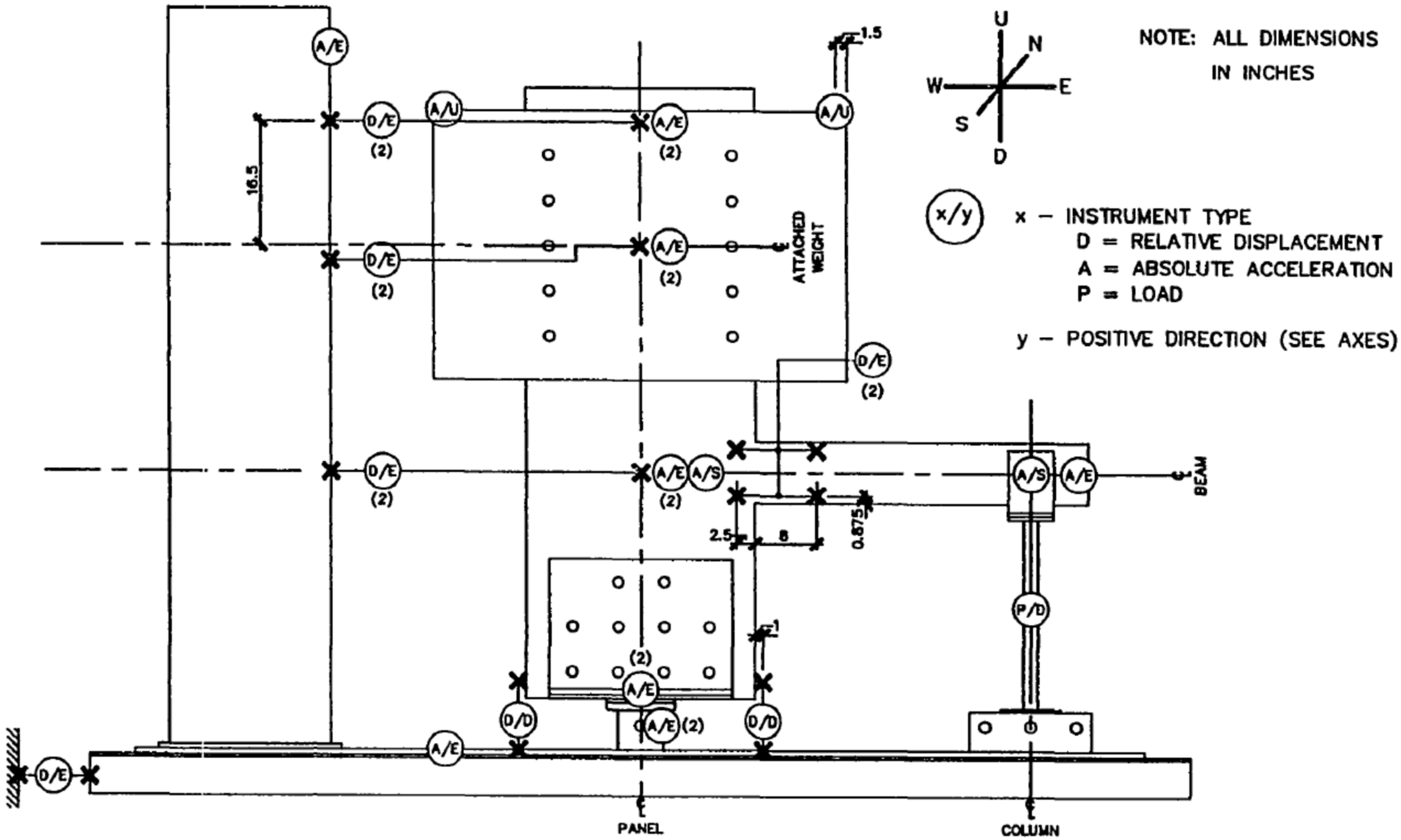

Figure C-6: Instrumentation layout of specimens tested by Bonacci (1989)

Note: Figure is taken from Bonacci (1989).

Free Body Diagram

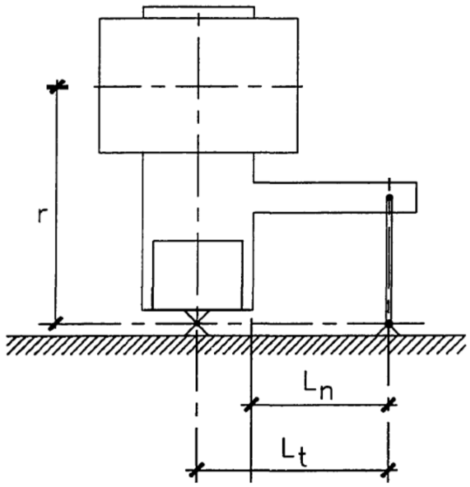

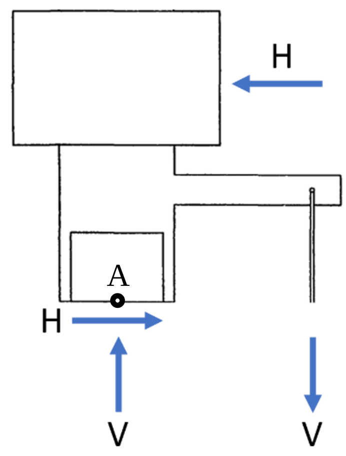

$$\sum M_A = H * r - V * L_t = 0$$

$$\boxed{H * r = V * L_t}$$

Virtual Work

External Work

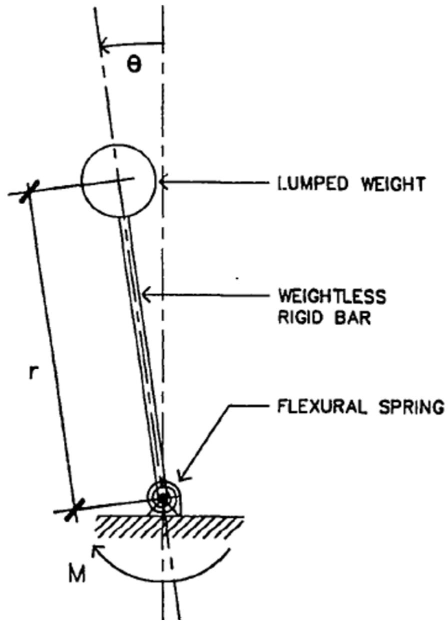

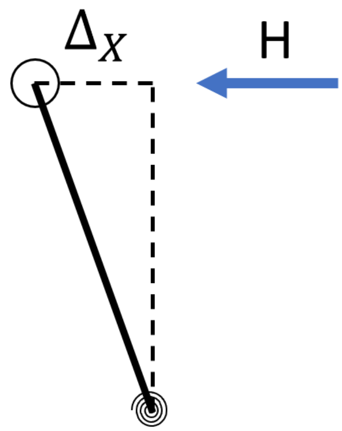

$$\boxed{EW = H * \Delta_X}$$

Figure C-7: Derivation of initial lateral stiffness of specimens tested by Bonacci (1989)

Internal Work

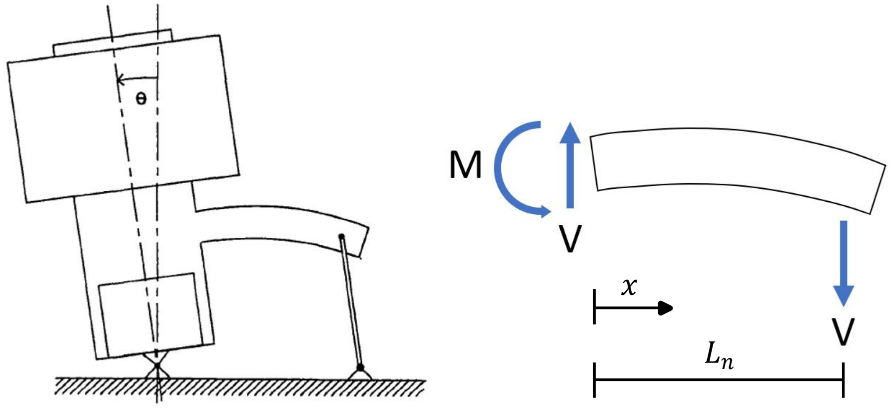

$$IW = \int_0^{L_n} \frac{V}{EI} * (L_n - x) * H * \frac{r}{L_t} * (L_n - x)\, dx$$

$$IW = \frac{VH}{EI} * \frac{r}{L_t} * \int_0^{L_n} (L_n - x)^2\, dx$$

$$IW = \frac{VH}{EI} * \frac{r}{L_t} * \int_0^{L_n} ({L_n}^2 - 2 * L_n * x + x^2)\, dx$$

$$IW = \frac{VH}{EI} * \frac{r}{L_t} * ({L_n}^2 * x - 2 * L_n * \frac{x^2}{2} + \frac{x^3}{3})\Big|_{x=0}^{x=L_n}$$

$$\boxed{IW = \frac{VH}{EI} * \frac{r}{L_t} * \frac{{L_n}^3}{3}}$$

$$\boldsymbol{EW = IW}$$

$$H * \Delta_X = \frac{VH}{EI} * \frac{r}{L_t} * \frac{{L_n}^3}{3}$$

$$\frac{V}{\Delta_X} = \frac{3EI}{{L_n}^3} * \frac{L_t}{r}$$

$$\boxed{K_o = \frac{H}{\Delta_X} = \frac{3EI}{{L_n}^3} * \left(\frac{L_t}{r}\right)^2}$$

Figure C-7 (cont.): Derivation of initial lateral stiffness of specimens tested by Bonacci (1989)

Note: Figures are taken from Bonacci (1989).

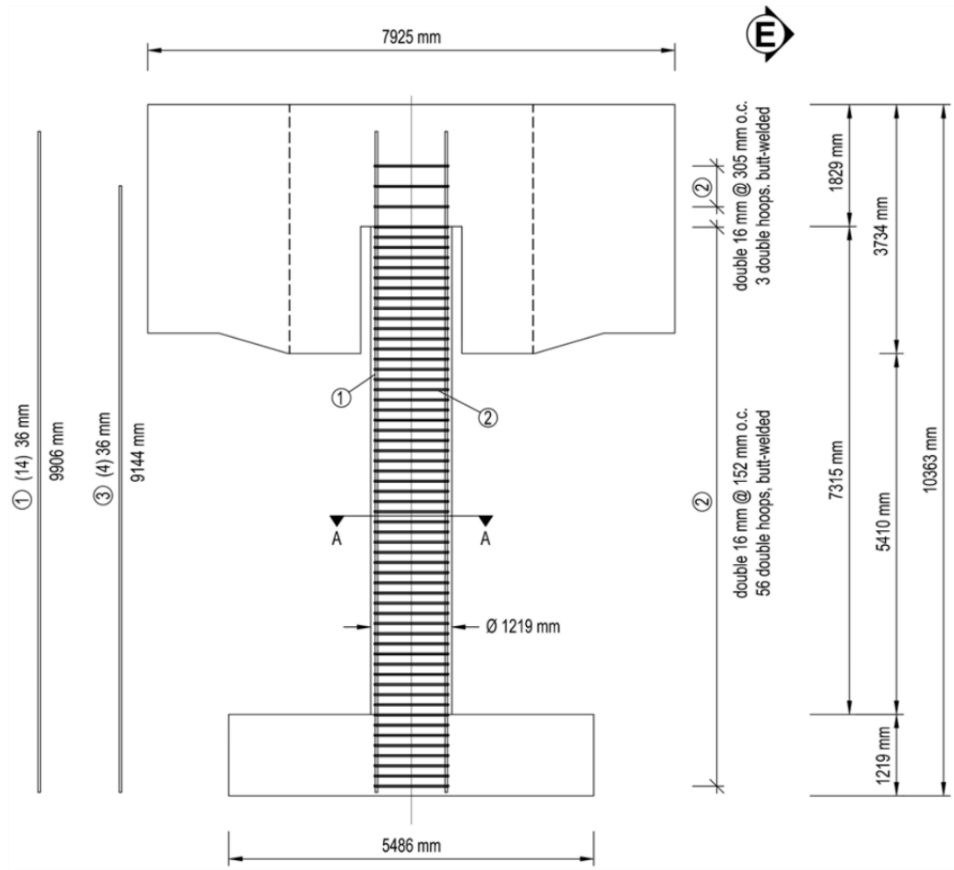

(a) Elevation of test specimen

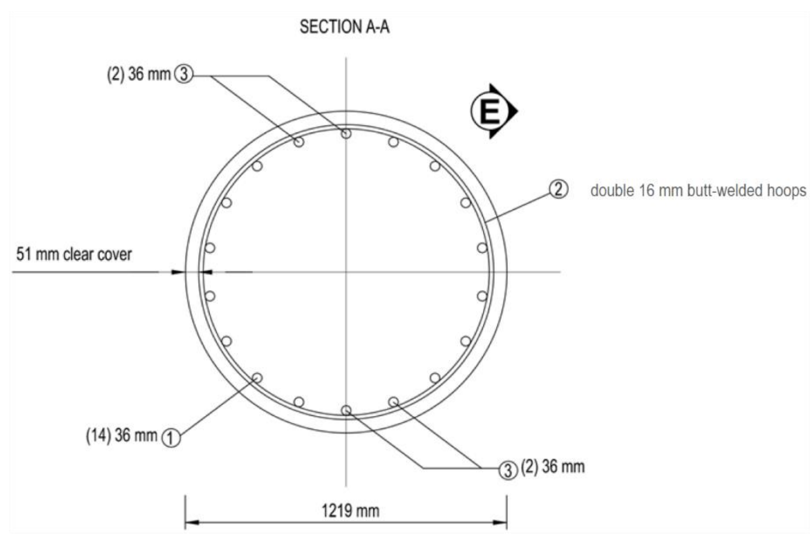

(b) Cross section of column

Figure C-8: Reinforced concrete bridge column tested by Schoettler (2015) at UCSD

Note: Figures are taken from Schoettler (2015).

(a) Isometric of test specimen

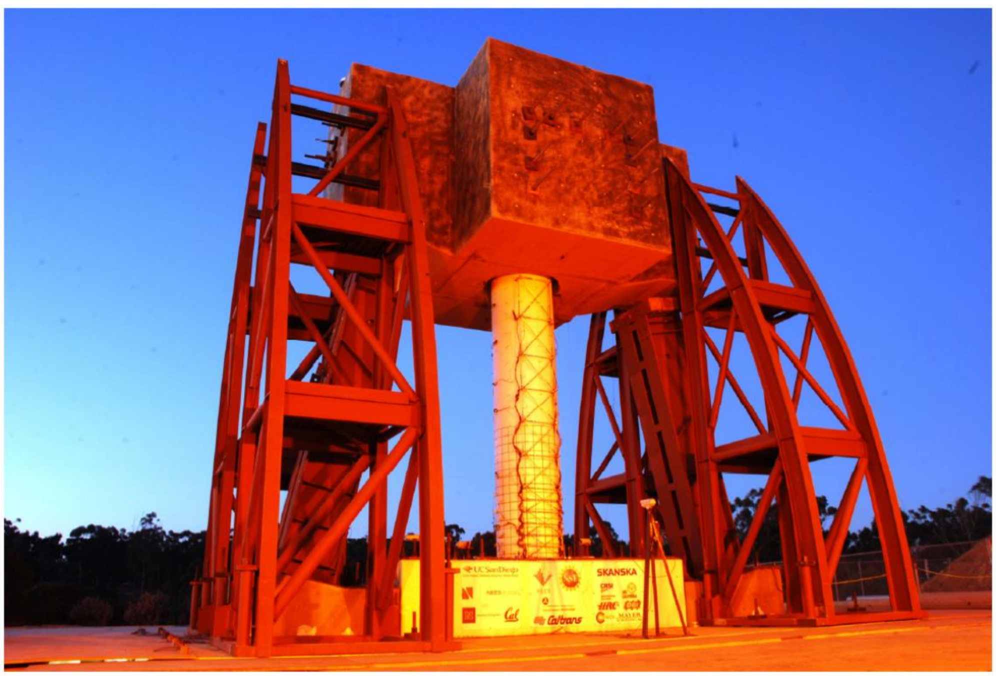

(b) Test setup

Figure C-9: Reinforced concrete bridge column tested by Schoettler (2015) at UCSD

Note: Photographs are taken from Schoettler (2015).

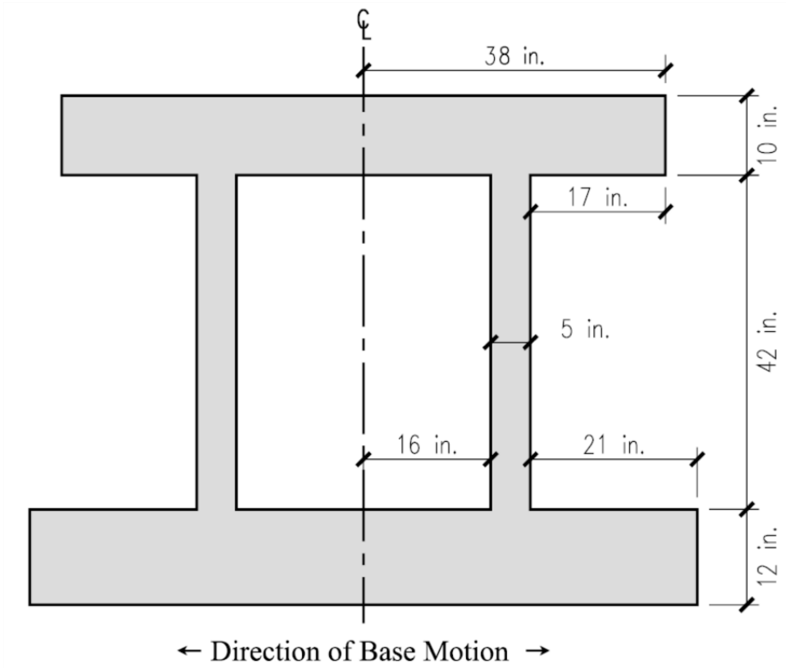

(a) Elevation of test specimens

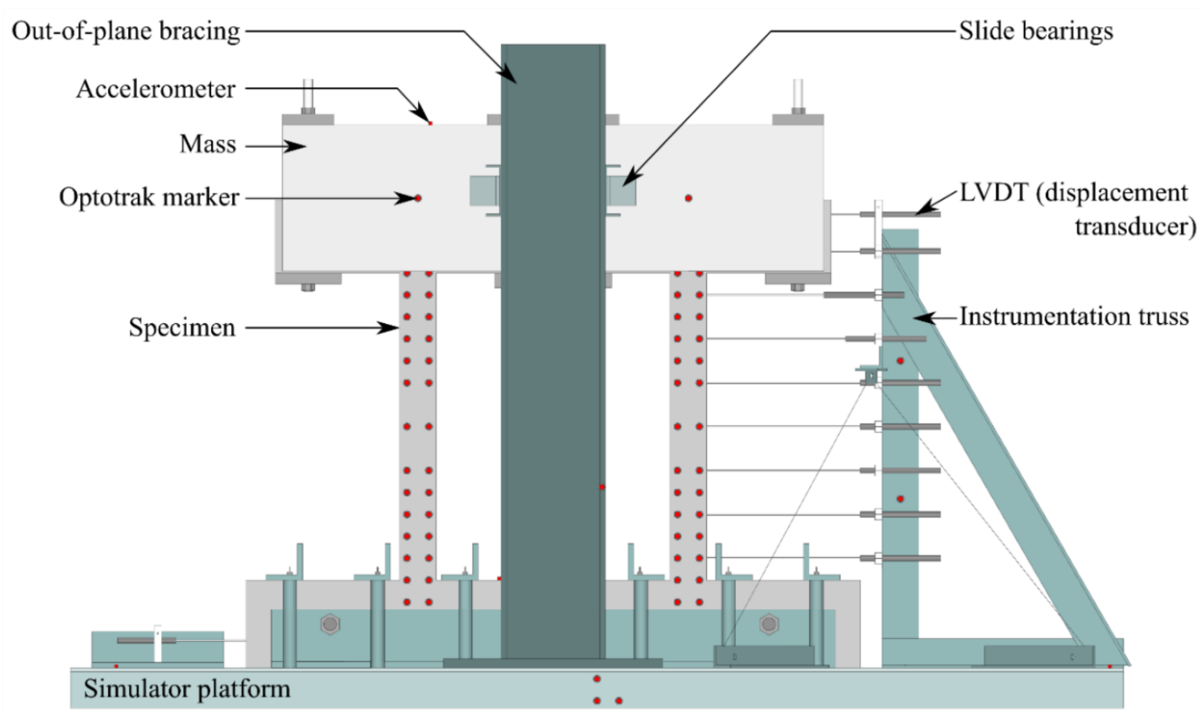

(b) Test setup

Figure C-10: Reinforced concrete frames tested by Laughery (2016) at Purdue University

Note: Figures are taken from Laughery (2016).

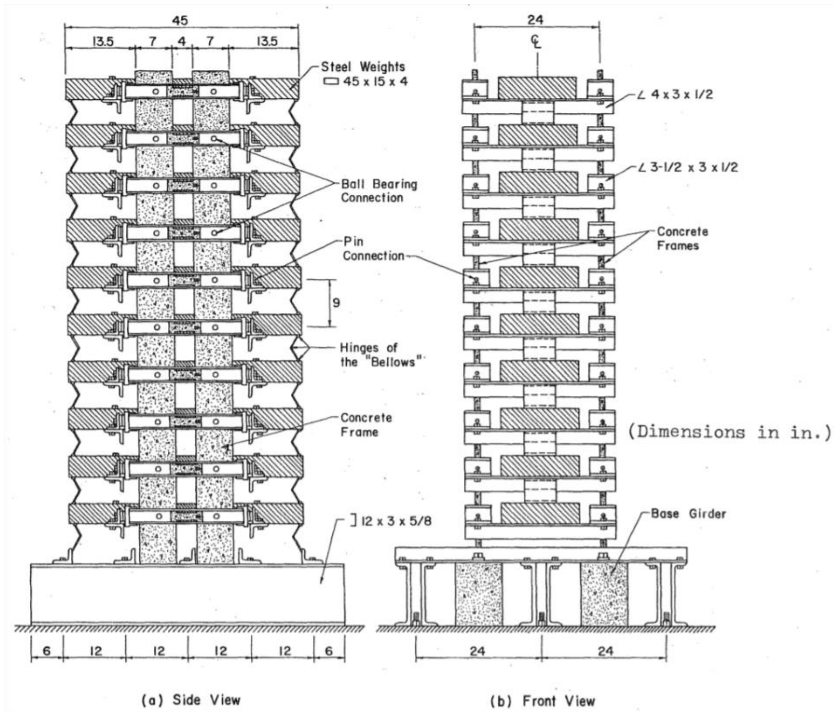

(a) Elevation of test specimens

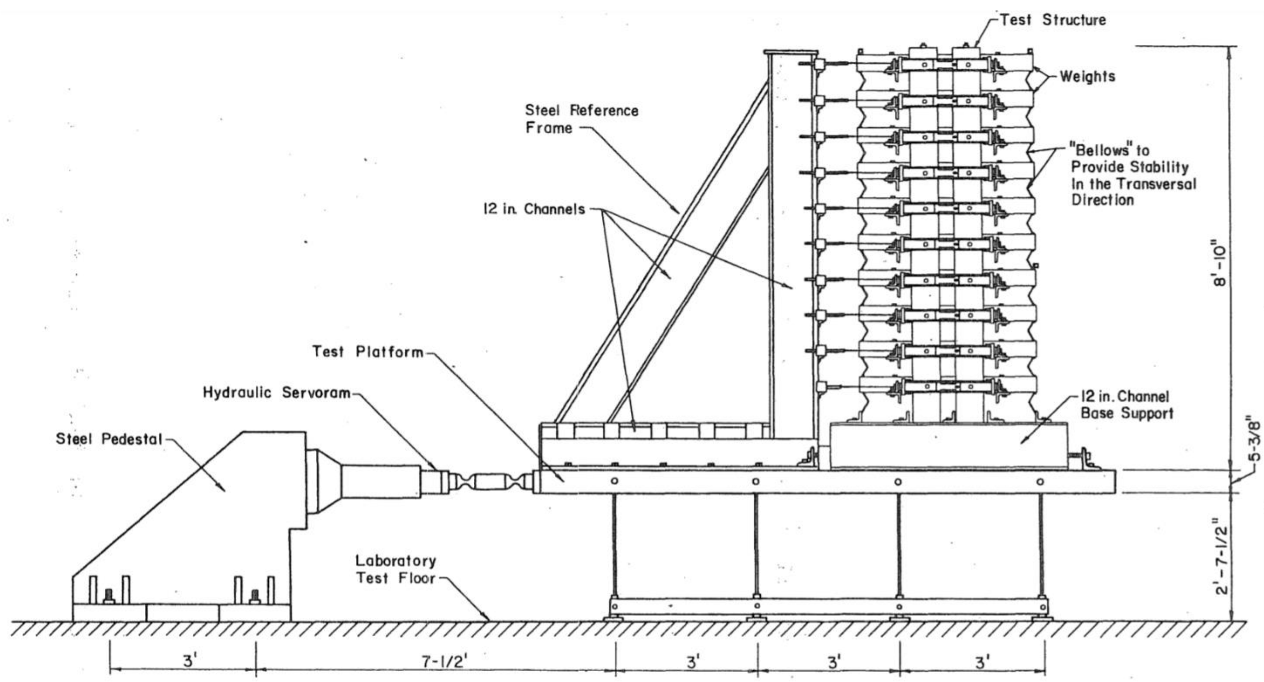

(b) Test setup

Figure C-11: Ten-story reinforced concrete wall specimens tested by Aristizabal (1976)

Note: Figures are taken from Aristizabal (1976).

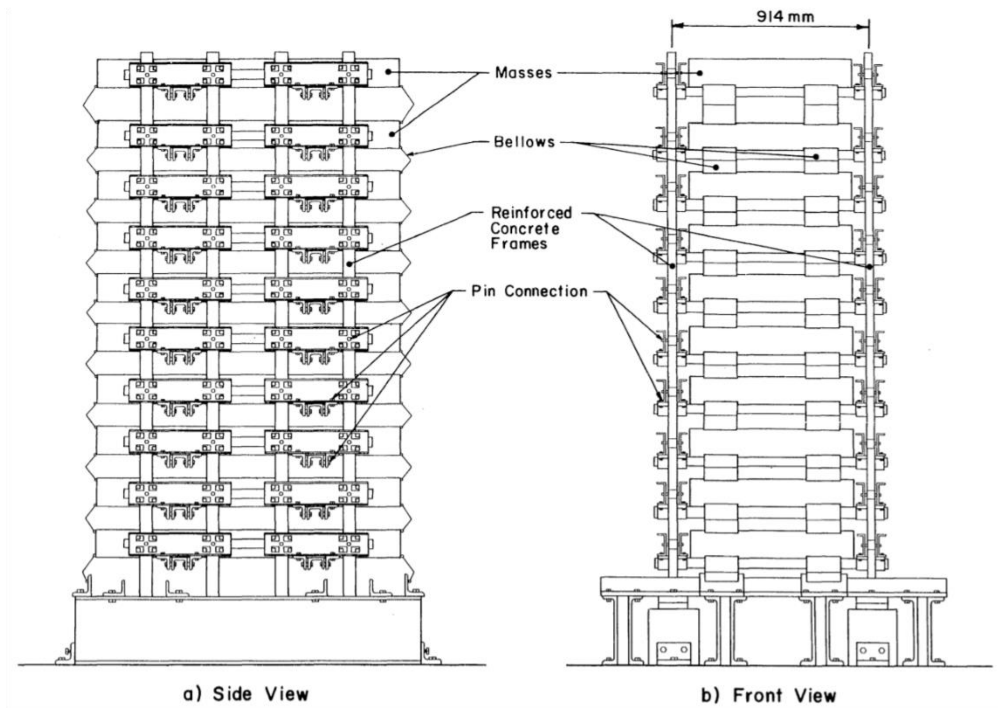

(a) Elevation of test specimen

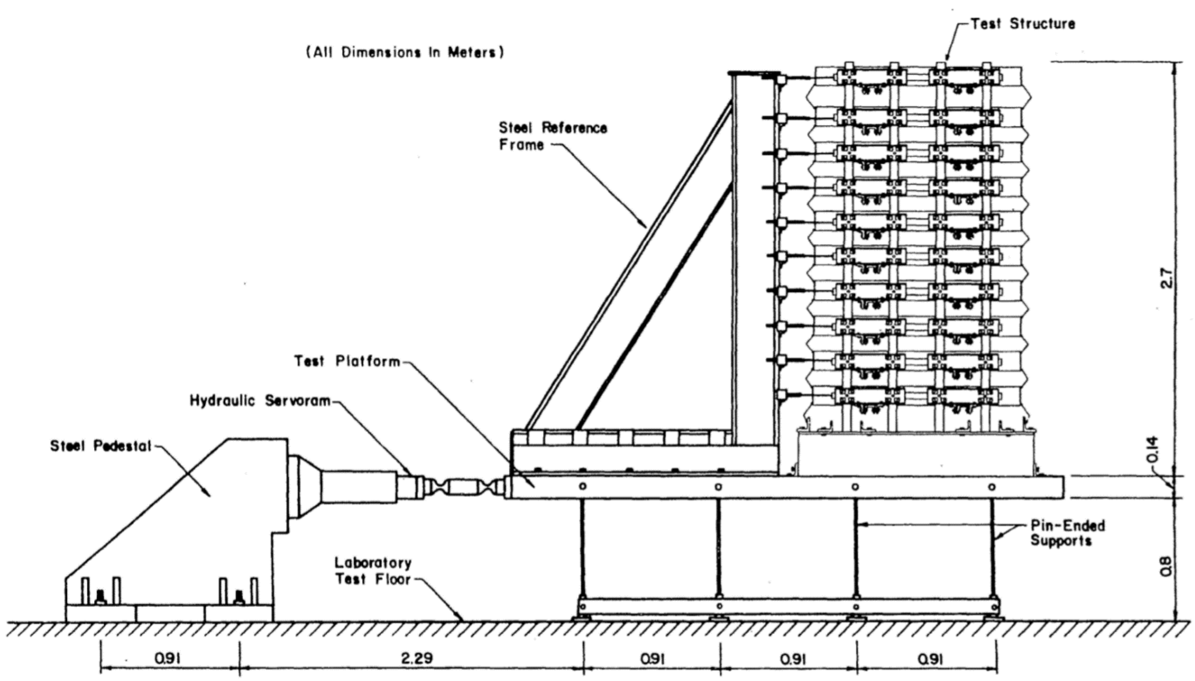

(b) Test setup

Figure C-12: Ten-story reinforced concrete frame specimen tested by Healey (1978)

Note: Figures are taken from Healey (1978).

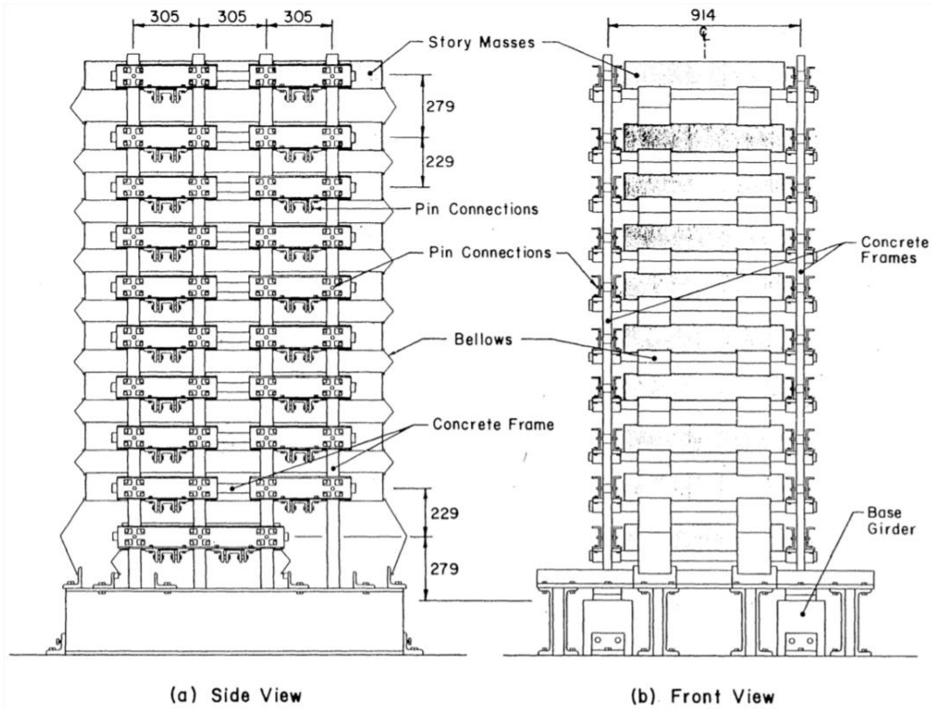

(a) Elevation of test specimen

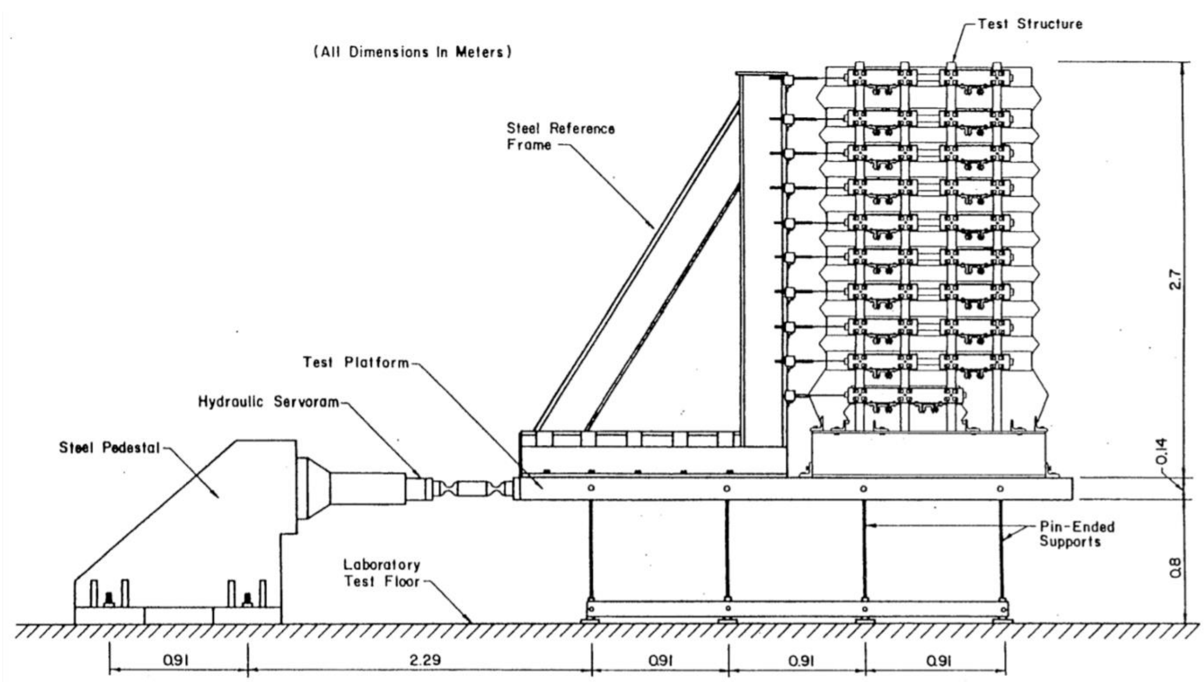

(b) Test setup

Figure C-13: Ten-story reinforced concrete frame specimen tested by Moehle (1978)

Note: Figures are taken from Moehle (1978).

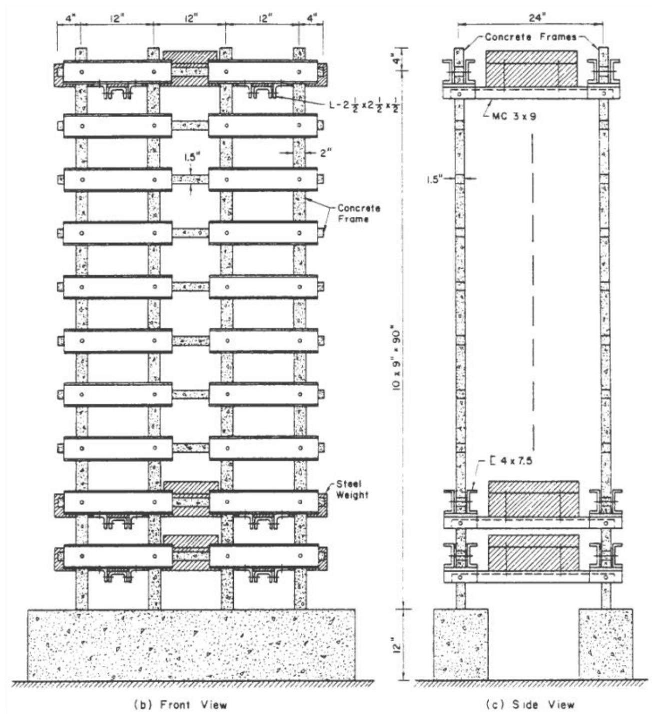

(a) Elevation of test specimens

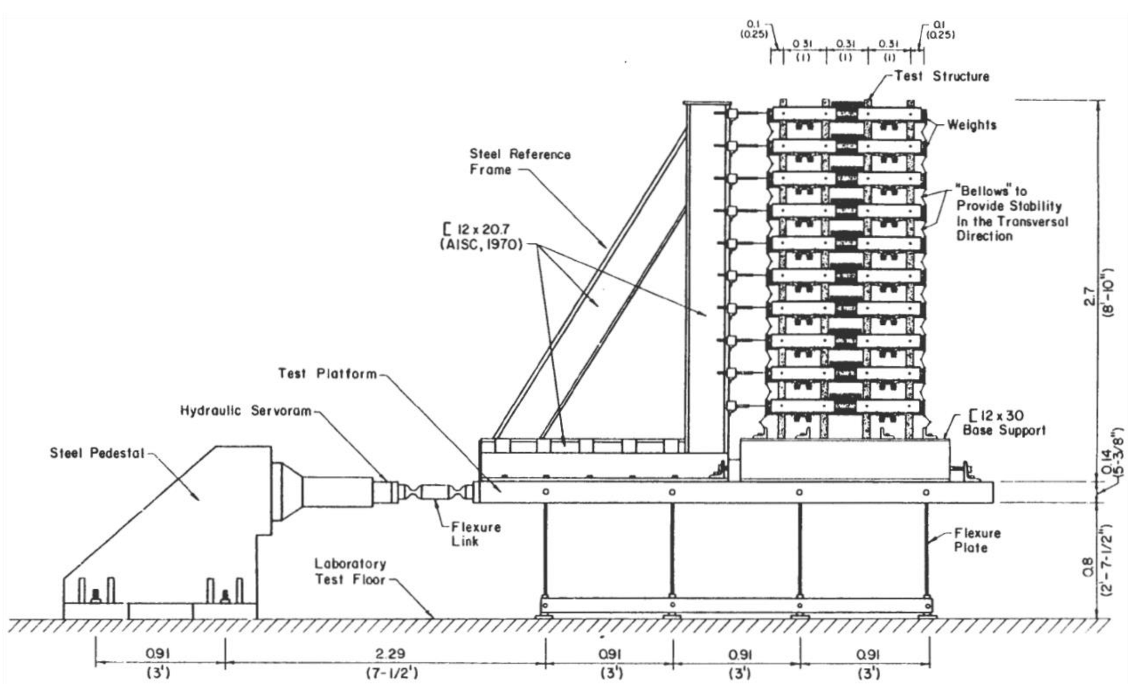

(b) Test setup

Figure C-14: Ten-story reinforced concrete frame specimens tested by Cecen (1979)

Note: Figures are taken from Cecen (1979).

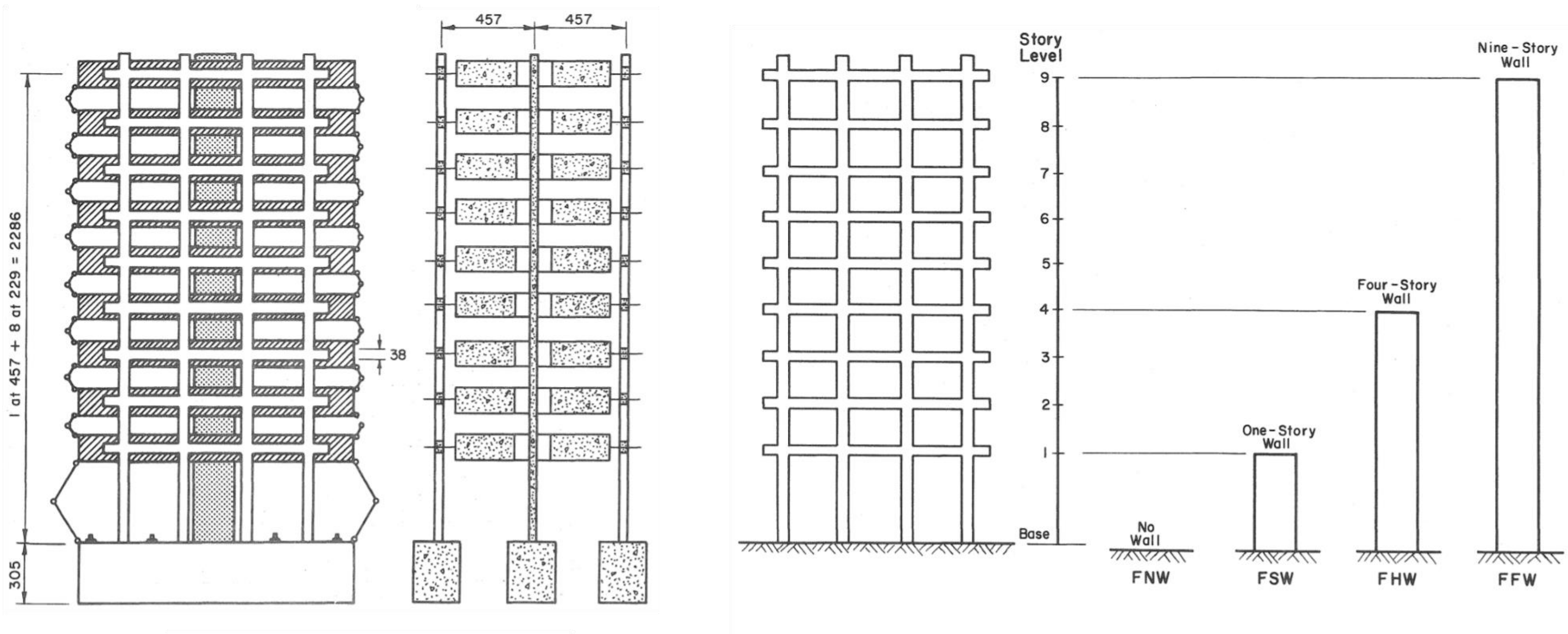

Test Structure Configuration

Frame Configuration

Wall Configurations

Figure C-15: Configurations of frame and wall specimens tested by Moehle (1980)

Note: Figures are taken from Moehle (1980).

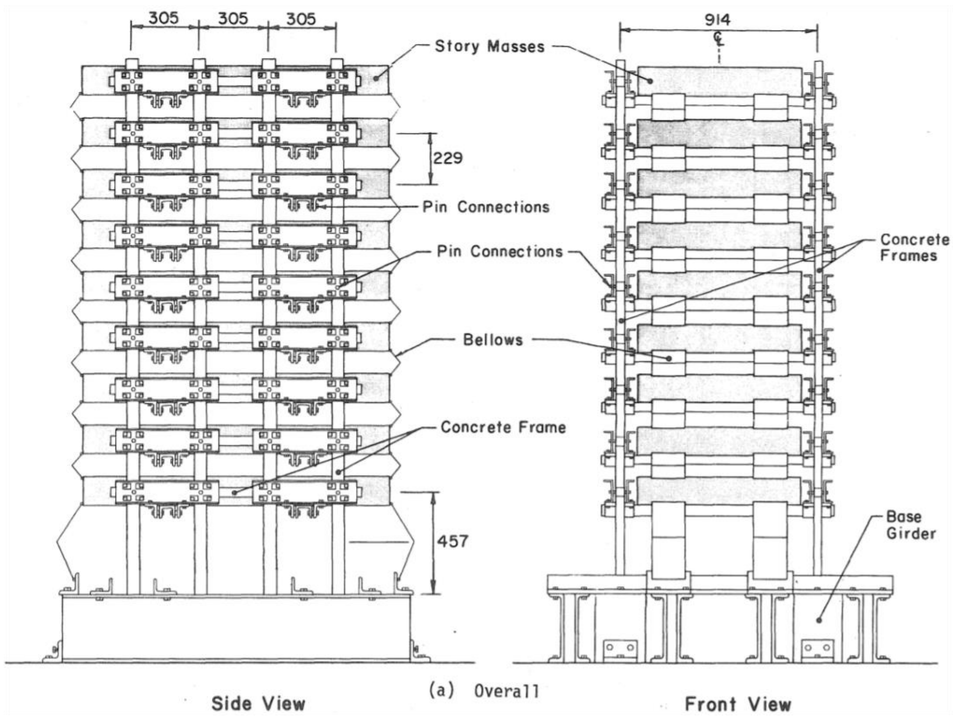

(a) Elevation of test specimens

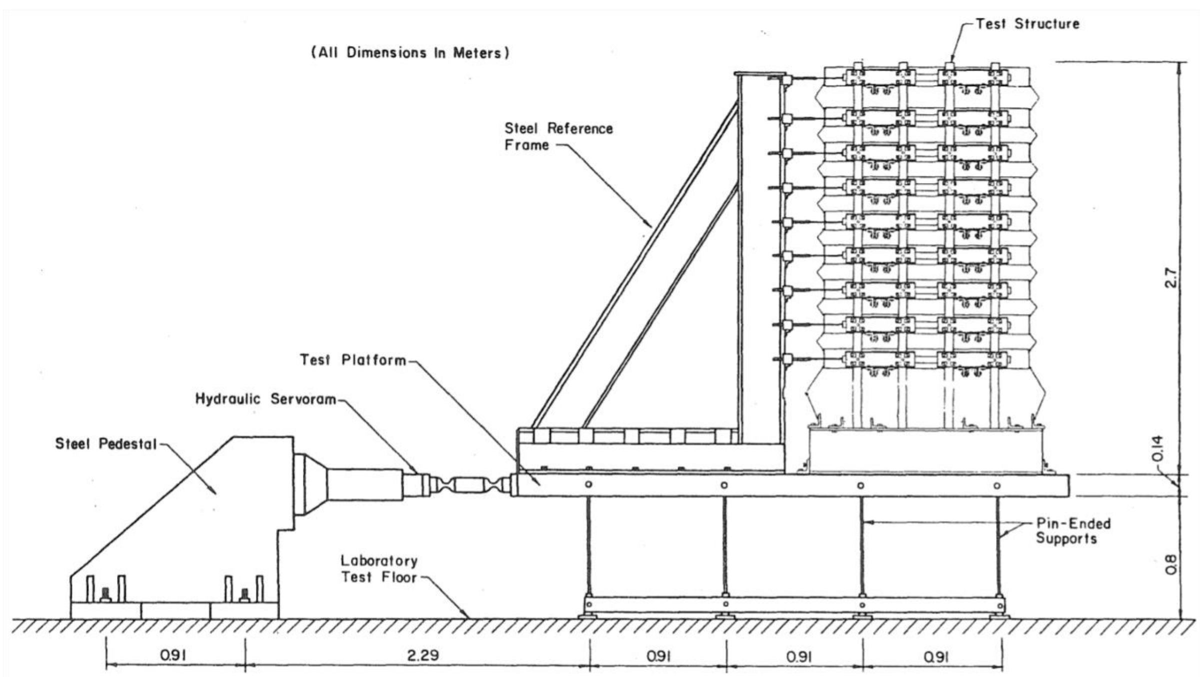

(b) Test setup

Figure C-16: Nine-story reinforced concrete frame and wall specimens tested by Moehle (1980)
Note: Figures are taken from Moehle (1980).

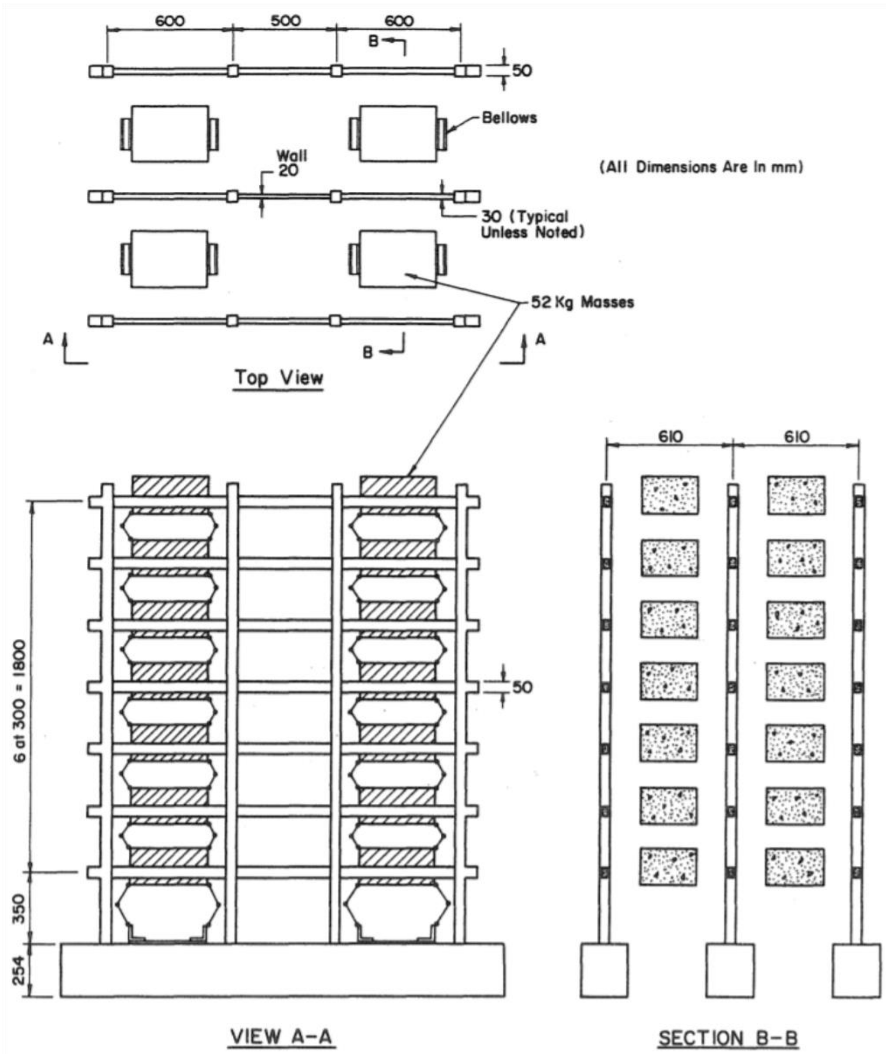

Figure C-17: Seven-story reinforced concrete frame and wall specimens tested by Wolfgram (1984)

Note: Figure is taken from Wolfgram (1984).

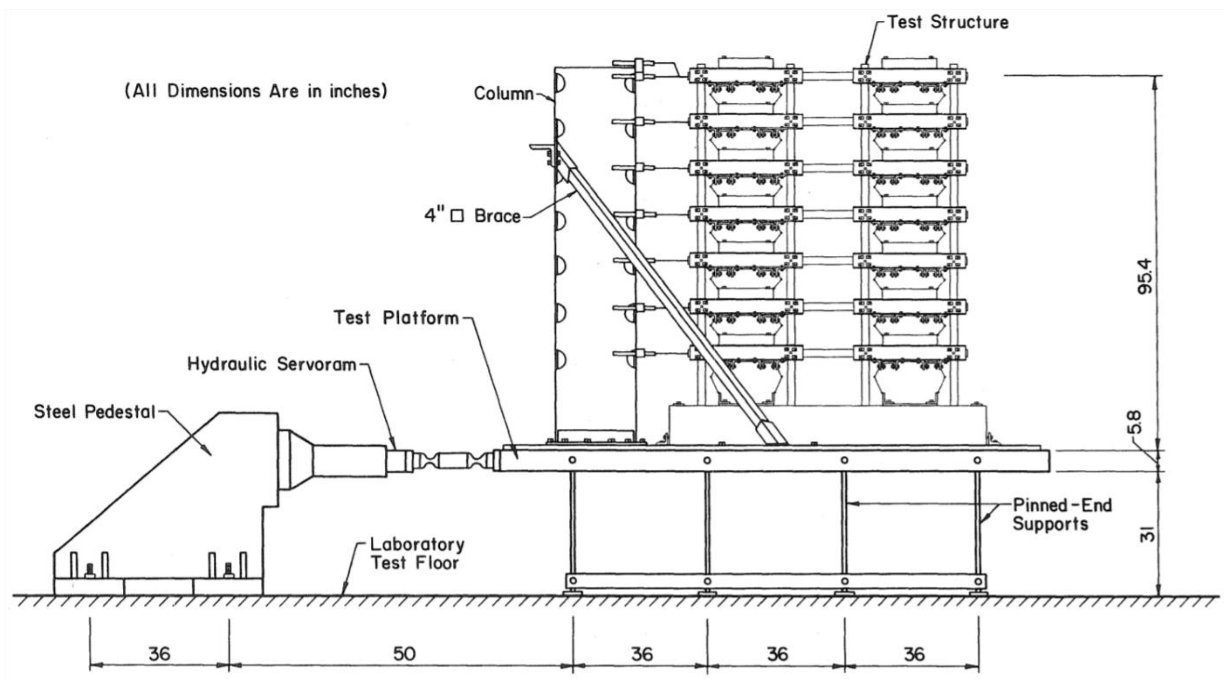

Figure C-18: Test setup of specimens tested by Wolfgram (1984)

Note: Figure is taken from Wolfgram (1984).

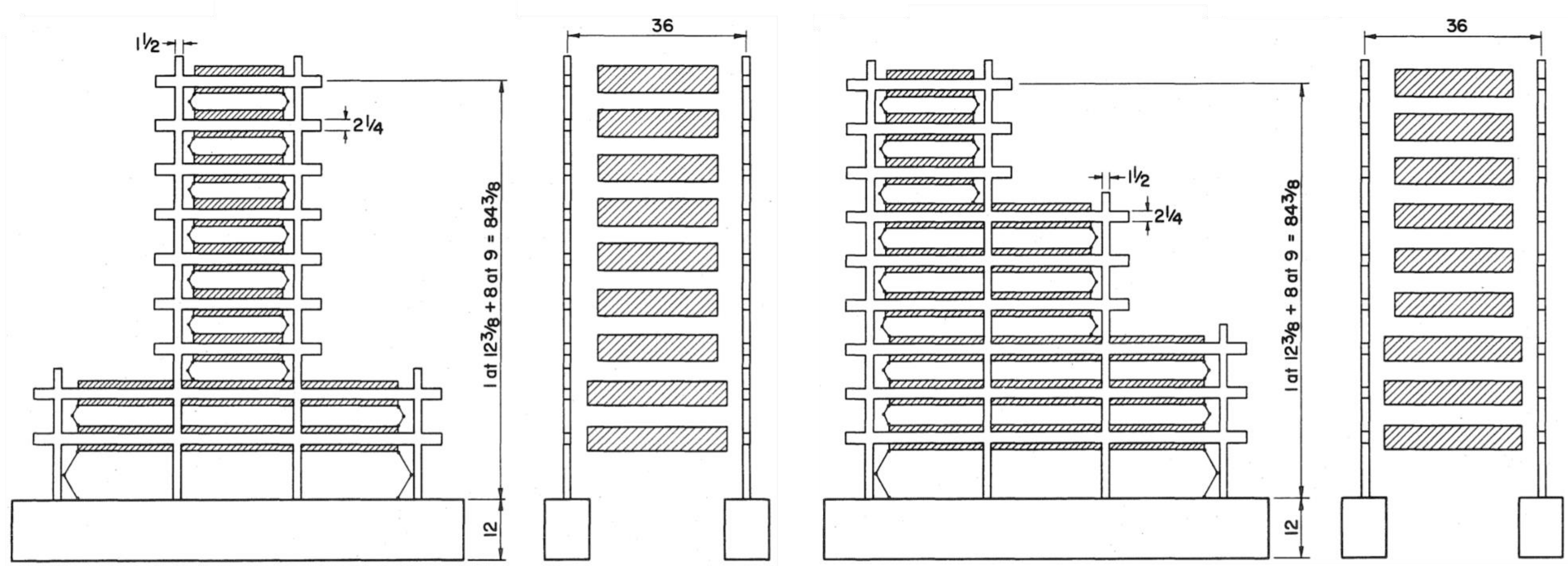

Tower Structure

Stepped Structure

Figure C-19: Configurations of frame specimens tested by Wood (1985)

Note: Figures are taken from Wood (1985).

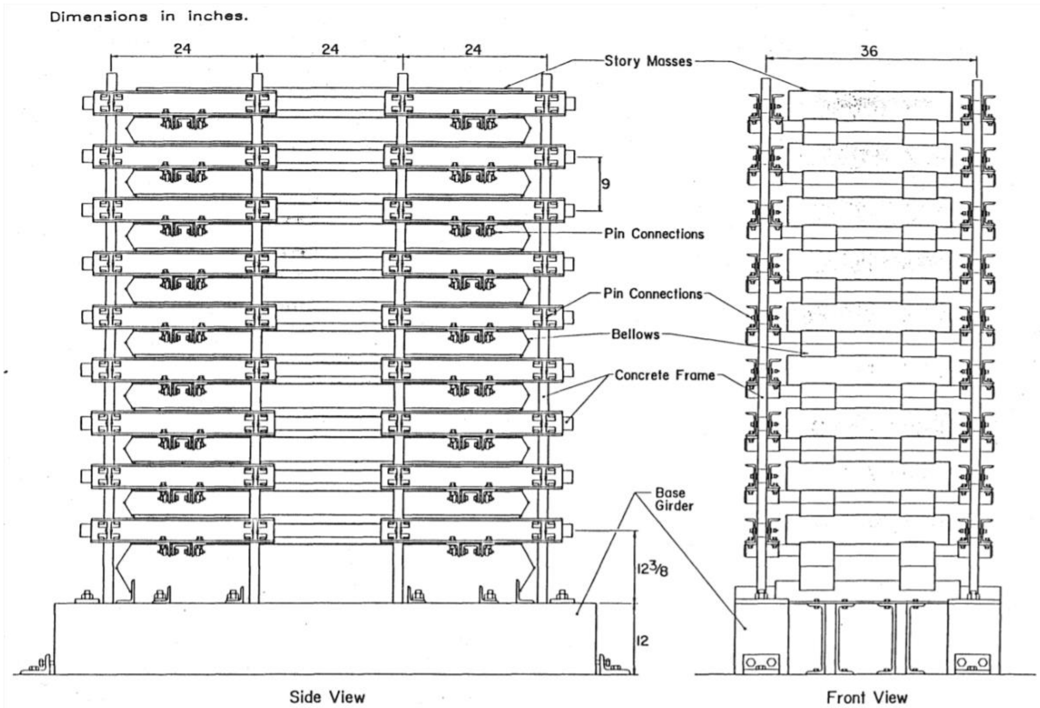

(a) Elevation of test specimens

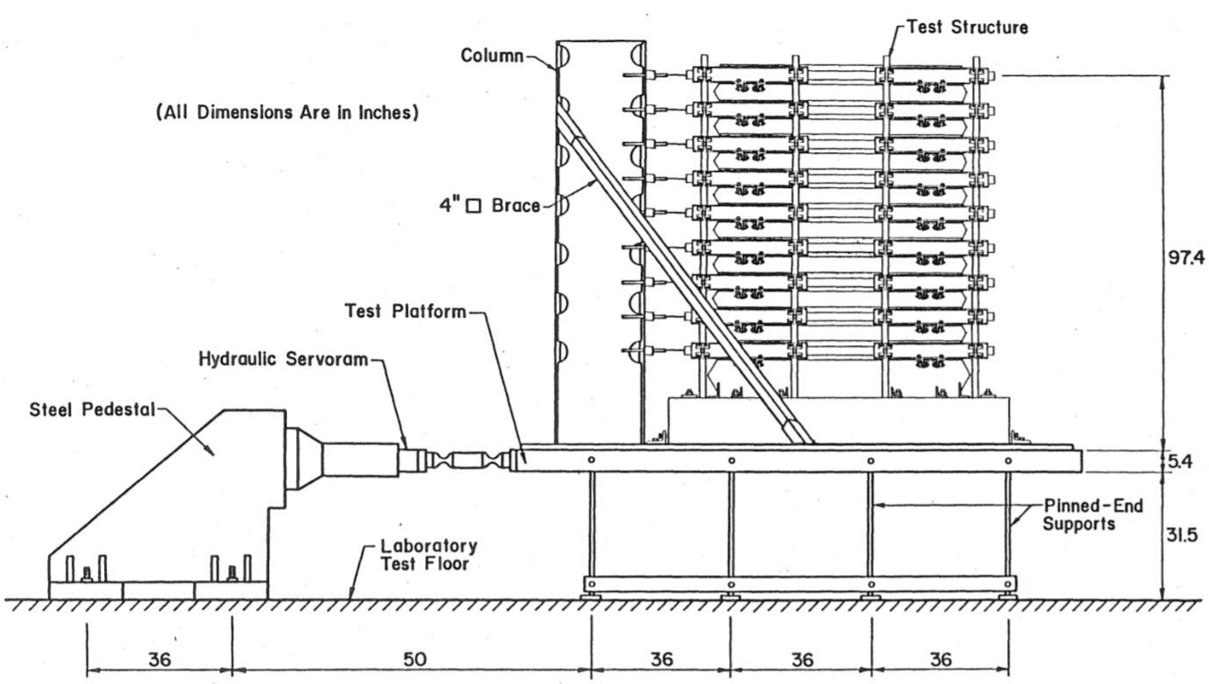

(b) Test setup

Figure C-20: Nine-story reinforced concrete frame specimens tested by Wood (1985)
Note: Figures are taken from Wood (1985).

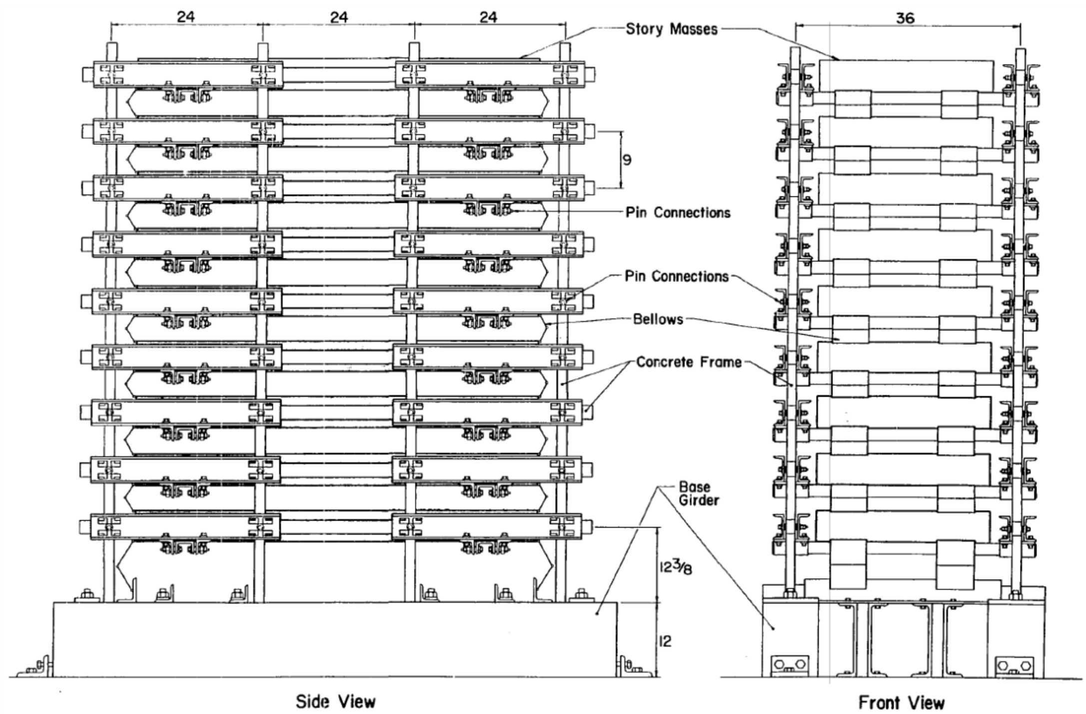

(a) Elevation of test specimens

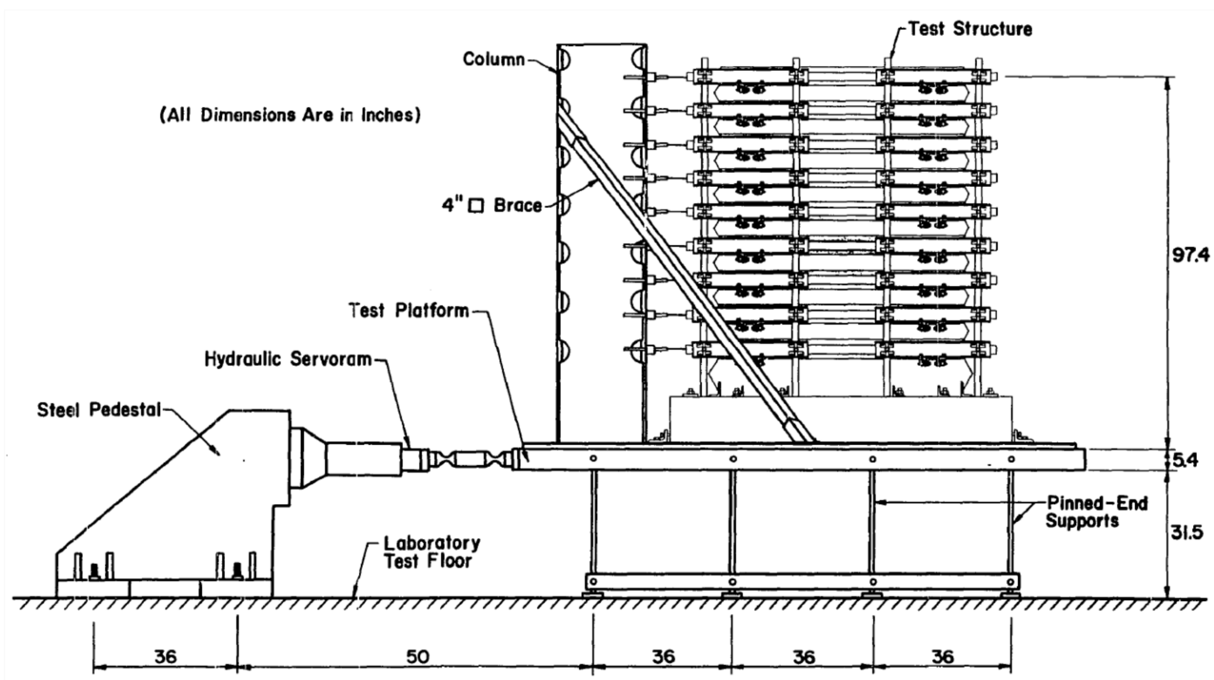

(b) Test setup

Figure C-21: Nine-story reinforced concrete frame specimens tested by Schultz (1986)

Note: Figures are taken from Schultz (1986).

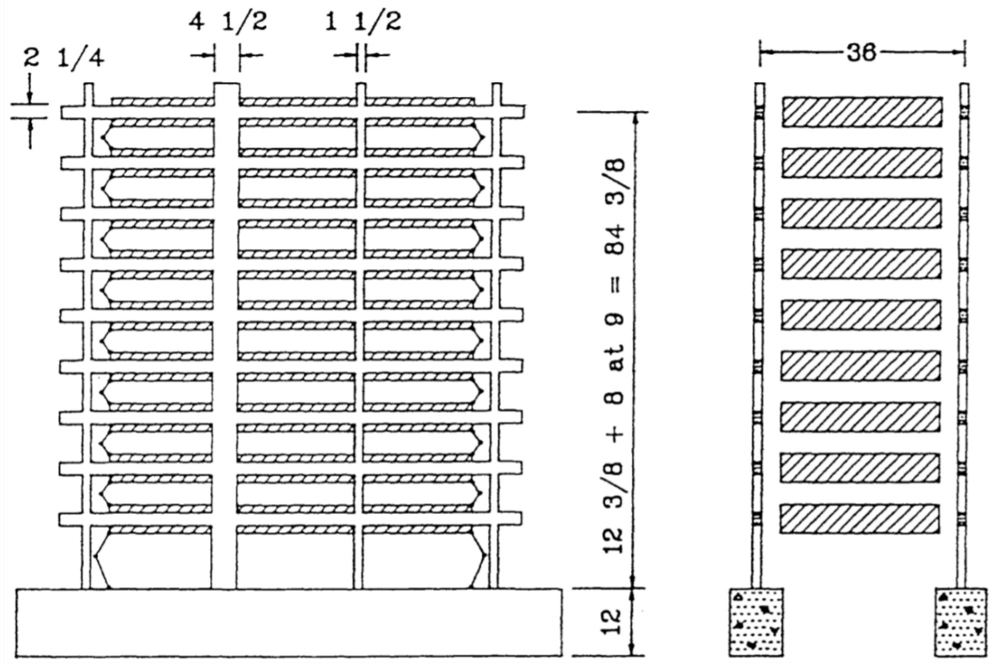

(a) Elevation of test specimens

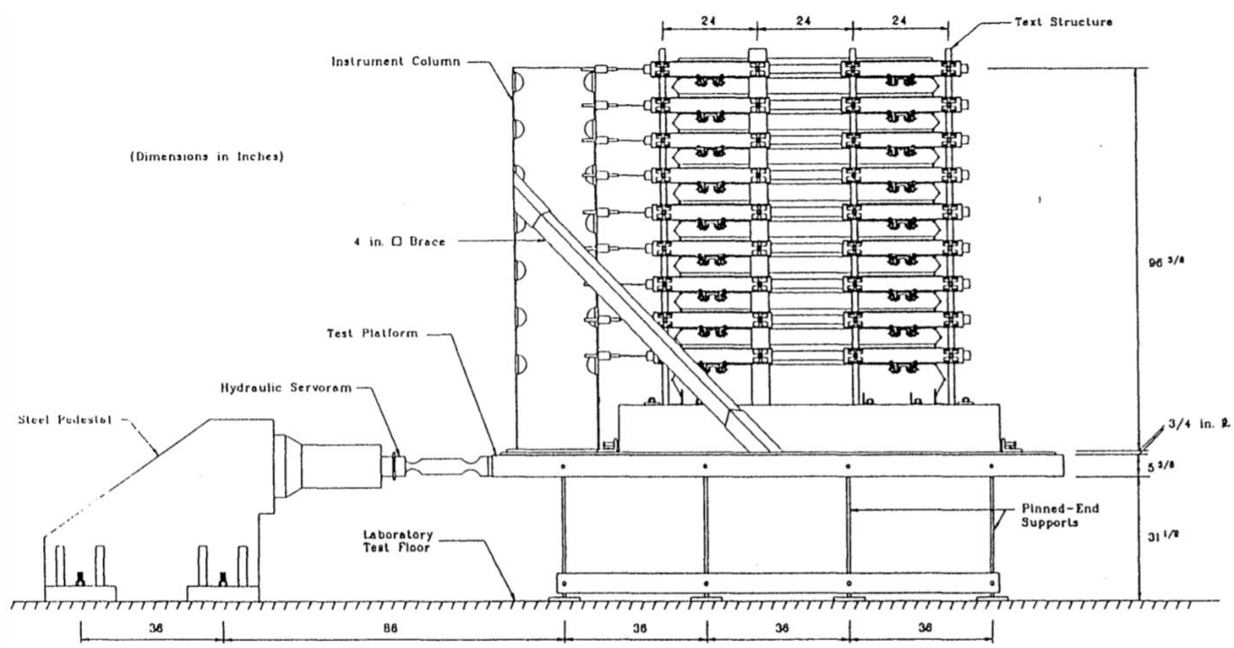

(b) Test setup

Figure C-22: Nine-story reinforced concrete frame and wall specimens tested by Eberhard (1989)
Note: Figures are taken from Eberhard (1989).

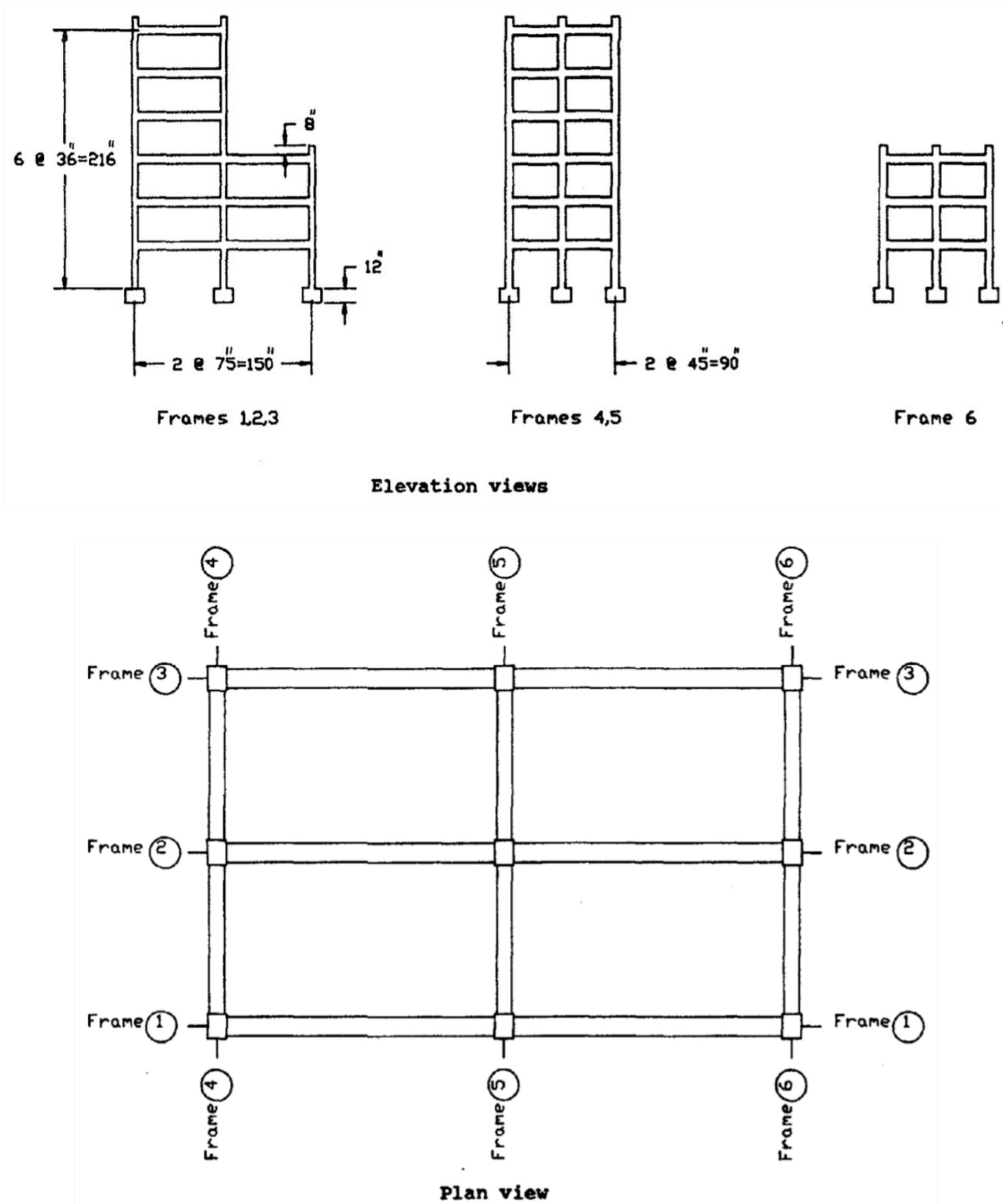

Figure C-23: Six-story reinforced concrete frame specimen tested by Shahrooz (1987)

Note: Figure is taken from Shahrooz (1987).

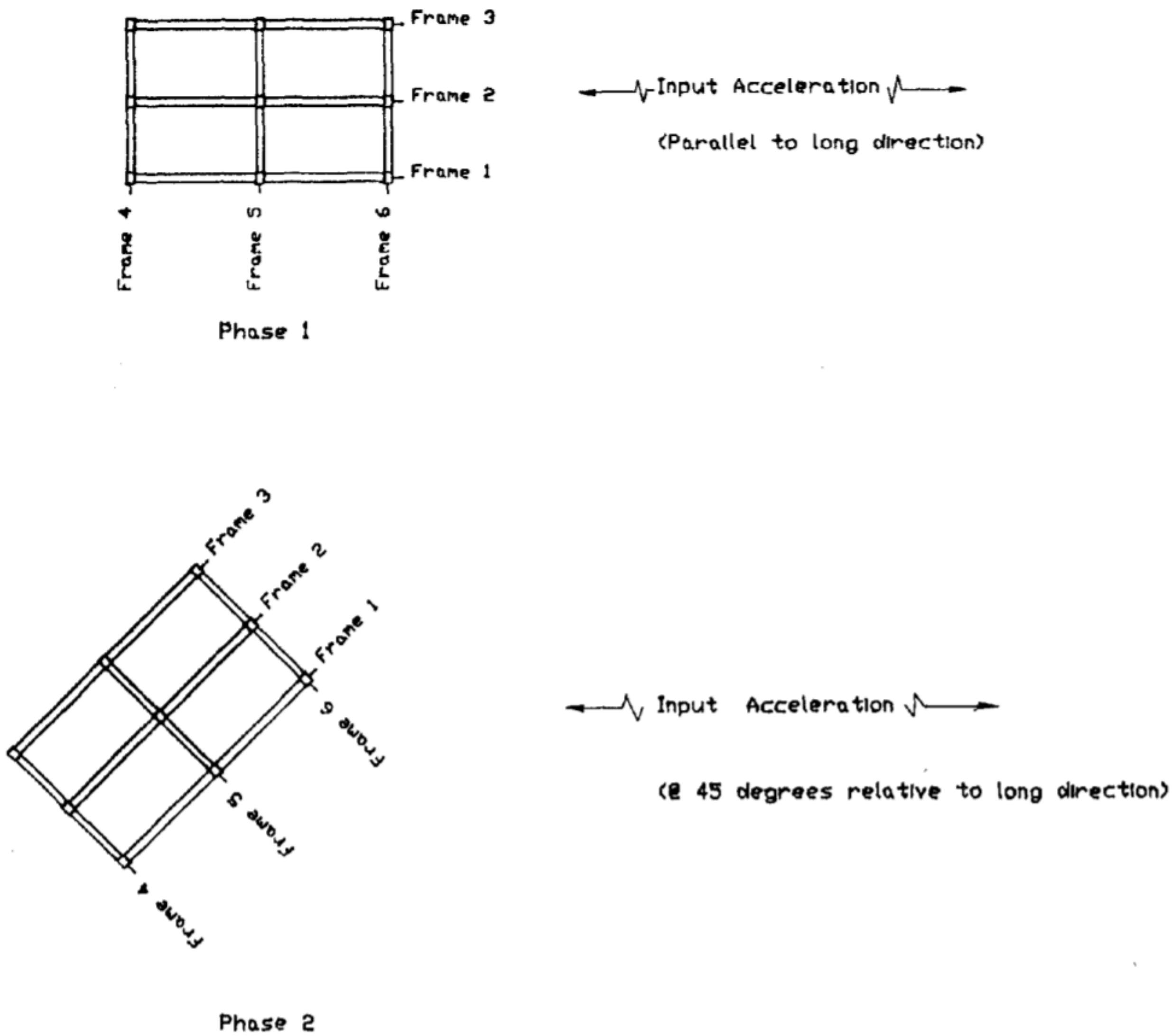

Figure C-24: Configurations of specimen tested by Shahrooz (1987)

Note: Figure is taken from Shahrooz (1987).

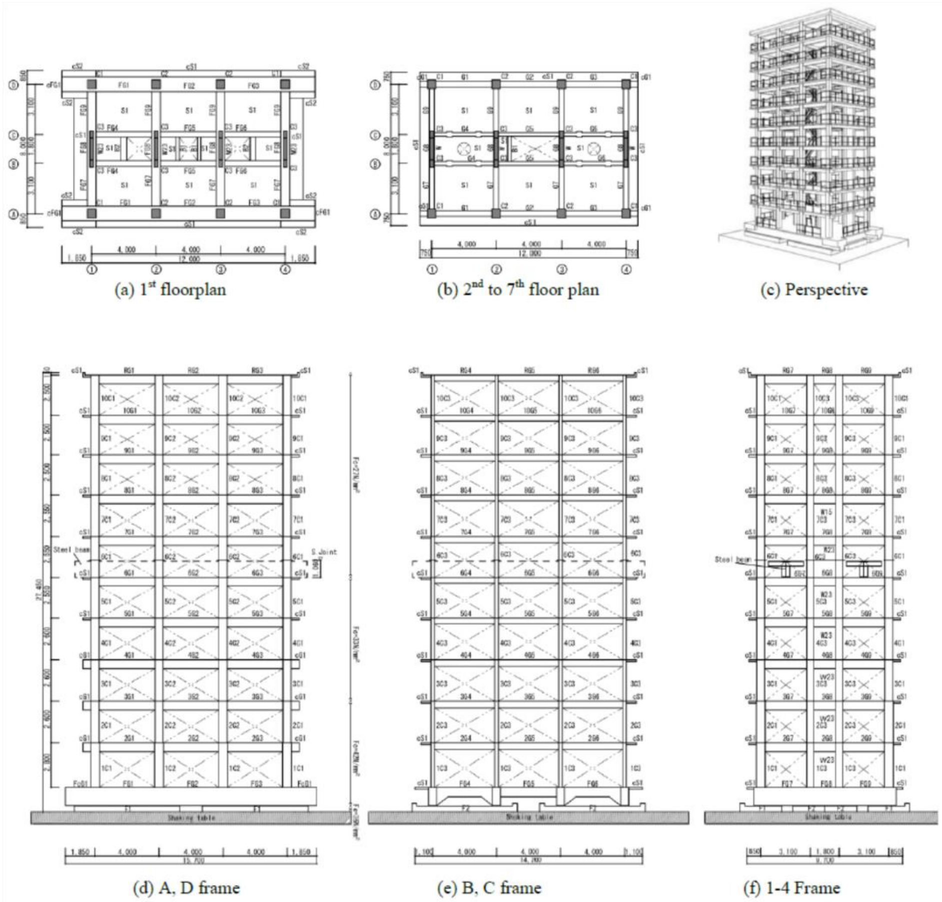

(a) Elevation of test specimens

(b) Test setup

Figure C-25: Ten-story reinforced concrete frame specimens tested at E-Defense

Note: Figure is taken from Kajiwara (2017).

APPENDIX D. MEASURED RESPONSE OF TEST SPECIMENS

Raw voltage data obtained during each test run are available at https://datacenterhub.org/deedsdv/publications/view/208 (DOI: 10.7277/W61K-FB26). Sensitivities listed in Table B-13, Table B-16, Table B-19, and Table B-22 may be used to convert voltage data into quantities with engineering units.

This appendix contains the base motion and structural response histories measured in each simulation of Specimens F1 and F2 (Figure D-1 through Figure D-175). Base motion data include base acceleration, base velocity, and base displacement histories corrected and/or inferred from measurements obtained from ADXL accelerometers mounted on foundation beams of specimens (described in Section 2.5.3). Structural response data include in-run story drift histories obtained from measurements from LVDTs attached to foundation and top beams of specimens (described in Section 2.5.1), lateral load histories obtained from measurements of the load cell (described in Section 2.5.2), and roof acceleration histories obtained from measurements of accelerometers attached to top of Specimen F1 in Series F1-M-C-OOP (described in Section 2.5.3). Force-displacement relationships measured in each simulation are plotted in Figure D-176 through Figure D-183.

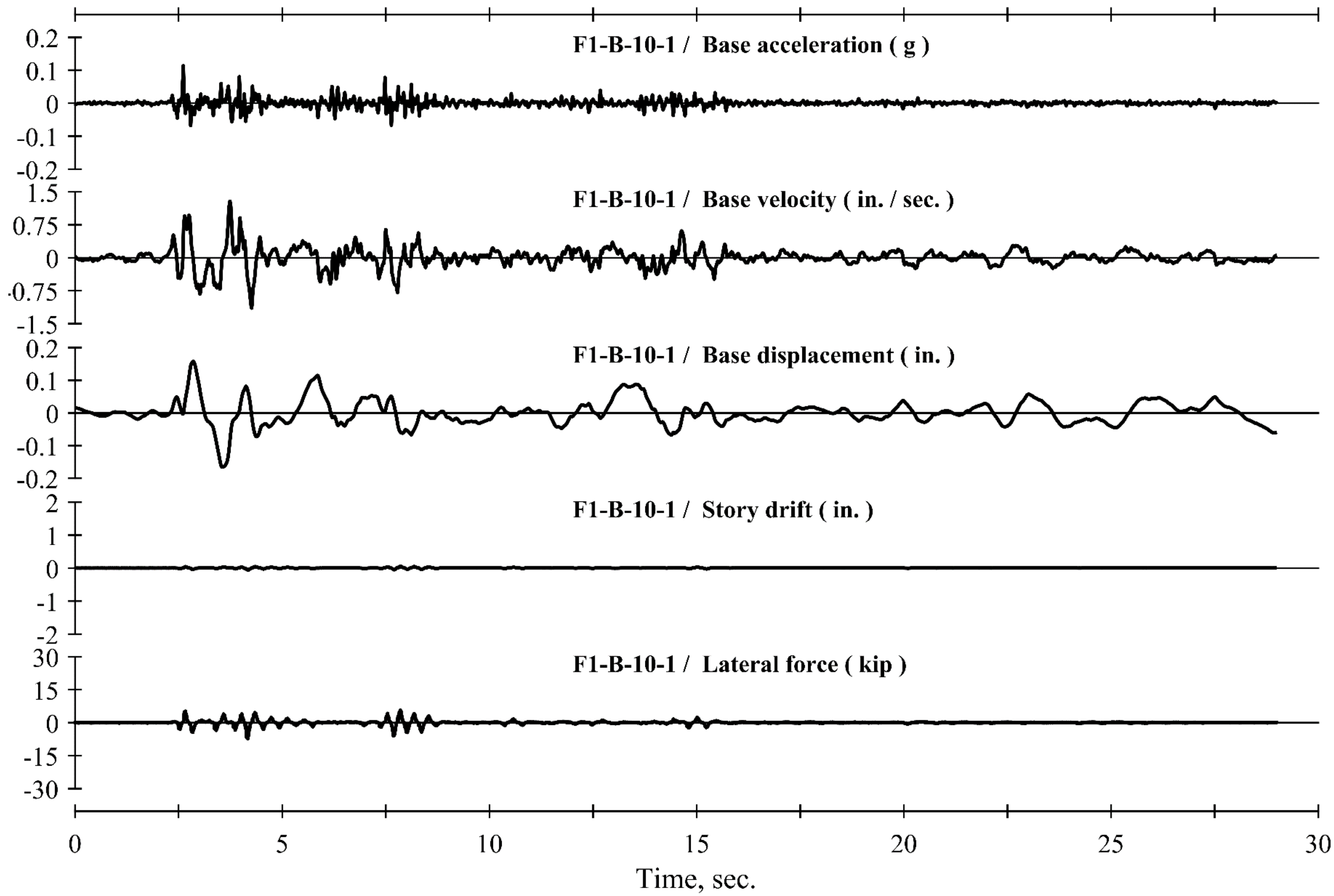

Figure D-1: Base motion and structural response histories in Run 1 of Specimen F1

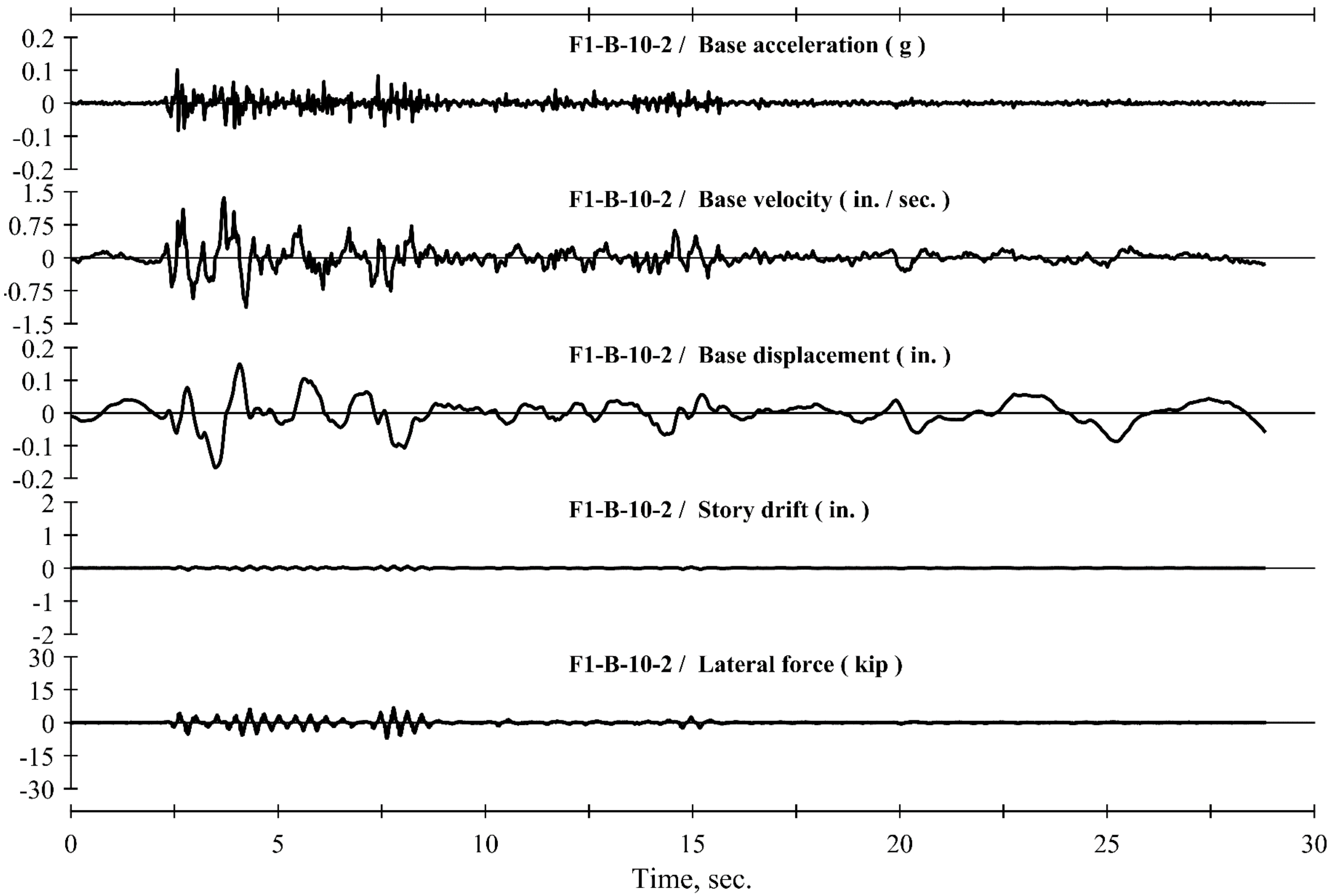

Figure D-2: Base motion and structural response histories in Run 2 of Specimen F1

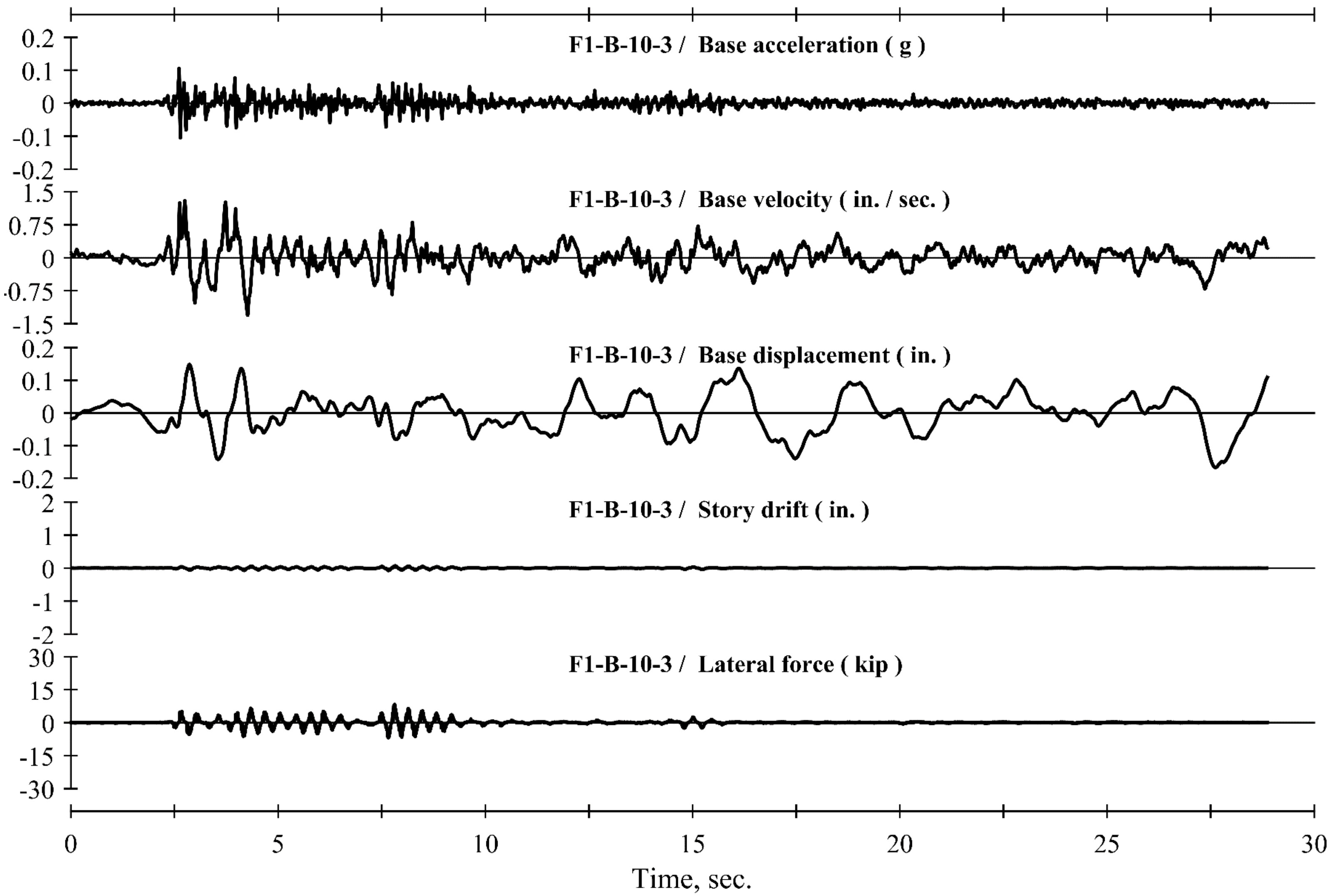

Figure D-3: Base motion and structural response histories in Run 3 of Specimen F1

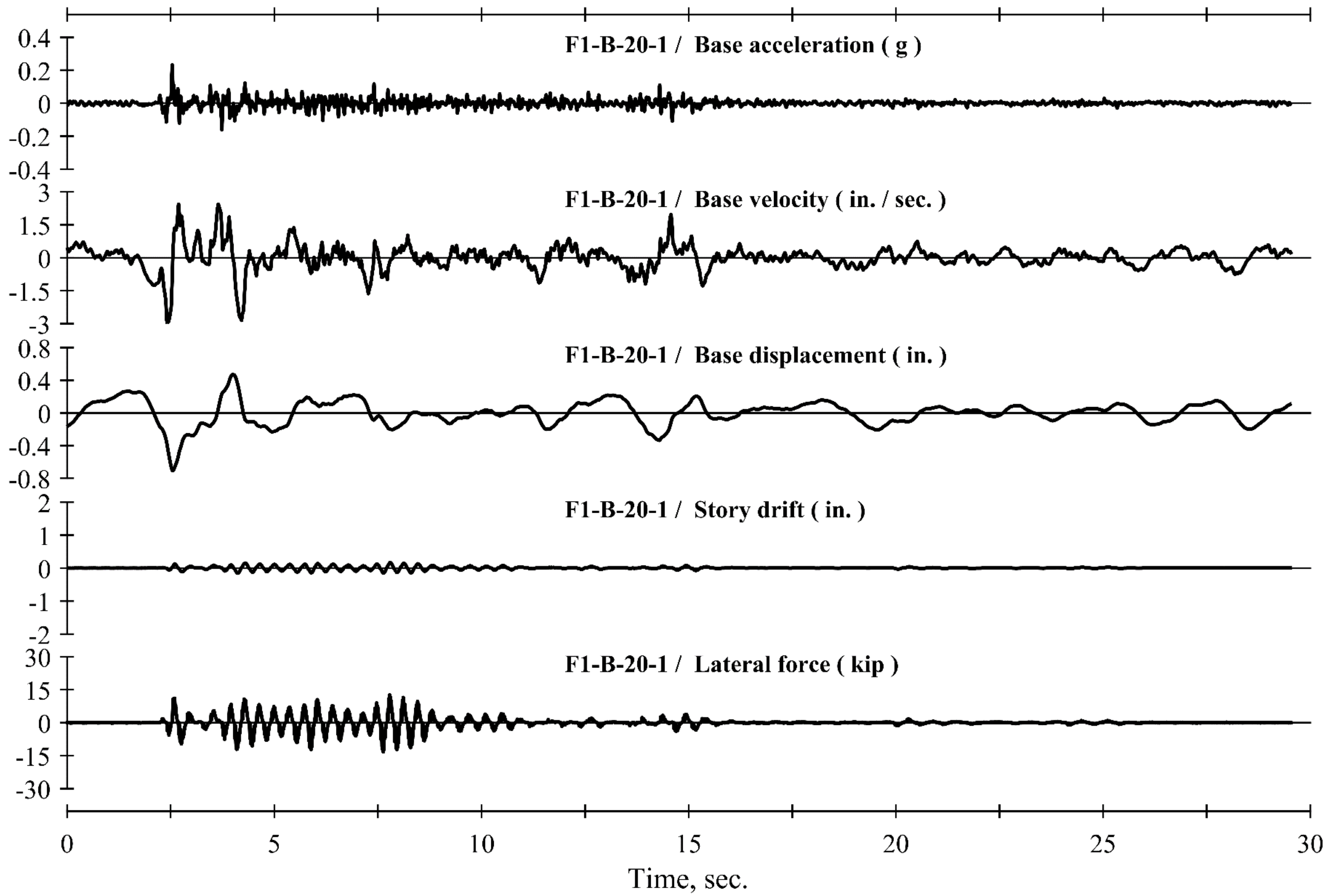

Figure D-4: Base motion and structural response histories in Run 4 of Specimen F1

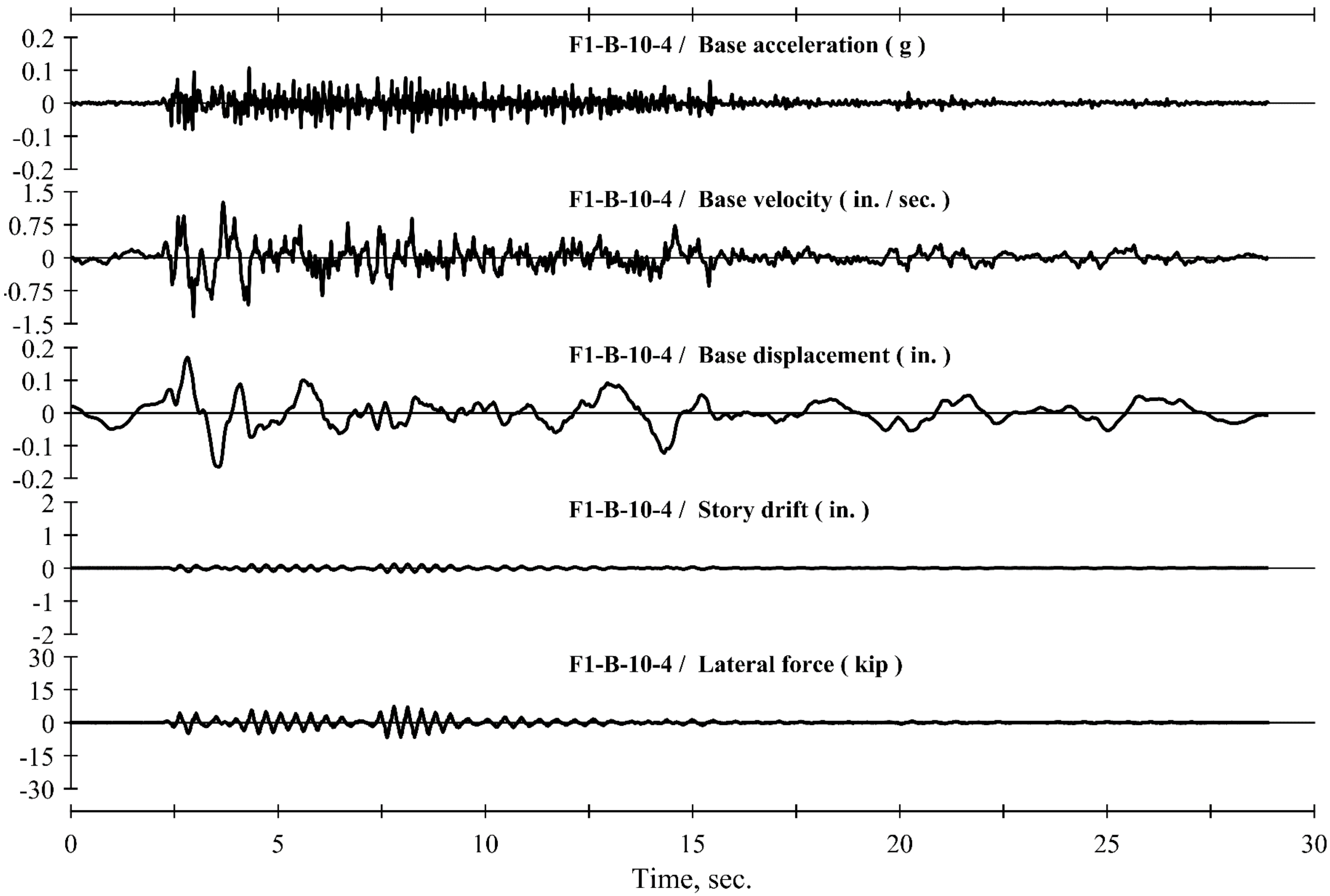

Figure D-5: Base motion and structural response histories in Run 5 of Specimen F1

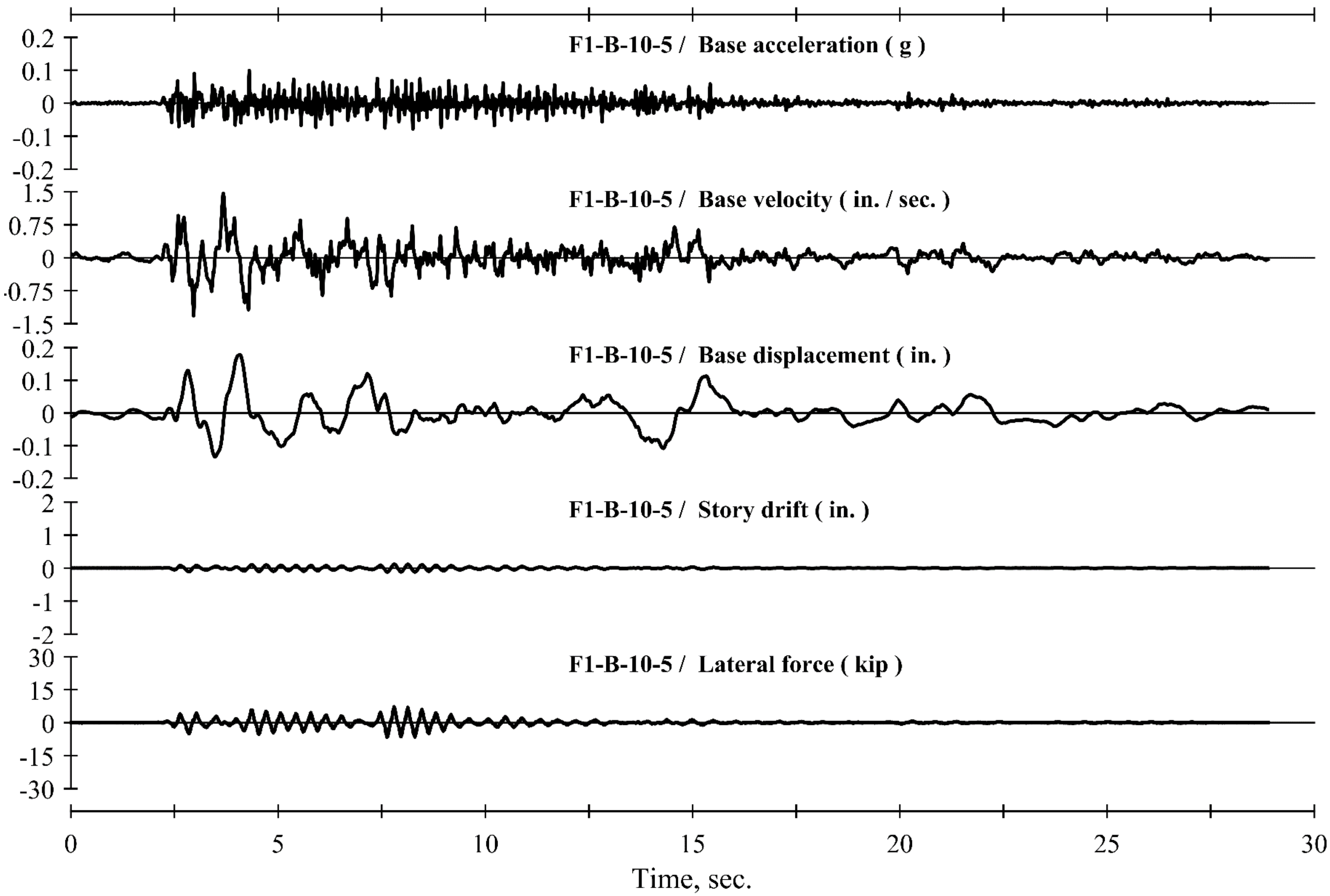

Figure D-6: Base motion and structural response histories in Run 6 of Specimen F1

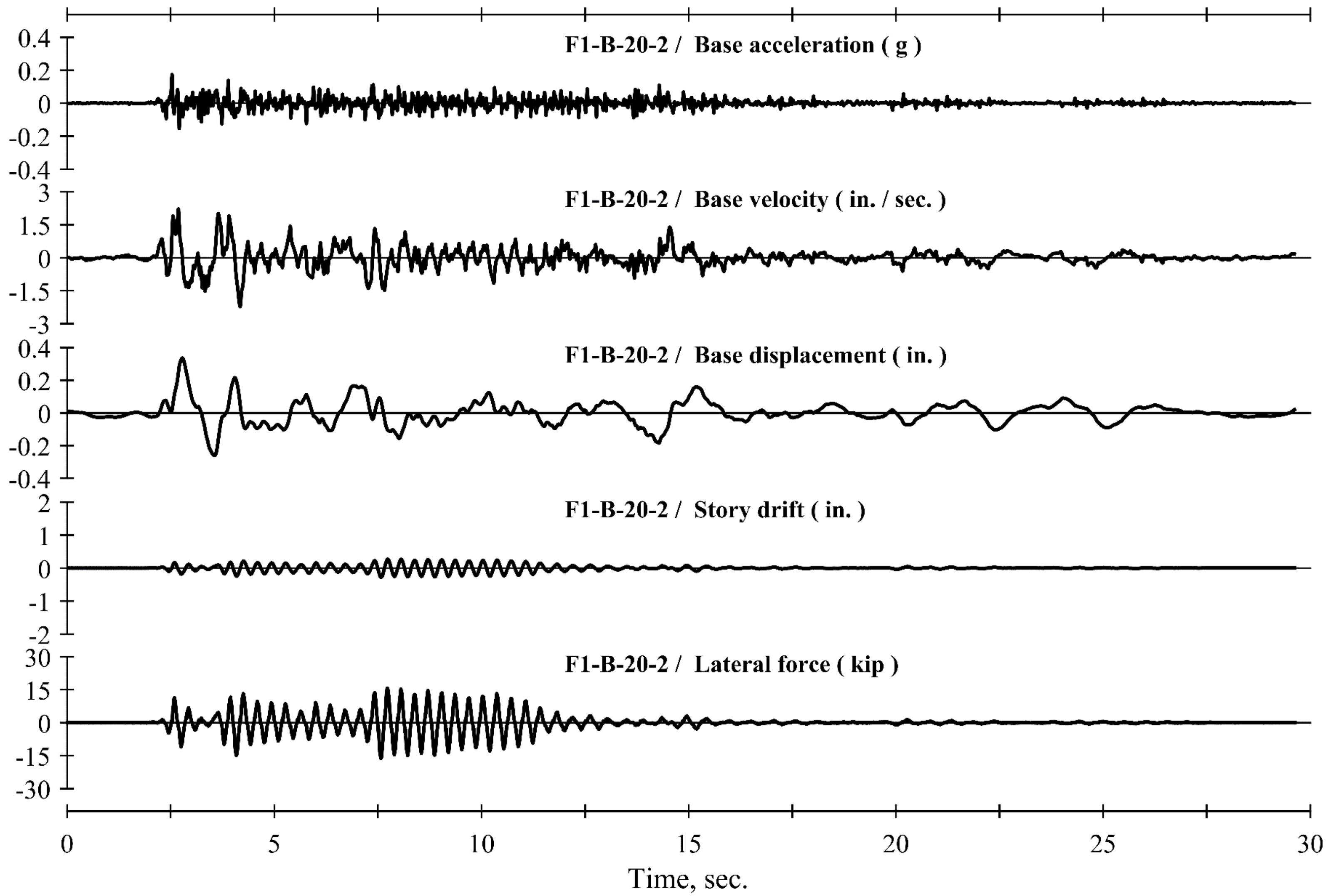

Figure D-7: Base motion and structural response histories in Run 7 of Specimen F1

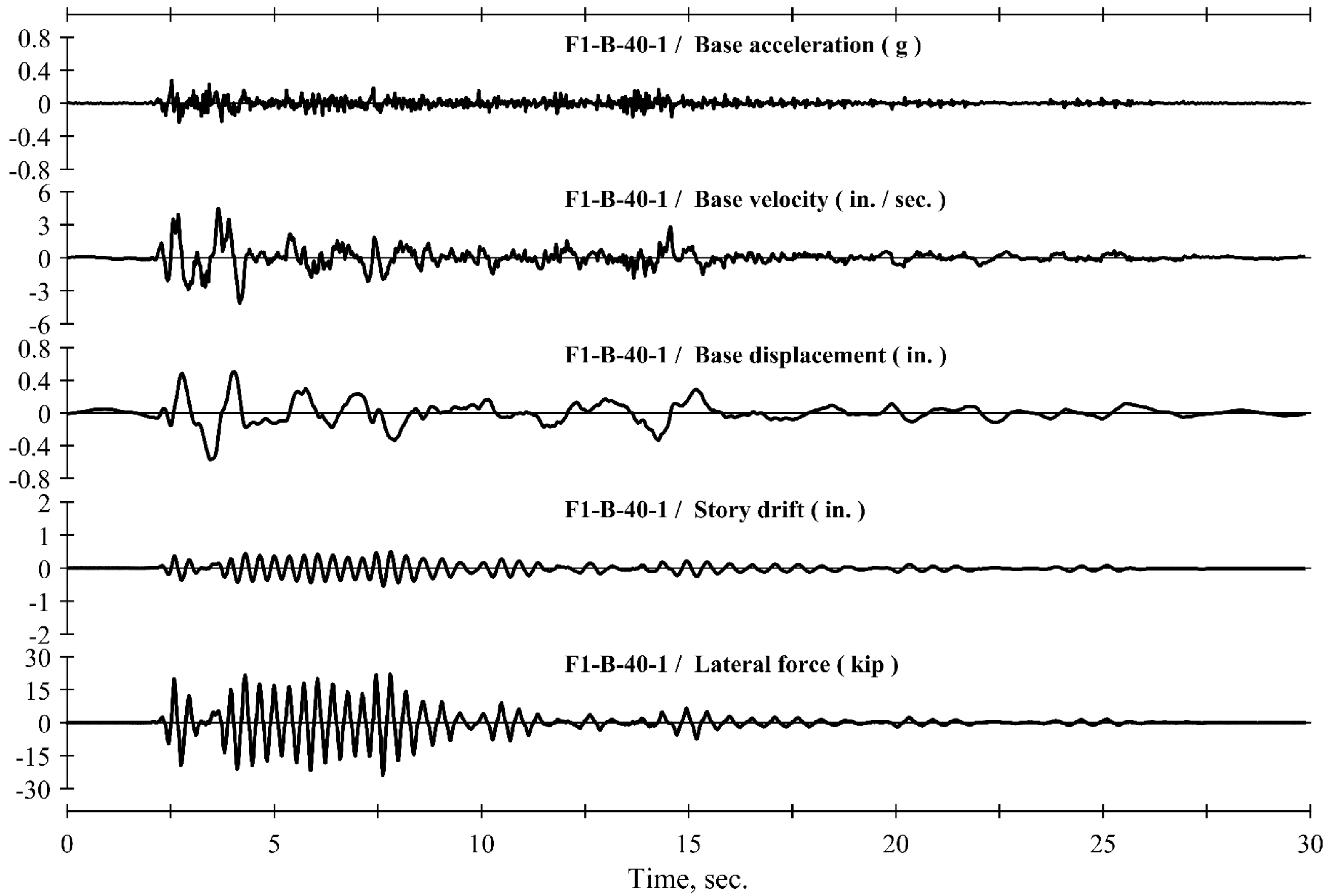

Figure D-8: Base motion and structural response histories in Run 8 of Specimen F1

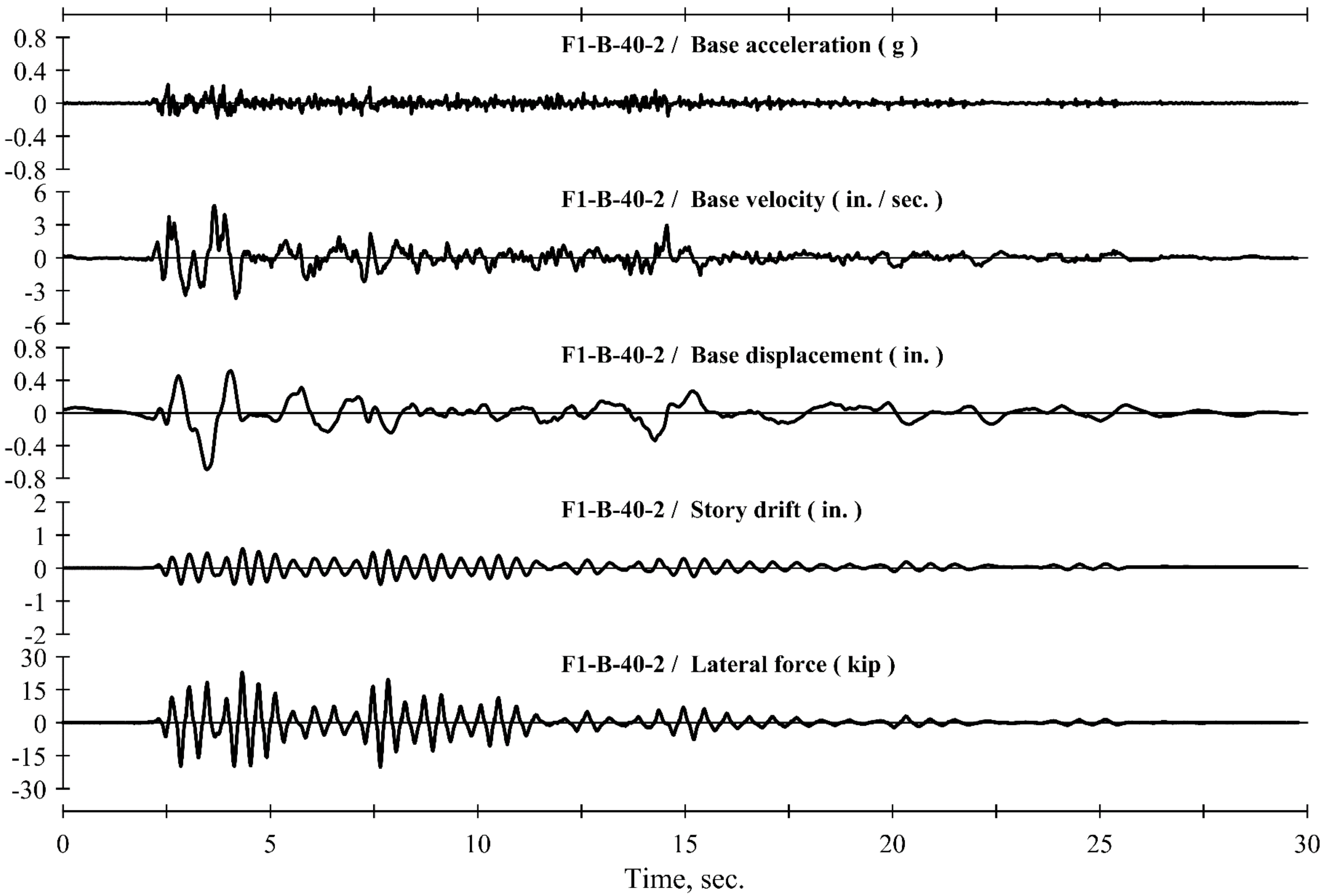

Figure D-9: Base motion and structural response histories in Run 9 of Specimen F1

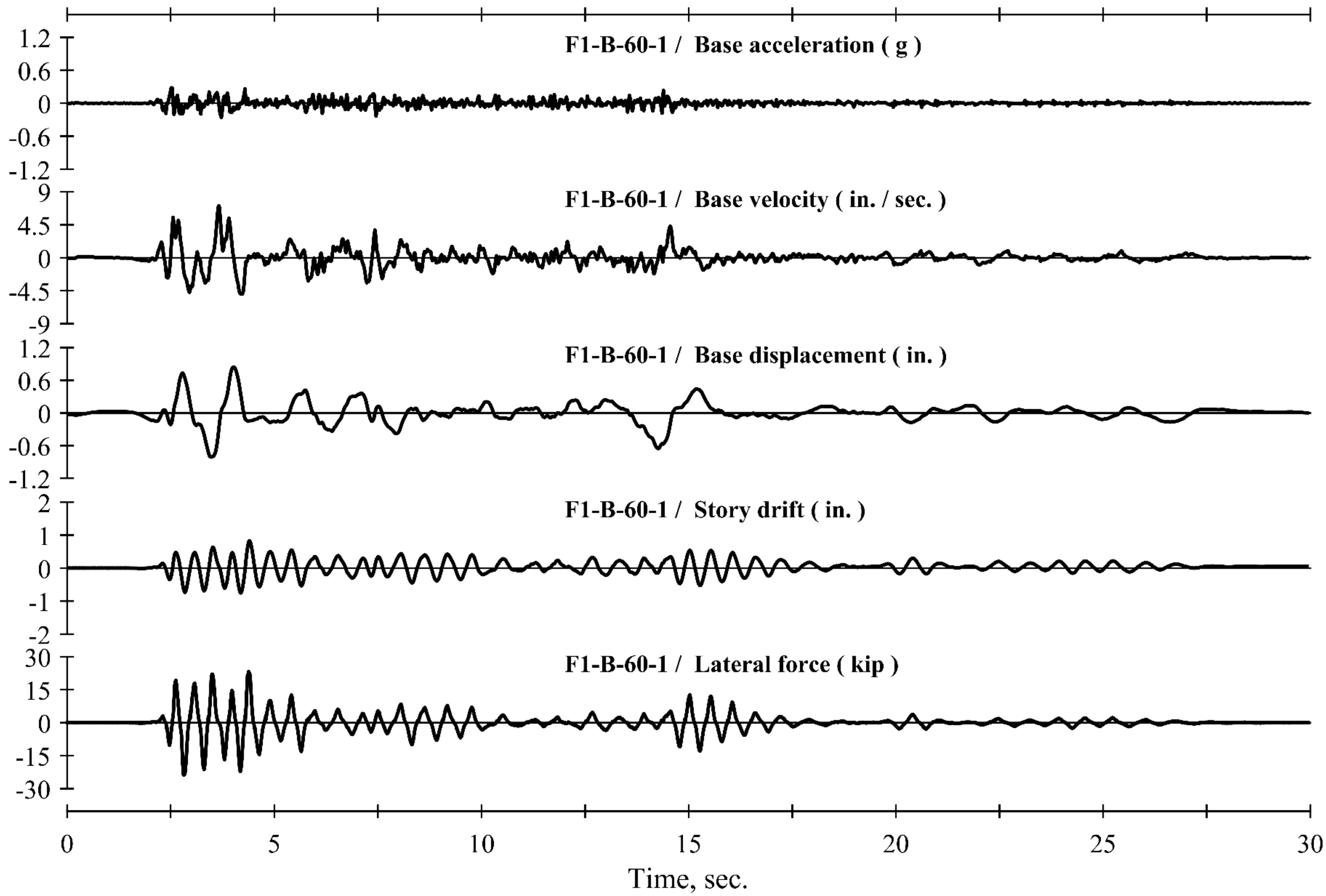

Figure D-10: Base motion and structural response histories in Run 10 of Specimen F1

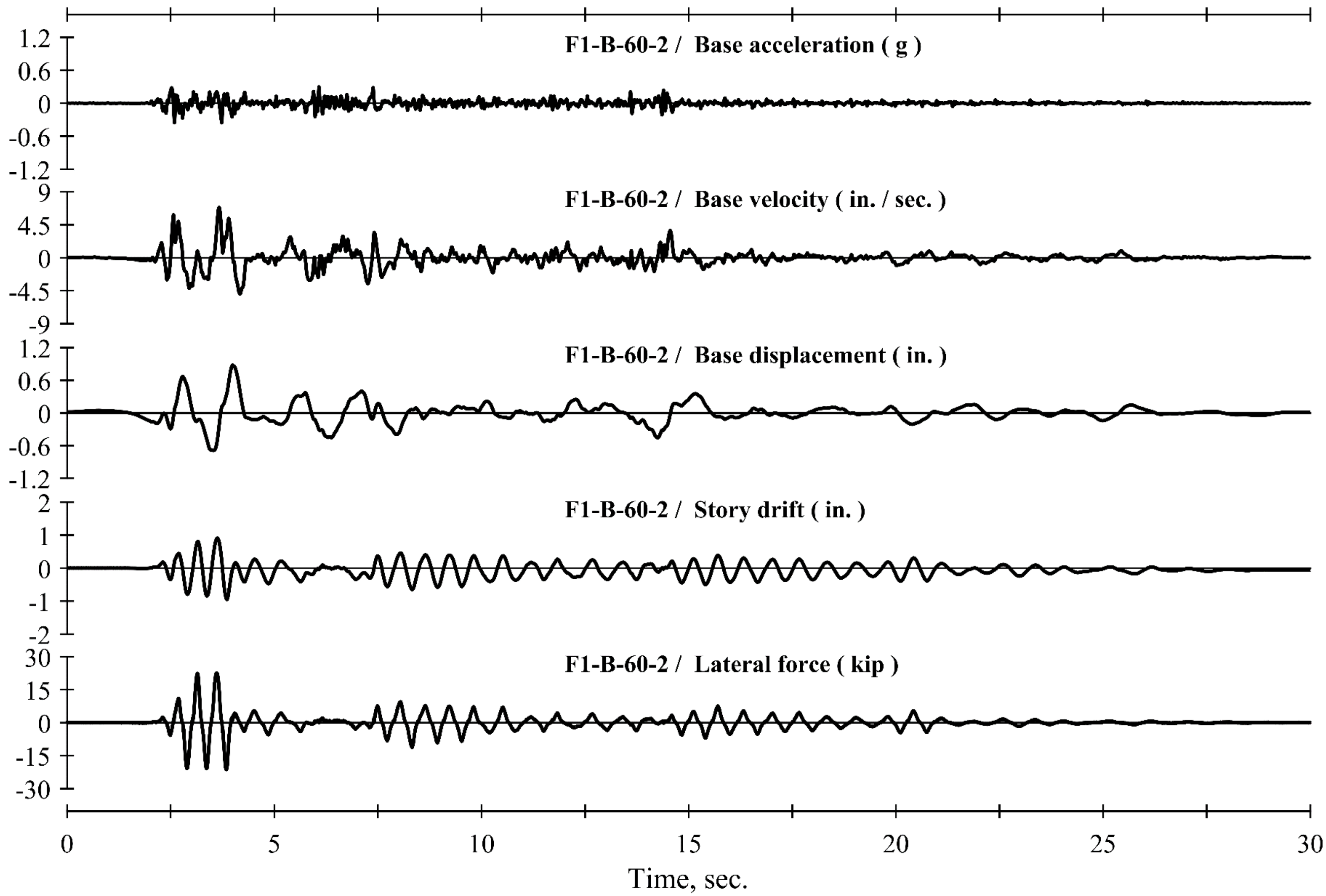

Figure D-11: Base motion and structural response histories in Run 11 of Specimen F1

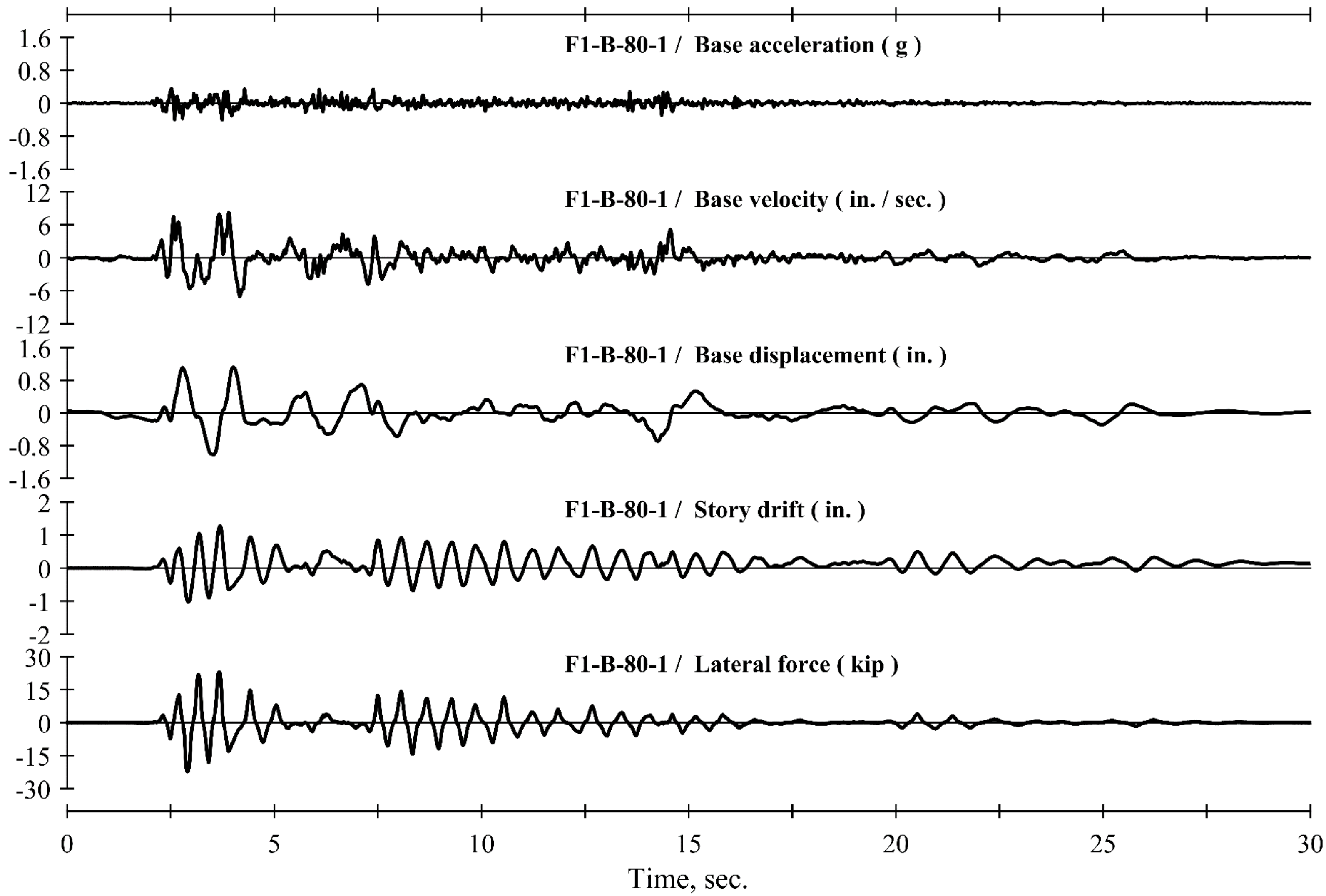

Figure D-12: Base motion and structural response histories in Run 12 of Specimen F1

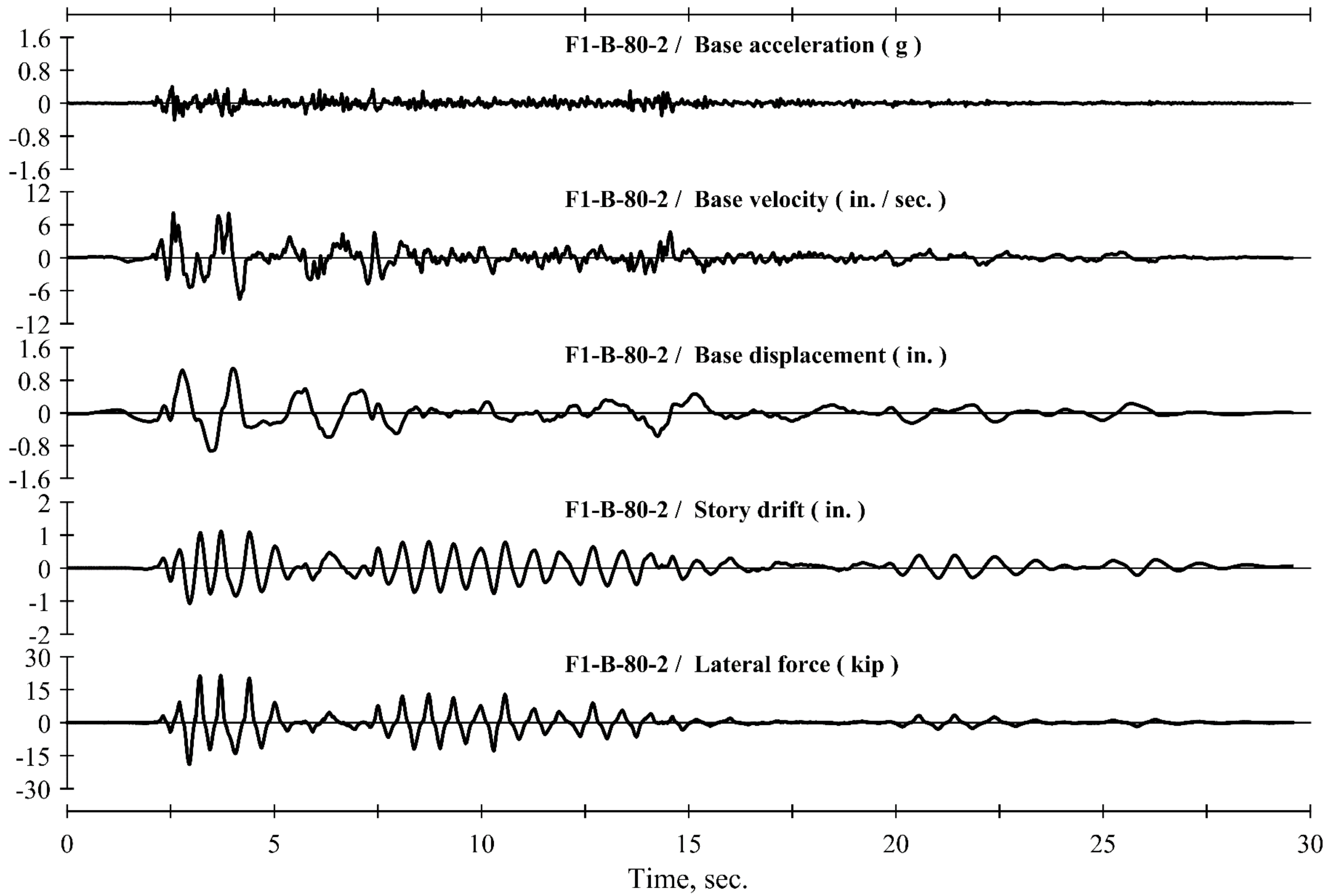

Figure D-13: Base motion and structural response histories in Run 13 of Specimen F1

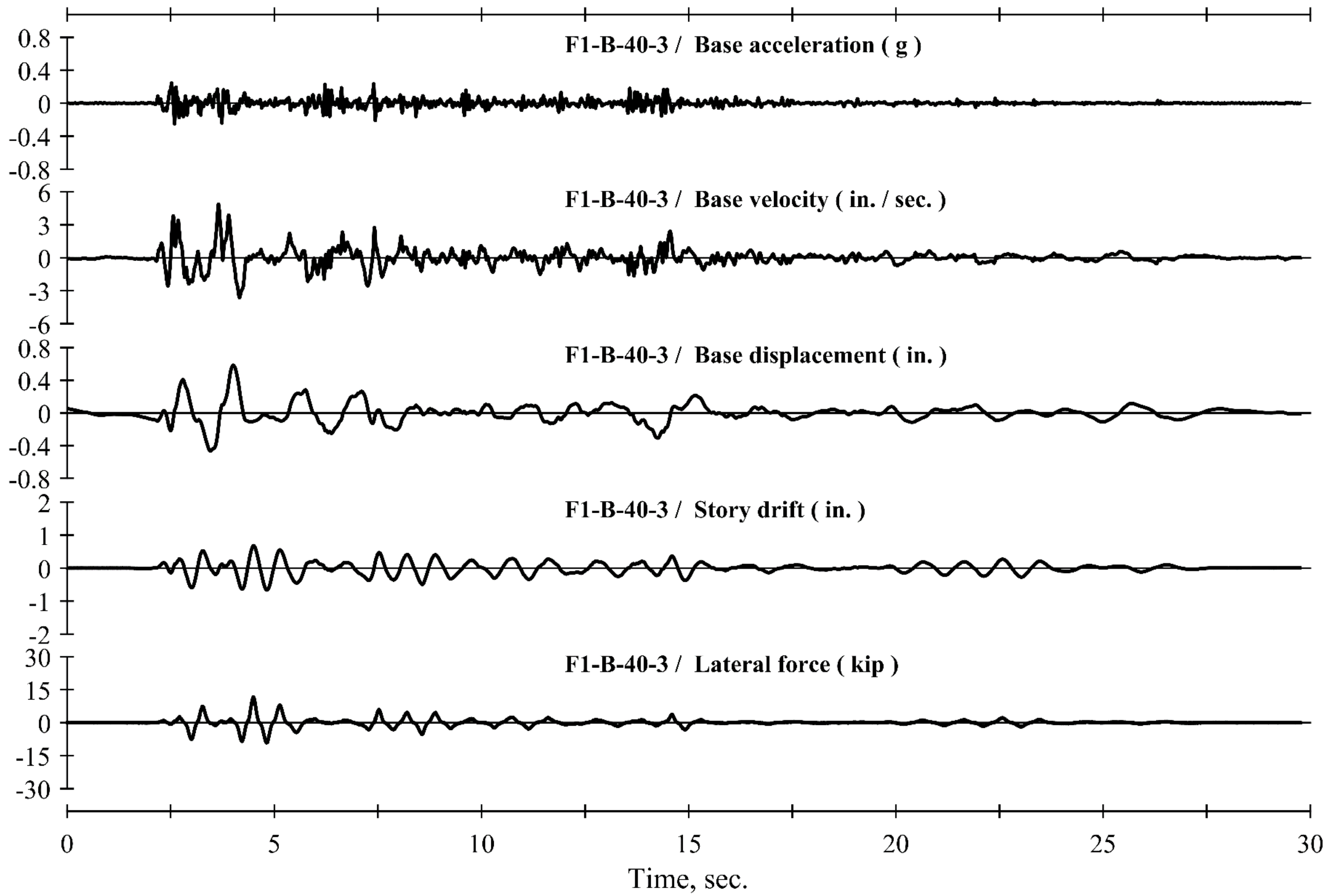

Figure D-14: Base motion and structural response histories in Run 14 of Specimen F1

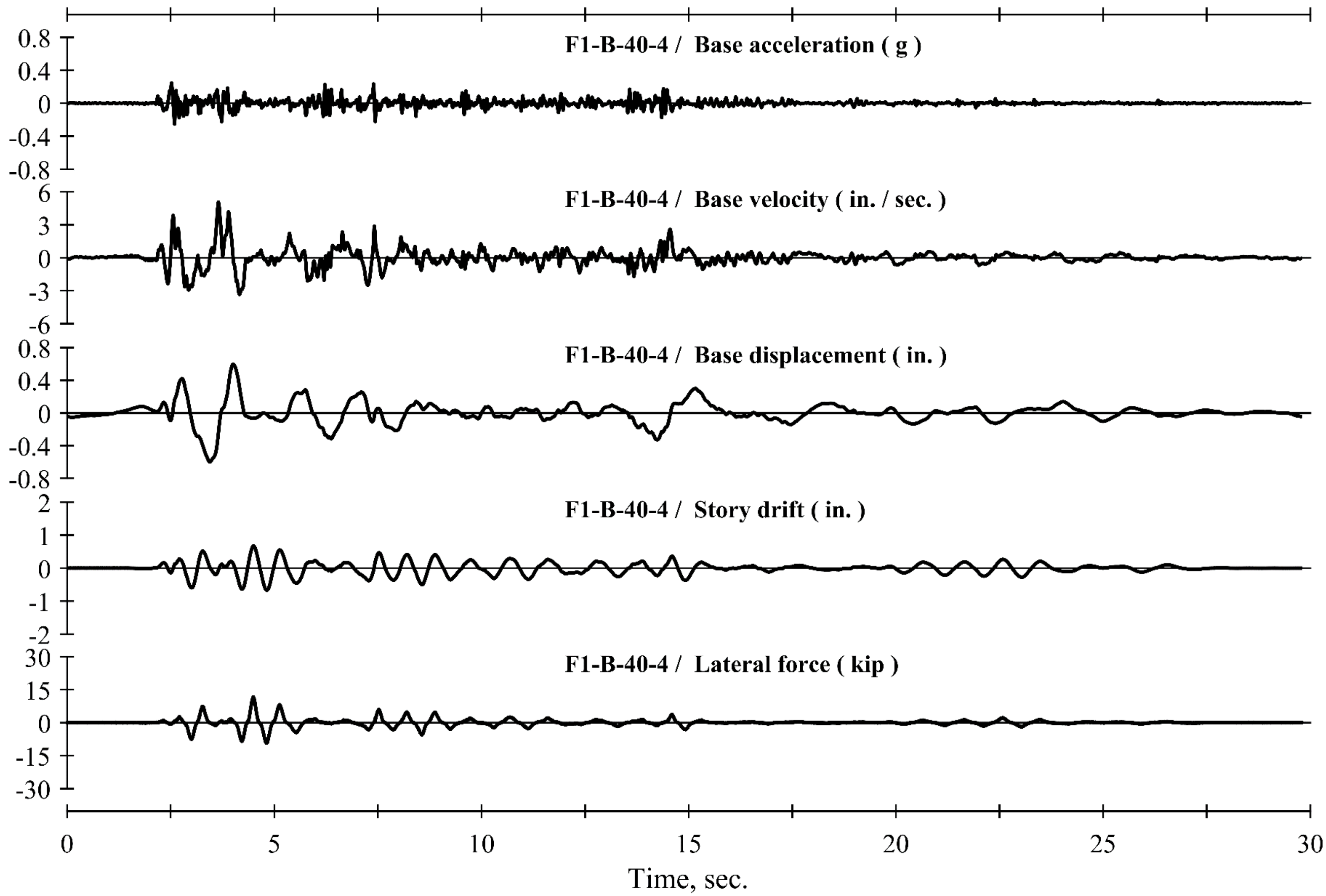

Figure D-15: Base motion and structural response histories in Run 15 of Specimen F1

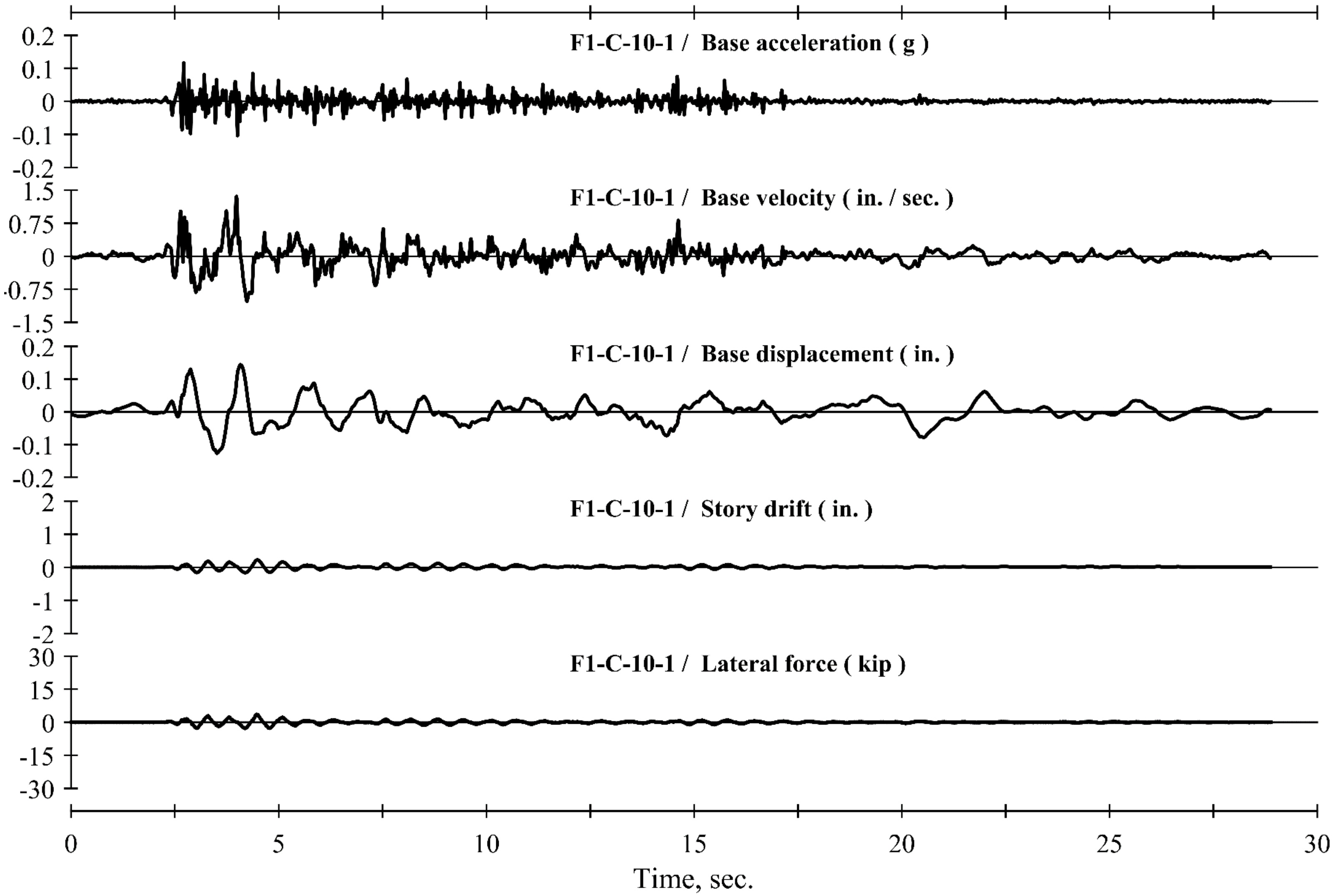

Figure D-16: Base motion and structural response histories in Run 16 of Specimen F1

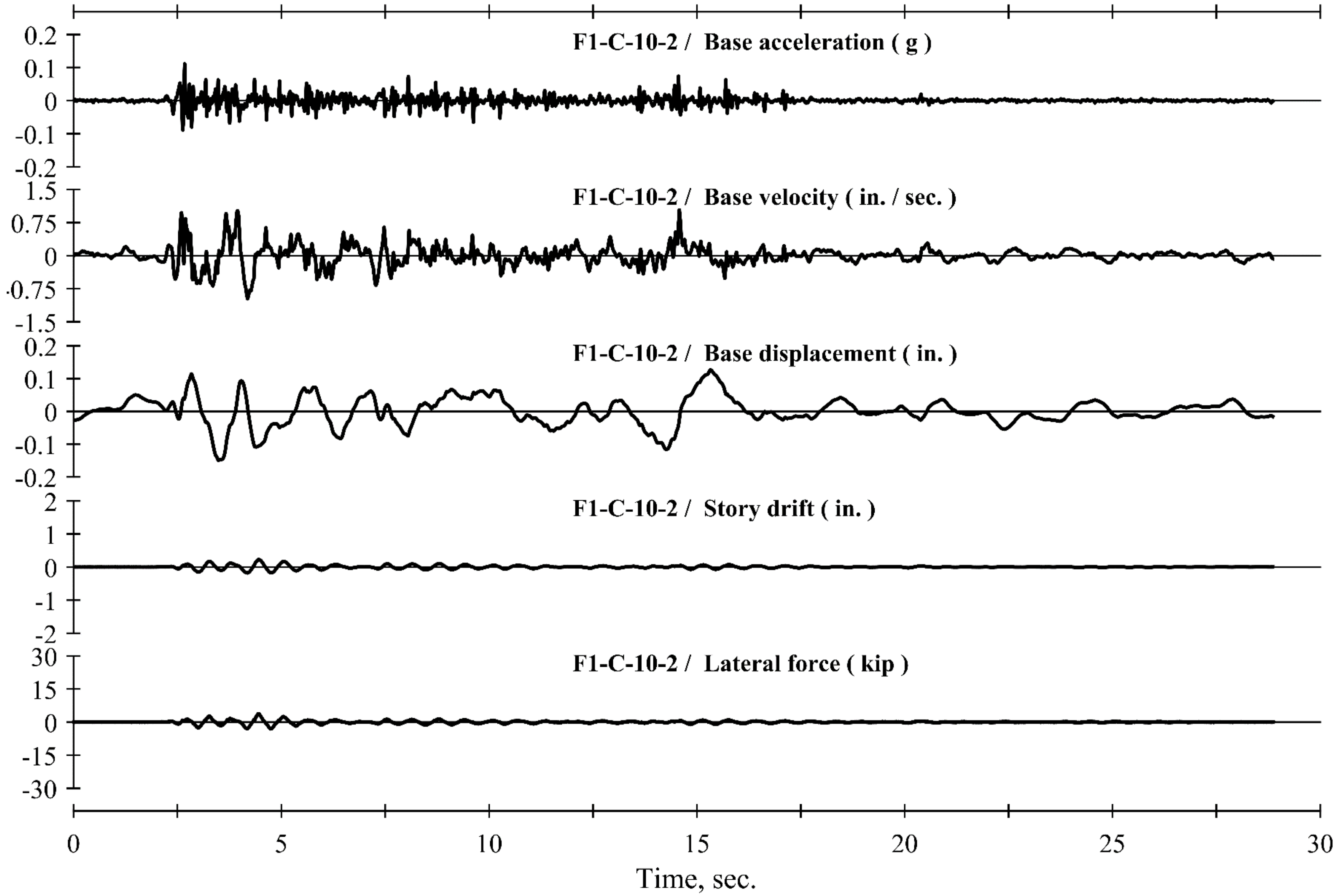

Figure D-17: Base motion and structural response histories in Run 17 of Specimen F1

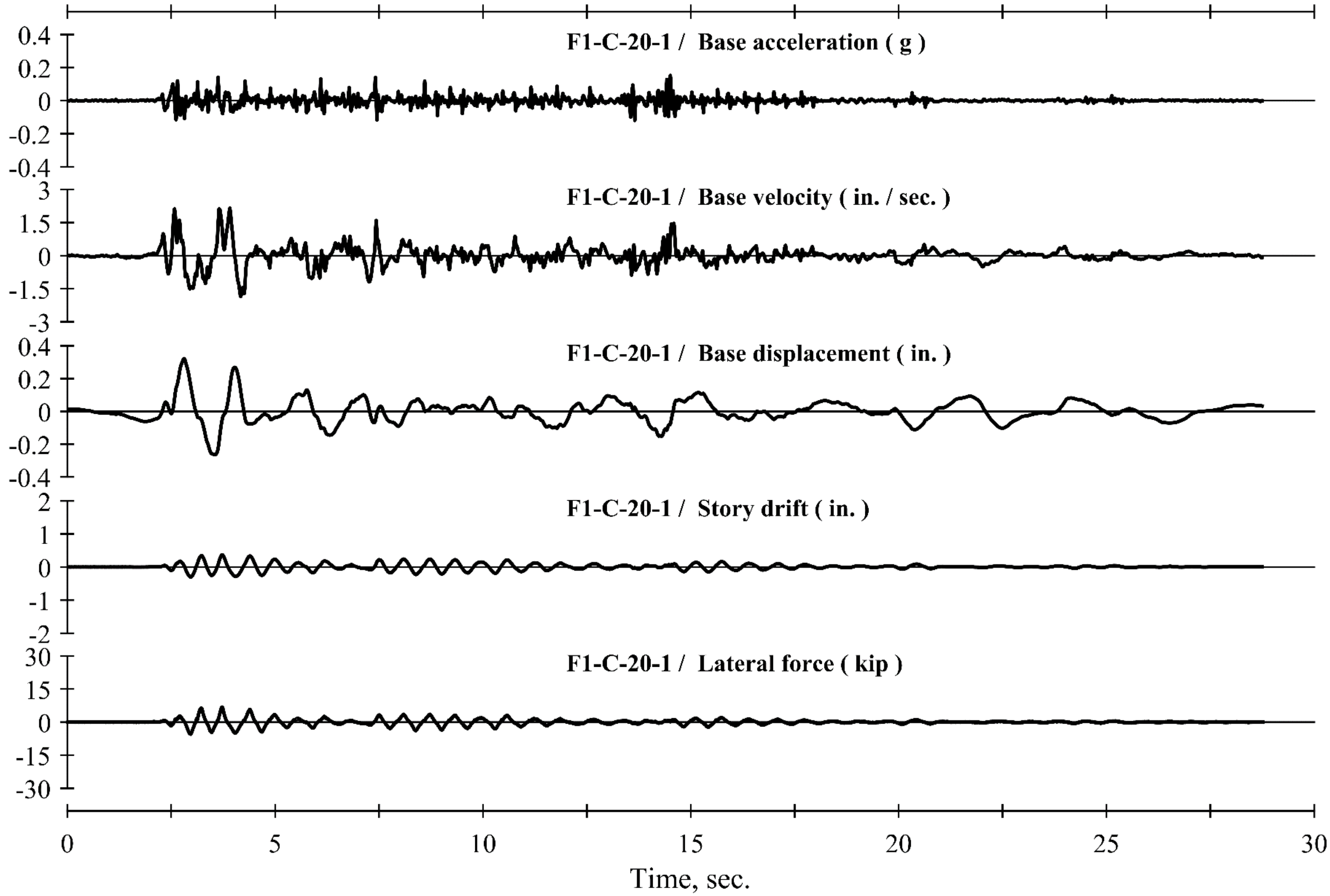

Figure D-18: Base motion and structural response histories in Run 18 of Specimen F1

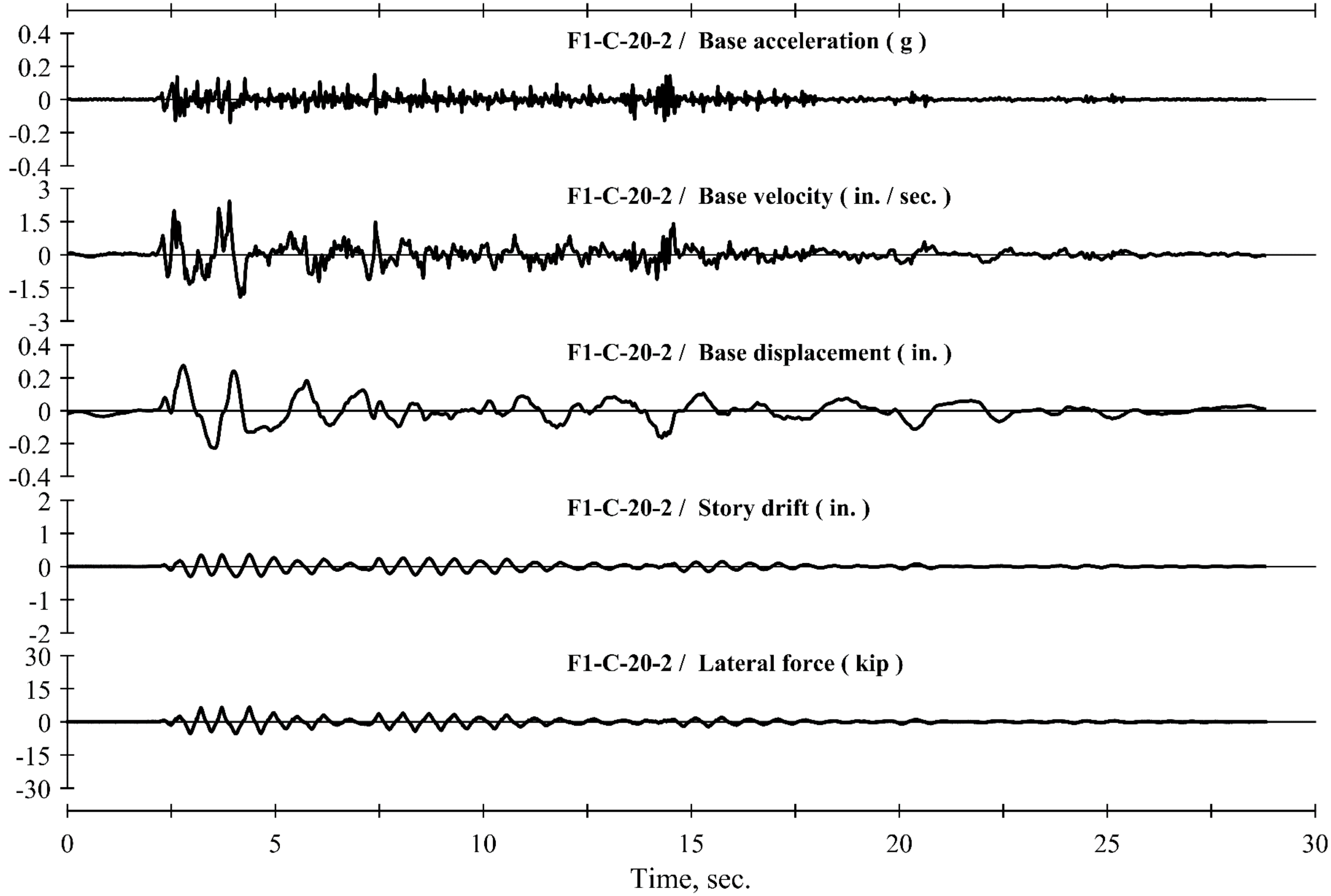

Figure D-19: Base motion and structural response histories in Run 19 of Specimen F1

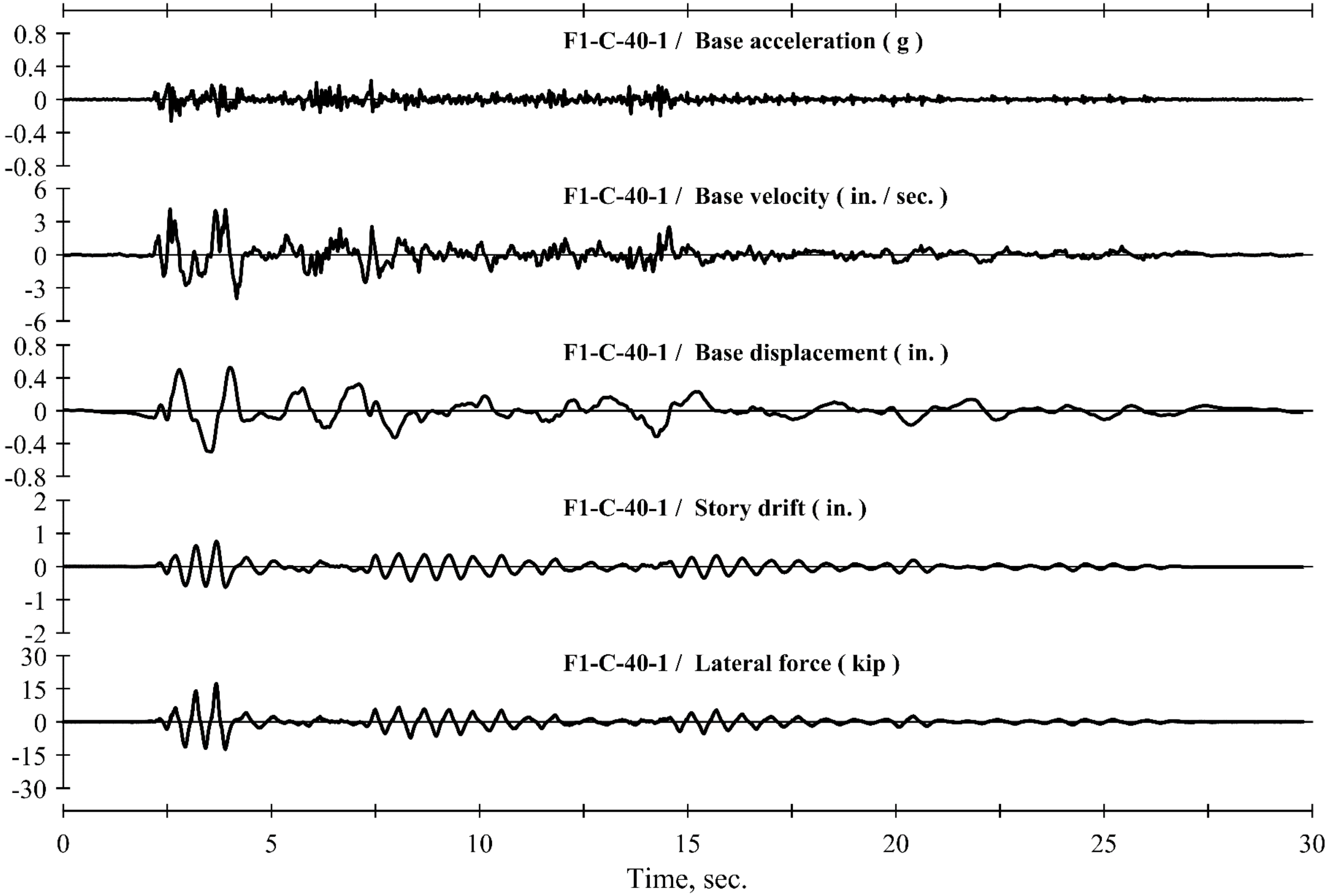

Figure D-20: Base motion and structural response histories in Run 20 of Specimen F1

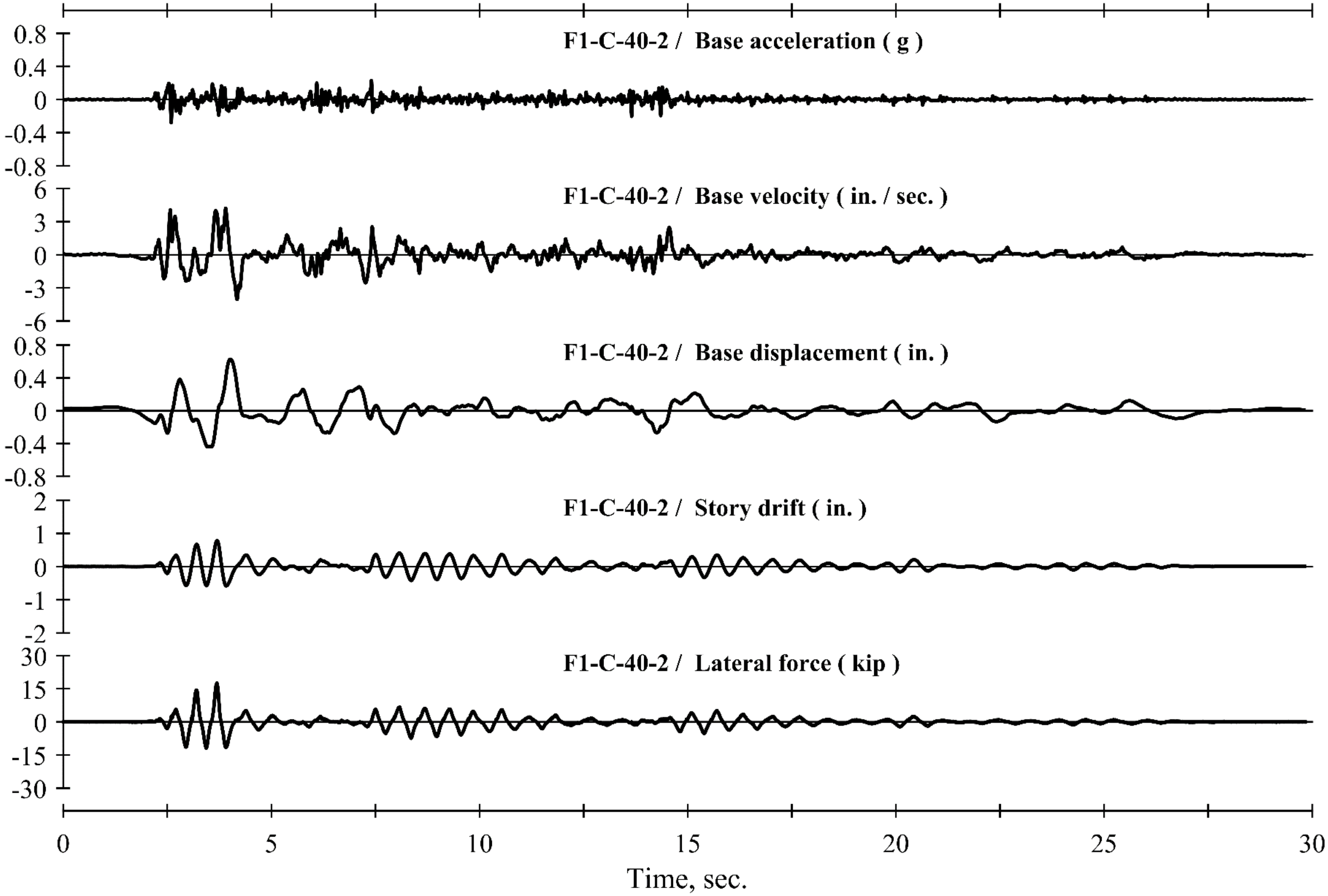

Figure D-21: Base motion and structural response histories in Run 21 of Specimen F1

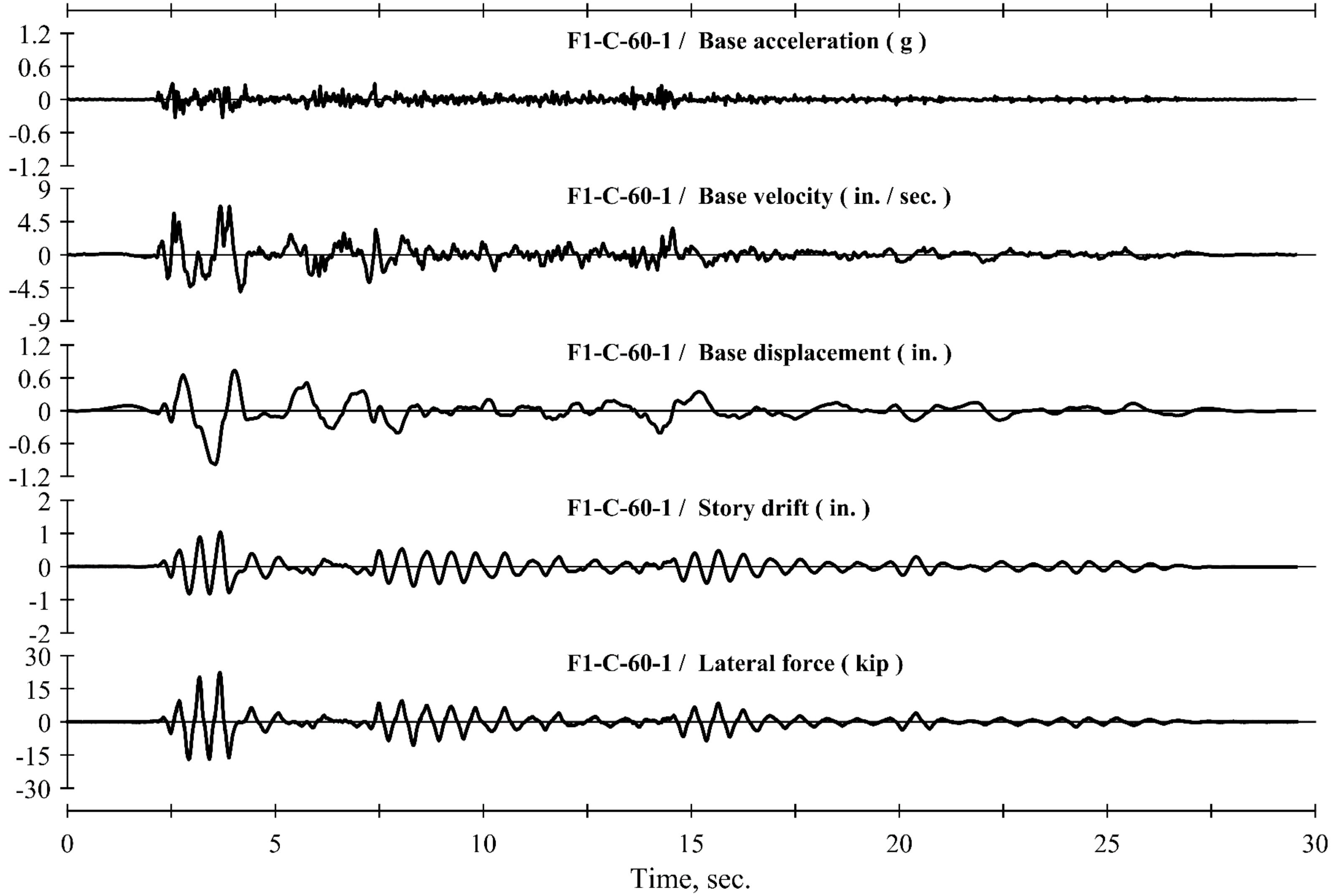

Figure D-22: Base motion and structural response histories in Run 22 of Specimen F1

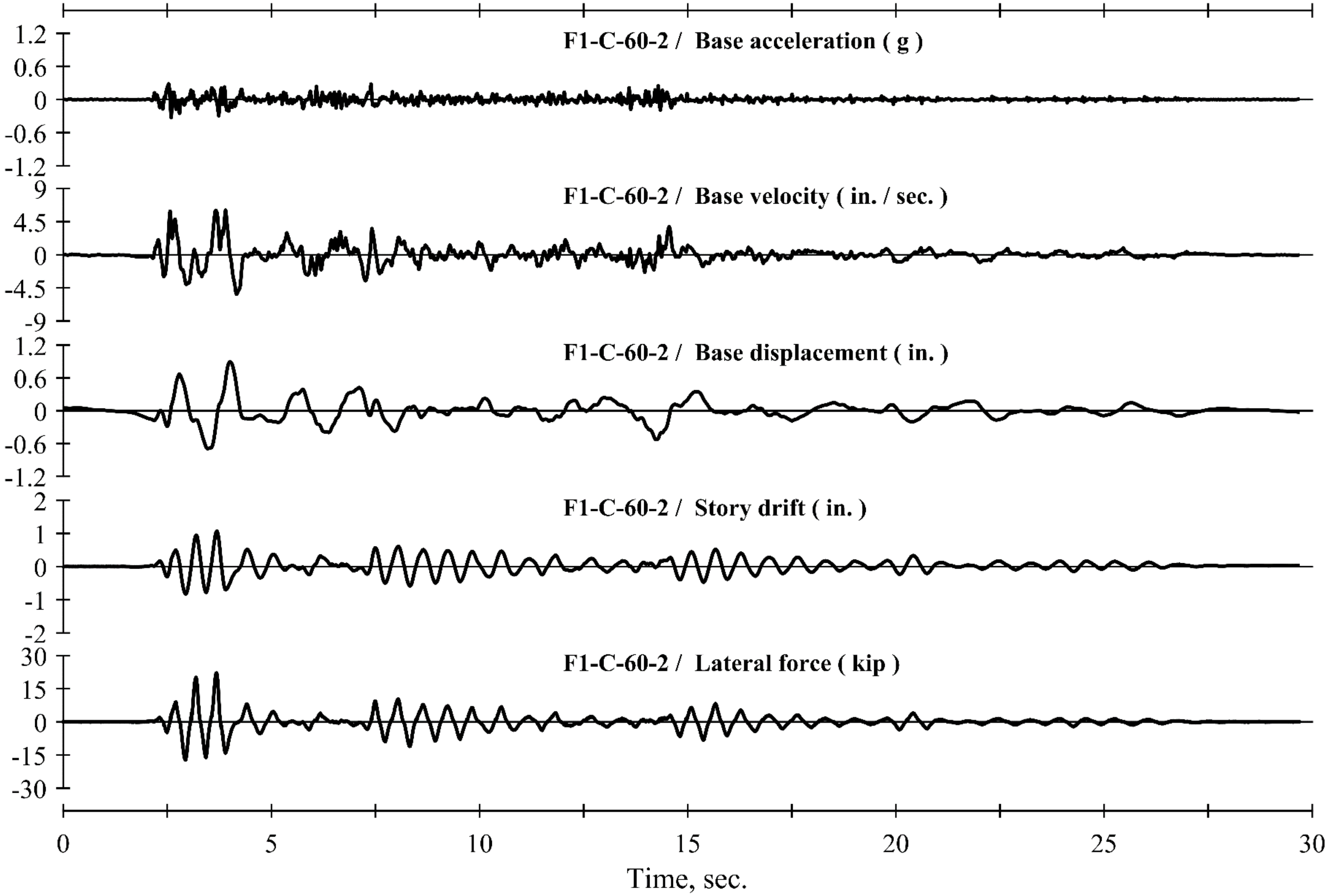

Figure D-23: Base motion and structural response histories in Run 23 of Specimen F1

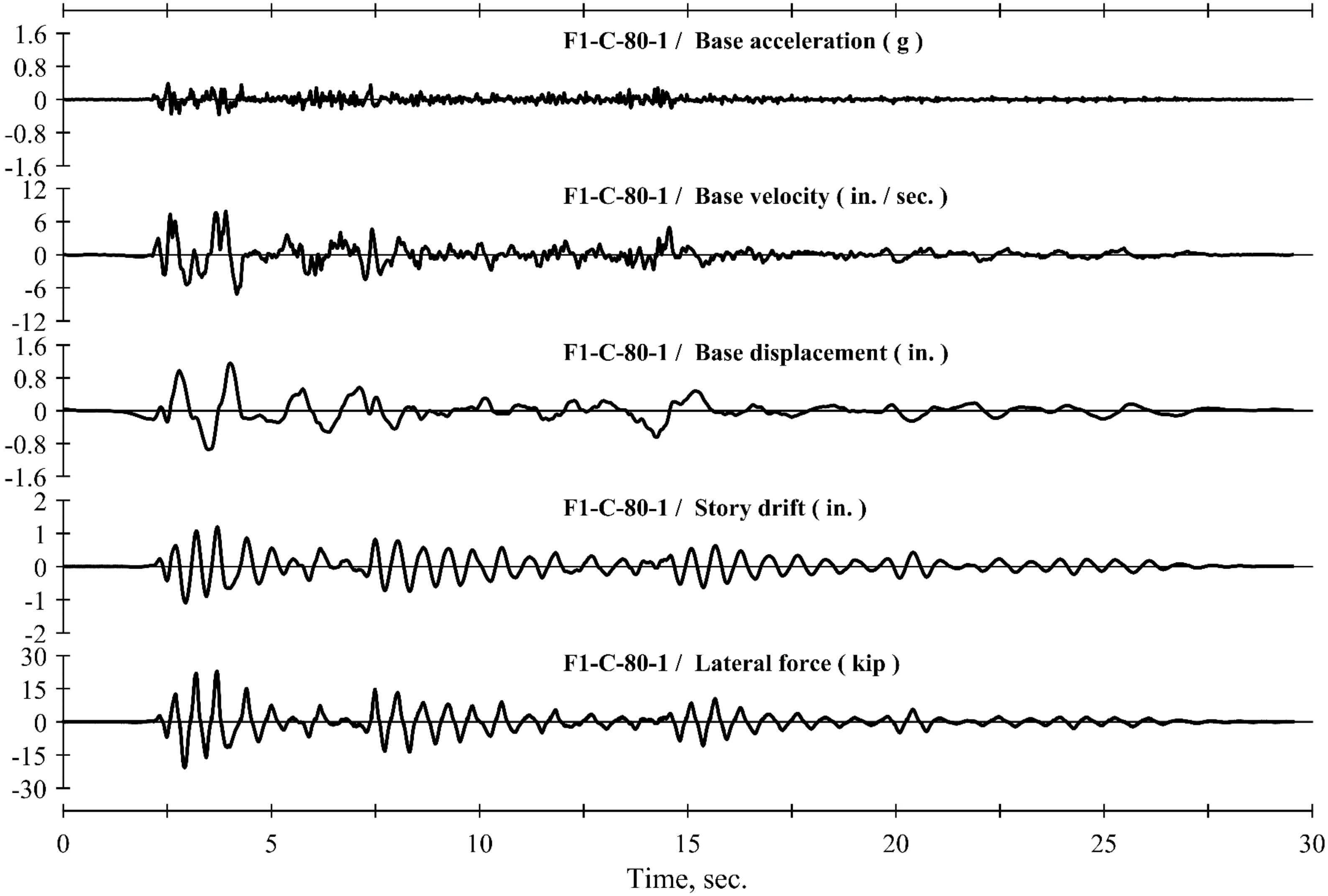

Figure D-24: Base motion and structural response histories in Run 24 of Specimen F1

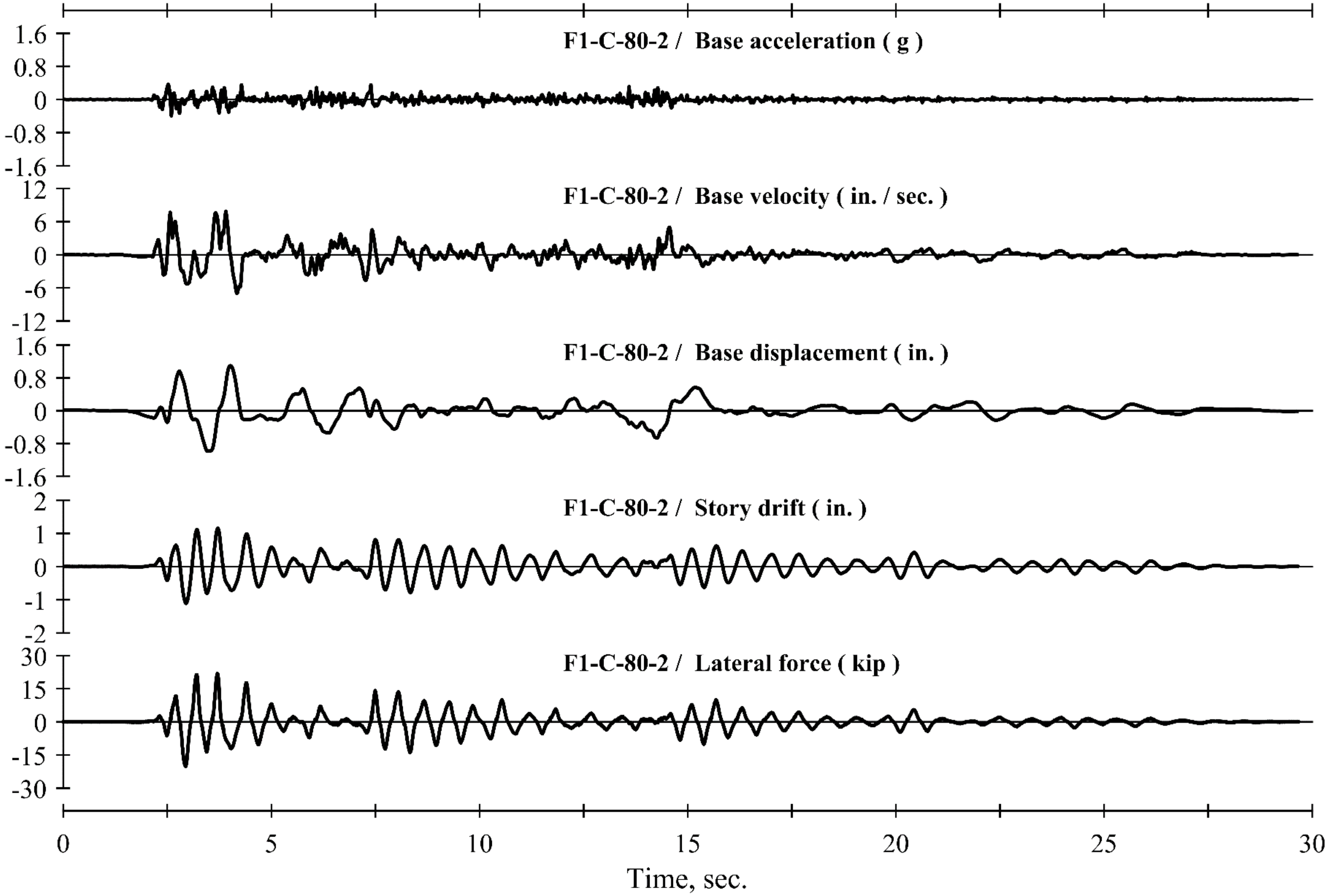

Figure D-25: Base motion and structural response histories in Run 25 of Specimen F1

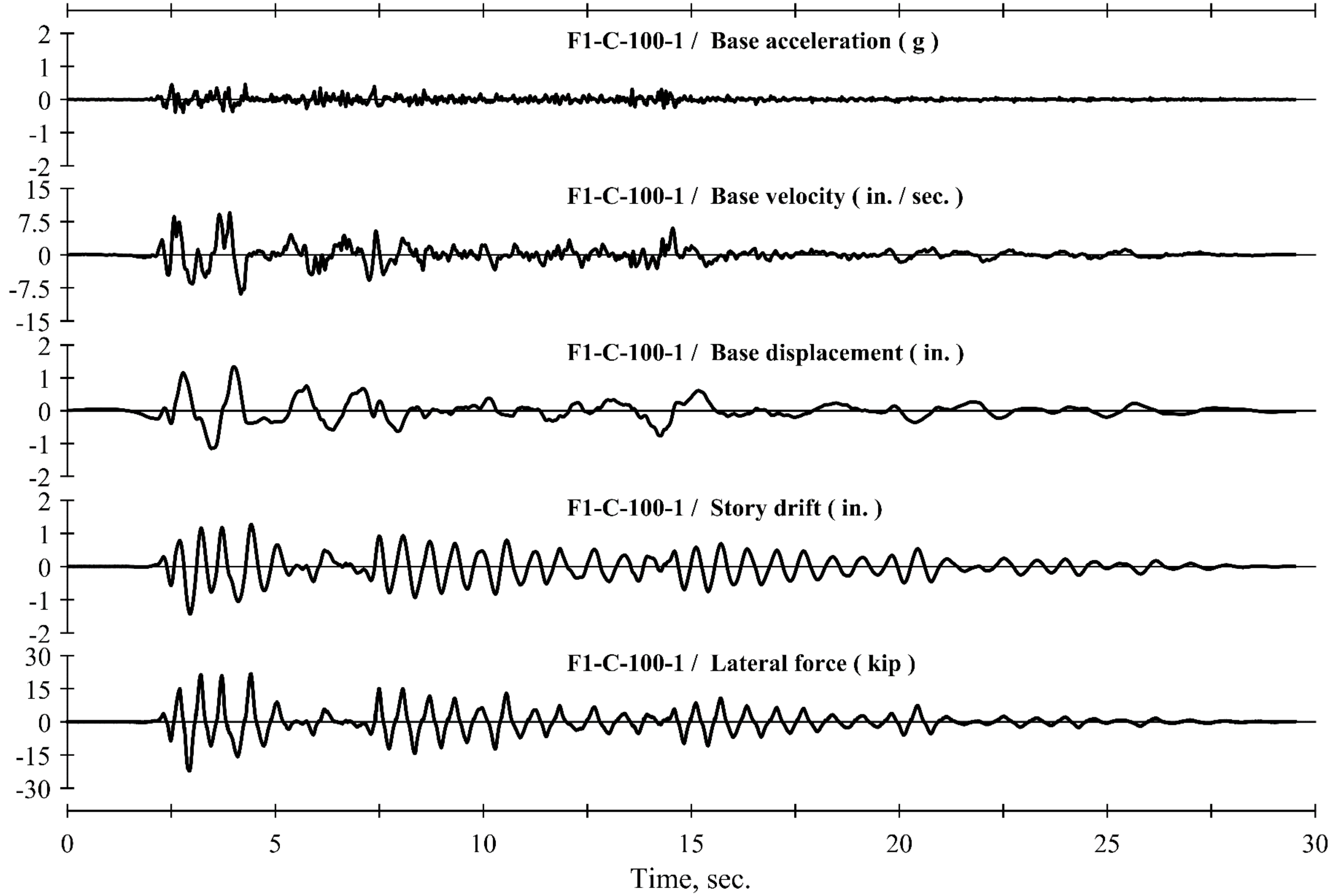

Figure D-26: Base motion and structural response histories in Run 26 of Specimen F1

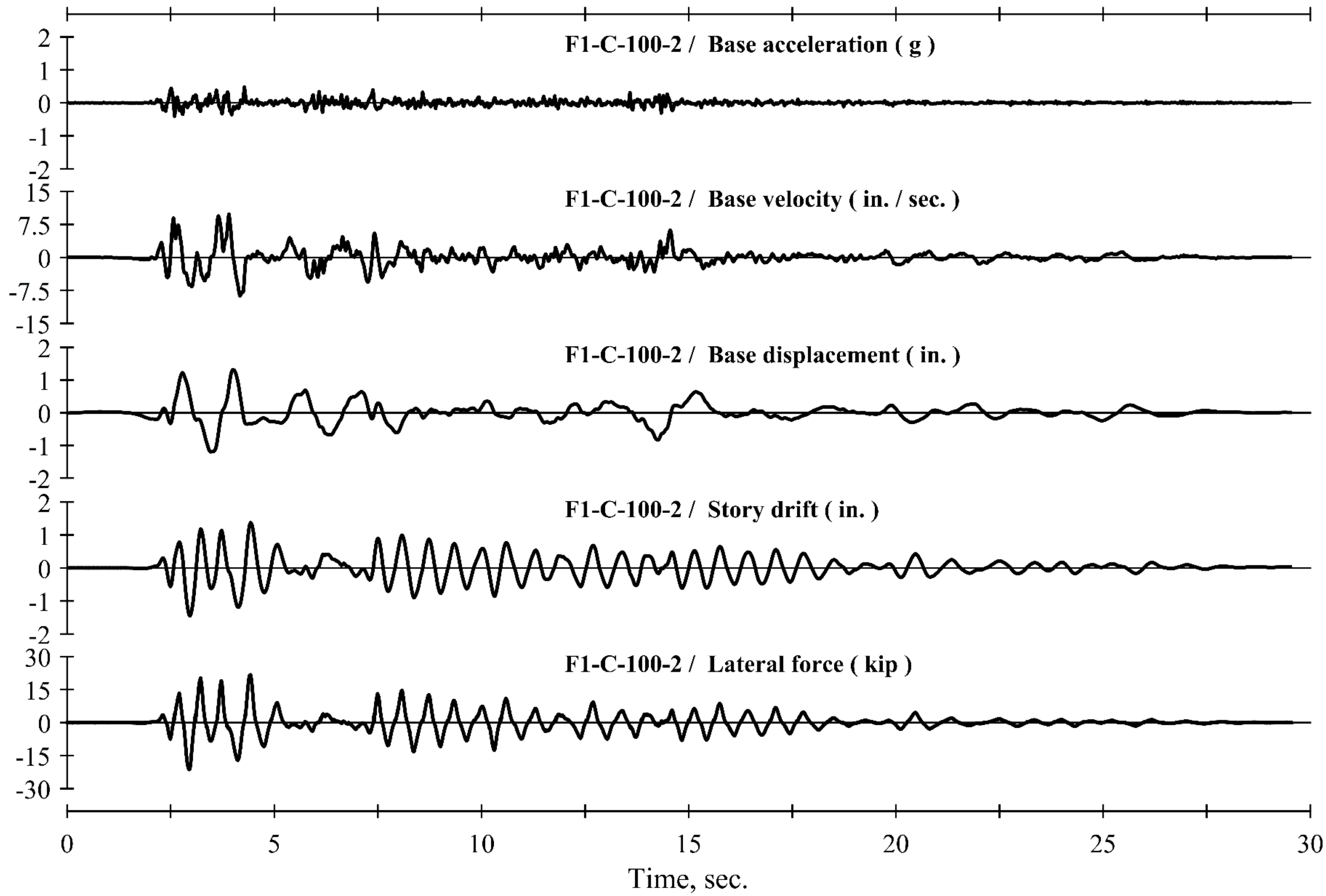

Figure D-27: Base motion and structural response histories in Run 27 of Specimen F1

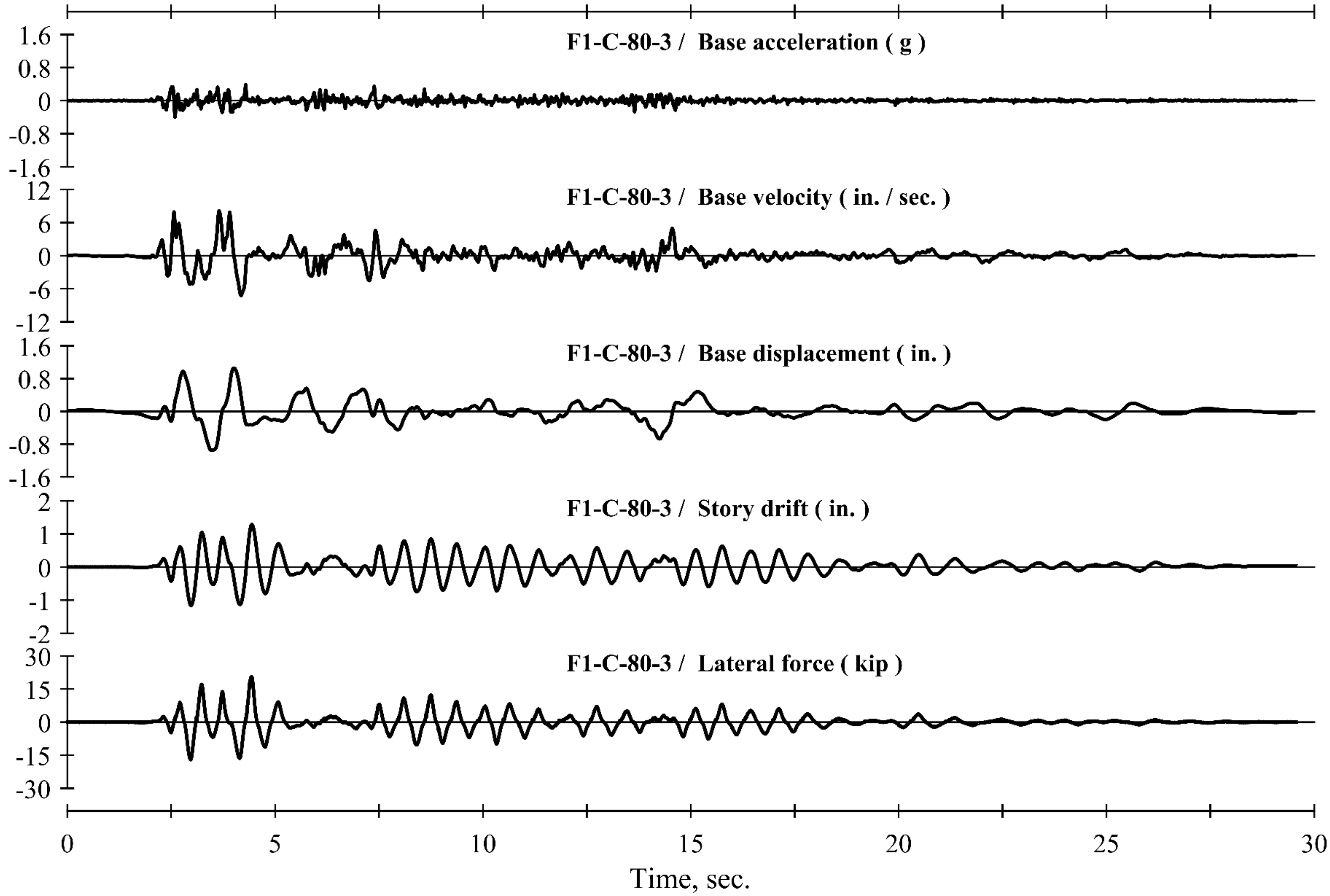

Figure D-28: Base motion and structural response histories in Run 28 of Specimen F1

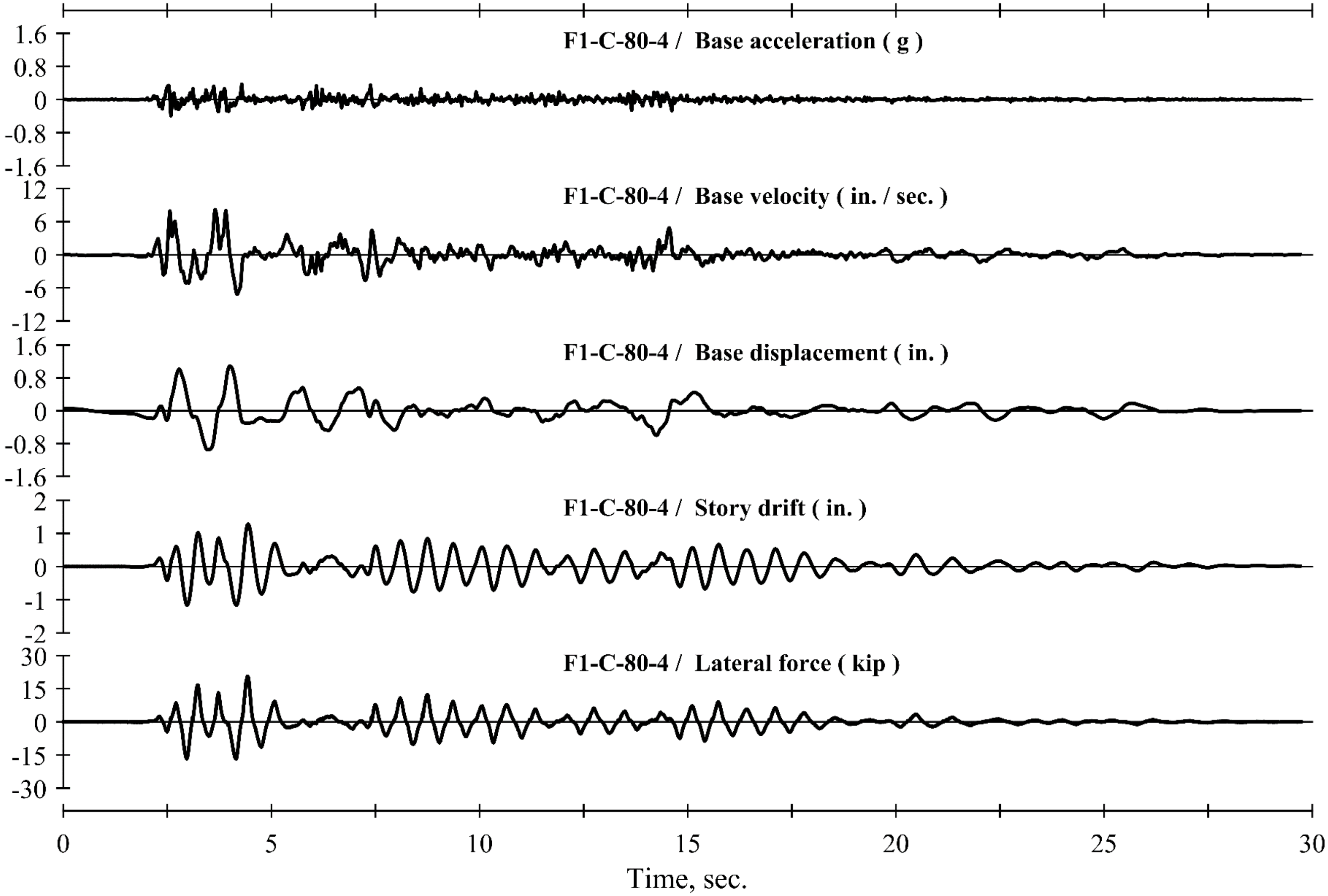

Figure D-29: Base motion and structural response histories in Run 29 of Specimen F1

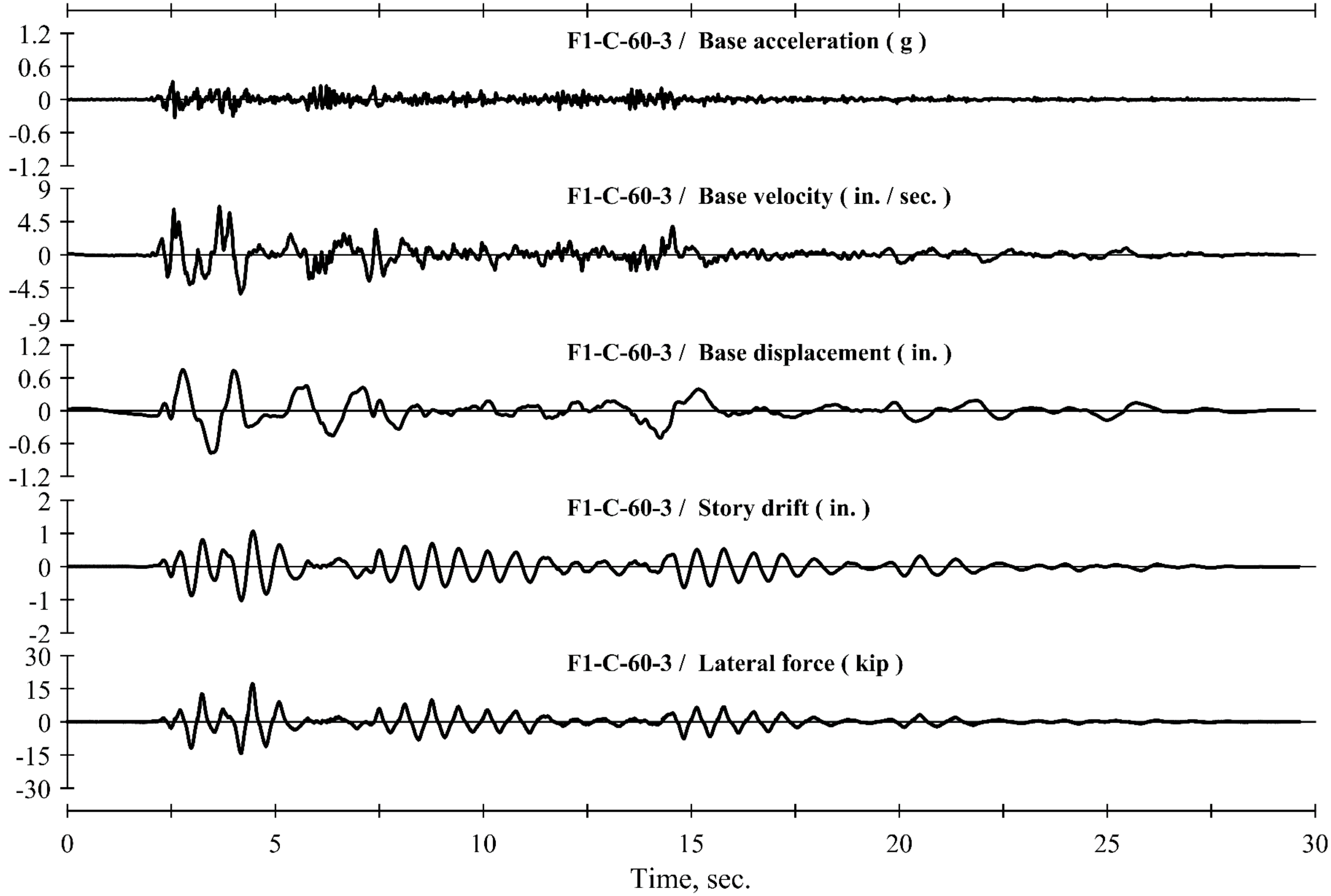

Figure D-30: Base motion and structural response histories in Run 30 of Specimen F1

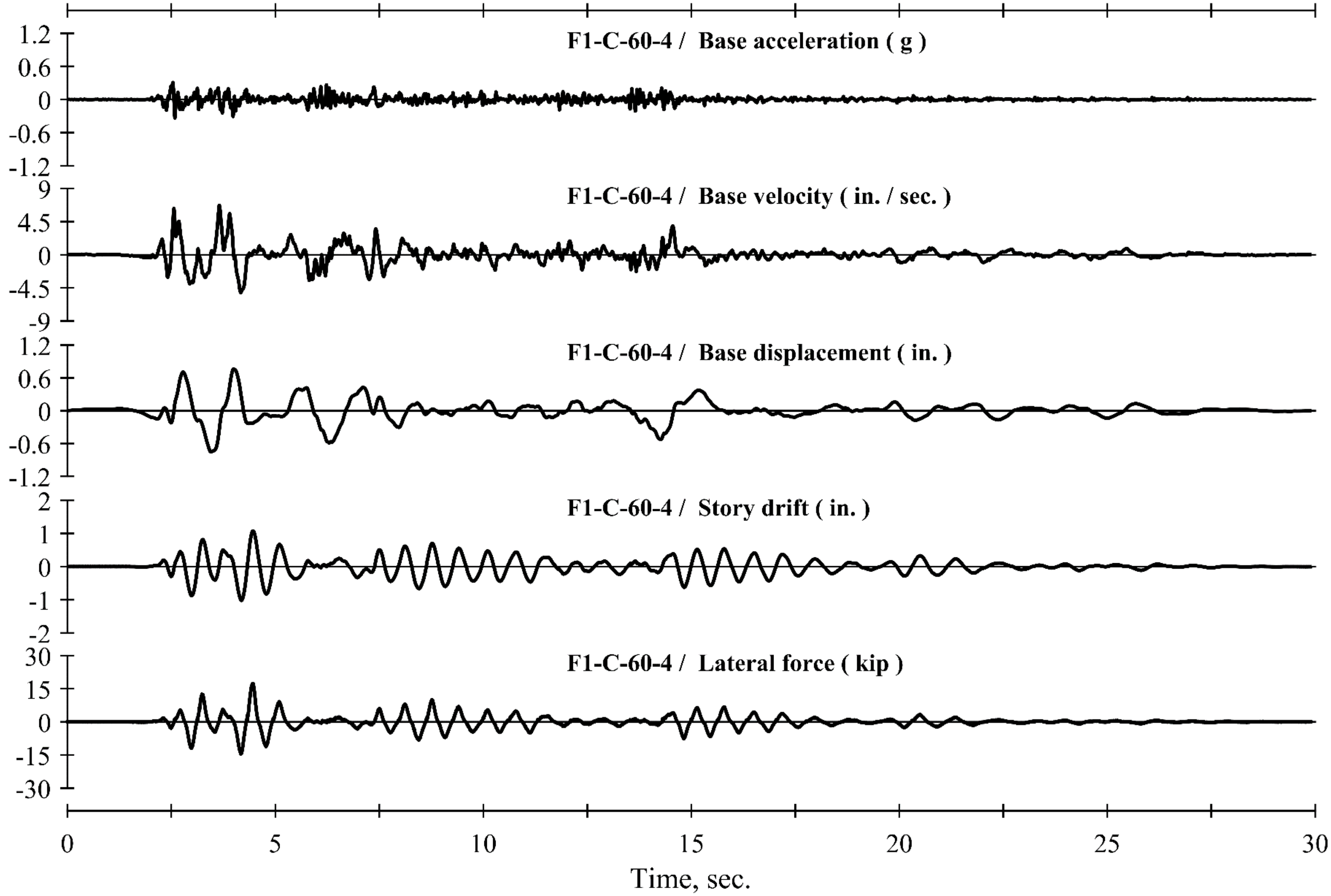

Figure D-31: Base motion and structural response histories in Run 31 of Specimen F1

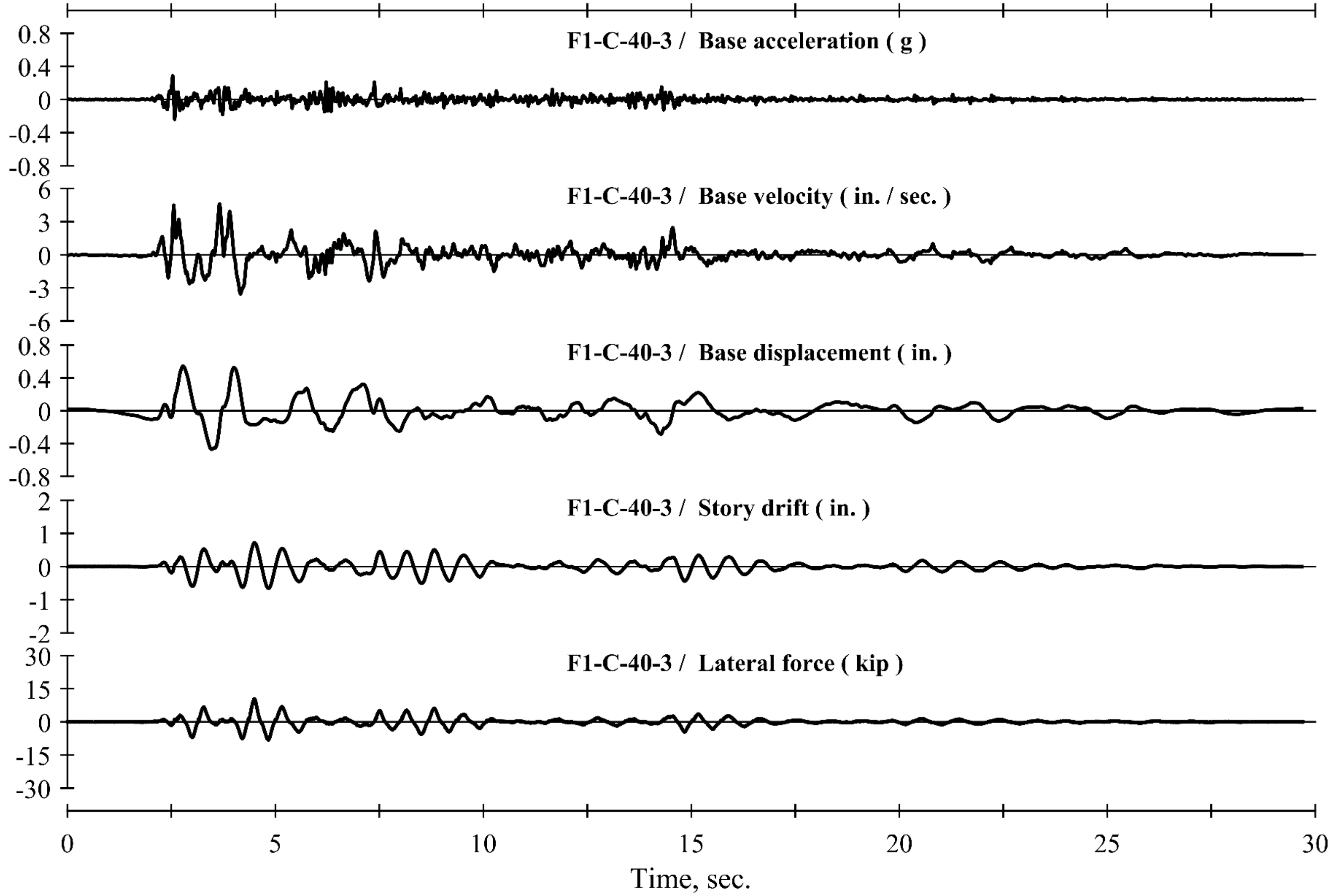

Figure D-32: Base motion and structural response histories in Run 32 of Specimen F1

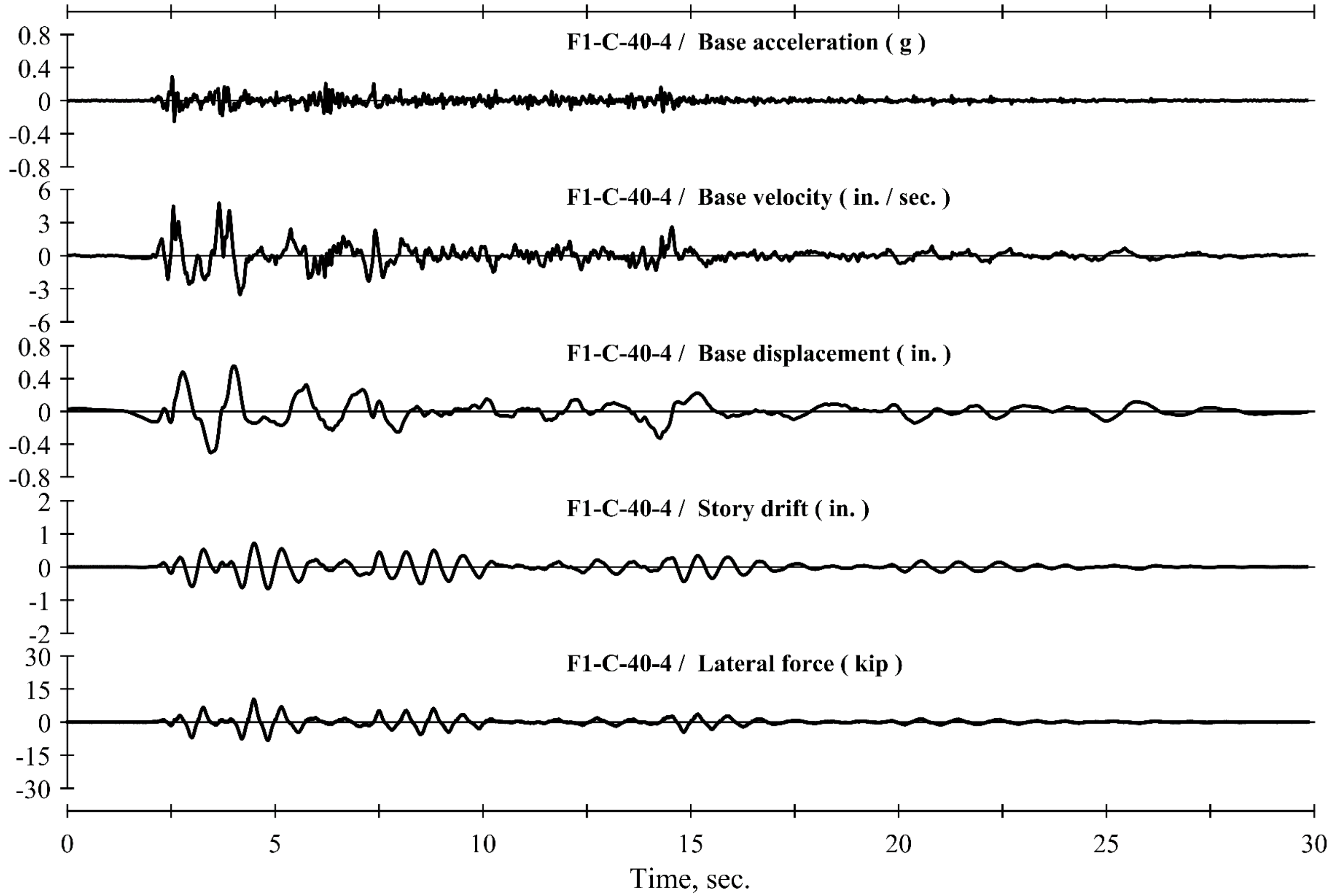

Figure D-33: Base motion and structural response histories in Run 33 of Specimen F1

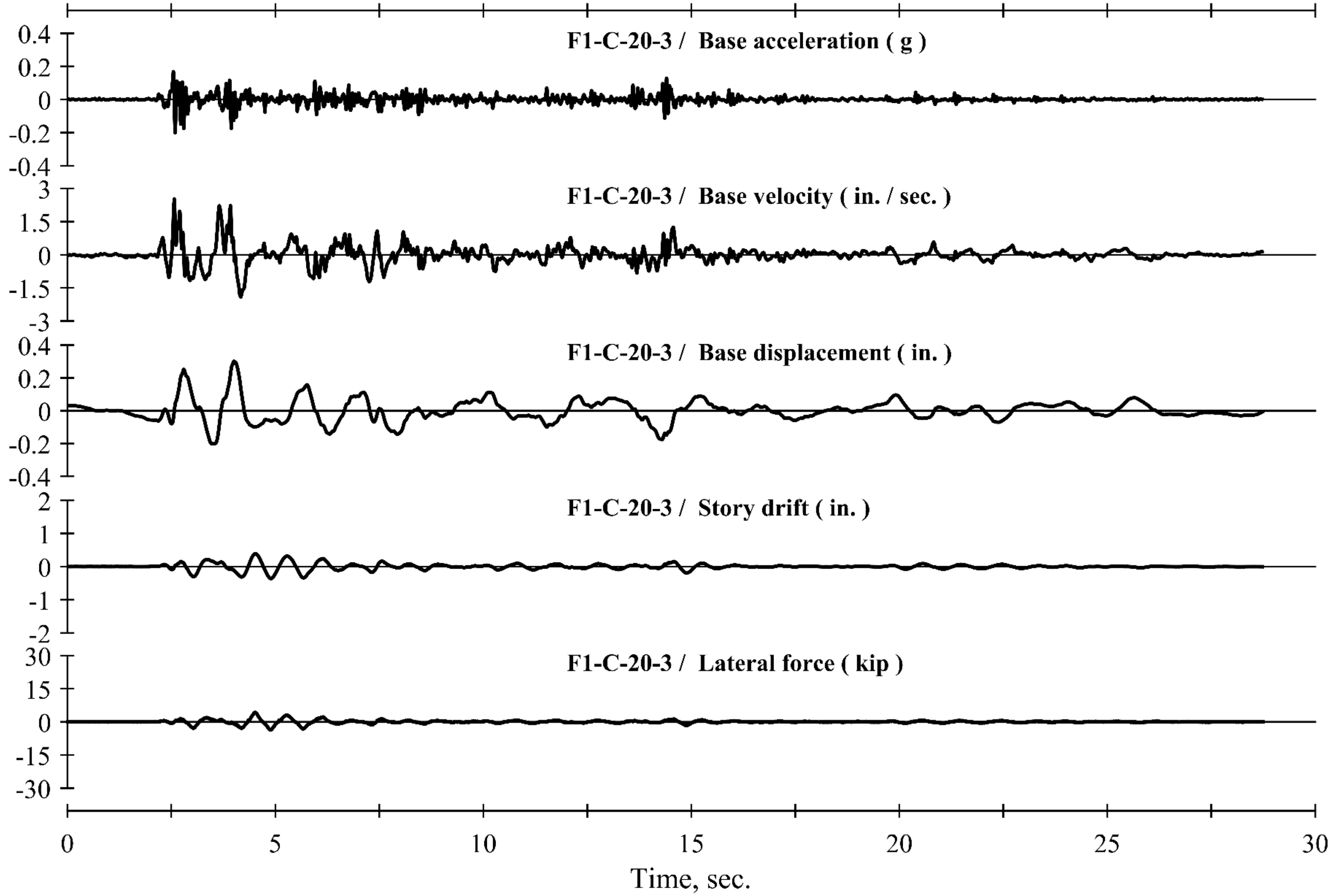

Figure D-34: Base motion and structural response histories in Run 34 of Specimen F1

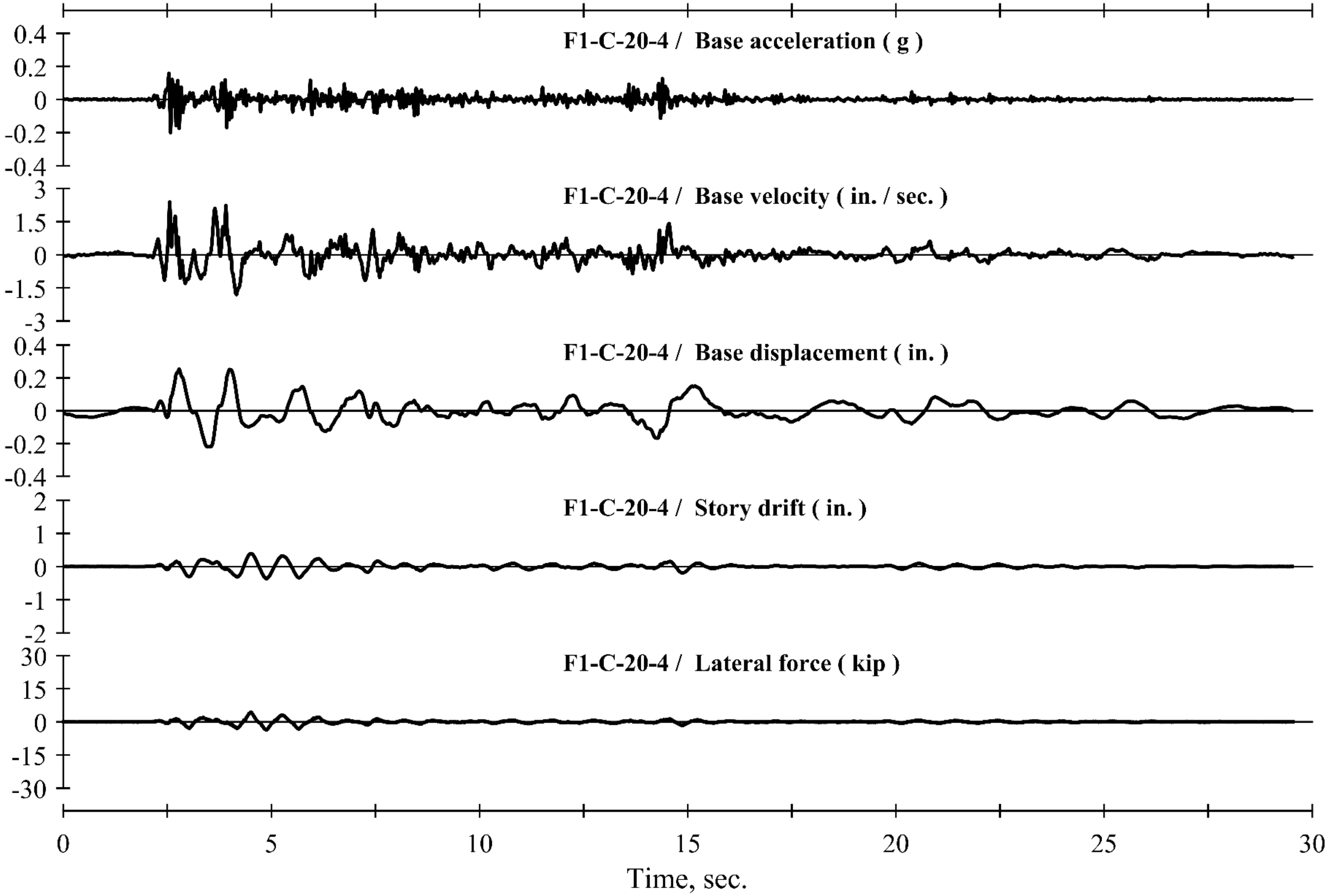

Figure D-35: Base motion and structural response histories in Run 35 of Specimen F1

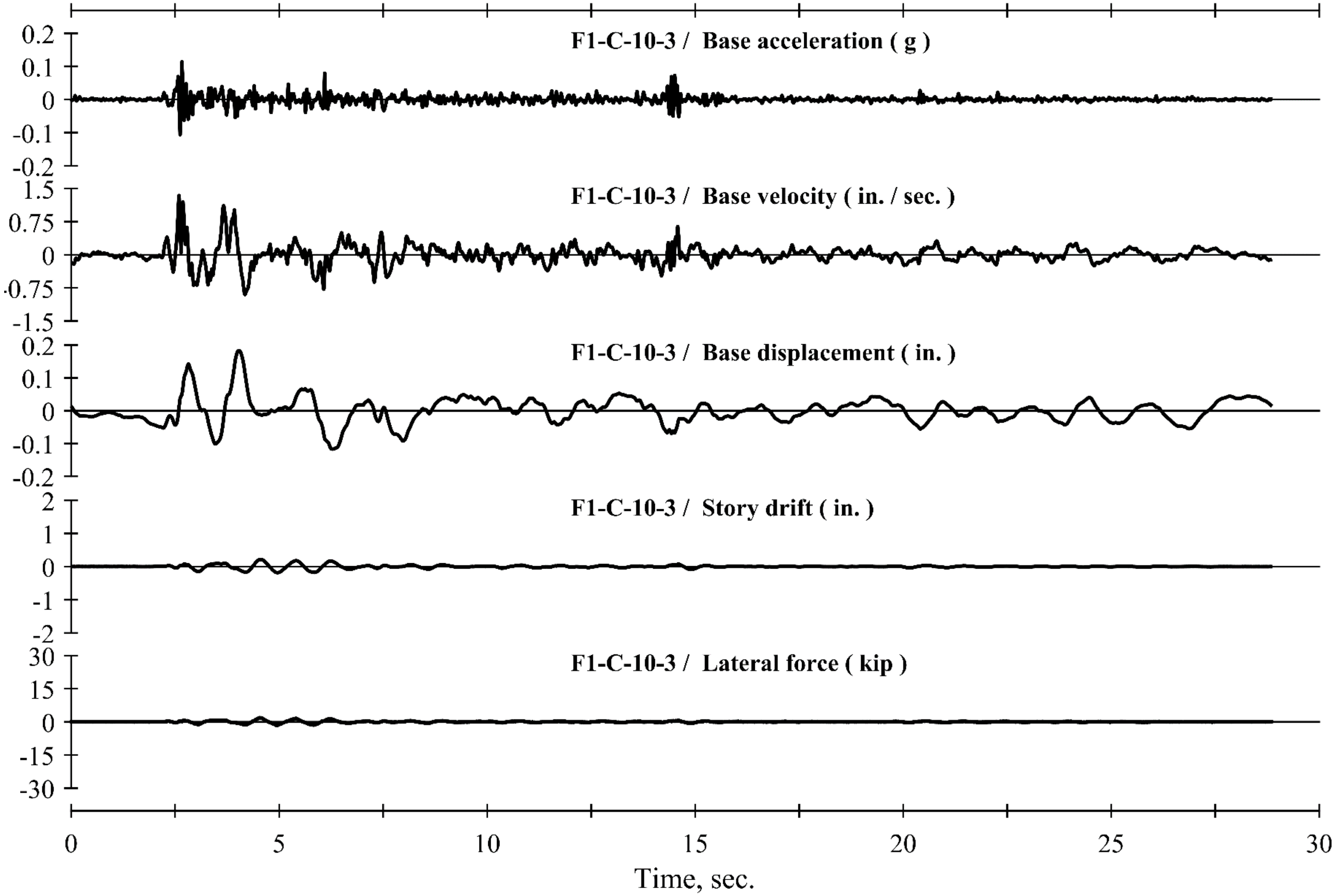

Figure D-36: Base motion and structural response histories in Run 36 of Specimen F1

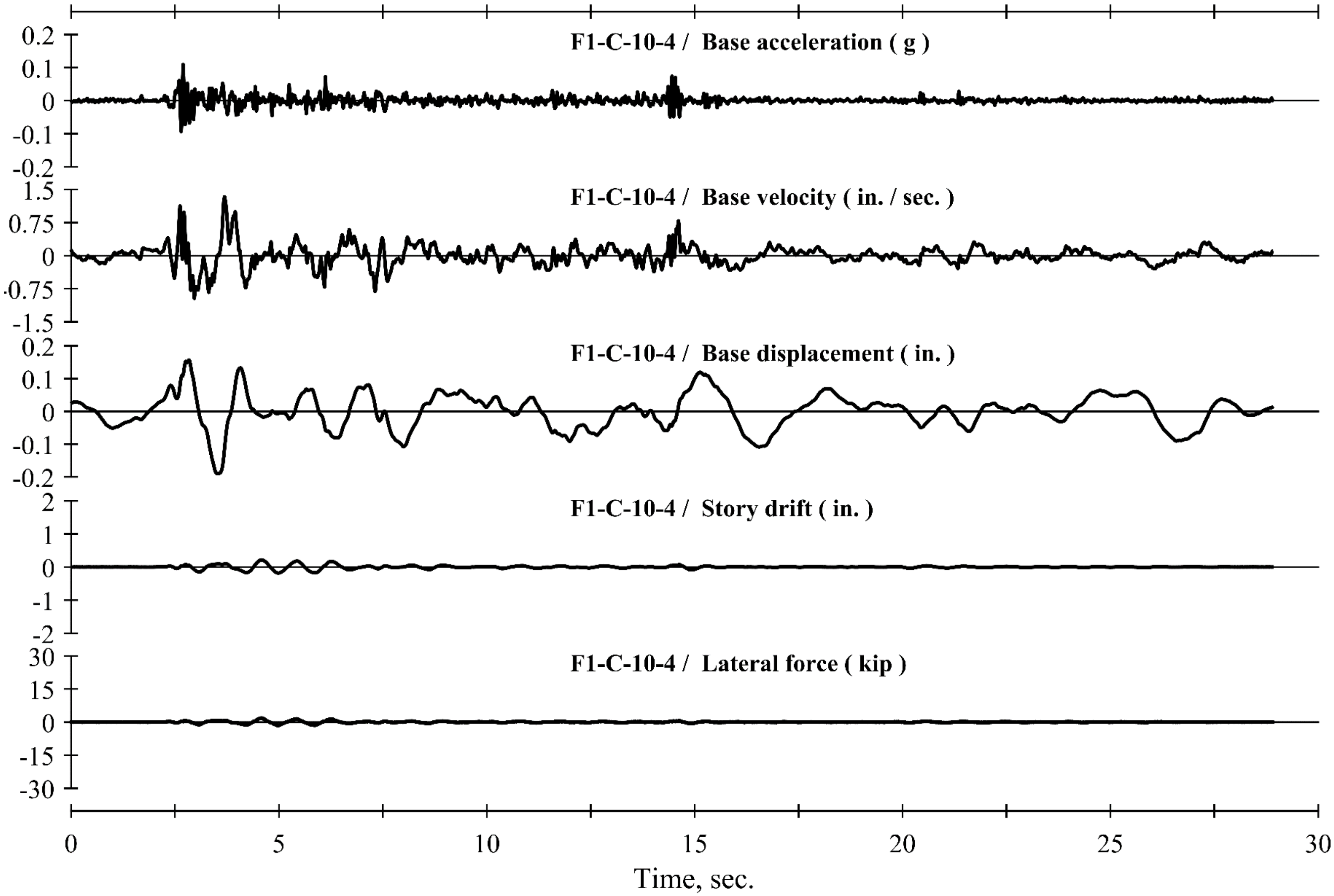

Figure D-37: Base motion and structural response histories in Run 37 of Specimen F1

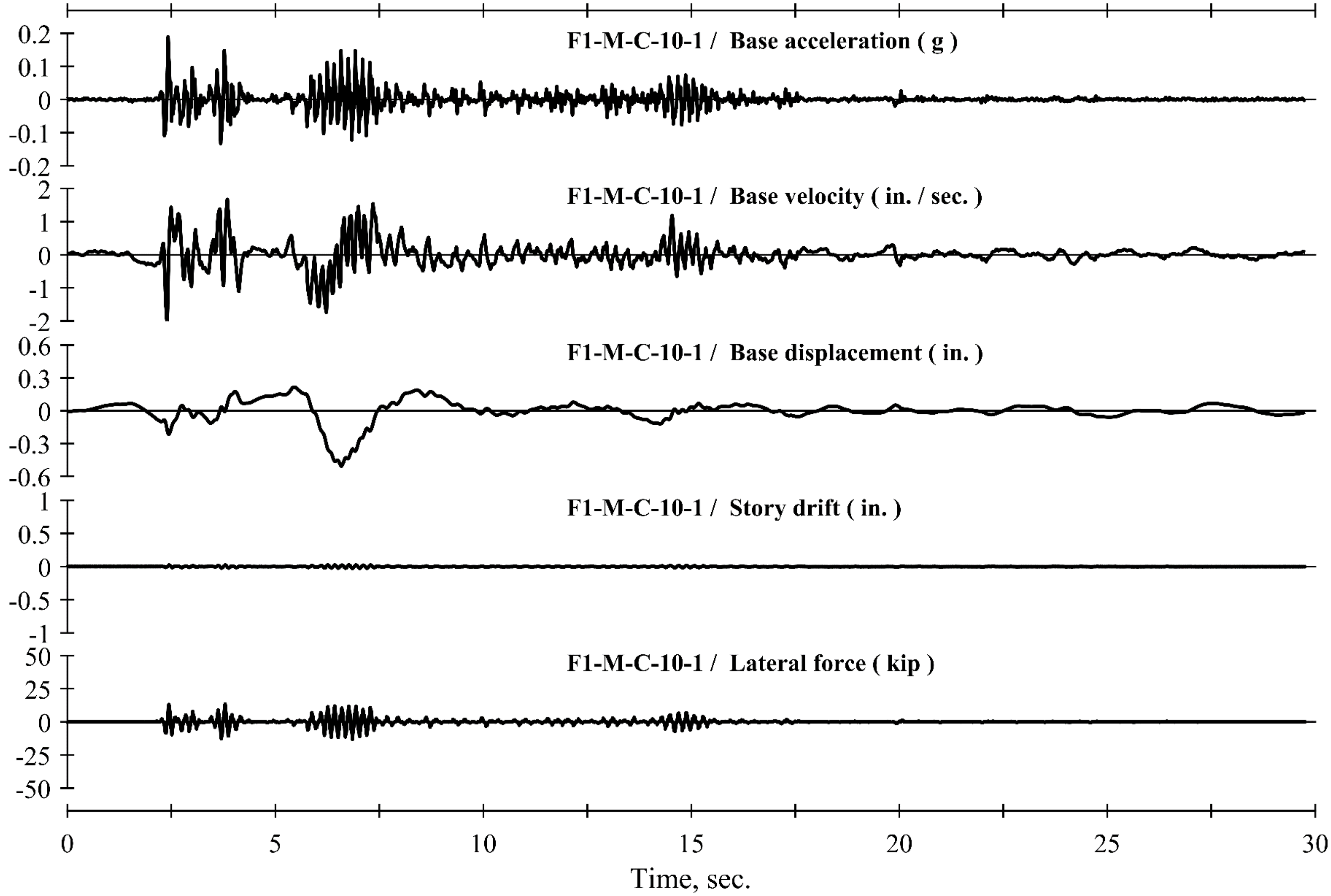

Figure D-38: Base motion and structural response histories in Run 38 of Specimen F1

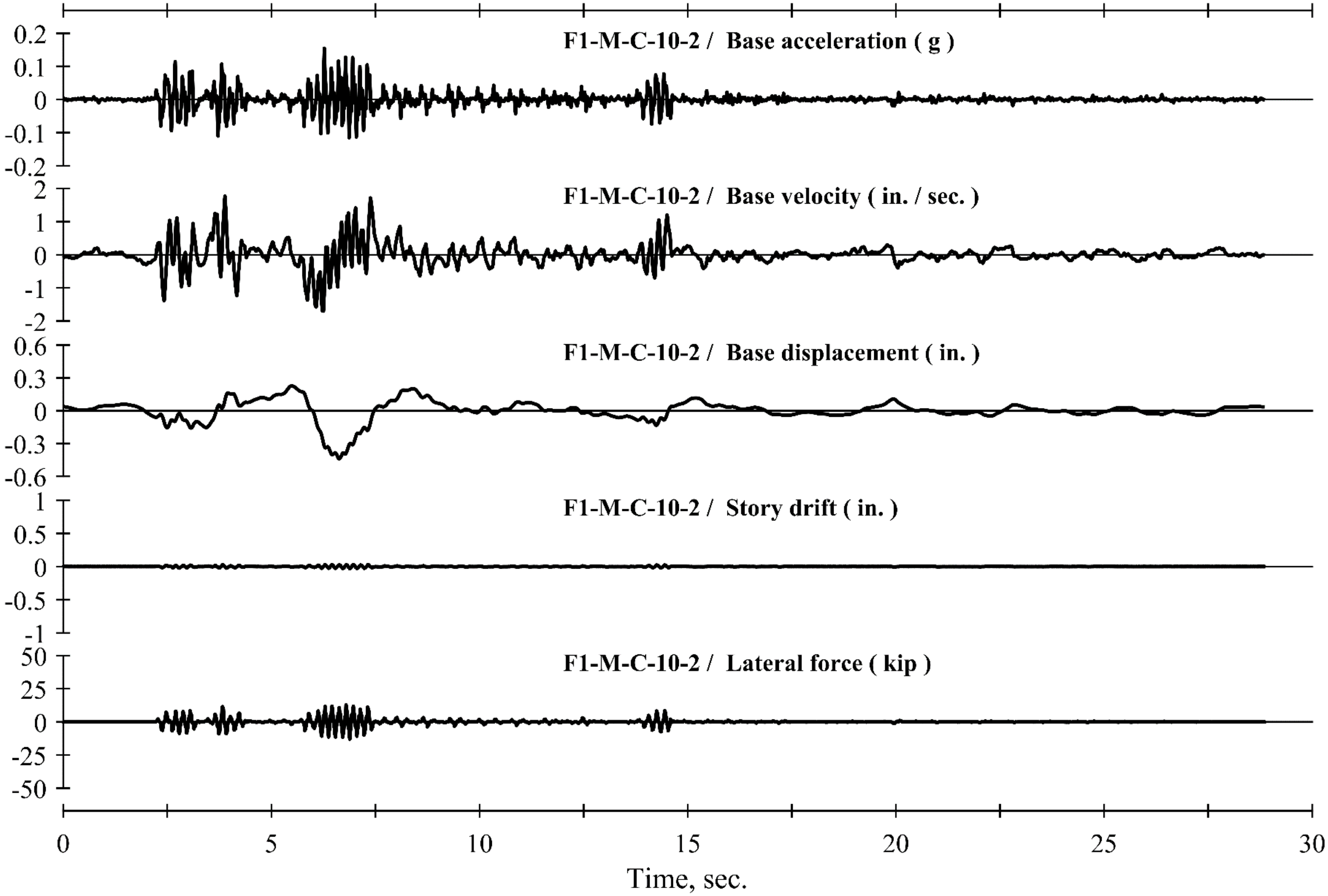

Figure D-39: Base motion and structural response histories in Run 39 of Specimen F1

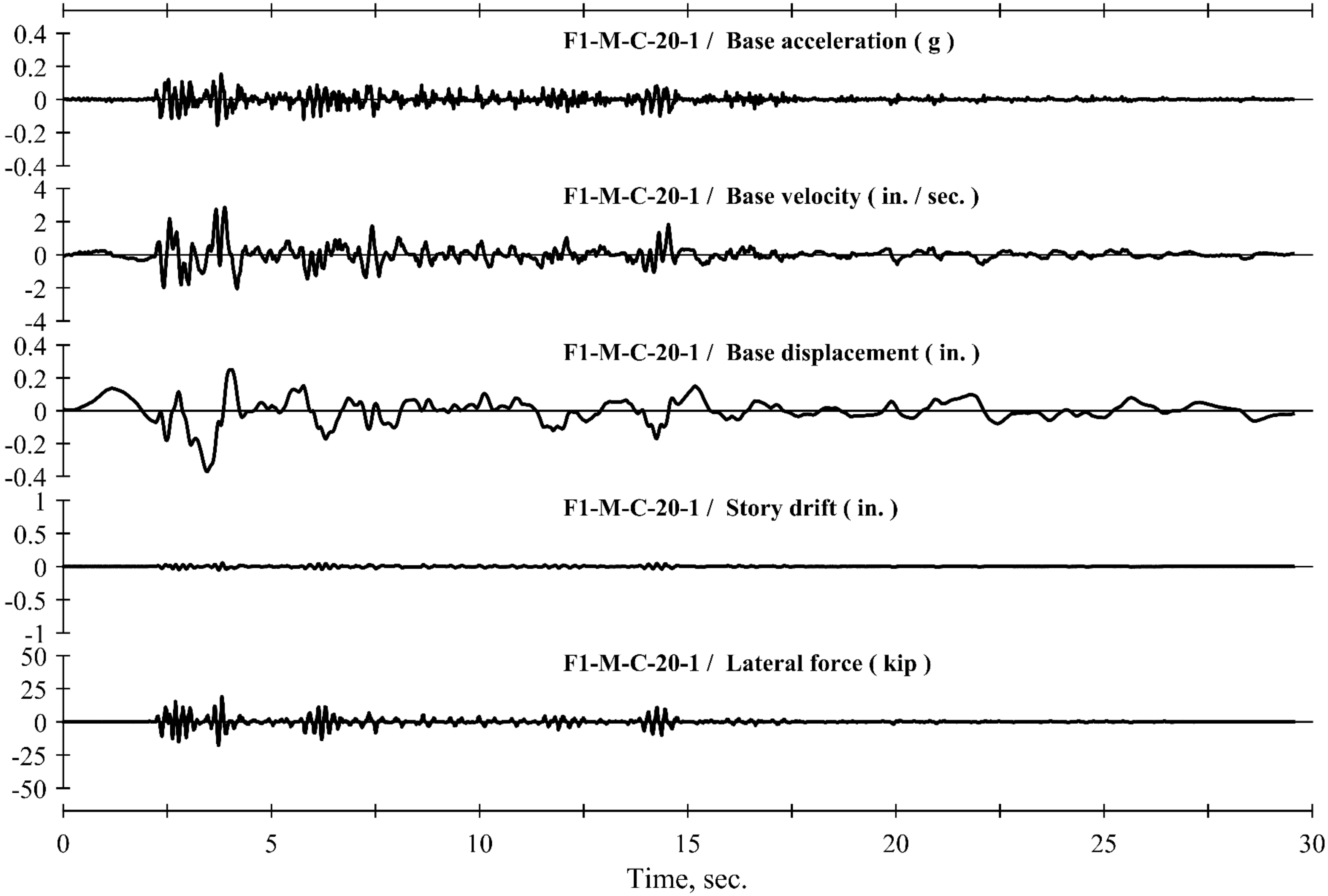

Figure D-40: Base motion and structural response histories in Run 40 of Specimen F1

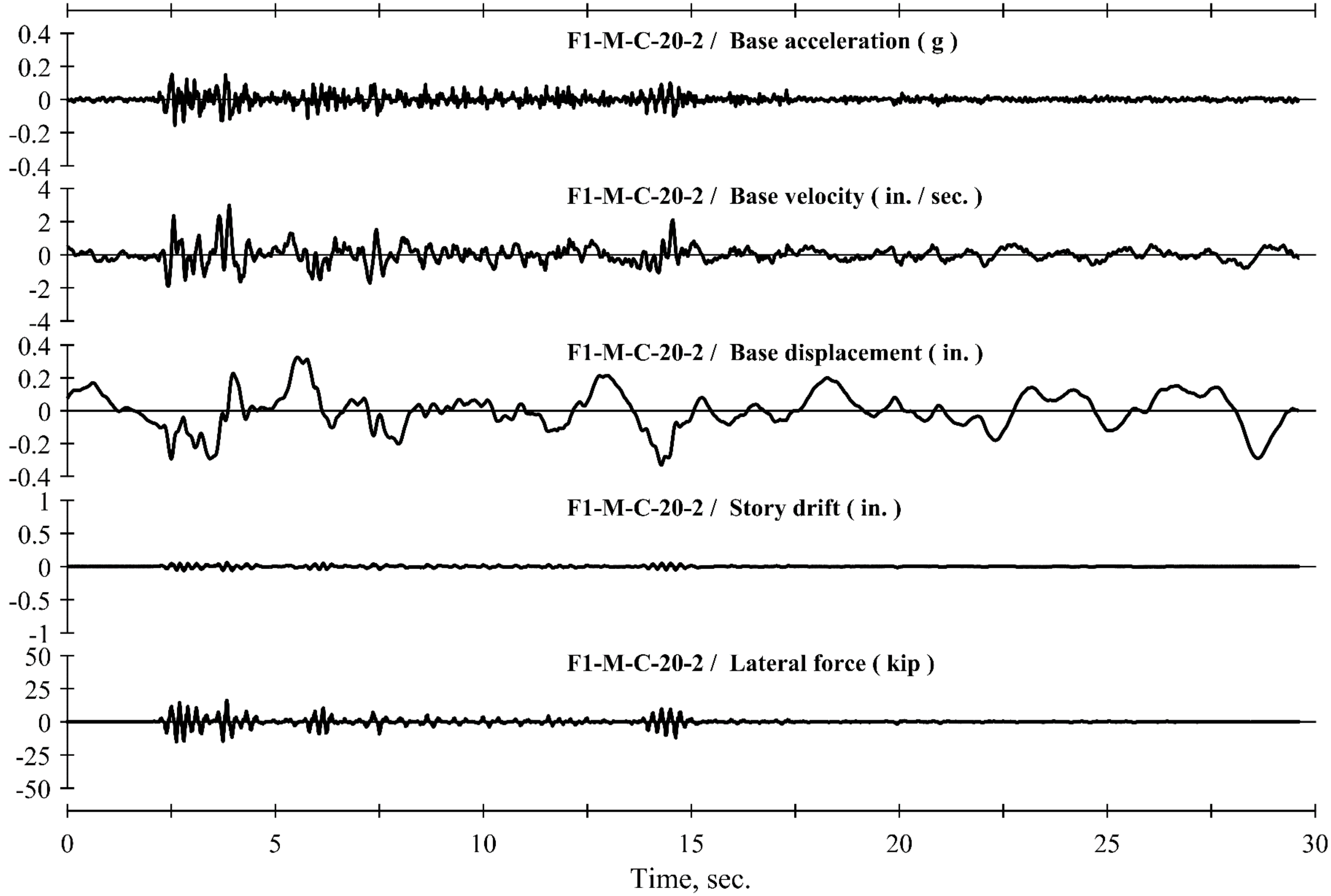

Figure D-41: Base motion and structural response histories in Run 41 of Specimen F1

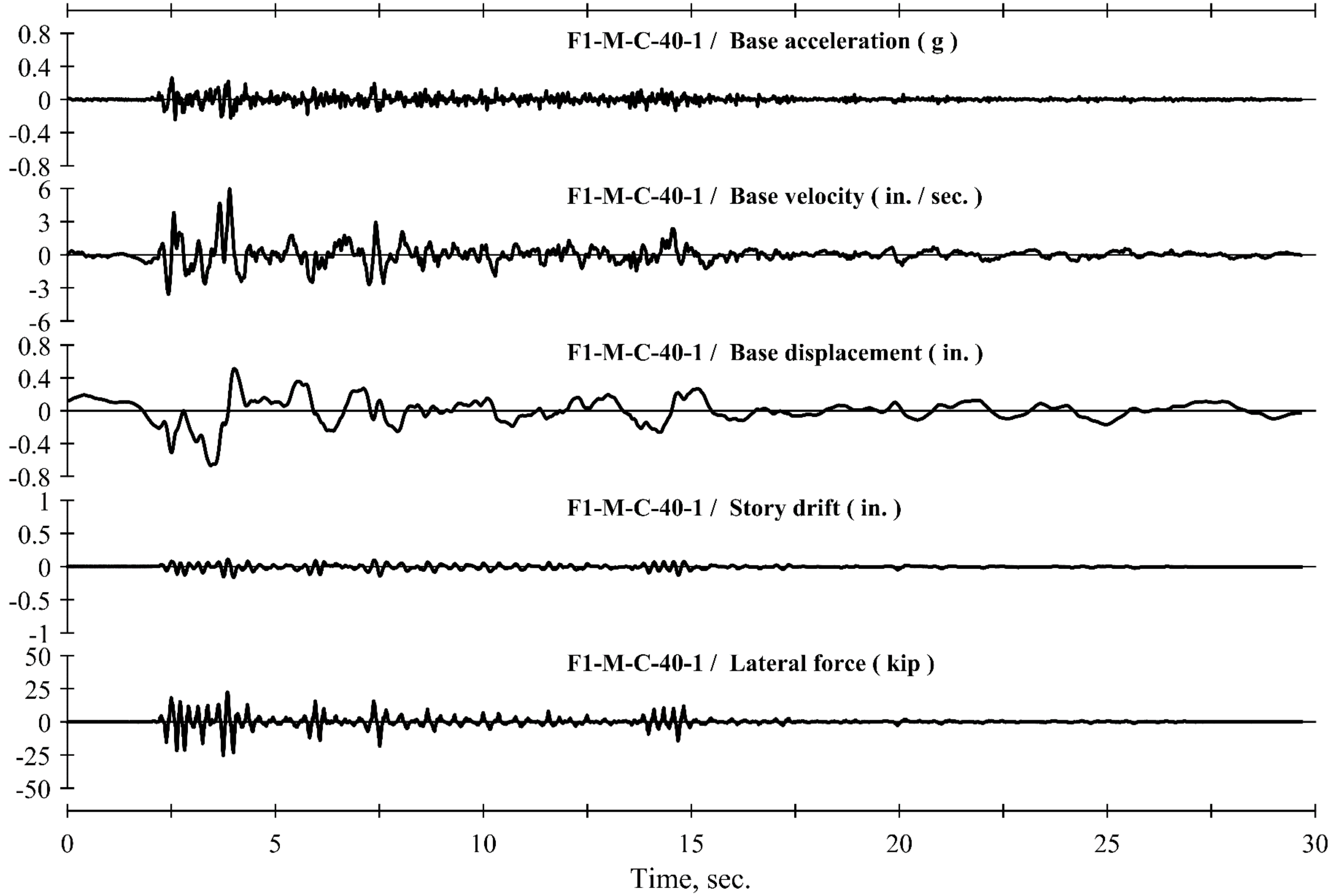

Figure D-42: Base motion and structural response histories in Run 42 of Specimen F1

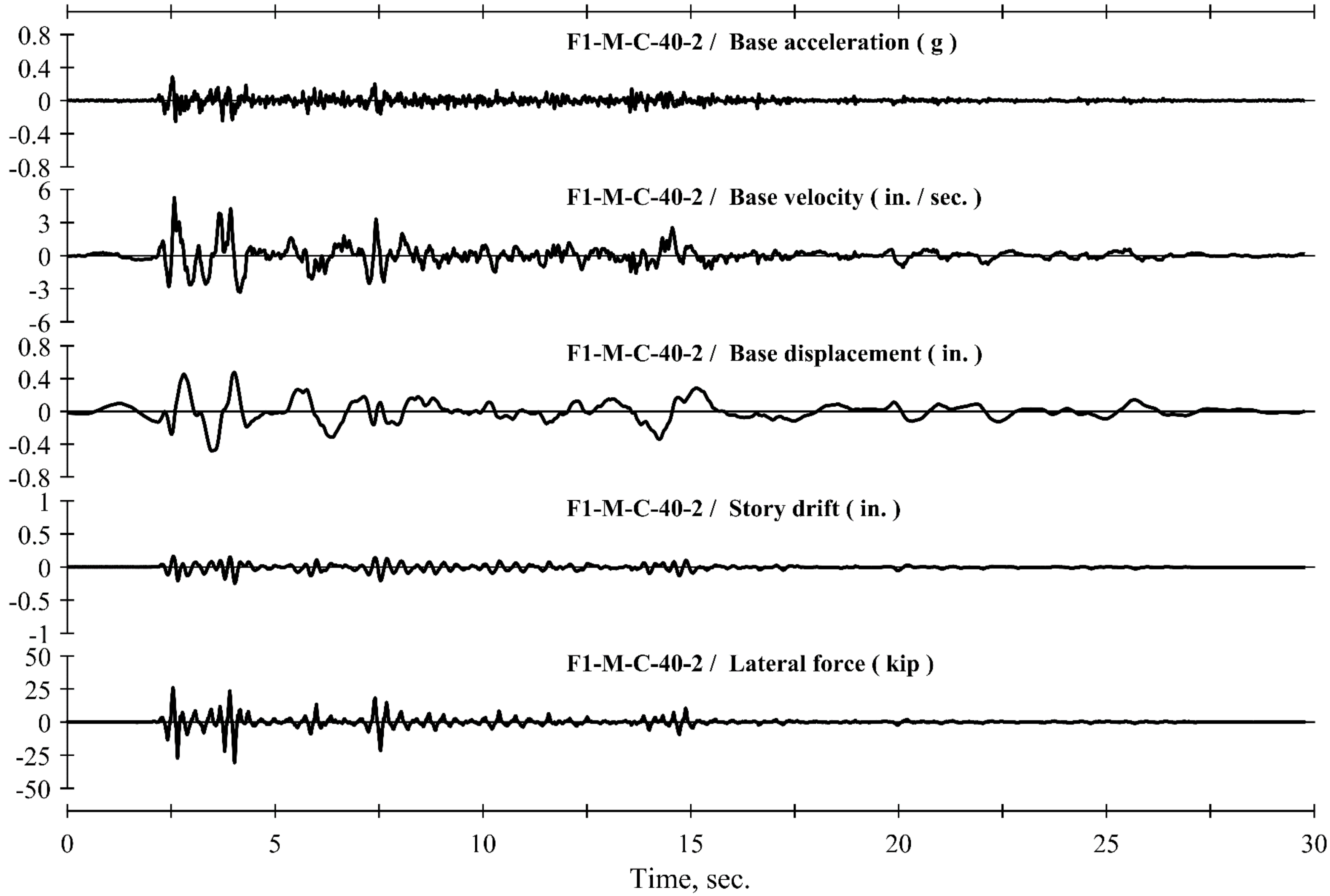

Figure D-43: Base motion and structural response histories in Run 43 of Specimen F1

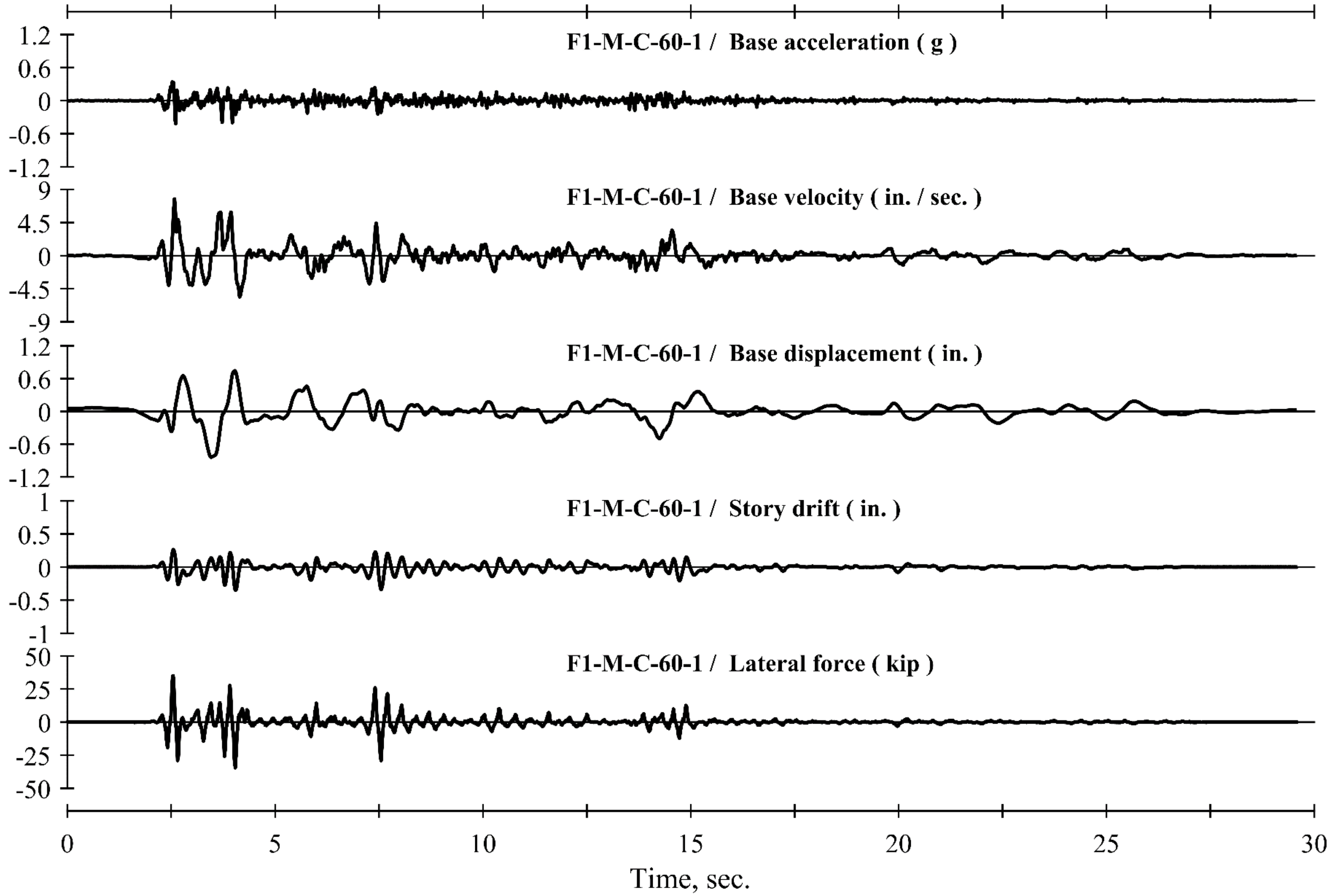

Figure D-44: Base motion and structural response histories in Run 44 of Specimen F1

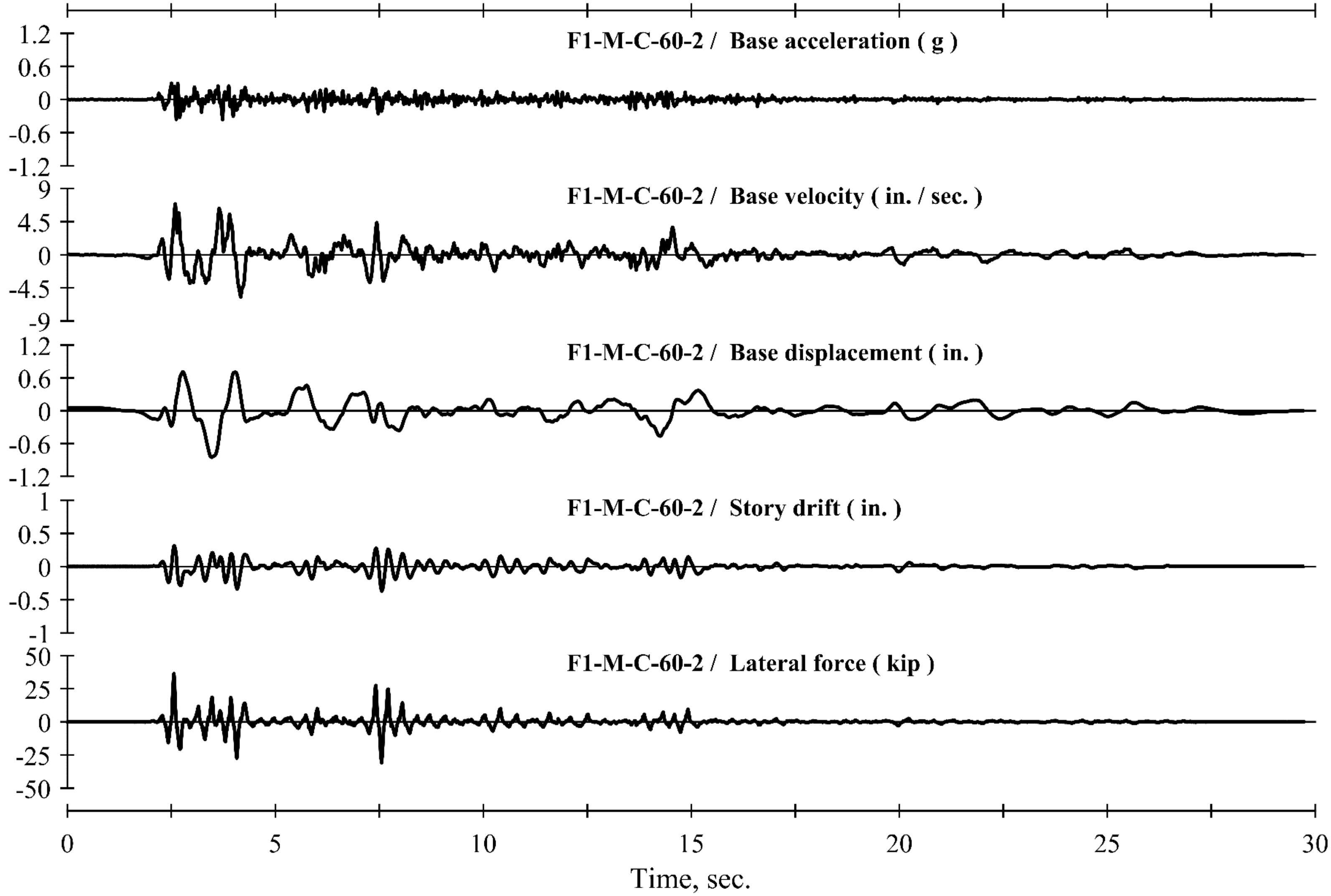

Figure D-45: Base motion and structural response histories in Run 45 of Specimen F1

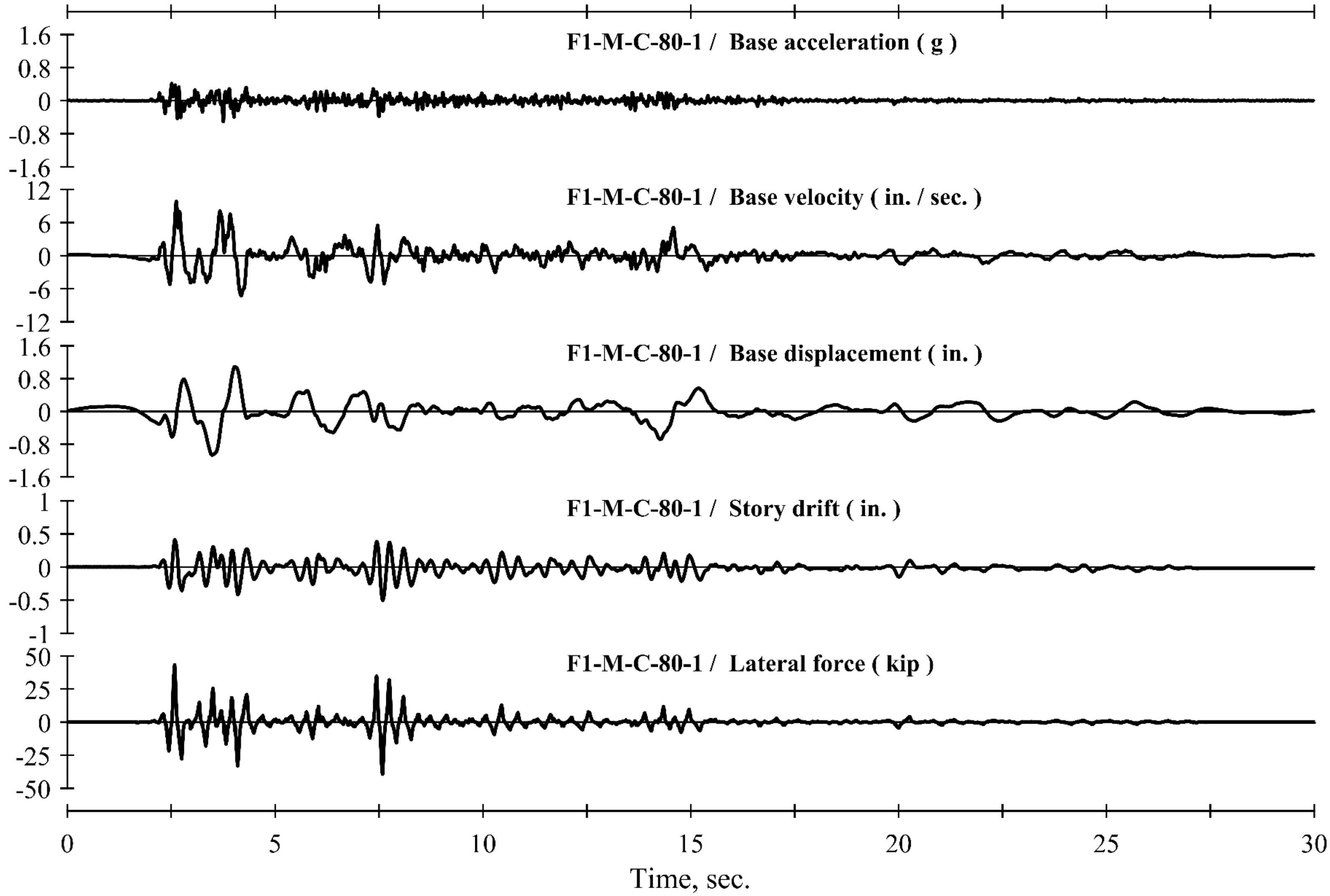

Figure D-46: Base motion and structural response histories in Run 46 of Specimen F1

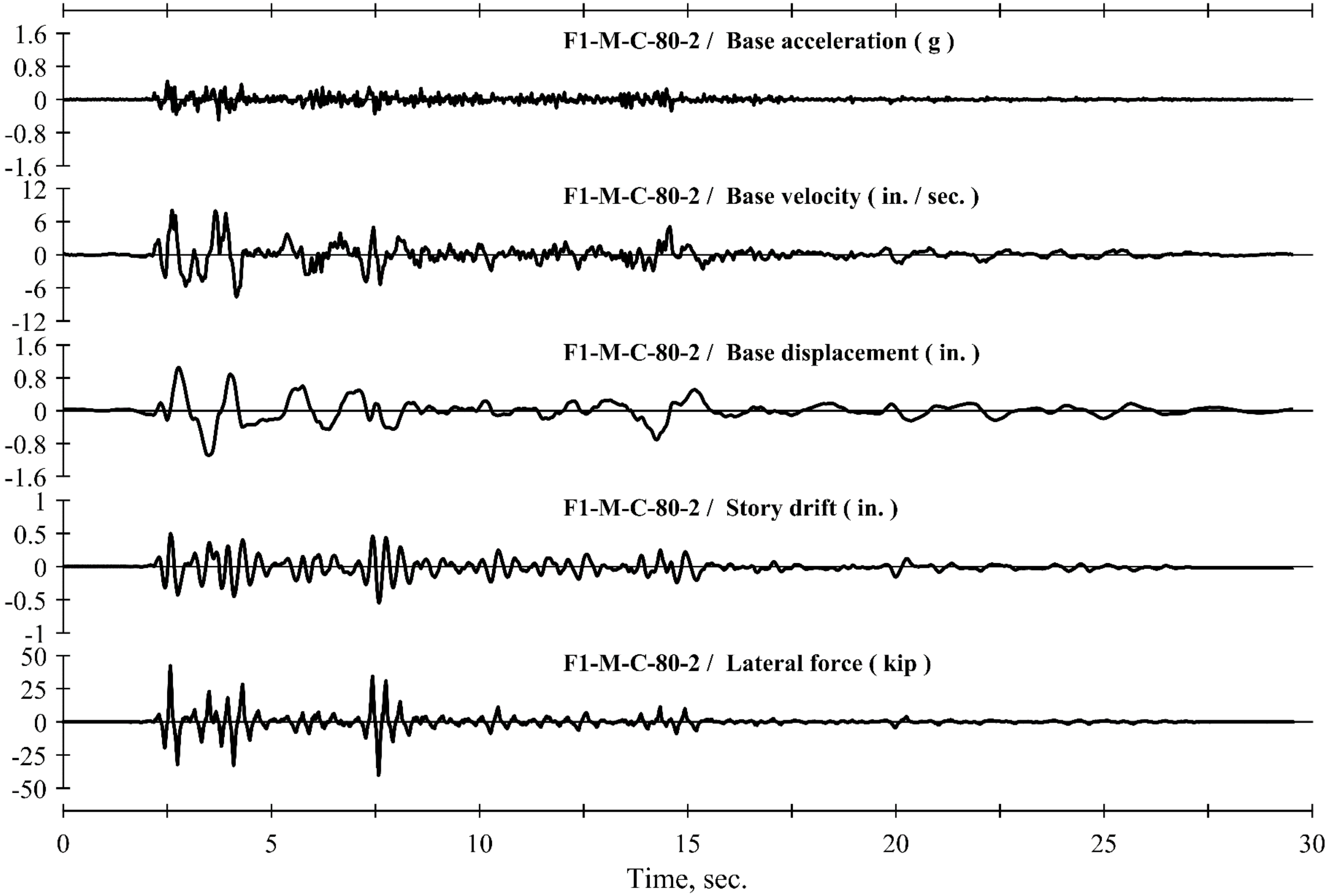

Figure D-47: Base motion and structural response histories in Run 47 of Specimen F1

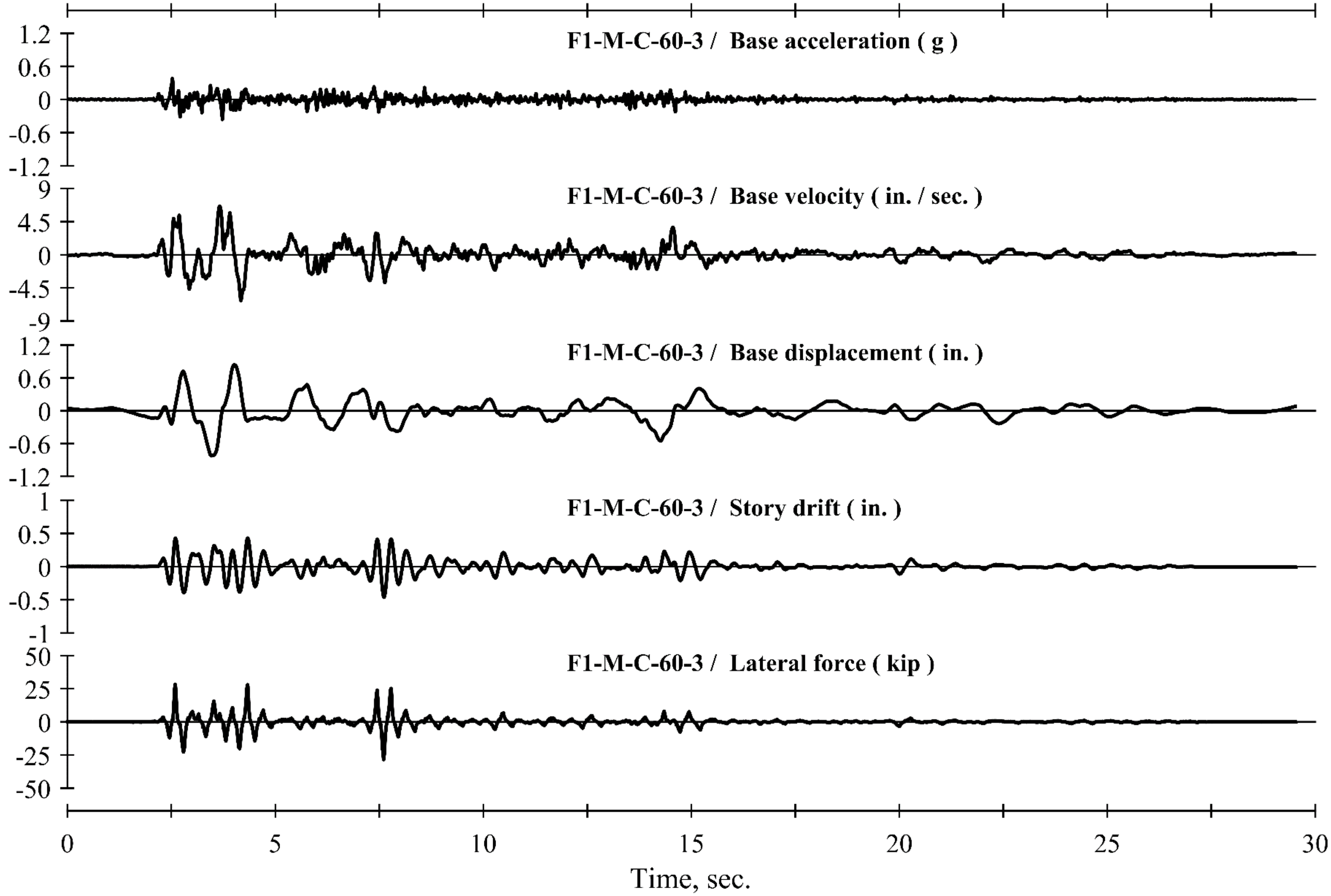

Figure D-48: Base motion and structural response histories in Run 48 of Specimen F1

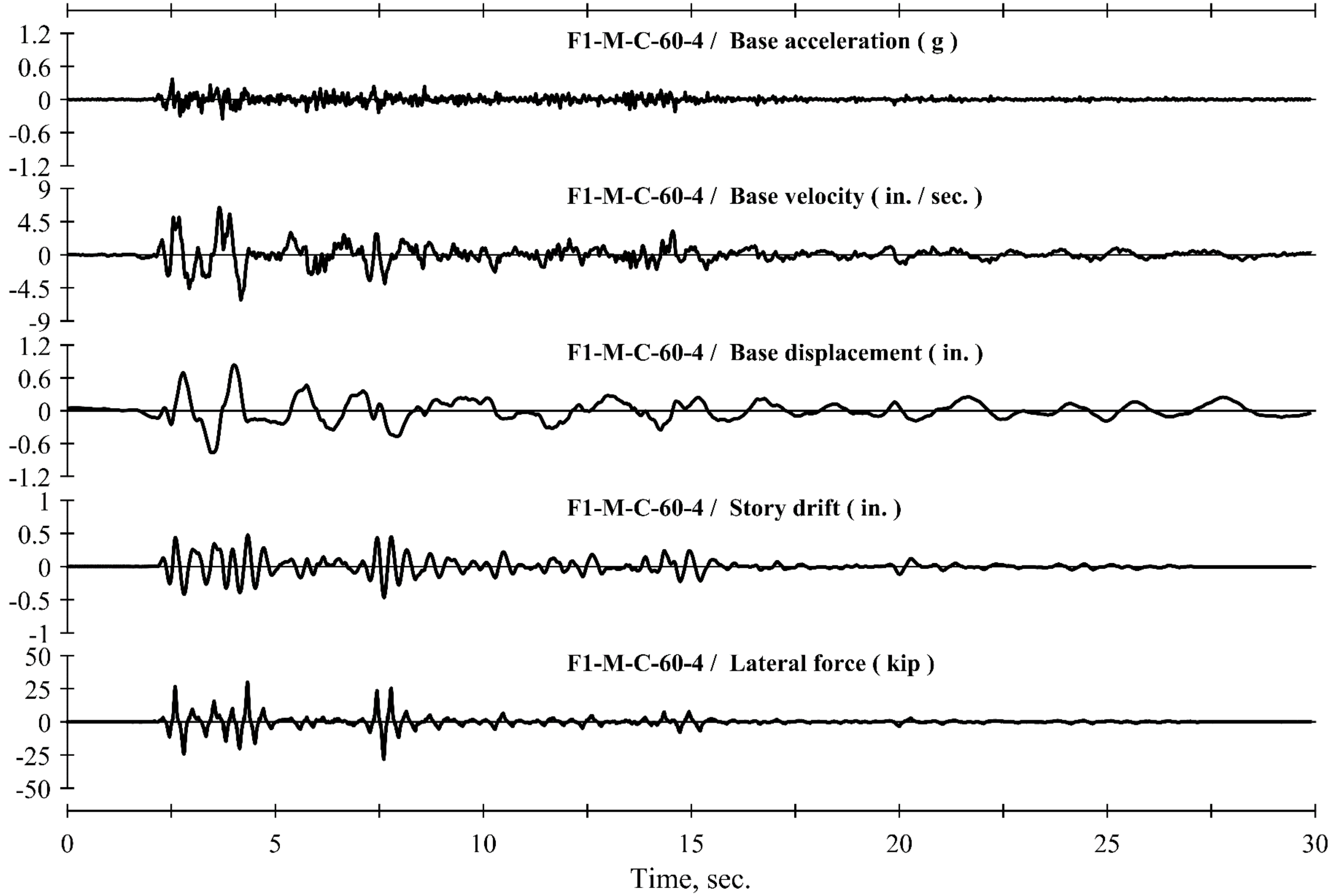

Figure D-49: Base motion and structural response histories in Run 49 of Specimen F1

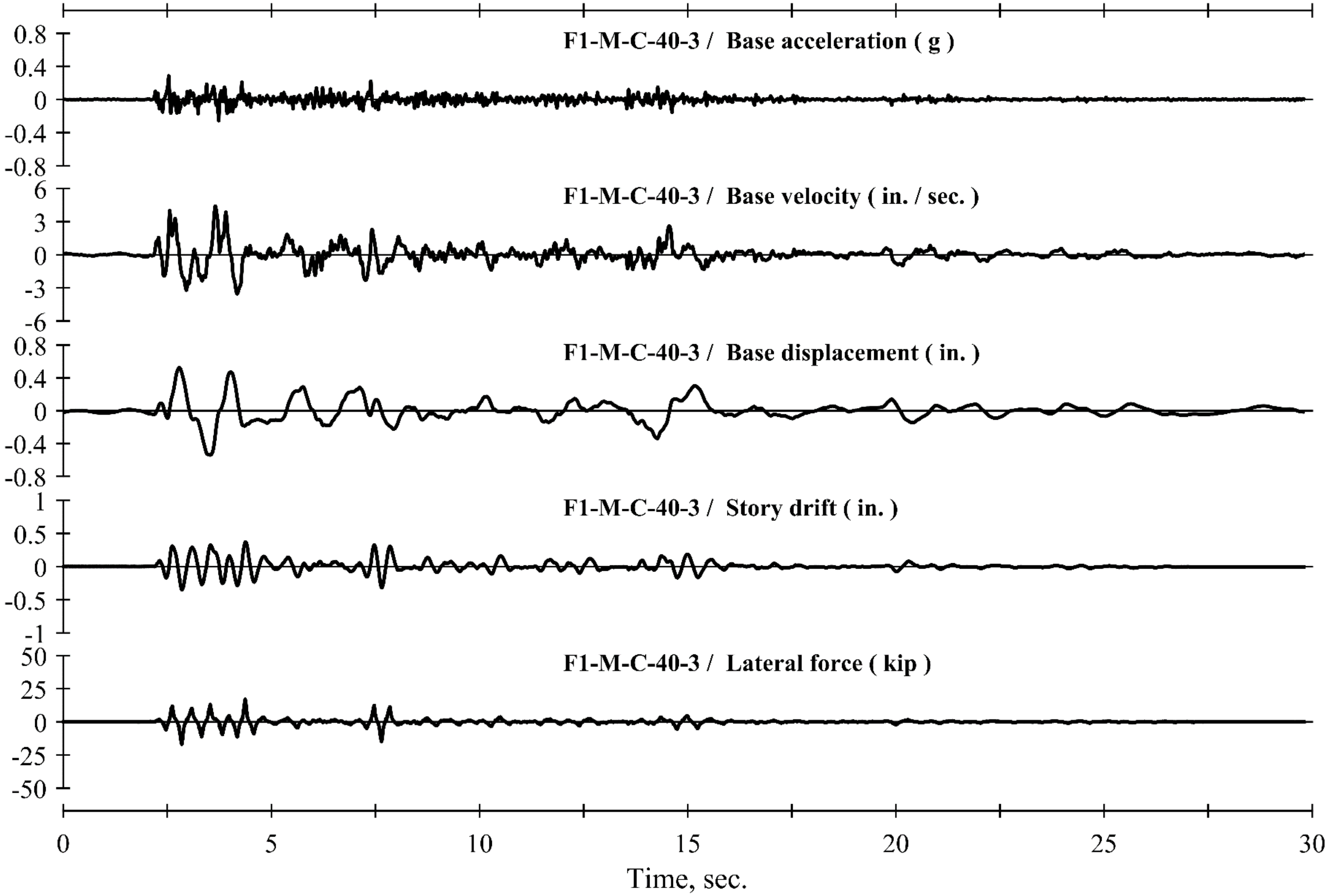

Figure D-50: Base motion and structural response histories in Run 50 of Specimen F1

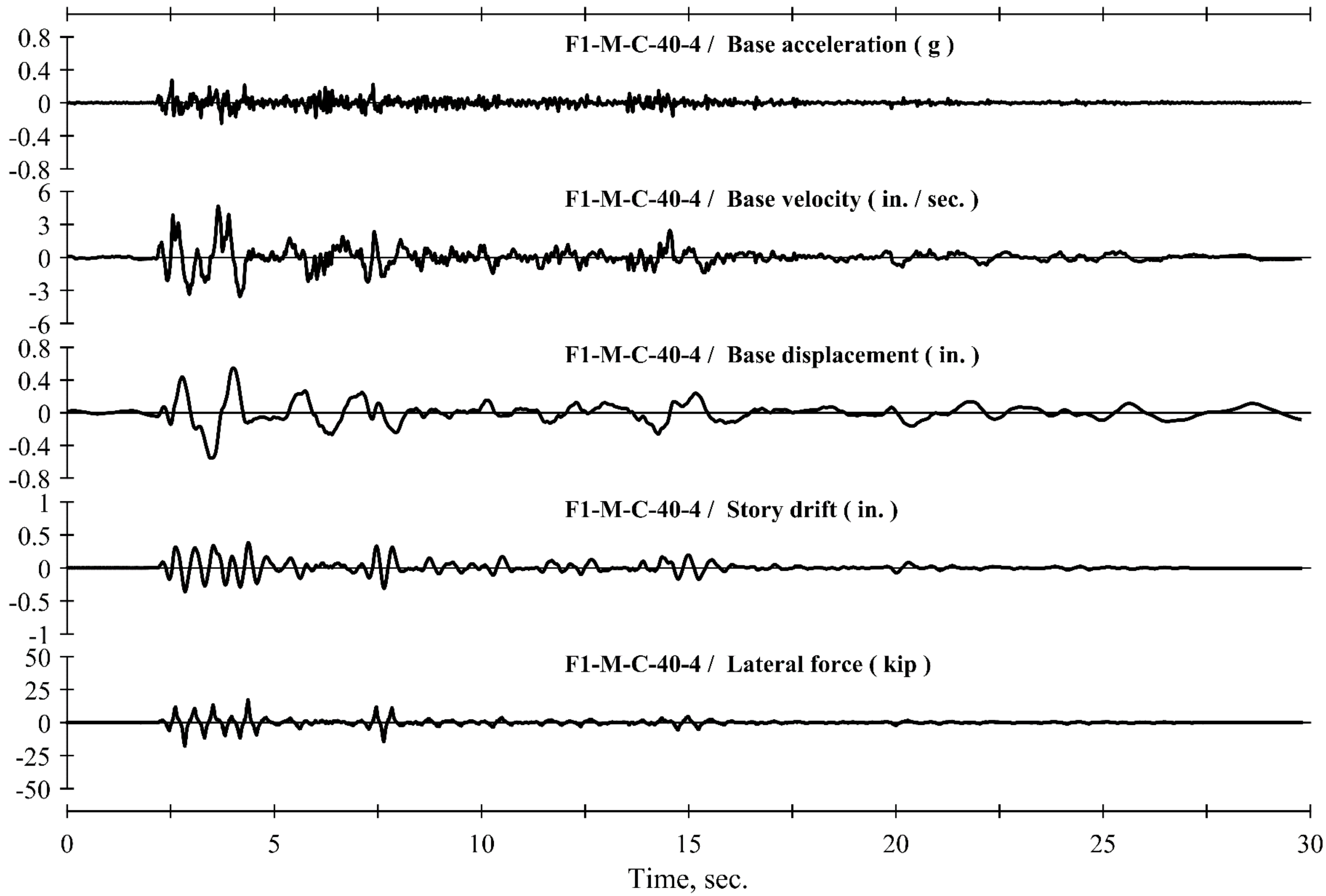

Figure D-51: Base motion and structural response histories in Run 51 of Specimen F1

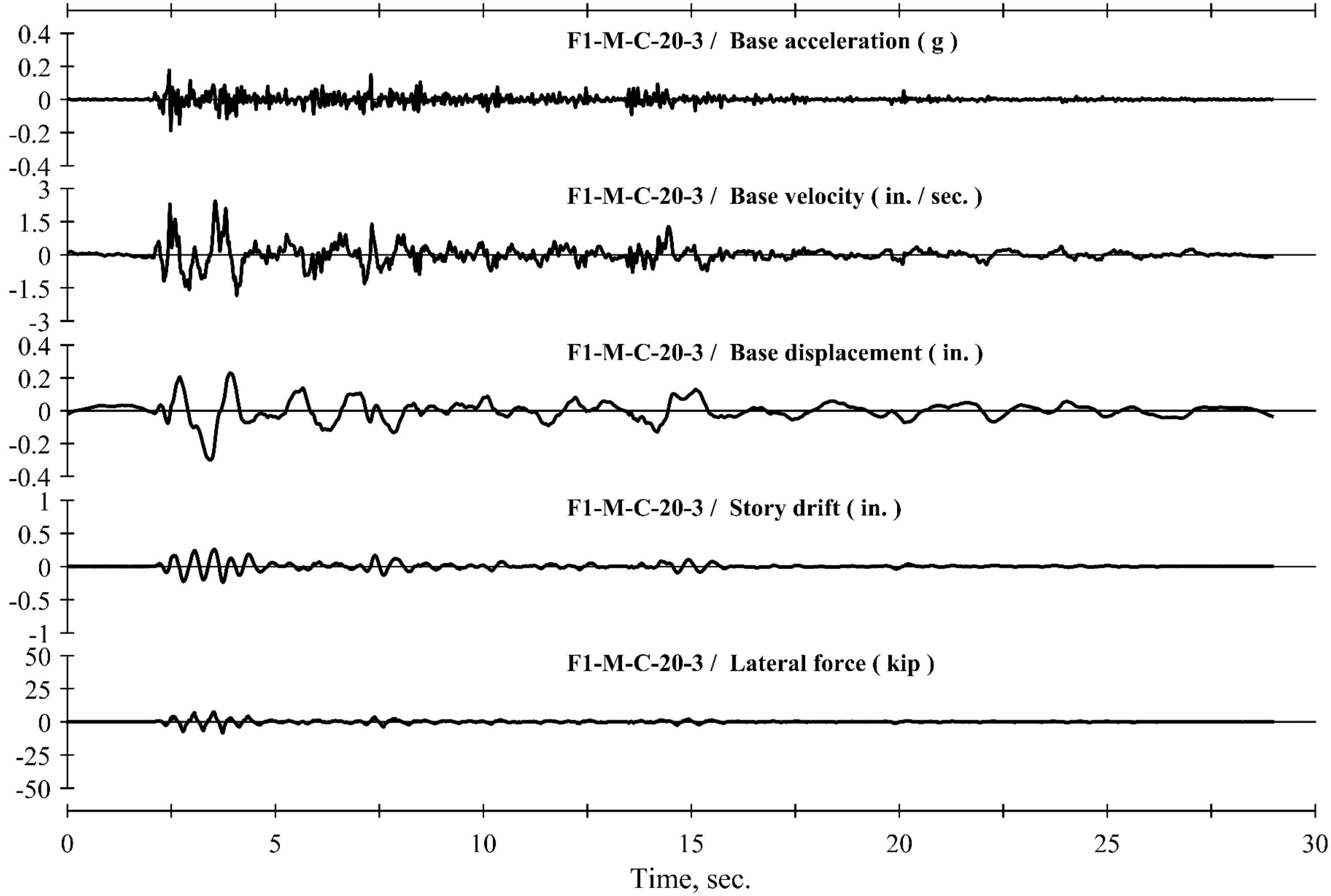

Figure D-52: Base motion and structural response histories in Run 52 of Specimen F1

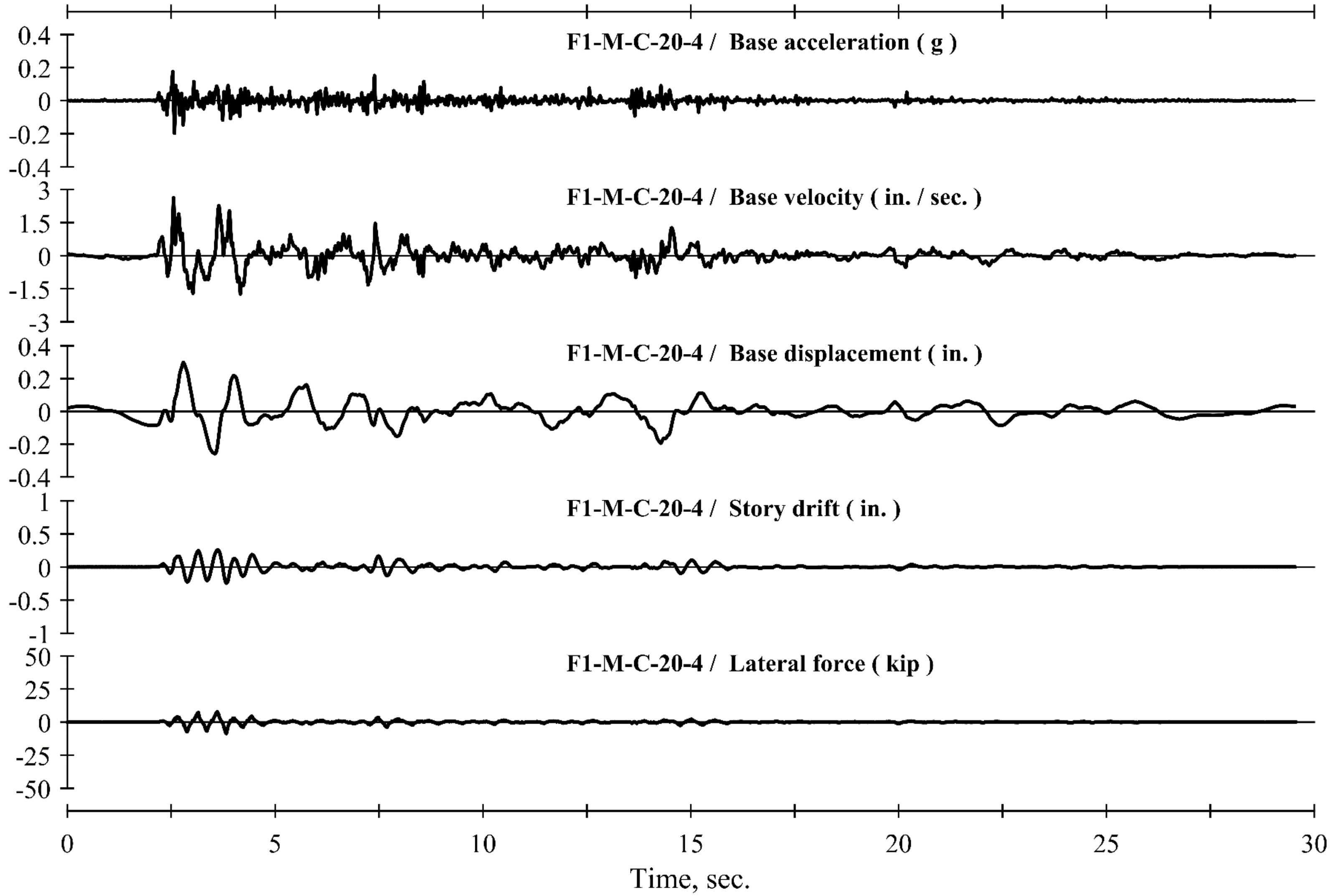

Figure D-53: Base motion and structural response histories in Run 53 of Specimen F1

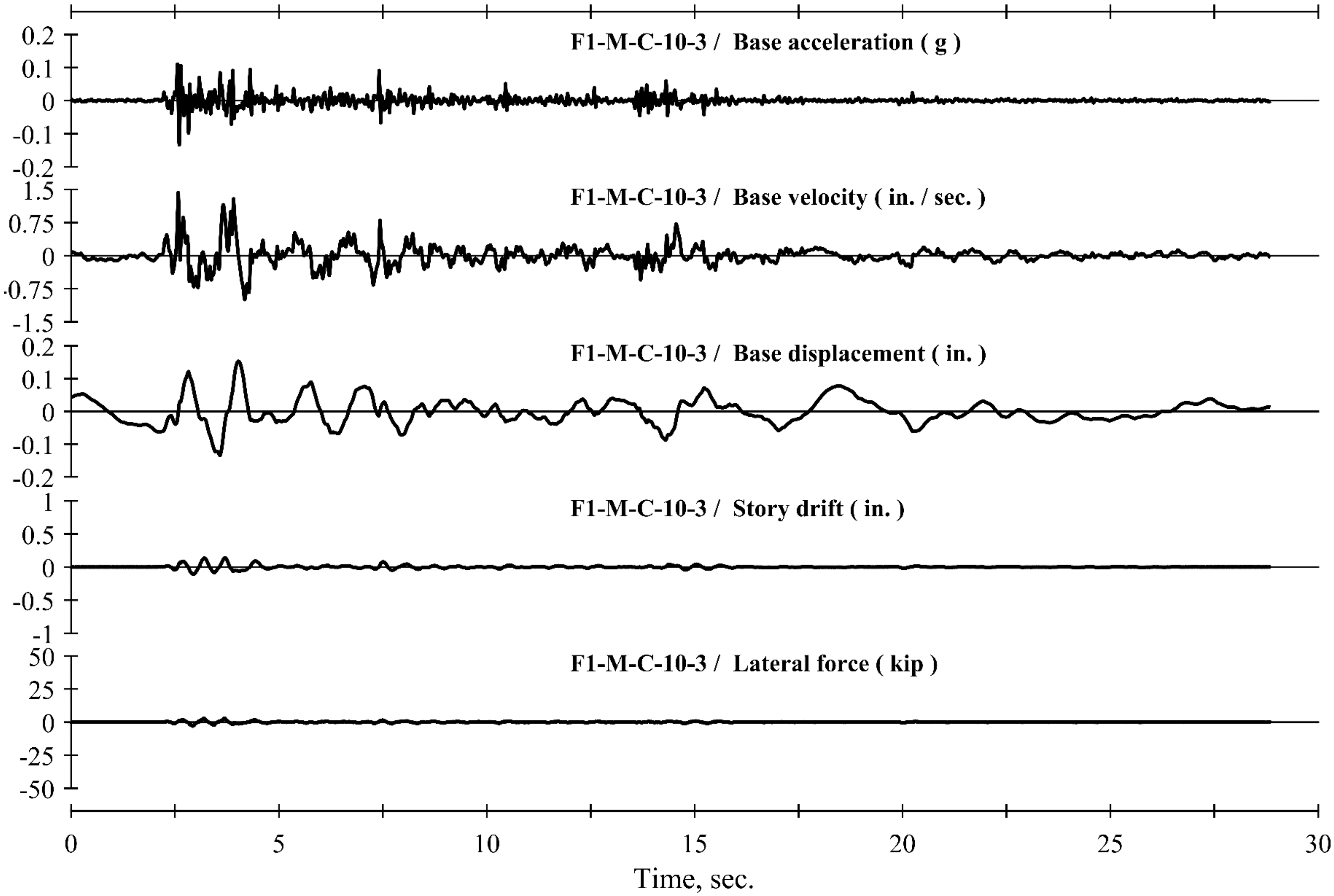

Figure D-54: Base motion and structural response histories in Run 54 of Specimen F1

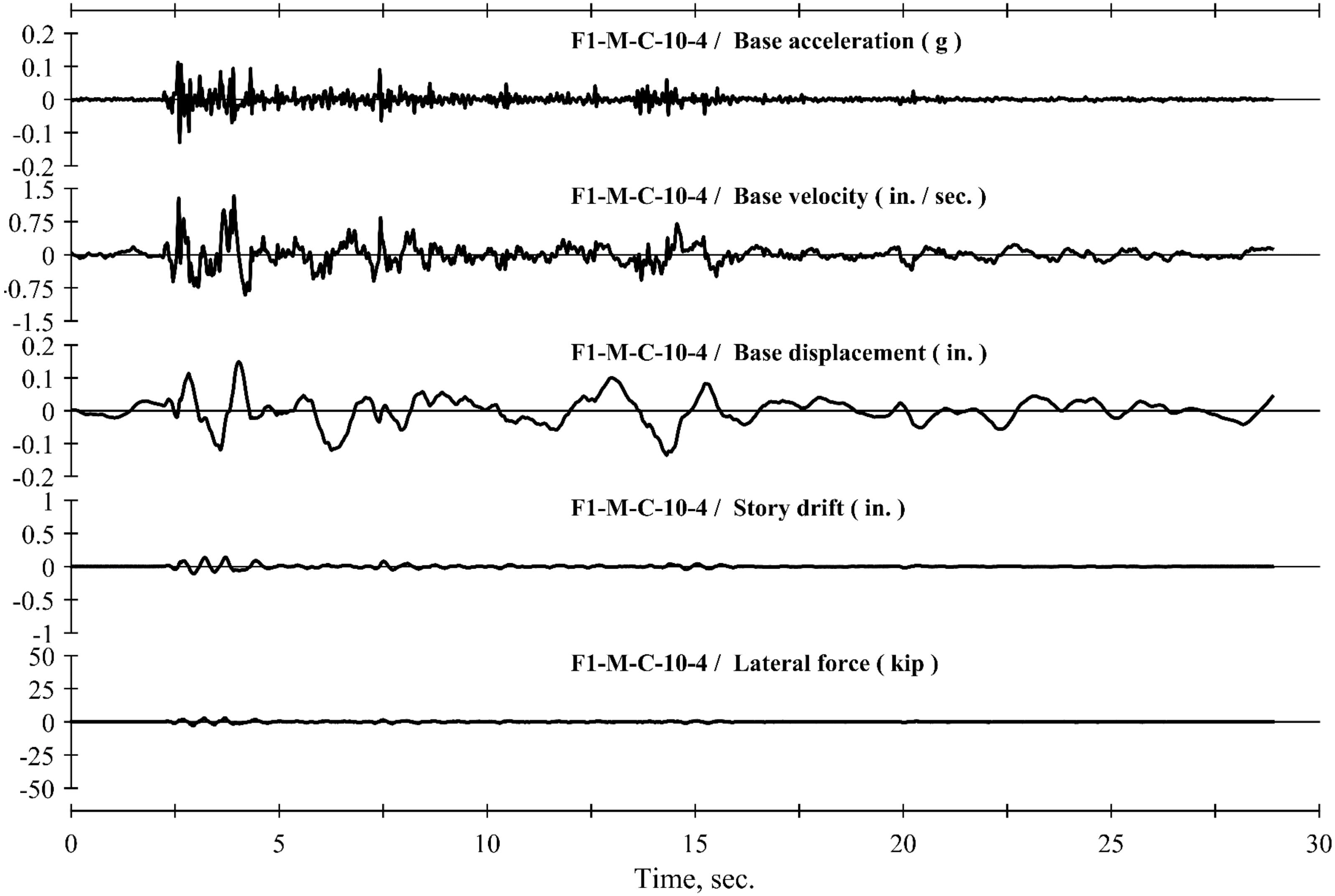

Figure D-55: Base motion and structural response histories in Run 55 of Specimen F1

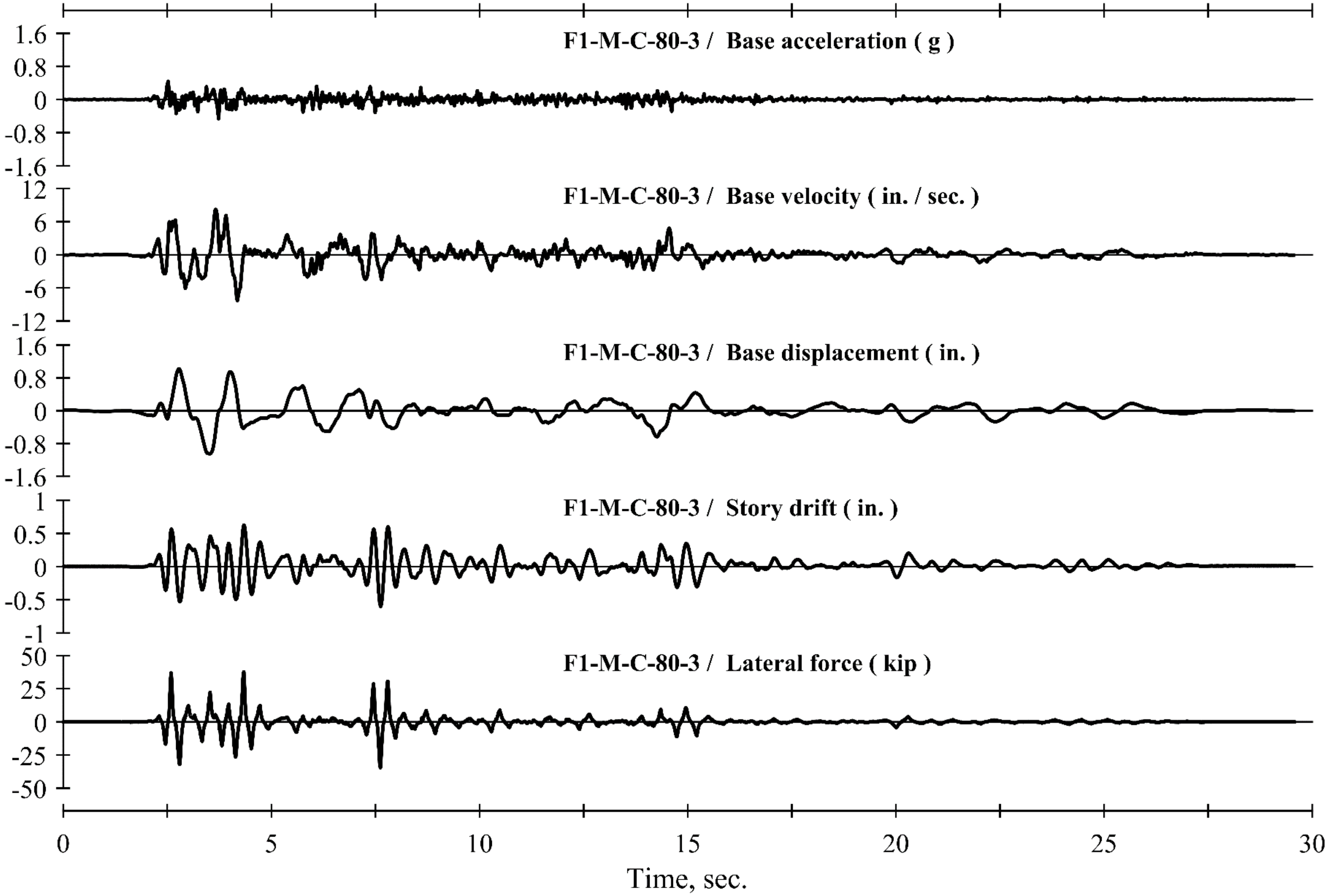

Figure D-56: Base motion and structural response histories in Run 56 of Specimen F1

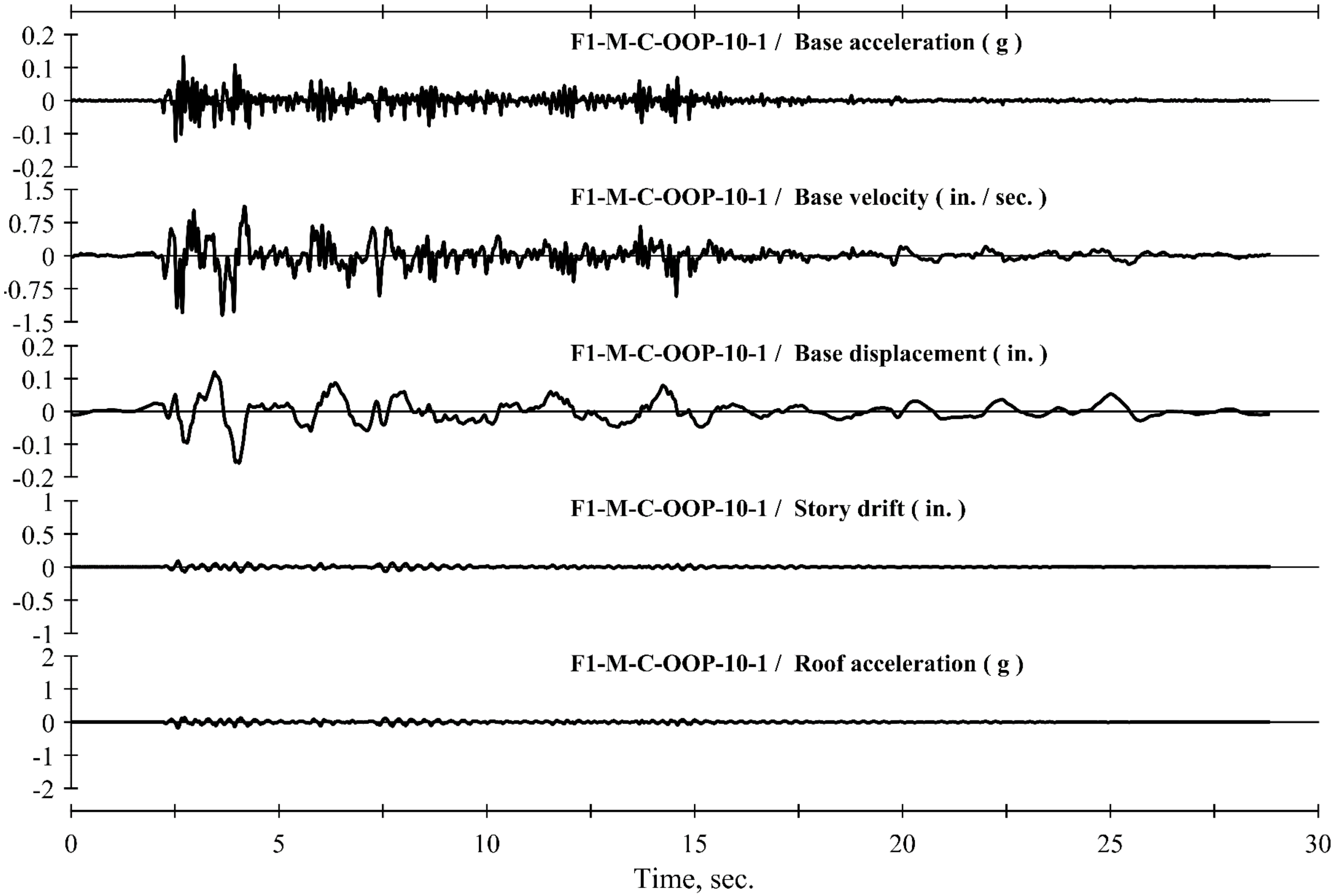

Figure D-57: Base motion and structural response histories in Run 57 of Specimen F1

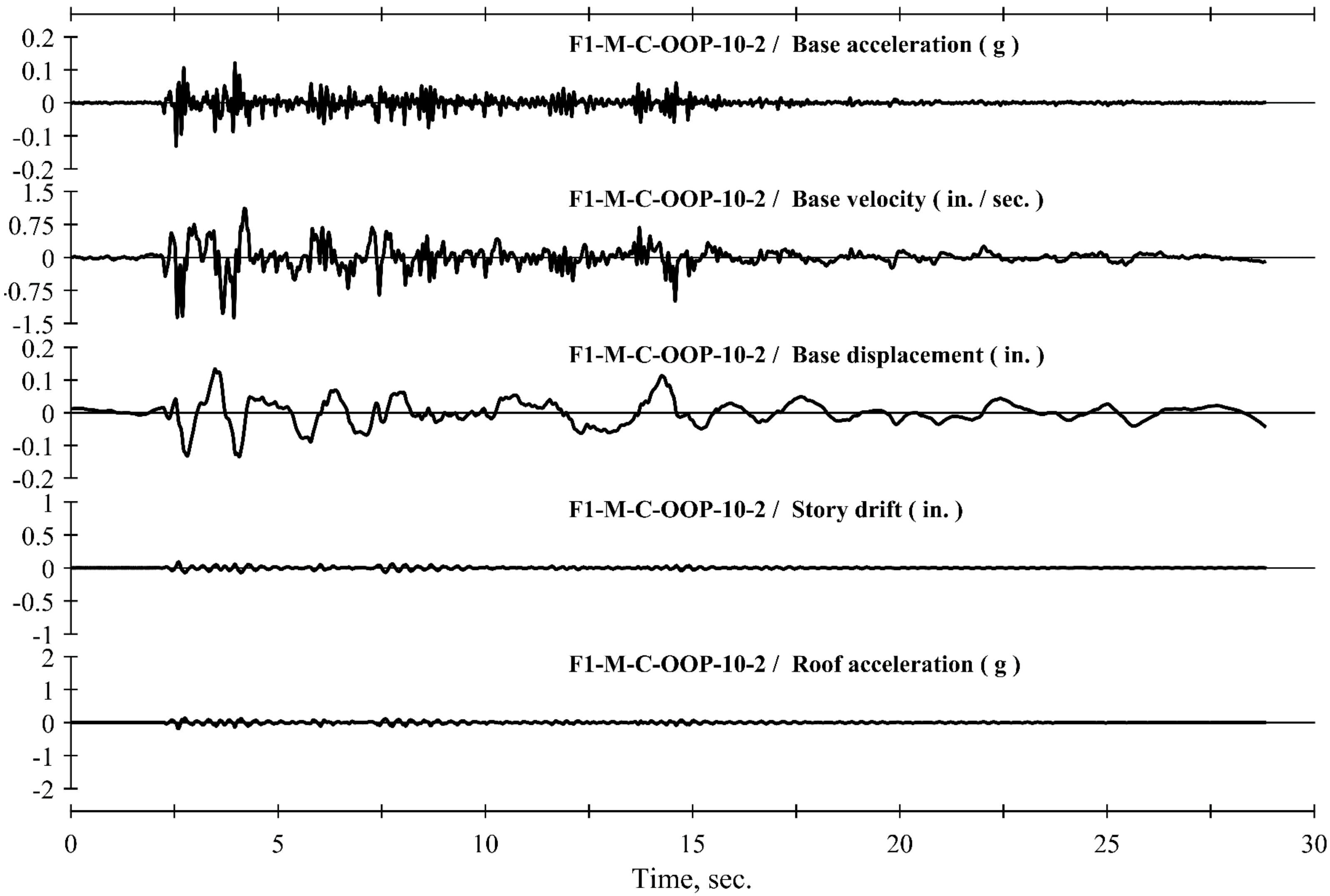

Figure D-58: Base motion and structural response histories in Run 58 of Specimen F1

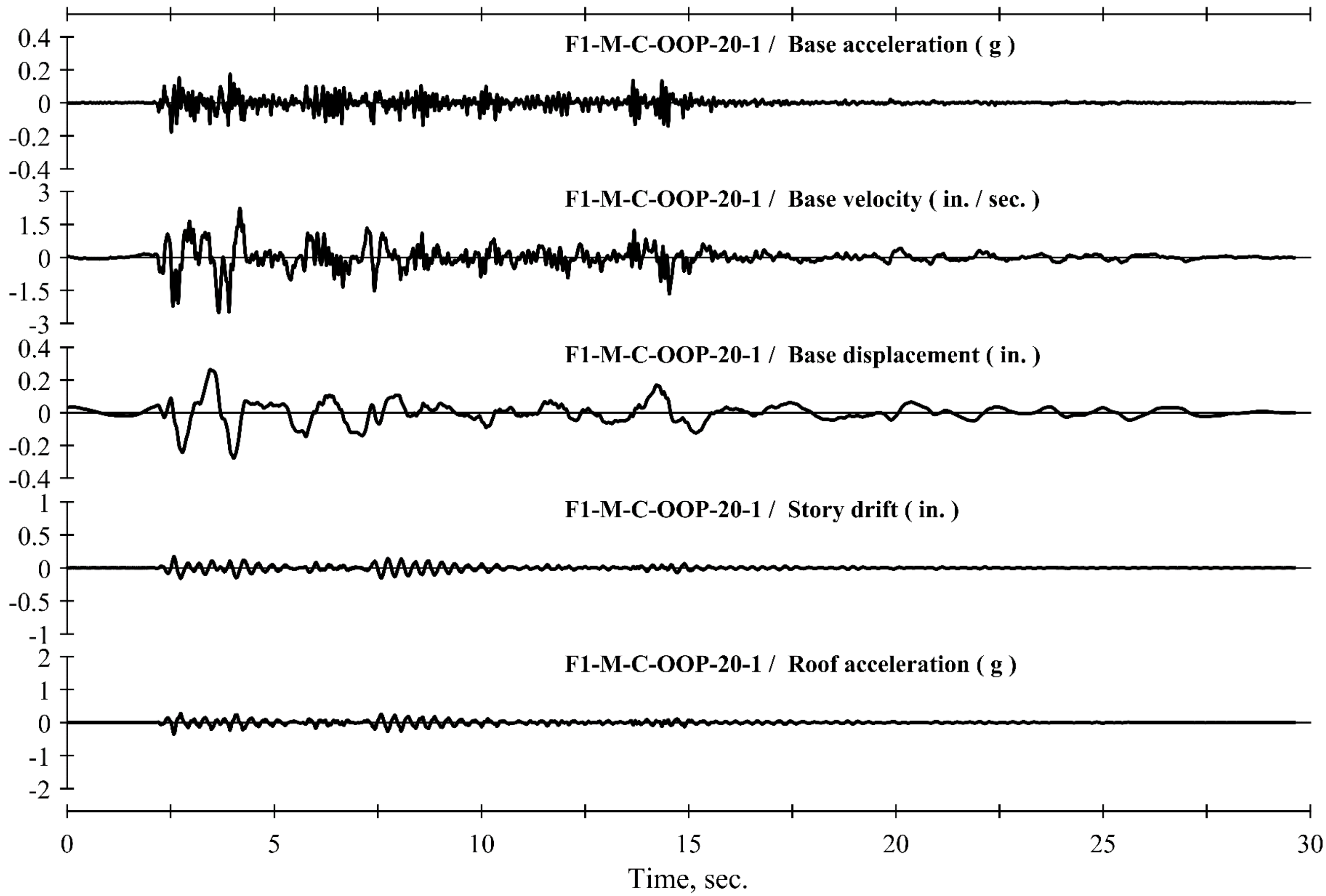

Figure D-59: Base motion and structural response histories in Run 59 of Specimen F1

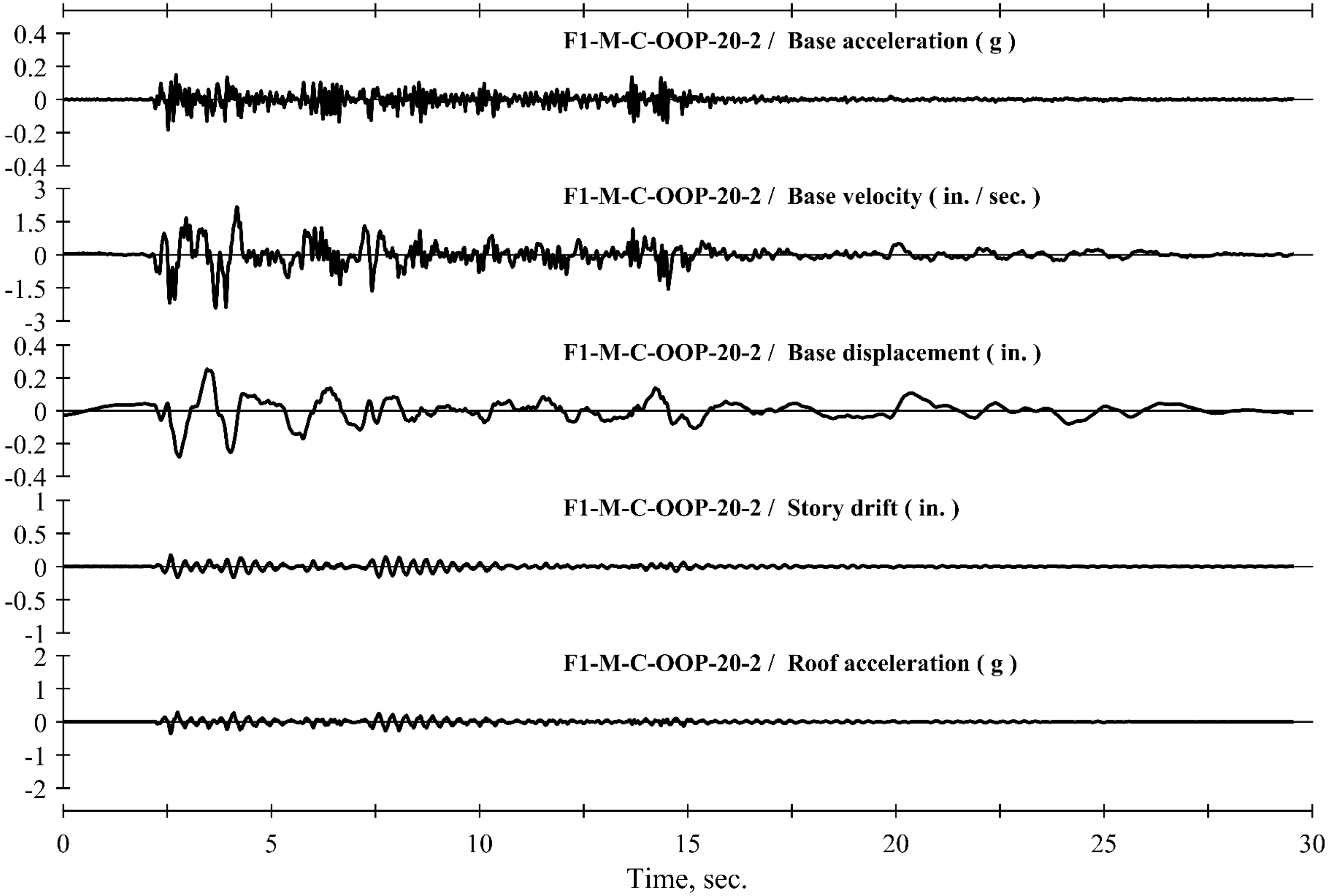

Figure D-60: Base motion and structural response histories in Run 60 of Specimen F1

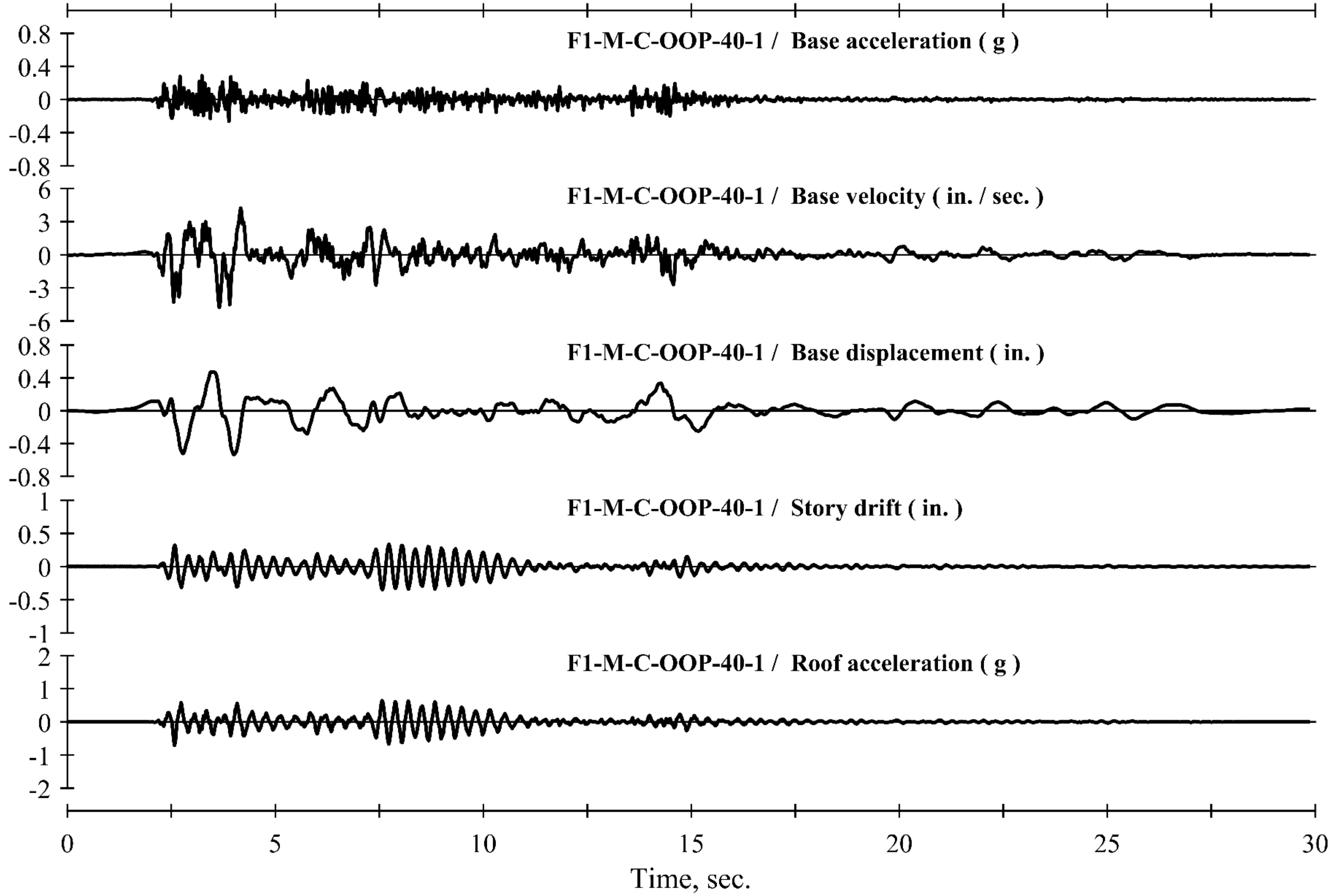

Figure D-61: Base motion and structural response histories in Run 61 of Specimen F1

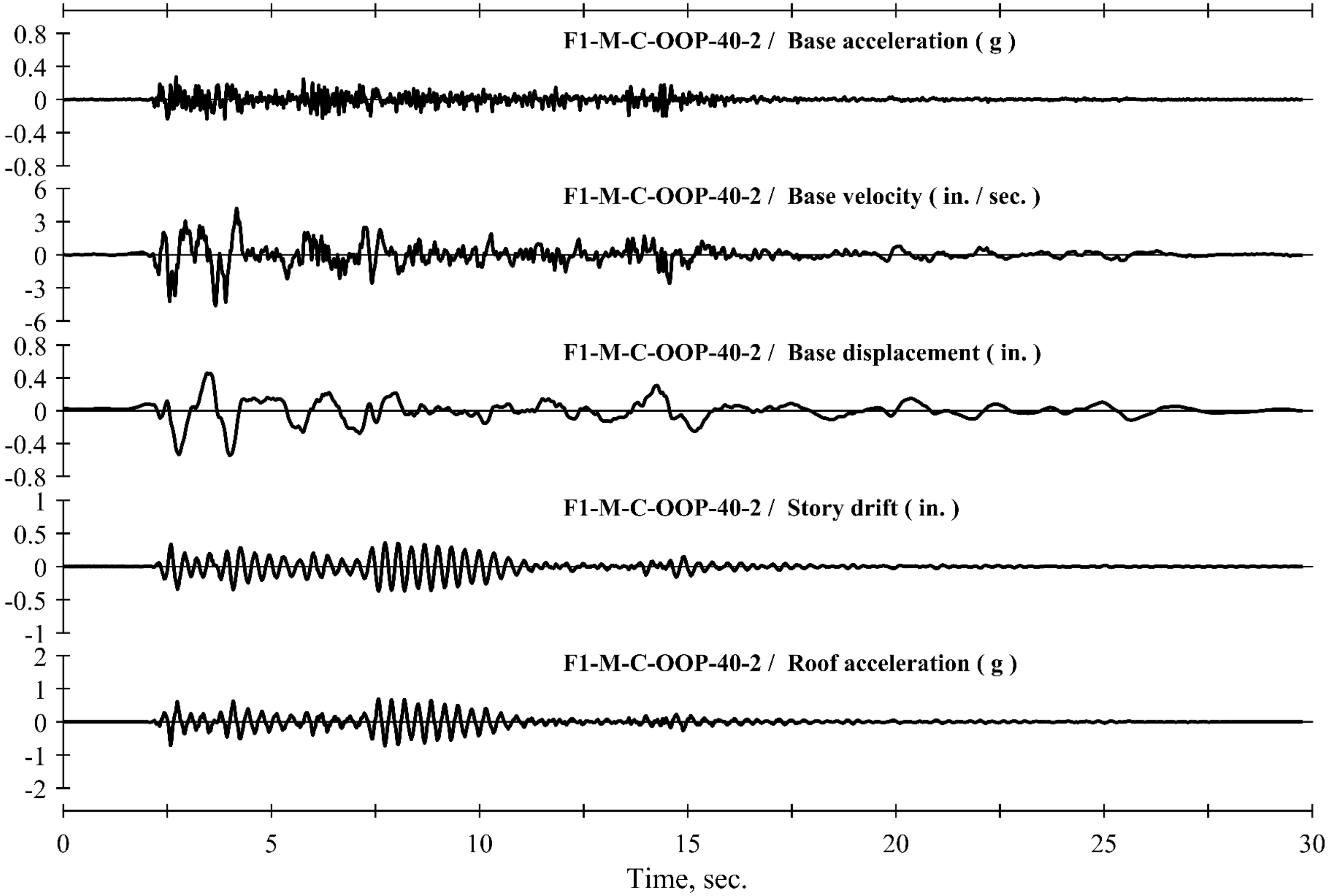

Figure D-62: Base motion and structural response histories in Run 62 of Specimen F1

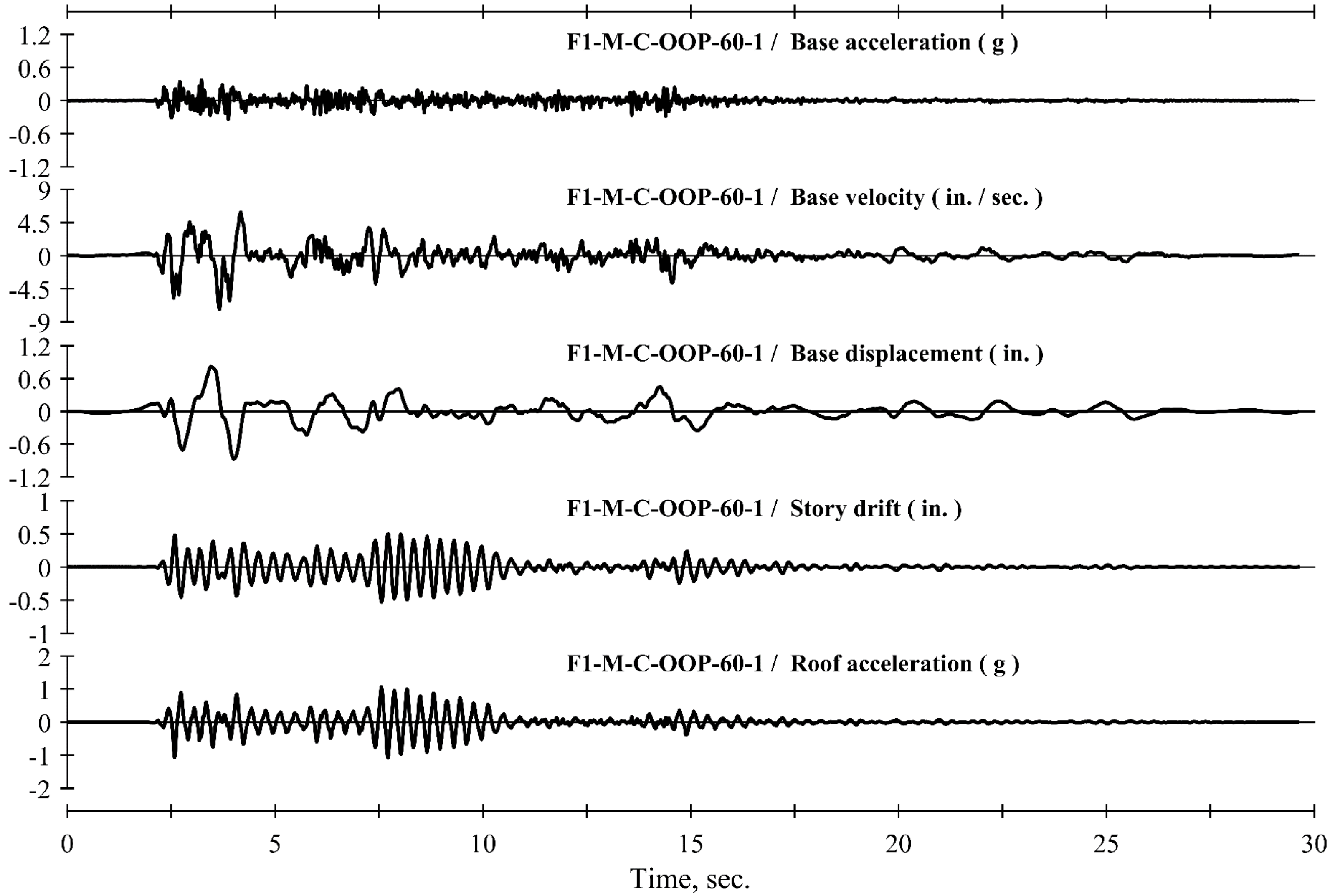

Figure D-63: Base motion and structural response histories in Run 63 of Specimen F1

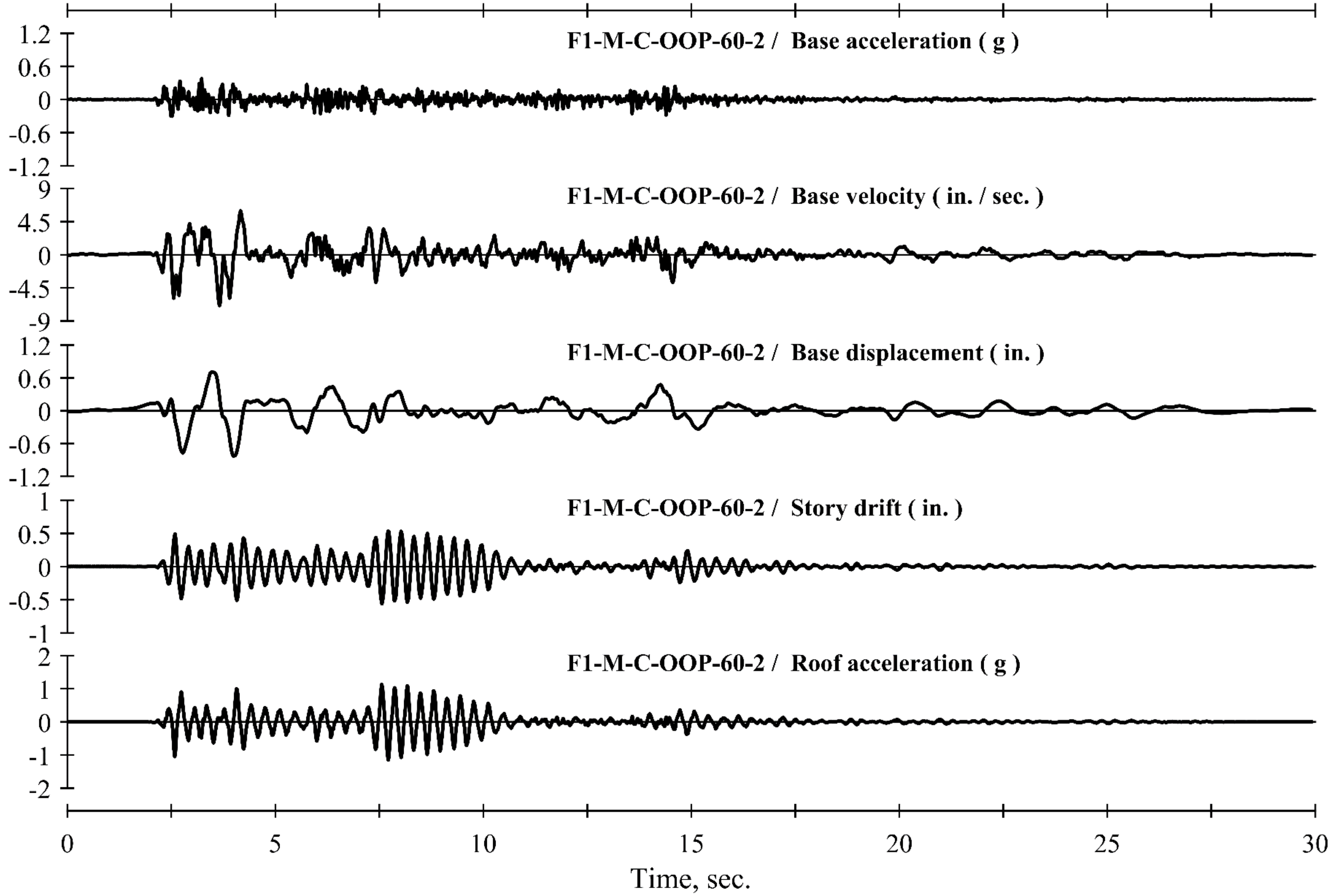

Figure D-64: Base motion and structural response histories in Run 64 of Specimen F1

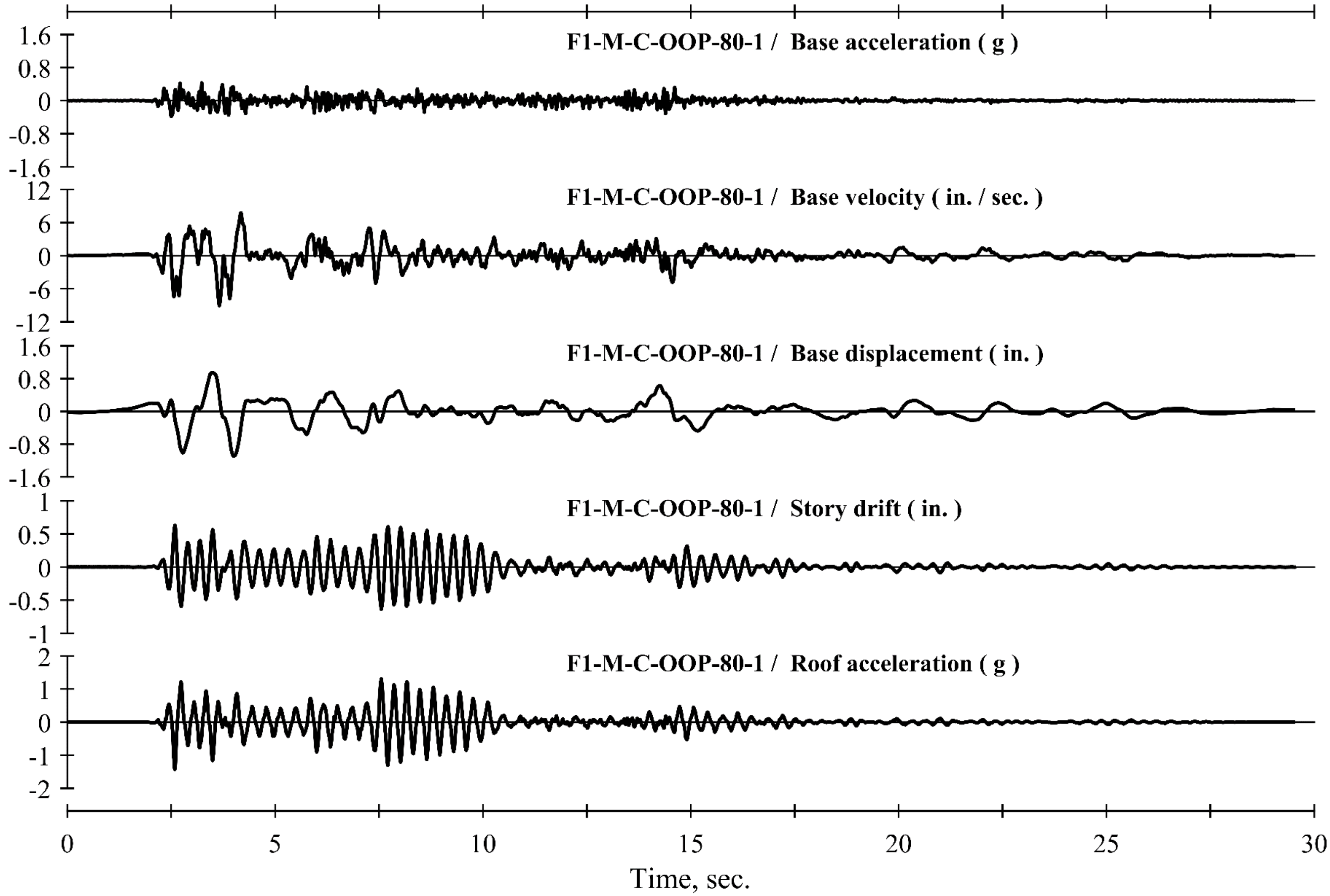

Figure D-65: Base motion and structural response histories in Run 65 of Specimen F1

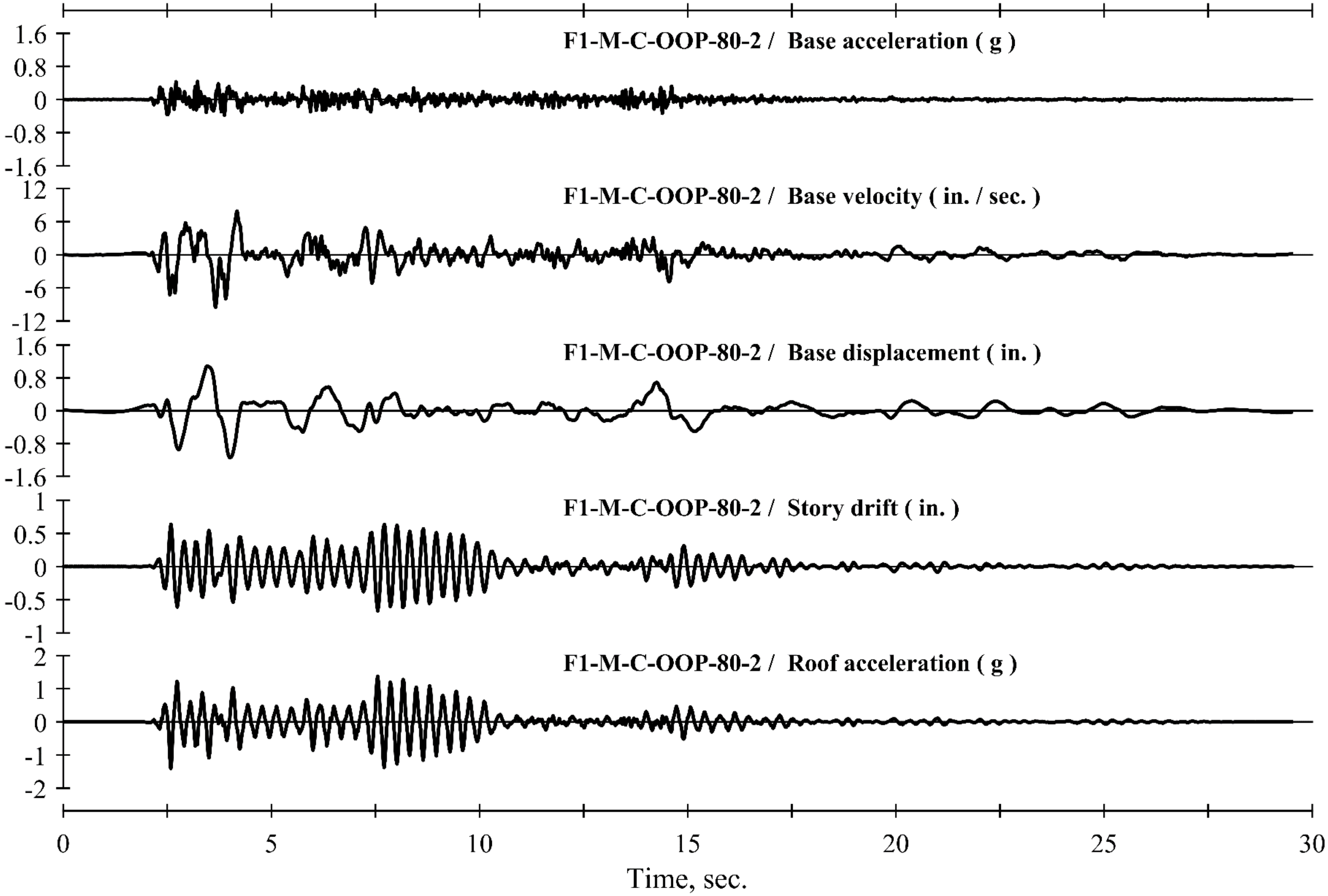

Figure D-66: Base motion and structural response histories in Run 66 of Specimen F1

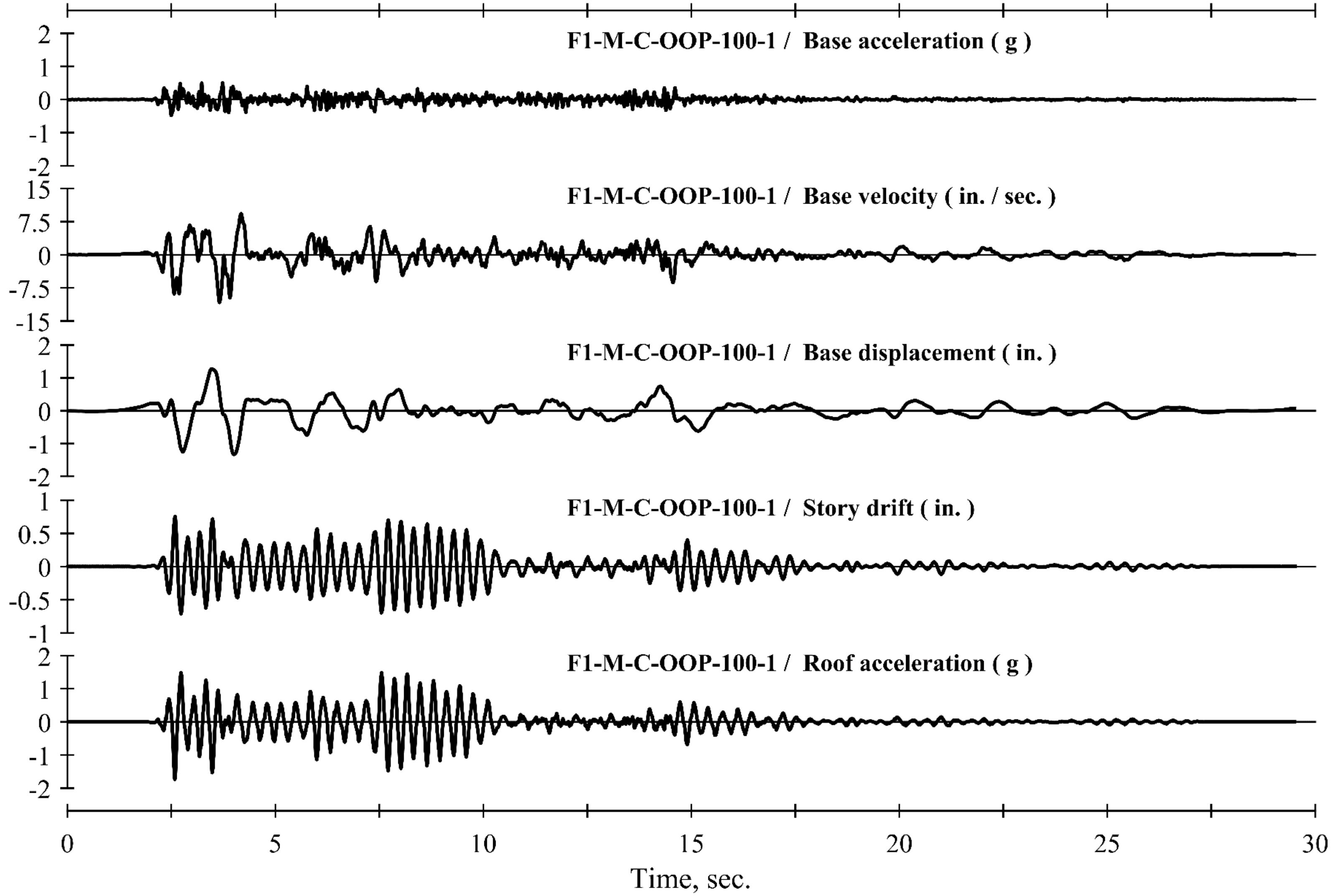

Figure D-67: Base motion and structural response histories in Run 67 of Specimen F1

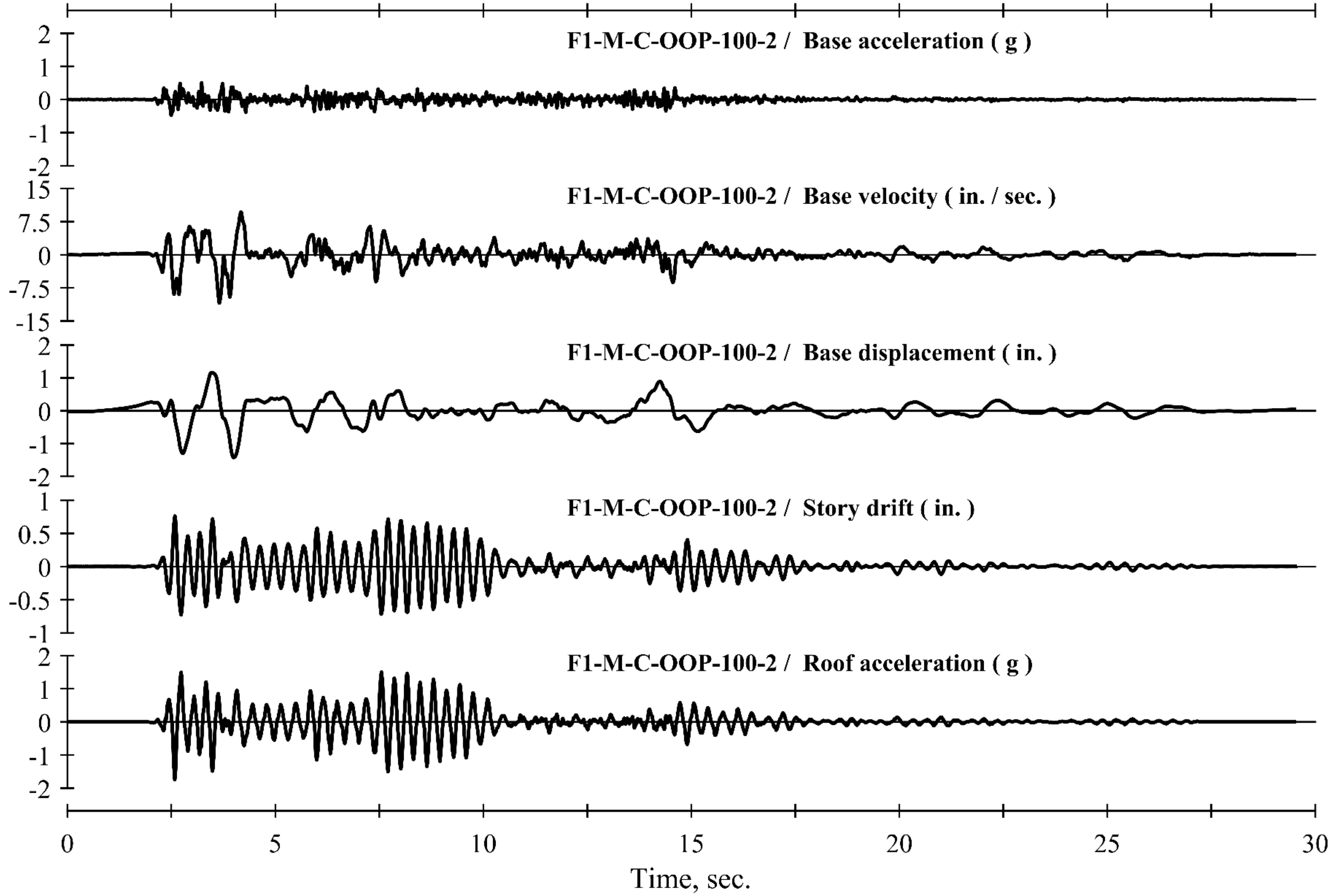

Figure D-68: Base motion and structural response histories in Run 68 of Specimen F1

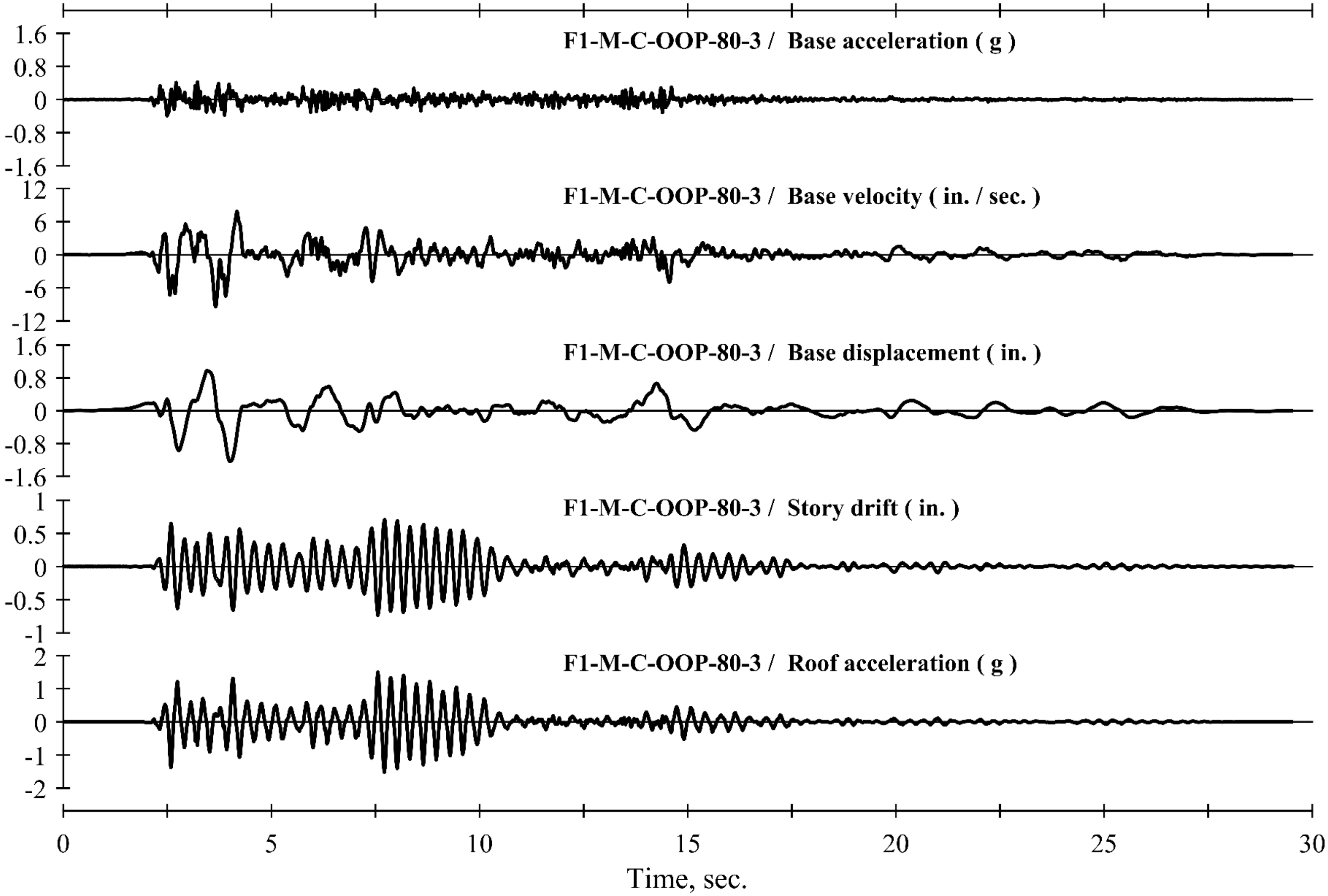

Figure D-69: Base motion and structural response histories in Run 69 of Specimen F1

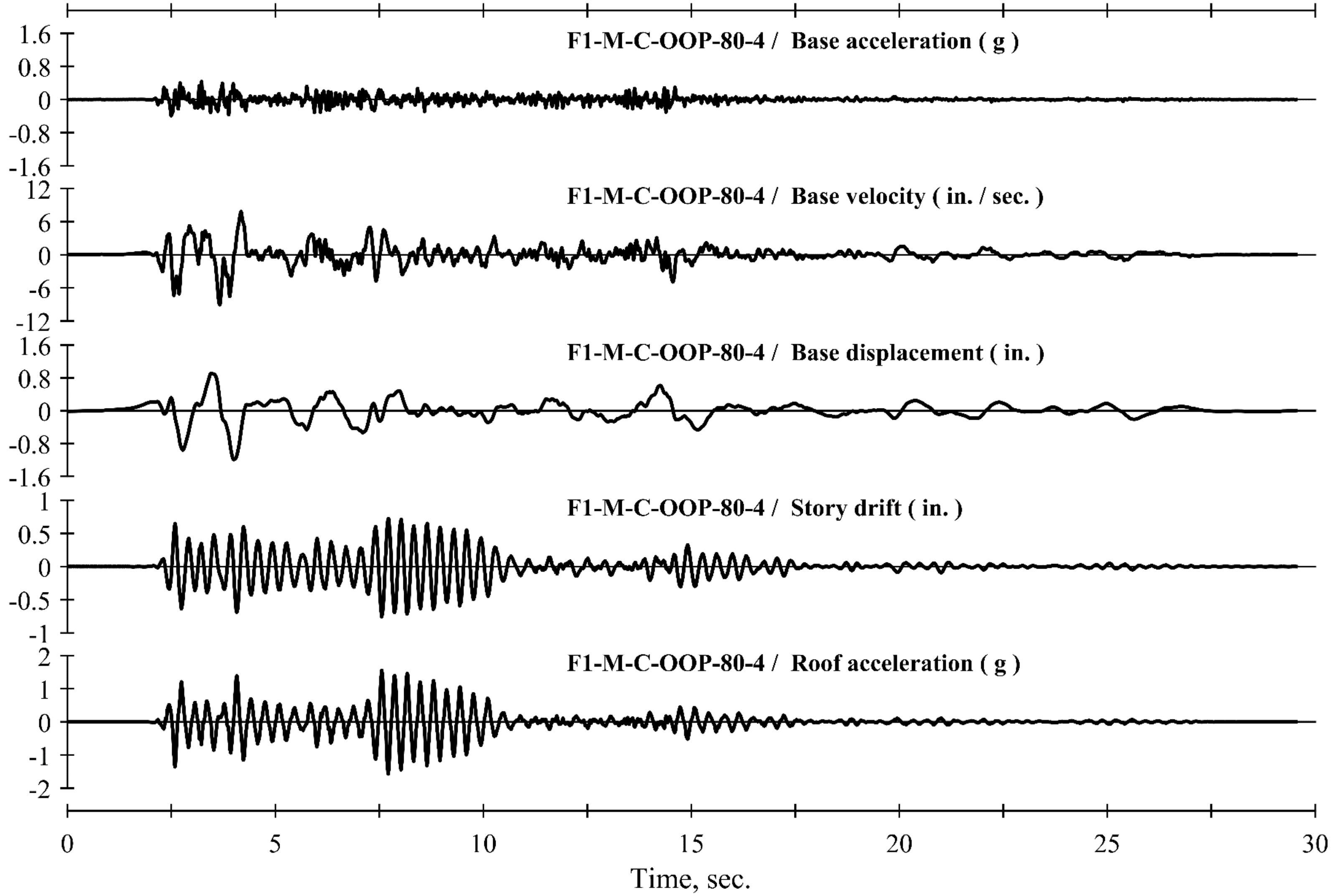

Figure D-70: Base motion and structural response histories in Run 70 of Specimen F1

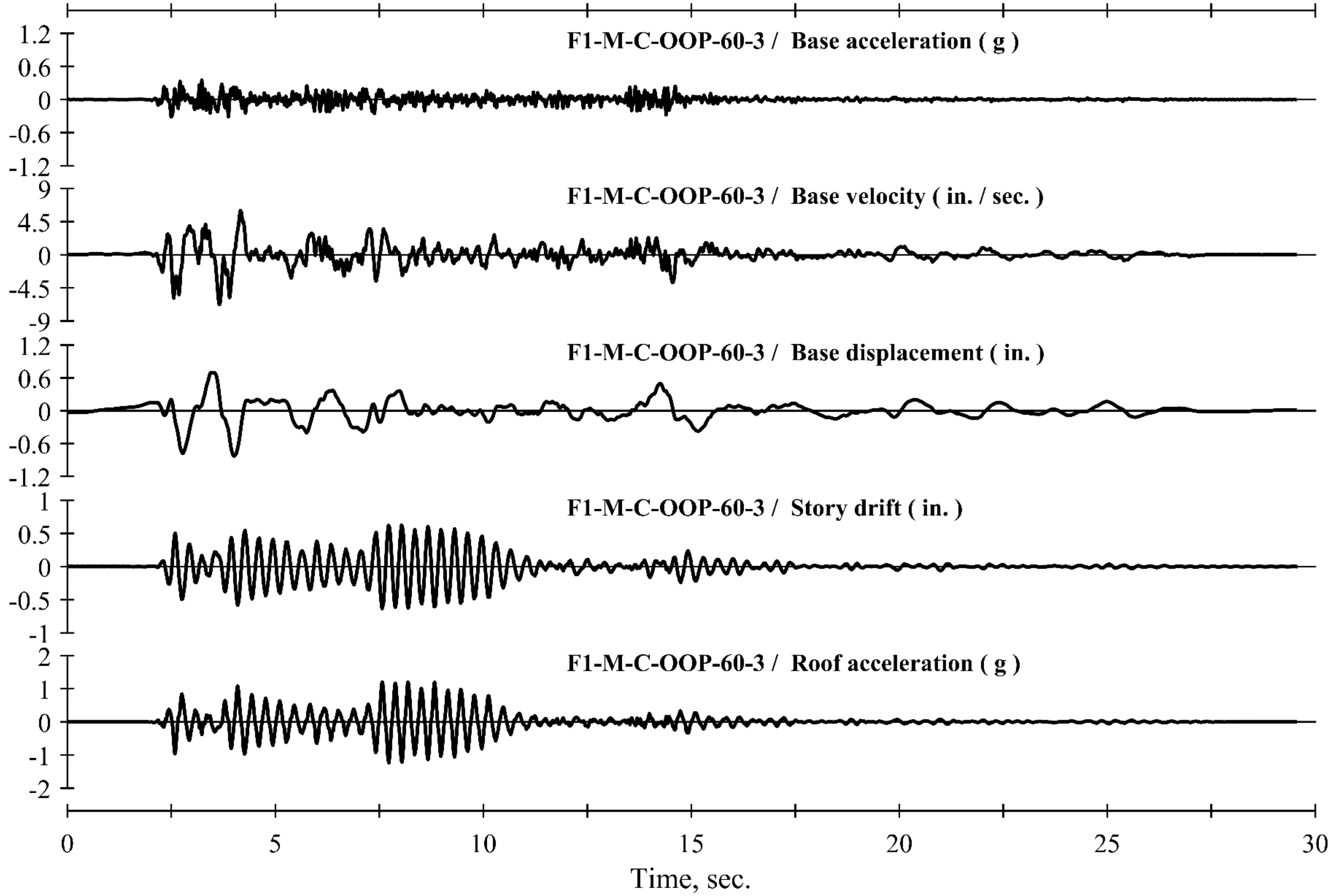

Figure D-71: Base motion and structural response histories in Run 71 of Specimen F1

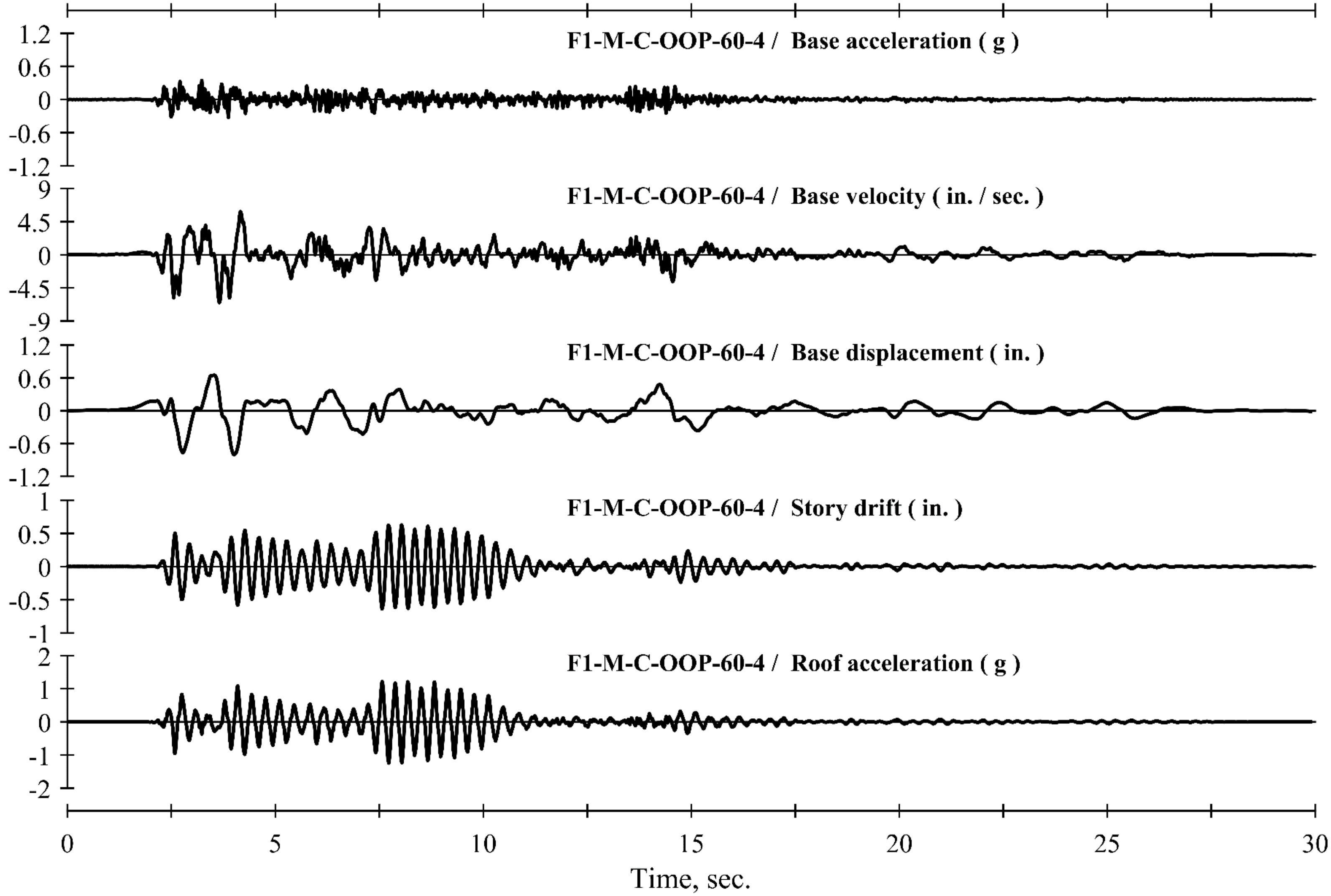

Figure D-72: Base motion and structural response histories in Run 72 of Specimen F1

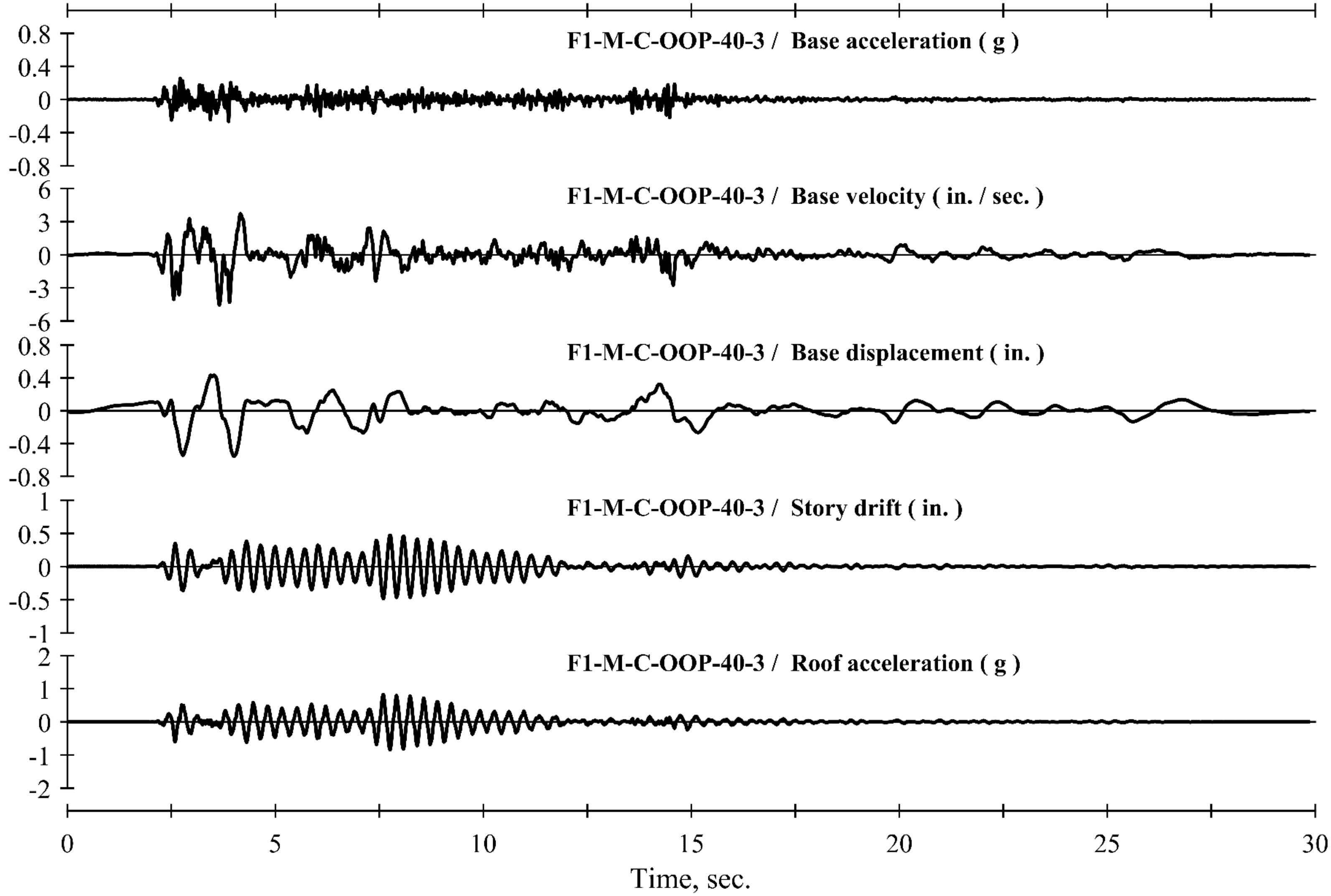

Figure D-73: Base motion and structural response histories in Run 73 of Specimen F1

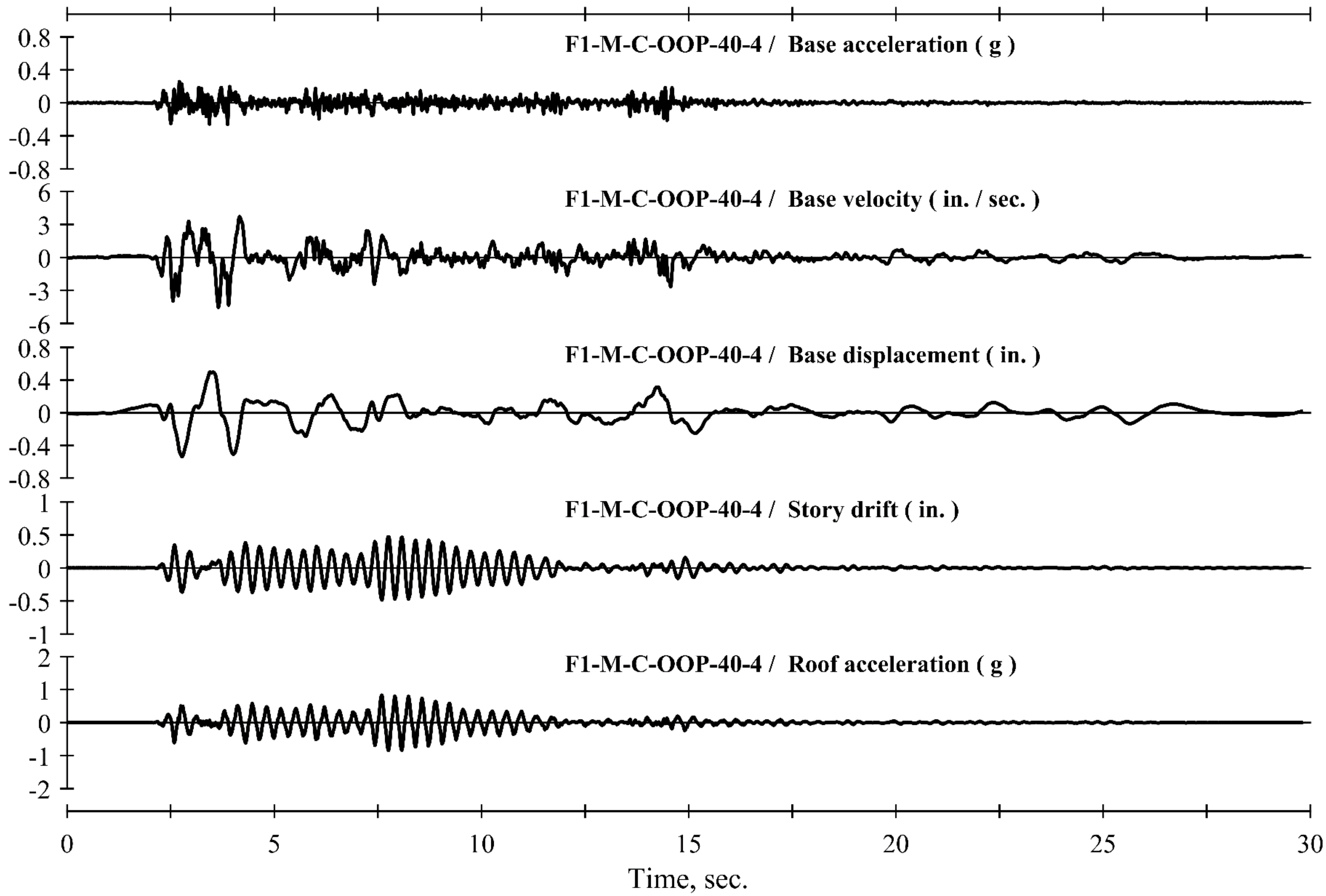

Figure D-74: Base motion and structural response histories in Run 74 of Specimen F1

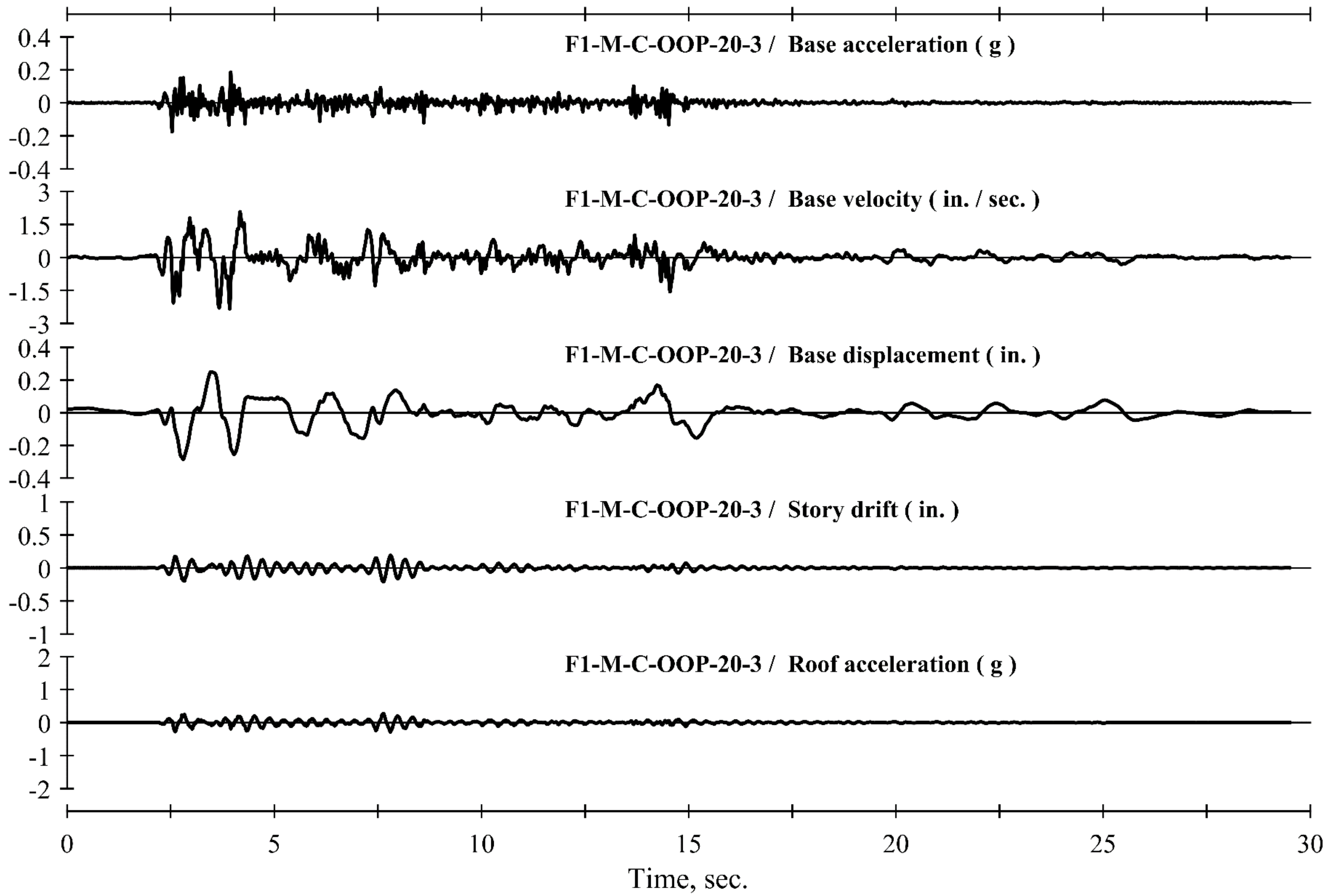

Figure D-75: Base motion and structural response histories in Run 75 of Specimen F1

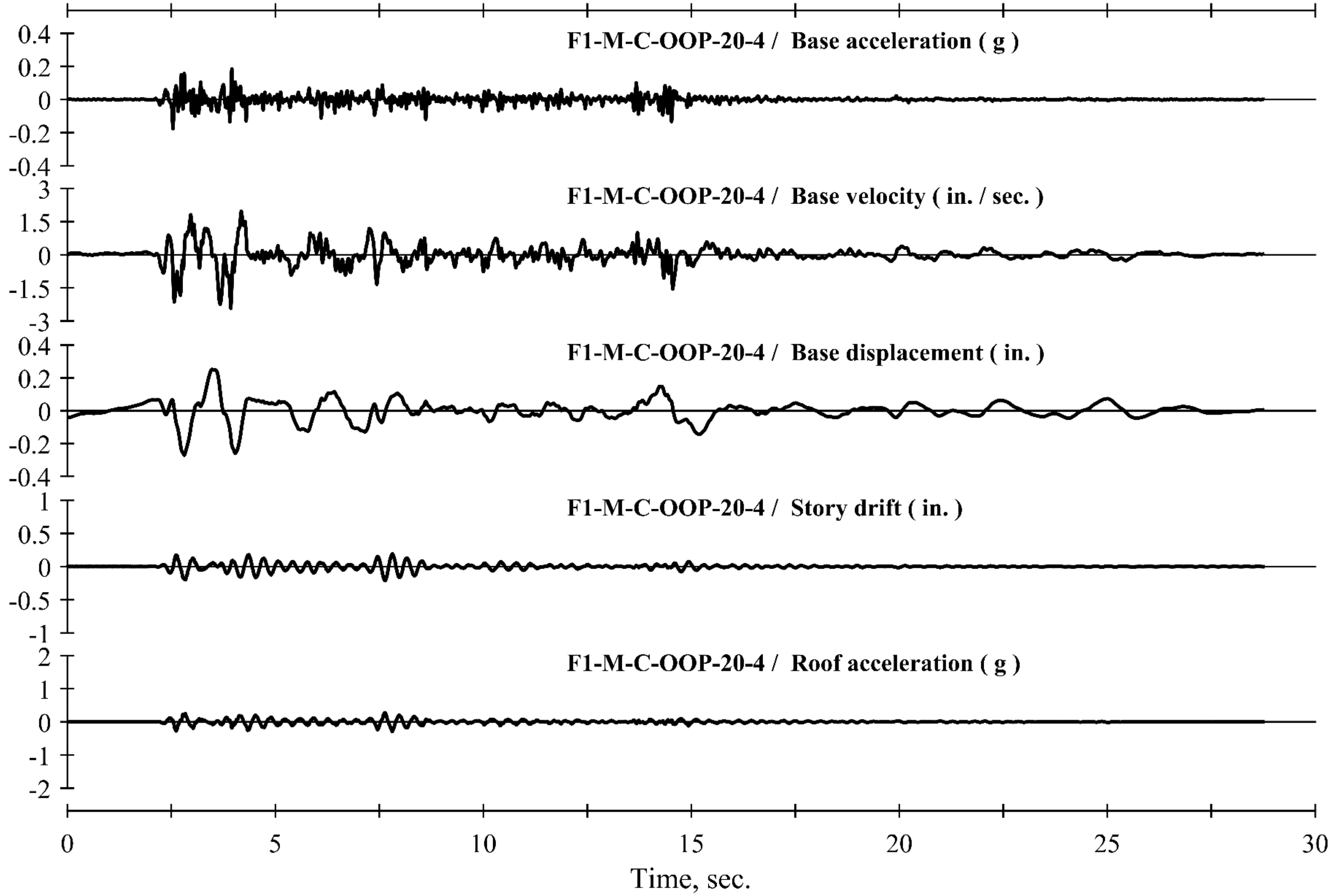

Figure D-76: Base motion and structural response histories in Run 76 of Specimen F1

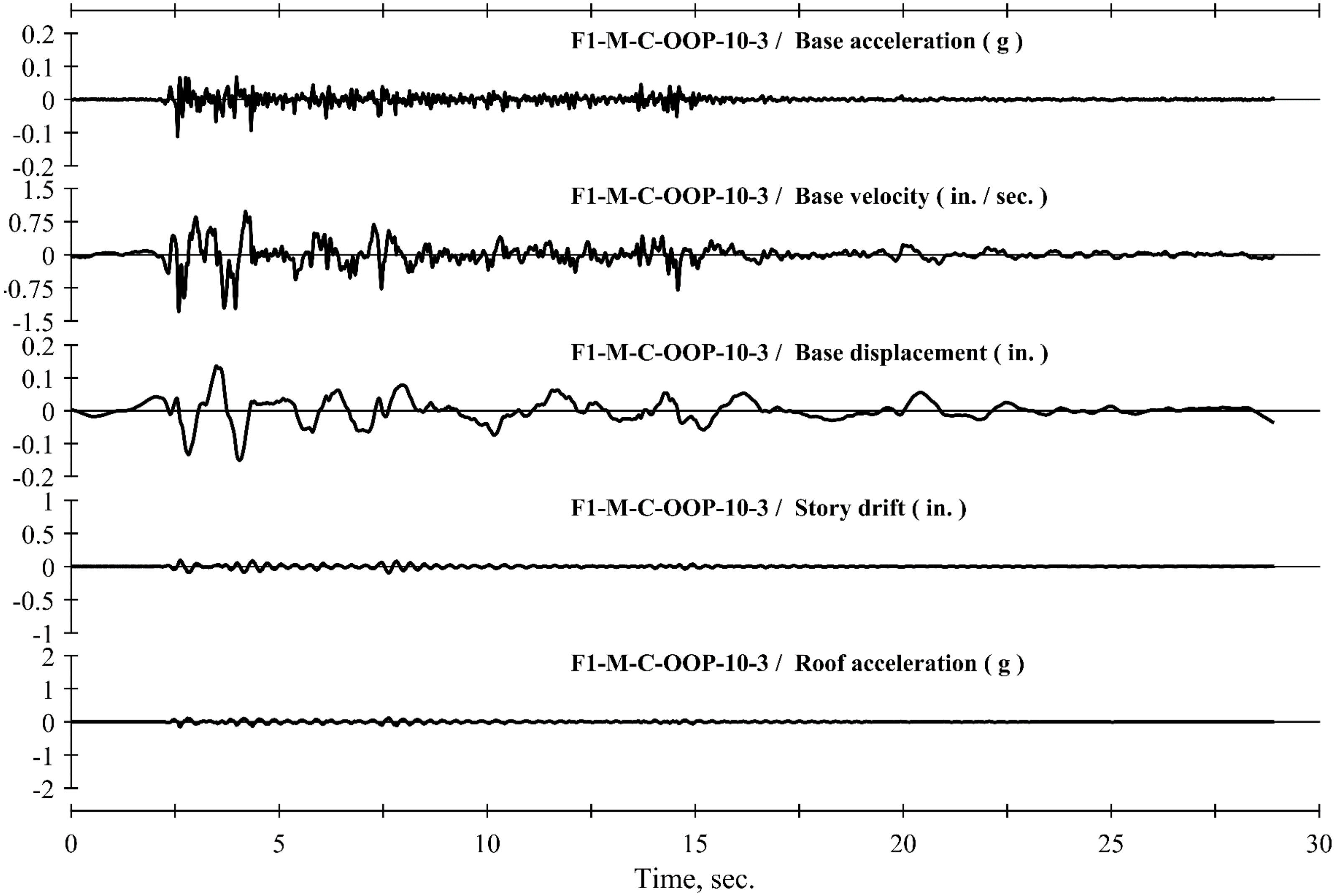

Figure D-77: Base motion and structural response histories in Run 77 of Specimen F1

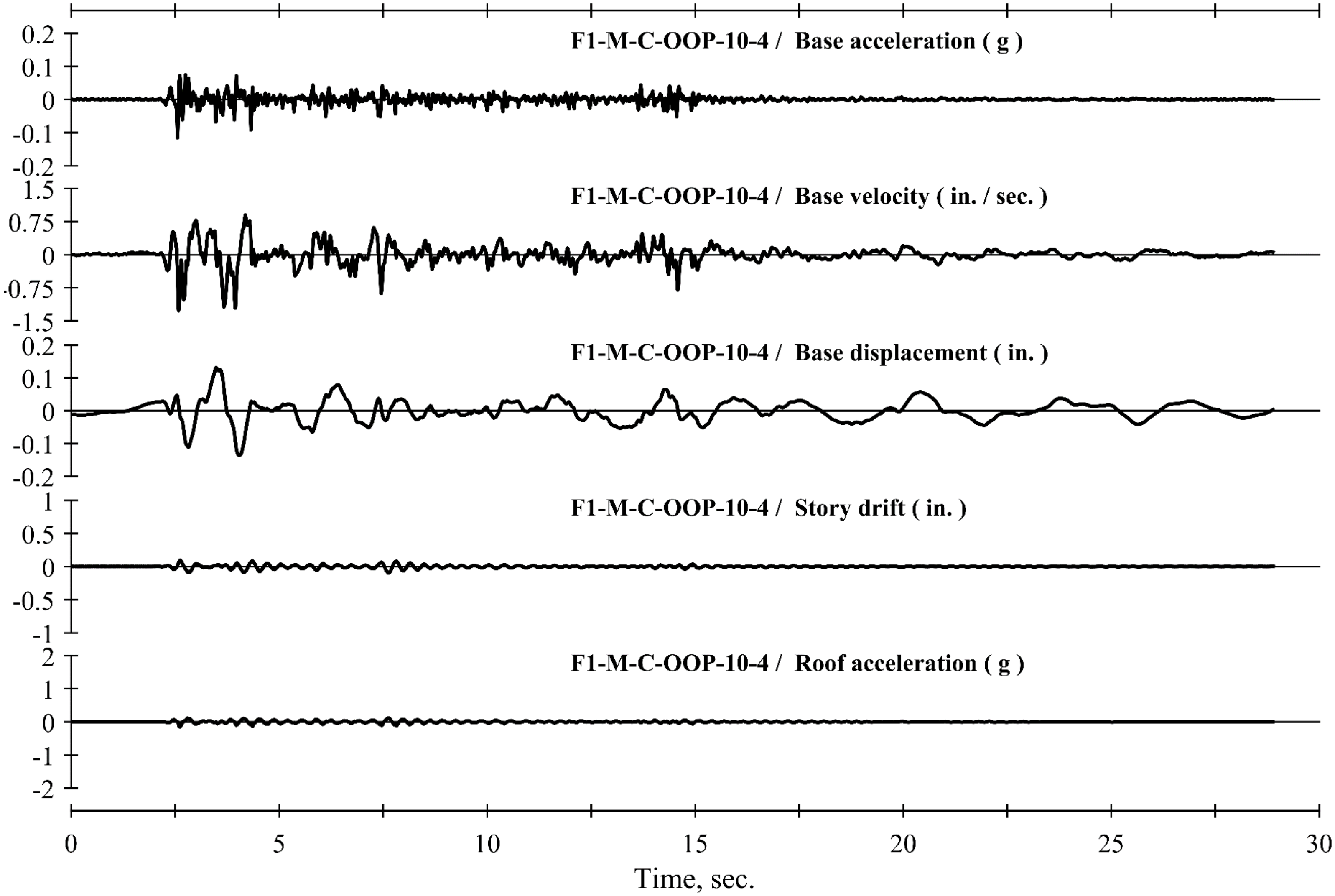

Figure D-78: Base motion and structural response histories in Run 78 of Specimen F1

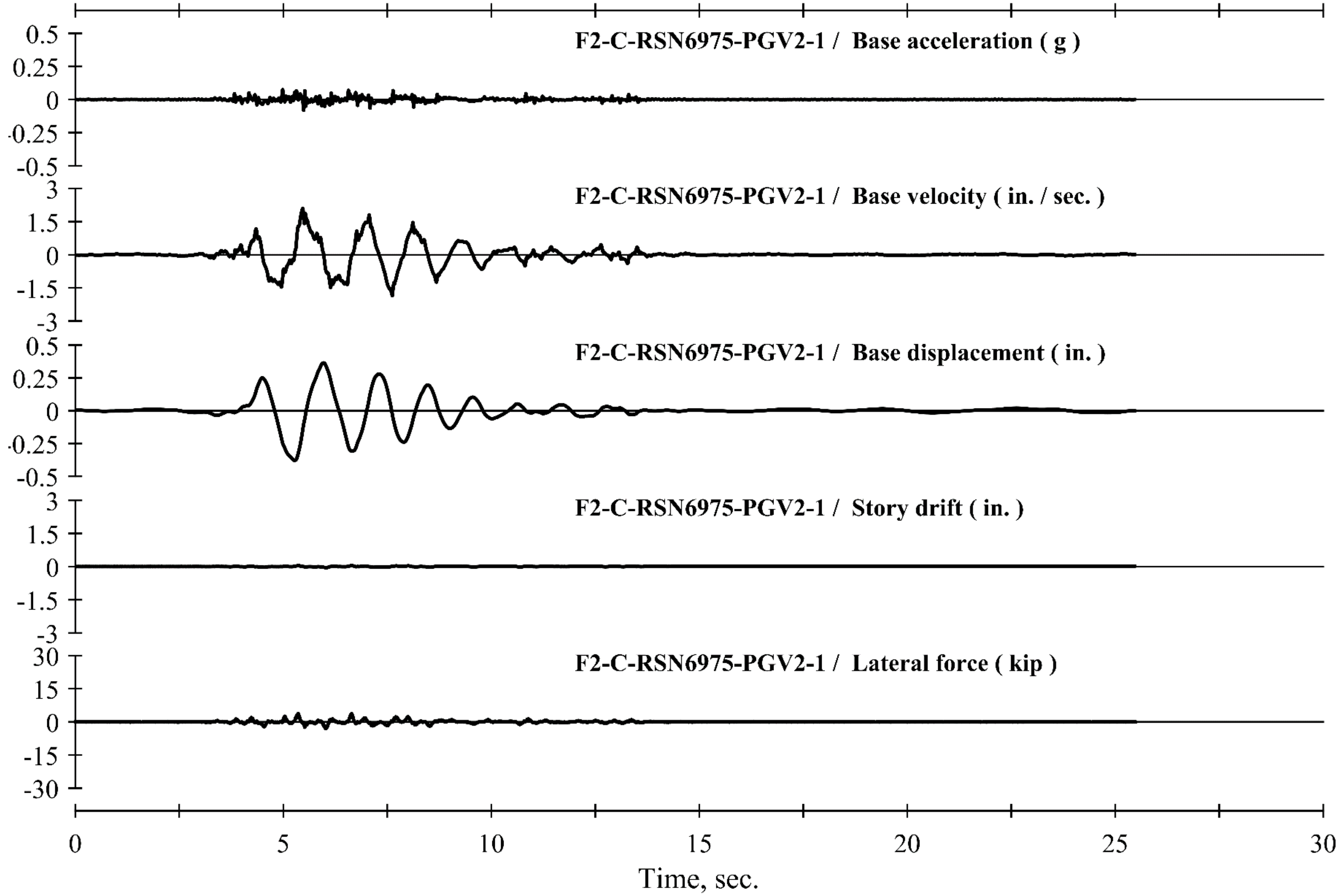

Figure D-79: Base motion and structural response histories in Run 1 of Specimen F2

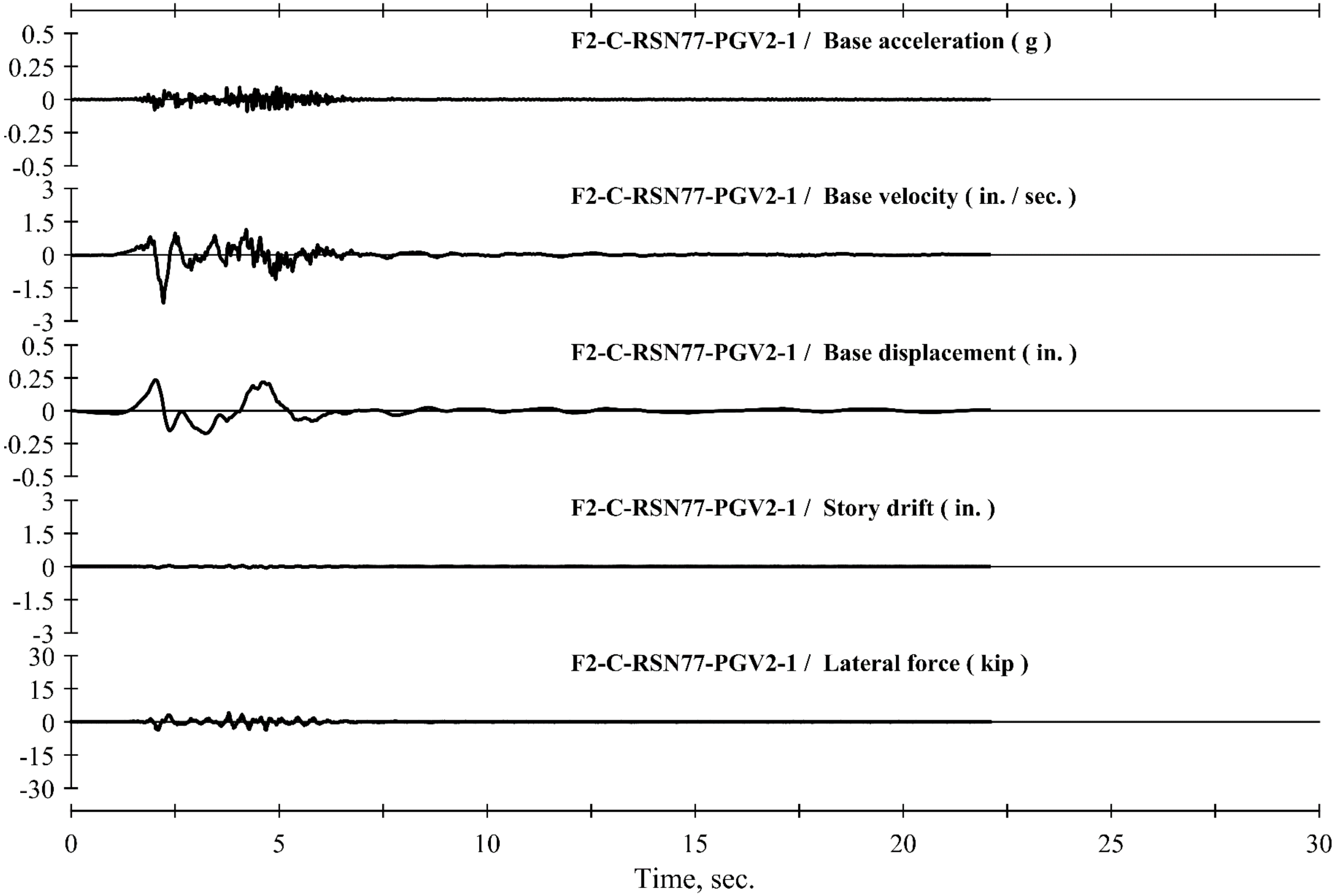

Figure D-80: Base motion and structural response histories in Run 2 of Specimen F2

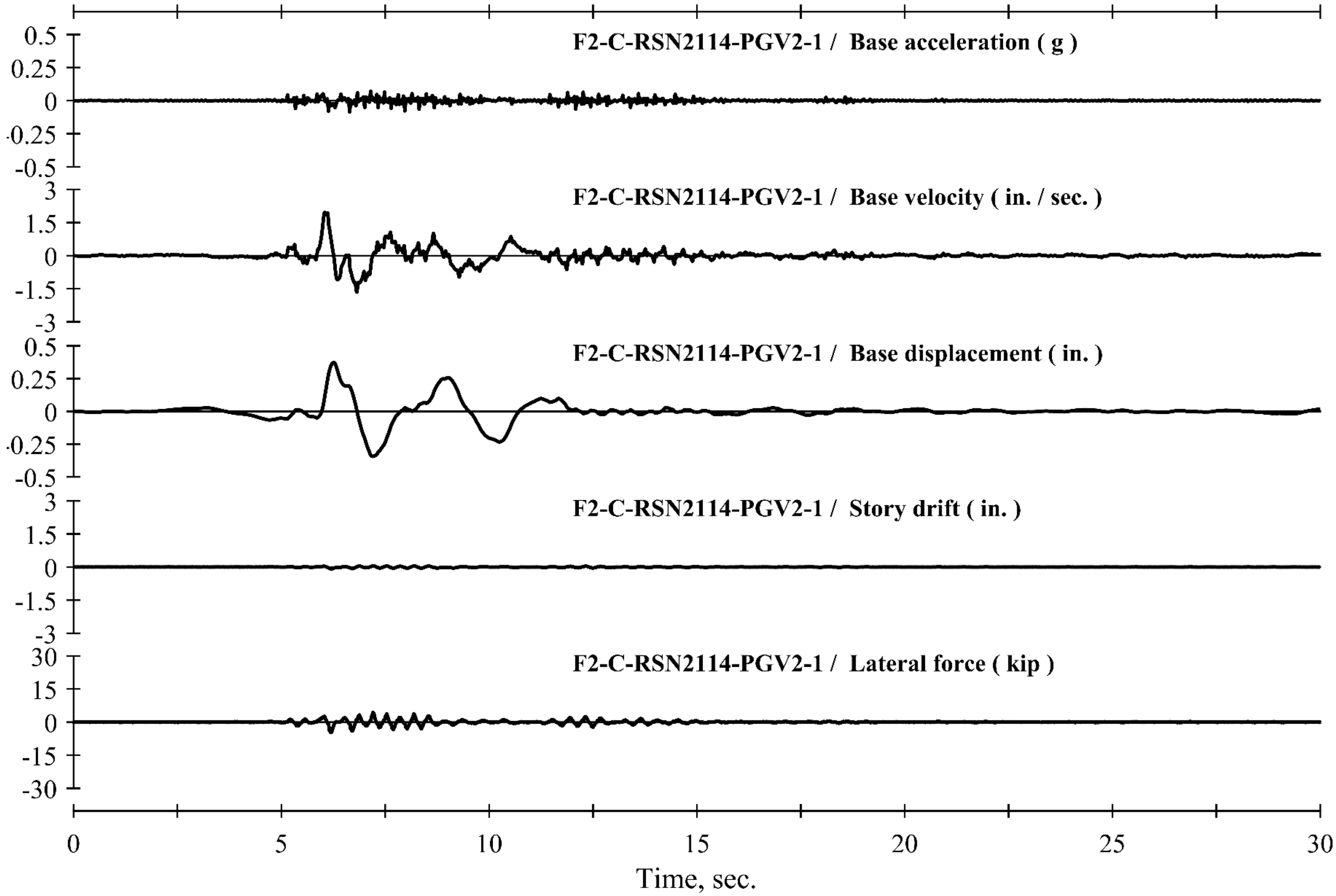

Figure D-81: Base motion and structural response histories in Run 3 of Specimen F2

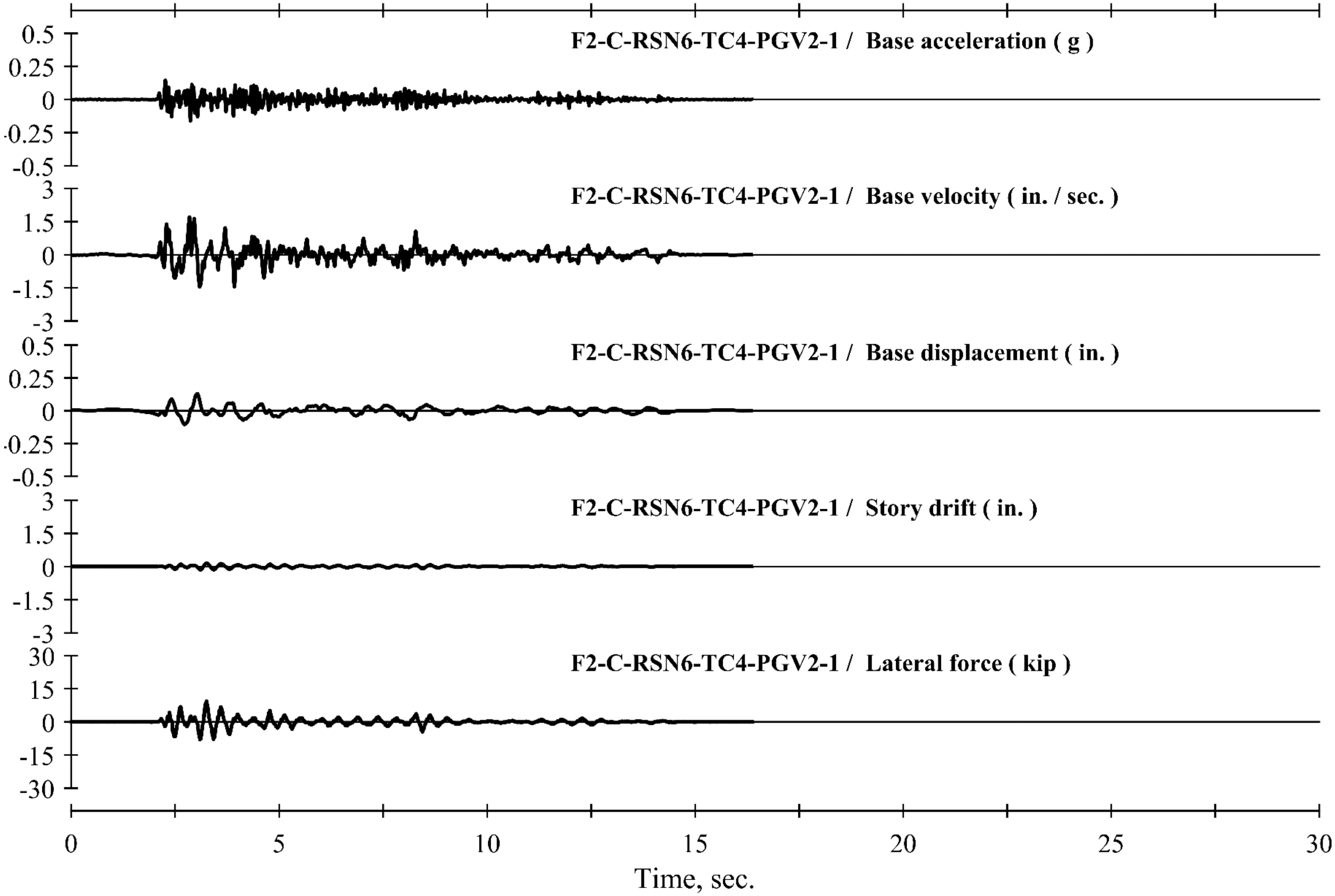

Figure D-82: Base motion and structural response histories in Run 4 of Specimen F2

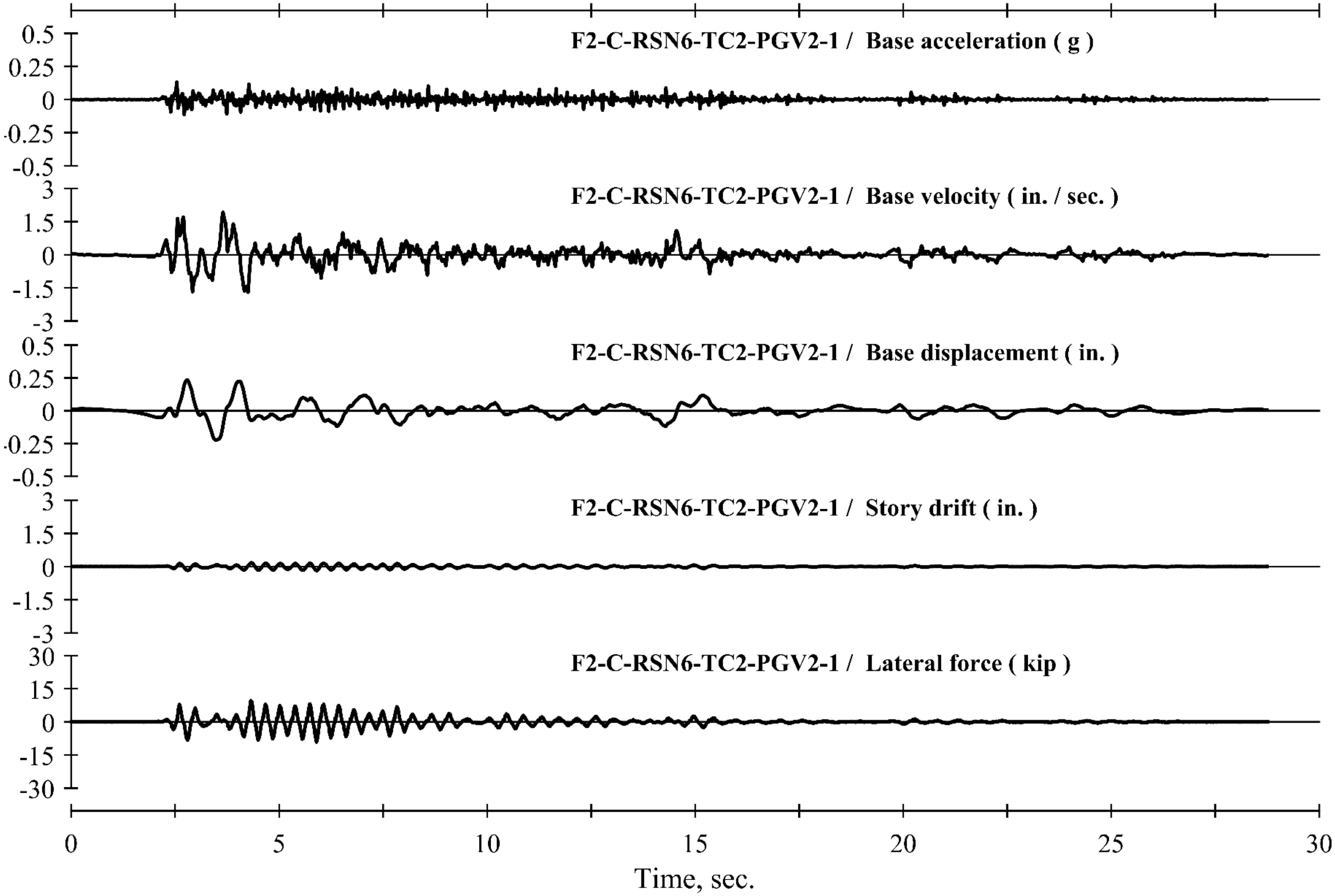

Figure D-83: Base motion and structural response histories in Run 5 of Specimen F2

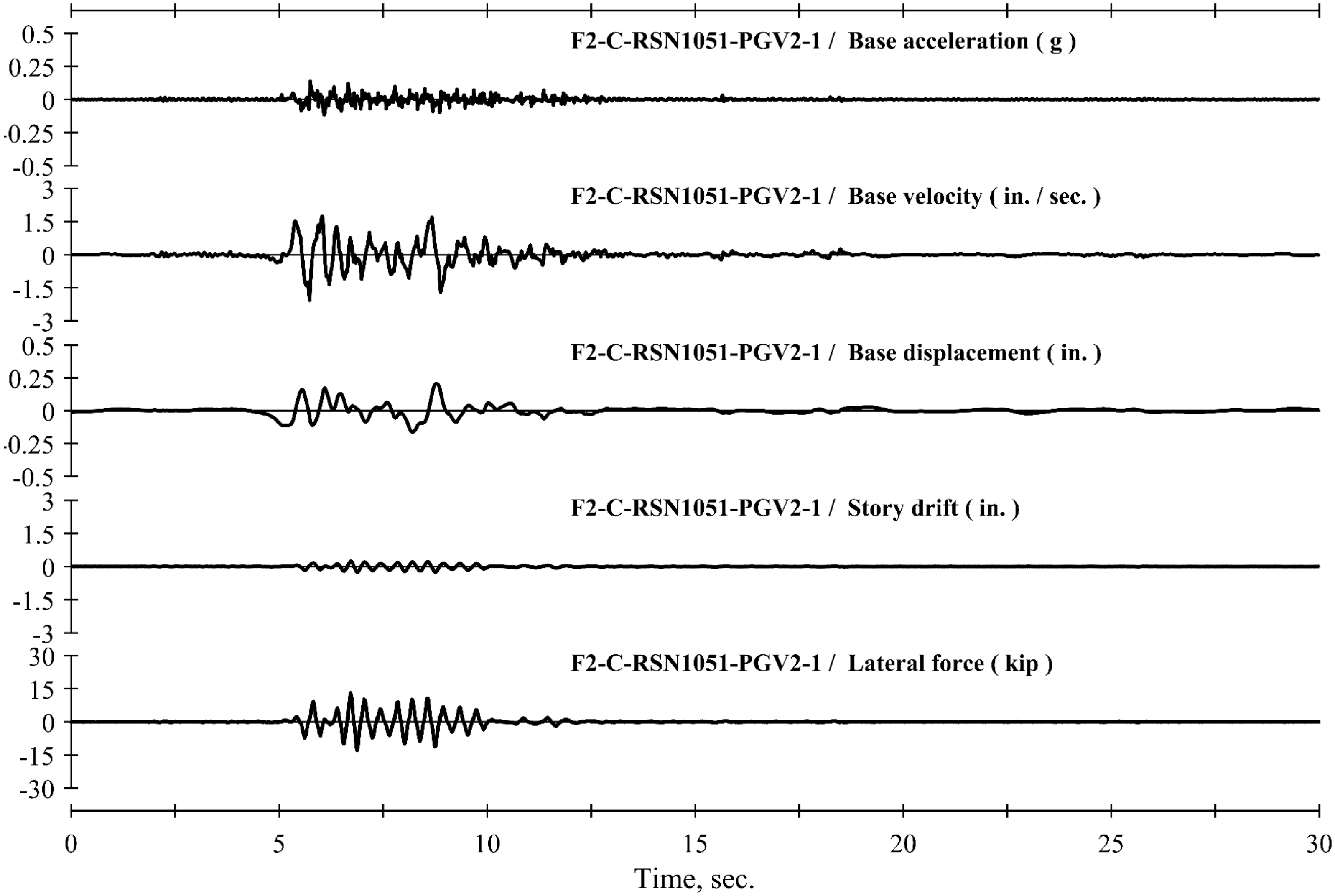

Figure D-84: Base motion and structural response histories in Run 6 of Specimen F2

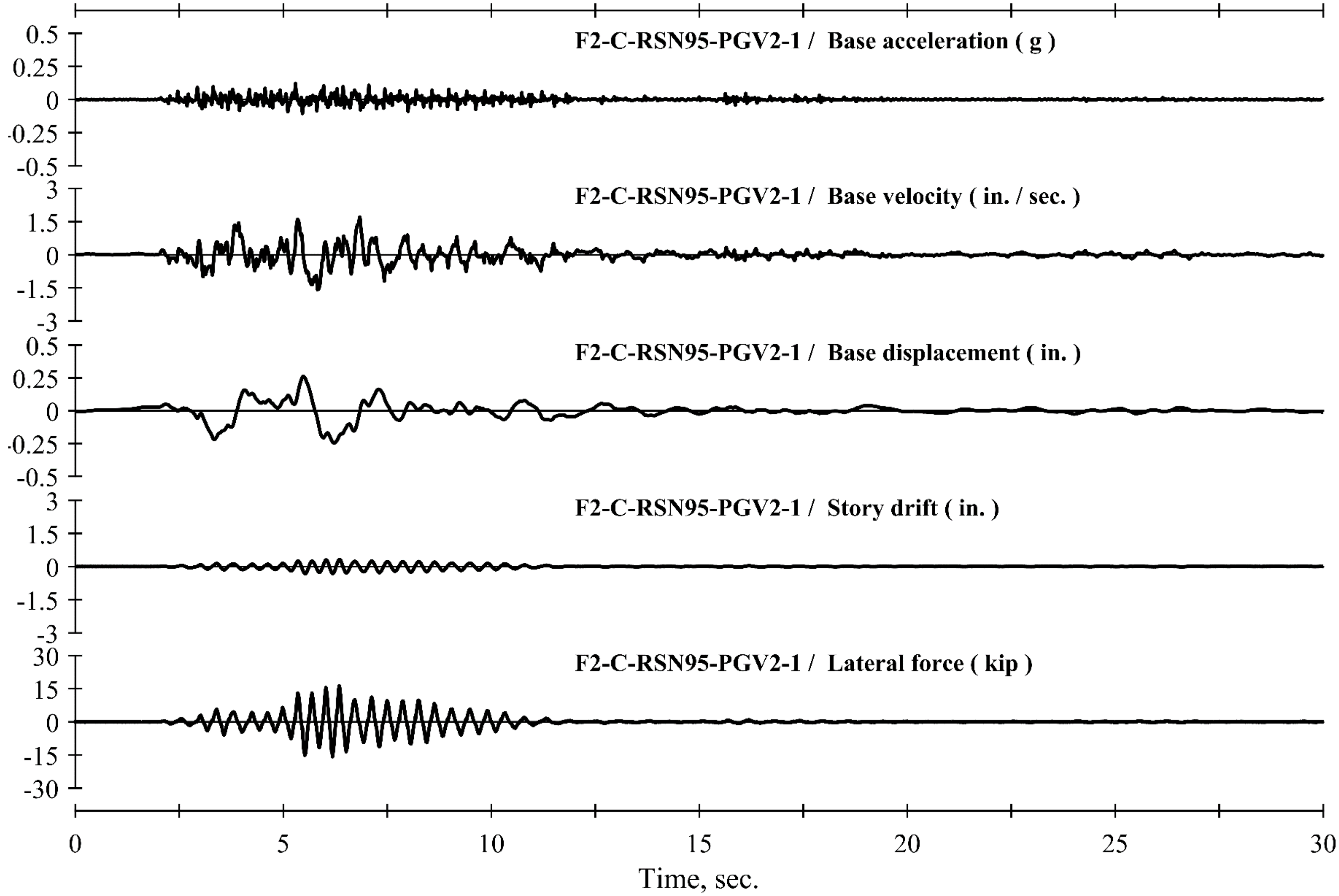

Figure D-85: Base motion and structural response histories in Run 7 of Specimen F2

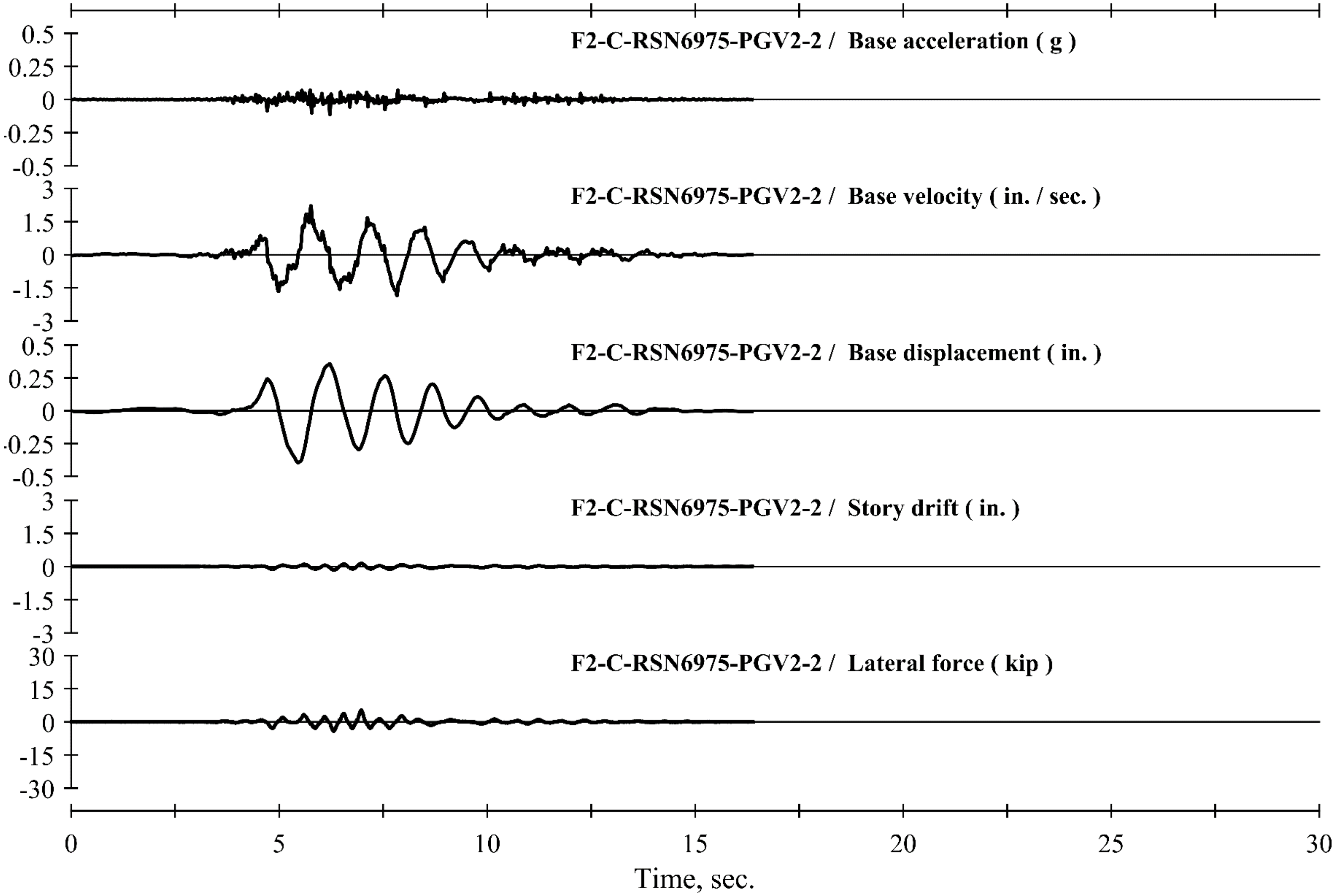

Figure D-86: Base motion and structural response histories in Run 8 of Specimen F2

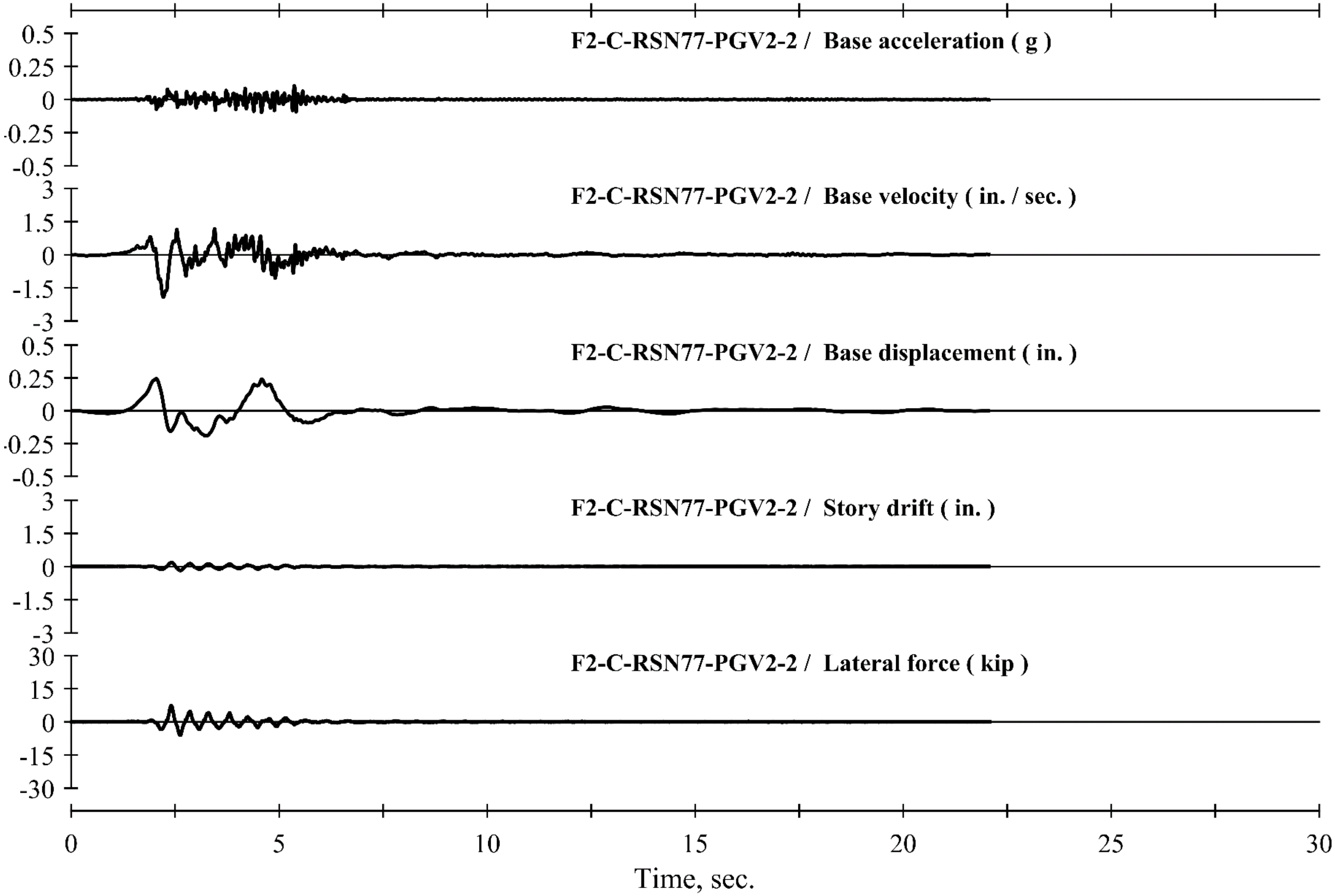

Figure D-87: Base motion and structural response histories in Run 9 of Specimen F2

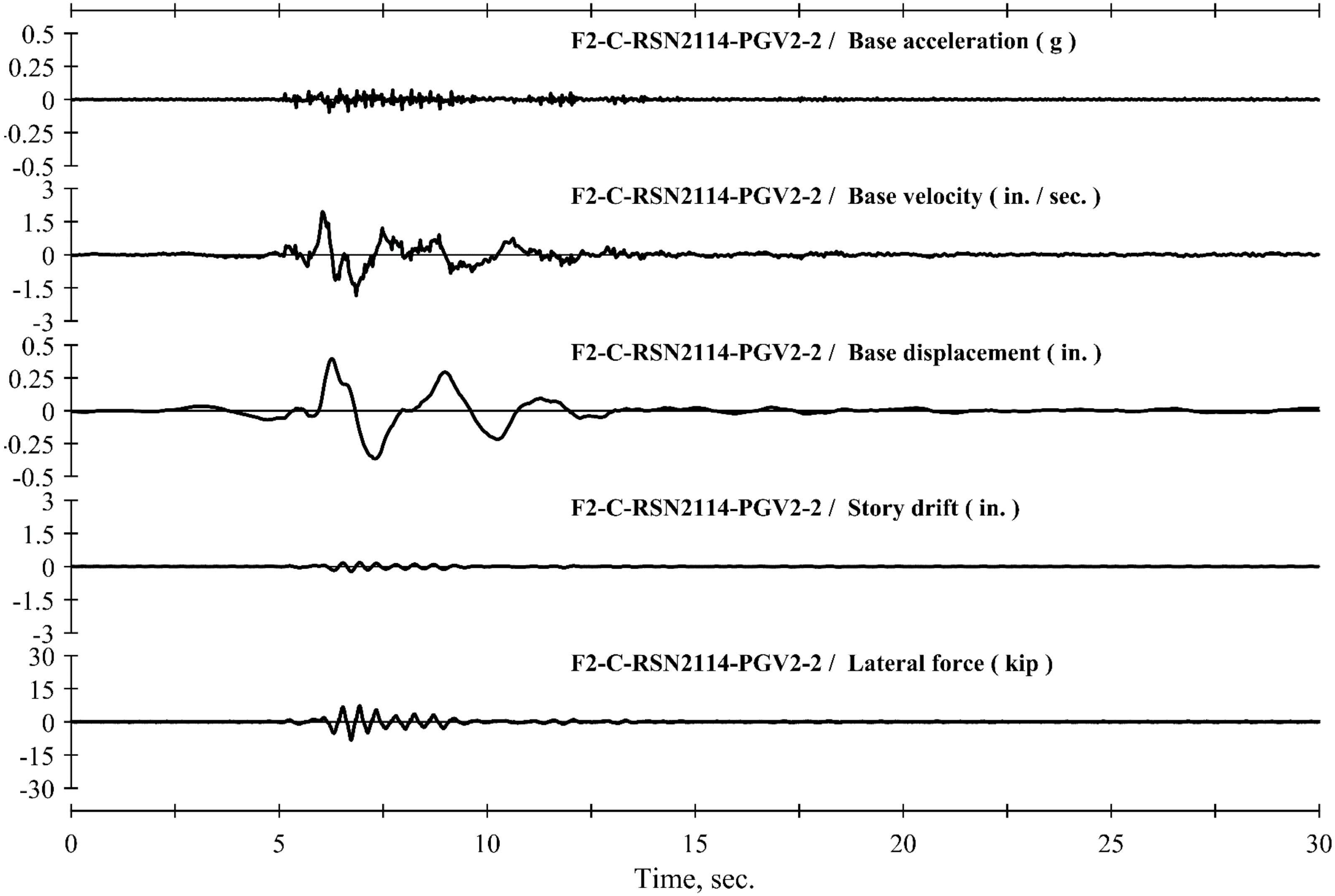

Figure D-88: Base motion and structural response histories in Run 10 of Specimen F2

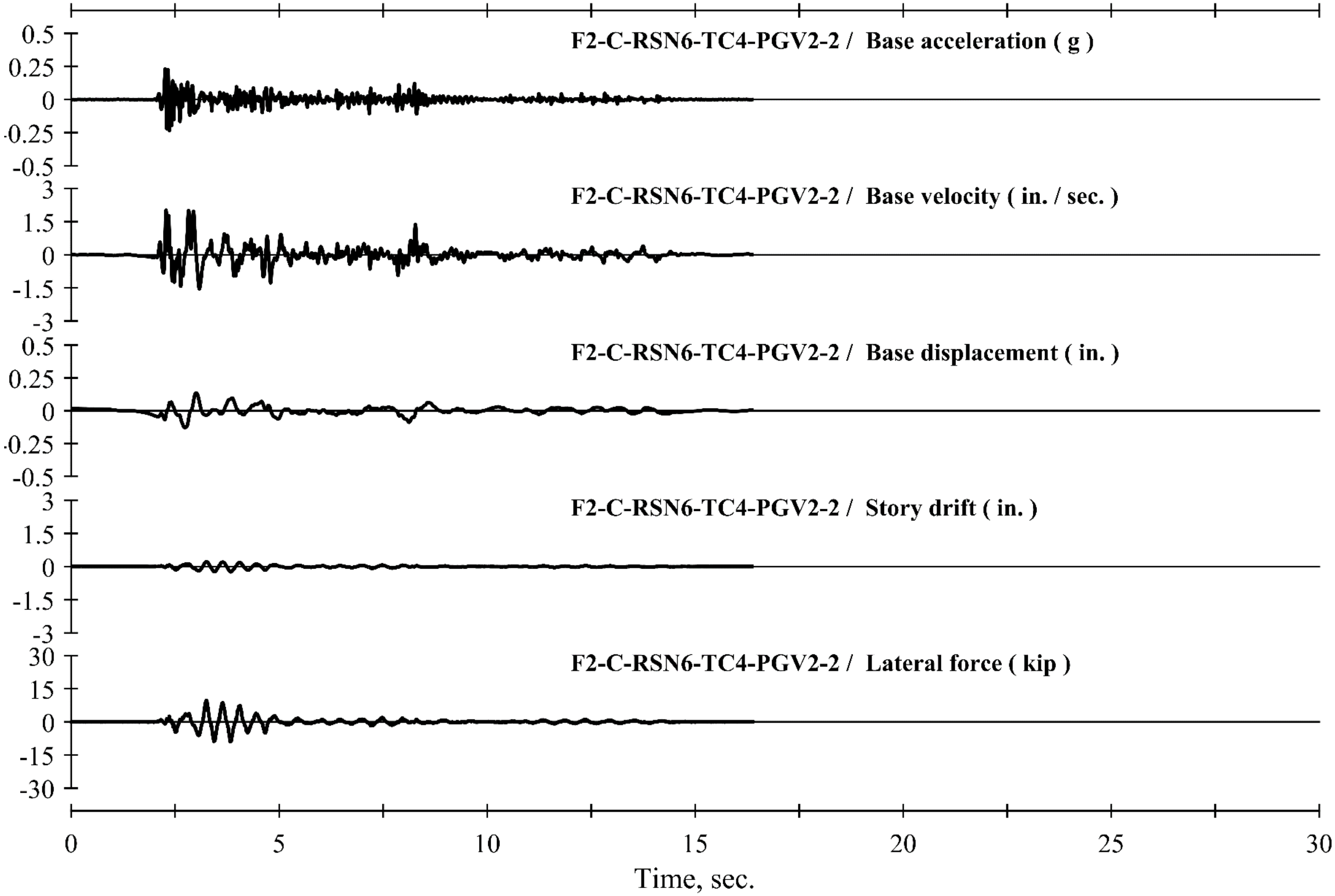

Figure D-89: Base motion and structural response histories in Run 11 of Specimen F2

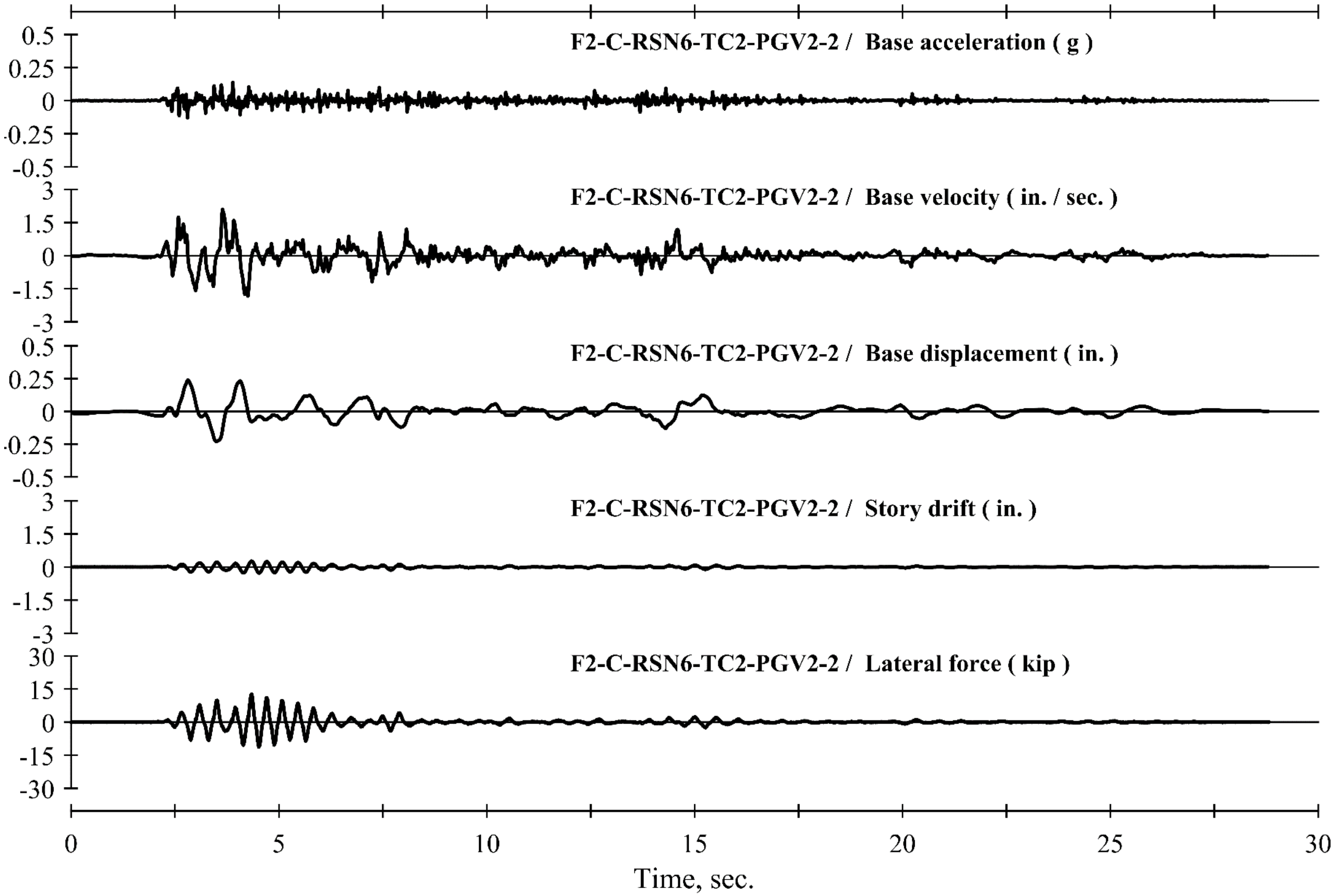

Figure D-90: Base motion and structural response histories in Run 12 of Specimen F2

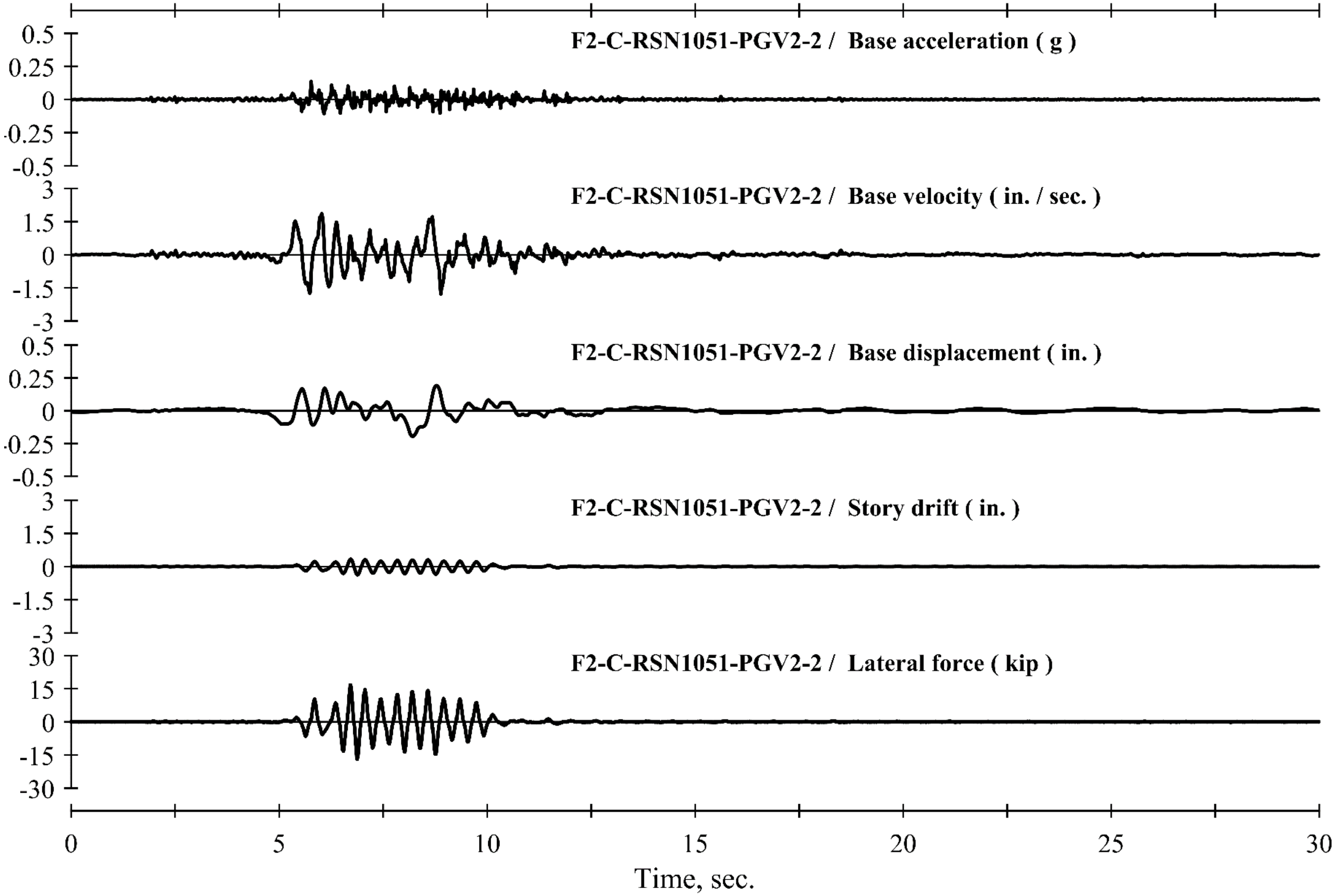

Figure D-91: Base motion and structural response histories in Run 13 of Specimen F2

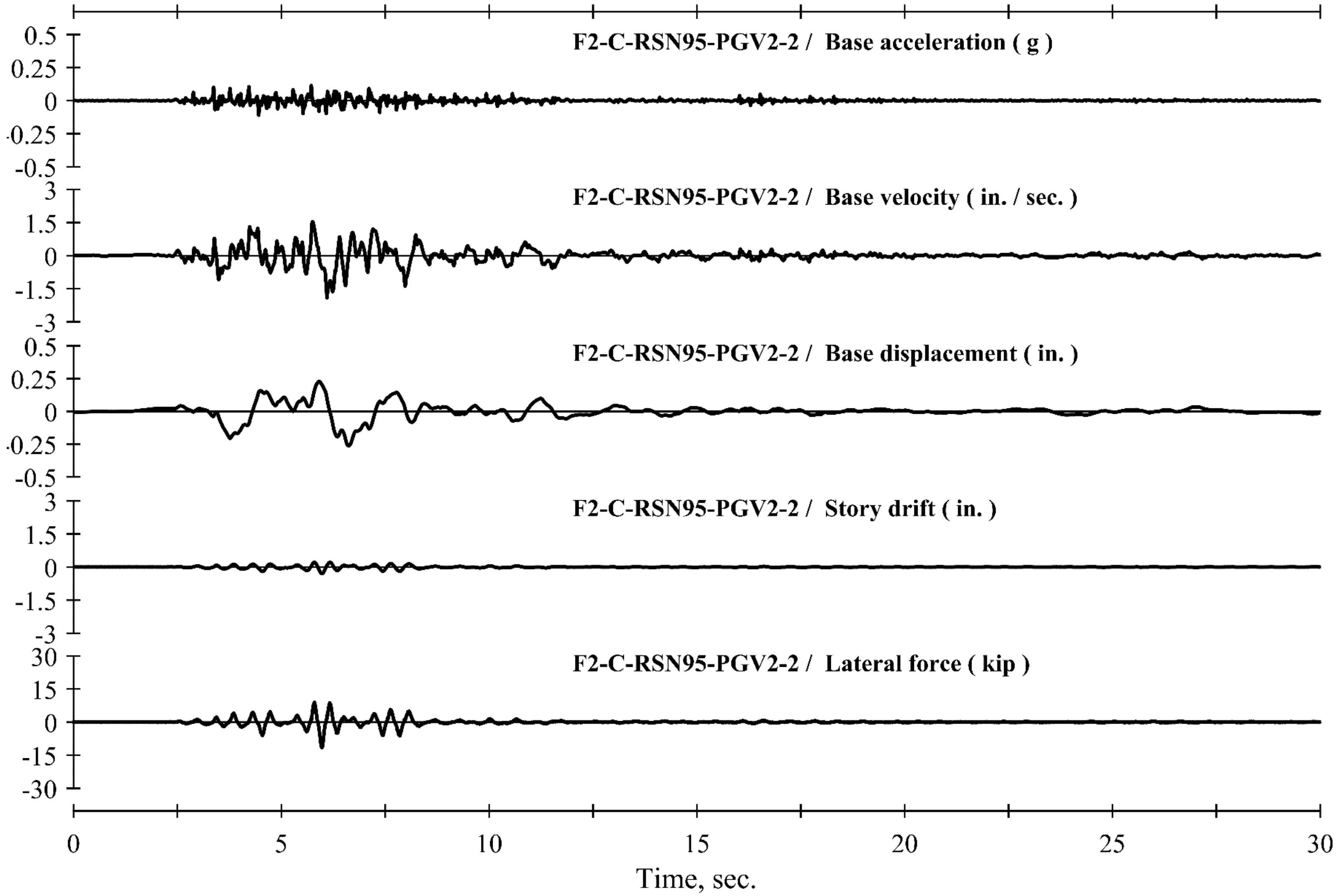

Figure D-92: Base motion and structural response histories in Run 14 of Specimen F2

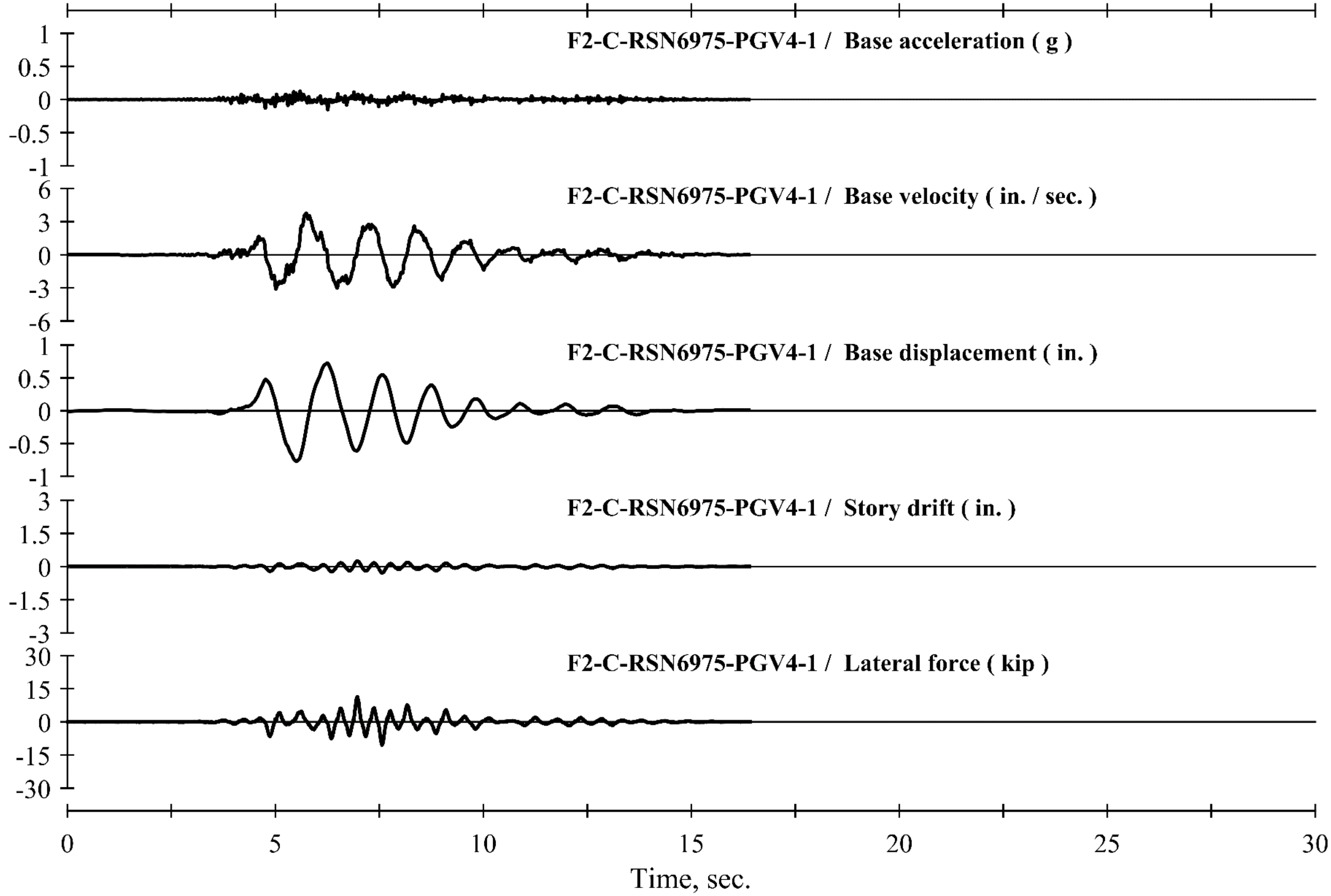

Figure D-93: Base motion and structural response histories in Run 15 of Specimen F2

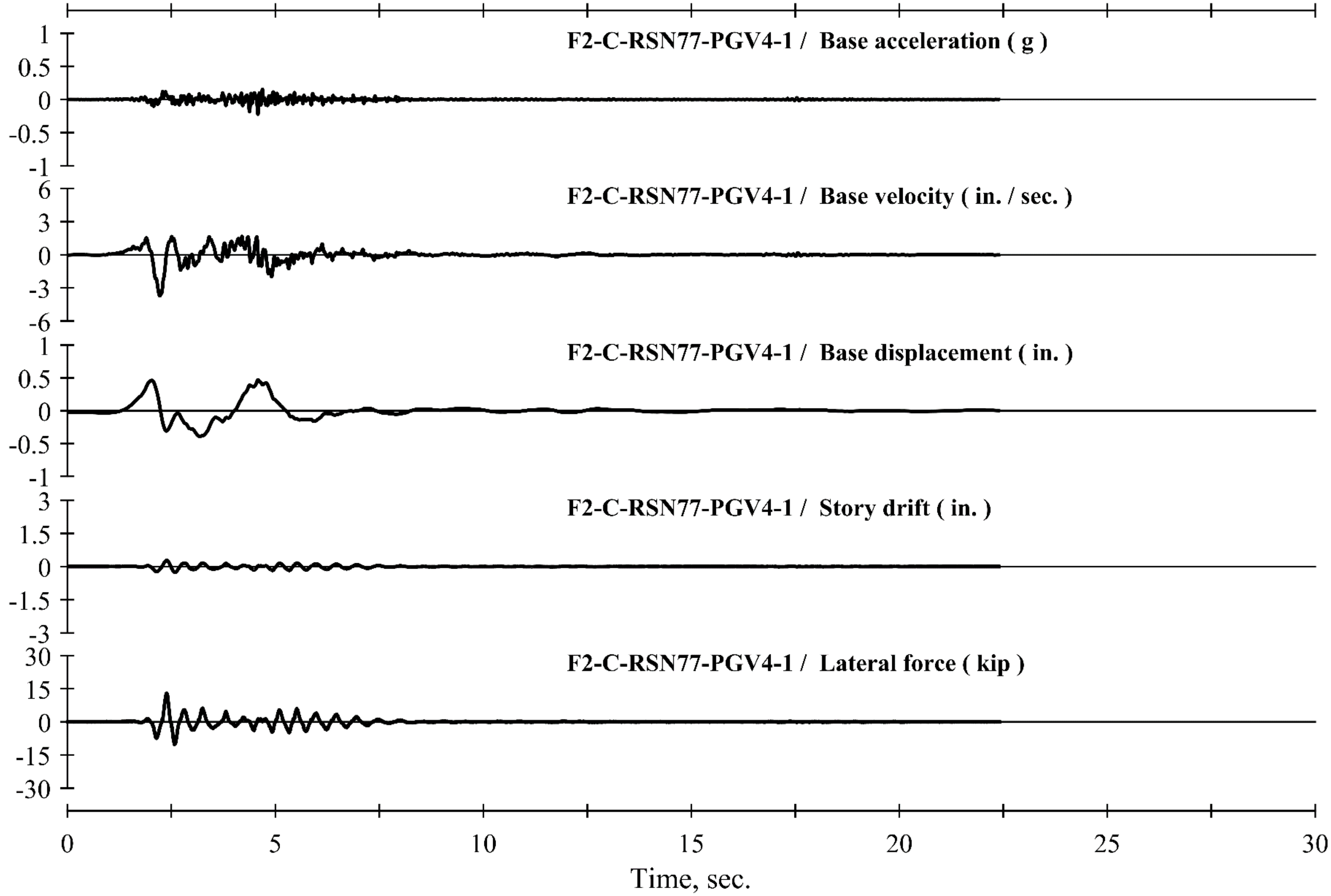

Figure D-94: Base motion and structural response histories in Run 16 of Specimen F2

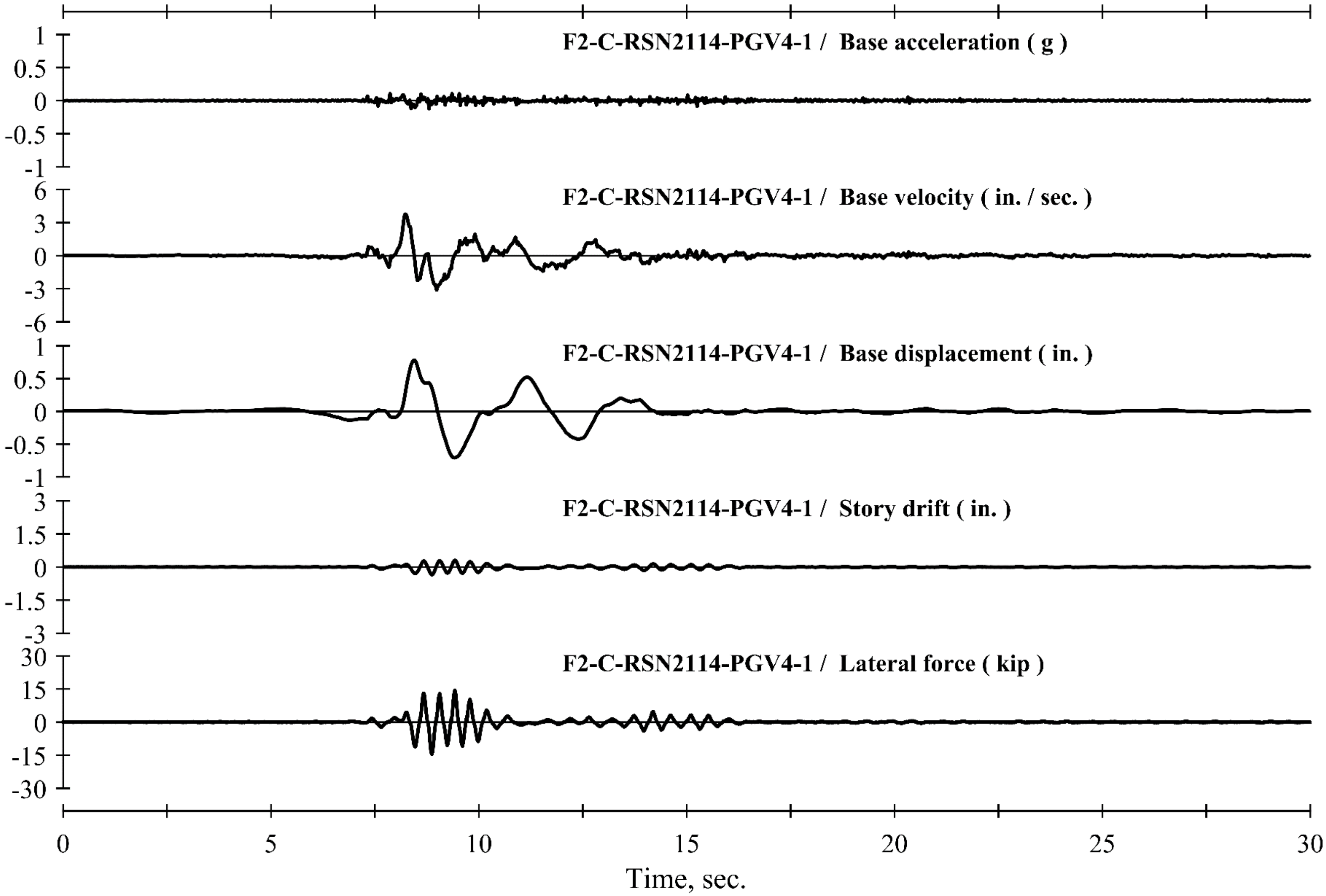

Figure D-95: Base motion and structural response histories in Run 17 of Specimen F2

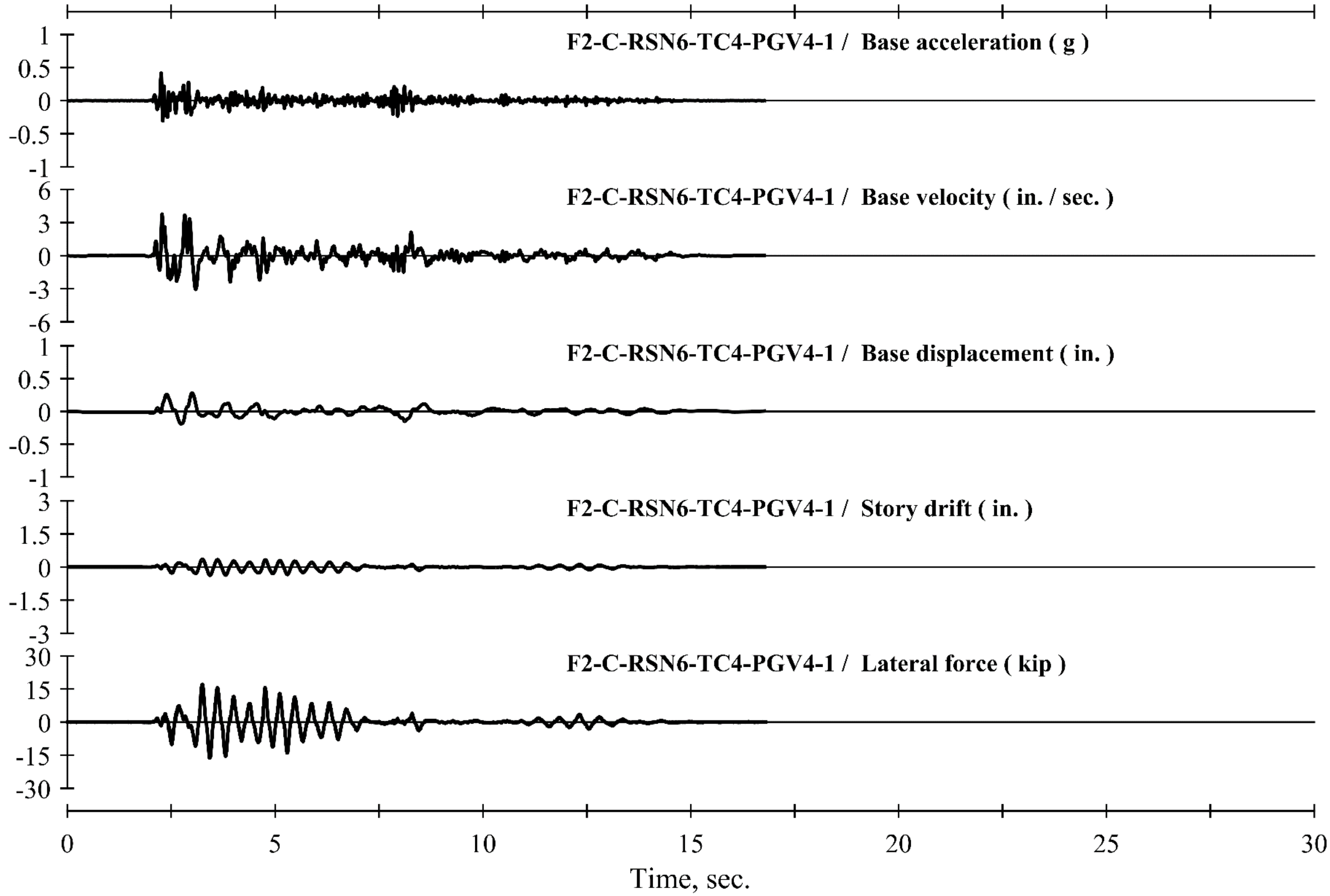

Figure D-96: Base motion and structural response histories in Run 18 of Specimen F2

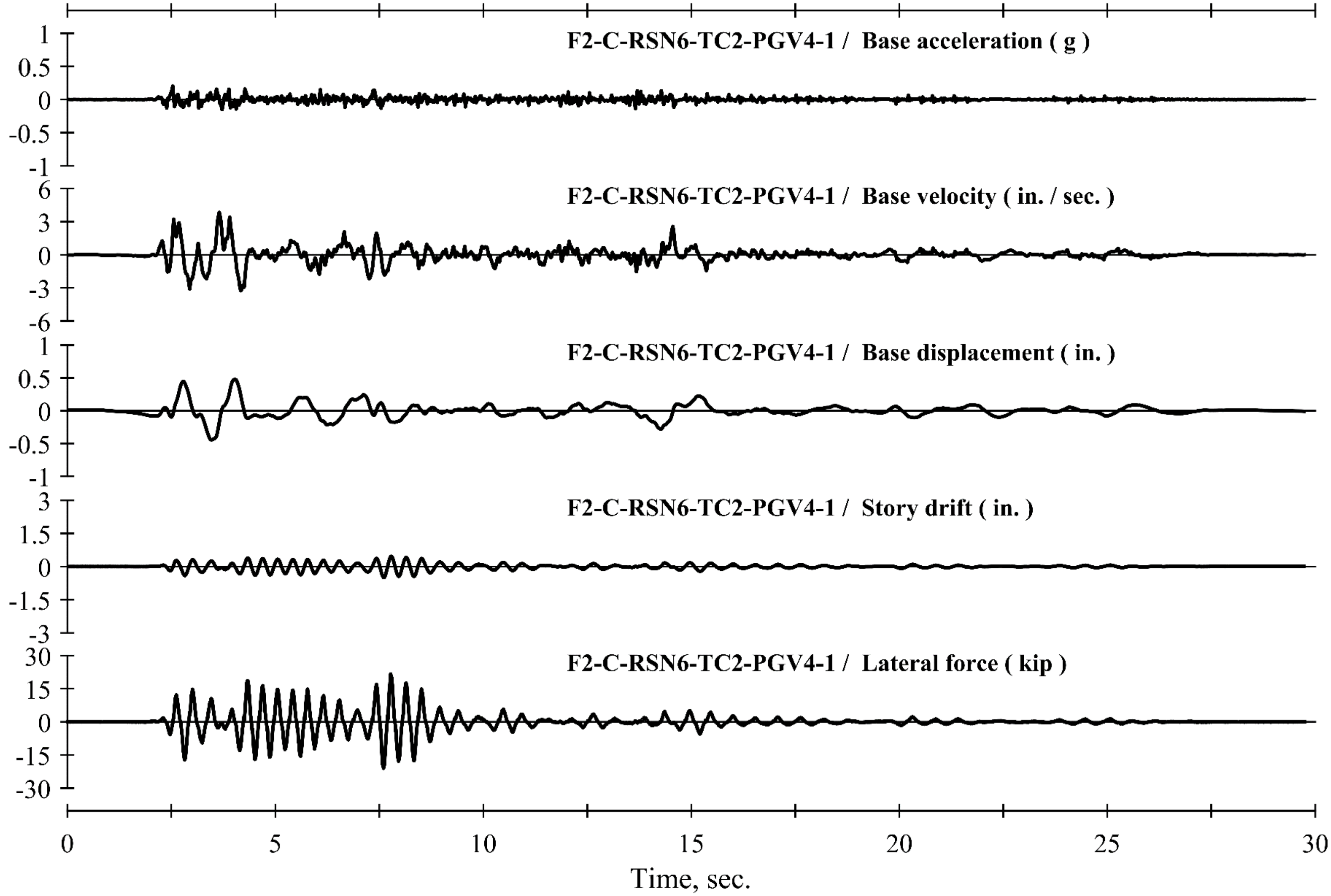

Figure D-97: Base motion and structural response histories in Run 19 of Specimen F2

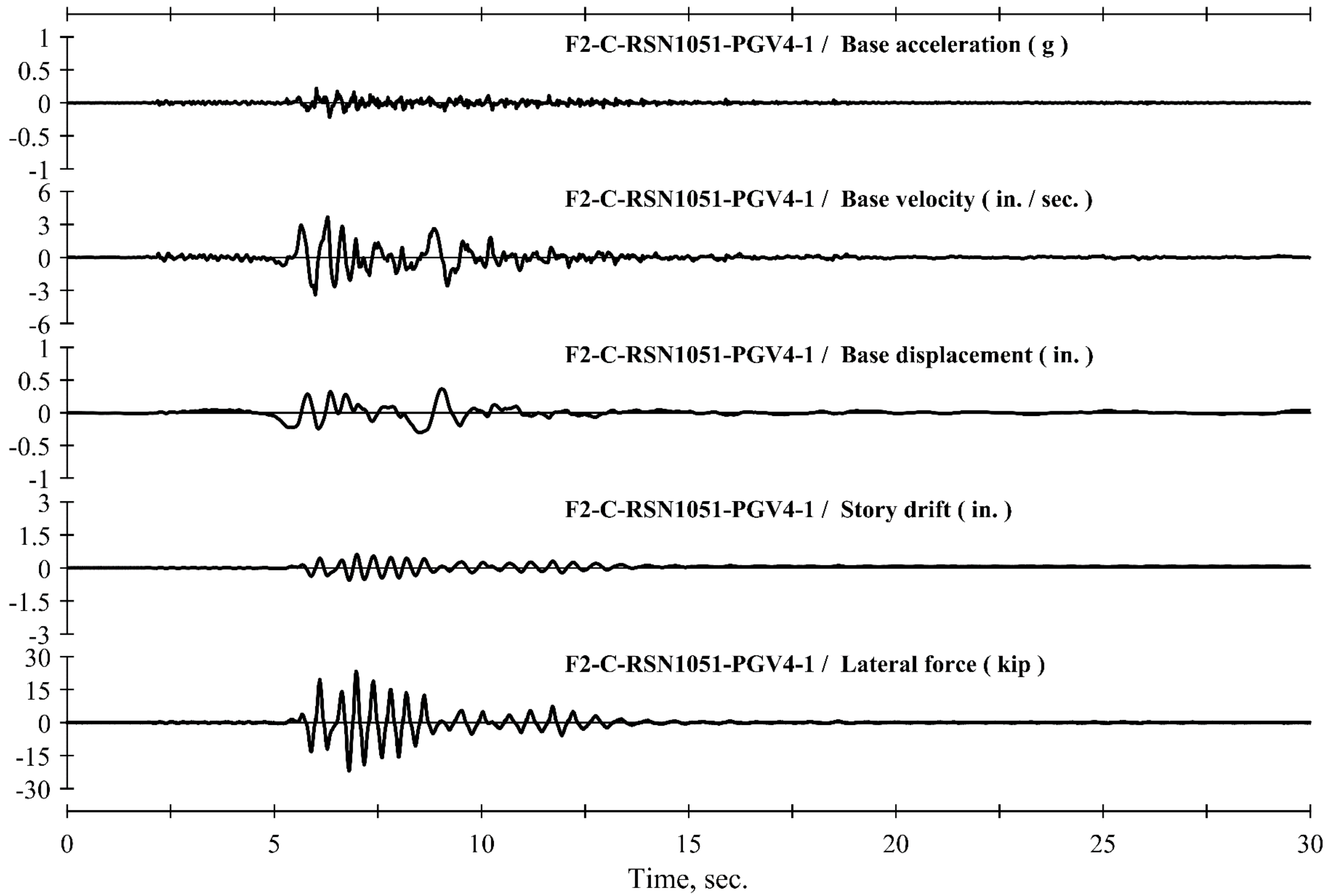

Figure D-98: Base motion and structural response histories in Run 20 of Specimen F2

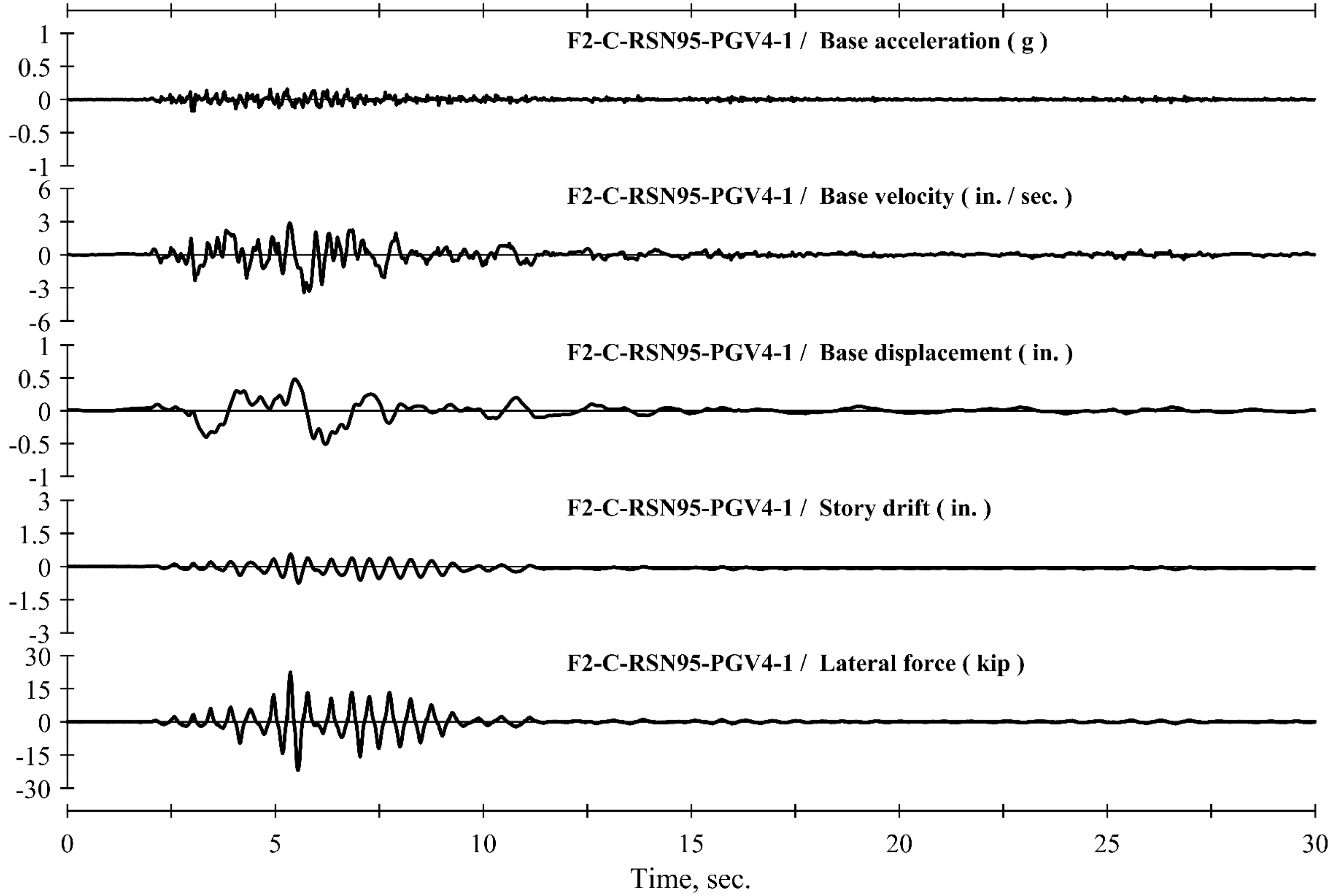

Figure D-99: Base motion and structural response histories in Run 21 of Specimen F2

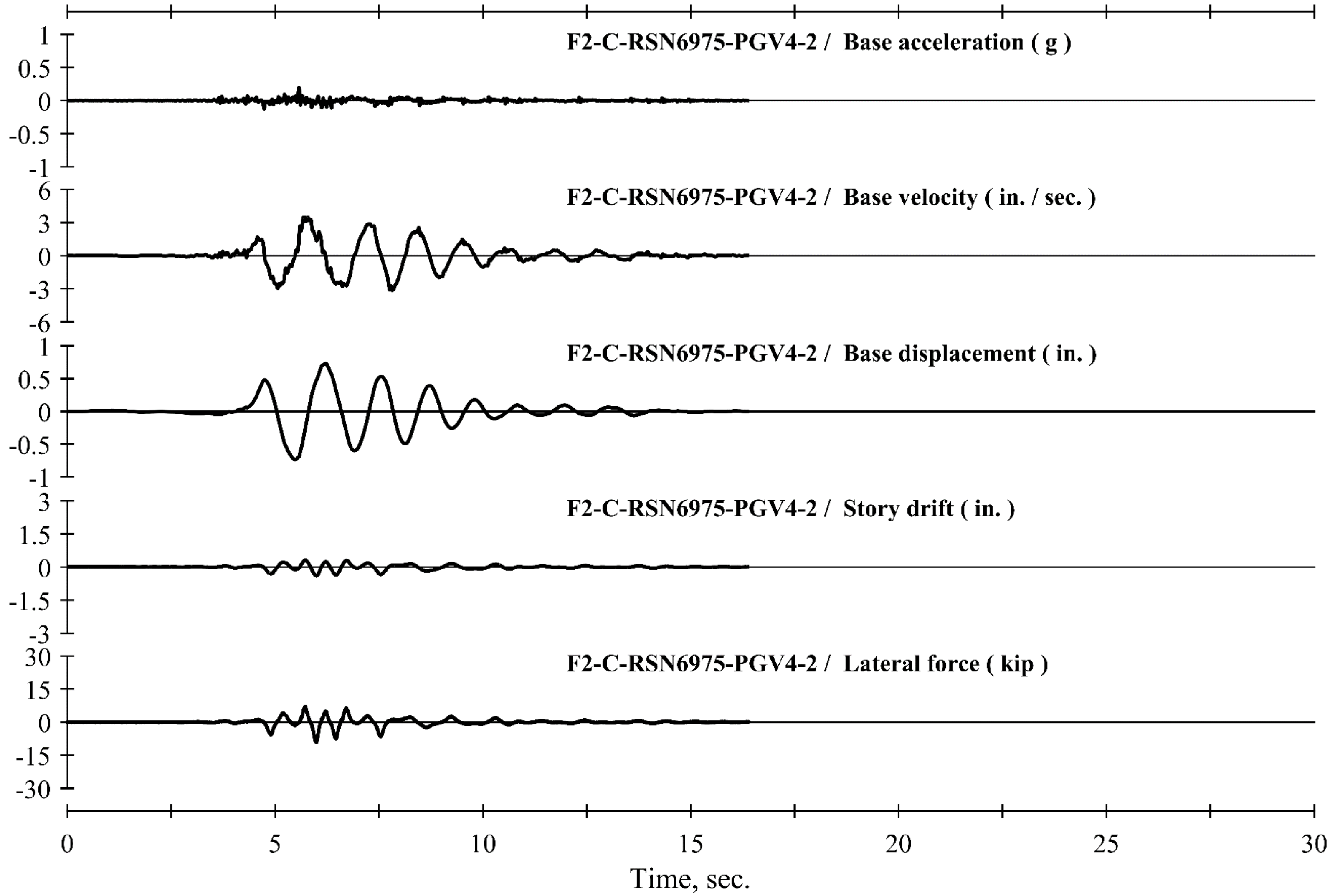

Figure D-100: Base motion and structural response histories in Run 22 of Specimen F2

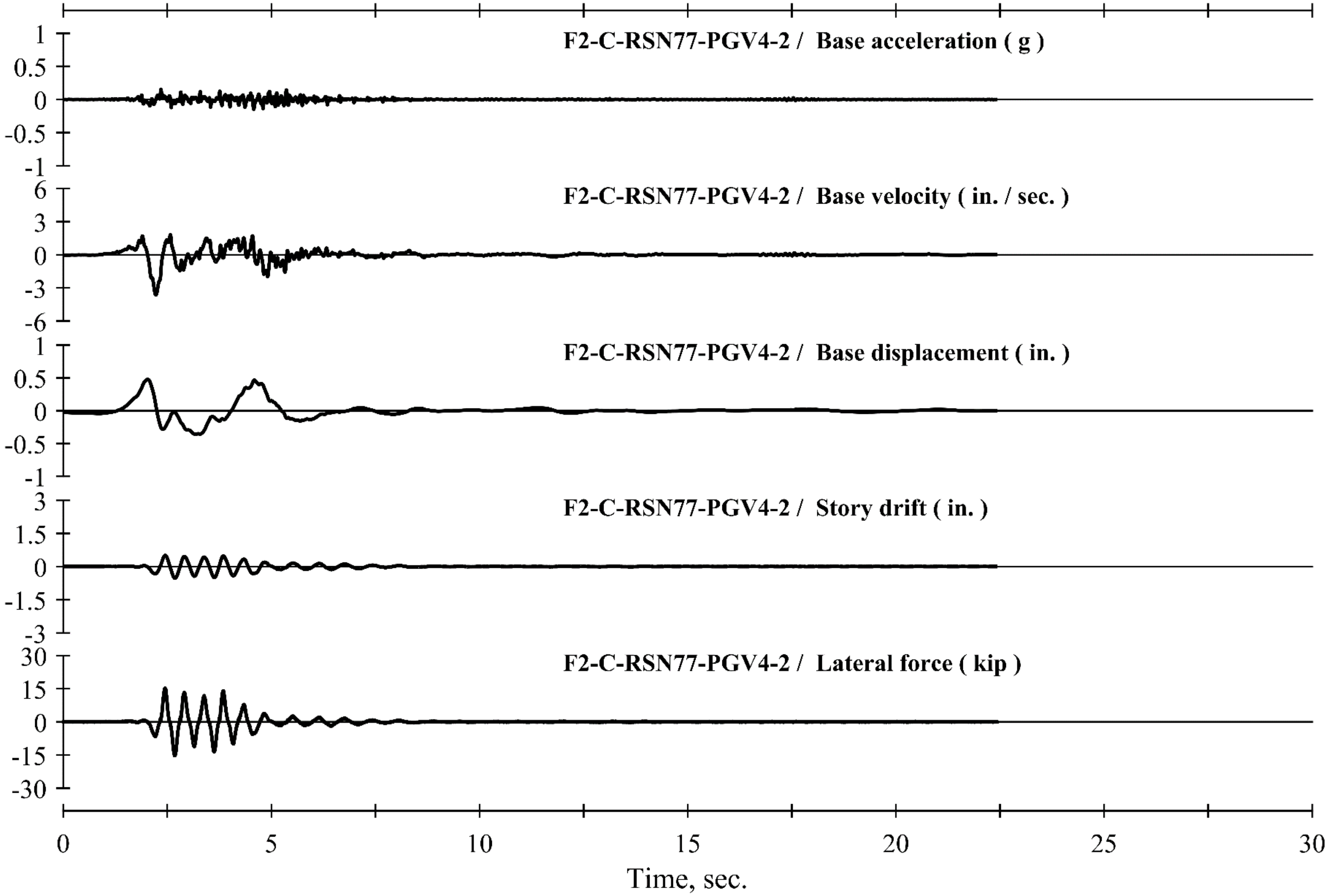

Figure D-101: Base motion and structural response histories in Run 23 of Specimen F2

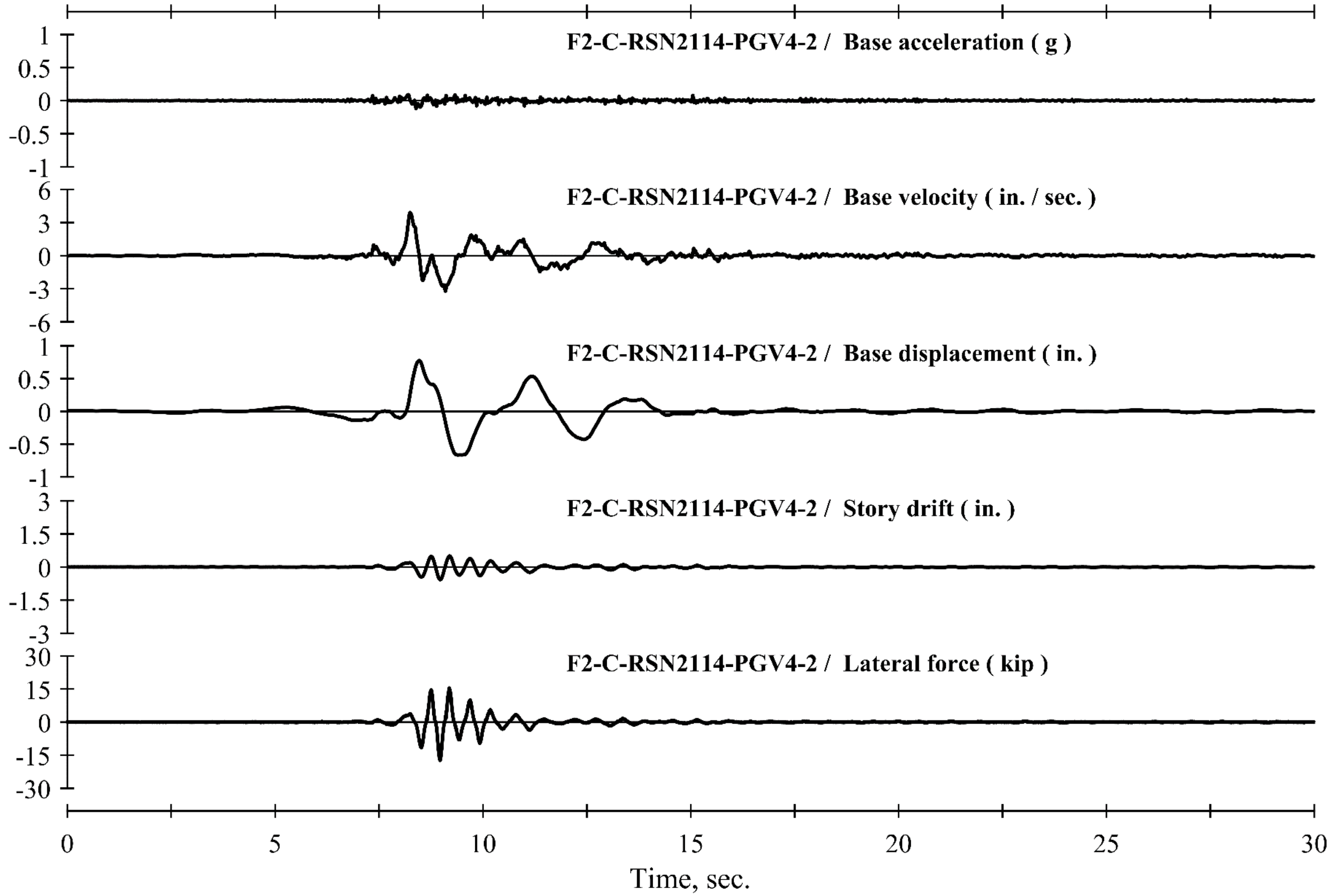

Figure D-102: Base motion and structural response histories in Run 24 of Specimen F2

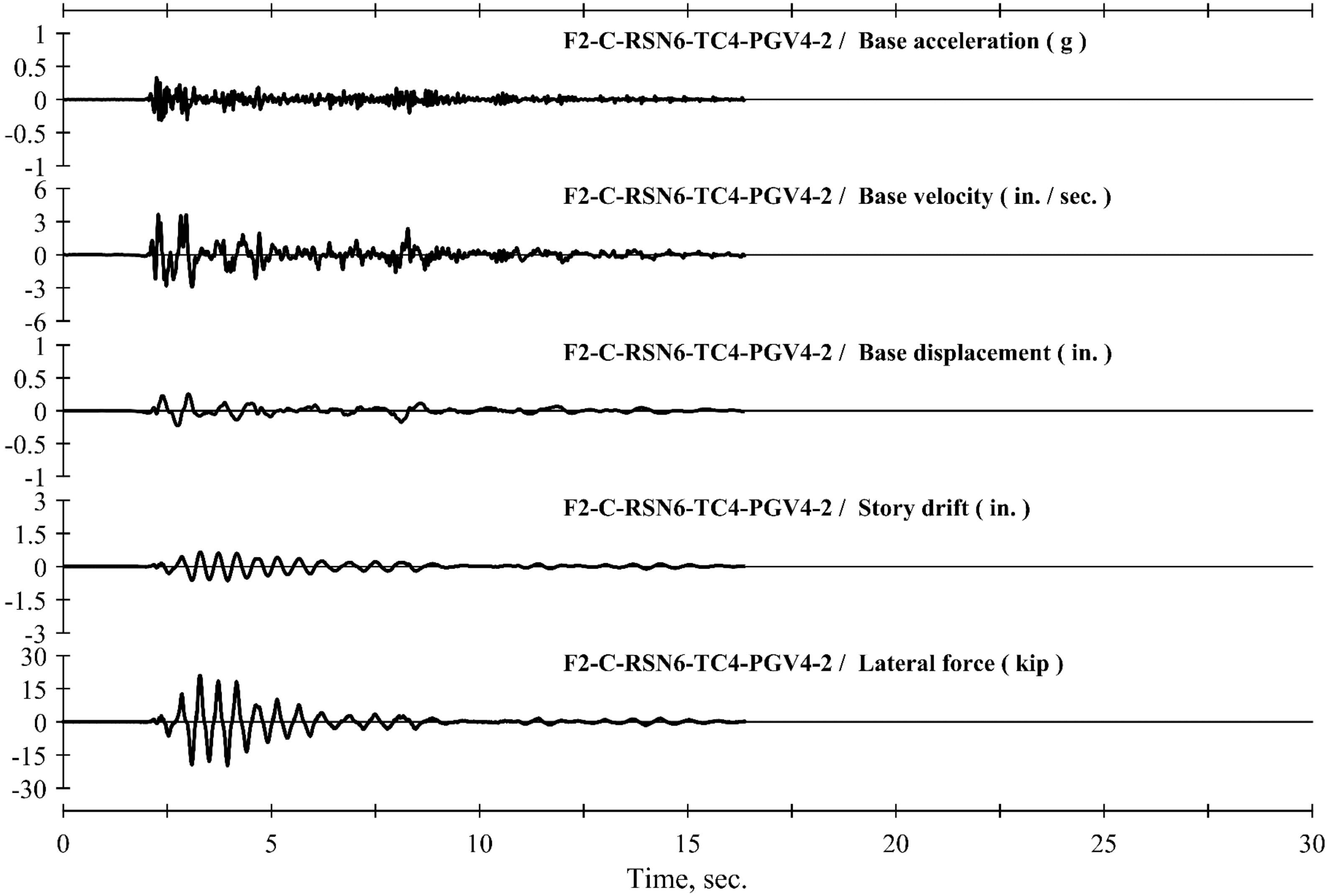

Figure D-103: Base motion and structural response histories in Run 25 of Specimen F2

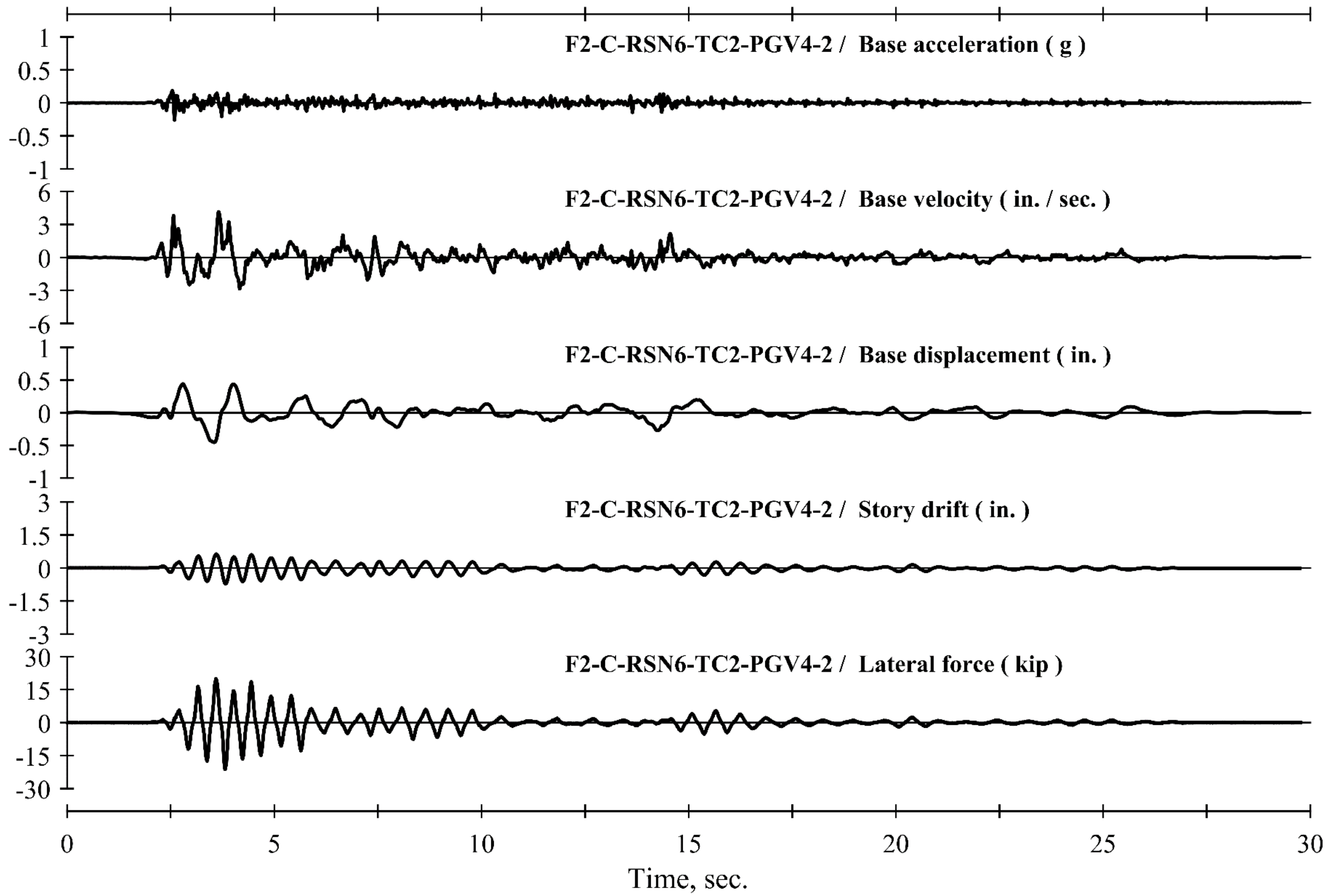

Figure D-104: Base motion and structural response histories in Run 26 of Specimen F2

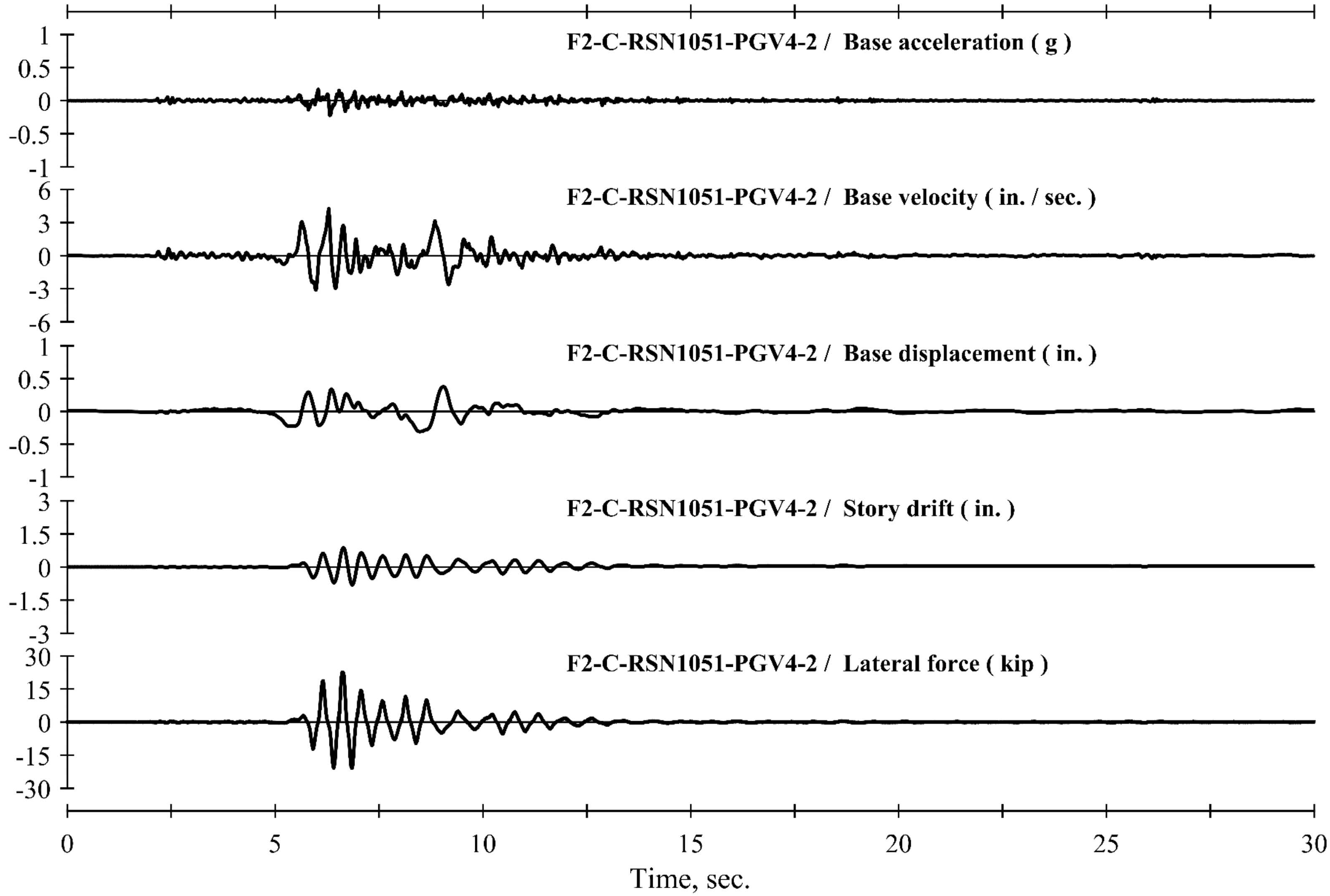

Figure D-105: Base motion and structural response histories in Run 27 of Specimen F2

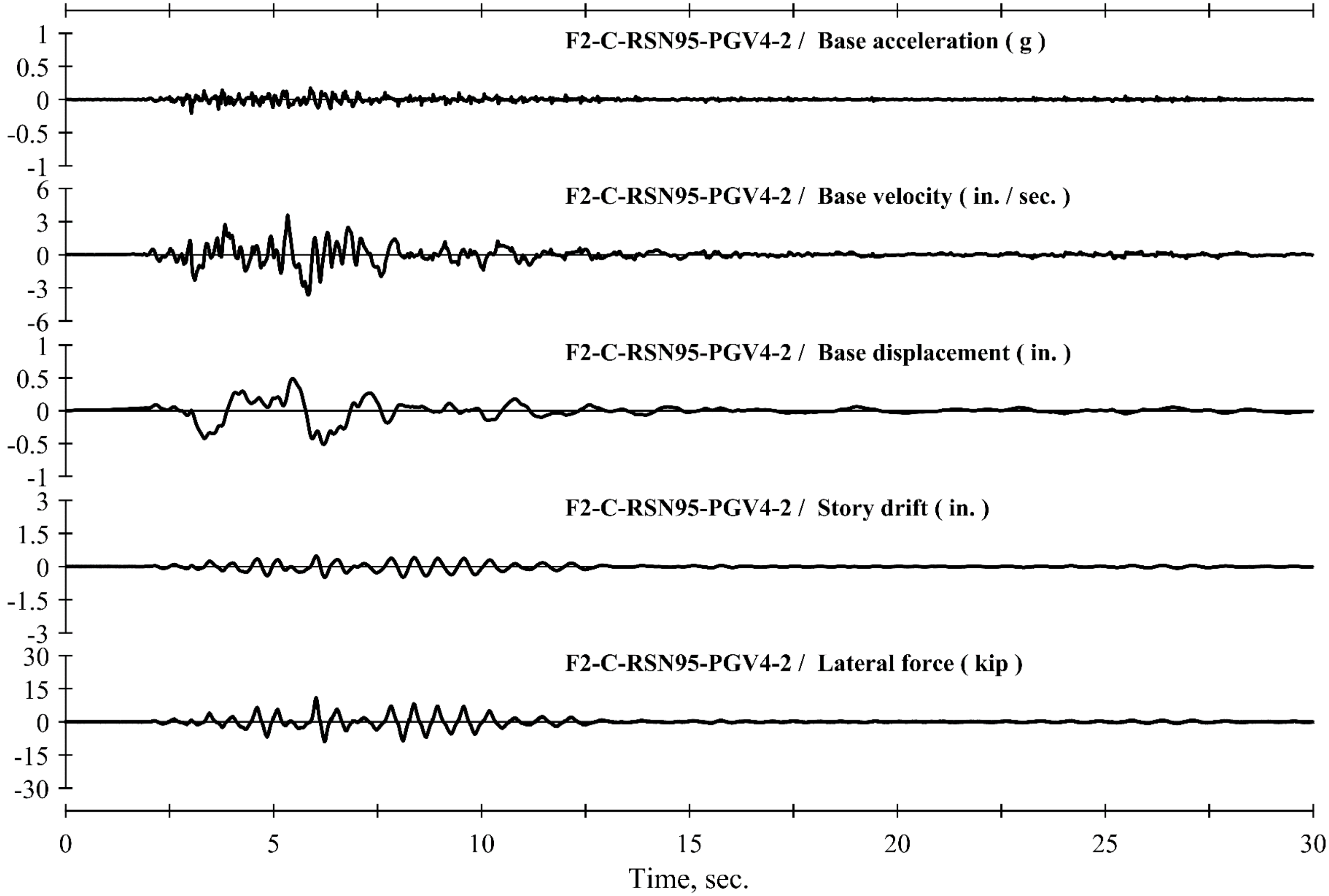

Figure D-106: Base motion and structural response histories in Run 28 of Specimen F2

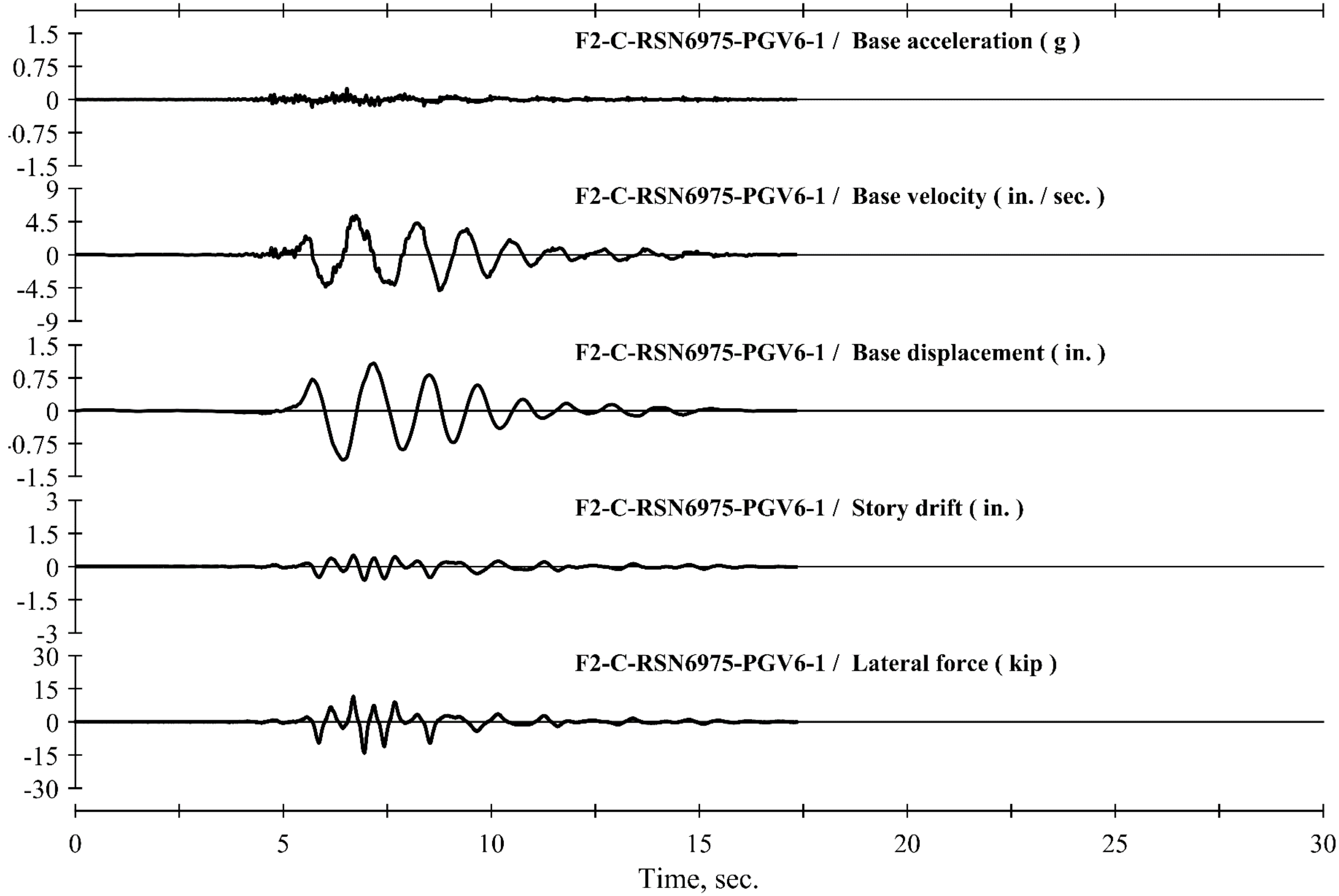

Figure D-107: Base motion and structural response histories in Run 29 of Specimen F2

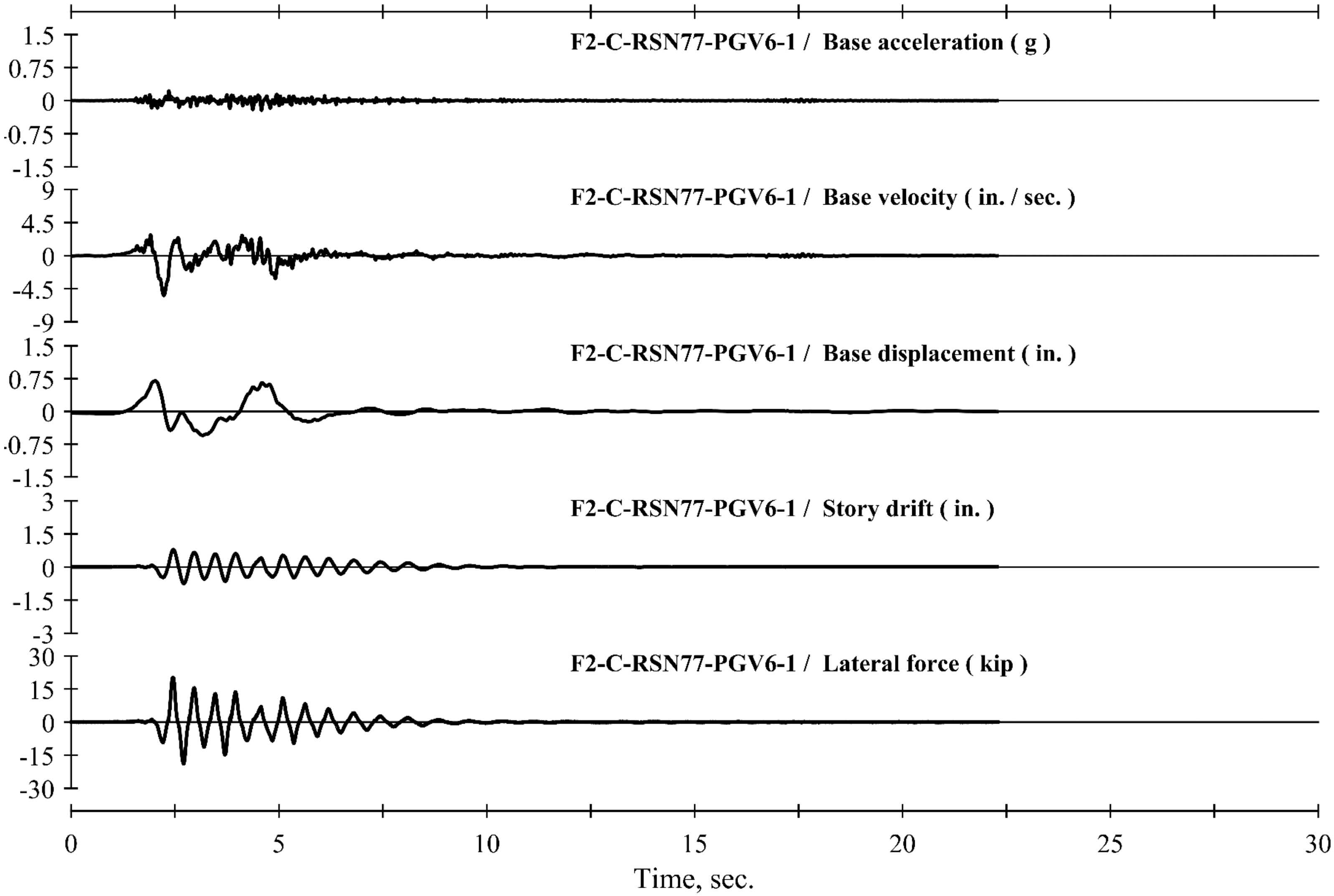

Figure D-108: Base motion and structural response histories in Run 30 of Specimen F2

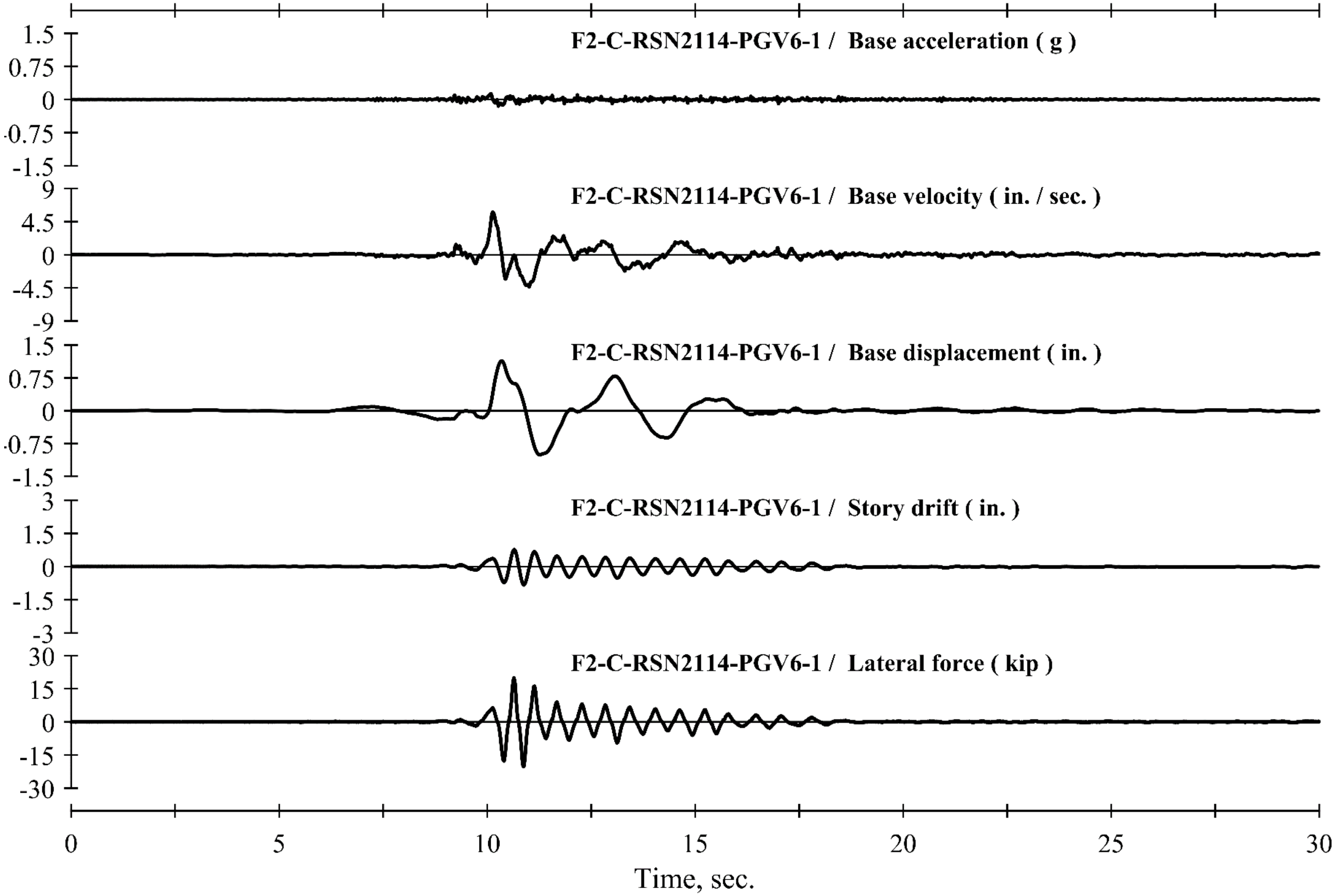

Figure D-109: Base motion and structural response histories in Run 31 of Specimen F2

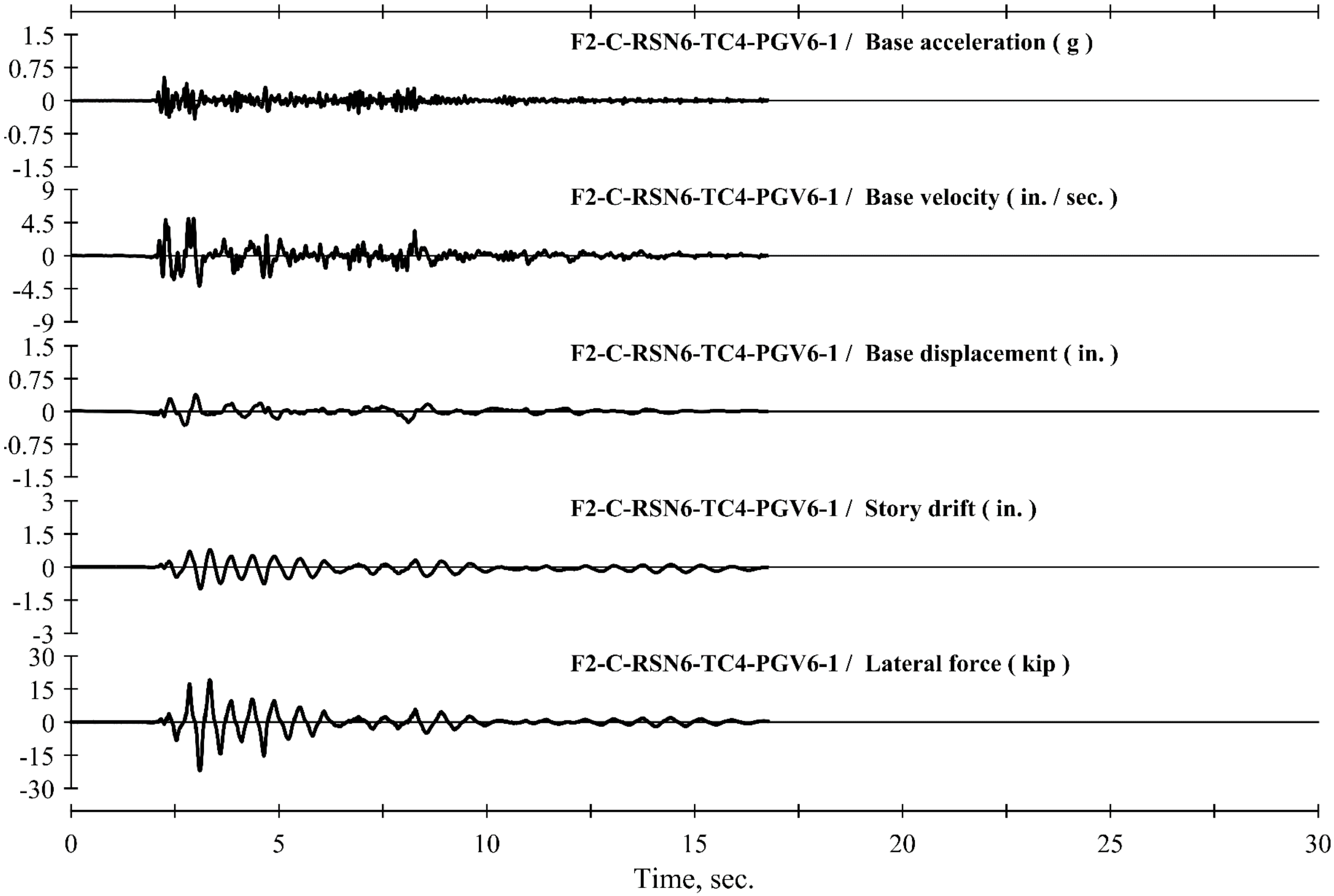

Figure D-110: Base motion and structural response histories in Run 32 of Specimen F2

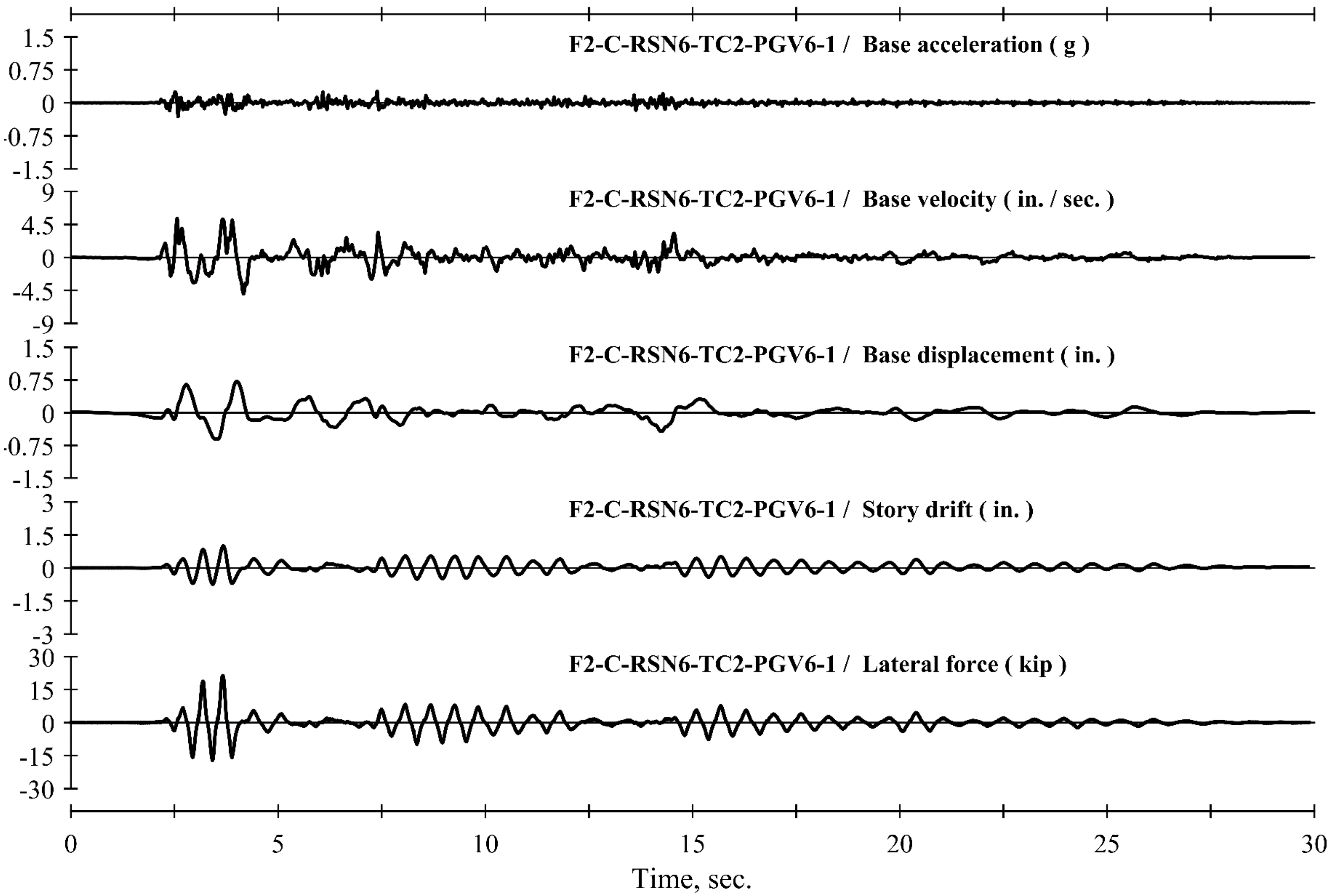

Figure D-111: Base motion and structural response histories in Run 33 of Specimen F2

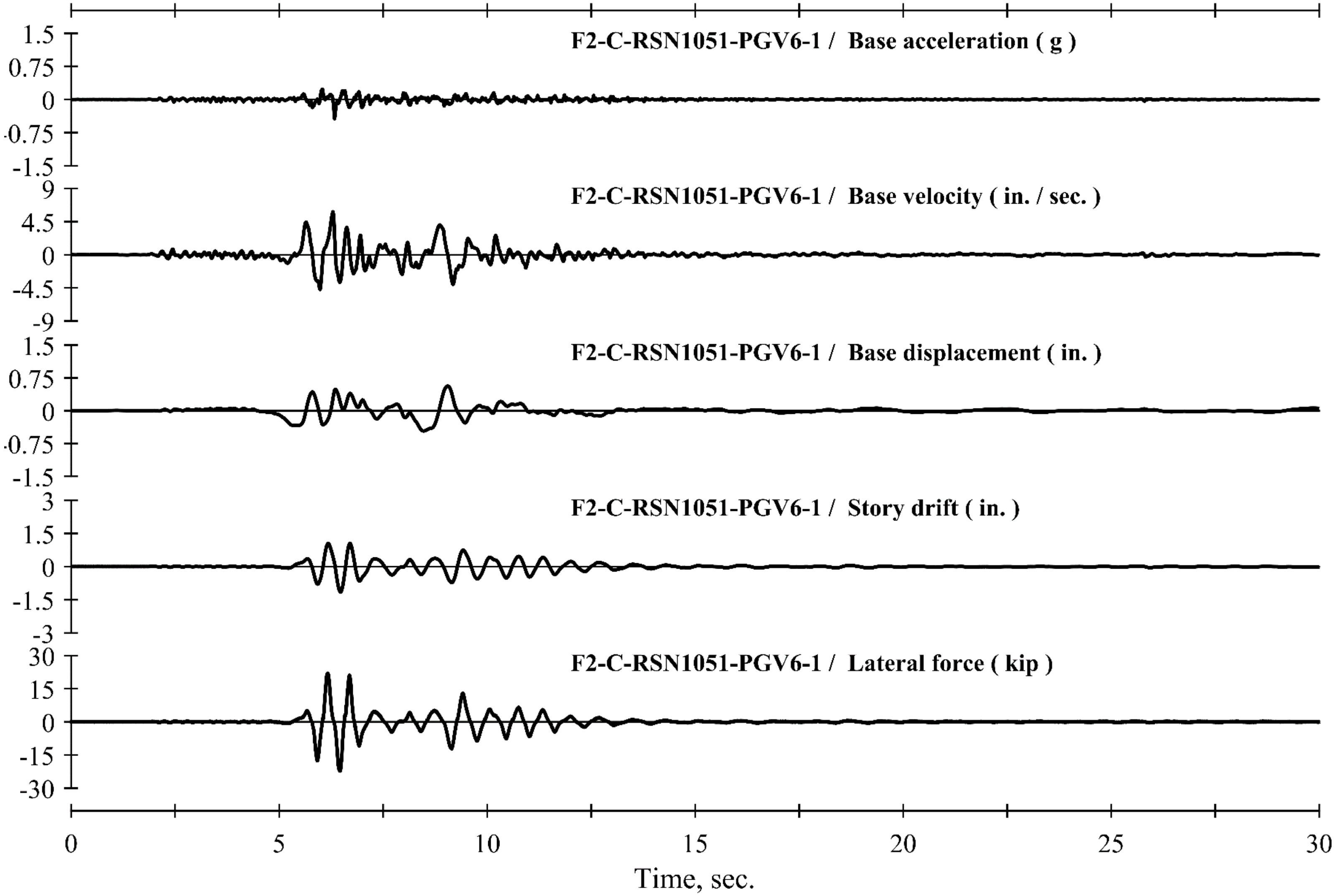

Figure D-112: Base motion and structural response histories in Run 34 of Specimen F2

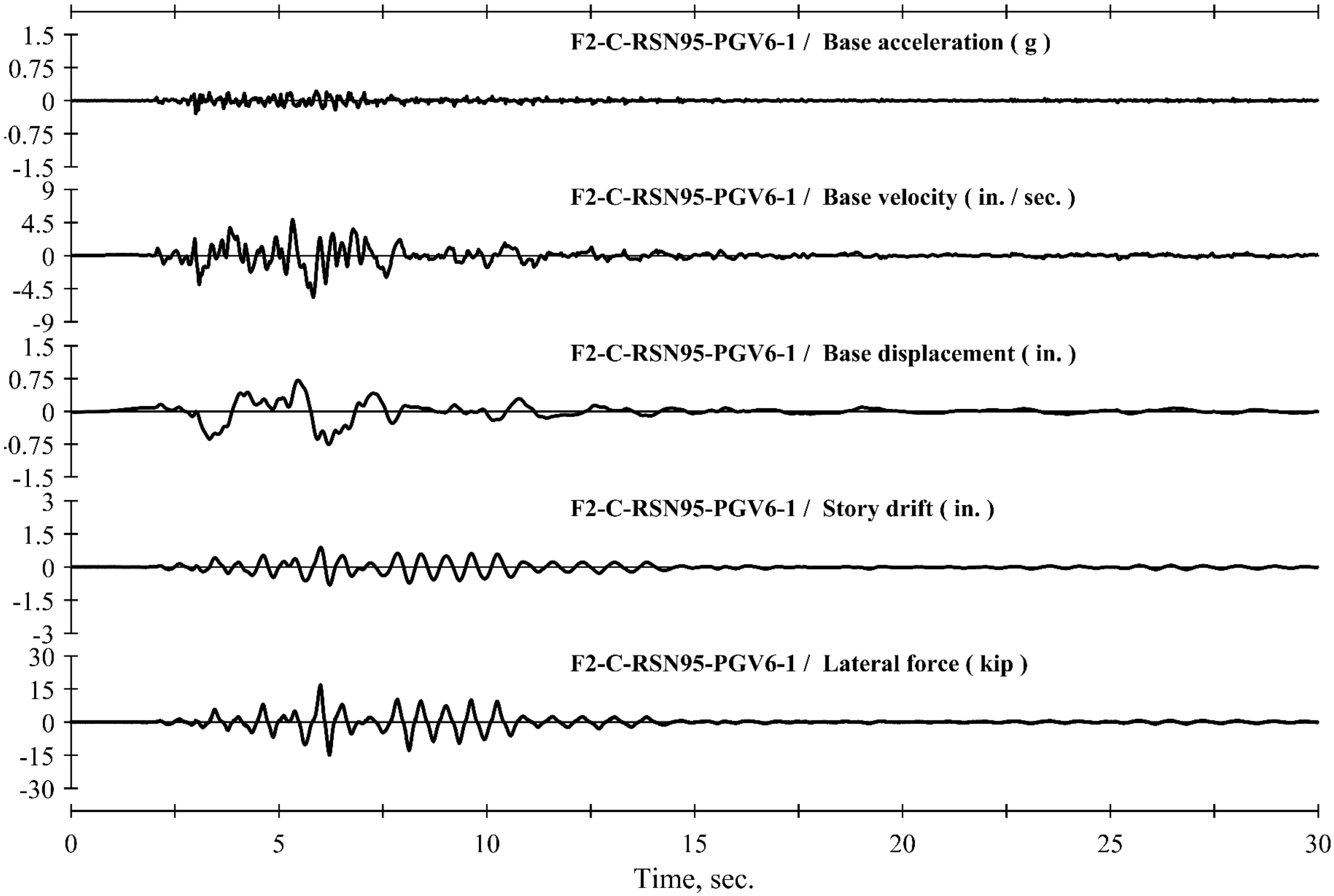

Figure D-113: Base motion and structural response histories in Run 35 of Specimen F2

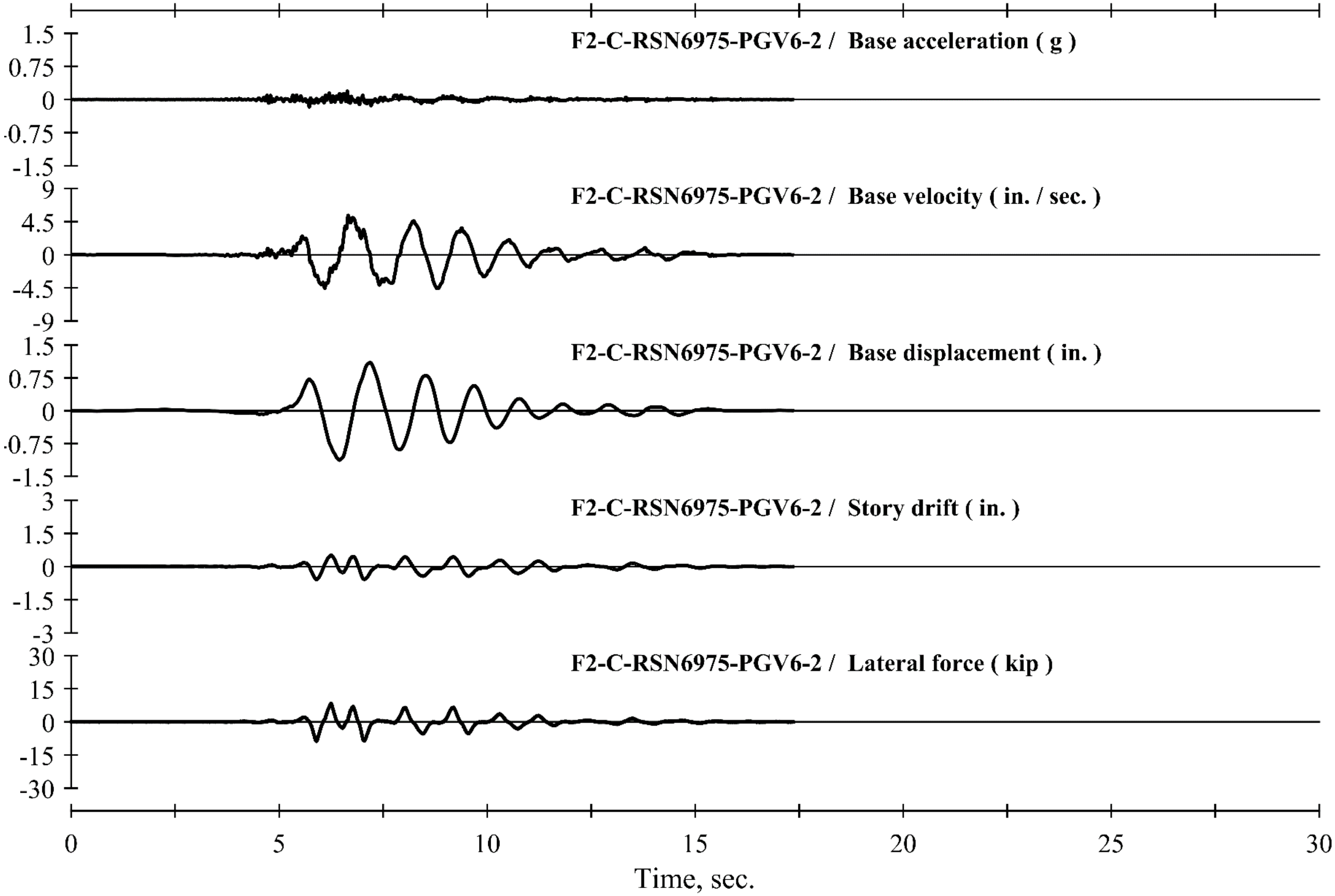

Figure D-114: Base motion and structural response histories in Run 36 of Specimen F2

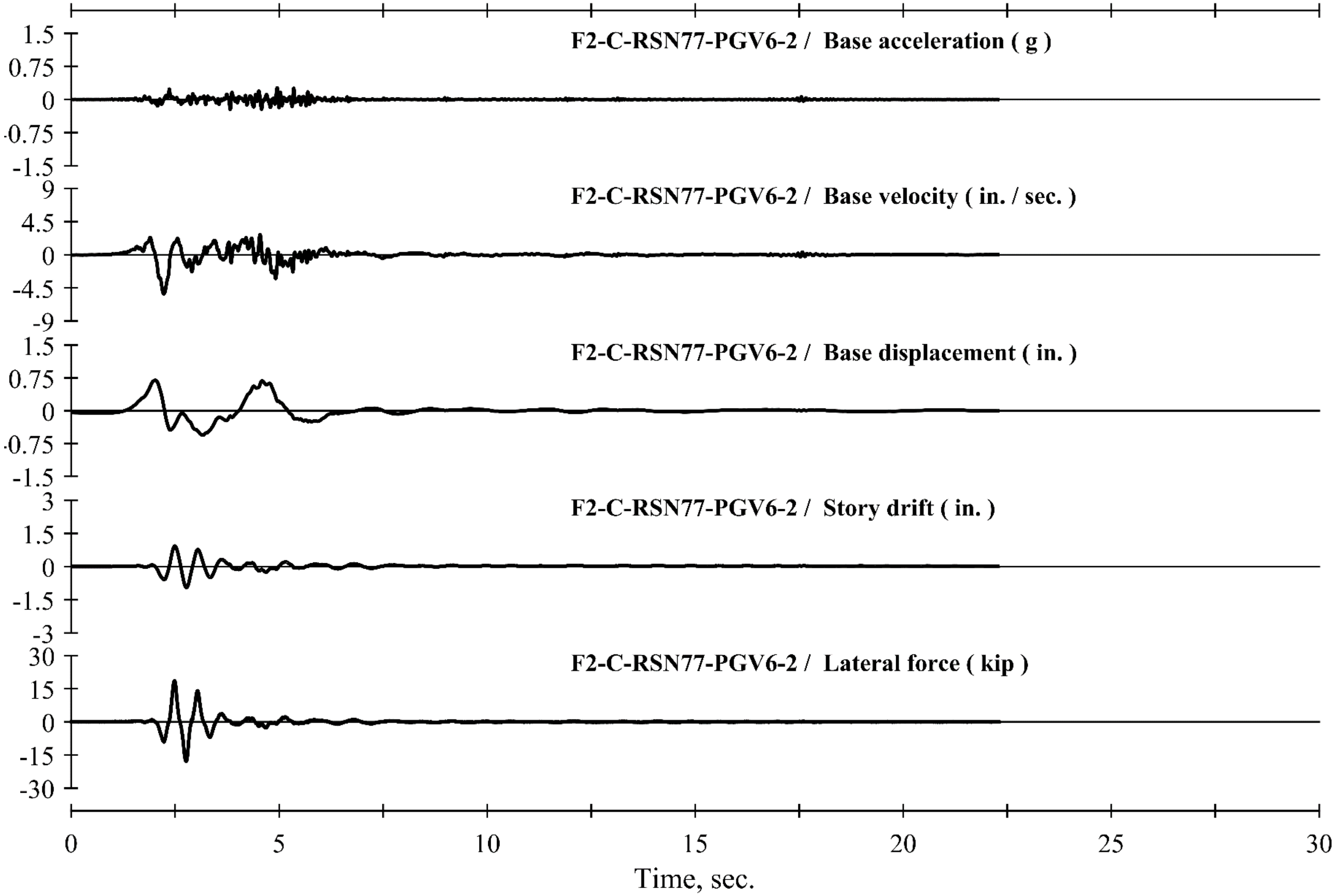

Figure D-115: Base motion and structural response histories in Run 37 of Specimen F2

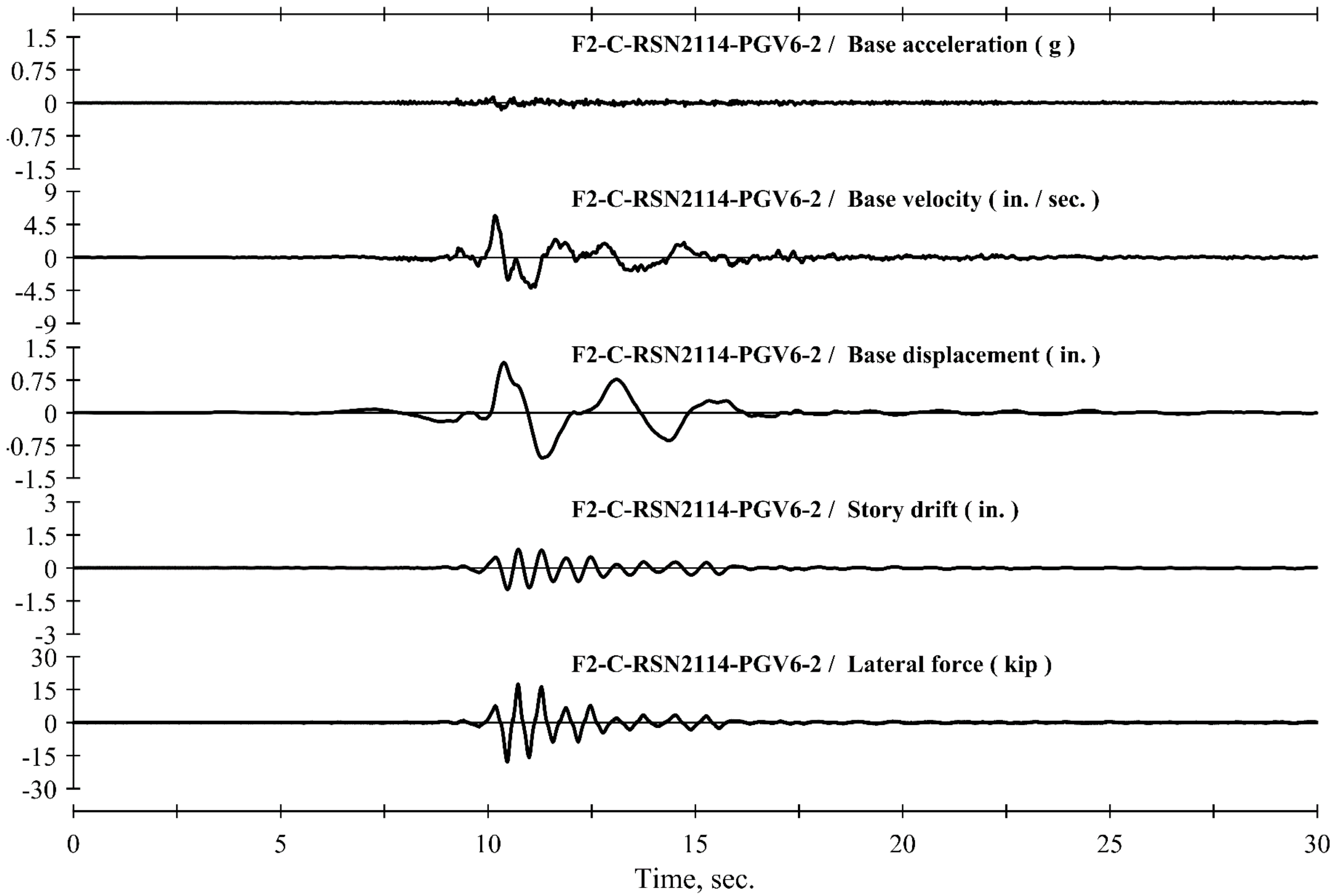

Figure D-116: Base motion and structural response histories in Run 38 of Specimen F2

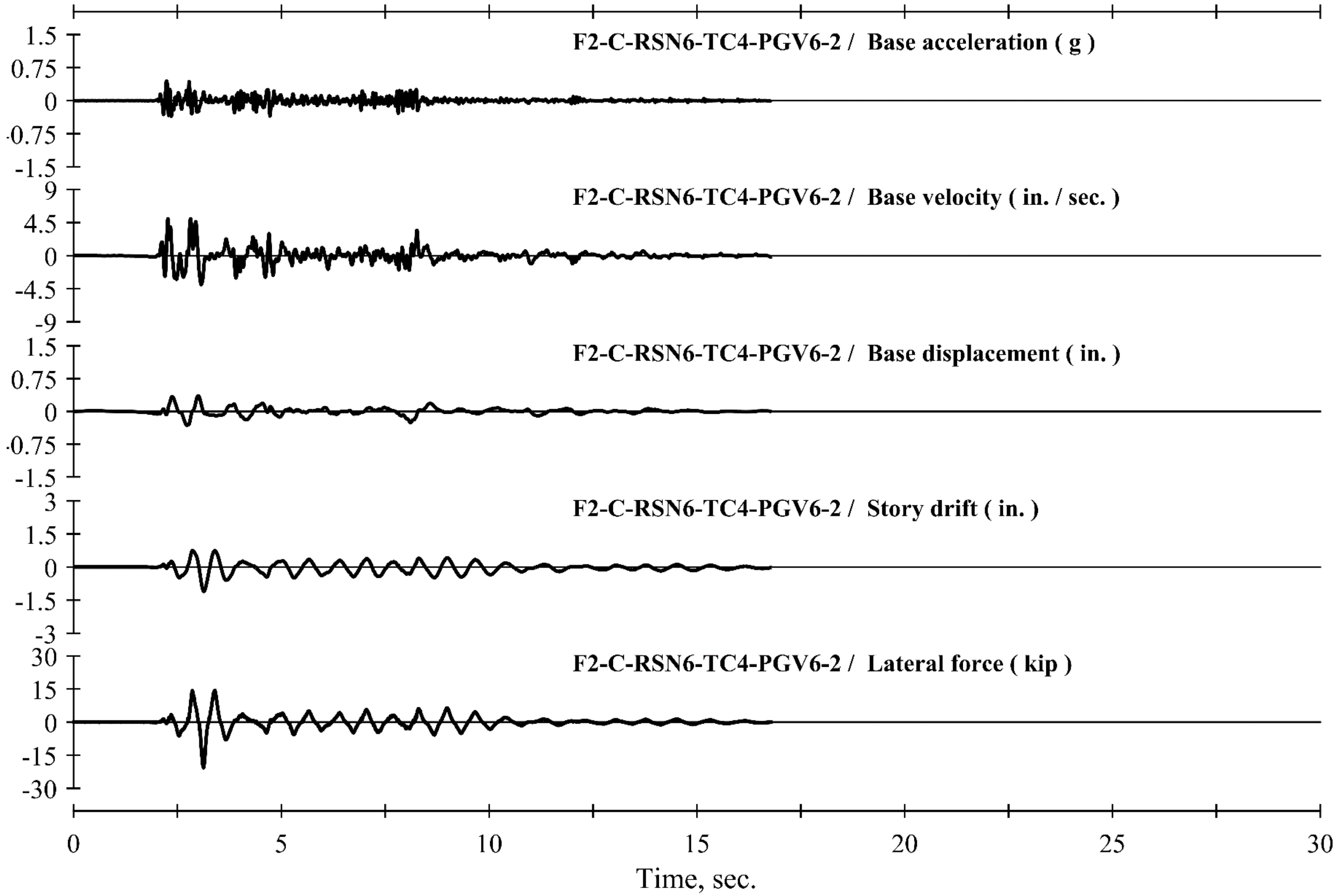

Figure D-117: Base motion and structural response histories in Run 39 of Specimen F2

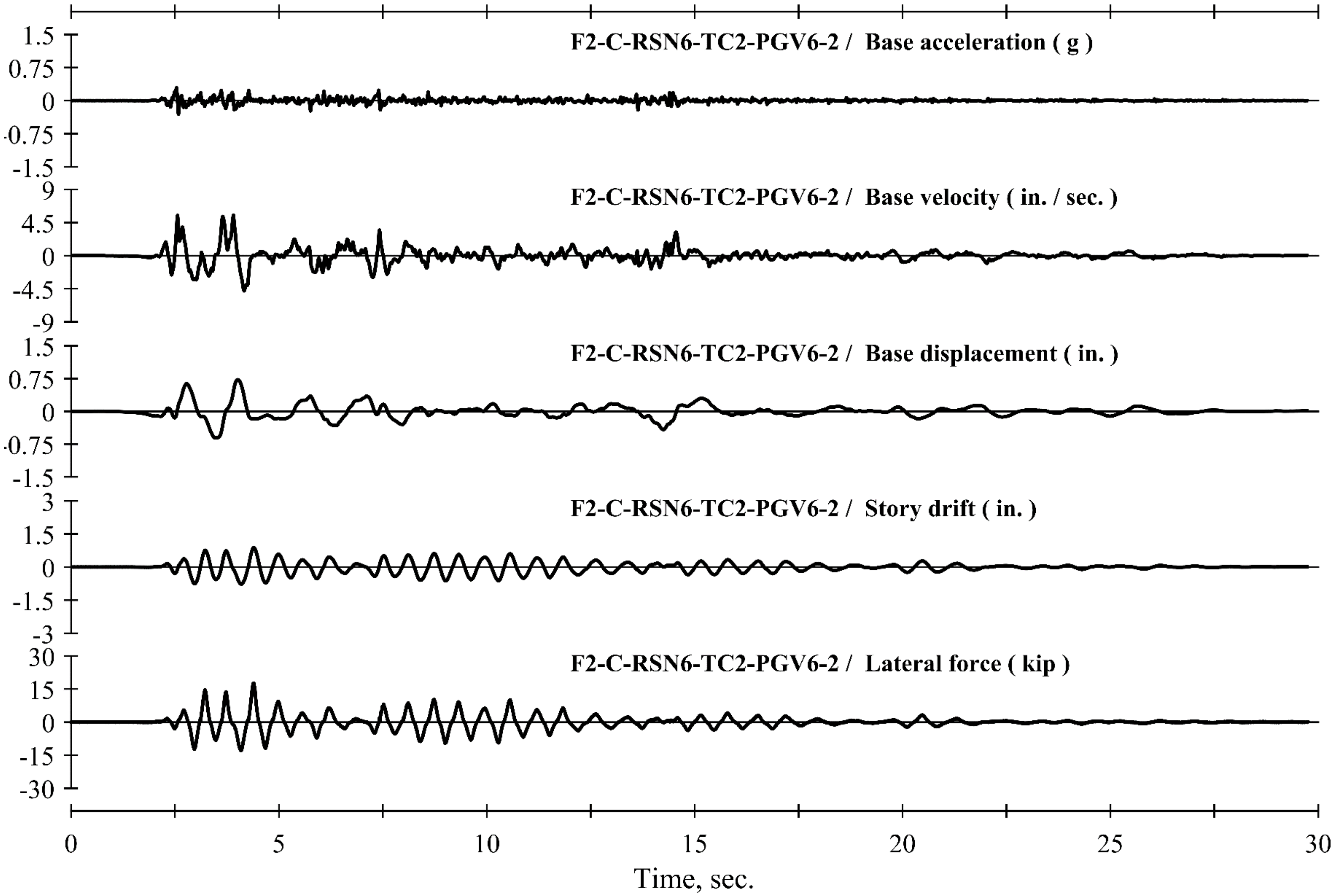

Figure D-118: Base motion and structural response histories in Run 40 of Specimen F2

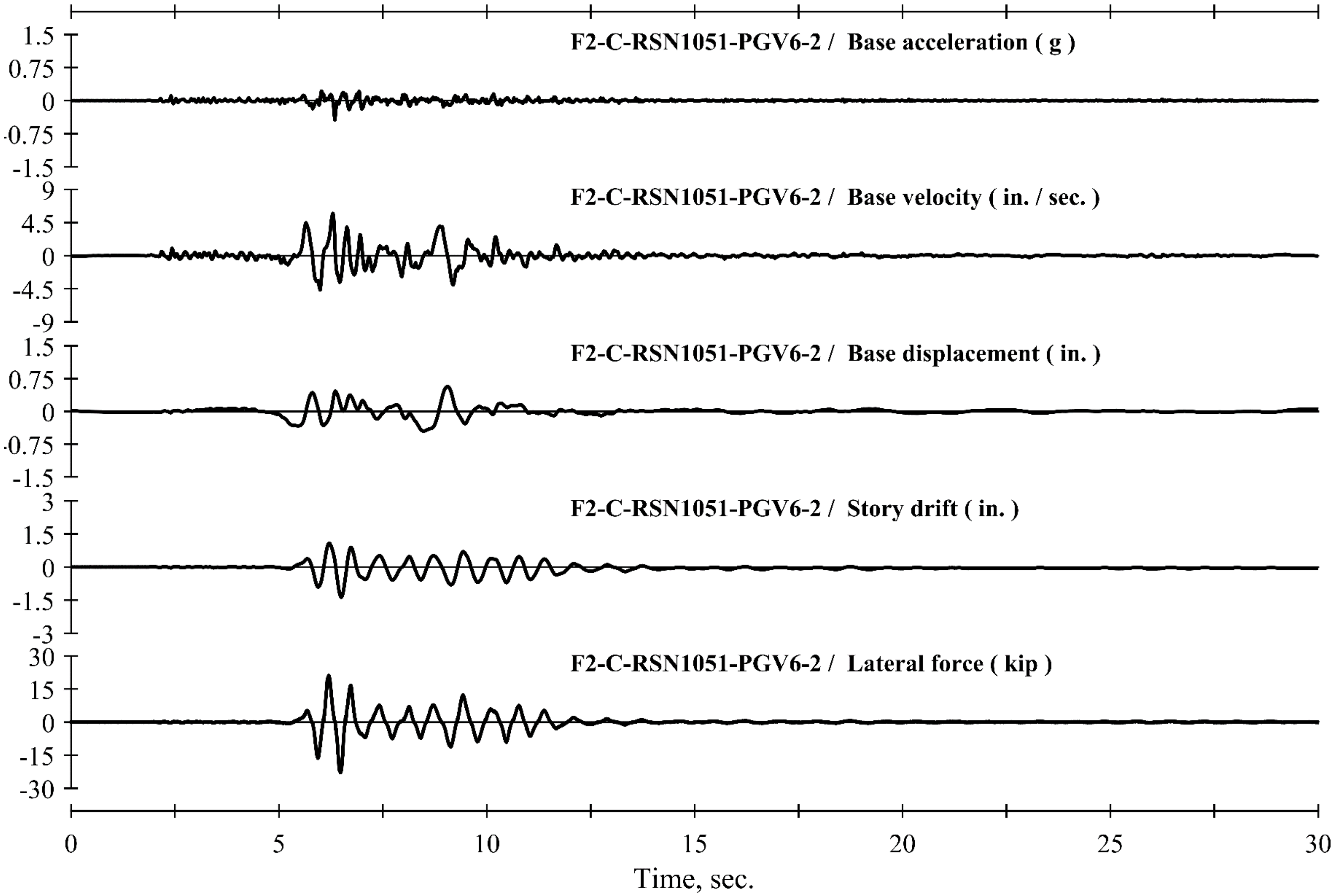

Figure D-119: Base motion and structural response histories in Run 41 of Specimen F2

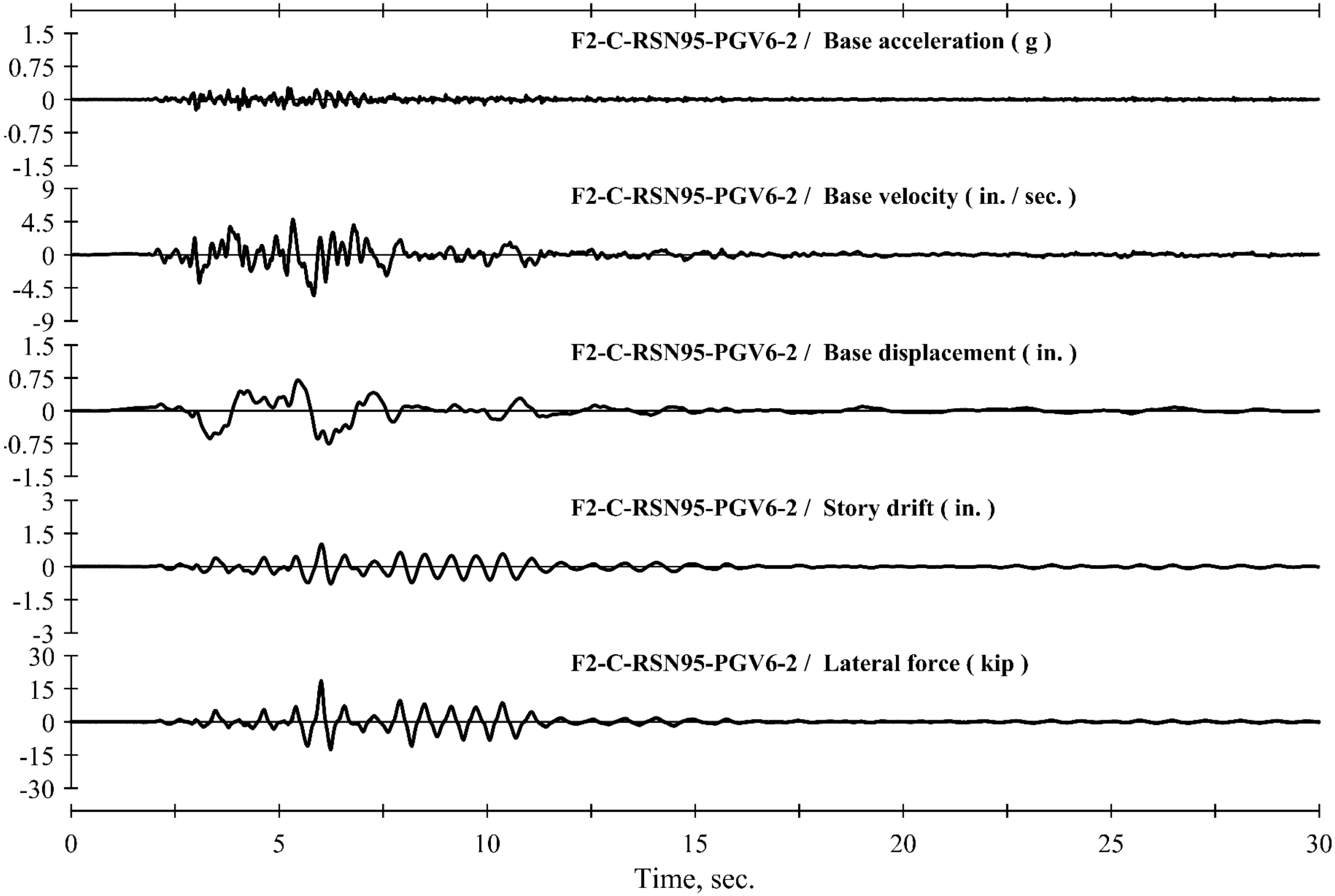

Figure D-120: Base motion and structural response histories in Run 42 of Specimen F2

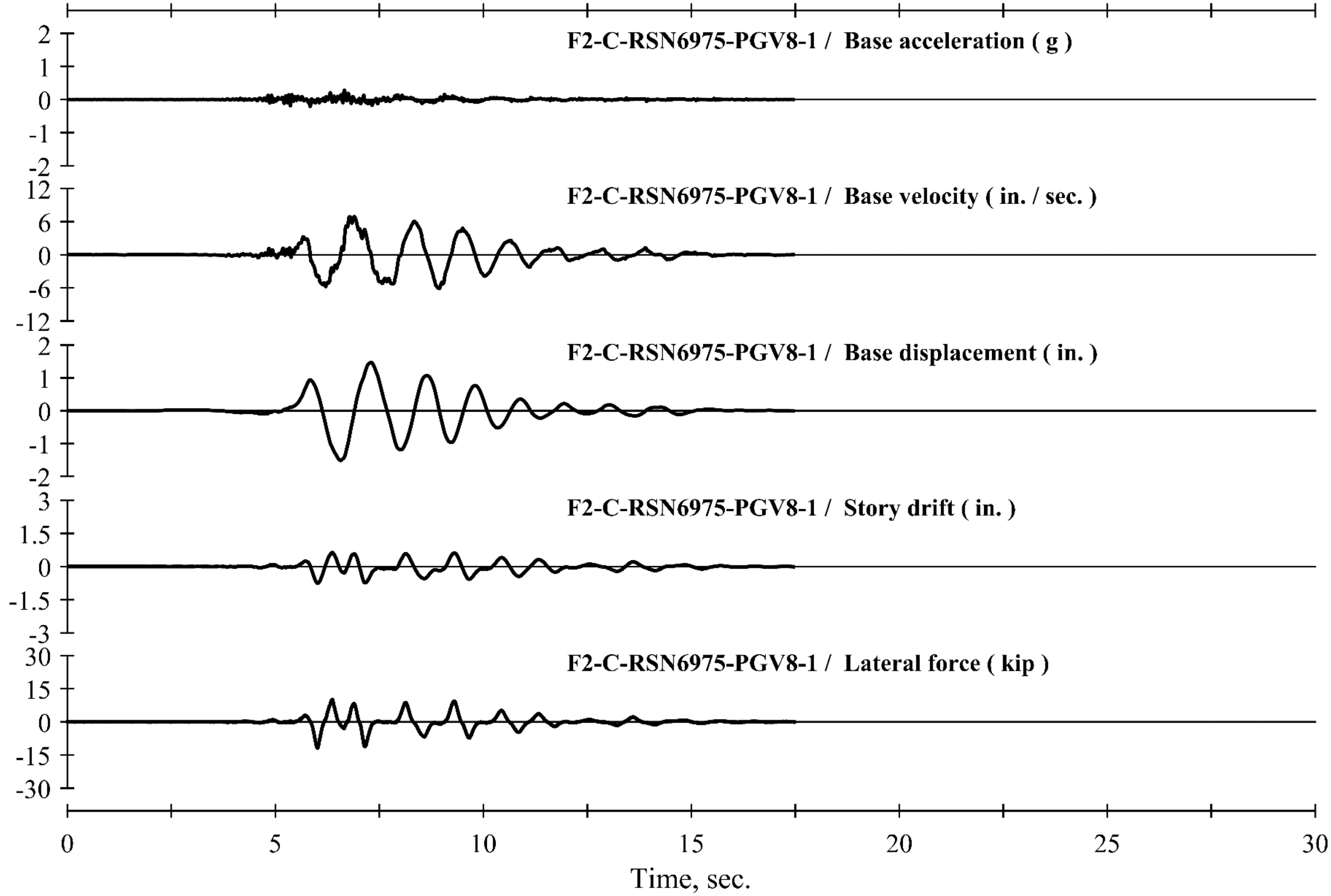

Figure D-121: Base motion and structural response histories in Run 43 of Specimen F2

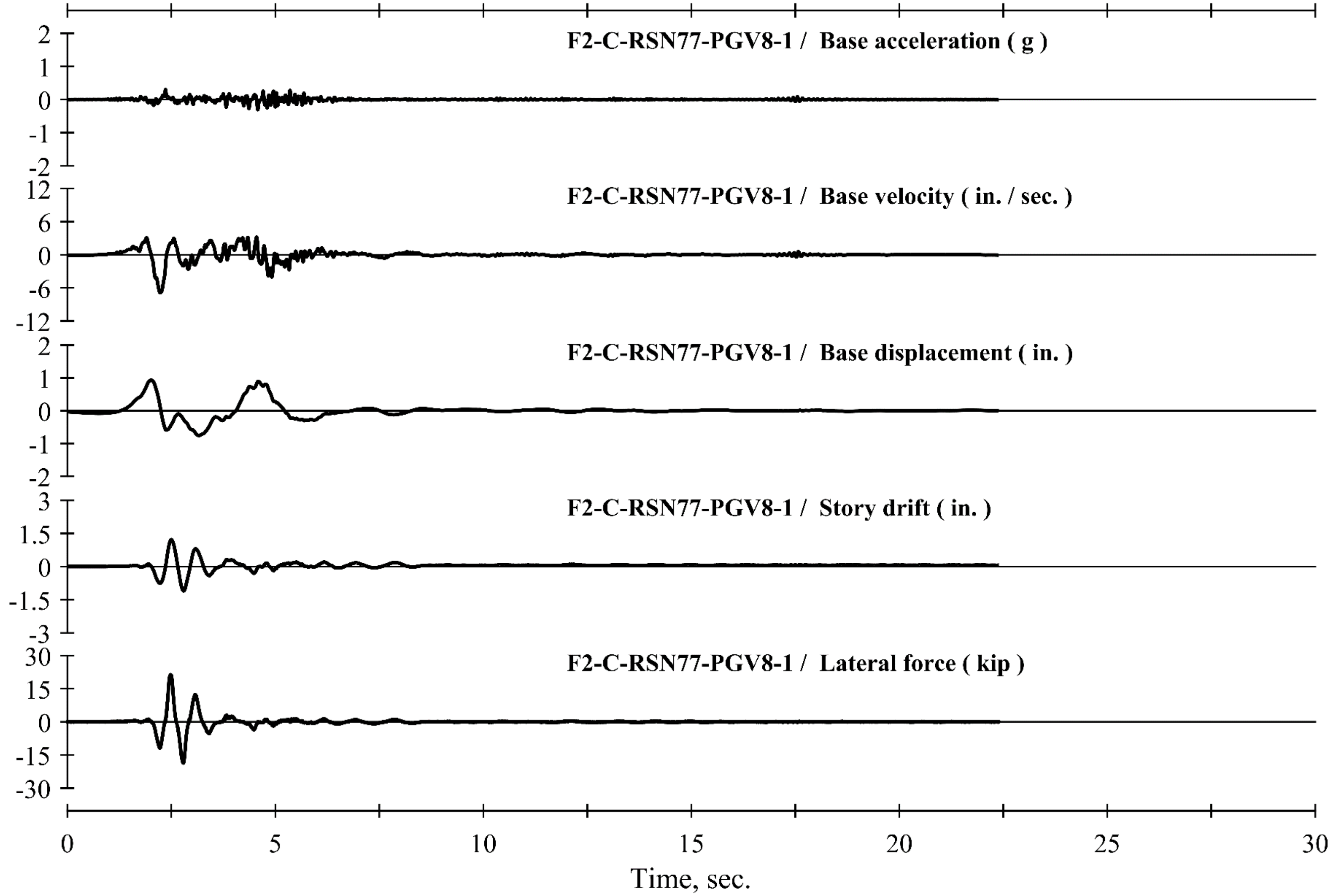

Figure D-122: Base motion and structural response histories in Run 44 of Specimen F2

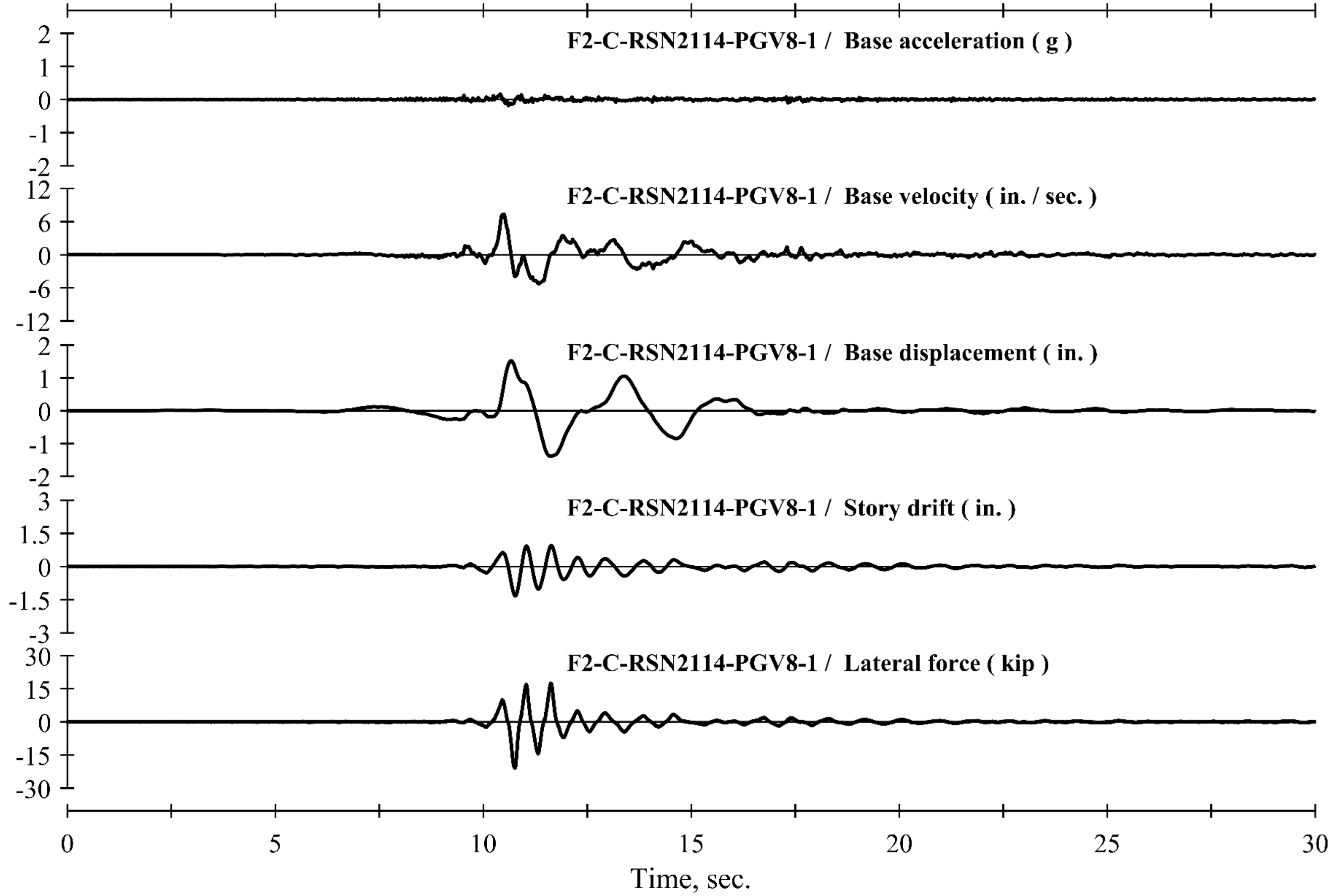

Figure D-123: Base motion and structural response histories in Run 45 of Specimen F2

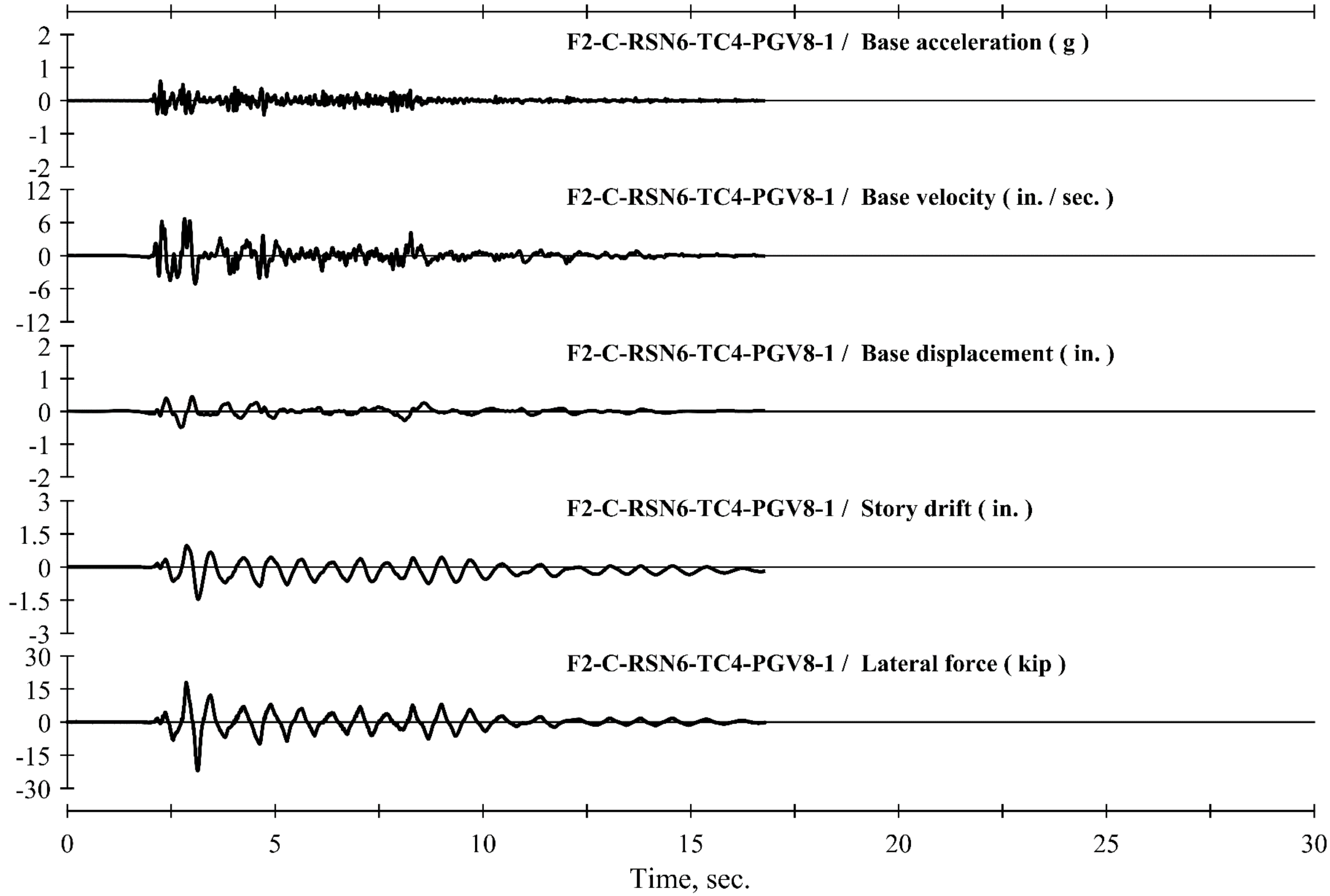

Figure D-124: Base motion and structural response histories in Run 46 of Specimen F2

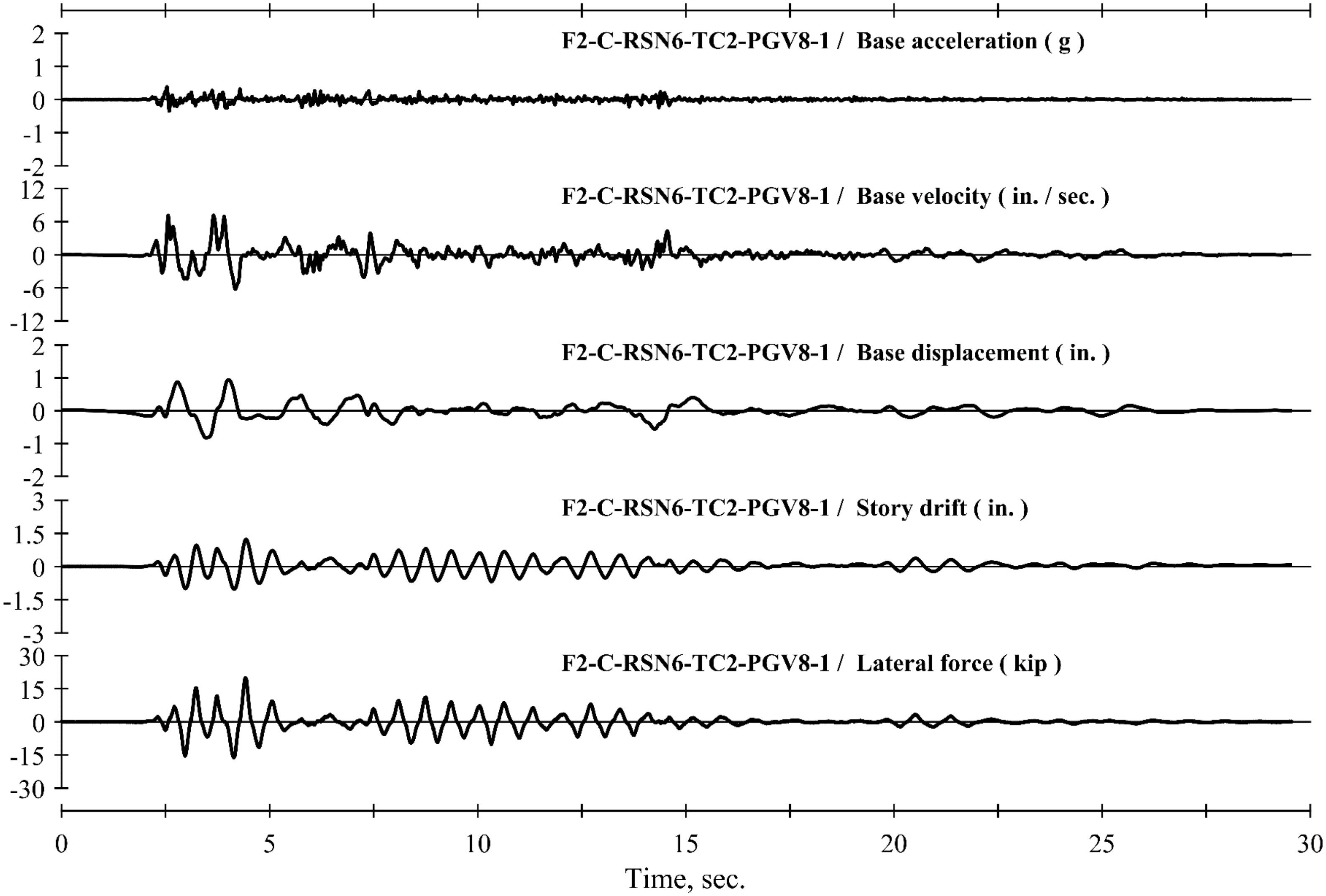

Figure D-125: Base motion and structural response histories in Run 47 of Specimen F2

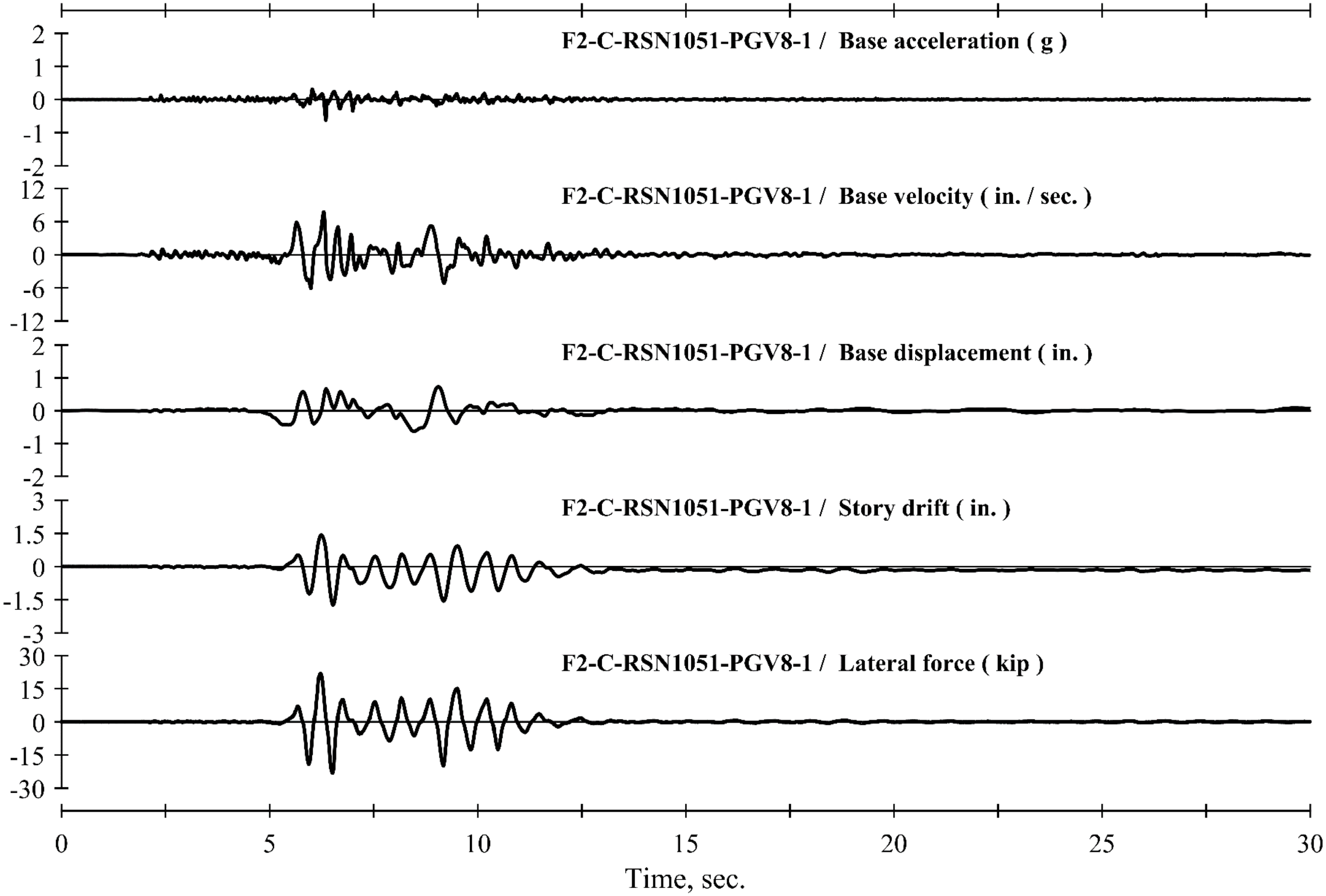

Figure D-126: Base motion and structural response histories in Run 48 of Specimen F2

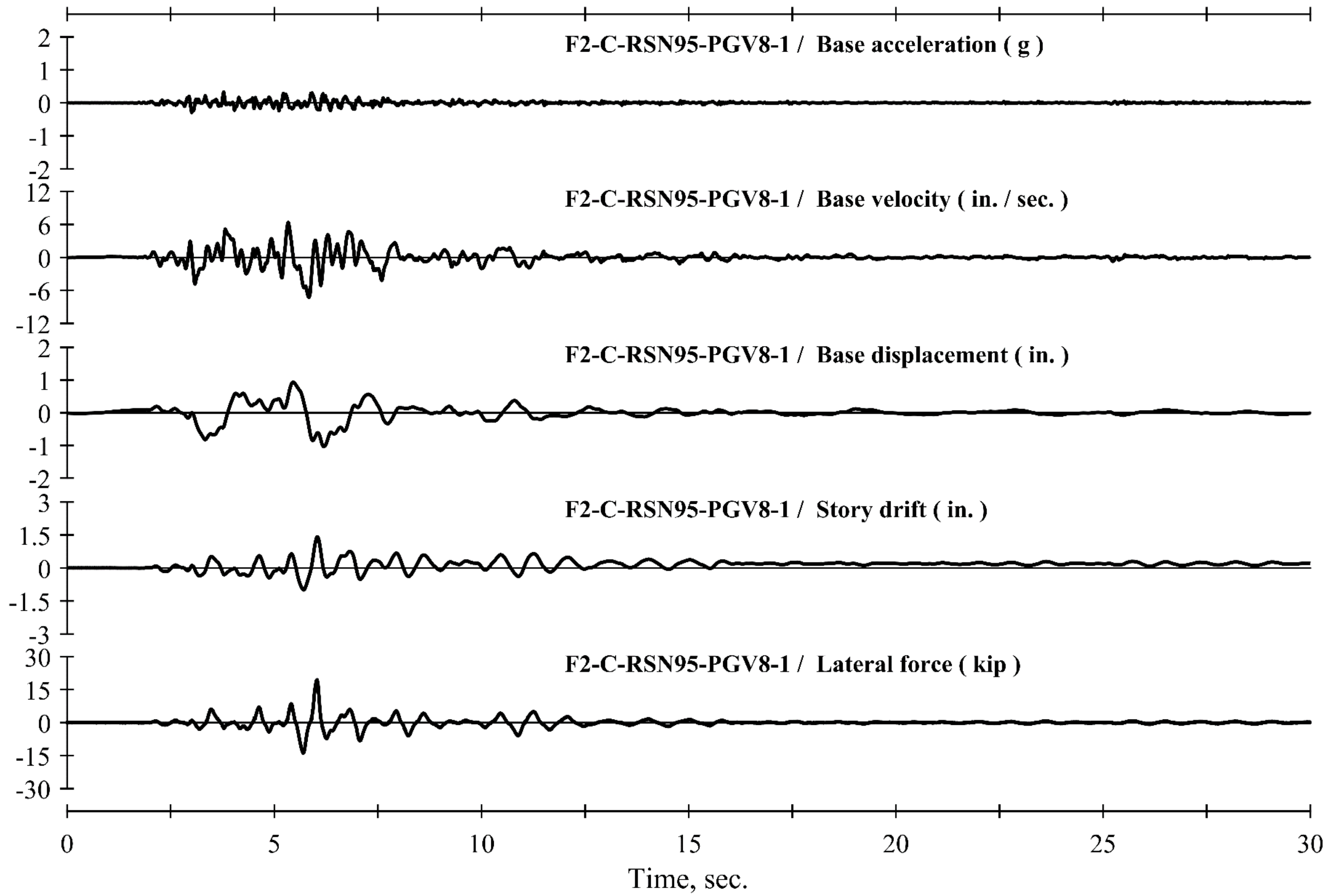

Figure D-127: Base motion and structural response histories in Run 49 of Specimen F2

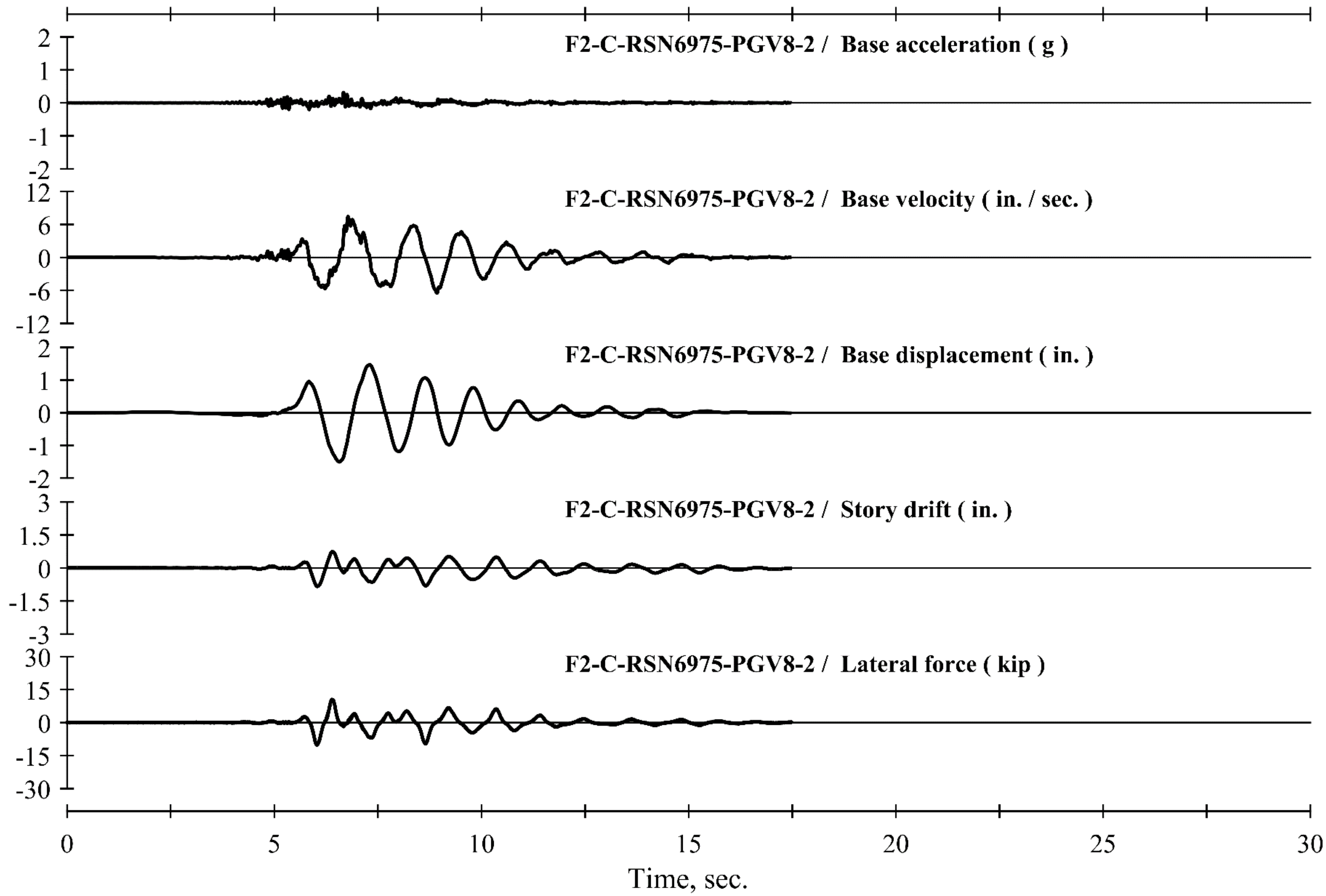

Figure D-128: Base motion and structural response histories in Run 50 of Specimen F2

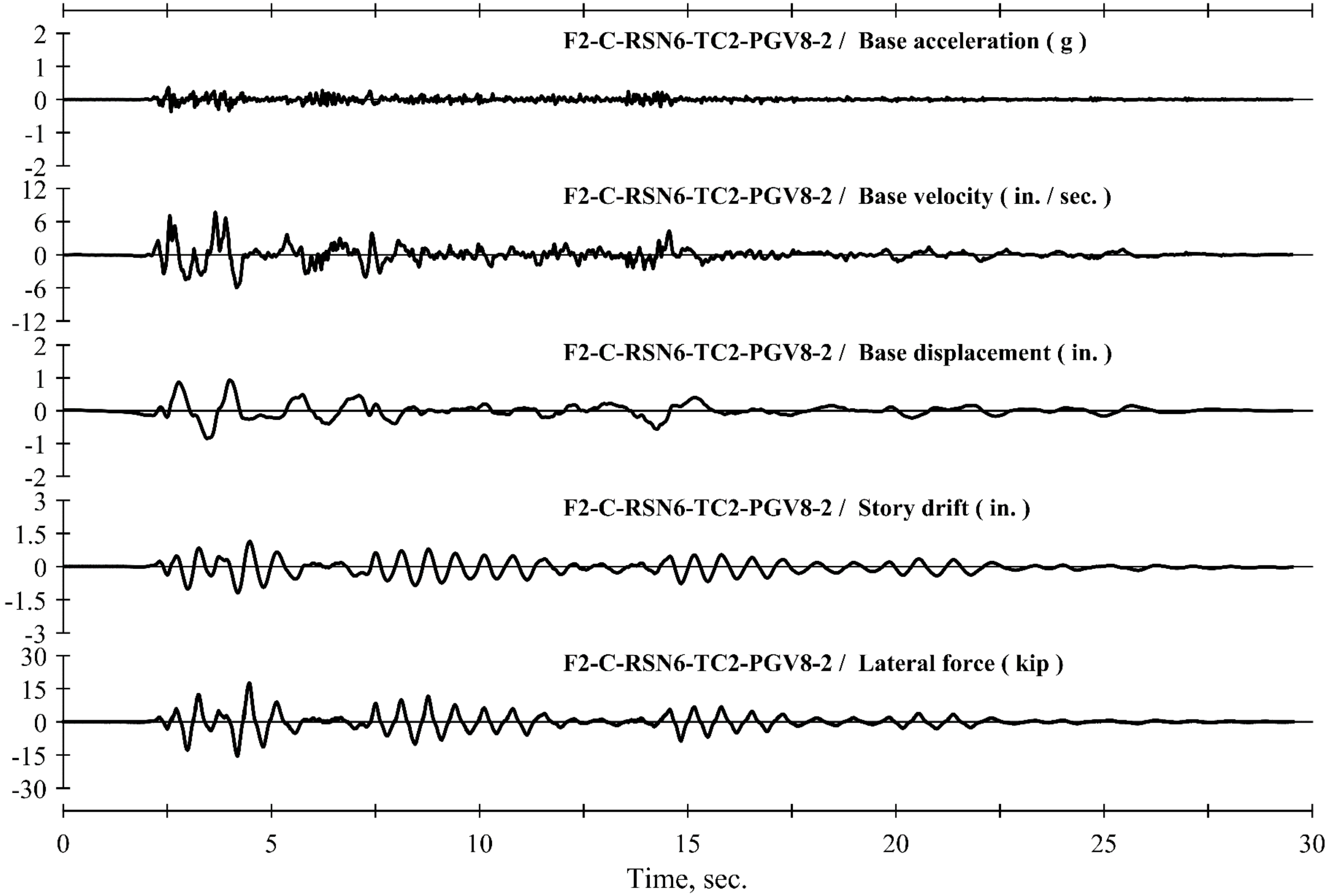

Figure D-129: Base motion and structural response histories in Run 51 of Specimen F2

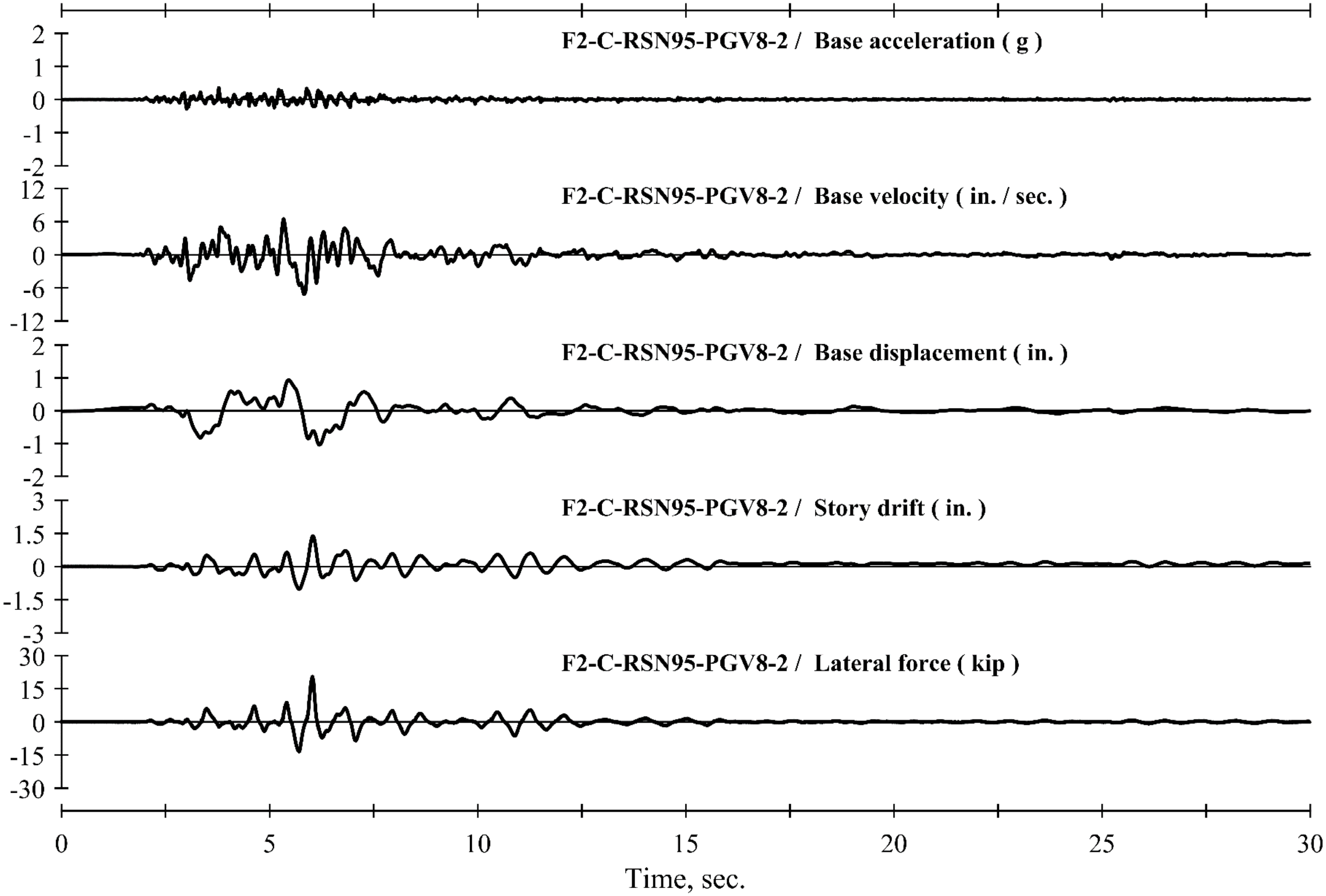

Figure D-130: Base motion and structural response histories in Run 52 of Specimen F2

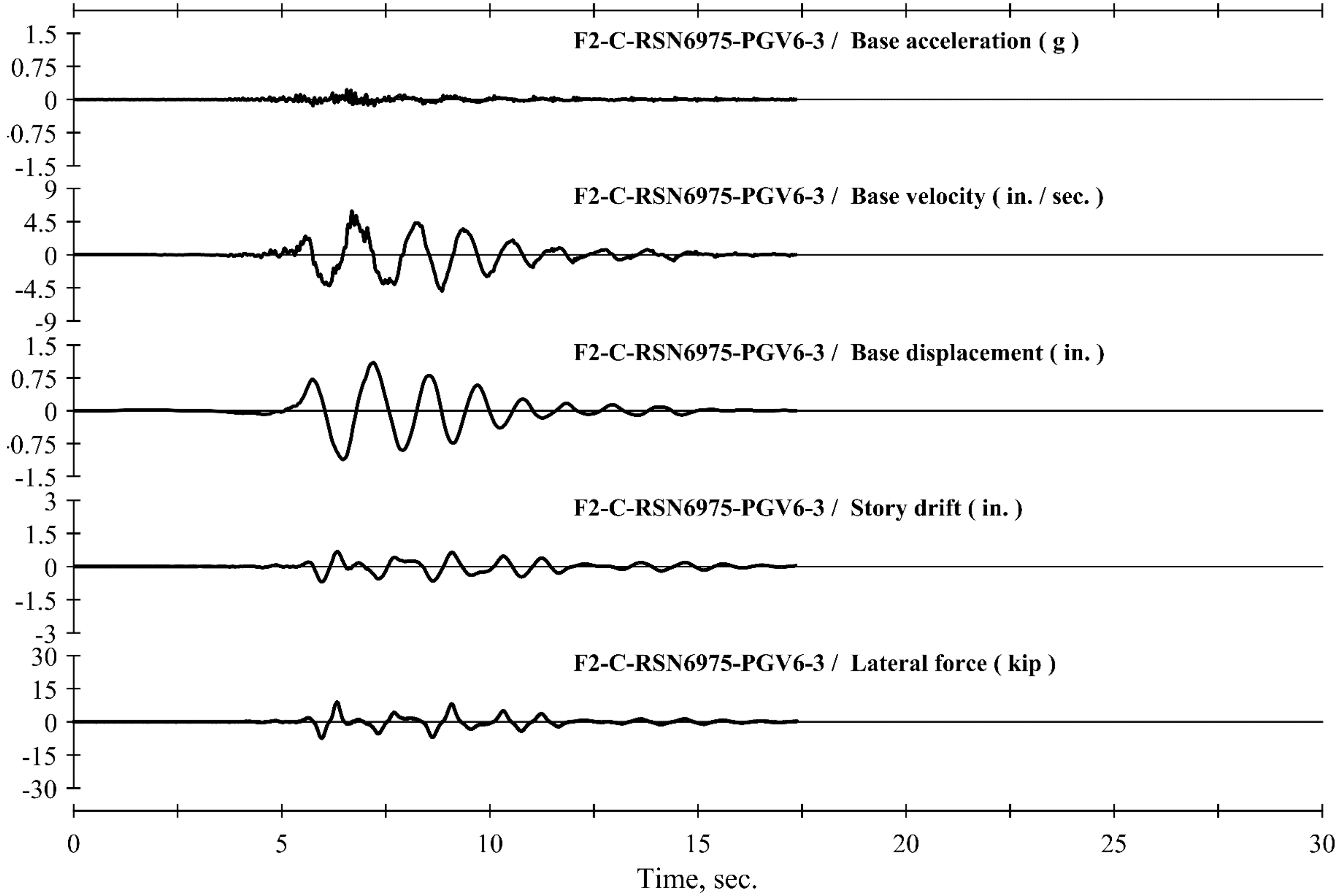

Figure D-131: Base motion and structural response histories in Run 53 of Specimen F2

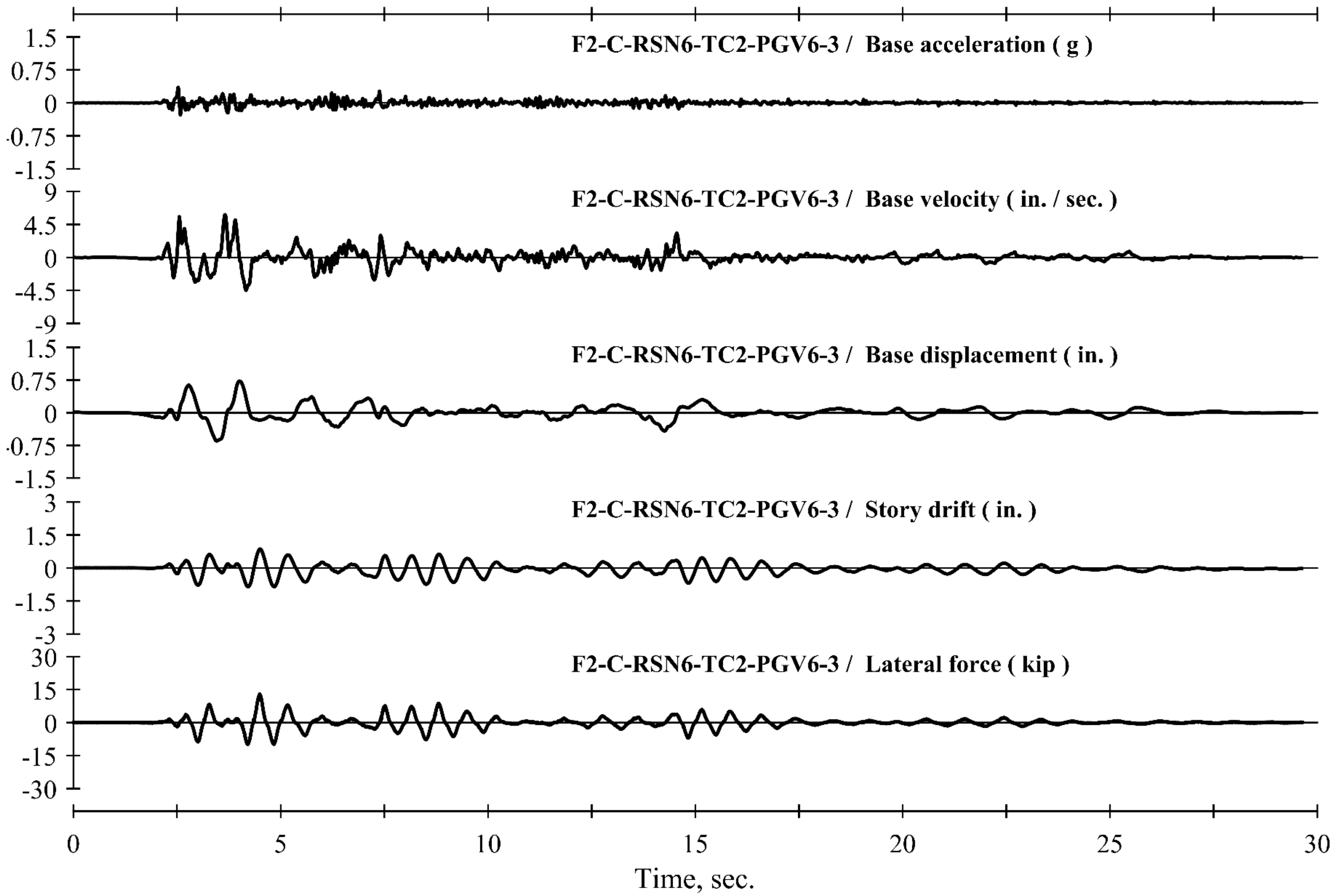

Figure D-132: Base motion and structural response histories in Run 54 of Specimen F2

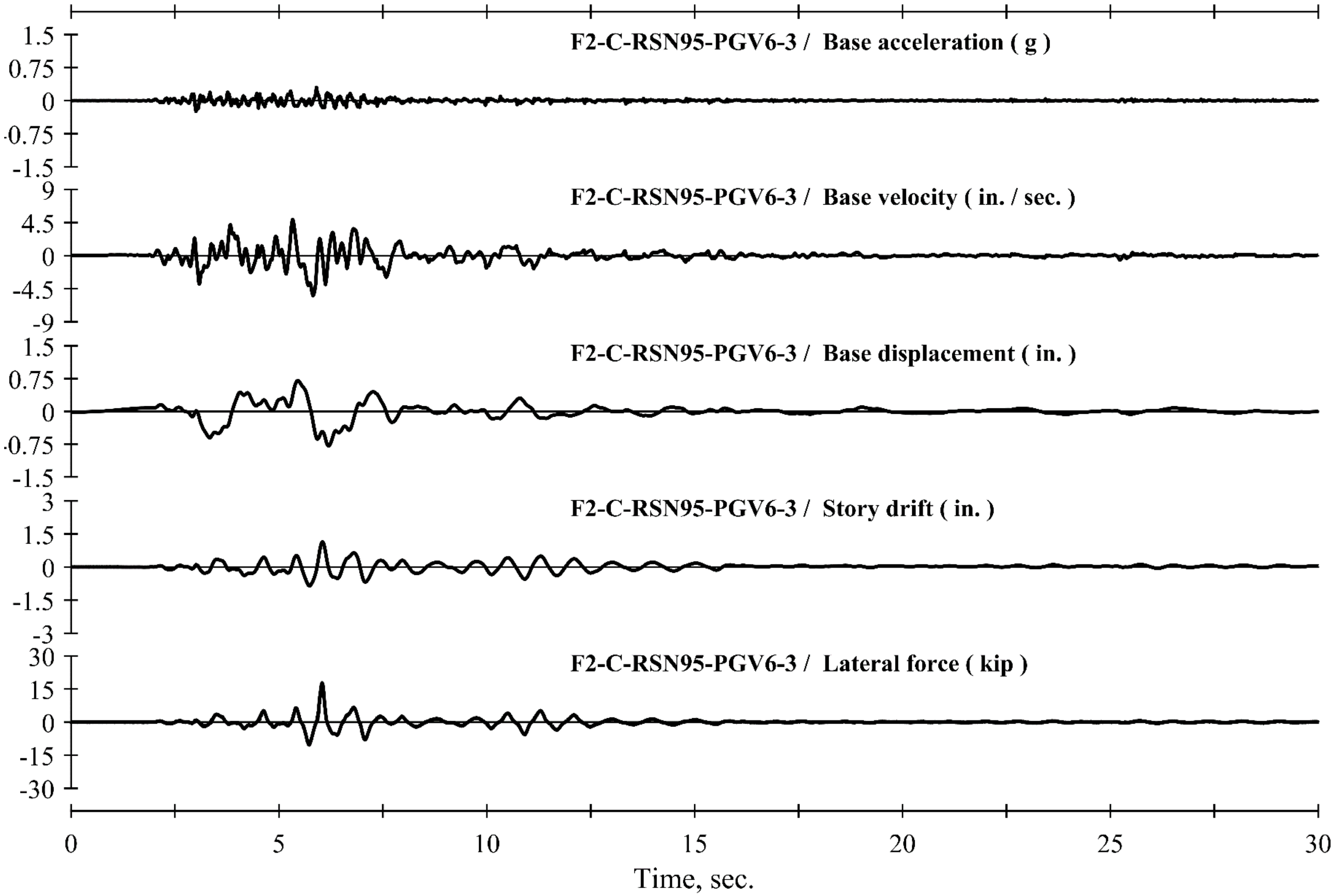

Figure D-133: Base motion and structural response histories in Run 55 of Specimen F2

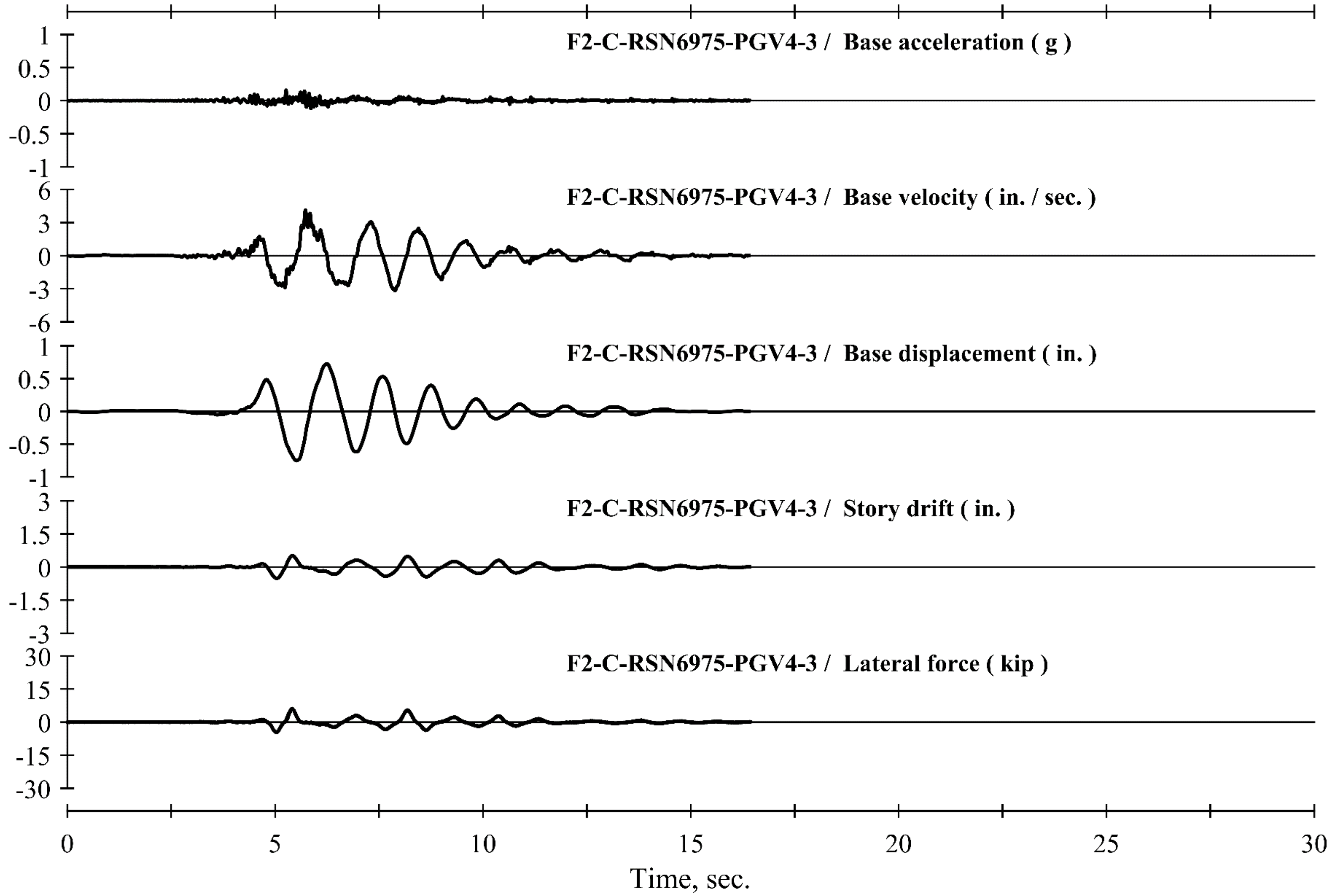

Figure D-134: Base motion and structural response histories in Run 56 of Specimen F2

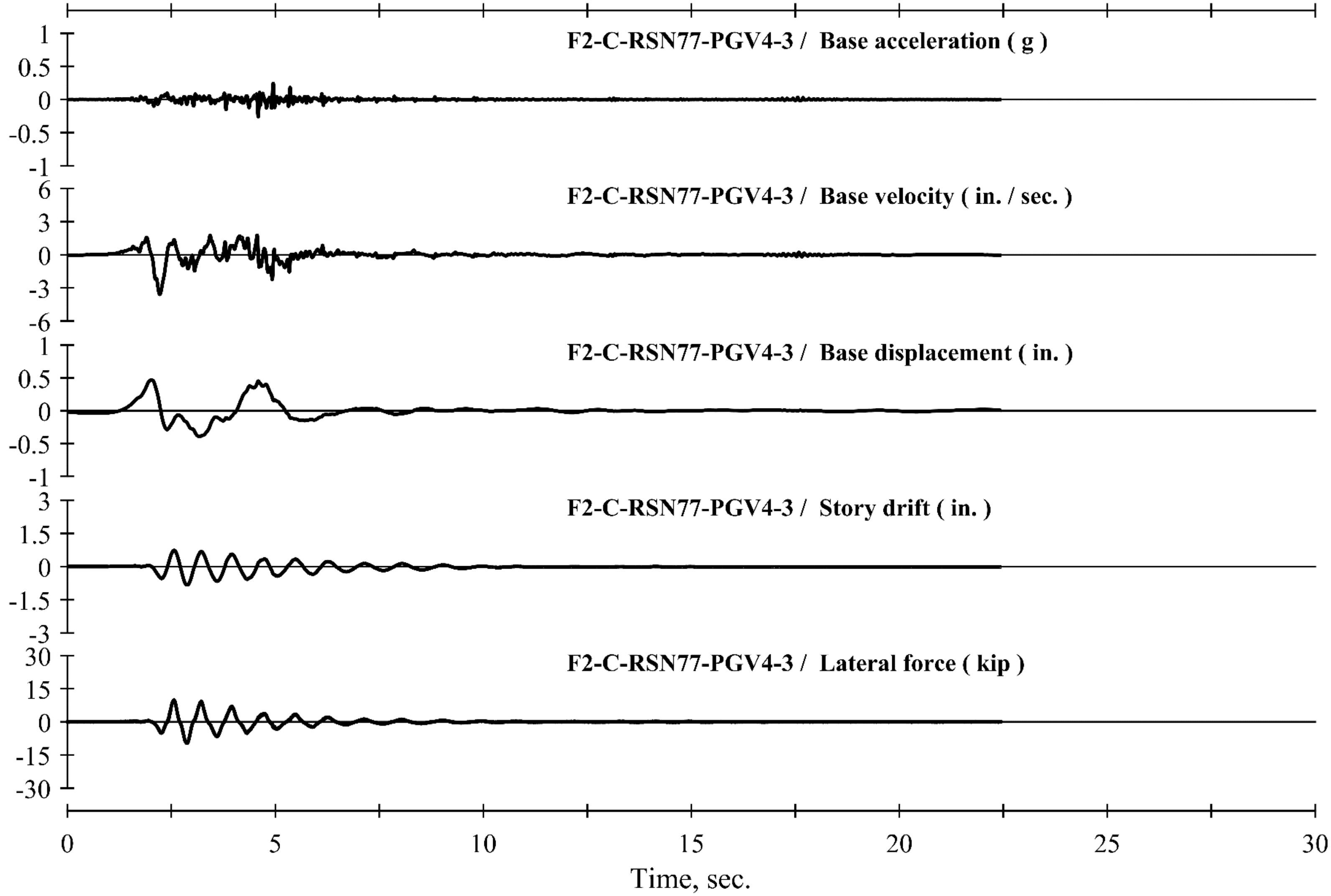

Figure D-135: Base motion and structural response histories in Run 57 of Specimen F2

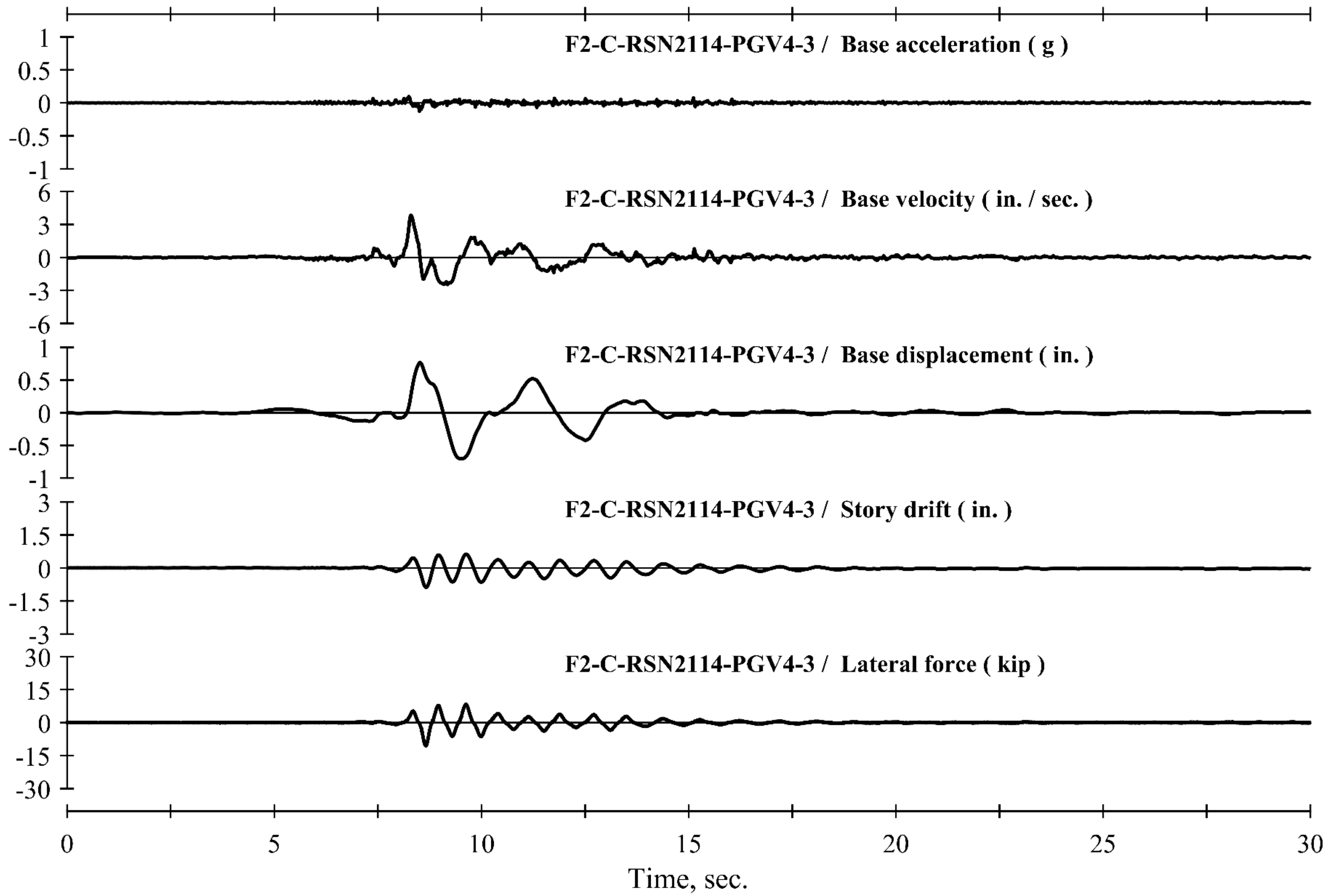

Figure D-136: Base motion and structural response histories in Run 58 of Specimen F2

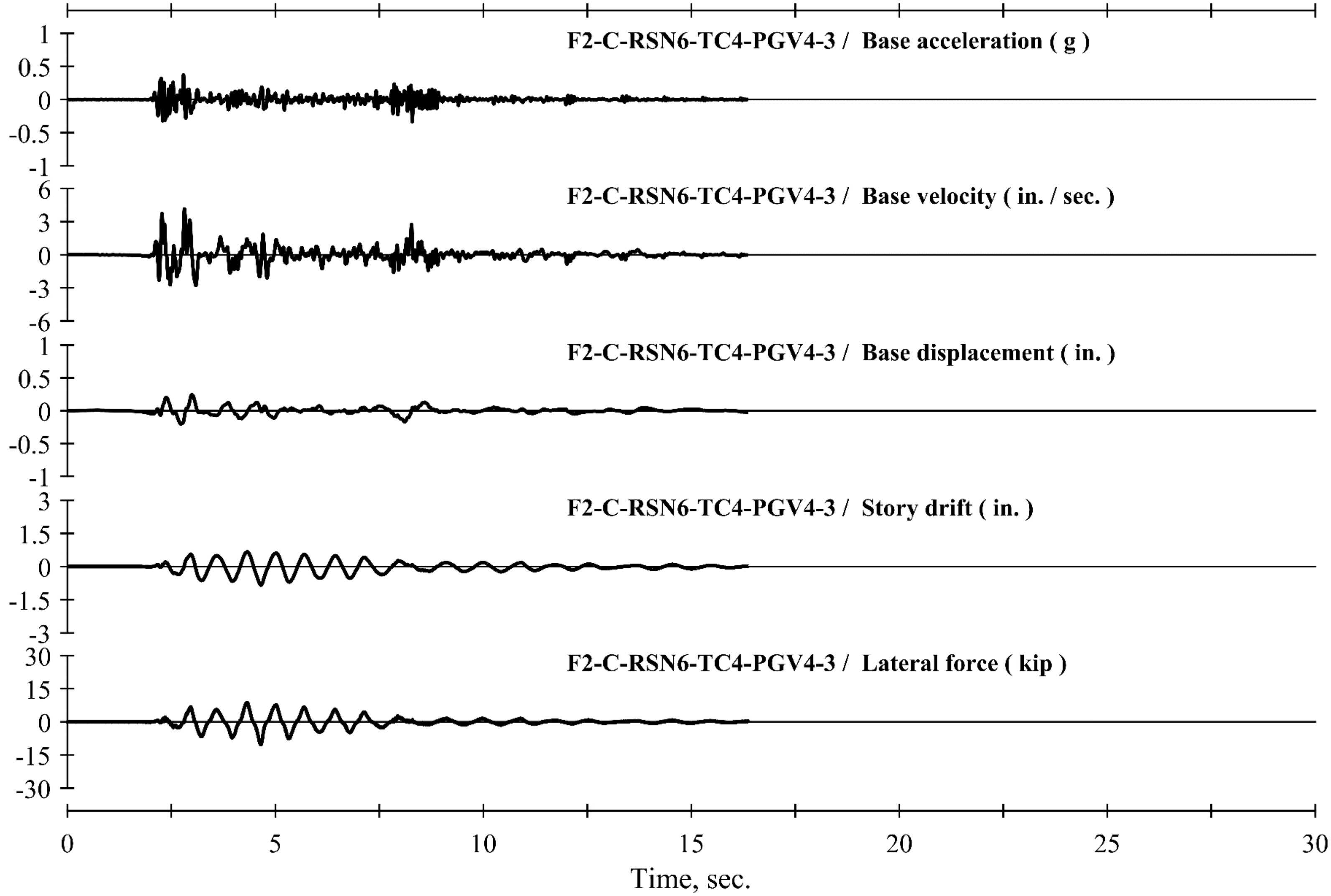

Figure D-137: Base motion and structural response histories in Run 59 of Specimen F2

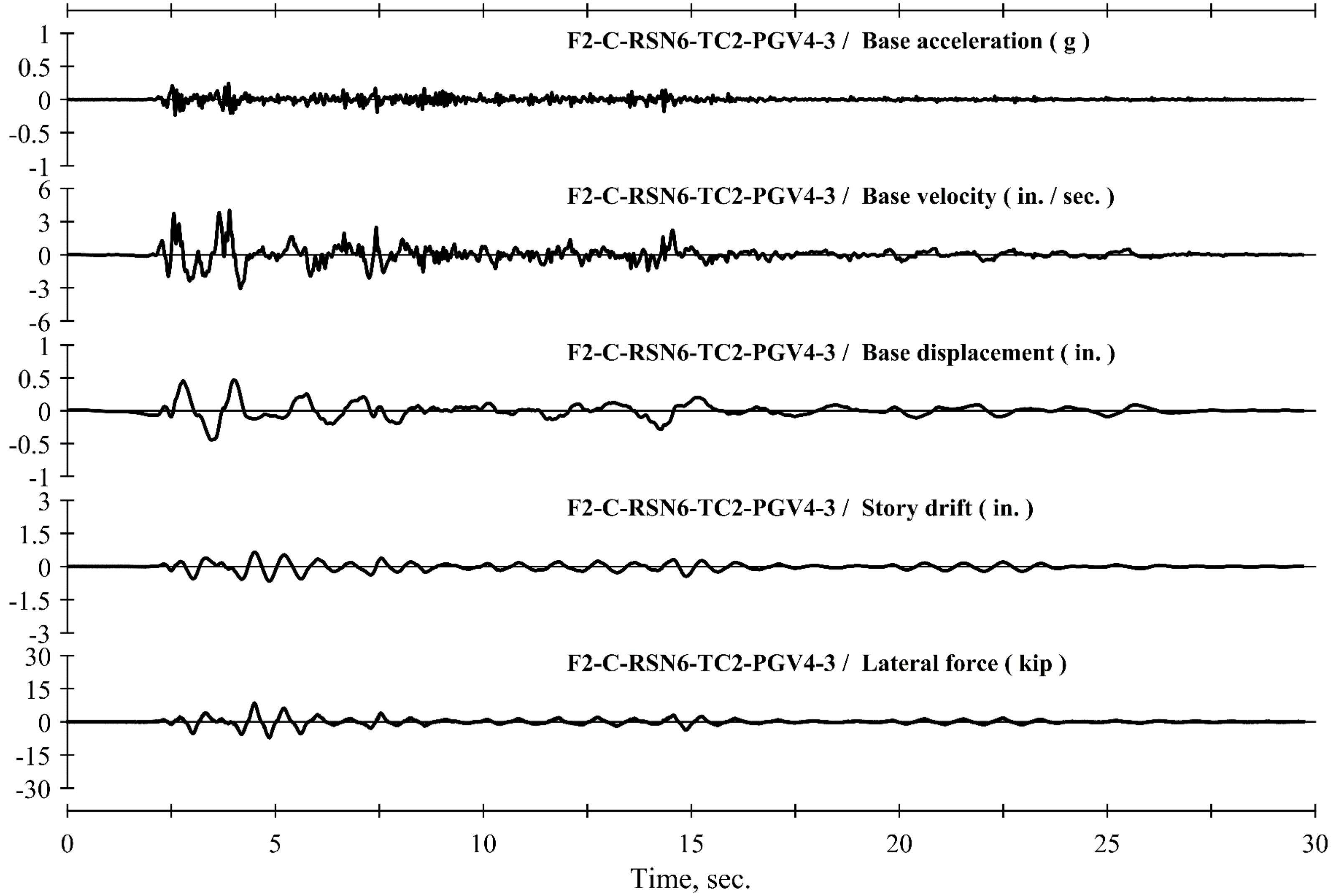

Figure D-138: Base motion and structural response histories in Run 60 of Specimen F2

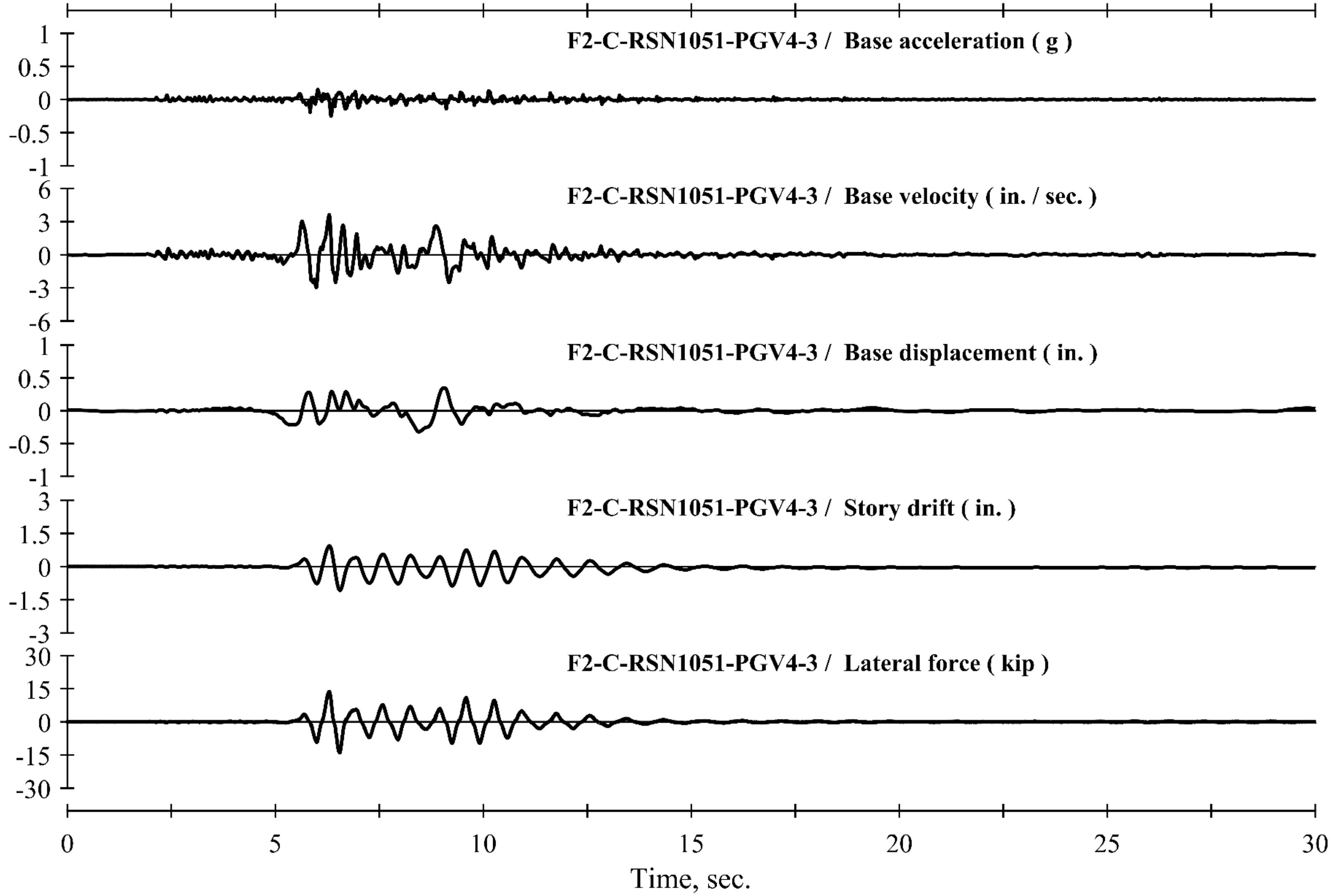

Figure D-139: Base motion and structural response histories in Run 61 of Specimen F2

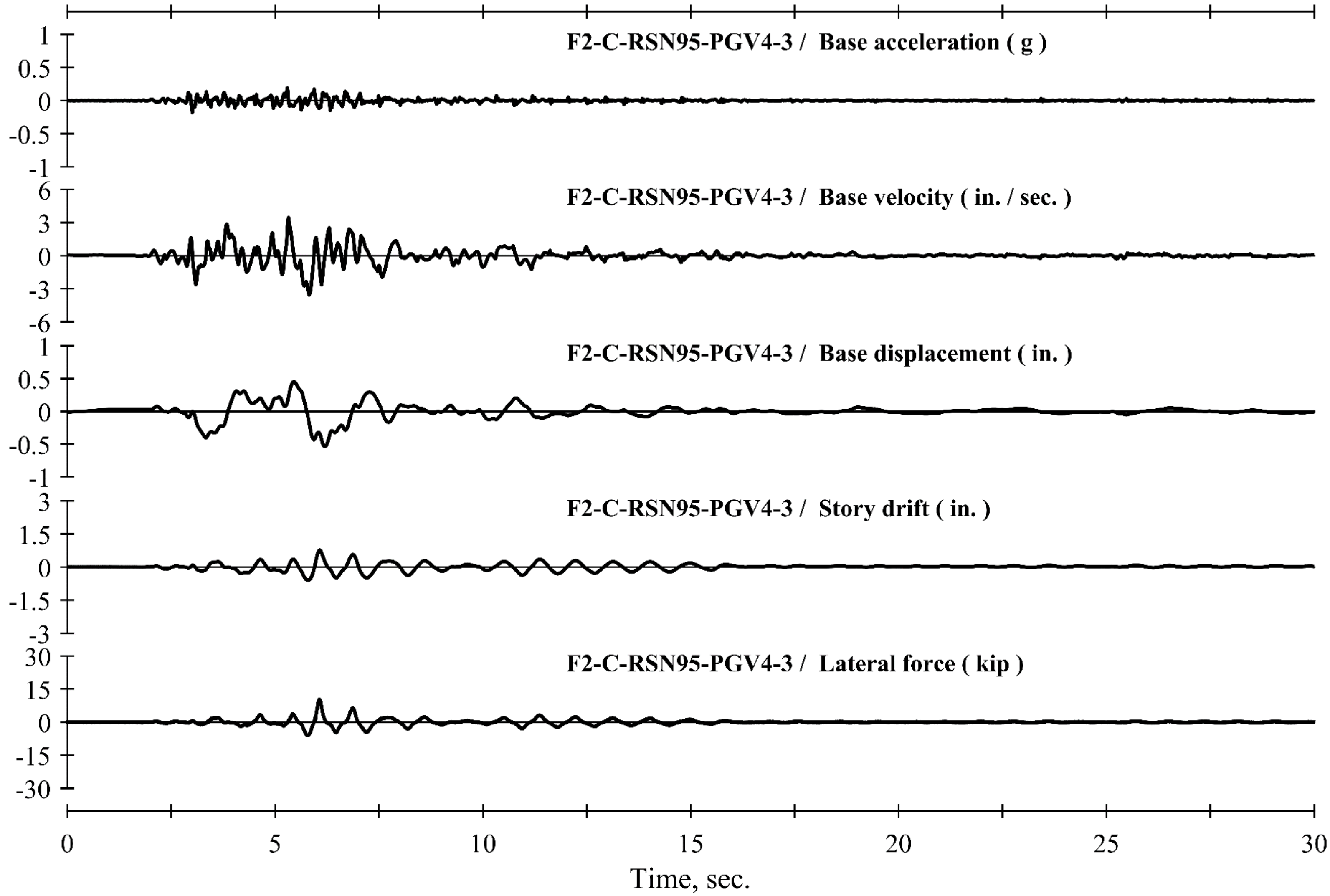

Figure D-140: Base motion and structural response histories in Run 62 of Specimen F2

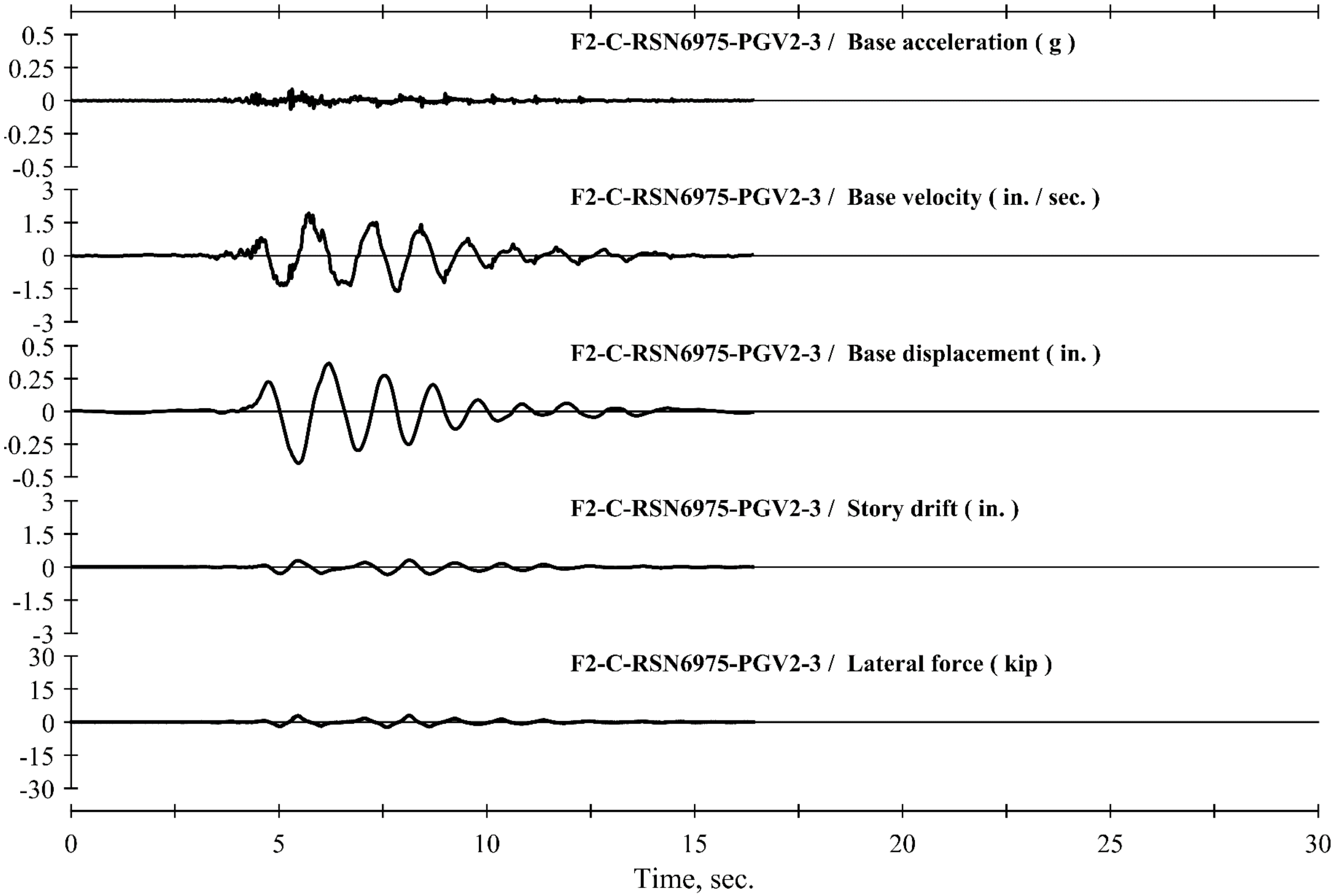

Figure D-141: Base motion and structural response histories in Run 63 of Specimen F2

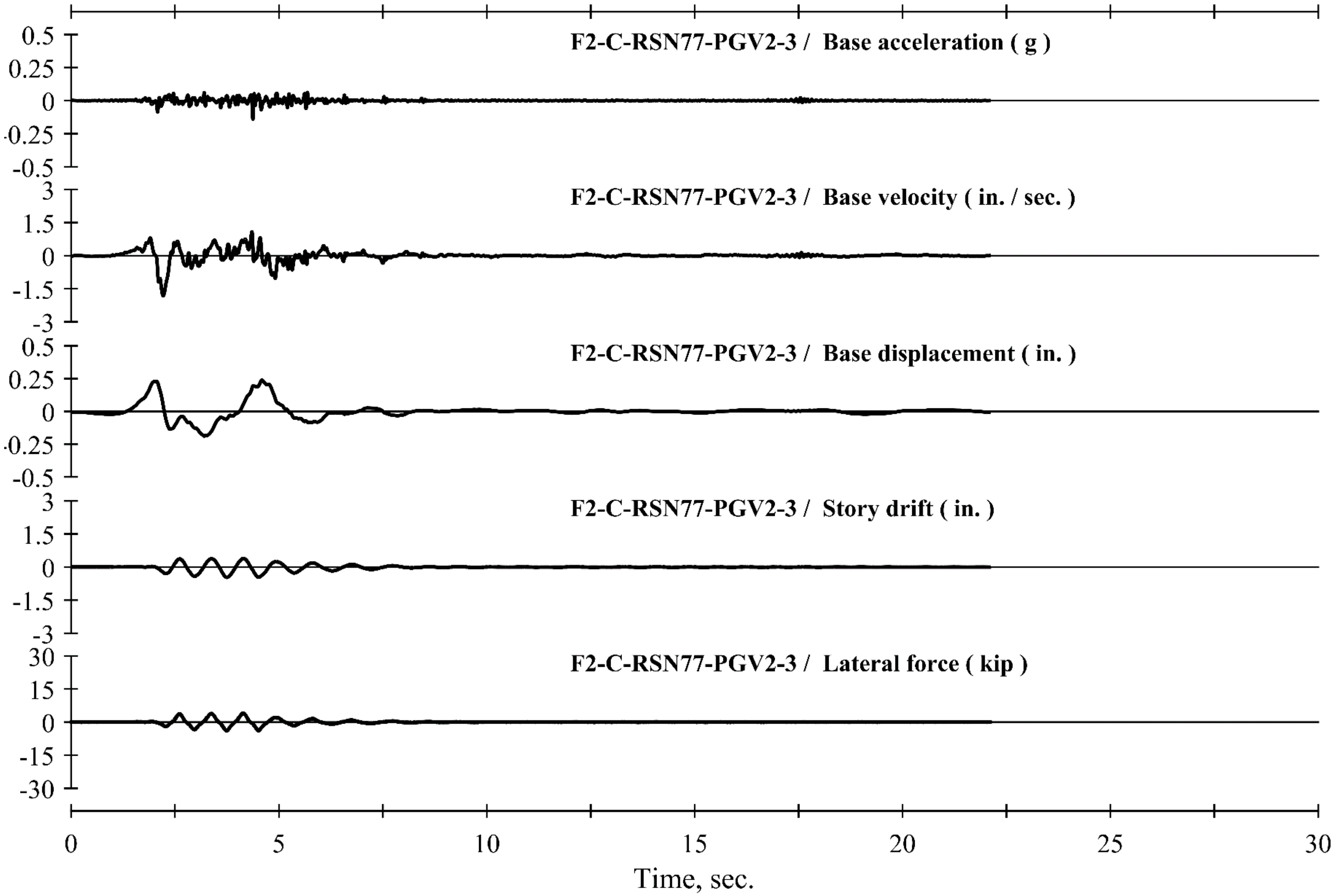

Figure D-142: Base motion and structural response histories in Run 64 of Specimen F2

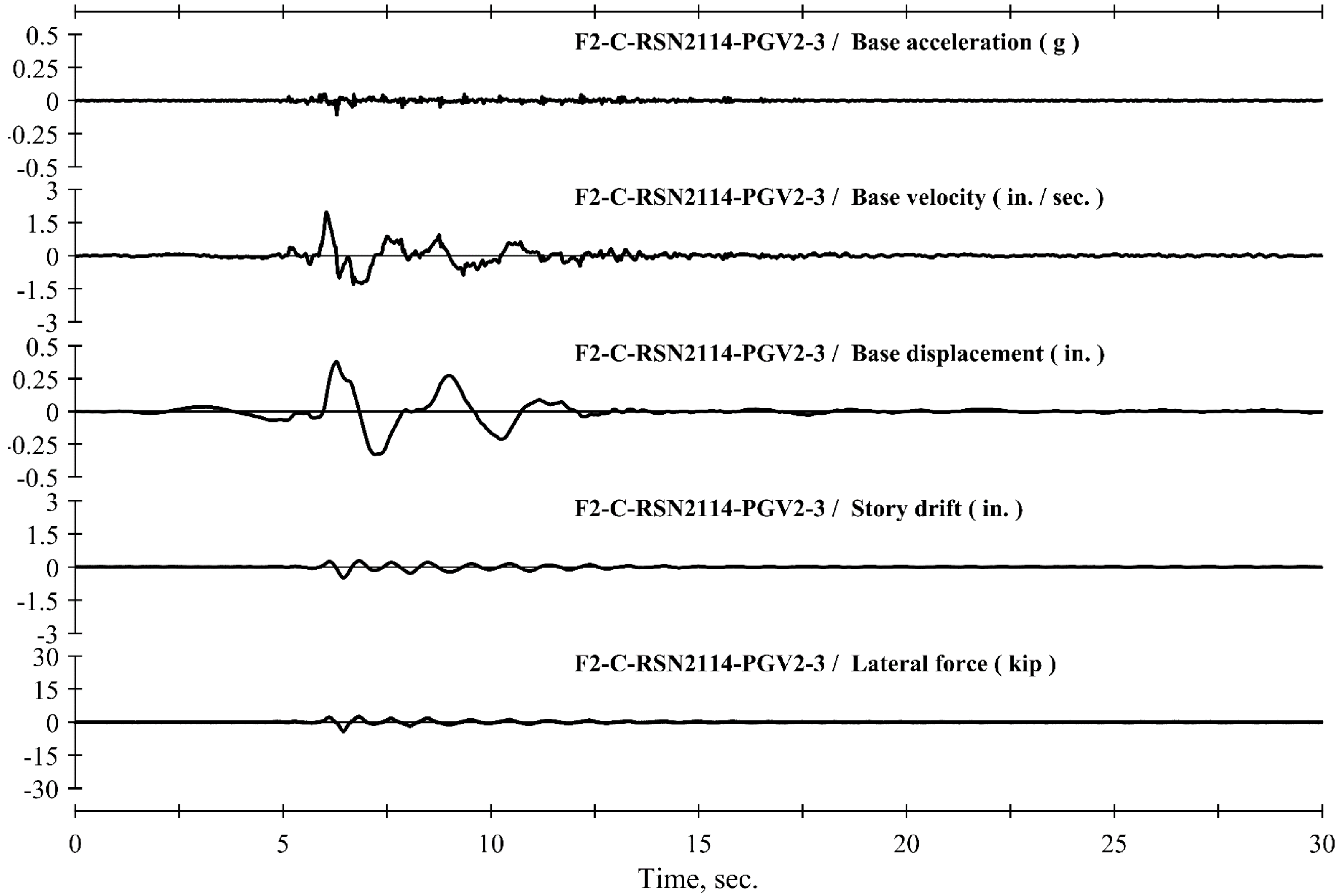

Figure D-143: Base motion and structural response histories in Run 65 of Specimen F2

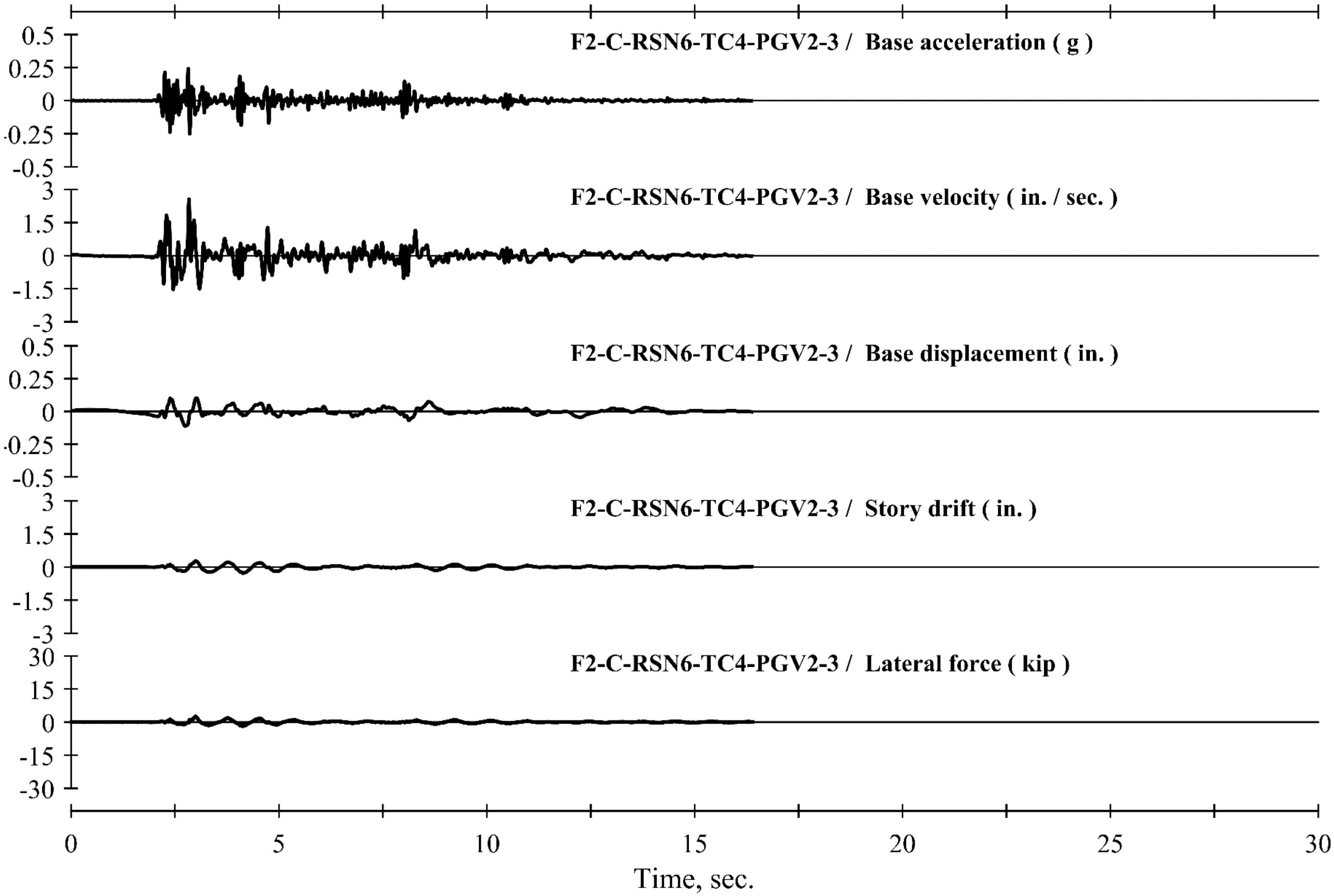

Figure D-144: Base motion and structural response histories in Run 66 of Specimen F2

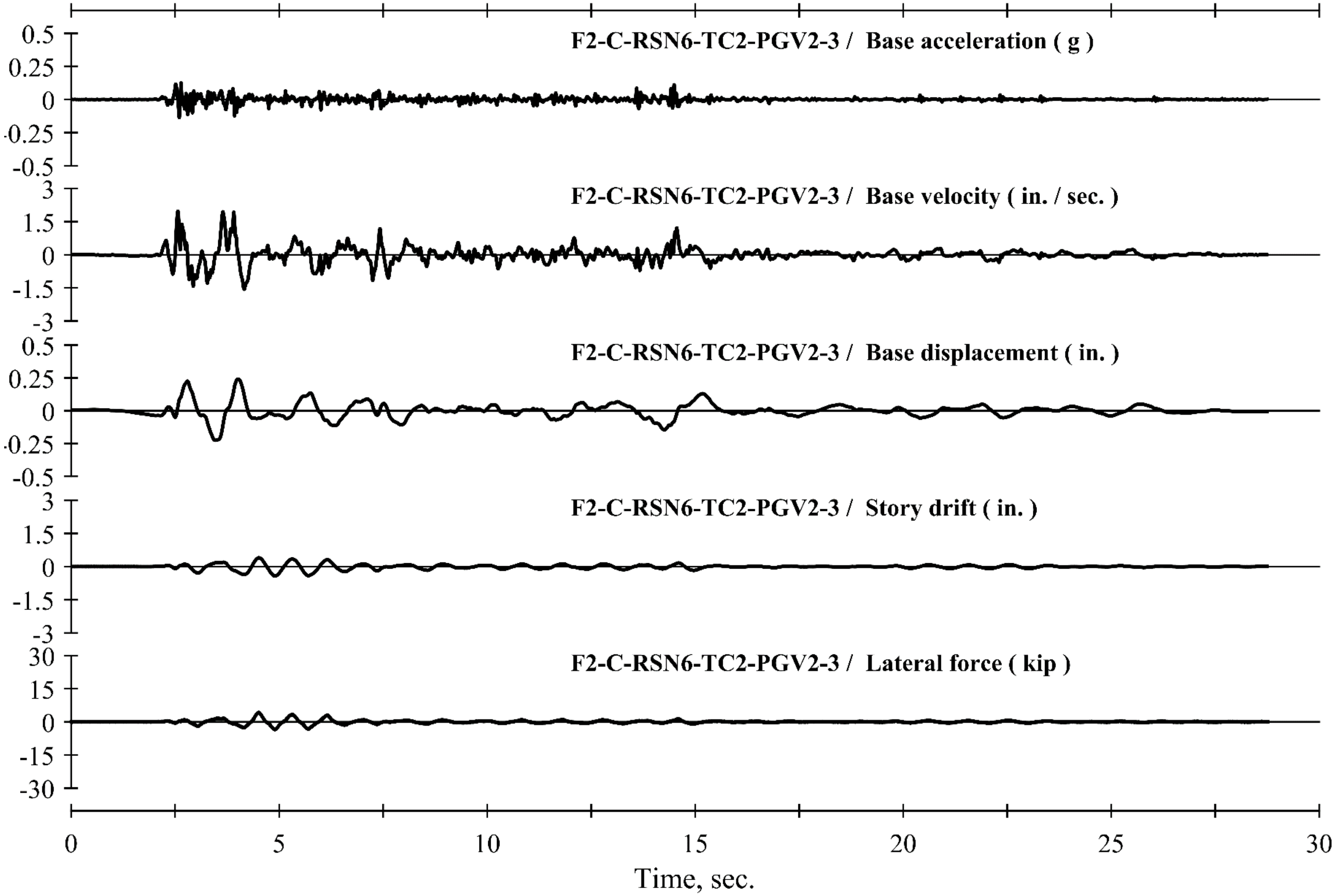

Figure D-145: Base motion and structural response histories in Run 67 of Specimen F2

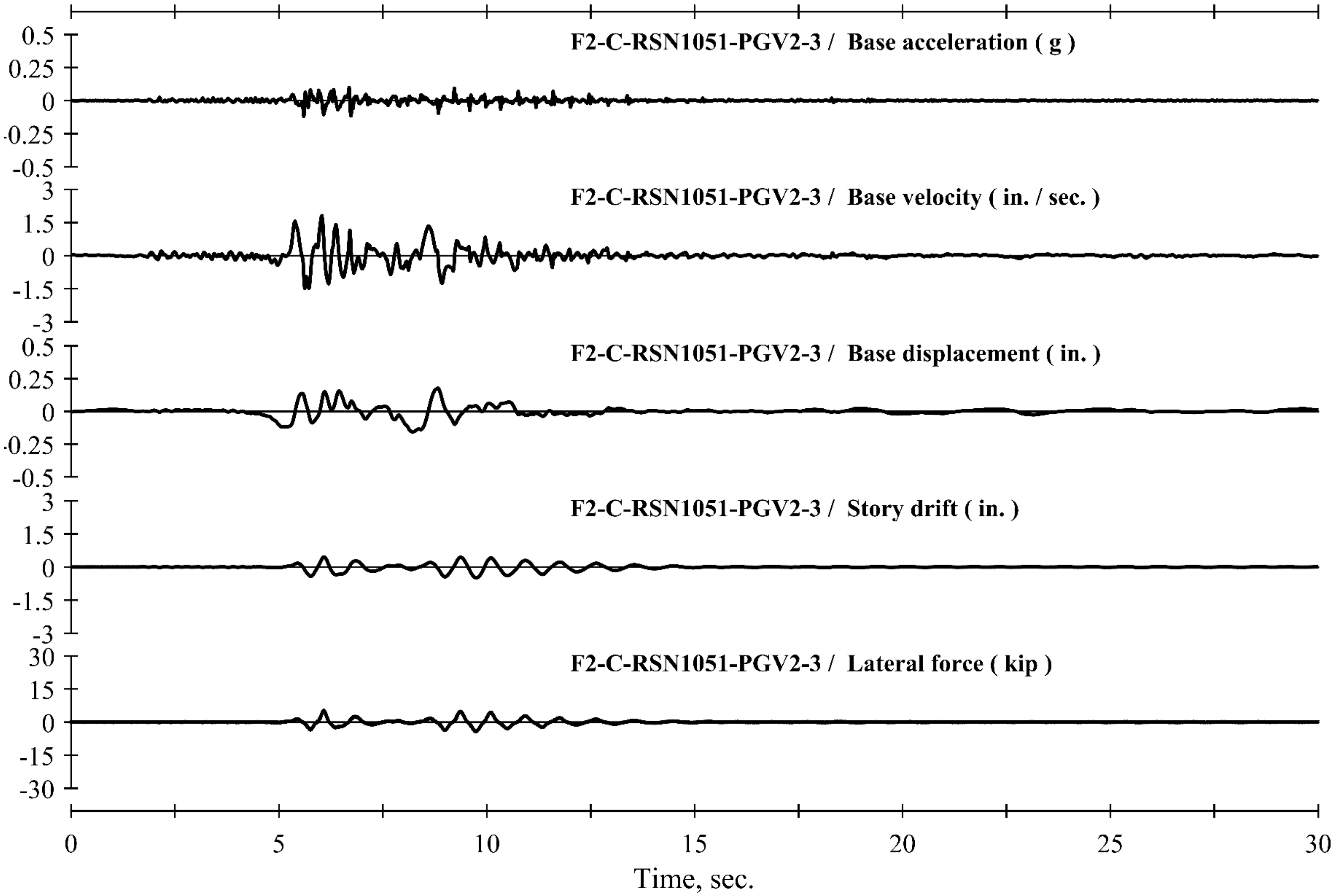

Figure D-146: Base motion and structural response histories in Run 68 of Specimen F2

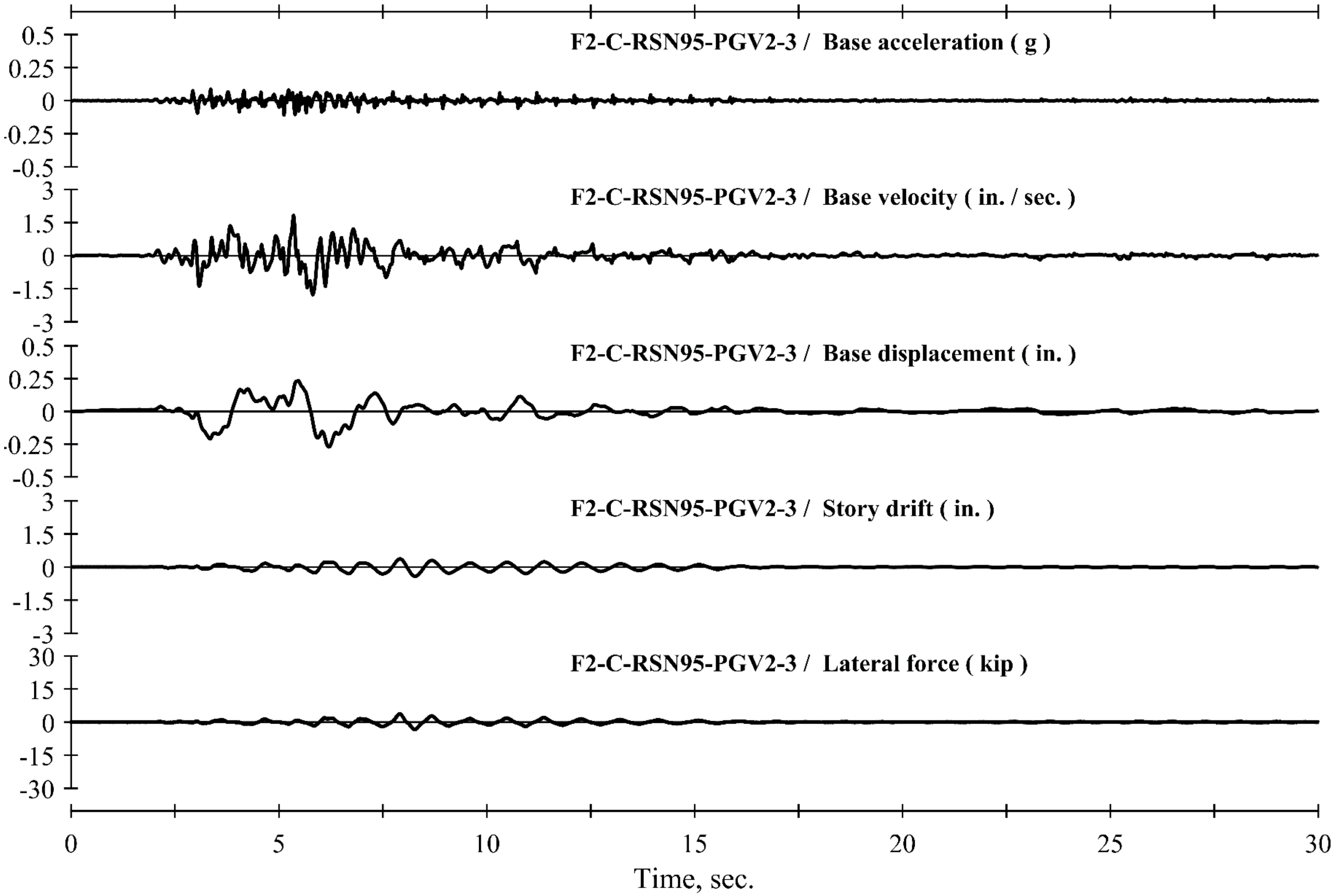

Figure D-147: Base motion and structural response histories in Run 69 of Specimen F2

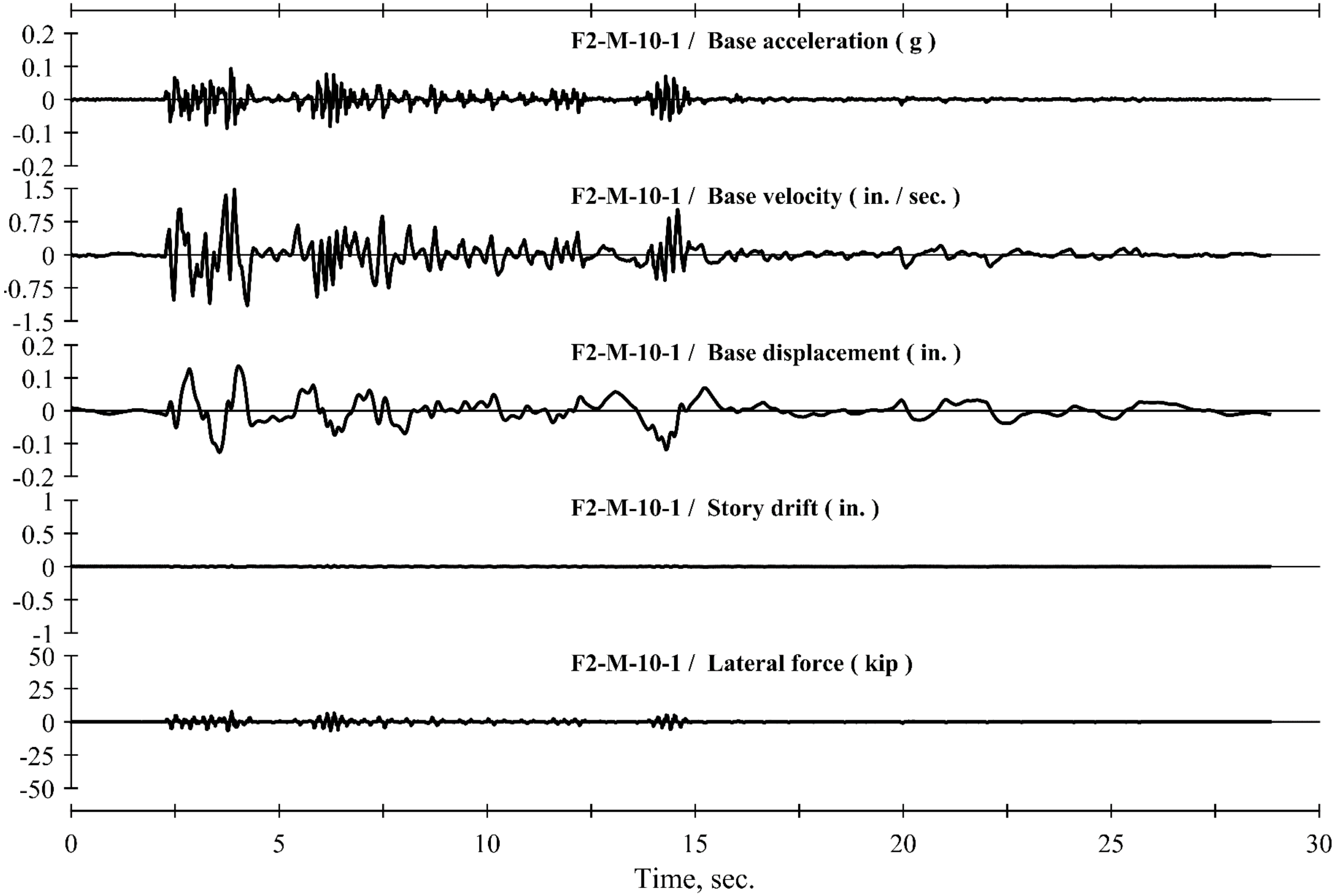

Figure D-148: Base motion and structural response histories in Run 70 of Specimen F2

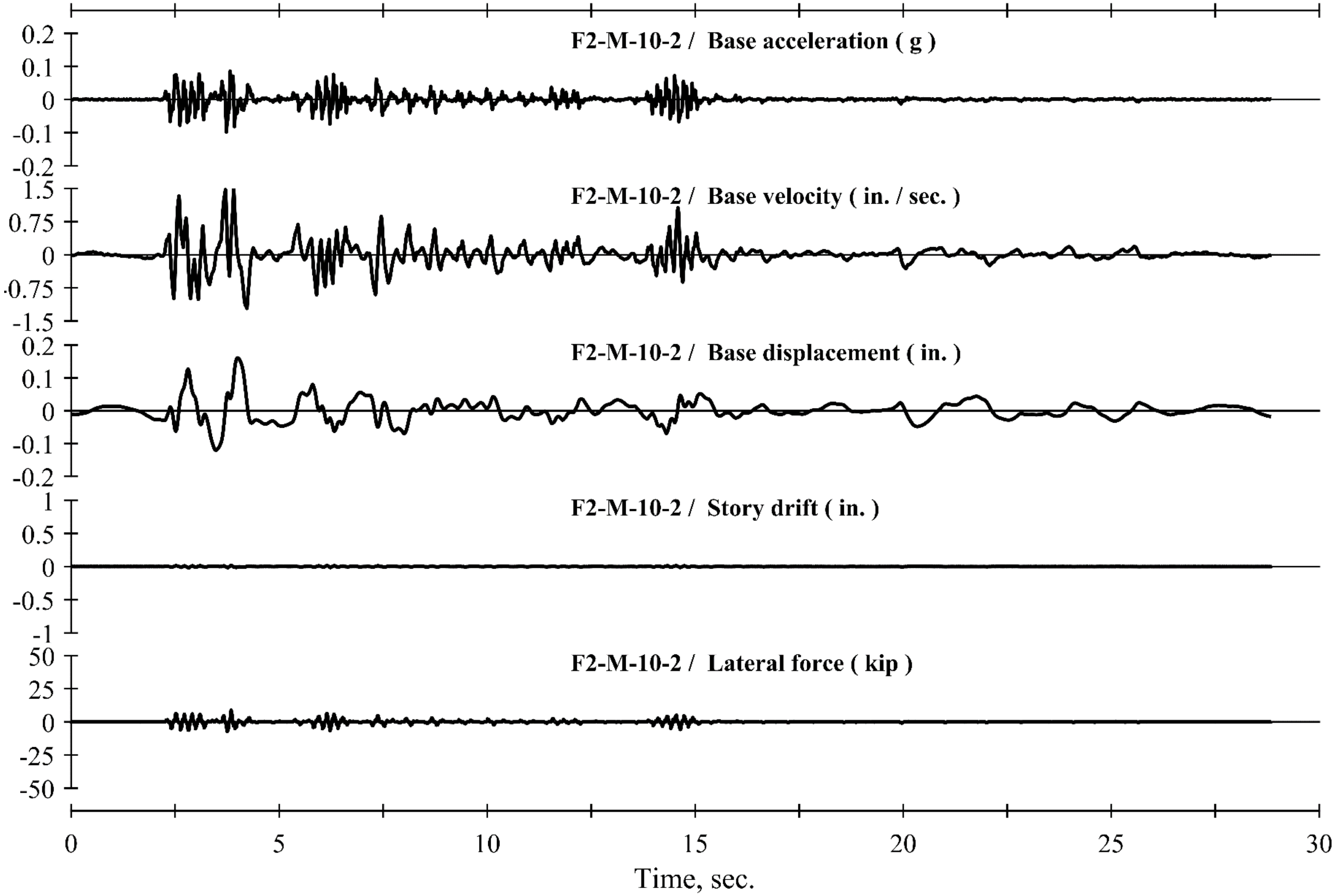

Figure D-149: Base motion and structural response histories in Run 71 of Specimen F2

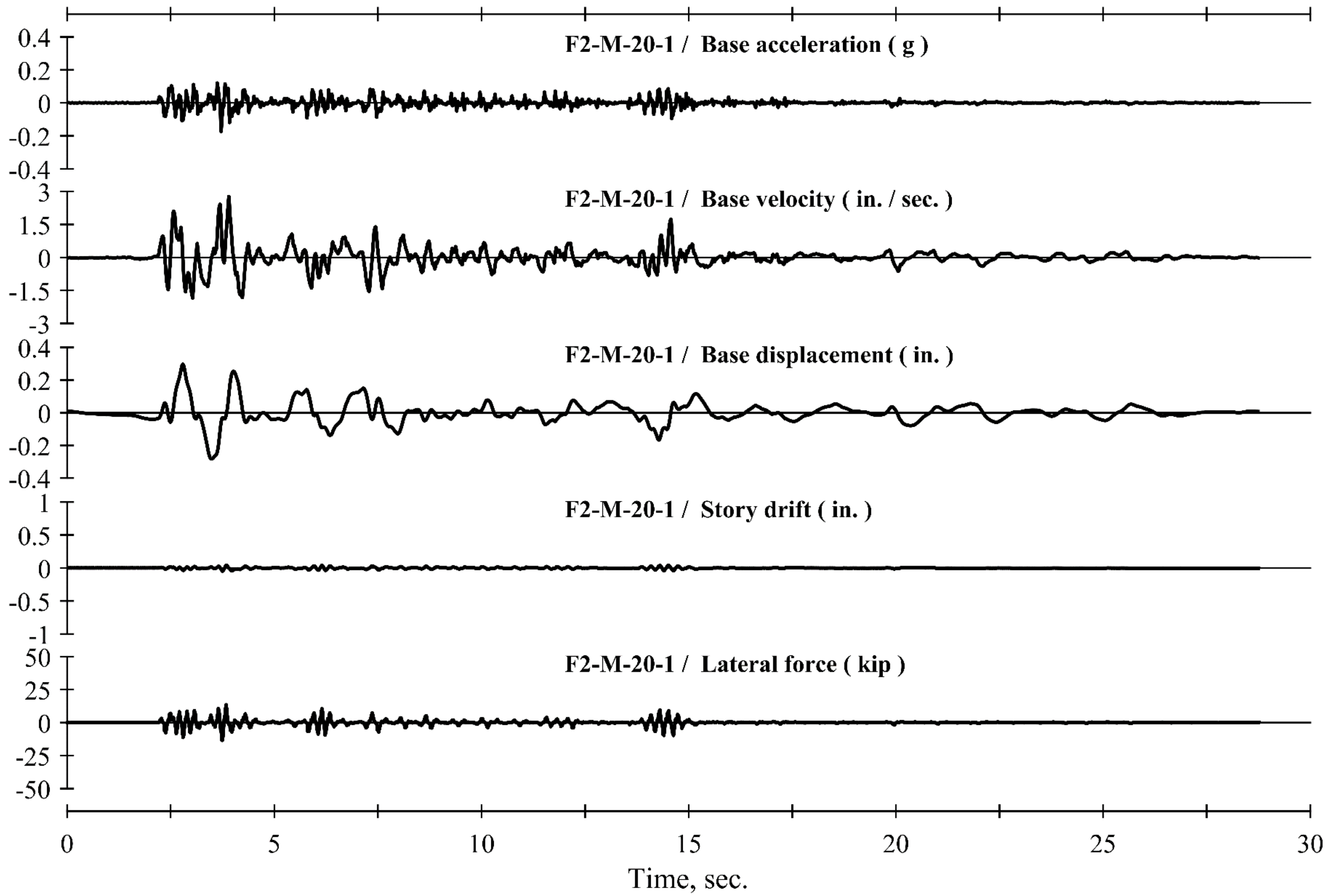

Figure D-150: Base motion and structural response histories in Run 72 of Specimen F2

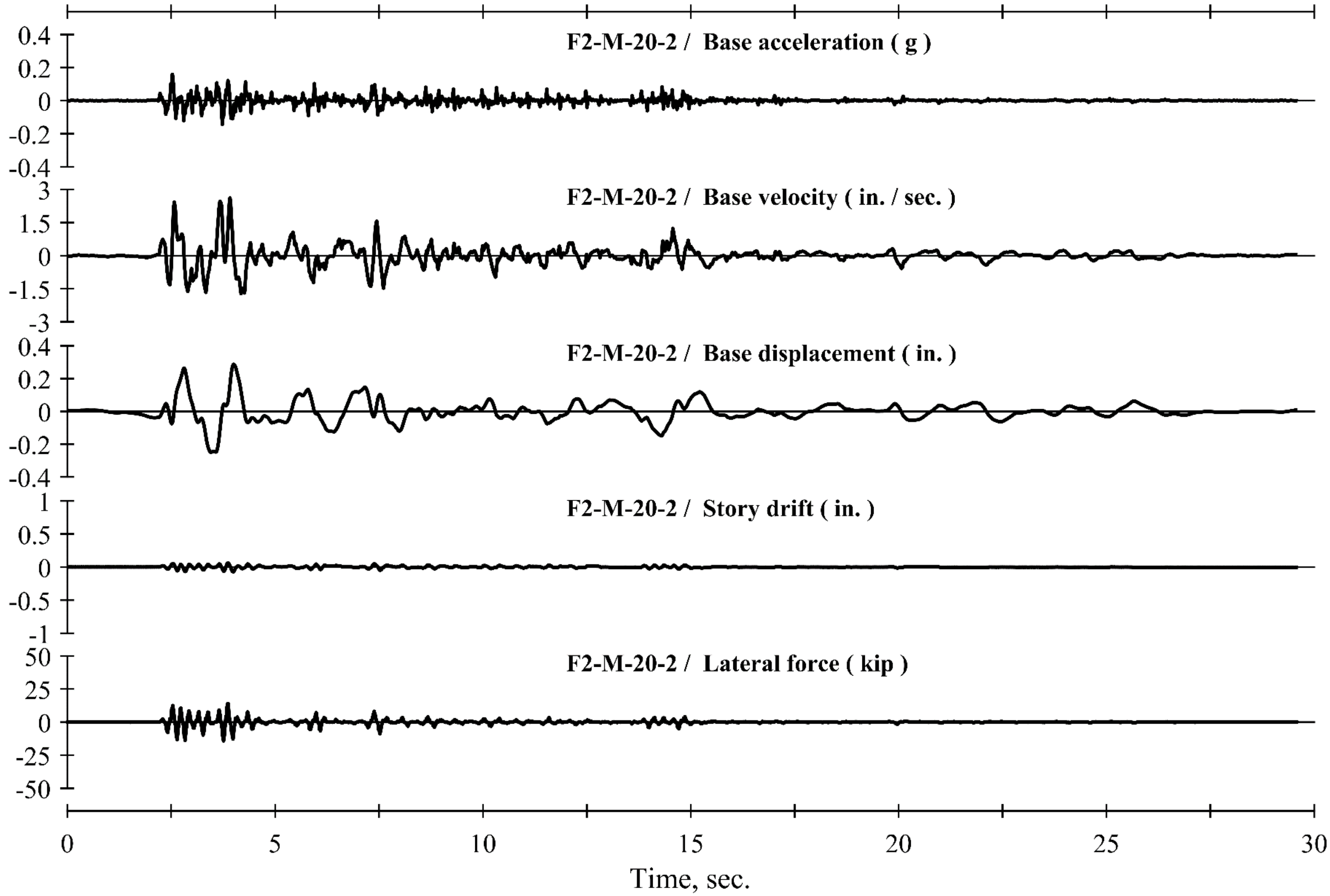

Figure D-151: Base motion and structural response histories in Run 73 of Specimen F2

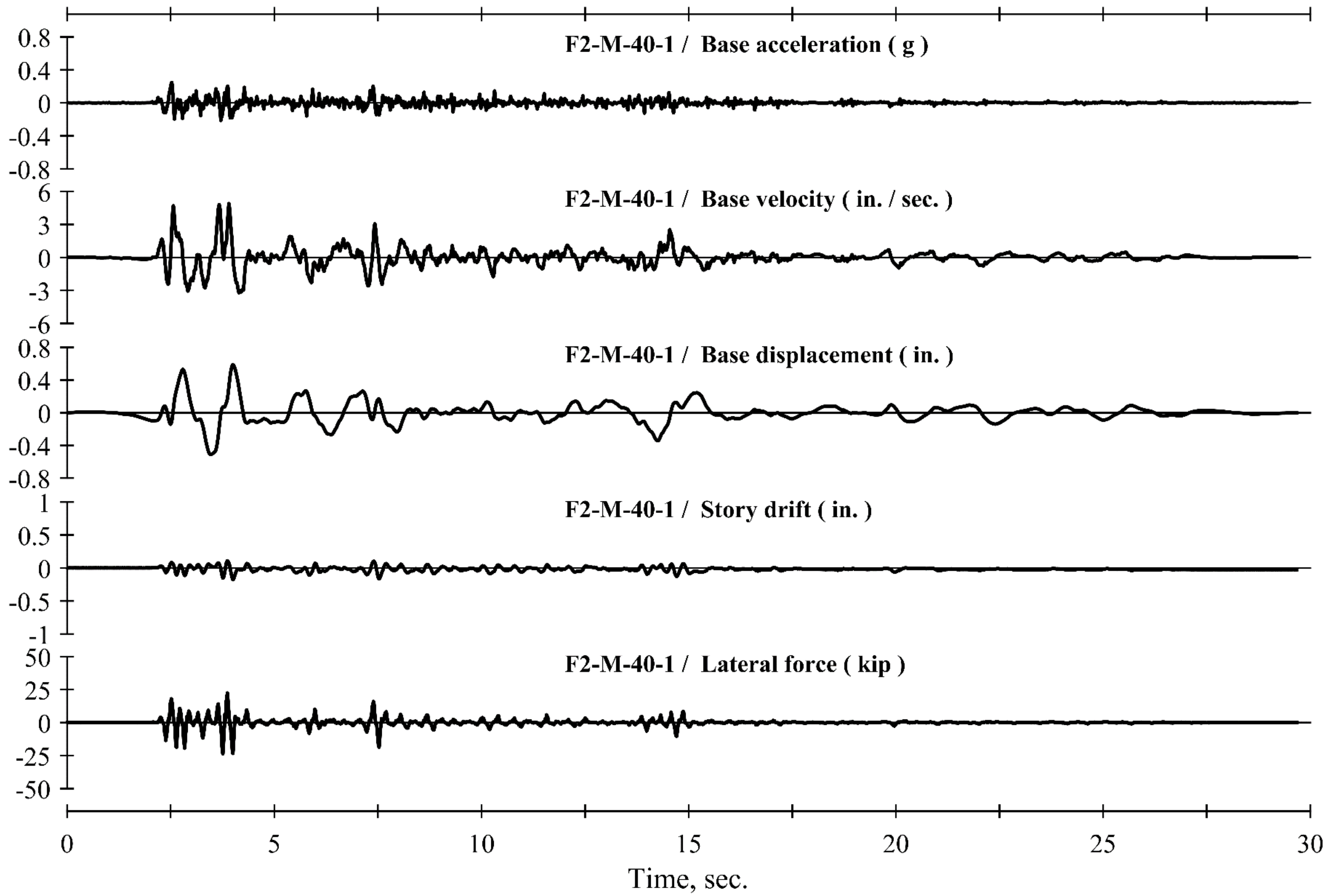

Figure D-152: Base motion and structural response histories in Run 74 of Specimen F2

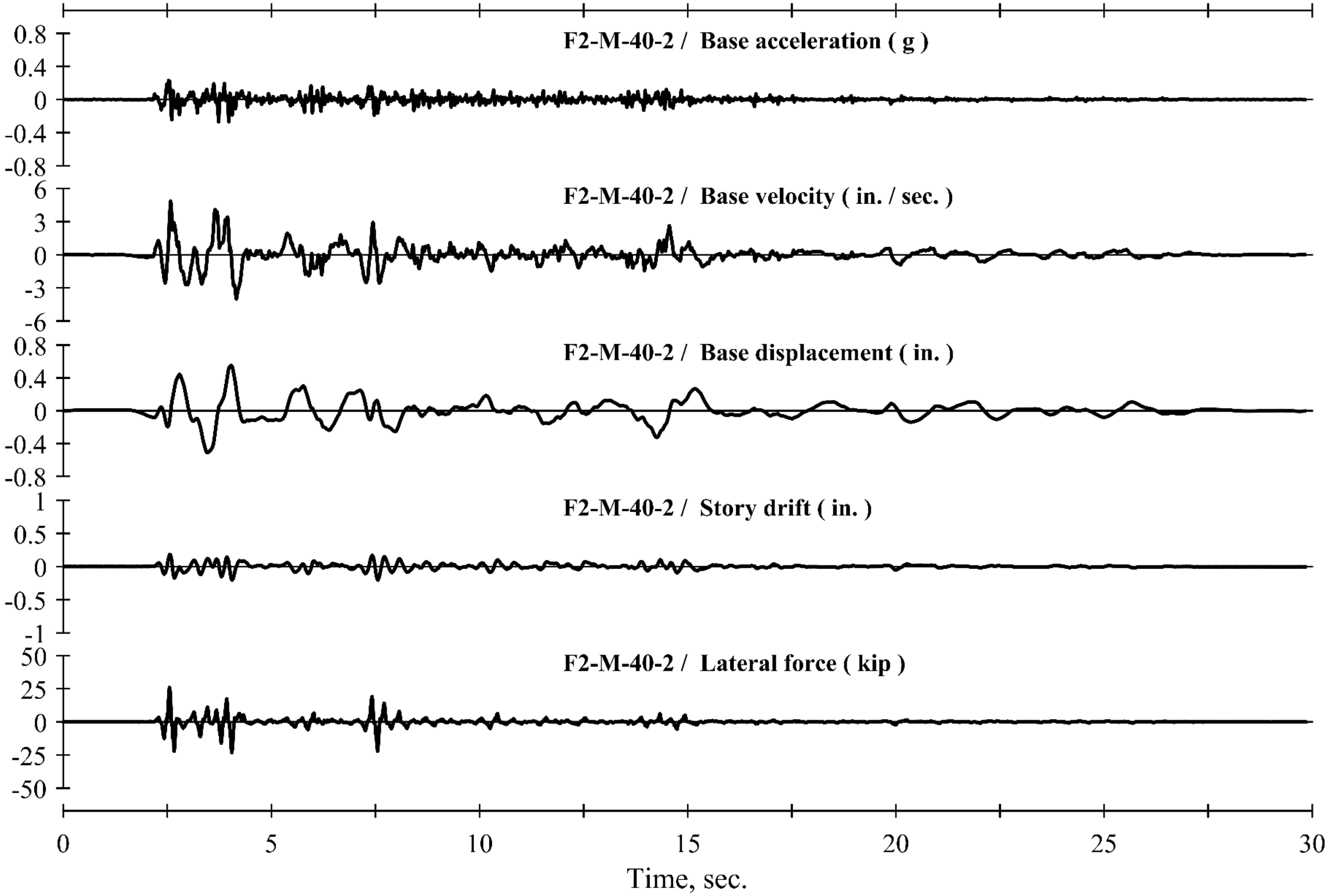

Figure D-153: Base motion and structural response histories in Run 75 of Specimen F2

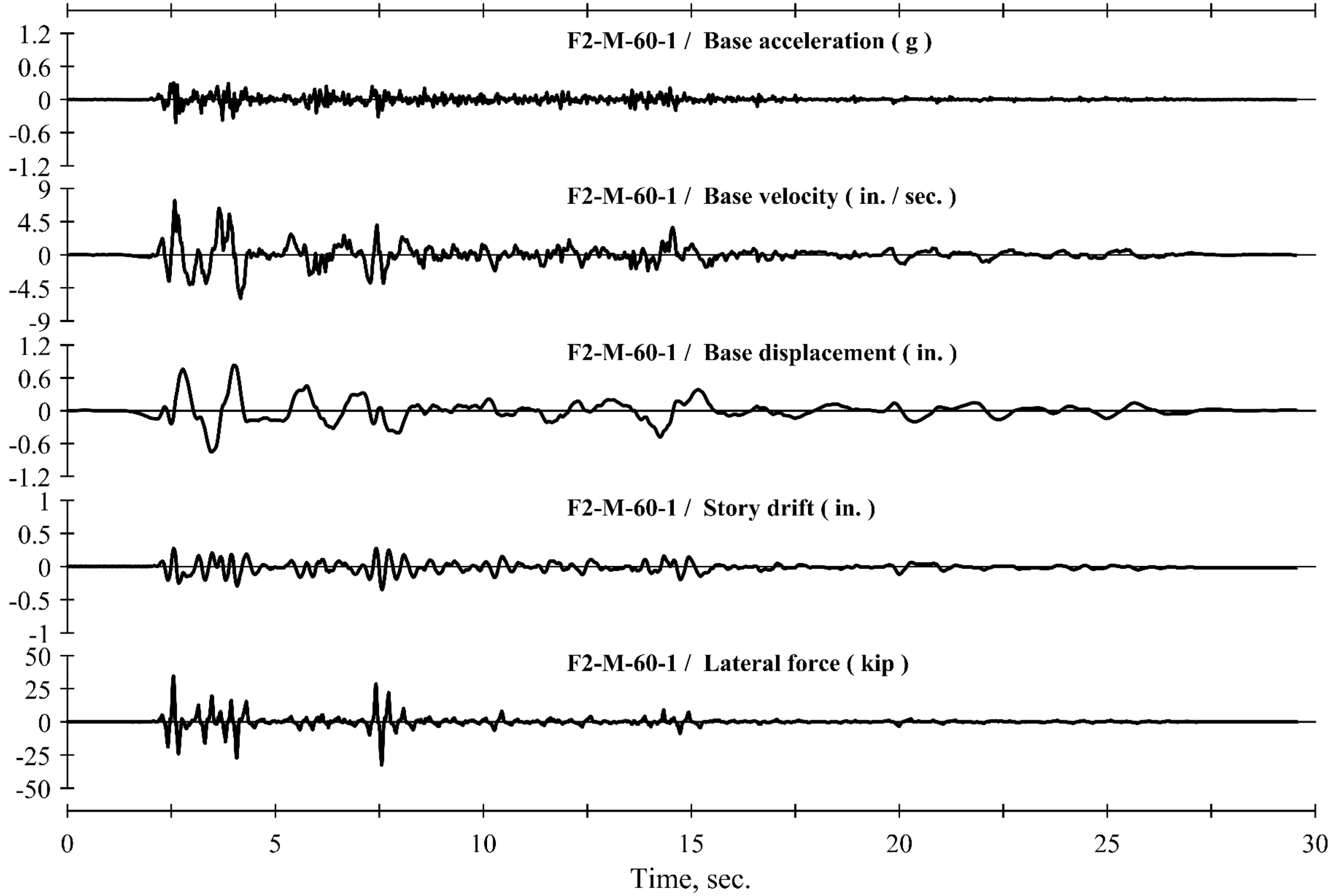

Figure D-154: Base motion and structural response histories in Run 76 of Specimen F2

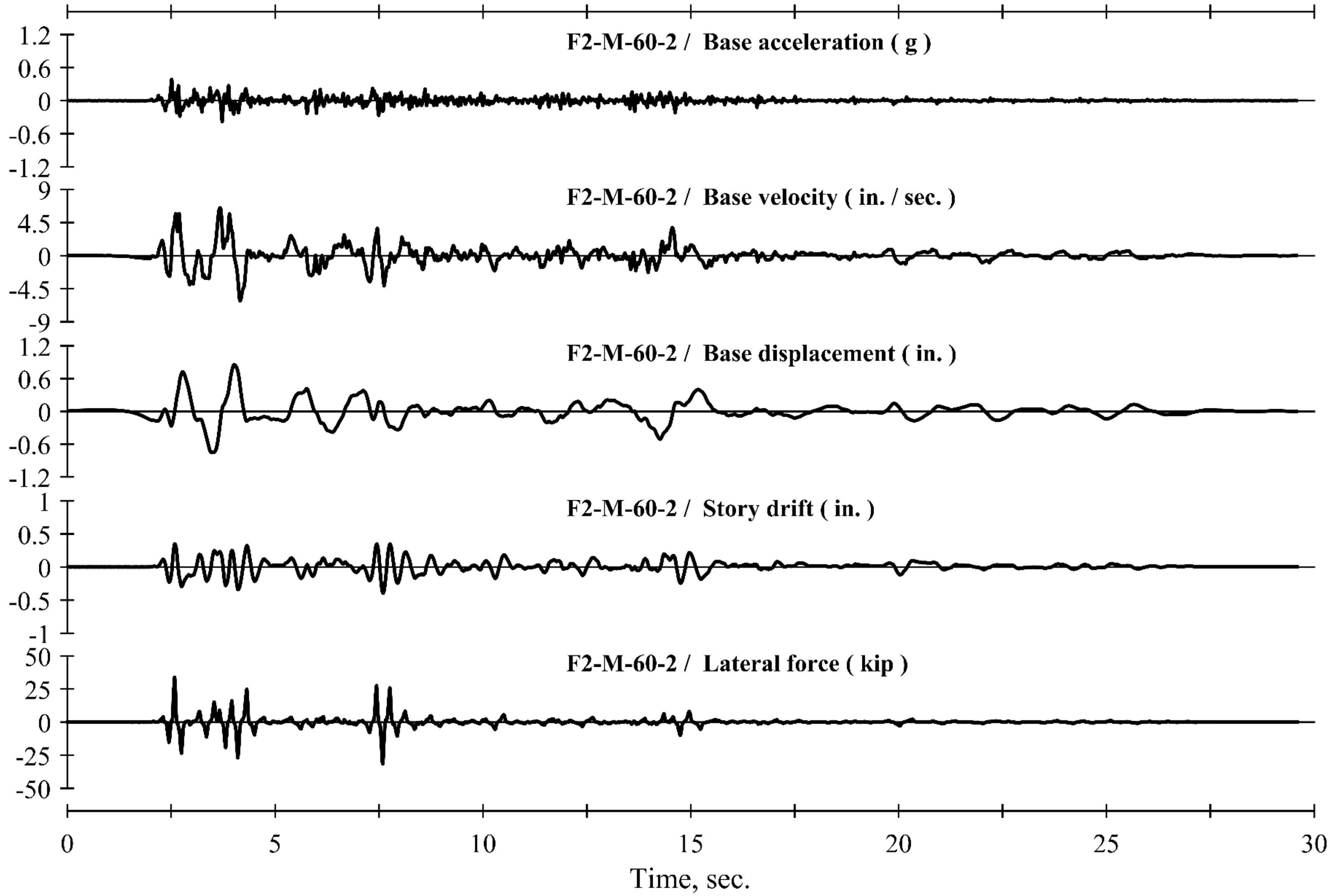

Figure D-155: Base motion and structural response histories in Run 77 of Specimen F2

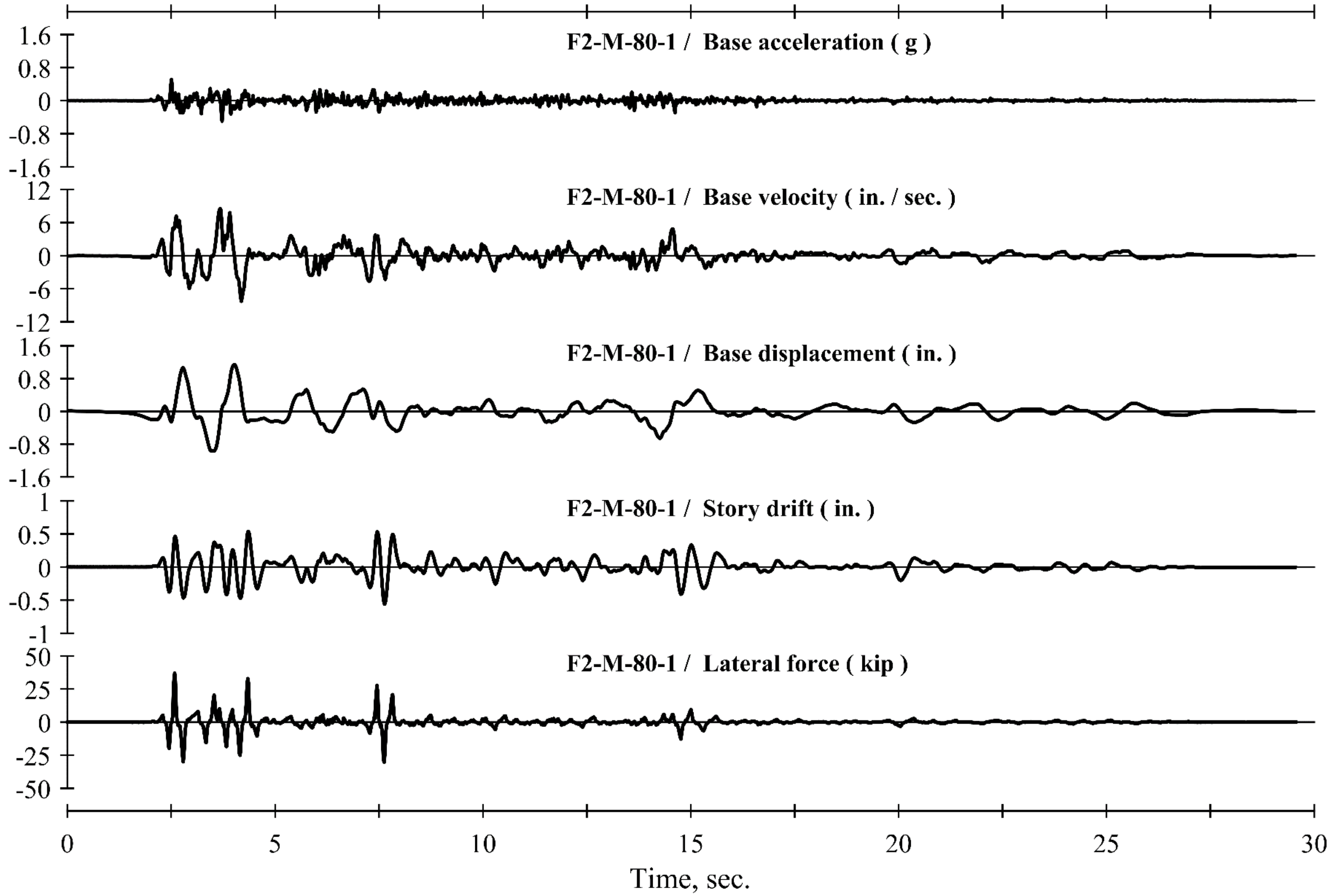

Figure D-156: Base motion and structural response histories in Run 78 of Specimen F2

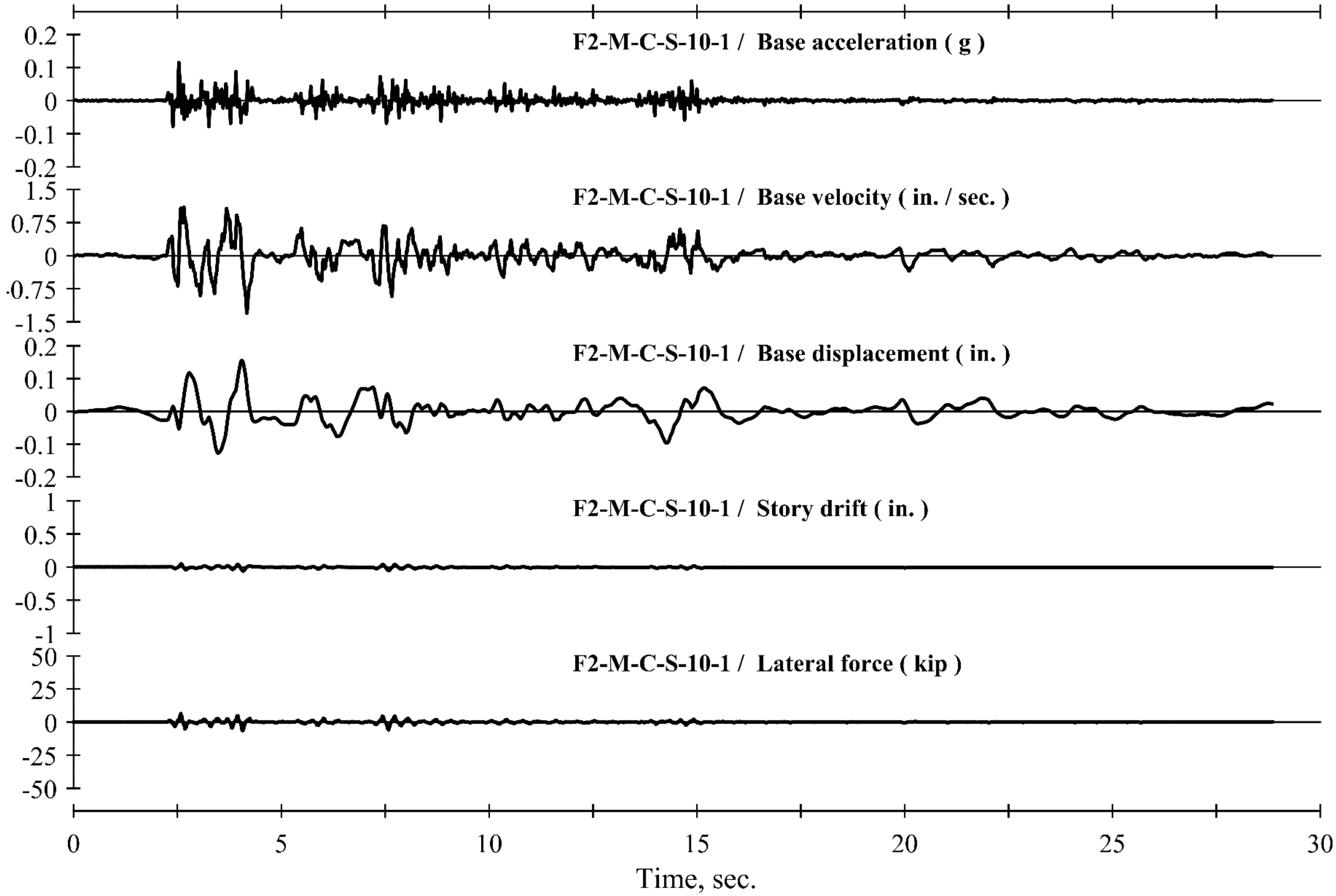

Figure D-157: Base motion and structural response histories in Run 79 of Specimen F2

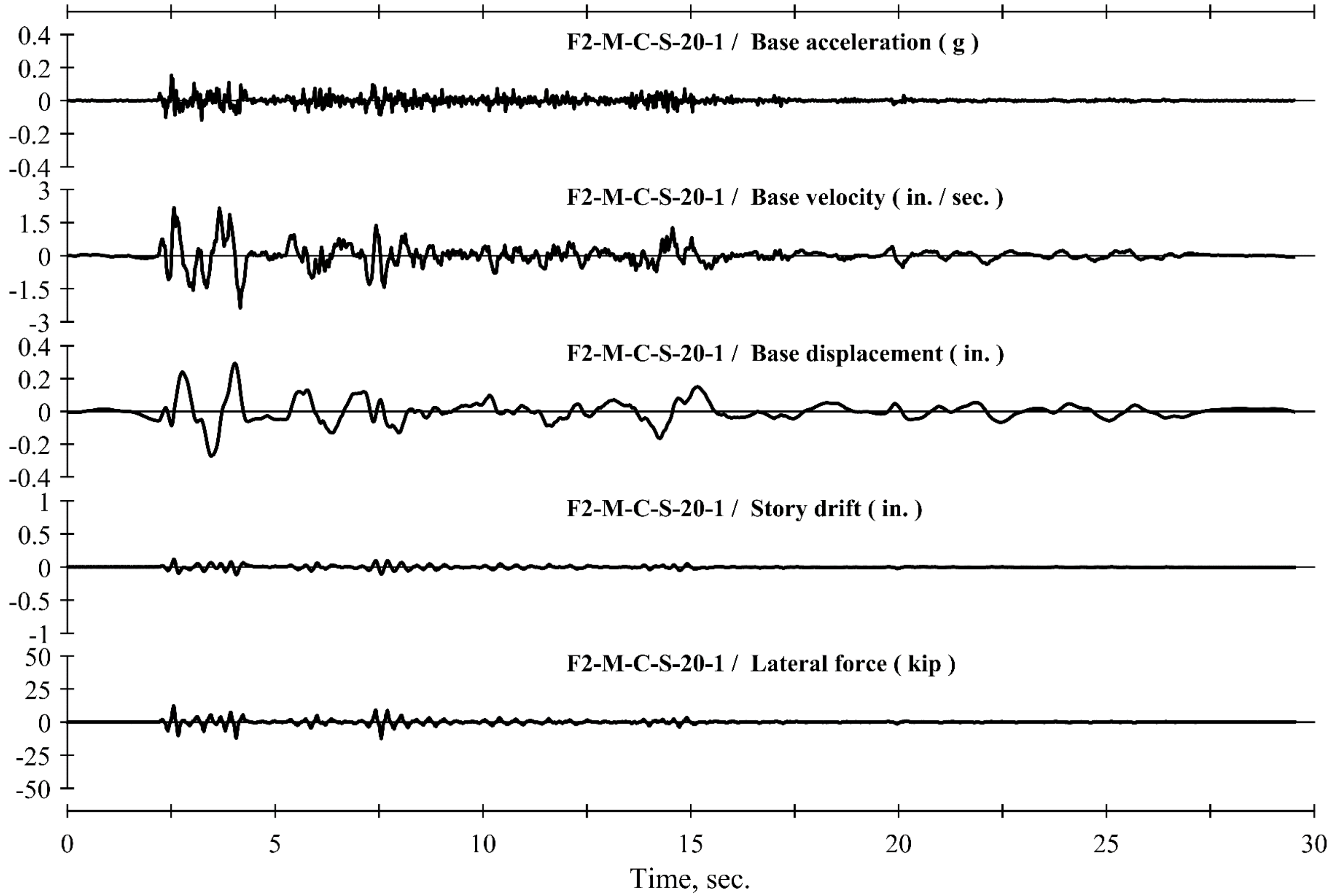

Figure D-158: Base motion and structural response histories in Run 80 of Specimen F2

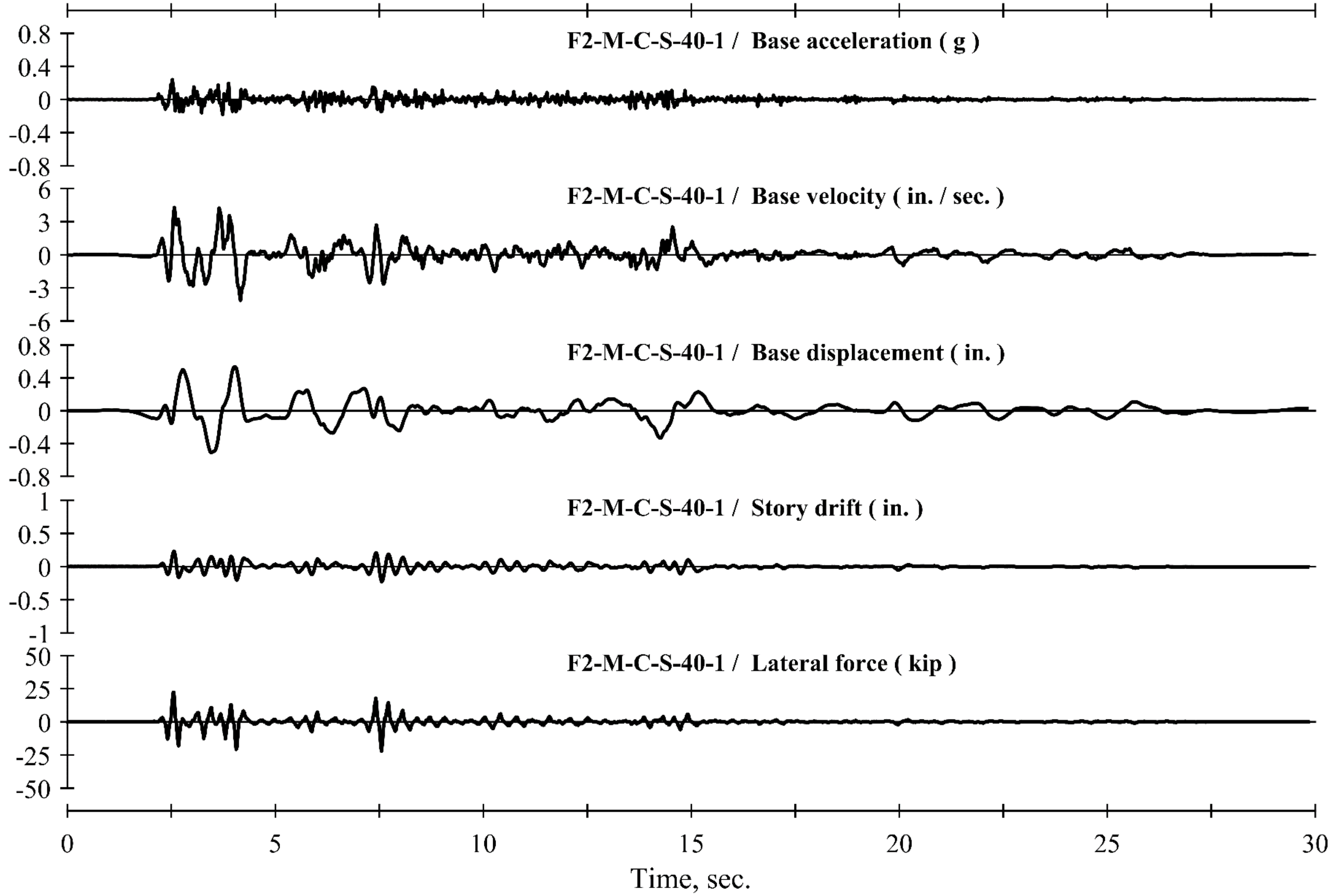

Figure D-159: Base motion and structural response histories in Run 81 of Specimen F2

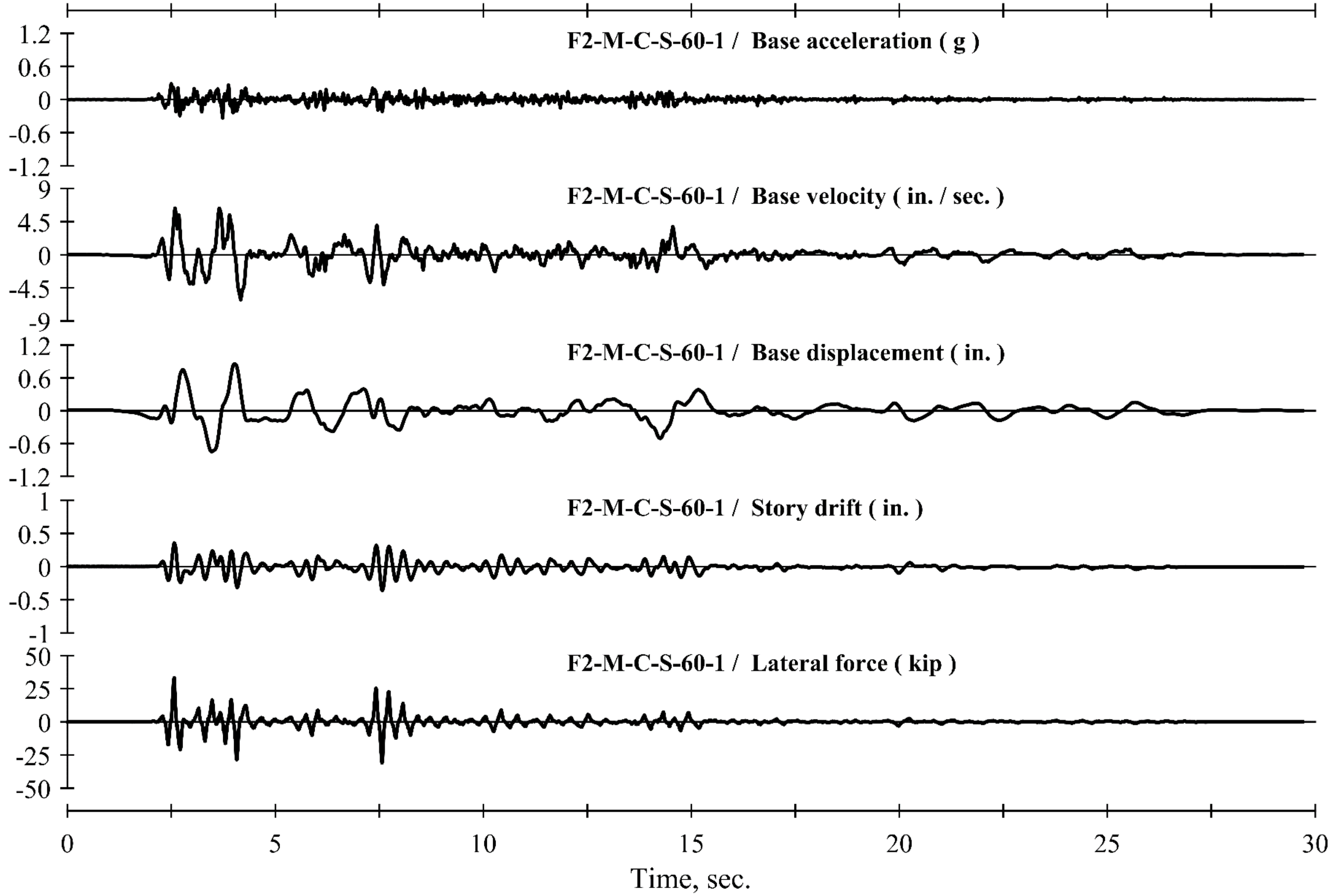

Figure D-160: Base motion and structural response histories in Run 82 of Specimen F2

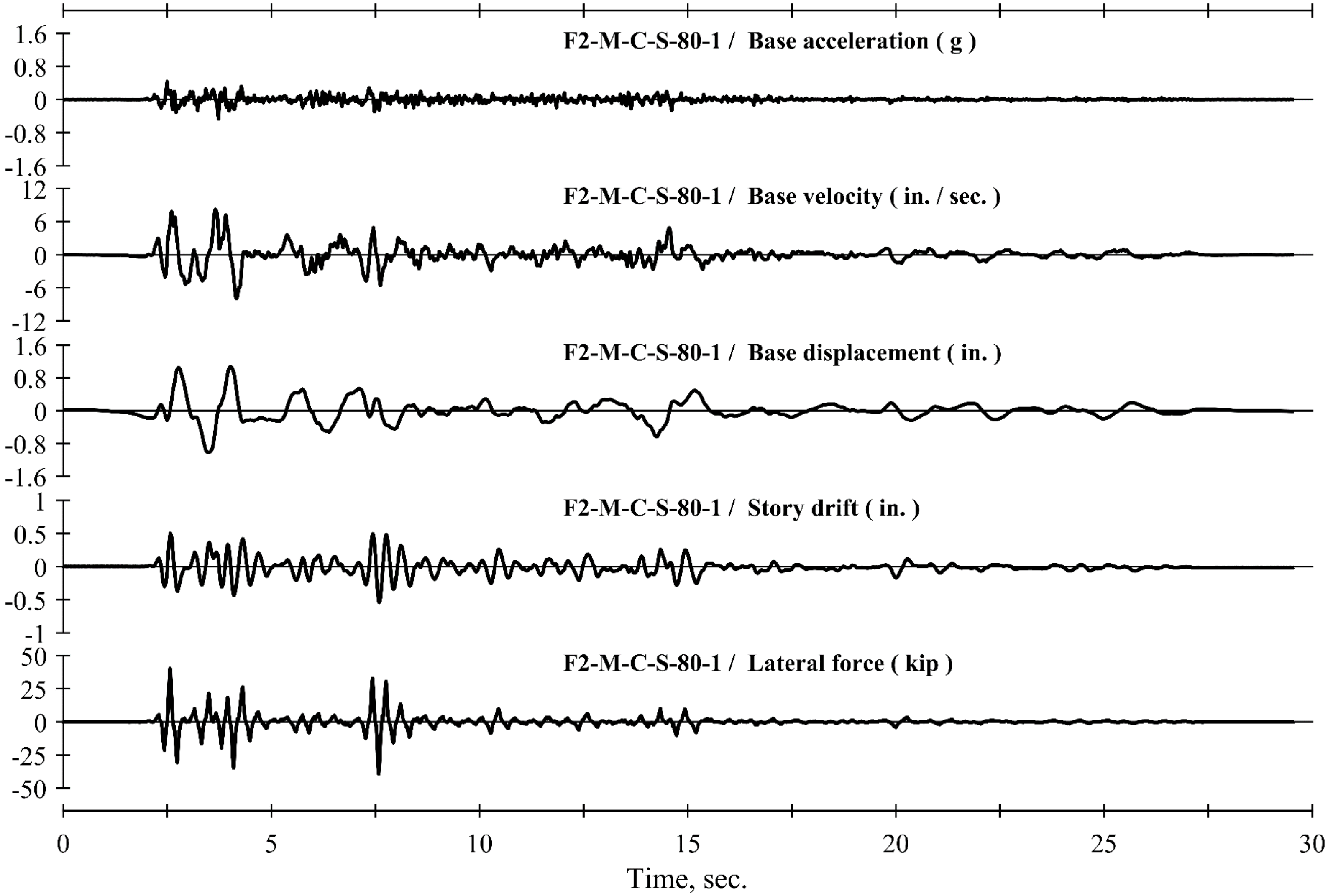

Figure D-161: Base motion and structural response histories in Run 83 of Specimen F2

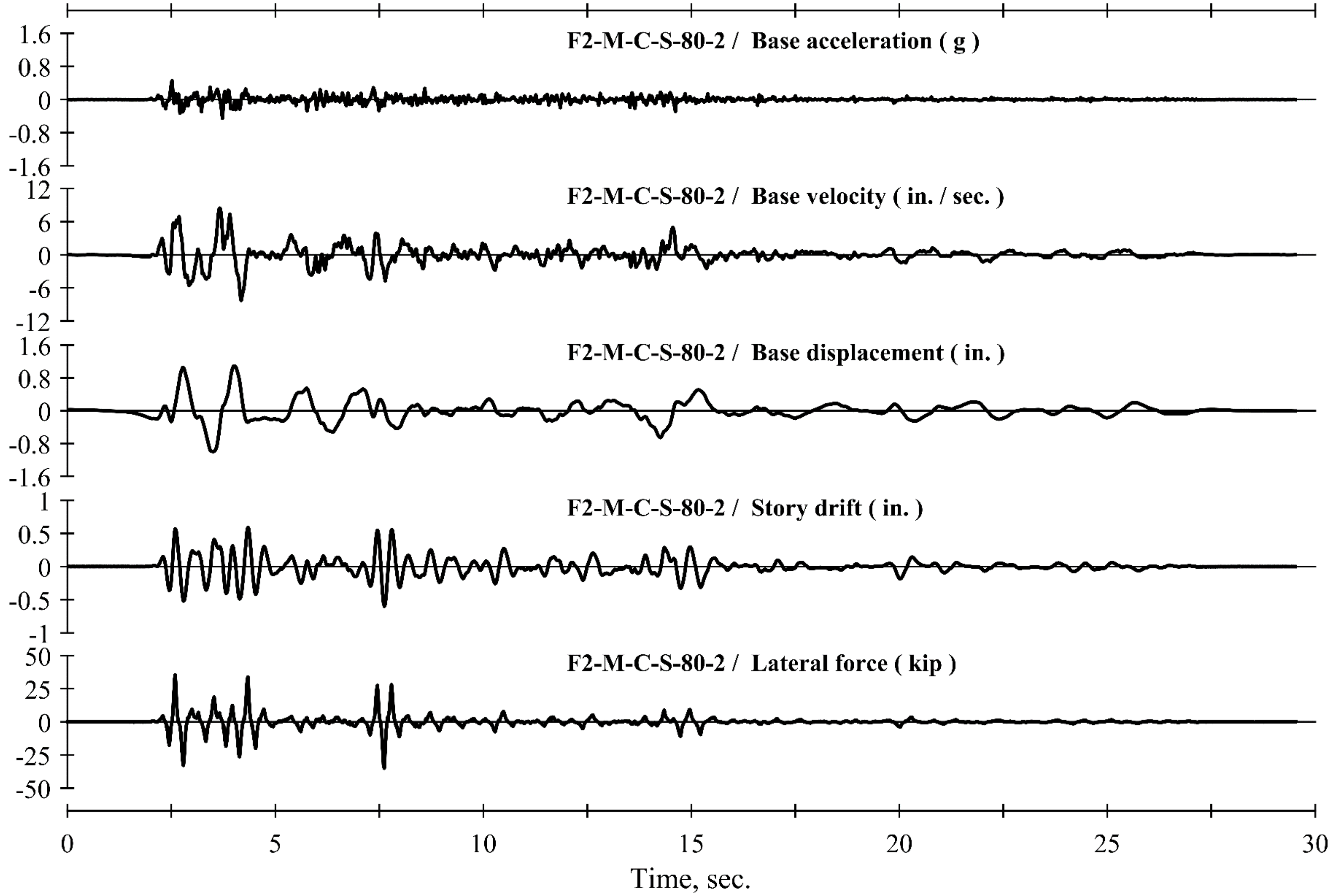

Figure D-162: Base motion and structural response histories in Run 84 of Specimen F2

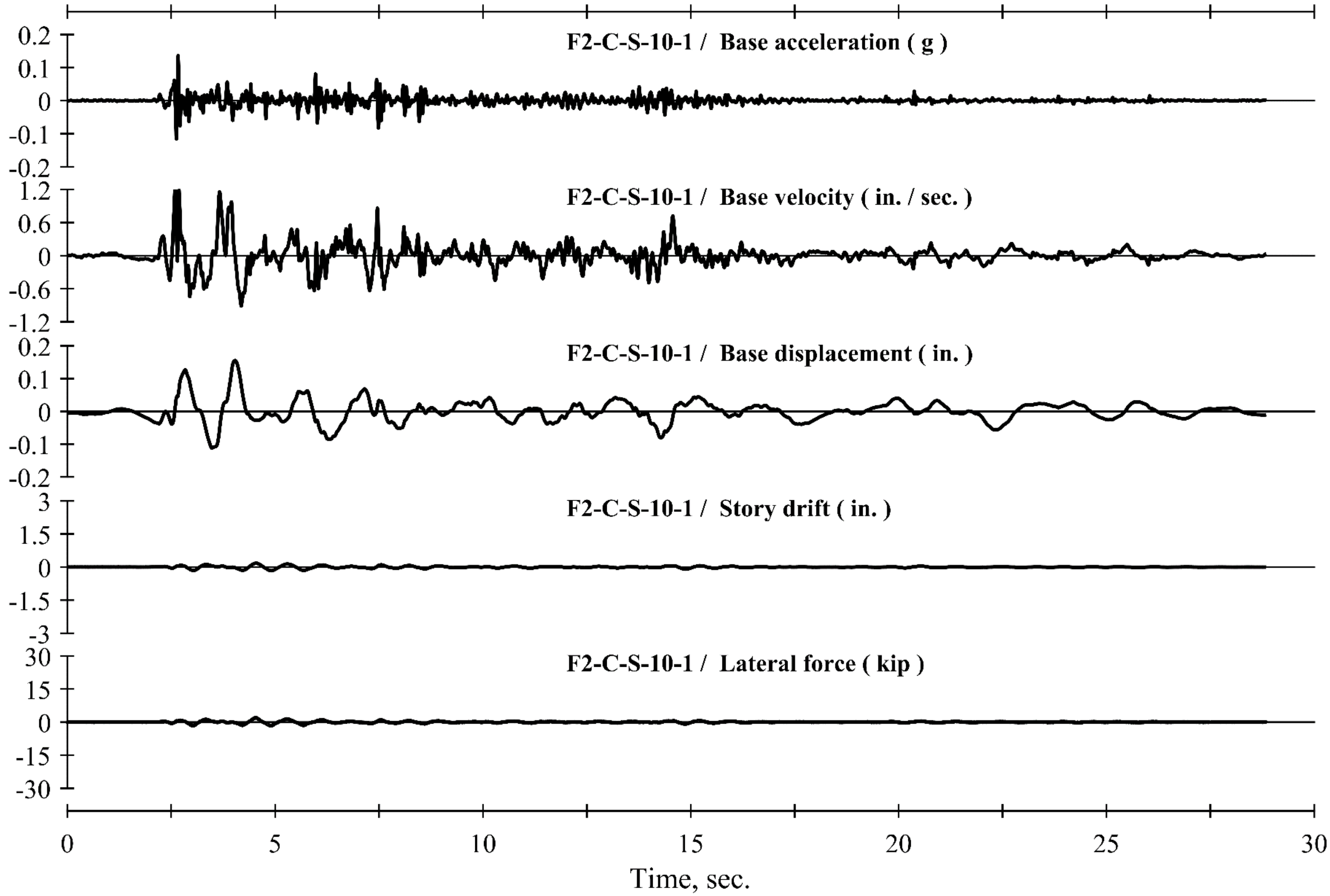

Figure D-163: Base motion and structural response histories in Run 85 of Specimen F2

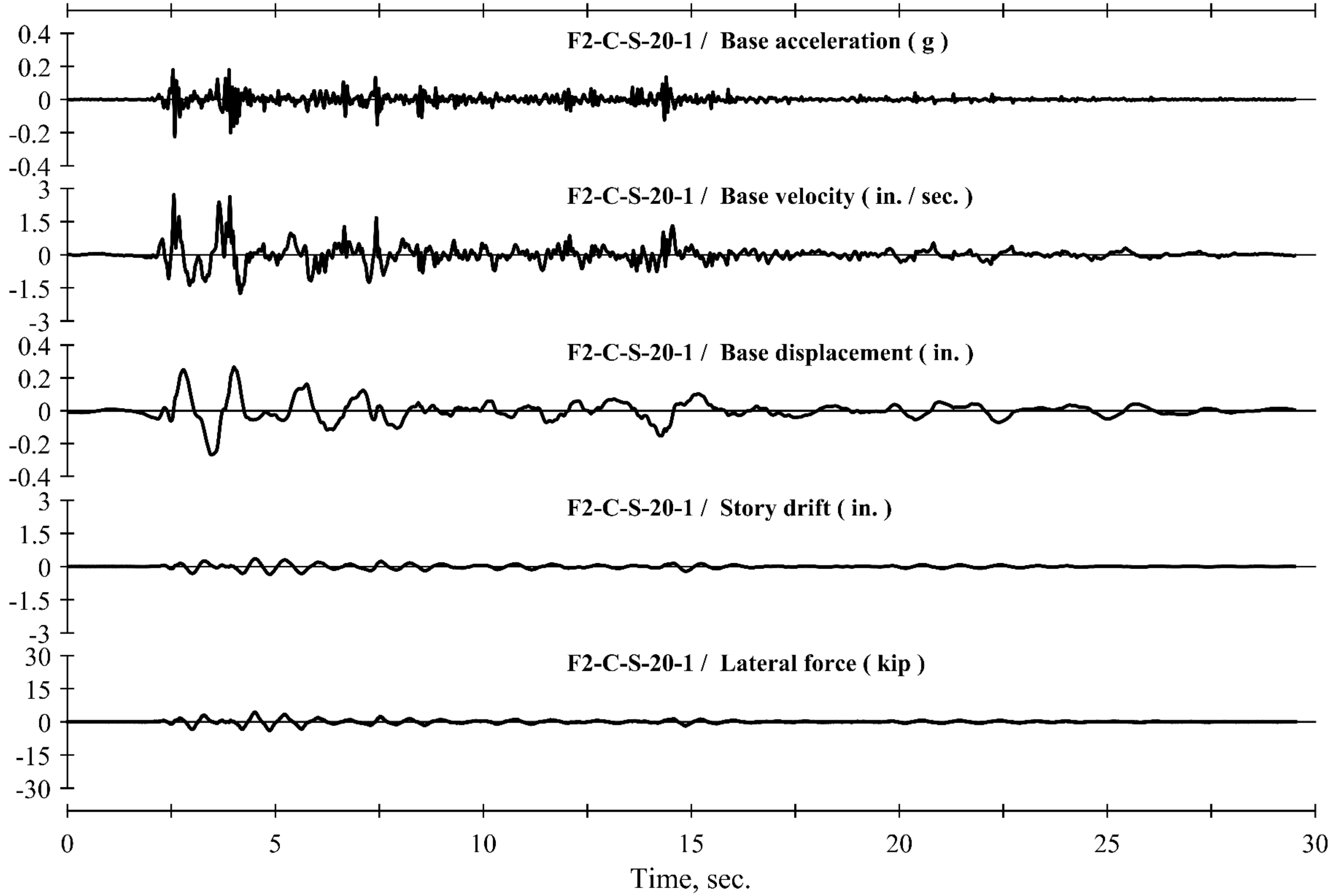

Figure D-164: Base motion and structural response histories in Run 86 of Specimen F2

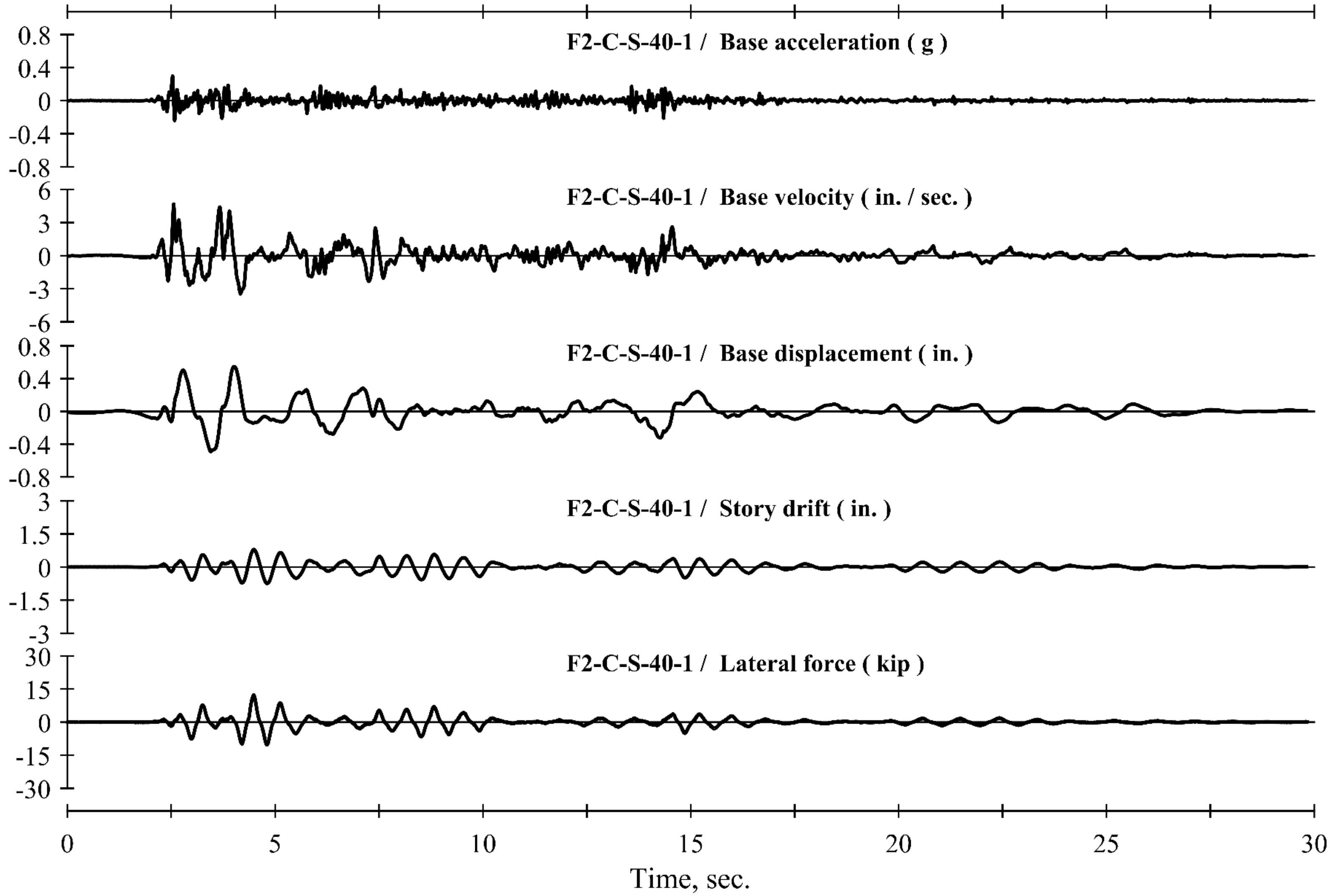

Figure D-165: Base motion and structural response histories in Run 87 of Specimen F2

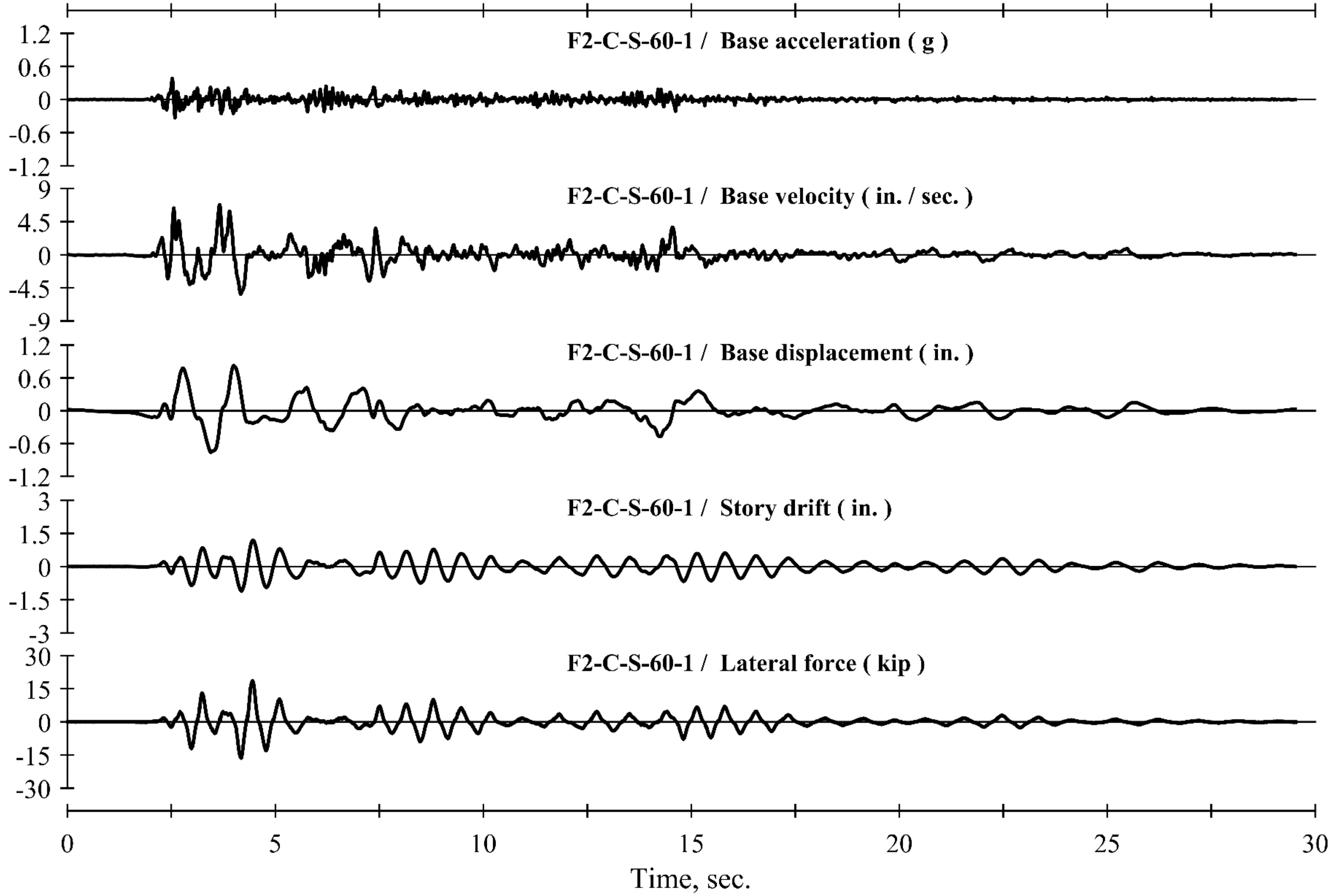

Figure D-166: Base motion and structural response histories in Run 88 of Specimen F2

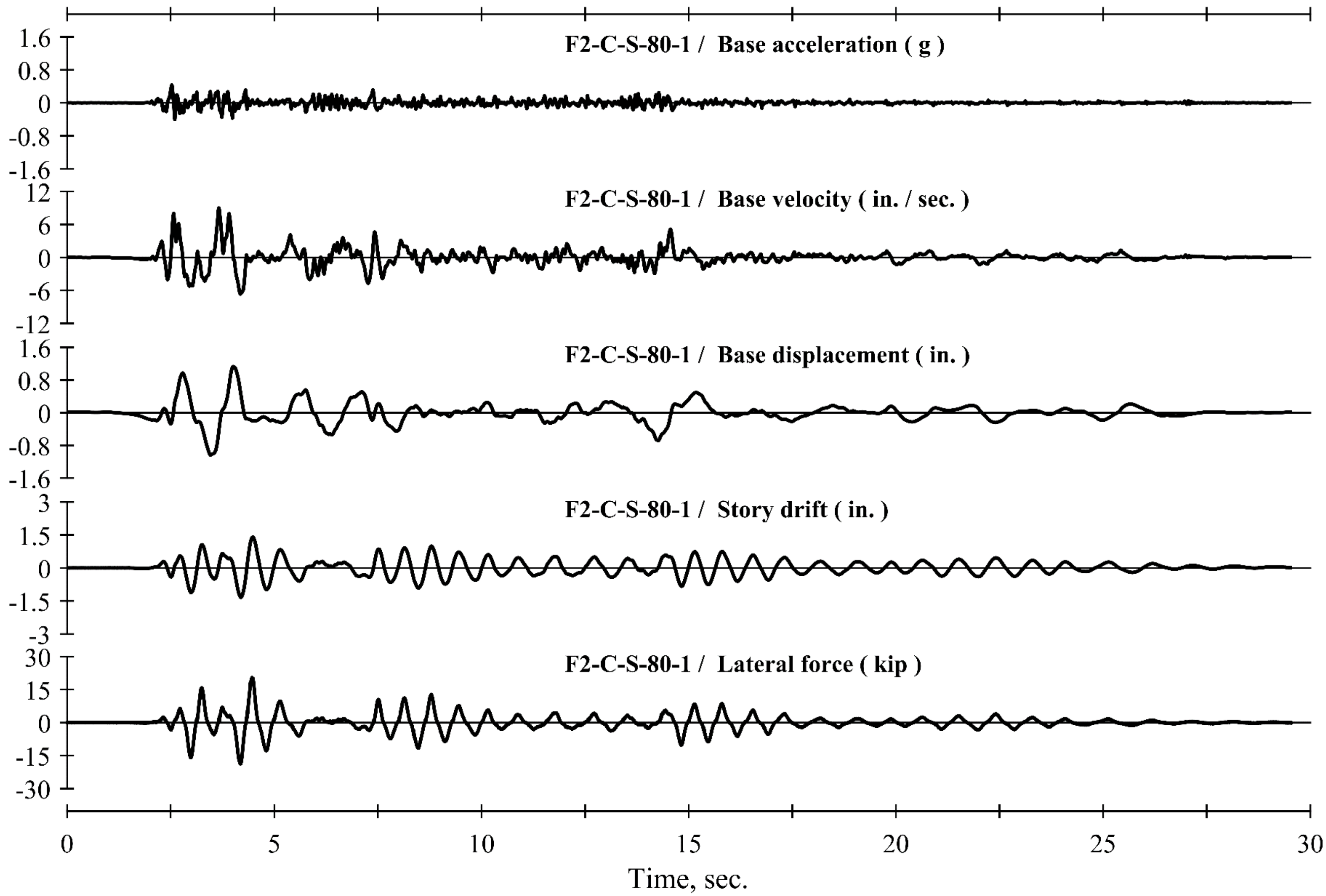

Figure D-167: Base motion and structural response histories in Run 89 of Specimen F2

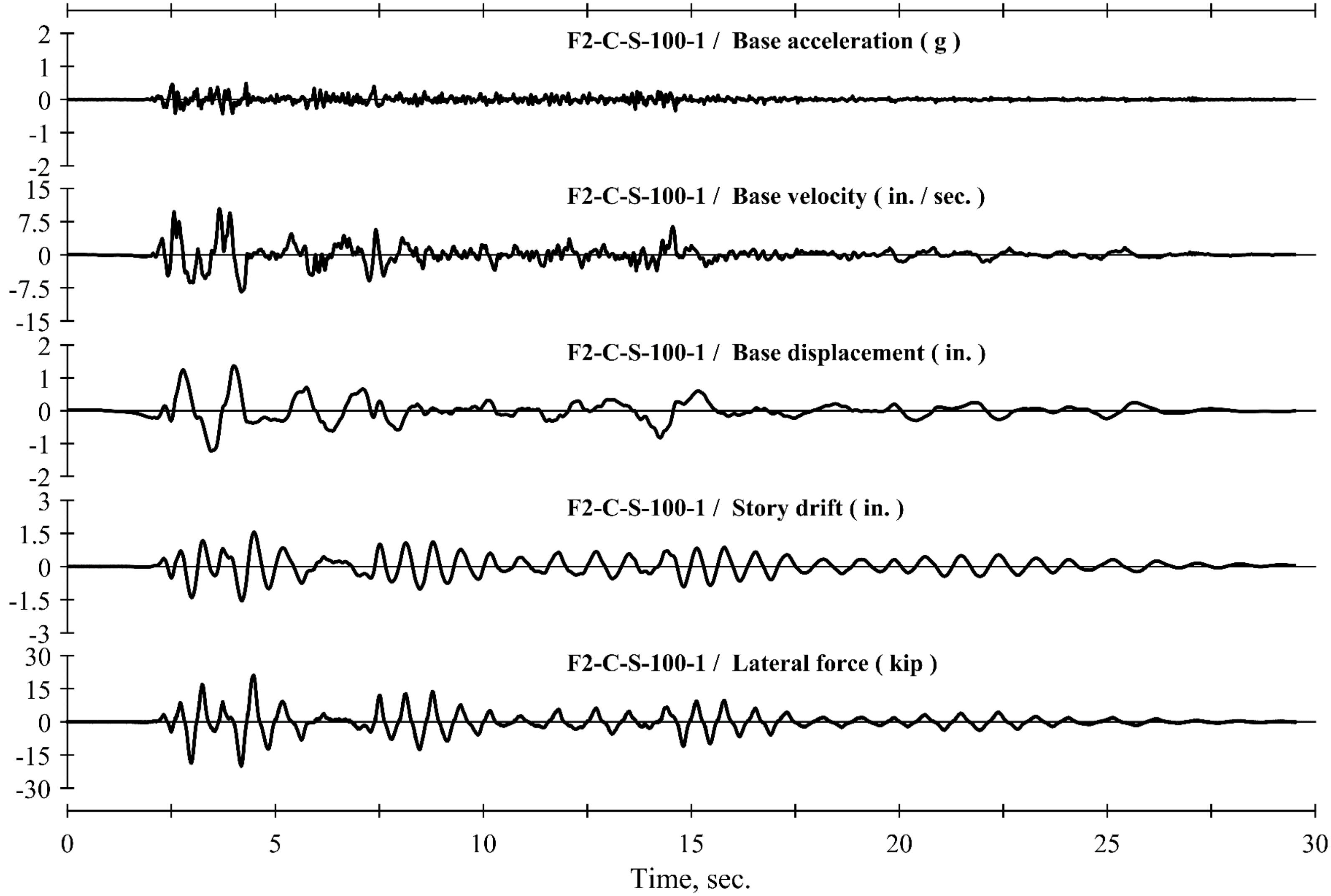

Figure D-168: Base motion and structural response histories in Run 90 of Specimen F2

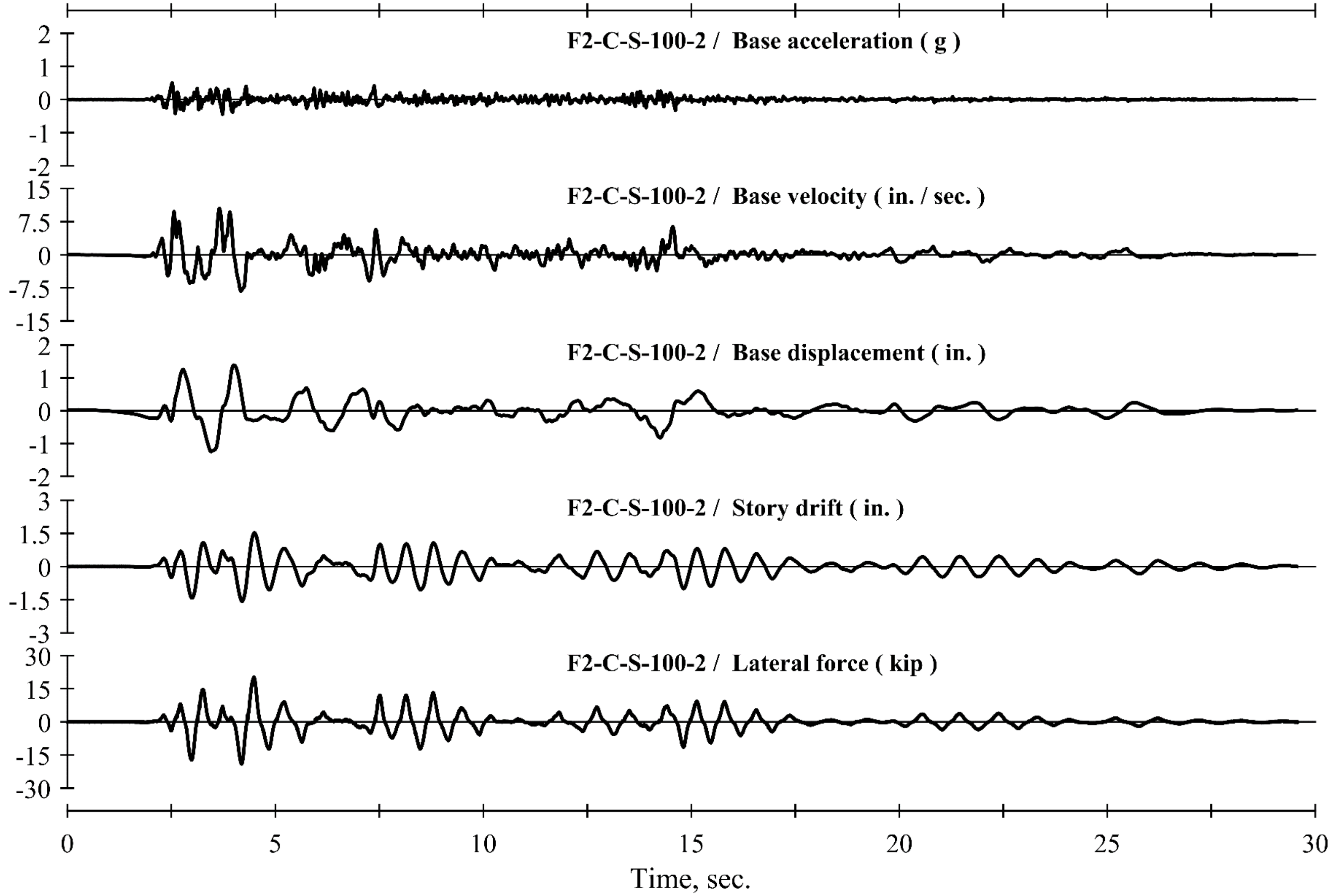

Figure D-169: Base motion and structural response histories in Run 91 of Specimen F2

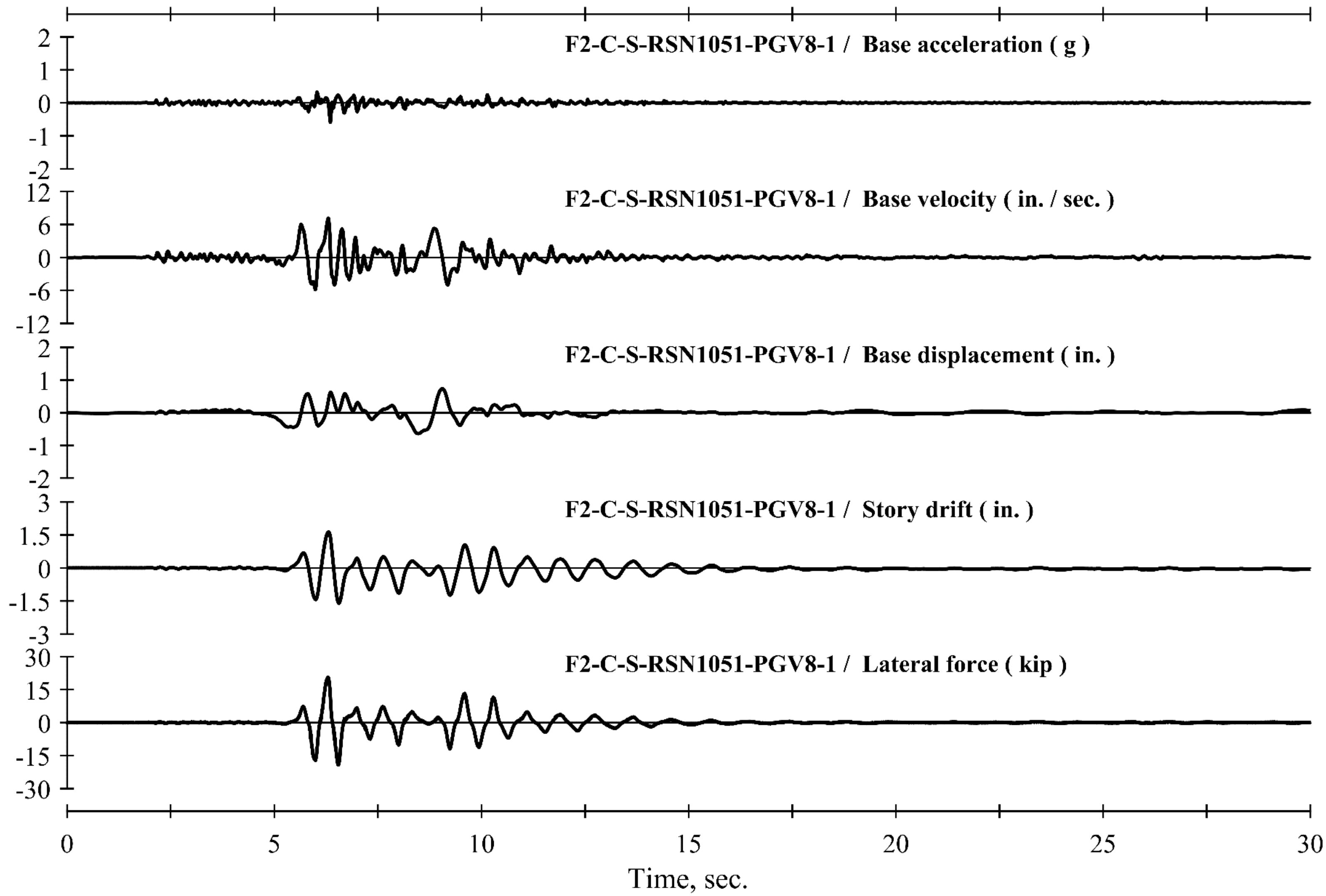

Figure D-170: Base motion and structural response histories in Run 92 of Specimen F2

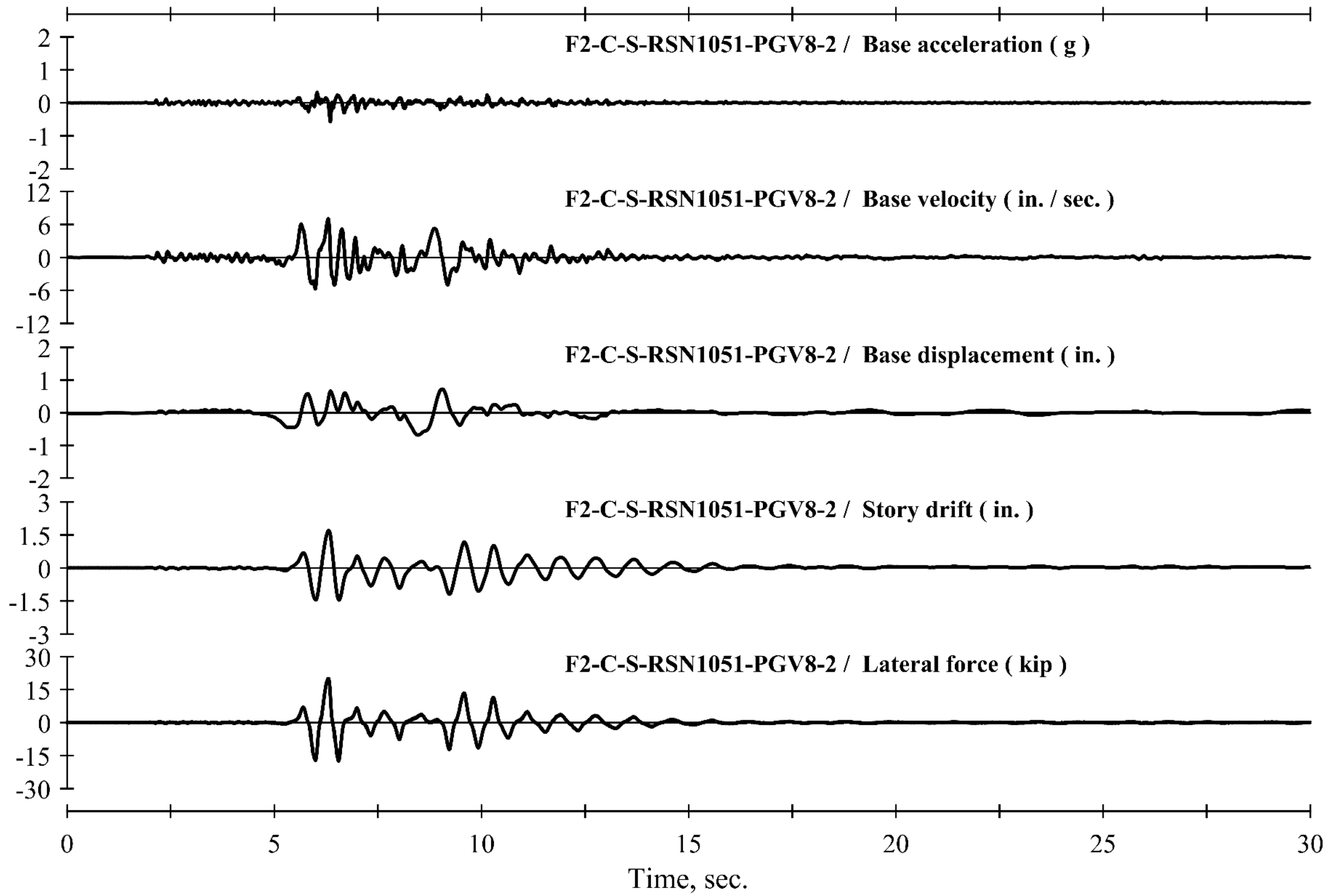

Figure D-171: Base motion and structural response histories in Run 93 of Specimen F2

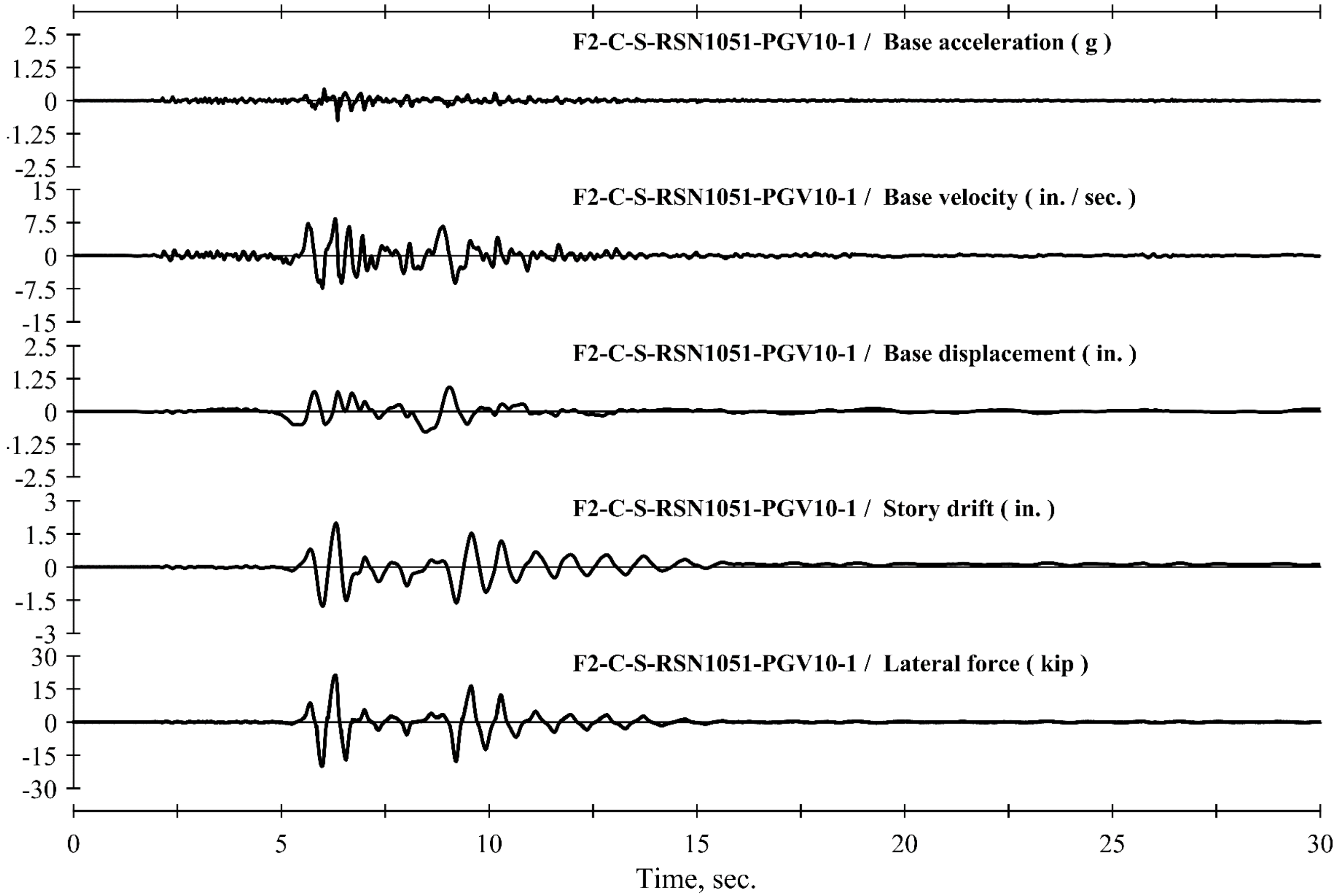

Figure D-172: Base motion and structural response histories in Run 94 of Specimen F2

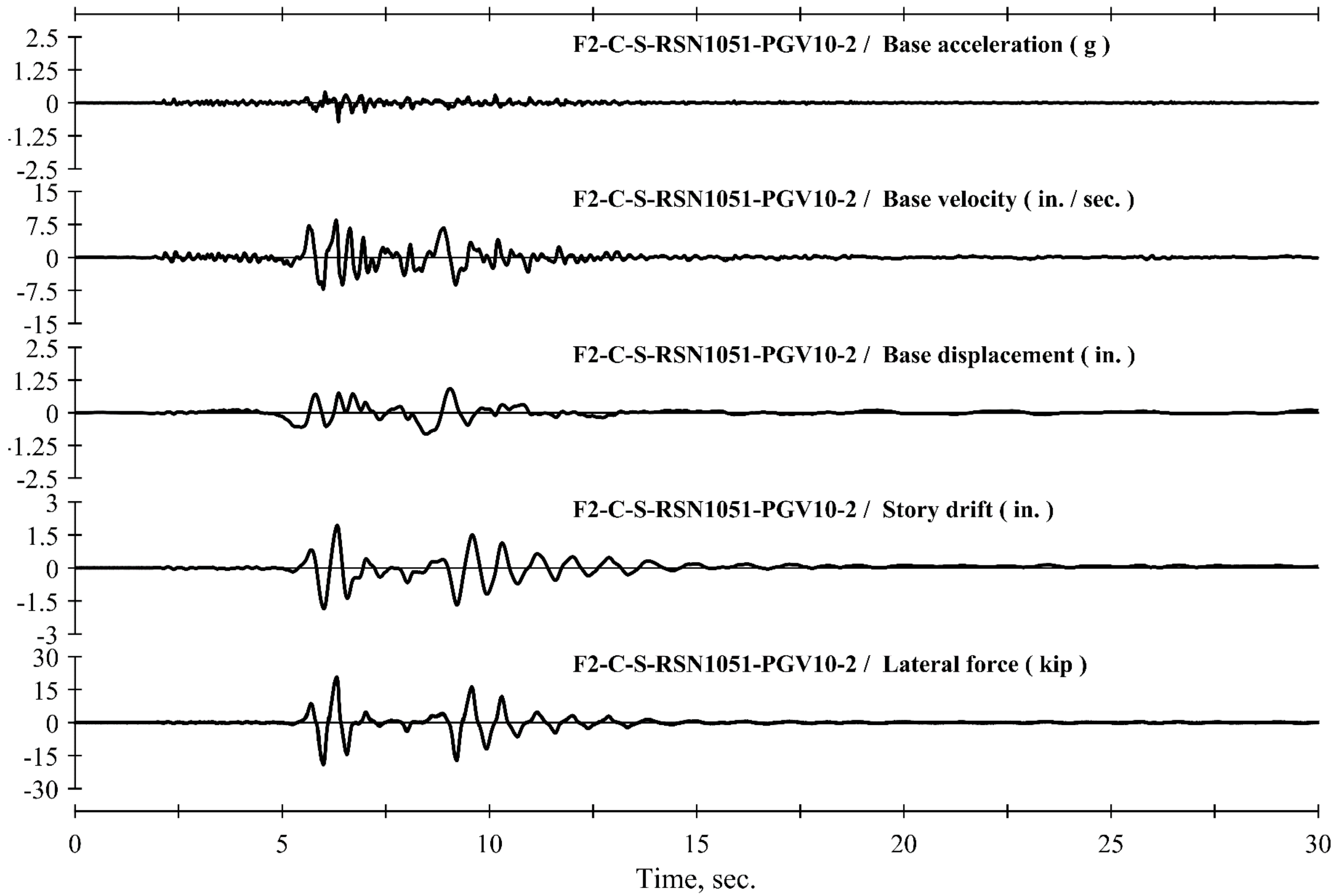

Figure D-173: Base motion and structural response histories in Run 95 of Specimen F2

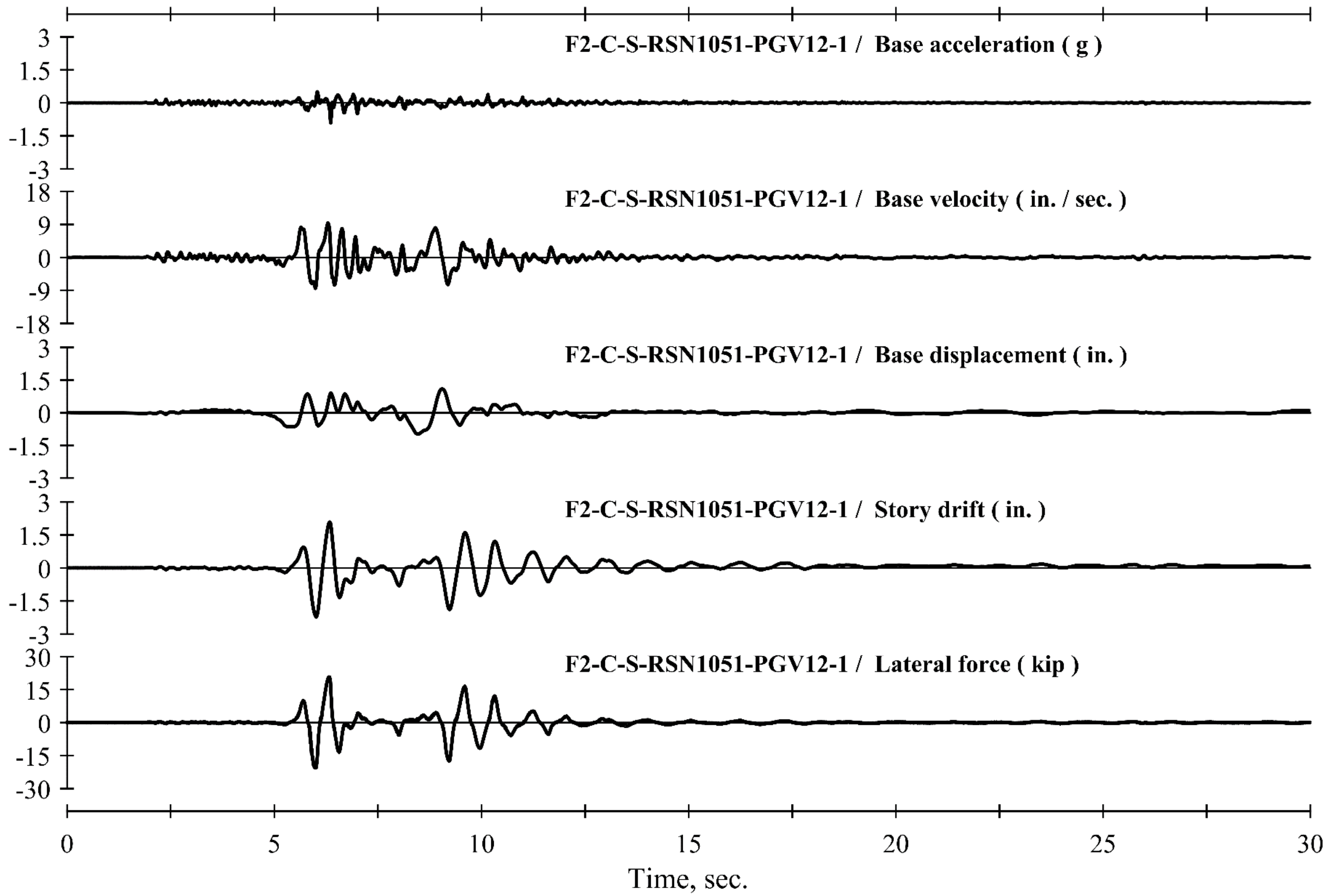

Figure D-174: Base motion and structural response histories in Run 96 of Specimen F2

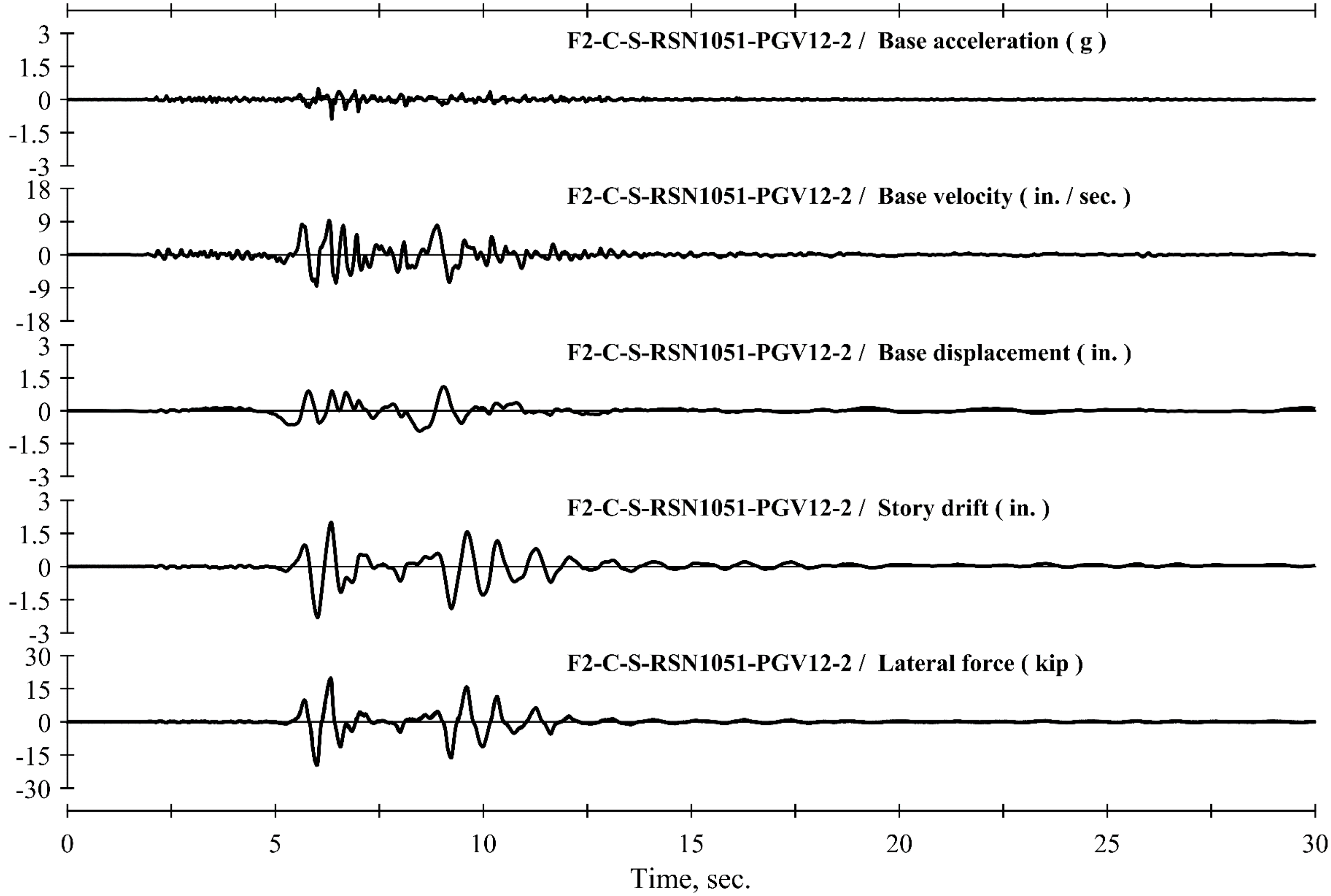

Figure D-175: Base motion and structural response histories in Run 97 of Specimen F2

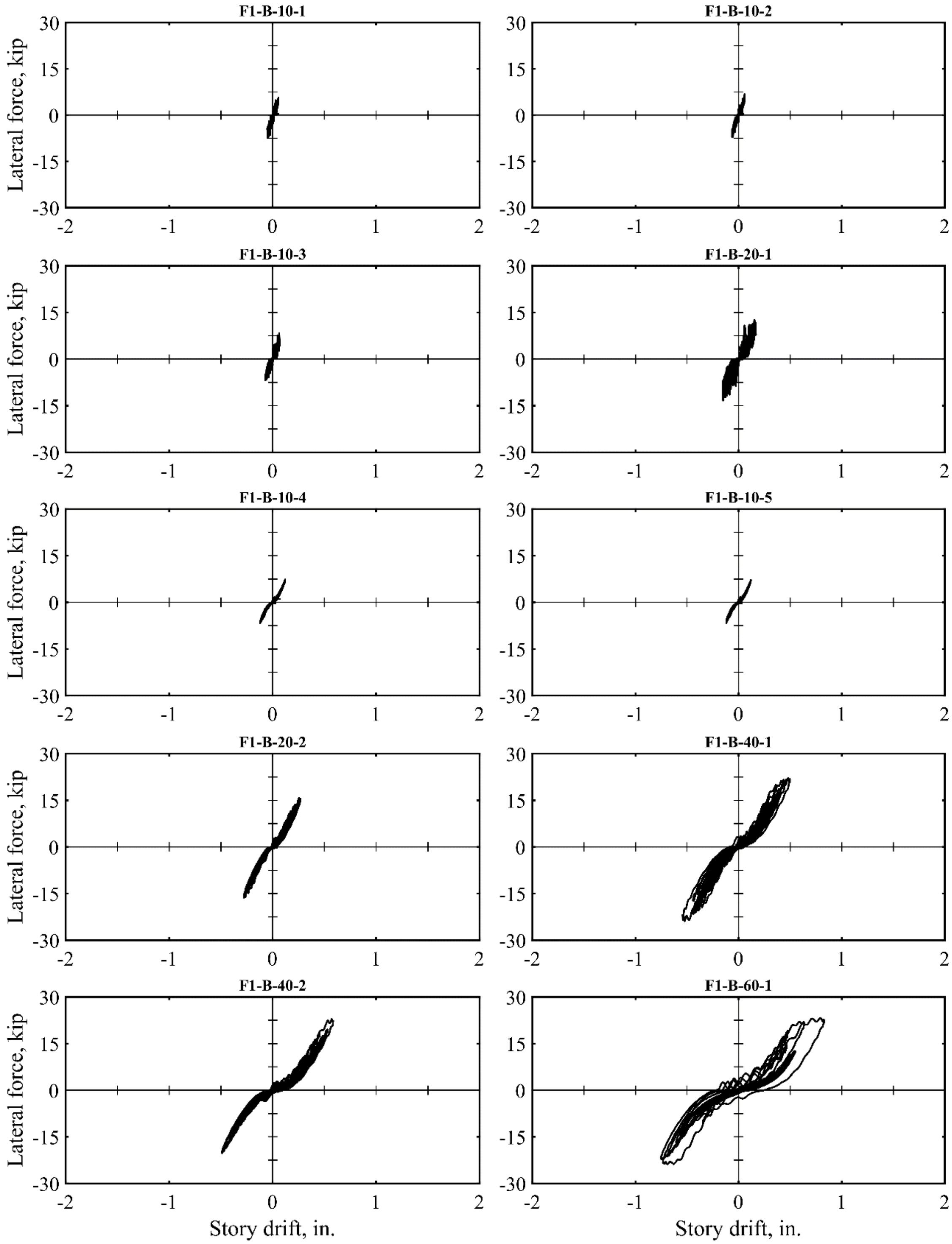

Figure D-176: Force-displacement response in Series F1-B

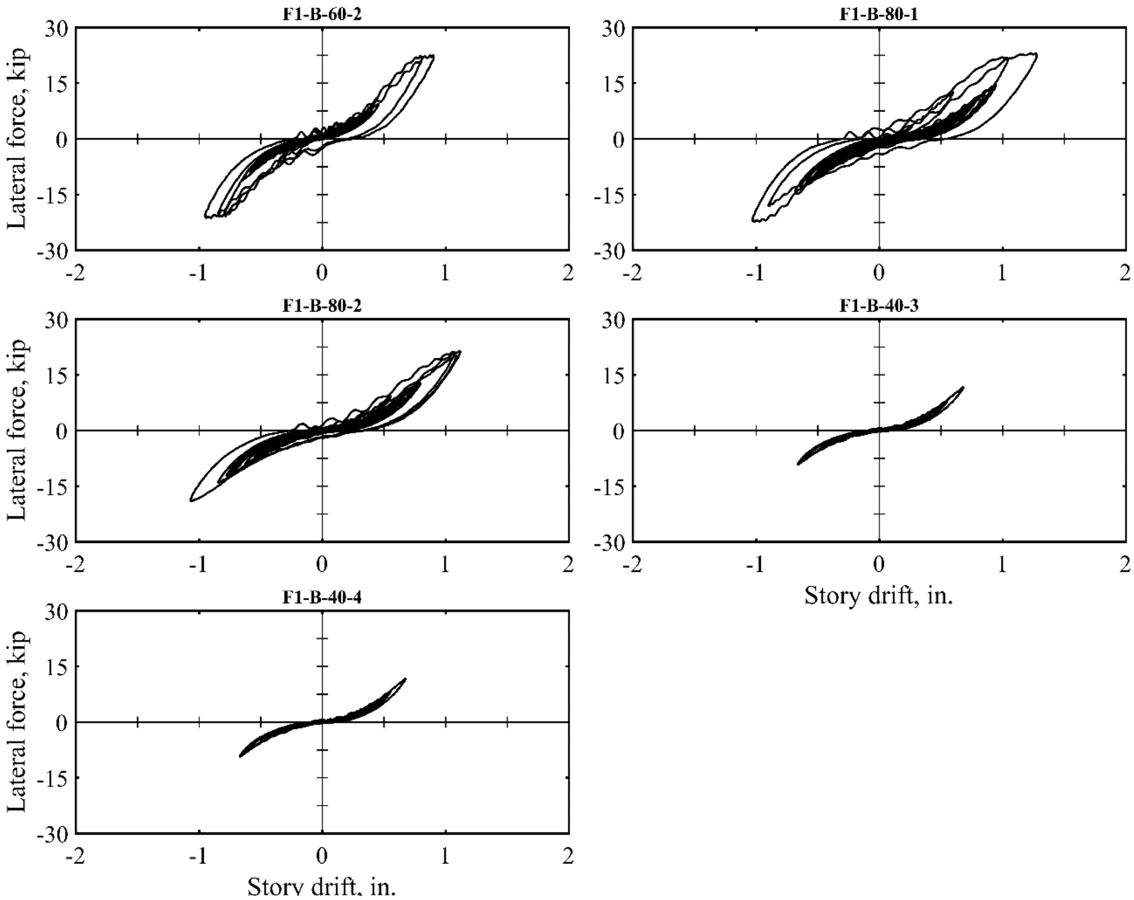

Figure D-176 (continued): Force-displacement response in Series F1-B

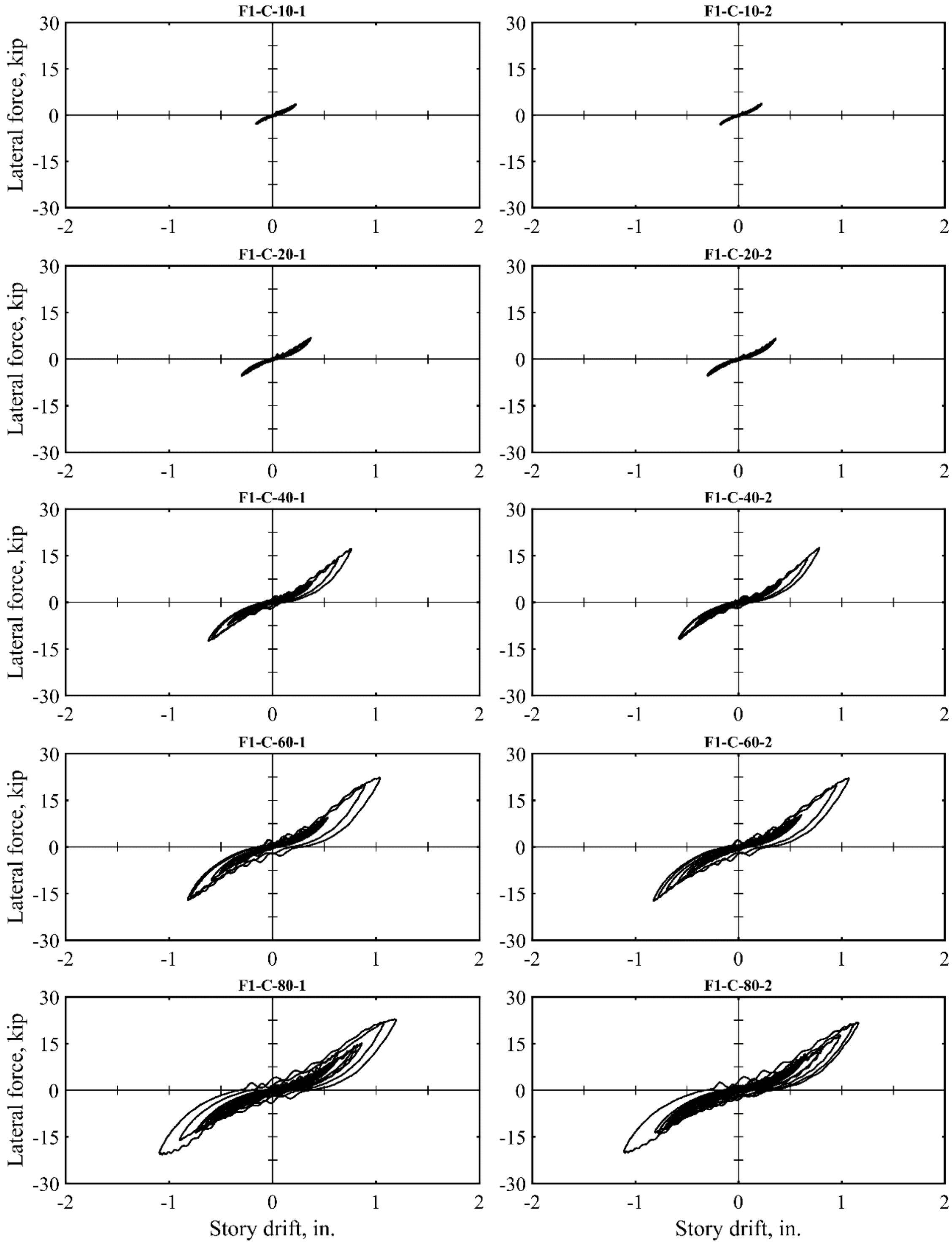

Figure D-177: Force-displacement response in Series F1-C

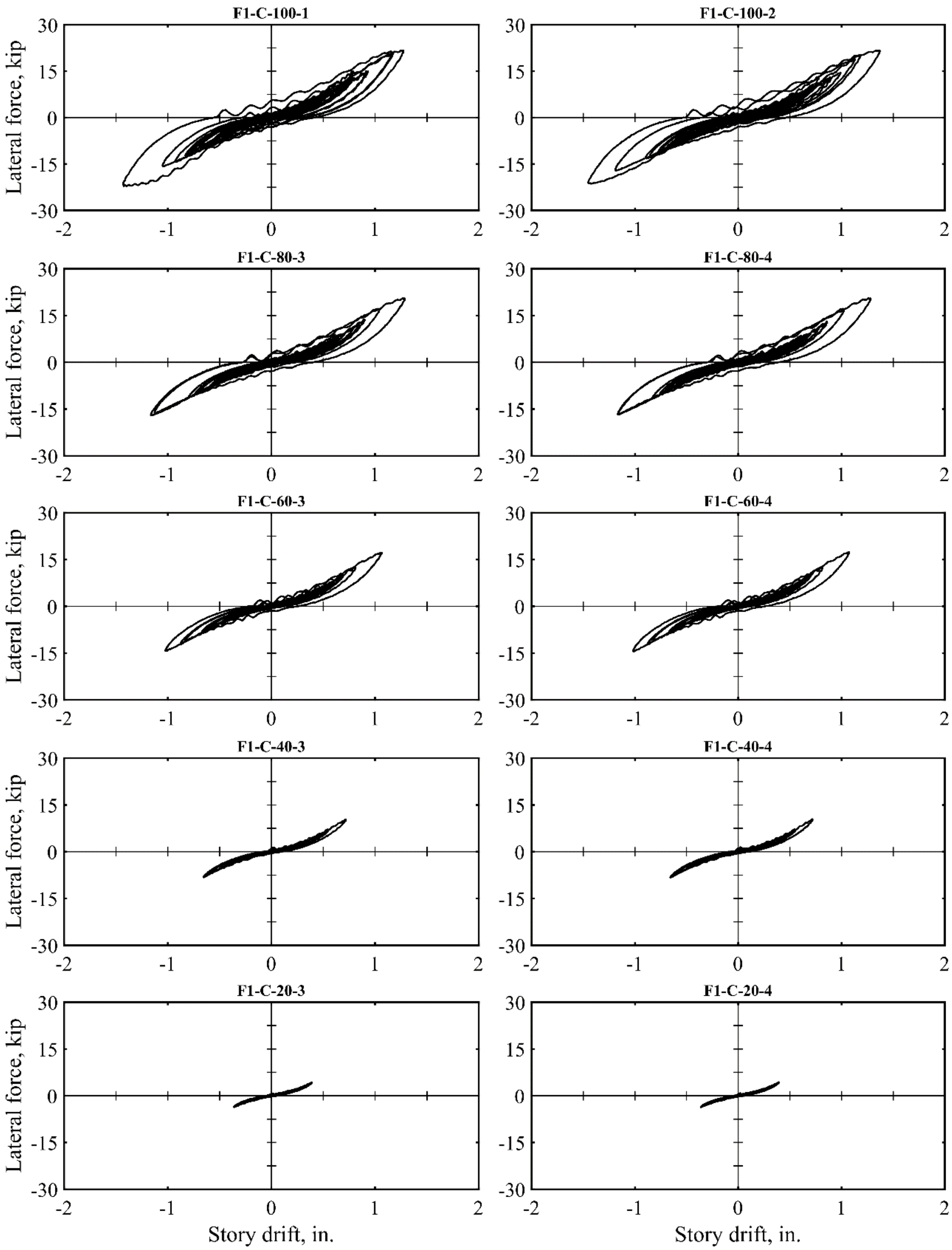

Figure D-177 (continued): Force-displacement response in Series F1-C

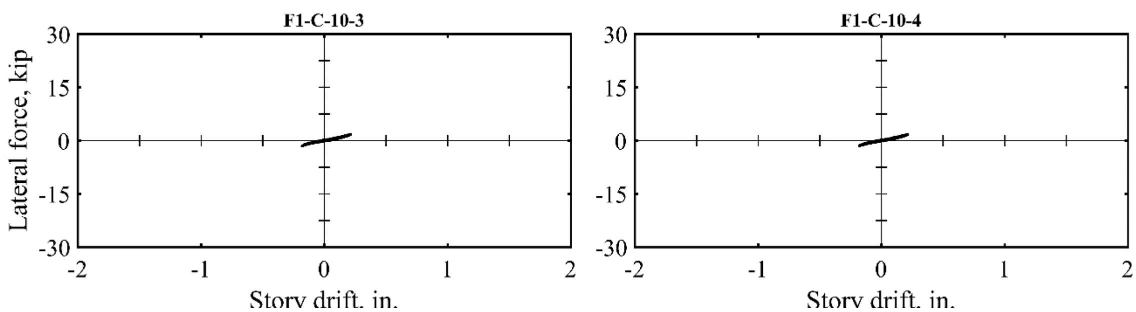

Figure D-177 (continued): Force-displacement response in Series F1-C

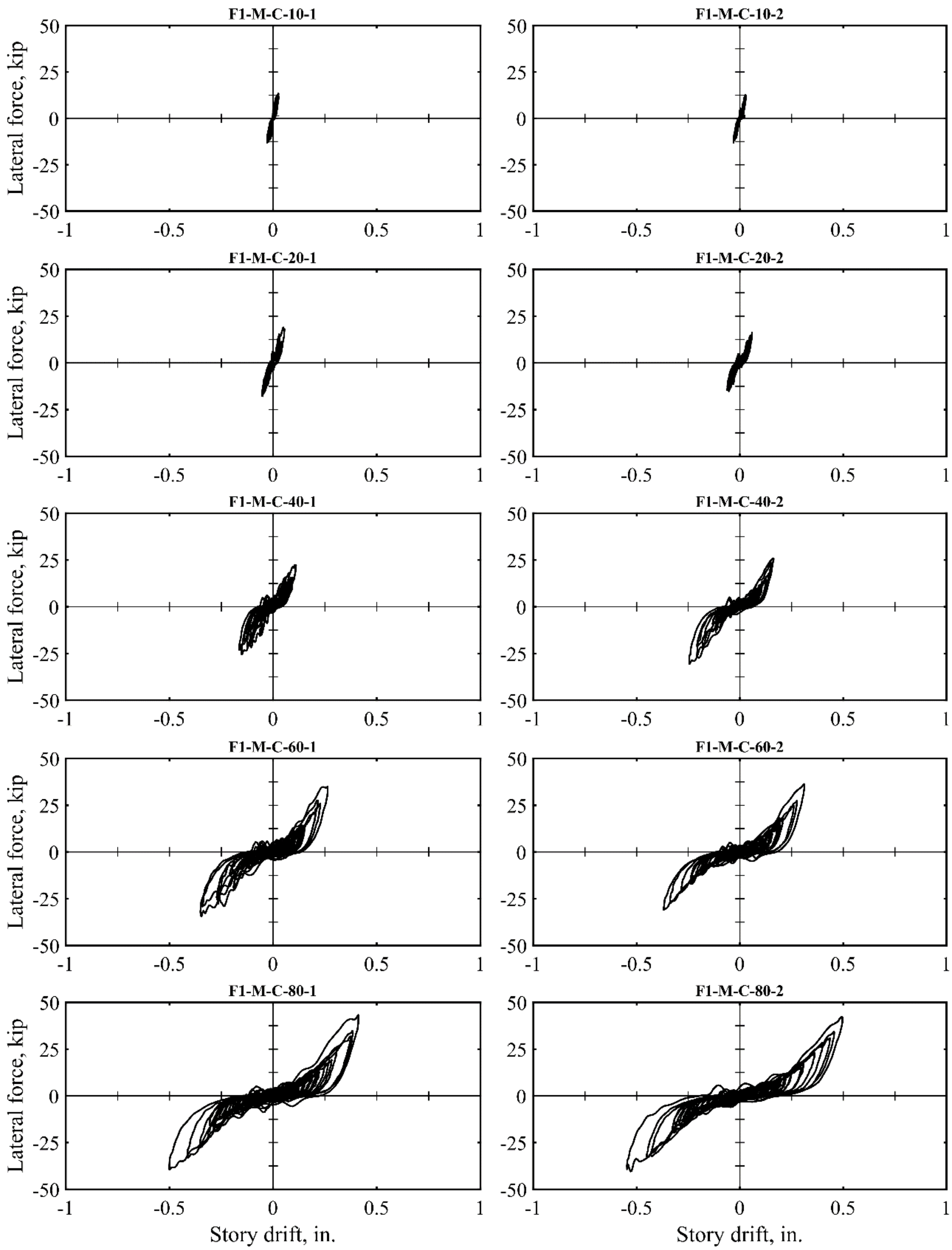

Figure D-178: Force-displacement response in Series F1-M-C

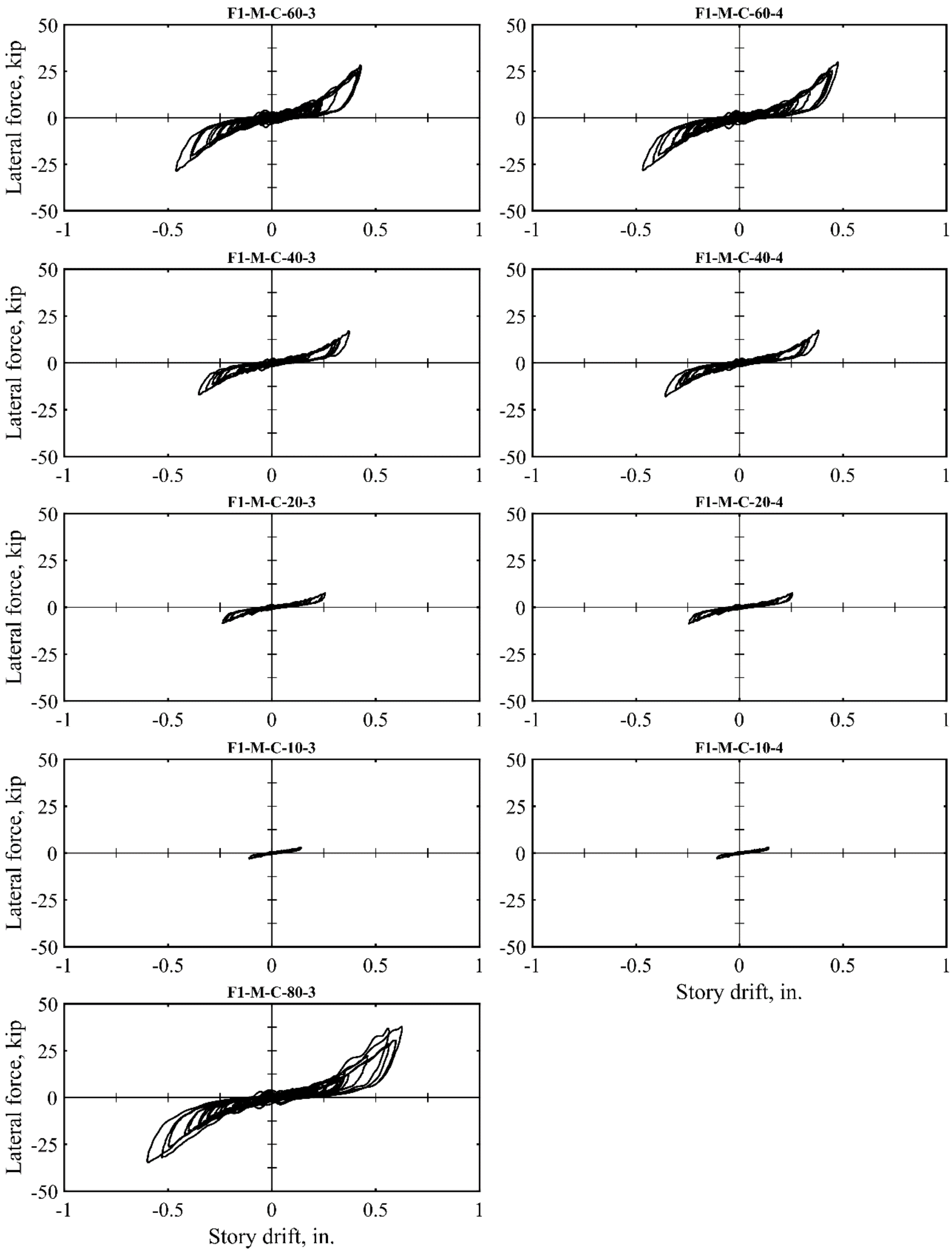

Figure D-178 (continued): Force-displacement response in Series F1-M-C

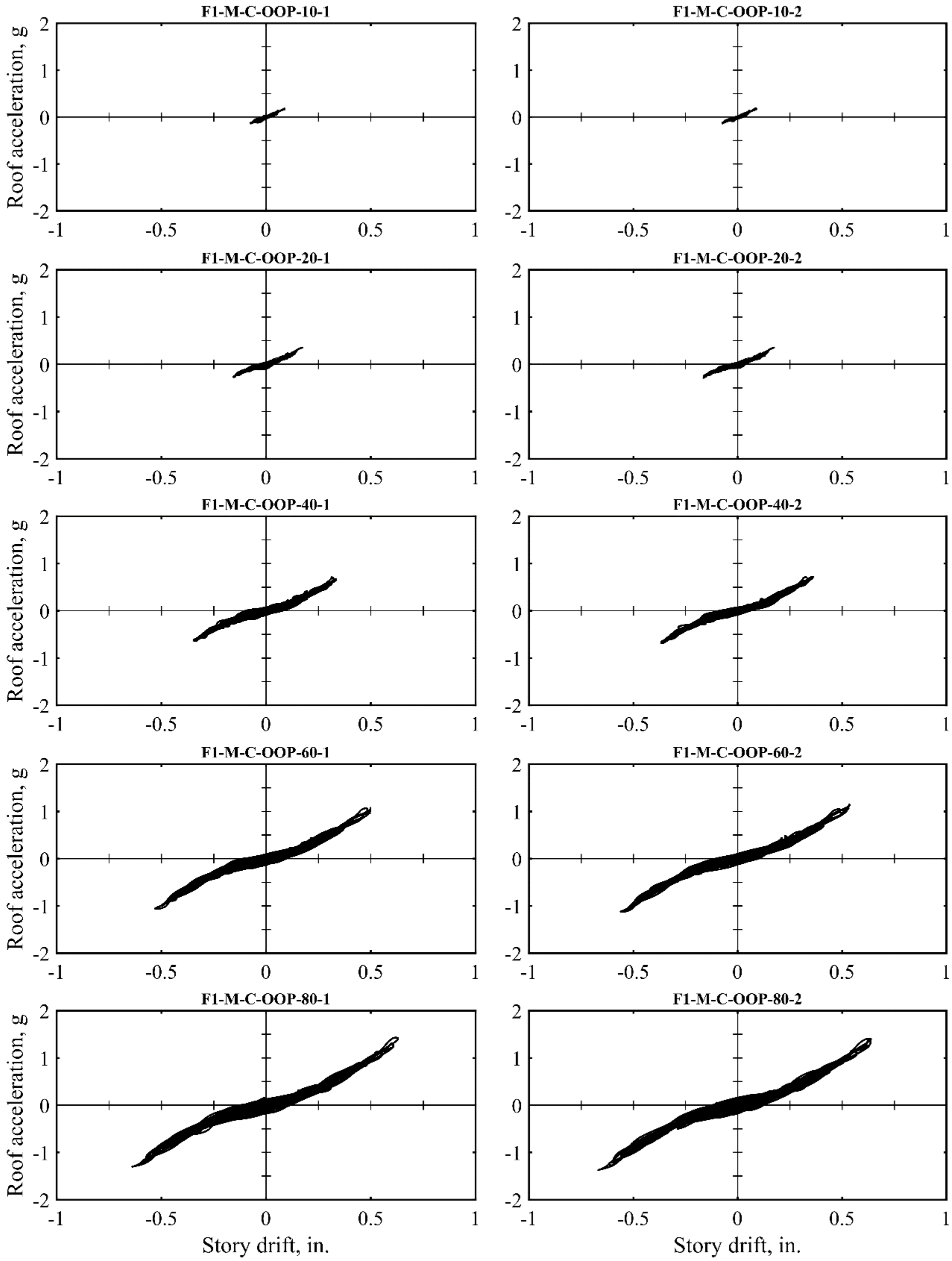

Figure D-179: Force-displacement response in Series F1-M-C-OOP

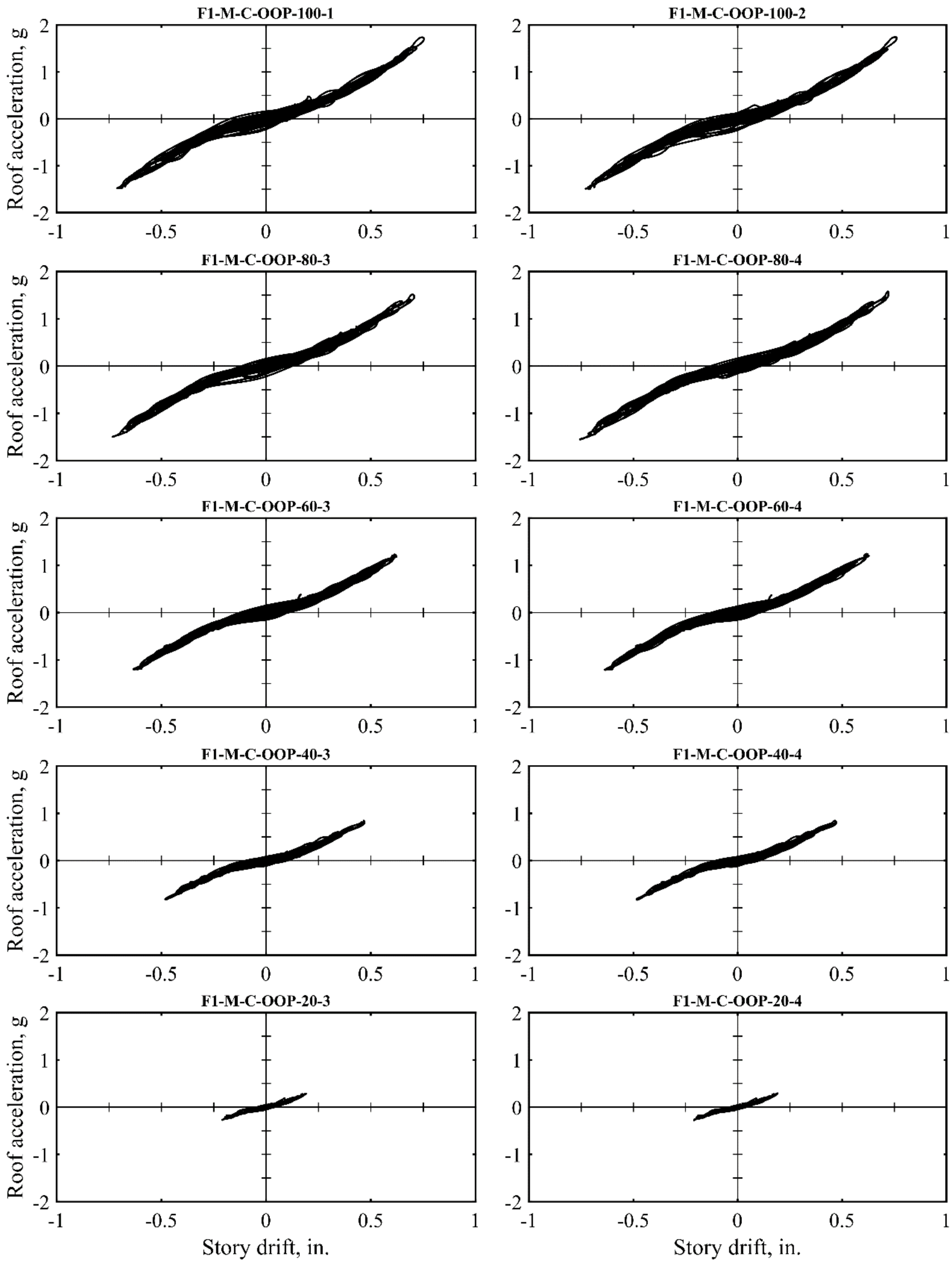

Figure D-179 (continued): Force-displacement response in Series F1-M-C-OOP

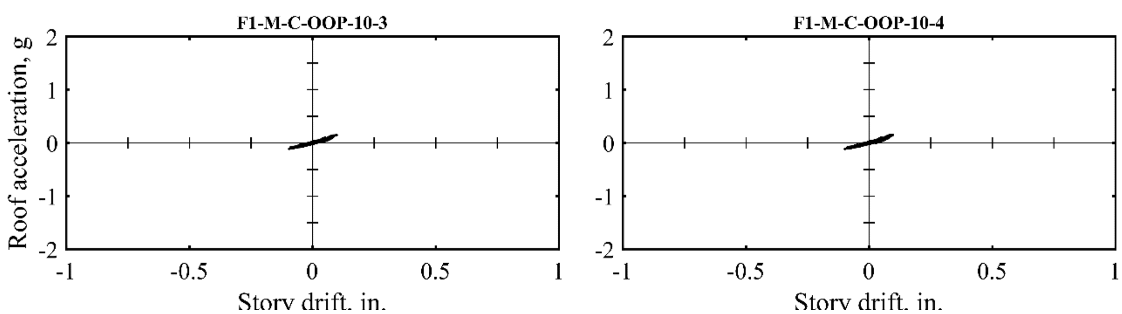

Figure D-179 (continued): Force-displacement response in Series F1-M-C-OOP

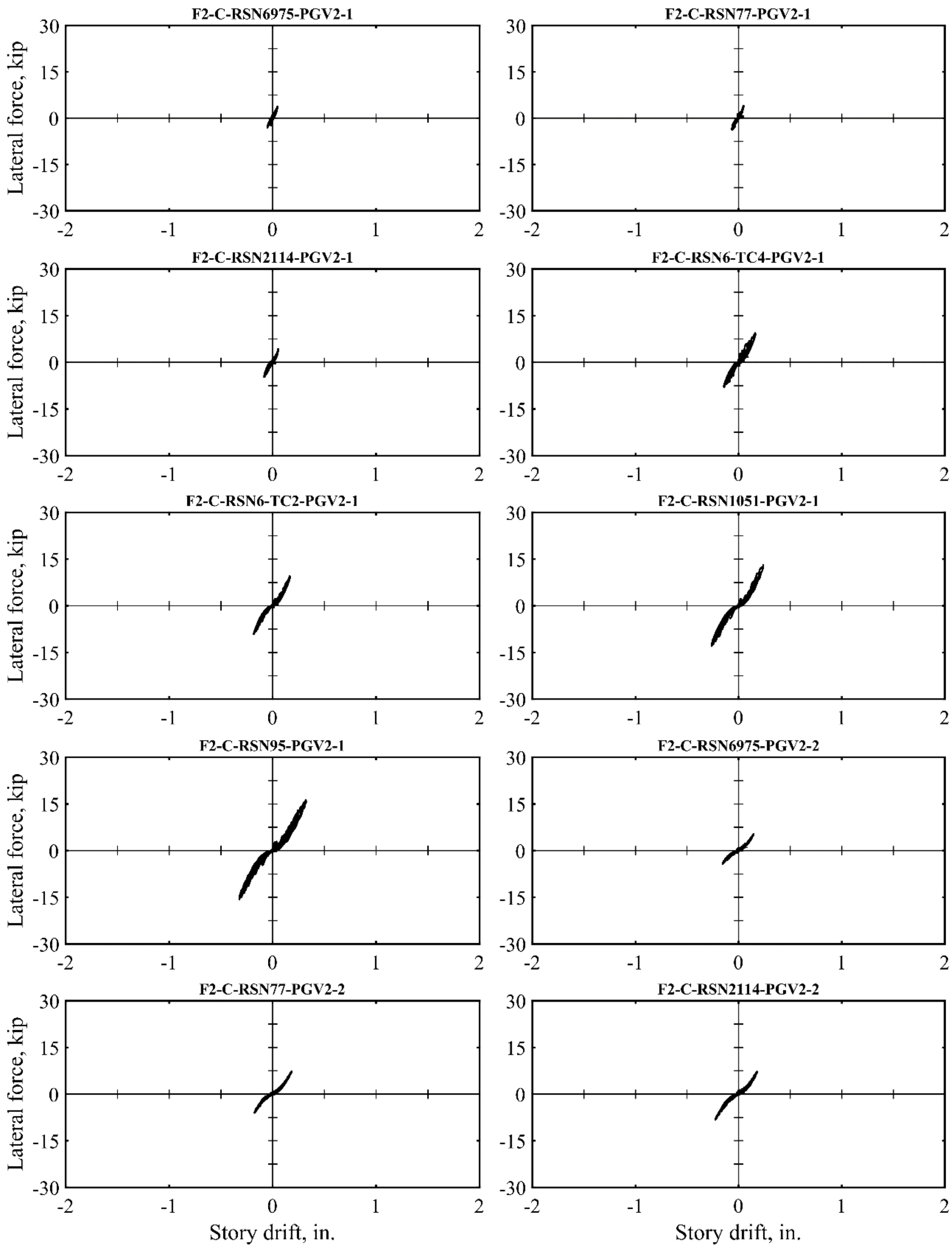

Figure D-180: Force-displacement response in Series F2-C

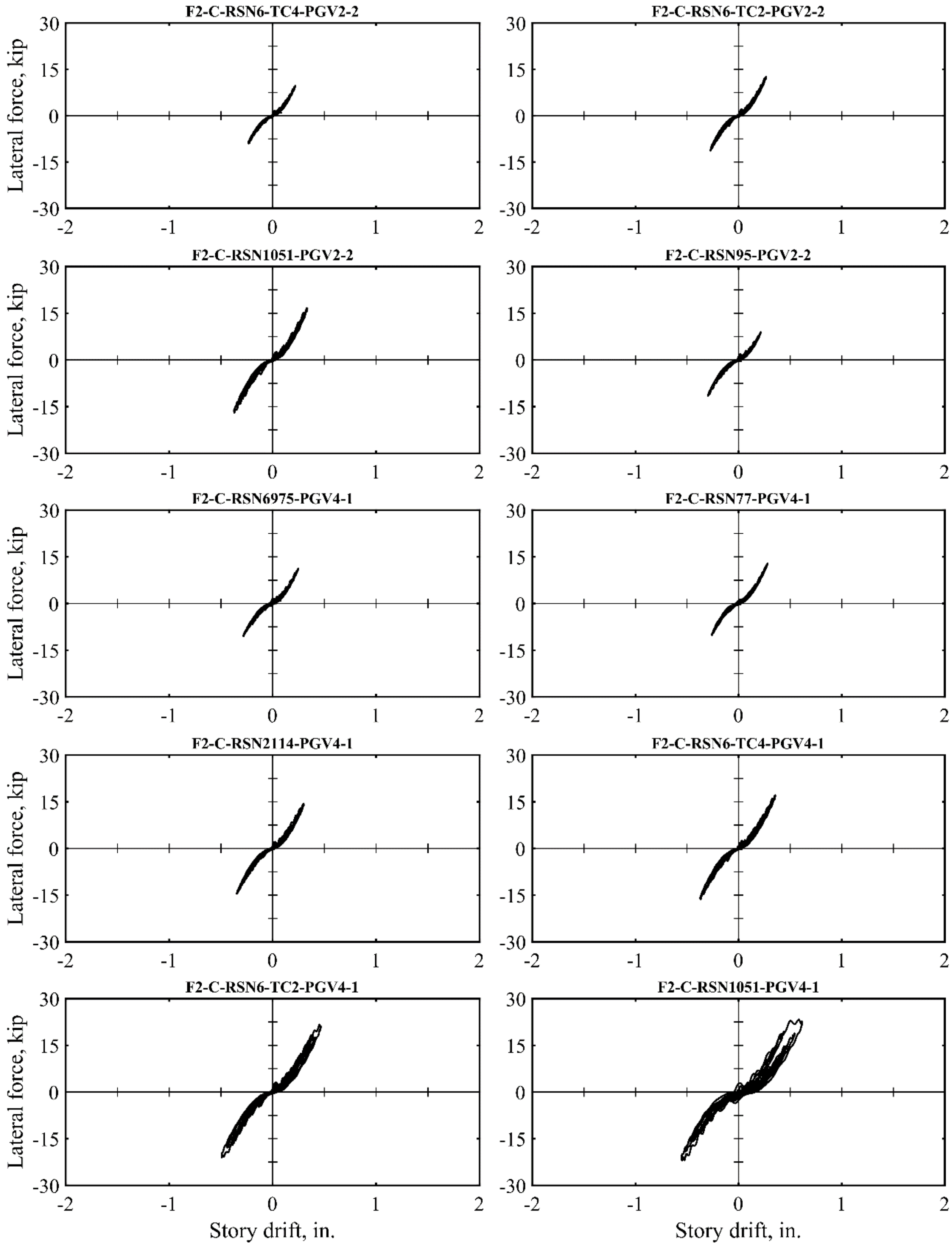

Figure D-180 (continued): Force-displacement response in Series F2-C

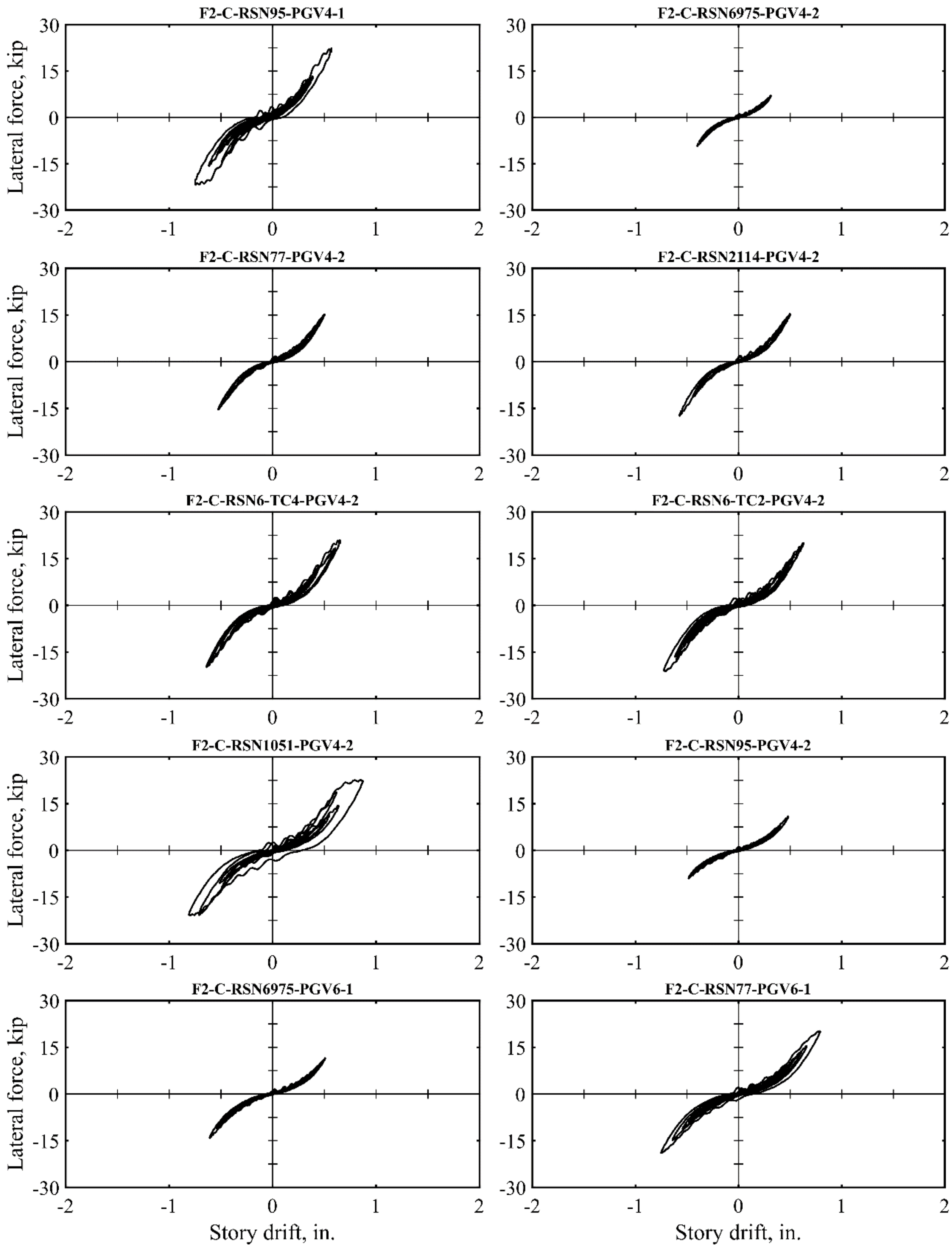

Figure D-180 (continued): Force-displacement response in Series F2-C

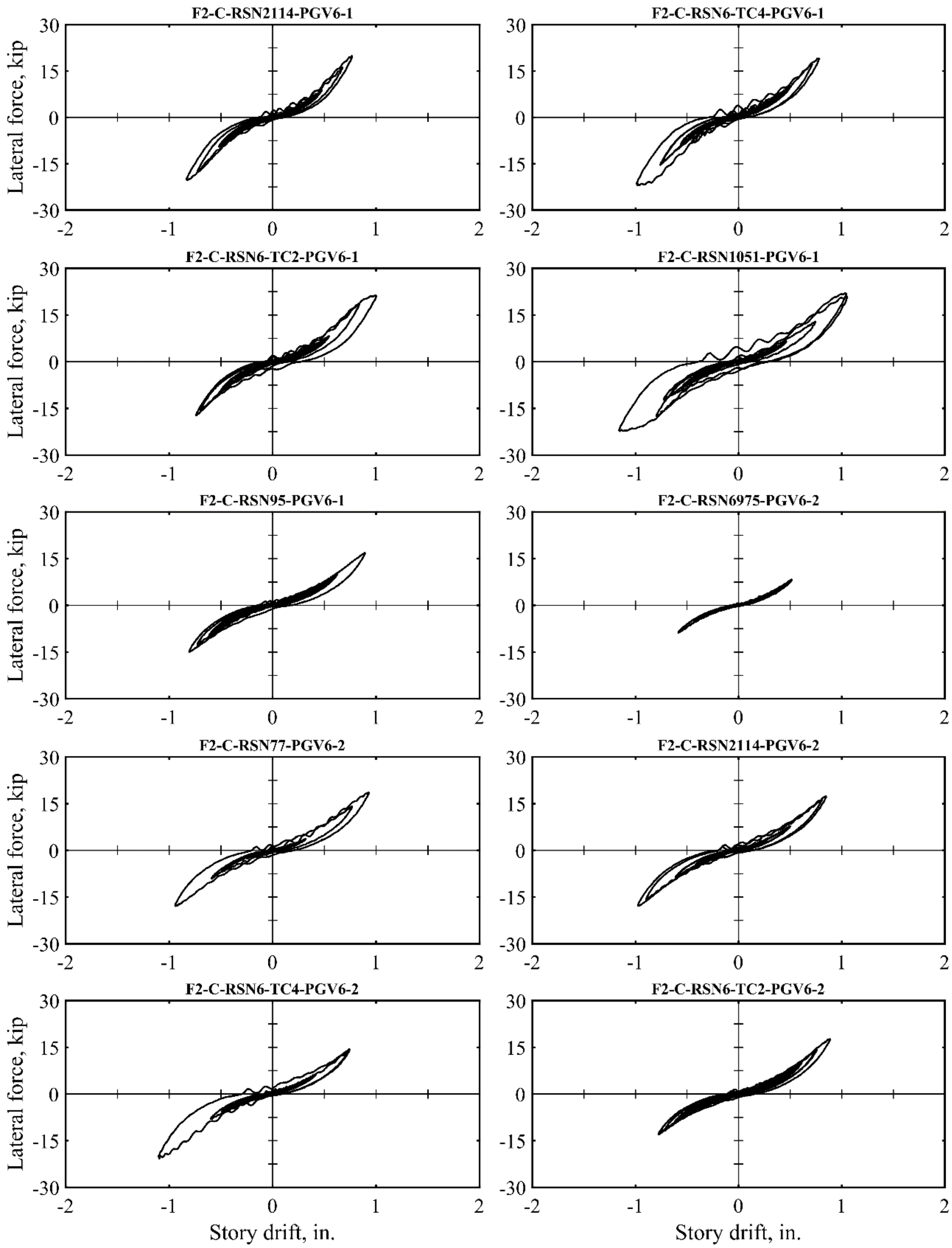

Figure D-180 (continued): Force-displacement response in Series F2-C

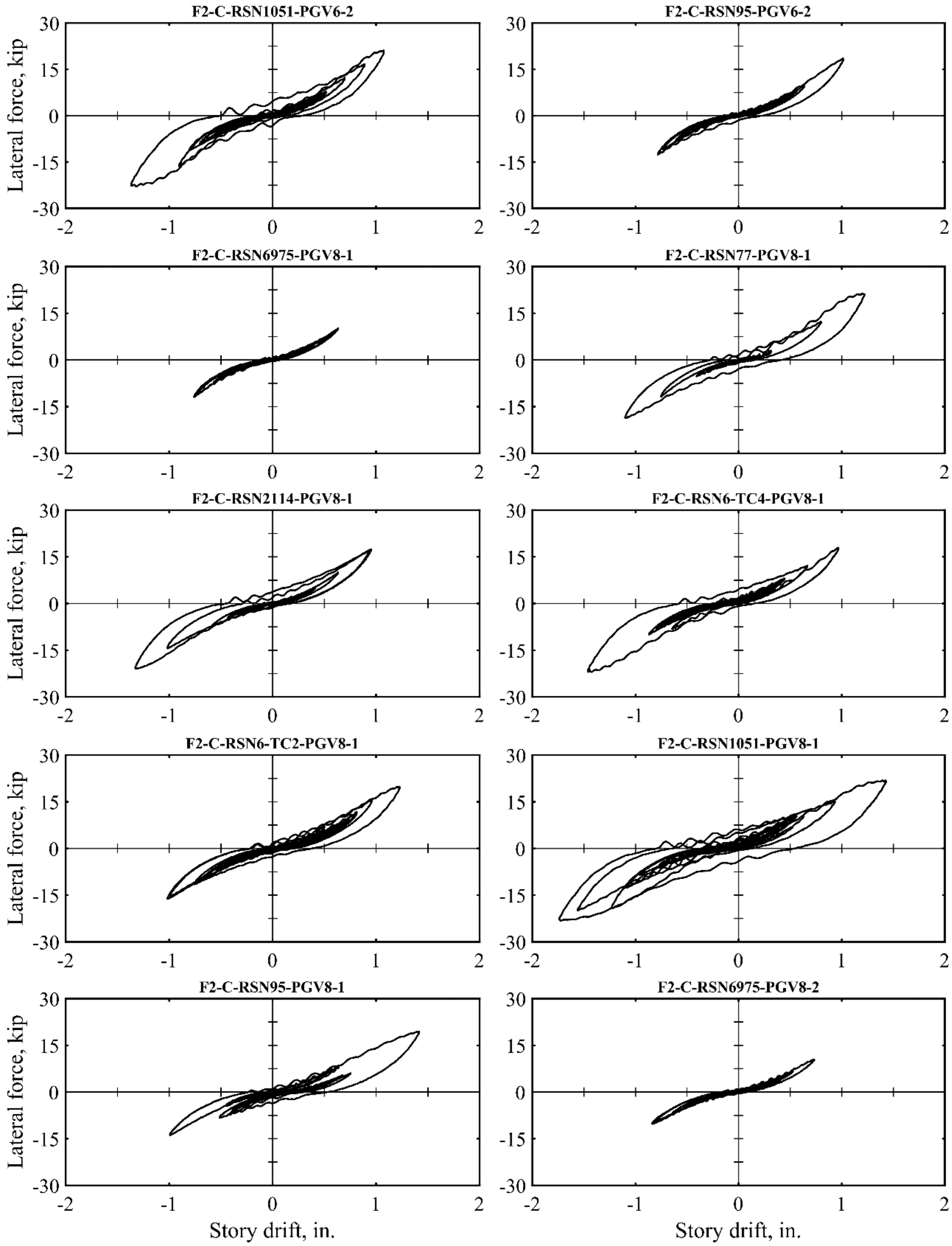

Figure D-180 (continued): Force-displacement response in Series F2-C

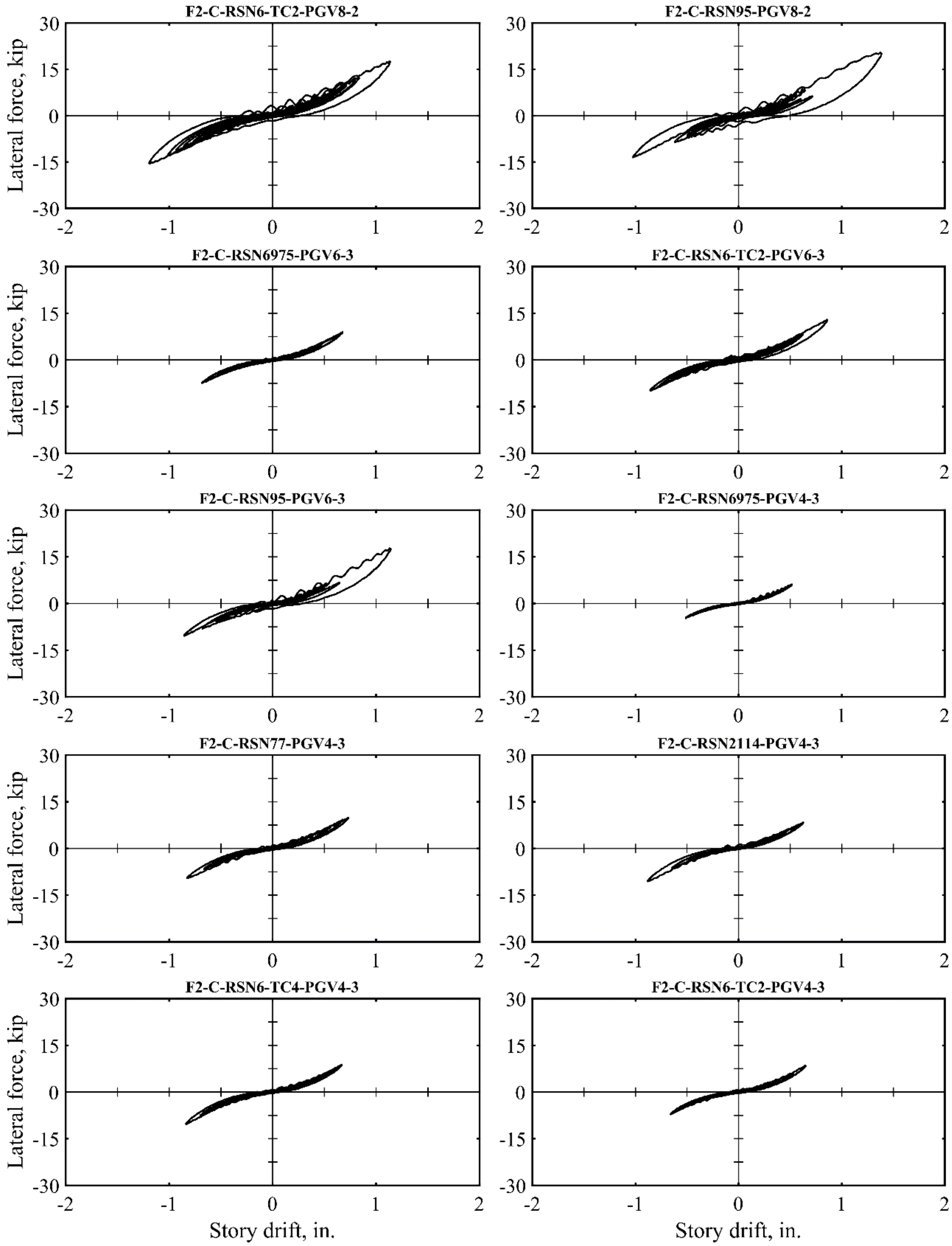

Figure D-180 (continued): Force-displacement response in Series F2-C

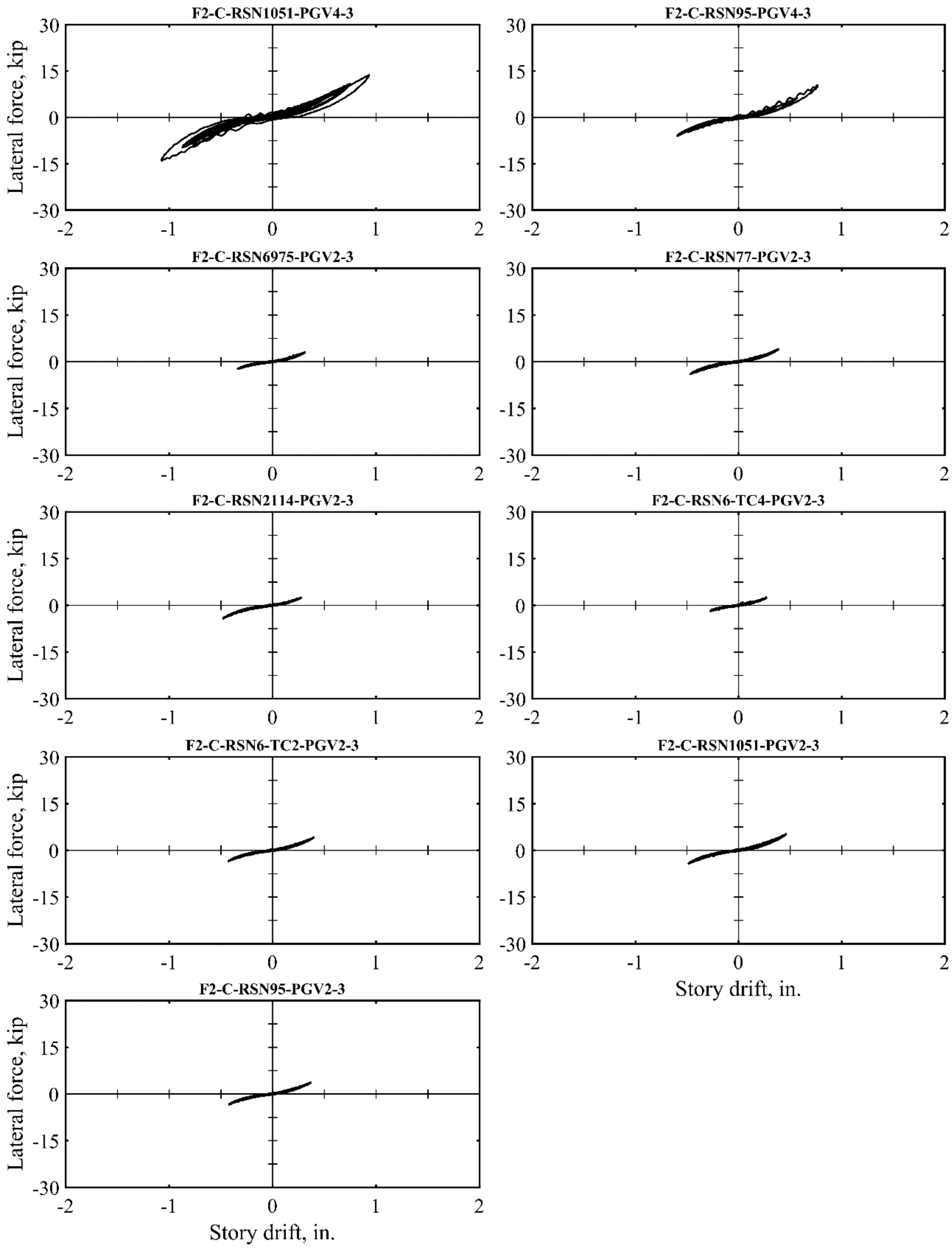

Figure D-180 (continued): Force-displacement response in Series F2-C

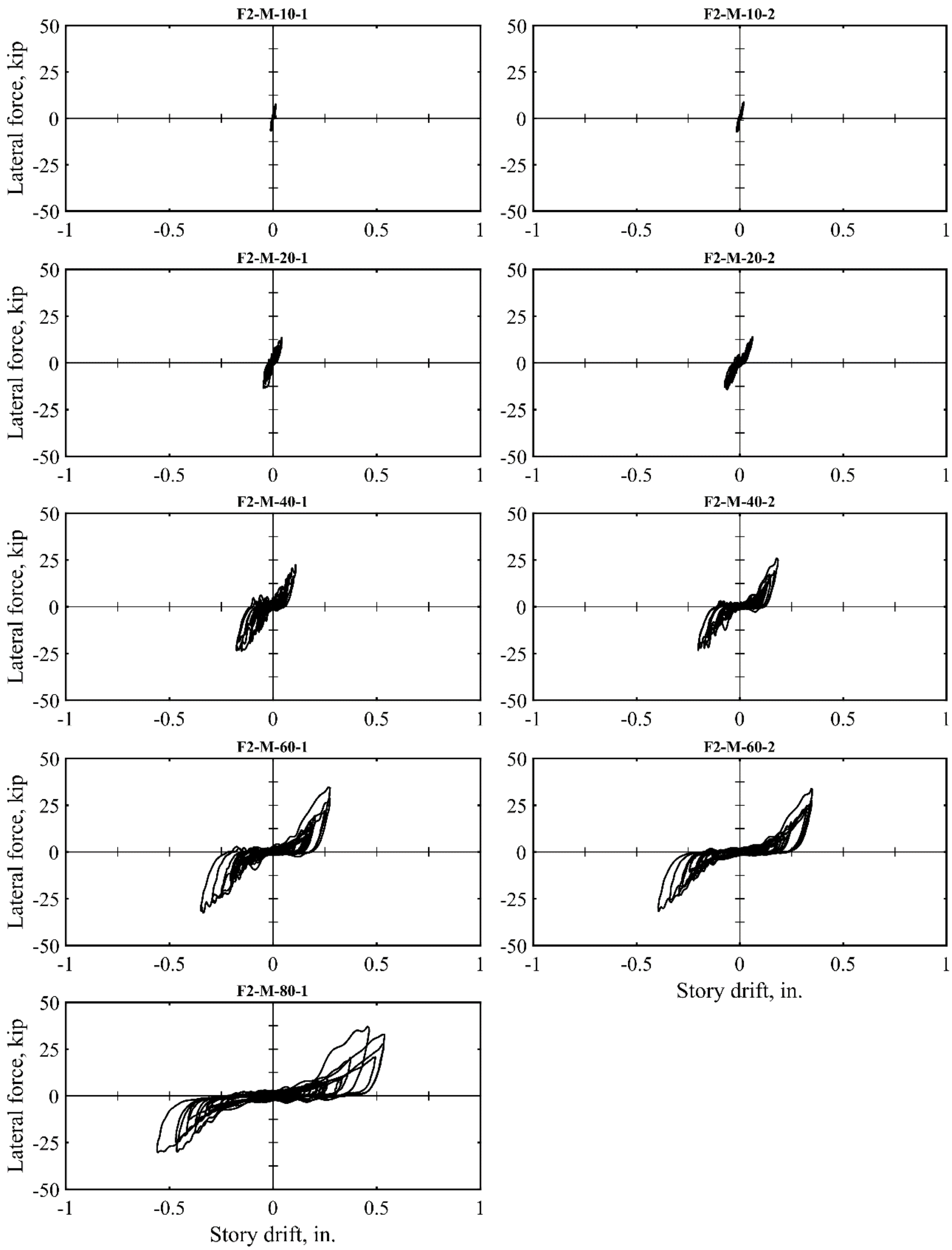

Figure D-181: Force-displacement response in Series F2-M

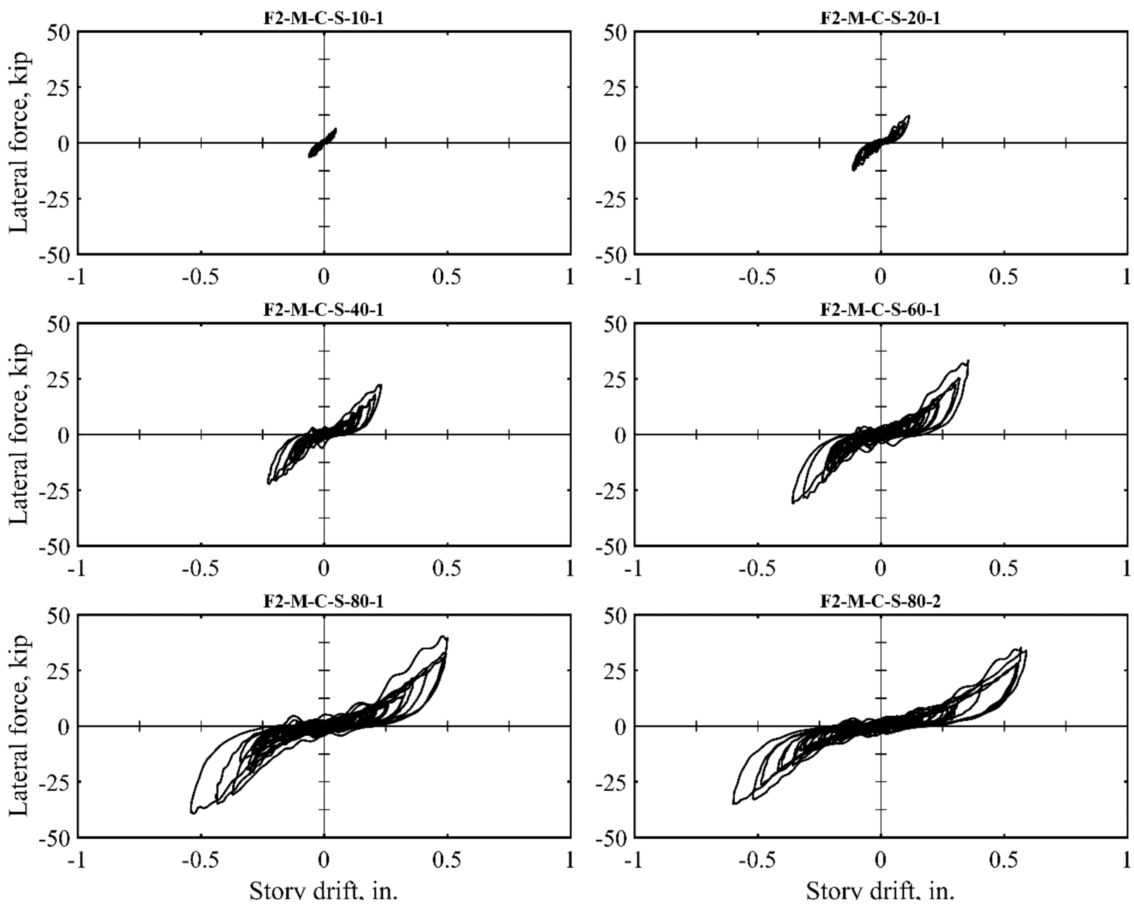

Figure D-182: Force-displacement response in Series F2-M-C-S

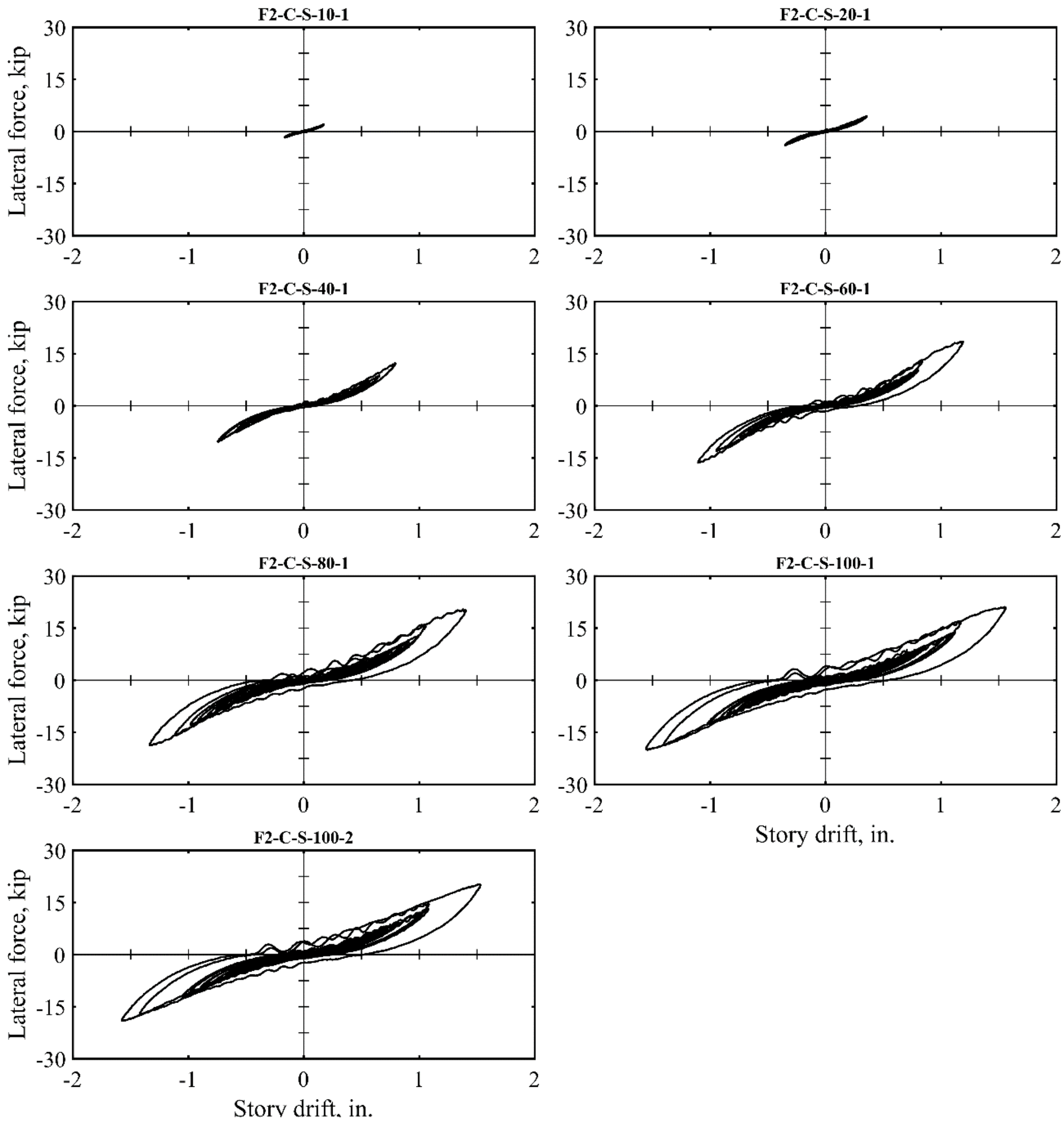

Figure D-183: Force-displacement response in Series F2-C-S

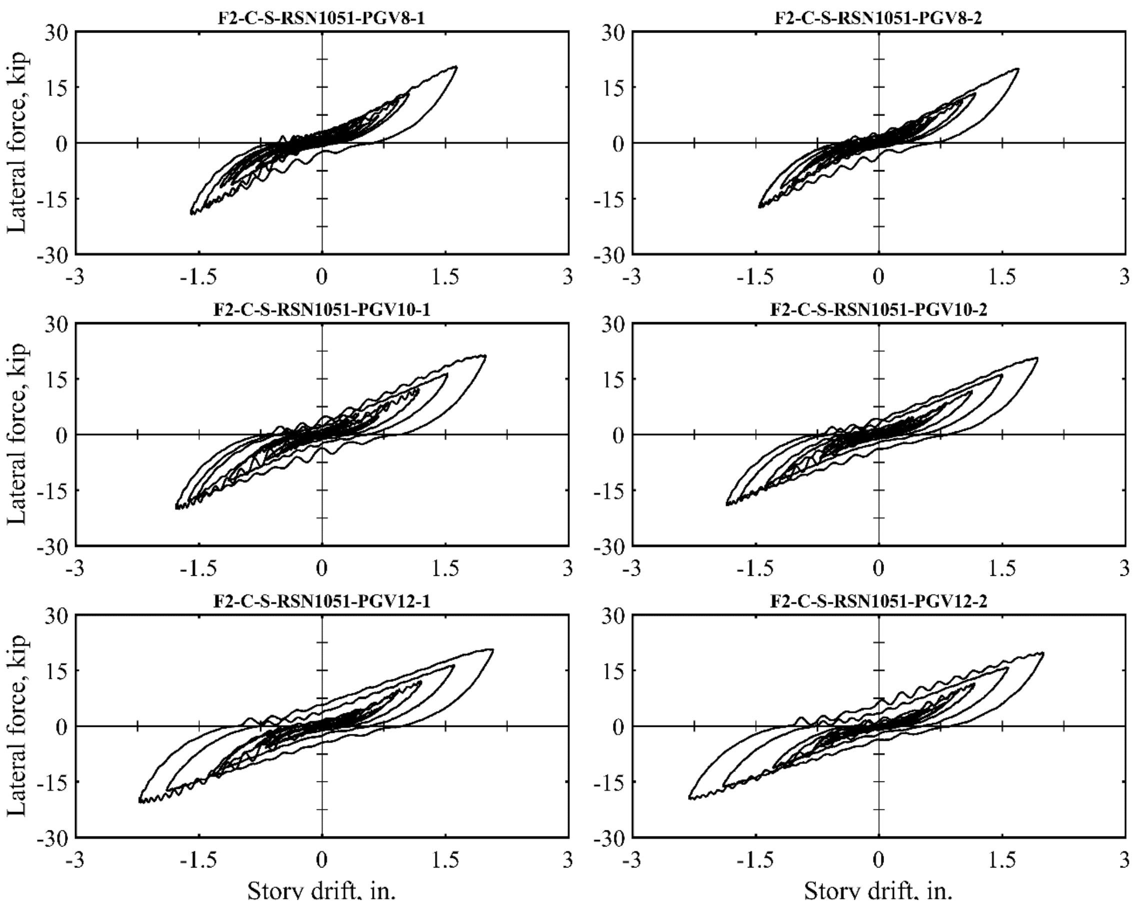

Figure D-183 (continued): Force-displacement response in Series F2-C-S